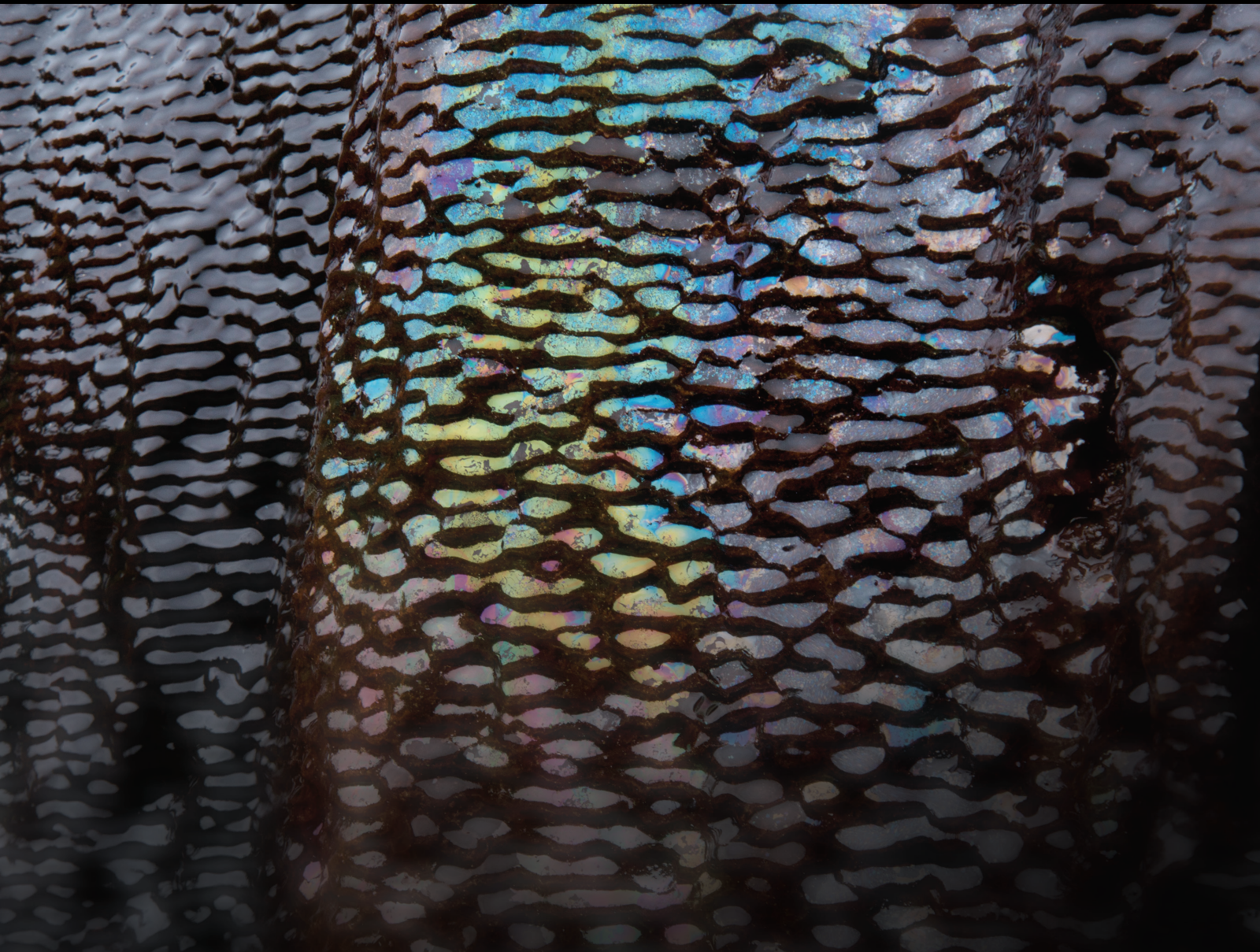


Geofluids in the Simultaneous Exploitation of Coal and Coalbed Methane

Lead Guest Editor: Feng Du

Guest Editors: Haiyan Wang, Wei Zhao, Bo Tan, Radovan Kukutsch, and Jia Lin





Geofluids in the Simultaneous Exploitation of Coal and Coalbed Methane

Geofluids

**Geofluids in the Simultaneous
Exploitation of Coal and Coalbed
Methane**

Lead Guest Editor: Feng Du

Guest Editors: Haiyan Wang, Wei Zhao, Bo Tan,
Radovan Kukutsch, and Jia Lin







Copyright © 2022 Hindawi Limited. All rights reserved.

This is a special issue published in "Geofluids." All articles are open access articles distributed under the Creative Commons Attribution License, which permits unrestricted use, distribution, and reproduction in any medium, provided the original work is properly cited.





























Chief Editor

































Umberta Tinivella, Italy

Associate Editors

Paolo Fulignati , Italy
Huazhou Li , Canada
Stefano Lo Russo , Italy
Julie K. Pearce , Australia

Academic Editors



Basim Abu-Jdayil , United Arab Emirates
Hasan Alsaedi , USA
Carmine Apollaro , Italy
Baojun Bai, USA
Marino Domenico Barberio , Italy
Andrea Brogi , Italy
Shengnan Nancy Chen , Canada
Tao Chen , Germany
Jianwei Cheng , China
Paola Cianfarra , Italy
Daniele Cinti , Italy
Timothy S. Collett , USA
Nicoló Colombani , Italy
Mercè Corbella , Spain
David Cruset, Spain
Jun Dong , China
Henrik Drake , Sweden
Farhad Ehya , Iran
Lionel Esteban , Australia
Zhiqiang Fan , China
Francesco Frondini, Italy
Ilaria Fuoco, Italy
Paola Gattinoni , Italy
Amin Gholami , Iran
Michela Giustiniani, Italy
Naser Golsanami, China
Fausto Grassa , Italy
Jianyong Han , China
Chris Harris , South Africa
Liang He , China
Sampath Hewage , Sri Lanka
Jian Hou, China
Guozhong Hu , China
Lanxiao Hu , China
Francesco Italiano , Italy
Azizollah Khormali , Iran
Hailing Kong, China

Karsten Kroeger, New Zealand
Cornelius Langenbruch, USA
Peter Leary , USA
Guangquan Li , China
Qingchao Li , China
Qibin Lin , China
Marcello Liotta , Italy
Shuyang Liu , China
Yong Liu, China
Yueliang Liu , China
Constantinos Loupasakis , Greece
Shouqing Lu, China
Tian-Shou Ma, China
Judit Mádl-Szonyi, Hungary
Paolo Madonia , Italy
Fabien Magri , Germany
Micòl Mastroicco , Italy
Agnes Mazot , New Zealand
Yuan Mei , Australia
Evgeniy M. Myshakin , USA
Muhammad Tayyab Naseer, Pakistan
Michele Paternoster , Italy
Mandadige S. A. Perera, Australia
Marco Petitta , Italy
Chao-Zhong Qin, China
Qingdong Qu, Australia
Reza Rezaee , Australia
Eliahu Rosenthal , Israel
Gernot Rother, USA
Edgar Santoyo , Mexico
Mohammad Sarmadivaleh, Australia
Venkatramanan Senapathi , India
Amin Shokrollahi, Australia
Rosa Sinisi , Italy
Zhao-Jie Song , China
Ondra Sracek , Czech Republic
Andri Stefansson , Iceland
Bailu Teng , China
Tivadar M. Tóth , Hungary
Orlando Vaselli , Italy
Benfeng Wang , China
Hetang Wang , China
Wensong Wang , China
Zhiyuan Wang , China
Ruud Weijermars , Saudi Arabia


Bisheng Wu , China
Da-yang Xuan , China
Yi Xue , China
HE YONGLIANG, China
Fan Yang , China
Zhenyuan Yin , China
Sohrab Zendehboudi, Canada
Zhixiong Zeng , Hong Kong
Yuanyuan Zha , China
Keni Zhang, China
Mingjie Zhang , China
Rongqing Zhang, China
Xianwei Zhang , China
Ye Zhang , USA
Zetian Zhang , China
Ling-Li Zhou , Ireland
Yingfang Zhou , United Kingdom
Daoyi Zhu , China
Quanle Zou, China
Martina Zucchi, Italy

Contents


Study on the Inerting Effect and Migration Law of Nitrogen and Carbon Dioxide in Large Inclined Goaf by Physical Simulation Model

Xiaolin Song, Chunlei Wu , Chun Liu, Yanlong Li, Zhiyu Wang, and Bobo Shi 
Research Article (16 pages), Article ID 9295411, Volume 2022 (2022)


Stability Control of a Roadway Surrounding Rock during the Cutting and Pressure Relief of a Coal-Bearing Roof at a Shallow Mining Depth

Chen Tian, Yingjie Liu , Hezhuang Lou, and Tinggui Jia
Research Article (16 pages), Article ID 5308530, Volume 2022 (2022)



Identification of Initial Crack and Fracture Development Monitoring under Uniaxial Compression of Coal with High Bump Proneness

Zuoqing Bi, Han Liang , and Qianjia Hui
Research Article (8 pages), Article ID 6561152, Volume 2021 (2021)



Optimization of the Plastic Area of a Borehole Based on the Gas Extraction Effect and Its Engineering Application

Kuan Wu, Shiliang Shi , Yi Lu, He Li, and Min Li
Research Article (13 pages), Article ID 8147366, Volume 2021 (2021)


Study on Mechanical Behavior and Seepage Characteristics of Coal Mass during Unloading

Yan Wang, Yongsheng Han , and Fei Liu 
Research Article (23 pages), Article ID 8446470, Volume 2021 (2021)

Prediction and Evaluation of Coal Mine Coal Bump Based on Improved Deep Neural Network

Shuang Gong , Yi Tan , and Wen Wang
Research Article (11 pages), Article ID 7794753, Volume 2021 (2021)








Study on the Influence of Liquid Nitrogen Cold Soaking on the Temperature Variations and Seepage Characteristics of Coal Samples with Different Moisture Contents

Bo Li , Chaohui Zong, Laisheng Huang, Yongjie Ren, and Xiaoquan Lv
Research Article (10 pages), Article ID 8924016, Volume 2021 (2021)


Study on Prediction of Coal-Gas Compound Dynamic Disaster Based on GRA-PCA-BP Model

Kai Wang, Kangnan Li, and Feng Du 
Research Article (11 pages), Article ID 3508806, Volume 2021 (2021)


Research on Control Mechanism of Surrounding Rock of Deep Gob-Side Entry Retaining

Jianxiong Liu , Jingke Wu , Yun Dong , Yanyan Gao , Jihua Zhang , Weizhong He , and Jiarui Chen 
Research Article (10 pages), Article ID 2729122, Volume 2021 (2021)


Gas Jet Coal-Breaking Behavior: An Elliptical Crushing Theoretical Model

Gongda Wang, Yuanyuan Wang , Xin Yang, and Xin Song
Research Article (16 pages), Article ID 4300088, Volume 2021 (2021)





Pressure-Relief Mechanism and Application of Large-Diameter Boreholes in Coal Seams with Rockburst Hazard

Zhen Hao , Guangzhong Sun, Haihang Wei, Jiayu Liu, Maolin Tian, Shuaiyi Liu, and Yikun Xu
Research Article (9 pages), Article ID 5469999, Volume 2021 (2021)



Investigation of Shale Permeability Evolution considering Bivalued Effective Stress Coefficients for CO₂ Injection

Yi Wang , Hao Wang, Shangyi Qi, Shimin Liu, Yixin Zhao, and Wenting Yue
Research Article (11 pages), Article ID 1132440, Volume 2021 (2021)








CFD-Based Determination of the Optimal Blowing and Suction Air Volume Ratio of Dual-Radial Swirl Shielding Ventilation in a Fully Mechanized Excavation Face

Kuan Wu , Shiliang Shi , Yijie Shi , and Yong Chen 
Research Article (12 pages), Article ID 5473256, Volume 2021 (2021)


Investigation of Seepage Law in Broken Coal and Rock Mass under Different Loading and Unloading Cycles

Zihao Kan , Lei Zhang , Mingxue Li, Xiaochuan Yuan, and Mengqian Huang
Research Article (14 pages), Article ID 8127250, Volume 2021 (2021)


Study on Pore and Fissure Structure Characteristics of Deep Soft Coal Rock

Minbo Zhang , Zhen Zhang , Dangyu Zhang , Delong Zou , Jinlei Du , Zichao Wang , and Chunxin Li 
Research Article (13 pages), Article ID 1475926, Volume 2021 (2021)

Study on the Permeability Evolution Model of Mining-Disturbed Coal

Hengyi Jia  and Delong Zou
Research Article (9 pages), Article ID 1810915, Volume 2021 (2021)

Combining K-Means Clustering and Random Forest to Evaluate the Gas Content of Coalbed Bed Methane Reservoirs

Jie Yu, Linqi Zhu , Ruibao Qin, Zhansong Zhang, Li Li, and Tao Huang
Research Article (8 pages), Article ID 9321565, Volume 2021 (2021)

Disastrous Mechanism and Concentration Distribution of Gas Migration in Fully Mechanized Caving Stope in Wuyang Coal Mine

Li Chong, He Sifeng , and Xu Zhijun
Research Article (16 pages), Article ID 4366942, Volume 2021 (2021)

Laws of Gas Diffusion in Coal Particles: A Study Based on Experiment and Numerical Simulation


Yongjiang Hao , Xiaofeng Ji , and Jiewen Pang 
Research Article (15 pages), Article ID 4561819, Volume 2021 (2021)

Contents


Influences of Coal Properties on the Principal Permeability Tensor during Primary Coalbed Methane Recovery: A Parametric Study

Jie Zang , Ze Ma, Yong Ge, and Chengxin Li
Research Article (17 pages), Article ID 2097503, Volume 2021 (2021)






Variation Law of Infrared Radiation Temperature of Unloading Fracture of Composite Coal-Rock

Xin Li , Xue Wang , Zhen Yang , Hao Li , Yan Li , and Weiman Sun 
Research Article (20 pages), Article ID 7108408, Volume 2021 (2021)

Numerical Simulation of the Volumetric Strain Distribution of a Protected Coal Seam

Hengyi Jia 
Research Article (11 pages), Article ID 3679862, Volume 2021 (2021)




A Statistical Damage Constitutive Model of Anisotropic Rock: Development and Validation

Tenglong Rong , Can Guan , Keliu Liu , Shuai Heng, Wenlong Shen , and Ruiyong Mou 
Research Article (16 pages), Article ID 6307895, Volume 2021 (2021)






The Law of Fracture Evolution of Overlying Strata and Gas Emission in Goaf under the Influence of Mining

Cheng Cheng, Xiaoyu Cheng , Rui Yu, Wenping Yue, and Chao Liu
Research Article (16 pages), Article ID 2752582, Volume 2021 (2021)


Effects of Thermal Treatment on Mineral Composition and Pore Structure of Coal

Bin Liu , Teng Teng , Zhenhua Jiao , and Shaobo Li
Research Article (14 pages), Article ID 5939690, Volume 2021 (2021)

Mechanical Characteristics and Energy Dissipation Trends of Coal-Rock Combination System Samples with Different Inclination Angles under Uniaxial Compression

Zhen Wei , Ke Yang , Xiang He, Xiaolou Chi , Xinyuan Zhao , and Jiqiang Zhang 
Research Article (12 pages), Article ID 7702751, Volume 2021 (2021)



Research and Optimization of Gas Extraction by Crossing-Seam Boreholes from Floor Roadway

Gang Li  and Jiafei Teng
Research Article (10 pages), Article ID 7499012, Volume 2021 (2021)




Numerical Simulation of Coal Spontaneous Combustion around a Borehole Induced by Negative Pressure Gas Drainage

Youxin Zhao , Qingjie Qi, Xinlei Jia , Yingjie Liu , and Jingwen Zhang
Research Article (11 pages), Article ID 3938243, Volume 2021 (2021)


Response Surface Method for Strength Analysis and Proportion Optimization of New Type Sealing Materials

Sheng Xue , Xin Guo , Chunshan Zheng, Yaobin Li, and Xiaoliang Zheng
Research Article (14 pages), Article ID 8769809, Volume 2021 (2021)







Failure Analysis of Deep Composite Roof Roadway and Support Optimization of Anchor Cable Parameters

Chen Li , Wenlong Zhang , Tianhong Huo, Rui Yu, Xidong Zhao , and Ming Luo
Research Article (13 pages), Article ID 5610058, Volume 2021 (2021)


Analysis of Key Factors Affecting Water Disaster in Deep Mining and Establishment of a Water Disaster Evaluation Method Suitable for Different Mining Depths

Jianghui He , Wenping Li , Wei Qiao, Zhi Yang, and Qiqing Wang 
Research Article (14 pages), Article ID 9948763, Volume 2021 (2021)



Crack Propagation Law and Failure Characteristics of Coal-Rock Combined Body with the Different Inclination Angle of Prefabricated Fissure

Chunlei Zhang , Yun Dong , Ruimin Feng , Ningbo Peng , Jihua Zhang , Jingke Wu , and Wei Shen
Research Article (13 pages), Article ID 4348912, Volume 2021 (2021)

Analysis on the Shape and Impact Pressure of the High-Pressure Water Jet during the Hydraulic Flushing Cavity Technique

Shouqing Lu, Chengfeng Wang, Wei Wang , Mingjie Li, and Dongti Zhang
Research Article (16 pages), Article ID 7496540, Volume 2021 (2021)

Pore Structure Characteristics and Evolution Law of Different-Rank Coal Samples

Zhihui Wen , Qi Wang , Yunpeng Yang, and Leilei Si
Research Article (17 pages), Article ID 1505306, Volume 2021 (2021)

Research Article

Study on the Inerting Effect and Migration Law of Nitrogen and Carbon Dioxide in Large Inclined Goaf by Physical Simulation Model

Xiaolin Song,^{1,2} Chunlei Wu ,^{1,2} Chun Liu,³ Yanlong Li,^{1,2} Zhiyu Wang,^{1,2} and Bobo Shi ^{1,2}

¹State Key Laboratory of Coal Resources and Safe Mining, China University of Mining and Technology, Xuzhou, Jiangsu 221116, China

²School of Safety Engineering, China University of Mining and Technology, Xuzhou, Jiangsu 221116, China

³IoT Perception Mine Research Center, China University of Mining and Technology, Xuzhou 221116, China

Correspondence should be addressed to Chunlei Wu; tb18120020b1@cumt.edu.cn and Bobo Shi; shibobo@cumt.edu.cn

Received 24 July 2021; Revised 28 June 2022; Accepted 22 July 2022; Published 31 August 2022

Academic Editor: E. Santoyo

Copyright © 2022 Xiaolin Song et al. This is an open access article distributed under the Creative Commons Attribution License, which permits unrestricted use, distribution, and reproduction in any medium, provided the original work is properly cited.

In this paper, the inerting effect and migration law of inert N₂ and CO₂ in large inclined goaf are studied using a physical simulation model. The differences in oxygen reduction and inert gas migration are analyzed and compared. The results show that as N₂ and CO₂ injection increased, the oxidation zone's range and width shrunk, and the end of the loose and oxidation zones moved closer to the working face. The migration profile of CO₂ and N₂ resembled a trumpet and an L shape, respectively, and under the same inerting flow rate, the effect of CO₂ inerting on oxygen reduction was much less significant than that of N₂.

1. Introduction

Steeply dipping coal seams with dip angles of 35° to 55° are considered challenging to mine internationally. Currently, coal reserves of steeply dipping coal seams account for about 20% of the total coal reserves in China [1], and its annual production accounts for about 10% of total coal production. With continuous mining, coal seams with good occurrence conditions in the eastern region are gradually exhausted. As a result, the coal mining center shifts to the western region, and the proportion of mined steeply dipping coal seams continues to increase [2]. However, spontaneous combustion, one of the major disasters in coal mine production, has become a major hindering factor of green, efficient, high-yield, and safe coal production in China. Spontaneous combustion causes secondary disasters such as gas explosions, coal dust explosions, and the release of toxic gases that seriously threaten the safety of miners and the profit of the mines. It is reported that over half of the coal mines in China are at risk of spontaneous combustion, 60% of which are

caused by fires in goafs [3]. However, mining large dip angle coal seams is easier to spontaneously combust than mining near horizontal coal seams. The mining methods of large dip angle coal seams mainly include horizontal slicing mining, roadway caving mining method, segmentalized horizontal slicing or oblique cutting slicing mining, pseudoinclined strike long wall caving mining, and so on [4]. The particularities of the coal mining methods could cause severe floating coal accumulation and asymmetric distribution in goafs, which increases the risk of spontaneous combustion [5]. Therefore, preventing floating coal spontaneous combustion in the goaf of steeply dipping working face is crucial for safe coal mine production.

Among the many fire prevention technologies reported, inert gas fire prevention technology has significant advantages due to its rapid oxygen, temperature, and air leakage reduction in goafs [6]. The inert gases adopted are mainly N₂ and CO₂. Inert gas fire prevention and fire extinguishing technologies in slightly inclined coal seams have been

TABLE 1: Basic parameters of the similar simulation experiment platform for goaf of high inclined working face.

Element	Conventional value	Simulated value	Element	Conventional value	Simulated value
The working face length (m)	126	2	The caving zone height (m)	12~21	0.2~0.33
The gob model length (m)	180	3	The fracture zone height (m)	39~48	0.67
The gob model height (m)	60	1	Inclination angle (°)	45	45

systematically studied. Chen and Wang [7] studied the law of spontaneous combustion in the goaf of comprehensive caving working face and the nitrogen injection technology to prevent and extinguish fires, concluding that the risk of spontaneous combustion in the goaf of comprehensive caving working face at a certain height could be eliminated with nitrogen injection. Zhuang et al. [8] investigated the mechanism of spontaneous combustion in the goaf of working face during the layered mining of thick coal seams and put forward the isolation nitrogen injection technology with optimal nitrogen injection parameters. Zheng [9] studied the mechanism and parameters of nitrogen injection to prevent and extinguish fires in goafs under different mining conditions.

Domestic and foreign scholars have carried out a lot of research work on the migration of N_2 and CO_2 in goaf. Cao et al. [10] analyzed the influence of nitrogen injection flow rate in the goaf on the nitrogen migration radius based on field measured data, concluding that increasing the nitrogen injection flow rate could increase the nitrogen migration radius in a nearly linear logarithmic form. But with the increase of nitrogen injection flow rate, the oxygen suppression efficiency of nitrogen injection to the oxidation zone in the goaf decreases gradually, so simply increasing nitrogen injection flow rate will not have an ideal effect. Cao et al. [11] studied the range of changes in the three spontaneous combustion zones before and after nitrogen injection through on-site monitoring and determined the optimal position and flow rate of nitrogen injection for the optimal inerting effect. Shao et al. [12, 13] studied the flow characteristics of CO_2 in the goaf through numerical simulation and concluded that injecting CO_2 into the goaf is more effective than injecting nitrogen. Wang et al. [14] adopted numerical test methods to study the distribution law of the three spontaneous combustion zones in the goaf of a fully mechanized working face with different positions and flow rates of carbon dioxide injection. Their results showed that the optimal carbon dioxide injection position is the inlet groove about 20 m from the working face, and the maximum width of the oxidation heating zone after carbon dioxide injection moves from the inlet side to the middle of the working face.

According to the literature review, scholars have conducted relatively little research on the migration law of inert gas in the goaf of the high-inclination working face, especially the goaf with complex coal and rock distribution under slicing mining in high-inclination thick coal seams. Therefore, effectively predicting the inert gas flow in the

goaf of the high-inclination thick coal seam under slicing mining and accurately implementing the fire prevention technology is of top priority in preventing and controlling spontaneous combustion in the goaf. This paper takes the Dongxia coal mine as the research object and conducts physical similarity simulation experiments to study the O_2 distribution and inert gas migration law in the goaf after inert gas injection. This study could guide fire prevention in mines and have important practical significance for preventing and controlling spontaneous combustion in goafs of large inclined coal seams.

2. Materials and Methods

2.1. Overview of 37121-1 Working Face. The 37121-1 working face with a large dip angle in the Dongxia coal mine is located in the 940-875 stage of the Dongxia coal mine. The average thickness of the coal seam in this face is 7.0 m, and the average dip angle of the working face is 45°. This coal seam has a high risk of spontaneous combustion with the smallest spontaneous combustion duration of 37 days. The working face's strike length is 1021 m, and the inclination length is 126 m. The comprehensive mechanized top coal caving mining method is adopted for mining, with a mining height of 2.7 m and a caving height of 4.3 m. The working face is set up at a level between +940 m and +875 m. The design air supply of the working face is 490 m^3/min , whereas the actual air supply is 750 m^3/min .

2.2. Experimental Platform

2.2.1. Experimental Platform Design. To investigate the effects of inert gas injection settings on O_2 distribution in large inclined goaf, a similarity simulation experiment platform based on working face 37121-1 in the Dongxia coal mine (similar ratio, 1:60) was established. The basic parameters of the similarity simulation experiment platform are shown in Table 1.

The similarity simulation experiment follows three similarity criteria: geometric similarity, kinematic similarity, and dynamic similarity, as shown below [15–17].

- (i) *Geometric similarity:* the similarity simulation experiment platform for goafs of high inclined working faces is proportional to the geometric parameters of the real goafs. The foam used to fill the goaf in the simulation is proportional to the size of the gravel in the real goaf
- (ii) *Kinematic similarity:* the time for the air to flow through the working face in the similarity

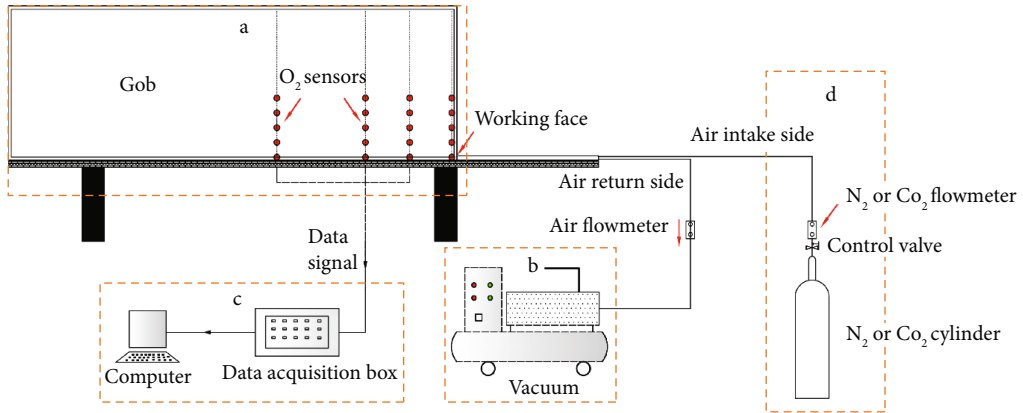


FIGURE 1: Schematic diagram of the experimental platform.

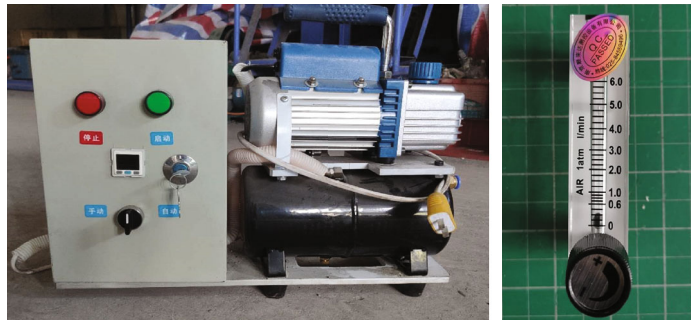


FIGURE 2: The negative pressure vacuum pump and rotameter.

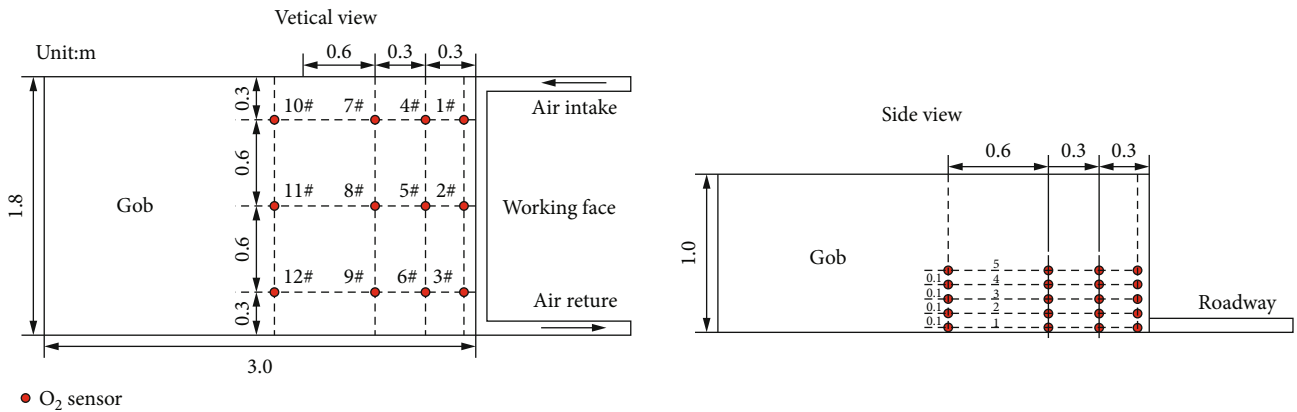


FIGURE 3: The layout of O₂ sensors.

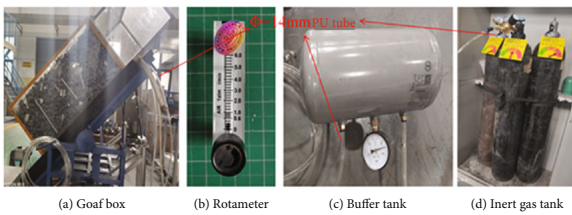


FIGURE 4: The N₂ and CO₂ injection system.

TABLE 2: The similarity simulation experiment scheme.

Inert	Inclination angle (°)	Depth of buried pipe (m)	Ventilation rate (L/min)
			1.1
N ₂ /CO ₂	45°	0.67	2.3
			3.4

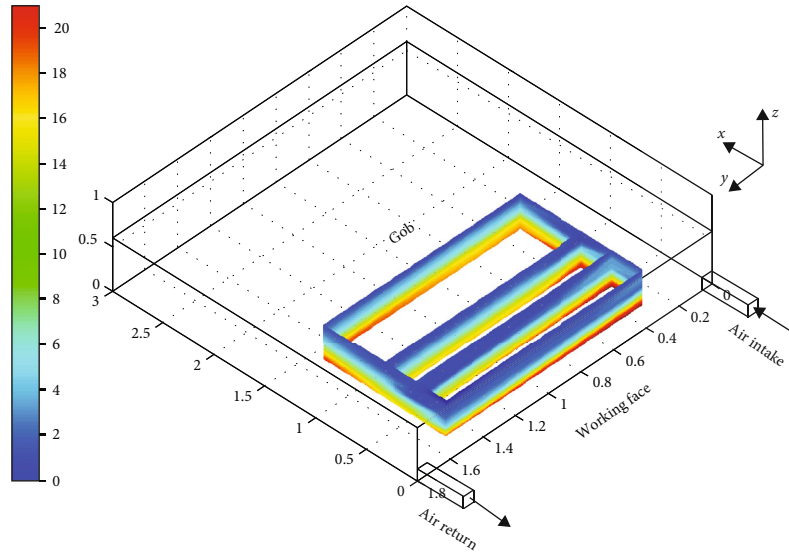


FIGURE 5: O_2 concentrations at $x = 0.2, 0.5, 0.8,$ and 1.4 m and $y = 0.3$ and 1.5 m with N_2 injection rate of 3.4 L/min, 0° .

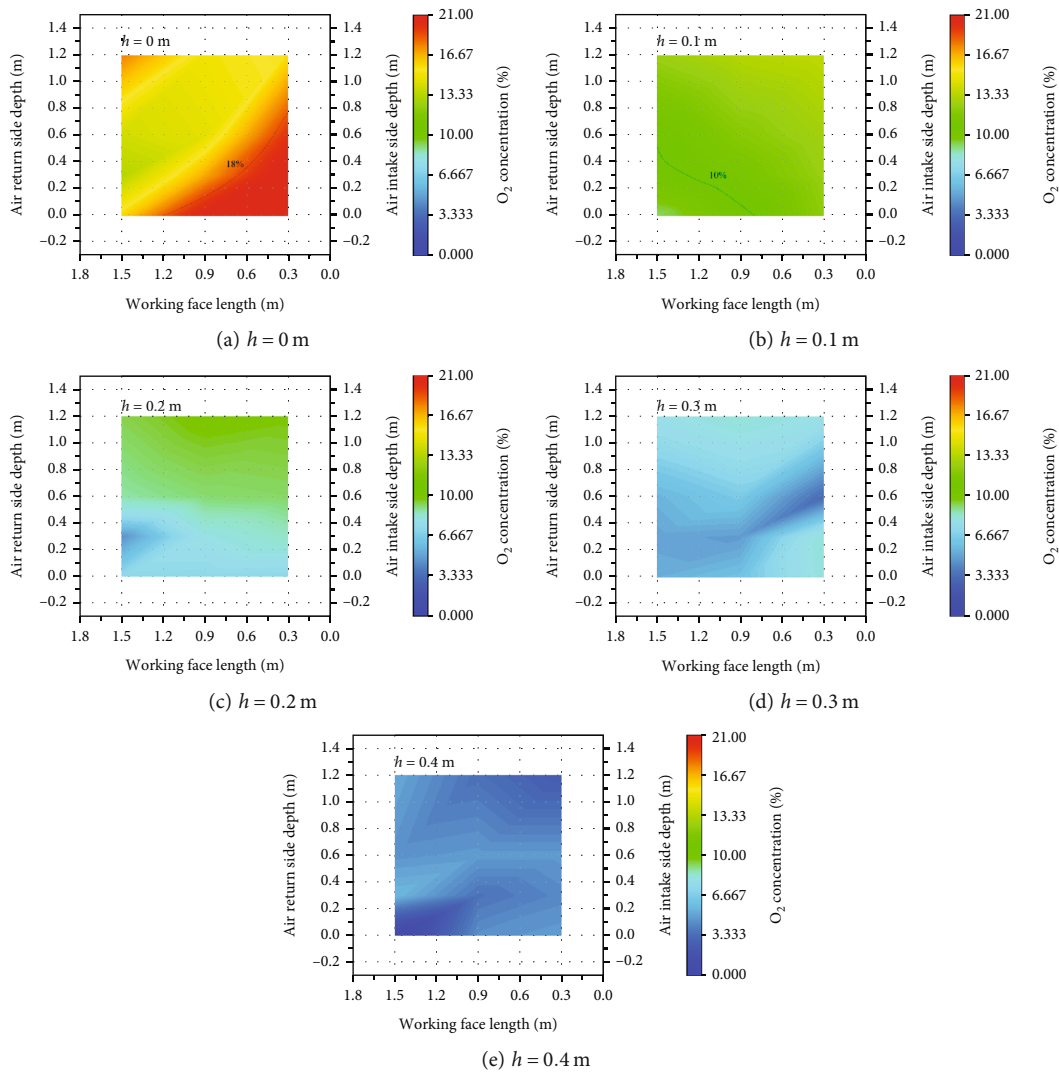


FIGURE 6: Cloud distribution of O_2 concentration at different heights with the N_2 injection rate of 3.4 L/min, 0° .

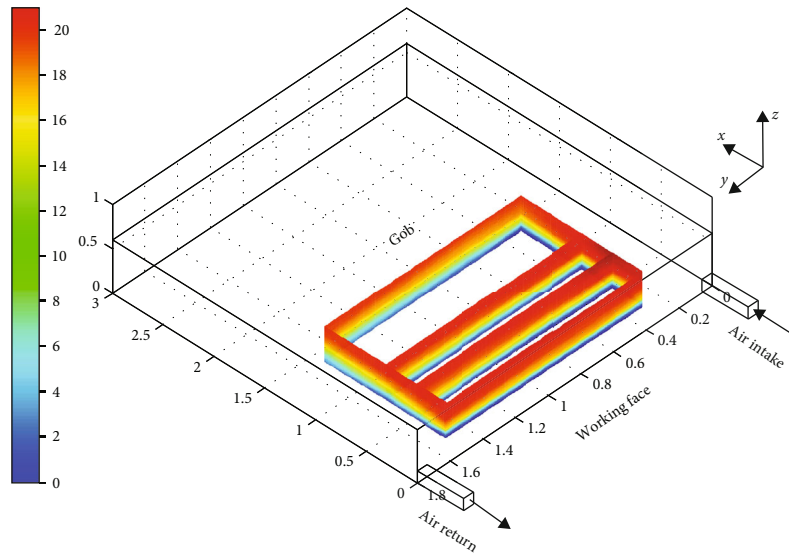


FIGURE 7: O_2 concentrations at $x = 0.2, 0.5, 0.8,$ and 1.4 m and $y = 0.3$ and 1.5 m with CO_2 injection rate of 3.4 L/min, 0° .

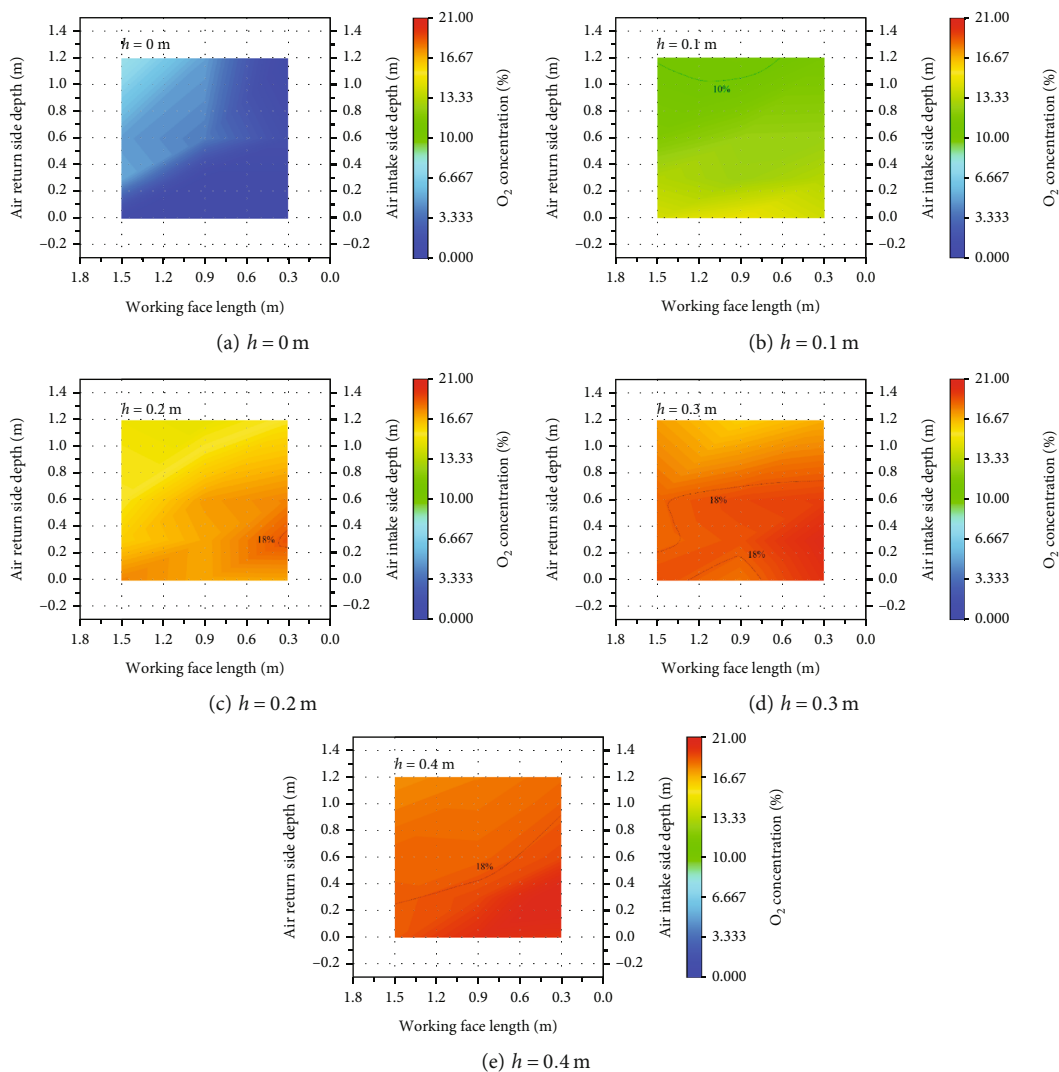


FIGURE 8: Cloud distribution of O_2 concentration at different heights with the CO_2 injection rate of 3.4 L/min, 0° .

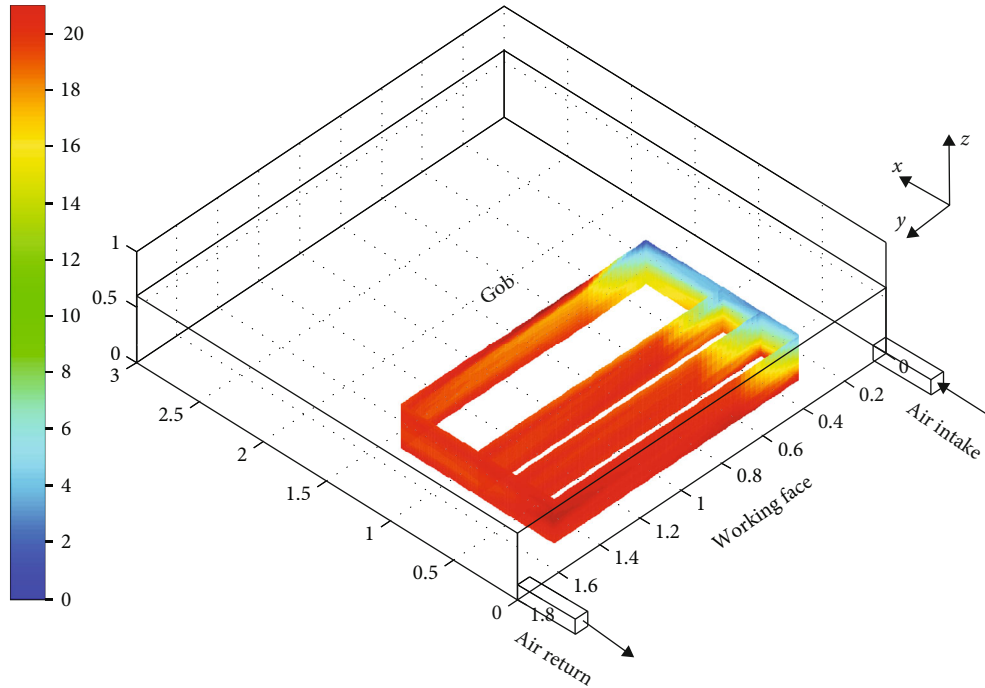


FIGURE 9: O₂ concentrations at $x = 0.2, 0.5, 0.8,$ and 1.4 m and $y = 0.3$ and 1.5 m with N₂ injection rate of 1.1 L/min, 45°.

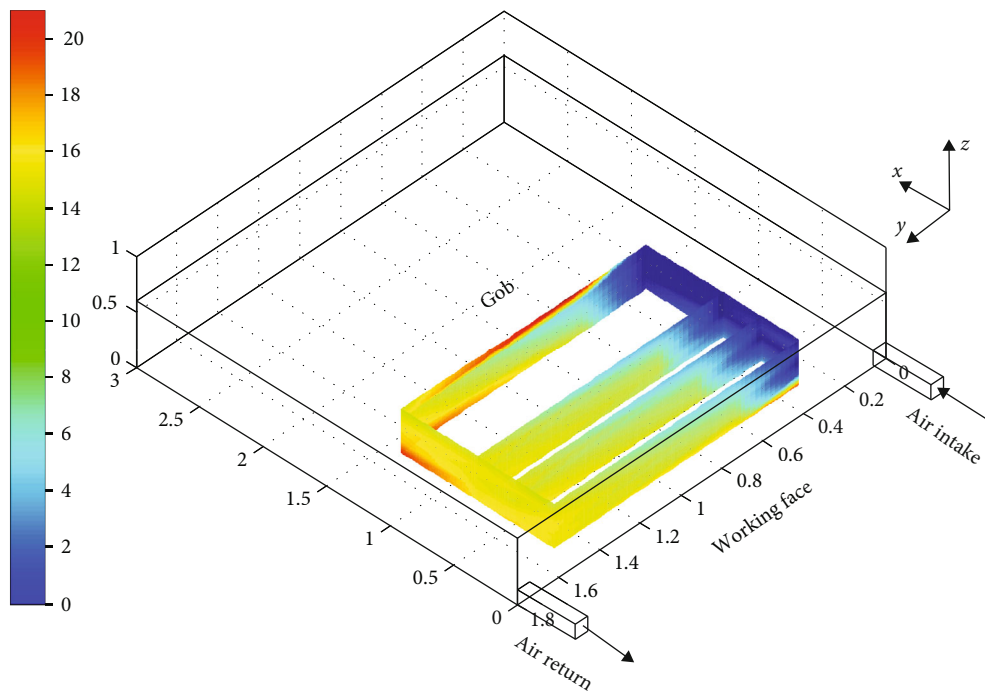


FIGURE 10: O₂ concentrations at $x = 0.2, 0.5, 0.8,$ and 1.4 m and $y = 0.3$ and 1.5 m with N₂ injection rate of 2.3 L/min, 45°.

simulation model is the same as that in the real goaf. The volume proportion of inert gas to air injected in the model is also the same as in the real goaf

- (iii) *Dynamic similarity*: the force of the airflow in the similarity simulation experiment platform of large inclined goaf is the same as that in the real goaf,

and force direction is also the same if secondary factors are not considered [18]

2.2.2. *Platform Construction*. The experimental platform simulated the O₂ distribution and inert gas migration law under different flow rates after injecting N₂ and CO₂ into

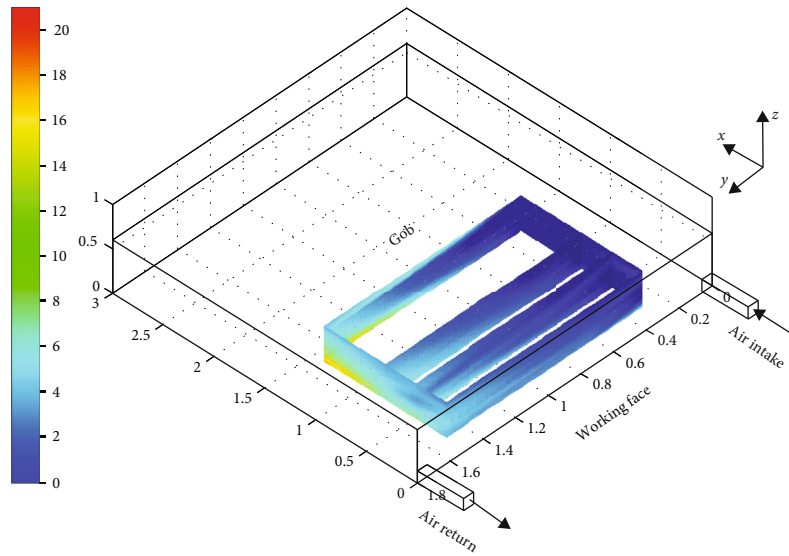


FIGURE 11: O_2 concentrations at $x = 0.2, 0.5, 0.8,$ and 1.4 m and $y = 0.3$ and 1.5 m with N_2 injection rate of 3.4 L/min, 45° .

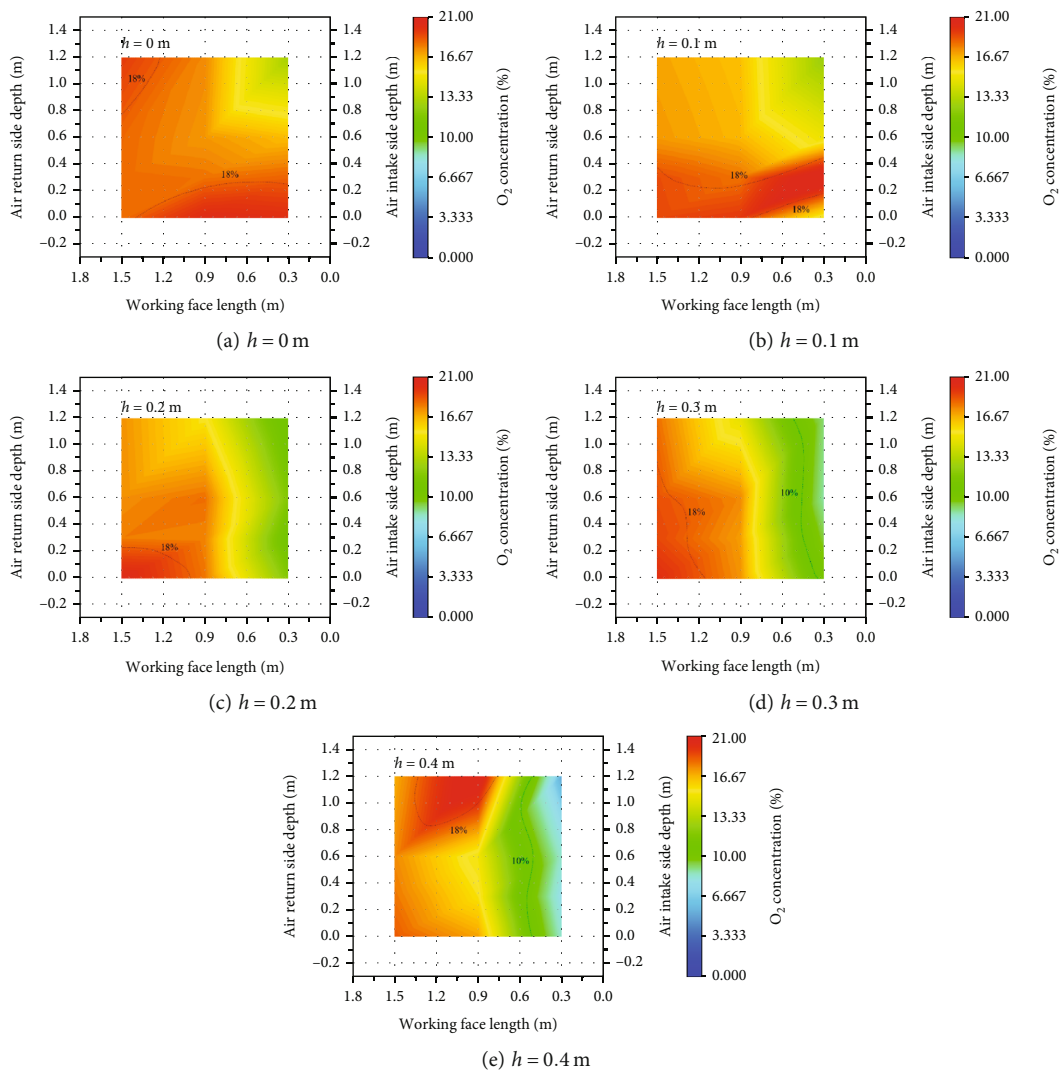


FIGURE 12: Cloud distribution of O_2 concentration at different heights with the N_2 injection rate of 1.1 L/min, 45° .

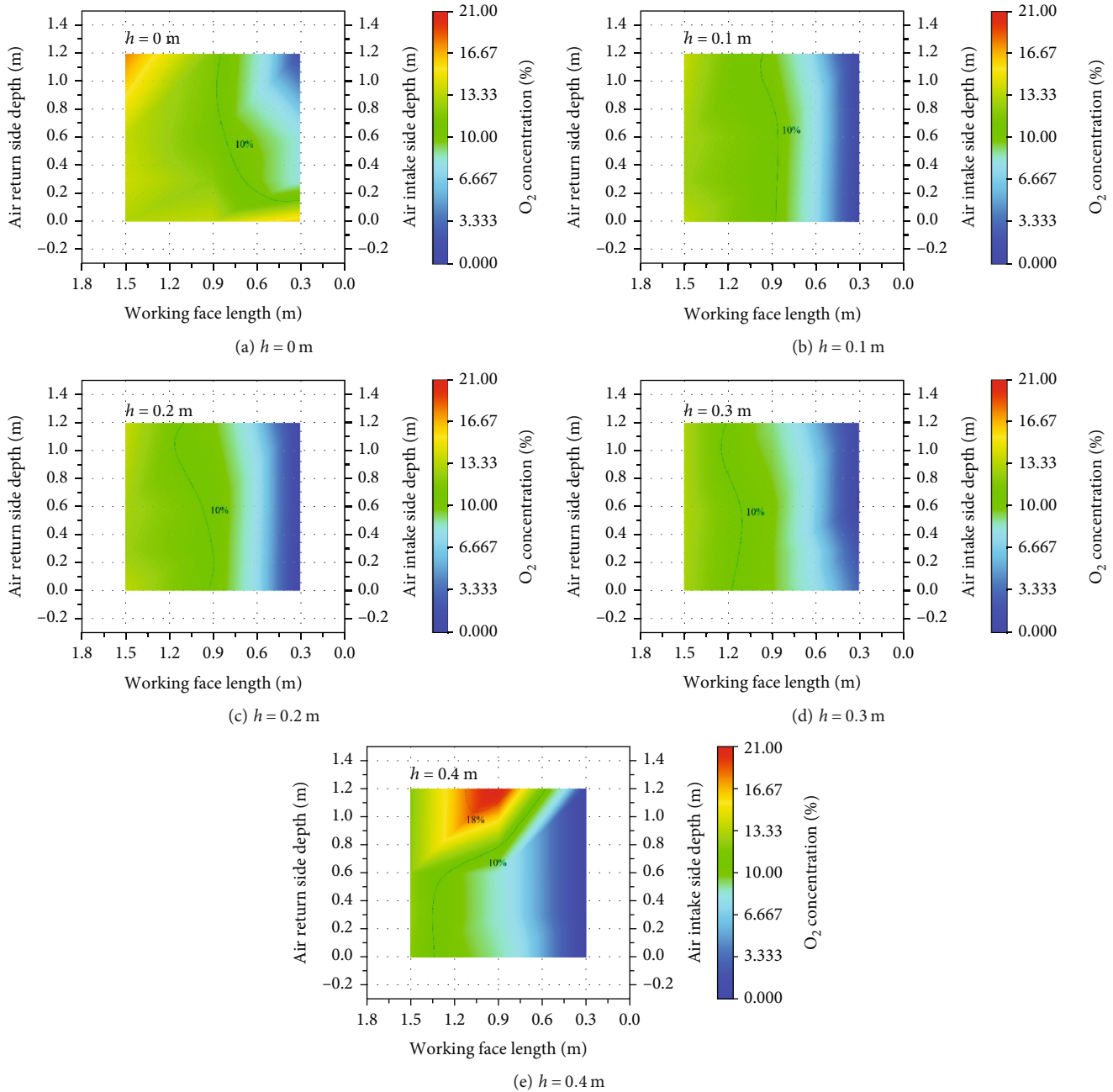


FIGURE 13: Cloud distribution of O_2 concentration at different heights with the N_2 injection rate of 2.3 L/min, 45° .

the large inclined goafs. The experimental platform includes the box, ventilation, data collection, and inert gas injection systems. The schematic diagram of the experimental platform is shown in Figure 1.

(1) *The Box System.* The box simulating a large inclined goaf is the main part of the experimental platform. It includes the box body and two long roadways. The box is made of a 50 mm angle steel frame and a 2 mm thick stainless steel bottom plate welded to the frame. The dimension of the main box is $3\text{ m} \times 2\text{ m} \times 1\text{ m}$. The goaf and roadway are constructed with transparent PMMA

acrylic plate to simulate the supporting coal wall. Two rotating supports are welded between the bottom plate and the frame. By synchronously rotating the two nuts, the whole platform can be tilted to the left in the range of 0° to 55° .

According to the coal and rock distribution law in large inclined goaf, the coal caving and the distribution of the remaining coal are very irregular. Thus, organic foams of different diameters are used to fill up the box and approximate the spatial characteristics of the porous medium in large inclined goafs. A layer of broken coal blocks is laid

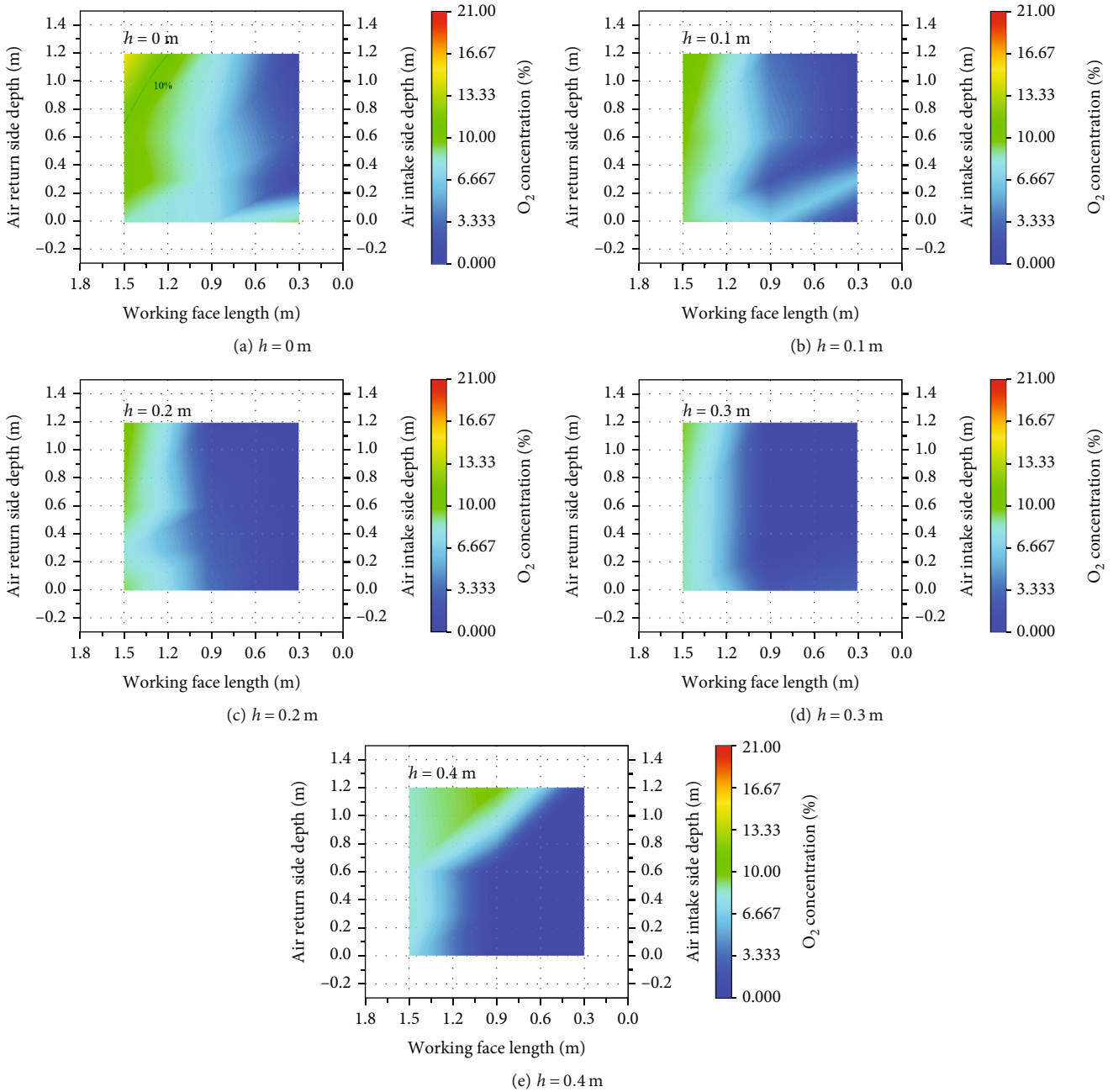


FIGURE 14: Cloud distribution of O_2 concentration at different heights with the N_2 injection rate of 3.4 L/min, 45°.

on the bottom of the box to simulate the residual coal in the goaf.

(2) *The Ventilation System.* The ventilation system is designed to adjust the ventilation parameters of the similarity simulation experiments. It includes a negative pressure vacuum pump and a rotameter. The vacuum pump is connected to the left air return roadway to simulate the extraction downward ventilation mode of the working face. The rotameter is used to measure and help control the air volume of the working face, as shown in Figure 2.

(3) *The Data Collection System.* The data collection system records the monitoring data in real time. Figure 3 shows a detailed layout of the oxygen measurement points. A total of 60 oxygen sensors were arranged in the goaf box to measure the spatial distribution of O_2 in the goaf and indirectly reflect the migration law of N_2/CO_2 in the goaf.

(4) *The Inert Gas Injection System.* The inert gas injection system simulates the inert gas injection into the goaf. The system includes the N_2 or CO_2 gas cylinders, gas pressure reducing valves, gas buffer tanks, air rotor flow meters, and

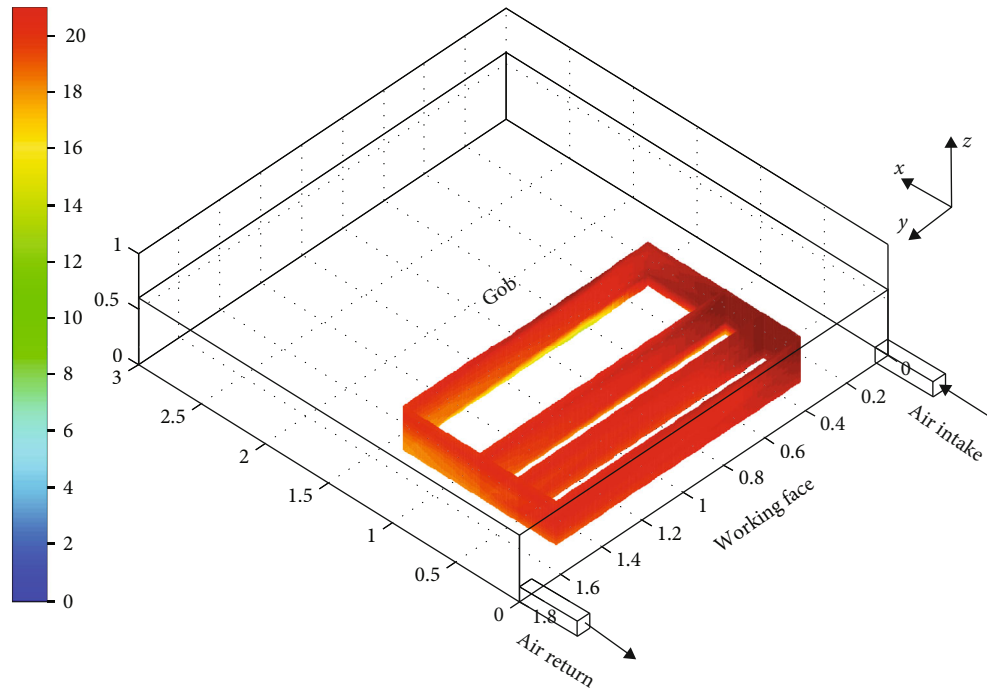


FIGURE 15: O_2 concentrations at $x = 0.2, 0.5, 0.8,$ and 1.4 m and $y = 0.3$ and 1.5 m with the CO_2 injection rate of 1.1 L/min, 45° .

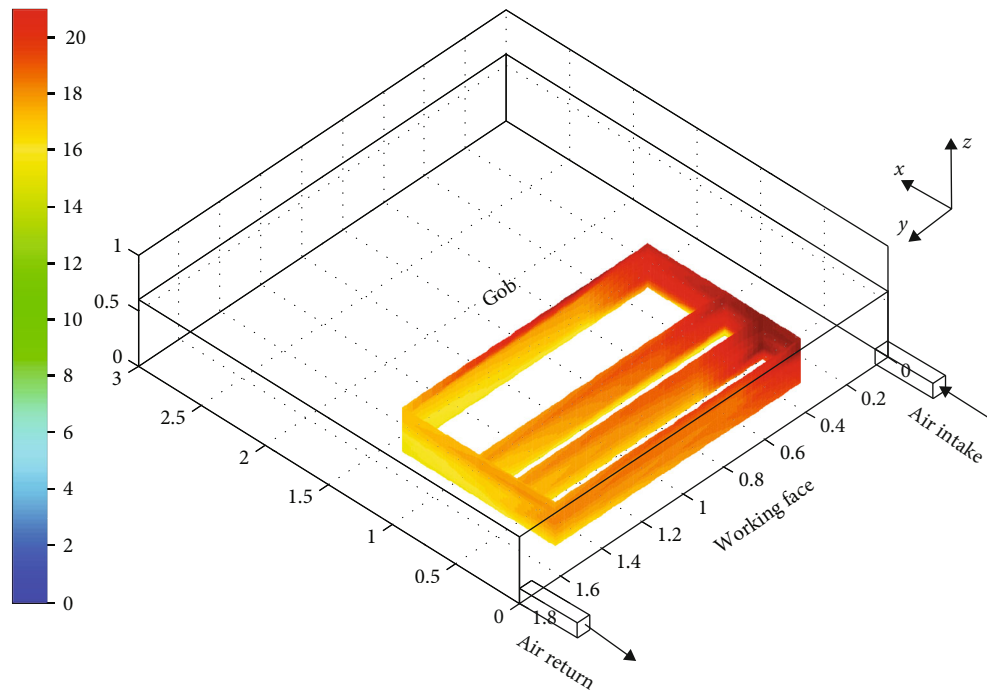


FIGURE 16: O_2 concentrations at $x = 0.2, 0.5, 0.8,$ and 1.4 m and $y = 0.3$ and 1.5 m with the CO_2 injection rate of 2.3 L/min, 45° .

transparent PU pipes with a diameter of 14 mm, as shown in Figure 4. The N_2 or CO_2 cylinders simulate the source of inert gas injected into the goaf. The two cylinders are connected with a three-way joint to ensure a sufficient inert gas source during the experiment. The gas pressure-reducing valve is connected to the gas cylinder to maintain an absolute pressure so that the outflow of inert gas is

smooth and continuous. Gas buffer tanks are used to buffer the airflow and a certain amount of inert gas and ensure the continuity of inert gas injection during the experiment.

2.3. Experimental Methods. The purpose of this experiment is to qualitatively analyze the inert gas migration law in the large inclination goaf under different flow

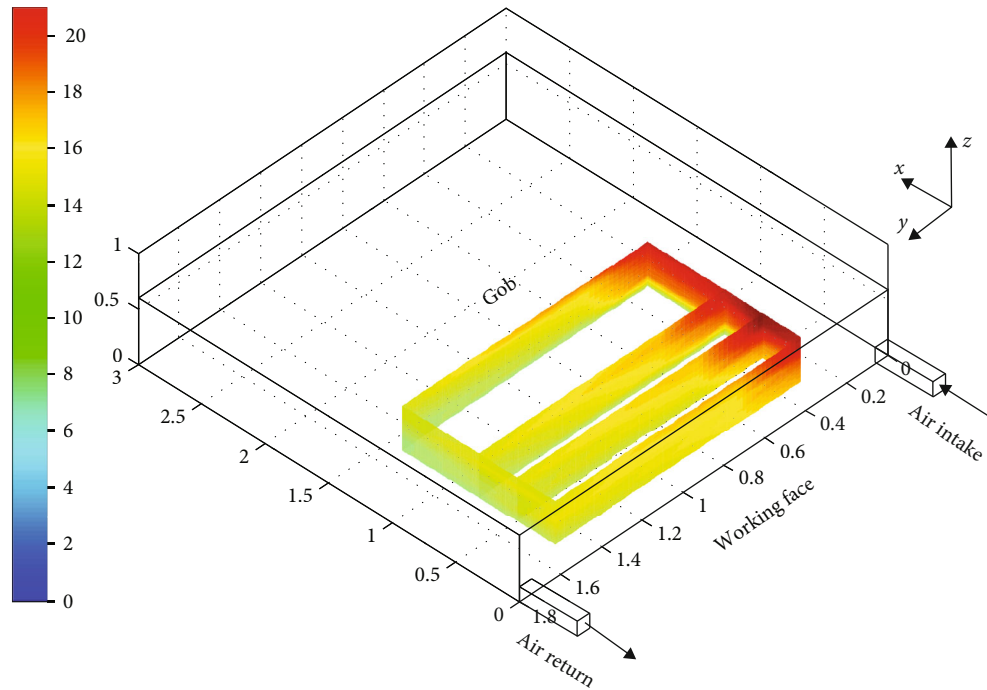


FIGURE 17: O_2 concentrations at $x = 0.2, 0.5, 0.8,$ and 1.4 m and $y = 0.3$ and 1.5 m with the CO_2 injection rate of 3.4 L/min, 45° .

conditions and the change law of the three spontaneous combustion zones in the goaf. Since the experiment indirectly analyzes the migration process of N_2 or CO_2 by monitoring the spatial distribution of O_2 , and the central area of N_2 or CO_2 inerting is the oxidation zone, it is assumed that the gas composition in the goaf is all air at the beginning of the experiment. The experiment includes two parts:

- (1) A simulation experiment with similar migration law of N_2 in the goaf
- (2) A simulation experiment with similar migration law of CO_2 in the goaf

The actual ventilation rate of working face 37121-1 in the Dongxia coal mine is 880 m³/min. According to the similarity criteria, the ventilation rate of the working face in the experiment is set to 5.0 L/min, and the flow rate of N_2 or CO_2 is set to 1.1 L/min, 2.3 L/min, and 3.4 L/min, corresponding to the actual N_2 or CO_2 injection flow rates of 200 m³/min, 400 m³/min, and 600 m³/min. The depth of the N_2 or CO_2 injection pipeline in the experiment is 0.67 m, corresponding to the actual depth of 40 m. Since the maximum inclination angle of working face 37121-1 is 45° , the rotation angle of the platform is set to 45° in the experiment. Table 2 shows the experimental scheme. The ventilation mode of the simulated working face is downward ventilation, and the position of N_2 or CO_2 injection is located in the high-level air intake side.

Before the experiment, the inclination angle of the experiment platform was set to 45° , and the negative pressure vac-

uum pump was connected to the air return side. At the same time, the gas injection pipeline was connected to the N_2/CO_2 perfusion system. The vacuum pump was turned on to pressurize the similarity model for at least 3 h to fill it with air and adjust the readings of the 60 oxygen sensors to 20.95%. After that, the ventilation system was turned on, and the negative pressure and the exhaust airflow were adjusted. The air rotor flowmeter read 5.0 L/min, indicating continuous and stable ventilation. Therefore, the typical ventilation environment of the working face was simulated. The N_2/CO_2 cylinder valve was opened, and the flow rate of N_2/CO_2 was adjusted through the rotameter to continuously and stably pass N_2/CO_2 into the similarity model. The data collection system recorded the data in real time. When the concentration was stable, the readings of each O_2 sensor were saved, and the experiment concluded.

3. Results and Discussions

3.1. Inclination Angle of 0° . To verify the feasibility of studying the dangerous area in the goaf and the inert gas migration law with a similarity model, we conducted N_2 and CO_2 injection experiments at the 0° inclination angle with a flow rate of 3.4 L/min. The oxygen concentration distribution in the six sections at $x = 0.2, x = 0.5, x = 0.8, x = 1.4, y = 0.3,$ and $y = 1.5$ m and the cloud distribution of O_2 concentration at $h = 0, h = 0.1, h = 0.2, h = 0.3,$ and $h = 0.4$ m are shown in the following figures.

As shown in Figures 5 and 6, the N_2 injection exerts inerting effects on the upper side of the goaf but no significant inerting effect on the lower side. The inerting effect of N_2 improves with the increase of the distance from the floor. The N_2 injection can reduce the oxygen concentration to

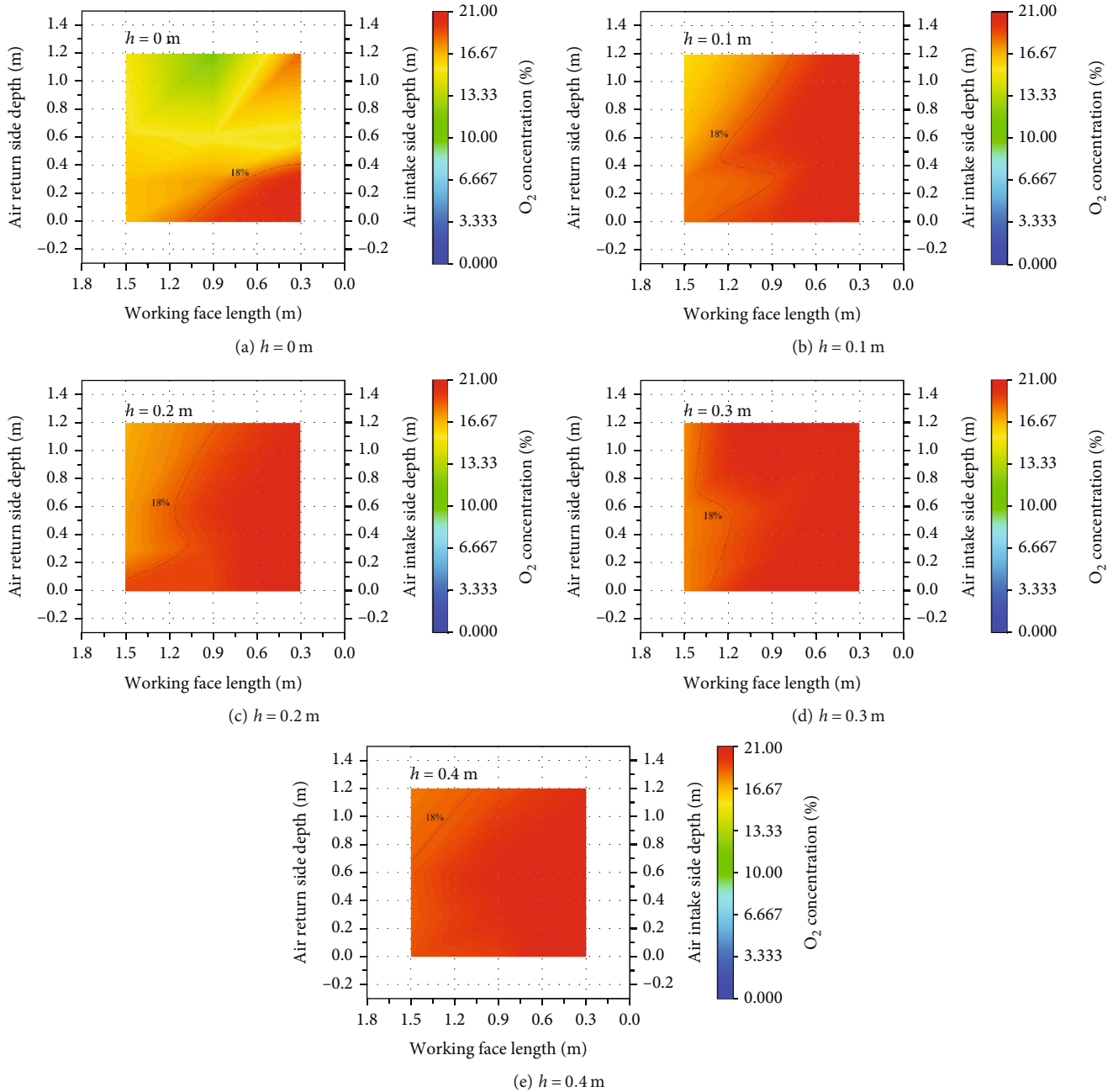


FIGURE 18: Cloud distribution of O_2 concentration at different heights with the CO_2 injection rate of 1.1 L/min, 45° .

below 10% at $h = 0.2$ m, 0.3 m, and 0.4 m and keep the coal entirely within the range of the suffocation zone. As shown in Figures 7 and 8, the CO_2 injection exerts apparent inerting effects on the lower side of the goaf but has poor inerting effects on the upper side. CO_2 only keeps the coal within the range of suffocation zone at $h = 0$ m, while the oxygen concentration at other heights is high, indicating that the CO_2 migration is much worse than that of N_2 .

3.2. Inclination Angle of 45°

3.2.1. N_2 Injection. When the N_2 injection rate is 1.1, 2.3, and 3.4 L/min, the oxygen concentration distributions at $x = 0.2$,

0.5, 0.8, and 1.4 m and $y = 0.3$ and 1.5 m are shown in Figures 9–11, respectively.

The deeper blue color in the high area indicates low oxygen concentration. With the increase of the injection rate, N_2 diffuses to a larger area. When the N_2 flow rate is 1.1 L/min, the areas on the upper side of the goaf have a low N_2 inerting effect, but most areas have no inerting effect and high oxygen concentration. When the N_2 injection rate increases to 2.3 L/min, the N_2 inerting range is larger with decreased oxygen concentration on the lower side of the goaf. When the N_2 injection rate increases to 3.4 L/min, the N_2 inerting effect on the lower side of the goaf is more significant, and the color of other areas is dark blue, indicating decreased

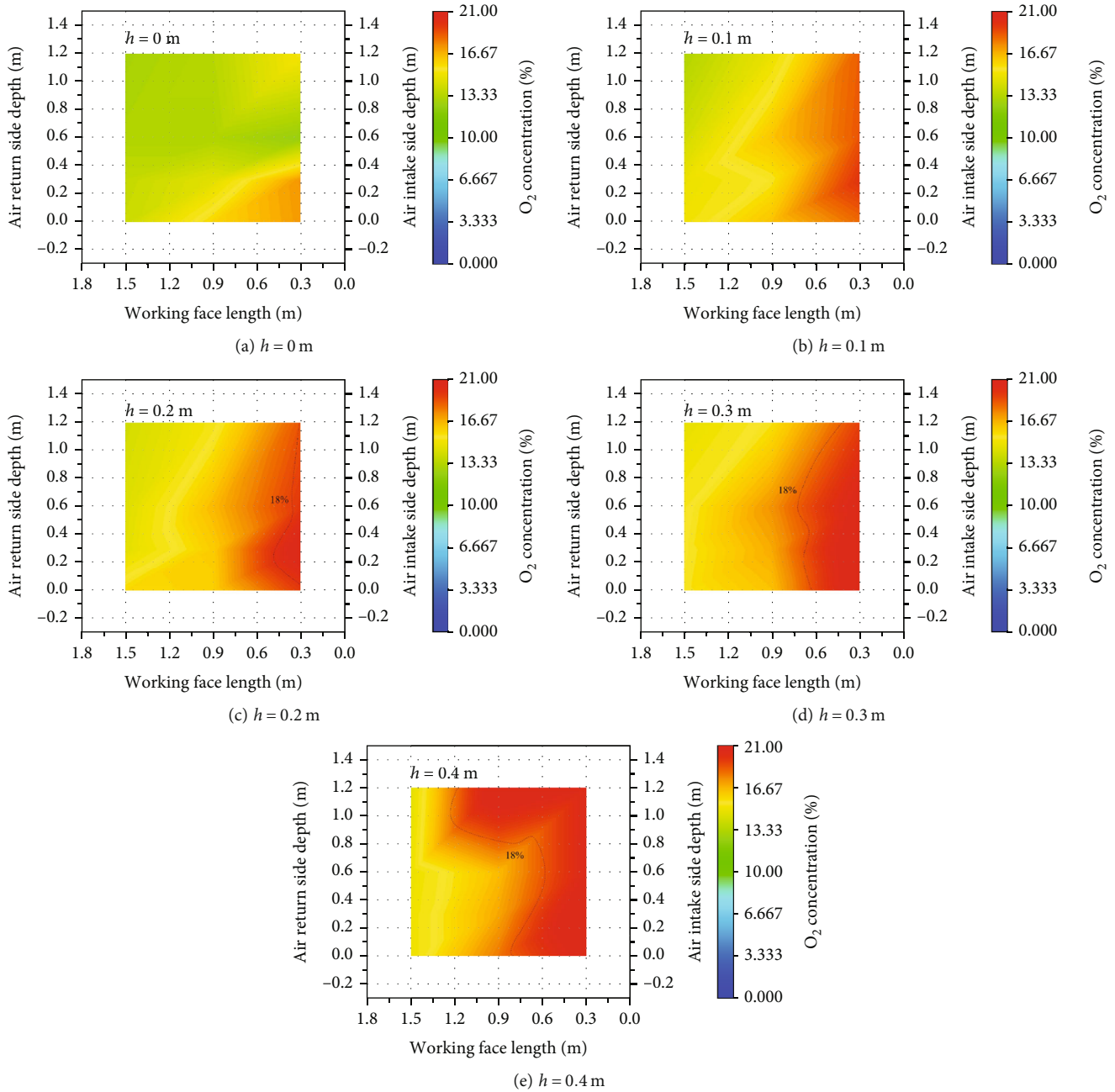


FIGURE 19: Cloud distribution of O₂ concentration at different heights with the CO₂ injection rate of 2.3 L/min, 45°.

oxygen concentration with the increased N₂ injection rate. Thus, a higher N₂ injection rate has a better inerting effect on the large inclined goaf.

As shown in Figures 12–14, the oxygen concentration distribution at different heights of the goaf is basically the same under different N₂ injection rates, and N₂ is mainly distributed at the air inlet side of the goaf. When the N₂ injection rate is 1.1 L/min, the oxygen concentration near the goaf floor is above 10% ($h = 0.1$ m and $h = 0.2$ m), and the oxidation zone of the goaf is large ($10\% < c_{O_2} < 18\%$). At 0.3 m and 0.4 m from the floor, the suffocation zone appears. When the N₂ injection rate is 2.3 L/min, the oxida-

tion zone decreases with the distance from the bottom plate. As the N₂ injection rate increases to 3.4 L/min, the whole goaf is basically within the range of the suffocation zone, and the residual coal in the goaf is not prone to spontaneous combustion.

3.2.2. CO₂ Injection. As shown in Figures 15–17, the inerting area of CO₂ is utterly different from that of N₂. The inerting area is mainly reflected by CO₂ injection. The CO₂ reaches the side of the low-level air return side at first and gradually diffuses from the low-level air return side to the high-level air intake side with the increase of the

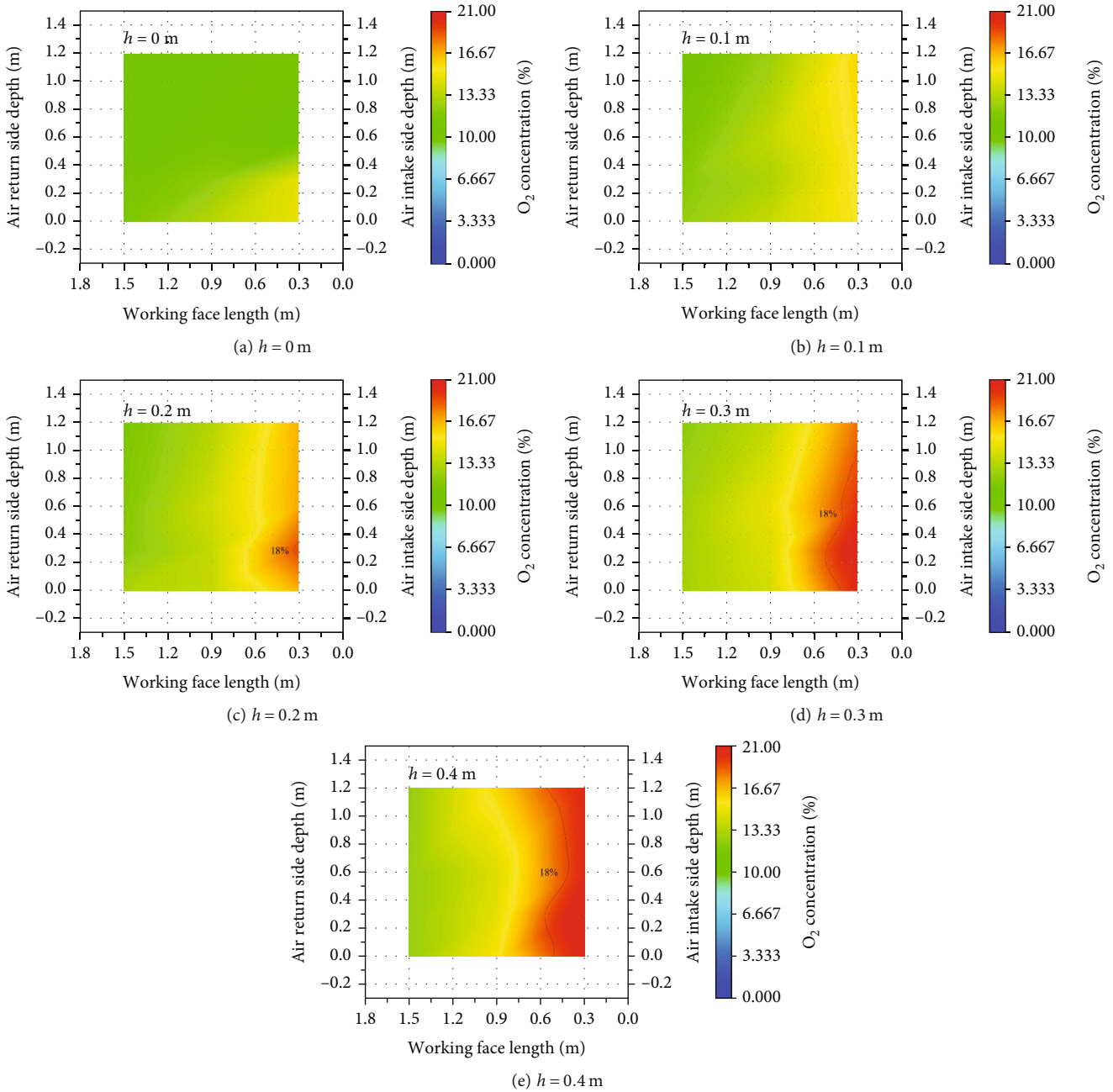


FIGURE 20: Cloud distribution of O_2 concentration at different heights with the CO_2 injection rate of 3.4 L/min, 45° .

CO_2 injection rate. When the CO_2 injection flow is 1.1 L/min, the inerting area is mainly located on the lower side of the goaf. The range of blue area is very limited, indicating that the injection flow is not enough to keep the goaf inert. As the CO_2 injection rate increases to 2.3 L/min, the CO_2 inerting area becomes larger, and the oxygen concentration on the lower side of the goaf decreases significantly. When the CO_2 injection rate increases to 3.4 L/min, the oxygen concentration on the lower side of the goaf decreases further, but that in the goaf cannot be reduced to a lower level.

As shown in Figures 18–20, the oxygen concentration distribution law is basically the same at different heights of the goaf under different CO_2 injection rates. CO_2 is mainly distributed on the return side of the goaf. When the CO_2 injection rate is 1.1 L/min, the oxygen concentration at each height from the goaf floor is above 10%. The oxygen concentration increases with the distance from the goaf floor, and the 18% oxygen concentration line at $h = 0.1, 0.2,$ and 0.3 m presents an S-type distribution. Even with the CO_2 injection rate increasing to 2.3 and 3.4 L/min, the oxygen concentration in the goaf is still high above 10%. Most of

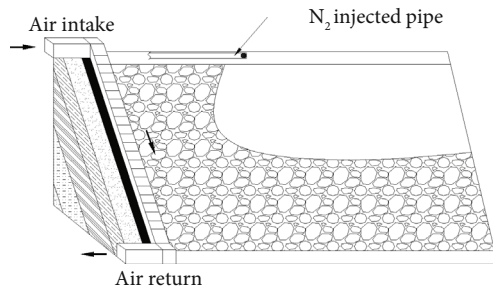


FIGURE 21: Schematic diagram of N_2 migration in large dip goaf.

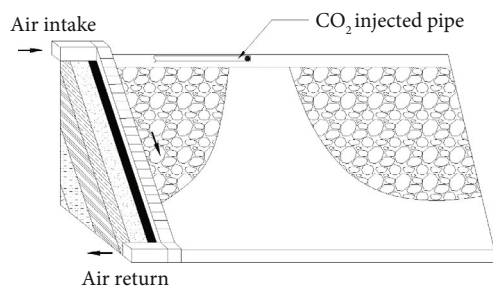


FIGURE 22: Schematic diagram of CO_2 migration in large dip goaf.

the goaf is in the oxidation zone, and the residual coal is prone to spontaneous combustion.

3.3. The N_2 and CO_2 Injection Migration Mechanisms and Laws

3.3.1. The N_2 and CO_2 Injection Migration Mechanisms. When injected into goafs with large inclinations, N_2 accumulates in the upper space of the air intake side due to gravity and then spreads downward and toward the air return side. The N_2 injection flow is crucial to the spontaneous combustion zone distribution in the goaf. With increased N_2 injection, the range and width of the oxidation zone decreased, and the end of the loose zone and oxidation zone moved forward to the working face, where the end of the oxidation zone moved further than that of the loose zone.

When injected into goafs with large inclinations, CO_2 diffuses along the goaf bottom to the side of the low-level air return side due to gravity and then slowly diffuses upward. The inerting effect of CO_2 on the floor area of goafs with large inclinations was less significant than that of horizontal goafs because CO_2 was denser than air. With large inclinations, CO_2 flows along the air intake side to the low-level air return side of the goaf. Part of CO_2 dissipates along with the airflow of the working face, which reduces CO_2 accumulation in the air return side, resulting in poor inerting effects.

3.3.2. The N_2 and CO_2 Injection Migration Laws. The N_2 and CO_2 inerting effects and migration laws in the goaf area with large inclinations are shown in Figures 21 and 22, respectively. When N_2 is injected into the goaf area with large inclinations, N_2 accumulates in the upper area of the lower part of the inlet side since N_2 is lighter than air and gradually dif-

fuses toward the low-level high oxygen area. The migration profile of N_2 approximates an L shape. When injected, CO_2 accumulates to the low-level air return side and gradually diffuses toward the high oxygen area in the deep part of the high-level air intake side since CO_2 is denser than air. There is also a high oxygen area near the working face due to ventilation. The migration profile of CO_2 resembles a trumpet shape, in which the bell mouthing is located in the CO_2 filling port of the air intake side.

4. Conclusion

In this paper, the inerting effects and migration laws of N_2 and CO_2 injections into the goaf with large inclinations were studied with a similarity simulation model. The results showed that with the increase of N_2 and CO_2 injection, the range and width of the oxidation zone decreased, and the end of the loose zone and the oxidation zone moved forward to the working face. When injected at the same flow rate, CO_2 flew to the air return side and dissipated with the airflow of the working face due to its higher density than air, and the inerting effects were far less significant than that of N_2 . The migration profile of N_2 in the goaf approximated an L shape, and that of CO_2 approximated a trumpet shape. Therefore, the inerting effects of N_2 were superior in terms of fire prevention and extinguishment in large inclined goafs.

Data Availability

The data used to support the findings of this study are included within the article.

Additional Points

Coal Mining Terminology. Working face: the first production site of coal, with narrow working space, mechanical equipment, poor visual environment, high temperature characteristics. Goaf: the cavity or cavity left after the underground coal or coal gangue is mined in the process of coal mining. Air intake: the fresh air flow for the working face. Air return: the turbid wind after fresh air passing through the working face and goaf.

Conflicts of Interest

The authors declare that they have no conflicts of interest.

Acknowledgments

This work was supported by the National Natural Science Foundation of China (Grant No. 52074277) and Natural Science Foundation of Jiangsu Province (Grant No. BK20211585).

References

- [1] M. Liu, "Research on fully mechanized mining technology of large inclined working face," *Shanxi Metallurgy*, vol. 42, no. 5, pp. 117-118, 2019.

- [2] L. Ma, X. Song, H. Wen, and X. Meng, "Research on fire prevention and control technology for seam spontaneous combustion in overlong fully mechanized longwall coal mining face," *Coal Engineering*, vol. 3, pp. 58–60, 2006.
- [3] S. Shao, C. Wu, M. Hao et al., "A novel coating technology for fast sealing of air leakage in underground coal mines," *International Journal of Mining Science and Technology*, vol. 31, no. 2, pp. 313–320, 2021.
- [4] B. Hao, X. Lv, and J. Wang, "Mining's choice in inclined thick seam," *Coal Technology*, vol. 27, no. 2, pp. 43–45, 2008.
- [5] L. Tao and Y. Wang, "Overlying strata movement and failure in steeply dipping coal seam," *Journal of China Coal Society*, vol. 6, pp. 23–26, 1996.
- [6] L. Ge, Y. Shao, Y. Wang, G. Zhang, Z. Zhang, and L. Liu, "Experimental research on inerting characteristics of carbon dioxide used for fire extinguishment in a large sealed space," *Process Safety and Environmental Protection*, vol. 142, pp. 174–190, 2020.
- [7] Q. Chen and X. Wang, "Research on the law of spontaneous combustion of coal and nitrogen injection fire-fighting technology in fully mechanized caving face," *Journal of China Coal Society*, vol. 6, pp. 618–623, 1996.
- [8] Y. Zhuang, G. Zhao, Q. Bao et al., "Isolated nitrogen injection fire prevention and extinguishing technology in layered mining of thick coal seam," *Coal Science & Technology*, vol. 11, pp. 31–34, 1998.
- [9] N. Zheng, "Discussion on nitrogen injection fire prevention and extinguishing technology in fully mechanized mining face under complex geological conditions," *Coal Technology*, vol. 12, pp. 49–50, 2003.
- [10] Z. Cao, J. Shi, H. Zhang, X. Chun, and K. Zhao, "Study on influence of nitrogen injection flow rate on nitrogen diffusion radius in goaf," *Mining Safety and Environmental Protection*, vol. 46, no. 5, pp. 12–15, 2019.
- [11] J. Cao, J. Wu, C. Zhou, and Y. Tang, "Division of spontaneous combustion dangerous region and determination of nitrogen injection position in goaf of low level top coal caving mining face," *Coal Science & Technology*, vol. 45, no. 2, pp. 89–94, 2017.
- [12] H. Shao, S. Jiang, Z. Wu, W. Zhang, and K. Wang, "Numerical simulation on fire prevention by infusing carbon dioxide into goaf," *Journal of Mining and Safety Engineering*, vol. 30, no. 1, pp. 154–158, 2013.
- [13] H. Shao, S. Jiang, Z. Wu, W. Zhang, and K. Wang, "Comparative research on the influence of dioxide carbon and nitrogen on performance of coal spontaneous combustion," *Journal of China Coal Society*, vol. 39, no. 11, pp. 2244–2249, 2014.
- [14] G. Wang, J. Deng, X. Zhang, Y. Xiao, and J. Sun, "Determination of parameters of injecting CO₂ to prevent spontaneous combustion in gob of fully mechanized top-coal caving," *Journal of Liaoning Technical University (Natural Science)*, vol. 28, no. 2, pp. 169–172, 2009.
- [15] H. Su, F. Zhou, X. Song, B. Shi, and S. Sun, "Risk analysis of coal self-ignition in longwall gob: a modeling study on three-dimensional hazard zones," *Fire Safety Journal*, vol. 83, pp. 54–65, 2016.
- [16] H. Su, F. Zhou, X. Song, and Z. Qiang, "Risk analysis of spontaneous coal combustion in steeply inclined longwall gobs using a scaled-down experimental set-up," *Process Safety and Environmental Protection*, vol. 111, pp. 1–12, 2017.
- [17] M. Hao, Y. Li, X. Song, J. Kang, H. Su, and F. Zhou, "Hazardous areas determination of coal spontaneous combustion in shallow-buried gobs of coal seam group: a physical simulation experimental study," *Environment and Earth Science*, vol. 78, no. 1, pp. 31–39, 2019.
- [18] M. Hao, Y. Li, X. Song, J. Kang, H. Su, and F. Zhou, *Hazardous Areas Distribution of Coal Spontaneous Combustion in Shallow-Buried Compound Gobs of Coal Seam Group*, vol. 78, no. 1, 2019, China University of mining and technology, Xuzhou, 2019.

Research Article

Stability Control of a Roadway Surrounding Rock during the Cutting and Pressure Relief of a Coal-Bearing Roof at a Shallow Mining Depth

Chen Tian,^{1,2} Yingjie Liu ,³ Hezhuang Lou,⁴ and Tinggui Jia⁵

¹Safety Engineering College, Heilongjiang University of Science and Technology, Harbin 150022, China

²CHN Energy Shandong Coal Group Corporation Ltd, Daliuta 719315, China

³Emergency Science Research Academy, China Coal Research Institute, China Coal Technology & Engineering Group Co., Ltd., Taiyuan 100013, China

⁴The No. 4 Pipe Network Operation Branch, Beijing Drainage Group Co., Ltd., Beijing 100044, China

⁵Inner Mongolia University of Science and Technology, Baotou 014000, China

Correspondence should be addressed to Yingjie Liu; 290783585@qq.com

Received 29 July 2021; Revised 23 December 2021; Accepted 24 January 2022; Published 9 March 2022

Academic Editor: Jia Lin

Copyright © 2022 Chen Tian et al. This is an open access article distributed under the Creative Commons Attribution License, which permits unrestricted use, distribution, and reproduction in any medium, provided the original work is properly cited.

Recent years have seen the widespread use of a new gob-side entry retaining technology, namely, automatic roadway forming based on roof cutting and pressure relief. However, because of the complex geological conditions, stability control methods for the surrounding rock remain unexplored. In this paper, through theoretical analysis, field measurement, and numerical simulation, the stability control of a roadway surrounding rock under roof-cutting and pressure-relief conditions is studied. The key stage in the steady-state control of this type of rock is determined by establishing a mechanical model of the hard roof in the process of automatic roadway formation. The results show that the roof-cutting and pressure-relief technology outperforms the conventional mining technology in terms of surface crack development and subsidence. The roadway roof movement can be divided into three stages: a direct roof-caving activity period, a basic roof-breaking activity period, and a roof-stabilizing period. The stress above the original roadway is gradually transferred to the adjacent working face, and a stress concentration is formed on the working face 6 m away from the roadway retaining section. In this scenario, the roadway is in a stress-reducing area, which ensures its safety. Based on the research results, we suggest adding a constant resistance and large deformation anchor cable near the cutting seam side for active support. A single-hydraulic prop + I-beam + steel mesh can support the working face, and a grouting bolt support can help reinforce the broken and loose surrounding rocks at the gangue-retaining side of the roadway. Thus, the movement of the surrounding rock can be effectively controlled. An industrial test shows that the effect of retaining roadway is evidently improved.

1. Introduction

Through nearly 60 years of exploration and practice, the gob-side entry retaining (GER) technology has achieved good results in applications, is now a relatively complete coal-pillar-free mining technology [1–5], and has promoted the development of coal-pillar-free mining. However, more attention should be paid to the stress concentration of the filling body and the poor matching between filling material and roof.

In the study of GER supports, various safety factors, support principles, and support methods have been proposed

depending on the geological conditions through theoretical derivation, physical simulation, numerical simulation, and field monitoring [6, 7]. Through a computer simulation analysis of a roadway bolt support design, a sensitivity analysis method for the roadway support safety factor has been proposed [8,9]. The bolt strength, bolt shotcrete thickness, and lithology significantly influence the GER effect [10]. A constitution model was analyzed using linear elasticity, nonlinear elastoplastic, and elastoplastic theories. The post deformation and failure behavior of the rock mass has an important impact on the displacement and stress distribution of roadway surrounding

rocks. With the analysis results of a bolt support experiment [11], corresponding support countermeasures have been proposed [12, 13]. In the GER approach, the roadway-side support controls the basic roof of the roadway, and the control of the roof inclination serves as a theoretical basis for designing the working resistance and shrinkage of the roadside support [14, 15]. The roof activity law in different periods has a varying influence on retaining the roadway, and the mechanism of roadway-side reinforcement support can be explained through mechanical derivation. Accordingly, a roadway-side support principle has been proposed [16–19]. The interaction angle between roof movement and roadway-side support under mining action has a certain influence on the strength of the filling body for roadway protection, and the corresponding theoretical calculation method has been proposed [20, 21]. In recent years, the “soft rock large deformation theory” coupling support principle has been applied to fully mobilize the strength of deep stable rock strata and realize support integration and load uniformity. The theory has been verified by conducting several field experiments [22–25].

Significant research has been made on the behavior law of underground pressure distribution during GER. Studies have shown that rocks surrounding a roadway move violently because of the primary weighting and periodic weighting of the basic roof, resulting in support deformation, damage to GER roadway, and roof cracks or broken rocks [26–28]. The violent deformation of the roadway has a synchronous effect with the mining face weighting [29], and the roof subsidence increases in direct proportion with the increase in the roadway width and the hanging roof distance [30]. With the increase in the cutting height of the roadway-side support body with a high resistance along the GER section, the height of the roadway-side support of the caving rock increases. The roadside support body and surrounding rock can be made to reach a new balanced state as soon as possible by fully utilizing the bearing capacity of the caving gangue, thereby reducing roadway deformation [31, 32]. Moreover, a GER support cannot easily prevent any changes in the upper stratum balance. Nevertheless, a sufficient support resistance can help avoid serious fractures on the direct roof, prevent the formation of a large separation layer between the upper layers, and directly realize basic roof cutting at the goaf side [33]. Therefore, improving the support strength has a positive effect on controlling the surrounding rock for retaining roadways [34–36].

Automatic roadway formation through roof cutting and pressure relief is a new pillar-free mining technology [37,38]. In this approach, the stress transfer of the overlying strata is cut off via bidirectional energy accumulation blasting at the cutting seam [39], and the roof rock mass collapses to form a roadway side, thus realizing an automatic roadway formation in working face mining. Self-formed roadways without coal pillars have been realized through the roof cutting and pressure relief of medium-thick coal seams [40–42]. Results have shown that the stress condition of roadway surrounding rocks during this process can be improved, and a support technology has been established to adapt to the deformation of roadway surrounding rocks and to control their stability. Currently, there is little research on the

stability control of the surrounding rocks of shallow-buried and deep-coal-bearing composite roadways under roof-cutting and pressure-relief conditions. Moreover, research on roof-cutting and pressure-relief technology under the condition of a shallow coal seam hard roof is insufficient.

Therefore, based on the rock mechanics during roof cutting and pressure relief, this study establishes a mechanical model of a hard roof in the process of roof cutting and pressure relief, analyzes the key stages in the stable control of a roadway, and obtains the surrounding of shallow-buried and deep-coal-bearing roadways. Finally, field verification was carried out to validate the results.

2. Geological Conditions of the 12201 Working Face

The 12201 fully mechanized face of Halagou Coal Mine was the first working face of the second panel of a coal mine 12#, with an inclined face 320 m in width and 747 m in length (from the cutting hole to the stopping line). The GER section was 580 m in length. As for the face, the coal seam thickness ranged from 0.8 m to 2.2 m. The average mining height was 2 m. The workable reserve reaches 61 Mt. The coal seam was relatively stable, with the 12202 face on the northwest, which was the only face nearby. Figure 1 shows the layout of the 12201 fully mechanized face.

In terms of the lithology of this face, the thickness of the overlying bedrock ranged from 55 m to 70 m, whereas the thickness and depth ranges of the unconsolidated layers were 0–33.48 m and 60–100 m, respectively. The immediate roof of the coal seam was composed of siltstone, which had an average thickness of 1.84 m. The No. 12 upper coal seam was laid above the immediate roof, and its average thickness was 1.56 m. The top of the coal seam contains mudstone with an average thickness of 1.35 m. The main roof of the coal seam was made of fine-sandstone and siltstone; the average thicknesses of which were 3.34 m and 4.05 m, respectively. The immediate floor of the face was made of siltstone with an average thickness of 3.67 m. At the bottom of the immediate floor was fine-sandstone with an average thickness of 4.23 m. Figure 2 shows the lithology of the 12201 fully mechanized face.

3. RCPR Gob-Side Entry Retaining Parameter Design

An adequate height is required for roof cutting to ensure that the movement of the rock beam on the main roof of the overlying strata in the goaf is supported by the caving gangue. Based on previous research and based on the analysis of key parameters of automatic roadway with RCPR, the influence of height and angle of roof cutting on the strata behaviors had been simulated and studied with the FLAC^{3D} numerical simulation software, which confirmed that the optimal roof cutting height and splitting angle of the 12201 working face of Halagou Coal mine were 6 m, respectively. The effect of automatic roadway with RCPR had been well implemented through conducting the bidirectional

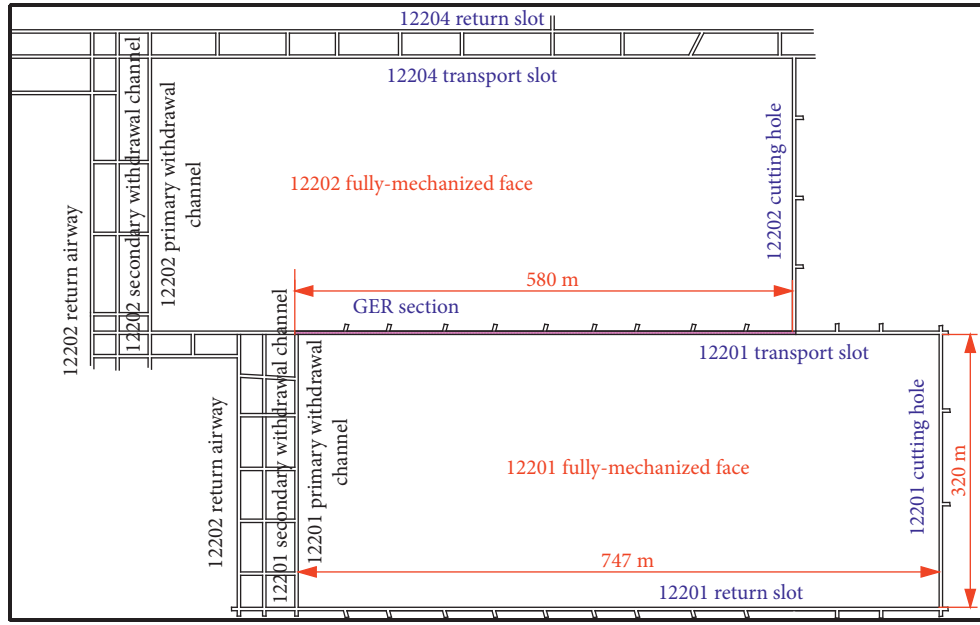


FIGURE 1: Diagram of the 12201 work surface layout.

Stratum	No.	Depth of stratum/ m	Histogram	Rock name
Yan'an group	1	$\frac{4.63-0.03}{4.05}$	[Histogram]	Siltstone
	2	$\frac{4.18-2.50}{3.34}$	[Histogram]	Fine sandstone
	3	$\frac{2.14-0.55}{1.35}$	[Histogram]	Mudstone
	4	$\frac{2.75-0.00}{1.56}$	[Histogram]	No. 12 uppercoal
	5	$\frac{3.90-0.52}{1.84}$	[Histogram]	Siltstone
	6	$\frac{2.30-0.80}{1.92}$	[Histogram]	No. 12 coal
	7	$\frac{10.40-0.15}{3.67}$	[Histogram]	Siltstone
	8	$\frac{7.75-2.40}{4.23}$	[Histogram]	Fine sandstone

FIGURE 2: Comprehensive histogram of the 12201 fully mechanized mining face.

cumulative blasting test on-site [43–45]. The height could be determined using the following equation:

$$H_m = \frac{(H_{coal} - \Delta H_1 - \Delta H_2)}{0.3} \quad (1)$$

Since the coal seam of the 12201 fully mechanized face had a composite roof, the roof-cutting height was set as 6 m. Considering the significant angle effect on the fracture, the cutting angle should be measured carefully to optimize the roof caving in the goaf and realize a reasonable stress distribution by adjusting the stress concentration area. In the present study, the cutting angle was set to 20° [46].

The bilateral cumulative tensile explosion was employed for directional roof cutting. In this approach, two shaped charges were placed in a gathering device with two preset blasting directions. After detonation, pressure from directions other than the preset ones was uniformly applied to the surrounding rock around the blasting boreholes, which were in tension in the preset directions simultaneously. In this study, the optimal charge quantity was set as 3 + 2+0 + 1. The distance between the boreholes was 0.6 m. The thickness of the boreholes was 6.0 m. The optimal luting length was 0.5 m. Ten boreholes were generated in each explosion. Figure 3 shows the borehole layout [47].

4. Ground Pressure Behavior Law of Roof-Cutting and Pressure-Relief Stope with Three Shallow-Buried Composite Roofs

4.1. Analysis of the Ground Pressure Behavior Law in Stope Area. The stope was mainly divided into three stratum pressure areas: a roof-cutting influence area, a nonaffected area in the middle, and a noncutting area, as shown in Figure 4.

Based on the division of the roadway under roof unloading, seven hydraulic supports, denoted by 5#, 10#, 20#, 90#, 100#, 125#, and 165#, were selected for ore-pressure monitoring, among which 5#, 10#, and 20# were located in the affected area of the roadway under roof unloading, 90# and 100# were located in the middle unaffected area, and 125# and 165# were located in the unroofed area. Figure 5 shows the pillar loads in the areas affected by roof cutting, pressure relief, and roadway retention.

4.1.1. Periodic Pressure Step Distance. The supports 5#, 10#, and 20# were in the conventional coal mining process area at the beginning of the mining stage of the working face. When

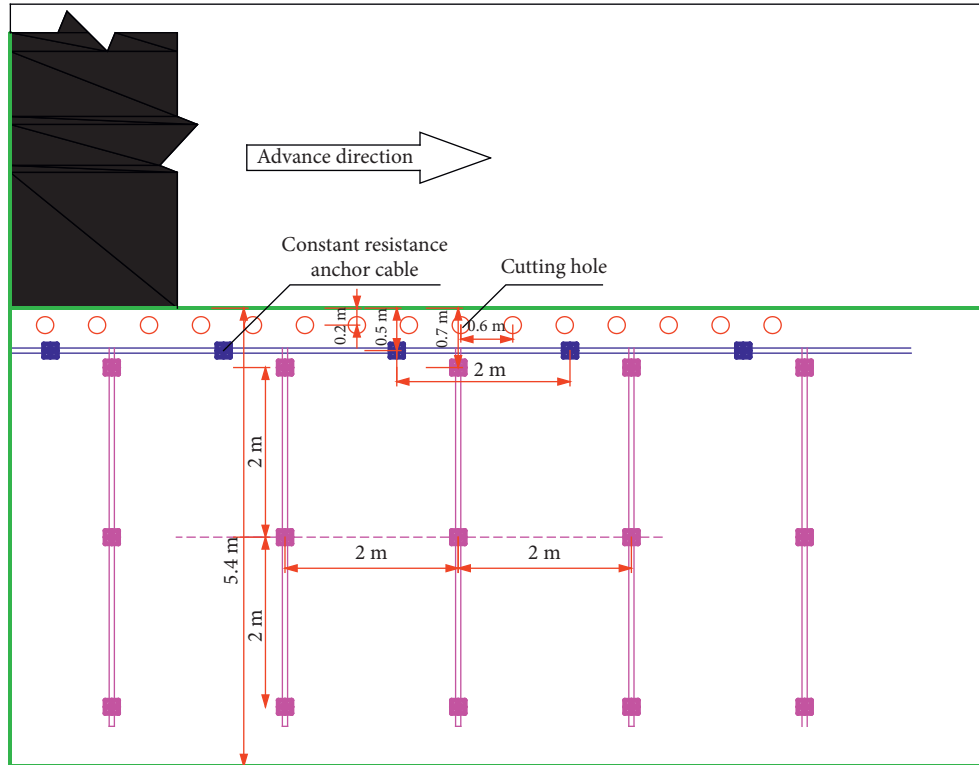


FIGURE 3: Slot hole layout plan.

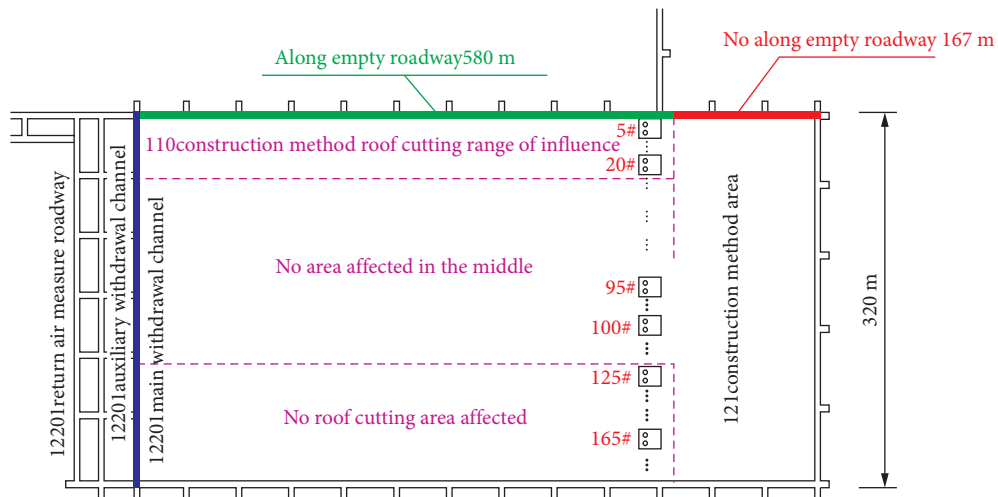


FIGURE 4: Division of the roof-cutting and pressure-relief roadway retaining project.

pushed to 173 m, the three supports enter the influence areas of roof cutting, pressure relief, and roadway retention. Table 1 lists the periodic pressure step distances of the 5#, 10#, and 20# brackets in the above two stages.

Compared with the conventional coal mining process area, the periodic pressure step distance in the area affected by the cutting of the roof unloading and retaining roadway increases by a range of 18–22 m, i.e., by approximately twofold. The periodic pressure step increased under the influence of roof cutting pressure relief shows large direct jacking height and small lumpiness at the end of the working

face (large coefficient of breaking expansion), the filling effect of goaf was good, the gangue formed into a burst could usually fill the goaf, and the base roof had less room for rotation. The smaller the rotation angle, the smaller the rotary deformation. As a result, the basic roof was not easy to break; the fracturing step was increased.

4.1.2. Support Resistance. In the process of advancing with the stope, the three supports passed through the conventional coal mining process area and the cutting roof

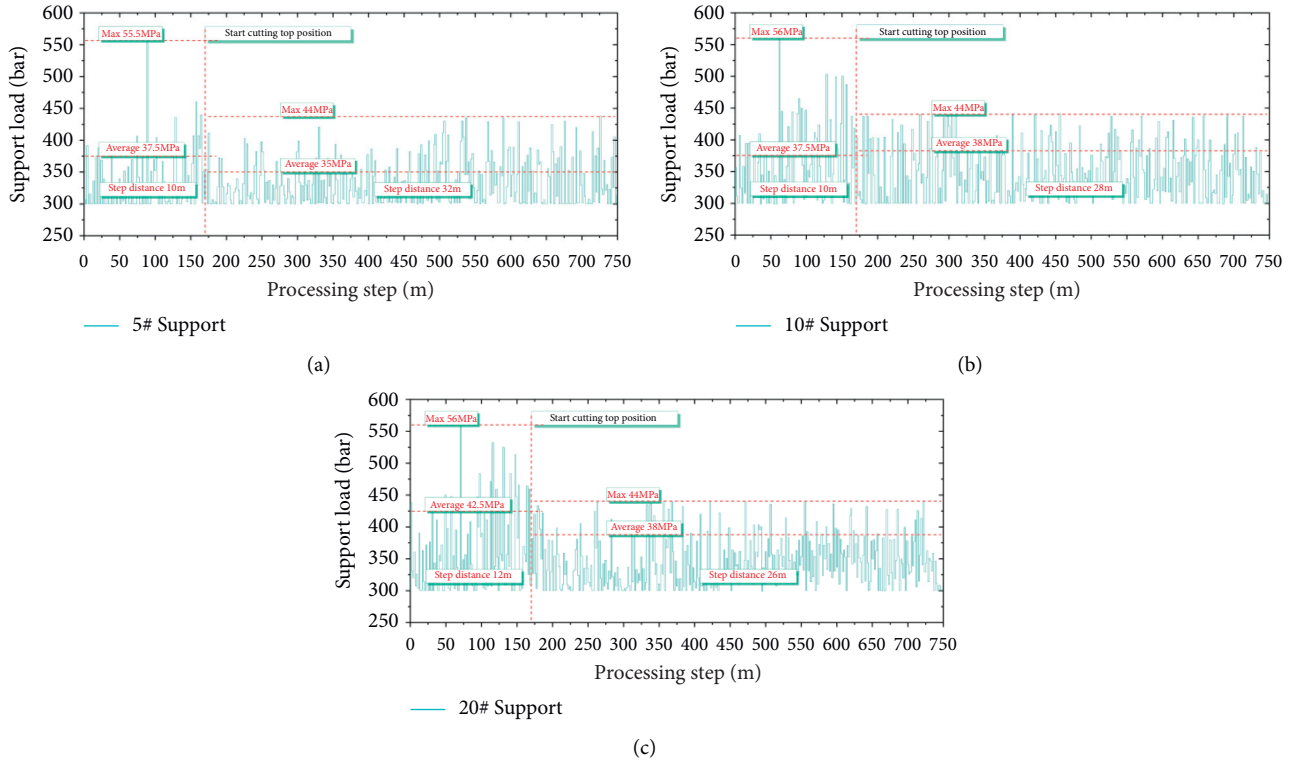


FIGURE 5: Load curves of support pillars in areas affected by roof cutting in the roof-unloading, retaining roadway: (a) No. 5, (b) No. 10, and (c) No. 20.

TABLE 1: Pressure cycle steps and pressure in areas affected by roof cutting in the roadway.

Hydraulic support	Conventional coal mining area (m)	Influence areas of cutting roof reserved for cutting-roof pressure relief (m)
No. 5	10	32
No. 10	10	28
No. 20	12	33

influenced areas of the roof unloading and retaining roadway. Table 2 provides the load statistics of the supports in the two stages.

The chart shows that, compared with the conventional coal mining process, the maximum pressure during the periods of roof cutting, pressure relief, and roadway retention was reduced by a range of 10–12 MPa or by approximately 20%. The basic roof fracture interval increased. However, the support working resistance decreased. The fracture step of the basic tip increased, but the working resistance of the support decreased. It showed that when the direct roof breaks down and falls behind, the broken and swollen gangue could basically fill the goaf under the influence of cutting head blasting. The base roof had less room to rotate. Therefore, the rotary deformation was also small, and the direct roof of the goaf retention lane was also small.

4.1.3. *Unaffected Area and Uncut Top Area in the Middle.* Figure 6 shows the load curves of the 95#, 100#, 125#, and 165# supports.

The maximum and average periodic pressures of the support in the middle of the working face were 60 and

44 MPa, and the step distance of the periodic pressure was in the range of 10–20 m. The maximum periodic pressure was 55 MPa, and the average value was 37 MPa. The step distance of the periodic pressure was in the range of 8–12 m. Based on the load curves of the support pillars in the middle unaffected area (95#, 100#) and uncut top area (125#, 165#), the values of the periodic pressure step and the support load are listed in Table 3.

4.2. *Analysis of the Variation Law of Force Expansion and Contraction of the Anchor Cable with Constant Resistance and Large Deformation.* Based on the advance of the working face and the arrangement of the anchor cable stress meter, we selected stress monitoring points 11# and 12# on the anchor cable, located 331 m away from the open-cut hole of the 12201 working face.

The analysis shows the following:

- (1) The advance concentrated stress generated by the advance of the working face had an impact on the stress of the anchor cable, and the advance influence range was generally up to 30 m, such as at the measuring points 15#, 14#, and 13#

TABLE 2: Support load (MPa) in areas affected by roof cutting in the roof-unloading and retaining roadway.

Hydraulic support	Conventional coal mining area			Influence area of cutting roof is reserved for cutting-roof pressure relief		
	Maximum	Minimum	Average	Maximum	Minimum	Average
No. 5	55.5	33	37.5	44	32	35
No. 10	56	31	37.5	44	30	38
No. 20	56	35	42.5	44	32	37.5

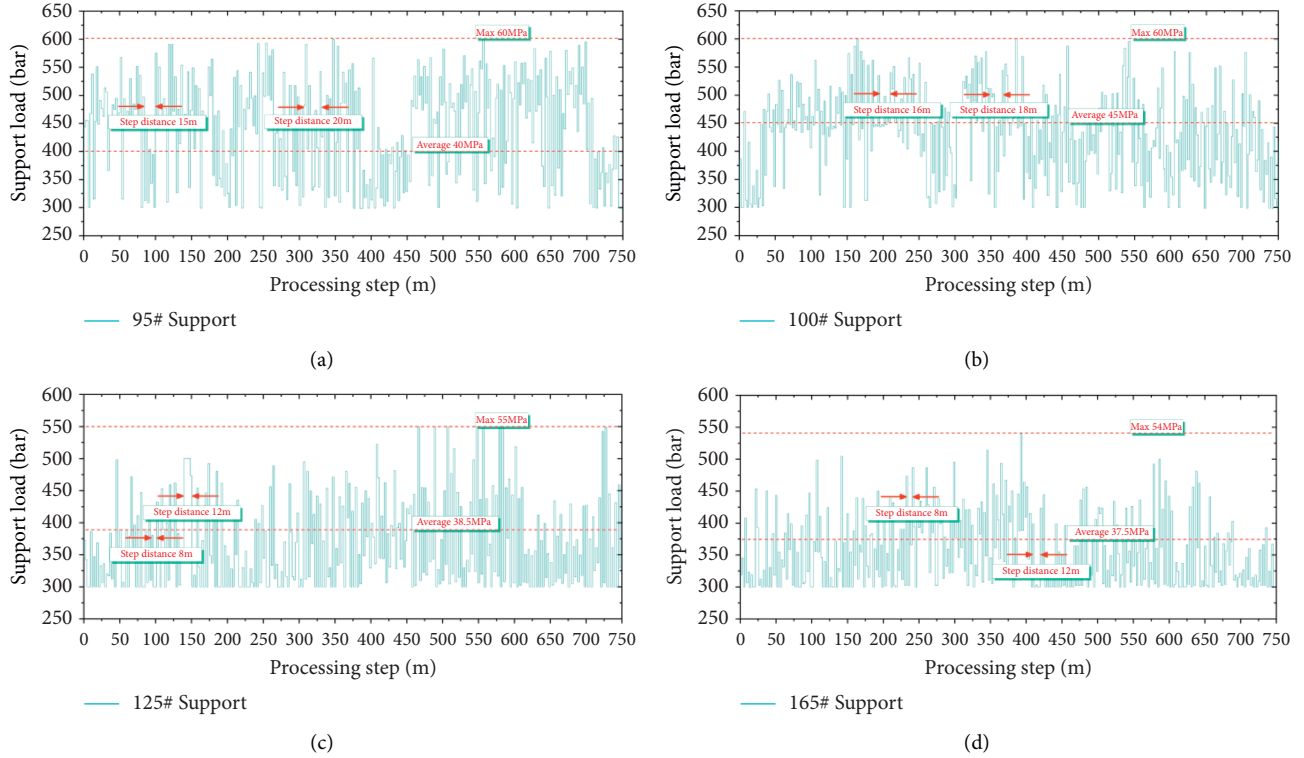


FIGURE 6: Pillar load curves of supports in the middle unaffected area and uncut top area: (a) No. 95, (b) No. 100, (c) No. 125, and (d) No. 165.

TABLE 3: Support load and periodic pressure step in the middle of the unaffected area and uncut top area.

Area	Hydraulic support	Hydraulic support load (MPa)			Periodic pressure step (m)
		Maximum	Minimum	Average	
Middle unaffected area	No. 95	60	32.5	44.2	10–20
	No. 100	60	34	45	10–20
Uncut top area	No. 125	55	32	38.5	8–12
	No. 165	54	31.5	37.5	8–12

(2) When the strike length of the goaf was equal to the trend length, the stress was concentrated, there was evident ore-pressure formation, the deformation of the roof and floor was large, and roof caving occurs easily

When the working face was pushed 319 m, a large stress concentration occurred, leading to an increase in the anchor stress value at the measuring points 11# and 12# in front of the working face. Figure 7 shows the change curve of the anchor stress value.

Table 4 presents the key position and maximum tensile stress on the stress curve of the anchor cable.

4.3. Analysis of the Variation Law of Roof Separation. Based on the advance of the working face and the arrangement of the roof separator, five monitoring points 1#, 2#, 4#, 5#, and 6# were selected, positioned 260, 280, 330, 430, and 480 m away from the open-cut eye of 12201 working face.

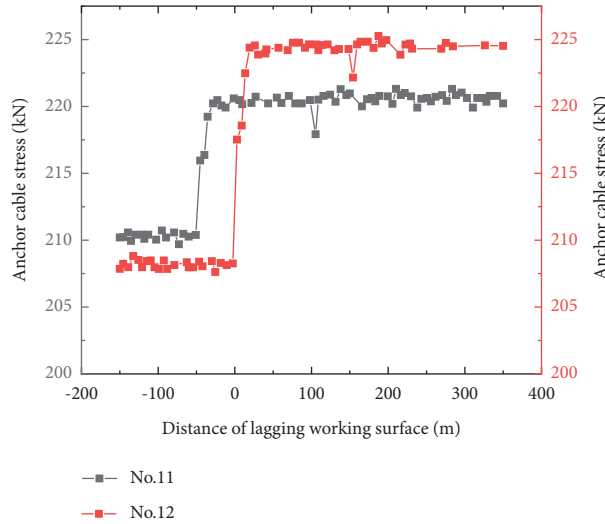


FIGURE 7: Variation curve of anchor cable stress obtained using a stress meter.

TABLE 4: Key positions and maximum tensile stress of the anchor cable stress change curve.

Anchor cable stress monitoring point	Distance from opening to 12201 sides (m)	Curve increases its starting position (lag face distance) (m)	Maximum tensile stress of the anchor cable (kN)
No. 15	241	-31	124.1
No. 14	261	-26	232.6
No. 13	281	-41	286.7
No. 12	331	-13 (fully mechanized face stopped to 319 m)	225.2
No. 11	381	-63 (fully mechanized face stopped to 319 m)	221.3

The analysis shows the following:

- (1) The advance of the working face had an impact on the roof separation of the roadway, which was generally within ± 50 m. When the roadway roof condition was poor, it was mainly affected by the advance concentrated stress of the working face, such as at measuring points 1# and 2#. When the roadway roof condition was good, it is mainly affected by the stress of the short-wall beam formed after mining, such as at measuring points 5# and 6#.
- (2) Based on the stable position of the curve at the monitoring points 4, 5, and 6, after the stopping of the working face, when the roof separation value tended to stabilize, the distances of the lagging working face were 81, 81, and 94 m, respectively.

In other words, when the distance of the lagging working face was greater than 95 m, the roadway roof separation tended to be stable. Figure 8 shows the variation curve of the roof separation value at the roof separation monitoring point. Table 5 shows the key position and maximum value of the roof separation change curve.

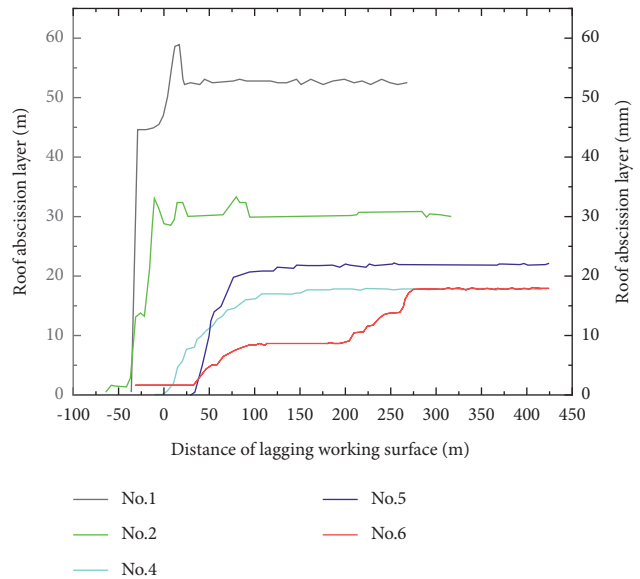


FIGURE 8: Variation curve of roof separation.

lagging single pillars (2#, 7#, 12#, and 13#) were selected, located 26, 73, 176, and 205 m away from the open-cut hole of the 12202 working face, respectively.

The analysis shows the following. (1) The abutment pressure of the lagging single pillar was mainly manifested in two ways. ① It quickly reaches the rated support force and

4.4. Analysis of the Variation Laws of the Abutment Pressure and Shrinkage under Lagging Single Pillar. Four monitoring points for the supporting pressure and shrinkage under

TABLE 5: Key positions and maximum value on the roof separation variation curve.

Roof separation monitoring point	Distance from opening to 12201 sides (m)	Curve increases its starting position (lag face distance) (m)	Curve starts at a smooth position (lag face distance) (m)	Maximum ceiling separation (mm)
No. 6	260	33	81	17.9
No. 5	280	31	82	22.0
No. 4	330	-2	94	17.8
No. 2	430	-48	8	33.4
No. 1	480	-34	-29	58.4

fluctuates in a certain range, such as at the pillar measurement points 7 and 12. ② After the working surface advances a certain distance, it gradually reached the rated support force and fluctuates within a certain range, such as at 2# and 13# pillar measuring points.

(2) From the stable position of the curve at the monitoring points 2, 7, 12, and 13, we found that after the stoping of the working face, when the maximum shrinkage under the active column tended to be stable, the distances of the lagging working face were 90, 92, 98, and 102 m, respectively.

When the distance of the hysteresis working face was greater than 100 m, the subsidence of the roadway roof tends to stabilize. This was consistent with the previous conclusion that “roadway roof separation tended to be stable only when the hysteresis working face distance was greater than 95 m.”

Figure 9 shows the curves of the abutment pressure and shrinkage under the active columns at the monitoring points on the single pillar. Table 6 shows the key positions and maximum value of the accumulated shrinkage of the active columns.

4.5. Analysis of the Variation Law of Roadway Lateral Pressure. Two side-pressure monitoring points were arranged at the side of the goaf of the roadway, 240 m and 302 m away from the open-cut hole of the 12202 working face. The maximum lateral pressure value at the monitoring point 1# is 2.0 MPa, and the average value was 1.7 MPa after stabilization, i.e., 30 m behind the working face. The maximum lateral pressure value at the monitoring point 2# is 0.8 MPa, and the average was 0.7 MPa after stabilization, i.e., 39 m from the lagging working face. Figure 10 shows the monitored lateral pressure values and their variation curves at the two lateral pressure monitoring points.

4.6. Comparative Analysis of Surface Deformation. A field observation showed that the surface deformation of the roof-cutting and the pressure-relief-retaining roadway was significantly lower than that under the conventional long-wall mining condition. The crack width was small, in the range of 1–3 mm. Table 7 compares the surface subsidence and damage. Figures 11 and 12 show a comparison of the surface fracture development zones and actual conditions.

Based on the above analysis, the roof movement along the goaf roadway could be divided into three stages: an active stage of direct roof caving, an active stage of basic roof breaking, and a stable roof stage.

4.6.1. Direct Jacking Falls Active Period. With the advance of the working face, the support constantly moved forward, and the roof strata at the rear of the working face lost support from the supports. The direct roof of the goaf side of the retention lane was under the action of cutting force generated by dead weight. The edge of the backfill near the direct roof roadway was broken. It is like an upside-down step in the state of the cantilever beam. At this stage, under the drive of the direct roof caving and the basic roof sinking, the deformation of the goaf roadway roof was mainly rotational deformation. The roof activity in this stage also was the direct roof-caving activity period. When the direct roof collapse could fill the goaf, the basic roof strata break and collapse. The basic roof could form a masonry structure to achieve stability in the balance process.

4.6.2. Active Period of Basic Roof Rupture. When the direct roof strata were not enough to fill the goaf, the basic roof strata would also collapse the flexure fracture, filling goaf forms masonry structure, and in the process of motion balance, because the stiffness of the coal body was greater than that of caved gangue in goaf. Therefore, the weight of the overburden on the basic roof was gradually transferred to the depth of the coal beside the roadway through the direct roof; stress concentration occurred in the deep part of the coal body and rotates with the basic roof block. The basic roof rock gradually stabilized under the support of falling gangue at the bottom, so that the surrounding rock stress along the goaf was lower than the original rock stress.

4.6.3. Roof Stabilization Period. The deformation is still largely driven by rotation, characterized by a high speed and magnitude. In this period, the deformation of the roof accounts for 60–70% of the total rotation-induced deformation of the roadway. With the gradual compaction of the gangue, the stable upper strata would also break, deform, and sink, thereby damaging the coal wall and even the direct roof. The abutment pressure range would increase, the peak value would continue to move inward, and the roof above the retaining roadway would sink in parallel. Because of the influence of the stratified collapse of the basic roof, the roof of the roadway would sink in a fluctuating manner. The roof movement was mainly parallel subsidence. However, the subsidence speed is low.

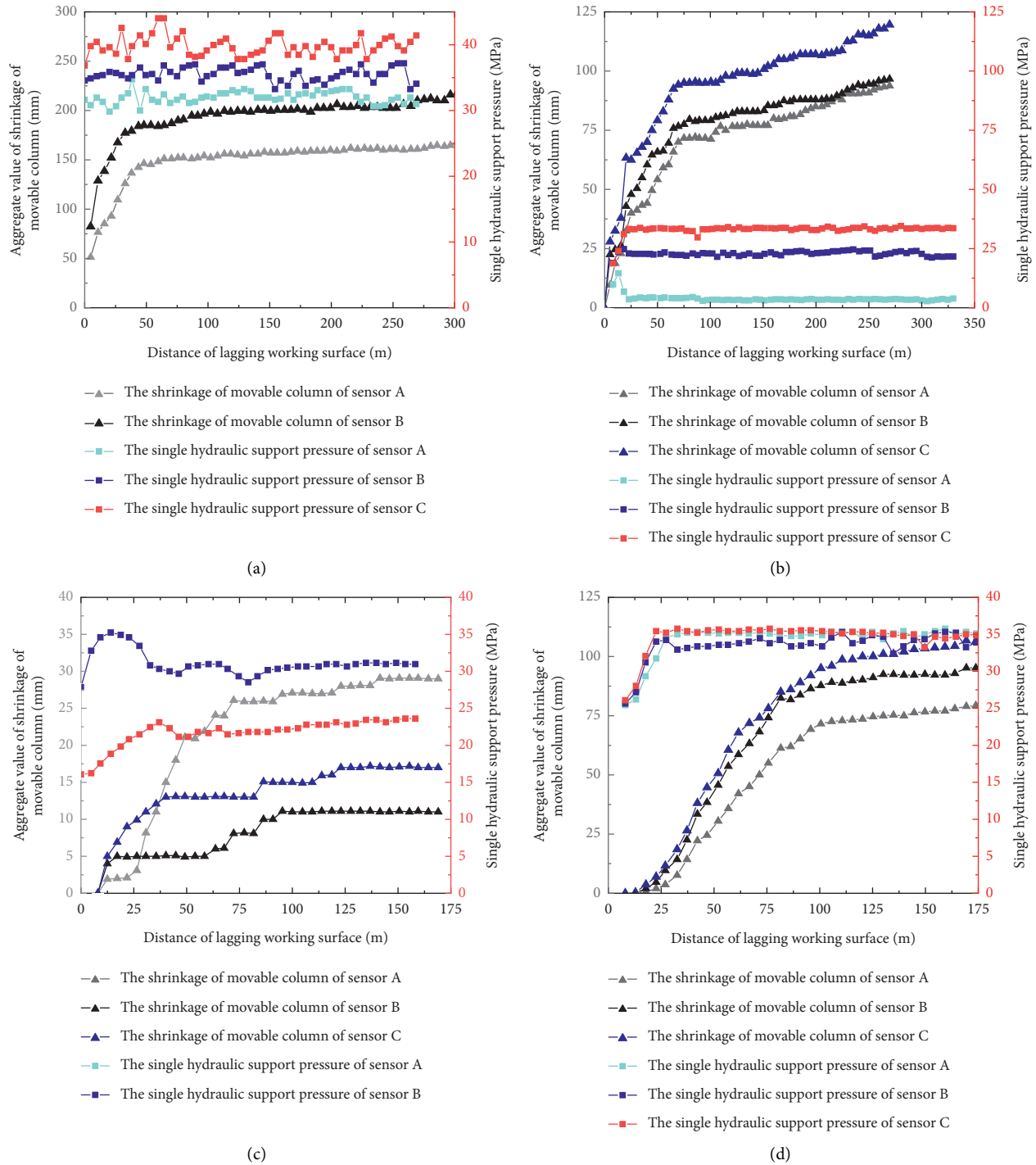


FIGURE 9: Data recorded at each monitoring point in the section along the hollow lane: (a) No. 2, (b) No. 7, (c) No. 12, and (d) No. 13.

5. Numerical Simulation of Mine Pressure Development in Shallow-Buried, Composite Roof-Cutting, Unloading Stope

To better study the mining pressure distribution rules of the automatic roadway formation working face under roof-cutting and pressure-relief conditions without coal pillar mining, we should analyze the movement mode of the stope roof and upper rock strata, understand the

movement mechanism and stress distribution of the surrounding rock more clearly, and effectively guide the selection of the support and corresponding equipment in the future.

Based on the actual situation on-site, a step-by-step numerical simulation of the mining process was carried out for a distance of 15 m each time, with the simulated stopping length being 60 m. The initial stresses imposed in the x -direction, y -direction, and z -direction are 10 MPa, 10 MPa,

TABLE 6: Key positions and maximum value of the accumulated lower shrinkage of active columns on the change curve.

Measure point	Curve starts at a smooth position (lag face distance) (m)	Maximum shrinkage under the active column (mm)
No. 2	92	217
No. 7	90	120
No. 12	98	29
No. 13	106	102

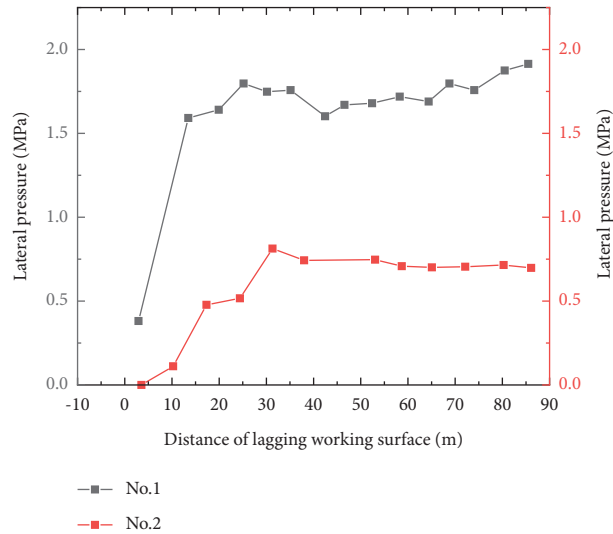


FIGURE 10: Variation curve of lateral pressure at the monitoring points.

TABLE 7: Comparison of surface subsidence and damage.

Classification	Cut off the roof pressure to leave the roadway area	Conventional coal mining area	Contrasting condition
Steps to sink (mm)	<5 mm	400–750 mm	Retaining roadway for roof-cutting pressure relief basically eliminate the step sinking
Crack width (mm)	1–3 mm	10–20 mm	Crack width reduction 75%
Crack interval (m)	30–40 m	8–10 m	Fracture density reduction 70%

and 15 MPa, respectively. The burial depth is set to 200 m. The working face width is 300 m.

As shown in Figure 13, when the working face was excavated for 15 m, the pressures on the tail and middle sides were relatively high. The vertical stress on the working face near the cutting seam alignment slot was 2.4 MPa and that on the end side was 3 MPa.

The horizontal stress on the working face close to the slotting groove was 0.9 MPa and that on the end side was 1.2 MPa. The pressure of the slotting groove was reduced by 25% compared with that on the end side.

As shown in Figure 14, after 30 m excavation of the working face, it experienced the initial pressure of the basic roof, and the initial pressure step distance was about 40 m. The overall pressure of the working face was small after the basic roof pressure at this time. The vertical stress of the working face close to the slotted groove was 2.09 MPa, the end side was 2.6 MPa, and the side pressure of the slotted groove was reduced by 20% compared with that of the end side. The horizontal stress on the working face close to the

slotted groove was 1.092 MPa and that on the end side was 1.4 MPa. The pressure on the slotted groove side was 22% less than that on the end side.

As shown in Figure 15, after 45 m of excavation, the vertical stress of the working face near the slotting groove was 1.8 MPa, whereas that on the tail side was 3.0 MPa. The side pressure of the slotting groove was reduced by 40% compared with that at the end. The horizontal stress on the working face close to the slotting groove was 0.9 MPa and that on the end side was 1.2 MPa. The pressure on the slotting groove side was reduced by 25% compared with that on the end side.

As shown in Figure 16, after 60 m of excavation, the working face experienced a periodic pressure, and the pressure step distance was 30 m. The vertical stress on the working face close to the slotted groove is 2.6 MPa, whereas that on the tail side was 3.12 MPa. The pressure on the slotted groove side was reduced by 30% compared with that at the end. The horizontal stress on the working face close to the slotting groove was 0.9 MPa and that on the end side was

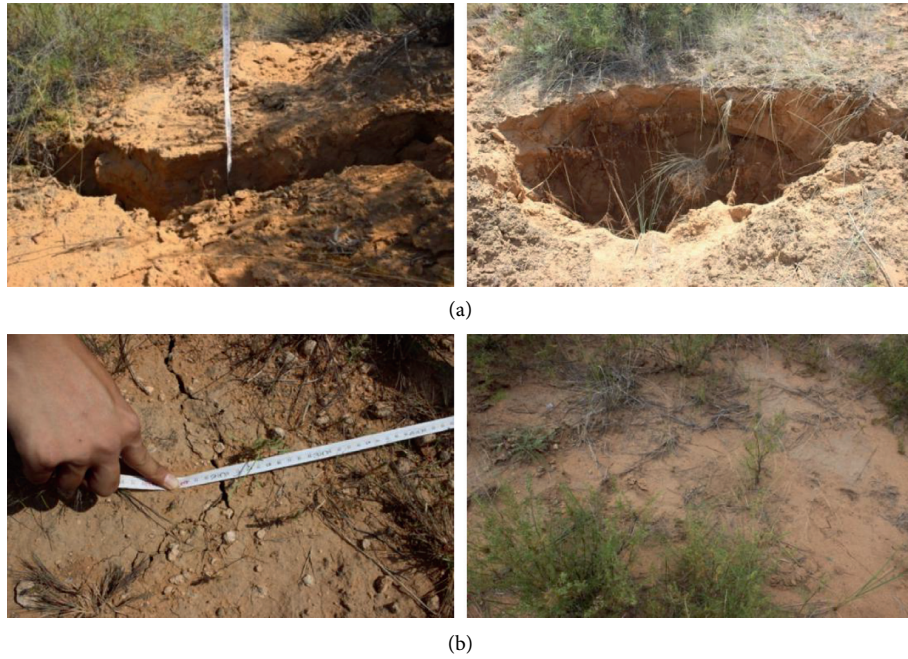


FIGURE 11: Comparison of surface fractures. (a) Surface fractures in the conventional coal mining process. (b) Surface cracks in the roadway retained by roof cutting and pressure relief.

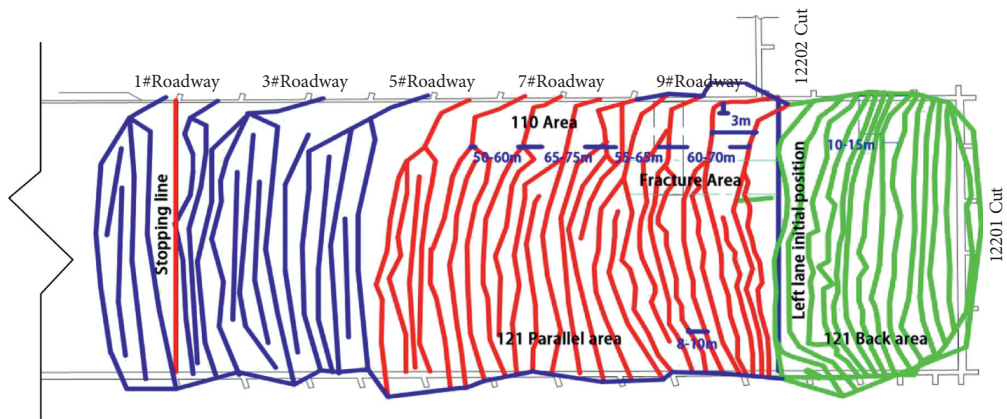


FIGURE 12: Surface fracture development zone comparison.

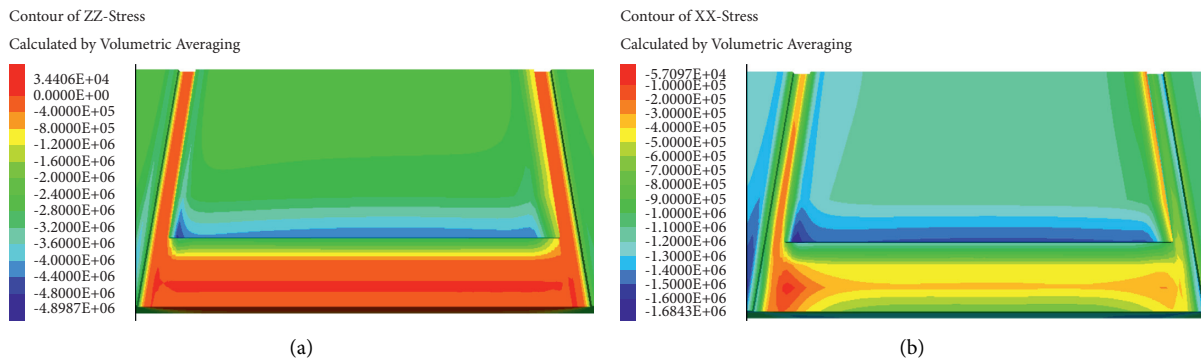


FIGURE 13: Stress distributions while excavating a face for 15 m. (a) Vertical stress. (b) Horizontal stress.

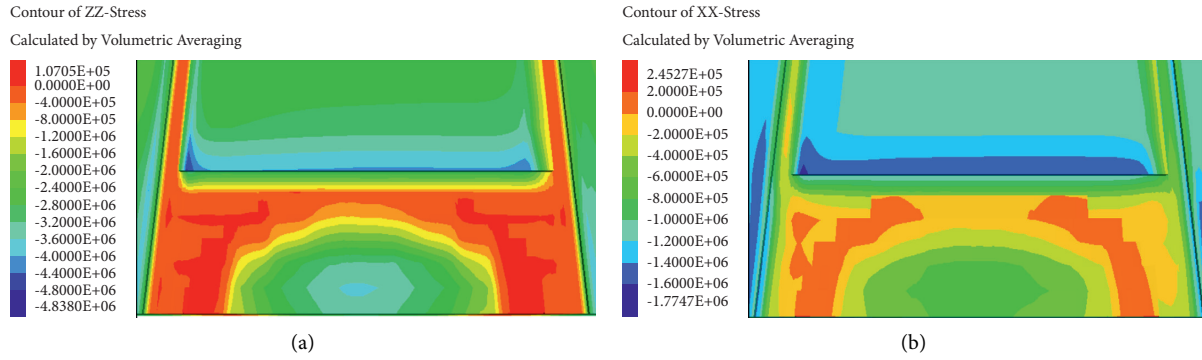


FIGURE 14: Stress distributions while excavating a face for 30 m. (a) Vertical stress. (b) Horizontal stress.

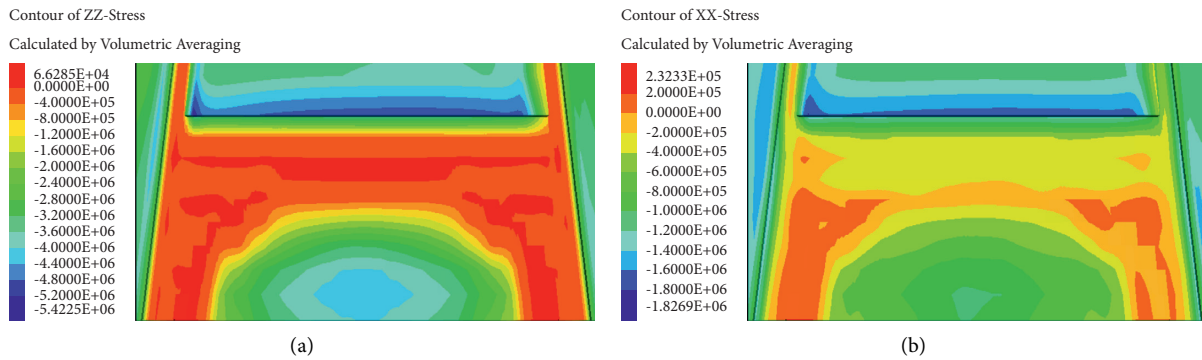


FIGURE 15: Stress distributions while excavating a face for 45 m. (a) Vertical stress. (b) Horizontal stress.

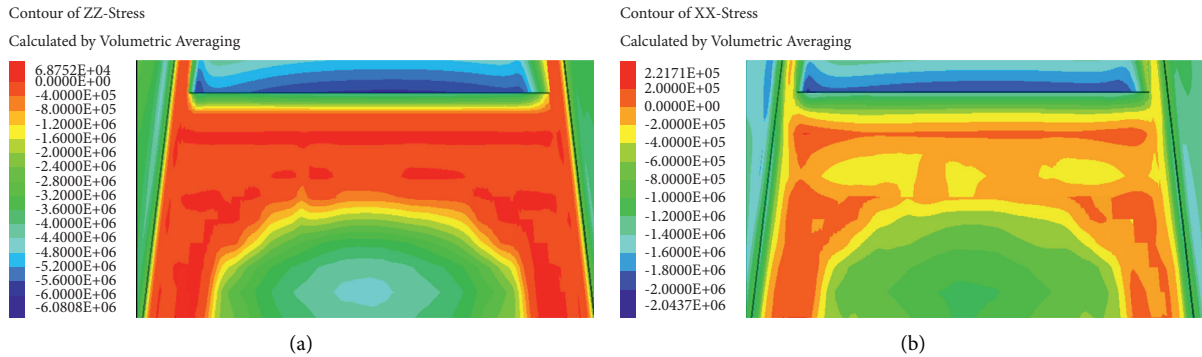


FIGURE 16: Stress distribution while excavating a face for 60 m. (a) Vertical stress. (b) Horizontal stress.

1.2 MPa. The pressure on the slotting groove side was reduced by 25% compared with that on the end side.

To sum up, in the cut after unloading without the coal pillar mining technology, the original stoppe stress distribution was changed, particularly on the cutting seam gateway side. After the mining face overburden formation of the cantilever beam structure, a protective space was formed along the trough; the safety of the tunnel was ensured. The original side pressure of the coal pillar along the trough was transferred to the depth of the adjacent working face. Moreover, the simulation results show that stress concentration was formed at 6 m away from the adjacent working face to the roadway, and the stress distribution of the original working face also changed.

By comparing the actual situation on-site with the numerical simulation, the following can be concluded:

- (1) The pressure on the working face of the slotting side was low, the vertical stress was reduced by approximately 27.5%, and the horizontal stress was reduced by 24.25%. The same numerical simulation shows that the influence range of the roadway on the mining pressure of the working face was 25 m, consistent with the actual measured data on-site.
- (2) The periodic pressure step of the working face was 30 m, and the actual on-site periodic pressure step was approximately 30 m, an increase of approximately 1 m compared with the original periodic pressure step.

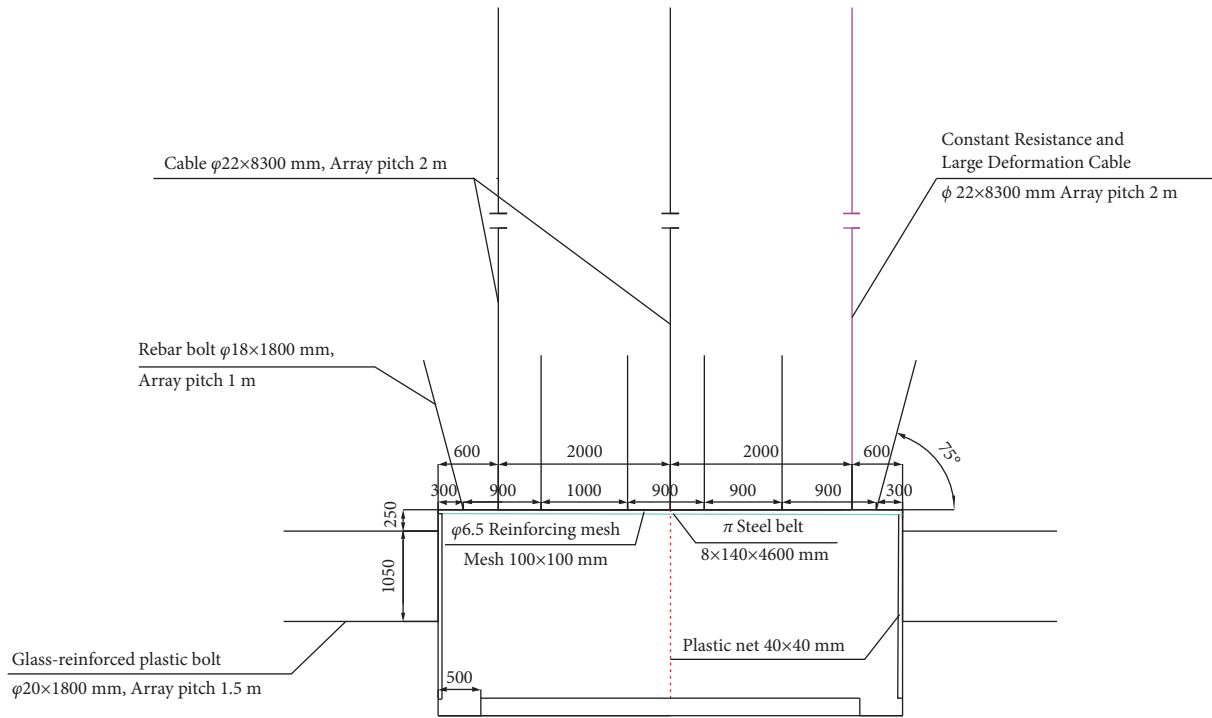


FIGURE 17: Design section of trough support.

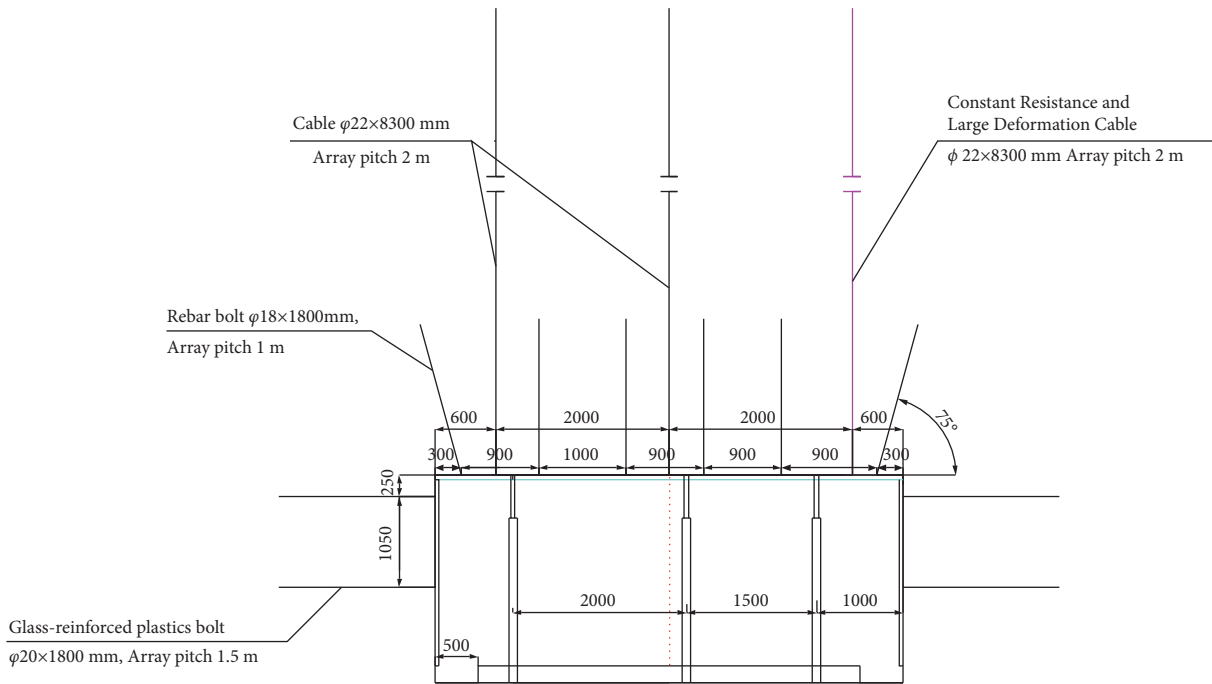


FIGURE 18: Sectional drawing of a single support in the lane.

(3) After the application of roof-cutting and pressure-relief technology, the stress above the original roadway was gradually transferred to the adjacent working face, forming a stress concentration inside the working face 6 m away from the retained roadway. Nevertheless, the retained roadway was in the stress-reduction zone, thus ensuring its safety.

6. Steady-State Control of the Surrounding Rock under Roof Pressure Relief

Based on the analysis results of field monitoring and numerical simulation, we optimized the relevant parameters of the coal-pillar-free mining technology for automatic roadway formation under the condition of a shallow-buried deep coal-bearing



FIGURE 19: Effect diagram of the roadway (a) before and (b) after optimization.

composite roof, to avoid repeated investment on support. The specific optimization parameters are as follows.

6.1. Support Parameters of the Chute

- ① The roof is supported by an ordinary anchor cable and large deformation anchor cable with constant resistance. Make a row of anchor and large deformation along the roadway strike at the reserved slit side. Anchor rod adopts rebar bolt; anchor cable was connected with type steel belt and spread 6.5 rigid mesh in the roof rock face.
- ② The upper part used a 20 mm × 2000 mm fiberglass bolt, the spacing between the rows was 1050 mm × 1500 mm, and the plastic mesh grid is 40 mm × 40 mm.
- ③ Roof anchor cable (common anchor cable and constant resistance large deformation anchor) used 22 mm × 8300 mm steel strand, with the row spacing of 2000 × 2000. Among them, the distance between the constant resistance and large deformation anchor cable was 600 mm, the rebar anchor rod was 18 mm × 1800 mm, and the spacing between rows was 900 mm × 1000 mm. The rock bolt near the side of the side and the vertical line were arranged at an angle of 15°. The steel belt was 8 mm × 140 mm × 4600 mm, the steel mesh was 6.6 mm in diameter, and the mesh size was 100 mm × 100 mm. Figure 17 shows the optimized supporting section along the groove.

6.2. Single Support in the Roadway. Based on the analysis of the practical application on-site, the influence of supporting pressure on the roadway was reduced after roof cutting, pressure relief, and roadway retention. The supporting form of the roadway could be “one beam and three columns,” as shown in Figure 18. Figure 19 shows the field application effect.

7. Conclusion

In this paper, through theoretical analysis, field measurement, and numerical simulation, the stability control of a roadway surrounding rock under roof-cutting and pressure-

relief conditions is studied. The main conclusions are as follows.

- (1) A stress model of a hard roof in an automatic roadway formation was established under roof-cutting and unloading conditions. A mechanical analysis was carried out on the deformation of the hard roof during roof cutting and unloading. When the working face was pushed past the cutting seam, the goaf roof was in a state of motion.
- (2) Based on a remote ore-pressure monitoring system, surface rock movement, and fracture observation, surface cracks and subsidence were significantly alleviated after roof cutting and pressure relief. Roadway roof movement could be divided into three stages: an active stage of direct roof caving, an active stage of basic roof breaking, and a stable roof stage. Through ore-pressure monitoring, compared with the conventional coal mining area, the affected area of roof-cutting pressure relief increased by 18–22 m, i.e., by approximately twice, a reduction of 20%. It could be known from the observation of drift separation, roof and floor displacement, anchor cable and pillar forced, and shrinkage of live columns. The deformation of the constant resistance anchor cable was less than the subsidence of the roof, which was mainly affected by the bending subsidence of the upper rock layer. However, in the control range of constant resistance anchor cable, the stratum separation value was small, which effectively improved the bearing function of the stratum. The influence range of face propulsion on cable stress was about 30 m and generally ±50 m from the coal of the working face. When the distance of the lagging working face was more than 100 m, the roadway roof separation and roof subsidence tended to be stable, and the maximum shrinkage under active columns was 217 mm. After the pillar was withdrawn for a week, the roof of the roadway tended to be stable. The accumulated subsidence was approximately 9 mm during the period.
- (3) A comparison between numerical simulation and actual working conditions showed that the working face pressure at the slotted side of the mining face

was low and that the vertical stress was reduced by approximately 27.5% and the horizontal stress by 24.25%. The influence range of the roadway on the working face's ore pressure was 25 m, and the working face's periodic pressure step distance was 30 m, consistent with the field measured data. After the application of roof-cutting and pressure-relief technology, the stress above the original roadway was gradually transferred to the adjacent working face, forming a stress concentration inside the working face 6 m away from the retained roadway. Nevertheless, the retained roadway was in the stress-reduction zone, thus ensuring the safety of the roadway.

- (4) Based on theoretical analysis, field measurement, and numerical simulation, we developed an integral control method for the surrounding rock of the roadway formed by the automatic roof cutting and pressure relief of the 12201 fully mechanized mining face, Halagou Coal Mine. A constant resistance and large deformation anchor cable was added to the side near the cut joint for active support, and a single-hydraulic prop +11# I-steel + steel mesh was used for a combined support at the back of the working face support. A grouting bolt support was used to reinforce the broken loose surrounding rocks at the gangue-retaining side of the tunnel. Through the optimization of the support design, the surrounding rock control effect was found to be remarkable.

Data Availability

The data used to support the findings of this study are included within the article.

Conflicts of Interest

The authors declare no conflicts of interest.

Acknowledgments

This work was supported by Liaoning Provincial Education Department Fund (LJ2017FAL002), Liaoning Innovation and Entrepreneurship Training Plan for College Students (2017101470001), and China Postdoctoral Science Foundation (2020M680490).

References

- [1] N. Zhang, C. L. Han, and J. G. Kaniaguang, "The theory and practice of surrounding rock control in retaining roadway along the goaf," *Journal of China Coal Society*, vol. 39, no. 8, pp. 1635–1641, 2014.
- [2] Y. Chen, J. B. Bai, and X. Y. Wang, "Research and application of support technology in retaining roadway along goaf," *Journal of China Coal Society*, vol. 37, no. 6, pp. 903–910, 2012.
- [3] Q. L. Liu and M. Wang, "The technology of coal pillar less mining in the roadway along the goaf in fully mechanized caving face," *Coal Science and Technology*, vol. 44, no. 5, pp. 122–127, 2016.
- [4] X. G. Ma, J. Wang, and H. L. Wu, "Experimental study on topless blasting of coal pillar less mining face in Tashan Coal mine," *Coal Science and Technology*, vol. 46, no. S1, pp. 27–32, 2018.
- [5] X. H. Zhang, P. F. Guo, and J. Wang, "Study on optimization experiment of pressure relief borehole spacing along the roadway," *Coal Technology*, vol. 35, no. 6, pp. 6–8, 2016.
- [6] Y. J. Wang, M. C. He, and K. X. Zhang, "Characteristics and control measures of mine pressure in mine roadway without coal pillars," *Journal of mining and Safety Engineering*, vol. 35, no. 4, pp. 677–685, 2018.
- [7] J. W. Guo and J. W. Zhao, "Study on the breaking rule and control mechanism of the lower roof of the retaining roadway along the goaf," *Journal of mining and Safety Engineering*, vol. 29, no. 6, pp. 802–807, 2012.
- [8] S. K. Palei and S. K. Das, "Sensitivity analysis of support safety factor for predicting the effects of contributing parameters on roof falls in underground coal mines," *International Journal of Coal Geology*, vol. 75, no. 4, pp. 241–247, 2008.
- [9] M. Lars, "Interaction of shotcrete with rock and rock bolts," *Science Direct*, vol. 45, pp. 538–553, 2007.
- [10] J. Hematian, I. Porter, and N. I. Aziz, "Design of roadway support using a strain softening model," in *Proceedings of the 13th International Conference. Ground Control in Mining*, Charlottesville, Virginia, August 1994.
- [11] B. G. D. Smart and D. O. Davies, "Application of the rock-title approach to pack design in an Arch-sharped roadway," *Mining Engineer*, vol. 12, 1982.
- [12] N. G. Baxter, T. P. Watson, and B. N. Whittaker, "A study of the application of T-H support systems in coal mine gate roadways in the UK," *Mining Science and Technology*, vol. 10, no. 2, pp. 167–176, 1990.
- [13] G. Williams, "Roof bolting in south wales," *Colliery Guardian*, vol. 11, 2004.
- [14] S. Bjurstrom, "Shear strength of hard rock joints reinforced by grouted tensioned bolts," *Proc. of 3rd Congress, ISRM Denver*, vol. II, 1974.
- [15] H. H. Sun and B. L. Zhao, *Theory and Practice of Gob Side Entry Retaining*, Coal Industry Press, Pennsylvania, PA, USA, 1993.
- [16] H. M. Li, "Design of roof strata control for gob side entry retaining," *Journal of rock mechanics and engineering*, vol. 19, no. 5, pp. 651–654, 2000.
- [17] T. Y. Qi, Y. Guo, and C. Hou, "Study on Adaptability of integral pouring roadway protection belt along gob side entry retaining," *Acta Sinica Sinica*, vol. 24, no. 3, pp. 256–260, 1999.
- [18] X. Z. Hua, J. F. Ma, and T. J. Xu, "Reinforcement support and parameter optimization of anchor cable beside gob side entry retaining," *Coal Science and Technology*, vol. 32, no. 8, pp. 60–64, 2004.
- [19] X. M. Sun and J. Yang, "Study on space-time action law of bolt mesh cable coupling support in deep mining roadway," *Journal of rock mechanics and engineering*, vol. 26, no. 5, pp. 895–897, 2007.
- [20] X. M. Fei, "Discussion on the present situation and existing problems of gob side entry retaining support technology in China," *China Science and technology information*, vol. 21, no. 3, pp. 31–33, 2008.
- [21] M. C. He and G. Qi, "Deformation failure mechanism and coupling support design of deep composite roof coal roadway," *Journal of rock mechanics and engineering*, vol. 26, no. 5, pp. 988–991, 2007.
- [22] X. M. Sun and M. C. He, "Study on nonlinear design method of bolt mesh cable coupling support for deep soft rock

- roadway," *Journal of rock mechanics and engineering*, vol. 27, no. 7, pp. 1061–1065, 2006.
- [23] X. W. Feng and Z. W. Zhang, "Surrounding rock control technology of rigid flexible secondary coupling support in deep coal roadway," *Mine pressure and roof management*, vol. 4, pp. 18–20, 2001.
- [24] F. Peng and X. M. Sun, "Study on the coupling support technology of anchor net and cable in deep coal roadway," *Mine Pressure and Roof Management*, vol. 4, pp. 21–24, 2001.
- [25] B. D. Han and C. Y. Peng, "Strata pressure behavior and control of gob side entry retaining," *Coal Science and Technology*, vol. 10, no. 3, pp. 5–8, 2000.
- [26] J. X. Liu, P. F. Gou, and Y. S. Zhang, "Analysis of strata pressure behavior in gob side entry retaining," *Ground pressure and roof management*, vol. 7, no. 3, pp. 1–6, 1996.
- [27] S. L. Lu, *Ground Pressure Behavior of Roadway Protection without Coal Pillars*, pp. 55–56, Coal Industry Press, Pennsylvania, PA, USA, 1982.
- [28] X. M. Guan, L. Lu, and L. S. Zhai, "Study on the law of mine pressure behavior when driving roadway along the goaf in fully mechanized caving face," *Mine pressure and roof management*, vol. 17, pp. 30–33, 2000.
- [29] H. M. Li and M. Gu, "Experimental study on gob side entry retaining of No. 9 coal seam in Jincheng mining area," *Journal of Jiaozuo Institute of Technology (NATURAL SCIENCE EDITION)*, vol. 3, pp. 90–93, 2000.
- [30] H. H. Sun, J. Wu, and Y. X. Qiu, "Strata behavior and strata control of gob side entry retaining," *Acta coal Sinica*, vol. 1, 1992.
- [31] J. Q. Jiang, *Stress and Movement of Stope Surrounding Rock*, Coal Industry Press, Pennsylvania, PA, USA, 1993.
- [32] D. Y. Li, *Study on Surrounding Rock Stability of Fully Mechanized Top Coal Caving Face*, Taiyuan University of Technology, Taiyuan, China, 2004.
- [33] Q. M. Chen, "Ground pressure behavior characteristics and control technology of gob side entry in fully mechanized top coal caving face," *Acta coal Sinica*, vol. 8, pp. 382–385, 1998.
- [34] Y. J. Yang and Y. L. Tan, "Study on the relationship between the deformation affected by mining and the width of coal pillar of roadway protection," *Jiangsu coal*, vol. 3, pp. 9–10, 1995.
- [35] D. R. Zhu, *Fracture Law of Main Roof in Longwall Face and its Application*, China University of mining and Technology, Xuzhou, China, 1987.
- [36] M. C. He and G. F. Zhang, "Study on the technology of no pillar mining in protective layer of Baijiao Coal Mine by cutting roof along goaf," *Journal of mining and safety engineering*, vol. 21, no. 4, pp. 511–513, 2011.
- [37] H. Liu, "Study on the technology of automatic coal roadway without coal pillars in large depth and medium thick seam of Chengjiao Coal mine," *Energy and Environment Protection*, vol. 40, no. 11, pp. 193–198, 2018.
- [38] H. H. Yang, E. L. Xue, and W. Luo, "Application of Shenhua Group's top-loading pressure relief automatic roadway without coal pillar mining technology," *Coal Science and Technology*, vol. 3, pp. 1–3, 2015.
- [39] M. C. He, W. F. Cao, and R. L. Shang, "A new technology of two-dimensional shaped energy stretch blasting," *Chinese Journal of Rock Mechanics and Engineering*, vol. 12, pp. 2047–2051, 2003.
- [40] M. C. He, Y. B. Gao, and J. Yang, "Experimental study on self-forming tunnel of quick-recovery and top-loading unloading and non-coal pillar in thick coal seam," *Rock and Soil Mechanics*, vol. 39, no. 1, pp. 254–264, 2018.
- [41] Y. B. Gao, J. Yang, and M. C. He, "Study on deformation mechanism and control technology of gravel gangway without coal pillar cutting in thick coal seam," *Chinese Journal of Rock Mechanics and Engineering*, vol. 36, no. 10, pp. 2492–2502, 2017.
- [42] G. F. Zhang, M. C. He, and X. P. Yu, "Study on mining technology of non-coal pillars along the goaf of Baijimine protection layer," *Journal of mining and Safety Engineering*, vol. 28, no. 4, pp. 511–516, 2011.
- [43] E. L. Xue, Z. H. Ma, and W. Luo, "Study on the mining pressure law of automatic roadway with shallow top-buried composite roof under pressure relief," *Coal Science and Technology*, vol. 2017, no. s1, pp. 34–38, 2017.
- [44] K. Wang, T. H. Kang, and H. T. Li, "Study on the method of controlling roof placement and reasonable suspension length of hard roof," *Chinese Journal of Rock Mechanics and Engineering*, vol. 28, no. 11, pp. 2320–2327, 2009.
- [45] Z. H. Chen, J. J. Feng, and C. C. Xiao, "Mechanical model of roof fracture in fully mechanized top coal caving mining in shallow deep seam," *Journal of China Coal Society*, vol. 32, no. 5, pp. 449–452, 2007.
- [46] P. F. Guo, G. F. Zhang, and Z. G. Tao, "Blasting technology of roadway retaining in hard and weak composite roof with top pressure relief," *Coal Science and Technology*, vol. 44, no. 10, pp. 120–124, 2016.
- [47] Z. B. Guo, J. Wang, and T. P. Cao, "Study on key parameters of automatic roadway of thin coal seam cutting and pressure relieving," *Journal of China University of Mining and Technology*, vol. 45, no. 5, pp. 879–885, 2016.

Research Article

Identification of Initial Crack and Fracture Development Monitoring under Uniaxial Compression of Coal with High Bump Proneness

Zuoqing Bi, Han Liang , and Qianjia Hui

College of Mining Engineering, Liaoning Technical University, Fuxin 123000, China

Correspondence should be addressed to Han Liang; 18641822228@163.com

Received 5 August 2021; Accepted 30 November 2021; Published 21 December 2021

Academic Editor: Jia Lin

Copyright © 2021 Zuoqing Bi et al. This is an open access article distributed under the Creative Commons Attribution License, which permits unrestricted use, distribution, and reproduction in any medium, provided the original work is properly cited.

The rock burst proneness of coal is closely related to the coal mass structure. Therefore, the initial crack distribution of high burst proneness coal, its fracture development, and failure process under loading conditions are of great significance for the prediction of rock burst. In this study, high burst proneness coal is used to prepare experiment samples. The surface cracks of the samples are identified and recorded. The internal crack of the sample is detected by nuclear magnetic resonance (NMR) technology to determine the crack ratio of each sample. Then, 3D-CAD technology is used to restore the initial crack of the samples. Uniaxial compression test is carried out, and AE properties are recorded in the test. The stress-strain curve, the distribution of the fractural points within the sample at different stress states, and the relationship between ring count and stress are obtained. Results show that the stress-strain curves of high burst proneness coal are almost linear, to which the stress-ring count curves are similar. The distributions of fractural points in different bearing states show that the fracture points emerge in the later load stage and finally penetrate to form macrofracture, resulting in sample failure. This study reveals the initial crack distribution of coal with high burst proneness and the fracture development under bearing conditions, which provides a theoretical basis for the prediction technology of rock burst and technical support for the research of coal structure.

1. Introduction

Coal bump, or coal burst, is a type of violent geological disaster that is described by sudden and rapid destruction of coal mass around the roadway or a coal pillar, causing casualties and significant economic loss. Along with deep underground mining, coal bump has become a major disaster for major coal-producing countries. For example, as the biggest producer and consumer of coal in the world, China currently has 132 burst proneness coal mines with an average mining depth of 653 m [1].

There are many factors related to rock burst. Firstly, geological conditions, such as buried depth, faults, and folds, are closely related to rock burst [2, 3]. Horizontal tectonic stress is identified as the force source of rock burst [4–6]. Rock burst may also be related to gas and water contents and their migration [7–9]. Mining-related disturbances are also an important factor to inducing rock burst [10–13]. In addition,

the property of coal and rock mass itself, that is, the so-called burst proneness, is another important factor in the occurrence of rock burst [14–17].

Coal is composed by matrix material and joints. Therefore, the impact tendency of coal is related to the structure of coal [18–20]. Regarding the research on the relationship between coal macrofracture and rock burst, Yin et al. [21] used CT technology to carry out uniaxial compressive test to analysis the CT of coal in each deformational stage from microcrack initiation, bifurcation, development, fracture, and failure. Pan et al. [22] analysed the energy storage and consumption of coal from the perspective of microstructure and constructed a quantitative relationship between the lithologic fabric of the coal and its impact tendency. Zhao et al. [23] used X-ray diffraction, SEM, and microphotometer to analyse the strength of coal burst proneness and obtained the relationship between coal internal mesostructural parameters and burst proneness. Jiang et al. [24] used

TABLE 1: Average physical and mechanical parameters of the coals.

Density (kg/m ³)	Compressive strength (MPa)	Tensile strength (MPa)	Cohesion (MPa)	Internal friction angle (°)	Elastic modulus (GPa)	Poisson ratio
1350	30.00	3.89	5.16	29.27	4.62	0.32

XRD, paramagnetic resonance, and SEM to obtain the structure of coal samples before and after rock burst and explored the characteristics of energy dissipation in the process of rock burst. Wu and Liu [25] studied the relationship between the pore development and the burst proneness of coal in the SEM image through the fractal method and proposed that the larger the fractal dimension is, the smaller the burst proneness is.

These studies show that the coal burst proneness is closely related to the coal structure. However, there are few methods to identify the initial cracks in coal body and to examine the fracture development under loading conditions, resulting in difficulties in the study of rock burst. In this study, the initial cracks of coal were identified by nuclear magnetic resonance (NMR) technology and represented by 3D-CAD technology. Acoustic emission (AE) technology is used to monitor the internal fracture point of coal under uniaxial compression, which is used to analyse the fracture development of the coal sample. This study provides a basis for the study of the relationship between coal structure and coal burst proneness and provides a technical support for coal burst prediction.

2. Materials and Methods

2.1. Sample Preparation. The coal samples studied in this paper were taken from Xinzhouyao Coal Mine, Datong, China. The average compressive strength of the coal samples is approximate 30 MPa with high bump proneness. Standard rock mechanics testing was conducted to measure the physical and mechanical parameters of the coals, including compressive, Brazilian tensile, varying angle shearing tests. The testing results of the samples are shown in Table 1.

For sample preparation, the coal blocks were cut by a cutting machine and then taken the core by a coring machine. Coal samples were finally processed into standard cylindrical specimens with dimensions of 50 mm (in diameter) \times 100 mm (in length), as shown in Figure 1. Sample preparation was in accordance with the International Rock Mechanics Test Recommendation (IRTM) that the error of the parallelism depth between the upper and lower surfaces was within 0.02 mm. To assure the accuracy of the experiment, 9 coal specimens were prepared.

After sample preparation, the cracks in the sample surface were measured. The main cracks of each sample before testing are listed in Table 2.

2.2. Experiment Equipment

2.2.1. NMR. The NMR equipment is shown in Figure 2. The applied intensity of the magnetic field is 0.3-0.5 T, and the main frequency of the instrument is 12 MHz. To ensure that



FIGURE 1: Prepared coal samples.

the sample is in the middle of the magnetic field, the coil diameter of the magnetic field was selected as 60 mm. The analysis equipment is a nuclear magnetic imaging software and a gradient pulse instrument. The imaging software can set the slice width, number of slices, and slice gap of the sample. After positioning, prescanning, formal scanning, and imaging of the sample, the crack structure inside the sample is displayed in the form of slices.

2.2.2. Loading Machine and AE Devices. WAW-600C computer-aided electrohydraulic servo universal testing machine is used to conduct the compressive test. AE monitoring device is simultaneously instrumented to observe the dynamic response of the specimen structure under uniaxial loading. The maximum loading capability is 600 kN, the measuring amplitude ranges from 2% to 100% of the maximum loads, the maximum piston rising velocity is 70 mm/min, the lifting velocity of the loading plate is 150 mm/min, the maximum piston stroke is 250 mm, and the maximum distance between the compression plates is 500 mm.

The AE technology is an effective method to detect the dynamic change of the material structure under the action of external loading through instrumentation. Each channel of the data acquisition system consists of measuring instrument, digital signal processor, computation program, and other peripheral apparatus, which are finally connected to a computer. The components of each channel include an AE sensor, a preamplifier, and a data acquisition card, as shown in Figure 3.

TABLE 2: The initial surface crack of each coal sample.

Crack no.	Position (mm)	Direction	Length (mm)	Width (mm)	Thickness (mm)	
1	1	Top 5.2	Horizontal	23.8	13.2	0.25
2	1	Bottom 12.3	Horizontal 30°	25.8	9.5	0.96
3	1	Bottom 38	Horizontal 45°	27.6	13.8	0.62
	2	Inclined	Vertical	25.3	19.3	0.78
4	1	Bottom 5	Horizontal	19.2	17	0.36
5	1	Top 45	Horizontal	33.1	16.4	0.40
	2	Top	Vertical	24.3	13.2	0.42
6	1	Top 55	Horizontal	19.5	17.9	1.00
	2	Top 50	Horizontal	27.4	16.3	0.3
	3	Top 10	Vertical	21.3	10.1	0.22
7	1	Top-middle	Vertical	38.3	15.3	0.1
8	1	Top-middle	Vertical	48.3	9.3	0.3
	2	Middle	Horizontal 80°	30.1	18.2	0.25
9	1	Bottom 10	Horizontal	26.3	16.1	0.5
	2	Bottom 20	Horizontal	28.4	15.0	0.5
	3	Bottom 35	Horizontal	23.4	21.5	0.52
	2	Bottom	Vertical	51.3	22.4	0.28
	3	Top 15	Horizontal	18.4	16.7	0.4
	4	Top 17	Vertical	23.4	8.4	0.23



FIGURE 2: NMR instrument.

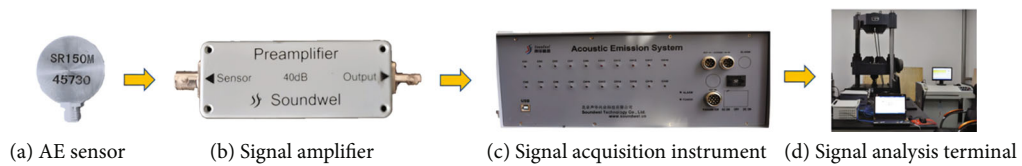


FIGURE 3: Acoustic emission signal transmission process.

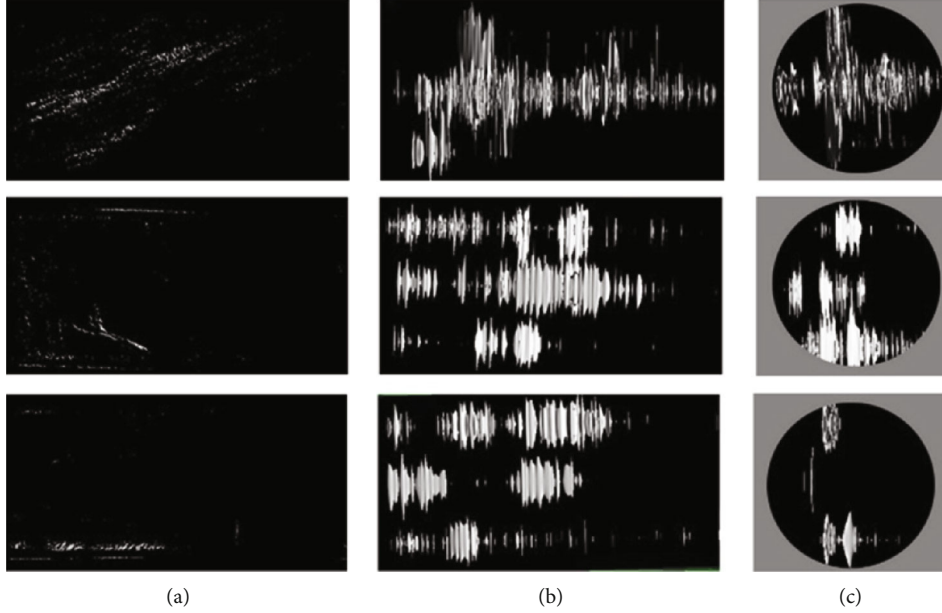


FIGURE 4: NMR reconstruction of coal samples: (a) main view, (b) top view, and (c) side view.



FIGURE 5: Testing procedure.

2.3. Experimental Procedure

2.3.1. Initial Crack Identification Using NMR. The internal crack distribution of the sample can be obtained by processing the 3D slice map using NMR 3D reconstruction software. The NMR 3D reconstruction map of typical samples is shown in Figure 4, in which the white areas indicate the crack.

2.3.2. Uniaxial Compressive Test. The uniaxial compression testing system and the AE monitoring system are used to dynamically monitor the experimental data. The uniaxial compression testing machine is controlled by displacement with a loading rate of 0.5 mm/min. For parameters of the AE instrument, the threshold of the AE monitoring is set as 45 dB to minimize the effect of surrounding noises. The peak definition time (PDT), the hit definition time (HDT),

TABLE 3: Dimension and crack ratio of coal sample.

Sample no.	Diameter (mm)	Height (mm)	Crack ratio (%)
1	50.14	100.84	0.04
2	50.21	100.10	0.12
3	50.11	100.03	0.32
4	50.17	100.05	0.06
5	50.12	100.63	0.18
6	50.08	100.42	0.27
7	50.04	100.04	0.03
8	50.17	100.84	0.14
9	50.02	100.45	0.35

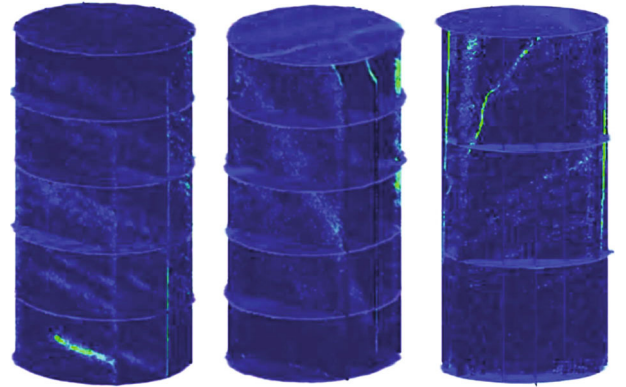


FIGURE 6: 3D-CAD sample reconstruction diagram.

and the hit locking time (HLT) are selected as 300, 600, and 1000 μ s, respectively. The sound velocity is set to be 1.8 km/s.

After parameter setting was completed, fusing test was conducted on the specimen to verify the sensitivity of each

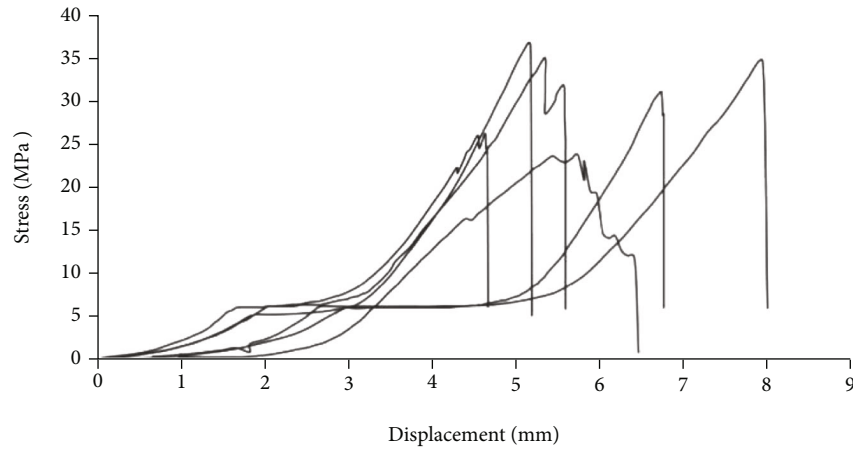


FIGURE 7: Stress-strain curves of testing sample.

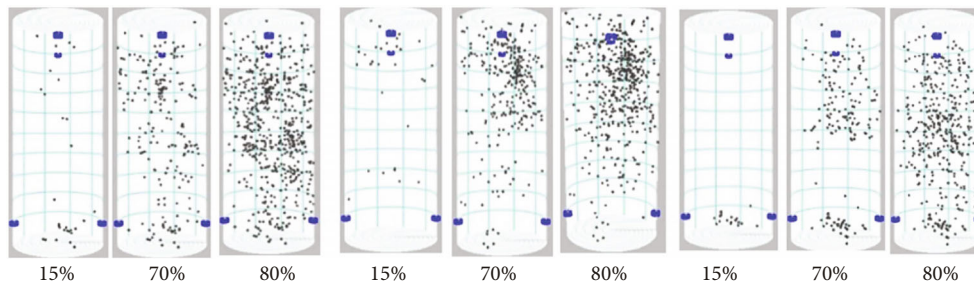


FIGURE 8: Distributions of the fractured sources of specimens 1-3.

sensor to guarantee the reliability of the experiment. Coupling agent needs be evenly pasted on the interface between the sensor and the testing sample for high-quality acquisition data. A piece of paper was placed between the testing machine and the specimen to eliminate friction. After the parameter setting and fusing testing are completed, uniaxial compression tests are carried out. The stress loading system and the AE monitoring system were turned on simultaneously. The experimental arrangement is shown in Figure 5.

3. Results and Discussion

3.1. Initial Crack Ratio. According to the NMR data, the initial crack ratio can be calculated. As the internal crack of the sample is an irregular body, to simplify the calculation, the internal crack of the sample is regarded as a regular cuboid, and the parameter index is length, width, and height. The crack ratio of each coal sample is shown in Table 3.

3.2. 3D-CAD Reconstruction of Initial Cracks. By import the 3D slice diagram of the sample into CAD software, the 3D-CAD reconstruction diagram of the initial cracks can be obtained. It provides a digital description for crack and fracture parameters, which can be used for fractural mechanism study and mesa-data analysis. Typical 3D-CAD crack reconstruction diagram of coal sample before testing is shown in Figure 6.

3.3. Results of Uniaxial Compression Tests. Figure 7 shows stress-strain curves of the testing samples. The deformational behaviour of hard coal shows a brittle property. After the compaction stage, the compressive stiffness of the coal is nearly uniform until sample failure.

3.4. AE Fracturing Point Distribution. The AE monitoring device identifies the locations of the fractured points in the coal specimen through sound waves released in the failing process of the specimen. Figure 8 shows the distributions of the wave sources at the stress levels of 15%, 70%, and 80% of peak stress of three testing samples.

Result shows that, along with increasing of axial load, the AE activities in the specimen increase, and the AE events are distributed nearly symmetrically along the central axis of the specimen. The AE events of the hard coal specimens are mainly concentrated near the central axis of the specimen, indicating there is a strong energy accumulation around the central axis. The AE events of the soft coal specimens are more sparsely distributed in the coal specimens and slightly concentrated near the middle part of the specimens.

3.5. AE Counts under Different Loading Conditions. AE count, also called ring count or ringdown count, refers to the number of times that the wave signals formed in AE beyond the threshold value. In this experiment, each wave signal exceeding the threshold is recorded as one AE count, which is regarded as one crack damage in the specimen. The

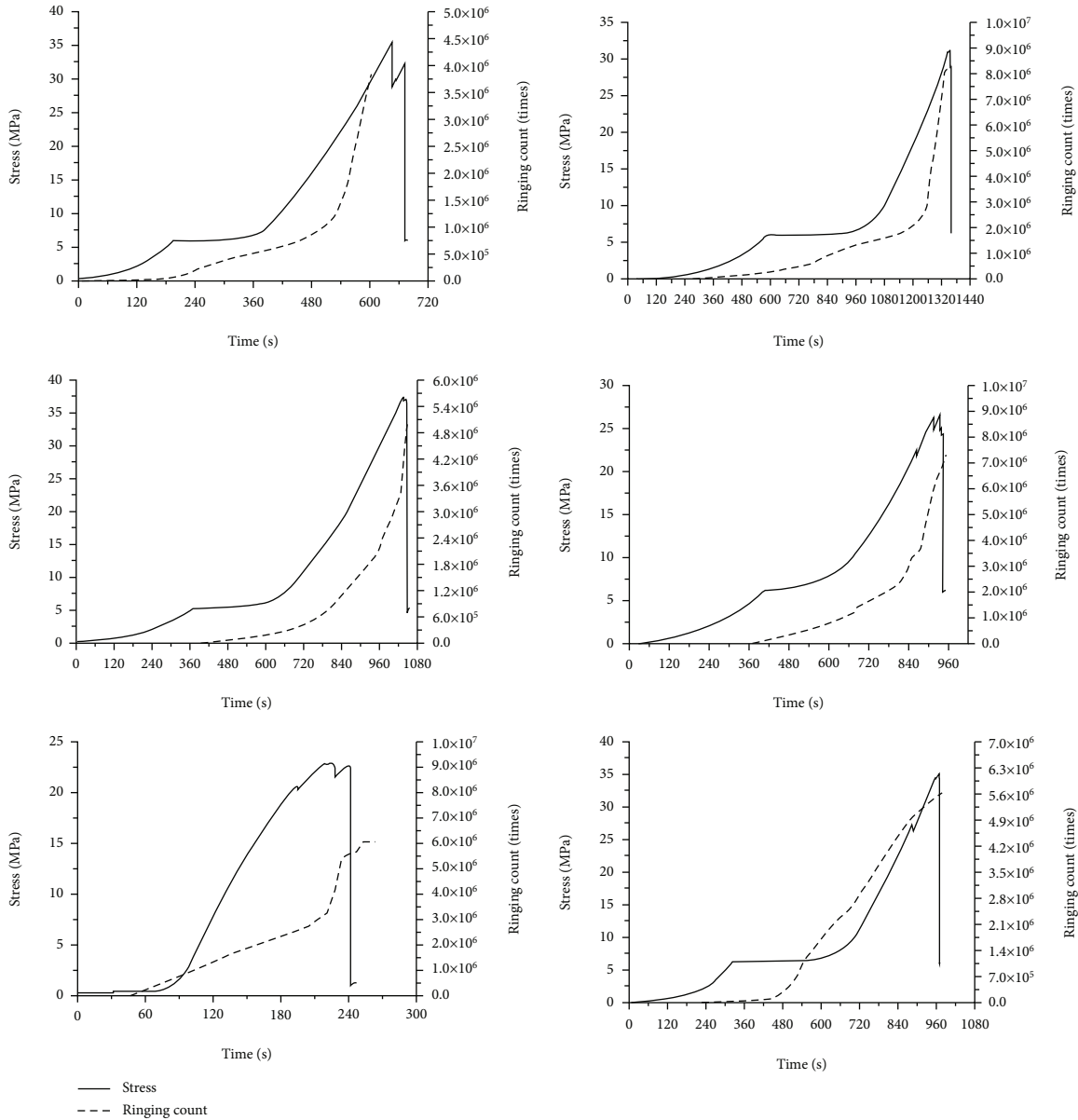


FIGURE 9: AE count results of specimens 1-6.

more AE counts suggest the more damage in the specimen at that moment. The number of the AE counts changes with time, as illustrated in Figure 9.

Result shows that the AE counts of the specimen appear in the early stage, and the maximum number is from 3.8×10^6 to 8.2×10^6 with average about 6.0×10^6 . It suggests that the coal specimens with higher strength have a slow growth of the AE events at the early stage of the loading process. At the middle elastic stage, the fractured sources increase gradually, and at the end of the linear stage, the AE fractured points increase sharply.

4. Discussion

Traditionally, the deformation of coal under uniaxial compression is divided into the following five stages: compaction, elastic, elasto-plastic, strain-softening, and residual

[26, 27]. In the compaction stage, the pore space and primary microcracks are compressed along with stress increasing. Elastic and elastoplastic stages are featured by linear relationship between the stress and strain. The specimen is compressed more tightly, and microcracks begin to develop within the specimen. In the strain softening stage, cracks propagate rapidly to form macrofracture. The peak stress is a point indicating failure of the coal sample along the main fracture. After peak, the deformation of the sample enters residual stage, in which the stress is residual strength of the coal.

For coal with high bump proneness, the testing result of this study suggests that, from the compaction to strain softening stage, the stress-strain curve is nearly linear, and the residual strength of the hard coal is close to zero rapidly. It suggests that such deformational behaviour is a feature for coal mass with high burst proneness.

AE event is often appeared in cluster model [28]. By comparing the fractured source locations at different stress levels, the testing result shows that, for hard coal, it has less AE events and when the loading stress is within the range of 10% to 20% of the peak stress. When the stress increases to 70%-80% of the peak value, the AE events became more active, suggesting rapid crack propagation in the coal specimen. After the stress reaches more than 80% of the peak stress, macrocracks propagate and expand rapidly and merge with each other, leading sudden failure of the specimen. It indicates that the AE events of hard coal increase slightly at the early stage of the compression. Then, it increases steadily in the linear elastic stage and increases sharply after linear elastic stage. Accordingly, the specimen undergoes primary crack coalescence, expansion, stable propagation, and ultimate macroscopic failure.

Combining the AE events with the deformational behaviour in the testing process, it suggests that, for hard coal, the cracks are developed in the later linear stage; that is, the AE counts comply with the growth of semiexponential function. The peak AE account of the coal specimen with high burst proneness takes place prepeak stress as the failure mode of the specimen is brittle; *i.e.*, there is nearly no energy that dissipates after the peak stress.

5. Conclusions

To study the structure of high burst proneness coal, NMR, 3D-CAD, and AE technology were used to identify the initial cracks and fracture development of coal samples under uniaxial compression condition. The following conclusions can be drawn.

- (1) The initial crack in the sample is detected by NMR, and the crack ratio of each sample is obtained, which is a dominant factor on the bearing performance and deformation characteristics of the coal sample. By observing the surface cracks of the sample, the initial cracks can be restored by 3D-CAD
- (2) The uniaxial compression test results show that the stress-strain curve of the sample has a remarkably high linearity, indicating that the coal with high burst proneness has the characteristic of brittleness
- (3) In the process of uniaxial compression, the relationship between ring count and stress is obtained by using AE technology. The results show that the increase of ring count is consistent with the change of stress. Therefore, for coal with high burst proneness, the monitoring of ring counts is an effective means of stress analysis
- (4) Through the analysis of fracture point distribution in different loading stages, it is considered that the fracture development of coal with high burst proneness is mainly concentrated in the later loading stage

This study reveals the initial crack distribution of coal with high burst proneness and the fracture development

under bearing conditions, which provides a theoretical basis for the prediction technology of rock burst and technical support for the research of coal structure.

Data Availability

All data of this article has been included in this manuscript.

Conflicts of Interest

The authors declare that there is no conflict of interest regarding the publication of this paper.

Acknowledgments

This work was financially supported by the National Natural Science Fund of China (51774174).

References

- [1] Q. X. Qi, Y. Z. Li, S. K. Zhao et al., "70 years development of coal mine rockburst in China: establishment and consideration of theory and technology system," *Coal Science and Technology*, vol. 47, no. 9, pp. 1–40, 2019.
- [2] Y. Jiang and Y. Zhao, "Research status of coal mine rockburst in China: mechanism, early warning and control," *Journal of Rock Mechanics and Engineering*, vol. 34, pp. 2188–2204, 2015.
- [3] K. Wang and F. Du, "Coal-gas compound dynamic disasters in China: a review," *Process Safety and Environmental Protection*, vol. 133, pp. 1–17, 2020.
- [4] Q. X. Qi, T. Q. Liu, and Y. W. Shi, "Mechanism of friction sliding de-stability of rock burst," *Mine Pressure and Roof Management*, vol. Z1, 1995.
- [5] S. Wang, D. Li, C. Li, C. Zhang, and Y. Zhang, "Thermal radiation characteristics of stress evolution of a circular tunnel excavation under different confining pressures," *Tunnelling and Underground Space Technology*, vol. 78, pp. 76–83, 2018.
- [6] J. Han, H. Liang, C. Cao, Z. Bi, and Z. Zhu, "A mechanical model for sheared joints based on Mohr-Coulomb material properties," *Géotechnique Letters*, vol. 8, no. 2, pp. 92–96, 2018.
- [7] L. Zhang, J. H. Li, J. H. Xue, C. Zhang, and X. Fang, "Experimental studies on the changing characteristics of the gas flow capacity on bituminous coal in CO₂-ECBM and N₂-ECBM," *Fuel*, vol. 291, article 120115, 2021.
- [8] J. Lin, T. Ren, G. Wang, P. Booth, and J. Némcik, "Experimental investigation of N₂ injection to enhance gas drainage in CO₂-rich low permeable seam," *Fuel*, vol. 215, pp. 665–674, 2018.
- [9] J. Lin, T. Ren, Y. P. Cheng, J. Némcik, and G. Wang, "Cyclic N₂ injection for enhanced coal seam gas recovery: a laboratory study," *Energy*, vol. 188, article 116115, 2019.
- [10] L. Dou and Z. Mu, *Rockburst Prevention and Control of Coal Mine*, Science Press, Beijing, China, 2018.
- [11] D. J. Xue, J. Wang, Y. Zhao, and H. Zhou, "Quantitative determination of mining-induced discontinuous stress drop in coal," *International Journal of Rock Mechanics and Mining Sciences*, vol. 111, pp. 1–11, 2018.
- [12] Q. Qingxin, C. Shangben, W. Huaixin, M. Debing, and W. Yongxiu, "Study on relations among coal bump, rockburst and mining tremor with numerical simulation," *Chinese Journal of Rock Mechanics and Engineering*, vol. 11, pp. 1852–1858, 2003.

- [13] D. J. Xue, Y. T. Liu, H. W. Zhou, J. Q. Wang, J. F. Liu, and J. Zhou, "Fractal characterization on anisotropy and fractal reconstruction of rough surface of granite under orthogonal shear," *Rock Mechanics and Rock Engineering*, vol. 53, no. 3, pp. 1225–1242, 2020.
- [14] Y. Jiang, Y. Pan, and F. Jiang, "State of the art review on mechanism and prevention of rock bumps in China," *Journal of China Coal Society*, vol. 39, no. 2, pp. 205–213, 2014.
- [15] W. Liu, Y. Jiang, H. Zhou, and Z. H. Chen, "Experimental study on outburst proneness coal seam of meso character and crack destabilization," *Journal of Hunan University of Science & Technology*, vol. 21, no. 4, pp. 14–18, 2006.
- [16] F. Jiang, Q. Wei, and S. Yao, "Key theory and technical analysis on mine pressure bumping prevention and control," *Coal Science and Technology*, vol. 41, no. 6, pp. 6–9, 2013.
- [17] Z. C. Feng and Y. S. Zhao, "Correlativity of rock inhomogeneity and rock burst trend," *Chinese Journal of Rock Mechanics and Engineering*, vol. 22, no. 11, pp. 1863–1865, 2003.
- [18] F. du, K. Wang, X. Zhang, C. Xin, L. Shu, and G. Wang, "Experimental study of coal-gas outburst: insights from coal-rock structure, gas pressure and adsorptivity," *Natural Resources Research*, vol. 29, no. 4, pp. 2481–2493, 2020.
- [19] L. Zhang, S. Chen, C. Zhang, X. Fang, and S. Li, "The characterization of bituminous coal microstructure and permeability by liquid nitrogen fracturing based on μ CT technology," *Fuel*, vol. 262, article 116635, 2020.
- [20] Y. X. Zhao, Y. D. Jiang, and S. P. Tian, "Investigation on the characteristics of energy dissipation in the preparation process of coal bumps," *Journal of China Coal Society*, vol. 35, no. 12, pp. 1979–1983, 2010.
- [21] G. Z. Yin, G. F. Dai, W. L. Pi, and D. W. Li, "CT experiment of coal rock damage evolution law under uniaxial compression load," *Chongqing University Journal*, vol. 26, no. 6, pp. 96–100, 2003.
- [22] J. N. Pan, Z. P. Meng, and B. M. Liu, "Relationship between rock composition and texture of coal-bearing formation and its burst potential," *Chinese Journal of Rock Mechanics and Engineering*, vol. 24, no. 24, pp. 4422–4427, 2005.
- [23] Y. X. Zhao, Y. D. Jiang, and Y. Zhang, "The relationship between bump-prone property and microstructure characteristics of coal," *Journal of China Coal Society*, vol. 32, no. 1, pp. 64–68, 2007.
- [24] Y. Jiang, Y. Lu, Y. Zhao, Y. Song, and L. Tao, "Multiparameter monitoring experiments for instability destruction of coal samples," *Chinese Journal of Rock Mechanics and Engineering*, vol. 31, no. 4, pp. 667–674, 2012.
- [25] X. Wu and C. W. Liu, "Evaluation of impact tendency of coal rock based on surface fractal features," *Underground Space and Engineering*, vol. 9, no. 5, pp. 1045–1049, 2013.
- [26] F. Du and K. Wang, "Unstable failure of gas-bearing coal-rock combination bodies: insights from physical experiments and numerical simulations," *Process Safety and Environmental Protection*, vol. 129, pp. 264–279, 2019.
- [27] L. Xue-wei, L. Quan-sheng, C. Yuan, and L. Qiang, "Experimental study of effects of fracture type on strength characteristic and failure modes of fractured rockmass," *Rock and Soil Mechanics*, vol. 36, no. S2, pp. 208–214, 2015.
- [28] D. Xue, L. Lu, J. Zhou, L. Lu, and Y. Liu, "Cluster modeling of the short-range correlation of acoustically emitted scattering signals," *International Journal of Coal Science & Technology*, vol. 8, pp. 1–15, 2021.

Research Article

Optimization of the Plastic Area of a Borehole Based on the Gas Extraction Effect and Its Engineering Application

Kuan Wu,^{1,2} Shiliang Shi ,¹ Yi Lu,¹ He Li,¹ and Min Li¹

¹Hunan University of Science and Technology, School of Resource, Environment and Safety Engineering, Xiangtan, Hunan 411201, China

²Hunan University of Science and Technology, Work Safety Key Lab on Prevention and Control of Gas and Roof Disasters for Southern Coal Mines, Xiangtan, Hunan 411201, China

Correspondence should be addressed to Shiliang Shi; sslhust@yeah.net

Received 22 July 2021; Accepted 15 October 2021; Published 11 November 2021

Academic Editor: Bo Tan

Copyright © 2021 Kuan Wu et al. This is an open access article distributed under the Creative Commons Attribution License, which permits unrestricted use, distribution, and reproduction in any medium, provided the original work is properly cited.

Gas extraction is most commonly used to control gas disasters in coal mines. The distribution of the plastic zone around a borehole and the sealing quality are key factors affecting gas extraction. In this paper, the plastic zone was simulated by COMSOL, and a theoretical equation of the plastic zone radius was derived. In addition, an antispray hole equipment and the “two plugging and one injection” sealing technology were proposed. The results show that a larger borehole pore size corresponds to a larger plastic zone and larger range of pressure relief of the borehole. The error between the calculated and simulated plastic zone radii is within 1%, and the modified equation is applicable to Puxi mine. The loss and harm caused by borehole spraying are reduced by applying antispray hole equipment. By applying the “two plugging and one injection” sealing technology and phosphogypsum-based self-produced gas expansion paste material to block the borehole, the sealing quality is improved and an accurate gas mixing flow, pure flow, and concentration were obtained. As the plastic zone enlarges, the gas extraction flow gradually increases with, but the relative variation of flow first increases and subsequently decreases. Considering the safety and economy of construction, the optimal radius of the plastic zone is 64.9 mm.

1. Introduction

Coal is a type of energy used throughout the world, and it is widely used in the power, fuel, and oil industries [1–4]. However, with the continuous depletion of shallow coal reserves and the increasing demand for coal, coal mine disasters gradually increase with the increase of the mining depth [5–8]. Among coal mine disasters, gas disasters are considered the most serious threat to the safety of China’s coal industry [9–13]. Over the past 70 years, there have been 25 catastrophic coal mine accidents, which have killed more than 100 people in China, and 18 of these accidents were gas disasters [14, 15]. Therefore, to prevent coal and gas outburst in the coal mining process, gas drainage, high-pressure water injection hydraulic fracturing, mine ventilation dilution gas, protective coal mining, and other technical measures are usually adopted in coal mines, among which gas drainage is the most commonly used method [16–19]. In some high-gas-

content mines in South China, drilling through the layer is often performed to control gas disasters [20–22].

One of the main factors affecting the effect of gas drainage is the borehole diameter [23–25]. Once a borehole is formed, the coal body around the borehole undergoes pressure relief and plastic damage, forming plastic zone for gas migration [26–29]. At present, based on the elastic-plastic theory, Guo et al. [30] studied the stress distribution characteristics and pressure relief range of coal around the borehole by analysing the borehole stress and air leakage form. Cheng et al. [31] established the mechanical model of borehole softening and expansion based on the Hoek Brown criterion and deduced the elastic area, plastic softening area, and fracture around the borehole. Su [32] used theoretical analysis and numerical simulation to analyse the failure mechanism of the coal body in a bedding hole, which formed the elastic deformation area around the hole. The stress distribution and displacement equation of the coal

body in the plastic softening zone and the pressure relief fracture zone were analysed.

Another main factor that affects the effect of gas drainage is the sealing quality of the borehole [33, 34]. In recent years, many new sealing methods and sealing materials have been proposed by a number of scholars. Zhang et al. [35, 36] developed the “strong-weak-strong” borehole sealing technology, which can improve the CMM drainage efficiency of a single high-gas low-permeability coal seam. Liu et al. [37] tested 10 groups of sealing materials and presented a new sealing method and an appropriate sealing equipment, including an automatic grout pump and two types of rubber bottom subs, which were used to improve the sealing performance of inclined cross-measure drainage boreholes. Zhou et al. [38] proposed a second-sealing-plugging technology for gas drainage and examined the migration law of gas movement in the fracture network of the coal seam. Ni et al. [39] studied the microcharacteristics of borehole sealing materials composed of frozen composite material with PU and expansive cement. Xiang et al. [40] developed a flexible gel sealing material and experimentally compared its sealing performance with that of conventional sealing materials. Ge et al. [41] conceived a novel hydraulic fracturing sealing material composed of cement, hardening, accelerating, and water-reducing admixtures; polypropylene fibre; and mixing water. Despite the emergence of new technologies and materials for anti-air leakage, these methods increase the drainage efficiency on the premise of a long sealing depth, which increases the construction difficulty and cost of sealing boreholes. An economical and effective sealing method with a short sealing depth for in-seam boreholes is necessary to prolong the efficient continuous drainage time and increase the drainage amount of methane [42–45].

In this paper, based on the elastic-plastic theory, the COMSOL simulation software was used to simulate the plastic area range of the coal body around a drill hole and verify whether the plastic area ranges of the theory and simulation were consistent with each other and analysed the relationship between different borehole diameters and plastic area ranges. The new type of blowout preventer was used to construct a test drilling hole, the “two plugging and one injection” sealing technology and phosphogypsum-based self-produced gas expansion slurry material were used to block the drilling hole, and the accurate gas mixed flow, pure flow, and concentration data were measured. Finally, the appropriate plastic area of the borehole was determined by analysing the gas drainage effect in different plastic areas of the drilling hole.

2. General Situation of Puxi Mine

Jiahe Mining Co., Ltd. is the raw coal company of Hunan Heijin Times Co., Ltd., and the subordinate Puxi mine is a gas outburst mine in the northeast of Jiahe County, Chenzhou, Hunan Province, as shown in Figure 1. The administrative area is under the jurisdiction of Xinglang town, Jiahe County. The geographical coordinates of the mining area are $112^{\circ} 24' 52'' \sim 112^{\circ} 27' 11''$ E and $25^{\circ} 35' 10'' \sim 25^{\circ} 39'$

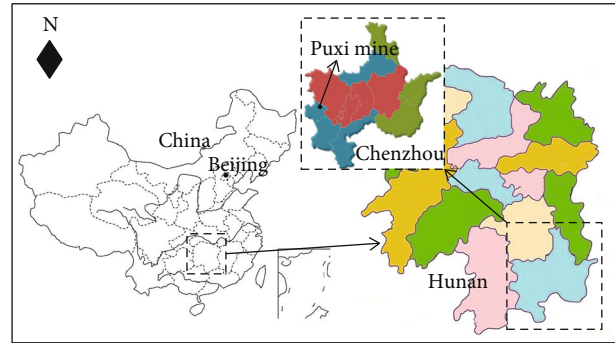


FIGURE 1: Location of Puxi mine.

$41''$ N. The north-south strike of the mine is 4.5 km; the east-west strike is 1.8 km, on average; the area is 8.6186 km^2 . There are seven coal seams in the mine: coal seam II, coal seam III, coal seam IV, coal seam V, coal seam V_2 , coal seam VI, and coal seam VII from top to bottom. Coal seam V has a stable occurrence and is the main coal seam of the mine, while coal seams II and VI are locally minable coal seams. The average thickness and inclination angle of coal seam V are 2.42 m and 25° , respectively. Since the mine was put into operation, coal and gas outburst have occurred 106 times, and the types of outburst are mainly extrusion and pour-out. The maximum coal outburst amount is 430 t, and the maximum gas outburst amount is $46,000 \text{ m}^3$. With the increase in mining depth, the outburst frequency and intensity are increasing. Although many projects have been performed in the borehole through the coal seam via the floor roadway in the mine, the borehole, which has a diameter of 65 mm, is not ideal. The extraction time is long, the extraction concentration is low, and regional outburst elimination cost is relatively high. Therefore, it is very important to determine the appropriate borehole diameter and plastic zone range.

3. Numerical Simulation of the Plastic Zone around the Borehole

3.1. Model and Calculation Parameters. In this paper, COMSOL Multiphysics was used to simulate and study the plastic zone in the coal body around crossing boreholes with different pore sizes. Model size selection depends on the range of the effects of stress changes around the borehole. According to theoretical analysis, a local change of the coal body only has a significant impact over a limited range, and stress changes are negligible far from the local construction site. According to the characteristics of 2254 working surfaces in Puxi mine, the model was established. Because of the symmetry of the model, only half of the computational domain was used to achieve a numerical solution. A $2 \text{ m} \times 2 \text{ m}$ model is established, as shown in Figure 2. The borehole is located at the centre of the left boundary of the model. The bottom boundary of the model is fixed, that is, the vertical displacement is 0, the left boundary is symmetric constraint, and the right boundary is horizontal constraint,

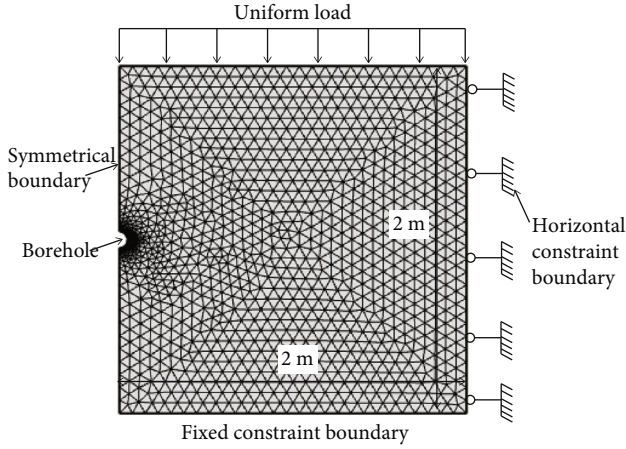


FIGURE 2: Geometric model.

that is, the horizontal displacement of the right boundary is 0, and the top boundary has a uniform load of 1.3 MPa to simulate the dead weight boundary of the overlying rock mass. The basic parameters of the coal seam are shown in Table 1.

3.2. Analysis of the Numerical Simulation Results. After completion of the borehole, the stress field around the borehole will change and redistribute. The coal body will expand, deform, and flow towards the borehole, causing plastic failure of the coal body. During borehole formation, the coal body adjacent to the borehole gradually bears the supported pressure of the coal body. The coal body adjacent to the borehole shows a state of stress concentration, which damages the coal body in the adjacent region because the strength is lower than the concentrated stress and forms a plastic zone.

As shown in Figure 3, after completion of the borehole, the plastic zone, elastic zone, and initial stress zone were successively formed around the borehole from inside to outside. Because the coal around the borehole was difficult to bear a large stress, the peak value of concentrated stress shifted away from the borehole wall, and the stress borne by the coal around the borehole gradually decreased and finally lowered than the original stress, which was the process of pressure relief. When the stress of the coal body at a certain distance from the borehole is lower than the strength of the coal body and only causes an elastic change but not a plastic change of the coal body, the pressure does not decrease in this area. Therefore, the range of the plastic zone, which can be expressed according the radius of the plastic zone, will affect the range of pressure relief of the borehole.

Figure 4 shows the distribution of the plastic zone around boreholes of 75 mm, 87 mm, 94 mm, 105 mm, and 113 mm from left to right. With the increased of the borehole pore size, the plastic zone around the borehole gradually increased. As shown in Figure 3, when the coal body entered the plastic state, the maximum tangential stress shifted from the periphery of the borehole to the junction of the elastic zone and plastic zone. As it extended into the coal body, the tangential stress gradually returned to the ini-

TABLE 1: Basic parameters of the coal seam.

No.	Model parameter	Parameter values
1	Elasticity modulus (MPa)	1180
2	Bulk modulus (MPa)	630
3	Cohesion (MPa)	0.68
4	Internal friction angle (°)	20.7
5	Tensile strength (MPa)	0.2
6	Density (kg·m ⁻³)	1350

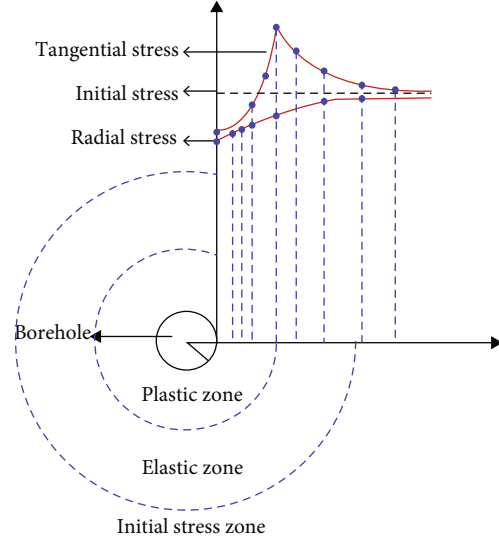


FIGURE 3: Stress distribution law around the borehole.

tial stress, so the peak point of tangential stress and the point of zero effective plastic strain were on the boundary of the plastic zone.

As shown in Figures 5 and 6, the tangential stress around the borehole first increased and subsequently decreased, while the effective plastic strain of the coal around the borehole gradually decreased with increasing distance from the borehole centre. Therefore, the x -coordinate that corresponds to the tangential stress peak point and the point where the effective plastic strain became 0 defined the radius of the plastic zone.

As shown in Table 2, the radii of the plastic zones of boreholes with pore sizes of 75 mm, 87 mm, 94 mm, 105 mm, and 113 mm are 46.3 mm, 53.9 mm, 57.6 mm, 65.0 mm, and 70.3 mm, respectively. Thus, a larger pore size corresponds to a larger plastic zone and larger range of pressure relief. From the perspective of gas extraction, a larger borehole diameter corresponds to a larger range of pressure relief of the coal body and a better gas extraction effect.

4. Modified Model of the Plastic Zone Range

4.1. Basic Model of Plastic Zone Range. Before analysing the plastic zone of the borehole, we can assume some conditions to transform the stress distribution around the borehole into a round hole problem of plane strain: (1) the surrounding

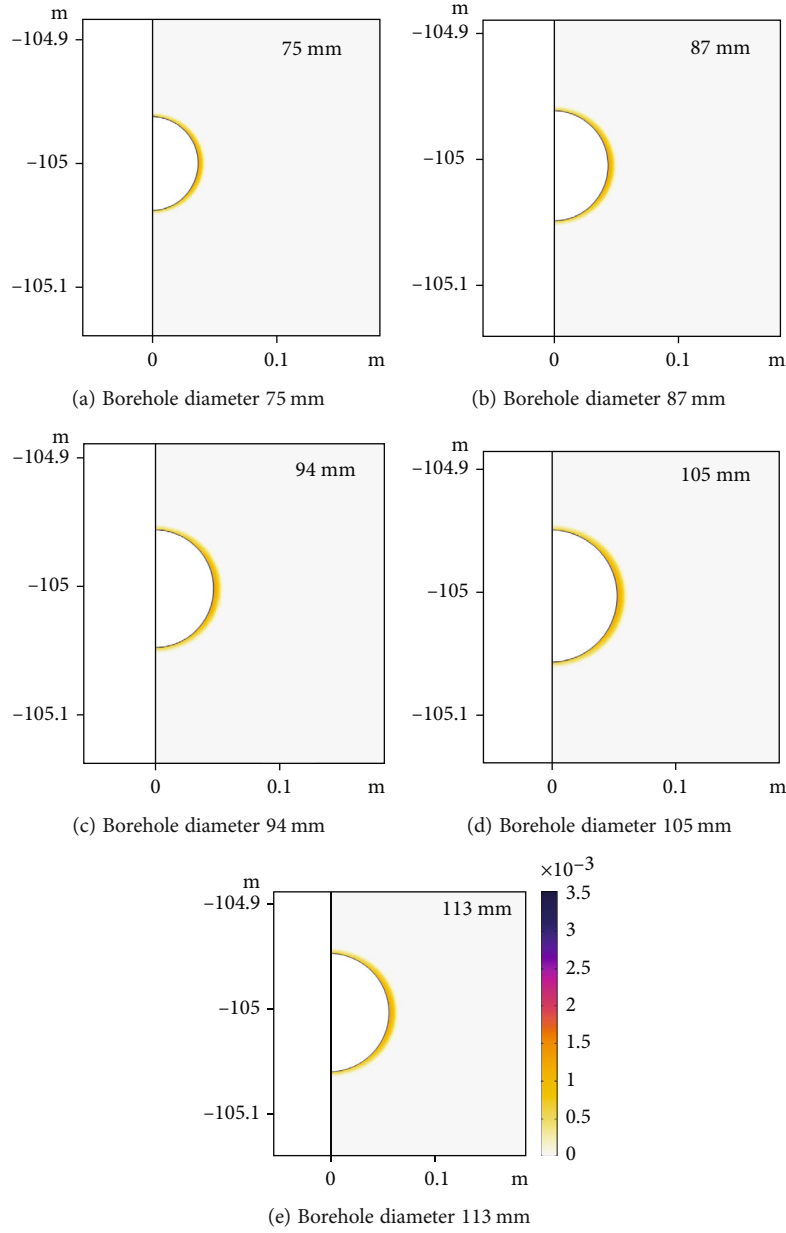


FIGURE 4: Plastic zone of different pore sizes.

rock mass of the borehole is a homogeneous, continuous, and isotropic ideal elastic-plastic body; (2) the properties of coal in different directions are identical; (3) after the borehole forms, the transverse and longitudinal displacement and deformation are small; (4) the lateral pressure coefficient of the surrounding rock is 1.

A plane coordinate system is established with the centre of the borehole as the origin. The distance between any point of the plane and the centre of the borehole is r . If the radius of plastic zone is R_p , the variation gradient of cohesion in the plastic zone can be expressed as Equation (1).

$$j_c = \frac{c_0 - c_s}{R_p - R}, \quad (1)$$

where j_c is the gradient of change; c_0 is the initial cohesion, MPa; c_s is the residual cohesion, MPa; R_p is the radius of plastic zone, m; and R is the borehole radius, m. In the plastic zone, the cohesion at distance r from the drilling centre can be expressed as Equation (2).

$$c^* = c_s + j_c(r - R). \quad (2)$$

In the elastic zone, $c^* = c_0$. For axisymmetric problems, the stress satisfies the equilibrium equation, so Equation (3) can be obtained.

$$\frac{d\sigma}{dr} + \frac{\sigma_r - \sigma_\theta}{r} = 0, \quad (3)$$

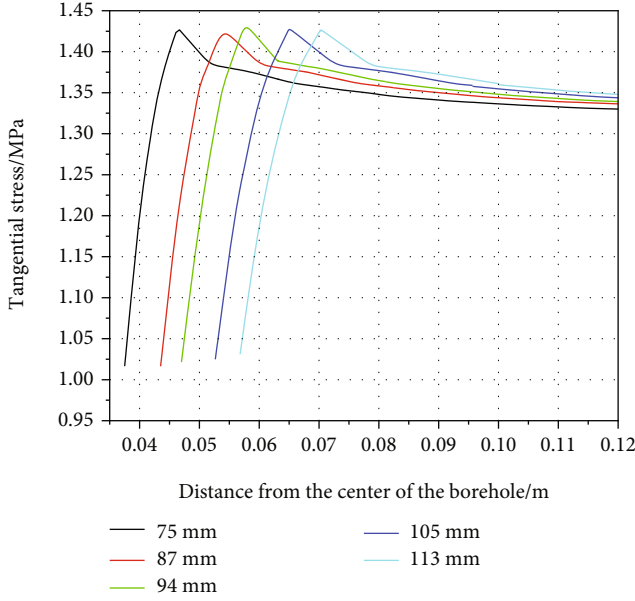


FIGURE 5: Tangential stress distribution of different pore sizes.

where σ_r is the radial stress, MPa, and σ_θ is the tangential stress, MPa. In the plastic zone, the rock mass material satisfies the equilibrium equation and the corresponding yield criterion. Hence, in this paper, the Mohr-Coulomb criterion, which is currently the most widely used criterion, is still used. In polar coordinates, the Mohr-Coulomb criterion can be expressed as Equation (4).

$$\sigma_\theta = \xi \sigma_r + \frac{2c^* \cos \varphi}{1 - \sin \varphi}, \quad (4)$$

where $\xi = 1 + \sin \varphi / 1 - \sin \varphi$; φ is the internal friction angle of coal, $^\circ$.

4.1.1. *Stress in the Plastic Zone.* Substitute Equation (4) into Equation (3) to obtain Equation (5).

$$\frac{d\sigma_r}{dr} + \frac{(1-\xi)}{r} \sigma_r = \frac{\sigma^*}{r}, \quad (5)$$

where $\sigma^* = 2c^* \cos \varphi / 1 - \sin \varphi$. Using the differential formula, Equation (6) is obtained.

$$\sigma_r = e^{-\int 1-\xi/r dr} \left(\int \frac{\sigma^*}{r} e^{\int 1-\xi/r dr} dr + C \right). \quad (6)$$

By substituting Equation (2) into Equation (6) and combining with $\xi = 1 + \sin \varphi / 1 - \sin \varphi$, we obtain Equation (7).

$$\sigma_r = (j_c R - c_s) \cot \varphi + \frac{2j_c \cos \varphi}{1 - 3 \sin \varphi} r + r^{\xi-1} C. \quad (7)$$

When r is equal to R , σ_r is equal to 0. Thus, the integral constant can be obtained by making $k_1 = (j_c R - c_s) \cot \varphi$ and $k_2 = 2j_c \cos \varphi / 1 - 3 \sin \varphi$ and combining the condition

of the stress boundary. Therefore, Equation (8) can be obtained.

$$\sigma_r = k_1 + k_2 r - k_1 \left(\frac{r}{R} \right)^{\xi-1} - k_2 r \left(\frac{r}{R} \right)^{\xi-2}. \quad (8)$$

By substituting Equation (8) into Equation (4), we obtain Equation (9).

$$\sigma_\theta = \xi k_1 + \xi k_2 r - \xi k_1 \left(\frac{r}{R} \right)^{\xi-1} - \xi k_2 r \left(\frac{r}{R} \right)^{\xi-2} + \sigma^*. \quad (9)$$

According to the total theory of plasticity, ε_Z is equal to 0 in the problem of plane strain. Thus, the plastic constitutive Equation (10) can be obtained.

$$\left\{ \begin{array}{l} \varepsilon_r = \frac{\psi}{4G^*} (\sigma_r - \sigma_\theta) \\ \varepsilon_\theta = \frac{\psi}{4G^*} (\sigma_\theta - \sigma_r) \end{array} \right\}, \quad (10)$$

where ε_r is the radial strain; ψ is the plastic index; G^* is the weakening shear modulus, MPa; and ε_θ is the tangential strain. The elastic constitutive Equation (11) is as follows:

$$\left\{ \begin{array}{l} \varepsilon_r = \frac{1-\nu^2}{E} \left(\sigma_r - \frac{\nu}{1-\nu} \sigma_\theta \right) \\ \varepsilon_\theta = \frac{1-\nu^2}{E} \left(\sigma_\theta - \frac{\nu}{1-\nu} \sigma_r \right) \end{array} \right\}, \quad (11)$$

where ν is Poisson's ratio; E is the modulus of elasticity, MPa. We substitute Equations (8) and (9) into Equations (10) and (11) to obtain the strain expression as Equation (12).

$$\left\{ \begin{array}{l} \varepsilon_r^p = \frac{\psi}{4G^*} [(1-\xi)\sigma_r - \sigma^*] + \frac{1-\nu^2}{E} \left[\left(\frac{1-(1+\xi)\nu}{1-\nu} \sigma_r \right) - \frac{\nu}{1-\nu} \sigma^* \right] \\ \varepsilon_\theta^p = \frac{\psi}{4G^*} [\sigma^* - (1-\xi)\sigma_r] + \frac{1-\nu^2}{E} \left[\left(\xi - \frac{\nu}{1-\nu} \right) \sigma_r + \sigma^* \right] \end{array} \right\}, \quad (12)$$

where ε_r^p and ε_θ^p are the radial strain and tangential strain in the plastic zone, MPa, respectively.

4.1.2. *Stress in the Elastic Zone.* The stress solution in the elastic region can be expressed as Equation (13).

$$\left. \begin{array}{l} \sigma_r \\ \sigma_\theta \end{array} \right\} = A \pm \frac{B}{r^2}, \quad (13)$$

where A and B are undetermined coefficients.

When r approaches infinity, $\sigma_r = \sigma_\theta = p_0 = A$; when r is equal to R_p , $\sigma^* = \sigma_0 = 2c_0 \cos \varphi / 1 - \sin \varphi$. Simultaneously, the elastic-plastic interface satisfies Equation (14).

$$\sigma_r + \sigma_\theta = 2p_0, \quad (14)$$

where p_0 is the initial stress, MPa.

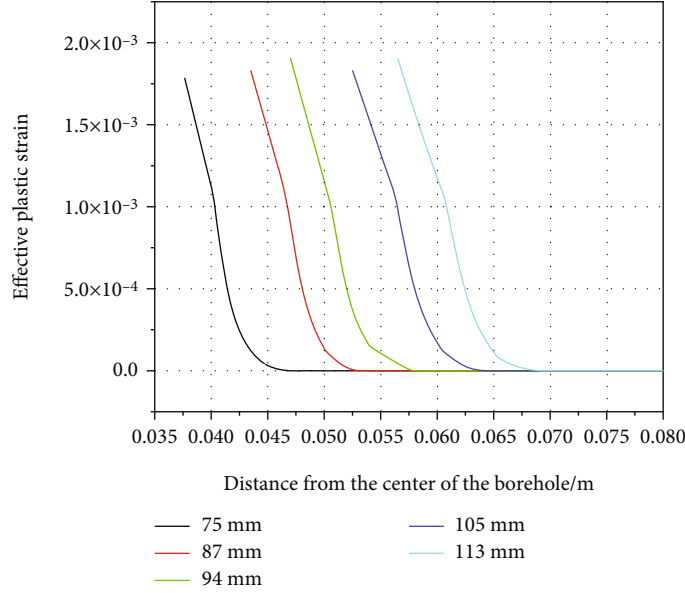


FIGURE 6: Effective plastic strain of different pore sizes.

TABLE 2: Radii of the simulated plastic zones of boreholes with different pore sizes.

Radius of borehole (mm)	37.5	43.5	47.0	52.5	56.5
Radius of plastic zone (mm)	46.3	53.9	57.6	65.0	70.3

Equation (15) can be obtained by substituting Equation (14) into Equation (3).

$$\begin{cases} \sigma_r|_{r=R_p} = p_0(1 - \sin \phi) - c_0 \cos \phi, \\ \sigma_\theta|_{r=R_p} = p_0(1 + \sin \phi) + c_0 \cos \phi. \end{cases} \quad (15)$$

Substituting Equation (15) into Equation (13), we obtain Equation (16).

$$\begin{cases} \sigma_r = p_0 - \frac{R_p^2}{r^2} (p_0 \sin \phi + c_0 \cos \phi), \\ \sigma_\theta = p_0 + \frac{R_p^2}{r^2} (p_0 \sin \phi + c_0 \cos \phi). \end{cases} \quad (16)$$

By substituting Equation (16) into Equation (11), we obtain the strain in the elastic region.

$$\begin{cases} \varepsilon_r^e = \frac{1+\nu}{E} \left[(1-2\nu)p_0 - (p_0 \sin \phi + c_0 \cos \phi) \frac{R_p^2}{r^2} \right], \\ \varepsilon_\theta^e = \frac{1+\nu}{E} \left[(1-2\nu)p_0 + (p_0 \sin \phi + c_0 \cos \phi) \frac{R_p^2}{r^2} \right], \end{cases} \quad (17)$$

where ε_r^e and ε_θ^e are the radial strain and tangential strain in the elastic zone, MPa, respectively.

4.1.3. *Radius of the Plastic Zone.* At the elastoplastic interface, $r = R_p$ and $\sigma^* = 2c_0 \cos \phi / (1 - \sin \phi)$. Because $\sigma_r^p = \sigma_r^e$, Equation (18) can be obtained according to Equations (8) and (16).

$$k_1 + k_2 R_p - k_1 \left(\frac{R_p}{R} \right)^{\xi-1} - k_2 r \left(\frac{R_p}{R} \right)^{\xi-2} + c_0 \cos \phi = p_0 (1 - \sin \phi). \quad (18)$$

By substituting Equation (1) and the expressions of k_1 and k_2 into Equation (18), we obtain the range of the plastic zone of the borehole.

$$\begin{aligned} & \left(\frac{R_p}{R} \right)^{\xi-1} \left[(c_0 - c_s) \frac{2 \cos \phi}{1 - 3 \sin \phi} + c_0 \cot \phi - c_s \cot \phi \left(\frac{R_p}{R} \right) \right] \\ & + \frac{R_p}{R} \left[p_0 (1 - \sin \phi) - c_0 \frac{3 \cos \phi (1 - \sin \phi)}{1 - 3 \sin \phi} + c_s \cot \phi \frac{1 - \sin \phi}{1 - 3 \sin \phi} \right] \\ & = p_0 (1 - \sin \phi) - c_0 (\cos \phi - \cot \phi). \end{aligned} \quad (19)$$

In particular, when the surrounding rock of the borehole is an ideal elastoplastic body, Equation (19) can be reduced to Equation (20).

$$R_p = R \left(\frac{p_0 (1 - \sin \phi) - c_0 (\cos \phi - \cot \phi)}{c_0 \cot \phi} \right)^{1 - \sin \phi / 2 \sin \phi}. \quad (20)$$

4.2. *Modified Model of the Plastic Zone Range.* The plastic zone radii of boreholes with different pore sizes, which were calculated by formula (20), are shown in Table 3.

TABLE 3: Calculated radii of the plastic zone of boreholes with different pore sizes.

Radius of borehole (mm)	37.5	43.5	47.0	52.5	56.5
Radius of plastic zone (mm)	41.9	48.6	52.5	58.6	63.1

Tables 2 and 3 show that there was an error between the numerically simulated and calculated radii of the plastic zones. Hence, formula (20) must be corrected. Figure 7 shows the variation law of the plastic zone range with the borehole radius and the variation law of the difference of the radius determined between the two methods.

As shown in Figure 7, the difference between the two methods shows an approximate first-order function with the radius as Equation (21).

$$R_1 = kR + c, \quad (21)$$

where R_1 is the difference, m; k is the slope. After calculation, the slope is 0.12, so the modified equation is shown in Equation (22).

$$R_{p1} = R_p + R_1 = R_p + 0.12R, \quad (22)$$

where R_{p1} is the modified radius of the plastic zone, m. Table 4 shows a comparison between the calculated radius of the plastic zone by Equation (22) and the simulated radius.

Table 4 shows that the error between the plastic zone radius calculated by Equation (22) and the simulated radius was within 1%, which proves that Equation (22) is applicable to Puxi mine. In Equation (22), the initial stress, cohesion, and internal friction angle are constants, so Equation (22) is a first-order function of the radius. According to Equation (22), when the radius increases, the plastic zone around the borehole also increases. The range of pressure relief of the borehole will increase, and the effect of gas extraction of the borehole will improve.

5. Analysis of the Gas Extraction Effect under Different Ranges of the Plastic Zone of the Borehole

5.1. Test Method. To study the relationship between the plastic zone of different boreholes and the gas extraction effect in Puxi mine, the effect of plastic zone radii of 46.4 mm, 53.8 mm, 58.1 mm, 64.9 mm, and 69.9 mm on the gas extraction effect was preliminarily determined and investigated, and the variations of the gas concentration, mixed flow rate, and pure flow in different plastic zones of the borehole were investigated. In principle, for the test area, we selected a newly excavated floor roadway with a length of more than 150 m, and the test site was determined to be the 2254 floor roadway in combination with the site conditions of Puxi mine.

5.2. Construction and Sealing of the Borehole

5.2.1. Application of the New Type of Antispray Hole Equipment in the Soft Coal Seam. During or after the con-

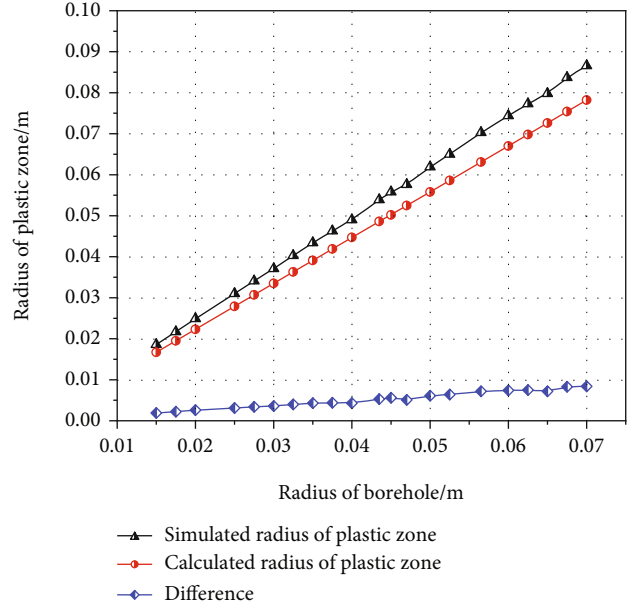


FIGURE 7: Comparison of the plastic zone radius.

struction of large boreholes, pulverized coal and gas are continuously ejected from the boreholes in a short period of time due to the soft coal quality of coal V in Puxi mine. This phenomenon is called borehole spraying. A large amount of gas emitted from the borehole over a short period of time would make the gas concentration in the tunnel abnormally increase and endanger the personal safety of underground construction personnel. To solve the problem of an abnormal increase of the gas concentration in the roadway caused by borehole spraying in the highly gassy and soft coal seam, a new type of antispray hole equipment was adopted in the test to reduce the damage caused by borehole spraying, as shown in Figure 8.

As shown in Figure 8, the equipment is composed of an upper cylinder and a lower semicircle arc plate. In the borehole construction process, if borehole spraying occurs, the gas extraction pump will be immediately opened. When pulverized coal and gas pass through the antispray hole equipment, gas enters the gas chamber through the pumping air hole under the effect of negative pressure and subsequently enters the gas extraction pump through the short extraction pipe. The pulverized coal loses kinetic energy and flows out from the space between the upper cylinder and the lower semicircle arc plate. In the usage process, the gas concentration can be monitored by the gas concentration monitor to determine whether borehole spraying has stopped. Compared with the existing equipment, the new type of antispray hole equipment has simple structure and convenient installation and disassembly. It can effectively reduce the gas concentration when the borehole spraying. At the same time, it can separate the pulverized coal and gas twice to ensure the gas drainage effect and finally ensure the safety of personnel in the roadway. Application of this new type of antispray hole equipment solved the problem that the gas concentration in the roadway abnormally

TABLE 4: Comparison of the radius of the plastic zone.

Radius of borehole (mm)	37.5	43.5	47.0	52.5	56.5
The simulated radius of plastic zone (mm)	46.3	53.9	57.6	65.0	70.3
The calculated radius of plastic zone (mm)	46.4	53.8	58.1	64.9	69.9
Error (%)	0.2	0.19	0.87	0.15	0.57

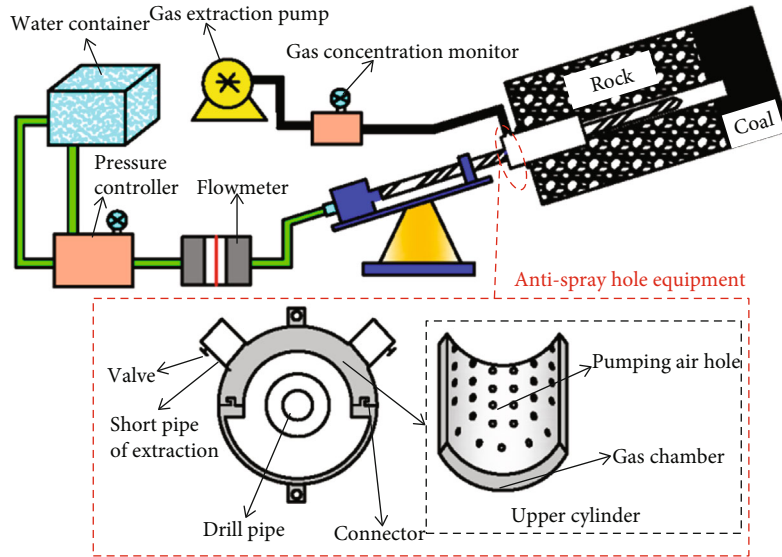


FIGURE 8: New type of antispray hole equipment.

increases due to gas gushing in the borehole construction process.

5.2.2. Borehole Sealing. The quality of borehole sealing directly affects the effect of gas extraction in the coal seam. By selecting the appropriate borehole sealing technology and materials, the quality of borehole sealing and the effect of gas extraction can be improved in the coal seam. Therefore, after borehole construction was completed, the “two blocks and one injection” sealing technology was selected for borehole sealing (see Figure 9). The process of grouting and hole sealing is depicted in Figure 10, a grouting pipe was used to inject phosphogypsum-based self-produced gas expansion paste material into the bag, and friction was generated between the bag and the borehole wall after the bag expanded. Under the continuous action of the grouting pump, the slurry would fill the cracks around the borehole wall to prevent gas from flowing out of the cracks.

The phosphogypsum-based self-produced gas expansion paste material is composed of the following components: 55 parts of phosphogypsum, 30 parts of water, 9 parts of cement, 0.18 parts of polyoxyethylene alkylamine, 0.9 parts of hydroxyethyl cellulose, 0.22 parts of acrylic acid, 0.39 parts of sodium methanesulfonate, 0.01 parts of ammonia persulfate, 4.0 parts of sodium bicarbonate, and 0.3 parts of microsilica powder. The preparation method is to add polyoxyethylene alkylamine and acrylic acid in water and stir to form a mixture. Then, cement, hydroxyethyl cellulose, ammonia persulfate, sodium methyl propylene sulfonate,

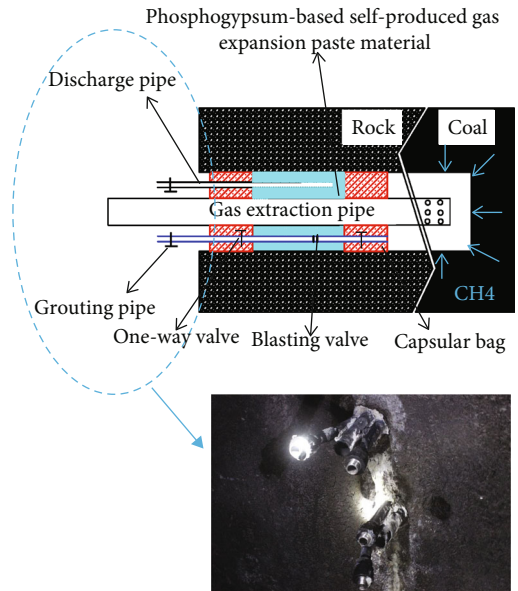


FIGURE 9: Principle of the “two blocks and one injection” sealing technology.

microsilica powder, and sodium bicarbonate are added to phosphogypsum to form mixed powder. Finally, the mixed powder is added to the mixture and stirred to make an expanded slurry. The phosphogypsum-based self-produced gas expansion paste material reacts slowly at room

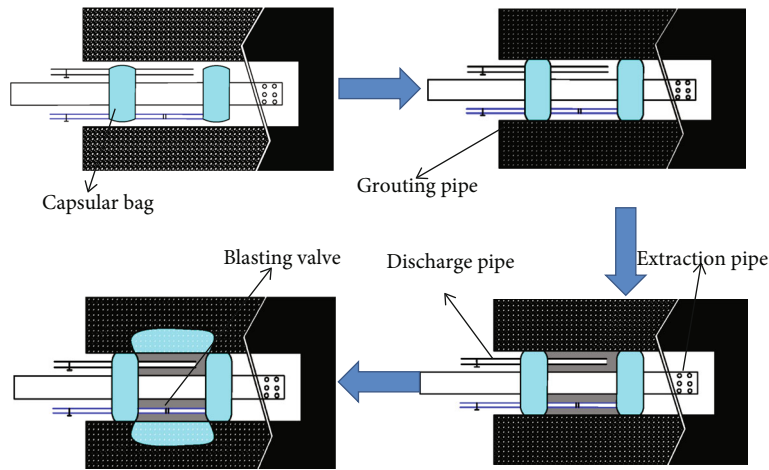


FIGURE 10: Hole-sealing process.

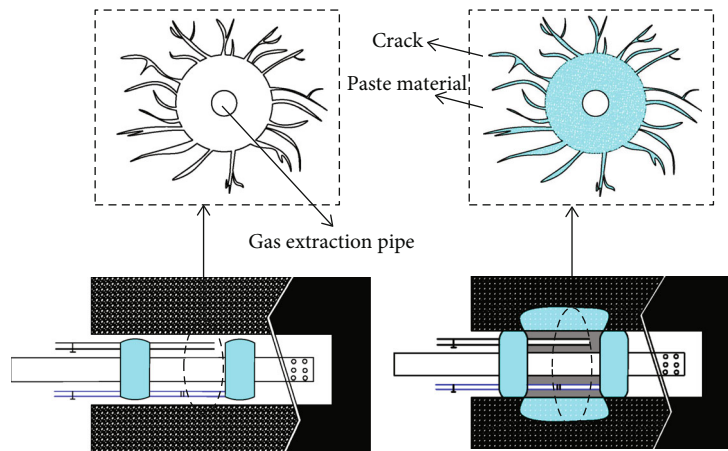


FIGURE 11: Comparison before and after grouting.

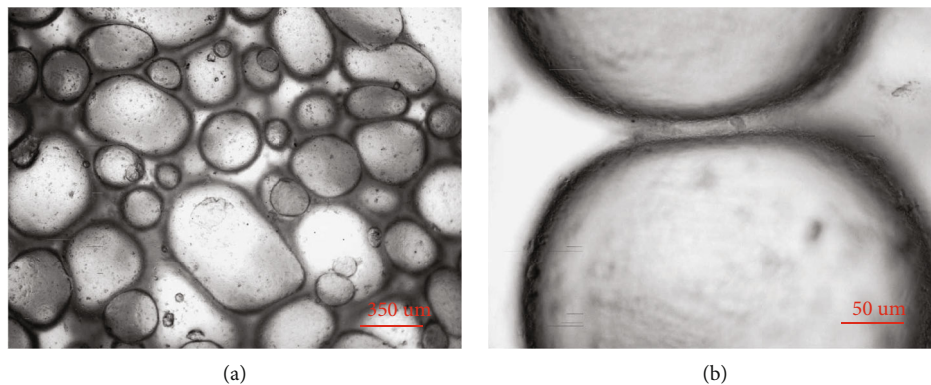


FIGURE 12: Optical microstructure of the paste material.

temperature, has good fluidity, can be injected into cracks, and has high compressive strength. At the same time, it improves the utilization rate of phosphogypsum and reduces its pollution to the environment.

A comparison of before and after the borehole wall cracks are filled with the phosphogypsum-based self-produced gas expansion paste material is shown in Figure 11. When the sealing section is full of the paste mate-

rial, the discharge pipe is closed and the paste material expands and fills the cracks around the borehole wall along the borehole diameter under the effect of the grouting pressure. In the preparation process of the phosphogypsum-based self-produced gas expansion paste material, the addition of polyoxyethylene alkyl and hydroxyethyl cellulose increases the bubble viscosity. Thus, the foam can expand, but the surface is not broken. As shown in Figure 12, the



FIGURE 13: Borehole construction and borehole networking.

foam distribution is homogeneous, and the structure of the foam wall is intact. Therefore, after the paste material enters the cracks, it can effectively seal the cracks and improve the sealing quality. In addition, at normal temperature, the paste material slowly reacts, which ensures good fluidity after the paste material enters into the cracks.

5.3. *Result of Test.* As shown in Figure 13, the investigation area of each borehole plastic zone was defined as a unit, which was divided into five investigation units, and each unit had five boreholes, and five boreholes of each unit were networked for extraction. The “two blocks and one injection” sealing technology and phosphogypsum-based self-produced gas expansion paste material were used in the test to improve the sealing quality and air tightness. Therefore, accurate data for the gas mixed flow, pure flow,

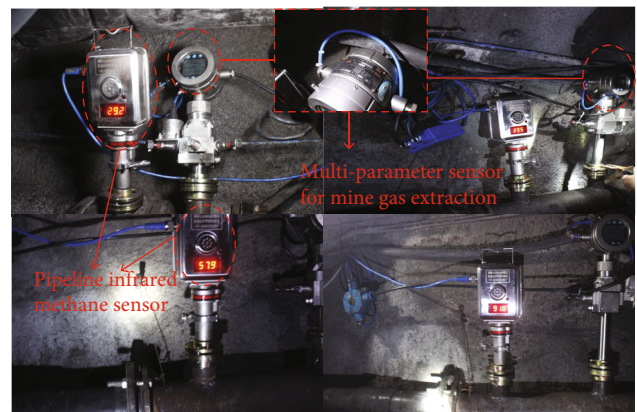


FIGURE 14: Gas flow concentration.

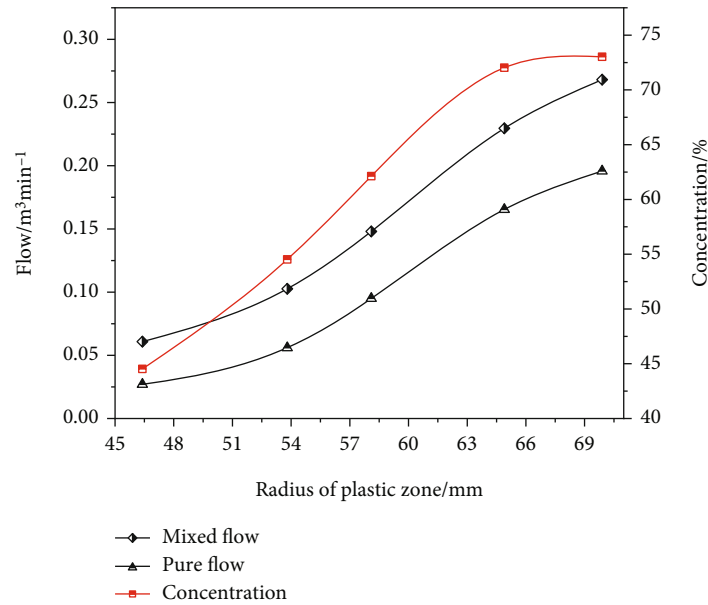


FIGURE 15: Changes in flow and concentration.

and concentration were measured. After the completion of borehole construction and sealing, the daily gas mixing flow, pure flow, and concentration of each unit were measured for 15 days. The reading on the pipeline infrared methane sensor is the gas concentration of each unit, and the reading on the multiparameter sensor for mine gas extraction is the mixed flow and pure flow of each unit, as shown in Figure 14.

The change rule of the average mixed flow, pure flow, and concentration in the first 15 days of different units is shown in Figure 15. In Figure 15, when the radius of the plastic zone of the borehole increased from 46.4 mm to 69.9 mm, the mixed flow increased from 0.061 m³/min to 0.268 m³/min, the pure flow increases from 0.027 m³/min to 0.196 m³/min, and the concentration increases from 44.53% to 73.03%. The increased in radius of the plastic zone improved the gas extraction effect.

On one hand, an increase of the plastic zone of the borehole results in an increase of the pressure relief circle around the borehole, which causes a better gas extraction effect. On the other hand, to increase the radius of the plastic zone of the borehole, it is necessary to expand the borehole diameter, which increases construction difficulty, construction cost, and construction risk. Therefore, to achieve safety, cost minimization, and extraction maximization, it is necessary to analyse the variation of the mixed flow and pure flow relative to the radius difference of the plastic zone with the increase of the plastic zone, as shown in Table 5.

As shown in Table 5, the relative variation of mixed flow increased from 5.68 to 21.58 and subsequently decreased to 7.60, while the relative variation of pure flow increased from 3.92 to 18.42 and subsequently decreased to 6.2. With the increased of the radius of the plastic zone, the rates of increased of the mixed flow and pure flow first increased and subsequently decreased. Therefore, consider-

TABLE 5: Relative change of the mixed flow and pure flow.

Radius (mm)	Radius difference of plastic (m)	Mixed flow (m ³ /min)	Relative variation of mixed flow	Pure flow (m ³ /min)	Relative variation of pure flow
46.4 mm	-	0.061	-	0.027	-
53.8 mm	0.0074	0.103	5.68	0.056	3.92
58.1 mm	0.0043	0.148	10.47	0.095	9.07
64.9 mm	0.0038	0.230	12.06	0.165	10.29
69.9 mm	0.005	0.268	7.60	0.196	6.2

ing the safety and economy of construction, the optimal radius of the plastic zone was 64.9 mm.

6. Conclusions

- (1) COMSOL Multiphysics is used to simulate the plastic zone of coal around a borehole. A larger borehole pore corresponds to a larger plastic zone and a larger range of pressure relief of the borehole. The basic model of the plastic zone range is established, and the stress in the elastic zone and radius of the plastic zone are derived step by step. By comparing the radii of the plastic zone from numerical simulation and calculation, the theoretical equation of the radius of the plastic zone is modified. The results show that the modified equation is suitable for Puxi mine
- (2) A new type of antispray hole equipment is used to construct a borehole, and the loss and harm caused by borehole spraying are reduced. The “two plugging and one injection” sealing technology and phosphogypsum-based self-produced gas expansion

paste material are used to block the borehole, and the sealing quality is improved

- (3) The accurate gas mixing flow, pure flow, and concentration are obtained. With the increase of the plastic zone, the flow of gas extraction gradually increases, but the relative variation of flow first increases and subsequently decreases. Therefore, considering the safety and economy of construction, the optimal radius of the plastic zone is 64.9 mm

Data Availability

The data used to support the findings of this study are included within the article.

Conflicts of Interest

The authors declare no conflict of interest.

Acknowledgments

This work is financially supported by the Hunan Provincial Innovation Foundation For Postgraduate (CX2018B657), the Foundation of Work Safety Key Lab on Prevention and Control of Gas and Roof Disasters for Southern Coal of China (E21825), the National Natural Science Foundation of China (51974299, 51904103, 51974120, and 51974119), the Youth Talent of Hunan Province (2020RC3047), and the Hunan Provincial Natural Science Foundation of China (2019JJ50180 and 2020JJ4023).

References

- [1] H. Li, S. L. Shi, B. Q. Lin et al., "Effects of microwave-assisted pyrolysis on the microstructure of bituminous coals," *Energy*, vol. 187, article 115986, 2019.
- [2] Q. G. Wang, D. Wang, F. W. Han, F. Yang, and Y. X. Sheng, "Study and application on foam-water mist integrated dust control technology in fully mechanized excavation face," *Process Safety and Environmental Protection*, vol. 133, pp. 41–50, 2020.
- [3] Z. L. Xi, X. D. Wang, X. L. Wang et al., "Polymorphic foam clay for inhibiting the spontaneous combustion of coal," *Process Safety and Environmental Protection*, vol. 122, pp. 263–270, 2019.
- [4] J. Lin, T. Ren, Y. P. Cheng, J. Nemcik, and G. D. Wang, "Cyclic N₂ injection for enhanced coal seam gas recovery: a laboratory study," *Energy*, vol. 188, article 116115, 2019.
- [5] Y. Lu, S. L. Shi, H. Q. Wang, Z. J. Tian, Q. Ye, and H. Y. Niu, "Thermal characteristics of cement microparticle-stabilized aqueous foam for sealing high-temperature mining fractures," *International Journal of Heat and Mass Transfer*, vol. 131, pp. 594–603, 2019.
- [6] Q. Ye, G. X. Wang, Z. Z. Jia, and C. S. Zheng, "Experimental study on the influence of wall heat effect on gas explosion and its propagation," *Applied Thermal Engineering*, vol. 118, pp. 392–397, 2017.
- [7] Y. Lu, "Laboratory study on the rising temperature of spontaneous combustion in coal stockpiles and a paste foam suppression technique," *Energy & Fuels*, vol. 31, no. 7, pp. 7290–7298, 2017.
- [8] Z. Z. Zhang, M. Deng, J. B. Bai, X. Y. Yu, Q. H. Wu, and L. S. Jiang, "Strain energy evolution and conversion under triaxial unloading confining pressure tests due to gob-side entry retained," *International Journal of Rock Mechanics and Mining Sciences*, vol. 126, article 104184, 2020.
- [9] Q. Ye, Z. Z. Jia, and C. S. Zheng, "Study on hydraulic-controlled blasting technology for pressure relief and permeability improvement in a deep hole," *Journal of Petroleum Science and Engineering*, vol. 159, pp. 433–442, 2017.
- [10] G. F. Li, H. A. Zheng, and D. S. Fu, "Research progress of polyurethane for coal mining borehole sealing engineering," *Clean Coal Technology*, vol. 20, pp. 94–98, 2014.
- [11] Q. G. Li, B. Q. Lin, and C. Zhai, "The effect of pulse frequency on the fracture extension during hydraulic fracturing," *Journal of Natural Gas Science and Engineering*, vol. 21, pp. 296–303, 2014.
- [12] C. J. Wang, S. Q. Yang, and X. W. Li, "Simulation of the hazard arising from the coupling of gas explosions and spontaneously combustible coal due to the gas drainage of a gob," *Process Safety and Environmental Protection*, vol. 118, pp. 296–306, 2018.
- [13] K. Noack, "Control of gas emissions in underground coal mines," *International Journal of Coal Geology*, vol. 35, no. 1–4, pp. 57–82, 1998.
- [14] X. L. Zhang, B. Q. Lin, C. Zhu et al., "Petrophysical variation of coal treated by cyclic high-voltage electrical pulse for coalbed methane recovery," *Journal of Petroleum Science and Engineering*, vol. 178, pp. 795–804, 2019.
- [15] G. H. Ni, H. C. Xie, Z. Li, and Y. Y. Niu, "Improving the permeability of coal seam with pulsating hydraulic fracturing technique: a case study in Changping coal mine, China," *Process Safety and Environmental Protection*, vol. 117, pp. 565–572, 2018.
- [16] C. Karacan, F. A. Ruiz, M. Cotè, and S. Phipps, "Coal mine methane: a review of capture and utilization practices with benefits to mining safety and to greenhouse gas reduction," *International Journal of Coal Geology*, vol. 86, no. 2–3, pp. 121–156, 2011.
- [17] M. Pillalamarry, S. Harpalani, and S. M. Liu, "Gas diffusion behavior of coal and its impact on production from coalbed methane reservoirs," *International Journal of Coal Geology*, vol. 86, no. 4, pp. 342–348, 2011.
- [18] H. Zhang, Y. P. Cheng, Q. Q. Liu et al., "A novel in-seam borehole hydraulic flushing gas extraction technology in the heading face: enhanced permeability mechanism, gas flow characteristics, and application," *Journal of Natural Gas Science and Engineering*, vol. 46, pp. 498–514, 2017.
- [19] J. Dong, Y. P. Cheng, K. Jin et al., "Effects of diffusion and suction negative pressure on coalbed methane extraction and a new measure to increase the methane utilization rate," *Fuel*, vol. 197, pp. 70–81, 2017.
- [20] L. Qin, C. Zhai, J. Z. Xu, S. M. Liu, C. Zhong, and G. Q. Yu, "Evolution of the pore structure in coal subjected to freeze–thaw using liquid nitrogen to enhance coalbed methane extraction," *Journal of Petroleum Science and Engineering*, vol. 175, pp. 129–139, 2019.
- [21] C. M. Shen, B. Q. Lin, C. Sun, Q. Z. Zhang, and Q. Z. Li, "Analysis of the stress-permeability coupling property in water jet slotting coal and its impact on methane drainage," *Journal of*

- Petroleum Science and Engineering*, vol. 126, pp. 231–241, 2015.
- [22] B. B. Li, K. Yang, P. Xu, J. Xu, M. Yuan, and M. Zhang, “An experimental study on permeability characteristics of coal with slippage and temperature effects,” *Journal of Petroleum Science and Engineering*, vol. 175, pp. 294–302, 2019.
- [23] B. Q. Lin, H. R. Song, Y. Zhao, T. Liu, J. Kong, and Z. B. Huang, “Significance of gas flow in anisotropic coal seams to underground gas drainage,” *Journal of Petroleum Science and Engineering*, vol. 180, pp. 808–819, 2019.
- [24] C. Karacan, W. Diamond, and S. Schatzel, “Numerical analysis of the influence of in-seam horizontal methane drainage boreholes on longwall face emission rates,” *International Journal of Coal Geology*, vol. 72, no. 1, pp. 15–32, 2007.
- [25] X. F. Liu, D. Z. Song, X. Q. He, Z. P. Wang, M. R. Zeng, and K. Deng, “Nanopore structure of deep-burial coals explored by AFM,” *Fuel*, vol. 246, pp. 9–17, 2019.
- [26] M. R. Islam, D. Hayashi, and A. Kamruzzaman, “Finite element modeling of stress distributions and problems for multi-slice longwall mining in Bangladesh, with special reference to the Barapukuria coal mine,” *International Journal of Coal Geology*, vol. 78, no. 2, pp. 91–109, 2009.
- [27] Y. F. Zhang, S. Y. Hu, T. Q. Xia, Y. K. Liu, Z. Pan, and F. B. Zhou, “A novel failure control technology of cross-measure borehole for gas drainage: a case study,” *Process Safety and Environmental Protection*, vol. 135, pp. 144–156, 2020.
- [28] Y. Niu, Z. H. Li, E. Y. Wang et al., “Study on characteristics of EP responding to coal mining,” *Engineering Fracture Mechanics*, vol. 224, article 106780, 2020.
- [29] Y. Niu, X. Y. Song, Z. H. Li et al., “Experimental study and field verification of stability monitoring of gas drainage borehole in mining coal seam,” *Journal of Petroleum Science and Engineering*, vol. 189, article 106985, 2020.
- [30] L. D. Guo, X. S. Zhao, and Y. J. Zhang, “Study on borehole sealing technique with sealing and isolation integration to gas drainage borehole along seam,” *Coal Science and Technology*, vol. 46, no. 5, pp. 114–119, 2018.
- [31] H. M. Cheng, Y. D. Qiao, and C. L. Dong, “Study on hydraulic fractured gas drainage effect based on Hoek-Brown criterion,” *Coal Science and Technology*, vol. 46, no. 9, pp. 111–116, 2018.
- [32] G. P. Su, “Pressure relief range and stress distribution of coal body around borehole for gas extraction along seam,” *China Energy and Environmental Protection*, vol. 41, no. 10, pp. 21–24, 2019.
- [33] H. Frank, R. Ting, and A. Naj, “Evolution and application of in-seam drilling for gas drainage,” *International Journal of Mining Science and Technology*, vol. 23, no. 4, pp. 543–553, 2013.
- [34] C. S. Zheng, B. Y. Jiang, S. Xue, Z. W. Chen, and H. Li, “Coalbed methane emissions and drainage methods in underground mining for mining safety and environmental benefits: a review,” *Process Safety and Environmental Protection*, vol. 127, pp. 103–124, 2019.
- [35] C. Zhang, B. Q. Lin, Y. Zhou, C. Zhai, and C. J. Zhu, “Study on “fracturing-sealing” integration technology based on high-energy gas fracturing in single seam with high gas and low air permeability,” *International Journal of Mining Science and Technology*, vol. 23, no. 6, pp. 841–846, 2013.
- [36] C. Zhang, B. Q. Lin, and Y. Zhou, “Strong-weak-strong borehole pressurized sealing technology for horizontal gas drainage borehole in mining seam,” *Journal of Mining and Safety Engineering*, vol. 30, pp. 935–939, 2013.
- [37] Q. Q. Liu, Y. P. Cheng, L. Yuan, Y. X. Fang, D. Z. Shi, and S. L. Kong, “A new effective method and new materials for high sealing performance of cross-measure CMM drainage boreholes,” *Journal of Natural Gas Science and Engineering*, vol. 21, pp. 805–813, 2014.
- [38] F. B. Zhou, J. H. Li, X. Ze, Y. K. Liu, R. G. Zhang, and S. J. Shen, “A study of the second hole sealing method to improve gas drainage in coal seams,” *Journal of China University of Mining & Technology*, vol. 38, pp. 764–768, 2009.
- [39] G. H. Ni, B. Q. Lin, and C. Zhai, “Microscopic properties of drilling sealing materials and their influence on the sealing performance of boreholes,” *Journal of University of Science and Technology Beijing*, vol. 35, pp. 572–579, 2013.
- [40] X. W. Xiang, C. Zhai, Y. M. Xu, X. Yu, and J. Z. Xu, “A flexible gel sealing material and a novel active sealing method for coalbed methane drainage boreholes,” *Journal of Natural Gas Science and Engineering*, vol. 26, pp. 1187–1199, 2015.
- [41] Z. L. Ge, X. D. Mei, and Y. Y. Lu, “Mechanical model and test study of sealed drilling for hydraulic fracturing in underground coal mines,” *Journal of Basic Science and Engineering*, vol. 22, pp. 1128–1139, 2014.
- [42] L. Qin, P. Wang, S. G. Li et al., “Gas adsorption capacity changes in coals of different ranks after liquid nitrogen freezing,” *Fuel*, vol. 292, article 120404, 2021.
- [43] L. Qin, P. Wang, S. G. Li et al., “Gas adsorption capacity of coal frozen with liquid nitrogen and variations in the proportions of the organic functional groups on the coal after freezing,” *Energy Fuels*, vol. 35, no. 2, pp. 1404–1413, 2021.
- [44] H. Li, L. Tian, B. X. Huang et al., “Experimental study on coal damage subjected to microwave heating,” *Rock Mechanics and Damage Engineering*, vol. 53, no. 12, pp. 5631–5640, 2020.
- [45] J. X. Lu, H. Li, S. L. Shi et al., “Microwave-induced microstructure evolution of coal and its effects on the methane adsorption characteristic,” *Energy Fuels*, vol. 35, no. 5, pp. 4081–4090, 2021.

Research Article

Study on Mechanical Behavior and Seepage Characteristics of Coal Mass during Unloading

Yan Wang,¹ Yongsheng Han ,² and Fei Liu ³

¹Rizhao Polytechnic, Rizhao, Shandong 276800, China

²Department of Water Resources Engineering, Shandong Water Conservancy Vocational College, Rizhao, Shandong 276826, China

³School of Resources and Civil Engineering, Suzhou University, Suzhou, Anhui 234000, China

Correspondence should be addressed to Fei Liu; szxylf@126.com

Received 23 June 2021; Revised 31 August 2021; Accepted 8 October 2021; Published 31 October 2021

Academic Editor: Feng Du

Copyright © 2021 Yan Wang et al. This is an open access article distributed under the Creative Commons Attribution License, which permits unrestricted use, distribution, and reproduction in any medium, provided the original work is properly cited.

With the increase of buried depth, the content of gas increases gradually. The gas in the mining process will lead to gas gush and other dynamic disasters, or even coal and gas gushing in front of the working face. Therefore, the study on the permeability distribution of coal and the surrounding rock is the core work of coal and gas mining at the same time. To study the mechanical behaviors and seepage characteristics of coal mass during unloading is to prepare for coal and gas mining in the future, which can not only ensure the safety of operators to the maximum extent but also increase the mining rate as much as possible. Based on the stress-strain curve and seepage curve, the brittleness index and seepage characteristics of coal are analyzed. The greater the brittleness index is, the more likely the coal mass is to produce cracks, and then to form large cracks, or even fracture. Through the study of brittleness index and seepage characteristics of coal mass, the mechanical behavior of coal mass can be easily obtained, so as to guide the mining of coal mass.

1. Introduction

China has been advocating the conversion of polluting energy to clean energy, but as a big energy consumer, coal energy will always play a dominant role in the future for a long time [1, 2]. The present situation in China is that there are a lot of coal resources but little oil resources. The proven coal reserves of China account for 12.6% of the world's coal reserves, and the recoverable amount ranks the third and the output ranks the first in the world [3–5]. As for the quality of coal, there are less high-quality coal and more inferior coal [6], and the surface coal reserves are limited after all, as well as the large demand for coal energy, the mining of coal must be advanced to a deeper level [7–9]. As a result, deeper mining will face more complex coal strata, and mining work will also face more complex surrounding rock stress state [10, 11], making mining work with more risks, such as gas explosion, coal and gas outburst, flooding, roof accident, poisoning, and asphyxiation [12, 13]. Therefore, while coal mining brings huge economic benefits to people, exploring

how to prevent and reduce the occurrence of hazards in the process of coal mining can not only guarantee the safe and efficient operation of coal work but also provide a strong scientific support for mining work [14, 15].

The study on coal mass under real external force can reveal the influence of mining on coal mass, so it is very important to reduce the stress of coal mass from the perspective of experiment [16, 17]. In view of this, we study the mechanical characteristics and seepage characteristics of coal mass affected by real external forces and to further explore the development law of coal mass fractures [18–20]. In view of the mechanical influence and seepage characteristics of coal mass under triaxial test, scholars have done a lot of research [21–23]. Bieniawski [24] studied the size effect of coal and the stress-strain law under triaxial conditions. Wang et al. [25] conducted coal permeability tests under different confining pressure to monitor the deformation and permeability evolution of coal. Yin et al. [26] studied the mechanical properties and seepage characteristics of raw coal by using triaxial tests. It was found that different

loading and unloading paths (different loading speed, unloading speed, and starting point of loading and unloading) have important influence on the mechanical and seepage characteristics of raw coal, and know that the failure mode of raw coal is tensile shear composite failure. In terms of numerical simulation, Xue et al. [27–29] established a permeability model for damaged excavated coal for simulation analysis. The research shows that the mechanical properties of coal will change significantly, and the permeability of coal will increase before and after the peak point, but the amount of increase is different. Liu [30] studied the deformation, failure, and seepage characteristics of coal containing gas and concluded that the strength and stiffness of raw coal decrease with the increase of gas, and the raw coal gradually transformed from the original brittle failure to the ductile shear failure. There are many pores in the interior of coal, and gas exists in free and adsorbed states. The damage and fracture of coal just release the adsorbed gas, which increases the mining benefit of gas. Yuan et al. [31] studied the thermal-fluid-solid coupling model of gas bearing coal seam, carried out the numerical simulation of heat injection promoting gas drainage, and verified the feasibility of injecting heat into coal seam to promote gas drainage. Zhao et al. [32] made a numerical analysis on the gas drainage performance of coal seams with different structural deformation coal seams and complete coal seams. Guo et al. [33] focused on the criterion of coal seam fracture caused by cumulative blasting and summarized the fracture zone and fracture propagation process of coal. Xue et al. [34–36] established the analytical model of coal seam gas fracturing damage characteristics by studying the media fracturing characteristics and its deformation characteristics and analyzed the law of gas diffusion and migration. Anyim et al. [37] studied the critical stress fault in geothermal area by using the thermal hydrological mechanical coupling model to explore the evolution law of its permeability. Sidiq et al. [38] studied the permeability of reservoir rocks under high temperature and high pressure. In terms of damage and fracture evolution in the process of coal seepage, Chen [39] studied the stress-strain-permeability variation characteristics of coal mass and concluded that soft coal has more pores, more gas adsorption, and higher gas content than hard coal. In addition, the permeability of coal mass shows a “V” shape change. Xia et al. [40] used coupled rock triaxial test system to study the characteristics of seepage in the post-peak fracture stage of rock. The permeability of coal decreases instead of increasing, which indicates that the deformation of coal fractures has an irreversible process and the fracture opening becomes smaller. When unloading to a certain value, all levels of permeability become smaller, indicating that the recovery of permeability of coal has a lag.

Based on the above research findings, the stress-axial strain curve was obtained through triaxial tests, and the whole stage from loading to failure of coal mass was analyzed. The permeability of coal mass measured by the tests was combined with the graph to analyze the seepage characteristics of coal mass. And draw on scholars on the research of brittleness index, combined with the obtained data to check the brittleness index, to get the pattern of specific brittleness index.

2. Study on Mechanical Behavior of Coal Mass

2.1. The Acquisition and Preparation of Coal. The coal samples of this test are collected from a working face of mine. Because there are significant differences in the internal structure of coal and rock under geological action, the mechanical properties are discrete and heterogeneous. Therefore, the samples of this test are all taken from rock strata at the same location and at the same depth. In addition, try to ensure that the sampled rock blocks are complete and uniform, large in size, and sufficient for sampling, so as to reduce the error of the experiment. The processing of coal samples is carried out in accordance with the coal industry standard “Determination Method of Physical and Mechanical Properties of Coal.” Cylinder with diameter of 50 mm is drilled through the diamond hollow drill of vertical core-taking machine, and then cylindrical samples of different lengths (100 mm) are cut by automatic rock cutting machine. Finally, the two end faces are ground flat on the double-end grindstone machine. There are eight sets of samples, labeled A-1 through A-8, respectively.

In order to study the permeability characteristics of coal mass, eight groups of samples were treated separately. The samples A-6 and A-8 were humidified for 0 h, and the moisture content was 2.4%. The humidification treatment time of A-2 and A-4 samples is 17 hours, and the moisture content of the samples is 3.4%. The humidification treatment time of A-3 and A-5 samples is 33 hours, and the moisture content is 4.4%. The humidification treatment time of A-1 and A-7 samples is 69 hours, and the moisture content is 5.5%. The eight groups of samples were divided into four groups with different water content. The confining pressure is 5 MPa.

2.2. Test Equipment. The loading system is microcomputer controlled electrohydraulic servo testing machine. During the loading process, the system can collect load, displacement, and other data at the same time. The data acquisition system uses stress sensor, displacement sensor, and static strain gauge to measure the load and longitudinal and transverse deformation of the coal sample. As shown in the figure, the strain acquisition instrument has 20 channels, and each measuring point is automatically balanced, respectively. The measurement results can also be modified according to the sensitivity coefficient of the strain gauge, wire resistance, bridge mode, and sensitivity of various bridge sensors. In this experiment, half bridge connection is used to measure.

2.3. Stress-Strain Study. Through experiments, transverse strain and volumetric strain data of eight groups of samples were obtained, and then the Origin software was used to draw the figure below. Figure 1 shows the axial stress-strain diagrams from sample A-1 to sample A-8.

In the whole process of stress-strain prepeak curve, axial strain, transverse strain, and volumetric strain all increase with the increase of stress. As for the postpeak curve, the stress is decreasing, and the axial strain, transverse strain, and volumetric strain are all increasing. It shows that after the peak point, the coal mass is in a state of failure, and

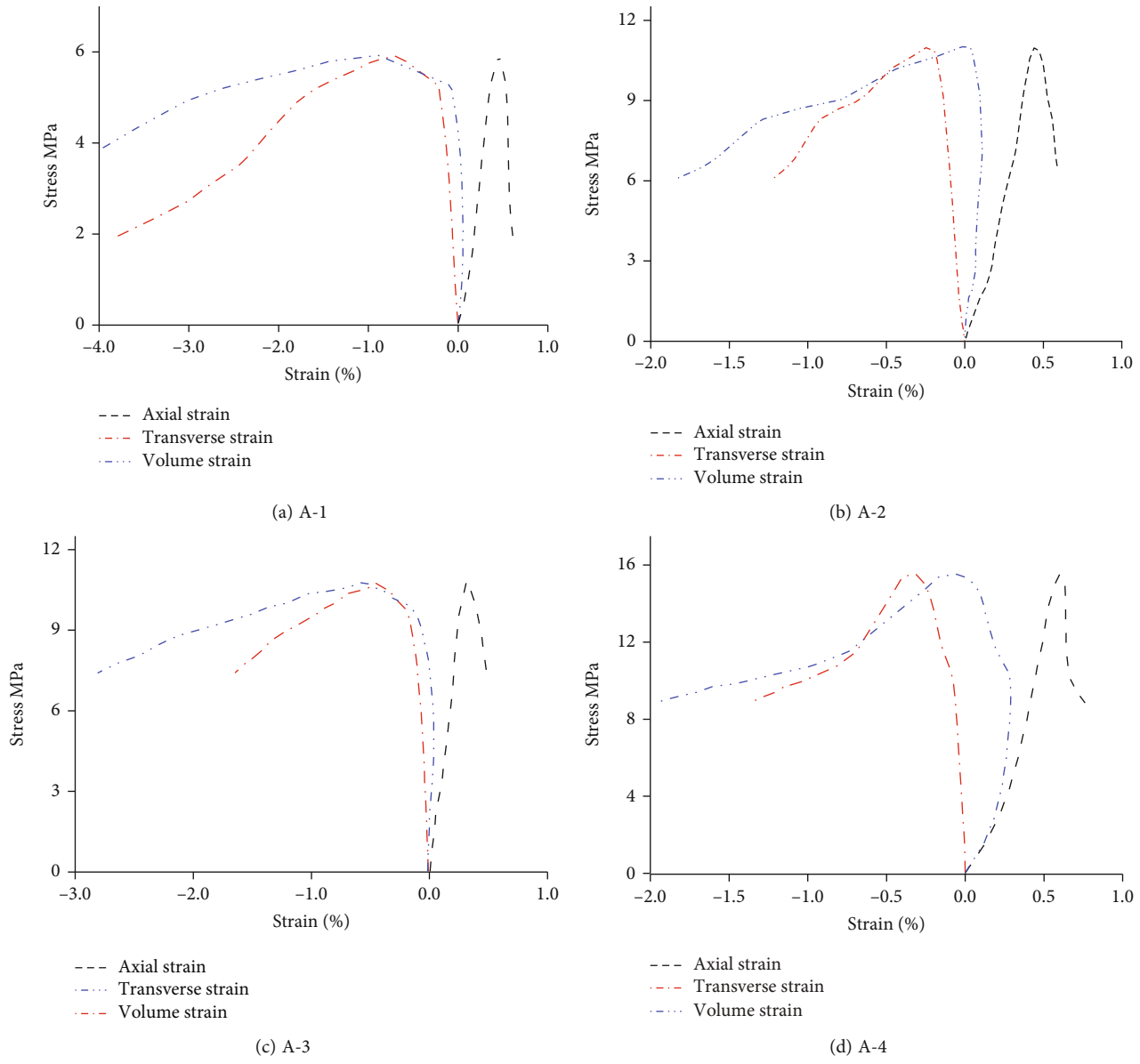


FIGURE 1: Continued.

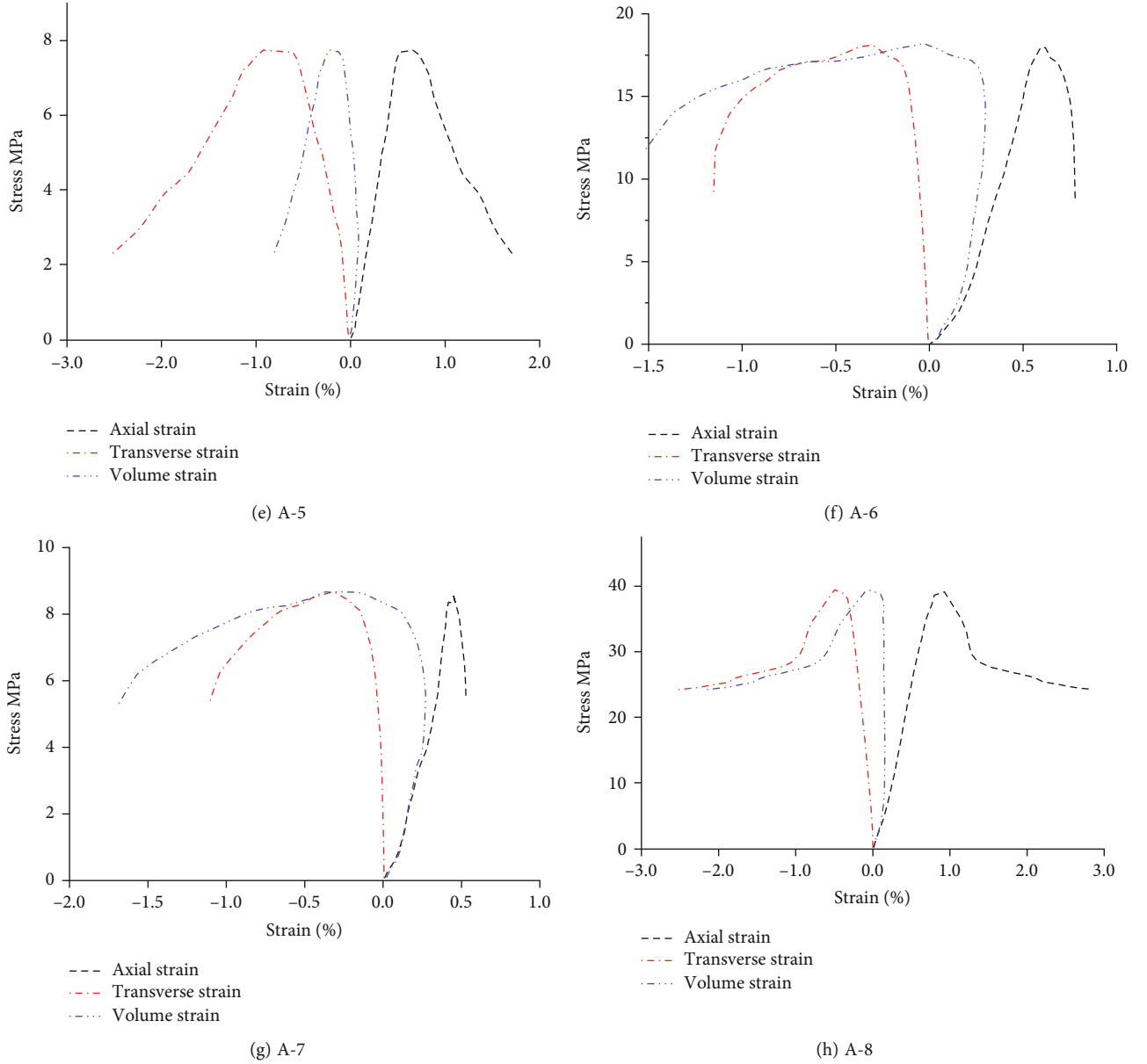


FIGURE 1: Axial stress-axial strain diagrams.

the deformation cannot be restored, which is consistent with the experiment. Before the peak, the increment of volumetric strain is smaller than the increment of axial strain and transverse strain, and the deformation of volumetric strain is smaller than that of axial and transverse strain. From the point of view that the component is compressed, the axial direction of the component is in the state of compression, while the transverse direction of the component is in the state of stretching. As a whole, the volumetric strain is first positive and then negative, indicating that the volume of the component decreases slightly in the process of unidirectional compression and then increases slightly with the destruction of the component, which is consistent with the theory.

2.4. Volumetric Strain Study. The primary condition of the crack volume strain should meet the small deformation con-

dition stipulated in “Elastic Mechanics,” which represents the volume strain generated by plastic deformation and fracture [41–43]. The detailed derivation process is as follows.

The axial force F , axial deformation Δl , and circumferential deformation value Δc of the whole process of rock loading and unloading failure can be obtained through the test.

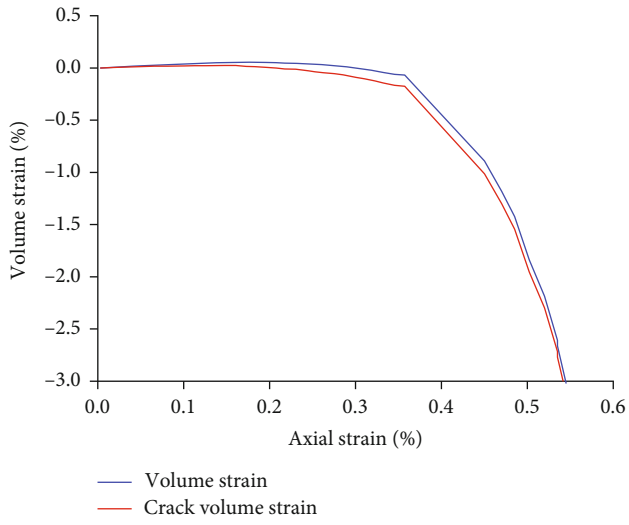
The axial strain is [44]

$$\varepsilon_1 = \frac{\Delta l}{l}, \quad (1)$$

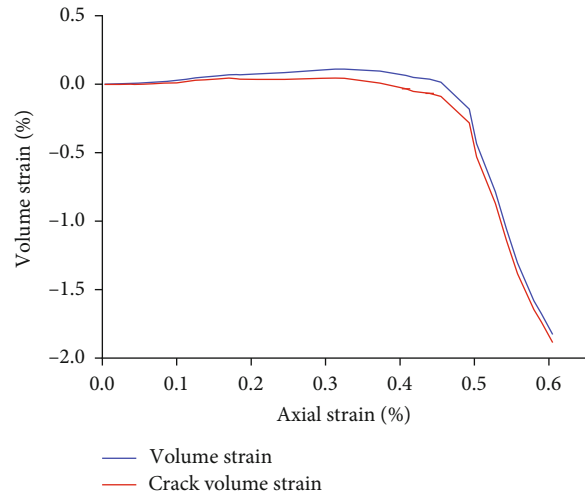
where l is the height of sample before loading.

The circumferential strain is [45]

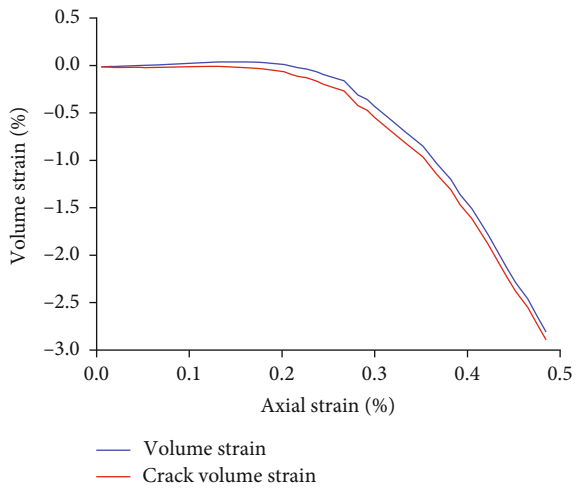
$$\varepsilon_2 = \frac{\Delta c}{c}, \quad (2)$$



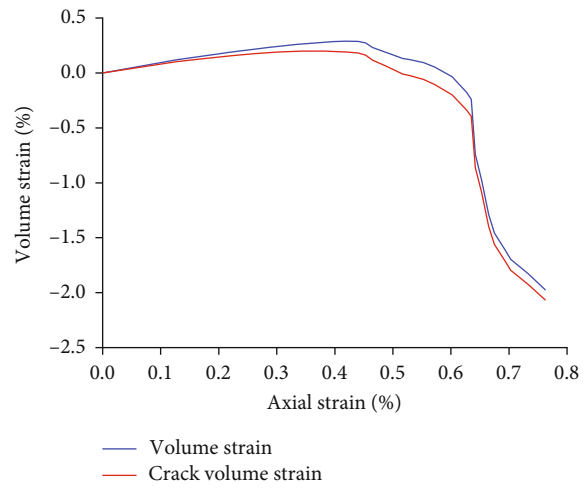
(a) A-1



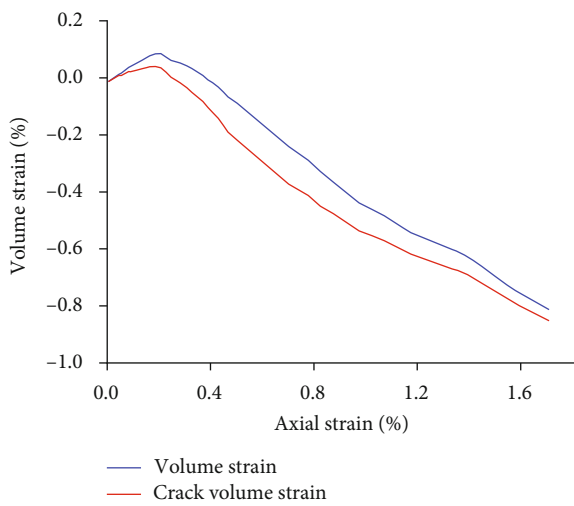
(b) A-2



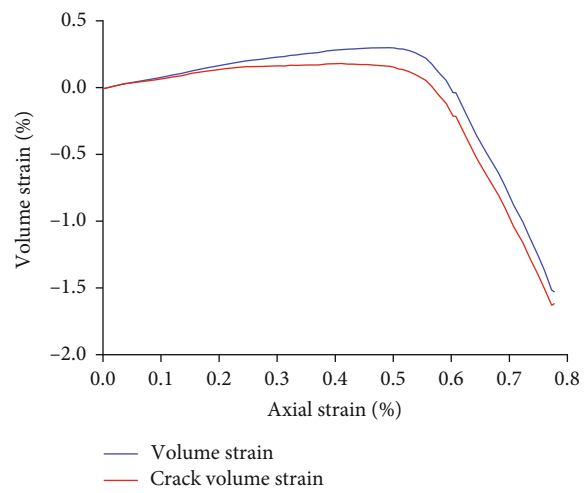
(c) A-3



(d) A-4



(e) A-5



(f) A-6

FIGURE 2: Continued.

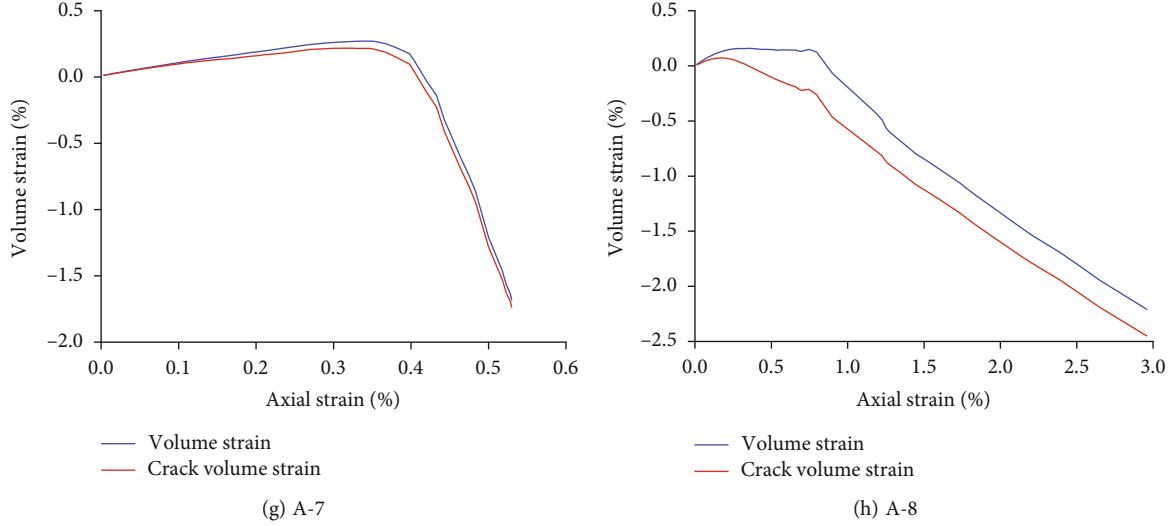


FIGURE 2: Volume strain-axial strain and crack volume strain-axial strain.

where Δc is the circumferential deformation, and c is the circumferential perimeter of the sample before deformation.

The volume strain is

$$\varepsilon_v = \varepsilon_1 + 2\varepsilon_2. \quad (3)$$

The volume strain of the crack of the circular specimen is

$$\varepsilon_{cv} = \varepsilon_v + \varepsilon_{ev}, \quad (4)$$

where ε_{cv} is the crack volume strain of the rock sample, and ε_{ev} is the projectile strain of the rock sample.

According to Hooke's Law:

$$\varepsilon_{e1} = \frac{1}{E}[\sigma_1 - \nu(\sigma_2 + \sigma_3)], \quad (5)$$

$$\varepsilon_{e2} = \frac{1}{E}[\sigma_2 - \nu(\sigma_1 + \sigma_3)], \quad (6)$$

where ε_{e1} is the axial elastic strain of the rock sample, and ε_{e2} is the circumferential elastic strain of rock sample.

For the conventional triaxial test, due to $\sigma_2 = \sigma_3$

$$\varepsilon_{cv} = \varepsilon_v - \frac{(1 - 2\nu)(\sigma_1 + 2\sigma_3)}{E}. \quad (7)$$

The equivalent plastic strain is

$$\varepsilon_{ep} = \frac{\sqrt{2}}{3} \sqrt{(\varepsilon_{1p} - \varepsilon_{2p})^2 + (\varepsilon_{2p} - \varepsilon_{3p})^2 + (\varepsilon_{1p} - \varepsilon_{3p})^2}, \quad (8)$$

where ε_{1p} , ε_{2p} , ε_{3p} are plastic strain in three principal stress directions.

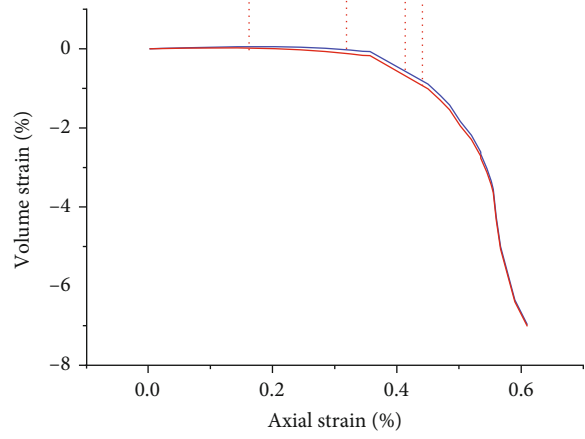
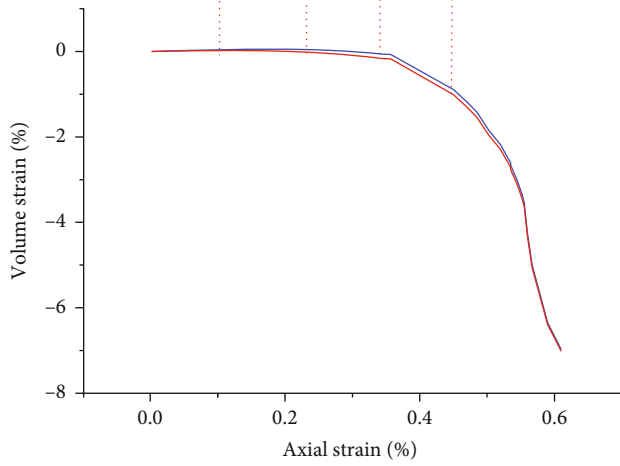
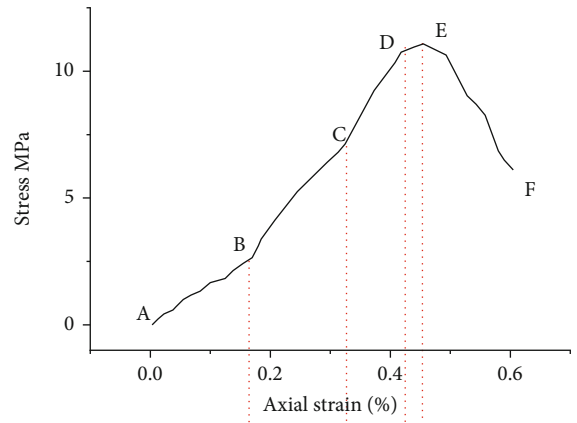
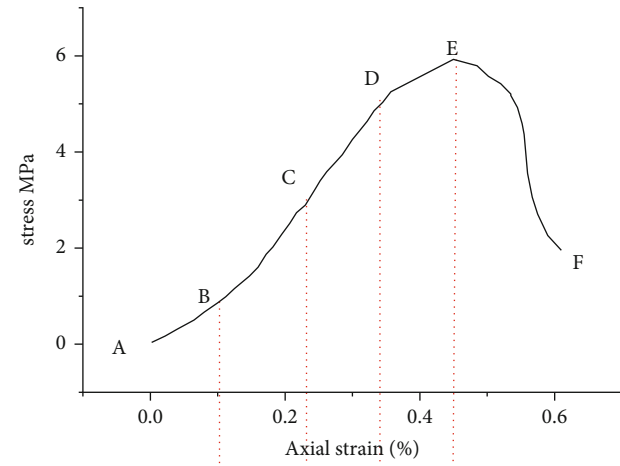
The above parameters were calculated from the experimental data, and Origin software was used to draw equivalent plastic strain-axial strain curve, as shown in Figure 2.

The analysis of the volume strain and crack volume strain shows that although the volume strain curve of the crack is close to volume strain curve, but it is always lower than the volume strain curve. In accordance with the physical meaning of crack volume strain, that is, under the condition of small deformation, the volume strain curve of the crack is similar to that of the volume strain. Through the study of crack volume strain, the degree and law of coal rock cracking can be further explained, which has certain guiding significance for coal mining.

2.5. Failure Process Analysis of Rock Samples. Based on the test data, volumetric strain-axial strain diagrams were drawn by software, and the failure of coal mass was analyzed by combining the graph with the test site situation.

According to Figure 3, coal mass experiences 6 stages from initial pressure to failure and then to residual deformation, and these six stages also show the nonlinear elastic behavior of rock. Because there are many small pores, cracks, and other defects in the rock, the stress-strain curve of rock under pressure is not linear, but nonlinear. The specific analysis is as follows:

- (1) *Crack Closure Stage (A-B in the Figure).* From the volume strain-axial strain curve of crack, it can be seen that there are natural cracks in the coal mass, and because of the external pressure, the natural cracks are constantly closed. When they reach point A, the natural cracks are completely closed, and the strain of the crack body tends to be 0
- (2) *The Elastic Stage (B-C in the Figure).* The volumetric strain of the crack is basically unchanged, and no new fracture occurs inside the rock. If the load is removed at this time, the coal mass will return to the original state, so this stage is called the elastic stage. Meanwhile, this relationship is linear elastic relationship



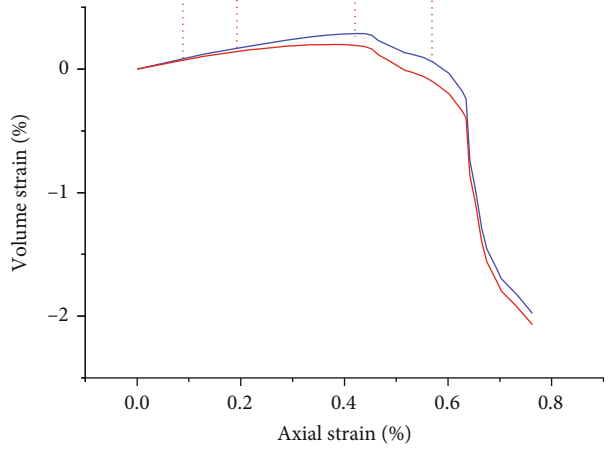
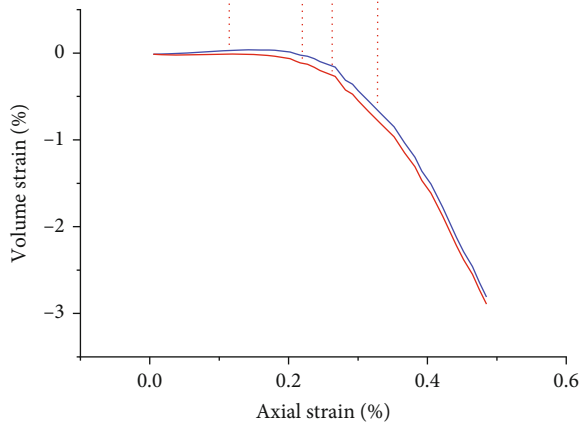
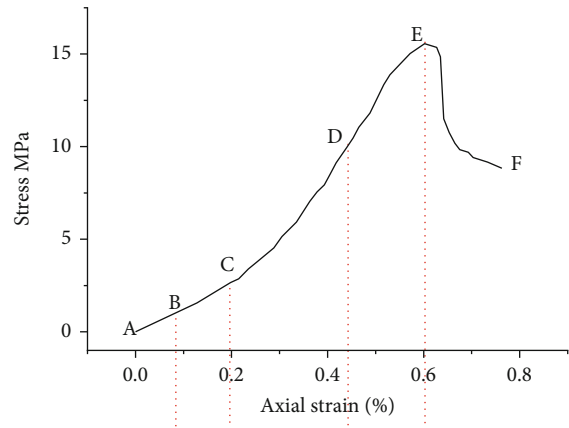
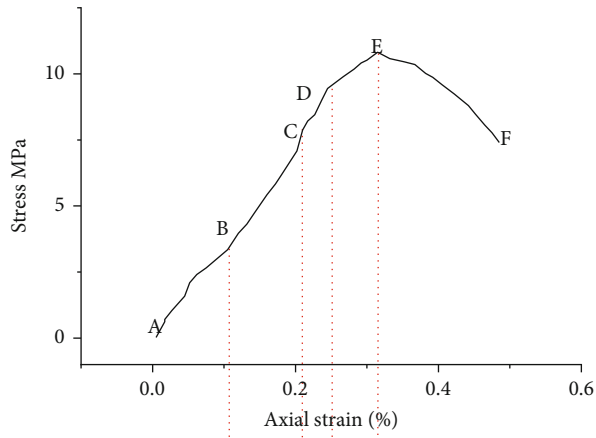
— Volume strain
— Crack volume strain

— Volume strain
— Crack volume strain

(a) A-1

(b) A-2

FIGURE 3: Continued.



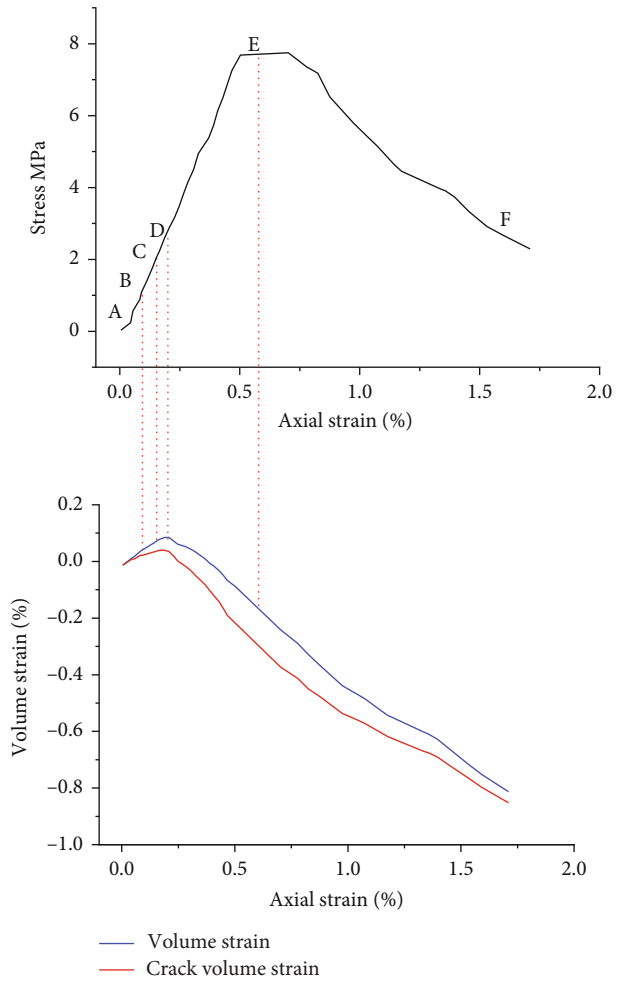
— Volume strain
— Crack volume strain

(c) A-3

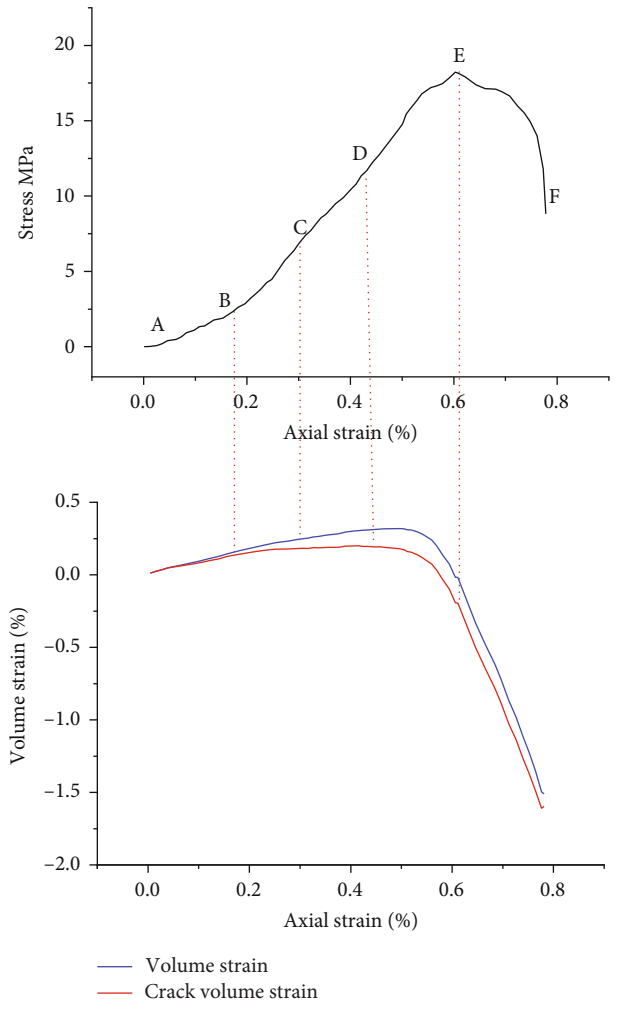
— Volume strain
— Crack volume strain

(d) A-4

FIGURE 3: Continued.



(e) A-5



(f) A-6

FIGURE 3: Continued.

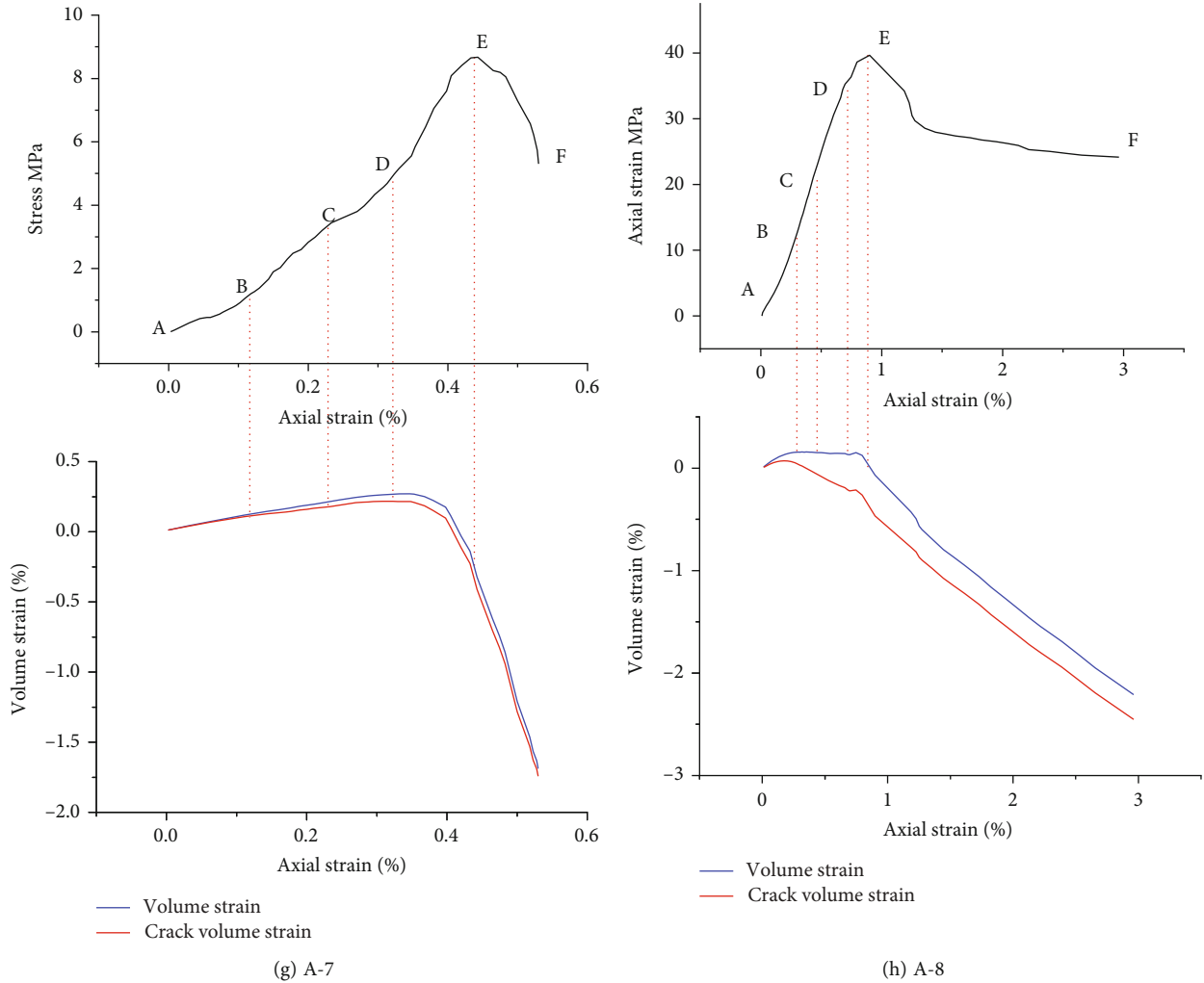


FIGURE 3: Stress-axial strain, volumetric strain-axial strain, and crack volume strain-axial strain.

- (3) *Tension Crack Development Stage (C-D in the Figure)*. New cracks begin to appear in the interior of coal mass, damage also begins to occur, and the volume strain of cracks keeps increasing. At this stage, the slope of volume strain-axial strain of the crack is low because the damage increase rate is relatively small. The failure process of rock samples is that the tensile cracks are generated first, and the shear failure is caused by the interaction of tensile cracks. Therefore, it can be considered that the stage (C-D section) when the crack volume strain begins to increase until the sudden change of volume strain occurs is the tensile failure inside the coal mass
- (4) *Macrocrack Development Stage (D-E in the Figure)*. When it reaches point D, the volume strain of coal mass changes abruptly, the slope of the volume strain curve of crack increases, the rate of damage increases, and the axial stress-strain curve begins to flatten. Therefore, it can be considered that at point D, tensile cracks run through each other and form

macroscopic cracks. The stage after point D can be considered as the development stage of macroscopic crack, and the coal mass changes from macroscopic continuous state to discontinuous state. However, the macrofailure mode of coal mass is determined by the interaction of tensile cracks, and pressure plays a certain control role on the interaction of tensile cracks, so pressure plays a control role on the macro-failure mode of coal mass

- (5) *Rock Structural Stage (E-F in the Figure)*. When it reaches point F, the axial strain of coal mass reaches the maximum. At this time, because of the penetration of macro cracks, coal mass can no longer be regarded as rock material, and coal mass bears load with rock structure. The postpeak stress-strain response of coal mass is not only related to the material properties and the macroscopic failure mode but also related to the stiffness of the test machine. This is because the postpeak behavior of rock is the coordination between rock structure and external forces tends to be stable

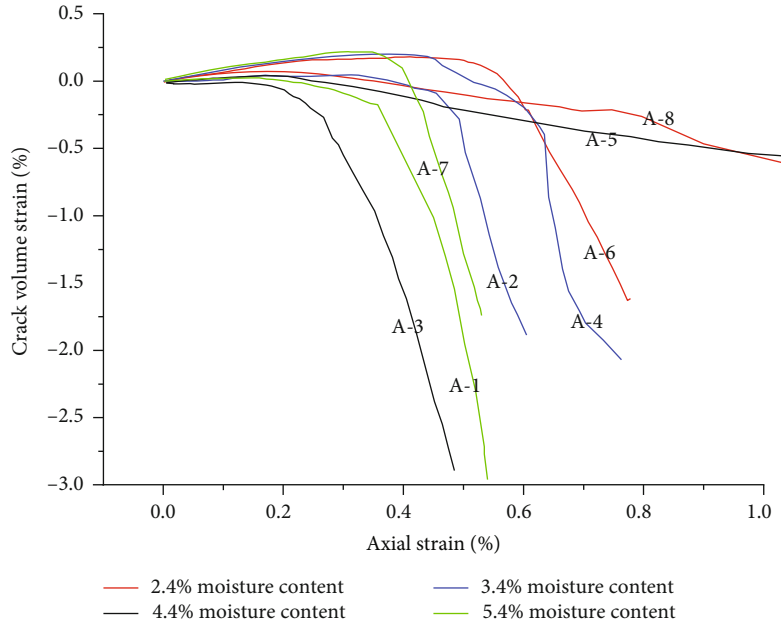


FIGURE 4: Volume strain-axial strain diagram of crack under different water content.

(6) *Residual Strength Stage (after F in the Figure)*. When it reaches point F, the damaged coal mass forms a stable rock structure and rock structure reaches a state of equilibrium. Therefore, the residual strength is shown on the axial stress-strain curve. The slope decreases at point F on the equivalent plastic strain-axial strain curve, indicating that the growth rate of the equivalent plastic strain decreases at point F, and the rock structure tends to be relatively stable and enters the residual strength. The volumetric strain slightly decreases after reaching point F, indicating that the rock structure tend to be stable

Figure 4 shows the volumetric strain-axial strain diagram of the crack under different water content, from which it can be concluded:

- (1) The volumetric strain-axial strain graphs of cracks with different water content have basically the same variation rule. The volume strain of the crack increases slightly at first and then decreases continuously. This is because at the beginning of pressure, the natural cracks in coal begin to close in the crack closure stage, and the crack volume strain approaches 0 at this time. In the subsequent elastic stage, the volume strain of the crack is basically unchanged. During the tensile crack development stage, new cracks appear and the volume strain of cracks begins to increase. At the macrocrack development stage, the slope of the crack increases and begins to decrease
- (2) The larger the moisture content is, the more rapidly the curve of the crack changes from the beginning to the residual strength. Because the higher the moisture content is, the more cracks in the coal mass

are, the weaker the ability to resist deformation is, and the faster it reaches the stage of residual strength

3. Study on Brittleness Index of Coal Mass

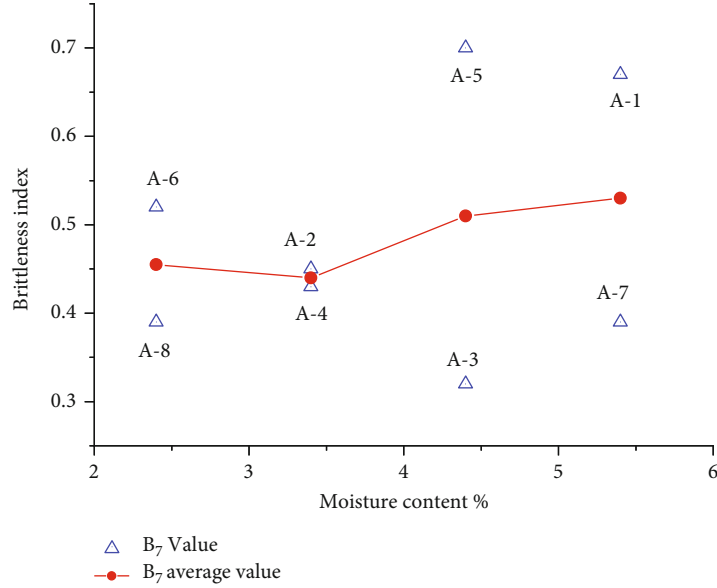
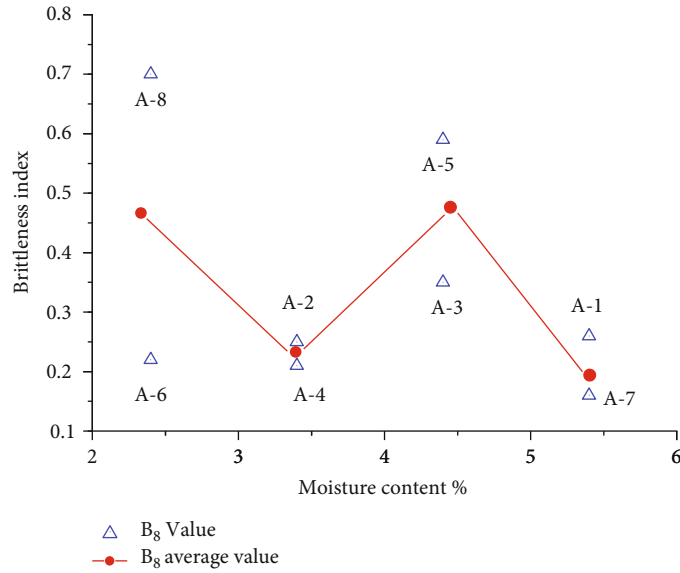
Brittleness is a physical attribute of coal mass, which is related to the mineral composition and stress action of coal mass [46–48]. Reservoir rock brittleness is mechanical properties evaluation, borehole wall stability evaluation, and the important indexes for evaluation of hydraulic fracturing effect. It has a good reference value for the safety analysis of rock engineering under the coupling effect of stress and seepage [49]. Although there is no unified standard of rock brittleness definition and testing method, but low strain or damage and fracture of tensile fracture damage, high-pressure ratio, high resilience, and after peak stress drop quickly recognized as is shown by the nature of the rock brittleness [50, 51]. The following are several common methods of brittleness evaluation.

3.1. Curve Method. Curve method is a brittleness evaluation method established according to each stage corresponding to axial stress-strain curve [52]. Thus, establishing the brittleness index

$$B_7 = \frac{\sigma_p - \sigma_r}{\sigma_p}, \tag{9}$$

where σ_p and σ_r are the peak stress and residual stress, respectively.

Based on the experimental data and the formula of the brittleness index B_7 , the image of the brittleness index B_7 under the different water content is made. As shown in Figure 5, the greater the value of B_7 , the stronger the brittleness of coal. It can be seen from the above figure that from

FIGURE 5: B_7 under different conditions.FIGURE 6: B_8 at different water content.

the B_7 value of each pattern, the B_7 value of A-5 with water content of 4.4% is the largest, and the brittleness is stronger, followed by A-1 with water content of 5.4%. From the mean value of the pattern, the pattern with water content of 5.4% has the highest B_7 value and the strongest brittleness, followed by the pattern with water content of 4.4%.

It is considered that the smaller the difference between the strain in which the friction strength reaches the maximum value (i.e., the peak strain) and the strain in which the cohesion weakens to the residual value (i.e., the residual strain)

$$B_8 = \frac{\varepsilon_r - \varepsilon_p}{\varepsilon_r}, \quad (10)$$

where ε_p and ε_r are the peak strain and residual strain, respectively.

According to the test data and the formula of B_8 , the image of B_8 with different water content is made by Origin software. According to Figure 6, the smaller the value of B_8 is, the stronger the brittleness of coal mass will be. From the B_8 value of each pattern, the B_8 value of A-7 with water content of 5.4% is the smallest, and the brittleness of coal is stronger, followed by A-4 with water content of 3.4%. From the average B_7 value of the pattern, the pattern with water content of 5.4% has the smallest value and the strongest brittleness, followed by the pattern with water content of 3.4%.

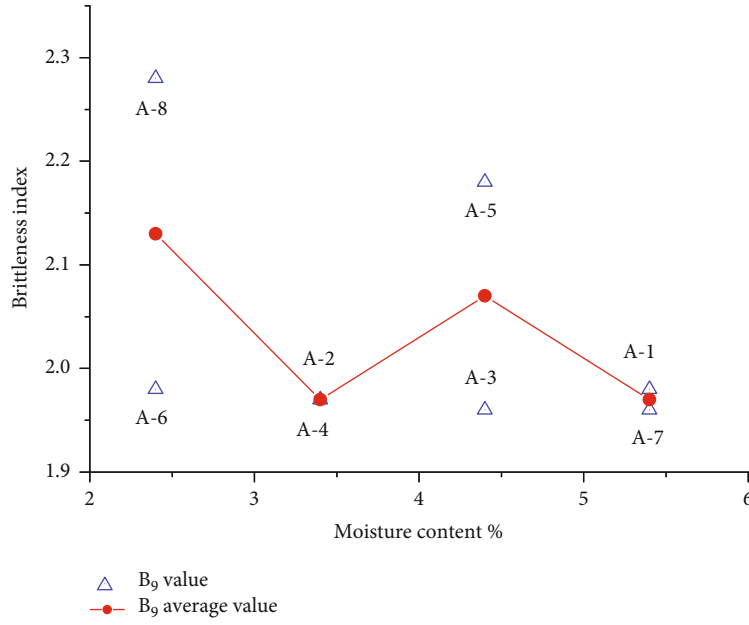


FIGURE 7: \$B_9\$ under different water content.

On the basis of summarizing the previous studies, a brittleness index which considered the mechanical characteristics of pre- and postpeak simultaneously.

$$B_9 = B'_9 + B''_9, \quad (11)$$

$$B''_9 = \alpha C_S + \beta C_S + \eta, \quad (12)$$

$$C_S = \frac{\varepsilon_p(\sigma_p - \sigma_r)}{\sigma_p(\varepsilon_r - \varepsilon_p)}, \quad (13)$$

where α , β , and η are the standardization coefficient, and C_S is the ratio of the absolute value of the postpeak curve slope to the prepeak curve slope.

According to the test data and the formula of B_9 , the image of B_9 under different water content is made by Origin software. According to Figure 7, the B_9 value of A-3 and A-7 is the smallest, which is 1.96. The value B_9 of A-8 is the largest, 2.28. It indicates that the brittleness of A-3 and A-7 is the strongest, while that of A-8 is the least. The average brittleness index with the water content of 3.4% is the smallest, and the brittleness is stronger. The average brittleness index of 2.4% is the largest and the weakest.

We studied the brittleness index

$$B_{10} = B'_{10} B''_{10}, \quad (14)$$

$$B'_{10} = \frac{\sigma_p - \sigma_r}{\sigma_p}, \quad (15)$$

$$B''_{10} = \frac{\lg |K_{ac}|}{10}, \quad (16)$$

where K_{ac} is the slope of the postpeak curve. The higher the value of B_{10} , the higher the degree of brittleness.

According to the test data and the formula of B_{10} , the image of B_{10} is made by Origin software. As shown in Figure 8, the greater the value of B_{10} is, the stronger the brittleness of coal mass is. From the B_{10} value of each pattern, the B_{10} value of A-1 with water content of 5.4% is the largest, and the brittleness of coal mass is stronger, followed by A-4 with water content of 3.4%. From the average B_{10} value of the pattern, the B_{10} value of the pattern with water content of 3.4% and 5.4% is equal and the largest, and the brittleness is the strongest.

3.2. Energy Method. The brittleness index is established by using the energy relation expressed by the axial stress-strain curve [53–55], which corresponds to the energy change of coal mass during the compression process. It defines the brittleness index by the ratio of

$$B_{11} = \frac{A_2}{A_1}, \quad (17)$$

where A_2 is defined as the recoverable energy (the area of BCD in Figure 9), and A_1 is defined as the total energy (the area of the OABD region in Figure 9). The greater the value of B_{11} is, the greater the recovery elastic energy and brittleness will be. Figure 9 shows a diagram of brittleness index B_{11} of coal.

According to the test data and the formula of B_{10} , the image of B_{11} under different water content is made by Origin software. Analysis: as shown in Figure 10, the greater the value of B_{11} , the greater the recovery elastic energy, and the stronger the brittleness of coal. From the B_{11} value of each pattern, A-6 with water content of 2.4% has the largest B_{11} value, and the brittleness is stronger, followed by A-3 with water content of 4.4%. From the average B_{11} value of the pattern, the pattern with 2.4% water content has the

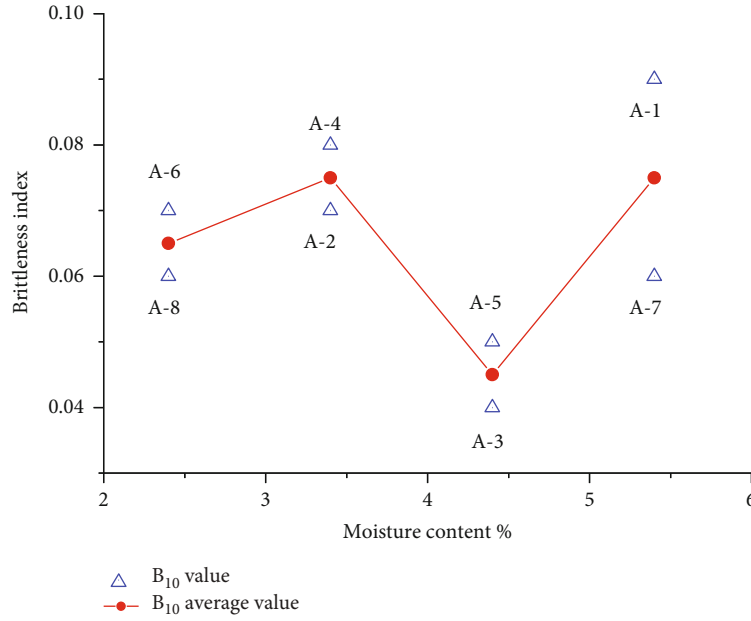


FIGURE 8: B_{10} under different water content.

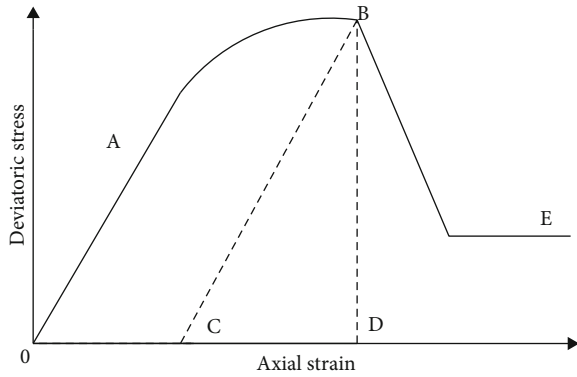


FIGURE 9: Schematic diagram of brittleness index B_{11} .

largest value and the strongest brittleness, followed by the pattern with 3.4% water content.

Tarasov et al. also considered the energy of postpeak process and proposed using the ratio of postpeak fracture energy to postpeak recoverable elastic energy as the brittleness index.

$$B_{12} = \frac{d_{wr}}{d_{we}}, \quad (18)$$

where d_{wr} is defined as the postpeak rupture energy (the gray area on the right and in Figure 11), and d_{we} is defined as the elastic energy behind the peak (the difference between the area of the large red triangle on the left of Figure 11 and the small red triangle on the right of Figure 11). The lower the value of B_{12} , the more brittle the rock is. Figure 11 shows a diagram of brittleness index B_{12} of coal.

According to the test data and the formula of B_{10} , the image of B_{12} under different water content is made by Origin software. As shown in Figure 12, the smaller the value of B_{12} , the stronger the brittleness of coal mass. From the B_{12} value of each pattern, the B_{12} value of A-1 with water content of 5.4% is the smallest, and the brittleness of coal is stronger, followed by A-7 with water content of 5.4%. From the average B_{12} value of the pattern, the pattern with water content of 5.4% has the smallest value and the strongest brittleness, followed by the pattern with water content of 3.4%.

After peak stress drop rate is of great significance to the rock brittleness characterization, but at the same time cannot be ignored before the peak stress-strain state for the influence of the rock brittleness. It is proposed that rock and rock damage when the release of elastic energy storage before total energy ratio and peak B_E common characterization of rock brittleness indexes

$$B_{14} = B_{\text{post}} + B_E, \quad (19)$$

$$B_{\text{post}} = \frac{\sigma_p - \sigma_r}{\varepsilon_r - \varepsilon_p}, \quad (20)$$

$$B_E = \frac{W_1}{W_2}, \quad (21)$$

where W_1 is defined as the elastic energy released by rock failure (the blue area in the figure). The higher the index B_{14} is, the more brittle the rock is. Figure 13 shows a diagram of brittleness index B_{14} of coal.

According to the test data and the formula of B_{10} , the image of B_{14} under different water content is made by Origin software. According to Figure 14, the greater the value of B_{14} is, the stronger the brittleness of coal mass will be. From the B_{14} value of each pattern, A-6 with water content of 2.4% has

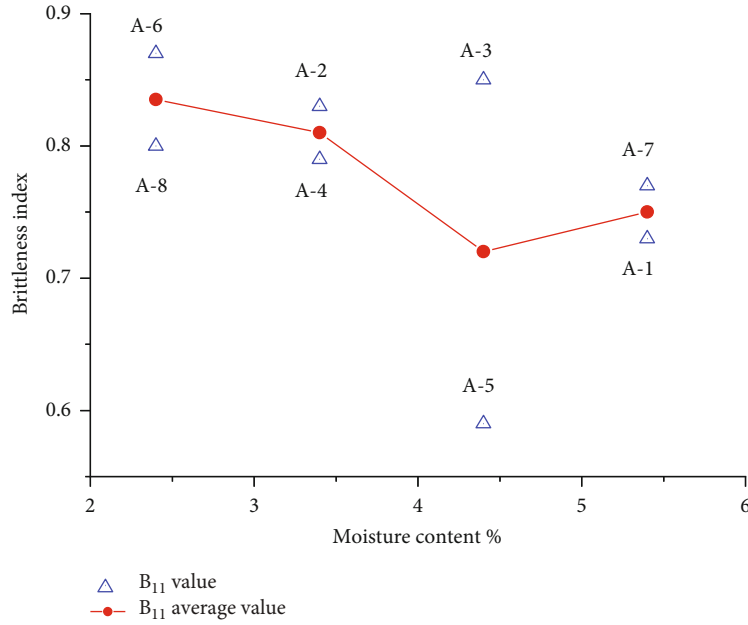


FIGURE 10: B_{11} under different water content.

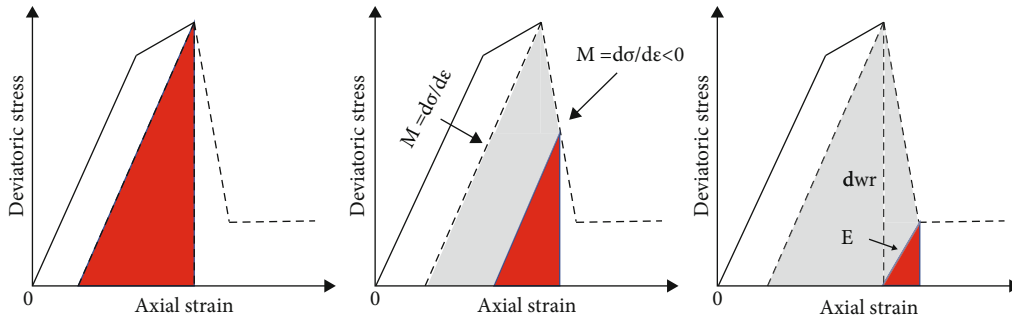


FIGURE 11: Schematic diagram of brittleness index B_{12} .

the largest B_{14} value, and the brittleness is stronger, followed by A-4 with water content of 3.4%. From the average B_{14} value of the pattern, the pattern with water content of 3.4% has the largest B_{14} value and the strongest brittleness, followed by the pattern with water content of 5.4%.

Table 1 shows a summary of B values at different water contents. The analysis shows that although the brittleness of samples with different water content is evaluated from different brittleness indexes, the results are consistent. The lower the water content, the greater the brittleness. With the increase of water content, the brittleness of coal samples decreases, showing certain softening characteristics.

4. Constitutive Model

The coal mass can be divided into six stages from loading to failure [56–58]: (1) crack closure stage, (2) elastic stage, (3) development stage of tensile crack, (4) the development stage of macrocrack, (5) rock structure stage, and (6) residual strength stage. However, the proportion of the crack closure stage to the axial strain stage cannot be ignored.

4.1. *Duncan-Chang Model.* Duncan-Chang model is described as follows [59, 60]:

$$\sigma = \frac{\varepsilon}{a + b\varepsilon}, \tag{22}$$

$$\sigma = \frac{\varepsilon}{a + b\varepsilon + c\varepsilon^2}, \tag{23}$$

where the coefficients of a , b , and c are $a = 1/E_0$, $b = 1/\sigma_c - 2/\varepsilon_c E_0$, $c = 1/E_0 \varepsilon_c^2$.

E_0 is the initial modulus of elasticity ($E_0 = d\sigma/d\varepsilon | \varepsilon \rightarrow 0$), σ_c is UCS strength (uniaxial compressive strength), and ε_c is the corresponding axial strain.

The model is described as follows [61]:

$$\sigma = E\varepsilon \exp \left[-\left(\frac{\varepsilon}{\varepsilon_0} \right)^m \right]. \tag{24}$$

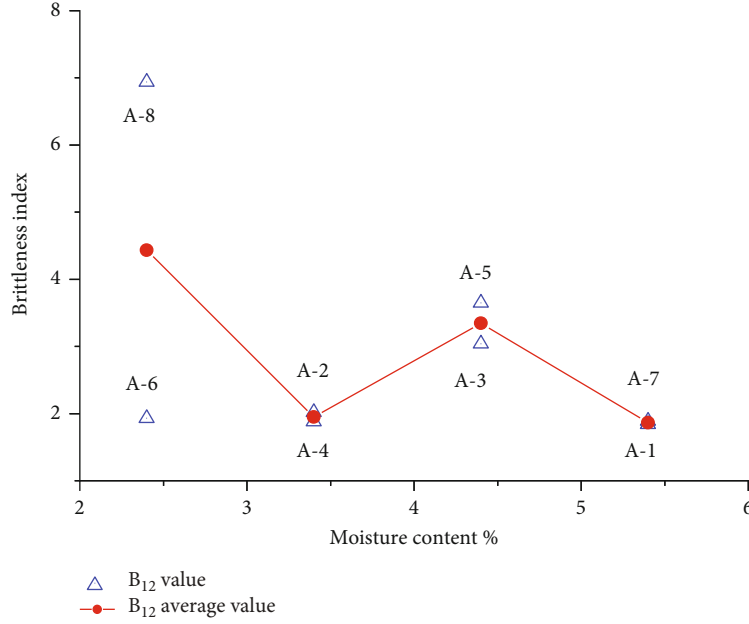


FIGURE 12: B_{12} under different moisture content.

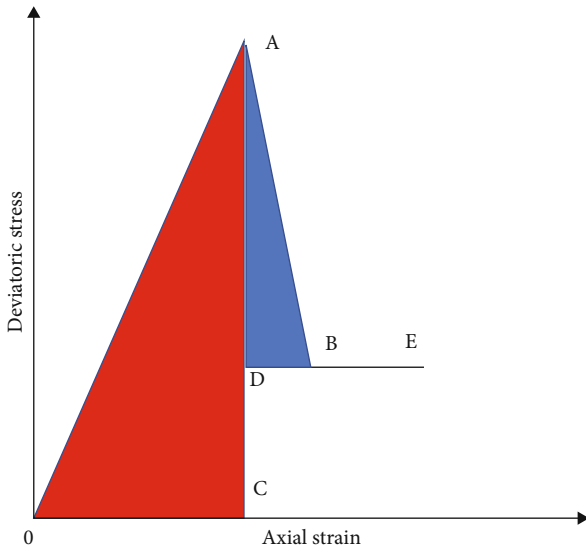


FIGURE 13: Schematic diagram of brittleness index B_{14} .

E is the modulus of elasticity.

$$m = \frac{1}{\ln(E\varepsilon_c/\sigma_c)}, \quad (25)$$

$$\varepsilon_0 = \frac{\varepsilon_c}{(1/m)^{1/m}}. \quad (26)$$

The stress-strain curve from the experiment is converted to the stress-strain curve ignoring the fracture closure stage.

The model calculation based on Weber distribution is as follows [62, 63]:

$$\sigma = E(\varepsilon - \varepsilon'_c) \exp \left[-\left(\frac{\varepsilon - \varepsilon'_c}{\varepsilon_0} \right)^m \right]. \quad (27)$$

The determination of the axial strain ε_x used for differentiation is based on experiment.

$$\sigma = \begin{cases} \frac{\varepsilon}{a + b\varepsilon + c\varepsilon^2} & \varepsilon \leq \varepsilon_x, \\ E(\varepsilon - \varepsilon'_c) \exp \left[-\left(\frac{\varepsilon - \varepsilon'_c}{\varepsilon_0} \right)^m \right] & \varepsilon > \varepsilon_x, \end{cases} \quad (28)$$

where $a = 1/E_0$, $b = 1/\sigma_c - 2/\varepsilon_2 E_0$, $c = 1/E_0 \varepsilon_c^2$, $m = 1/\ln E\varepsilon_c/\sigma_c$, and $\varepsilon_0 = \varepsilon_c/(1/m)^{1/m}$.

4.2. Practice of Duncan-Chang Model. The experimental data were put into the Duncan-Chang model, and the Origin software was used to draw the corresponding graphs. Table 2 shows the parameters of Duncan-Chang model.

As you can see from Figure 15, at the prepeak stage, the fitting curve is very close to the actual curve, which indicates the correctness of Duncan-Chang model and that the Duncan-Chang model has a correct direction for the study of coal mass.

From the strength of coal and rock, under the same water content and the same axial stress, the axial strain of sample A-6 is greater than that of sample A-8, indicating that under the same conditions, the structure and texture of sample A-6 are looser and softer than that of sample A-8, so the axial strain is larger. The axial strain of sample A-4 is greater than that of sample A-2, indicating that under

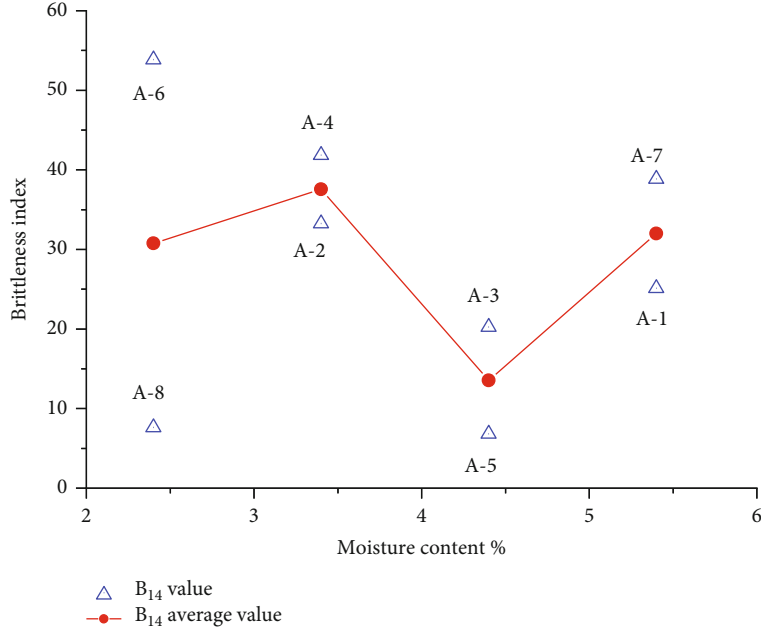


FIGURE 14: B_{14} under different moisture content.

TABLE 1: Summary of B values at different water content.

Experimental group no.	Moisture content (%)	B_7	B_8	B_9	B_{10}	B_{11}	B_{12}	B_{14}
A-8	2.4	0.39	0.7	2.28	0.06	0.8	6.94	7.62
A-6	2.4	0.52	0.22	1.98	0.07	0.87	1.93	53.88
A-2	3.4	0.45	0.25	1.97	0.07	0.83	2.02	33.28
A-4	3.4	0.43	0.21	1.97	0.08	0.79	1.88	41.86
A-3	4.4	0.32	0.35	1.96	0.04	0.85	3.04	20.25
A-5	4.4	0.7	0.59	2.18	0.05	0.59	3.65	6.83
A-7	5.4	0.39	0.16	1.96	0.06	0.77	1.89	38.86
A-1	5.4	0.67	0.26	1.98	0.09	0.73	1.84	25.14

TABLE 2: Parameters of Duncan-Chang model.

	a	b	c	E	ϵ_0	ϵ'_c	m
A-1	0.13866	-0.19682	-0.30191	18.51	0.4968	0.069	6.286
A-2	0.08417	-0.20721	0.26803	39.53	0.3787	0.141	11.51
A-3	0.02849	-0.11827	1.39539	39.91	0.362	0.018	11.6
A-4	0.10949	-0.19167	0.09463	43.58	0.4959	0.211	10.06
A-5	0.10036	-0.19886	0.30131	20.4	0.6961	0.103	5.237
A-6	0.15007	-0.57475	0.74232	40.45	0.535	0.135	23.34
A-7	0.18879	-1.04542	2.26044	24.51	8.882	0.101	6.081
A-8	0.03317	-0.00628	-0.09582	60.65	1.103	0.089	4.97

the same conditions, the structure and texture of sample A-4 are looser and softer than that of sample A-2, so the axial strain is larger. The intersection point in the figure is because A-2 of the sample has passed the peak stress point and started to decline. Because the Duncan-Chang model studies the stage before the peak stress, the part of A-2 decline can

be ignored. The axial strain of sample A-5 is greater than that of sample A-3, indicating that under the same conditions, and the structure and texture of sample A-5 are looser and softer than that of sample A-3, so the axial strain is larger. The axial strain of sample A-1 is greater than that of sample A-7, indicating that under the same conditions, the structure and texture of sample A-1 are looser and softer than that of sample A-7, so the axial strain is larger. However, the fitting situation of the second half of sample A-7 is not very good, because the test data of the second half do not conform to the Duncan-Chang model and changes irregularly.

4.3. *Function Fitting.* When the Duncan-Chang model was used to fit the test data, a function was occasionally obtained that fitted the test data well, as shown below [64, 65]:

$$\sigma = \begin{cases} \frac{\epsilon}{a + b\epsilon + c\epsilon^2} & \epsilon \leq \epsilon_x, \\ d - e\epsilon^e & \epsilon > \epsilon_x. \end{cases} \quad (29)$$

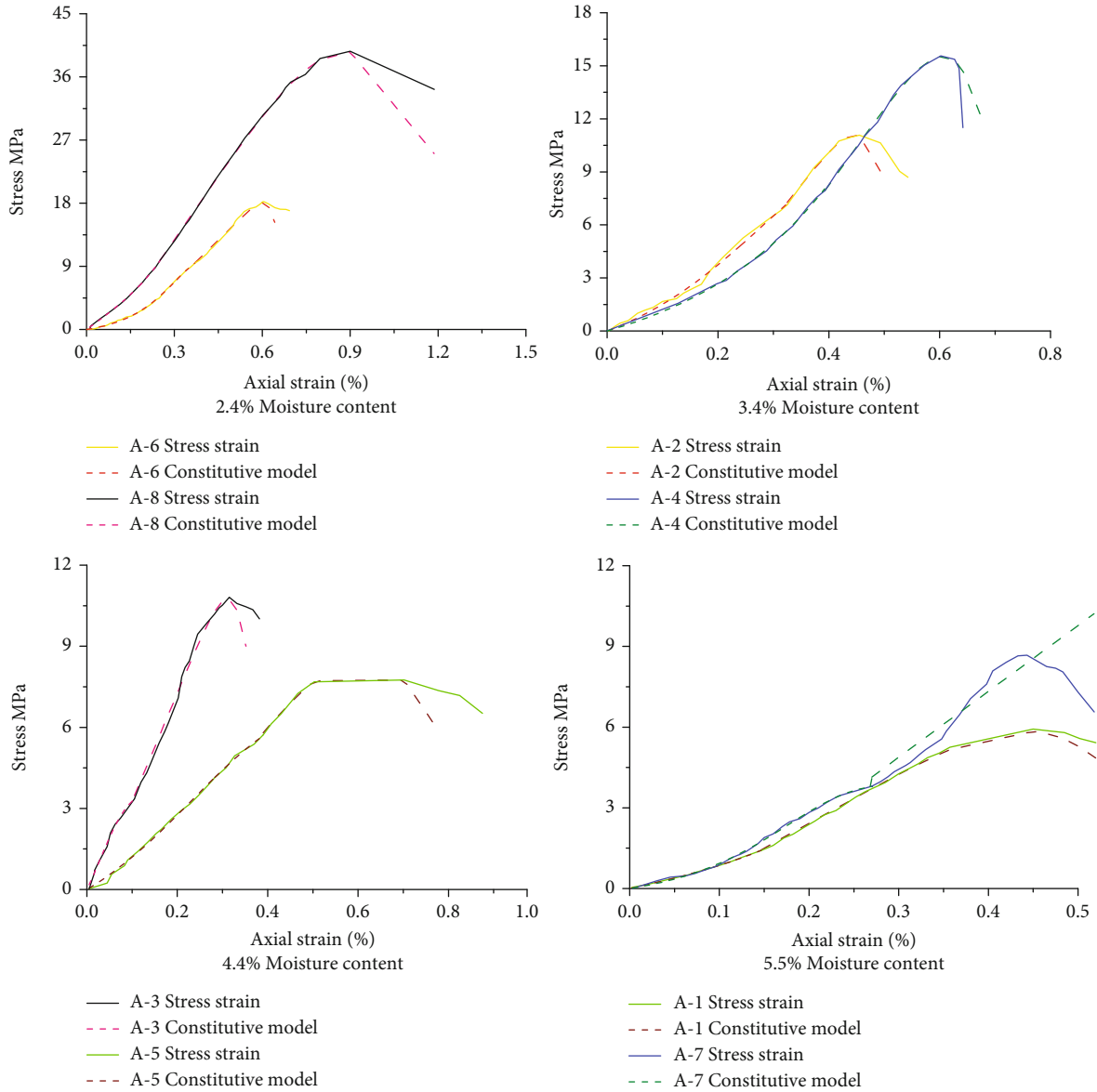


FIGURE 15: Constitutive model diagram of different water content.

The first half of this function is the same as the Duncan-Chang model ($\epsilon \leq \epsilon_\chi$), and the second half refers to a new function.

The fitting Figure 16 is as follows:

The axial stress-strain diagrams at different water content fitted by this function are very close to the results fitted by the Duncan-Chang model, and the conclusions are the same. Water content has softened effect on coal and rock. Under the same conditions, sample A-8 is denser and harder than sample A-6. The structure of sample A-2 is denser, and the texture is harder than that of sample A-4. The structure of sample A-3 is denser, and the texture is harder than that of sample A-5. The structure of sample A-7 is denser, and the texture is harder than that of sample A-1. The failure mechanism of media cracks is further revealed through Figure 16. First, the primary cracks are compacted, and the

cracks are reduced. Then, with the increase of load, new cracks appear and more cracks become.

In addition, it can be seen from Figure 16 that the peak stress of coal samples with different moisture content is also different. With the increase of moisture content, the peak stress of coal samples generally shows a downward trend. The peak stress of coal samples with moisture content of 2.4% is the largest, the peak stress of coal samples with moisture content of 5.4% is the smallest, and the peak stress decreases by about 75%.

5. Study on Seepage Characteristics

According to the permeability measured by the test combined with other data from the test, the graph is drawn as follows:

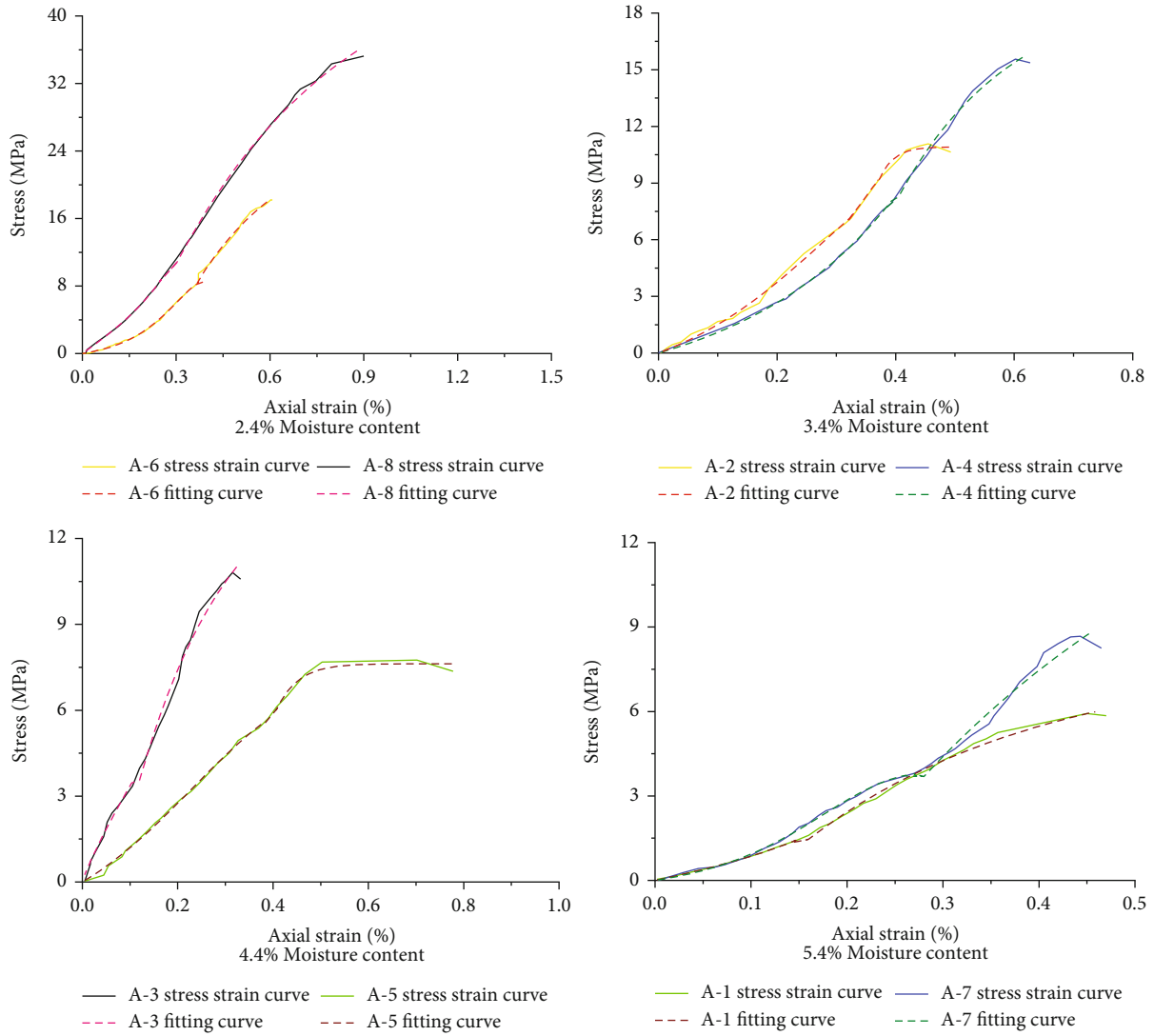


FIGURE 16: Fitting diagram of different water content.

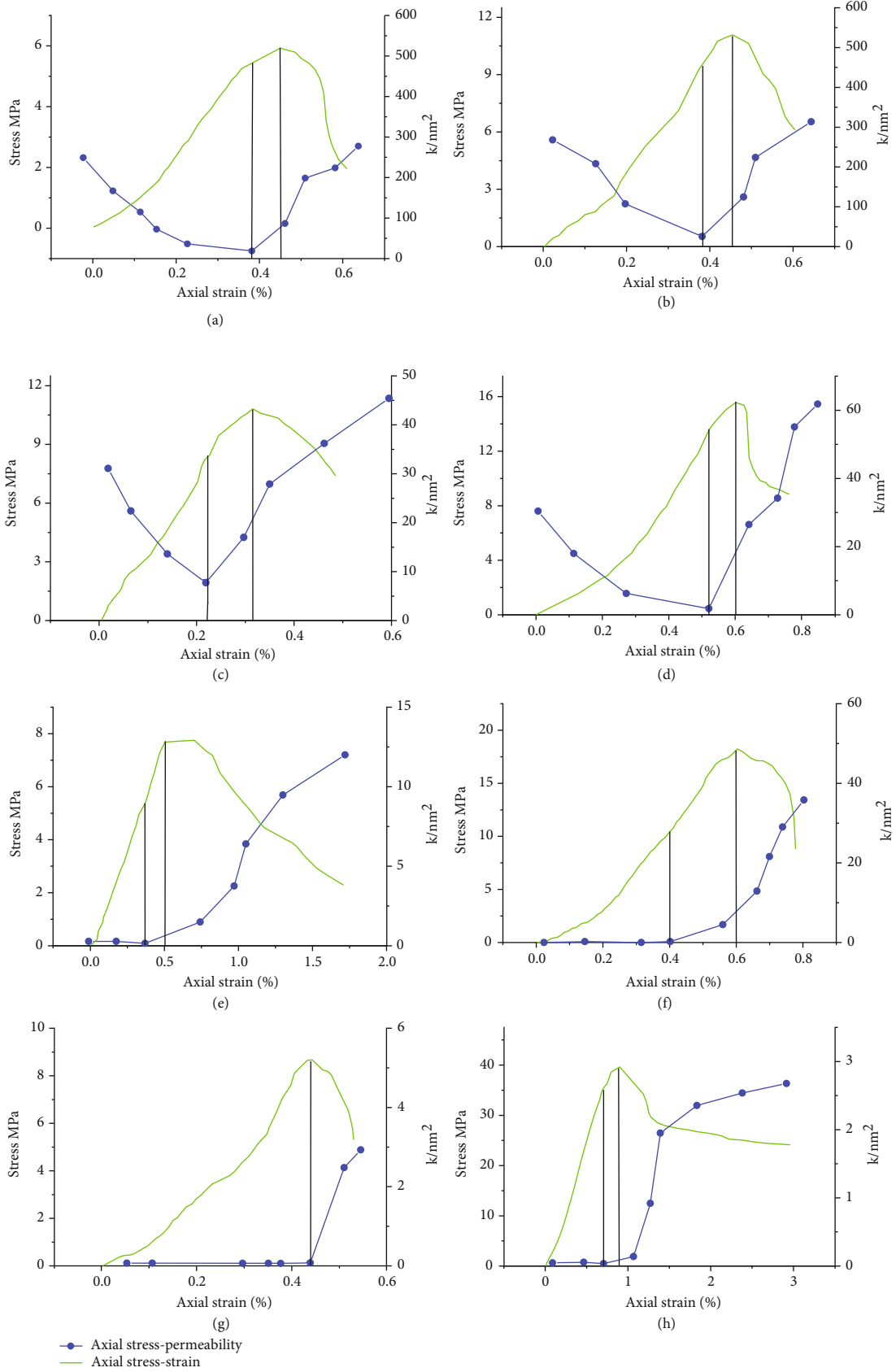


FIGURE 17: Stress-axial strain, permeability-axial strain diagram of the pattern.

As you can see from Figure 17, the permeability changes of different coal types are basically the same, and the permeability of coal masses decreases first and then increases. At the initial loading and elastic deformation stage, the pattern cracks close gradually, and the permeability decreases with the increase of axial stress and strain. With the increase of the axial load, the axial stress and strain gradually increase, new cracks appear inside the pattern, new channels are added, and the permeability of the pattern gradually increases. After entering the failure stage, macrocracks appear and permeability increases rapidly.

6. Conclusion

In this paper, triaxial compression test combined with Origin graphic processing technology is used to carry out loading and unloading tests and image processing on coal mass patterns, identify and obtain useful information, and then analyze the mechanical behavior of coal mass and the study of seepage characteristics in unloading process. In data processing, many kinds of software have been used in numerical calculation and drawing, mainly including MATLAB, ABAQUS, EXCEL, and other software. In the analysis and research of this paper, the following conclusions are obtained:

According to the analysis of axial stress-strain graph, the coal mass can be divided into six stages from the initial loading to the failure stage: crack closure stage, elastic stage, development stage of tensile crack, the development stage of macrocrack, rock structure stage, and residual strength stage. It is also very important to know the crack closure stage of coal mass through the constitutive model, and the proportion of the crack in the axial strain cannot be ignored.

Through the analysis of permeability axial strain curve, it can be concluded that the permeability of coal and rock mass first decreases and then increases with the increase of load. Because at the beginning of loading, the crack of coal and rock mass begins to close, the channel in coal and rock body decreases, and the permeability decreases. As the load continues to increase, the coal and rock mass begin to produce new cracks, the channels increase, and the permeability increases. After loading to the failure stage, the coal and rock masses are completely destroyed, a large number of macrocracks are generated, and the permeability increases rapidly. The moisture content also reduces the strength of coal and rock, and the mechanical properties become worse. Through the in-depth study on the strength, mechanical properties, and permeability characteristics of damaged coal samples, the law is obtained, which plays a guiding role in coal mining and gas extraction, and can avoid coal mine disasters and accidents as much as possible.

Data Availability

The raw/processed data required to reproduce these findings are available upon request by contact with the corresponding author.

Conflicts of Interest

The authors declare that they have no conflicts of interest.

References

- [1] L. Yuan, "Innovation and development of safety science and technology in coal industry of China," *Safety in Coal Mines*, vol. 46, no. S1, pp. 5–11, 2015.
- [2] W. U. Cai, L. I. Ren, and F. U. Gui, "Training content design of preventing gas explosion accidents from the perspective of statistics of accident cases," *Safety in Coal Mines*, vol. 49, no. 8, pp. 266–268, 2018.
- [3] G. Fu and Z. Zheng, "Research on reasons classification for unsafe acts in coalmine water accidents," *Safety in coal mines*, vol. 47, no. 7, p. 244, 2016.
- [4] S. V. Valiulin, A. A. Onischuk, A. M. Baklanov et al., "Effect of coal mine organic aerosol on the methane/air lower explosive limit," *International Journal of Coal Science & Technology*, vol. 7, no. 4, pp. 778–786, 2020.
- [5] M. Więckowski, N. Howaniec, and A. Smoliński, "Effect of flow rates of gases flowing through a coal bed during coal heating and cooling on concentrations of gases emitted and fire hazard assessment," *International Journal of Coal Science & Technology*, vol. 7, no. 1, pp. 107–121, 2020.
- [6] G. U. Wei-juan, Z. H. Guo-shu, Z. H. Zhi-gen, C. H. Qing-hua, C. H. Ming-qiang, and X. U. Guang-quan, "Multi-index comprehensive identification and real-time warning of coal and gas outburst," *Journal of Mining and Safety Engineering*, vol. 30, no. 6, p. 922, 2013.
- [7] J. Tan, C. L. Jiang, X. W. Li, and Y. J. Chen, "Relationship and research progress of coal and gas outburst mechanism and outburst prediction," *Safety in Coal Mines*, vol. 47, no. 4, pp. 186–190, 2016.
- [8] C. Zhang, Z. T. Wang, D. Y. Yang, and C. C. Tian, "Study on mine safety manufacture accidents by factorial analysis," *Coal Technology*, vol. 35, no. 6, pp. 314–315, 2016.
- [9] P. Gao and G. Fu, "Study on characteristics and occurrence regularities of roof accidents in Chinese coal mines," *Industrial Safety and Environmental Protection*, vol. 40, no. 8, pp. 46–48, 2014.
- [10] K. Wang and F. Du, "Coal-gas compound dynamic disasters in China: a review," *Process Safety and Environmental Protection*, vol. 133, pp. 1–17, 2020.
- [11] L. Zhu, F. Dang, Y. Xue, K. Jiao, and W. Ding, "Multivariate analysis of effects of microencapsulated phase change materials on mechanical behaviors in light-weight aggregate concrete," *Journal of Building Engineering*, vol. 42, article 102783, 2021.
- [12] H. Cheng, N. Zhang, Y. Yang, Y. Dong, and W. Peng, "3-D dynamic evolution analysis of coal-rock damaged field and gas seepage field during the gas extraction process," *Journal of Natural Gas Science and Engineering*, vol. 56, pp. 444–454, 2018.
- [13] Z. Zhao, N. Ma, H. Jia, and Y. Cheng, "Partitioning characteristics of gas channel of coal-rock mass in mining space and gas orientation method," *International Journal of Mining Science and Technology*, vol. 23, no. 6, pp. 873–877, 2013.
- [14] J. I. Hou, "Coal and gas outburst hazard analysis of complex coal seam based on fuzzy clustering method," *Safety in Coal Mines*, vol. 48, no. 6, p. 160, 2017.

- [15] F. Du, K. Wang, X. Zhang, C. Xin, L. Shu, and G. Wang, "Experimental study of coal-gas outburst: insights from coal-rock structure, gas pressure and adsorptivity," *Natural Resources Research*, vol. 29, no. 4, pp. 2481–2493, 2020.
- [16] W. J. Yu, J. Zhang, Z. G. Yuan, and P. Wang, "Engineering mechanics behavior and surrounding rock control of mine loose coal and rock roadway," *Coal Science and Technology*, vol. 44, no. 6, pp. 52–59, 2016.
- [17] Y. Weijian, F. Tao, W. Weijun et al., "Support problems and solutions of roadway surrounding rock for thin coal seams under complex conditions in southern China," *Journal of China Coal Society*, vol. 40, no. 10, pp. 2370–2379, 2015.
- [18] P. F. Wu, W. G. Liang, M. T. Cao, J. F. Yang, and L. Li, "Experimental investigation on model I fracture characteristics of coal in different stratification," *Chinese Journal of Underground Space and Engineering*, vol. 13, no. S2, pp. 538–545, 2017.
- [19] C. Zhang, S. G. Li, Q. Zeng, and H. F. Lin, "Numerical simulation on permeation laws of grouting in coal and rock fracture," *Safety in coal mines*, vol. 46, no. 12, p. 19, 2015.
- [20] X. C. Li, L. Zhang, and Y. L. Zhao, "Evolution of gas-filled coal creep-seepage under conventional triaxial compression," *Advanced Engineering Sciences*, vol. 50, no. 4, pp. 55–62, 2018.
- [21] Y. Huang, L. T. Zhou, and Z. F. Zhou, "Equations for permeability variation of fractured rock mass under high water pressure," *Journal of Engineering Geology*, vol. 26, no. 6, pp. 1433–1438, 2018.
- [22] T. L. Xiao, X. P. Li, and Y. H. Guo, "Experimental study of failure characteristic of single jointed rock mass under triaxial compression tests," *Rock and Soil Mechanics*, vol. 33, no. 11, pp. 3251–3261, 2012.
- [23] X. Wang, Z. Feng, H. Li, J. Wei, and L. Wang, "Reliability analysis of acoustic emission for coal and gas outburst under triaxial loading," *Safety in Coal Mines*, vol. 46, no. 8, pp. 160–163, 2015.
- [24] Z. T. Bieniawski, "The effect of specimen size on compressive strength of coal," *International Journal of Rock Mechanics and Mining Sciences & Geomechanics Abstracts*, vol. 5, no. 4, pp. 325–335, 1968.
- [25] S. Wang, D. Elsworth, and J. Liu, "Permeability evolution during progressive deformation of intact coal and implications for instability in underground coal seams," *International Journal of Rock Mechanics and Mining Sciences*, vol. 58, pp. 34–45, 2013.
- [26] G. Yin, Y. Liu, M. Li, B. Deng, and J. Lu, "Influence of true triaxial loading-unloading stress paths on mechanical property and permeability of coal," *Journal of the China Coal Society*, vol. 43, no. 1, pp. 131–136, 2018.
- [27] Y. Xue, F. Gao, Y. N. Gao, and X. Liang, "Research on mining-induced permeability evolution model of damaged coal in post-peak stage," *Journal of China University of Mining & Technology*, vol. 46, no. 3, pp. 521–527, 2017.
- [28] Y. Xue, F. Gao, Y. Gao, X. Liang, Z. Zhang, and Y. Xing, "Thermo-hydro-mechanical coupled mathematical model for controlling the pre-mining coal seam gas extraction with slotted boreholes," *International Journal of Mining Science and Technology*, vol. 27, no. 3, pp. 473–479, 2017.
- [29] Y. Xue, F. Gao, T. Teng, and Y. Xing, "Effect of gas pressure on rock burst proneness indexes and energy dissipation of coal samples," *Geotechnical and Geological Engineering*, vol. 34, no. 6, pp. 1737–1748, 2016.
- [30] X. G. Liu, *Study on the Deformation and Failure Characteristics and the Permeation Behavior of Gas-Saturated Coal*, China University of Mining & Technology, 2013.
- [31] R. Yuan, C. Chen, X. Wei, and X. Li, "Heat-fluid-solid coupling model for gas-bearing coal seam and numerical modeling on gas drainage promotion by heat injection," *International Journal of Coal Science & Technology*, vol. 6, no. 4, pp. 564–576, 2019.
- [32] W. Zhao, K. Wang, R. Zhang, H. Dong, Z. Lou, and F. An, "Influence of combination forms of intact sub-layer and tectonically deformed sub-layer of coal on the gas drainage performance of boreholes: a numerical study," *International Journal of Coal Science & Technology*, vol. 7, no. 3, pp. 571–580, 2020.
- [33] D. Guo, P. Lv, J. Zhao, and C. Zhang, "Research progress on permeability improvement mechanisms and technologies of coalbed deep-hole cumulative blasting," *International Journal of Coal Science & Technology*, vol. 7, pp. 329–336, 2020.
- [34] Y. Xue, J. Liu, F. Dang, X. Liang, S. Wang, and Z. Ma, "Influence of CH₄ adsorption diffusion and CH₄-water two-phase flow on sealing efficiency of caprock in underground energy storage," *Sustainable Energy Technologies and Assessments*, vol. 42, p. 100874, 2020.
- [35] Y. Xue, P. G. Ranjith, F. Dang et al., "Analysis of deformation, permeability and energy evolution characteristics of coal mass around borehole after excavation," *Natural Resources Research*, vol. 29, no. 5, pp. 3159–3177, 2020.
- [36] Y. Xue, T. Teng, F. Dang, Z. Ma, S. Wang, and H. Xue, "Productivity analysis of fractured wells in reservoir of hydrogen and carbon based on dual-porosity medium model," *International Journal of Hydrogen Energy*, vol. 45, no. 39, pp. 20240–20249, 2020.
- [37] K. Anyim and Q. Gan, "Fault zone exploitation in geothermal reservoirs: production optimization, permeability evolution and induced seismicity," *Advances in Geo-Energy Research*, vol. 4, no. 1, pp. 1–12, 2020.
- [38] H. Sidiq, R. Amin, and T. Kennaird, "The study of relative permeability and residual gas saturation at high pressures and high temperatures," *Advances in Geo-Energy Research*, vol. 1, no. 1, pp. 64–68, 2017.
- [39] L. Chen, *Research on Failure Strain and Permeability Evolution of the Coal Ahead of Working Face and Its Application*, China University of Mining & Technology, Beijing, 2016.
- [40] Z. H. Xia, X. B. Zhang, C. Yao et al., "Experimental studies on seepage characteristics during the loading and unloading confining pressure of post-peak fractured rock," *Journal of China Coal Society*, vol. 44, no. 11, pp. 3379–3387, 2019.
- [41] P. Hou, X. Liang, Y. Zhang, J. He, F. Gao, and J. Liu, "3D multi-scale reconstruction of fractured shale and influence of fracture morphology on shale gas flow," *Natural Resources Research*, vol. 30, no. 3, pp. 2463–2481, 2021.
- [42] Y. Xue, Z. Cao, and Z. Li, "Destabilization mechanism and energy evolution of coal pillar in rockburst disaster," *Arabian Journal of Geosciences*, vol. 13, no. 13, pp. 1–13, 2020.
- [43] Y. Xue, J. Liu, P. G. Ranjith, X. Liang, and S. Wang, "Investigation of the influence of gas fracturing on fracturing characteristics of coal mass and gas extraction efficiency based on a multi-physical field model," *Journal of Petroleum Science and Engineering*, vol. 206, p. 109018, 2021.
- [44] F. Ghasemi, M. Ghaedi, and M. Escrochi, "A new scaling equation for imbibition process in naturally fractured gas

- reservoirs,” *Advances in Geo-Energy Research*, vol. 4, no. 1, pp. 99–106, 2020.
- [45] Y. Xue, J. Liu, X. Liang, and Z. Y. Ma, “Nonlinear evolution characteristics of acoustic emission and fracture mechanism of coal under gas pressure,” *Chinese Journal of Geotechnical Engineering*, vol. 43, pp. 241–245, 2021.
- [46] Y. Rafiei and M. Motie, “Improved reservoir characterization by employing hydraulic flow unit classification in one of Iranian carbonate reservoirs,” *Advances in Geo-Energy Research*, vol. 3, no. 3, pp. 277–286, 2019.
- [47] J. Liu, Y. Xue, Q. Zhang, K. Yao, X. Liang, and S. Wang, “Micro-cracking behavior of shale matrix during thermal recovery: insights from phase-field modeling,” *Engineering Fracture Mechanics*, vol. 239, p. 107301, 2020.
- [48] J. Liu, X. Liang, Y. Xue, K. Yao, and Y. Fu, “Numerical evaluation on multiphase flow and heat transfer during thermal stimulation enhanced shale gas recovery,” *Applied Thermal Engineering*, vol. 178, p. 115554, 2020.
- [49] Y. Xue, P. G. Ranjith, F. Gao et al., “Mechanical behaviour and permeability evolution of gas-containing coal from unloading confining pressure tests,” *Journal of Natural Gas Science and Engineering*, vol. 40, pp. 336–346, 2017.
- [50] Z. Z. Cao, Y. L. Ren, Q. T. Wang, B. H. Yao, and X. C. Zhang, “Evolution mechanism of water-conducting channel of collapse column in karst mining area of southwest China,” *Geofluids*, vol. 2021, Article ID 6630462, 2021.
- [51] Y. Xue, F. Dang, F. Liu et al., “An elastoplastic model for gas flow characteristics around drainage borehole considering post-peak failure and elastic compaction,” *Environmental Earth Sciences*, vol. 77, no. 19, pp. 1–18, 2018.
- [52] E. Broni-Bediako and R. Amarin, “Experimental study on the effects of cement contamination in a water based mud,” *Advances in Geo-Energy Research*, vol. 3, no. 3, pp. 314–319, 2019.
- [53] Y. Xue, T. Teng, L. Zhu et al., “Evaluation of the non-Darcy effect of water inrush from karst collapse columns by means of a nonlinear flow model,” *Water*, vol. 10, no. 9, p. 1234, 2018.
- [54] J. Liu, Y. Xue, W. Chen, P. Hou, S. Wang, and X. Liang, “Variational phase-field model based on lower-dimensional interfacial element in FEM framework for investigating fracture behavior in layered rocks,” *Engineering Fracture Mechanics*, vol. 255, p. 107962, 2021.
- [55] Y. Xue, F. Dang, Z. Cao et al., “Deformation, permeability and acoustic emission characteristics of coal masses under mining-induced stress paths,” *Energies*, vol. 11, no. 9, p. 2233, 2018.
- [56] P. Hou, X. Liang, F. Gao, J. B. Dong, J. He, and Y. Xue, “Quantitative visualization and characteristics of gas flow in 3D pore-fracture system of tight rock based on Lattice Boltzmann simulation,” *Journal of Natural Gas Science and Engineering*, vol. 89, article 103867, 2021.
- [57] L. Zhu, F. Dang, Y. Xue, W. Ding, and L. Zhang, “Analysis of micro-structural damage evolution of concrete through coupled X-ray computed tomography and gray-level co-occurrence matrices method,” *Construction and Building Materials*, vol. 224, pp. 534–550, 2019.
- [58] Y. Xue, F. Gao, and X. Liu, “Effect of damage evolution of coal on permeability variation and analysis of gas outburst hazard with coal mining,” *Natural Hazards*, vol. 79, no. 2, pp. 999–1013, 2015.
- [59] T. Teng, Y. Xue, and C. Zhang, “Modeling and simulation on heat-injection enhanced coal seam gas recovery with experimentally validated non-Darcy gas flow,” *Journal of Petroleum Science and Engineering*, vol. 177, pp. 734–744, 2019.
- [60] Z. Z. Cao, P. Xu, Z. H. Li, M. X. Zhang, Y. Zhao, and W. L. Shen, “Joint bearing mechanism of coal pillar and backfilling body in roadway backfilling mining technology,” *CMC-Computers Materials & Continua*, vol. 54, no. 2, pp. 137–159, 2018.
- [61] X. Liang, P. Hou, Y. Xue, X. J. Yang, F. Gao, and J. Liu, “A fractal perspective on fracture initiation and propagation of reservoir rocks under water and nitrogen fracturing,” *Fractals*, vol. 29, no. 7, p. 2150189, 2021.
- [62] J. Liu, X. Liang, Y. Xue, Y. Fu, K. Yao, and F. Dou, “Investigation on crack initiation and propagation in hydraulic fracturing of bedded shale by hybrid phase-field modeling,” *Theoretical and Applied Fracture Mechanics*, vol. 108, p. 102651, 2020.
- [63] L. Zhu, F. Dang, Y. Xue, W. Ding, L. Zhang, and X. Xiong, “Meso-scale damage detection and assessment of concrete under dynamic compression loading using X-ray computed tomography,” *Materials Characterization*, vol. 176, p. 111149, 2021.
- [64] J. Liu, K. Yao, Y. Xue, X. Zhang, Z. Chong, and X. Liang, “Study on fracture behavior of bedded shale in three-point-bending test based on hybrid phase-field modelling,” *Theoretical and Applied Fracture Mechanics*, vol. 104, p. 102382, 2019.
- [65] L. Zhu, F. Dang, Y. Xue, W. Ding, and K. Jiao, “Experimental investigation of the thermal and mechanical properties of lightweight aggregate concrete mixed with microencapsulated phase change materials,” *International Journal of Energy Research*, vol. 45, no. 9, pp. 12864–12878, 2021.

Research Article

Prediction and Evaluation of Coal Mine Coal Bump Based on Improved Deep Neural Network

Shuang Gong ^{1,2,3,4}, Yi Tan ^{1,2} and Wen Wang^{2,3}

¹State Key Laboratory of Water Resource Protection and Utilization in Coal Mining, Beijing 100011, China

²School of Energy Science and Engineering, Henan Polytechnic University, Jiaozuo 454000, China

³Henan Key Laboratory for Green and Efficient Mining & Comprehensive Utilization of Mineral Resources, Jiaozuo 454000, China

⁴Collaborative Innovation Center of Coal Work Safety, Jiaozuo, Henan Province 454000, China

Correspondence should be addressed to Yi Tan; 517237667@qq.com

Received 3 August 2021; Accepted 24 September 2021; Published 20 October 2021

Academic Editor: Haiyan Wang

Copyright © 2021 Shuang Gong et al. This is an open access article distributed under the Creative Commons Attribution License, which permits unrestricted use, distribution, and reproduction in any medium, provided the original work is properly cited.

Coal bump prediction is one of the key problems in deep coal mining engineering. To predict coal bump disaster accurately and reliably, we propose a depth neural network (DNN) prediction model based on the dropout method and improved Adam algorithm. The coal bump accident examples were counted in order to analyze the influencing factors, characteristics, and causes of this type of accidents. Finally, four indexes of maximum tangential stress of surrounding rock, uniaxial compressive strength of rock, uniaxial tensile strength of rock, and elastic energy of rock are selected to form the prediction index system of coal bump. Based on the research results of rock burst, 305 groups of rock burst engineering case data are collected as the sample data of coal bump prediction, and then, the prediction model based on a dropout and improved Adam-based deep neural network (DA-DNN) is established by using deep learning technology. The DA-DNN model avoids the problem of determining the index weight, is completely data-driven, reduces the influence of human factors, and can realize the learning of complex and subtle deep relationships in incomplete, imprecise, and noisy limited data sets. A coal mine in Shanxi Province is used to predict coal bump with the improved depth learning method. The prediction results verify the effectiveness and correctness of the DA-DNN coal bump prediction model. Finally, it is proved that the model can effectively provide a scientific basis for coal bump prediction of similar projects.

1. Introduction

Coal bump is a dynamic phenomenon characterized by sudden, rapid, and violent destruction of coal (rock) around roadway or mining face due to the instantaneous release of elastic deformation energy [1]. This kind of disaster is a bottleneck problem in underground mining engineering, which directly threatens the safety of construction personnel and equipment and then seriously affects the project progress. Therefore, the prediction of coal bump is very important. Prediction is the core of coal bump prevention and control. Accurate and reliable prediction of high-intensity coal bump disaster is to effectively avoid and control it [2]. The prediction of coal bump has become a research hotspot in the fields of large-scale underground geotechnical engineering and deep coal mineral resources mining.

The current research on prediction of coal bump can be generally divided into three categories: The first category is the criteria established on the basis of coal bump mechanism, such as Russense criterion, Barton criterion, Turchaninov criterion, and Hoek criterion [3]. The second category is the prediction method based on field measurement, mainly including the microgravity method [4], acoustic emission method [5], and microseismic method [6]. The third type is the prediction method considering the influence of various factors. The third kind of method considers the problems relatively comprehensively and has good guiding significance for engineering practice. In recent years, this kind of method has attracted extensive attention of scholars. The third method is divided into two subcategories: (1) comprehensive prediction method based on coal bump index criterion. Among them, Tan [7] proposed a prediction method

for comprehensively judging the possibility and intensity of coal bump based on fuzzy mathematics theory. Adoko et al. [8] and Wang et al. [9] conducted in-depth research; prediction models based on fuzzy mathematics theory are established, respectively, but the determination of index weight in this method depends on subjective factors. Hu et al. [10] established an improved matter-element extension model for coal bump intensity prediction, which is difficult to predict mixed and intermediate coal bumps. Chen et al. [11] established the prediction model of ideal point method by calculating the index weight through the combination weighting method, but the ideal point method is only an evaluation and analysis method, and it is necessary to determine reasonable evaluation factors and ideal points when using. Hu et al. [12] applied the combination weight to assign weight to the index and established the coal bump grade preside model based on the approximate ideal solution ranking method. This method is difficult to determine the index weight under the condition of multiple factors. Li et al. [13] proposed an improved cloud model to predict coal bump by fusing the index weights through cloud atomization. The prediction accuracy will be reduced for the indexes that do not obey the normal distribution. (2) The comprehensive prediction method of coal bump based on the sample data of examples, among which the representative ones are as follows: Gong et al. [14] established a Bayesian discriminant model for coal bump prediction, and the prediction accuracy of the model is easily affected by the representativeness of the original data and the sample size. Luo and Cao [15] used principal component analysis to calculate the weight matrix and established a weighted distance discrimination model. This method is greatly affected by the representativeness and accuracy of the original data. Wu et al. [16] established the coal bump prediction model of least squares support vector machine based on particle swarm optimization algorithm. The kernel function is the core of support vector machine, and its selection directly affects the prediction accuracy and calculation time. Pu et al. [17] established a coal bump prediction model based on decision tree. The decision tree is suitable for high-dimensional data, but it is easy to over fit.

The above methods and theories of coal bump prediction have achieved certain prediction results from different angles, which have played a great role in promoting the research of this problem. However, due to the complexity of coal bump mechanism, the diversity of influencing factors, and the defects of various methods, there are still the following deficiencies in practical engineering application: (1) the main ideas of most methods belong to comprehensive evaluation, and the core problem is the determination of the weight of each index. However, the determination of the weight will inevitably be subjective and arbitrary; the rationality of weight is the key to the reliability of coal bump prediction results. (2) Coal bump prediction is a complex nonlinear problem. The occurrence of coal bump is the result of the joint action of many factors. Some of these influencing factors are determined and quantitative, while others are random, qualitative, and fuzzy. It is difficult to describe comprehensively and accurately by using mathe-

tical or mechanical methods and theories, which is greatly affected by human factors and one sidedness. Therefore, it is still necessary to explore new prediction methods and carry out the research on coal bump intensity classification prediction. In 1994, Feng [18] first proposed an adaptive pattern recognition method for rock burst prediction by using neural network theory, and then, some scholars also carried out research in this field. Jia et al. [19], Roohollah and Abbas [20], and Wu et al. [21] established generalized regression neural network, emotional neural network, and probabilistic neural network coal bump prediction models, respectively. Coal bump is a special form of mine pressure manifestation. The prediction of the breeding mechanism, time of occurrence, and intensity of coal bump has been an outstanding problem. The key to effective prevention and control of coal bump lies in the research of monitoring and early warning of coal bump. The current mine monitoring mostly uses microseismic for global monitoring. For the monitoring of mine seismic and impact ground pressure at the mining face, most of the traditional monitoring means such as drill chip method and stress monitoring are used at present. The accuracy of the prediction needs to be enhanced, and the development and arrangement of the monitoring system needs to be further optimized. With the development of big data and artificial intelligence technology, people gradually began to use computer models to predict the impact hazard of coal bump. However, the prediction is mostly based on geological factors and mining technology factors, as well as monitoring data. The prediction methods and algorithms are relatively single, and the prediction results are fixed, which is poor guidance for the site. Further research is needed in the comprehensive utilization and integration analysis of the information obtained by various techniques reflecting different aspects of coal bump.

This paper studies the deep neural network model based on the dropout method and improved Adam algorithm. The model makes full use of the stronger nonlinear learning ability and deeper network depth of deep neural network (DNN) [22]. The model avoids the problem of determining the index weight and is completely data-driven. The qualitative and quantitative analyses are effectively combined to avoid the influence of human factors. It can mine complex and subtle deep relationships in incomplete, imprecise, and noisy limited data sets. Therefore, the research on the application of depth neural network in coal bump prediction is of great significance to expand the coal bump prediction system and improve the ability of prediction.

2. Prediction Sample Database

2.1. Selection of Evaluation Indicators. The occurrence mechanism of coal bump is complex, and there are many influencing factors. The selection of indicators is the key to prediction. Too many indicators will make it difficult to obtain the measured values of some indicators and increase the complexity of the prediction process. Too few indicators cannot reflect the comprehensiveness of the prediction process, resulting in the inconsistency between the results and

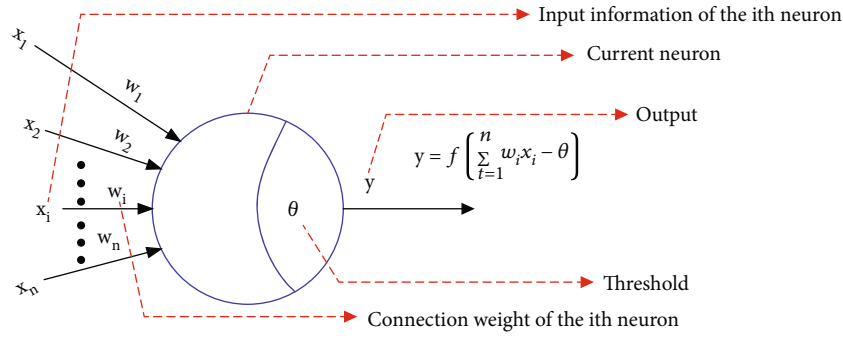


FIGURE 1: Schematic diagram of perceptron.

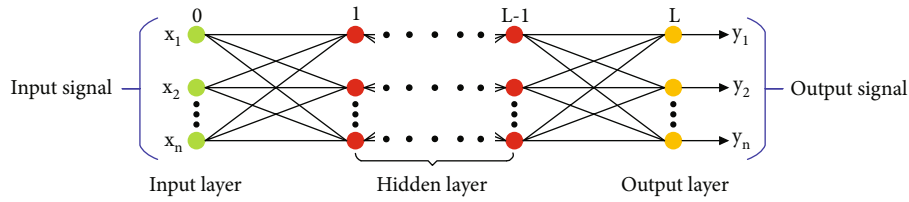


FIGURE 2: Topology of deep neural network.

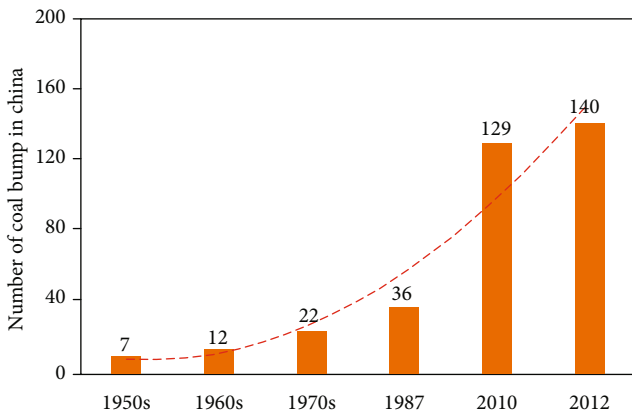


FIGURE 3: Number of coal bump mines in China.

the reality. The research of this paper is to determine the coal bump prediction and evaluation index through the analysis of three coal bump engineering examples of Qianqiu coal mine, Zhaolou coal mine, and Wulong coal mine. The purpose of analyzing coal bump engineering examples is to convert fuzzy and nonquantifiable influencing factors into quantifiable physical and mechanical indexes. At the same time, the selected indexes should also be common, easy to measure in practice, and recorded in previous coal bump examples.

From the in situ stress level and the location of coal bump in the example, coal bump usually occurs in the rock mass with high stress concentration. Therefore, the maximum tangential stress of tunnel wall surrounding rock is selected as one of the coal bump prediction indexes. In terms of landform, coal bump usually occurs in mountains or deep underground projects, or in rock mass with high tectonic stress. From the structural layout, the more irregular the excavation section, the greater the possibility of coal bump,

and the above factors can be reflected by the maximum tangential stress of the surrounding rock. In the example, the coal bump section form is mainly tensile failure, accompanied by shear failure, so the tensile strength and shear strength of rock are selected. Through reading the existing literature, it is found that there are few records of shear strength in the actual coal bump example, which is difficult to analyze. Therefore, only the tensile strength of the rock is selected as a predictor of coal bump, and the tensile strength is considered to represent the tensile and shear properties of the rock.

In addition, coal bump mainly occurs in hard coal or rock with complete structure, and the common index to measure the hardness of coal rock is the compressive strength of coal rock, and the compressive strength of rock should be measured in almost any coal mass engineering. Therefore, the compressive strength of coal is also selected as the prediction index of coal bump. The formation of high-energy reservoir in surrounding rock must meet two conditions: one is that the rock mass can store large elastic strain energy and second is that the internal stress of the rock mass is highly concentrated. The coal bump tendency index reflects the energy storage and release performance of rock mass. Under the same stress conditions, the greater the rock mass, the better the energy storage and release performance of rock mass. Therefore, the coal bump tendency index is selected as the coal bump evaluation index.

Through the above analysis, it is considered that the role of many influencing factors in coal bump can be reflected by the four physical and mechanical indexes of maximum tangential stress, uniaxial compressive strength, uniaxial tensile strength, and elastic energy index of surrounding rock. Therefore, four indexes are selected as the prediction and evaluation indexes of coal bump in this study.

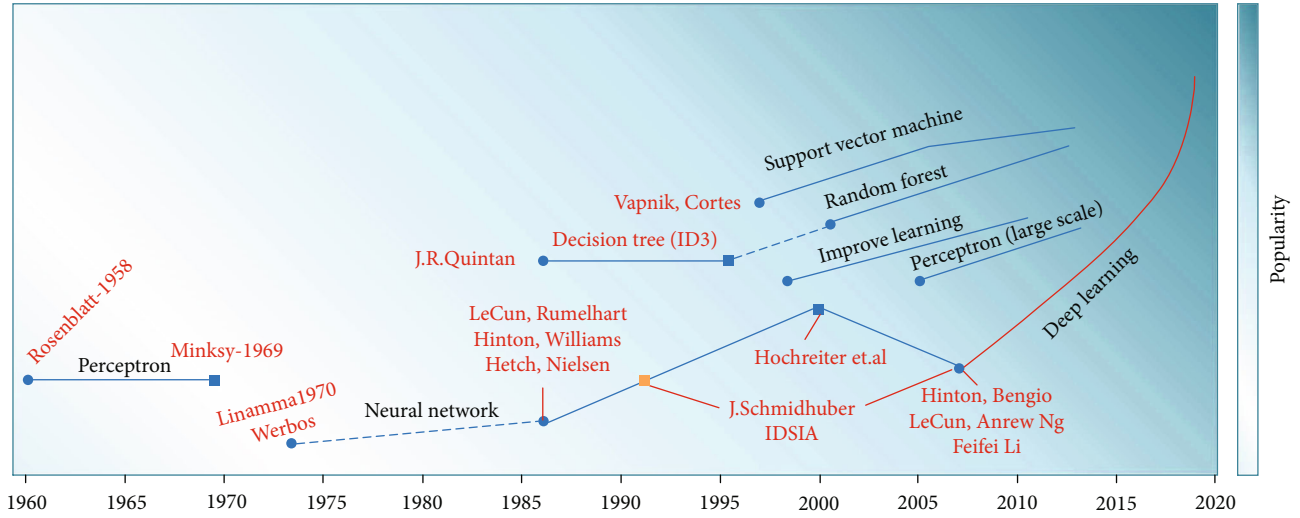


FIGURE 4: A brief history of machine learning.

Improved Adam algorithm

1. Initialization: initial learning efficiency, $\eta = 0.001$; Exponential decay rate of first-order moment and second-order moment estimation, $\beta_1 = 0.9$, $\beta_2 = 0.999$, $\beta_1, \beta_2 \in [0, 1)$; Small constants for numerical stability, $\delta = 1e - 08$
2. Initialization parameter θ
3. Initialization: first order moment vector $m_0 = 0$, second order moment vector $v_0 = 0$; time step $t_0 = 0$; iterative direction of improved Adam algorithm $p_0^\lambda = 0$
4. When the stop criterion is not reached
5. A small batch of m samples $\{x^1, x^2, \dots, x^m\}$ was collected from the training set
6. Calculate the gradient y^i for the target $g_t \leftarrow 1/m \nabla_{\theta_{t-1}} \sum_i L((x^i; \theta), y^i)$
7. $t \leftarrow t + 1$
8. Updated biased first-order moment estimation: $m_t \leftarrow \beta_1 \cdot m_{t-1} + (1 - \beta_1) \cdot g_t$
9. Updated biased second-order moment estimation: $v_t \leftarrow \beta_2 \cdot v_{t-1} + (1 - \beta_2) \cdot g_t \odot g_t$
10. Correct the deviation of the first moment: $\hat{m} \leftarrow m_t / (1 - \beta_1^t)$
11. Correct the deviation of the second moment: $\hat{v} \leftarrow v_t / (1 - \beta_2^t)$
12. The amount of update per iteration of the improved Adam algorithm: $P_t^A = \hat{m}_t / \sqrt{\hat{v} + \delta} P_t^{AM} \leftarrow \lambda \cdot P_{t-1}^{AM} + \eta \cdot P_t^A$
13. Parameter update: $\theta_t \leftarrow \theta_{t-1} - P_t^{AM}$
14. end while

ALGORITHM 1: Steps of improved Adam algorithm.

2.2. Acquisition of Sample Data. According to the selected evaluation indexes and based on the research results of coal bump [23–26], 305 groups of coal bump engineering case data are collected as the sample data of coal bump prediction. All data samples have complete independent four factors.

3. Improved Deep Neural Network Model

In recent years, deep learning technology has attracted extensive attention. As a deep learning model fitting complex nonlinear relationships, deep neural network has not only made a breakthrough in image classification but also significantly improved the accuracy of speech recognition.

3.1. Deep Neural Network Model. The DNN model is derived from the perceptron model (as shown in Figure 1). The perceptron model can only be used for binary classification and is unable to learn more complex nonlinear models. DNN is

extended based on perceptron model by adding hidden layer, expanding activation function, and adding neurons in output layer. The interior of DNN can be divided into three categories: input layer, hidden layer, and output layer. Its structure is shown in Figure 2. The outstanding feature of DNN is that it has multiple hidden layers. Each link between network units is a causal chain that can be learned and trained. If the same network unit is used, DNN has far more expression ability than shallow network and stronger ability to deal with complex problems. Figure 3 shows the trend of the number of coal bump mines in China according to the China Energy Statistics Yearbook 2013. Figure 4 shows the history of the development of machine learning theory based on a comprehensive analysis of previous literature.

Activation function simulates the threshold activation characteristics of human brain neurons, introduces nonlinear features into DNN, and realizes the transformation from simple linear space to highly nonlinear space. The

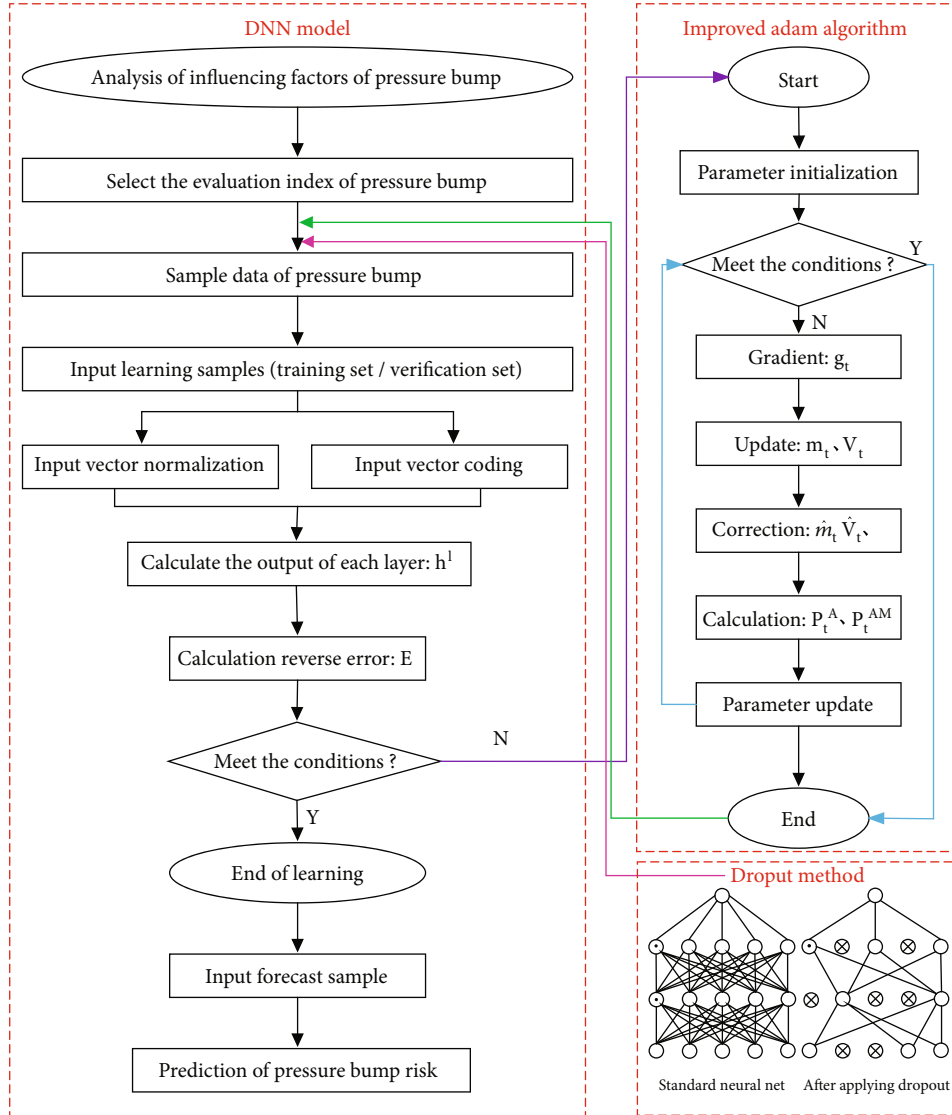


FIGURE 5: Flow chart of coal bump prediction based on improved neural network model.

commonly used activation functions include sigmoid function, Tanh function, ReLu function, and softplus function. Considering the advantages of fast convergence and strong generalization ability of model training using ReLu function [27], ReLu is selected as the hidden layer activation function in this paper, and its function form is as follows:

$$f_1(z^l) = \max(0, z^l). \quad (1)$$

The activation function of the output layer is determined according to the problems to be solved. Coal bump prediction belongs to the classification task, which usually adopts softmax function, and its function form is as follows:

$$u = h_k^L = \frac{\exp(z_k^L)}{\sum_{i=1}^n \exp(z_i^L)}, \quad (2)$$

where h_k^L is the output of the k th neuron in the output layer.

Forward calculation cannot learn the best parameters (weight and bias) based on learning samples. Therefore, Rumelhart et al. [28] proposed the backpropagation (BP), which outputs the parameters of each layer in turn from the error of the predicted value and the actual value from the output layer backwards. When using BP algorithm to optimize parameters, for classification tasks, the loss function generally selects cross-entropy error, and its function form is as follows:

$$E = - \sum_{i=1}^N \sum_{k=1}^T y_i^k \log \hat{y}_i^k, \quad (3)$$

where y_i^k is the actual value, \hat{y}_i^k is the predicted value, N is the learning sample number, and T is the number of classifications.

TABLE 1: Parameters of coal bump prediction model.

Serial number	Parameter	Value
1	Number of neurons in input layer	6
2	Number of hidden layer neurons	32, 64, 16
3	Number of neurons in output layer	6
4	Hidden layer activation function	ReLU
5	Output layer activation function	Softmax
6	Loss function	Cross-entropy error
7	Suppress overfitting	Dropout method
8	Drop rate in dropout model	$P = 0.4$
9	Training function	Improved Adam algorithm
10	Initial learning rate	$\eta = 0.001$
11	Momentum coefficient	$\lambda = 0.95$
12	Error target value	0.001
13	Batch size	10
14	Training times	70

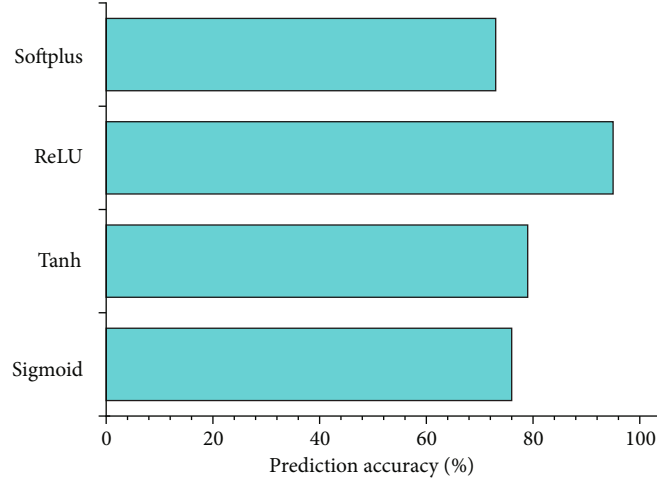


FIGURE 6: Selection and comparison of activation functions.

3.2. Algorithm Improvement of Neural Network Model.

Overfitting refers to the state that only the training data can be fitted, but other data not included in the training data cannot be well fitted. Generally, the reasons for overfitting are as follows: (1) the model has many parameters and strong expressiveness and (2) less training data. Since there are few parameters in the model, only reason 2 can be considered. Considering the limitation of coal bump data, in order to prevent overfitting in the training process of the DNN model, this paper uses the dropout method to regularize the model. The basic idea of the dropout method is to randomly discard a certain proportion of neurons in the input layer and hidden layer in the DNN training process. Dropout reduces the feature extraction process of irrelevant feature data.

The goal of DNN training is to reduce the error until the global optimal or suboptimal solution is reached based on stochastic gradient descent, momentum, AdaGrad, and

adaptive motion estimation (Adam). SGD is the simplest and commonly used optimization algorithm in DNN training. Compared with SGD algorithm, Adam algorithm combines the advantages of momentum algorithm and Adagrad algorithm, automatically adjusts the learning rate, and efficiently searches the parameter space. It is suitable for solving the problem of coal bump prediction with high noise. Although Adam algorithm theoretically solves the adaptive problem of learning rate, Wilson et al. [29] found that Adam algorithm not only has higher training effect but also brings nearly half of the test error. To solve this problem, we integrate the idea of momentum [30] into Adam's algorithm, which is more stable. The optimization and update steps of the improved Adam algorithm are shown as Algorithm 1.

3.3. Prediction of Coal Bump Based on Improved Neural Network Model.

In this paper, the dropout method and improved Adam algorithm are applied to the coal bump

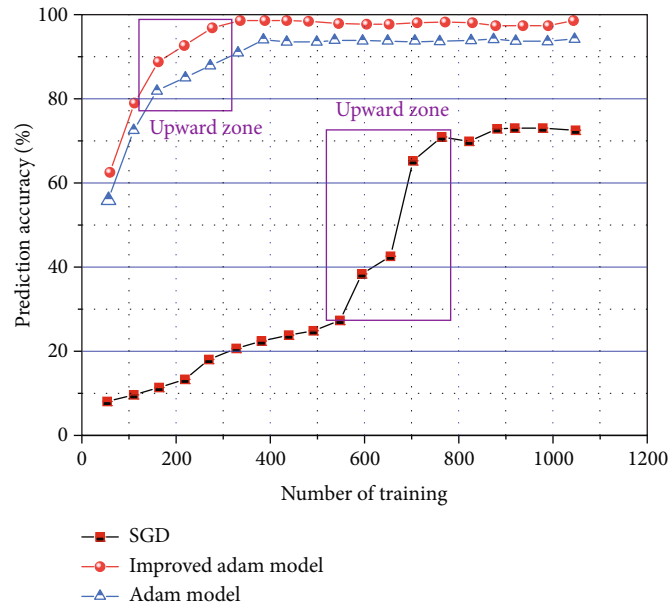


FIGURE 7: Comparison of prediction accuracy of three algorithms.

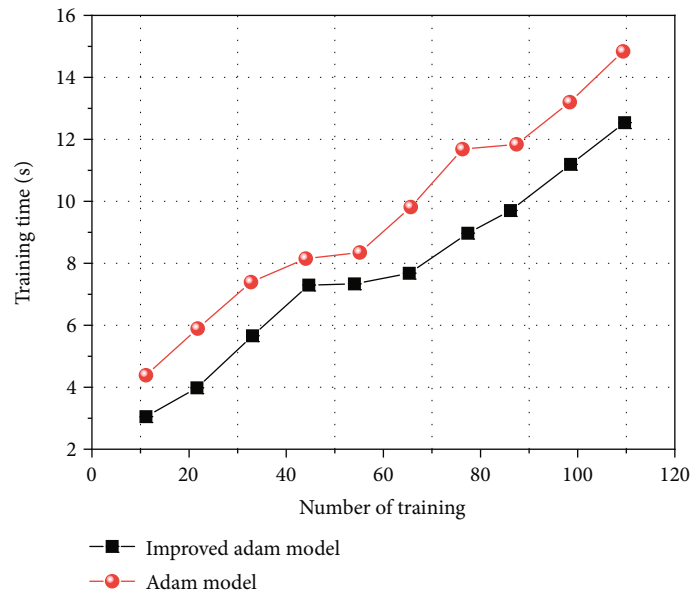


FIGURE 8: Comparison of training time before and after algorithm improvement.

prediction model based on DNN. The flow of the coal bump prediction model based on DA-DNN is shown in Figure 5. Considering the limited amount of coal bump sample data, refer to the data set division method commonly used in the field of deep learning; that is, the training set, verification set, and test set are divided according to 6:2:2. Firstly, 61 groups are randomly selected from 305 groups of sample data as the test set. The extracted data features can represent the whole data set and are the same as those of the training set. The remaining 244 groups of sample data are taken as the learning samples of the DA-DNN model. During the training process, 80% of the learning samples are taken as

the training set and 20% as the verification set. There is no intersection between the training set and the verification set. The training set is used for model training and updating parameters. The validation set is used to test the accuracy of the model, adjust the super parameters (training times, learning rate, etc.), and monitor whether the model has been fitted. The test set is used to evaluate the generalization ability and test the real prediction accuracy after the final training of the model.

The input layer includes 4 neurons. Comprehensively considering the training accuracy, training time, and other factors, according to the empirical formula, it is determined

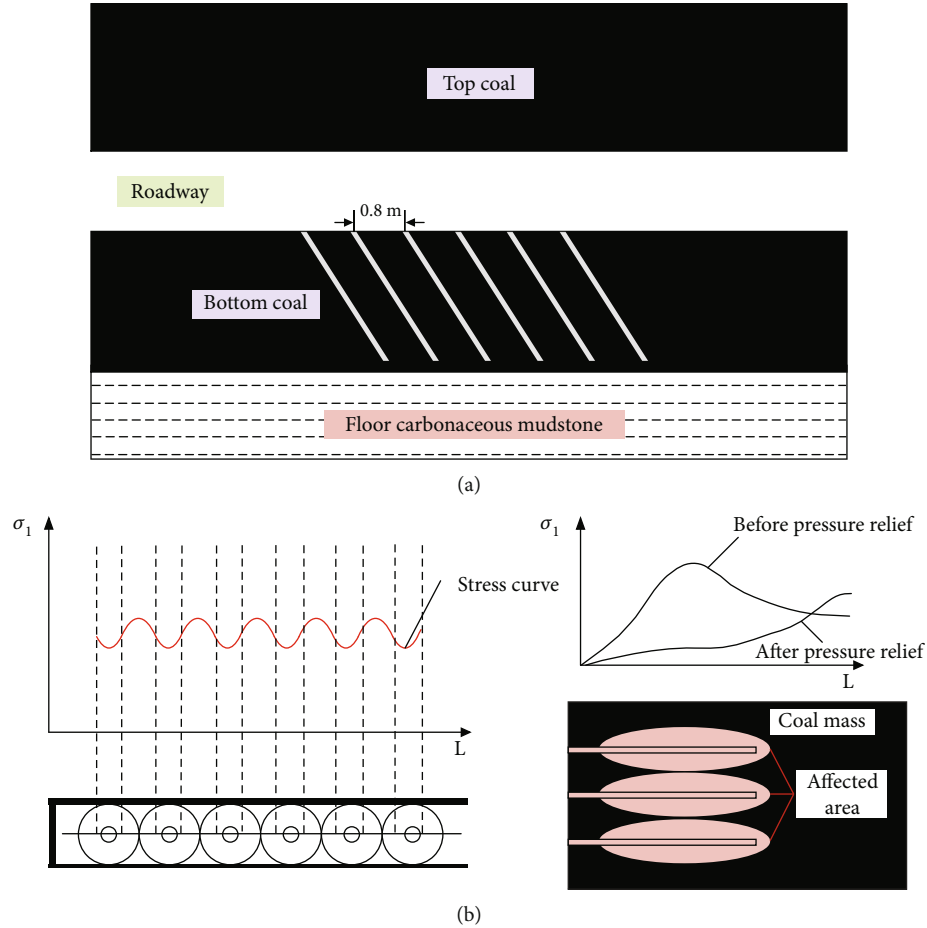


FIGURE 9: Measures to prevent impact hazards. (a) Layout of tunnel floor pressure relief drilling. (b) Stress variation diagram of coal affected by large-diameter pressure relief hole.

that the hidden layer is three layers, and the number of neuron nodes is 32, 64, and 16, respectively. As shown in Table 1, coal bump intensity is often divided into four levels, namely, no coal bump (level I), slight coal bump (level II), intermediate coal bump (level III), and strong coal bump (level IV). Considering that the input and output of the DA-DNN model are numerical values, the above coal bump levels are coded, and the four levels of “no rock burst”, “slight rock burst”, “intermediate rock burst”, and “strong rock burst” are represented by numbers “0”, “1”, “2”, and “3”, respectively. The four neurons in the output layer are “0”, “1”, “2”, and “3”.

The activation function of hidden layer is ReLU function. Because coal bump prediction is a classification task, the output layer activation function is softmax function, and the loss function is cross-entropy error. To verify the superiority of ReLU function, the prediction accuracy of test set is taken as the verification target, which is compared with other three common activation functions. It can be seen from Figure 6 that the prediction accuracy of selecting ReLU as the activation function is more than 95%, and the rest are less than 85%. Obviously, the prediction accuracy of selecting ReLU function is higher.

The improved Adam algorithm is adopted in this study. To verify the superiority of the improved Adam algorithm, it is compared with SGD, Adam, and improved Adam. It can

be seen from Figure 7 that taking the prediction accuracy of the test set as the verification target, when the training times (epochs) are less than 700, the prediction accuracy of SGD algorithm is less than 62%. When the training times are 100, the accuracy of Adam and improved Adam algorithm has reached more than 70%, while when the training times are 300, the accuracy of improved Adam algorithm has reached more than 95%. And it is obviously better than Adam algorithm. Only when the training times are greater than 700, the prediction accuracy of SGD algorithm can reach more than 70%. As can be seen from Figure 8, the training time of the improved Adam algorithm is significantly lower than that of the Adam algorithm, indicating that its loss convergence speed is better. The main parameters of the DA-DNN coal bump prediction model are shown in Table 1. In this paper, the DA-DNN algorithm is programmed in Python language, the development environment is Python 3.7, and the code implementation is based on keras algorithm package.

4. Case Study of Coal Bumping Based on Improved Neural Network Model

Taking a coal mine in Shanxi Province as an example, the mining depth of the mine is 500 m, there are many impact

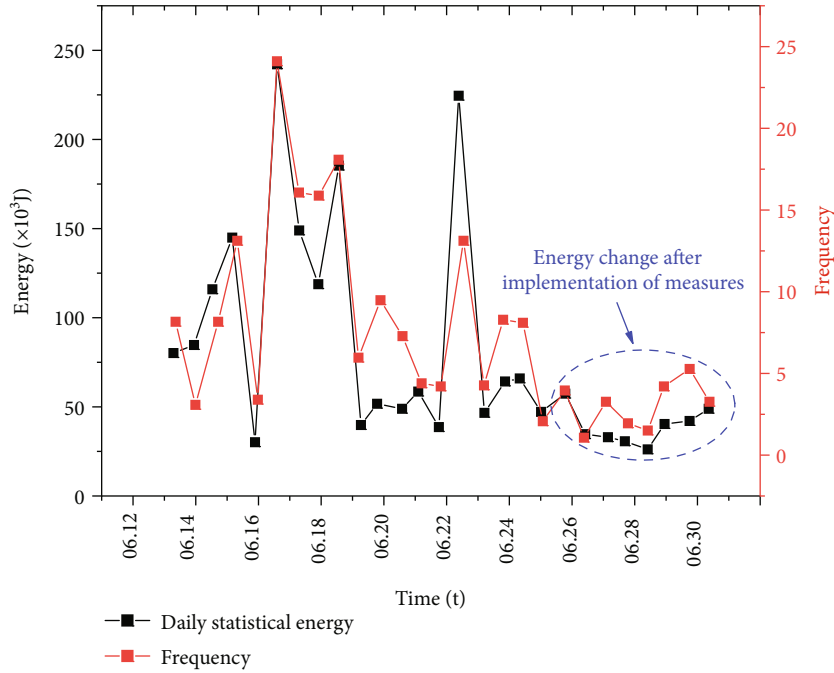


FIGURE 10: Variation of microseismic energy and frequency after borehole pressure relief.

dynamic phenomena during roadway excavation, and there has been a rock burst accident, which belongs to a strong rock burst mine. According to the prediction results of the above indexes, it is consistent with the actual situation of the mine. Borehole pressure relief is a method to form surrounding rock fracture area by constructing large-diameter holes on the coal wall to eliminate stress concentration and reduce impact risk. The crushing zone formed by drilling and unloading pressure can attenuate the vibration waves caused by mine earthquakes, rapidly weaken the vibration wave energy transmitted to the roadway, and protect the roadway from vibration damage. The principle of pressure relief by large-diameter drilling is shown in Figure 9.

During the mining of 401101 working face and the excavation of central main roadway in a coal mine, the pressure is relieved by drilling holes on both sides of the roadway. The drilling direction is inclined along the coal seam, the hole spacing is 0.7 m, the hole depth is 20 m, and the hole is 1.2~1.5 m from the roadway floor. It can be seen from Figure 10 that the total daily energy was in the low energy stage for five consecutive days after the coal bump event on June 16, and the large energy release event occurred again on June 22, but no coal bump accident was caused. Since then, the comprehensive prevention and control scheme combined with composite support technology and large-diameter borehole pressure relief was implemented in the roadway, and the energy has been lower than 7.5×10^4 J for 4 consecutive days after the implementation of the scheme; the frequency is less than 3 times, indicating that this scheme can effectively reduce the energy stored in coal and rock mass and its vibration frequency.

It can be seen from the above that after the comprehensive prevention and control scheme is adopted in the roadway excavation process, the occurrence frequency and

strength of coal bump are significantly reduced, while there is no impact in the area with low stress level, indicating that the effect of the comprehensive prevention and control scheme has played a good control role and achieved certain results in the prevention and control of coal bump.

5. Conclusions

- (a) When the training times (epochs) are less than 700, the prediction accuracy of SGD algorithm is less than 60%. When the training times are 100, the accuracy of Adam and improved Adam algorithm has reached more than 70%, while when the training times are 300, the accuracy of improved Adam algorithm has reached more than 95%
- (b) The comprehensive prevention and control scheme combined with composite support technology and large-diameter borehole pressure relief was implemented in the roadway, and the energy has been lower than 7.5×10^4 J for 4 consecutive days after the implementation of the scheme; the frequency is less than 3 times, indicating that this scheme can effectively reduce the energy stored in coal and rock mass and its vibration frequency
- (c) After the comprehensive prevention and control scheme is adopted in the roadway excavation process, the occurrence frequency and strength of coal bump are significantly reduced, while there is no impact in the area with low stress level, indicating that the effect of the comprehensive prevention and control scheme has played a good control role and

achieved certain results in the prevention and control of coal bump

- (d) Coal bump data is growing rapidly and is being produced in large quantities in mining engineering. The traditional data processing methods cannot adapt gradually. It is an urgent direction to develop artificial intelligence data processing methods and use deep learning technology to learn and mine coal bump data

Data Availability

The data used to support the findings of this study are available from the corresponding author upon request.

Conflicts of Interest

The authors declare that there is no conflict of interest regarding the publication of this paper.

Acknowledgments

This work was financially supported by the State Key Laboratory of Water Resource Protection and Utilization in Coal Mining (GJNY-18-73.16), the Support Plan for Scientific and Technological Innovation Talents in Colleges and Universities of Henan Province (21HASTIT024), the Scientific and Technological Innovation Research Team of Henan Polytechnic University (T2021-5), the National Natural Science Foundation of China (51974105), the Fundamental Research Funds for the Universities of Henan Province (Grant No. NSFRF200332), the Key Research and Development and Promotion of Special (Science and Technology) Project of Henan Province (No. 212102310379), the Key Scientific Research Project Fund of Colleges and Universities of Henan Province (No. 21A610005 and No. 20B440001), the Henan Key Laboratory for Green and Efficient Mining and Comprehensive Utilization of Mineral Resources (Henan Polytechnic University) (KCF201804), and the Doctoral Foundation of Henan Polytechnic University (No. B2019-22). All support is greatly appreciated.

References

- [1] S. Gong, "Investigation of tensile and fracture mechanical properties of bituminous coal at different strain rates," *Journal of Materials Research and Technology*, vol. 15, pp. 834–845, 2021.
- [2] S. Gong, Z. Wang, L. Zhou, and W. Wang, "Experimental investigation on the tensile and fracture properties of burst-prone coal under quasistatic condition," *Shock and Vibration*, vol. 2021, no. 1, 13 pages, 2021.
- [3] X. B. Li, F. Q. Gong, S. F. Wang et al., "Coupled static-dynamic loading mechanical mechanism and dynamic criterion of rockburst in deep hard rock mines," *Chinese Journal of Rock Mechanics and Engineering*, vol. 38, no. 4, pp. 708–723, 2019.
- [4] Z. T. Bieniawski, "Mechanism of brittle fracture of rock," *International Journal of Rock Mechanics and Mining Sciences & Geomechanics Abstracts*, vol. 4, no. 4, pp. 405–430, 1967.
- [5] C. P. Lu, L. Yang, and Z. Nong, "In-situ and experimental investigations of rockburst precursor and prevention induced by fault slip," *International Journal of Rock Mechanics and Mining Sciences*, vol. 108, pp. 86–95, 2018.
- [6] P. M. Duncan and L. Eisner, "Reservoir characterization using surface microseismic monitoring," *Geophysics*, vol. 75, no. 3, pp. 75139–75146, 2010.
- [7] Y. A. Tan, "Application of comprehensive assessment using fuzzy mathematics to rockburst prediction in underground caverns," in *Proceedings of the 2nd National Congress of Chinese Society for Rock Mechanics and Engineering*, pp. 247–253, Knowledge Press, Beijing, 1989.
- [8] A. C. Adoko, C. Gokceoglu, L. Wu, and Q. J. Zuo, "Knowledge-based and data-driven fuzzy modeling for rockburst prediction," *International Journal of Rock Mechanics and Mining Sciences*, vol. 61, no. 4, pp. 86–95, 2013.
- [9] C. Wang, A. Wu, H. Lu, T. Bao, and X. Liu, "Predicting rockburst tendency based on fuzzy matter-element model," *International Journal of Rock Mechanics & Mining Sciences*, vol. 75, pp. 224–232, 2015.
- [10] J. H. Hu, J. L. Shang, and K. P. Zhou, "Improved matter-element extension model and its application to prediction of rockburst intensity," *The Chinese Journal of Nonferrous Metals*, vol. 23, no. 2, pp. 495–502, 2013.
- [11] C. Xu, X. L. Liu, E. Z. Wang, and S. J. Wang, "Prediction and classification of strain mode rockburst based on five-factor criterion and combined weight-ideal point method," *Chinese Journal of Geotechnical Engineering*, vol. 39, no. 12, pp. 2245–2252, 2017.
- [12] Q. G. Hu, F. M. Chen, and G. Z. Ning, "Rockburst evaluation model and application of CW-TOPSIS," *Journal of Shandong University (Engineering Science)*, vol. 47, no. 2, pp. 20–25, 2017.
- [13] S. H. Li, S. Y. Wang, J. D. Zhu, B. Li, J. Yang, and L. Z. Wu, "Prediction of rockburst tendency based on weighted fusion and improved cloud model," *Chinese Journal of Geotechnical Engineering*, vol. 40, no. 6, pp. 1075–1083, 2018.
- [14] F. Q. Gong, X. B. Li, and W. Zhang, "Rockburst prediction of underground engineering based on Bayes discriminant analysis method," *Rock and Soil Mechanics*, vol. 31, pp. 370–377, 2010.
- [15] L. Luo and P. Cao, "Model of weighted distance discriminant analysis and application for deep roadway," *Journal of Central South University (Science and Technology)*, vol. 43, no. 10, pp. 3971–3975, 2012.
- [16] S. C. Wu, Z. G. Wu, and C. X. Zhang, "Rock burst prediction probability model based on case analysis," *Tunnelling and Underground Space Technology*, vol. 93, p. 103069, 2019.
- [17] Y. Y. Pu, D. B. Apel, and B. Lingga, "Rockburst prediction in kimberlite with unsupervised learning method and support vector classifier," *Tunnelling and Underground Space Technology*, vol. 90, pp. 12–18, 2019.
- [18] X. T. Feng, "Adaptive pattern recognition to predict rockburst in underground openings," *Journal of Northeastern University*, vol. 15, no. 5, pp. 471–475, 1994.
- [19] Y. P. Jia, Q. Lu, and Y. Shang, "Rockburst prediction using particle swarm optimization algorithm and general regression neural network," *Chinese Journal of Rock Mechanics and Engineering*, vol. 32, no. 2, pp. 343–348, 2013.
- [20] S. F. Roohollah and T. Abbas, "Long term prediction of rockburst hazard in deep underground openings using three robust

- data mining techniques,” *Engineering with Computers*, vol. 35, no. 2, pp. 659–675, 2019.
- [21] S. C. Wu, C. X. Zhang, and Z. Q. Cheng, “The prediction of intensity classification of rockburst based on PCA-PNN,” *Journal of China Coal Society*, vol. 44, no. 9, pp. 2767–2776, 2019.
- [22] G. E. Hinton, S. Osindero, and Y. W. Teh, “A fast learning algorithm for deep belief nets,” *Neural Computation*, vol. 18, no. 7, pp. 1527–1554, 2006.
- [23] Q. H. Qian, “Definition, mechanism, classification and quantitative forecast model for rockburst and coal bump,” *Rock & Soil Mechanics*, vol. 35, no. 1, pp. 1–6, 2014.
- [24] H. A. Warda, S. H. Haddara, E. M. Wahba, and M. Sedahmed, “Lattice Boltzmann simulations of the capillary pressure bump phenomenon in heterogeneous porous media,” *Journal of Petroleum Science & Engineering*, vol. 157, pp. 558–569, 2017.
- [25] H. Wang, Y. Jiang, Z. Jie, S. Ruyue, and W. Chen, “Numerical investigation on the assessment and mitigation of coal bump in an island longwall panel,” *International Journal of Mining Science & Technology*, vol. 5, pp. 625–630, 2013.
- [26] Y. Zhao and Y. Jiang, “Acoustic emission and thermal infrared precursors associated with bump-prone coal failure,” *International Journal of Coal Geology*, vol. 83, no. 1, pp. 11–20, 2010.
- [27] Y. Liu, X. Wang, L. Wang, and D. Liu, “A modified leaky ReLU scheme (MLRS) for topology optimization with multiple materials,” *Applied Mathematics and Computation*, vol. 352, pp. 188–204, 2019.
- [28] D. E. Rumelhart, G. E. Hinton, and R. J. Williams, “Learning representations by back-propagating errors,” *Nature*, vol. 323, no. 6088, pp. 533–536, 1986.
- [29] A. C. Wilson, R. Roelofs, M. Stern, N. Srebro, and B. Recht, “The marginal value of adaptive gradient methods in machine learning,” in *Proceedings of the 31st Conference on Neural Information Processing Systems*, pp. 1–14, Long Beach, USA, 2017.
- [30] H. Zhang, *Research and Improvement of Optimization Algorithms in Deep Learning*, Beijing University of Posts and Telecommunications, Beijing, 2017.

Research Article

Study on the Influence of Liquid Nitrogen Cold Soaking on the Temperature Variations and Seepage Characteristics of Coal Samples with Different Moisture Contents

Bo Li ^{1,2,3}, Chaohui Zong,¹ Laisheng Huang,¹ Yongjie Ren,¹ and Xiaoquan Lv¹

¹School of Safety Science and Engineering, Henan Polytechnic University, Jiaozuo 454003, China

²Collaborative Innovation Center of Coal Work Safety and Clean High Efficiency Utilization, Henan Polytechnic University, Jiaozuo 454003, China

³State Key Laboratory Cultivation Base for Gas Geology and Gas Control, Henan Polytechnic University, Jiaozuo, Henan 454003, China

Correspondence should be addressed to Bo Li; anquanlibo@163.com

Received 5 August 2021; Revised 4 September 2021; Accepted 9 September 2021; Published 19 October 2021

Academic Editor: Feng Du

Copyright © 2021 Bo Li et al. This is an open access article distributed under the Creative Commons Attribution License, which permits unrestricted use, distribution, and reproduction in any medium, provided the original work is properly cited.

Due to its advantages such as environmental friendliness and remarkable permeability enhancement effect, the technology of liquid nitrogen cold soaking (LNCS) cracking coal has become a hot spot in the research on coal seam permeability enhancement in recent years. The frost heave force generated by water-ice phase transformation and the temperature stress are the main mechanisms of LNCS cracking water-containing coal. This paper focuses on the effect of LNCS on the temperature variations and seepage characteristics of coal. To further this purpose, the temperature measurement test and the permeability test were conducted on coal samples with different moisture contents under LNCS, respectively. In addition, by comparing the computer tomography test results of coal samples before and after LNCS, the internal pore structure changes of coal samples were further analyzed from a three-dimensional perspective. The test results show that the coal sample with a higher moisture content consumes a shorter time to reach internal temperature equilibrium and experiences faster temperature changes. LNCS can enhance coal permeability, and the growth rate of permeability increases exponentially with the increase of moisture content. After the LNCS treatment, the dried coal sample is mainly sprouting new pores on the basis of primary pores; in contrast, for water-containing coal samples, new pores are sprouted while primary pores will penetrate each other spatially to form a fracture network. In the process of LNCS, moisture has a significant effect on the seepage characteristics of coal, so appropriately increasing the moisture content of the coal seam conduces to achieving a better permeability enhancement effect.

1. Introduction

Coalbed methane (CBM), an associated energy source with coal, is a clean fuel and chemical raw material [1]. Coal is generally considered to be composed of a coal matrix and a natural crack network. The low permeability of coal seams directly restricts the efficient extraction of CBM [2–4]. Therefore, auxiliary methods are needed to enhance coal seam permeability. The liquid nitrogen cracking technology is a green and efficient waterless cracking technology which enhances coal seam permeability by injecting large amounts of low-temperature liquid nitrogen into the coal seam

through surface drilling or downhole drilling. When used as the cracking fluid, liquid nitrogen boasts the advantages of no pollution, low cost, and easy preparation. It can not only effectively solve the problems of waste of massive water resources, water lock, water sensitivity, etc., but it can also improve the cracking effect [5–7].

In the low-temperature environment, the temperature change of coal rock is a very important research point, and some have conducted related studies on the temperature variation of rock-soil mass under the effect of low-temperature environment. Liu et al. [8] established a microscopic structural model of frozen rock using the digital

image processing technique and converted the model into a finite element physical model by means of geometric vector conversion. Based on the converted model, they analyzed the temperature field distribution law during freeze-thaw cycles of inhomogeneous frozen rock under negative temperature conditions. By adopting the research methods of numerical simulation and experimental research, Xiong et al. [9] analyzed the basic law of heat transfer in frozen soil under freeze-thaw cycles based on the influence mechanism of heat conduction and latent heat of phase transformation on temperature, and studied the characteristics of temperature propagation in frozen soil after construction. Tan et al. [10] investigated the temperature field variation of tunnel-surrounding rock mass in a cold region by using a combination of numerical simulations and engineering field measurements, and they found that the latent heat released by the water-ice phase transformation process can change the temperature field of rock and soil porous media by changing the rate of ice formation. Park et al. [11] investigated the variation of thermophysical parameters of rocks with ambient temperature by physical parameter testing experiments. The results showed that when the temperature was reduced from 40°C to -160°C, the coefficient of thermal expansion and specific heat of rocks decreased with decreasing temperature, while the thermal conductivity changed less significantly with decreasing temperature. The above researches gave an insight into the variation pattern of the internal temperature of coal rock under the effect of a low-temperature environment. However, previous researches on coal rock temperature field variations under low-temperature freezing conditions were mostly conducted by means of numerical simulation, and few experimental studies in this field have been reported.

During liquid nitrogen cold soaking (LNCS) on coal rock, the temperature stress generated by the temperature gradient, the expansion stress generated by liquid nitrogen vaporization, and the freezing and swelling force generated by the volume expansion of water-ice phase transformation will all promote fracture generation, development, and connection, thus enhancing coal rock permeability. Cai et al. [12] tested permeability changes of a coal sample before and after liquid nitrogen treatment under the conditions of 0.25 MPa air pressure and 2.25 MPa surrounding pressure. In addition, considering the effect of moisture content, a series of liquid nitrogen permeability enhancement techniques have been proposed. Li et al. [13, 14] investigated the effect of LNCS on the permeability and pore structure of coal rock, and they found increases in the permeability, porosity, and pore radius of coal rock treated with LNCS. Yang et al. [15] treated saturated and dried coal samples under -10°C, -25°C, -40°C, and LNCS conditions, respectively, and tested their permeabilities. The results revealed that the coal sample experienced more significant permeability variations under LNCS conditions than under -10°C, -25°C, and -40°C conditions. Cai et al. [16, 17] conducted NMR analysis on rock samples that had been frozen with liquid nitrogen and found that the freezing effect of liquid nitrogen caused fracture expansion and porosity and permeability enhancement of the samples. By conducting NMR tests on coal samples before and after

LNCS, Wei et al. [18] found that the porosity and pore radius of coal increased with the increase of water content saturation. This finding indicated that pore water played a crucial role in coal; besides, the higher the water saturation, the more obvious the damage characteristics of coal after LNCS. The above studies show that LNCS freezing promotes the pore development and seepage characteristics of coal rocks, but there is a lack of studies on the effects of LNCS on the seepage characteristics of coal with different moisture contents.

At present, the influence of moisture content on the coal cracking effect of LNCS has been extensively researched on. However, most of the researches are focused on the effect of moisture content on pore structure variations before and after LNCS cracking, and crack variations are often characterized by parameters such as sound velocity and crack expansion [19–23]. The influences on temperature changes and seepage characteristics in coal are rarely considered. In this paper, the influences of LNCS on the temperature changes and seepage characteristics of coal samples with different moisture contents were explored. First, coal samples with different moisture contents were prepared. Next, a series of tests related to LNCS were carried out on the coal samples. Furthermore, the temperature variations and permeability characteristics of coal are analyzed and discussed on the basis of the experimental results. The research results are beneficial for the improvement of coal permeability and the enhancement of CBM extraction efficiency.

2. Experimental Methods and Sample Preparation

2.1. Experimental Facilities. The temperature measurement test was conducted with the aid of a temperature measurement device independently developed by the laboratory, as shown in Figure 1. The permeability test was conducted with the aid of a laboratory coal rock triaxial creep-seepage test system (Figure 2) which consisted of a high-pressure gas cylinder, a clamping device, a flow rate acquisition device, an axial pressure and confining pressure loading device, and a constant-temperature device. The observation experiment of the development and expansion of the internal cracks in the coal samples used a laboratory coal and rock industrial CT scanning system (Figure 2).

2.2. Preparation of Test Samples. The test coal samples were anthracite taken from the Zhujiao Coal Mine of Henan Energy and Chemical Industry Group Co., Ltd., Anyang, China. The size of the coal samples used for the metrology measurement test was $\Phi 50 \text{ mm} \times 100 \text{ mm}$. The basic parameter information of the coal samples is shown in Table 1. Coal samples for temperature measurement tests require internal temperature collection through temperature measurement boreholes. Please refer to the previous work for detailed processing information of experimental sample preparation for temperature measurement [24]. The prepared coal samples are shown in Figure 3. The coal samples with different

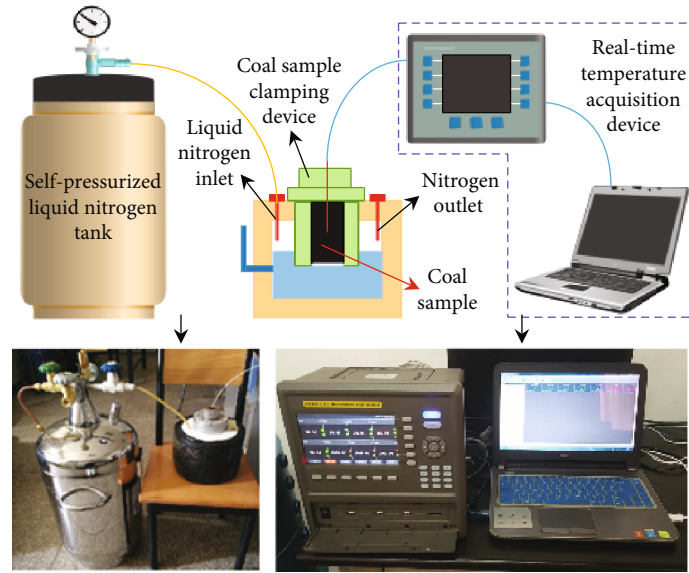


FIGURE 1: Temperature measurement test device.

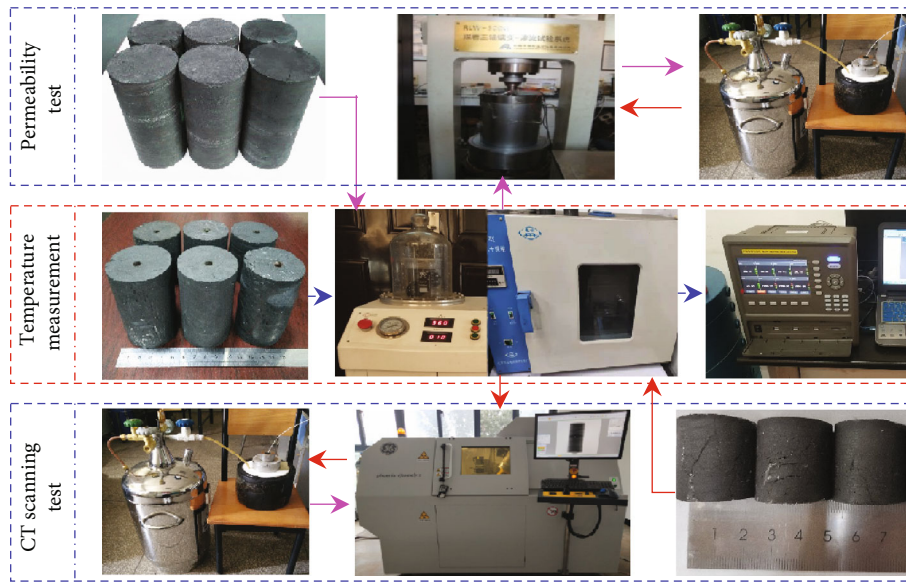


FIGURE 2: Experimental overall flowchart.

TABLE 1: Basic parameters of coal samples.

Sample	TRD ($\text{g}\cdot\text{cm}^{-3}$)	ARD ($\text{g}\cdot\text{cm}^{-3}$)	M_{ad} (wt%)	A_{ad} (wt%)	V_{daf} (wt%)	FC_{ad} (wt%)
Coking coal	1.45	1.33	0.74	8.25	20.21	70.09

Note: TRD represents true density; ARD represents apparent density; M_{ad} represents moisture, air-drying base; A_{ad} represents ash yield, air-drying base; V_{daf} represents volatile matter, dry ash-free basis; FC_{ad} represents fixed carbon content.

moisture contents used in the test were prepared in accordance with the following procedure.

- (1) The prepared coal sample was placed in the drying oven whose temperature was set to 70°C to be dried for over 48 h. The mass of the coal sample after drying was recorded as m_{d}

- (2) The coal sample was subjected to vacuum water saturation treatment through a water saturation device, during which it was taken out to be weighed every 12 h until its mass no longer increased. In this case, the coal sample was considered to be saturated. At this time, the mass of the water-saturated coal sample was recorded as m_{s}



FIGURE 3: Test coal samples.

TABLE 2: Permeability test conditions.

Axial pressure (MPa)	Confining pressure (MPa)	Pressure at the high-pressure seepage end (MPa)	Pressure at the low-pressure seepage end (MPa)	Seepage gas
1	2	0.45	0.1	N ₂

(3) The saturated coal sample was put into the drying oven, during which it was constantly taken out to be weighed. The time for weighing was adjusted according to actual needs. When reaching the target drying mass, the coal sample was taken out and immediately put in a sealing bag to cool to room temperature for later use. The preset water saturation degrees were 0%, 20%, 40%, 60%, 80%, and 100%, respectively. The target drying mass was calculated by $m = s_t(m_s - m_d) + m_d$, where m is the target drying mass, s_t is the preset water content saturation, and m_s is the mass of the saturated coal sample

(4) The above steps were repeated to prepare coal samples with different water saturation degrees. The drying oven and the vacuum water saturation device are shown in Figure 2

2.3. Experimental Process

2.3.1. Temperature Measurement Test. First, liquid nitrogen was injected into the heat preservation tank through the self-pressurized liquid nitrogen tank, and the air outlet port was kept open. The liquid nitrogen interface was kept constant by controlling the amount of liquid nitrogen injected in line with the amount of liquid nitrogen vaporized. Meanwhile, the internal measurement point temperature of the coal sample was acquired in real time at an interval of 1 min. During this period, liquid nitrogen was intermittently injected into the sample container, and the liquid nitrogen interface should always just submerge to the bottom of the coal sample. When the temperature change at the measuring point became less than 0.05°C/min, the internal temperature of the coal sample was considered to have reached equilibrium stability, and the data acquisition could stop. Finally, the coal sample must be taken out. During the coal sample

temperature measurement, silicone rubber was applied to the bottom part of the sample holder in contact with the coal sample in order to prevent the low-temperature nitrogen gas generated by liquid nitrogen vaporization from penetrating the wall of the sample and interfering with the experiment

2.3.2. Permeability Test. The permeability tests of coal samples with different moisture contents before and after LNCS were carried out through the laboratory coal rock triaxial creep-seepage test system (sample size: $\Phi 50 \text{ mm} \times 100 \text{ mm}$). In order to exclude the influence of the temperature measurement borehole on the native pore structure of the coal samples, the permeability test coal samples were left untreated. In addition, the experimental conditions during the liquid nitrogen cold soaking were the same as the temperature measurement tests. The permeability test conditions are listed in Table 2

The flow rate data acquired in the seepage experiment are used to calculate the permeabilities of samples:

$$k = \frac{2p_0\mu LQ}{A(p_1^2 - p_2^2)}, \quad (1)$$

where k is the permeability of the coal sample (mD); p_0 is the atmospheric pressure (0.1 MPa); μ is the nitrogen dynamic viscosity ($10^{-6} \text{ Pa}\cdot\text{s}$); L is the length of the coal sample (cm); Q is the average flow rate of gas permeating the coal sample (cm^3/s); A is the size of the bottom and top area of the coal sample (cm^2); p_1 and p_2 are the pressures at the inlet and the outlet, respectively (MPa).

The specific test steps are as follows: (1) The permeabilities of all coal samples were measured by the triaxial seepage test system. Each coal sample was measured 3 times, and the calculated average value was taken as its permeability before LNCS. (2) After the initial permeability test was completed,

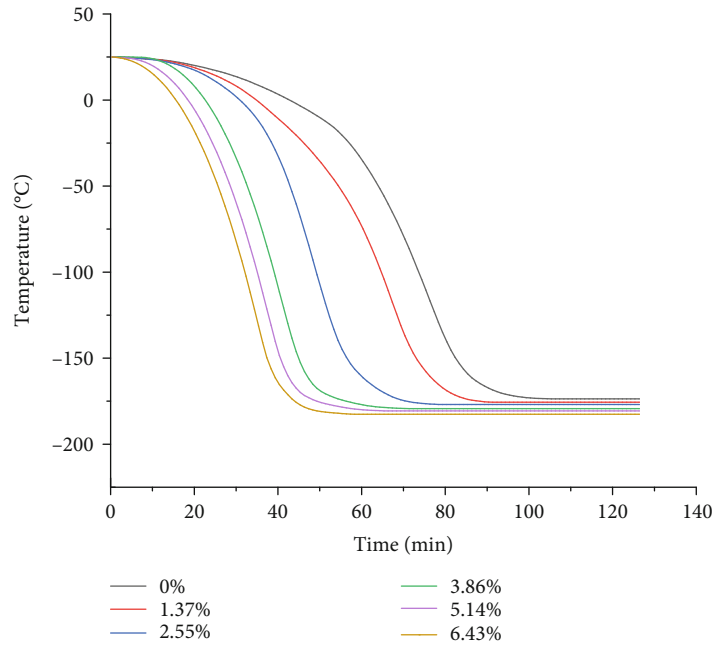


FIGURE 4: Temperature change curve of internal measurement points of coal samples with time.

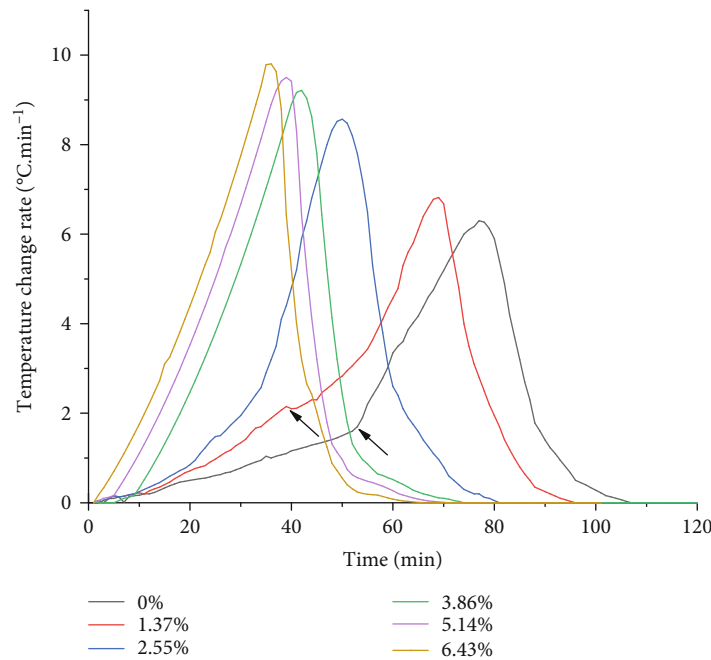


FIGURE 5: Temperature change rate curve of internal measurement points of coal samples with time.

the LNCS temperature measurement system was employed to perform LNCS treatment on coal samples, and the treatment time was the same the temperature measurement time. (3) After completion of LNCS temperature measurement, the permeability of the coal sample was measured after it returned to room temperature.

2.3.3. *Micro-CT Scanning Test.* LNCS treatment was carried out on coal samples through the liquid nitrogen temperature measurement system (the test conditions were the same as

the temperature measurement test), and the samples were scanned before and after LNCS, respectively. The resolution of industrial CT scanning is related to the size of the sample, and the smaller the size, the more accurate the CT scanning. To improve the scanning accuracy, small size coal samples ($\Phi 50 \text{ mm} \times 100 \text{ mm}$) were used to observe the changes of pore structure. The CT image reconstruction and processing method is as follows: CT data reconstruction software was used to define the sample CT reconstruction area, the reconstruction parameters are set, beam hardening correction is

TABLE 3: Contrast of permeability of coal samples before and after treatment.

Sample	Moisture content (%)	Water saturation (%)	Average permeability (mD)		Permeability increase rate (%)
			Before LNCS	After LNCS	
J_1	0	0	0.1365	0.2406	76.26
J_2	1.37	20	0.1432	0.3214	124.44
J_3	2.55	40	0.1392	0.4403	216.31
J_4	3.86	60	0.0949	0.3869	307.70
J_5	5.12	80	0.1288	0.6979	441.85
J_6	6.43	100	0.0828	0.6492	684.06

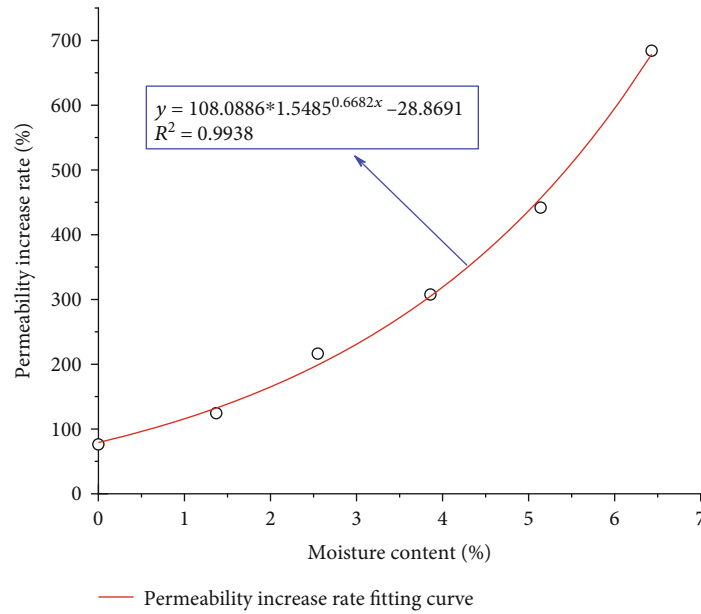


FIGURE 6: Fitting curve of permeability increase rates of coal samples after LNCS.

performed, automatic geometry correction is performed, and artifact compensation on the acquired raw images is performed to obtain better imaging quality. After the image reconstruction was completed, the image analysis was performed using VGStudio MAX image processing software to extract the internal fracture information of the coal samples at different scanning points and analyze them to obtain the pore structure changes inside the coal samples. The experimental flowchart is given in Figure 2

3. Results and Discussion

3.1. Effect of LNCS on the Temperature Variation of Coal. To disclose the effect of LNCS on the temperature variations within coal under different moisture content conditions and further explore the effect of moisture on the temperature variation of coal under LNCS, the experiment of temperature measurement of a coal sample under LNCS was carried out. Based on the results of the temperature measurement test, the temperature change curves of coal samples with different moisture contents under LNCS conditions were obtained (Figure 4).

As can be seen in Figure 4, the dried coal sample consumes about 110 min to reach temperature equilibrium at the internal measurement point, while the saturated coal sample only consumes 65 min. Besides, the larger the moisture content of a coal sample, the shorter the time it consumes to reach temperature equilibrium at the internal measurement point. As shown in Figure 5, for the coal sample with a higher moisture content, its temperature change rate requires a shorter time to reach the peak value and the peak value is larger. Considering the water-ice phase transformation aspect, when the coal sample is exposed to liquid nitrogen, an ultra-low-temperature medium, the pore water inside it will quickly freeze into ice. Since the thermal conductivity changes suddenly after water turns into ice, it affects the variation of the internal temperature of coal. As early as 1958, Hobbs obtained the following conclusion about the heat conduction between ice and water by summarizing previous experiments: when the temperature drops to 0°C , the thermal conductivities of ice and water are $2.2\text{ W/m}^{\circ}\text{C}$ and $0.58\text{ W/m}^{\circ}\text{C}$, respectively. In addition, the thermal conductivity of ice will continue to increase continuously as the ambient temperature decreases [25].

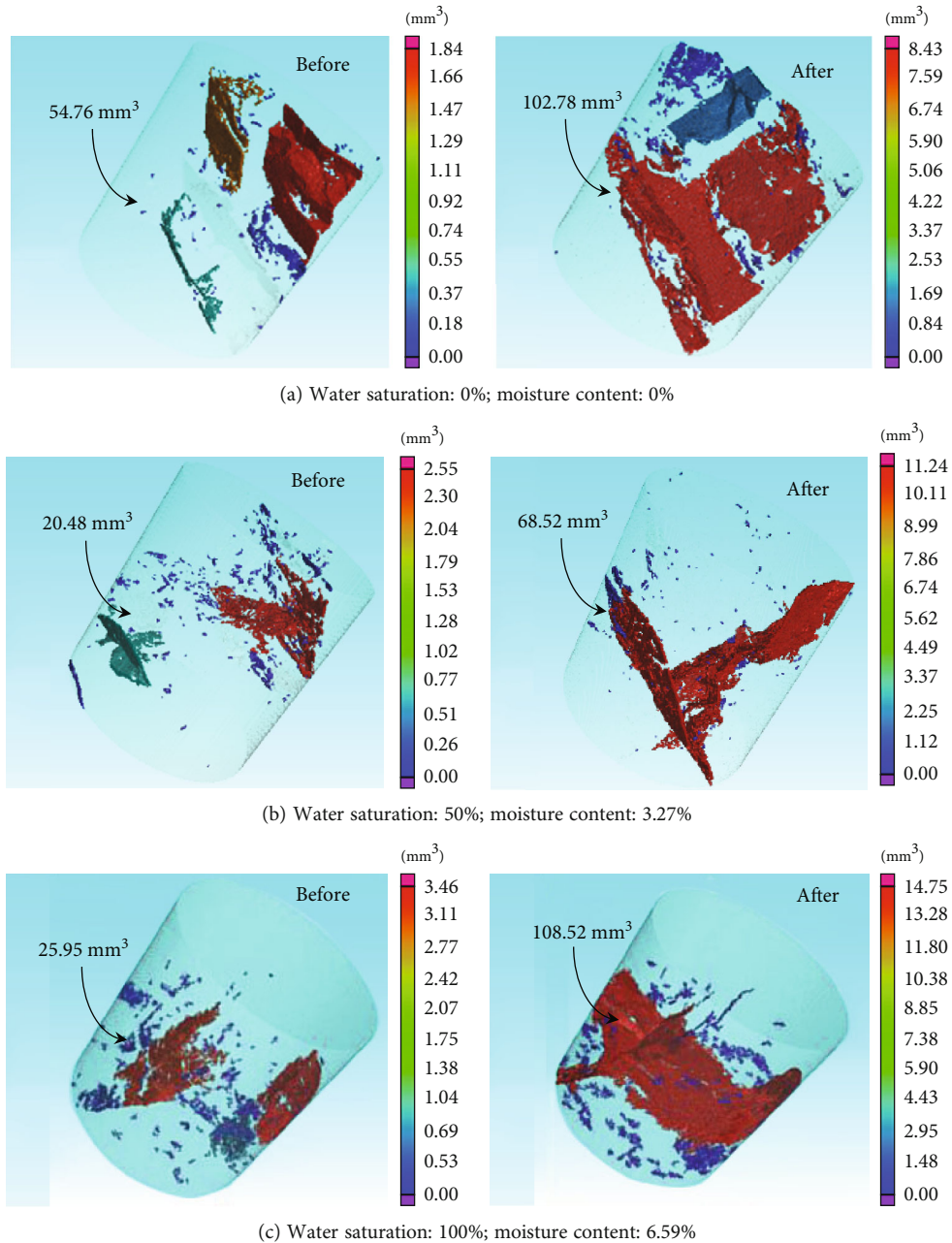


FIGURE 7: 3D views of coal samples.

Since liquid nitrogen is an ultra-low-temperature medium, it has a greater influence on the thermal conductivity of the ice inside coal. Therefore, the coal sample with 6.43% water content corresponds to the highest temperature change rate. In Figure 5, sudden change points (marked by the arrows) occur on the temperature change curves of coal samples with 0% and 1.37% moisture contents, which agrees with the results of Li et al. The reason for such a phenomenon is that the infiltration of low-temperature nitrogen into the internal temperature measurement points of the coal samples accelerates temperature variation [24].

3.2. *Effect of LNCS on the Permeability Changes of Coal.* Coal is a porous medium containing pores and fractures instead

of an idealized continuous medium [26, 27]. When coal is frozen by liquid nitrogen, the difference in thermal conductivities will produce uneven temperature stress, and the phase transformation effect of pore water will cause volume expansion, which will induce the expansion and connectivity of pores in coal. To investigate the effect of LNCS on the change of permeability of coal under different moisture content conditions, the changes of permeability of coal samples before and after LNCS were comparatively analyzed, as shown in Table 3 and Figure 6.

As presented in Table 3 and Figure 6, the permeabilities of all coal samples exhibit a rising trend after LNCS. Among them, the dried coal sample corresponds to the lowest permeability increase rate, and the saturated coal sample

corresponds to the highest rate which is 8.97 times higher than that of dried coal samples. The relationship between the moisture content and the permeability increase rate is not linear but exponential (Figure 6). The mechanism and degree of influence of LNCS on the permeability changes of dried and water-containing coal samples are different.

The pore structure change of the dried coal sample results from the temperature stress caused by the temperature difference effect. When the coal sample is exposed to the low-temperature medium, the temperature field of the coal at the contact surface of the cold source will change rapidly, and part of the coal matrix grains will undergo volume contraction, so a large local temperature stress will be formed between the internal grains. The increase of temperature stress to a certain degree will promote the pore structure of coal to expand and connect, and then the coal permeability will increase. For water-containing coal samples, the pore structure change mainly results from the frost swelling force generated by the water-ice phase transformation and the temperature stress generated by the temperature difference effect, and the frost swelling force gradually becomes dominant as the water saturation increases. When the water-containing coal samples come into contact with the low-temperature medium, the water-ice phase transformation of the pore water can produce a volume expansion of about 9%, and the frost heave force generated by the phase transformation action is theoretically capable of reaching 207 MPa [28–30]. When the combined effect of frost heave force and temperature stress exceeds the strength limit of coal, their synergistic effect causes a large number of new pores to be generated as well as the connectivity of the primary crack network.

The following conclusion can be drawn based on the above analysis. The damage mechanism of dried coal is relatively single, dominated by the pore and fracture damage caused by temperature stress. With the introduction of moisture, the damage effect caused by moisture occurs in addition to the internal structure damage caused by temperature stress. In the case of a low moisture content, some water inside coal freezes and generates pressure. When coal gets saturated, the water inside pores and fractures is completely frozen, and volume expansion causes the contraction and destruction of the coal matrix. In short, the larger the moisture content of a coal sample, the better the permeability enhancement effect.

3.3. Effect of LNCS on the Pore Structures of Coal. The permeability test results suggest that LNCS has a remarkable promotion effect on the permeabilities of coal samples under different moisture content conditions, especially for the saturated coal sample. To investigate the permeability enhancement effect of LNCS on coal samples under different moisture content conditions, the pore structure of coal samples were analyzed by CT scanning test from a 3D perspective.

Figure 7 shows the 3D views of the CT scanning test results of coal samples with different water saturation degrees before and after LNCS. By comparing the spatial distribution of coal pores before and after LNCS, the effect

of LNCS on the development and expansion of the pore structure of coal samples with different water saturation degrees is analyzed. Before LNCS, the total pore volumes of coal samples with 0%, 50%, and 100% water saturation are 54.76 mm^3 , 20.48 mm^3 , and 25.95 mm^3 , respectively. After LNCS, they increase to 102.78 mm^3 , 68.52 mm^3 , and 108.52 mm^3 by 87.69%, 234.57%, and 318.19%, respectively. Compared with an unsaturated water coal sample, the total pore volume of a saturated coal sample increased more significantly. The total pore volume increase of the saturated coal water sample is 3.63 times that of the dried coal sample. A comparison among the 3D micro-CT pore models of coal samples with different water saturation degrees reveals that the dried coal sample is mainly sprouting new pores on the basis of primary pores after LNCS; in contrast, after the coal samples with 50% and 100% water saturation degrees are treated with liquid nitrogen, new pores sprouted while primary pores will penetrate each other spatially to form a crack network.

From the above analysis, it can be seen that after LNCS treatment, the coal sample with a higher moisture content experiences more vigorous development and expansion of its pore structure and a greater change in its seepage characteristics. Therefore, when applied to a water-containing reservoir, LNCS can significantly improve the permeability of the reservoir, thereby promoting the rate of CBM drainage.

4. Conclusions

In this study, the effect of LNCS on the temperature variations within coal samples with different moisture contents were studied. Moreover, the pore structure of coal samples was quantitatively and qualitatively characterized by permeability and CT scanning tests. The study draws the following conclusions

- (1) The experimental results of coal temperature changes during LNCS show that the coal sample with a higher moisture content consumes a shorter time to reach internal temperature equilibrium and experiences faster temperature changes. The continuous increase of thermal conductivity after phase transformation of water-ice under low-temperature freezing conditions can accelerate the coal temperature change rate
- (2) The permeability test results of coal samples reveal that the permeability increase grows exponentially with the increase of moisture content under the effect of LNCS, and the permeabilities of coal samples are enhanced by 76.26%–684.06%
- (3) The 3D CT scanning results of coal samples disclose that after the LNCS treatment, the dried coal sample is mainly sprouting new pores on the basis of primary pores; in contrast, for water-containing coal samples, new pores sprouted while primary pores will penetrate each other spatially to form a crack network

(4) Moisture has a remarkable effect on the seepage characteristics of coal during LNCS, and the freezing and swelling force generated by volume expansion resulting from the water-ice phase transformation promote the development and connection of coal fractures and enhance coal permeability. The joint action of temperature difference effect and water-ice phase transformation exerts a stronger promotion effect on coal permeability. In the process of LNCS cracking coal, the integrated consideration of moisture content conduces to achieving a better permeability enhancement effect

Data Availability

The data used to support the findings of this study are available from the corresponding author upon request.

Conflicts of Interest

The authors declare no competing interests.

Acknowledgments

The authors would like to thank the financial support from the National Natural Science Foundation of China (51874125, 51974109, and 51704099), the Project of Youth Talent Promotion in Henan Province (2020HYTP020), the Outstanding Youth Fund of Henan Polytechnic University in 2020 (J2020-4), the Young Key Teachers from Henan Polytechnic University (2019XQG-10), the Zhongyuan Talent Program-Zhongyuan Top Talent (ZYYCYU202012155), and the Training Plan for Young Backbone Teachers of Colleges and Universities in Henan Province (2021GGJS051).

References

- [1] S. H. Zhang, S. H. Tang, Z. Qian, Z. J. Pan, and Q. L. Guo, "Evaluation of geological features for deep coalbed methane reservoirs in the Dacheng Salient, Jizhong Depression, China," *International Journal of Coal Geology*, vol. 133, pp. 60–71, 2014.
- [2] B. Li, J. X. Zhang, Z. B. Ding, B. Wang, and P. Li, "A dynamic evolution model of coal permeability during enhanced coalbed methane recovery by N_2 injection: experimental observations and numerical simulation," *RSC Advances*, vol. 11, no. 28, pp. 17249–17258, 2021.
- [3] A. Liu, S. M. Liu, G. Wang, and G. J. Sang, "Modeling of coal matrix apparent strains for sorbing gases using a transversely isotropic approach," *Rock Mechanics and Rock Engineering*, vol. 53, no. 9, pp. 4163–4181, 2020.
- [4] F. Du, K. Wang, Y. Y. Guo et al., "The mechanism of rockburst-outburst coupling disaster considering the coal-rock combination: an experiment study," *Geomechanics and Engineering*, vol. 22, no. 3, pp. 255–264, 2020.
- [5] A. Vengosh, R. B. Jackson, N. Warner, T. H. Darrah, and A. Kondash, "A critical review of the risks to water resources from unconventional shale gas development and hydraulic fracturing in the United States," *Environmental Science & Technology*, vol. 48, no. 15, pp. 8334–8348, 2014.
- [6] D. Zhao, Q. Wang, D. Li, and Z. Feng, "Experimental study on infiltration and freeze-thaw damage of water-bearing coal samples with cryogenic liquid nitrogen," *Journal of Natural Gas Science and Engineering*, vol. 60, pp. 24–31, 2018.
- [7] Z. F. Li, H. F. Xu, and C. Y. Zhang, "Liquid nitrogen gasification fracturing technology for shale gas development," *Journal of Petroleum Science Engineering*, vol. 138, pp. 253–256, 2016.
- [8] H. Liu, G. S. Yang, and J. X. Ren, "Numerical analysis method for temperature field of freezing-thawing shale based on digital image processing," *Chinese Journal of Rock Mechanics and Engineering*, vol. 26, no. 8, pp. 1678–1683, 2007.
- [9] W. Xiong, M. G. Liu, Q. H. Zhang, and Z. M. Wang, "Temperature distribution along piles in permafrost regions," *Rock and Soil Mechanics*, vol. 30, no. 6, pp. 1658–1664, 2009.
- [10] X. J. Tan, W. Z. Chen, G. J. Wu, and J. P. Yang, "Numerical simulations of heat transfer with ice-water phase change occurring in porous media and application to a cold-region tunnel," *Tunnelling and Underground Space Technology*, vol. 38, pp. 170–179, 2013.
- [11] C. Park, J. H. Synn, H. S. Shin, H. D. Lim, and S. W. Jeon, "An experimental study on the thermal characteristics of rock at low temperatures," *International Journal of Rock Mechanics and Mining Sciences*, vol. 41, no. 3, pp. 367–368, 2004.
- [12] C. Z. Cai, G. S. Li, Z. W. Huang, Z. H. Shen, S. C. Tian, and J. W. Wei, "Experimental study of the effect of liquid nitrogen cooling on rock pore structure," *Journal of Natural Gas Science Engineering*, vol. 21, pp. 507–517, 2014.
- [13] B. Li, Y. J. Ren, and X. Q. Lv, "The evolution of thermal conductivity and pore structure for coal under liquid nitrogen soaking," *Advances in Civil Engineering*, vol. 2020, 8 pages, 2020.
- [14] B. Li, L. L. Zhang, J. P. Wei, and Y. J. Ren, "Pore damage properties and permeability change of coal caused by freeze-thaw action of liquid nitrogen," *Advances in Civil Engineering*, vol. 2018, 9 pages, 2018.
- [15] Z. Z. Yang, Y. P. Zhang, J. Min, X. G. Li, W. Zhou, and Z. Lu, "Experimental research on influence of low temperature on coal permeability," *Rock and Soil Mechanics*, vol. 38, no. 2, pp. 354–360, 2017.
- [16] C. Z. Cai, G. S. Li, Z. W. Huang, Z. H. Shen, and S. C. Tian, "Rock pore structure damage due to freeze during liquid nitrogen fracturing," *Arabian Journal for Science and Engineering*, vol. 39, no. 12, pp. 9249–9257, 2014.
- [17] C. Z. Cai, Z. W. Huang, G. S. Li, F. Gao, J. W. Wei, and R. Li, "Feasibility of reservoir fracturing stimulation with liquid nitrogen jet," *Journal of Petroleum Science and Engineering*, vol. 144, pp. 59–65, 2016.
- [18] J. P. Wei, L. L. Zhang, B. Li, and Z. H. Wen, "Non-uniformity of coal damage caused by liquid nitrogen freeze-thaw," *Journal of Natural Gas Science and Engineering*, vol. 69, p. 102946, 2019.
- [19] L. Qin, C. Zhai, S. M. Liu, and J. Z. Xu, "Factors controlling the mechanical properties degradation and permeability of coal subjected to liquid nitrogen freeze-thaw," *Scientific Reports*, vol. 7, no. 1, pp. 1–11, 2017.
- [20] L. Qin, C. Zhai, S. M. Liu, J. Z. Xu, G. Q. Yu, and Y. Sun, "Changes in the petrophysical properties of coal subjected to liquid nitrogen freeze-thaw—a nuclear magnetic resonance investigation," *Fuel*, vol. 194, pp. 102–114, 2017.

- [21] B. Li, L. S. Huang, X. Q. Lv, and Y. J. Ren, "Variation features of unfrozen water content of water-saturated coal under low freezing temperature," *Scientific Reports*, vol. 11, no. 1, pp. 1–12, 2021.
- [22] X. C. Li, Y. Y. Meng, C. L. Yang, B. S. Nie, Y. J. Mao, and X. H. Chen, "Effects of pore structure on acoustic wave velocity of coal samples," *Journal of Nanoscience and Nanotechnology*, vol. 17, no. 9, pp. 6532–6538, 2017.
- [23] L. Liu, X. Li, D. Wang, and Z. Zhang, "Experimental study on temperature response of different ranks of coal to liquid nitrogen soaking," *Natural Resources Research*, vol. 30, no. 2, pp. 1467–1480, 2021.
- [24] B. Li, L. S. Huang, X. Q. Lv, and Y. J. Ren, "Study on temperature variation and pore structure evolution within coal under the effect of liquid nitrogen mass transfer," *ACS Omega*, vol. 6, no. 30, pp. 19685–19694, 2021.
- [25] P. V. Hobbs, *Ice Physics*, Oxford University Press, Oxford, England, 1974.
- [26] C. F. Rodrigues and M. J. Lemos de Sousa, "The measurement of coal porosity with different gases," *International Journal of Coal Geology*, vol. 48, no. 3-4, pp. 245–251, 2002.
- [27] F. Du, K. Wang, G. D. Wang, Y. F. Jiang, C. P. Xin, and X. Zhang, "Investigation of the acoustic emission characteristics during deformation and failure of gas-bearing coal-rock combined bodies," *Journal of Loss Prevention in the Process Industries*, vol. 55, pp. 253–266, 2018.
- [28] Y. F. Cheng, L. Jiang, H. D. Wang, U. Ansari, Z. Y. Han, and J. P. Ding, "Experimental study on pore structure and mechanical properties of stratified coal," *International Journal of Geomechanics*, vol. 17, no. 12, p. 04017116, 2017.
- [29] L. Qin, C. Zhai, S. M. Liu, and J. Z. Xu, "Mechanical behavior and fracture spatial propagation of coal injected with liquid nitrogen under triaxial stress applied for coalbed methane recovery," *Engineering Geology*, vol. 233, pp. 1–10, 2018.
- [30] C. Z. Cai, G. S. Li, Z. W. Huang, S. C. Tian, Z. H. Shen, and X. Fu, "Experiment of coal damage due to super-cooling with liquid nitrogen," *Journal of Natural Gas Science and Engineering*, vol. 22, pp. 42–48, 2015.

Research Article

Study on Prediction of Coal-Gas Compound Dynamic Disaster Based on GRA-PCA-BP Model

Kai Wang,^{1,2} Kangnan Li,^{1,2} and Feng Du ^{1,2}

¹Beijing Key Laboratory for Precise Mining of Intergrown Energy and Resources, China University of Mining and Technology (Beijing), Beijing 100083, China

²School of Emergency Management and Safety Engineering, China University of Mining & Technology (Beijing), Beijing 100083, China

Correspondence should be addressed to Feng Du; fengducumbt@126.com

Received 4 August 2021; Accepted 29 September 2021; Published 14 October 2021

Academic Editor: Qingquan Liu

Copyright © 2021 Kai Wang et al. This is an open access article distributed under the Creative Commons Attribution License, which permits unrestricted use, distribution, and reproduction in any medium, provided the original work is properly cited.

The intensity and depth of China's coal mining are increasing, and the risk of coal-gas compound dynamic disaster is prominent, which seriously restricts the green, safe, and efficient mining of China's coal resources. How to accurately predict the risk of disasters is an important basis for disaster prevention and control. In this paper, the Pingdingshan No. 8 coal mine is taken as the research object, and the grey relational analysis (GRA), principal component analysis (PCA), and BP neural network are combined to predict the coal-gas compound dynamic disaster. First, the weights of 13 influencing factors are sorted and screened by grey relational analysis. Next, principal component analysis is carried out on the influencing factors with high weight value to extract common factors. Then, the common factor is used as the input parameter of BP neural network to train the previous data. Finally, the coal-gas compound dynamic disaster prediction model based on GRA-PCA-BP neural network is established. After verification, the model can effectively predict the occurrence of coal-gas compound dynamic disaster. The prediction results are consistent with the actual situation of the coal mine with high accuracy and practicality. This work is of great significance to ensure the safe and efficient production of deep mines.

1. Introduction

With the increase of mining intensity and mining depth of China's coal resources, when the coal under high ground stress and high gas pressure is disturbed by mining, the coupling effect of rockburst and coal-gas outburst becomes intense [1–3]. In particular, after entering deep mining, the interaction between rockburst and coal-gas outburst becomes serious, which no longer exists in the form of a single disaster. It shows the characteristics of compound disaster. It is called coal-gas compound dynamic disaster [4–6]. In the process of the occurrence of coal-gas compound dynamic disaster, many factors are intertwined with each other, which may be used as incentives and strengthen each other before, during, and after the accident. Compared with single dynamic disaster, the coupling of two disasters may make the coal-gas compound dynamic disaster more intense and violent, resulting in a large number of property losses

and casualties. Coal-gas compound dynamic disaster has become a major disaster restricting the safe and efficient mining of coal resources in China. Therefore, how to accurately predict the occurrence of disasters has become a major scientific issue in the field of coal mine safety under the form of new disasters.

Compared with rockburst and coal-gas outburst, the threshold of coal-gas compound dynamic disaster is lower, and the disaster mechanism is more complex [7–11]. The previous single disaster prediction method is no longer applicable, and the prediction difficulty of coal-gas compound dynamic disaster is greatly increased [12]. At present, the previous research on the prediction of rockburst and coal-gas outburst is quite fruitful [13–18]. However, the research on the prediction of coal-gas compound dynamic disaster is relatively less. Pan [19] put forward three kinds of integrated forecasting technologies, including multi-indexes integrated monitoring of drilling cutting method,

real-time continuous monitoring of coal temperature, and real-time continuous monitoring of coal charge, and applied them in Pingdingshan and other mining areas. Luo et al. [20] used the analytic hierarchy process (AHP) to build a multiparameter risk assessment model of mine dynamic disasters and carried out classification early warning for rockburst, coal-gas outburst, and coal-gas compound dynamic disaster. The model is verified by some examples, and it is concluded that the model has strong applicability to the prediction of dynamic disasters in deep mines. Yuan [21] and Meng and Zhang [22] proposed that through the comprehensive detection method, the coal drilling cutting quantity, the initial gas emission velocity, and the gas desorption quantity should be used as the sensitive indexes for the risk assessment, prediction, and effective inspection of the coal-gas compound dynamic disaster. According to the multifactor coupling unified catastrophe characteristics of deep coal-gas dynamic disaster in Pingdingshan mining area, Yuan [23] proposed the unified prediction theory of deep coal-gas dynamic disaster based on geological dynamic zoning and the probability prediction method of pattern recognition and established the risk evaluation and prediction technical index system of deep coal-gas dynamic disaster in Pingdingshan mining area. By analyzing the correlation between “direction” and “mechanism” of the precursor of coal-gas compound dynamic disaster, Jiang et al. [24] put forward the multiparameter monitoring and joint early warning method of real-time danger. Through the construction of multiparameter joint warning platform, the test is carried out in many coal mines, and the preliminary results are obtained. Dou et al. [25] summarized the monitoring and early warning technologies of gas-bearing coal rock dynamic disasters. They include zoning and grading monitoring and early warning, microseism monitoring method, electromagnetic radiation, elastic wave CT and vibration wave CT in the aspect of rock burst monitoring, drilling gas gushing initial velocity method, R-index method, and electromagnetic radiation method in the aspect of coal and gas outburst monitoring. They pointed out that for the monitoring and early warning of coal-gas compound dynamic disaster, we should focus on the establishment of multiparameter normalized dimensionless monitoring and early warning model and criteria for dynamic disaster risk, build the monitoring and early warning index system suitable for coal-gas compound dynamic disaster, and develop the corresponding monitoring technology and equipment.

It can be seen that although relevant scholars have made some meaningful researches on the prediction of coal-gas compound dynamic disaster, most of them are still in the qualitative stage, and the application of quantitative mathematical methods in the prediction of coal-gas compound dynamic disaster is rarely reported. Therefore, combined with the application of mathematical method in the prediction of coal-gas outburst and rockburst [26–29], a method predicting the coal-gas compound dynamic disaster based on the GRA-PCA-BP model is put forward, and the model is verified, and good results are achieved.

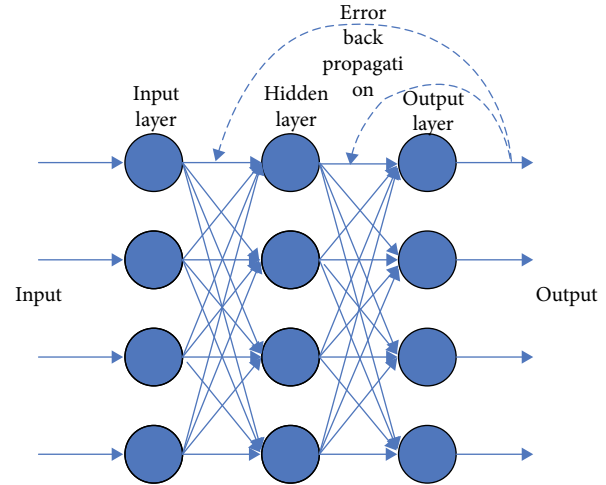


FIGURE 1: Error back propagation of three-layer network structure.

2. Occurrence Law and Influencing Factors of Coal-Gas Compound Dynamic Disaster

2.1. Occurrence Law of Coal-Gas Compound Dynamic Disaster. Coal-gas compound dynamic disaster is an atypical dynamic disaster induced by mining activities. With the increase of mining depth and complex geological structure, a considerable number of mines are facing the double danger of coal-gas outburst and rockburst. Coal-gas compound dynamic disaster will occur under specific conditions. Based on the field investigation records and extensive literature review of coal-gas compound dynamic disaster in multitime period for multicoal mines, the occurrence laws and destructive characteristics of coal-gas compound dynamic disaster are summarized as follows:

- (1) Compared with coal-gas outburst and rockburst, when coal-gas compound dynamic disaster occurs, the critical value of main controlling factors is lower, and the intensity and damage degree of disasters are obviously higher. Compared with the coal-gas outburst disaster, the gas pressure of coal-gas compound dynamic disaster is lower, and the coal strength is higher. Compared with rockburst disaster, when coal-gas compound dynamic disaster occurs, the gas pressure is higher, and the strength of coal seam roof strength is lower
- (2) The damage type of coal-gas compound dynamic disaster is obviously different from coal-gas outburst and rockburst, which shows new disaster characteristics. The damage type of coal-gas compound dynamic disaster includes part of the damage characteristics of coal-gas outburst and rockburst disaster. When the coal-gas compound dynamic disaster occurs, the impact power is stronger, and gas emission is higher

2.2. Analysis of Factors Influencing Coal-Gas Compound Dynamic Disaster. To explore the influencing factors of

TABLE 1: Partial initial data of coal-gas compound dynamic disaster in No. 8 coal mine.

Number	t_1/m	t_2	t_3	t_4	t_5	t_6	t_7	t_8/m	t_9/m	$t_{10}/^\circ$	t_{11}	t_{12}/mmHg	t_{13}	Disaster or not
1	535	0	0	0	0.5	1.47	3	5.4	0.8	11	0.06	11.23	0.32	1
2	554	0	0.08	0	1	1.47	3	5.4	0.7	11	0.05	15.47	0.28	1
11	566	1	0	0	0.5	1.78	2	3.5	0	16	0	7.93	0.57	1
12	566	1	0	0	0.5	1.78	2	3.5	0	16	0	9.00	0.81	1
20	484	0	0	0	0.5	2.13	3	3.5	0	10	0	12.56	0.29	1
21	530	3	0	0	1	1.72	3	4.3	0.65	24	0.11	11.48	0.67	1
29	540	0	0	0.13	0.5	2.03	3	4.7	1.2	11	0.10	12.05	0.27	1
30	457	0	0	0.14	0.5	1.07	4	3.5	0.4	31	0.06	5.09	0.15	0
38	510	0	0	0	0.5	1.54	3	4.5	1.5	20	0.13	12.74	0.26	1
39	800	1	0.17	0.39	0.5	2.03	3	3.0	0	11	0	15.89	0.18	0

Note: In the column “Disaster or not”, the “1” represents that the disaster occurs, and the “0” represents the disaster does not occur.

TABLE 2: Partial dimensionless data of coal-gas compound dynamic disaster in No. 8 coal mine.

Number	t_1	t_2	t_3	t_4	t_5	t_6	t_7	t_8	t_9	t_{10}	t_{11}	t_{12}	t_{13}	Disaster or not
1	0.9397	0	0	0	0.9331	0.8567	1.0455	1.3431	1.237	0.7863	0.7863	0.8955	0.8746	1
2	0.9731	0	2.7259	0	1.8661	0.8567	1.0455	1.3431	1.0824	0.7863	0.6553	1.2336	0.7653	1
11	0.9942	1.3529	0	0	0.9331	1.0374	0.697	0.8705	0	1.1437	0	0.6323	1.5579	1
12	0.9942	1.3529	0	0	0.9331	1.0374	0.697	0.8705	0	1.1437	0	0.7177	2.2139	1
20	0.8501	0	0	0	0.9331	1.2414	1.0455	0.8705	0	0.7148	0	1.0015	0.7926	1
21	0.9309	4.0588	0	0	1.8661	1.0024	1.0455	1.0695	1.005	1.7156	1.4416	0.9154	1.8313	1
29	0.9485	0	0	1.1178	0.9331	1.1831	1.0455	1.169	1.8555	0.7863	1.31	0.9609	0.738	1
30	0.8027	0	0	1.2037	0.9331	0.6236	1.3939	0.8705	0.6185	2.216	0.7863	0.4059	0.41	0
38	0.8958	0	0	0	0.9331	0.8975	1.0455	1.1192	2.3193	1.4297	1.7037	1.0159	0.7106	1
39	1.4052	1.3529	5.7926	3.3533	0.9331	1.1831	1.0455	0.7461	0	0.7863	0	1.2671	0.492	0

TABLE 3: Partial correlation coefficient and correlation degree.

Number	Correlation coefficient												
	t_1	t_2	t_3	t_4	t_5	t_6	t_7	t_8	t_9	t_{10}	t_{11}	t_{12}	t_{13}
1	0.9046	0.7433	0.7433	0.7433	0.9032	0.8876	0.9272	0.9975	0.9713	0.8737	0.8737	0.8955	0.8912
2	0.9116	0.7433	0.7405	0.7433	0.8842	0.8876	0.9272	0.9975	0.9354	0.8737	0.8489	0.9704	0.8696
11	0.9161	1	0.7433	0.7433	0.9032	0.9255	0.8566	0.8904	0.7433	0.9493	0.7433	0.8447	0.9503
12	0.9161	1	0.7433	0.7433	0.9032	0.9255	0.8566	0.8904	0.7433	0.9493	0.7433	0.8605	0.8199
20	0.8863	0.7433	0.7433	0.7433	0.9032	0.9723	0.9272	0.8904	0.7433	0.86	0.7433	0.9177	0.8749
21	0.9028	0.5915	0.7433	0.7433	0.8842	0.9179	0.9272	0.9325	0.9185	0.9153	0.9779	0.8996	0.8912
29	0.9064	0.7433	0.7433	0.9434	0.9032	0.9585	0.9272	0.9552	0.8863	0.8737	0.9893	0.909	0.8643
30	0.83	1	1	0.765	0.8077	0.8627	0.7376	0.8182	0.8637	0.6388	0.8329	0.9061	0.9053
38	0.8955	0.7433	0.7433	0.7433	0.9032	0.8959	0.9272	0.9437	0.8022	0.9808	0.9178	0.9208	0.8592
39	0.7361	0.7433	0.4035	0.5389	0.8077	0.7681	0.7894	0.84	1	0.8329	1	0.7557	0.8885
t_1	Correlation degree												
	t_2	t_3	t_4	t_5	t_6	t_7	t_8	t_9	t_{10}	t_{11}	t_{12}	t_{13}	
0.8804	0.8317	0.7346	0.7556	0.8717	0.8923	0.8712	0.8988	0.8197	0.8717	0.8117	0.8531		0.9077
4	Correlation degree ranking												
	9	13	12	6	3	7	2	10	5	11	8		1

coal-gas compound dynamic disaster, we need to understand the occurrence and development process of the disaster. Under the influence of mining disturbance, the coal-rock composite structure in critical state begins to deform and

lose stability and release elastic strain energy. A large amount of gas expansion energy is accumulated in the pores of coal mass in coal-rock composite structure. The release of gas expansion energy has tensile damage to coal mass. Coal

TABLE 4: Kaiser-Meyer-Olkin and Bartlett tests.

Kaiser-Meyer-Olkin		0.543
	Approximate chi-square	91.012
Bartlett sphericity test	Degree of freedom	28
	Significance	0

mass failure will further promote the release of elastic energy of coal mass and rock mass. At this time, the overall failure and instability of coal-rock composite structure induce the occurrence of coal-gas compound dynamic disaster. Combined with the influencing factors of coal-gas outburst disaster and rockburst disaster and the occurrence and development process of coal-gas compound dynamic disaster, the preliminary analysis is made to obtain the 13 influence factors of coal-gas compound dynamic disaster, which is buried depth (t_1), fault number (t_2), variation coefficient of coal thickness (t_3), variation coefficient of coal seam dip angle (t_4), soft stratification change (t_5), surrounding rock combination (t_6), type of coal mass failure (t_7), coal thickness (t_8), soft stratification thickness (t_9), coal seam dip angle (t_{10}), wrinkle coefficient (t_{11}), initial velocity of gas emission (t_{12}), and firmness coefficient (t_{13}).

3. Principles of the GRA-PCA-BP Model

3.1. Grey Relational Analysis (GRA). Grey relational analysis is a method of quantitative description and comparison of the development and change situation of a system. By determining the geometric similarity between the reference data column and several comparison data columns, we can judge whether they are closely related, reflecting the degree of correlation between the curves. The grey relational analysis method has several characteristics: it does not need huge data. It can find the corresponding statistical law even in the case of less data. It has no requirement for whether the sample obeys the classical probability distribution function. It will not cause the problem that the qualitative analysis results and quantitative analysis results are inconsistent. The rules and relations of the studied system will not be misinterpreted [30–32].

This method can be used to analyze the correlation degree between each influencing factor and the result when selecting the prediction index of coal-gas compound dynamic disaster. By evaluating the importance of each influencing factor, the main factors affecting the occurrence of coal-gas compound dynamic disaster are screened out from many parameters, and the interference of secondary factors on the prediction process and result is abandoned, which can improve the accuracy of the results and lay a good foundation for the operation of the model.

The specific implementation steps of grey relational analysis are as follows:

- (1) Suppose the parent sequence is Y_0 , and each influencing factors be the comparison subfactors sequence Y_i ($i = 1, 2, \dots, n$). The observed values of the parent factors are as follows:

$$Y_0 = \{y_0(1), y_0(2), \dots, y_0(n)\} \quad (1)$$

The observed values of the subfactors are as follows:

$$Y_i = \{y_i(1), y_i(2), \dots, y_i(n)\}. \quad (2)$$

- (2) The original data of each sequence are dimensionless processed. Supposing that X_0, X_i ($i = 1, 2, \dots, m$) are the observed values of parent factor and subfactor, respectively, after dimensionless treatment, then (the average method is used to process the data)

$$x_0(k) = \frac{y_0(k)}{1/n \sum_{t=1}^n y_0(t)}, x_i(k) = \frac{y_i(k)}{1/n \sum_{t=1}^n y_i(t)} \quad (3)$$

- (3) After dimensionless processing of original data, the correlation coefficient ζ between x_0 and x_i ($i = 1, 2, 3, \dots, n$) at point k is

$$\zeta_i(k) = \frac{\min_i \min_k |x_0(k) - x_i(k)| + \rho \max_i \max_k |x_0(k) - x_i(k)|}{|x_0(k) - x_i(k)| + \rho \max_i \max_k |x_0(k) - x_i(k)|} \quad (4)$$

In formula (4), the formula $\Delta_i(k) = |x_0(k) - x_i(k)|$, ($i = 1, 2, 3, \dots, n$) is called the absolute difference between x_0 and x_i at point k . The formula $\min_i \min_k |x_0(k) - x_i(k)|$ and the formula $\max_i \max_k |x_0(k) - x_i(k)|$ are two-level minimum difference and two-level maximum difference, respectively. The coefficient ρ is the resolution coefficient, generally $\rho = 0.5$.

- (4) Calculation of the grey relational degree r_i value

$$r_i = \frac{1}{n} \sum_{k=1}^n \zeta_i(k) \quad (5)$$

3.2. Principal Component Analysis (PCA). Principal component analysis (PCA) is a statistical technique to extract common factors from variable groups. This technique can find out the hidden representative factors among many variables and classify the same essential variables into one new factor to effectively reduce the number of variables. This intelligent optimization algorithm has unique advantages in local and global optimization and robust performance.

The advantages of principal component analysis are very suitable for the prediction of coal-gas compound dynamic disaster. The number of factors initially screened by GRA is large, and the correlation between the factors is high. There may be multicollinearity among the factors, which makes the model estimation distorted or difficult to estimate accurately due to the accurate correlation or high correlation

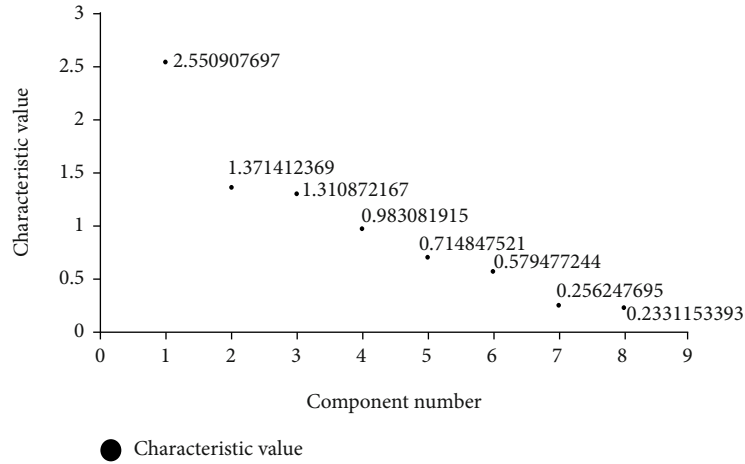


FIGURE 2: Gravel diagram.

TABLE 5: Total variance explained.

Common factor	Total variance explained			Extract the sum of squares of the load		
	Total	Initial eigenvalue Variance percentage	Cumulative percentage	Total	Variance percentage	Cumulative percentage
1	2.551	31.886	31.886	2.551	31.886	31.886
2	1.371	17.143	49.029	1.371	17.143	49.029
3	1.311	16.386	65.415	1.311	16.386	65.415
4	0.983	12.289	77.703	0.983	12.289	77.703
5	0.715	8.936	86.639			
6	0.579	7.243	93.882			
7	0.256	3.203	97.086			
8	0.233	2.914	100			

TABLE 6: Composition matrix.

	Component			
	F_1	F_2	F_3	F_4
Buried depth (t_1)	0.576	0.009	-0.661	-0.05
Change of soft stratification (t_9)	0.202	0.286	0.617	0.518
Surrounding rock combination (t_6)	-0.214	0.235	-0.49	0.762
Coal failure type (t_7)	0.844	-0.198	0.145	0.119
Coal thickness (t_8)	0.104	0.717	0.346	-0.19
Coal seam dip angle (t_{10})	-0.098	-0.816	0.328	0.17
Initial velocity of gas emission (t_{12})	0.892	0.082	-0.022	-0.133
Coal firmness coefficient (t_{13})	-0.778	0.095	-0.057	-0.183

between the factors, thus affecting the accuracy of BP neural network prediction. PCA simplification of influencing factors can effectively avoid the occurrence of this problem and can further reduce the dimension of influencing factors by obtaining new common factors [33–35].

The specific implementation steps of principal component analysis are as follows:

(1) Standardized collection of original index data

There are p -dimensional random vector $x = (x_1, x_2, \dots, x_p)^T$, n samples $x_i = (x_{i1}, x_{i2}, \dots, x_{ip})^T$, $i = 1, 2, \dots, n, n > p$, constructing a sample matrix, performing the following standardized transformations on the sample matrix elements:

$$Z_{ij} = \frac{x_{ij} - \bar{x}_j}{s_j}, i = 1, 2, \dots, n; j = 1, 2, \dots, p, \quad (6)$$

where $\bar{x}_j = \sum_{i=1}^n x_{ij}/n$, $s_j^2 = \sum_{i=1}^n (x_{ij} - \bar{x}_j)^2/n - 1$. The normalized matrix Z is obtained.

- (2) The correlation coefficient matrix of standardized matrix Z is calculated

$$R = [r_{ij}]_p \times p = \frac{Z^T Z}{n-1}, \quad (7)$$

where $r_{ij} = \sum z_{kj} \cdot z_{ki}/n - 1$, $i, j = 1, 2, \dots, p$.

- (3) The characteristic equation $|R - \lambda I_p| = 0$ is used to solve the sample correlation matrix R . Then, p characteristic roots are obtained to determine the principal component. Through equation $\sum_{j=1}^m \lambda_j / \sum_{j=1}^p \lambda_j \geq t$ ($t < 1$), the value of m is determined, which makes the utilization of information more than t . For each λ_j , $j = 1, 2, \dots, m$, the equation $Rb = \lambda_j b$ is solved to get the unit eigenvector b_j^0

- (4) The standardized index variables are transformed into main components

$$U_{ij} = z_i^T b_j^0, j = 1, 2, \dots, m \quad (8)$$

U_1 is the first principal component, U_2 is the second principal component, ..., and U_p is the p principal component.

3.3. BP Neural Network. BP neural network is a kind of multilayer feedforward neural network trained according to the error back propagation algorithm, which is the most widely used neural network [36, 37]. The topological structure of BP neural network model is composed of three layers: input layer, hidden layer, and output layer. Gradient shrinkage technique is used to calculate the solution weight by iterative operation. The addition of hidden nodes makes the adjustable parameters increase and approach the accurate value. There is no uniform regulation on the number of neurons in the implied layer, which is generally determined by empirical formula. The empirical formula for determining the number of neurons N in the hidden layer is as follows:

$$N = \sqrt{n \times m}, \quad (9)$$

$$N = \sqrt{n \times m} + a, \quad (10)$$

$$N = m(n+1), \quad (11)$$

$$N = 2m + 1, \quad (12)$$

where n is the number of input layer nodes, m is the number of output layer nodes, and a is a constant between 1 and 10. From the input layer to the hidden layer and from

TABLE 7: Some common factor data after calculation.

Number	X_1	X_2	X_3	X_4
1	1.60969737	0.74749536	0.339417928	0.812900035
2	2.204036798	1.03198924	0.891851959	1.269598519
11	0.457772706	0.272297774	0.084938237	0.966876527
12	0.02353326	0.341611389	0.045670799	0.835486048
20	1.592037485	0.557492709	0.025542212	1.189012618
21	0.915941684	0.186560304	1.004711086	1.439935842
29	1.691453877	0.691818614	0.119806084	1.110542908
30	1.610308877	-0.967254621	0.937421456	1.166563328
38	1.724334178	0.065505757	0.48872312	1.012079589
39	2.375037821	0.394508286	-0.321069244	1.172335713

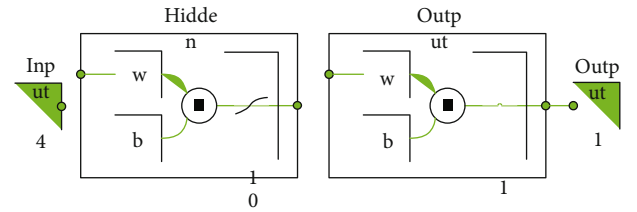


FIGURE 3: BP neural network model.

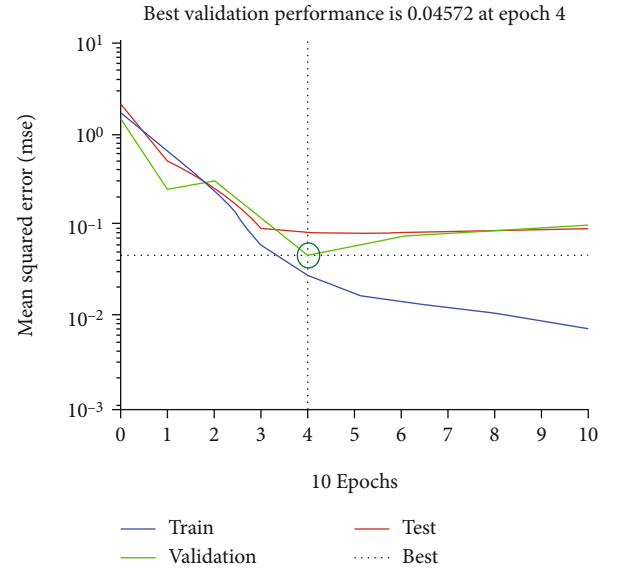


FIGURE 4: Working performance of neural network.

the hidden layer to the output layer, the actual output value is obtained. When the output layer error exceeds the error tolerance range, it will be back propagation. By modifying the weights of the neural nodes, the mean square error of the expected output and the actual output is minimized. Therefore, the results meet the requirements. The structure diagram is shown in Figure 1.

3.4. GRA-PCA-BP Model. In the GRA-PCA-BP model, firstly, the influencing factors with high weight are screened by grey relational analysis. Secondly, the influencing factors

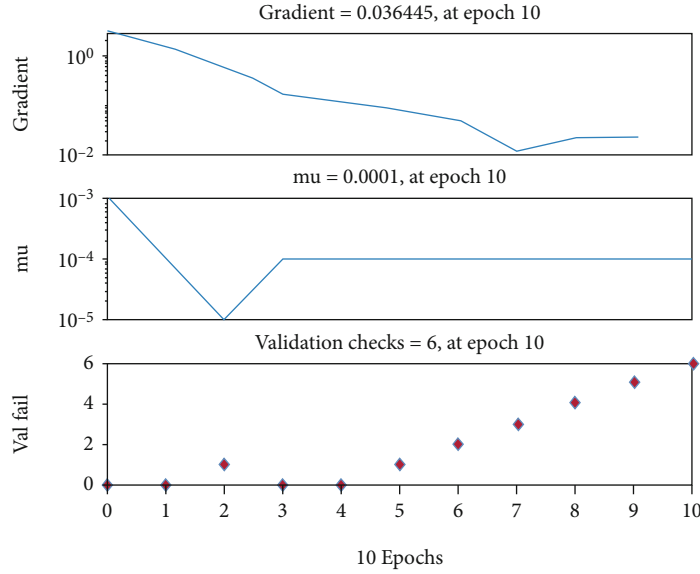


FIGURE 5: Training status diagram.

are integrated into representative common factors through principal component analysis, and the number of factors is further reduced. Finally, the common factor data is substituted into the input layer of BP neural network, and the training of prediction model is started to obtain a model that can accurately predict whether disasters occur. Grey relational analysis eliminates irrelevant or small influence factors. Principal component analysis eliminates multicollinearity between independent variables and further reduces the dimension of input data. The BP neural network has good predictability. The combination of the three methods can make full use of the advantages and avoid the disadvantages and can accurately and quickly predict the coal-gas compound dynamic disaster.

4. Case Analysis

4.1. Grey Relational Analysis of Influencing Factors. The influencing factors of 13 kinds of coal-gas compound dynamic disasters were analyzed. In this paper, we need to compare the 13 factors with whether the occurrence of compound disasters and calculate the correlation degree, so the parent sequence Y_0 is whether the occurrence of compound disasters. The 46 groups of data of Pingdingshan No. 8 coal mine are selected and analyzed by the SPSS software. Some initial data are shown in Table 1, some dimensionless data are shown in Table 2, and correlation coefficient and correlation degree are shown in Table 3.

Through the process of grey relational analysis, the order of 13 factors affecting the strength of coal-gas compound dynamic disaster is obtained: coal firmness coefficient (t_{13}) > coal thickness (t_8) > surrounding rock combination (t_6) > buried depth (t_1) > coal seam dip angle (t_{10}) > change of soft stratification (t_5) > coal failure type (t_7) > initial velocity of gas emission (t_{12}) > number of faults (t_2) > thickness of soft stratification (t_9) > wrinkle coefficient (t_{11}) > variation coefficient of coal seam dip angle (t_4) > variation coefficient of coal

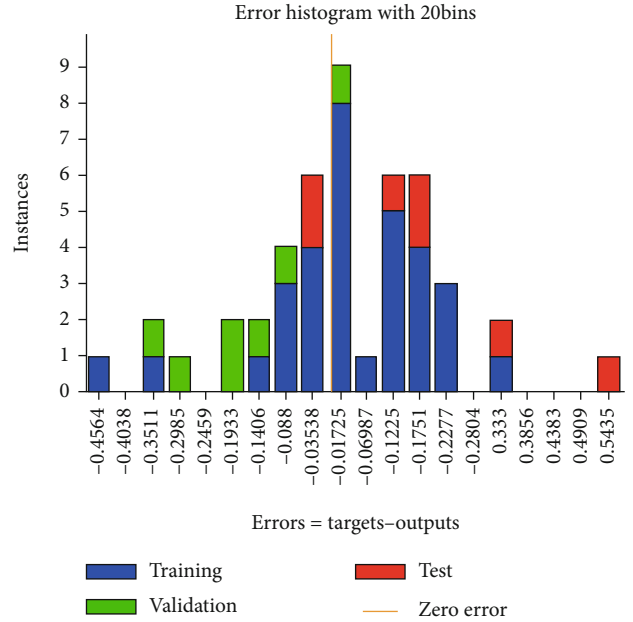


FIGURE 6: Error histogram.

thickness (t_3). Some of the influencing factors with a small degree of relevance (less than 0.85) are deduced, and the first eight influencing factors are kept.

4.2. Using PCA to Simplify the Main Influencing Factors. The first eight retained factors were simplified by PCA using the SPSS software. After the process of inspection, extraction, and calculation, four common factor data were finally obtained. The following are the specific steps.

KMO (Kaiser-Meyer-Olkin) and Bartlett test results are shown in Table 4. KMO test statistics show whether the partial correlation between variables is strong enough. Bartlett sphericity test is used to judge whether the correlation

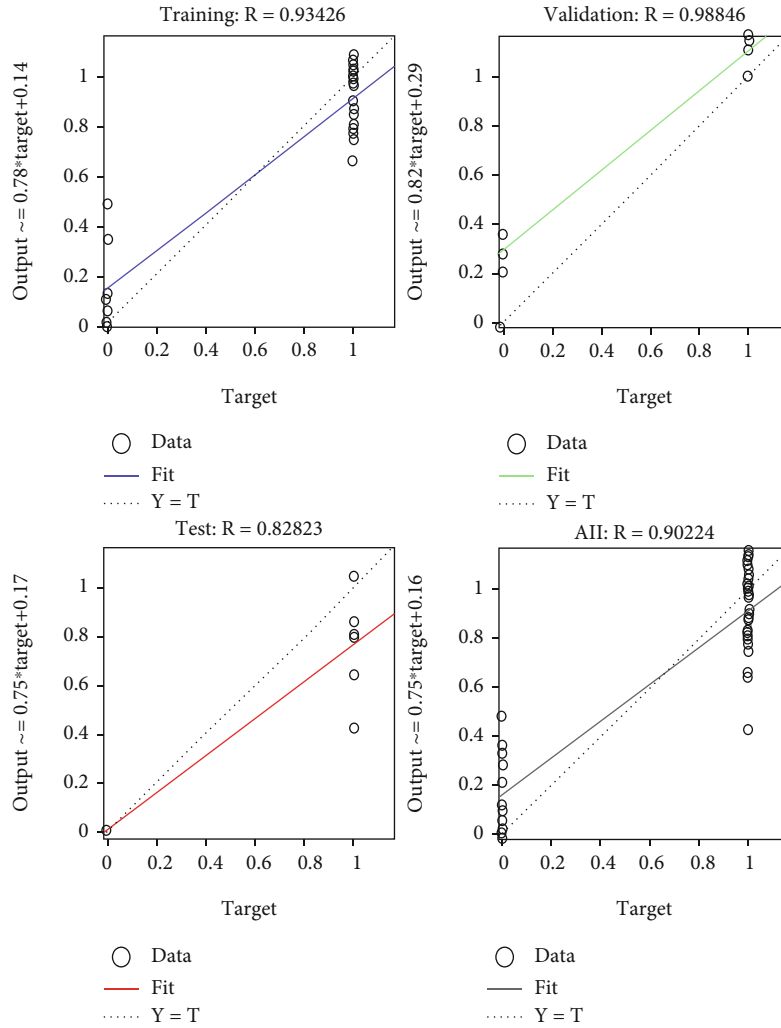


FIGURE 7: Linear regression analysis.

matrix is the identity matrix. It can be seen from Table 4 that the value of KMO test statistic is 0.543, which indicates that the degree of information overlap among the variables is acceptable and can be used for principal component analysis. In Bartlett's sphericity test, the value of significance is 0, which indicates that the hypothesis that each variable is independent is rejected and there is a strong correlation between variables.

Figure 2 is the gravel diagram, and Table 5 shows the explanation of total variance. The horizontal axis of the gravel diagram is the number of each common factor, and the vertical axis represents the size of its characteristic value. The diagram can intuitively get the importance of each common factor. The detailed information of each common factor is listed on the left side of the total variance explanation table, and the information of extracting the common factor is on the right side. It can be seen from Figure 2 and Table 5 that the eigenvalues of the first four common factors are close to or greater than 1, and the sum of the variance percentages reaches 77.7%, that is, the first four common factors can represent eight influencing factors.

Table 6 is the component matrix, and Table 7 shows part of the calculated common factor data. Component matrix, also known as factor load matrix, is the coefficient of the factor expression of each original variable, which expresses the influence degree of the extracted common factor on the original variable. Through the factor load matrix, we can get the linear combination of the original index variables, such as $X_1 = a_{11} \times F_1 + a_{12} \times F_1 + a_{13} \times F_1 + \dots + a_{18} \times F_1$, where X_1 is the common factor data 1. $a_{11} \setminus a_{12} \setminus a_{13} \dots a_{18}$ are the factor loads on the same line as component F_1 . F_1 is the extracted component.

4.3. Construction of BP Neural Network. As shown in Figure 3, this paper uses the MATLAB software to build a neural network model, repeatedly trains and verifies the common factor data, and finally obtains a model that can effectively predict coal-gas compound dynamic disaster.

The MATLAB software includes input layer, hidden layer, and output layer. The common factor data in Table 7 takes the output type of numerical matrix as the input data of BP neural network, and the output type of

TABLE 8: Prediction results of common factor test set of coal-gas compound dynamic disaster.

Number	X_1	X_2	X_3	X_4	Forecast results	Expected results
44	1.399042495	0.785939655	-0.11810208	1.141111803	1	1
45	1.190427325	0.760470516	-0.219058963	1.091743892	1	1
46	2.44822473	-0.227521877	0.287181263	1.03121518	0	0

numerical matrix is taken as the output data of BP neural network in the column of “Disaster or not” in Table 1.

The 32 sets (70%) of data are randomly selected as the training set. The 7 sets (15%) of data are selected as the validation set. The other 7 sets (15%) of data are selected as the test set. For the number of neurons in the hidden layer, formula (9) is used for calculation, $a = 8$. Thus, the prediction model structure is set as a 3-layer 4-10-1 structure.

During the model training, the parameters are set as follows: the maximum number of network training is set to 1000 times, the training accuracy is set to 0.0001, and the learning rate is set to 0.01.

Figure 4 shows the performance of the neural network. The ordinate is the mean square error, and the abscissa is the number of iterations. It can be seen from the figure that after training the neural network using the Levenberg-Marquardt method, the number of iterations of the neural network is very small, and the network training is completed in only 10 steps. And the best verification of the neural network is obtained when the number of iteration steps is 4. The square error value is 0.04572.

Figure 5 shows the visualization of gradient, μ factor, and generalization ability transformation in the network training process. It can be seen from the figure that the actual gradient of the network is 0.036, and the actual value of the damping factor μ in the Levenberg-Marquardt algorithm used by the network is $1e^{-4}$. Validation checks indicate the generalization ability check standard of the network. If the training error cannot be reduced for 6 consecutive times, the training task will be ended.

Figure 6 shows the error histogram. In the figure, the abscissa represents the median of the error interval, and the ordinate represents the number of samples located in the error interval. From this figure, the error between the output value of the neural network and the original target value of the sample can be obtained.

Figure 7 shows the fitting results of the linear regression analysis of the test set, training set, and validation set. From the figure, the regression fitting situation of the data can be obtained. The regression R value measures the correlation between the output and the target. An R value of 1 indicates a close relationship, and 0 indicates a random relationship. The overall R value of the three sets is 0.90224, indicating that the regression fitting effect is good.

4.4. Test of GRA-PCA-BP Model. The last three groups of data are selected to input the model for prediction, testing whether the model constructed in this paper meets the target requirements. The prediction results are shown in Table 8. From the prediction results, it can be seen that the prediction results of GRA-PCA-BP model are completely consis-

tent with the actual situation, which indicates that this method is feasible to predict the risk of coal-gas compound dynamic disaster and has good promotion value in practice.

5. Conclusion

The prediction of coal-gas compound dynamic disaster is of great significance for the safe and efficient mining of coal mine. Firstly, the grey relational analysis method is used to eliminate irrelevant or small influential factors, and then, the principal component analysis method is used to eliminate the multicollinearity between the independent variables. Moreover, the input data dimension is further reduced. Combined with the good prediction effect of BP neural network, the coal-gas compound dynamic disaster prediction model based on GRA-PCA-BP is finally obtained. The model has high prediction accuracy and convenient operation.

Model verification of the disaster case of Pingdingshan No. 8 mine shows that the coal-gas compound dynamic disaster prediction model based on GRA-PCA-BP neural network has high accuracy and practicability, which provides a new method for the disaster prediction of the coal mines with coal-gas compound dynamic disaster risk, and provides a theoretical basis for the safe and efficient mining of coal resources in deep mining areas in China.

To the best of our knowledge, this is the first work using mathematical methods to predict coal-gas compound dynamic disaster. But only relying on the limited data of Pingdingshan No. 8 mine for research, the accuracy still needs to be verified by using more data of the coal mine. Meanwhile, the model used in this article is relatively simple. It is necessary to continue to study more accurate mathematical models to accurately predict coal-gas compound dynamic disaster. This is our focus in the future.

Data Availability

The data used to support the findings of this study are available from the corresponding author upon request.

Additional Points

Bullet Points. (1) The influencing factors of coal-gas compound dynamic disaster were analyzed. (2) A prediction model of coal-gas compound dynamic disaster based on GRA-PCA-BP was established. (3) The prediction model is verified by the case study of Pingdingshan No. 8 coal mine.

Conflicts of Interest

All the authors declare that they have no conflict of interest.

Authors' Contributions

Kai Wang contributed to the formal analysis and writing—original draft. Kangnan Li contributed to the investigation and writing—review and editing. Feng Du contributed to the methodology, investigation, writing—review and editing, and supervision.

Acknowledgments

This research was funded by the National Natural Science Foundation of China (52130409, 52121003, 51874314, and 52004291).

References

- [1] Q. Tu, Y. Cheng, Q. Liu et al., "Investigation of the formation mechanism of coal spallation through the cross-coupling relations of multiple physical processes," *International Journal of Rock Mechanics & Mining Sciences*, vol. 105, pp. 133–144, 2018.
- [2] K. Wang, A. Zhou, J. Zhang, and P. Zhang, "Real-time numerical simulations and experimental research for the propagation characteristics of shock waves and gas flow during coal and gas outburst," *Safety Science*, vol. 50, no. 4, pp. 835–841, 2012.
- [3] H. Xie, Y. Ju, F. Gao, M. Gao, and R. Zhang, "Groundbreaking theoretical and technical conceptualization of fluidized mining of deep underground solid mineral resources," *Tunnelling & Underground Space Technology*, vol. 67, pp. 68–70, 2017.
- [4] K. Wang and F. Du, "Coal-gas compound dynamic disasters in China: a review," *Process Safety and Environmental Protection*, vol. 133, pp. 1–17, 2020.
- [5] C. P. Lu, L. M. Dou, N. Zhang, J. H. Xue, and G. J. Liu, "Microseismic and acoustic emission effect on gas outburst hazard triggered by shock wave: a case study," *Natural Hazards*, vol. 73, no. 3, pp. 1715–1731, 2014.
- [6] F. Du and K. Wang, "Unstable failure of gas-bearing coal-rock combination bodies: insights from physical experiments and numerical simulations," *Process Safety and Environmental Protection*, vol. 129, pp. 264–279, 2019.
- [7] P. Konicek, K. Soucek, L. Stas, and R. Singh, "Long-hole destress blasting for rock-burst control during deep underground coal mining," *International Journal of Rock Mechanics and Mining Sciences*, vol. 61, pp. 141–153, 2013.
- [8] Q. T. Hu, S. T. Zhang, G. C. Wen, L. Dai, and B. Wang, "Coal-like material for coal and gas outburst simulation tests," *International Journal of Rock Mechanics and Mining Sciences*, vol. 74, pp. 151–156, 2015.
- [9] T. Li, M. F. Cai, and M. Cai, "A review of mining-induced seismicity in China," *International Journal of Rock Mechanics and Mining Sciences*, vol. 44, no. 8, pp. 1149–1171, 2007.
- [10] F. Du, K. Wang, X. Zhang, C. Xin, L. Shu, and G. Wang, "Experimental study of coal-gas outburst: insights from coal-rock structure, gas pressure and adsorptivity," *Natural Resources Research*, vol. 29, no. 4, pp. 2481–2493, 2020.
- [11] X. L. Li, S. J. Chen, Z. H. Li, and E. Y. Wang, "Rockburst mechanism in coal rock with structural surface and the microseismic (MS) and electromagnetic radiation (EMR) response," *Engineering Failure Analysis*, vol. 124, no. 6, p. 105396, 2021.
- [12] B. Gao, F. Mi, and R. Zhang, "Research status and prospect of compound dynamic disaster of deep mining in coal mine," *Coal mine safety*, vol. 44, no. 11, pp. 175–178, 2013.
- [13] C. WANG, E. WANG, X. U. Jiankun, X. LIU, and L. LING, "Bayesian discriminant analysis for prediction of coal and gas outbursts and application," *Mining Science and Technology (China)*, vol. 20, no. 4, pp. 520–523, 2010.
- [14] B. Jta, D. Cwc, B. Yca et al., "Determination of critical value of an outburst risk prediction index of working face in a coal roadway based on initial gas emission from a borehole and its application: a case study," *Fuel*, vol. 267, p. 117229, 2020.
- [15] J. Tang, C. Jiang, Y. Chen, X. Li, G. Wang, and D. Yang, "Line prediction technology for forecasting coal and gas outbursts during coal roadway tunneling," *Journal of Natural Gas Science & Engineering*, vol. 34, pp. 412–418, 2016.
- [16] L. Qiu, Z. Liu, E. Wang, X. He, J. Feng, and B. Li, "Early-warning of rock burst in coal mine by low-frequency electromagnetic radiation," *Engineering Geology*, vol. 279, no. 1, p. 105755, 2020.
- [17] C. Zhang, G. Jin, C. Liu et al., "Prediction of rockbursts in a typical island working face of a coal mine through microseismic monitoring technology," *Tunnelling and Underground Space Technology*, vol. 113, p. 103972, 2021.
- [18] X. Li, F. Pan, H. Li, M. Zhao, L. Ding, and W. Zhang, "Prediction of rock-burst-threatened areas in an island coal face and its prevention: a case study," *International Journal of Mining Science and Technology*, vol. 26, no. 6, pp. 1125–1133, 2016.
- [19] Y. Pan, "Integrated study on compound dynamic disaster of coal-gas outburst and rockburst," *Journal of coal industry*, vol. 41, no. 1, pp. 105–112, 2016.
- [20] Y. Luo, Y. Pan, and X. Xiao, "Multi-parameter risk evaluation and graded early warning of mine dynamic disaster," *Chinese Journal of Safety Science*, vol. 23, no. 11, pp. 85–90, 2013.
- [21] R. Yuan, "Features of dynamic disasters combined rockburst and gas outburst in deep coal mine and its preventive measures," *Coal science and technology*, vol. 41, no. 8, pp. 6–10, 2013.
- [22] X. Meng and Y. Zhang, "Temporal evolution of stress field-based drilling method outburst prediction theory and practice. Intelligent Information Technology Application Association," in *Proceedings of 2011 AASRI conference on information technology and economic development (AASRI-ITED 2011 VI). Intelligent Information Technology Application Association: Intelligent information technology application society*, p. 4, Kuala Lumpur, Malaysia, 2011.
- [23] R. Yuan, *Study on the Disaster Mechanism and Prevention Key Technologies of Deep Mine Dynamic Disasters in Pingdingshan Coal Mine*, China University of mining and Technology, 2012.
- [24] F. Jiang, G. Yang, and Q. Wei, "Study and prospect on coal mine composite dynamic disaster real-time prewarning platform," *Journal of coal industry*, vol. 43, no. 2, pp. 333–339, 2018.
- [25] L. Dou, X. He, and R. E. N. Ting, "Mechanism of coal-gas dynamic disasters caused by the superposition of static and dynamic loads and its control technology," *Journal of China University of Mining and Technology*, vol. 47, no. 1, pp. 48–59, 2018.
- [26] S. Jian, W. Lian-guo, Z. Hua-lei, and S. Yi-feng, "Application of fuzzy neural network in predicting the risk of rock burst,"

- Procedia Earth and Planetary Science*, vol. 1, no. 1, pp. 536–543, 2009.
- [27] Y. Li, Y. Yang, and B. Jiang, “Prediction of coal and gas outbursts by a novel model based on multisource information fusion,” *Energy Exploration & Exploitation*, vol. 38, no. 5, article 014459872091307, pp. 1320–1348, 2020.
- [28] S. Wu, Z. Wu, and C. Zhang, “Rock burst prediction probability model based on case analysis,” *Tunnelling and underground space technology*, vol. 93, p. 103069, 2019.
- [29] B. Li, E. Wang, Z. Shang et al., “Deep learning approach to coal and gas outburst recognition employing modified AE and EMR signal from empirical mode decomposition and time-frequency analysis,” *Journal of Natural Gas Science and Engineering*, vol. 90, p. 103942, 2021.
- [30] S. J. Ren, C. P. Wang, Y. Xiao et al., “Thermal properties of coal during low temperature oxidation using a grey correlation method,” *Fuel*, vol. 260, p. 116287, 2020.
- [31] Q. Nian, S. Shi, and R. Li, “Research and application of safety assessment method of gas explosion accident in coal mine based on GRA-ANP-FCE,” *Procedia Engineering*, vol. 45, no. 2, pp. 106–111, 2012.
- [32] X. Yang and W. Li, “Research on coal mine safety accident based on grey relational analysis,” *Innovative Computing and Information*, vol. 231, pp. 101–108, 2011.
- [33] X. Yang and Z. Su, “Prediction of the protein O-glycosylation by kernel principal component analysis and support vector machines,” *Science technology and Engineering*, vol. 13, no. 25, pp. 7371–7376, 2013.
- [34] T. Parhizkar, E. Rafieipour, and A. Parhizkar, “Evaluation and improvement of energy consumption prediction models using principal component analysis based feature reduction,” *Journal of Cleaner Production*, vol. 279, p. 123866, 2021.
- [35] A. Roy, H. Dhawan, S. Upadhyayula, and H. Kodamana, “Insights from principal component analysis applied to Py-GCMS study of Indian coals and their solvent extracted clean coal products,” *International Journal of Coal Science & Technology*, 2021.
- [36] Y. Wu, R. Gao, and J. Yang, “Prediction of coal and gas outburst: a method based on the BP neural network optimized by GASA,” *Process Safety and Environmental Protection*, vol. 133, pp. 64–72, 2020.
- [37] C. Y. Ping, “An incorporate genetic algorithm based back propagation neural network model for coal and gas outburst intensity prediction,” *Procedia Earth and Planetary Science*, vol. 1, no. 1, pp. 1285–1292, 2009.

Research Article

Research on Control Mechanism of Surrounding Rock of Deep Gob-Side Entry Retaining

Jianxiong Liu ¹, Jingke Wu ^{1,2}, Yun Dong ¹, Yanyan Gao ¹, Jihua Zhang ¹,
Weizhong He ¹ and Jiarui Chen ¹

¹Jiangsu Engineering Laboratory of Assembly Technology on Urban and Rural Residence Structure, Huaiyin Institute of Technology, Huai'an, Jiangsu 223003, China

²School of Transportation, Southeast University, Nanjing, Jiangsu 211189, China

Correspondence should be addressed to Jingke Wu; wujingke@hyit.edu.cn

Received 2 August 2021; Accepted 27 September 2021; Published 13 October 2021

Academic Editor: Jia Lin

Copyright © 2021 Jianxiong Liu et al. This is an open access article distributed under the Creative Commons Attribution License, which permits unrestricted use, distribution, and reproduction in any medium, provided the original work is properly cited.

To address the large deformation of the surrounding rock of deep gob-side entry retaining under high stress, lithological characteristics of the surrounding rock and failure model of support body and their evolutionary processes are analyzed through field investigation and theoretical analysis. Failure mechanisms of surrounding rock and the technology to control it are studied systematically. The results show that the causes of the large deformation of the surrounding rock are weak thick mudstones with softening property and water absorption behavior, as well as its fragmentation, dilatancy, and long-term creep during strong disturbance and highly centralized stress states. The cross-section shape of the roadway after deformation and failure of the surrounding rock is obviously asymmetric in both the horizontal and vertical directions. Since the original system supporting the surrounding rock is unable to completely bear the load, each part of the supporting system is destroyed one after the other. The failure sequences of the surrounding rock are as follows: (1) roadway roof fracture in the filling area, (2) filling body fracture under eccentric load, (3) rapid subsidence of the roadway roof, and (4) external crack drum and rib spalling at the solid coal side. Due to this failure sequence, the entire surrounding rock becomes unstable. A partitioned coupling support and a quaternary control technology to support the surrounding rock are proposed, in which the roof of the filling area plays a key role. The technology can improve the overall stability of gob-side entry retaining, prevent support structure instability caused by local failure of the surrounding rock, and ensure the safety and smoothness of roadways.

1. Introduction

The deformation of surrounding rock of gob-side entry roadways in deep and shallow coal mines is very different. The coal-rock mass is in an environment of high ground stress, high geothermal temperature, and high water pressure and experiences multiple strong effects from mining activity [1, 2]. In the deep gob-side entry retaining in the Huainan Mining Group, the strata often behave violently, resulting in severe damage to the surrounding rock. This damage includes the incline and sinking of the broken roof due to insufficient load-bearing capacity of the load-bearing structure, structure fracturing of the filling body, external crack drum and rib spal-

ling of the solid coal side, and serious floor heave. At present, a method of grading gob-side entry retaining is widely adopted by the Huainan Mining Group. However, the surrounding rock is difficult to control, resulting in serious large-scale deformation, which is very unfavorable for the safe construction, ventilation, and reuse of gob-side entry retaining. Therefore, a systematic investigation of the failure mechanism and control method of the surrounding rock in deep gob-side entry retaining is of practical significance for gob-side entry retaining technology in deep mines.

Many studies have been conducted on the failure mechanism, control theory, and technology of surrounding rock in coal mines. Kang et al. [3] proposed design principles

and suggestions for supporting surrounding rock by analyzing the deformation and failure characteristics of gob-side entry retaining of a working face with multiple roadways; Xie et al. [4] presented a new method of roadside support using a concrete-filled steel tubular scaffold by investigating the settlement and failure of surrounding rock structures of gob-side entry retaining with large mining height; Han et al. [5] presented a concept of roadside composite bearing and revealed the stability mechanism of roadside structures. Tan et al. [6] investigated the mechanical relationship between the overlying strata of a gob-side entry retaining and the filling body and proposed a support technology comprising a soft and hard composite layer filling body; Chen et al. [7] clarified the mechanism of roadside support by analyzing the response characteristics between the roadside support and the distribution of the stress field and displacement field in surrounding rock. From a national perspective, the mine has a larger burial depth resulting in strong mine pressure, large deformation, expansion, and poor stability of the deep gob-side entry retaining, which makes it difficult to reuse. It is still necessary to further study the stability of the surrounding rock and supporting technology under conditions of high pressure and large deformation [8–11].

Using gob-side entry retaining of the 12512 working face as the research object, this article systematically analyzes the characteristics of the surrounding rock, the failure characteristics of the supporting structure, and the deformation and failure process of gob-side entry retaining under deep soft rock conditions. This study illustrates the failure mechanism of the surrounding rock and proposes a quaternity control technology and roof partition coupling support to support the surrounding rock, with the filling area's roof playing a key role. This technology is also verified through field engineering to determine whether it provides a good supporting effect.

2. Engineering Condition Analysis

2.1. Geological Conditions. Located in the south of the anticline transition, the eastern area of the coal mine, on the whole, is a south-dipping monoclinic structure with a relatively simple geological structure. The dip angle of the coal seam in the 12512 working face is 3° , the coal seam floor elevation is -821.4– -853.2 m, and the depth is more than 900 m. According to the geological conditions of the mining area, an in situ stress test of the rock in the 12512 working face floor was carried out; the results show that the direction of the maximum horizontal principal stress of the coal seam is approximately east-west and that its magnitude is about 29.1–30.8 MPa; the magnitude of the vertical stress is 23.54 MPa. Figure 1 shows the section of the roadway roof and floor rock layers.

The mineral compositions of the mudstone samples in roadway roof and floor as tested by X-ray diffraction are as follows: 65.3% kaolinite, 14.2% quartz, 10.9% montmorillonite, 5.1% illite, and 4.5% of other minerals. According to the classification criteria of expansive soft rock proposed by academician He Manchao [12], it is determined to be a moderately expansive soft rock; the strength of which is reduced after soaking in water.

Histogram	Lithology	Thickness (m)
	Sandy mudstone	$\frac{1.0\sim 5.3}{3.2}$
	Fine sandstone	$\frac{0.8\sim 9.6}{2.6}$
	Carbon mudstone	$\frac{1.7\sim 10.0}{3.5}$
	Sandy mudstone	$\frac{0.9\sim 6.7}{3.1}$
	11-2 coal	$\frac{0.5\sim 6.9}{2.5}$
	Sandy mudstone	$\frac{1.4\sim 4.2}{4.5}$
	Carbon mudstone	$\frac{0.6\sim 7.2}{3.5}$

FIGURE 1: Strata distributions of roadway roof and floor.

2.2. General Engineering Situation. Figure 2 shows the 12512 working face; the section net width \times net height = 4.8 m \times 2.8 m. For mining, gob-side entry retaining is adopted by the half in situ mode with an opening gap width in the working face end, a filling body width \times height = 2.5 m \times 2.5 m, and a shift distance of 0.6 m toward the roadway with a width of 4.2 m.

- (1) The support parameters of the section track drift: there are 6 anchor bolts of Φ 20 mm \times L2 200 mm in each row of the roadway roof with a yow line space of 850 mm \times 850 mm. A row of anchor cables with Φ 20 mm \times L7 300 mm are vertically arranged between the two rows of anchor bolts in accordance with the “3-3” mode and a yow line space of 1200 mm \times 850 mm. The support parameters of the coal sides: there are 4 anchor bolts in each row with a yow line space of 850 mm \times 850 mm and a metal mesh. Finally, the top slope is sprayed to seal the surrounding rock
- (2) The support parameters of the opening gap in the roadway roof at the working face end: there are 4 anchor bolts in each row with a yow line space of 850 mm \times 850 mm. A Φ 20 mm \times L7 300 mm single anchor cable is vertically arranged between the two rows of anchor bolts, adopting 4 rows of canopy auxiliary support

Utilizing the above supporting parameters, at the first mining stage of the 12512 working face, serious deformation and failure of the surrounding rock occurred in gob-side entry retaining accompanied by the crushing of the shallow surrounding rock and an obvious decrease in the mechanical properties of the surrounding rock.

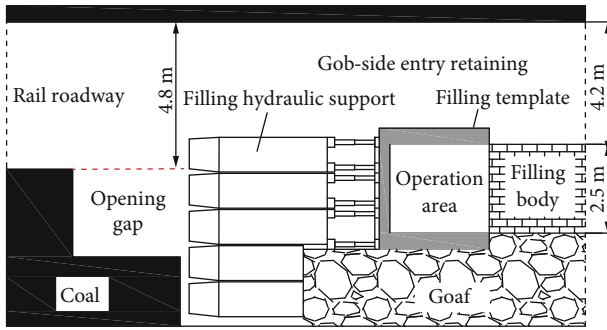


FIGURE 2: Spatial layout of the working face end.

3. Failure Law of the Deep Gob-Side Entry Retaining in High-Stress Soft Rock

3.1. Failure Form of the Surrounding Rock. To fully understand the internal destruction of the surrounding rock, a borehole peeping instrument was used to detect and analyze the damage within the rock. There are 5 boreholes in each section of gob-side entry retaining. Based on the development of borehole fractures, the fractured area and fissure area of the surrounding rock were drawn as shown in Figure 3. As can be seen in the figure, the fracture development degree of the surrounding rock in gob-side entry retaining ranges from large to small as follows: the filling area roof (6.9 m) > the roadway roof (4.0 m) > the roof of the solid coal side (3.8 m) > the upper part of the solid coal side (2.8 m) > the lower part of the solid coal side (2.1 m). Thus, the damage degree of the filling area roof and the upper part of the solid coal side is obviously larger than that of the solid coal side, respectively. Moreover, the overall deformation and failure of the surrounding rock are obviously asymmetric relative to the vertical and horizontal directions of the roadway cross-section.

3.2. Failure Process Analysis of the Surrounding Rock. The activity of the surrounding rock and its deformation characteristics in gob-side entry retaining can be divided into 3 stages, which in chronological order are initial activity, transition period activity, and later stage activity [13–17]. Considering the strong mining impact at the front section of the section track drift, the deformation and failure process of the surrounding rock can be roughly divided into 4 stages. Figure 4 shows the mining period of the leading working face, the early stage of a gob-side entry retaining, the active period of the overlying rock (the deformation and subsidence period of the overlying rock), and the creep period of the surrounding rock; among these, the creep period of the surrounding rock is lengthy and restricted by space resulting in the monitored data only being available in the range within 200 m behind the working face. The deformation and failure of the surrounding rock are as follows:

(1) The mining-affected period of the leading working face (0–100 m ahead of the working face): at 80 m ahead of the working face, the deformation velocity of the surrounding rock increases, especially at the

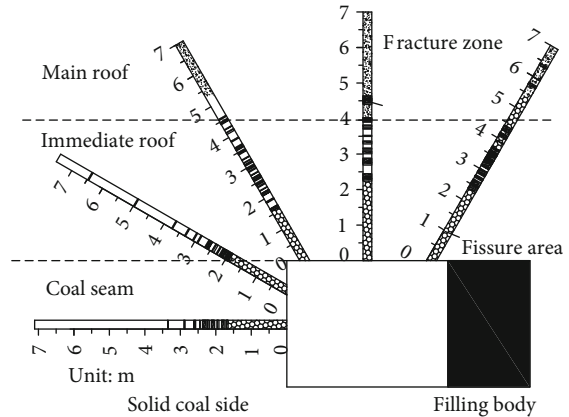


FIGURE 3: Fracture development status of the surrounding rock.

coal side and floor, which show the fastest deformation rate. Together with the effect of the high abutment pressure in the working face and the repeated “jacking and pressing” disturbance of the end hydraulic support in the working face, the mudstone of the filling area’s roof shows shallow fragmentation and deep separation

- (2) The initial stage of gob-side entry retaining (0–50 m behind the working face): with the advancing of the working face, the soft immediate roof at the edge of the goaf loses support and then falls, resulting in a gradual increase in the roof pressure and the stress concentration degree. Due to the influence of the main roof and the vertical stress of the upper strata on the thick soft immediate roof, the stratum at the edge of the goaf first undergoes tensile and shear failure, as well as loose expansion, and then flows in the direction of the goaf. The deformation and failure of the surrounding rock in this stage are mainly manifested as follows: ① The filling area’s roof is in a weak support state and does not form a complete bearing structure with the roadway roof, leading to the rapid subsidence of the roof and a direct pressing on the filling template (see Figure 5(a)). ② The load of the filling area’s roof on the filling body is large and uneven, and together with the low strength of the early filling body and the poor roof connection, it gives rise to the asymmetric fracturing of the weak area on both sides and a decreased width of the main bearing area
- (3) The active period of the overlying strata of gob-side entry retaining (-50–110 m behind the working face): due to the severe activity and higher stress concentration degree of the surrounding rock, the roof, floor, and solid coal side all move at 10–25 mm/d accompanied by a fast deformation speed. The main roof of the stope edge is broken at one side of the solid coal and inclined to the goaf edge, which forces

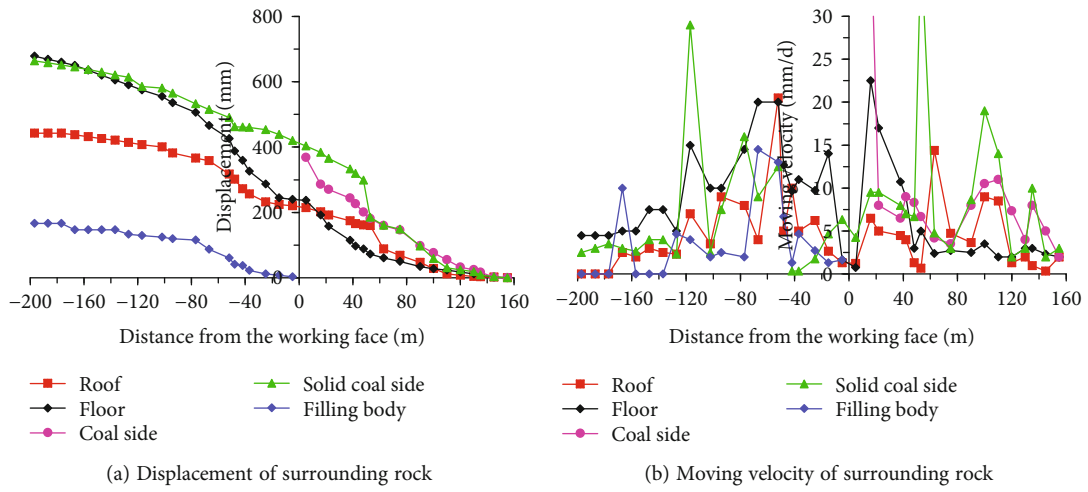


FIGURE 4: Displacement curves of surrounding rock of deep gob-side entry retaining.

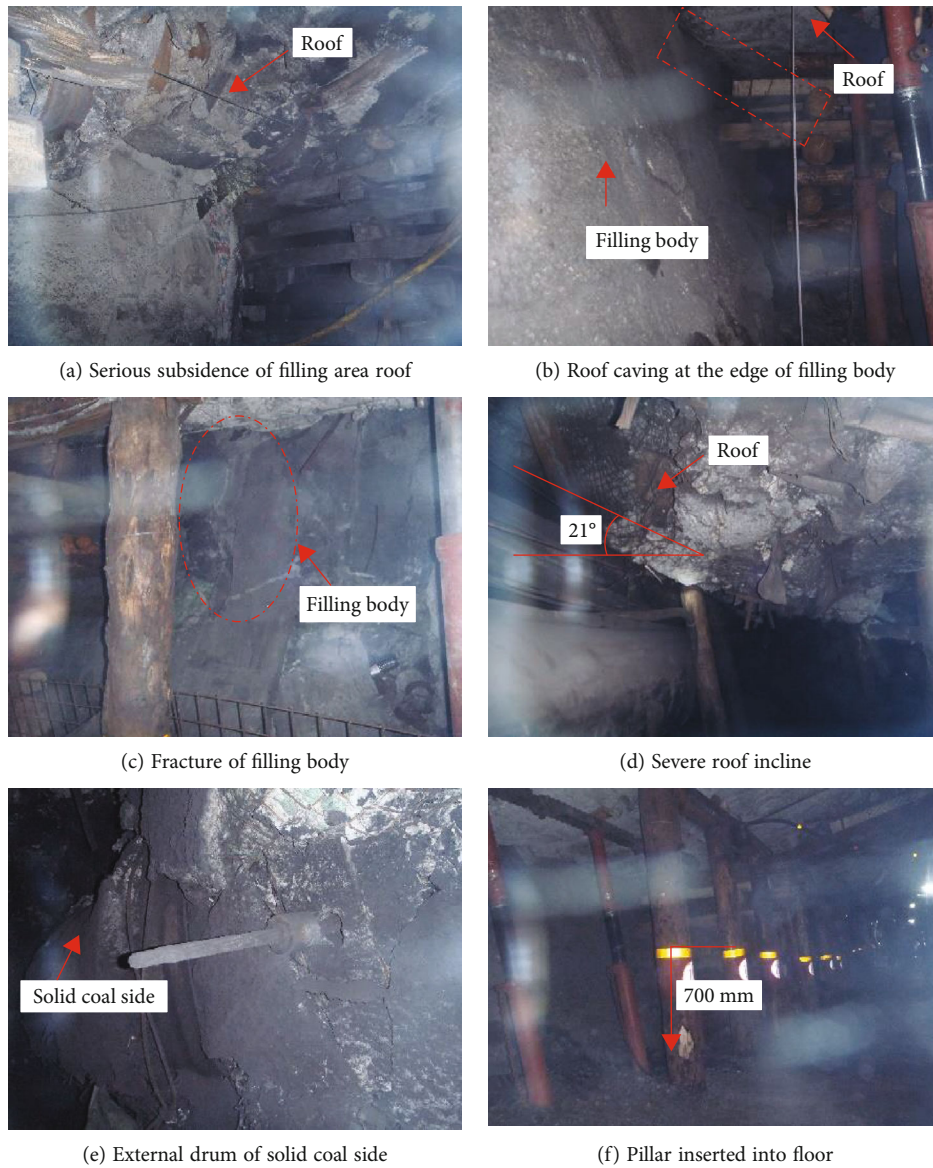


FIGURE 5: Failure status of deep gob-side entry retaining.

the filling body and roof to bear the high abutment pressure that is further transferred to and concentrated at the deeper part of the solid coal seam; this causes a marked expansion of the fracture zone, the fissure zone, and the plastic zone in the surrounding rock. The deformation and failure of the surrounding rock in this stage are mainly manifested by the following: ① The filling area's roof is strongly disturbed and extremely broken, causing roof caving along the filling body (see Figure 5(b)). ② The filling body is inclined and rotated; the crack extending to the filling body makes it unable to reach its designed carrying capacity and destroys its stability ahead of time (see Figure 5(c)). ③ The filling body and its roof are continuously destroyed in the filling area. The load on the anchor bolt (cable) vertically arranged on the roof increases linearly with the inclined subsidence of the roof, the shearing dislocation, and the separation layer, causing more tensile failure of the anchor bolt (cable); the roadway roof shows an unstable state of multizone separation (see Figure 5(d)). ④ In the upper part of the solid coal side, there is an outer drum and even severe spalling (see Figure 5(e)) as well as an overall shift. ⑤ A large amount of water accumulated in gob-side entry retaining leads to the softening expansion of the thick mudstone soaked in water. In addition, the filling body with the heavy load is embedded in the floor, causing serious floor heave (see Figure 5(f))

- (4) The creep period of the surrounding rock (over 200 m behind the working face): the activity of the overlying strata slows down. The stress of the surrounding rock is relatively balanced, but the creep rate is still high, especially in the floor (4.5 mm/d), followed by the solid coal (3.5 mm/d). Before the completion of the working face and the roadway repair, after 11 months or more, the displacement of the roof-floor and the coal sides and the roadway section shrinkage rate can be up to 1211 mm, 743 mm, and 54%, respectively; this does not meet the production requirements of the next working face due to a huge amount of roadway repair works needing to be completed

The deformation and failure of support structures in gob-side entry retaining are uneven, which causes the overall instability of the structure due to the significant deformation and a part failure [18, 19]. Based on the results of field investigations and simulation tests on the deformation and failure of the surrounding rock in gob-side entry retaining (Figure 6), the following conclusions are drawn: the support structure of the surrounding rock is first destroyed at the edge of the goaf and then toward the solid coal side. The evolution process of the deformation and failure of the surrounding rock is roadway excavation → stress state change in the surrounding rock → plastic collapse expansion in the surrounding rock → shallow fissure increase in the surrounding rock → slow creep period of the surrounding rock → restress of overlying strata in the stope edge caused by mining → fracture development in

the filling area's roof → filling body instability under eccentric load or roof cutting at the edge of the filling body → crack increase in the roadway roof in the course of turning and sinking → transfer of high support stress from the roof to the solid coal side → fracture propagation in the solid coal seam → sharp increase in the vertical and horizontal displacements in the solid coal seam leading to rib spalling and outer drum → acceleration unbalance of the roof strata; all this finally causes gob-side entry retaining to become completely unstable.

The above analysis shows that the support system of gob-side entry retaining does not form a complete whole integer and the original supporting system cannot fully mobilize the bearing capacity of the deep surrounding rock, resulting in damage to the support structure one after the other. This is generally manifested in the following 4 aspects: ① The roof support structure exhibits poor integrity and weak bearing capacity. Especially in the filling area, the roof is seriously damaged and unstable, which is the key component to strengthen the support. ② The anchoring depth of the solid coal side is not enough, causing the overall displacement. ③ The filling body has low strength and uneven force. ④ The bare soft thick mudstone floor without the support structure is affected by water.

4. Support Technology of Deep Gob-Side Entry Retaining in High-Stress Soft Rock

Based on the movement characteristics of the surrounding rock in the deep gob-side entry retaining in high-stress soft rock, and considering the initial point and key point of the chain reaction of the deformation and failure of the support structure, a quaternary control technology and roof partition coupling support to support the surrounding rock is proposed, with the filling area's roof playing a key role. This quaternary control technology consists of the roof P_1 with anchor bolt and mesh injection coupling support, solid coal support P_2 with anchor bolt (cable) support, P_3 with high bearing capacity, and roadway auxiliary support P_4 . Among them, the roadway roof P_1 is divided into 3 areas, namely, the filling area roof I zone, the roadway roof II zone, and solid coal side roof III zone. Among these, the filling area roof I zone is the key surrounding rock supporting structure in both the horizontal and vertical directions of gob-side entry retaining. The support structure model of gob-side entry retaining and the quaternary control technology for the surrounding rock are shown in Figure 7.

4.1. Coupling Support in the Roof 3 Zone. The key to successful gob-side entry retaining is to maintain roof integrity. To achieve the best supporting effect requires making all-round plans for the roof 3 partition coupling support. The coupling supporting steps in the roof 3 zone are as follows. The first step is to arrange the cable stayed anchor in the section track drift roof near both the coal sides. The anchor cable end goes deep into the crack-free area of the shoulder corner of the roadway roof, including the deep strata of the I and III zones, which strengthens the support of the roadway shoulder corner to prevent the roof from falling at the edges of the corners of the coal during gob-side entry retaining. The

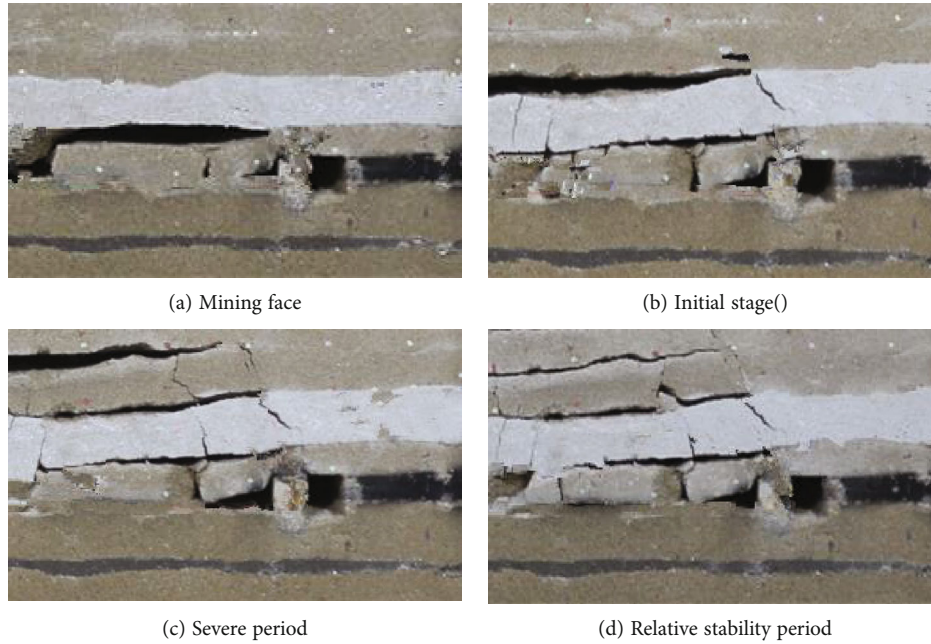


FIGURE 6: Fracture development process of deep gob-side entry retaining.

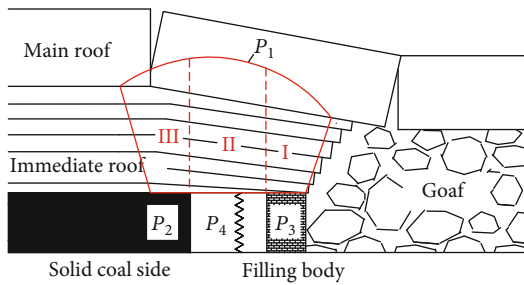


FIGURE 7: The support structure model of gob-side entry retaining.

second step is to provide support at a certain distance ahead of the working face. A hollow grouting anchor rope^[120-21] is arranged in the II zone of the roadway roof to achieve grouting and integration of the bolting and grouting, which will reconsolidate the deep and shallow cracks and the broken strata in the roadway roof, improve the mechanical properties of the coal-rock mass and its bearing capacity, provide a reliable basis for the anchor (cable), improve the stress condition of surrounding rock, and ensure anchor bolt (cable) anchorage reliability. The third step is to utilize the “three high” (high strength, high stiffness, and high pretension) anchor bolts and the large diameter anchor cables to strengthen the working face end to prevent the collapse of the filling area’s roof and provide a good condition for the smooth implementation of the roadside filling. The roof 3 partition coupling support will eventually fix the roof together to prevent its discontinuous deformation, including roof layer separation, dislocation, crack opening, and new crack generation; this will also ensure roof leveling.

4.2. Reinforcement of the Solid Coal Side. Strong support can not only improve the vertical bearing capacity of the roof but also restrain floor heave [22–24]. The formation of the serious outer drum is attributed to the insufficiently effective anchor length of the anchor bolt, which leads to the entire displacement of the bolt-grouting body. From the section track drift to gob-side entry retaining, a fracture zone, plastic zone, and elastic zone have formed on the solid coal side from the outside to the inside. To maintain stability, the anchorage range should be greater than the sum of width of the broken zone and the plastic zone, which is the limit equilibrium area width x_0 that is calculated by the following equation [25]:

$$x_0 = \frac{MA}{2 \tan \varphi_0} \ln \left(\frac{k\gamma H + (c_0/\tan \varphi_0)}{(c_0/\tan \varphi_0) + (p_x/A)} \right), \quad (1)$$

where M is the mining height with a value of 2.50 m, A is the lateral pressure coefficient with a value of 0.42, H is the mining depth with a value of 820 m, φ_0 is the coal-rock interface internal friction angle with a value of 30° , c_0 is the cohesion of the coal-rock interface with a value of 0.34 MPa, k is the maximum stress concentration factor with a value of 2.7, γ is the overburden average value with a value of 22 kN/m^3 , and p_x is the support strength of the solid coal side with a value of 0.21 MPa. These values are based on engineering experience and the designed quantity and pretightening force of the bolt (cable) per unit area of the coal side.

According to the formula, the limit equilibrium area width of the solid coal side is 3.54 m. Because of the soft coal body, the anchor bolt is designed to enter more than 2.30 m into the elastic zone, and the anchor cable length for the solid coal body is finally determined to be 7.30 m.

4.3. *Optimization of Bearing Capacity of Filling Body.* The vertical bearing capacity and deformation capacity of the filling body should match the support mode and strength of the roof-floor; this makes the filling body match the roof-floor movement and fully provide its packing effect. Improving the bearing capacity of the filling body is mainly achieved in the following 3 ways:

- (1) Select filling materials that in the early stage have rapid solidification and high strength: paste material, which is mainly composed of silicate, fly ash, sand, water, and additives, is used in gob-side entry retaining because of its advantages of being extensive, low cost, high strength, and so on

To verify the bearing performance of the filling body, the strength of the paste filling material was tested. 4 groups of specimens were directly sampled and manufactured in the roadside filling field. There are 3 specimens with a length of 150 mm, a width of 150 mm, and a height of 150 mm in each group. The change in the uniaxial compressive strength of the specimens with time as measured in the laboratory is shown in Table 1. The values in the table indicate that the strength of the filling material can meet the relevant regulations.

- (2) The reasonable reinforcement of reinforced skeleton in the filling body: for a large volume of a filling body, the uniaxial compressive strength of filling body is much lower than the uniaxial compressive strength. Moreover, during the interaction with the overlying strata, the filling body is unevenly subjected to both the vertical and horizontal forces. To increase the compressive strength and shear strength of the filling body and prevent the filling body from slipping to the goaf, a reinforcing steel skeleton should be preset in the filling body
- (3) The optimization of construction technology: when filling work is carried out beside a section track drift, the filling body should be fully connected to the roof so that the load can be uniformly borne; the contact floor area of the filling body should be increased to prevent the filling body from getting embedded in the thick mudstone of the roadway floor; the filling body should also be connected to the roof-floor to form a composite bearing structure of "roof-filling body-floor" to avoid the slippage or rotation of the filling body

4.4. *Auxiliary Strengthening Support.* During the violent activity of overlying strata, the roof pressure is high and the support structure is still unable to maintain the stability of the roadway. Therefore, it is necessary to make use of auxiliary strengthening support to brace the roof, assist the filling body to bear the load, and restrain the floor deformation. The auxiliary support in a roadway is mainly composed of a single hydraulic prop+ π type steel beam+high strength and large postbase, which can ensure an initial large support force at the beginning of mining. Because of the deformation of the roof-floor, the load on the single hydraulic prop

TABLE 1: Strength tests of filling material.

Days (d)	Compressive strength value (MPa)
1	4~7
3	10~15
7	15~20
28	29~33

increases; the hydraulic prop can restrain roof separation and floor heave in time by yield and additional resistance limiting its deformation to finally achieve the double control of the roof and floor.

5. Support Scheme Optimization and Control Effect Analysis

5.1. *Optimization of the Supporting Scheme.* Considering the field conditions, a quaternary control technology for deep gob-side entry retaining is optimized reasonably. The optimized support scheme is shown in Figure 8.

- (1) The coupling support on the roof 3 zone: a group of large diameter anchor cables with $\Phi 20 \text{ mm} \times L7 300 \text{ mm}$ and 16[#] channel beam with a length of 3000 mm and a hole distance of 850 mm are arranged on both sides of the section track drift roof. At 110 m ahead of the working face, a hollow grouting anchor cable with $\Phi 20 \text{ mm} \times L7 300 \text{ mm}$ and high-strength tray are added to each row of the anchor beam end on the roof via the step-by-step arrangement method, and spray grouting operations are performed to reinforce the roof
- (2) The reinforcement of the solid coal side: three $\Phi 20 \text{ mm} \times L7 300 \text{ mm}$ anchor cables equipped with 20[#] channel steel are arranged along the roadway; these three cables are 400 mm, 1200 mm, and 2000 mm away from the roof
- (3) The reinforcement of the opening gap roof at the working face end: there are four $\Phi 20 \text{ mm} \times L2 200 \text{ mm}$ "three high" bolts equipped with M5 steel belts in each row; the pretightening force is 60~80 kN, and the yow line space is 850 mm \times 850 mm; then, an anchor cable with $\Phi 20 \text{ mm} \times L7 300 \text{ mm}$ and high-strength tray are arranged between the two rows of bolts. The pretightening force is 80~100 kN, and the array pitch is 850 mm; two rows of anchor cables with 16[#] channel are arranged along the tunnel direction layout, and the hole distance is 1200 mm
- (4) The bearing performance optimization of the filling body: when the special paste filling material is selected, the water-cement ratio should be strictly controlled to ensure that the material strength is up to standard. Three-dimensional reinforcing steel bars are preset in the formwork before roadside filling, and the reinforcing ribs are replaced by $\Phi 20 \text{ mm} \times L2 200 \text{ mm}$ bolts, with $\Phi 6 \text{ mm}$ grid bars

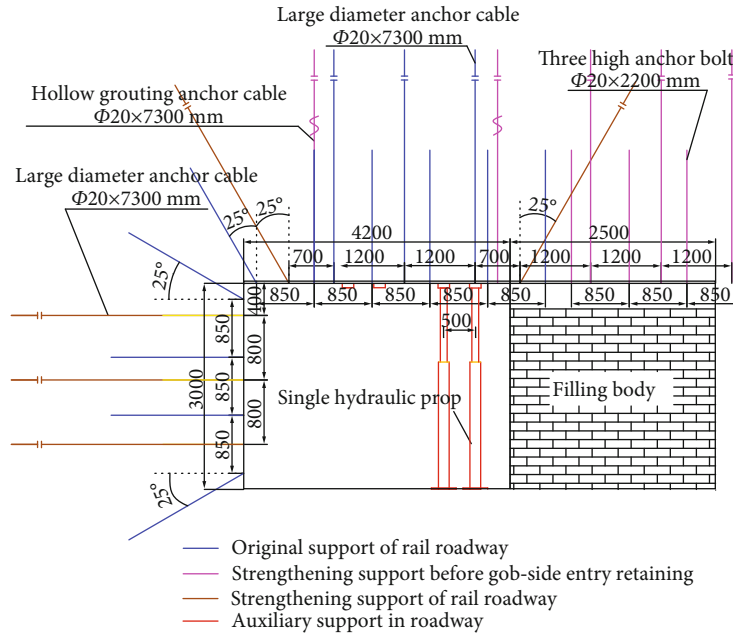


FIGURE 8: Support scheme of deep gob-side entry retaining.

which mutually butt to form a three-dimensional framework; here, the upper anchor bolts and lower anchor bolts of the vertical 3D stiffener are fixed inside the roof and floor, respectively. In addition, a 4000 mm long I-beam is placed under the filling body with a spacing of 800 mm, which increases the contact area and prevents the filling body from cutting into the thick mudstone of the floor

- (5) The auxiliary strengthening support in the roadway: the auxiliary reinforcement in the roadway is arranged close to the filling body layout by setting one single hydraulic prop with an $11^{\#}\pi$ type steel beam and $300\text{ mm} \times 300\text{ mm} \times 10\text{ mm}$ postbase with high strength and large postbase along the roadway. There are 2 single hydraulic props in each section and two sides near the filling body and the roadway center; this is an asymmetric support state with an initial bearing capacity not less than 100 kN

5.2. Control Effect of the Surrounding Rock. After adopting this scheme, five sets of displacement measuring stations were installed in the surrounding rock of gob-side entry retaining of the 12512 working face, and these were used to monitor the deformation of the surrounding rock at different distances behind the working face. The displacement curve of the surrounding rock along gob-side entry retaining was shown in Figure 9.

After gob-side entry retaining in the range of 250 m behind the working face experienced strong dynamic pressure, the displacement of the filling body, the solid coal, and the roof was 40 mm, 294 mm, and 152 mm, respectively. The floor heave was 351 mm. The filling body and roof were basically stable, and the displacement of solid coal and floor

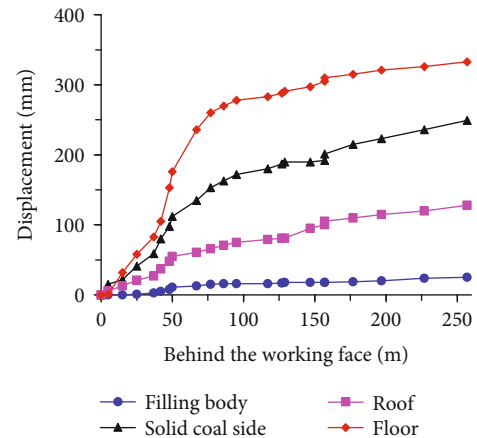


FIGURE 9: Periodical deformation curves of gob-side entry retaining.

increases slowly. The roadway cross-section can meet the requirements of gob-side entry retaining at different stages.

For the record, in this paper, a new support method is proposed for gob-side entry retaining in soft rock with high stress. The deformation of the surrounding rock is effectively controlled to a certain extent, which is beneficial for the safe reuse of the next working face. However, more simple, economic, and effective methods are needed to continually improve the supporting technology and reduce the cost.

6. Conclusion

- (1) The large deformation of the deep gob-side entry retaining in soft rock with high stress is mainly attributed to the low uniaxial compressive strength,

softening and swelling of thick mudstone under the influence of water, cataclastic dilatancy, and long-term creep under strong mining activity and high-stress states; through verifying the failure characteristics of shallow and deep surrounding rock, the overall deformation and failure are obviously asymmetrical relative to the vertical and horizontal directions of the cross-section of the roadway

- (2) By analyzing the deformation and failure characteristics of the deep gob-side entry retaining in soft rock with high stress and the failure mechanism of the surrounding rock, it is found that the original supporting system of gob-side entry retaining is not sufficient, leading to the supporting system getting destroyed one by one. The surrounding rock first starts from the filling area's roof, resulting in an eccentric loading fracturing of the filling body. Then, the roadway roof begins to incline and sink steeply due to the external drum and rib spalling at the solid coal side and severe floor heave, which eventually leads to the instability of the surrounding rock
- (3) The gob-side entry retaining roof is divided into three zones for coupling support. A quaternary control technology for controlling surrounding rock is proposed with the filling area's roof as the key factor. This technology mainly includes the roof with anchor bolt mesh grouting coupling support, solid coal with anchor bolt (cable) support, roadside filling body with high bearing performance, and auxiliary strengthening support in the roadway during the mining stress adjustment period. The technology has been applied to gob-side entry retaining of the 12512 working face and has achieved good results and satisfied the ventilation demand of gob-side entry retaining at different stages

Data Availability

All data used to support the findings of this study are included within the article. There is not any restriction on data access.

Conflicts of Interest

The authors declare no conflicts of interests.

Acknowledgments

This research was financially supported by the Jiangsu University Blue Project Talent Project, the Huaishang Talent Plan Project, the National Natural Science Foundation of China (Nos. 51804129, 51904112, and 51904113), the General Program of China Postdoctoral Science Foundation (No. 2020M671301), the Postdoctoral Science Foundation of Jiangsu Province (No. 2019K139), the Open Project of Jiangsu Engineering Laboratory of Assembly Technology on Urban and Rural Residence Structure (No. JSZP201902), the Industry Education Research Cooperation Projects in

Jiangsu Province (No. BY2020007), and the Natural Science Foundation of Jiangsu Higher Education Institutions (No. 20KJB440002).

References

- [1] Z. Wu, W. Z. Li, F.-q. Gao, Z.-y. Jiang, and J.-z. Li, "Roadway soft coal control technology by means of grouting bolts with high pressure-shotcreting in synergy in more than 1 000 m deep coal mines," *Journal of China Coal Society*, vol. 46, no. 3, pp. 747–762, 2021.
- [2] X.-g. Zheng, T.-l. An, G. Yu, C. C. Liu, and C. Cheng, "Surrounding rock control mechanism and engineering application of in-situ coal pillar in gob-side entry retaining," *Journal of China University of Mining & Technology*, vol. 35, no. 6, pp. 1091–1098, 2018.
- [3] H. P. Kang, L. X. Yan, X. P. Guo, Z. T. Zhang, and F. Q. Gao, "Characteristics of surrounding rock deformation and reinforcement technology of retained entry in working face with multi-entry layout," *Chinese Journal of Rock Mechanics and Engineering*, vol. 31, no. 10, pp. 2022–2036, 2012.
- [4] S.-r. Xie, Q. Zhang, and D.-d. Chen, "Research and application of asymmetric anchorage deep beam bearing structure model in gob-side entry retaining roof," *Journal of Mining & Safety Engineering*, vol. 37, no. 2, pp. 298–310, 2020.
- [5] C.-l. Han, N. Zhang, B.-y. Li, G.-y. Si, and X.-g. Zheng, "Pressure relief and structure stability mechanism of hard roof for gob-side entry retaining," *Chinese Journal of Geotechnical Engineering*, vol. 22, pp. 4445–4455, 2015.
- [6] Y. L. Tan, F. H. Yu, J. G. Ning, and T. B. Zhao, "Adaptability theory of roadside support in gob-side entry retaining and its supporting design," *Journal of China Coal Society*, vol. 41, no. 2, pp. 376–382, 2016.
- [7] Y. Chen, J. B. Bai, T. L. Zhu, S. Yan, S. H. Zhao, and X. C. Li, "Mechanisms of roadside support in gob-side entry retaining and its application," *Rock and Soil Mechanics*, vol. 33, no. 5, pp. 1427–1432, 2012.
- [8] F. P. Schumacher and E. Kim, "Evaluation of directional drilling implication of double layered pipe umbrella system for the coal mine roof support with composite material and beam element methods using FLAC 3D," *Journal of Mining Science*, vol. 50, no. 2, pp. 335–348, 2014.
- [9] W. Cai, Z. Chang, D. Zhang, X. Wang, W. Cao, and Y. Zhou, "Roof filling control technology and application to mine roadway damage in small pit goaf," *International Journal of Mining Science and Technology*, vol. 29, no. 3, pp. 477–482, 2019.
- [10] X. Guo, Z. Zhao, X. Gao, X. Wu, and N. Ma, "Analytical solutions for characteristic radii of circular roadway surrounding rock plastic zone and their application," *International Journal of Mining Science and Technology*, vol. 29, no. 2, pp. 263–272, 2019.
- [11] Y. Li, M. Lei, H. Wang et al., "Abutment pressure distribution for longwall face mining through abandoned roadways," *International Journal of Mining Science and Technology*, vol. 29, no. 1, pp. 59–64, 2019.
- [12] E. Karampinos, J. Hadjigeorgiou, J. Hazzard, and P. Turcotte, "Discrete element modelling of the buckling phenomenon in deep hard rock mines," *International Journal of Rock Mechanics and Mining Sciences*, vol. 80, pp. 346–356, 2015.
- [13] M. R. Zareifard and A. Fahimifar, "Analytical solutions for the stresses and deformations of deep tunnels in an elastic-brittle-

- plastic rock mass considering the damaged zone,” *Tunnelling and Underground Space Technology*, vol. 58, pp. 186–196, 2016.
- [14] J.-k. Wu, Y. Dong, J. Chen et al., “Short cantilever rock beam structure and mechanism of gob-side entry retaining roof in reuse period,” *Shock and Vibration*, vol. 2020, Article ID 8835820, 14 pages, 2020.
- [15] S. Ji, J. Zhang, R. Pan, and J. Karlovšek, “Local acceleration monitoring and its application in physical modelling of underground mining,” *International Journal of Rock Mechanics and Mining Sciences*, vol. 128, no. 6, p. 104282, 2020.
- [16] X. Sun, C. Zhao, Y. Zhang, F. Chen, S. Zhang, and K. Zhang, “Physical model test and numerical simulation on the failure mechanism of the roadway in layered soft rocks,” *International Journal of Mining Science and Technology*, vol. 31, no. 2, pp. 291–302, 2021.
- [17] H. Jing, J. Wu, Q. Yin, and K. Wang, “Deformation and failure characteristics of anchorage structure of surrounding rock in deep roadway,” *International Journal of Mining Science and Technology*, vol. 30, no. 5, pp. 593–604, 2020.
- [18] J. Wu, Y. Dong, Y. Jiang et al., “Research on plastic zone evolution law of surrounding rock of gob-side entry retaining under typical roof conditions in deep mine,” *Shock and Vibration*, vol. 2020, Article ID 8864991, 13 pages, 2020.
- [19] S. Renliang, X. Kong, Z. T. Wei, M. Li, S. Yang, and L. Tian, “Theory and application of strong support for coal roadway sidewall,” *Chinese Journal of Rock Mechanics and Engineering*, vol. 32, no. 7, pp. 1304–1313, 2013.
- [20] G.-c. Zhang, F.-l. He, H.-g. Jia, and Y.-h. Lai, “Analysis of gate-road stability in relation to yield pillar size: A case study,” *Rock Mechanics and Rock Engineering*, vol. 50, no. 5, pp. 1263–1278, 2017.
- [21] Y.-q. Zhao, F.-l. He, and J.-k. Wu, “A new cable-truss structure for roadway driving next to goaf,” *Geotechnical and Geological Engineering*, vol. 37, no. 1, pp. 389–400, 2019.
- [22] J. Hadjigeorgiou and E. Karampinos, “Use of predictive numerical models in exploring new reinforcement options for mining drives,” *Tunnelling and Underground Space Technology*, vol. 67, pp. 27–38, 2017.
- [23] P. Konicek, K. Soucek, L. Stas, and R. Singh, “Long-hole destress blasting for rockburst control during deep underground coal mining,” *International Journal of Rock Mechanics and Mining Sciences*, vol. 61, pp. 141–153, 2013.
- [24] G.-c. Zhang, Z.-j. Wen, S.-j. Liang et al., “Ground response of a gob-side entry in a longwall panel extracting 17 m-thick coal seam: a case study,” *Rock Mechanics and Rock Engineering*, vol. 53, no. 2, pp. 497–516, 2020.
- [25] J. B. Bai, H. Q. Zhou, and C. J. Hou, “Development of support technology beside roadway in gob-side entry retaining for next sublevel,” *China University of Mining and Technology*, vol. 33, no. 2, pp. 183–186, 2004.

Research Article

Gas Jet Coal-Breaking Behavior: An Elliptical Crushing Theoretical Model

Gongda Wang,^{1,2} Yuanyuan Wang^{1,2} , Xin Yang,^{1,2} and Xin Song^{1,2}

¹School of Civil and Resources Engineering, University of Science and Technology Beijing, Beijing 100083, China

²State Key Laboratory of the Ministry of Education of China for High-Efficiency Mining and Safety of Metal Mines, University of Science and Technology Beijing, Beijing 100083, China

Correspondence should be addressed to Yuanyuan Wang; g20198146@xs.ustb.edu.cn

Received 26 July 2021; Revised 20 August 2021; Accepted 21 September 2021; Published 12 October 2021

Academic Editor: Afshin Davarpanah

Copyright © 2021 Gongda Wang et al. This is an open access article distributed under the Creative Commons Attribution License, which permits unrestricted use, distribution, and reproduction in any medium, provided the original work is properly cited.

Coalbed methane (CBM) is a source of clean energy and has been recovered in past decades all over the world. Gas dynamic disaster is the primary disaster in outburst coal, and methane drainage plays a key role in eliminating this danger. As an efficient technology, a gas jet is widely used in CBM development and methane drainage. In this work, the full impinging process of coal and rock fracturing by a supersonic gas jet was studied. To understand how jet parameters affect coal and rock fracturing results, an elliptical crushing theoretical model was proposed. In addition, a laboratory experiment was designed to examine the proposed model, and four key parameters affecting the fracturing results were studied. The results show that different from the monotonic variation of theoretical values, there is a turning point in the variation of experimental values under some parameters. Considering the influence of the depth and radius of the erosion pit, the rock-breaking effect is better when the nozzle size is 2.75 Ma. The optimal target distance is 30 mm, and the impact pressure of a gas jet should be continuously increased in order to achieve certain rock-breaking effects under the impact of the jet.

1. Introduction

Coalbed methane (CBM) is a source of clean energy and has been recovered in past decades all over the world [1–4]. In terms of coal mining, methane is the primary cause of mine disasters especially for outburst mines [5–7]. Therefore, methane drainage plays a key role in eliminating gas outbursts. To enhance CBM recovery or drainage efficiency, water jet technology has been proposed and has been proven effective [8–12]. However, in the low permeability soft coal seams, the use of water jet technology frequently leads to the collapse of a borehole and the inhabitation of the gas desorption [13–16]. Due to the fact that the use of a gas jet for the fracture of coal can effectively avoid these problems, more and more attention has been paid to gas jet technology.

Gas jet technology is widely used in the fields of glass cutting, hole drilling, and cooling [17–19]. Komori et al. [20] proposed a supersonic gas jet technology based on the Laval nozzle. Frendi and Brown [21] studied the flow structures from a supersonic impinging jet and indicated a strong

interaction between the acoustic waves emanating from the impingement plate and the jet plume. Due to the high impact force of a high-pressure gas jet, it has been extended to the fracture of coal and rock in recent years. Kutter and Fairhurst [22] carried out the research of high-pressure gas punching fracture earlier, and they proposed that the pressure distribution along the normal direction of a rock fracture can be produced in the rock when high-pressure gas impacts rock materials. Hagan [23] proposed the “gas wedge effect” by comparing the action form of high-pressure gas with the mechanism of a water jet. On the basis of previous studies, Nilson et al. [24] established a model of high-pressure gas punching fracture. Eslamian et al. [25] studied the crushing effect of a supersonic gas jet on a cylindrical brittle gypsum deposit. It was found that both jet angle and sediment hardness can affect the crushing efficiency. Liu et al. [26–29] proposed a high-pressure abrasive gas jet technology for coal breakage and systematically investigated the stress wave effect, the wear mechanism of abrasive air jet erosion, and the effects of nozzle pressure ratios on the

pulsation frequency of air jets. Ranjith et al. [30] studied the effect of mass flow on the abrasive acceleration of gas jets. They found that pressure is also important. When the mass flow increases, the abrasive acceleration distance and time decrease.

Previous studies mainly focused on optimizing the nozzle structure and jet parameters to improve the efficiency of fracturing coal and rock [25, 28]. However, high-pressure gas jet coal breaking is a continuous and comprehensive process including the transportation of high-pressure gas in the pipeline, the free development of high-pressure gas in the air medium, and the final coal breaking. Researchers mainly focused on the stage of final coal breaking by jet punching, and the study on the whole continuous process of gas jet impinging coal and rock is relatively rare. Moreover, as for the research on the damage characteristics of a high-pressure gas jet, there is lack of the corresponding criterion for coal breaking by a gas jet. Therefore, in this work, the full process of a high-pressure gas jet was systematically considered, and a mathematical model was proposed. The supersonic air jet impinging laboratory experiment was designed to examine the proposed model and four key parameters affecting the fracturing results were tested, including jet pressure, target distance, nozzle size, and strength of coal and rock. This study is intended to enrich the theories of gas jet coal breaking, providing some guidance for the development of CBM and the prevention of mine gas disasters.

2. Mathematical Model of the Full Impinging Progress of a Supersonic Gas Jet

As for a full impinging system, considering the risk of high-pressure gas, the air compressor and high-pressure gas storage tank were placed in an underground chamber, and then the high-pressure air reaches the nozzle through the pipeline to fracture the coal and rock. The system is shown in Figure 1. The introduction of the mathematical model of the full impinging progress of a supersonic gas jet follows.

2.1. Flow Model of High-Pressure Gas in a Pipeline. The viscosity of gas shall be considered in the mechanical energy balance formula of pipeline calculation gas, that is, there shall be resistance loss term h_f in the formula:

$$gz_1 + \frac{u_1^2}{2} + \int_{p_1}^{p_2} \frac{dp}{\rho} = gz_2 + \frac{u_2^2}{2} + h_f. \quad (1)$$

When the gas flows in the pipeline, the volume flow rate and average flow rate change along the length of the pipe, and the resistance loss per unit length of the pipe must also change along the length of the pipe. Formula (1) above is changed to the differential form below:

$$gdz + d\frac{u^2}{2} + vdp + \lambda \frac{(dl)}{d} \times \frac{u^2}{2} = 0, \quad (2)$$

where $v = (1/\rho) = (RT/Mp)$ is the specific volume of gas

(m^3/kg), L is the pipe length (m), d is the pipe diameter (m), friction coefficient λ is a function of Re and ε/d , and we have

$$\text{Re} = \frac{du\rho}{\mu} = \frac{dG}{\mu}. \quad (3)$$

In the case of equal pipe diameter transportation, since the mass flow rate G is a constant along the pipe length, Re is only related to the temperature of the gas. Therefore, λ can be regarded as a constant along the length of the tube for the flow process with little change in isothermal flow or temperature:

$$G = \frac{q_m}{A}, \quad (4)$$

where q_m is the mass flow (kg/S), A is the cross-sectional area of the pipe (m^2):

$$u = \frac{G}{\rho} = Gv. \quad (5)$$

For isothermal flow, p^*v is equal to the constant. And substituting equation (5) into equation (2), we can get

$$G^2 \ln \frac{p_1}{p_2} + \frac{p_2^2 - p_1^2}{(2RT/M)} + \lambda \frac{l}{2d} G^2 = 0. \quad (6)$$

If the pressure drop Δp in the tube is very small, the kinetic energy difference of the first term in equation (6) can be ignored. In this case, equation (6) is the special form of the energy equation of the incompressible fluid to the horizontal tube. For the transportation of high-pressure gas, $(p_1 - p_2)/p_2$ is smaller and can be treated as an incompressible fluid. After finishing formula (6), we can conclude the following:

$$(p_2^2 - p_1^2) \frac{M}{2RT} + \lambda \frac{l}{2d} G^2 = 0. \quad (7)$$

Under the condition of known T , pipeline parameters, pipeline outlet pressure p_2 (equal to nozzle inlet pressure), and the pressure p_1 at the pipeline inlet can be obtained. Therefore, p_2 can be achieved by adjusting p_1 to supply high-pressure gas remotely.

2.2. Mathematical Model of Continuous Process and Criterion of Coal Breaking by Jet. The jet is accelerated through the nozzle, improving the transition from subsonic to supersonic in the throat. Then, the gas jet is ejected from the nozzle into the environmental medium. Finally, the supersonic jet impinges on the coal wall and forms an erosion pit on the target surface. This process can be divided into three parts: the acceleration of the gas jet, the development of the gas jet, and the impact of the gas jet.

2.2.1. Mathematical Model of Acceleration Stage. The nozzle is the key factor affecting jet velocity. The straight or conical

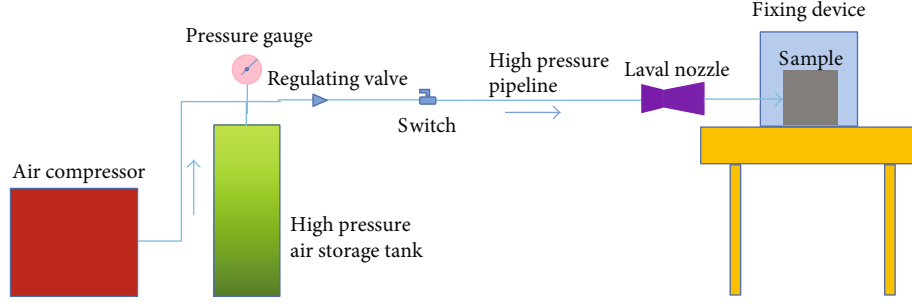


FIGURE 1: Schematic diagram of full impinging system.

convergent nozzles are generally used in traditional gas jet technology, and the highest speed that a gas jet can reach is sonic. In order to improve the working efficiency, the common conical contraction nozzle is often used in engineering applications. After the high-pressure gas flows through the contraction nozzle, the maximum can only reach one Mach number, which is equivalent to the sound velocity flow of local air. Under the same external parameters, the Laval nozzle can achieve speeds several times the sound velocity. The nozzle is usually composed of a convergence section, a throat part, and an expansion section. Its structure is shown in Figure 2.

The aerodynamics theory indicates that when the high-pressure gas flows through the nozzle with known parameters, the gas state after acceleration depends on the nozzle parameters, inlet air pressure, temperature, and outlet external back pressure. When the ratio of a nozzle area to the throat area is determined, the Mach number after the acceleration can be obtained from the following formula [31]:

$$\frac{S}{S_e} = \frac{1}{\text{Ma}} \left[\left(1 + \frac{k-1}{2} \text{Ma}^2 \right) \times \left(\frac{2}{k+1} \right) \right]^{(k+1/2)(k-1)}. \quad (8)$$

In order to simplify the complexity of the problem, an imaginary reference state is introduced in the study of aerodynamics. The state where the velocity of air decreases to zero after the absolute energy isentropic process from a real state is called the stagnation state corresponding to the real state. In the stagnation state, it is assumed that the flow process of high-pressure gas in the nozzle is a one-dimensional steady isentropic adiabatic flow. There is no heat and work exchange between the gas in the flow and the outside world. No flow is added or drawn out, and the friction between the high-pressure gas and the nozzle wall is ignored. For the Laval nozzle, the supersonic flow in the nozzle can be expressed by the flow parameters in the stagnation state:

$$\begin{cases} \frac{P^*}{P} = \left(1 + \frac{k-1}{2} \text{Ma}^2 \right)^{(k/k-1)}, \\ \frac{\rho^*}{\rho} = \left(1 + \frac{k-1}{2} \text{Ma}^2 \right)^{(k/(k-1))}, \\ \frac{T^*}{T} = 1 + \frac{k-1}{2} \text{Ma}^2, \end{cases} \quad (9)$$

where P is the gas pressure, P^* is the gas pressure under stagnation state, ρ^* is the gas density under the stagnation state, ρ is the gas density, T is the gas thermodynamic temperature, T^* is the gas thermodynamic temperature under the stagnation state, and Ma is the Mach number, which means

$$\text{Ma} = \frac{V}{a}, \quad (10)$$

where a is the corresponding local air sound velocity in this state, which can be obtained from $a = \sqrt{kRT}$; R is the gas constant, and the value for air is $287.06 \text{ J}/(\text{kg}\cdot\text{K})$; T is the gas thermodynamic temperature.

According to formulas (8) to (10), the flow velocity at the nozzle exit section can be obtained from formula (11) combining the total pressure at the nozzle inlet, the total temperature at the nozzle outlet, and the external back pressure at the nozzle outlet:

$$U_0 = \begin{cases} \sqrt{\frac{2}{k-1} \left[\left(\frac{P^*}{P} \right)^{(k-1/k)} - 1 \right]} \cdot \sqrt{kRT}, & \text{Ma} < \text{Ma}_{\max}, \\ \text{Ma}_{\max} \cdot \sqrt{kRT}, & \text{Ma} = \text{Ma}_{\max}, \end{cases} \quad (11)$$

where Ma_{\max} is the maximum Mach number that can be reached at the outlet under the given nozzle parameters.

2.2.2. Mathematical Model of Development Stage. The gas jet is ejected from the nozzle into the environmental medium until it strikes a certain wall. The development characteristics of the jet can be divided into three typical zones, namely, the free jet zone, the impinging zone, and the wall jet zone [32, 33]. The zoning diagram is shown in Figure 3.

In the free jet zone, the shear driving interactions exist between the outer boundary of the jet and the surrounding air medium. The existence of shear stress would lead to the generation of turbulence, which causes the attenuation of the jet velocity in the axial direction. Meanwhile, it would aggravate the entrainment of the air fluid around the jet, resulting in the increase of the total jet flow and the continuous expansion of the jet cross-section along the radial direction. However, the static pressure of the

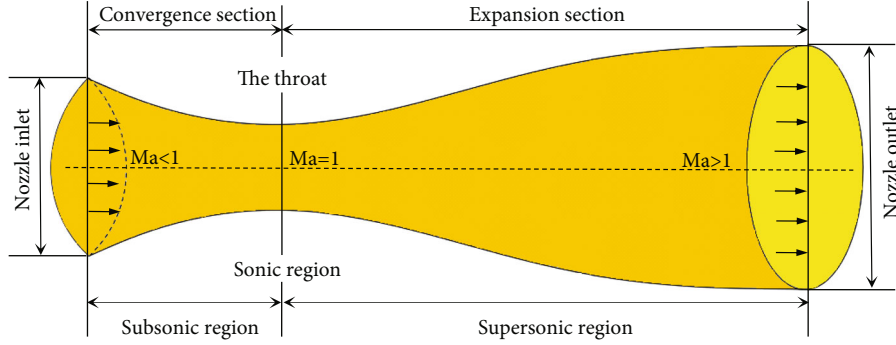


FIGURE 2: Schematic diagram of a scaled nozzle structure.

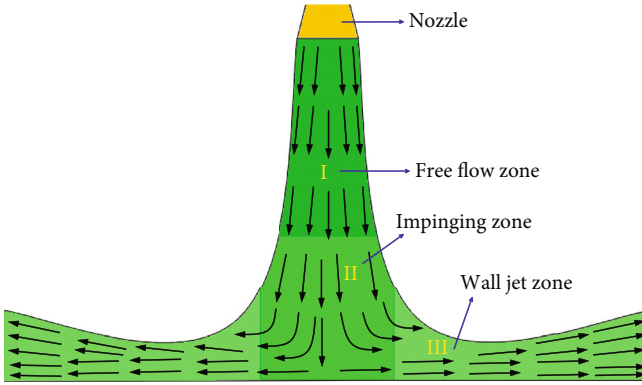


FIGURE 3: Schematic diagram of gas jet development zones.

jet on the wall begins to rise, showing a large pressure gradient and forcing the jet streamline to produce rapid bending. The jet flow changes from the original axial flow to the near wall flow, which is characterized by the existence of a stagnation point and the radial bending of the jet streamline. In the wall jet zone, the jet generally presents along the diameter. Due to the shear interaction between the wall and the air medium, the jet velocity begins to decay to zero after a long distance from the stagnation point.

The influence factors of the development stage of the gas jet include nozzle radius b_0 , nozzle plate distance H , incidence angle θ , and jet initial velocity U_0 . In order to facilitate the analysis, a rectangular coordinate system (x, y) is established in the jet flow field to analyze the free jet zone and the impingement zone, and the coordinate system (x_1, y_1) is used to analyze the impinging zone and the wall jet zone, as shown in Figure 4.

The axial pressure of a jet is defined as P_m . The pressure at the stagnation point and the wall pressure are P_s and P_w , respectively. U_m represents the jet velocity, and U_{m1} is the maximum value of U_m in the x_1 direction of any cross-section. b_u represents the radial length dimension of the fluid cross-section velocity of $1/2U_m$ in the free jet section. According to the analysis, starting from the stagnation point, U_{m1} increases with the increase of x_1 until the maximum value. Then, the velocity decreases and tends to be zero at U_{m1} far away from the jet axis due to the fact that the turbu-

lence is mixed with the surrounding air medium. In the free jet zone, the axial velocity U_{mf} and radial length b_f can be expressed as follows:

$$U_{mf}, b_f = f_{1,2}(M_0, \rho, x), \quad (12)$$

where $M_0 = \rho \cdot 2b_0^2 \cdot U_0^2$; it is the momentum flux of the nozzle section.

In the impinging zone, the jet velocity U_m , the section length size b_u , and the pressure distribution P_m exist as follows:

$$U_m, b_u = f_{3,4}(M_0, \rho, x, H), \quad (13)$$

$$P_m = f_5(M_0, \rho, x, H). \quad (14)$$

By using dimensional analysis and referring to relevant research conclusions in similar fields [34], we establish the following:

$$\frac{U_m}{U_0} \sqrt{\frac{H}{2b_0}} = g_1\left(\frac{x}{H}\right). \quad (15)$$

$$\frac{b_u}{H} = g_2\left(\frac{x}{H}\right). \quad (16)$$

$$\frac{P_m}{\rho U_0^2} \frac{H}{2b_0} = g_3\left(\frac{x}{H}\right). \quad (17)$$

For the free jet zone, the following could be obtained:

$$\frac{U_{mf}}{U_0} \sqrt{\frac{x}{2b_0}} = C. \quad (18)$$

According to the simultaneous equations (14) and (17), the following results can be obtained:

$$\frac{U_m}{U_{mf}} = h\left(\frac{x}{H}\right). \quad (19)$$

Based on the analysis of the pressure in the jet impinging zone, combined with equation (16), the pressure value at the

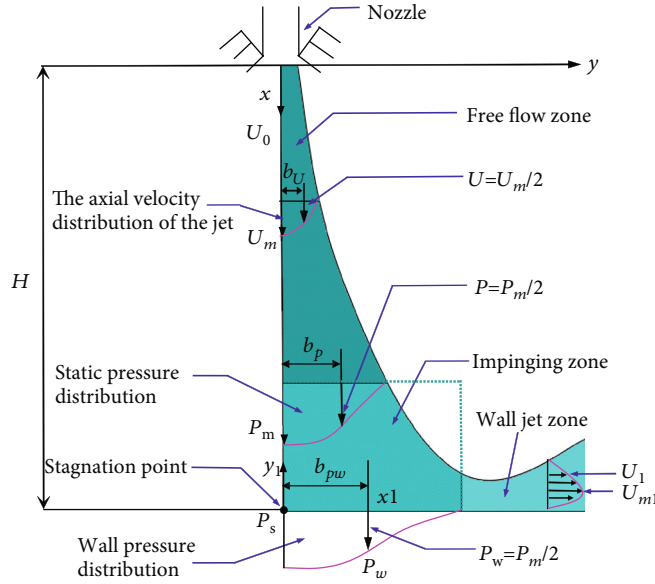


FIGURE 4: The coordinate system of gas jet development stage.

stagnation point can be obtained as follows:

$$\frac{P_s}{\rho U_0^2/2} \cdot \frac{H}{2b_0} = g_3 \left(\frac{x}{H} = 1 \right). \quad (20)$$

According to the simultaneous equations (16) and (19), the following results can be obtained:

$$\frac{P_m}{P_s} = g_4 \left(\frac{x}{H} \right). \quad (21)$$

When the jet impinges on the coal, the wall pressure distribution at \$x_1\$ away from the jet axis is as follows:

$$\frac{P_w}{\rho U_0^2/2} \cdot \frac{H}{2b_0} = g_5 \left(\frac{x_1}{H} \right). \quad (22)$$

For the simultaneous equations (19) and (21), the pressure on the inner wall of the impinging zone has the following relationship with the pressure at the stagnation point:

$$\frac{P_w}{P_s} = g_6 \left(\frac{x_1}{H} \right). \quad (23)$$

According to the conclusion in Beltaos and Rajaratnam's work [35], equation (22) can be written as follows:

$$\frac{P_w}{P_s} = e^{-38.5(x_1/H)^2}. \quad (24)$$

The pressure distribution of the jet acting on the wall of the coal body is directly related to the feasibility of the jet breaking coal. The jet velocity and jet pressure in the

impinging zone are analyzed as follows:

$$\frac{\partial}{\Delta y} (uv)_{y \rightarrow 0} = -K_1, \quad (25)$$

$$\left(u \frac{\Delta v}{\Delta y} + v \frac{\Delta u}{\Delta y} \right)_{y \rightarrow 0} = -K_1. \quad (26)$$

Equation (25) can be written by using the following continuity equation:

$$\left(-u \frac{\Delta u}{\Delta x} + v \frac{\Delta u}{\Delta y} \right)_{y \rightarrow 0} = -K_1. \quad (27)$$

When \$y\$ is 0, in the direction of the jet axis, we have

$$\frac{d}{dx} U_m^2 = 2K_1. \quad (28)$$

The integral treatment of equation (28) is as follows:

$$U_m^2 = 2K_1 x + K_2. \quad (29)$$

Combining with equation (15), the axial velocity distribution of the jet flow can be written as follows:

$$\left(\frac{U_m}{U_0} \right)^2 \frac{H}{2b_0} = K_3 \left(\frac{x}{H} \right) + K_4, \quad (30)$$

$$\left(\frac{U_m}{U_0} \right)^2 \frac{H}{2b_0} = K_5^2 \left(1 - \frac{x}{H} \right) + K_6. \quad (31)$$

In combination with the law of momentum conservation, the pressure value at the stagnation point can be

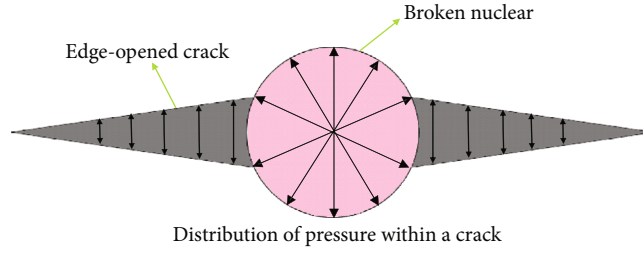


FIGURE 5: Schematic diagram of pressure inside a crack.

expressed as follows:

$$P_s = \frac{\rho U_0^2}{2} \cdot \frac{2b_0}{H} \cdot \frac{1}{K_{pw}}, \quad (32)$$

where $K_{pw} = \int_0^\infty (P_w/P_s) \cdot d(x_1/H)$, which can be set as 0.13 [34].

In the impinging zone, it is assumed that the turbulence phenomenon and gas viscosity effect caused by jet impinging can be ignored, and we have

$$P_w + \frac{\rho U_{m1}^2}{2} = P_s. \quad (33)$$

By combining equations (20) and (24), the velocity distribution along the x_1 direction of the wall surface can be obtained as follows:

$$\frac{U_{m1}}{U_0} \sqrt{\frac{H}{2b_0}} = 2.77 \left[1 - e^{-38.5(x_1/H)^2} \right]^{1/2}. \quad (34)$$

2.2.3. Mathematical Model of Impact Stage. The ideal elastic-plastic material failure process is different from the elastic-plastic fracture theory [36] and forging extrusion theory [37]. This is because coal is a brittle material with dual medium characteristics of fracture and pore. When the instantaneous jet impinges on coal under a certain kinetic energy, the instantaneous jet velocity decreases rapidly and produces a back pressure gradient, which produces a blasting shock wave. Meanwhile, it strongly influences the energy compression force of coal, which destroys the coal wall and leads to the formation of a plastic compression crushing zone. Under the action of the blasting shock wave, stress waves are generated inside the coal and rock mass. Under the tensile action of the stress incident wave and the free surface reflected wave, the coal and rock mass are damaged to a certain extent. The particles inside the coal and rock mass are dislocated. Meanwhile, the medium units are tangentially stretched and radially compressed, leading to the further generation of an initial radial crack.

Given that the high-viscosity liquid water is different from the high-pressure gas jet in a continuous impact wave damage to the formation of a break zone and the initial crack, the low viscous gas flows quickly within the crack space. The pressure effect on the crack wall (Figure 5) follows the law of quasistatic pressure distribution, which can

be approximately equal to the pressure of a jet under the action of the stagnation pressure [38]. The quasistatic pressure promotes the initial crack propagation, extension, and communication, and it generates a cross crack network inside the coal body. If the tensile stress of the gas in the fracture exceeds the tensile strength limit of the coal mass, the coal body will be destroyed and the coal particles will peel off, thus forming a plastic failure zone centered on the jet axis and forming erosion pits. The entry of the high-pressure gas in these cracks decreases gradually after expansion, and the crack stops cracking when the pressure drops to the point where it is not sufficient to support further crack expansion.

Because the action time of the gas quasistatic pressure is much longer than that of the shock wave, it is generally believed that in the stage of gas jet impingement on rock breaking, quasistatic pressure failure is the main part, and tensile failure should be the main mechanism of gas jet impingement on coal pit formation.

For coal with jet action on the surface, the stress concentration in the crushing core and the extended crack is composed of the jet stagnation pressure and induced stress. The coal failure criterion can be defined by the following formula:

$$P + \sigma_t \geq S_t, \quad (35)$$

where P is the normal pressure acting on the crack. P is the induced tensile stress generated and developed under the action of the jet impact. It can be understood as the stagnation pressure of the jet, and the induced pressure depends on the characteristics of the jet impact and the geometry of the crack.

Considering that an infinite plate is subjected to the vertical impact of a high-pressure gas jet (shown in Figure 5), the pressure distribution along the normal direction of the wall is $P = P(x, y)$. The stress distribution in the column coordinate system can be expressed as follows:

$$\begin{cases} \sigma_r = \frac{P}{2\pi} \left\{ (1-2\nu) \left(\frac{1}{r^2} - \frac{Z}{r^2} (r^2 + Z^2)^{-1/2} \right) - 3r^2 Z (r^2 + Z^2)^{-5/2} \right\}, \\ \sigma_z = -\frac{3P}{2\pi} Z^3 (r^2 + Z^2)^{-5/2}, \\ \sigma_\theta = \frac{P}{2\pi} (1-2\nu) \left\{ -\frac{1}{r^2} + \frac{Z}{r^2} (r^2 + Z^2)^{-1/2} + Z (r^2 + Z^2)^{-3/2} \right\}, \end{cases} \quad (36)$$

In equation ((36)), r is the radial distance from the z -axis. The equation represents the pressure at any point of the object induced by the existence of normal pressure. When the pressure P applied to the object is known, the stress induced by normal pressure can be obtained by integration. When a jet impinges on the flat panel wall surface, there is a point Q on the surface of the panel. And x and y point to the tangent direction of point Q , respectively. The superposition principle is used at $Z = 0$, as follows:

$$\begin{cases} \sigma_x = (\sigma_r(l, \theta) \cos \theta^2 + \sigma_\theta(l, \theta) \sin \theta^2) dl d\theta, \\ \sigma_y = (\sigma_r(l, \theta) \sin \theta^2 + \sigma_\theta(l, \theta) \cos \theta^2) dl d\theta. \end{cases} \quad (37)$$

The two formulas of equation (37) are divided into the local term with Z and the nonlocal term without Z . The local term can be expressed as follows:

$$\begin{cases} \sigma_{r1} = \frac{P}{2\pi} \left\{ (1-2\nu) \left(-\frac{Z}{r^2} (r^2 + z^2)^{-1/2} \right) - 3r^2 Z (r^2 + Z^2)^{-5/2} \right\}, \\ \sigma_{\theta1} = \frac{P}{2\pi} (1-2\nu) \left\{ \frac{Z}{r^2} (r^2 + z^2)^{-1/2} + Z (r^2 + Z^2)^{-3/2} \right\}. \end{cases} \quad (38)$$

The analysis of the above equation shows that the value of Z is very small, and the values on the right side of the equation are very small except the value near point Q . Since the pressure distribution around point Q is not obvious, it is approximately considered that the pressure is equal to that at point Q . In this case, the pressure is not affected. By integrating equation (37), we can obtain the following:

$$\sigma_{x1} = \sigma_{y1} = \frac{P_Q}{2\pi} \left[-(1-2\nu)(l^2 + Z^2)^{-5/2} \times 3\pi r^2 Z + Z(l^2 + Z^2)^{-3/2} \pi \right] dl. \quad (39)$$

By integrating the above formula within a circle with a small radius (when l is set to a), we can get the following:

$$\sigma_{x1} = \sigma_{y1} = \frac{P_Q}{2} \left[-(1+2\nu) + \frac{2(1+2\nu)Z}{\sqrt{a^2 + Z^2}} - \left(\frac{Z}{\sqrt{a^2 + Z^2}} \right)^3 \right]. \quad (40)$$

When Z approaches 0, there is

$$\sigma_{x1} = \sigma_{y1} = -\frac{P_Q}{2} (1+2\nu). \quad (41)$$

For the nonlocal phase, there is

$$\sigma_{x2} = -\sigma_{y2} = \frac{1}{2\pi} (1-2\nu) - \frac{P(x, y)}{l^2} (\cos \theta^2 - \sin \theta^2) dl d\theta. \quad (42)$$

Considering that the value of the nonlocal phase is much smaller than that of the local phase and the value of the nonlocal phase gradually disappears as it approaches the axis

direction, only local terms are generally considered. Combining the local stress failure criterion and local terms, the relationship between jet pressure and Poisson's ratio and tensile strength of a coal body under the tensile failure criterion of a coal body would be established as follows:

$$P \geq \frac{2}{1-2\nu} S_t. \quad (43)$$

2.2.4. Criteria for Identification of Coal Breaking Capacity and Erosion Pit Characteristics by Gas Jet. Combining with the mathematical model that illustrates the continuous process of coal breaking by a gas jet, when the jet pressure is greater than the critical failure pressure of coal, erosion holes will be formed. After combining equations (9), (11), (32), and (43), the criteria for determining whether a gas jet can break coal can be obtained:

$$\begin{aligned} & \frac{7.7kRb_0}{H} \cdot \frac{T}{(P^*/P)^{(k-1/k)}} \cdot \frac{\rho}{(P^*/P)^{1/k}} \\ & \cdot \frac{2}{k-1} \left[\left(\frac{P^*}{P} \right)^{(k-1/k)} - 1 \right] \geq \frac{2}{1-2\nu} S_t, \end{aligned} \quad (44)$$

where the adiabatic coefficient k is 1.4 for air, the gas constant R is 287.06 J/(kg·k) for air, b_0 is the section area of the nozzle outlet, H is the initial jet impact distance, and other relevant parameters are defined as equation (9). The ratio of gas stagnation parameters to static parameters is defined as follows:

$$a = \left(\frac{P^*}{P} \right)^{1/k}. \quad (45)$$

After the simplification of equation (44), we can obtain the following:

$$\frac{1.54 \times 10^4 T \rho b_0 (a^{0.4} - 1)}{H \cdot a^{1.4}} \geq \frac{2}{1-2\nu} S_t. \quad (46)$$

When the coal particles are eroded and stripped by a jet, the impact distance of the jet gradually increases, and the pressure value at the stagnation point gradually decreases. When the pressure is less than the critical failure pressure of coal and rock mass, the jet is insufficient to cause damage to the coal body. Under the premise that the nozzle geometric parameters, gas state parameters, and coal mechanics parameters are known, the initial impact distance of the jet is determined, and the axial depth of the hole formed by jet erosion can be obtained from the following formula:

$$\Delta h = \frac{kRb_0(1-2\nu)}{(k-1)S_t k_{pw}} \left[\left(\frac{P^*}{P} \right)^{(k-1/k)} - 1 \right] \frac{T\rho P}{P^*} - H, \quad (47)$$

$$\Delta h = \frac{7.7 \times 10^3 T \rho b_0 (1-2\nu) \cdot [a^{0.4} - 1]}{S_t a^{1.4}} - H. \quad (48)$$

TABLE 1: The theoretical values of the parameters under different jet pressures.

P_2 (MPa)	T (K)	Ma	H (mm)	P_w (MPa)	P_s (MPa)	U_0 (m/s)	Δh (mm)	x (mm)
2	298	3.5	30	2.667	54.181	652.104	3.647	1.80
4	298	3.5	30	2.667	108.362	652.104	37.293	3.99
6	298	3.5	30	2.667	162.543	652.104	70.940	4.30
8	298	3.5	30	2.667	216.724	652.104	94.587	4.69
10	298	3.5	30	2.667	270.905	652.104	108.234	5.13
12	298	3.5	30	2.667	325.086	652.104	111.880	5.62

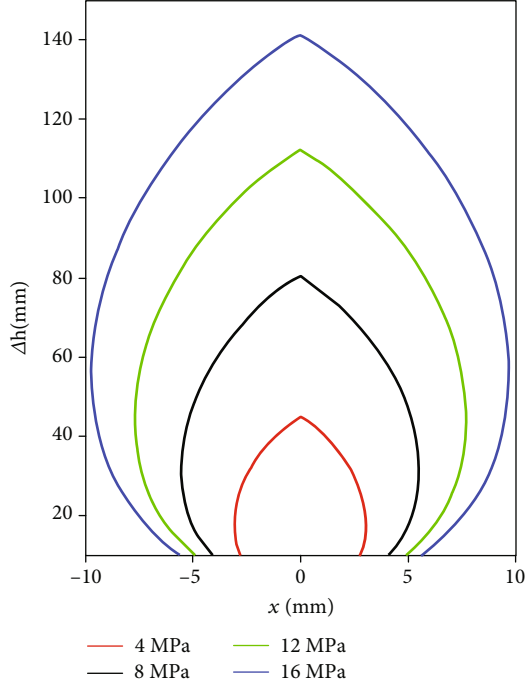


FIGURE 6: Characteristics of erosion pit under different jet conditions.

TABLE 2: Pressure at pipeline inlet under different jet pressures.

P_2 (MPa)	l (m)	d (m)	A (m ²)	λ	G	P_1 (Pa)
2	1000	0.2	0.0314	1.6	0.47	2000037.43
4	1000	0.2	0.0314	1.6	0.94	4000074.87
6	1000	0.2	0.0314	1.6	1.40	6000112.30
8	1000	0.2	0.0314	1.6	1.87	8000149.73
10	1000	0.2	0.0314	1.6	2.34	10000187.17
12	1000	0.2	0.0314	1.6	2.81	12000224.60

In terms of the radial pressure distribution of the jet impact on the coal, when the pressure is greater than the critical failure pressure, the radius of the erosion hole at the corresponding impact distance can be calculated as follows:

$$x = \frac{7.7 \times 10^3 T \rho b_0 [a^{0.4} - 1]}{S_t \cdot (1 - 2\nu)^{-1} a^{1.4}} \cdot \sqrt{\frac{\log(P_w^*/P_s^*)}{-38.5}}, \quad (49)$$

where P_w^* represents the critical failure pressure of the

TABLE 3: Mass flow rate at nozzle outlet under different jet pressures.

P_2 (MPa)	T (K)	Radius of nozzle throat, b_1 (mm)	m (kg/s)
2	298	1	0.0147
4	298	1	0.0294
6	298	1	0.0441
8	298	1	0.0588
10	298	1	0.0735
12	298	1	0.0882



FIGURE 7: Physical diagram of a test block fixing device.



FIGURE 8: Physical diagram of nozzle.

wall under the action of the jet impact, and P_s^* represents the pressure value at the stagnation point under the impact distance H .

It can be seen from equations (48) and (49) that, in addition to environmental factors, the coal-fracturing capacity of a gas jet could be also affected by jet pressure, target distance, nozzle radius, and coal strength.

2.3. Mass Flow Rate at Nozzle Outlet. According to the continuity equation of gas steady flow, the flow rate of gas is the same through any section of the nozzle. However, the flow rate of all kinds of nozzles is limited by their minimum

TABLE 4: Material ratio and mechanical parameters.

No.	Cement	Gypsum	Sand	Water	Sand cement ratio	Water solid ratio	S_t	v
1	3	1	10	3	2.5	0.214	0.64	0.24
2	3	1	8	2	2.0	0.167	0.70	0.26
3	3	1	6	1.5	1.5	0.150	0.78	0.29
4	1	3	8	2	2.0	0.167	0.50	0.22

cross-section. Therefore, the flow rate is usually calculated according to the minimum cross-section [39, 40].

$$q_m = Sa^* \rho^*, \quad (50)$$

where S is the area of the nozzle throat; a^* is the velocity of the jet in the throat, and ρ^* is the density of the jet in the throat.

When the gas velocity through the nozzle reaches the speed of sound, the gas mass flow will reach the maximum value. In this work, the gas jet reaches the speed of sound at the nozzle throat. Therefore, the mass flow at the nozzle outlet is equal to that speed at the throat.

3. Theoretical Calculation and Experimental Verification

3.1. Theoretical Calculation. In order to preliminarily analyze the coal-breaking capacity of a gas jet and the law of pit formation, the coal-breaking law of a gas jet is theoretically calculated according to an established mathematical model. Due to space limitations, only the theoretical values of the parameters under different jet pressures are listed in Table 1.

In order to visually investigate the characteristics of erosion pits formed by a gas jet impinged on coal and rock mass, the initial impact distance is selected to be 30 mm, and the nozzle specification is 3 Ma. According to equations (48) and (49), the shape of erosion pits under different jet pressures is calculated, and the results are shown in Figure 6. With the increase of the pressure at the nozzle inlet, the depth and radial length of erosion pits formed by a jet impact increase continuously, but the increase of the axial depth of holes is much larger than that of radial length. When the pressure at the nozzle inlet increases, the jet impact kinetic energy increases and the gas stagnation pressure acting on the crack increases, which is reflected in the expansion of the axial and radial crushing range of the erosion hole. Because the wall pressure attenuates rapidly from the axial direction, the increment of hole radial length is much smaller than that of axial depth. Further observation shows that with the increase of nozzle inlet pressure, the shape of the erosion hole formed by the jet impact on the same coal and rock mass gradually changes from the initial conical shape to an elliptical shape.

For the pipeline part, a new seamless steel tube is selected as the research object (at this point, the absolute friction degree of the pipeline $\varepsilon = 0.15$). Under the condition that the temperature $T = 298$ K and the outlet pressure of the pipeline is known as the inlet pressure of the nozzle, the

pressure value at the inlet of the pipeline is calculated, as shown in Table 2.

It can be found from Table 2 that the pressure at the outlet of the pipeline is slightly higher than that at the inlet under the assumption that the gas flows in the pipeline are in a constant temperature environment.

In the case of only changing the jet pressure, the mass flow rate at the nozzle outlet under different jet parameters is calculated, as shown in Table 3.

It is found from the Table 3 that the mass flow rate at the nozzle outlet only increases with the increase of jet pressure under the condition of constant external back pressure.

3.2. Experimental Verification of the Size of the Erosion Pit.

According to the established mathematical model, the theoretical values of the depth and radius of the erosion pit under different jet parameters are calculated and verified by experiments. Considering the difficulty and safety of obtaining gas raw materials, air was selected for the experiment in this task. The following analyses include the influence of Mach number Ma , target distance H , jet pressure P , and tensile strength S_t on the coal-breaking ability of a gas jet.

3.2.1. Experimental System. As shown in Figure 1, the experimental system consists of three parts: high-pressure supersonic gas jet forming and controlling device, test block fixing device, and nozzle system. These three parts of the experimental system are independent of each other in structure and are easy to assemble and disassemble. They are connected with each other through a high-pressure rubber hose and a high-pressure steel pipe. When the gas is repeatedly compressed by the air compressor, the normal temperature and atmospheric pressure gas is stored in the high-pressure gas storage tank. After the manual pressure regulating valve is opened, the high-pressure gas flows through the pipeline and nozzle and ejects outwards. Then, the jet continuously impacts on the wall of the coal and rock mass, resulting in erosion damage. The following are the details of the experiment.

(1) The High-Pressure Supersonic Gas Jet Forming and Controlling Device. The gas jet forming and controlling device in the system is composed of a piston air compressor, a high-pressure gas storage tank, a high-pressure pipeline, a pressure gauge, and a pressure regulating valve. The air with normal temperature and atmospheric pressure is first repeatedly pressurized by the air compressor and then stored in the high-pressure gas storage tank. The pressure is read by the pressure gauge installed on the intake pipeline, and the

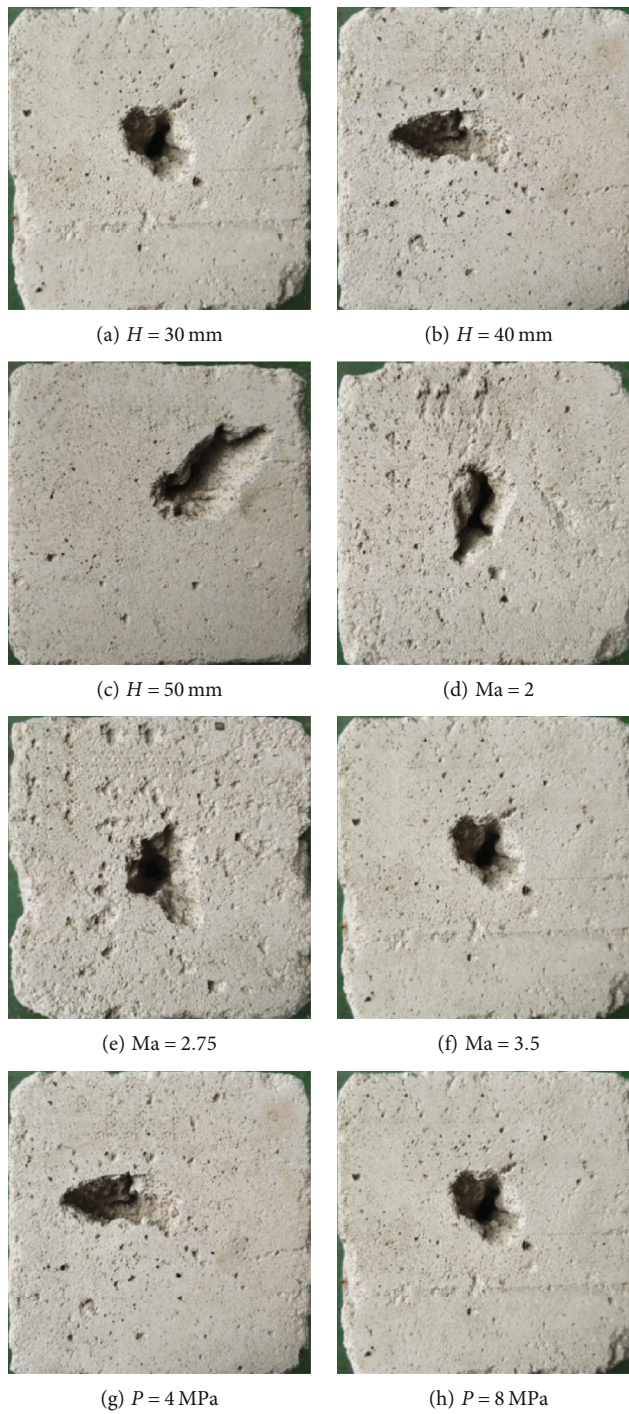


FIGURE 9: Continued.

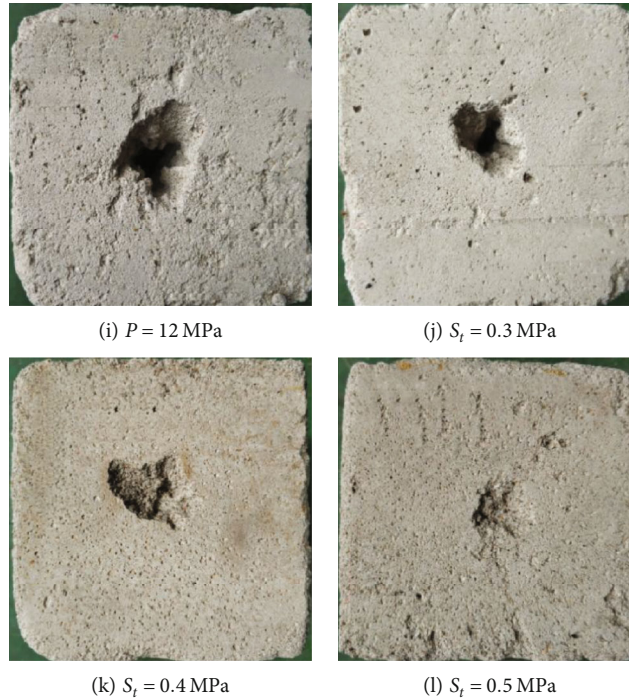


FIGURE 9: Shape of erosion pit formed by different jet parameters (Ma , H , P , S_t).

start-up and stop of the air compressor are controlled. When the specified pressure is reached, the required gas pressure is manually adjusted by the pressure regulating valve.

(2) *Test Block Fixing Device*. Due to the large impact dynamic pressure in the process of gas jet impingement, it is necessary to fix the test block in order to ensure that the test block is not displaced in the impact process. The RLCJ-1 device produced by Nantong Renlong Scientific Research Instrument Co., Ltd. was used to fix the test block. The loading pressure is 0-60 MPa, the loading accuracy is 0.01 MPa, and the size of loading chamber is 250 mm \times 250 mm \times 300 mm. Because the size of the test block made of similar material is 100 mm \times 100 mm \times 100 mm and the stroke of the piston column of the loading device is limited (30 mm), in order to load the pressure to similar materials, adding a gasket in the confining pressure loading chamber was considered. Because the cabin space is larger than that of similar materials, the size of the high-strength finish rolling pad commonly used in confining pressure loading should also be large enough. Considering the convenience of the experimental process, a high molecular polyethylene backing plate is used. The physical figure is shown in Figure 7.

(3) *Nozzle System*. In order to realize supersonic flow, the jet velocity must be realized by the Laval nozzle. In this test, a high-pressure rubber pipe and a high-pressure steel pipe were installed at the outlet of the pressure regulating valve, and the screw thread was processed at the end of the high-pressure steel pipe to connect the Laval nozzle. The nozzle specifications include 2 Ma, 2.25 Ma, 2.5 Ma, 2.75 Ma, 3 Ma,

3.25 Ma, and 3.5 Ma. The inlet diameter of the nozzle is 7 mm, and the rear diameter is 2 mm. The outlet diameter is different. The larger the Mach number, the larger the section diameter of the corresponding nozzle outlet. The physical figure is shown in Figure 8.

3.2.2. *Experimental Method and Sample Preparation*. The pressure regulating valve is adjusted to the required experimental pressure, the impact target distance and the nozzle specification of the nozzle are adjusted, the air outlet valve is opened, and the high-pressure gas flows through the nozzle to form a high-pressure supersonic gas jet, causing erosion damage to the sample. After the jet pressure is significantly reduced, the valve is closed. After impact, a vernier caliper is used to measure the depth and width of the erosion pit. After the measurement, the first test is completed. Other different test blocks are replaced for repeated tests.

In order to achieve good results in the jet impingement experiment, raw coal is the best impact material. However, due to the randomness of the development of the actual coal joints and fissures, the mechanical structure is complex, and it is very easily broken in the process of sampling and sample preparation. It is difficult to obtain coal blocks with regular or similar mechanical parameters, and the number of test blocks required in the experiment is large. Therefore, cement, gypsum, river sand, and other similar materials are considered as a replacement for raw coal for processing. According to the mechanical parameters of raw coal, the proportion of raw materials is carried out to ensure that the stress-strain, compressive strength, tensile strength, elastic modulus, and Poisson's ratio of similar materials are as

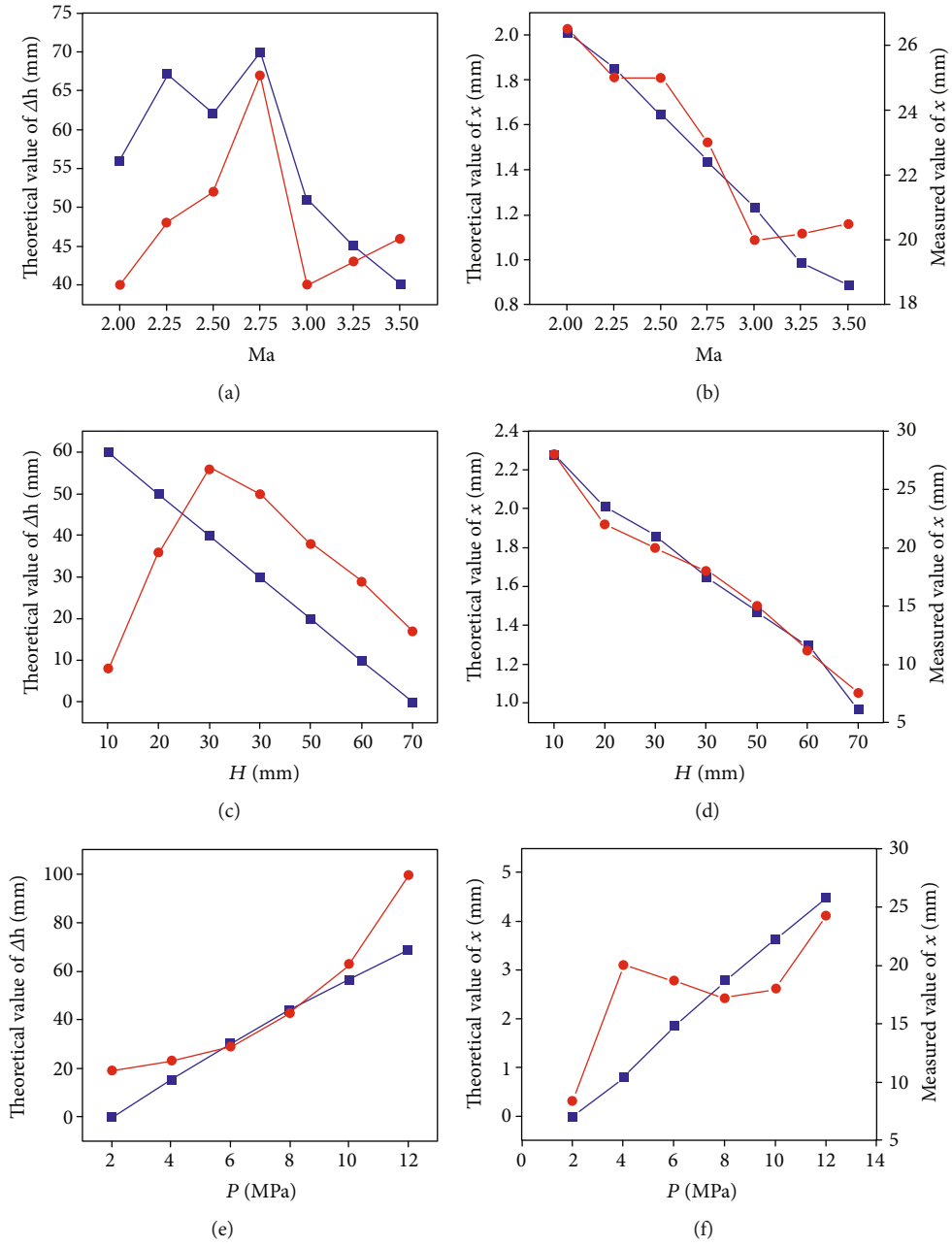


FIGURE 10: Continued.

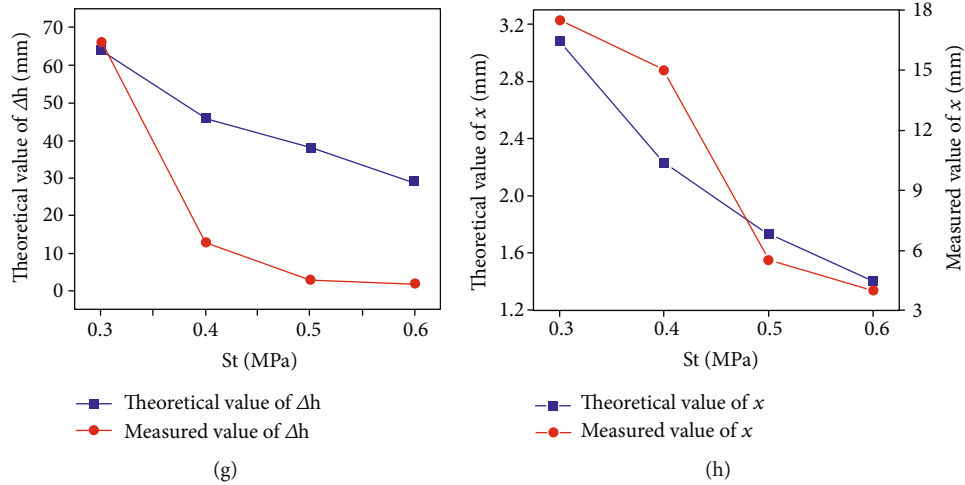


FIGURE 10: Theoretical and measured values of erosion pit size under different fracture parameters (Ma, H, P, St).

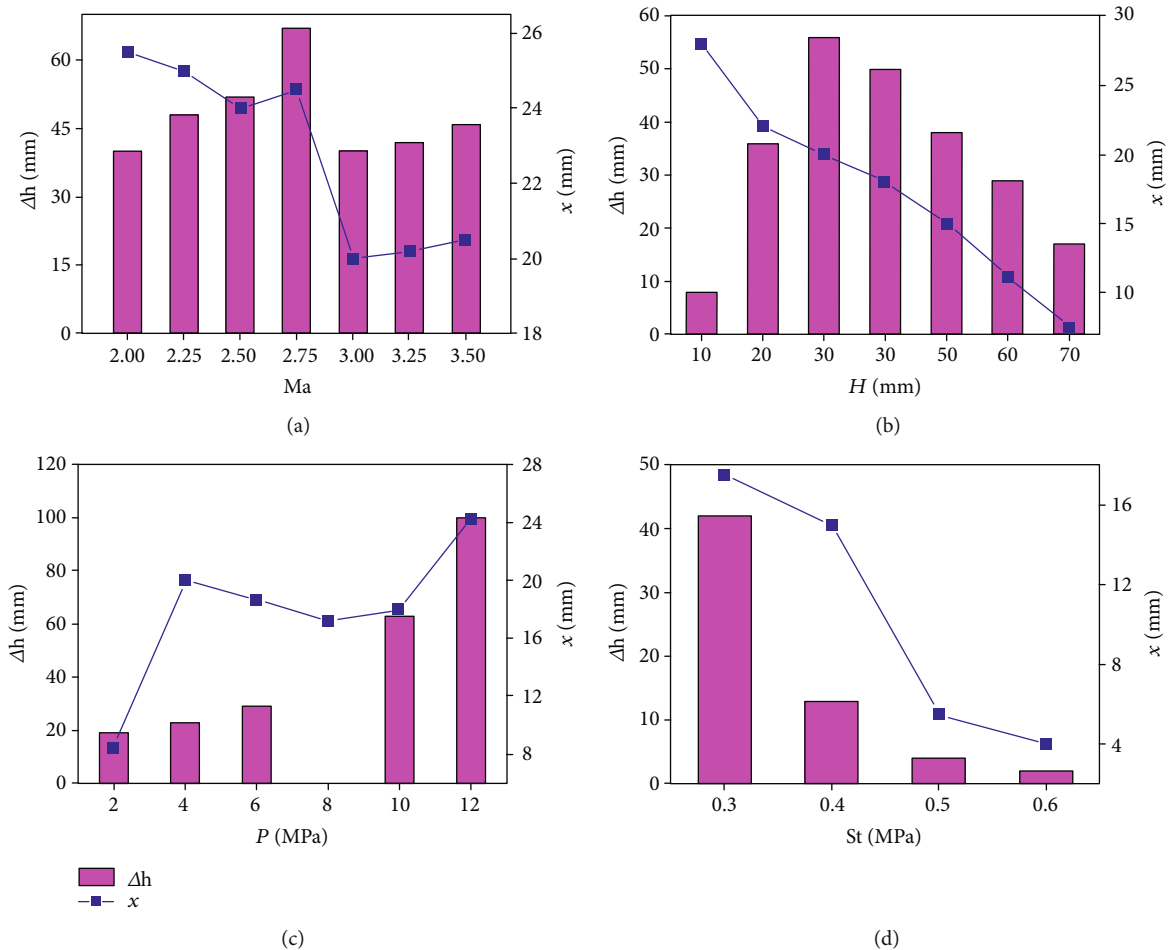


FIGURE 11: Variation of depth and radius of an erosion pit with different jet parameters (Ma, H, P, St).

close as possible to the raw coal, as shown in Table 4. The size of the test block is 100 mm × 100 mm × 100 mm for experimental verification.

3.2.3. *Verification.* After the installation of the experimental device, we carried out four groups of experiments under the condition of changing the jet parameters. The following

analyses include the influence of Mach number Ma (2, 2.25, 2.5, 2.75, 3, 3.25, 3.5 Ma), target distance H (10, 20, 30, 40, 50, 60, and 70 mm), jet pressure P (2, 4, 6, 8, 10, and 12 MPa), and tensile strength S_t (0.3, 0.4, 0.5, and 0.6 MPa) on the coal-breaking ability of a gas jet. The size of the erosion pit directly reflects the coal-breaking ability of each jet parameter, so the radius and depth of the erosion pit are taken as the comparison parameters. The sample after the experiment is shown in Figure 9. After measuring the erosion pit, the experimental value is compared with the theoretical value, and the results are shown in Figure 10.

As shown in Figure 10, the theoretical and measured values under some parameters have roughly the same variation trend after ignoring the large error in the experimental data. However, with the increase of Mach number and target distance, the theoretical value of erosion pit depth decreases gradually, while the measured value increases first and then decreases. With the increase of jet pressure, the change in the radius of an erosion pit is opposite to the Mach number and target distance.

Differently from the monotonic variation of theoretical values, there is a turning point in the variation of experimental values under some parameters. Taking the variation under different target distances as an example, the depth of the erosion pit increases with the increase of the target distance and reaches the deepest depth when the target distance is 30 mm. The radius of the erosion pit also remains almost unchanged after the target distance is 30 mm. Therefore, the optimal impinging distance is 30 mm, rather than that the smaller distance would cause a better impinging effect.

In order to determine these optimal values within the paper's research scope, experimental data under various jet parameters are analyzed, and the results are shown in Figure 11.

Under the condition of a constant nozzle Mach number and impingement distance, the depth of an erosion pit formed by high-pressure gas jet impact and the area of an erosion pit both increase with the increase of nozzle inlet pressure. Considering the influence of the depth and radius of an erosion pit comprehensively, certain rock breaking can be achieved under the action of jet impingement. The impact pressure of a gas jet should be increased continuously.

Under the condition of a constant nozzle inlet pressure and nozzle Mach number, the depth of an erosion pit formed by high-pressure gas jet impact first increases and then decreases with the increase of target distance. Besides the large area peeling data of test block surface with 10 mm spacing, the erosion pit area also shows the trend of first increasing and then decreasing. It is considered that an optimum distance of 30 mm exists under the action of jet impingement.

Under the condition of a constant nozzle inlet pressure and impingement distance, the depth of an erosion pit formed by high-pressure jet impingement increases with the increase of nozzle Mach number, and the erosion pit area reaches the maximum when the nozzle Mach number is 2.75 Ma . Considering the influence of the depth and radius of the erosion pit, the rock-breaking effect is better when the nozzle size is 2.75 Ma .

Under the condition of constant nozzle inlet pressure, nozzle Mach number, and impingement distance, the depth of an erosion pit formed by high-pressure gas jet impact and the area of an erosion pit both decrease with the increase of coal strength.

4. Discussion

Gas jet breaking coal and rock is a new type of pressure relief and permeability increasing technology. By studying the continuous action mechanism of a gas jet and the influence law of different jet parameters on erosion and coal breaking, the theory of gas jet impacting coal and rock breaking is enriched and developed, and the selection of jet parameters is optimized, which is of great significance for the application of gas jet engineering. Although the mechanism and law of coal breaking by gas jet impingement have been studied in this work, there are still some deficiencies which need to be further studied and improved. (1) Limited by the influence of a high-pressure gas source, it is impossible to realize a high-pressure and long-time jet impingement experiment. In the selection of experimental factors, the influence of impact time on the experimental results is ignored, and the optimal value of jet parameters cannot be completely accurately selected. (2) Because the raw coal sample is not easily obtained and its demand is usually large, it is replaced by similar materials in this work. The results show that the similar materials do not have the joint structure of raw coal, and the experimental results will have a certain degree of deviation. Moreover, raw coal exists in the complex stress field, which is not easily achieved in the laboratory conditions. Therefore, the field test of a gas jet breaking coal and rock is needed in our future research.

5. Conclusion

- (1) The mathematical model of the full impinging process of coal and rock fracturing by a supersonic gas jet is established. In particular, the transport of high-pressure gas in a pipeline is included in the model. The relationship between the pressure at the inlet and the pressure at the outlet of the pipeline is obtained, and the remote supply of high-pressure gas can be achieved. Moreover, the criteria for distinguishing the coal-fracturing ability of a gas jet and the characteristics of an erosion pit are deduced, and it is found that the shape of the erosion pit is ellipse, which lays a foundation for further theoretical research and field process design.
- (2) Laboratory experiment results show that different from the monotonic variation of theoretical values, a turning point exists in the variation of experimental values under some parameters. Taking the variation under different target distances as an example, the depth of the erosion pit increases with the increase of the target distance and reaches the deepest depth when the target distance is 30 mm. The

radius of the erosion pit also remains almost unchanged after the target distance is 30 mm

- (3) Considering the influence of the depth and radius of erosion pit comprehensively, certain rock-breaking effects can be achieved under the action of jet impingement. The impact pressure of a gas jet should be increased continuously. The rock-breaking effect is better when the nozzle size is 2.75 Ma

Nomenclature

g :	Gravitational acceleration (m/s^2)
u_1 :	Speed at pipeline inlet (m/s)
u_2 :	Speed at pipeline outlet (m/s)
p_1 :	Pressure at pipeline inlet (Pa)
p_2 :	Pressure at pipeline outlet (Pa)
h_f :	Resistance loss (J/kg)
ρ :	Density (kg/m^3)
v :	Specific volume of gas (m^3/kg)
L :	Length of pipeline (m)
d :	Diameter of pipeline (m)
Re:	Reynolds number
λ :	Friction coefficient
μ :	Viscosity (Pa·s)
q_m :	Mass flow rate (kg/s)
A :	Section area of pipeline (m^2)
G :	Mass flow rate (kg/s)
R :	Gas constant, $287.06 \text{ J}/(\text{kg}\cdot\text{K})$ for air
T :	Thermodynamic temperature (K)
M :	Molar mass (g/mol)
S :	Any cross-sectional area of nozzle (m^2)
S_e :	Nozzle throat area (m^2)
Ma:	Mach number
Ma_{\max} :	Maximum Mach number
k :	Adiabatic coefficient, 1.4 for air
P :	Gas pressure (Pa)
P^* :	Gas pressure under stagnation state (Pa)
ρ^* :	Gas density at stagnation state (kg/m^3)
T^* :	Thermodynamic temperature of gas in stagnation state (K)
a :	Sound velocity (m/s)
b_0 :	Radius at nozzle outlet (m)
H :	Target distance: the distance from the nozzle outlet to the plate (m)
θ :	Jet angle ($^\circ$)
U_0 :	Initial velocity of a jet (m/s)
P_m :	Jet axial pressure (Pa)
P_s :	Pressure at stagnation point (Pa)
P_s^* :	Pressure value at stagnation point at impact distance H (Pa)
P_w :	Pressure at wall (Pa)
P_w^* :	Critical failure pressure at the wall (Pa)
U_m :	Jet velocity (m/s)
ν :	Poisson's ratio
S_t :	Tensile strength (Pa)
K_{pw} :	Constant (0.13)
U_{m1} :	Maximum value of U_m in x_1 direction of any cross-section (m/s)

b_u :	Radial length dimension of fluid cross-section velocity of $1/2U_m$ in a free jet section (m)
U_{mf} :	Axial velocity of jet (m/s)
b_f :	Radial length of jet (m)
x :	Radius of erosion pit (m)
Δh :	Depth of erosion pit (m).

Data Availability

The datasets used or analyzed during the current study are available from the corresponding author on reasonable request.

Conflicts of Interest

The authors declare that they have no known competing financial interests or personal relationships that could have appeared to influence the work reported in this paper.

Authors' Contributions

Gongda Wang performed formal analysis and wrote the original draft of the manuscript. Yuanyuan Wang conducted the investigation and wrote, reviewed, and edited the manuscript. Xin Yang performed formal analysis. Xin Song contributed in the conduct of the investigation.

Acknowledgments

This work was supported by National Natural Science Foundation of China (51974161, 51804161, 52074156, and 52004291) and the Chinese Postdoctoral Science Foundation (2019M660861).

References

- [1] T. Moore, "Coalbed methane: a review," *International Journal of Coal Geology*, vol. 101, pp. 36–81, 2012.
- [2] J. Liu, Z. Chen, D. Elsworth, H. Qu, and D. Chen, "Interactions of multiple processes during CBM extraction: a critical review," *International Journal of Coal Geology*, vol. 87, no. 3–4, pp. 175–189, 2011.
- [3] C. Fan, D. Elsworth, S. Li et al., "Modelling and optimization of enhanced coalbed methane recovery using CO_2/N_2 mixtures," *Fuel*, vol. 253, pp. 1114–1129, 2019.
- [4] A. S. Ranathunga, M. S. A. Perera, P. G. Ranjith, and C. H. Wei, "An experimental investigation of applicability of CO_2 enhanced coal bed methane recovery to low rank coal," *Fuel*, vol. 189, pp. 391–399, 2017.
- [5] K. Jin, Y. Cheng, T. Ren et al., "Experimental investigation on the formation and transport mechanism of outburst coal-gas flow: implications for the role of gas desorption in the development stage of outburst," *International Journal of Coal Geology*, vol. 194, pp. 45–58, 2018.
- [6] J. Sobczyk, "A comparison of the influence of adsorbed gases on gas stresses leading to coal and gas outburst," *Fuel*, vol. 115, pp. 288–294, 2014.
- [7] S. Xue, Y. Wang, J. Xie, and G. Wang, "A coupled approach to simulate initiation of outbursts of coal and gas—model

- development,” *International Journal of Coal Geology*, vol. 86, no. 2-3, pp. 222–230, 2011.
- [8] T. Lu, H. Yu, T. Zhou, J. Mao, and B. Guo, “Improvement of methane drainage in high gassy coal seam using waterjet technique,” *International Journal of Coal Geology*, vol. 79, no. 1-2, pp. 40–48, 2009.
- [9] L. Li, F. Wang, T. Li, X. Dai, X. Xing, and X. Yang, “The effects of inclined particle water jet on rock failure mechanism: experimental and numerical study,” *Journal of Petroleum Science and Engineering*, vol. 185, article 106639, 2020.
- [10] C. Cai, X. Wang, X. Yuan et al., “Experimental investigation on perforation of shale with ultra-high pressure abrasive water jet: shape, mechanism and sensitivity,” *Journal of Natural Gas Science and Engineering*, vol. 67, pp. 196–213, 2019.
- [11] S. Liu, F. Zhou, H. Li, Y. Chen, F. Wang, and C. Guo, “Experimental investigation of hard rock breaking using a conical pick assisted by abrasive water jet,” *Rock Mechanics and Rock Engineering*, vol. 53, no. 9, pp. 4221–4230, 2020.
- [12] Y. Xue, H. Si, D. Xu, and Z. Yang, “Experiments on the microscopic damage of coal induced by pure water jets and abrasive water jets,” *Powder Technology*, vol. 332, pp. 139–149, 2018.
- [13] D. Li, “A new technology for the drilling of long boreholes for gas drainage in a soft coal seam,” *Journal of Petroleum Science and Engineering*, vol. 137, pp. 107–112, 2016.
- [14] X. Li, D. Zhou, Y. Lu, Y. Kang, Y. Zhao, and X. Wang, “Dynamic effects of high-pressure pulsed water jet in low-permeability coal seams,” *Journal of Coal Science & Engineering*, vol. 15, no. 3, pp. 284–288, 2009.
- [15] S. Chen, T. Yang, P. G. Ranjith, and C. Wei, “Mechanism of the two-phase flow model for water and gas based on adsorption and desorption in fractured coal and rock,” *Rock Mechanics & Rock Engineering*, vol. 50, no. 3, pp. 571–586, 2017.
- [16] J. Dong, Y. Cheng, K. Jin et al., “Effects of diffusion and suction negative pressure on coalbed methane extraction and a new measure to increase the methane utilization rate,” *Fuel*, vol. 197, pp. 70–81, 2017.
- [17] A. R. Shahani and M. Seyyedian, “Simulation of glass cutting with an impinging hot air jet,” *International Journal of Solids and Structures*, vol. 41, no. 5-6, pp. 1313–1329, 2004.
- [18] Y. Masip, A. Campo, and S. M. Nuñez, “Experimental analysis of the thermal performance on electronic cooling by a combination of cross-flow and an impinging air jet,” *Applied Thermal Engineering*, vol. 167, p. 114779, 2020.
- [19] Y. Lu, A. Klimenko, H. Russell, Y. Dai, J. Warner, and K. Hooman, “A conceptual study on air jet-induced swirling plume for performance improvement of natural draft cooling towers,” *Applied Energy*, vol. 217, no. 18, pp. 496–508, 2018.
- [20] T. Komori, M. Miura, S. Horiki, and M. Osakabe, “ICOPE-15-1158. Supersonic air and wet steam jet using simplified de Laval nozzle,” in *Proceedings of the International Conference on Power Engineering*, Yokohama, Japan, 2015.
- [21] A. Frendi and M. Brown, “Flow structures and noise from a supersonic impinging jet,” *International Journal of Numerical Methods for Heat and Fluid Flow*, vol. 26, no. 8, pp. 2509–2527, 2016.
- [22] H. Kutter and C. Fairhurst, “On the fracture process in blasting,” *International Journal of Rock Mechanics and Mining Sciences & Geomechanics Abstracts*, vol. 8, no. 3, pp. 181–202, 1971.
- [23] T. N. Hagan, “Rock breakage by explosives,” *Acta Astronautica*, vol. 6, no. 3-4, pp. 329–340, 1979.
- [24] R. Nilson, W. Proffer, and R. Duff, “Modelling of gas-driven fractures induced by propellant combustion within a borehole,” *International Journal of Rock Mechanics and Mining Sciences & Geomechanics Abstracts*, vol. 22, no. 1, pp. 3–19, 1985.
- [25] M. Eslamian, A. Pophali, M. Bussmann, and H. N. Tran, “Breakup of brittle deposits by supersonic air jet: the effects of varying jet and deposit characteristics,” *International Journal of Impact Engineering*, vol. 36, no. 2, pp. 199–209, 2009.
- [26] Y. Liu, H. Zhang, P. G. Ranjith, J. Wei, and X. Liu, “Wear mechanism of abrasive gas jet erosion on a rock and the effect of abrasive hardness on it,” *Geofluids*, vol. 2019, Article ID 4125363, 14 pages, 2019.
- [27] Y. Liu, T. Zhang, and X. Liu, “Analysis of the stress wave effect during coal breakage by a high-pressure abrasive air jet,” *Advances in Mechanical Engineering*, vol. 10, no. 6, 2018.
- [28] Y. Liu, J. Zhang, J. P. Wei, and X. T. Liu, “Optimum structure of a Laval nozzle for an abrasive air jet based on nozzle pressure ratio,” *Powder Technology*, vol. 364, no. 3, pp. 343–362, 2020.
- [29] Y. Liu, C. Wang, J. P. Wei, and C. Chen, “Effect of nozzle pressure ratio on pulsation frequency of air jets used in hole drilling,” *Journal of Petroleum Science and Engineering*, vol. 196, article 107399, 2021.
- [30] P. G. Ranjith, Y. Liu, J. Wei, and X. Liu, “Effect of abrasive mass flow on the abrasive acceleration and erosion rates of abrasive gas jets,” *Rock Mechanics and Rock Engineering*, vol. 52, no. 9, pp. 3085–3102, 2019.
- [31] X. Song, G. Wang, H. Ma, H. Gong, and C. Cui, “Mechanism and mathematical model of the continuous process of gas jet breaking coal,” *Journal of China Coal Society*, vol. 45, no. 9, pp. 3176–3185, 2020.
- [32] S. M. Simionescu, N. O. Tănase, D. Broboană, and C. Bălan, “Impinging air jets on flat surfaces at low Reynolds numbers,” *Energy Procedia*, vol. 112, pp. 194–203, 2017.
- [33] M. J. Tummers, J. Jacobse, and S. G. Voorbrood, “Turbulent flow in the near field of a round impinging jet,” *International Journal of Heat and Mass Transfer*, vol. 54, no. 23-24, pp. 4939–4948, 2011.
- [34] S. Beltaos and N. Rajaratnam, “Plane turbulent impinging jets,” *Journal of Hydraulic Research*, vol. 11, no. 1, pp. 29–59, 1973.
- [35] S. Beltaos and N. Rajaratnam, “Impingement of axisymmetric developing jets,” *Journal of Hydraulic Research*, vol. 15, no. 4, pp. 311–326, 1977.
- [36] J. G. A. Bitter, “A study of erosion phenomena part I,” *Wear*, vol. 6, no. 1, pp. 5–21, 1963.
- [37] A. V. Levy and W. Buqian, “Erosion of hard material coating systems,” *Wear*, vol. 121, no. 3, pp. 325–346, 1988.
- [38] A. Kaliazine, M. Eslamian, and H. N. Tran, “On the failure of a brittle material by high velocity gas jet impact,” *International Journal of Impact Engineering*, vol. 37, no. 2, pp. 131–140, 2010.
- [39] S. Nakao and M. Takamoto, “Choking phenomena of sonic nozzles at low Reynolds numbers,” *Flow Measurement and Instrumentation*, vol. 11, no. 4, pp. 285–291, 2000.
- [40] S. Nakao, Y. Yokoi, and M. Takamoto, “Development of a calibration facility for small mass flow rates of gas and the uncertainty of a sonic Venturi transfer standard,” *Flow Measurement and Instrumentation*, vol. 7, no. 2, pp. 77–83, 1996.

Research Article

Pressure-Relief Mechanism and Application of Large-Diameter Boreholes in Coal Seams with Rockburst Hazard

Zhen Hao ^{1,2}, Guangzhong Sun,¹ Haihang Wei,¹ Jiayu Liu,¹ Maolin Tian,¹ Shuaiyi Liu,¹ and Yikun Xu¹

¹School of Resources and Safety Engineering, Henan University of Engineering, Zhengzhou 451191, China

²State and Local Joint Engineering Laboratory for Gas Drainage & Ground Control of Deep Mines, Henan Polytechnic University, Jiaozuo 454003, China

Correspondence should be addressed to Zhen Hao; haozhen09@163.com

Received 19 July 2021; Accepted 24 September 2021; Published 7 October 2021

Academic Editor: Haiyan Wang

Copyright © 2021 Zhen Hao et al. This is an open access article distributed under the Creative Commons Attribution License, which permits unrestricted use, distribution, and reproduction in any medium, provided the original work is properly cited.

Drilling of large-diameter boreholes is regarded as an effective measure for rockburst prevention. By investigating the morphological characteristic and evolution of plastic zone in borehole surrounding rock, the pressure-relief mechanism of large-diameter borehole was ascertained, and the engineering application of large-diameter boreholes was assessed in the 13230 working face of Gengcun Coal Mine, Henan Province, China. The results showed that (1) the plastic zone in surrounding rock of borehole appear as circular, elliptical, and butterfly shapes, in which the maximum size of the butterfly wings of the plastic zone is several times larger than the borehole diameter; (2) under certain stress conditions, multiple large-diameter boreholes distributed in coal seam with rockburst risk lead to the generation and coalescence of large-range butterfly-shape plastic zone. They reduce the stress concentration and capacity for storing elastic energy of coal seam, thus reducing the rockburst risk of the coal seam; (3) large-diameter boreholes significantly decrease the stress concentration in front of the 13230 working face and improve the stress environment in the head entry, promoting the safe mining of the working face.

1. Introduction

Rockburst is one of the major engineering disasters caused by the violent release of accumulated strain energy in deep underground projects [1]. This phenomenon is often accompanied with the ejection of rock fragments, which would directly threaten the safety of workers [2, 3].

In recent years, rockburst have become more serious due to the increasing mining intensity and depth. For a long time, rockburst prevention and control in coal mines, as one of major research topics on prevention and control of mine disasters, has attracted much interest among scholars and engineering technologists. In early studies, many scholars elaborated the causes of static and dynamic failure of coal and rock mass from different perspectives and formed many classical theories, such as energy theory, strength theory, stiffness theory [4, 5], burst proneness theory

[6], instability theory [7], and “three factors” theory [8]. With the introduction of interdisciplinary disciplines such as mathematics and mechanics into this research field, burst start-up theory [9], catastrophe theory, and chaos theory have been formed [10, 11].

At present, the consensus is that the stress concentration degree and accumulation capacity for elastic energy in coal and rocks can be artificially lowered to prevent and control the rockburst. The type of pressure-relief measures in coal seams mainly include coal-seam water infusion, deep-hole blasting, and pressure relief through large-diameter borehole. Due to some unique advantages such as convenient and fast construction and small disturbance, large diameter pressure-relief borehole has been widely used in many mines prone to rockburst in China as an effective and conventional measure for rockburst prevention [12]. In engineering practice, large diameter pressure-relief borehole was investigated

in Yuejin Coal Mine, and more than 3100 boreholes were drilled along the haulage gateway in the coal body [13]. In order to reduce the influence of geo-stress distribution on safety mining near the fault areas, the large diameter borehole large diameter method was used to conduct in situ geo-stress measurements [14]. Therefore, investigation on the pressure-relief mechanism of large-diameter boreholes is of significance for further enriching the theory on rockburst prevention and control and promoting the safe and efficient working of mines prone to rockburst.

In terms of pressure-relief and rockburst-prevention mechanism and the effect evaluation of large-diameter boreholes, many scholars have conducted effective studies from different perspectives. Jia et al. [15] thought that the fundamental reason why large-diameter boreholes show the pressure-relief effect is that cracks around borehole propagate and coalesce, releasing the concentrated stress accumulating in coal seams; moreover, the pressure-relief effect of boreholes is directly proportional to the borehole diameter and depth while inversely proportional to the borehole spacing. Jiao et al. [16] suggested that large-diameter boreholes distributed in coal seams may decrease the peak particle velocity in dynamic conditions velocity and degree of stress concentration and its extent in the rock surrounding a roadway subjected to dynamic loads and increase the attenuation length of the elastic energy, thus greatly decreasing the possibility of a rockburst in the roadway. To reduce the rockburst risk in large coal pillars, Li et al. [17] realized the passive transfer of the concentrated stress in large coal pillars by distributing large-diameter boreholes with reasonable depth and spacing. Xiao et al. [18] found that the area subject to stress-concentration on the floor is shifted to greater depth by distributing large-diameter boreholes across the floor and increasing their diameter. In this way, the range of the stress-drop zone is expanded, and the rockburst risk in the roadway floor is decreased. By further exploring the pressure-relief mechanism afforded by boreholes through the similar simulation tests, Qi et al. [19] found that the borehole diameter delivers a significant size effect on the pressure-relief effect and they provided a reasonable range of the borehole diameters acceptable to provision of pressure relief. By analyzing the pressure-relief effects of boreholes with different diameters through numerical simulation, Li et al. [20] showed that the borehole diameter is directly proportional to the pressure-relief effect, which is weakened when the spacing between boreholes for pressure relief exceeds some critical value. Zhu et al. [21] proposed to assess the residual hazard of pressure-relieved coal seams with rockburst hazard by using an energy dissipation index and proposed a method with which to quantify the parameters of large-diameter boreholes. Wei [22] suggested that the growth of the borehole diameter and depth can improve the pressure-relief effect of coal seams prone to rockburst. Many scholars have explored the failure mechanism of brittle hard rock drilling by means of laboratory experiments and numerical simulation and discussed the influence of drilling size, rock strength, load, and other parameters on the failure range of drilling [23–27]. However, the above research is only limited to sandstone or

marble with high strength and rarely involved in coal with low strength drilling. The research results provide a basis for the present study.

By taking the specific engineering and geological conditions in Gengcun Coal Mine, Henan Province, China, as the research background, the rockburst-prevention mechanism of large-diameter boreholes was analyzed by studying the morphological characteristics and evolution of plastic zone in the borehole surrounding rock based on the butterfly-shape plastic zone theory. In addition, an engineering case study was performed.

2. Pressure-Relief Mechanism of Large-Diameter Borehole

2.1. The Formation Mechanism and Morphological Characteristic of Plastic Zone of Large-Diameter Borehole Surrounding Rock. The construction of large-diameter boreholes in coal seam is similar to the layout of a small roadway [28]. After excavating a roadway or drilling a borehole in coal and rocks, the stress in the surrounding rock of the roadway or borehole is redistributed, and plastic zone appear in the shallow part of the surrounding rock. Therefore, it is feasible to establish a mechanical model (Figure 1) for the surrounding rock of borehole in a nonconstant stress field by taking the zone with borehole with a radius of a (generally being five times the borehole radius) as the separator. The loads on the boundary of the model are determined as P_1 and P_3 .

The equation for the boundary of the plastic zone in surrounding rock of circular borehole in nonuniform stress field conditions derived according to literature [29] is described as follows:

$$\begin{aligned}
 & 9 \left(1 - \frac{P_1}{P_3}\right)^2 \left(\frac{a}{r}\right)^8 + \left[-12 \left(1 - \frac{P_1}{P_3}\right)^2 + 6 \left(1 - \frac{P_1^2}{P_3^2}\right) \cos 2\theta\right] \left(\frac{a}{r}\right)^6 \\
 & + \left[10 \left(1 - \frac{P_1}{P_3}\right)^2 \cos^2 2\theta - 4 \left(1 - \frac{P_1}{P_3}\right)^2 \sin^2 \varphi \cos^2 2\theta - 2 \right. \\
 & \cdot \left. \left(1 - \frac{P_1}{P_3}\right)^2 \sin^2 2\theta - 4 \left(1 - \frac{P_1^2}{P_3^2}\right) \cos 2\theta + \left(1 + \frac{P_1}{P_3}\right)^2\right] \left(\frac{a}{r}\right)^4 \\
 & + \left[-4 \left(1 - \frac{P_1}{P_3}\right)^2 \cos 4\theta + 2 \left(1 - \frac{P_1^2}{P_3^2}\right) \cos 2\theta - 4 \right. \\
 & \cdot \left. \left(1 - \frac{P_1^2}{P_3^2}\right) \sin^2 \varphi \cos 2\theta - \frac{4C(P_3 - P_1) \sin 2\varphi \cos 2\theta}{P_3^2}\right] \left(\frac{a}{r}\right)^2 \\
 & + \left[\left(1 - \frac{P_1}{P_3}\right)^2 - \sin^2 \varphi \left(1 + \frac{P_1}{P_3} + \frac{2C \cos \varphi}{P_3 \sin \varphi}\right)^2\right] = 0,
 \end{aligned} \tag{1}$$

where C and φ separately refer to the cohesion and internal friction angle of the borehole surrounding rock; r and θ separately represent the polar coordinates of the boundary of the plastic zone in the borehole surrounding rock; a stands for the radius of the borehole; and P_1 and P_3 denote the loads on the boundary of the model.

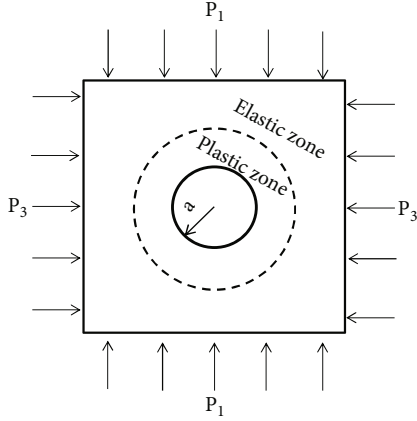


FIGURE 1: The mechanical model for the surrounding rock of borehole in nonconstant stress field.

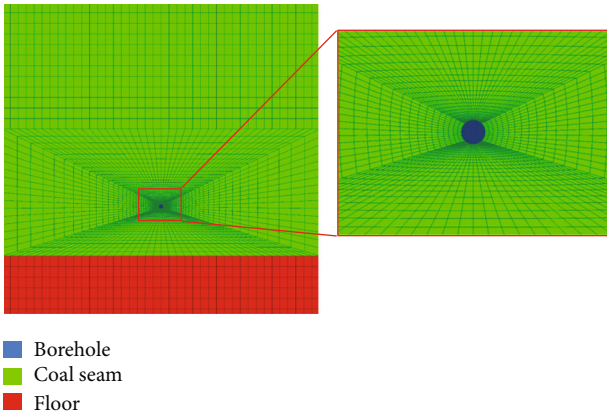


FIGURE 2: The numerical calculation model of borehole.

Therefore, the morphological characteristic and size of the plastic zone in the borehole surrounding rock depends on the stress field (that is, the bidirectional boundary load ratio P_1/P_3) of the boreholes and on fixed mechanical properties (C and φ) of the surrounding rock.

The morphological characteristics of the plastic zone in surrounding rock of the borehole were analyzed by numerical simulation method. A numerical calculation model (Figure 2) with dimensions of $40\text{ m} \times 40\text{ m} \times 1\text{ m}$ (length \times width \times thickness) was established, with the borehole diameter being 153 mm. The displacements around the model in three directions (x , y , and z) were fixed and that in the y -direction was fixed as for both the front and back boundaries. The immediate floor of the model exhibits consistent mechanical parameters with the coal seam, and the loads on the vertical and horizontal boundaries were separately set to P_1 and P_3 . The mechanical parameters of coal seam and floor are shown in Table 1.

Under different stress conditions, the plastic zone morphological characteristics of borehole surrounding rock are obviously different (Figure 3). As shown in Figure 3, when the bidirectional boundaries load ratio P_1/P_3 is 1, Figure 1 shows a mechanical model under bidirectional constant

TABLE 1: The mechanical parameters of coal seam and floor.

Lithology	σ_c /MPa	σ_t /MPa	C /MPa	φ / $^\circ$
Coal seam and floor	26	1.3	3	25

σ_c : compressive strength; σ_t : tensile strength; C : cohesion; φ : friction angle.

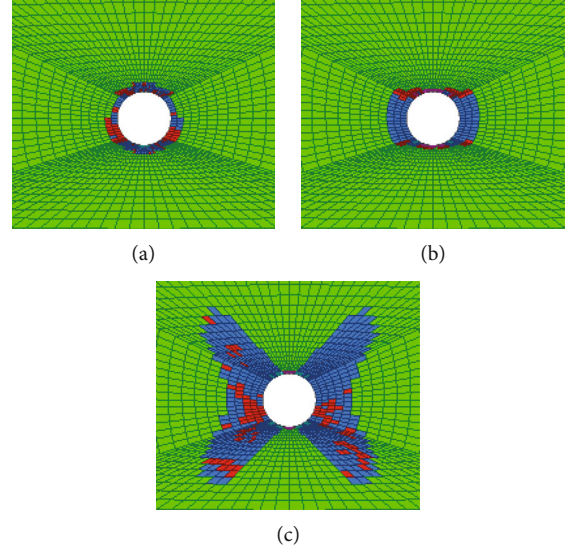


FIGURE 3: The plastic zone morphological characteristics of borehole surrounding rock under different stress conditions.

stress field, and Equation (1) for the boundary of plastic zone in borehole surrounding rock is the standard equation for circle. In this case, the boundary of the plastic zone is circular (Figure 3(a)). When P_3 remains unchanged and P_1/P_3 increases to 1.7, the boundary in the horizontal direction gradually broadens while that in the vertical direction becomes narrower. The maximum and minimum radii of the boundary of the plastic zone separately occur in the transverse and longitudinal axes, and the boundary of the plastic zone becomes ellipse-like in shape (Figure 3(b)). When P_1/P_3 reaches 2.5, the profile of the plastic zone boundary is concave at coordinate axes while protrudes in four quadrants, thus appearing as a butterfly shape (Figure 3(c)). Moreover, the maximum radius of the boundary of butterfly-shape plastic zone occurs in the vicinity of the angular bisector of the included angle between coordinate axes.

2.2. The Pressure-Relief Mechanism of Large-Diameter Borehole

2.2.1. Evolution of Plastic Zone of Large-Diameter Borehole.

According to the literature [30], Figure 4 shows the morphological characteristics of the plastic zone around boreholes with different distances to the 13230 working face in Gengcun Coal Mine when the working face is advanced by 30 m, and the borehole diameter is 153 mm.

As shown in Figure 4, at different distances to the working face, both the maximum and minimum principal stresses differ as do the morphological characteristics and range of

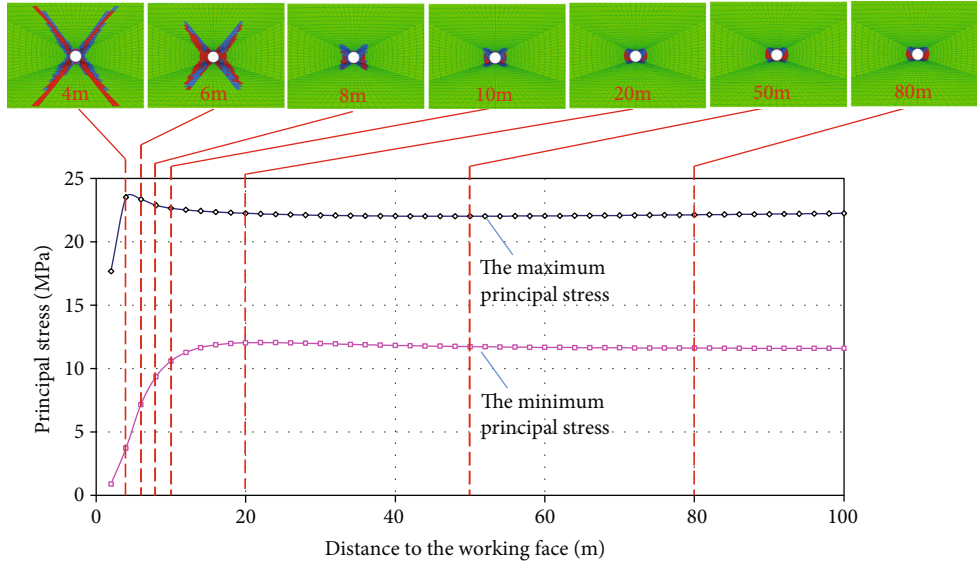


FIGURE 4: Evolution of the plastic zone around large-diameter boreholes.

the plastic zone around the large-diameter boreholes. In the range of 100 m from the working face, the plastic zone of the surrounding rock is elliptic and butterfly shape influenced by mining stress, and the smaller the distance to the working surface, the larger the size of plastic zone. At a position to the working face not lower than 20 m, the ratio of the maximum principal stress to the minimum principal stress is about 1.9, and the plastic zone is distributed in an elliptical shape, with the maximum radius occurring along the transverse axis.

The plastic zone around four shoulder angles of a borehole extend outwards at a position 10 m from the working face. With decreasing distance from the working face, the ratio of the maximum principal stress to the minimum principal stress gradually rises, and the boundary of the plastic zone in vertical and horizontal directions varies (albeit only slightly). The maximum size of the plastic zone gradually extends to the deep part along the angular bisector of the included angle between coordinate axes, and the plastic zone gradually evolves into a butterfly shape. At positions 4 m and 6 m from the working face, the maximum sizes of the butterfly wings of plastic zone are 0.91 m and 0.65 m, which are 11.9 and 8.5 times of the borehole radius.

2.2.2. The Pressure-Relief Mechanism of Large-Diameter Borehole. When constructing large-diameter boreholes in coal seam with rockburst hazard, a certain range of plastic zone is generated after coal around the boreholes is subjected to mining stress. Under certain stress conditions, the maximum radius of the plastic zone of a single borehole can be several times larger than the borehole diameter. In the case that large range plastic zones are generated and coalesce around multiple large-diameter boreholes (Figure 5), the elastic energy accumulated in the coal seam is slowly released, and the peak stress reduced as well; thus, large pressure-relief areas are formed, and the area of stress

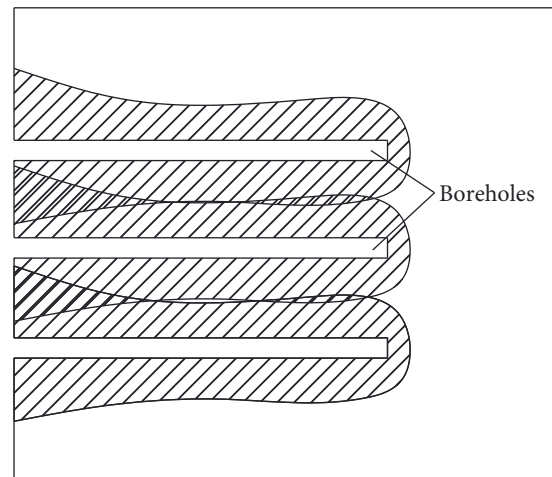


FIGURE 5: The pressure-relief principle of large-diameter boreholes.

concentration is shifted to greater depth in the coal seam. Therefore, in terms of the prevention and control of rockburst, the large-diameter borehole mainly function in two ways. One is relieving pressure, that is, the coalesced plastic zone around boreholes can alleviate the stress concentration and the rockburst hazard in coal seam. The other way is by changing the mechanical properties of coal seam, that is, the generation of plastic zone around boreholes weakens the capacity of coal seam to store elastic energy, thus decreasing the risk of rockburst [15, 31].

3. Engineering Application

3.1. Engineering Background. The Gengcun Coal Mine, located in the middle part of Yima Coalfield, Henan Province, China, is the main mine of Yima Coal Company, Henan Energy and Chemical Industry Group Co., Ltd. In the mine, the 2-3 coal seam with a dip angle of 9° to 13° is

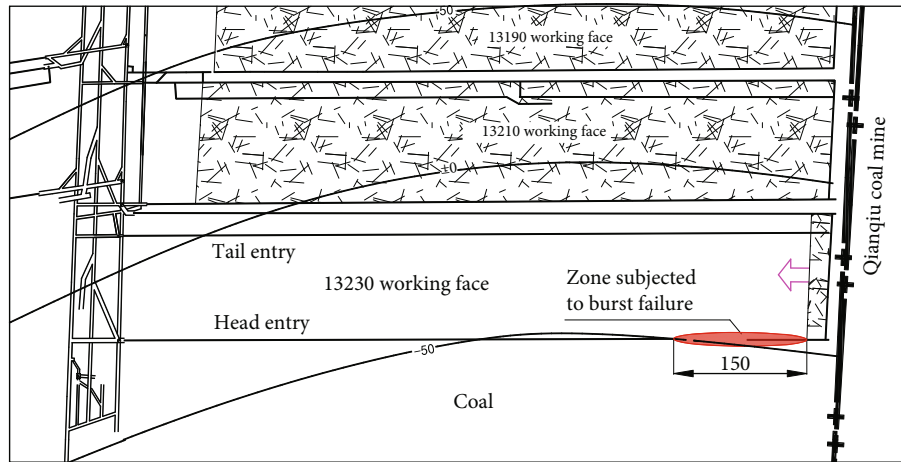


FIGURE 6: The layout of the working face of Gengcun Coal Mine.

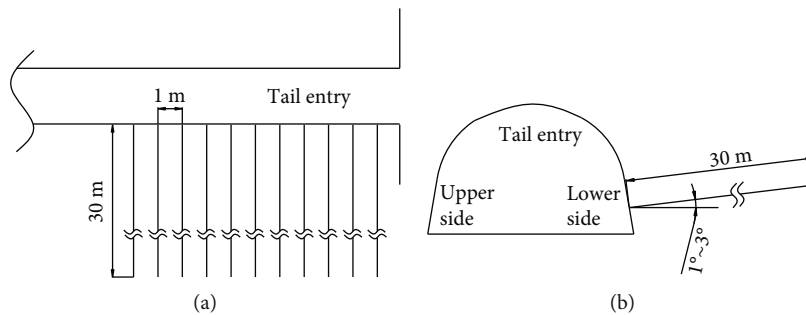


FIGURE 7: The layout of large-diameter boreholes drilled in tail entry. (a) The plan view of the large-diameter boreholes layout. (b) The crosssection of the layout of large-diameter boreholes.

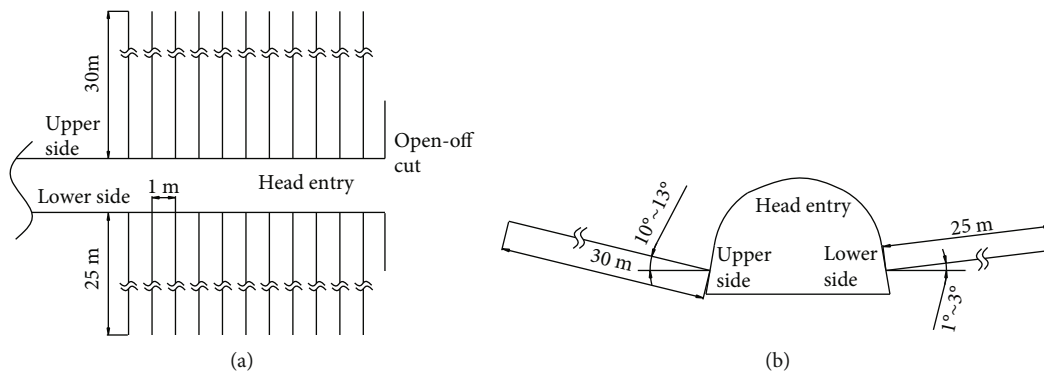


FIGURE 8: The distribution of large-diameter boreholes drilled in the head entry. (a) The plan view of the large-diameter boreholes layout. (b) The crosssection of the layout of large-diameter boreholes.

mainly mined, showing strong rockburst proneness. In December 2015, a severe rockburst accident happened in the head entry of the 13230 working face affected by the mining stress. It caused different degrees of burst failure in the roadway about 150m in front of the working face of the head entry and led to casualties and economic loss. The layout of the working face is shown in Figure 6.

Both the crosssection of the head entry and tail entry of the 13230 working face appeared as a semicircular arch mea-

suring $6.2 \text{ m} \times 4.15 \text{ m}$ (width \times height). A coal pillar with the width of 8m was set between the tail entry of the 13230 working face and the goaf of the adjacent 13210 working face.

3.2. *The Engineering Application of Large-Diameter Boreholes for Pressure Relief.* To reduce the risk of the burst failure occurring again in roadways during the mining of the 13230 working face, large-diameter boreholes were drilled

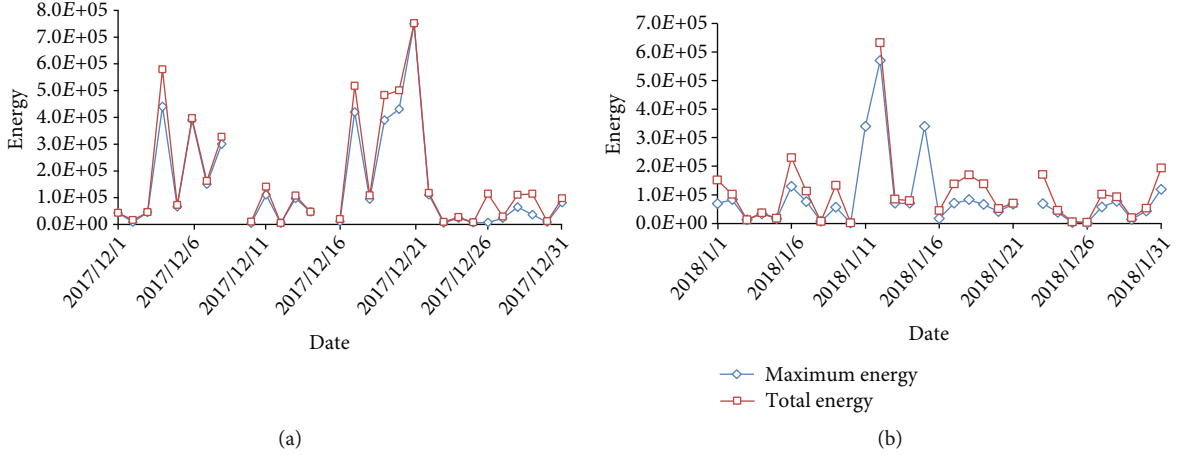


FIGURE 9: Curves of the energy and its frequency obtained based on MS monitoring. (a) MS monitoring data in December 2017. (b) MS monitoring data in January 2018.

from the lower side of the tail entry and upper and lower sides of the head entry within the range of 300 m ahead of the working face (as shown in Figures 7 and 8). To alleviate the stress concentration of the advanced abutment pressure on the working face, the depths of the large-diameter boreholes drilled from the lower side of the tail entry and the upper side of the head entry in the 13230 working face were no less than 30 m and that from the lower side of the head entry were no less than 25 m. In addition, the dip angle of the large-diameter boreholes was adjusted (as appropriate) to guarantee that the boreholes were always distributed within coal, in which the dip angle of those boreholes drilled from the upper side of the head entry was within 10° to 13° and those from the lower side of the tail entry and the lower side of the head entry were between 1° and 3° . Existing studies showed that the larger the borehole diameter, the better the pressure-relief effect; moreover, large-diameter boreholes were difficult to construct, resulting in a certain loss of construction efficiency [32]; therefore, according to the existing equipment and technical conditions, the diameter of the large-diameter boreholes for pressure relief in the 13230 working face was determined as 153 mm, and the distance between the outlet of boreholes and the roadway floor was not less than 1 m. To ensure coalescence of plastic zone around boreholes, the borehole spacing was set to 1 m.

3.3. Analysis of the Pressure-Relief Effect of Large-Diameter Boreholes

3.3.1. In Situ Monitoring. After the resumption of production in the 13230 working face, multiple rockburst-prevention measures (such as pressure relief with large-diameter borehole and coal-seam water injection) were implemented in Gengcun Coal Mine, and a monitoring and warning system (involving microseismic (MS) event monitoring and drill-cutting monitoring) was established.

Figure 9 shows MS event monitoring data from December 2017 to January 2018: the peak energy recorded reaches 10^5 J, and the maximum energy does not increase constantly

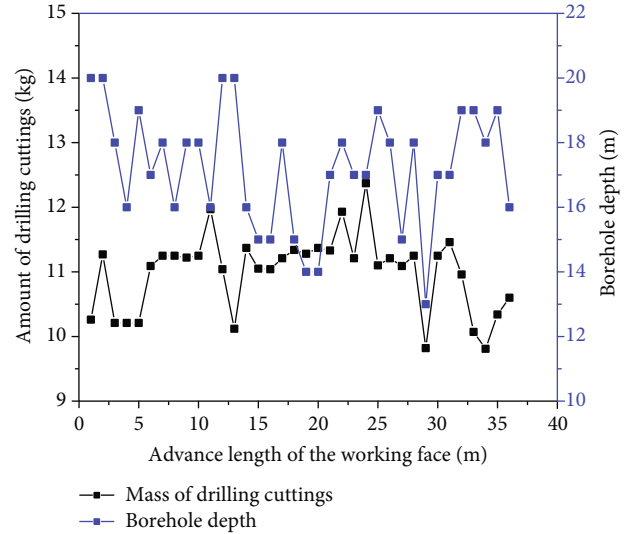


FIGURE 10: Monitored data of drill-cuttings.

TABLE 2: The critical mass of drill-cuttings to be monitored.

Borehole depth/m	4~7	7~10	10~13	13~16	16~20
Critical mass/kg	8	11	17	23	29

within 3 days. Through observation for two months, the maximum energy within each month was found to be 7.5×10^5 J and 5.7×10^5 J, respectively.

During the mining of the 13230 working face, the advance length of the working face and the borehole depth and maximum amount of drill-cuttings monitored on each occasion (with a borehole diameter of 75 mm) were recorded according to the preset monitoring range and various parameters such as the borehole depth and spacing.

The monitored results of the advance length of the working face and the maximum amount of drill-cuttings are shown in Figure 10: the 13230 working face was excavated

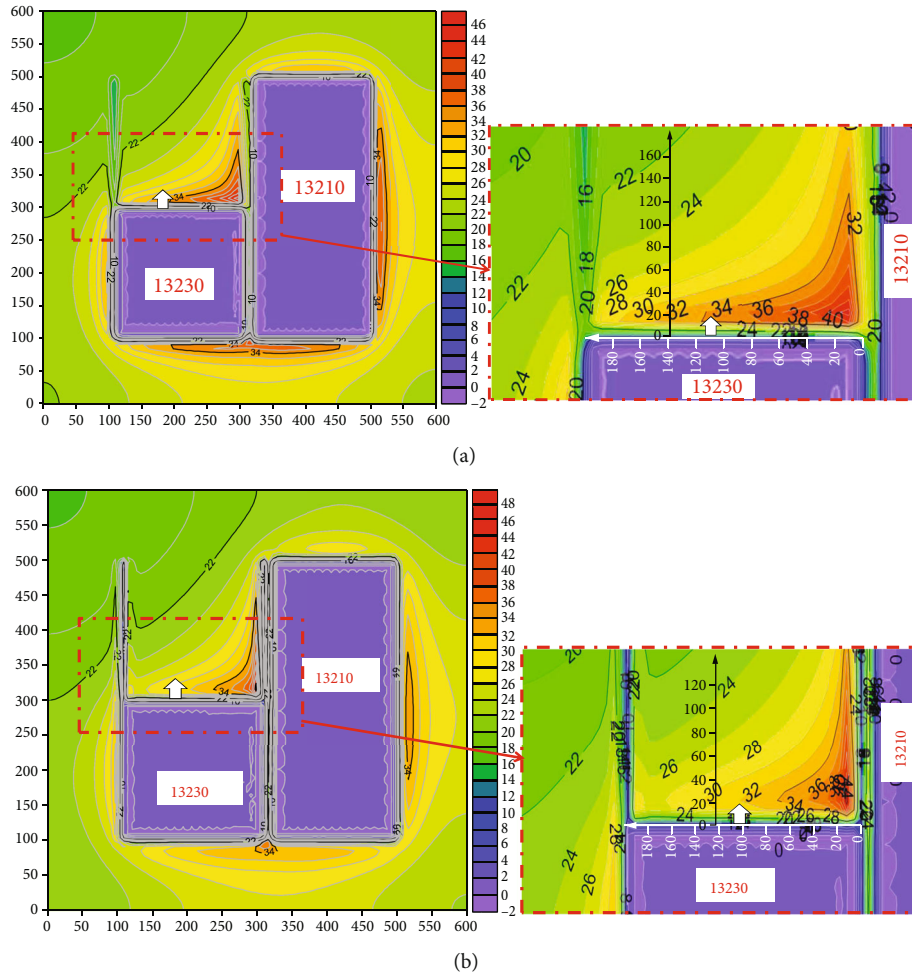


FIGURE 11: Distributions of vertical stress. (a) Without large-diameter boreholes. (b) With large-diameter boreholes.

for 36 m in total during the monitoring period; the amounts of drill-cuttings at different borehole depths were all lower than the critical value, showing insignificant fluctuations therein. The maximum amount of drilling cuttings was 12.37 kg, which corresponded to a borehole depth of 17 m, and it was much lower than the critical value (Table 2). Additionally, no burst failure appeared in the two roadways in the 13230 working face after resumption of production, allowing safe production from the mine.

3.3.2. Numerical Simulation Analysis. Before and after distributing large-diameter boreholes in segments ahead of the two roadways in the 13230 working face of Gengcun Coal Mine, the pressure-relief effect of large-diameter boreholes is compared in terms of the distribution of vertical stress in coal seam by way of numerical simulation. At first, a large numerical calculation model is established by $FLAC^{3D}$; afterwards, boreholes are excavated in the two roadways, and the 13210 and 13230 working face is mined in turn. Finally, the vertical stress on the roof of coal seam is extracted. Boundary conditions and other information about the numerical simulation analysis can be obtained from the literature [30]. After graphical postprocessing, the nephogram of the vertical stress is plotted (Figure 11).

As shown in Figure 9, the concentrated areas of vertical stress are found in front of the 13230 working face near the goaf of the 13210 working face both before and after distributing large-diameter boreholes in segments ahead of the head entry and tail entry in the 13230 working face. After large-diameter boreholes are drilled, the stress concentration in segments ahead of the head entry decreases to a significant extent. When large-diameter boreholes are not drilled to relieve this pressure, by taking the 34 MPa contour as an example, the lengths of the contour along the dip the 13230 working face are about 120 (Figure 9(a)); after relieving pressure by constructing large-diameter boreholes, the lengths of the same contour (34 MPa) along the dip of the 13230 working face are 70 (Figure 9(b)). Through comparison, it can be found that the distribution of large-diameter boreholes in two roadways can decrease the degree of stress concentration in front of the working face, thus improving the stress field around the head entry.

4. Discussion

As an effective measure for rockburst prevention, large-diameter boreholes are widely used in coal seam with rockburst risk. Many scholars have studied the pressure-relief

mechanism of large-diameter boreholes from different angles. In this paper, based on the plastic zone morphology of the surrounding rock of boreholes, it is considered that a large range of butterfly-shaped plastic zone will be produced and connected by several large-diameter boreholes in the coal seam under the mining pressure, so as to reduce the stress concentration degree of the coal seam and the capacity of storing elastic energy. Combined with the research results of existing literature, the research results of this paper will further enrich the prevention theory of rockburst and promote the safe and efficient mining of rockburst mines. In addition, there are still some limitations, such as butterfly shape plastic zone is formed in a certain surrounding rock and stress condition, and butterfly-shape plastic zone is directional, only when the butterfly wing and coal seam direction is consistent; the pressure relief effect of large-diameter drilling is the best.

5. Conclusion

Through the systematic study on the pressure-relief mechanism of large-diameter boreholes and the engineering application, we mainly get the following conclusions.

- (1) The plastic zone of borehole surrounding rock appeared in three forms, i.e., circular, elliptical, and butterfly shape. When the bidirectional boundaries load ratio reached a certain value, the length of the butterfly wings of a butterfly-shape plastic zone could be several times greater than the borehole diameter
- (2) Under certain stress conditions, multiple large-diameter boreholes drilled in coal seam with rockburst hazard induce the generation and coalescence of large-range butterfly-shaped plastic zone; moreover, they alleviate the stress concentration therein and capacity for storing elastic energy of coal seam, thus reducing the rockburst proneness of coal seam
- (3) An engineering case study was analyzed based on the performance of two roadways in the 13230 working face of Gengcun Coal Mine. The results showed that the use of large-diameter boreholes can significantly decrease the degree of stress concentration in front of the working face and improve the stress field in the head entry, thus promoting the safe mining of the working face

Data Availability

The data used to support the findings of this study are available from the corresponding author upon request.

Conflicts of Interest

The authors declare no conflict of interest.

Acknowledgments

This work was partially supported by the Natural Science Foundation of China (Grant no. 52104126), the Key Scientific Research Project of Higher Education Institutions of Henan Province (Grant nos. 20A440002 and 21A440001), the Research Fund of State and Local Joint Engineering Laboratory for Gas Drainage & Ground Control of Deep Mines (Henan Polytechnic University) (Grant no. SJF202008), and The Doctoral Cultivation Fund of Henan University of Engineering (Grant no. DKJ2019003).

References

- [1] P. Leveille, M. Sepehri, and D. B. Apel, "Rockbursting potential of kimberlite: a case study of Diavik diamond mine," *Rock Mechanics and Rock Engineering*, vol. 50, no. 12, pp. 3223–3231, 2017.
- [2] W. D. Ortlepp and T. R. Stacey, "Rockburst mechanisms in tunnels and shafts," *Tunnelling and Underground Space Technology*, vol. 9, no. 1, pp. 59–65, 1994.
- [3] W. Z. Liang, B. Dai, G. Y. Zhao, and H. Wu, "A scientometric review on rockburst in hard rock: two decades of review from 2000 to 2019," *Geofluids*, vol. 2020, 17 pages, 2020.
- [4] P. P. Procházka, "Application of discrete element methods to fracture mechanics of rock bursts," *Engineering Fracture Mechanics*, vol. 71, no. 4-6, pp. 601–618, 2004.
- [5] L. M. Dou, C. P. Lu, Z. L. Mu, Y. H. Qin, and J. M. Yao, "Intensity weakening theory for rockburst and its application," *Journal of China Coal Society*, vol. 30, no. 5, pp. 690–694, 2005.
- [6] S. V. Tsirel and N. V. Krotov, "Probability interpretation of indirect risk criteria and estimate of rock-burst hazard in mining anthracite seams," *Journal of Mining Science*, vol. 37, no. 3, pp. 240–260, 2001.
- [7] M. T. Zhang, "Instability theory and mathematical model for coal/rock bursts," *Chinese Journal of Rock Mechanics and Engineering*, vol. 6, no. 3, pp. 197–204, 1987.
- [8] Q. X. Qi and L. M. Dou, *Theory and Technology of Rockburst*, China University of Mining and Technology Press, 2008.
- [9] J. F. Pan, Y. Ning, D. B. Mao, H. Lan, T. T. Du, and Y. W. Peng, "Theory of rockburst start-up during coal mine," *Chinese Journal of Rock Mechanics and Engineering*, vol. 31, no. 3, pp. 586–596, 2012.
- [10] Y. S. Pan and M. T. Zhang, "The study of coalburst by catastrophic theory," *Journal of Fuxin Mining Institute*, vol. 11, no. 1, pp. 12–18, 1992.
- [11] S. H. Liu, "Nonlinear catastrophe model and chaotic dynamic mechanism of compound coal-rock unstable failure under coupled static-dynamic loading," *Journal of China Coal Society*, vol. 39, no. 2, pp. 292–300, 2014.
- [12] S. C. Zhang, Y. Y. Li, B. T. Shen, X. Z. Sun, and L. Q. Gao, "Effective evaluation of pressure relief drilling for reducing rock bursts and its application in underground coal mines," *International Journal of Rock Mechanics and Mining Science*, vol. 114, pp. 7–16, 2019.
- [13] Z. L. Li, L. M. Dou, W. Cai, G. F. Wang, Y. L. Ding, and Y. Kong, "Roadway stagger layout for effective control of gob-side rock bursts in the longwall mining of a thick coal seam," *Rock Mechanics and Rock Engineering*, vol. 49, no. 2, pp. 621–629, 2016.

- [14] M. Q. Huang, A. X. Wu, Y. M. Wang, and B. Han, "Geostress measurements near fault areas using borehole stress-relief method," *Transactions of Nonferrous Metals Society of China*, vol. 24, no. 11, pp. 3660–3665, 2014.
- [15] C. Y. Jia, Y. J. Jiang, X. P. Zhang, D. Wang, H. J. Luan, and C. S. Wang, "Laboratory and numerical experiments on pressure relief mechanism of large-diameter boreholes," *Chinese Journal of Geotechnical Engineering*, vol. 39, no. 6, pp. 1115–1122, 2017.
- [16] J. K. Jiao, W. J. Ju, and Y. Z. Wu, "Multi-layer control technologies for surrounding rock stability of dynamic-loading rock burst roadway," *Coal Science and Technology*, vol. 47, no. 12, pp. 10–17, 2019.
- [17] D. Li, F. X. Jiang, Y. Chen, D. C. Gai, Y. Wang, and W. B. Wang, "Study on impact mechanism and prevention technology of drainage lane of large coal pillars near deep wells," *Journal of Mining & Safety Engineering*, vol. 36, no. 2, pp. 265–271, 2019.
- [18] Z. M. Xiao, J. Liu, H. Wang, L. Sun, and H. Zhou, "Study on mechanism and control of rock burst instability of roadway floor induced by dynamic load disturbance," *Chinese Journal of Underground Space and Engineering*, vol. 15, no. 5, pp. 1573–1581, 2019.
- [19] Y. J. Qi, H. W. Jing, B. Meng, Z. X. Dong, and D. J. Liu, "Experimental modelling on size effect of pressure relief hole," *Journal of Mining & Safety Engineering*, vol. 35, no. 3, pp. 538–544, 2018.
- [20] Y. P. Li, H. W. Zhang, Z. J. Zhu, and C. Guo, "Study on safety parameters of pressure relief borehole in rockburst coal seam," *China Safety Science Journal*, vol. 28, no. 11, pp. 122–128, 2018.
- [21] S. T. Zhu, F. X. Jiang, X. F. Shi et al., "Energy dissipation index method for determining rockburst prevention drilling parameters," *Rock and Soil Mechanics*, vol. 36, no. 8, pp. 2270–2276, 2015.
- [22] H. C. Wei, "Technology and equipment of large diameter borehole construction applied to prevent and control pressure bump in coal mine," *Coal Science and Technology*, vol. 45, no. 10, pp. 140–143, 2017.
- [23] Z. P. Ba Ant, F. Lin, and H. Lippmann, "Fracture energy release and size effect in borehole breakout," *International Journal for Numerical and Analytical Methods in Geomechanics*, vol. 17, no. 1, pp. 1–14, 1993.
- [24] T. Meier, E. Rybacki, A. Reinicke, and G. Dresen, "Influence of borehole diameter on the formation of borehole breakouts in black shale," *International Journal of Rock Mechanics and Mining Science*, vol. 62, pp. 74–85, 2013.
- [25] T. Meier, E. Rybacki, T. Backers, and G. Dresen, "Influence of bedding angle on borehole stability: a laboratory investigation of transverse isotropic oil shale," *Rock Mechanics and Rock Engineering*, vol. 48, no. 4, pp. 1535–1546, 2015.
- [26] H. Lee, T. Moon, and B. C. Haimson, "Borehole breakouts induced in arkosic sandstones and a discrete element analysis," *Rock Mechanics and Rock Engineering*, vol. 49, no. 4, pp. 1369–1388, 2016.
- [27] D. P. Sahara, M. Schoenball, E. Gerolymatou, and T. Kohl, "Analysis of borehole breakout development using continuum damage mechanics," *International Journal of Rock Mechanics and Mining Science*, vol. 97, pp. 134–143, 2017.
- [28] Y. Han and F. Y. Zhang, "Progress in research on instability mechanism of coalbed borehole," *Journal of Safety Science and Technology*, vol. 10, no. 4, pp. 114–119, 2014.
- [29] X. F. Yu, Y. R. Zheng, H. H. Liu, and Z. C. Fang, *The Stability Analysis of Surrounding Rocks of Underground Engineering*, China Coal Industry Press, 1983.
- [30] H. T. Liu, Z. Hao, X. Y. Wu, X. D. Zhao, L. F. Guo, and Z. Y. Ma, "Mechanism of blast disaster induced by instantaneous malignant expansion of plastic zone," *Journal of China Coal Society*, vol. 42, no. 6, pp. 1392–1399, 2017.
- [31] J. Liu, Z. H. Ouyang, Q. X. Qi, S. K. Zhao, and X. L. Li, "Rigid-flexibility integrated energy absorption support technology applied in deep mine with pressure bumping," *Coal Science and Technology*, vol. 41, no. 6, pp. 17–20, 2013.
- [32] H. J. Liu, "Drilling pressure relief technology and effect of bilateral goaf island working face," *Coal Engineering*, vol. 48, no. 4, pp. 58–61, 2016.

Research Article

Investigation of Shale Permeability Evolution considering Bivalued Effective Stress Coefficients for CO₂ Injection

Yi Wang^{1,2,3}, Hao Wang⁴, Shangyi Qi⁵, Shimin Liu⁶, Yixin Zhao^{1,2,3} and Wenting Yue⁷

¹School of Energy & Mining Engineering, China University of Mining and Technology, Beijing 100083, China

²State Key Laboratory of Coal Resources and Safe Mining, China University of Mining and Technology, Beijing 100083, China

³Beijing Key Laboratory of Precision Mining of Intergrown Energy and Resources, China University of Mining and Technology, Beijing 100083, China

⁴Liaohu Oilfield Gas Storage Company, PetroChina, Panjin 124010, China

⁵Research Institute of Petroleum Engineering, Sinopec, Beijing 102206, China

⁶Department of Energy and Mineral Engineering, G³ Center and Energy Institute, The Pennsylvania State University, University Park, PA 16802, USA

⁷Research Institute of Petroleum Exploration and Development, China National Petroleum Corporation, Beijing 100083, China

Correspondence should be addressed to Yi Wang; yiwan.evan@cumtb.edu.cn

Received 3 August 2021; Revised 29 August 2021; Accepted 30 August 2021; Published 1 October 2021

Academic Editor: Afshin Davarpanah

Copyright © 2021 Yi Wang et al. This is an open access article distributed under the Creative Commons Attribution License, which permits unrestricted use, distribution, and reproduction in any medium, provided the original work is properly cited.

Because of the existence of multiscale pores from nano- to macroscale, a multimechanistic shale gas flow process involving the Darcy and Knudsen flows occurs during gas shale well depletion. The respective contribution of the Darcy and Knudsen flows to the permeability is constantly changing with pressure evolution. In this study, laboratory measurements of shale permeability with CO₂ injections were carried out under hydrostatic conditions, using the transient pulse-decay method. The “U”-shape permeability curve resulted in both positive and negative effective stress coefficients (Biot’s coefficient) χ . A permeability turning point was thus created to partition permeability curves into the Darcy and Knudsen sections. The Knudsen effect was proven to be significant at low pressure/late time in the laboratory. Effective stress and sorption-induced deformation have been found to govern the Darcy permeability evolution under the tested experimental conditions. Thus, negative effective stress coefficients, together with the positive ones, should be applied to a nonmonotonic pressure-permeability evolution to explain the concurrent effect of the Darcy flow and Knudsen flow at different pore pressures.

1. Introduction

Gas shale reservoirs have played an important role in natural gas world supply. Hydraulic fracturing stimulation is an effective method to create fracture networks that can connect shale formations to horizontal boreholes [1]. However, low matrix permeability retards gas migration from the tight matrix into the fracture networks. Pore diameters of the shale matrix can be smaller than 2 nm, which is significantly smaller than average pore size in conventional sandstone and carbonate reservoirs [2–5]. The shale matrix, which includes organic matter and clay minerals, serves as the storehouse for gas but limits gas transport due to its low permeability and low diffusivity. The tight structure can involve

a variety of flow dynamics processes, making the evaluation of gas migration behaviors intricate and challenging.

Gas transport in shales contains Darcy flow and Knudsen flow [6, 7] and the shrinkage/swelling response of organic components of shale due to gas desorption/adsorption [8–10]. The extremely tight structure of a shale core sample without apparent fractures can limit the gas transmission flux under high effective stress conditions during shale permeability laboratory tests. Since permeability testing time scales with the square of diffusion length, shorter shale core samples were used for permeability measurement which practically made laboratory testing feasible and time effective. In addition, permeability values obtained using classic Darcy’s law may not be valid if non-Darcian flow is

taking place [11]. Nanopore and micropore gas flow along with sorption effect needs to be separately characterized and integrated to account for the multimechanistic shale gas flow process [12]. In the above laboratory and modeling researches, they have massively discussed gas flow mechanisms in shale with different stress conditions under various pore scales. However, there is no certain conclusion either on how to reflect those flow types in a gas permeability test or on giving a comprehensive physical understanding to the effective stress in a shale gas flow process. In an actual shale gas flow process, due to the extremely small pore size and/or volume in shale formations and the complex matrix shrinkage/swelling effect, conventional Darcy flow and diffusion models cannot, on their own, describe gas flow transport in shale formations [6]. A multimechanical method includes the analysis and breakdown of the Darcy viscous flow, and the Knudsen flow is thus needed.

In this study, two cut and polished shale samples were used to conduct permeability tests using the pulse-decay method. The Darcy flow and Knudsen flow were separately analyzed to determine their respective contributions to total gas transport. Other important effects—such as effective stress and sorption-induced deformation, which have been frequently reported in unconventional rock studies—were considered to influence gas transport properties. Gas flow mechanisms and effective stress law were fully considered, and their physical meaning was discussed in a laboratory scale through data analysis.

2. Background

2.1. Shale Gas Flow Regimes. During shale gas reservoir production, the Darcy flow permeability is still a prevailing term used to quantify gas deliverability through shale fractures and matrices. However, the Knudsen diffusion is just as important as Darcy's convective flow in unconventional gas production prediction. Figure 1 shows multiple flow mechanisms during gas shale reservoir depletion according to some existing flow partitioning criteria [13, 14]. The average monthly production for 15 wells in the Eagleford Shale formation shows that peak production occurred late in the second month after the fracturing treatment. This was followed by a rapid decline until the 20th month; then, there was a production plateau at a relatively low production rate. Early in production, fracture (Darcy) flow dominated since free gas molecules were flowing through hydraulic fractures (large-diameter flow channels) and occupying the flow path, driven by pressure gradient. Production reached its peak very quickly due to fracture flow. Following peak production, rapid decline occurred due to quick depletion of compressive fracture gas storage.

However, desorption could be involved during the pressure decline stage; only a negligible amount of matrix gas contributed to production because of the slow diffusion process [16–18]. Generally, the Knudsen diffusion flow at this stage does not dominate total gas production compared to the free gas flowing through the fractures. Gas transport mechanism moves from continuum flow to a transition zone between the Darcy flow and Knudsen diffusion. This transi-

tion zone includes slip flow ($0.001 < K_n < 0.1$) and transition flow ($0.1 < K_n < 1$), where neither continuum flow nor free molecular flow is valid [16]. Gas flow in this zone can be considered a combination of the Darcy flow and Knudsen diffusion. After the fractures are depleted, a late-time asymptotic flow takes place, when reservoir fracture pressure becomes very low. At this stage, although fracture permeability is sufficient, gas influx from the matrix towards the fractures will take over the role of fracture permeability to control the well production. This mass influx from the matrix towards the fracture is a multimechanistic micro/nanoscale transport. Methane molecules first desorb from the internal surfaces of the matrix within the nanopore system due to fluid pressure driving force and become free gas [19, 20]. During the desorption process, the distance between the shale gas surface molecule layer and the adjacent molecules decreases, and the effective surface energy on the shale kerogen surface increases [21]. As a result, kerogen shrinkage also occurs in the shale matrix and enhances the nanopore flow path for gas molecules (Figure 2). Because of the wide range of pore sizes within the shale matrix, a combination of multiple flow regimes can be expected. Most gas molecules migrate through the nanopores by means of the Knudsen diffusion flow. The diffusion-dominated flow can remain operational for decades, contributing to the late production flat tail. Gas flow permeability evolution at the late-time production stage is critical and significantly influences the production behaviors [18]. In short, shale gas transport during production includes different flow regimes (Darcy, slip flow, transition flow, and Knudsen diffusion with gas desorption) at every stage, but their respective contributions to the total production change with decreasing pore pressure as the depletion continues.

The breakdown of different flow regimes, such as the Darcy flow, slip flow, and transition flow, can be classified and distinguished by the Knudsen number (K_n), which is a function of pore size and pore pressure [22, 23]:

$$K_n = \frac{\lambda}{2r}, \quad (1)$$

where λ is the gas mean free path, defined in Nomenclature and Greek Symbols:

$$\lambda = \frac{k_B T}{\sqrt{2} \pi d_m^2 P}. \quad (2)$$

The relationship between K_n , pore size, and pressure for CO₂ is also plotted in Figure 3, over the experimental pressure range used for the subsequent laboratory study. The temperature was at 296 K (room temperature). For Marcellus Shale reservoirs, the pore diameter is expressed in nanometers and micrometers [24]. Within the pore size range given in Figure 3, gas flow in the shale matrix lies mostly within the transition flow and slip flow region. It can potentially involve the Darcy flow regime if the pressure is sufficiently large or include the Knudsen diffusion when this pressure is low. In order to assess these flow mechanisms,

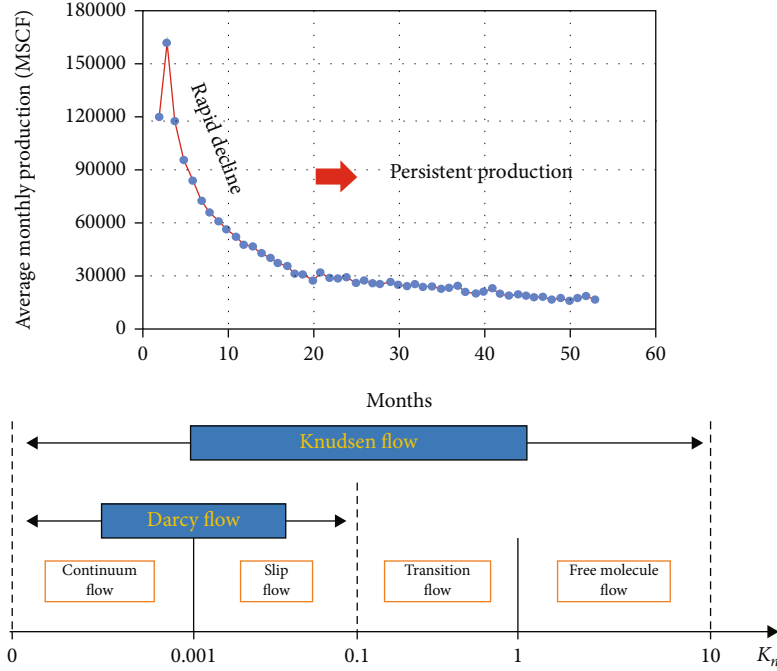


FIGURE 1: Average monthly gas production of 15 production wells in the Eagleford Shale Group with flow regime breakdown from large-scale Darcy/continuum flow to Knudsen diffusion/molecular flow, from [15].

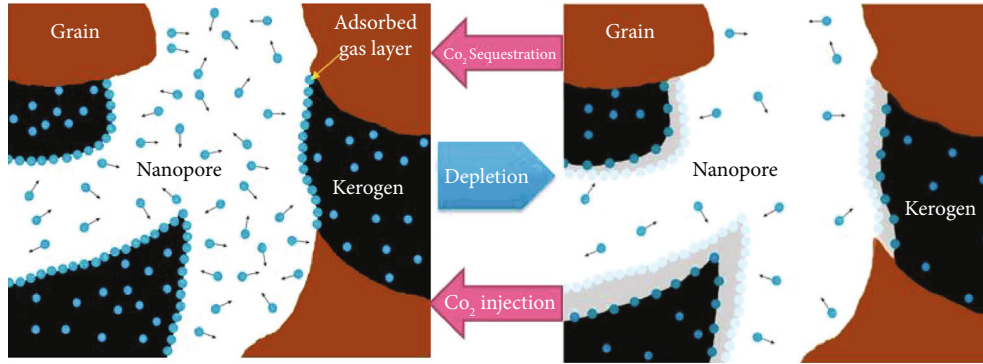


FIGURE 2: Gas desorption process in nanoscale. During gas production, gas molecules firstly desorb from the kerogen surface to the pore and then move outward due to pressure/concentration drop. Then, kerogen tends to shrink, together with the matrix.

the permeability measurements in this work were all conducted at relatively low pore pressures (<10 MPa) to ensure that 2~3 flow regimes can be covered. Since transition flow and slip flow can be modeled as a weighted combination of the pure Poiseuille flow (Darcy) and Knudsen flow [13, 25], coupled flow regimes were applied to describe gas flow and permeability evolution for gas flow in the shale matrix.

2.2. Permeability Measurement. Brace et al. first introduced the pulse-decay technique as a transient method derived from Darcy’s law and used to measure permeability by applying a pressure difference between two sides of a core sample [26]. Hsieh et al. derived more restrictive analytical solutions of the differential equation, describing decay curves from permeability measurement with compressive storage effect [27]. The exact solution of the differential

equation for dimensionless pressure difference and dimensionless time was improved and shown as [28]

$$\Delta p_D = 2 \sum_{n=1}^{\infty} \frac{a(b^2 + \theta_n^2) - (-1)^n b \sqrt{(a^2 + \theta_n^2)(b^2 + \theta_n^2)}}{\theta_n^2(\theta_n^2 + a + a^2 + b + b^2) + ab(a + b + ab)} \times e^{(-\theta_n^2 t_d)}, \quad (3)$$

where a and b are the ratio of the sample’s storage capacity to that of the upstream reservoir and downstream reservoir and θ_n is the n th root of the following equation:

$$\tan \theta = \frac{(a + b)\theta}{\theta^2 - ab}, \quad (4)$$

where $a = V_p/V_u$ and $b = V_p/V_d$.

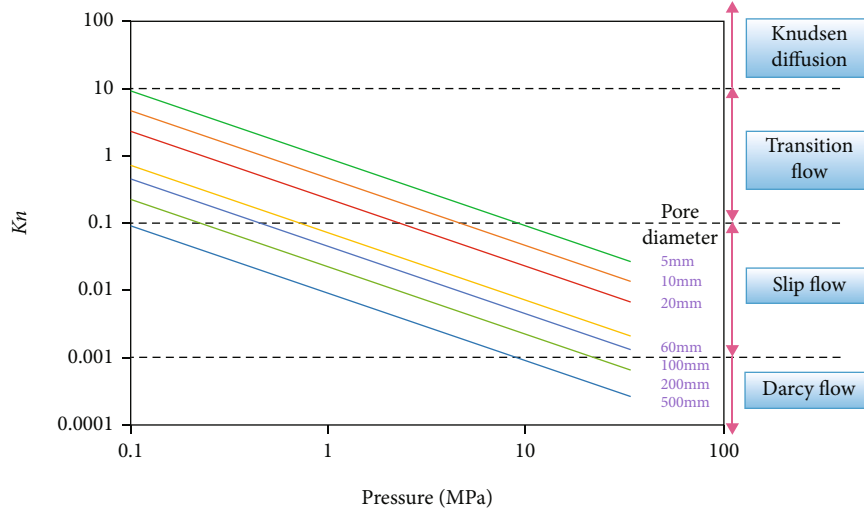


FIGURE 3: K_n changing with pressure and pore diameter for CO_2 at 296 K. Mostly, the flow is lying in the transition flow and slip flow region.

To simplify the above method, Jones introduced a factor f as follows [29]:

$$f = \frac{\theta^2}{a + b}. \quad (5)$$

The pulse-decay equation can be described as

$$P_u(t) - P_d(t) = (P_u(t_0) - P_d(t_0))e^{-\alpha t}, \quad (6)$$

$$\alpha = \left(\frac{fkA}{\mu c_g L} \right) \left(\frac{1}{V_u} + \frac{1}{V_d} \right). \quad (7)$$

Laboratory estimation of shale permeability for unconventional reservoir rocks conducted under hydrostatic conditions with an adsorption effect was reported by Cui et al. An effective adsorption porosity term was introduced to account for the contribution of gas molecule adsorption. The Langmuir model was used to quantify gas adsorption volume as a function of pressure [30] and mathematically described as follows:

$$V_a = \frac{V_L P}{P_L + P}. \quad (8)$$

So, the sample storage capacity ratio in Cui et al.'s approach becomes

$$a = \frac{V_p(1 + (\phi_a/\phi))}{V_u}, \quad (9)$$

$$b = \frac{V_p(1 + (\phi_a/\phi))}{V_d},$$

where $\phi_a = \rho_s(1 - \phi)P_L V_a / \rho V_{std} C_g (P_L + P)^2$. Recently, Wang et al. pointed out that Cui et al.'s method highlighted the contribution of the sorption effect in permeability calculation, demonstrating how the gas sorption effect can help to



FIGURE 4: Photograph of a slice of the Marcellus shale drilled core sample cut into a disk with 5.39 mm in thickness and 25.4 mm in diameter.

predict gas permeability [31]. Since our study involved handling organic-rich shale samples, the pulse-decay permeability calculation method proposed by Cui et al. was chosen to estimate apparent permeability for sorbing gas.

2.3. Effective Stress. To quantify the influence of effective stress on gas permeability, confining and pore pressures should be carefully related to rock and gas properties in pulse-decay tests. Terzaghi effective stress (or simple effective stress), as a function of confining and pore pressure according to Terzaghi's principle, is defined as [32]

$$\sigma_{\text{Ter}} = P_c - P. \quad (10)$$

However, for permeability tests, the effective stress law with an appropriate coefficient has been used instead of Terzaghi's principle [14, 33, 34]:

$$\sigma_e = P_c - \chi P. \quad (11)$$

To experimentally calculate the effective stress coefficient χ , the ratio of the slope method was presented by Kwon et al.:

$$\chi = - \frac{(\partial \log k / \partial p)}{(\partial \log k / \partial p_c)}. \quad (12)$$

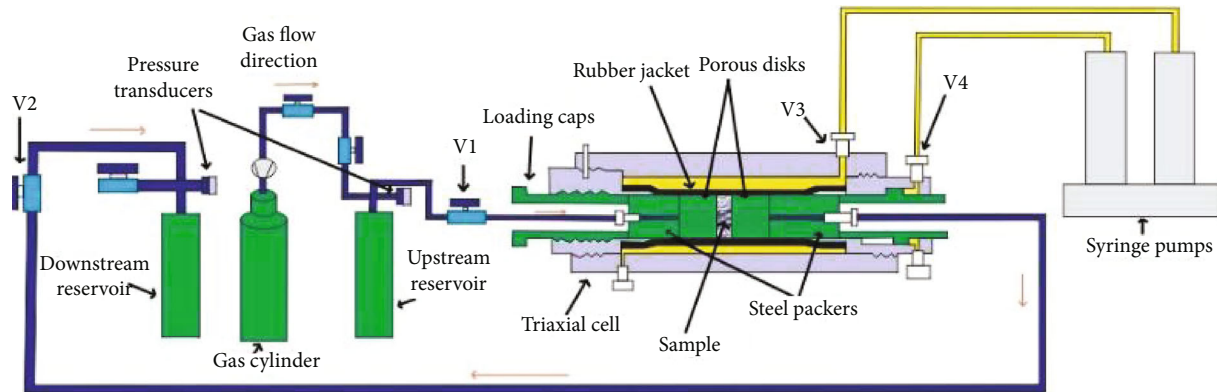


FIGURE 5: Schematic view of the pulse-decay experimental setup for the permeability evolution test. V1 is the valve controlling inlet gas flow from upstream, V2 is the valve controlling outlet gas flow to downstream, and V3/V4 is the valve controlling the confining/axial pressure applied on the sample.

The effective stress coefficient represents the sensitivity of permeability to the changes in confining and pore pressures.

3. Experimental Methods

3.1. Sample Procurement and Preparation. With tight structure, equilibrium time for pressure pulse-decay is extremely long for long core samples. This long equilibrium time reduces the efficiency of lab testing, and no pressure drop was observed under very high stress conditions after a few hours of pulse injection. Therefore, shale disks were preferable for permeability measurements; they can significantly shorten equilibrium time and are commonly used for shale permeability measurements [14]. Thus, in this study, Marcellus Shale drilled cores were prepared as thin disks for the gas apparent permeability tests. The prepared thin disks ranged in thickness from 3 to 6 mm and were 25.4 mm in diameter. All trimmed surfaces were polished to enable proper placement in the triaxial cell. Two well-prepared shale samples of different thickness are used in this work, and one of them is shown in Figure 4. Each disk sample has been weighed and placed in an oven for the first 24 hours at 150°C to remove the moisture. The second weighing was conducted before they were put into the oven again. We repeated this procedure until the sample weights remain stable. After the shale sample disks were dried in the oven, they were weighed in a dry and clean plastic sample bag in a lab-use alloy box for 3 hours before testing.

3.2. Experimental Stress Boundary Conditions. Hydrostatic conditions were applied in this series of shale permeability measurements, in which axial stress was equal to confining pressure (p_c) at a constant value throughout the duration of each experiment. Hydraulic stresses were regulated with computer-controlled syringe pumps using software developed in the LabView environment.

3.3. Experimental Setup and Procedure. The measurements presented in this study are recovered from a standard triaxial apparatus arranged for flow-through or pulse permeability

testing as shown in Figure 5. The apparent permeabilities of two Marcellus Shale samples of different thickness were measured under hydrostatic pressure. Using carbon dioxide as the test gas, the permeability of sorbing gas (CO_2) was compared by using a high-pressure pump for confining pressure loading and gas pressurization. The experiment process is as follows: (1) apply a certain confining pressure to the sample chamber, and vacuum the fluid pipeline and sample at the same time. (2) In the upstream of the system to the part of valve 1, inject a certain pressure of the test gas, the sample, and the downstream part of the original state. (3) After the injection pressure is stabilized, open valve 1, drive the gas pulse through the shale sample by the pressure difference between the upstream and downstream, read the pressure data after the overall pressure balance of the system, and close valve 1. (4) Repeat steps (1) to (3) until all planned pressure levels are tested.

The balancing time lasts for 30 minutes to ensure that the balancing process is complete. In the experiment, four groups of complete cycle permeability tests were carried out on samples of 5.39 mm and 3.71 mm with CO_2 under hydrostatic pressure of 11 and 21 MPa, respectively. Each group of tests was repeated once, and a total of 16 groups of tests were carried out. Finally, based on multiple groups of pressure data obtained in the experiment, equations (6) and (7) were used to calculate sample permeability. An entire CO_2 injection cycle on the 5.39 mm sample at 11 MPa is displayed in Figure 6.

4. Results

The measured permeability results of CO_2 for two disk samples (two cycles each) are shown in Figure 7. According to Figure 7, the repeatability of the permeability measurements is good. Also, the permeability data for the two samples are extremely close to each other, with very similar trends. In our experiments, the structures of the shale sample matrix were not damaged due to the application of a high confining and/or pore pressure. Our measured permeability values are relatively high among some reported shale permeabilities [35], due to the microfractures present in the shale disk

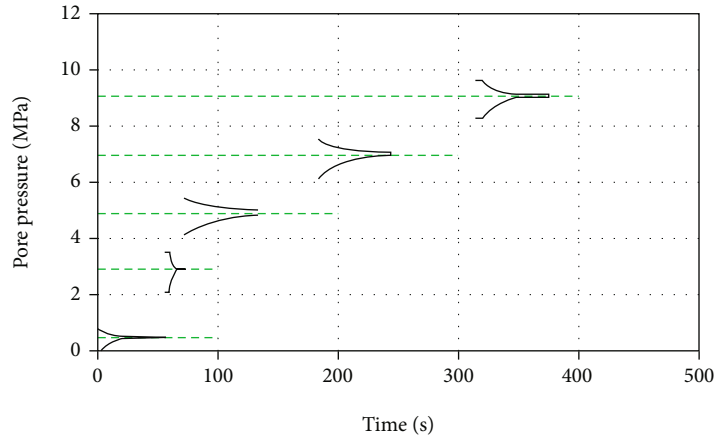


FIGURE 6: Pulse-decay pressure responses for the CO_2 injection test with the confining (hydrostatic) pressure at 11 MPa.

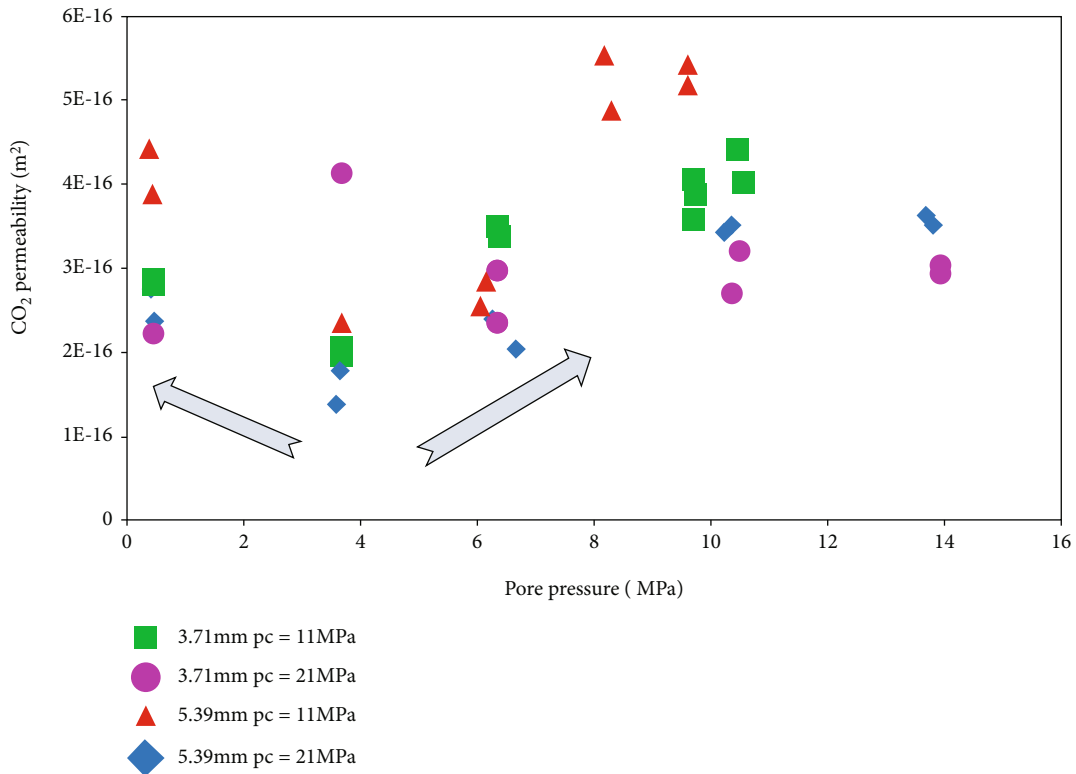


FIGURE 7: Permeability data with CO_2 injection on shale thin disks (3.71 mm and 5.39 mm) under 11 and 21 MPa confining (hydrostatic) pressure, processed by using Cui et al.'s method.

samples. These permeability measurements are still reasonable because Gensterblum reported a collection of permeability data for an organic shale sample case, with permeability ranging from $1\text{E} - 15 \text{ m}^2$ to $3\text{E} - 19 \text{ m}^2$ with a porosity of 2-8%. And the measured porosity of our Marcellus drilled samples ranges from 2% to 5.1%, obtained using the Small-Angle Neutron Scattering (SANS) technique, with a permeability range of 1.5 to $7\text{E} - 16 \text{ m}^2$. Based on the two sample observations in this study, the consistency of data between samples different in length indicates that the matrix structures for the sample collected from the same source can be

very similar. Consistent and accurate results help us justify the utility of collected experimental data and consolidate any hypotheses and conclusions based on them.

4.1. Permeability Evolution with Pore Pressure. For both samples, shale permeabilities showed similar evolution patterns. All the permeability values initially declined when pore pressure ranges from 0.35 to 4 MPa, then started to make a slight or sharp turn, and increased with the decrease in the Terzaghi stress, since the Terzaghi stress is negatively and linearly associated with pore pressure. At low pore

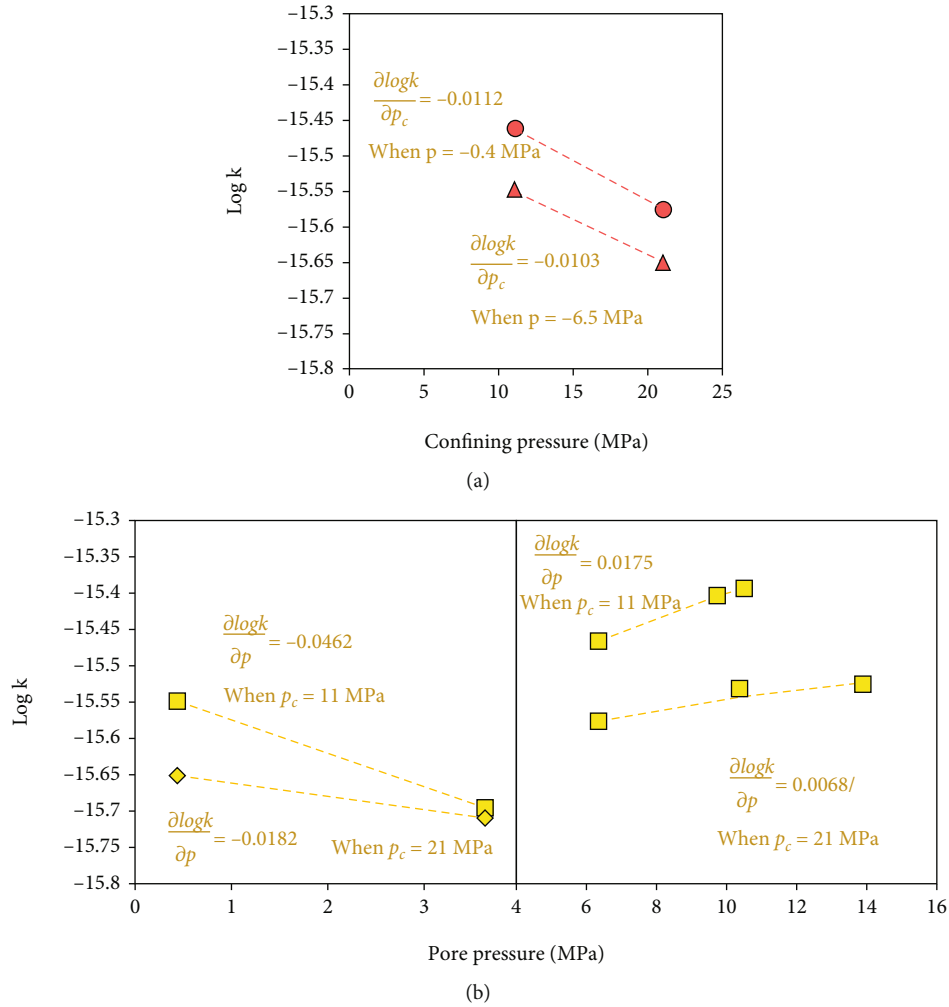


FIGURE 8: (a) CO₂ permeability data of a 3.71 mm shale disk linearized by plotting a logarithm of permeability versus confining pressures at constant pore pressures to determine the sensitivity of confining pressure to permeability. (b) CO₂ permeability data of a 3.71 mm shale disk linearized by plotting a logarithm of permeability versus p at constant confining pressures to determine the sensitivity of pore pressure to permeability. The slopes are positive when pressures are above ~4 MPa and negative when below ~4 MPa.

pressure, nano-/microscale transport, such as the Knudsen diffusion, dominates and has a decreasing contribution with increasing average pore pressure. With decreasing Terzaghi stress, shale gas permeability still has a decreasing tendency in the pore pressure range 4 to 14 MPa. This is because the nano- and micropores and the low gas pressure limit the contribution of the Darcy flow.

4.2. Permeability Evolution with Effective Stress. In order to further study and address the impact of effective stress on shale permeability, confining pressures (p_c) and pore pressures (p) were linearly plotted with the logarithm of apparent permeability (k) to determine the effective stress coefficient (χ) and the effective stress (σ_e). The result of permeability versus confining pressures at constant pore pressures for the 3.71 mm shale sample is shown in Figure 8(a). Almost the same slopes were obtained from two pore pressure points, which led to $\Delta \log k / \Delta p_c$ equal to -0.0112 when pore pressure is 0.4 MPa and -0.0103 when pore pressure is 6.5 MPa. The negative values indicate that

apparent permeabilities decrease with the increase in confining pressure [14, 34].

Then, we plotted $\partial \log k / \partial p$ values when p_c is equal to 11 MPa and 21 MPa for the 3.71 mm sample, respectively, breaking down the pressure at ~4 MPa into two divisions. In Figure 8(b), we can clearly observe that the slopes for $\log k$ versus p are always positive at high pore pressure division (>4 MPa) and negative at low pressure division (<4 MPa). These unexpected slopes resulted from the change of the controlling flow regime during pressure depletion. The Knudsen diffusion and slip are more important because the ratio of the mean free path to the pore throat is larger. This is due to lower pressure and narrowing of pore throats (flow paths).

On the other hand, Kwon et al. and Heller et al. obtained only one positive slope when plotting $\log k$ versus p . They may have assumed χ as one property for identical rock samples and only vary with the distribution of quartz and clay minerals. This means that the number of effective stress coefficients obtained depends on the monotony of the

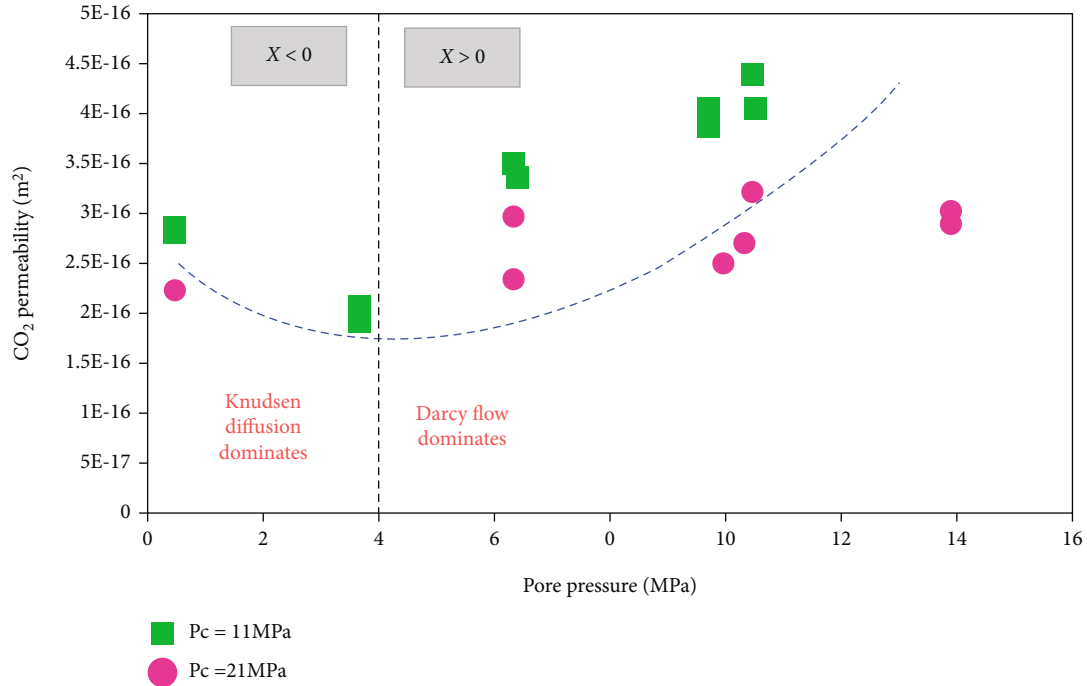


FIGURE 9: Permeability evolution curve evaluated by bivalued effective stress coefficients for the 3.71 mm shale disk sample.

permeability data profile, and it may not be valid to apply a unique χ value to evaluate the relationship between permeability and effective stress.

Using equation (12), we calculated the effective stress coefficients for each individual $\partial \log k / \partial p$. Corresponding to the $\partial \log k / \partial p$ values, χ became negative at low pressure (<4 MPa) and positive at high pressure (>4 MPa). According to equation (12), we will obtain a positive χ when $\partial \log k / \partial p$ is positive and vice versa. Within both low and high pressure sections, permeability decreases with the raise of effective stress based on effective stress law, which is consistent with previous results presented by Kwon et al. and Heller et al. In this study, we applied both positive and negative effective stress coefficients based on “U”-shape permeability evolution trends at varying pressure levels. These two different χ approaches will allow us to account for the non-Darcian flow components using the traditional effective stress concept.

5. Discussion

5.1. Impact of Flow Mechanisms on Permeability. Our permeability measurements were conducted at a relatively low pressure (<10 MPa), in order to address the diffusion and transition flow effect. Permeability values can reach an extremely high peak due to opening of the transport pore space resulting from confining pressure reduction. So, at the early stage of gas shale well production, low confining pressure (due to high initial reservoir pressure) and highly opened fractures significantly promote the Darcy flow suggested by high apparent permeability. The Darcy flow plays a more important role at this circumstance while the Knudsen flow always happens simultaneously, according to Figure 1. At the late stage, low pore pressure combined with

narrow flow paths not only increases the Knudsen number but also increases the contribution of Knudsen flow components [36]. This is one of the main reasons for researchers to integrate multiple flow influxes into an apparent permeability model framework to describe the pore pressure-dependent gas transport property in the shale matrix.

We know that in CO₂ capture in coal seams, carbon dioxide acts as a “plasticizer” for coal, lowering the temperature required to cause the transition from a brittle structure to a plastic structure after CO₂ is adsorbed by the coal matrix [37]. Permeability can be thus affected by the sequent changes of shale structure due to high stress and matrix swelling/shrinkage. In the shale layer, kerogen softening was observed quite significantly with CO₂ injection (supercritical CO₂ in many cases) employed as an enhanced recovery process [38]. So, our measured permeability data increase with CO₂ injection at higher pressure can be explained, since this enhancement was found when $p > 6.9$ MPa at 295 K when CO₂ has encountered phase change—CO₂ transforms from gaseous condition to supercritical condition. Supercritical CO₂ can result in the decrease in its maximum adsorption amount compared to gaseous condition [39]. With less adsorption, the shale matrix tends to shrink and permeability will thus increase. This observation proves that gas adsorption behavior and sorption-induced matrix deformation in the shale matrix are very critical in describing shale gas apparent permeability evolution. In practice, the matrix swelling strain associated with gas adsorption tends to close the cleat aperture and thus decrease permeability [40]. With the increasing upstream pressure from a very low level, a reduction in permeability can be seen until the Darcian flow starts to take control, and permeability increases again with the gradual loss of

effective stress. In conclusion, both sorption-induced deformation and diverse flow behavior between gases explain the CO₂ permeability trends. We need to couple the influence of sorption-induced rock deformation and the change of flow regimes to account for shale gas production.

5.2. Effective Stress Coefficient. When pressure is larger than 4 MPa, the effective stress coefficient was found to be positive and less than unity, indicating that the shale sample is experimentally more sensitive to changes in confining pressure than changes in pressure. This may result from very low clay content in the rock sample [34]. On the other hand, the absolute value of χ is larger than unity at low pressure (<4 MPa), meaning that permeability is more sensitive to pore pressure change. The difference in χ values and monotony of permeability indicate that the “check”-shape or “U”-shape permeability trends can be explained by certain physical theories rather than by random occurrence, as shown in Figure 9. 4 MPa was found to be a good reference pore pressure for permeability turning point in most of our data. Although this number may not be a guaranteed value for other samples or other conditions, this phenomenon has been captured a lot in theory and practice. The relationship between effective stress and gas apparent permeability contains critical information, not only about tectonic stress change and geological deformation but also about the pore pressure response that reflects how multiple flow regimes influence permeability evolution at varying pressure conditions. All these findings from shale permeability data and effective stresses lead to the conclusion that it is critical to consider the concurrent effect of both geomechanical deformation and macro/microflows.

6. Conclusions

A laboratory study has been conducted to investigate the gas transport in thin shale disk samples through CO₂ injections. The influence of effective stress and sorption-induced matrix swelling/shrinkage on permeability was investigated. The following conclusions are made and summarized:

- (1) The non-Darcy flow effect, basically the Knudsen flow and transition flow, has significant influence on shale gas behavior and overall gas deliverability at low reservoir pressure and in the late production stage
- (2) The relationship between permeability and pore pressure results in both positive and negative slopes when plotted. The negative slope indicates that the Knudsen flow effect has more significant enhancement on permeability than the reduction from increasing effective stress. Thus, bivalued effective stress coefficients (positive and negative) should be applied to a nonmonotonic pressure-permeability evolution profile
- (3) For “U”-shape permeability evolution, the effective stress coefficient can be estimated by partitioning permeability into two regions at the turning point.

This bivalued effective stress coefficient approach can use the effective stress law concept to explain and model the Knudsen flow at the low-pressure region. In the study, it was found that 4 MPa is the turning point, and we obtained bivalued coefficients that modeled experimental data well

Nomenclature

A :	Cross-sectional area of the sample (m ²)
a :	Ratio of the sample's storage capacity to that of the upstream reservoir (dimensionless)
b :	Ratio of the sample's storage capacity to that of the downstream reservoir (dimensionless)
C_g :	Gas compressibility (Pa ⁻¹)
d_m :	Molecular diameter (m)
f :	Mass flow correction factor (dimensionless)
L :	Sample length (m)
k :	Gas apparent permeability (m ²)
k_B :	Boltzmann constant (1.3805×10^{-23} J/K)
P :	Pore pressure (Pa)
P_c :	Confining pressure (Pa)
$P_d(t)$:	Pressure of downstream at time t (Pa)
$P_d(t_0)$:	Initial pressure of downstream (Pa)
P_L :	Langmuir pressure (Pa)
$P_u(t)$:	Pressure of upstream at time t (Pa)
$P_u(t_0)$:	Initial pressure of upstream (Pa)
r :	Pore radius (m)
T :	Temperature (K)
V_a :	Gas adsorbed volume (cm ³ ·g ⁻¹)
V_d :	Downstream reservoir volume (m ³)
V_L :	Langmuir volume (cm ³ ·g ⁻¹)
V_P :	Effective total sample pore volume (m ³)
V_{std} :	Mole volume of gas at standard temperature (273.15 K) and pressure (101 325 Pa) (22.413×10^{-3} m ³ ·mol ⁻¹)
V_u :	Upstream reservoir volume (m ³).

Greek Symbols

α :	Slope of the line when plotting the pressure decay $P_u(t) - P_d(t)$ against time on a semilog plot (dimensionless)
ΔP_D :	Dimensionless pressure difference (dimensionless)
θ_n :	The n th root of the transcendental equation ($\tan \theta = (a + b)\theta/(\theta^2 - ab)$) (dimensionless)
λ :	Gas mean free path (m)
μ :	Gas viscosity (Pa·s)
ρ :	Gas density (kg/m ³)
ρ_s :	Density of the solid adsorbent (kg/m ³)
σ_e :	Effective stress (Pa)
σ_{Ter} :	Terzaghi effective stress (Pa)
ϕ :	Matrix porosity (dimensionless)
χ :	Effective stress coefficient (dimensionless).

Data Availability

The data used to support the findings of this study are available from the first author upon request.

Conflicts of Interest

The authors declare that there are no conflicts of interest regarding the publication of this article.

Acknowledgments

This work is supported in part by the Beijing Municipal Natural Science Foundation (No. 8214063), the Fundamental Research Funds for the Central Universities (No. 2021YQNY08), and the National Natural Science Foundation of China (Nos. 51861145403 and 51874312).

References

- [1] S. Yang, S. Liu, N. Zhang, G. Li, and J. Zhang, "A fully automatic-image-based approach to quantifying the geological strength index of underground rock mass," *International Journal of Rock Mechanics and Mining Sciences*, vol. 140, article 104585, 2021.
- [2] V. Swami, C. Clarkson, and A. Settari, "Non-Darcy flow in shale nanopores: do we have a final answer?," in *SPE Canadian Unconventional Resources*, pp. 1–17, Calgary, Alberta, Canada, 2012.
- [3] S. Liu, *Estimation of different coal compressibilities of coalbed methane reservoirs under replicated in situ condition*, Southern Illinois University at Carbondale, 2012.
- [4] J. E. Heath, T. A. Dewers, B. J. O. L. McPherson et al., "Pore networks in continental and marine mudstones: characteristics and controls on sealing behavior," *Geosphere*, vol. 7, no. 2, pp. 429–454, 2011.
- [5] T. A. Dewers, J. Heath, R. Ewy, and L. Duranti, "Three-dimensional pore networks and transport properties of a shale gas formation determined from focused ion beam serial imaging," *International Journal of Oil, Gas and Coal Technology*, vol. 5, no. 2/3, p. 229, 2012.
- [6] F. Javadpour, "Nanopores and apparent permeability of gas flow in mudrocks (shales and siltstone)," *Journal of Canadian Petroleum Technology*, vol. 48, no. 8, pp. 16–21, 2009.
- [7] Y. Li, X. Li, J. Shi, H. Wang, L. Wu, and S. Teng, "A nano-pore scale gas flow model for shale gas reservoir flow characteristic of shale gas reservoir in various pole scales and molecule scales," in *SPE Energy Resources Conference*, pp. 9–11, Trinidad and Tobago, Spain, 2014.
- [8] K. Wu, X. Li, C. Wang, Z. Chen, and W. Yu, "A model for gas transport in microfractures of shale and tight gas reservoirs," *AIChE Journal*, vol. 61, no. 6, pp. 2079–2088, 2015.
- [9] X. Cui, A. M. M. Bustin, and R. M. Bustin, "Measurements of gas permeability and diffusivity of tight reservoir rocks: different approaches and their applications," *Geofluids*, vol. 9, no. 3, p. 223, 2009.
- [10] H. Kumar, D. Elsworth, J. P. Mathews, and C. Marone, "Permeability evolution in sorbing media: analogies between organic-rich shale and coal," *Geofluids*, vol. 16, no. 1, p. 55, 2016.
- [11] A. Liu, P. Liu, and S. Liu, "Gas diffusion coefficient estimation of coal: a dimensionless numerical method and its experimental validation," *International Journal of Heat and Mass Transfer*, vol. 162, article 120336, 2020.
- [12] F. Civan, C. Rai, and C. Sondergeld, "Shale-gas permeability and diffusivity inferred by improved formulation of relevant retention and transport mechanisms," *Transport in Porous Media*, vol. 86, no. 3, pp. 925–944, 2011.
- [13] H. Darabi, A. Etehad, F. Javadpour, and K. Sepehrnoori, "Gas flow in ultra-tight shale strata," *Journal of Fluid Mechanics*, vol. 710, pp. 641–658, 2012.
- [14] R. Heller, J. Vermylen, and M. Zoback, "Experimental investigation of matrix permeability of gas shales," *American Association of Petroleum Geologists Bulletin*, vol. 98, no. 5, pp. 975–995, 2014.
- [15] Y. Wang, *Laboratory Estimation and Modeling of Apparent Permeability for Ultra-Tight Anthracite and Shale Matrix: A Multi-Mechanistic Flow Approach*, The Pennsylvania State University, 2017.
- [16] E. Robertson and R. Christiansen, "A permeability model for coal and other fractured, sorptive-elastic media," *SPE Journal*, vol. 13, no. 3, pp. 314–324, 2008.
- [17] W. Yuan, Z. Pan, X. Li et al., "Experimental study and modeling of methane adsorption and diffusion in shale," *Fuel*, vol. 117, pp. 509–519, 2014.
- [18] Y. Wang and S. Liu, "Estimation of pressure-dependent diffusive permeability of coal using methane diffusion coefficient: laboratory measurements and modeling," *Energy and Fuels*, vol. 30, no. 11, pp. 8968–8976, 2016.
- [19] D. D. Do, *Adsorption Analysis: Equilibria and Kinetics*, Imperial College Press, 1998.
- [20] J. Fan, P. Liu, J. Li, and D. Jiang, "A coupled methane/air flow model for coal gas drainage: model development and finite-difference solution," *Process Safety and Environment Protection*, vol. 141, pp. 288–304, 2020.
- [21] S. Liu and S. Harpalani, "Compressibility of sorptive porous media: part 1. Background and theory," *AAPG Bulletin*, vol. 98, no. 9, pp. 1761–1772, 2014.
- [22] F. Zeng, Y. Zhang, J. Guo et al., "A unified multiple transport mechanism model for gas through shale pores," *Geofluids*, vol. 2020, Article ID 894149, 17 pages, 2020.
- [23] G. Karniadakis, A. Beskok, and A. Narayan, *Microflows and Nanoflows*, Springer Science & Business Media, 2005.
- [24] C. R. Clarkson, N. Solano, R. Bustin et al., "Pore structure characterization of North American shale gas reservoirs using USANS/SANS, gas adsorption, and mercury intrusion," *Fuel*, vol. 103, pp. 606–616, 2013.
- [25] U. Kuila, M. Prasad, and H. Kazemi, "Assessing Knudsen flow in gas-flow models of shale reservoirs," *Recorder*, vol. 38, pp. 23–27, 2013.
- [26] W. F. Brace, J. B. Walsh, and W. T. Frangos, "Permeability of granite under high pressure," *Journal of Geophysical Research*, vol. 73, no. 6, pp. 2225–2236, 1968.
- [27] P. A. Hsieh, J. V. Tracy, C. E. Neuzil, J. D. Bredehoeft, and S. E. Silliman, "A transient laboratory method for determining the hydraulic properties of 'tight' rocks—I. Theory," *International Journal of Rock Mechanics and Mining Science and Geomechanics Abstracts*, vol. 18, no. 3, pp. 245–252, 1981.
- [28] A. I. Dicker and R. M. Smits, "A practical approach for determining permeability from laboratory pressure-pulse decay measurements," in *SPE International Meeting on Petroleum Engineering*, pp. 285–292, Tianjin, China, 1988.
- [29] S. C. Jones, "A technique for faster pulse-decay permeability measurements in tight rocks," *SPE Formation Evaluation*, vol. 12, no. 1, pp. 19–26, 1997.

- [30] I. Langmuir, "The adsorption of gases on plane surfaces of glass, mica and platinum," *Journal of the American Chemical Society*, vol. 345, p. 1918, 1914.
- [31] Y. Wang, S. Liu, and D. Elsworth, "Laboratory investigations of gas flow behaviors in tight anthracite and evaluation of different pulse-decay methods on permeability estimation," *International Journal of Coal Geology*, vol. 149, pp. 118–128, 2015.
- [32] K. Terzaghi, *Theoretical Soil Mechanics*, John Wiley & Sons, Inc., New York, London, 1943.
- [33] M. D. Zoback and J. D. Byerlee, "Permeability and effective stress: geological notes," *AAPG Bulletin*, vol. 59, no. 1, pp. 154–158, 1975.
- [34] O. Kwon, A. K. Kronenberg, A. F. Gangi, and B. Johnson, "Permeability of Wilcox shale and its effective pressure law," *Journal of Geophysical Research*, vol. 106, no. B9, pp. 19339–19353, 2001.
- [35] Y. Gensterblum, A. Ghanizadeh, R. J. Cuss et al., "Gas transport and storage capacity in shale gas reservoirs - a review. Part a: transport processes," *Journal of Unconventional Oil and Gas Resources*, vol. 12, pp. 87–122, 2015.
- [36] Y. Wang, S. Liu, and Y. Zhao, "Modeling of permeability for ultra-tight coal and shale matrix: a multi-mechanistic flow approach," *Fuel*, vol. 232, pp. 60–70, 2018.
- [37] O. Bolland, *Carbon Dioxide Capture*, Cambridge University Press, 2009.
- [38] S. Lee, J. G. Speight, and S. K. Loyalka, *Handbook of Alternative Fuel Technologies*, CRC Press, 2015.
- [39] P. Chareonsuppanimit, S. A. Mohammad, R. L. Robinson Jr., and K. A. M. Gasem, "High-pressure adsorption of gases on shales: measurements and modeling," *International Journal of Coal Geology*, vol. 95, pp. 34–46, 2012.
- [40] S. Liu, Y. Wang, and S. Harpalani, "Anisotropy characteristics of coal shrinkage/swelling and its impact on coal permeability evolution with CO₂ injection," *Greenhouse Gases: Science and Technology*, vol. 6, no. 5, pp. 615–632, 2016.

Research Article

CFD-Based Determination of the Optimal Blowing and Suction Air Volume Ratio of Dual-Radial Swirl Shielding Ventilation in a Fully Mechanized Excavation Face

Kuan Wu ^{1,2}, Shiliang Shi ^{1,2}, Yijie Shi ^{1,2} and Yong Chen ^{1,3,4}

¹School of Resource & Environment and Safety Engineering, Hunan University of Science and Technology, Xiangtan, China

²Hunan University of Science and Technology Southern Coal Mine Gas and Roof Disaster Prevention and Control and Safety Production Key Experiment, China

³China Coal Technology Engineering Group Chongqing Research Institute, Chongqing 400037, China

⁴National Key Laboratory of Gas Disaster Detecting, Preventing and Emergency Controlling, Chongqing 400037, China

Correspondence should be addressed to Kuan Wu; 170101020001@mail.hnust.edu.cn

Received 21 June 2021; Accepted 21 August 2021; Published 17 September 2021

Academic Editor: Bo Tan

Copyright © 2021 Kuan Wu et al. This is an open access article distributed under the Creative Commons Attribution License, which permits unrestricted use, distribution, and reproduction in any medium, provided the original work is properly cited.

Dust is one of the main pollutants in coal mines, which seriously affects the physical and mental health of workers, as well as the safe production in underground mines. Dual-radial swirl shielding ventilation is a new ventilation method for a fully mechanized excavation face and can effectively reduce the dust concentration in the underground. The dust control effect of dual-radial swirl shielding ventilation is mainly affected by the thickness and integrity of the shielding air curtain, as well as the disturbance of the flow field near the air curtain. By changing the blowing and suction air volume ratio of the air duct, the strength of the radial air curtain can be improved, and the dust control effect of the dual-radial swirl shielding ventilation system can be effectively improved. In order to determine the optimal operating parameters of the dual-radial swirl shielding ventilation system, a numerical simulation method was used to conduct an in-depth study on the blowing and suction air volume ratio of the system. The results showed that when the blowing and suction air volume ratio of the air duct was 1.5, the radial air curtain had the highest strength. Under this condition, the dust concentration at the driver's position of the roadheader was the lowest, and the dual-radial swirl shielding ventilation system can achieve an ideal dust control effect.

1. Introduction

Coal resources are an important energy mineral resource. China's total coal consumption accounts for about 60% of the country's total energy consumption [1, 2]. With the increasing level of intelligence, mechanization, and automation of mines, potential hazards such as gas, coal dust, and fires have increased, especially dust pollution of mines, which seriously affects the safety of enterprises and the occupational health of workers [3–5]. In 2019, China reported 19,428 new cases of various occupational diseases, of which 15,898 were occupational pneumoconiosis, accounting for 81.8% of the new cases of various occupational diseases [6–8]. The direct economic loss caused by pneumoconiosis in China is more than 8 billion RMB per year, and the indirect loss is even

more difficult to calculate. There is still a lot of room for improvement in the development of dust control theory and technology [9, 10].

The fully mechanized excavation face has the most serious dust hazard in underground coal mines [11–13]. At present, the fully mechanized excavation face mainly uses coal seam water injection, spraying, and ventilation to reduce the dust concentration. Due to the characteristics of large dust production and small dust particle size in the fully mechanized excavation face, compared with other dust removal technologies, ventilation and dust control are the most convenient and efficient technology to reduce the concentration of dust in the fully mechanized excavation face without affecting the working environment in the roadway [14–16]. The ventilation and dust control technology of the fully mechanized

excavation face are to control the dust within a certain area around the fully mechanized excavation face by regulating the airflow field and to prevent the spread of dust from the excavation face [17, 18]. Currently, coal mines in China and other countries mainly adopt long-pressure and short-extraction ventilation to dilute the excavated dust and suck the dust-containing airflow into the dust collector for purification [19, 20]. However, since the use of circulating air is prohibited, the traditional long-pressure and short-exhaust ventilation requires the air supply volume to be greater than the suction air volume, so the dust-containing gas at the tunneling end cannot be exhausted by the suction tube. As a result, the dust is widespread in the roadway under the action of the air supply flow [21–24]. In order to prevent the large-scale spread of dust in the roadway, former West Germany first developed a wall-attached air duct. A wall-attached duct is a duct with an air outlet on the side of the air supply duct to improve the distribution of the airflow field in the fully mechanized excavation face. The airflow from the side air outlet forms a shielding air curtain on the roadway to prevent the spread of dust and improve the dust-catching effect of the air inlet. The wall-attached air duct can greatly improve the working environment of the fully mechanized excavation face, prevent gas accumulation on the top of the roadway, and ensure the safe production of the mine [25, 26]. However, the radial air curtain produced by the wall-attached air duct has a relatively weak rotation ability, and it is very easy to form a hollow air curtain due to the serious impact of the roadway environment. As a result, the dust-blocking ability is insufficient [27, 28].

In order to solve the problems of high dust concentration and turbulent air organization in the fully mechanized excavation face, the wall-attached swirl ventilation system was improved to form a new type of ventilation system for the fully mechanized excavation face, i.e., the dual-radial swirl shielding ventilation system. In this study, by taking the fully mechanized excavation face of a coal mine in northern China as the research object, a new dual-radial swirl shielding ventilation system for the fully mechanized face was designed. A simulated tunnel model was built to scale, and the airflow field structure and dust movement rules in the roadway under the dual-radial swirl shielding ventilation system were studied using Fluent software, especially the dust concentration in the working area of the roadheader driver. The validity of the numerical simulation was verified through a custom-built roadway model experiment platform. Finally, numerical simulations were used to study the dust control effect of the dual-radial swirl shielding ventilation system under different air duct blowing and suction volume ratios, and the working condition parameters for the best dust control were obtained.

2. Principle of Dual-Radial Swirl Shielding Ventilation and Dust Control

Dual-radial swirl shielding ventilation is a new ventilation method for a fully mechanized excavation face. Its working principle is somewhat similar to that of wall swirling ventilation; that is, a radial air curtain is formed on the section of

the roadway to block the spread of dust. Compared with the radial air curtain formed by the wall swirling ventilation, the radial air curtain formed by the dual-radial swirl shielding ventilation has a higher strength. It is because in the dual-radial swirl shielding ventilation, the formed rotating air curtain on the fully mechanized excavation face is produced by an arc-shaped wind deflector. Compared with the rotating air curtain produced by the attachment of the roadway, the shielding air curtain formed by the dual-radial swirl shielding ventilation system has a larger radial wind speed, even distribution, and a larger thickness. Therefore, the dual-radial swirl ventilation has a better effect in preventing the spread of dust.

During the excavation, the dust concentration in the roadway is extremely high. Turn on the dust removal fan and the blower, adjust the air valve, and deliver all the airflow to the air pressure sleeve; then, the air is discharged radially from the air curtain generator device at both ends of the sleeve. Under the action of the air curtain generating device, a rotating radial solid air curtain is formed between the tunneling end and the driver's cab of the roadheader, and another radial air curtain is formed between the driver's cab and the transfer point. Under the negative pressure of the suction port, the 1# air curtain near the tunneling end forms an umbrella-shaped swirling air curtain that rushes toward the tunneling end to control the dust produced by the tunneling within a small area. The controlled dust is drawn out by the suction tube to prevent the dust from spreading to the driver's cab, thus providing a good working environment for the driver. The 2# air curtain located in front of the transfer point isolates the dust at the transfer point from the driver's position, thus preventing dust from spreading from the transfer point to the driver's position. The synergistic action of the two air curtains can effectively isolate the two main dust sources of the fully mechanized excavation face from the area of the driver of roadheader, providing a good working environment for the driver. Figure 1 shows a schematic diagram of dual-radial swirl shielding ventilation on the fully mechanized excavation face when the roadheader works normally.

3. Calculation Model and Validation

3.1. Calculation Model and Meshing. By taking the fully mechanized excavation face of a coal mine in China as a prototype, a numerical simulation geometric model with a ratio of 1:1 was established by Solidworks software. The fully mechanized excavation face is a semicircular arched roadway with a cross-section of 4.6 m × 4.5 m and a cross-sectional area of 15.81 m². The fully mechanized excavation face is tunneled with an EBZ160 roadheader. Figure 2 shows the diagram of the roadway model. From the figure, the air supply tube I has a diameter of 0.8 m and a tube length of 25 m. It is attached to a sidewall of the roadway. Its axis is 2.7 m away from the ground of the roadway, and the air outlet at the end is 5 m away from the excavation face. The sleeve is composed of air supply tube II and the air suction tube. The air supply tube II is outside, and the suction tube is inside. The center axis of the sleeve is 2.7 m from the

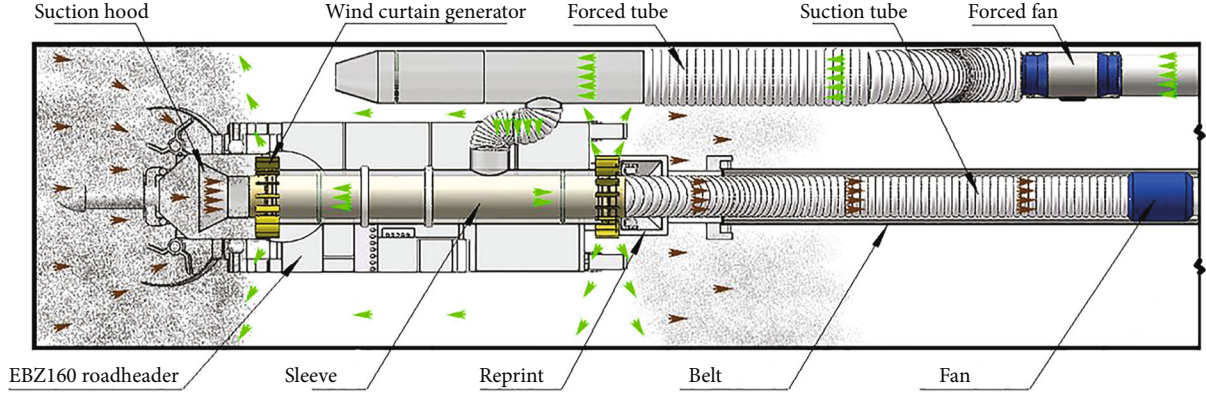


FIGURE 1: Schematic diagram of dual-radial swirl shielding ventilation.

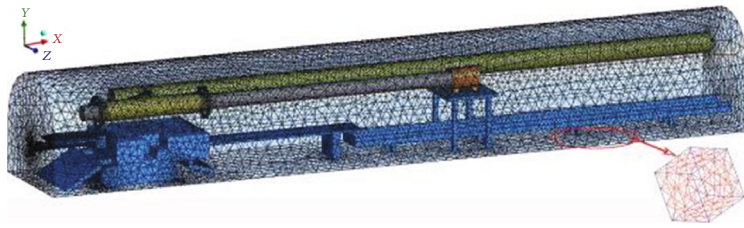


FIGURE 2: Schematic diagram of meshing.

ground of the roadway. There is an annular slit with a width of 0.09 m at each end of the air supply cylinder II, and an air curtain-generating device is arranged outside the annular slit. The diameter of the suction tube is 0.6 m, and its suction outlet at the end is 2.3 m away from the excavation face. A 1.8 m high roadheader, a first conveyor, and a second conveyor are arranged under the sleeve. The driver is 5 m from the excavation face.

Mesh software was used to mesh the built roadway model. Because the geometric model was relatively complex, the model was meshed with an adaptable unstructured grid and the global grid size was set to 0.4 mm. For arc-shaped wind deflectors and annular slits, 0.01 m grids were used for local densification. For other more complex structures, 0.05 m grids were used for local densification. A total of 932,351 grids were generated.

3.2. Mathematical Model. Since the volume fraction of dust in the fully mechanized excavation face was far below 10%, when using Fluent software to analyze the characteristics of the wind flow field and dust distribution, the $k-\varepsilon$ double equation model from the Euler model was used to establish the mathematical model of the wind flow field in the fully mechanized excavation face. In addition, according to the characteristics of the gas-dust particle two-phase flow and the theory of the gas-solid two-phase flow, the Euler-Euler model and the Euler-Lagrangian model were combined for calculation.

3.2.1. Hydrodynamic Equation. Based on the law of conservation of energy, the law of conservation of momentum, and the law of conservation of mass, the characteristics of

fluid motion are expressed in terms of continuity equation, momentum equation, and energy equation [29, 30].

Continuity equation:

$$\frac{\partial \rho}{\partial t} + \frac{\partial}{\partial x_i} (\rho u_i) = S_m \quad (1)$$

Momentum equation:

$$\frac{\partial}{\partial t} (\rho u_i) + \frac{\partial}{\partial x_j} (\rho u_i u_j) = -\frac{\partial p}{\partial x_i} + \frac{\partial \tau_{ij}}{\partial x_j} + \rho g_i + F_i \quad (2)$$

Energy equation:

$$\frac{\partial}{\partial t} (\rho E) + \frac{\partial}{\partial x_i} (u_i (\rho E + p)) = \frac{\partial}{\partial x_i} \left(k_{\text{eff}} \frac{\partial T}{\partial x_i} - \sum_j h_j J_j' + u_j (\tau_{ij})_{\text{eff}} \right) + S_h \quad (3)$$

where S_m is the mass added to the continuous phase from the dispersed secondary phase; p is the static pressure; τ_{ij} is the stress tensor that will be described below; ρg_i and F_i are the gravitational volume force and external volume force in i direction, respectively; k_{eff} is the effective heat transfer coefficient; J_j' is the diffusion flow of component j ; and S_h includes the heat of chemical reaction and the volume heat source term.

3.2.2. Turbulence Equation. Turbulence occurs where the velocity changes. Compared with the standard $k-\varepsilon$ model, the realizable $k-\varepsilon$ model can accurately predict the divergence ratio of the cylindrical jet and it has been used to

describe uniform shear flow with the rotating, free flow of the mixed flow and boundary layer flow effectively. And the realizable k - ε model in the turbulence model can achieve a higher degree of simulation in terms of the vortex, strong streamline bending, and rotation. In addition, among many k - ε models, the realizable k - ε model has a good effect on the complicated secondary flow and separation flow. The realizable k - ε model consists of a k equation (turbulent energy equation) and an ε equation (turbulent energy dissipation rate equation) [31, 32]. Therefore, this study selected realizable k - ε for describing airflow motion.

κ equation:

$$\frac{\partial(\rho k)}{\partial t} + \frac{\partial(\rho k u_i)}{\partial x_i} = \frac{\partial}{\partial x_j} \left[\left(\mu + \frac{\mu_t}{\sigma_k} \right) \frac{\partial k}{\partial x_j} \right] + G_k - \rho \varepsilon. \quad (4)$$

ε equation:

$$\frac{\partial(\rho \varepsilon)}{\partial t} + \frac{\partial(\rho \varepsilon u_i)}{\partial x_i} = \frac{\partial}{\partial x_j} \left[\left(\mu + \frac{\mu_t}{\sigma_\varepsilon} \right) \frac{\partial \varepsilon}{\partial x_j} \right] + \rho C_1 E \varepsilon - \rho C_2 \frac{\varepsilon^2}{k + \sqrt{v \varepsilon}}. \quad (5)$$

In the formulas, μ_t is the eddy viscosity coefficient; σ_k and σ_ε are the Prandtl coefficients corresponding to k and ε , respectively; G_k is the turbulent flow energy generation term caused by the average velocity gradient; C_1 and C_2 are constants; u is the fluid velocity; and J_i is the material diffusion flux produced by the concentration gradient.

3.2.3. Equations of Motion for Particles. ANSYS Fluent predicts the trajectory of a discrete phase particle (or droplet or bubble) by integrating the force balance on the particle, which is written in a Lagrangian reference frame. This force balance equates the particle inertia with the forces acting on the particle and can be written as

$$m_p \frac{d\vec{u}_p}{dt} = m_p \frac{\vec{u} - \vec{u}_p}{\tau_r} + m_p \frac{\vec{g}(\rho_p - \rho)}{\rho_p} + \vec{F}, \quad (6)$$

where m_p is the particle mass, \vec{u} is the fluid phase velocity, \vec{u}_p is the particle velocity, ρ is the fluid density, ρ_p is the density of the particle, \vec{F} is an additional force, $m_p((\vec{u} - \vec{u}_p)/\tau_r)$ is the drag force, and τ_r is the droplet or particle relaxation time calculated by

$$\tau_r = \frac{\rho_p d_p^2}{18\mu C_d \text{Re}}, \quad (7)$$

where μ is the molecular viscosity of the fluid, d_p is the particle diameter, and Re is the relative Reynolds number, which is defined as

$$\text{Re} = \frac{\rho d |\vec{u}_p - \vec{u}|}{\mu}. \quad (8)$$

3.3. Model Validation. In order to verify the validity of the numerical simulation model of dual-radial swirl shielding ventilation, similar experiments were carried out on the dual-radial swirl shielding ventilation system of a fully mechanized excavation face. A custom-developed dual-radial swirl shielding ventilation experiment system for a fully mechanized excavation face was used to record the airflow field structure and dust concentration distribution in the roadway under the dual-radial swirl shielding ventilation, and the experimental results were compared with the numerical simulation results.

3.3.1. Experimental System and Equipment. This verification experiment used a custom-designed experimental model and a custom-built experimental platform. The roadway model was built according to the actual roadway of a coal mine in China at the ratio of 1:10. The main body of the semicircular arched roadway was assembled by three pieces of transparent plexiglass. The total length of the roadway was 3.00 m, the width was 0.46 m, the height was 0.45 m, and the cross-sectional area was 0.16 m². There were 10 cm round holes on the end surface of the roadway and one sidewall, which can be connected with the dust generator to simulate the dust production of tunneling and the dust emission at the transfer point, respectively. The interior of the tunnel was equipped with air supply ducts, suction ducts, blowers, dust removal fans, simulated roadheaders, and simulated conveyors. The layout of the experimental model is shown in Figure 3.

In the flow field analysis experiment, the PIV particle image velocity measurement system produced by LaVision, Germany, was used to record the flow field of different sections in the roadway model. The flow situation and the spatial distribution of the flow field were obtained. In the dust similarity verification experiment, the German AG420 aerosol generator was used to generate dusts, and compressed air was used as the driving force to transport the dust from the tunneling end and the round holes on the sidewall of the tunnel to the tunnel model to simulate dust production in the tunnel and dust emission at the transfer point. An FCC-25 explosion-proof dust sampler was used for dust sampling to measure the dust concentration at the measurement points.

3.3.2. Experimental Program. The verification experiment tested the flow field and the dust control effect. In the flow field verification experiment, smoke particles with a sufficiently small and uniform particle size were used as tracer particles. The smoke was transported to the study area through a blower. When the flow field was stable, the flow field of the studied roadway section was recorded using a PIV system. The velocity vector diagram of the tunnel section obtained by the experiment was compared with the numerical simulation for verification. In the dust control effect verification experiment, the dust collected by the dust sampler at different measurement points was weighed, and the dust concentration at different measurement points under different working conditions was calculated according to the sampling time and sampling flow rate set by the sampler.

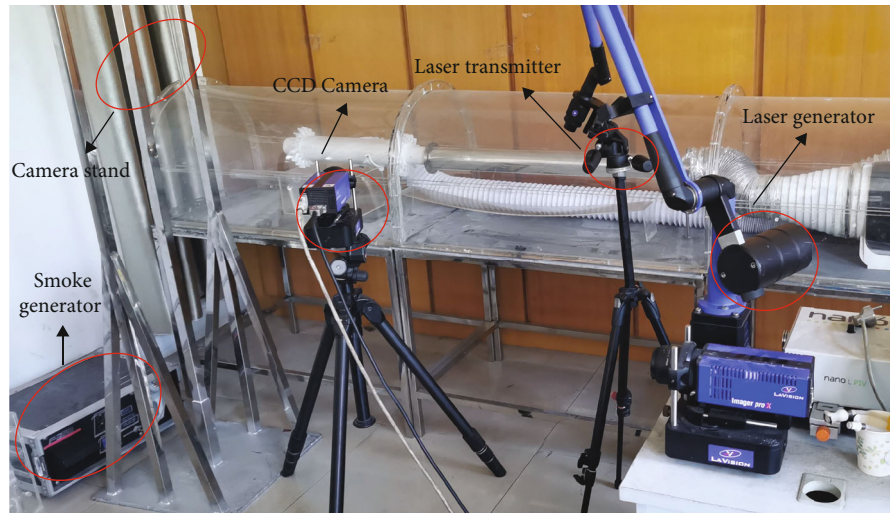


FIGURE 3: Experimental model of the fully mechanized excavation face.

Based on the dust concentration at different points, the dust control capability of the dual-radial swirl shielding ventilation system was investigated. The dust concentration distribution obtained from the experiment was compared with the numerical simulation to verify the validity of the simulation.

We selected three representative flow field measurement surfaces that were not disturbed by the model and used the PIV system to record the flow field. The 1# measurement surface was in parallel with the tunneling end face and 5 cm away from the tunneling end face, the 2# measurement surface was perpendicular to the tunneling end face and the ground and passed through the center of the sleeve, and the 3# measurement surface was in parallel with the ground and passed through the center of the sleeve. The three dust sampling points were arranged in the model roadway along the length of the roadway (x -axis), i.e., at the tunneling end (point A, $x = 3$ cm), at the roadheader's cab (point B, $x = 50$ cm), and the transfer point (point C, $x = 100$ cm). The flow field measurement surfaces and the arrangement of dust sampling points are shown in Figure 4.

3.3.3. Experimental Results and Analysis. Figures 5(a)–5(c) show the PIV experimental record results of the flow field test in the surfaces of 1#, 2#, and 3#, respectively, and Figures 5(d)–5(f) are the corresponding simulation results. Comparing Figure 5(a) with Figure 5(d), Figure 5(b) with Figure 5(e), Figure 5(c) with Figure 5(f), it can be found that the numerically calculated wind flow field structure is consistent with the PIV results. Due to limited experimental conditions, the appearance of the roadheader in the experiment was much simpler than that in the numerical simulation modeling. Compared with the internal flow in the roadway model in the simulation, the airflow field in the experiments was more idealized. Thus, the wind velocity in similar experiments was slightly larger than the numerical simulation results.

Figure 6 shows the dust concentration at different measurement points under the same working condition by experiment and numerical simulation. From the experimen-

tal data in the figure, among the three measurement points, point A (the tunneling end area) has the highest dust concentration and point B (the roadheader driver's cab) has the lowest dust concentration. Under the action of the dual-radial swirl shielding ventilation and dust control system in the fully mechanized excavation face, the tunneling dust was controlled within the tunneling end area, and the dust at the transfer point was also shielded in the area outside the driver's cab. Therefore, the radial air curtain can effectively prevent the spread of dust from various dust sources.

Based on the comprehensive comparison of similar experiments and numerical simulation results, we revealed that the approximate numerical results had the same trend as the experimental results. Therefore, the relevant mathematical model established in this study can be used in the numerical simulation research of the wind flow field in a fully mechanized excavation face. Since the similar experimental roadway model was built at a scale of 1/10 of the actual roadway, the volume of the dust sampler in the roadway model was relatively large, and the dust sampler had a large interference to the airflow field inside the roadway model, destroying the airflow field structure and reducing the dust control effect of the ventilation system. Thus, the dust concentration at each measurement point measured by similar experiments was higher than the numerical simulation result. Comparing the results of similar experiments and numerical simulations, it can be found that although the dust concentrations obtained by similar experiments and numerical simulations were different in numerical values, the dust concentration distribution patterns were the same.

4. Analysis of Dust Control Effect and Parameter Optimization of Dual-Radial Swirl Shielding Ventilation

The blowing and suction air volume ratio γ of the air duct plays a decisive role in the overall movement direction of the airflow in the tunnel. When the value of γ is less than

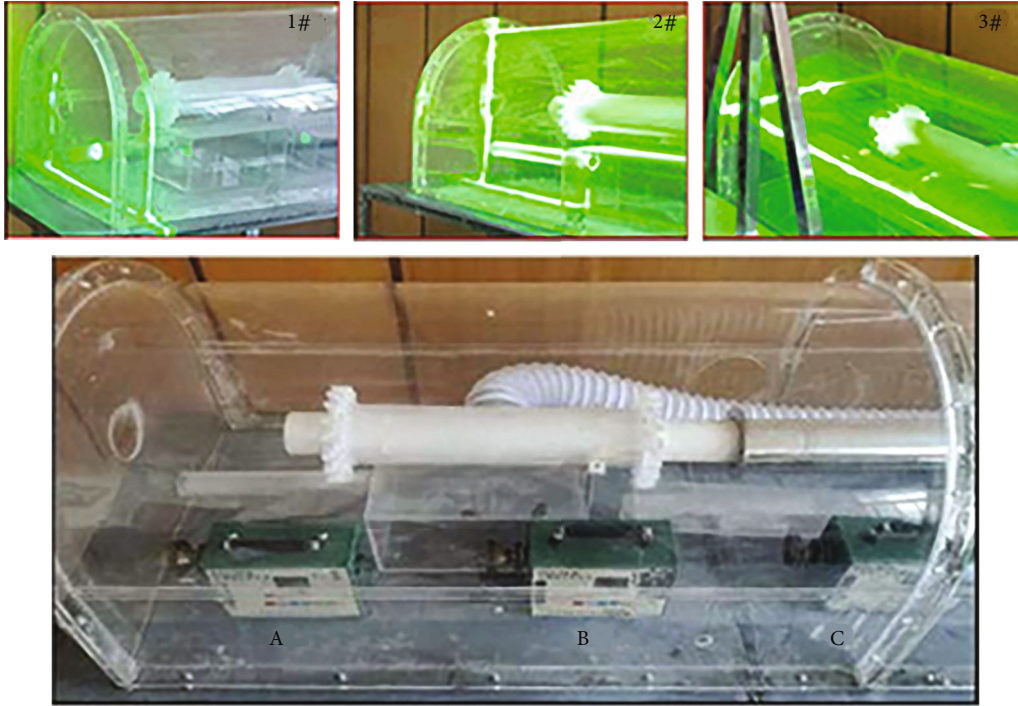


FIGURE 4: PIV measurement surfaces and dust sampling points.

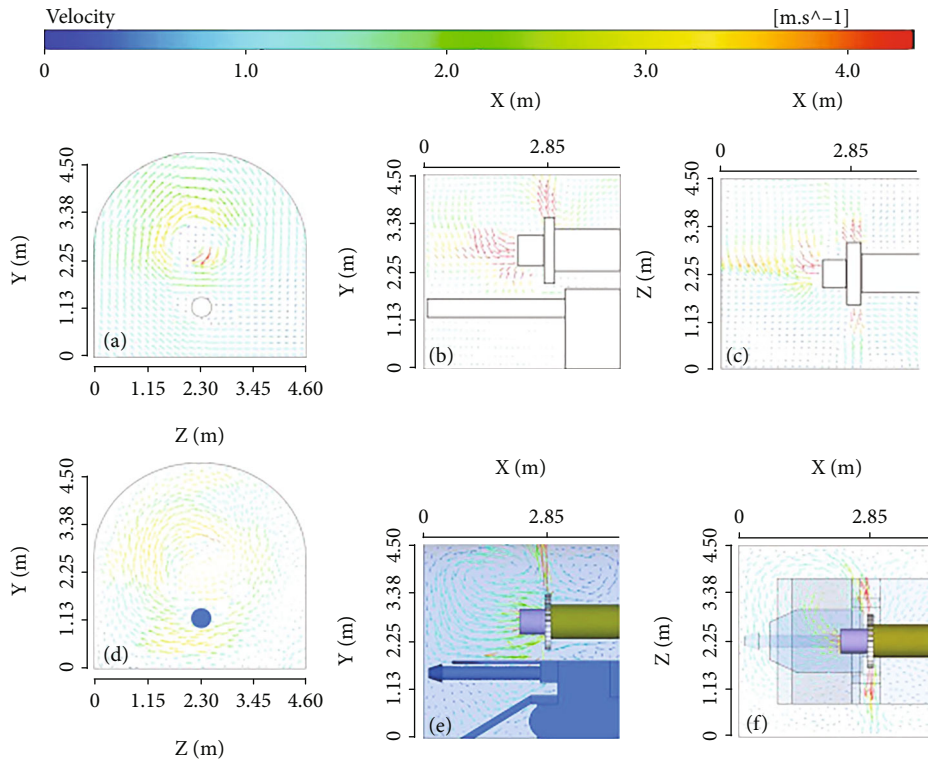


FIGURE 5: Comparison of experimental and numerical simulation flow fields.

1, the airflow in the roadway moves towards the suction outlet of the suction tube, and the dust at the transfer point will spread to the driver's cab of the roadheader with the 2# air curtain. When the value of γ is large, the tunneling dust

spreads to the driver's cab of the roadheader with part of the wind flow of the 1# air curtain, and the insufficient negative pressure at the suction outlet seriously reduces the dust collection efficiency of the suction tube, resulting

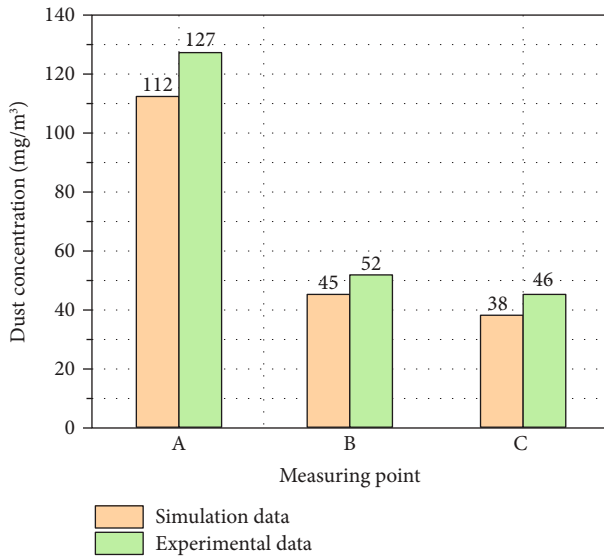


FIGURE 6: Comparison chart of different measurement points under the same working condition.

in an increase in the burden of the 1# air curtain and a decrease in the shielding effect of the tunneling dust. Therefore, a too small or too large γ value is not conducive to the dust shielding of the air curtain on the fully mechanized excavation face.

4.1. Parameter Settings. In order to investigate the influence of the air duct blowing and suction volume ratio γ on the effect of dual-radial swirl shielding ventilation and dust control, this simulation sets a total of six air duct blowing and suction volume ratios, i.e., 1.2, 1.3, 1.4, 1.5, 1.6, and 1.7. According to the relevant specifications of the air volume in the mine tunnel and on-site measured data, the blowing volume of the air supply tube was set to 300 m³/min, and the air suction volume of the suction tube was calculated by the air tube blowing and suction volume ratio γ . The specific parameters are shown in Table 1.

4.2. Effect of the Blowing and Suction Air Volume Ratio on the Flow Field. Figure 7 shows the speed vector diagram of the section at $Z = 2.3$ m perpendicular to the tunneling end under different air duct blowing and suction air volume ratios. It can be seen from the figure that a too small or too large air duct blowing and suction ratio γ is not conducive to shielding the dusts within the tunnel section by the radial air curtain.

For the 1# air curtain, when the γ value was small, the suction volume of the suction tube was relatively large, and the 1# air curtain close to the air inlet was affected by the large negative pressure at the suction outlet, and the airflow from the 1# slit was caught by the suction tube before reaching the roadway. As a result, the 1# air curtain was unable to completely block the tunnel section, which was not conducive to dust control. As the value of γ gradually increased, the suction volume of the suction tube gradually decreased, the negative pressure generated at the suction outlet also gradually decreased, the airflow gradually reached the road-

way wall, and the 1# air curtain moved toward the tunneling end face in an umbrella shape to completely block the roadway. When the γ value was 1.5, the airflow from the 1# slit was blown to the roadway wall at a certain angle under the action of negative pressure, moved along the tunneling end face of the roadway wall, and finally flowed to the air suction outlet under the action of the negative pressure at the air suction outlet. Under this condition, the 1# air curtain achieved a complete wrapping effect in the tunneling end area, and the best flow field in the tunneling end area was achieved. When the γ value was too large, the suction volume of the suction tube was small, and it was difficult for the negative pressure generated by the suction outlet to affect the high-speed airflow from the 1# slit. The high-speed airflow blew vertically to the roadway wall, causing strong wind flow disturbance in the area near the roadway wall. As a result, local vortex wind flow was produced, which led to wind flow turbulence in the tunneling end area and reduced the strength of the 1# air curtain.

For the 2# air curtain, when the γ value was small, the suction volume of the suction tube was much larger than the air volume of the 1# slit, and a large part of the airflow from the 2# slit moved toward the tunneling end face, reducing the strength of the 2# air curtain to block the roadway and weakening the movement of the 2# air curtain in the direction away from the tunneling end. As the γ value increased, the air suction volume gradually decreased, the air volume of the 2# air curtain flowing toward the tunneling end area decreased, the shielding ability of the 2# air curtain gradually increased, and the ability of the air curtain to move away from the tunneling end gradually increased.

Figure 8 shows the velocity vector diagram at the 1# and 2# slits in the roadway section in parallel with the tunneling end face under different air duct blowing and suction ratios γ . It can be seen from the figure that under the action of the external arc-shaped wind deflector, a radial air curtain with a good rotating effect was formed in the entire roadway section. Due to the complex environment in the tunnel, the integrity of the 1# and 2# air curtains was greatly affected. The 2# air curtain was approximately in parallel with the tunneling end face, which can be seen more completely in the figure. Since the 1# air curtain rushed toward the tunneling end in an umbrella shape, the wind flow of the 1# air curtain at the 1# slit was higher at the center of the roadway but lower near the wall of the roadway. When the value of γ was smaller, the inclination of the 1# air curtain was larger, the central area with larger wind speed on the cross section was smaller, and the low wind speed area was larger. With the increase in the γ value, the inclination amplitude of the 1# air curtain was reduced, and a more obvious wind velocity flow field appeared in the entire roadway section. As the γ value increased, the 2# air curtain had no obvious change. When the value of γ was larger, a large wind speed appeared on the wall of the roadway, and the wind flow with a large wind speed blowing vertically to the wall can easily generate turbulence and reduce the anti-interference ability of the air curtain.

4.3. Effect of the Blowing and Suction Air Volume Ratio on Dust Distribution. Figure 9 is a cloud diagram of the

TABLE 1: Parameter setting of boundary conditions.

Blowing and suction air volume ratio γ	The air volume of the suction tube (m^3/min)	Suction outlet wind speed (m/s)	Air volume out of annular slit (m^3/min)		Outlet wind speed of annular slit (m/s)	
			1#	2#	3#	4#
1.2	250.00	14.74				
1.3	230.77	13.61				
1.4	214.29	12.64				
1.5	200.00	11.80	175.00	125.00	12.90	9.22
1.6	187.50	11.06				
1.7	176.47	10.41				

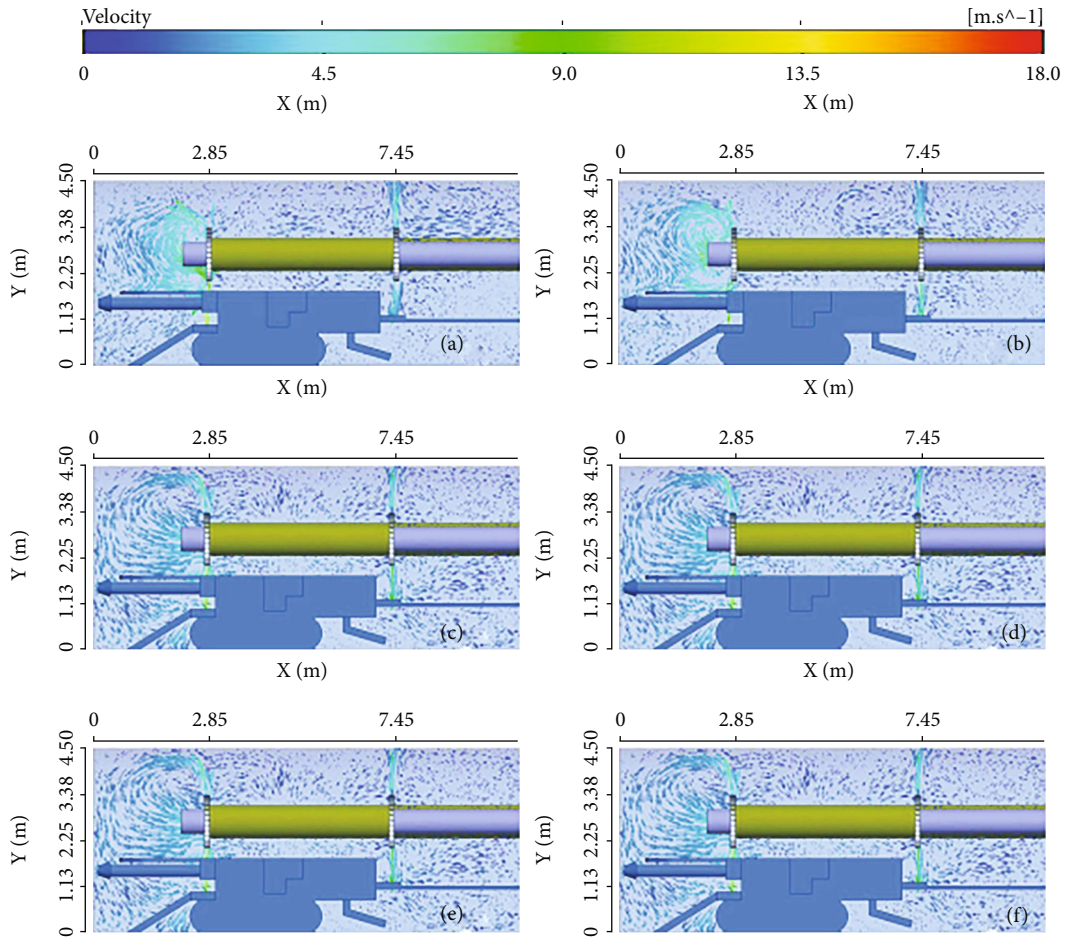


FIGURE 7: Speed vector diagram of the heading area at the $Z = 2.3$ m section: (a) $\gamma = 1.2$ mm; (b) $\gamma = 1.3$ mm; (c) $\gamma = 1.4$ mm; (d) $\gamma = 1.5$ mm; (e) $\gamma = 1.6$ mm; (f) $\gamma = 1.7$ mm.

distribution of dust concentration in the cross section of $Y = 1.7$ m, which is the height of the breathing zone, under different air duct blowing and suction volume ratios. It can be seen from the figure that as the γ value gradually increased, the dust concentration at the driver's position first decreased and then increased and the dust shielding ability of the dual-radial swirl shielding ventilation system first strengthened and then weakened. When the γ value was

smaller, the negative pressure generated by the large suction volume caused a relatively small wind speed of the 1# air curtain at the wall of the roadway, which destroyed the integrity of the 1# air curtain. As a result, the dust in the tunneling end area broke through the shielding of the 1# air curtain along the roadway wall and spread to the driver's cab of the roadheader. Since most of the air volume flowed out to the tunneling end area, the strength of the 2# air

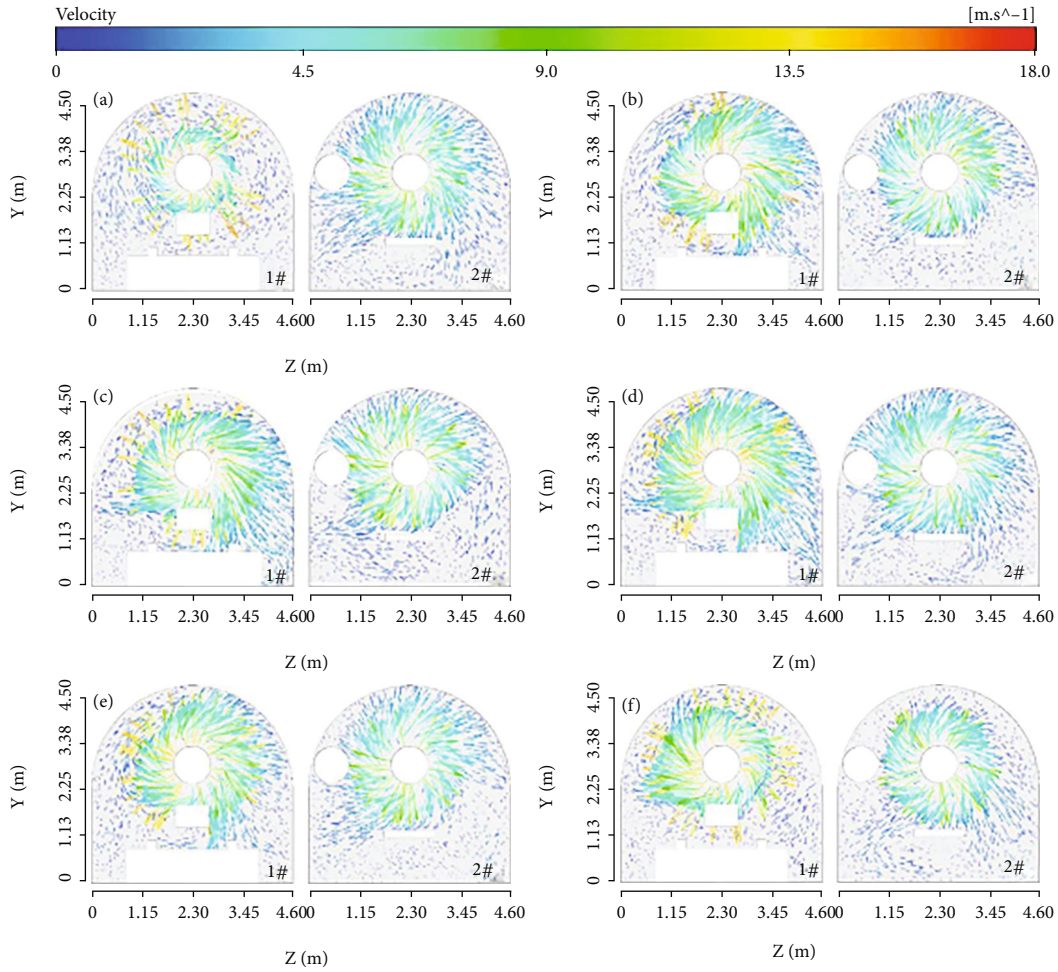


FIGURE 8: Vector diagrams of cross-sectional velocities at 1# and 2# slit air vents under different blowing and suction ratios: (a) $\gamma = 1.2$; (b) $\gamma = 1.3$; (c) $\gamma = 1.4$; (d) $\gamma = 1.5$; (e) $\gamma = 1.6$; (f) $\gamma = 1.7$.

curtain moving away from the tunneling end face was insufficient, so a large amount of dust accumulated at the transfer point, which increased the burden of the 2# air curtain. As a result, the dust control capacity of the 2# air curtain was seriously inadequate, and the dust at the transfer point spread to the driver's position of the roadheader. As the value of γ increased, the dust blocking ability of 1# and 2# air curtains gradually increased, the dust diffusion ability of each dust source to the driver's position of the roadheader was weakened, and the dust concentration at the driver's position of the roadheader gradually decreased. When the γ value was 1.5, the air curtain showed the best dust shielding effect. When γ continued to increase, the dust control ability of the 1# air curtain weakened and the dust control ability of the 2# air curtain increased. When the γ value was too large, large turbulence can be formed near the 1# air curtain, resulting in the turbulence of the flow field in the tunneling end area. Under this condition, it was difficult for the dust to accumulate. At the same time, due to the reduction of the air suction volume, the dust catching capacity of the suction tube was also reduced, so the dust removal capacity in the tunneling end area was reduced, and the dust

concentration increased, which increased the burden of the 1# air curtain. As a result, the dust control ability of the 1# air curtain was weakened, and the dust produced by the tunneling was diffused to the driver's position of the roadheader. Increasing the γ value can improve the strength of the 2# air curtain. Since the total air supply volume was much larger than the suction volume, under the action of the blowing and suction airflow, the 2# air curtain had a strong ability to move away from the tunneling end, so the dust shielding ability of the 2# air curtain at the transfer point continued to increase.

Figure 10 shows the variation curve of the dust concentration at the driver's position with the blowing and suction air volume ratio. From Figure 10, as the blowing and suction volume ratio of the air duct increased, the dust concentration at the driver first decreased and then increased. The dust concentration at the driver's position reached the lowest value when the blowing and suction volume ratio γ is 1.5. From the above analysis, it can be concluded that using the dual-radial swirl shielding ventilation in the fully mechanized excavation face, when the blowing and suction air volume ratio was set to 1.5, the best dust control effect can be obtained.

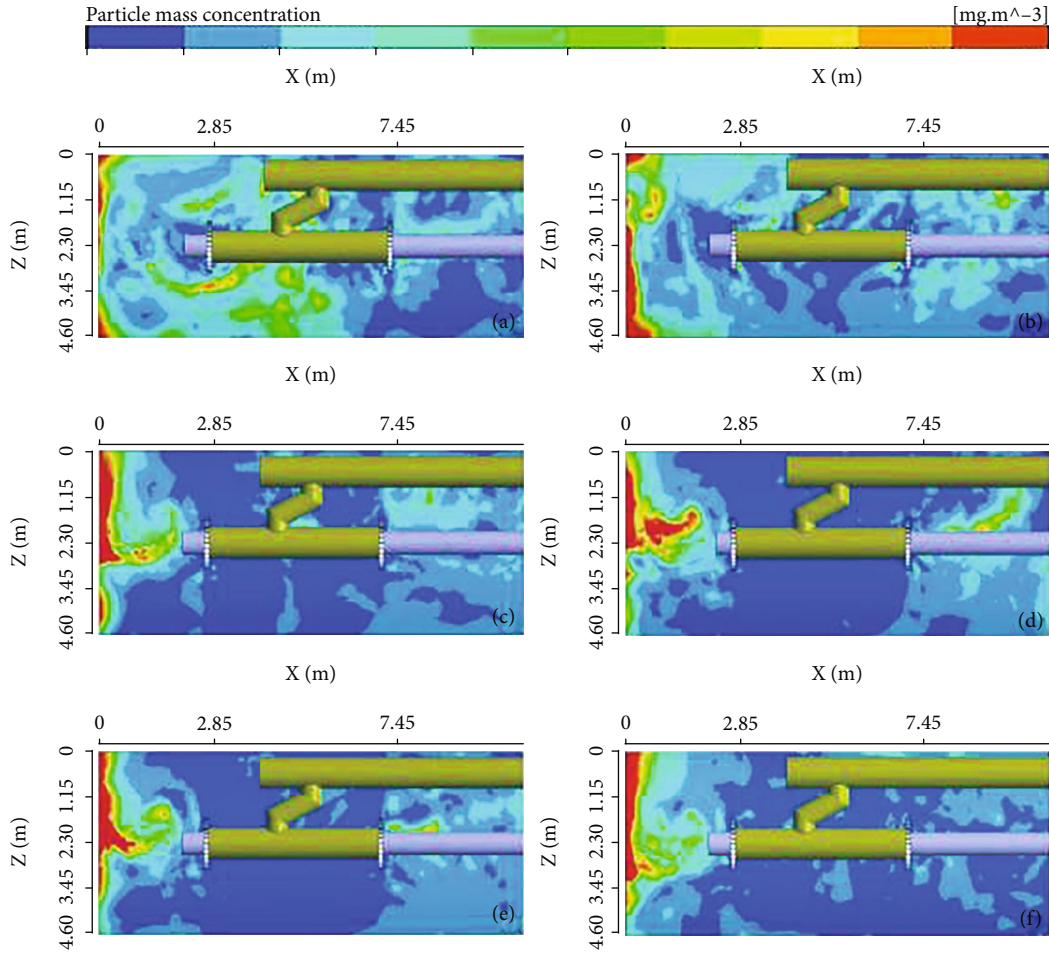


FIGURE 9: Cloud diagram of dust concentration distribution at the cross section of $Y = 1.7$ m under different blowing and suction ratios: (a) $\gamma = 1.2$; (b) $\gamma = 1.3$; (c) $\gamma = 1.4$; (d) $\gamma = 1.5$; (e) $\gamma = 1.6$; (f) $\gamma = 1.7$.

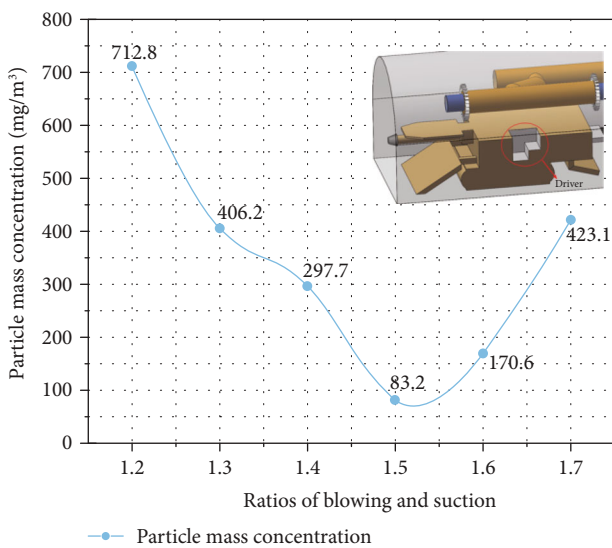


FIGURE 10: Dust concentration at the driver's position.

5. Conclusions

In this study, based on the actual geometric dimensions of the fully mechanized excavation face, the dual-radial swirl shielding ventilation system was modeled using Solidworks software, and the model was numerically simulated by the Fluent software. The validity of the model was verified by a custom-designed experimental model which is geometrically proportional to the real roadway. In the experimental model, the PIV particle image velocimetry system and the FCC-25 explosion-proof dust sampler were used to record the flow field and the dust concentration in the experimental model, respectively. Under the same working conditions with the numerical simulation, the experimental results and numerical simulation results were compared to verify that the numerical model of the dual-radial swirl shielding ventilation system was effective and can be used for more in-depth researches on system dust control optimization. From this research, it can be seen that the blowing and suction air volume ratio of the air dust has a significant impact on the dust control effect of the dual-radial swirl shielding ventilation system in the fully mechanized excavation face. A proper setting of the ratio can greatly improve the air

organization of the dual-radial swirl shielding ventilation system, thereby improving the dust control effect of the system. A too small blowing and suction air volume ratio destroyed the integrity of the 1# air curtain that was used to block the roadway section. A too large blowing and suction air volume ratio led to gradual turbulence of airflow and local circulating air. Therefore, a too large or too small blowing and suction volume ratio can decrease the dust control capability of the ventilation system. As the blowing and suction volume ratio of the air duct increased, the dust control effect of the dual-radial swirl shielding ventilation system showed a trend of first strengthening and then weakening. When the blowing and suction air volume ratio of the air duct was 1.5, the dust shielding effect was the best.

Due to the limitation of research time and experimental conditions, as well as the complex equipment layout and operation process of the actual fully mechanized mining face, the research results need to be further tested on-site.

Data Availability

Data sharing is not applicable to this article as no datasets were generated or analyzed during the current study.

Conflicts of Interest

The authors declare that they have no conflicts of interest.

Acknowledgments

This research was financially supported by the National Natural Science Foundation of China (51774135, 51974120), the Hunan Postgraduate Research and Innovation Funding Project (CX2018B657), and the Open Fund Project of Southern Coal Mine Gas and Roof Disaster Prevention and Control Work Safety Key Laboratory (E21825).



References

- [1] Y. H. Liu, W. Nie, Y. B. Mu et al., "A synthesis and performance evaluation of a highly efficient ecological dust depressor based on the sodium lignosulfonate-acrylic acid graft copolymer," *RSC Advances*, vol. 8, no. 21, pp. 11498–11508, 2018.
- [2] S. Yin, W. Nie, L. Guo et al., "CFD simulations of air curtain dust removal effect by ventilation parameters during tunneling," *Advanced Powder Technology*, vol. 31, no. 6, pp. 2456–2468, 2020.
- [3] B. Tan, H. Liu, B. Xu, and T. Wang, "Comparative study of the explosion pressure characteristics of micro- and nano-sized coal dust and methane-coal dust mixtures in a pipe," *International Journal of Coal Science & Technology*, vol. 7, no. 1, pp. 68–78, 2020.
- [4] P. F. Wang, X. H. Tan, W. M. Cheng, G. Guo, and R. H. Liu, "Dust removal efficiency of high pressure atomization in underground coal mine, *International Journal of Mining Science and Technology*," vol. 28, no. 4, pp. 685–690, 2018.
- [5] P. F. Wang, K. Zhang, and R. H. Liu, "Influence of air supply pressure on atomization characteristics and dust-suppression efficiency of internal-mixing air-assisted atomizing nozzle," *Powder Technology*, vol. 355, pp. 393–407, 2019.
- [6] Y. J. Li, P. F. Wang, R. H. Liu, Y. D. Jiang, and H. Han, "Determination of the optimal axial-to-radial flow ratio of the wall-mounted swirling ventilation in fully mechanized excavation face," *Powder Technology*, vol. 360, pp. 890–910, 2020.
- [7] Q. Bao, W. Nie, C. Q. Liu et al., "The preparation of a novel hydrogel based on crosslinked polymers for suppressing coal dusts," *Journal of Cleaner Production*, vol. 294, p. 1193, 2019.
- [8] P. F. Wang, Y. J. Shi, L. Y. Zhang, and Y. J. Li, "Effect of structural parameters on atomization characteristics and dust reduction performance of internal-mixing air-assisted atomizer nozzle," *Process Safety and Environmental Protection*, vol. 128, pp. 316–328, 2019.
- [9] H. Han, P. F. Wang, Y. J. Li, R. H. Liu, and C. Tian, "Effect of water supply pressure on atomization characteristics and dust-reduction efficiency of internal mixing air atomizing nozzle," *Advanced Powder Technology*, vol. 31, no. 1, pp. 252–268, 2020.
- [10] Q. Liu, W. Nie, Y. Hua, H. T. Peng, and Z. Q. Liu, "The effects of the installation position of a multi-radial swirling air-curtain generator on dust diffusion and pollution rules in a fully-mechanized excavation face: a case study," *Powder Technology*, vol. 329, pp. 371–385, 2018.
- [11] P. F. Wang, R. Z. Gao, R. H. Liu, and F. Q. Yang, "CFD-based optimization of the installation location of the wall-mounted air duct in a fully mechanized excavation face," *Process Safety and Environmental Protection*, vol. 141, pp. 234–245, 2020.
- [12] S. Akhshik, M. Behzad, and M. Rajabi, "CFD-DEM approach to investigate the effect of drill pipe rotation on cuttings transport behavior," *Journal of Petroleum Science and Engineering*, vol. 127, pp. 229–244, 2015.
- [13] D. W. Chen, W. Nie, P. Cai, and Z. Q. Liu, "The diffusion of dust in a fully-mechanized mining face with a mining height of 7 m and the application of wet dust-collecting nets," *Journal of Cleaner Production*, vol. 205, pp. 463–476, 2018.
- [14] Z. A. Jiang, "Study on similarity of gas-solid two-phase flow in ventilation and dust removal," *Coal Engineer*, vol. 40, pp. 12–15, 1993.
- [15] F. Camelli, G. Byrne, and R. Löhner, "Modeling subway air flow using CFD," *Tunneling and Underground Space Technology*, vol. 43, pp. 20–31, 2014.
- [16] Z. A. Jiang, P. Yan, J. S. Chen, and Z. Y. Zhang, "Optimization on parameters of long distance forced and short distance exhausted ventilation system in mine rock heading roadway," *Coal Science and Technology*, vol. 43, pp. 54–58, 2019.
- [17] S. Y. Hu, Q. Liao, G. R. Feng et al., "Numerical study of gas-solid two-phase flow around road-header drivers in a fully mechanized excavation face," *Powder Technology*, vol. 344, pp. 959–969, 2019.
- [18] Z. Korecki and W. Skoczynski, "KOMAG mining mechanization center-service to the cause of mining from 1945-1985," *Mechanizacja Automatykacja Gornictwa*, vol. 24, pp. 12–26, 1986.
- [19] C. Q. Liu, W. Nie, Q. Bao, Q. Liu, C. H. Wei, and Y. Hua, "The effects of the pressure outlet's position on the diffusion and pollution of dust in tunnel using a shield tunneling machine," *Energy & Buildings*, vol. 176, pp. 232–245, 2018.
- [20] W. Nie, W. L. Wei, P. Cai et al., "Simulation experiments on the controllability of dust diffusion by means of multi-radial vortex airflow," *Advanced Powder Technology*, vol. 29, no. 3, pp. 835–847, 2018.

- [21] X. F. Ren, X. M. Hu, D. Xue et al., “Novel sodium silicate/polymer composite gels for the prevention of spontaneous combustion of coal,” *Journal of Hazardous Materials*, vol. 371, pp. 643–654, 2019.
- [22] Z. Q. Liu, W. Nie, H. T. Peng, S. B. Yang, D. W. Chen, and Q. Liu, “The effects of the spraying pressure and nozzle orifice diameter on the atomizing rules and dust suppression performances of an external spraying system in a fully-mechanized excavation face,” *Powder Technology*, vol. 350, pp. 62–80, 2019.
- [23] J. P. Minier, “On Lagrangian stochastic methods for turbulent polydisperse two-phase reactive flows,” *Progress in Energy and Combustion Science*, vol. 50, pp. 1–62, 2015.
- [24] W. Nie, W. L. Wei, X. Ma, Y. H. Liu, H. T. Peng, and Q. Liu, “The effects of ventilation parameters on the migration behaviors of head-on dusts in the heading face,” *Tunnelling and Underground Space Technology*, vol. 70, pp. 400–408, 2017.
- [25] Q. Zhou, B. T. Qin, F. Wang, H. T. Wang, J. Hou, and Z. R. Wang, “Effects of droplet formation patterns on the atomization characteristics of a dust removal spray in a coal cutter,” *Powder Technology*, vol. 344, pp. 570–580, 2019.
- [26] Y. J. Shi, P. F. Wang, R. H. Liu, X. H. Tan, and W. Zhang, “Numerical simulation and engineering application of coalbed water injection,” *Mathematical Problems in Engineering*, vol. 2019, Article ID 6309160, 12 pages, 2019.
- [27] P. F. Wang, Y. J. Li, R. H. Liu, and Y. J. Shi, “Effects of forced-to-exhaust ratio of air volume on dust control of wall- attached swirling ventilation for mechanized excavation face,” *Tunnelling and Underground Space Technology*, vol. 90, pp. 194–207, 2019.
- [28] C. Tan, Z. A. Jiang, M. Wang, and Y. Chen, “Similarity experiment on multi-source dust diffusion law in fully mechanized caving face,” *China National Coal Association*, vol. 40, pp. 122–127, 2015.
- [29] Q. Zhou, B. T. Qin, F. Wang, and H. T. Wang, “Experimental investigation on the performance of a novel magnetized apparatus used to improve the dust suppression ability of surfactant-magnetized water,” *Powder Technology*, vol. 354, pp. 149–157, 2019.
- [30] W. J. Yin, G. Zhou, and D. H. Gao, “Simulation analysis and engineering application of distribution characteristics about multi-stage atomization field for cutting dust in fully mechanized mining face,” *Advanced Powder Technology*, vol. 30, no. 11, pp. 2600–2615, 2019.
- [31] S. Yin, W. Nie, Q. Liu, and Y. Hua, “Transient CFD modelling of space-time evolution of dust pollutants and air- curtain generator position during tunneling,” *Journal of Cleaner Production*, vol. 239, article 117924, 2019.
- [32] B. Sun, W. M. Cheng, J. Y. Wang, and H. Wang, “Effects of turbulent airflow from coal cutting on pollution characteristics of coal dust in fully-mechanized mining face: a case study,” *Journal of Cleaner Production*, vol. 201, pp. 308–324, 2018.

Research Article

Investigation of Seepage Law in Broken Coal and Rock Mass under Different Loading and Unloading Cycles

Zihao Kan ¹, Lei Zhang ¹, Mingxue Li,² Xiaochuan Yuan,¹ and Mengqian Huang³

¹School of Mines, State Key Laboratory of Coal Resources and Safe Mining, China University of Mining and Technology, Xuzhou, Jiangsu 221116, China

²School of Materials Science and Physics, China University of Mining and Technology, Xuzhou, Jiangsu 221116, China

³Shaanxi Yubei Coal Industry Xiaobaodang Mining Co. Ltd., Yulin, Shaanxi 719300, China

Correspondence should be addressed to Lei Zhang; leizhangcumt@163.com

Received 13 July 2021; Revised 4 August 2021; Accepted 16 August 2021; Published 1 September 2021

Academic Editor: Ondra Sracek

Copyright © 2021 Zihao Kan et al. This is an open access article distributed under the Creative Commons Attribution License, which permits unrestricted use, distribution, and reproduction in any medium, provided the original work is properly cited.

In order to study the seepage law of broken coal seams affected by multiple mining operations, a cyclic loading and unloading seepage experiment was carried out. For this purpose, the seepage law of broken samples with different coal and rock ratios was analyzed. The results of our study demonstrated that the permeability of the broken samples showed a decreasing trend. After a loading and unloading cycle, the permeability was significantly reduced. The impact of the loading stage on the broken sample was higher than that of the unloading phase. When the proportion of coal particles in the mixed samples of broken coal and rock was 50%, the irreversible permeability loss rate and permeability loss rate of the samples showed the highest values. The irreversible permeability loss rate and permeability loss rate of the broken rock mass were greater than those displayed by the broken coal mass. The stress sensitivity coefficient curves of the 5 types of broken coal and rock masses presented the same changes. The stress sensitivity coefficient curve and the effective stress displayed an exponential relationship.

1. Introduction

As coal mining is gradually performed at deeper depths, the occurrence of coal seam groups is more frequent [1]. During the mining of deep coal seams, the mining stress path experienced by the coal seams, the evolution of the surrounding rock fissure field, and the gas seepage become complex and unstable. This makes difficult to understand the characteristics of gas migration and enrichment during repeated mining of the coal seams. The reason is that coal seam mining produces pressure release and pressurization on unmined coal seams. This causes that some coal seams repeatedly undergo loading and unloading processes during coal seam mining [2]. As effect of periodic pressure, as the working face advances the overlying rock in the goaf redistributes the stress field. This causes that the overlying rock in the goaf is always present in the pressurization zone or pressure relief zone. Under this repeated loading and unloading action, the coal seam gradually changes from a complete

state to a broken state. This process changes the pore structure of the coal seam, and in consequence, the gas seepage law cannot be accurately determined. When the coal body is broken, the coal seam includes the broken coal particles. It is particularly important to study the pore structure and permeability of the broken coal rock mass that is subjected to cyclic loading and unloading processes.

Scholars have carried out research on the pore structure and seepage law of broken coal and rock mass under stress. Mccorquodale et al. [3] conducted multiple permeability tests and obtained dimensionless equations for the permeability coefficients of broken rocks with various particle sizes. Pradeepkumar et al. [4] determined that the seepage flow of broken rock obeys the Forchheimer equation and the Missbach equation. Qian et al. [5] summed up a large number of test results and concluded that, under high pressure, the permeability coefficient of broken rock masses increased an order of magnitude as compared with that of intact rock masses. In addition, the seepage of broken rock

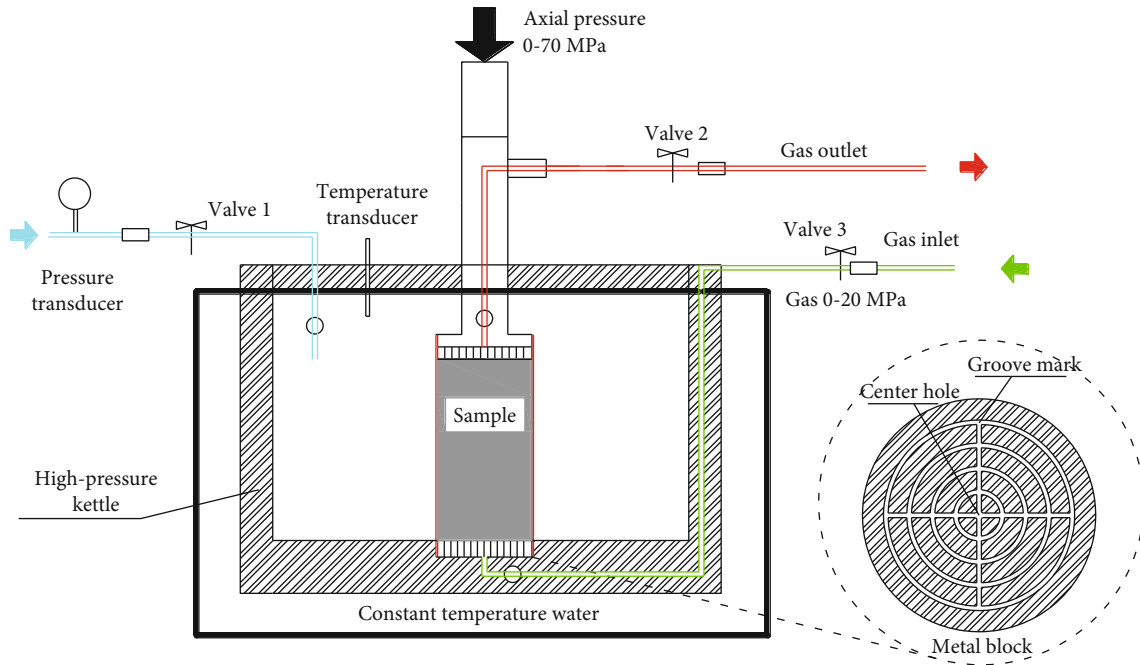


FIGURE 1: Gas flow and displacement testing equipment [15].

masses during in situ mining generally does not conform to Darcy's law. Shang et al. [6] obtained the porosity of broken coal samples at various particle sizes. According to their results, porosity gradually decreased with the increase of effective stress. In addition, this parameter was negatively correlated with the changing law of confining pressure. Wang et al. [7] found out that the main reason for the decrease in pore space and permeability loss of broken coal and rock samples under loading and unloading cycles is the rebreaking of coal and rock particles. According to Chu et al., the porosity and permeability of the broken coal sample gradually decreased with increasing stress. During the stress loading process, the inner physical structure of the broken coal sample changed, and the coal particles broke again. This process further affected their permeability. Yu et al. [8] determined that in the initial stage of stress loading, as porosity decreased, the permeability decreased in a linear way. Later, the permeability decreased more slowly, and finally, the permeability suddenly decreased with the decrease in porosity. Zhang et al. [9, 10] reported that the larger the proportion of coal in the mixed sample of broken coal and rock, the smaller the permeability, and the higher the stress sensitivity of permeability. As the number of loading and unloading cycles increased, the stress sensitivity gradually decreased. Wang et al. [11] identified that the relationship between seepage velocity and permeability and porosity can be fitted using power and exponential functions. When the porosity of a broken coal sample is high, the permeability is related to the stress loading process. When the porosity is small, the permeability tends to stabilize and does not show a relationship with the stress loading process. Zhang et al. [12] found out that the higher the proportion of large coal particles (20-25 mm) in the broken coal samples, the higher the permeability and stability. In

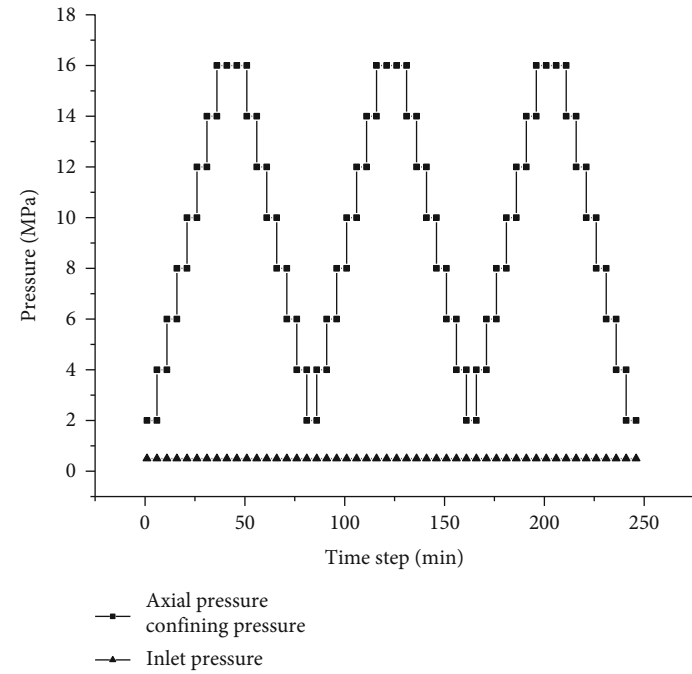
addition, the larger the proportion of small coal particles (5-10 mm), the greater the permeability. Small coal particles presented a filling effect on large coal particles.

These researchers have also analyzed the seepage law of broken coal using data on stress effect and pore structure and compared and analyzed coal samples of different particle sizes. However, in the experimental research on broken samples, there are few researches on the broken samples mixed with coal and rock particles, and there are fewer researches on cyclic loading and unloading as the stress path. Therefore, in this paper, combining the above two aspects, five kinds of broken samples with different coal-rock ratios are made, and the permeability changes of the five kinds of samples are studied under the action of cyclic loading and unloading. The purpose of testing the permeability of broken samples is to improve the efficiency of coal seam gas drainage. The model established in the literature [13, 14] effectively reflects the law of gas permeability changes under fracturing.

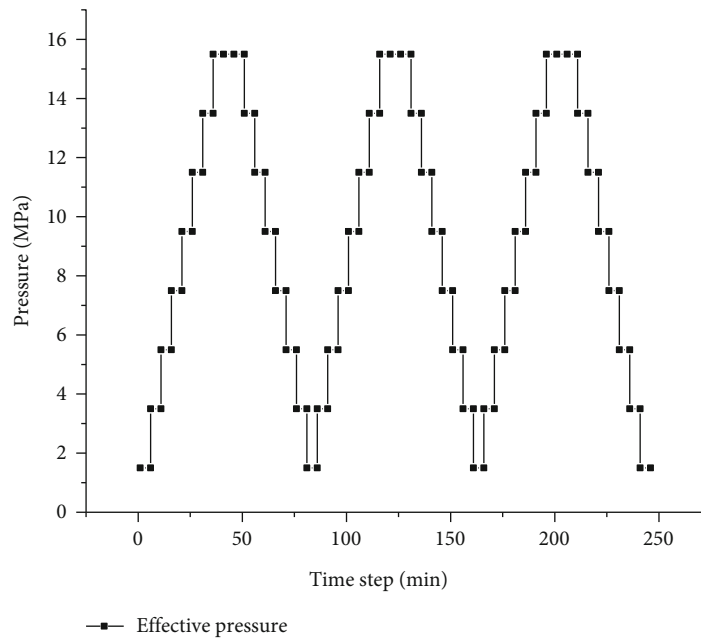
2. Experiments

2.1. Laboratory Equipment. The gas flow and displacement testing equipment consisted of a loading system, autoclave, air supply and pressure reduction system, temperature simulation system, and acquisition control system, as shown in Figure 1. The loading system is able to load the coal sample and at the same time maintain a radial pressure. The gas passes through the coal sample and enters the flow meter in order to measure permeability. The principle of the experimental device is shown in Figure 2.

2.2. Experimental Samples. The coal and rock blocks were selected from Huaibei coalfield 3_2 coal seam, located in the



(a)



(b)

FIGURE 2: (a) Stress path and (b) effective stress path.

Anhui Province. The mine ground elevation was +24.5~+25.2 m, and the working face elevation was -509~-680 m. The coal seams selected for these experiments corresponded to bituminous coal shown between medium and high metamorphic degrees. The rock mass was selected from the caving zone of this working face. The coal and rock blocks were ground until particles with approximately the same diameter were obtained. The diameter of the selected coal and rock particles was between 5 and 10 mm. The coal and rock particles were mixed in order to obtain samples with

a diameter of 50 mm and a height of 100 mm, as shown in Table 1 and Figure 3.

2.3. Experimental Program. The cyclic loading and unloading stress path is shown in Figure 2. After the sample was placed in the experimental device, temperature was adjusted to 20°C and tests were performed at a constant temperature. During the loading process, the axial pressure and confining pressure were set up to 2 MPa, the inlet pressure was adjusted to 0.5 MPa, helium was charged into the

TABLE 1: Basic data of coal samples.

Sample	Size (mm)	Coal to rock volume ratio	Volume (%)		Quality (g)	
			Coal	Rock	Coal	Rock
C1	50 × 100	1	100	0	162.1	0
C2	50 × 100	0.7	70	30	112.1	75.2
C3	50 × 100	0.5	50	50	83.4	130.1
C4	50 × 100	0.3	30	70	34.4	187.9
C5	50 × 100	0	0	100	0	263.7

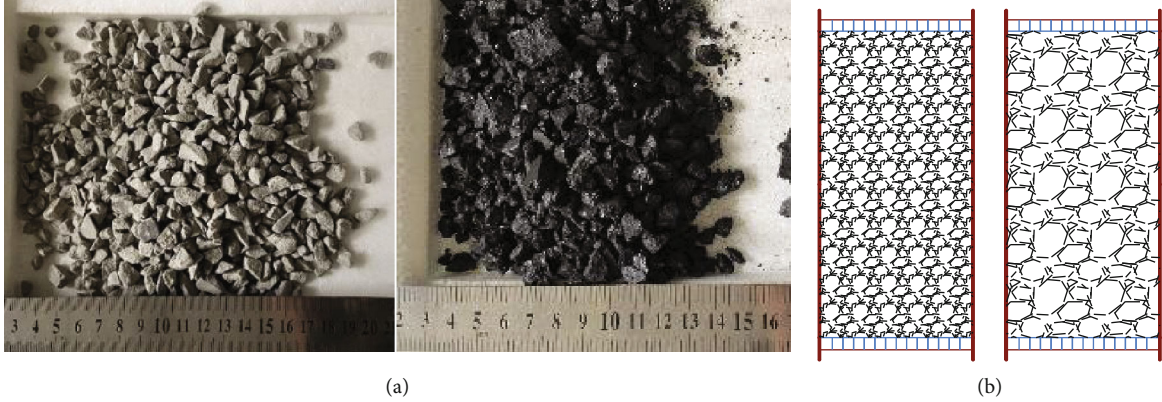


FIGURE 3: (a) Broken coal and rock and (b) coal samples.

experimental device, and the axial pressure and confining pressure were maintained constant for 5 minutes. The shaft confining pressure was loaded at intervals of 2 MPa until the axial pressure and confining pressure reached 16 MPa. The unloading process started with an interval of 20 minutes after each loading. During the unloading process, the axial and confining pressures were unloaded in steps of 2 MPa, until final values were 2 MPa and the first loading and unloading cycle and permeability test were completed [16]. Later, the same method was used to carry out the permeability test during the second and third stages of axial and confining loading and unloading processes. When the axial and confining pressures in the third stage were unloaded to reach 2 MPa, the permeability test was completed. The test for loading and unloading path and effective loading and unloading stress path is shown in Figure 2.

Equation (1) has been widely used to calculate the average effective stress in cylindrical coal samples:

$$\sigma_e = \sigma_a - P, \quad (1)$$

where σ_e is average effective stress (MPa), σ_a is axial pressure (MPa), and P_1 is the inlet pressure in the coal sample (MPa).

Since coal is a porous medium, the gas flow in the coal seam can be roughly described by a linear seepage law. The formula used to calculate axial permeability of a compressible gas can be obtained by normalizing the flow rate and pressure in Darcy's theorem permeability formula:

$$K = \frac{2PQ\mu L}{A(P_1^2 - P_2^2)}, \quad (2)$$

where K is coal permeability (md), Q corresponds to gas flow rate (cm^3/s), μ is the gas viscosity coefficient (Pa-s), L indicates the coal sample length (cm), A is the coal sample base area (cm^2), and P_1 and P_2 correspond to the relative gas pressures at the inlet and outlet of the raw coal sample, respectively (MPa).

In order to eliminate potential differences in pore structure caused by volume and shape variations of broken coal and rock particles, the concept of dimensionless permeability was introduced. The dimensionless permeability considers the initial permeability as the benchmark and the subsequent permeability as the benchmark and was used to express the degree of permeability change at every stress point:

$$k = \frac{K_n}{K}, \quad (3)$$

where k is the dimensionless permeability and K_n corresponds to permeability in the subsequent stress point, excluding the first stress point (md).

3. Experimental Results and Discussion

3.1. Changes in Permeability of Broken Samples. According to the stress path shown in Figure 2, the loading and unloading cycles were performed to obtain five different ratios of broken coal and rock mass permeability changes. As shown in Figure 4, the permeability of broken coal and rock mass showed a decreasing trend with increasing number of loading and unloading cycles. Given the different compositions

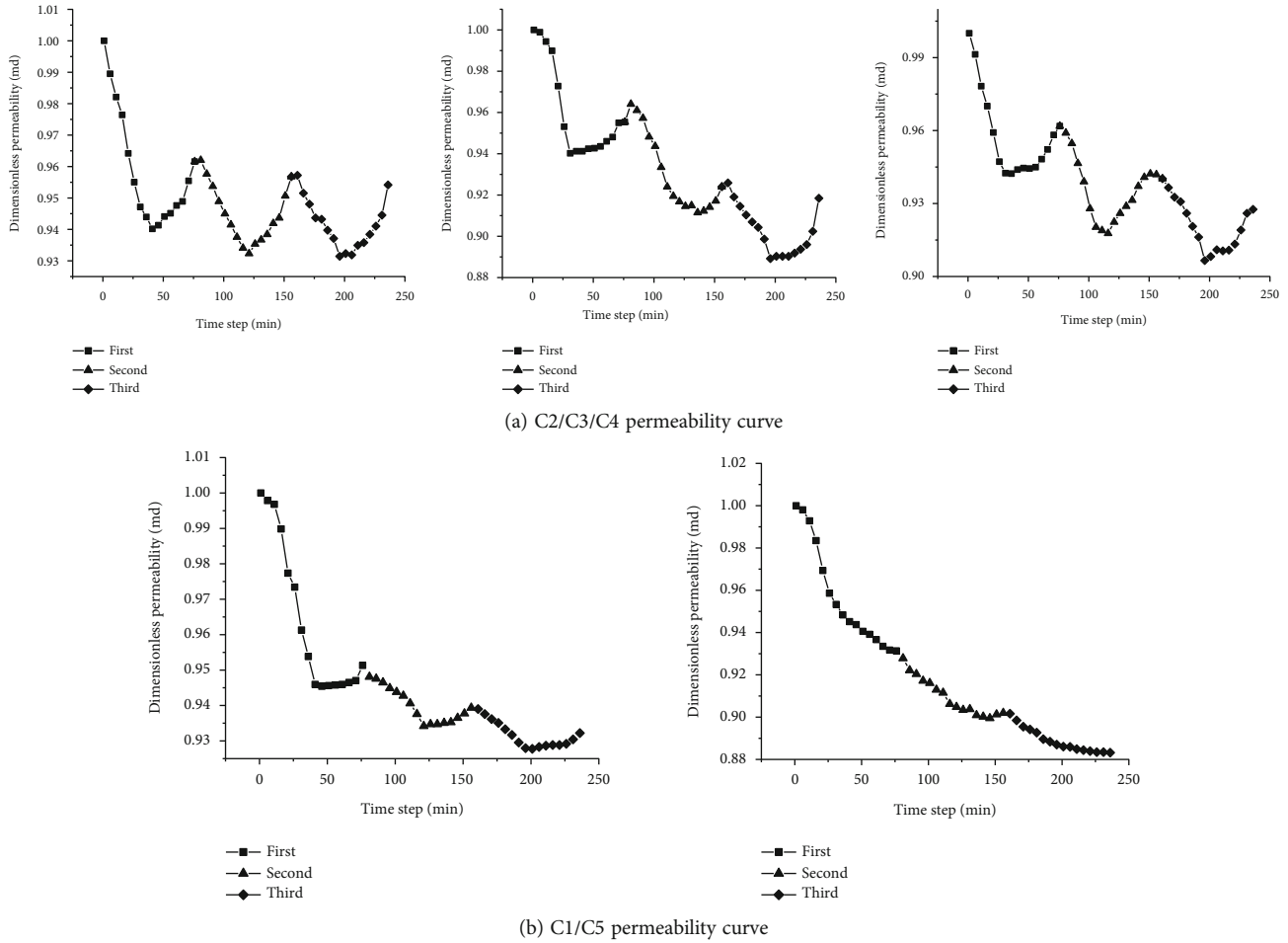


FIGURE 4: Permeability curve for samples C1/C2/C3/C4/C5.

of the five types of broken coal and rock masses, they were divided in two groups: C1/C5 and C2/C3/C4. In this case, C1/C5 corresponded to coal and rock samples, respectively. In addition, C2/3/4 indicated mixed samples. During the three loading and unloading cycles of C2/3/4 broken coal and rock samples, the permeability and effective stress were inversely proportional. During the loading process, the permeability of the broken coal rock decreased and later increased during the unloading stage. Data indicated that stress during loading and unloading stages presented two maximum points. In addition, the permeability curve displayed three minimum points. Permeability of C2/3/4 decreased as the number of loading and unloading cycles increased. It was also observed that the damage to the broken coal and rock mass gradually increased after three loading and unloading cycles. During the cyclic loading and unloading of C1 crushed coal, the overall change was the same as the one observed in C2/3/4. In addition, the change range of the extreme point inside the permeability curve was small, even smaller than the one observed in the C2/3/4 sample. The permeability of C5 broken rock mass always decreased, and no extreme point was present. These results differed from those obtained for C1 fractured coal mass. During cyclic loading and unloading processes of the

TABLE 2: Permeability variation.

Sample	C1	C2	C3	C4	C5
Loading 1	0.046	0.056	0.059	0.058	0.052
Unloading 2	-0.005	-0.021	-0.014	-0.018	0.014
Loading 2	0.011	0.028	0.045	0.041	0.022
Unloading 2	-0.005	-0.024	-0.007	-0.020	0.003
Loading 3	0.011	0.026	0.037	0.034	0.015
Unloading 3	-0.004	-0.022	-0.028	-0.019	0.003

broken coal and rock mass, the particles resulted from three different processes: extrusion deformation, particle crushing, and structural adjustment; the permeability changes of C1/2/3/4/5 at each stage are shown in Table 2. When coal and rocks were mixed, for example, in C2/3/4, particle crushing and extrusion deformation represented the main factors. On the other hand, in broken coal and rock samples mixtures (i.e., C1/5), structural adjustment and extrusion deformation represented the main processes. The specific shape is shown in Figure 5.

In order to further illustrate potential changes in permeability of broken coal and rock mass subjected to three

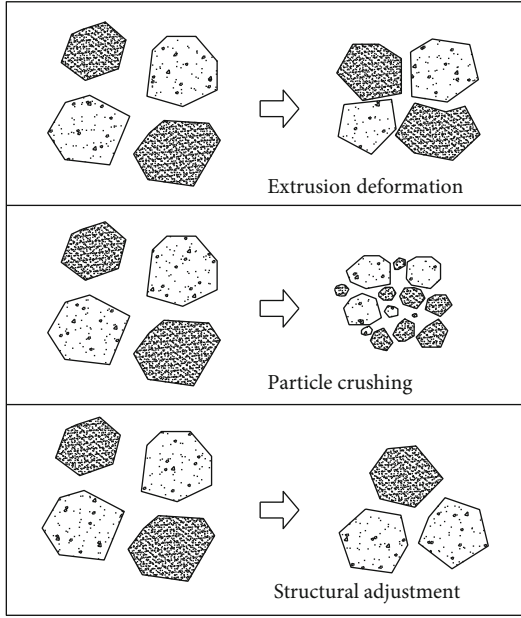


FIGURE 5: Three different processes occurring during loading and unloading of broken coal and rock mass samples.

loading and unloading cycles, the deformation of the granular particles was calculated using the Hertz contact deformation principle [17]. Before loading and unloading of the broken coal and rock mass, multiple particles presented high porosity. Herein, particle size and volume of the fracture channel present inside the sample were large. At this point, permeability presented the highest value. It was observed that, at high values of effective stress, no cohesion between the particles occurred, and the multiparticle pore structure started breaking down. At this time, the area of the pore seepage channel was greatly reduced. As stress further increased, a relatively stable pore structure was eventually formed. At the same time, because of the low strength and irregular shape of broken coal and rocks, samples were again broken during the loading and unloading cycle (Figure 5). The diameter of broken particles after loading and unloading cycles was significantly smaller than that of large particles. Also, the fracture channels composed of tiny particles were smaller than those composed of large particles. In addition, some small broken particles were able to fill the pore space of large particles, and at the same time, the particle structure was again adjusted [18], as shown in Figure 6. The pore structure of broken coal rocks was not restored during the unloading stage. This process produced a significant loss of permeability of the broken coal rock sample during the first loading and unloading process. In subsequent loading and unloading cycles, the coal and rock samples were broken again to a much lower degree as compared to the first loading process, and the structure between the particles was relatively stable [19]. Therefore, the permeability of the broken coal and rock samples during the secondary and tertiary loading and unloading processes decreased to a small extent. In addition to the irreversible permeation loss that resulted from changes of the pore structure of the broken coal samples and recrushing, the squeezing deformation

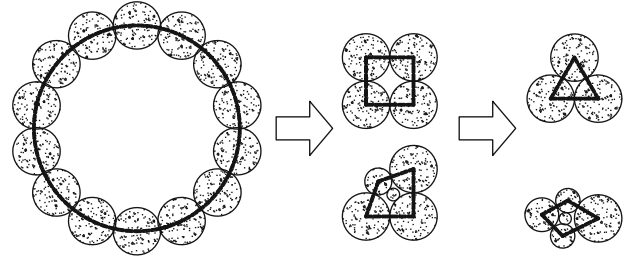


FIGURE 6: Changes in pore structure of broken coal and rock mass.

of the broken particles during the formation of the pore structure was also the reason for the reduction of porosity.

In order to determine the cause for the continuous decrease in permeability of broken coal and rock masses during the cyclic loading and unloading processes [20], the concept of the cubic law was introduced. Different researchers have [21] studied the seepage mechanism of water in rough fractures and have proposed use of the cubic law. The formula is presented in

$$Q = \frac{e^3}{12\mu} \frac{P_2 - P_1}{JRC^{0.03}}, \quad (4)$$

where Q represents the flow through the pipeline (m^3/s), e is the crack opening (m), μ corresponds to the fluid viscosity coefficient, JRC is the roughness coefficient, and $P_2 - P_1$ is the pressure difference between adjacent fluid domains (MPa), and a positive value indicates that the direction of flow velocity occurs from fluid domain 2 to fluid domain 1.

Different researchers [22] have used the root mean square Z of the structural surface to estimate the roughness coefficient JRC and have obtained

$$JRC = 32.2 + 32.47 \lg Z. \quad (5)$$

The root mean square Z formula of the surface profile is shown in

$$Z = \frac{1}{L} \sqrt{\int_{x=0}^{x=L} \left(\frac{dy}{dx} \right)^2 dx}, \quad (6)$$

where L corresponds to the length of the pipe (m). As shown in Figure 7, $L = r_1 + r_2$.

During the experiments, the broken coal and rock mass underwent three processes including deformation, particle crushing, and structural adjustment. The initial particle size was relatively large. After loading and unloading cycles, the coal and rock mass broke again and the particle size was reduced. The width of the cracks between them was reduced, as well as the length of the cracked pipes. According to Equation (4), L decreased and the root mean square Z_2 of the surface profile increased. In addition, as shown in Equation (3), in general, JRC increased. Furthermore, according to Equation (2), the flow rate of crushed coal and rock mass decreased, and coal was compressed. The permeability of the coal and rock mass decreased accordingly. Thus, the permeability of the broken coal rock always

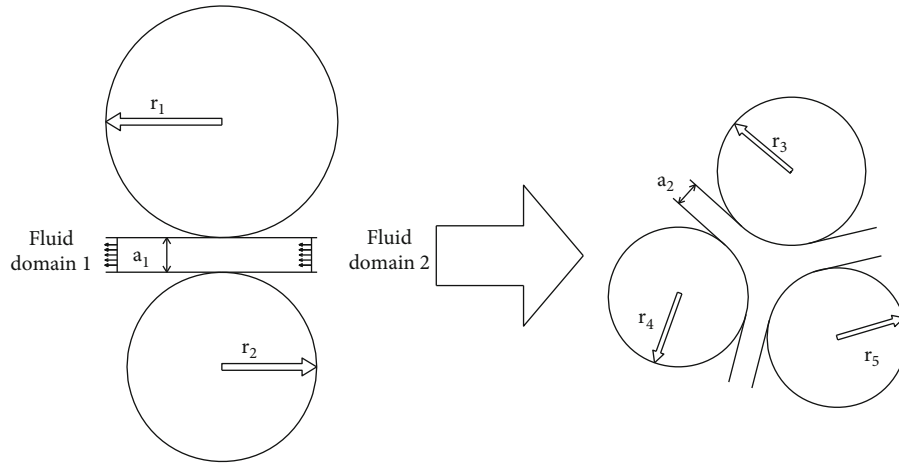
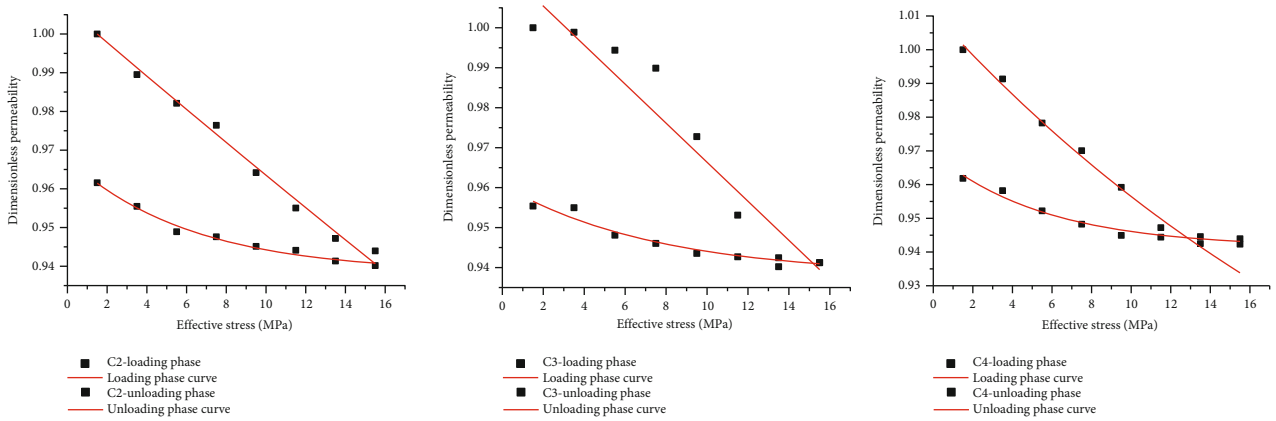
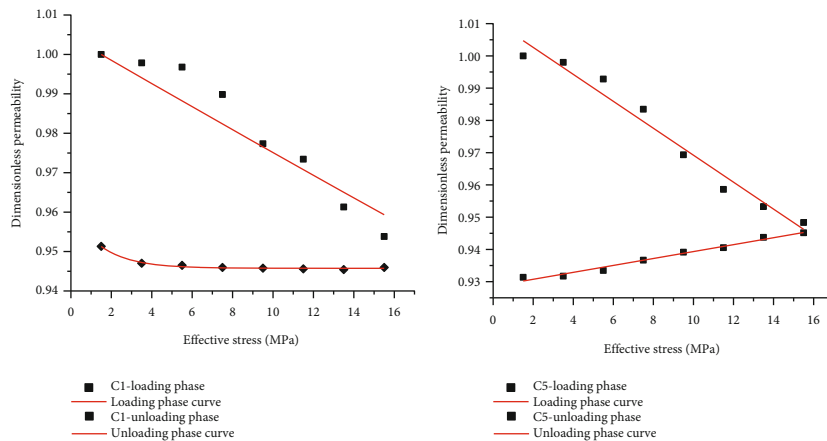


FIGURE 7: Seepage channel changes in broken coal and rock mass during loading and unloading processes.



(a) C2/3/4 coal sample



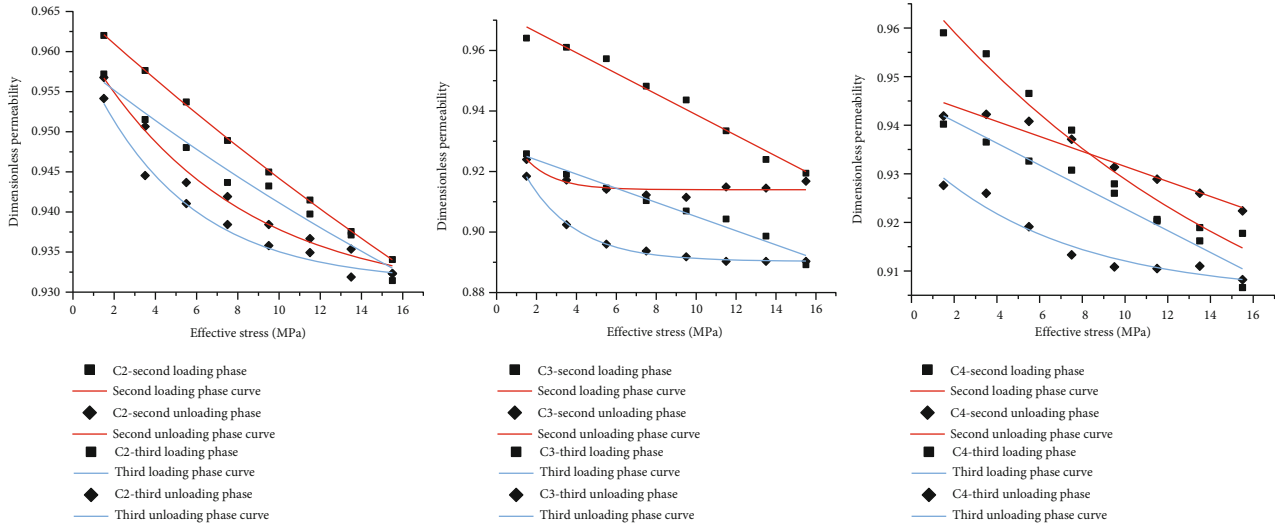
(b) C1/5 coal sample

FIGURE 8: Permeability curve for the first loading and unloading cycle.

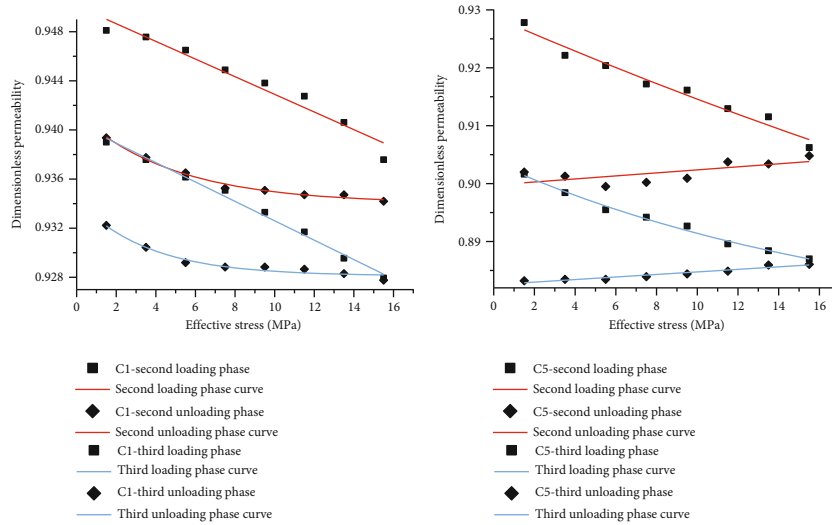
showed a decreasing trend during the loading and unloading cycles.

According to our results, significant changes in permeability were observed when broken coal rock masses C1/2/3/4/5 passed through one loading and unloading cycle. Figures 8 and 9 show the permeability curves for 5 different types of broken coal rock masses with effective stress as the

independent variable. Figure 8 shows data obtained in the first cycle. In addition, Figure 9 presents the permeability of the samples during the second and third loading and unloading cycles. Data indicated that, throughout the loading stage, the highest slope of the permeability curve corresponded to the C3 sample, followed by that of C4 and C2. At the beginning of the first loading step, small differences



(a) C2/3/4 coal sample



(b) C1/5 coal sample

FIGURE 9: Permeability curves for the second and third loading and unloading cycles.

in permeability were observed in the three samples. However, as effective stress increased, the permeability of the C3 sample decreased, and the slope increased. This occurred because the n value for the samples C2, C3, and C4 was 0.7, 0.5, and 0.3, respectively. Thus, the volume of coal and rock particles in the sample accounted for 70%, 50%, and 30%. During the loading process, the internal particles were mainly ground by extrusion. Since the hardness of the rock was higher than that of the coal, the internal coal particles were fractured again during the loading process. These particles filled the internal cracks of the rock. When the proportion of coal particles was 30%, the volume of the internal fissures present in the rock particles was larger, the filling volume of the coal particles was smaller, and the structural change of the pores was smaller than the ones observed in samples containing a coal ratio of 50%. When the proportion of coal particles was 70%, the coal particles in contact with the rock units were broken through particle crushing. On the other hand, when coal particles were not in contact



FIGURE 10: C2 and C3 samples after loading and unloading cycle.

with the rock particles, fragmentation was mainly due to extrusion, deformation, and structural adjustment. Moreover, when the proportion of particles was 50%, the coal and rocks were fully mixed and in full contact. For this reason, coal particles were fragmented again after being squeezed [23]. Figure 10 shows that, after three loading

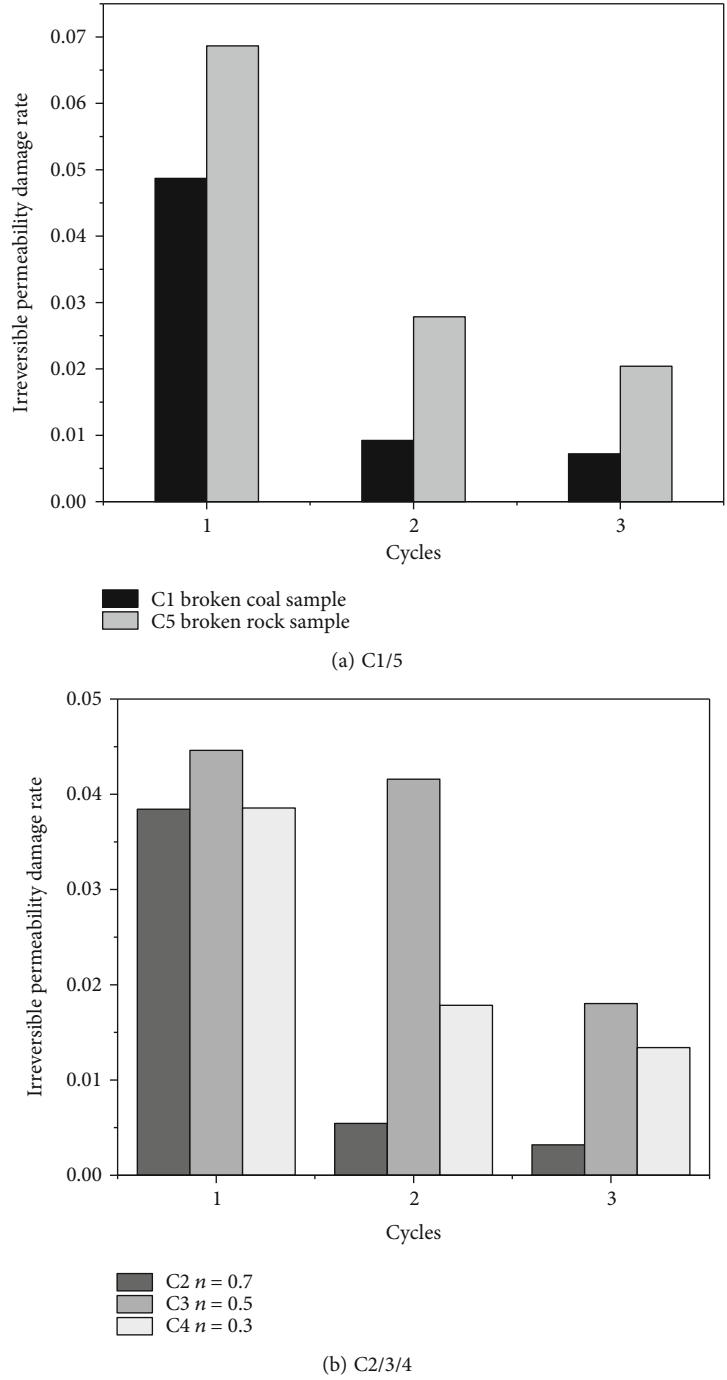


FIGURE 11: Irreversible permeability loss rate of C1~5 during three loading and unloading cycles.

and unloading cycles, the degree of fragmentation in the C3 sample was greater than that observed in the C2 sample. When the coal-to-rock ratio was 0.5, significant deformation of the broken coal and rock was observed, and the pore structure was notably damaged.

3.2. Permeability Damage Rate. In order to explore the influence of cyclic loading and unloading processes on the permeability of broken coal and rocks, the concept of irreversible permeability damage rate was introduced. The irreversible permeability damage rate represents the change in the perme-

ability of the broken sample during the cyclic loading and unloading process, considering that this change is irreversible. The irreversible permeability damage rate (%) is expressed as shown in Equation (7) and indicates to which degree the permeability of the coal reservoir cannot be recovered [24]:

$$D_{k_1} = \frac{k_1 - k_{1r}}{k_1} \cdot 100\%, \tag{7}$$

where D_{k_1} corresponds to the irreversible permeability damage rate after stress is returned to the first stress point, k_1

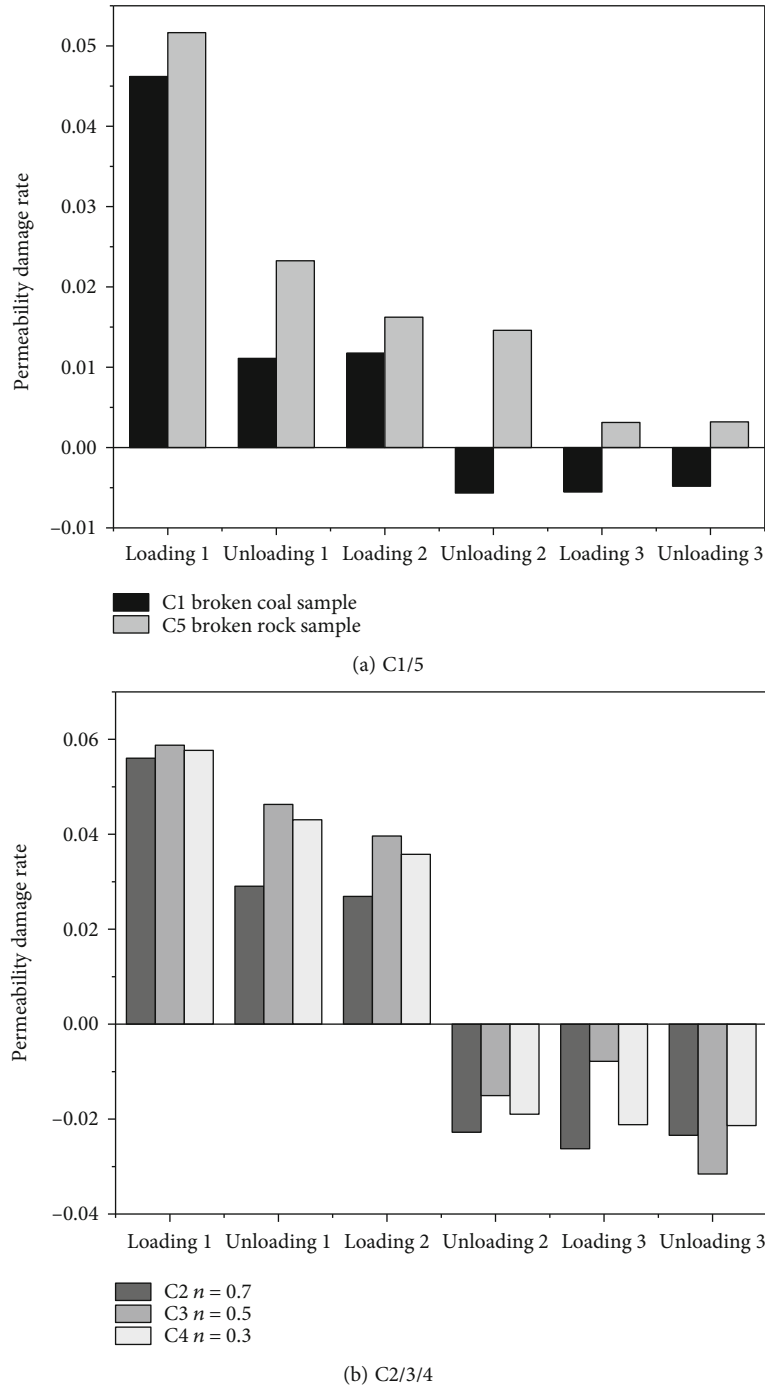


FIGURE 12: Rate of permeability loss in samples C1~5 under three loading and unloading cycles.

indicates the permeability at the first stress point (md), and k_{1r} is the permeability after the stress returns to the first stress point (md).

According to the data shown in Figure 11, the irreversible loss rate of the five broken samples gradually decreased when the number of loading and unloading cycles increased. Results for samples C1 and C5 indicated that, during the three loading and unloading cycles, the irreversible damage rate of the broken rock sample was higher than that of the broken coal sample. The coal used for the broken sample

was taken from the 3_2 coal seam of the Huaibei Coal Field. This coal seam corresponds to an outburst coal seam. Therefore, the coal sample displayed a plastic change relative to the rock sample during the cyclic loading and unloading process. The compression deformation during the loading and unloading process caused that the ratio of the broken rock was higher than that of the coal. In C2/3/4, which corresponds to three different types of crushed mixed samples, the irreversible damage rate after three loading and unloading cycles followed the order $C3 > C4 > C2$. When the coal-

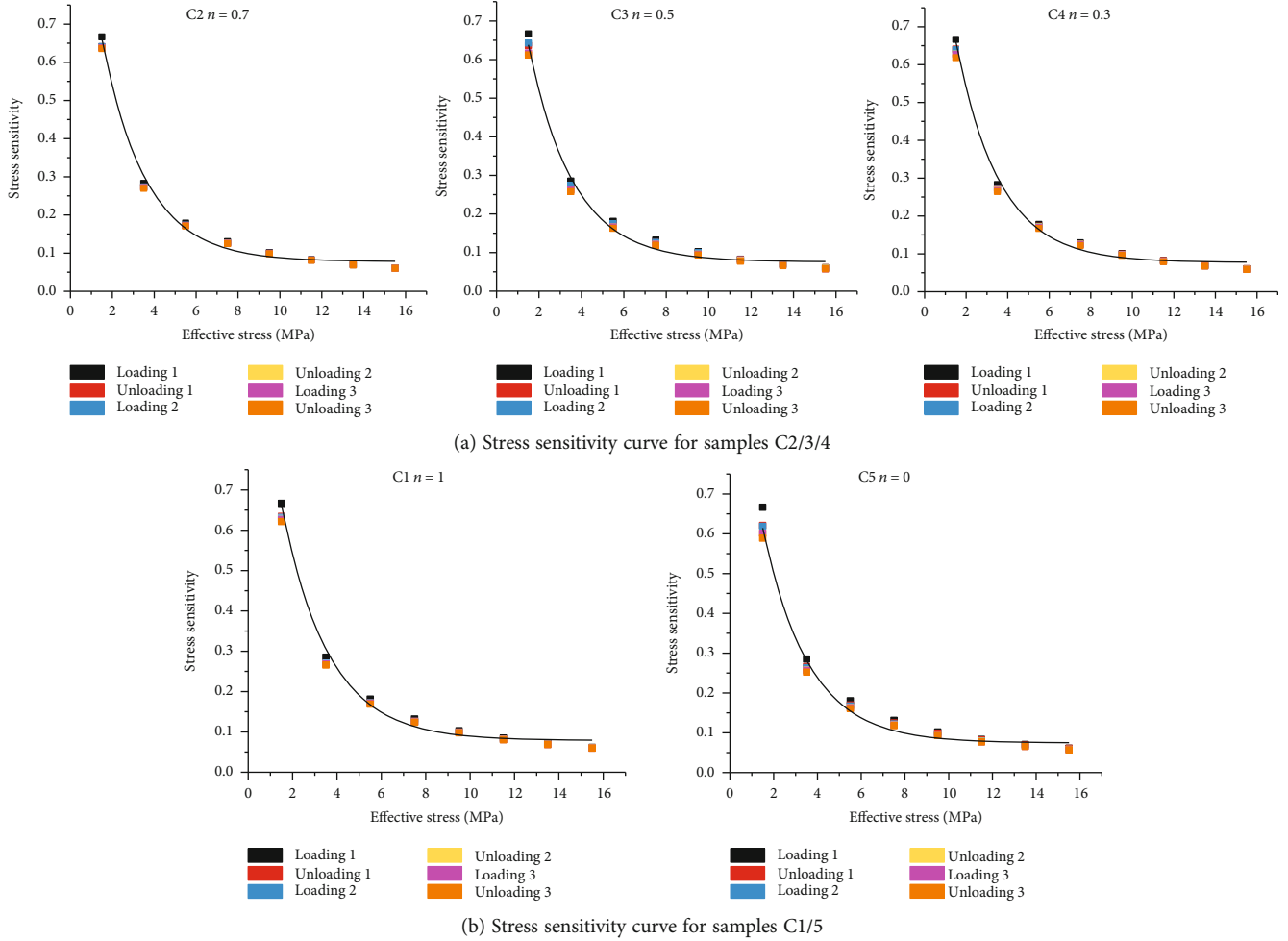


FIGURE 13: Stress sensitivity curve for samples C1 to C5.

to-rock ratio was 0.5, the coal-rock was fully mixed and the refragmentation of the internal particles resulted in a large difference in permeability of C3 crushed coal and rock, as well as a high irreversible damage rate. For C2 and C4 samples, differences in the irreversible damage rate between the first loading and unloading cycle were small. In addition, this difference increased as the number of loading and unloading cycles increased. The irreversible permeability of the C4 sample was greater than that of C2. In broken coal and rocks, when the proportion of rock particles was relatively large, the degree of damage in the internal particles and the degree of pore structural change increased. Moreover, when the proportion of coal and rock was the same, the degree of change presented the highest value.

In order to determine the impact of the test on each section of the broken coal and rock mass during loading and unloading processes, the concept of permeability damage rate (%) was introduced, and it is shown in [25]

$$D_{k_2} = \frac{k_1 - k_2}{k_1} \cdot 100\%, \quad (8)$$

where D_{k_2} represents the permeability damage rate at a

certain loading and unloading stage, k_1 is the permeability corresponding to a stress point at the beginning of a given loading or unloading stage (md), and k_2 indicates the permeability corresponding to a stress point at the end of a given loading or unloading stage (md).

Figure 12 shows that the permeability damage rate of the five types of broken coal and rock masses gradually decreased during the loading stage. In the case of C1/5, the permeability damage rate of the broken rock sample was greater than that of the broken coal sample. In addition, when performing the three loadings of the C2/3/4 broken mixtures, it was observed that the permeability damage rate of the C3 broken sample was greater than that of the C2/4 broken samples. The permeability damage rate of the C4 broken sample with a proportion of coal particles of 0.3 was greater than that of C2. The internal particle change law and the permeability differences were in agreement. In the unloading stage, the permeability damage rate of C5 fractured rocks was all greater than “0,” and the permeability damage rate of samples containing coal particles was less than “0.” This occurred because of the inverse relationship between permeability and effective stress. In relation to C2/3/4 crushed mixed samples, the permeability damage rate of C3 was smaller than that of C2/4. It was also observed

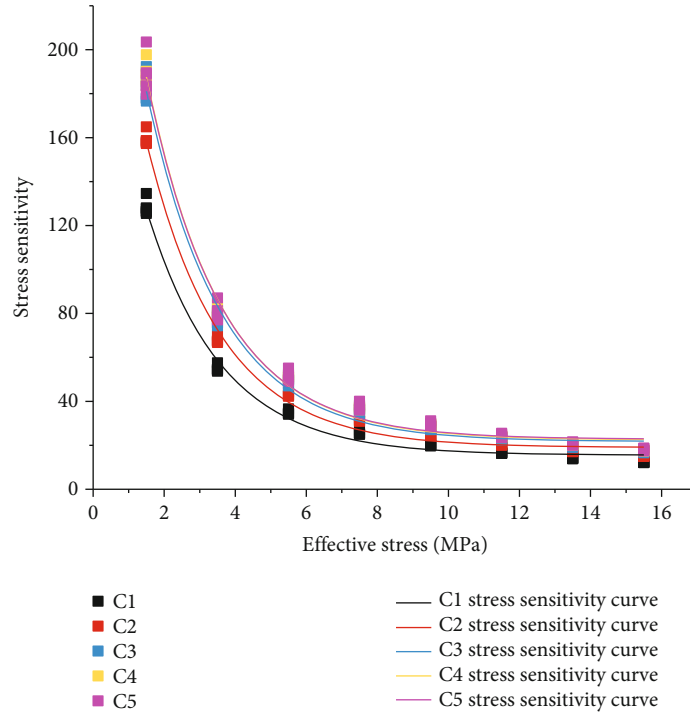


FIGURE 14: Comparison of sensitivity curves of five broken samples.

that, in the third unloading stage, the penetration damage rate of C3 was greater than the one observed in C2/4 broken samples.

3.3. Stress Sensitivity Analysis. In order to quantify the sensitivity of permeability to stress changes under cyclic loading and unloading conditions, the stress sensitivity coefficient C_k of permeability was determined using

$$C_k = \left| \frac{\partial k}{\partial \sigma_e} \right|, \quad (9)$$

where K represents the permeability of the coal sample (md) and σ_e is the effective stress (MPa).

In order to perform the analysis, permeability data for samples C1~5 were loaded into the formula, and the relationship between stress sensitivity and effective stress of broken coal sample permeability under cyclic loading and unloading conditions was calculated. Results are shown in Figure 13.

Data shown in Figure 13 indicated that the stress sensitivity of the permeability of the broken coal and rock mass in the cyclic loading and unloading process gradually decreased with the increase of the effective stress. It was also observed that, regardless of the stage, the stress sensitivity of permeability in broken coal samples gradually decreased with the increase in the number of loading and unloading cycles. The stress sensitivity of coal sample permeability at the loading stage was greater than the stress sensitivity in the corresponding unloading step. From the first loading and unloading to the third loading and unloading cycles, the stress sensitivity coefficient of the broken coal and rock mass gradually decreased.

Figure 14 presents a comparison of the stress sensitivity of the five broken samples. The ordinate in Figure 14 is different from that in Figure 13. The ordinate corresponds to the stress sensitivity resulting from the real permeability of the broken coal sample. As this figure shows, the highest point in the stress sensitivity curve gradually increased as samples went from C1 to C5, which is related to the initial permeability of the broken sample when the effective stress was 1.5 MPa. The higher the initial permeability, the initial stress sensitivity coefficient increased. In addition, the range of stress sensitivity variation for samples C1~5 gradually increased. The higher the amount of rock particles inside the broken sample, the higher the sensitivity of the sample to the effective stress and the greater the degree of change.

4. Conclusion

- (a) The internal particles in broken coal and rock were mainly caused by extrusion, deformation, and structural adjustment. In the case of broken coal and rock, the main processes were extrusion, deformation, and particle crushing. The permeability of the broken sample showed a decreasing trend. In addition, the permeability of the broken sample was significantly reduced after a loading and unloading cycle. The loading stage had a greater impact on the broken sample as compared to the unloading stage
- (b) When the proportion of coal particles in the broken sample was 50%, the irreversible permeability damage rate and the permeability damage rate of the sample presented the highest values. This result was bigger than that obtained for the broken samples

containing a proportion of coal particles of 0.3 and 0.7. The irreversible permeability damage rate and permeability damage rate of the broken rock mass were greater than those of the broken coal mass. In relation to broken coal rock, when the proportion of rock particles was relatively large, the damage degree of the internal particles and the degree of change of the pore structure were significantly higher. When the proportion of coal and rock was the same, the degree of change presented the highest value

- (c) The stress sensitivity coefficient curves of the five types of broken coal and rock masses were consistent. In addition, the stress sensitivity coefficient and effective stress can be fitted to the Darcy equation. The higher the number of rock particles inside the broken sample, the higher the sensitivity of the sample to effective stress and the greater the degree of change

Abbreviations

n :	Coal to rock volume ratio
k :	Dimensionless permeability
σ_e :	Average effective stress
K_n :	Permeability in the subsequent stress point
σ_a :	Axial pressure
e :	Crack opening
$P_1 - P_2$:	Air pressure difference
JRC:	The roughness coefficient
K :	Permeability
Z :	The root mean square
Q :	Gas flow rate
D_{k_1} :	The irreversible permeability damage rate
μ :	The fluid viscosity coefficient
D_{k_2} :	The permeability damage rate
L :	Coal sample length
A :	Coal sample base area.

Data Availability

The data obtained in the present research are available from the corresponding author upon request.

Conflicts of Interest

The authors declare that there are no conflicts of interest regarding the publication of this paper.

Acknowledgments

This research is supported by the National Natural Science Foundation of China (Grant Nos. 51704274 and 52174129), the Project of “Youth Elite Scientists Sponsorship Program by Cast” of China Association for Science and Technology (Grant No. 2017QNRC001), and the Jiangsu Province Scientific Research and Practice Innovation Project (Grant No. KYCX21_2390).

References

- [1] Z. H. Cheng, Q. X. Qi, H. Y. Li, L. Zhang, and X. G. Liu, “Evolution of the super imposed mining induced stress-fissure field under extracting of close distance coal seam group,” *Journal of China Coal Society*, vol. 41, no. 2, pp. 367–375, 2016.
- [2] C. Zhang and L. Zhang, “Permeability characteristics of broken coal and rock under cyclic loading and unloading,” *Natural Resources Research*, vol. 28, no. 3, pp. 1055–1069, 2019.
- [3] J. A. Mccorquodale, A.-A. A. Hannoura, and M. Sam Nasser, “Hydraulic conductivity of rockfill,” *Journal of Hydraulic Research*, vol. 16, no. 2, pp. 123–137, 1978.
- [4] P. GN and P. Venkataraman, “P. Non-Darcy converging flow through coarse granular media,” *Journal of the Institution of Engineers (India): Civil Engineering Division*, vol. 76, pp. 6–11, 1995.
- [5] M. G. Qian, X. X. Miao, J. L. Xu, and S. G. Cao, “On scientized mining,” *Journal of Mining & Safety Engineering*, vol. 1, pp. 1–10, 2008.
- [6] H. B. Shang, D. W. Jin, T. J. Zhang et al., “Permeability evolution of broken coal under triaxial stress,” *Journal of China Coal Society*, vol. 44, no. 4, pp. 1066–1075, 2019.
- [7] W. Wang, C. Zhang, S. X. Wu, S. Jia, and Y. S. Yang, “Experimental study on seepage characteristics of broken coal and rock samples in caving zone under cyclic loading and unloading,” *Journal of Mining Science and Technology*, vol. 5, no. 4, pp. 374–381, 2020.
- [8] M. G. Yu, J. K. Chao, T. X. Chu, F. Teng, and P. Li, “Experimental study on permeability parameter evolution of pressure-bearing broken coal,” *Journal of China Coal Society*, vol. 42, no. 4, pp. 916–922, 2017.
- [9] C. Zhang, S. H. Tu, and L. Zhang, “Study of stress sensitivity of coal samples with different mining damage in overlying strata,” *Journal of China University of Mining & Technology*, vol. 47, no. 3, pp. 502–511, 2018.
- [10] C. Zhang, *Coupling Mechanism of Stress-Fracture-Flow in High Gas Coal Seam Group and Its Impact on Pressure Relief Extraction*, [Ph.D. Thesis], China University of Mining and Technology, Xuzhou, 2017.
- [11] L. Z. Wang, Z. Q. Chen, H. L. Kong, and H. D. Shen, “Experimental study of impact of loading history on permeability characteristics of broken coal with different grain size gradations,” *Rock and Soil Mechanics*, vol. 34, no. 5, pp. 1325–1330, 2013.
- [12] T. J. Zhang, M. K. Pang, W. Q. Peng, N. Liu, and Y. G. Huang, “Seepage stability of cemented and fractured coal rock mass under tri-axial stress,” *Journal of Mining & Safety Engineering*, vol. 36, no. 4, pp. 834–840, 2019.
- [13] Y. Xue, J. Liu, P. G. Ranjith, X. Liang, and S. Wang, “Investigation of the influence of gas fracturing on fracturing characteristics of coal mass and gas extraction efficiency based on a multi-physical field model,” *Journal of Petroleum Science and Engineering*, vol. 206, article 109018, 2021.
- [14] Y. Xue, T. Teng, F. Dang, Z. Ma, S. Wang, and H. Xue, “Productivity analysis of fractured wells in reservoir of hydrogen and carbon based on dual-porosity medium model,” *International Journal of Hydrogen Energy*, vol. 45, no. 39, pp. 20240–20249, 2020.
- [15] L. Zhang, Z. W. Ye, M. Q. Huang, and C. Zhang, “Characteristics of bituminous coal permeability response to the pore pressure and effective shear stress in the Huaibei coalfield in

- China,” *Geofluids*, vol. 2019, Article ID 5489051, 12 pages, 2019.
- [16] J. Lin, T. Ren, Y. Cheng, J. Nemcik, and G. Wang, “Cyclic N₂ injection for enhanced coal seam gas recovery: a laboratory study,” *Energy*, vol. 188, article 116115, 2019.
- [17] G. Lei, P. C. Dong, S. Yang, B. Wang, Z. S. Wu, and S. Y. Mo, “Study of stress-sensitivity of low-permeability reservoir based on arrangement of particles,” *Rock and Soil Mechanics*, vol. 35, Supplement 1, pp. 209–214, 2014.
- [18] H. Ahn, S. Kim, M. Lee, and S. Wang, “Migration and residual trapping of immiscible fluids during cyclic injection: pore-scale observation and quantitative analysis,” *Geofluids*, vol. 2020, Article ID 4569208, 13 pages, 2020.
- [19] L. Zhang, J. H. Li, J. H. Xue, C. Zhang, and X. Q. Fang, “Experimental studies on the changing characteristics of the gas flow capacity on bituminous coal in CO₂-ECBM and N₂-ECBM,” *Fuel*, vol. 291, article 120115, 2021.
- [20] G. Wang, S. B. Wang, H. X. Li, X. J. Qin, and S. P. Li, “Study on water phase seepage evolution model considering mesoscale characteristics of pore and fissure in coal,” *Chinese Journal of Rock Mechanics and Engineering*, vol. 40, no. 8, pp. 1547–1558, 2021.
- [21] Q. Zhao, *Study on Fluid-Solid Coupling Flow Mechanism of Fracture*, Chengdu Southwest Petroleum University, 2015.
- [22] M. N. Testamanti and R. Rezaee, “Considerations for the acquisition and inversion of NMR T₂ data in shales,” *Journal of Petroleum Science and Engineering*, vol. 174, pp. 177–188, 2019.
- [23] L. Zhang, S. Lu, C. Zhang, and S. Chen, “Effect of cyclic hot/cold shock treatment on the permeability characteristics of bituminous coal under different temperature gradients,” *Journal of Natural Gas Science and Engineering*, vol. 75, article 103121, 2020.
- [24] Z. P. Meng and Q. L. Hou, “Experimental research on stress sensitivity of coal reservoir and its influencing factors,” *Journal of China Coal Society*, vol. 37, no. 3, pp. 430–437, 2012.
- [25] L. Zhang, S. Chen, J. H. Xue, T. X. Ren, and C. Zhang, “Permeability of bituminous coal and its stress sensitivity under liquid nitrogen fracturing,” *Journal of Mining & Safety Engineering*, vol. 37, no. 2, pp. 401–408, 2020.

Research Article

Study on Pore and Fissure Structure Characteristics of Deep Soft Coal Rock

Minbo Zhang ^{1,2}, Zhen Zhang ¹, Dangyu Zhang ², Delong Zou ³, Jinlei Du ¹,
Zichao Wang ¹ and Chunxin Li ¹

¹Xingfa School of Mining Engineering, Wuhan Institute of Technology, Wuhan 430073, China

²Jizhong Energy Resources Co., Ltd., Xingtai 054000, China

³Shenyang Research Institute of CCTEG, Shenyang 110016, China

Correspondence should be addressed to Zhen Zhang; zhangzhen_19971125@163.com

Received 20 June 2021; Accepted 16 August 2021; Published 31 August 2021

Academic Editor: Feng Du

Copyright © 2021 Minbo Zhang et al. This is an open access article distributed under the Creative Commons Attribution License, which permits unrestricted use, distribution, and reproduction in any medium, provided the original work is properly cited.

The microscopic pore and fissure structure is the key factor affecting the exploitation, storage, and migration of coalbed methane and coal spontaneous combustion tendency. For further research of the microstructure of deep soft coal rock, such as pores and fissures, the coal samples from the Yangdong mining area were qualitatively and quantitatively analyzed in terms of morphological characteristics, pore shape, pore specific surface area, pore volume, and pore diameter by a scanning electron microscope (SEM) and a low-temperature liquid nitrogen adsorption experiment. The results show that there are three major categories and five minor categories of pores with different genetic types, including metamorphic pore, exogenous pore, and mineral pore, and there are endogenous fissures, exogenous tensile fissures, and exogenous shear fissures developed in the coal body. According to the results of the low-temperature liquid nitrogen adsorption experiment, the hysteresis curves of coal samples can be divided into two types. The I type curve produces a loop. There is a “hysteresis loop” which is obvious, and there is an inflection point that is not obvious. The pore system is mainly composed of open pores. The II type curve has no adsorption back line and no obvious inflection point. The pore structure is mainly composed of an impermeable hole closed at one end. The BET specific surface area of coal samples ranges from 0.2810 to 4.7569 m²/g, with an average of 1.27984 m²/g. The BJH pore volume ranges from 0.002864 to 0.007377 cm³/g, with an average of 0.0041246 cm³/g. The average BJH pore diameter of coal samples ranges from 4.3935 to 20.1501 nm, with an average of 16.0313 nm. The pore specific surface area of coal is mainly contributed by micropores, and the transition pores contribute the most to pore volume. The distribution of pore volume in each pore section of a coal sample has the rule that the transition pore is larger than the micropore, and the micropore is larger than the mesopore, and the maximum ratio is 66.2%. The distribution of pore specific surface area has the rule that the micropore is larger than the transition pore, and the transition pore is larger than the mesopore. The maximum ratio is 91.2%.

1. Introduction

Coal is a kind of porous medium material, and its microscopic pore structure determines the adsorption, desorption, diffusion, seepage, and mechanical properties of coal. [1, 2] The pore and fissure structure of a coal body has a significant influence on the exploitation, storage, migration, and spontaneous combustion tendency of coal, and it is also a key factor affecting the extractability of coalbed methane [3, 4]. As early as the 1960s, domestic and foreign scholars

have begun to study the micropore structure of coal. Gan et al. believes that with the demand for energy and the development and utilization of coal and coalbed methane, people pay more and more attention to the study of coal pore structure [5]. The research methods of domestic and foreign scholars on the distribution characteristics of coal's microstructure and morphological development, pore and fracture types, and pore volume and specific surface area mainly include observation description and physical tests [6]. The observation description method mainly includes

macrodescription and imaging of coal samples with an optical microscope, while common physical test methods include the densitometer algorithm, the mercury injection method (MIP), the low-temperature nitrogen or CO₂ adsorption method, the scanning electron microscope (SEM), the nuclear magnetic resonance method, and the microscopic CT scanning method [7–9].

Li et al. [10] studied the relationship between the pore structure characteristics and structural deformation of tectonic coal in the Hancheng mining area using the microscopic CT test, and the study showed that cataclastic coal had the best pore connectivity and permeability, while mylonite coal had the worst. Meng et al. [11] studied Dongqu coking coal by using the microscopic CT and mercury injection test, and they obtained its pore diameter and morphology and other characteristics and believed that micropores were the main cause of poor permeability and connectivity. Thompson et al. and Kueper et al. [12, 13] first studied the porous material and calculated its fractal dimension. Wang et al. [14] studied the influence of coalification on the pore structure of the middle and high rank coal, and they found that micropores and transition pores accounted for the largest proportion of volume and specific surface area in middle and high rank coal. With the increase of coal rank, the fractal dimension of micropores gradually increased. Nie et al. [15] labeled the pore types in SEM images of coals with different metamorphic degrees. According to Mahamud's research [16], when the pressure of mercury injection is greater than 10 Mpa, the coal sample will produce a compression effect and destroy the coal's primary pore system. Cai et al. [17] used a small-angled ray combined with a scanning electron microscope to study and find out if the coal pores are mostly spheroid in low coal rank and ellipsoid in high coal rank. Klimenko et al. [18] used the conditional moment model to study the fractal characteristics of transportation, storage, and adsorption processes in the pores of CO₂ porous media. Li et al. [19] adopted SEM, low-temperature liquid nitrogen adsorption methods, and CO₂ adsorption methods for 8 kinds of coals with different metamorphic degrees to analyze parameters such as pore volume, pore diameter, specific surface area, and pore shape, and they obtained the heterogeneity of the pore morphology of coals with different ranks. Jiang et al. [20] studied the pore characteristics of structural coal and divided the low-temperature liquid nitrogen adsorption loop lines of coal samples into three categories. It is considered that there are four kinds of pores in coal: cylindrical pores with openings at both ends, cylindrical pores with openings at one end, ink bottle pores, and slit flat pores. Sun, Li and Wang, and Li et al. [21–23] also conducted low-temperature liquid nitrogen adsorption experiments under different metamorphic coals, different temperatures, different coal body structures, and different coal mines, so as to study the pore structure, pore volume and pore diameter distribution, and adsorption characteristics of coals under different conditions.

The pore-fissure structure of coal rock is closely related to coal seam mining and gas extraction, and it has a certain influence on coal spontaneous combustion. The pore-fissure

structure in deep soft coal rock is extremely complex, and the pore size distribution varies from millimeter to nanometer. The different pore sizes control the adsorption, apportionment, diffusion, and seepage of coalbed methane. The traditional scanning electron microscope method only qualitatively studies the pore and crack parameters on the polished surface of a coal sample, but it cannot deeply study the internal pore structure of coal, which has limitations. In this paper, the method of SEM and low-temperature liquid nitrogen adsorption experiment is adopted. It is of great significance to the coalbed methane resource evaluation, exploration, and development for a qualitative and quantitative characterization of the innovative ways of combining different scales of deep soft coal rock micropore structure research and analysis of the changing rule of the specific surface area and pore volume of coal and the pore size distribution of laws and so on.

2. Experimental Samples and Methods

The coal sample in this experiment is taken from the Yangdong well field of the Fengfeng coalfield, which is located in the east wing of the middle part of the Fengfeng coalfield. The coal quality belongs to the section of coking coal, thin coal, and lean coal in the metamorphic zone of the Fengfeng coalfield. The industrial analysis of raw coal quality is shown in Table 1:

According to the relevant standards of “GB/T482-2008 Coal Sample Method for Coal Seam” and “SY/T6154-1995 Determination of Static Nitrogen Adsorption Capacity by Rock Specific Surface and Pore Diameter Distribution,” the no. 2 coal (large coal) of the Permian Shanxi Formation in Yangdong Mine was collected as experimental coal samples, and the collected coal samples were sealed and stored in sealed bags with labels and transported to the laboratory.

2.1. Scanning Electron Microscope Observation Method.

According to the test requirements of the samples in the laboratory, the collected large coal samples are cut at a slow speed. The size of the cut is generally about 1 cm × 1 cm × 1 cm, which is a relatively regular cube. If there is secondary damage to the coal in the cutting process, the sample will be scrapped. One side of the qualified small sample is ground and disassembled; that is, the gauze is used for smooth and slow grinding, respectively. The side after disassembling is selected as the observation surface, and its surface is purged for clean treatment, and then dried. Then, conductive treatment (the observation surface is plated with a conductive layer) is conducted for experimental observation. The experimental instrument utilized here was the JSM-5510LV scanning electron microscope from Japan Electron Optics Laboratory Co., Ltd., as shown in Figure 1. The instrument resolution was 3.2 nm, and the magnification was continuously adjustable from 18 to 300,000. The surface of the sample was observed by secondary electronic imaging, and the apparent morphology and pore-fissure structure of the sample were analyzed.

TABLE 1: Raw coal industry analysis results.

Coal sample	Mad (%)	Ad (%)	Vdaf (%)	Std (%)	Qgrad (MJ/kg)	GR-I	CR-C (1-8)
Large coal	0.54 ~ 2.08	11.97 ~ 38.34	16.78 ~ 33.75	0.20 ~ 0.70	20.74 ~ 31.93	3 ~ 79	4 ~ 7
	1.31	25.16	25.27	0.32	26.34	41	6



FIGURE 1: JSM-5510LV scanning electron microscope.

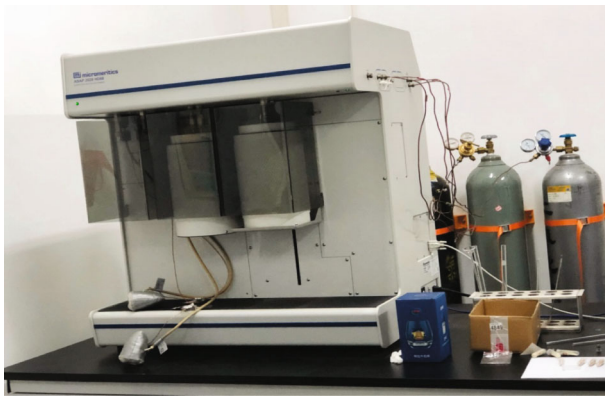


FIGURE 2: ASAP-2000 automatic surface and aperture analyzer.

2.2. Low-Temperature Liquid Nitrogen Adsorption Method.

According to the requirements of the experimental test, the large coal samples collected were crushed with a crusher in the laboratory, and then the crushed coal samples with a particle size of 60 to 80 mesh were screened out by a standard sieve. The prepared coal samples were put into a 105°C electric heating blast drying oven to dry, and then they were bottled and sealed for storage for experimental use. The experimental instrument utilized here was the ASAP-2000 automatic specific surface and aperture analyzer produced by Micromeritics Instrument Co., Ltd., as shown in Figure 2. The test was carried out according to the national standard “Determination of specific surface area of solid substance by gas adsorption BET method” (GB/T19587-2017). The instrument has high testing accuracy, the specific surface area analysis range is from 0.0005 m²/g to none, the pore diameter analysis range is 0.5 to 500.0 nm, and the pore volume minimum can detect

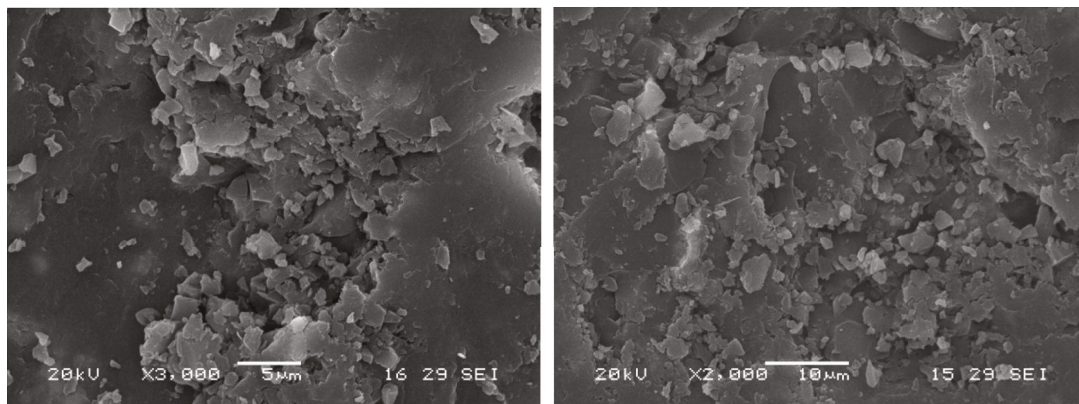
0.0001 cm³/g. The nitrogen adsorption method is used to measure the pore structure distribution characteristics of the coal sample, such as the specific surface area, pore diameter, and pore volume.

3. Analysis of Microstructure Characteristics of Coal under Scanning Electron Microscope

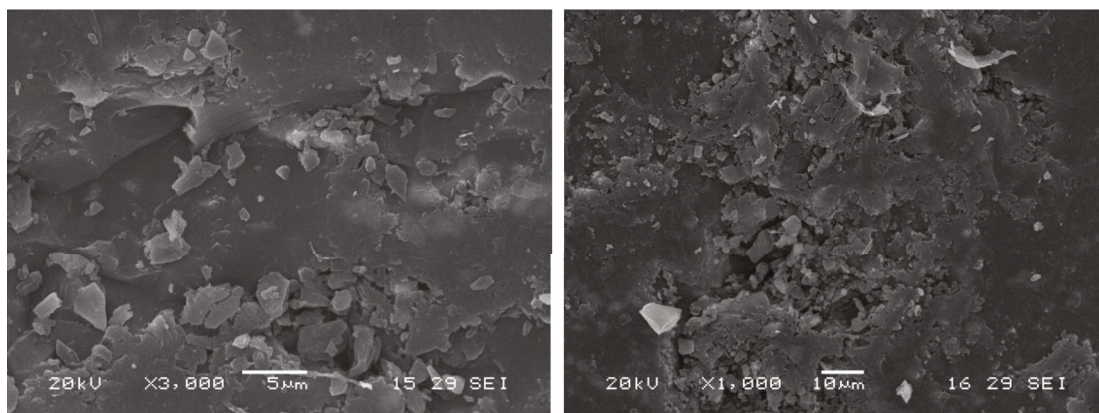
3.1. Analysis of Pore Characteristics of Coal Body. The pore and fissure results observed by a large number of scanning electron microscopy (SEM) analyses are shown in Figures 3 and 4. The coal samples are observed at different magnification ratios, and the pore and fissure characteristics of each coal sample can be clearly seen.

According to the scanning electron microscopy results of the coal samples in Figure 3, five types of pores are developed in the coal samples, including the granular pore, the breccia pore, the friction pore, the intergranular pore, and the air vent. The coal body as a whole is a collection of broken particles; the structure is loose, the whole coal body is flaky, the granular pore is attached to the surface of the coal body, and they have different shapes and sizes, irregular shapes, and relatively developed pore structures. Most of the pores are filled and stacked with minerals, including granular pores (Figure 3(a)), breccia pores (Figures 3(a) and 3(b)), and intergranular pores (Figure 3(c)). The coal body is damaged by the weak tectonic stress field or external factors, and it forms a sharp corner shape with a relatively regular shape. There is basically no displacement between the holes, and the connectivity is good. The holes formed between the breccia (i.e., the breccia holes) are exogenous holes. The pore diameter generally ranges from 2 μm to 10 μm, which is usually found in cataclastic coal. There are some clastic minerals filling in the pore, but it will not seriously block the pore fissure and has a certain permeability. A fragmentary hole is a kind of exogenous hole formed after being damaged by strong tectonic stress, and the shape of the crushed grain is mostly a sheet, block, or semicircle. It is small in volume and easy to accumulate. It is a displacement hole formed between the crushed grains and has good connectivity. The pore diameter range is generally 0.5 to 5 μm, and it is mostly found in cataclastic coal and crushed coal. Because severe fissures will block the pore and fissure, it has a certain influence on the permeability of a coal reservoir. Intergranular pore is the pore between the mineral grains, and it is a mineral pore. The pore diameter is generally micron sized, which is less developed in the coal body and has little influence on the permeability of a coal reservoir.

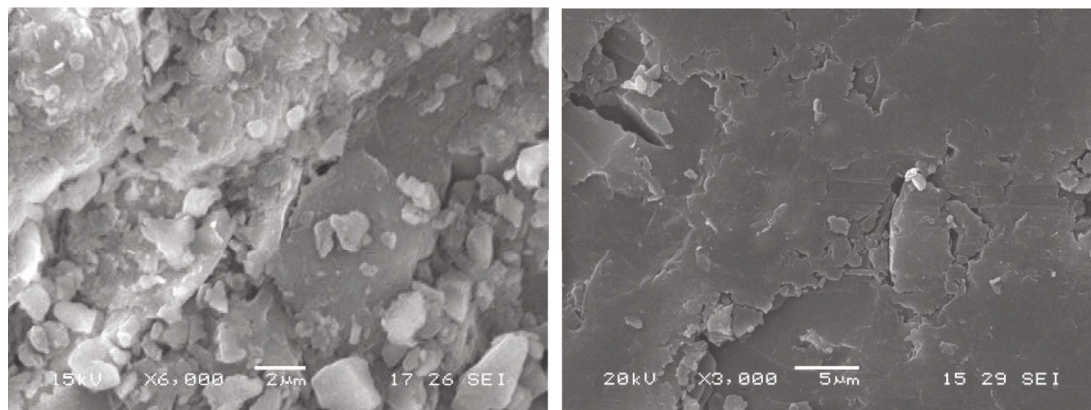
It can also be seen from the figure that the structure on the surface of the coal body is becoming denser, with fewer fissures and macropores. The pores are more elliptical and



(a) Granular hole and breccia hole

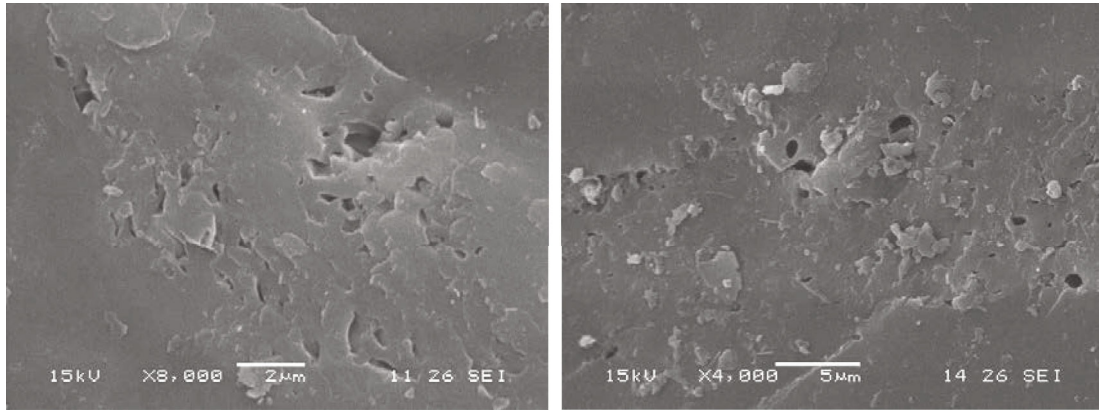


(b) Breccia hole and friction hole



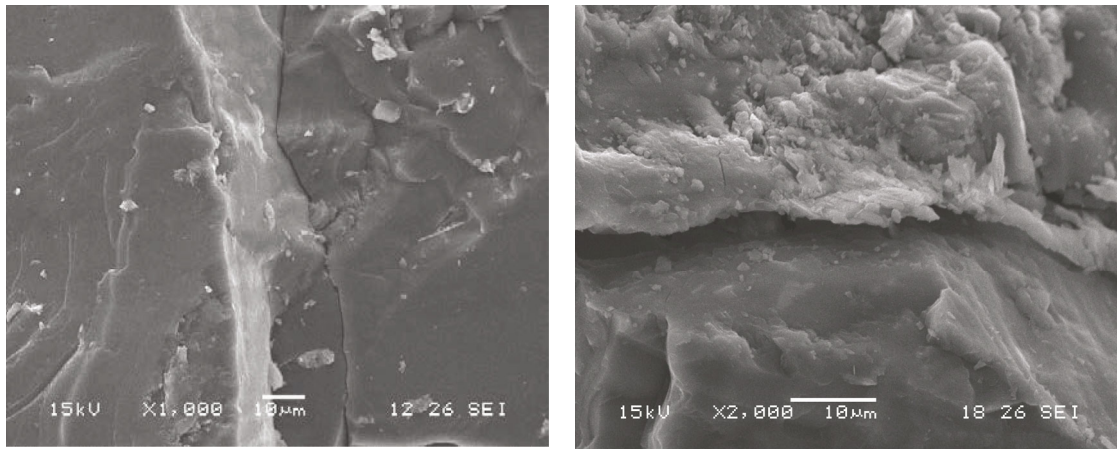
(c) Intergranular pore and friction hole

FIGURE 3: Continued.



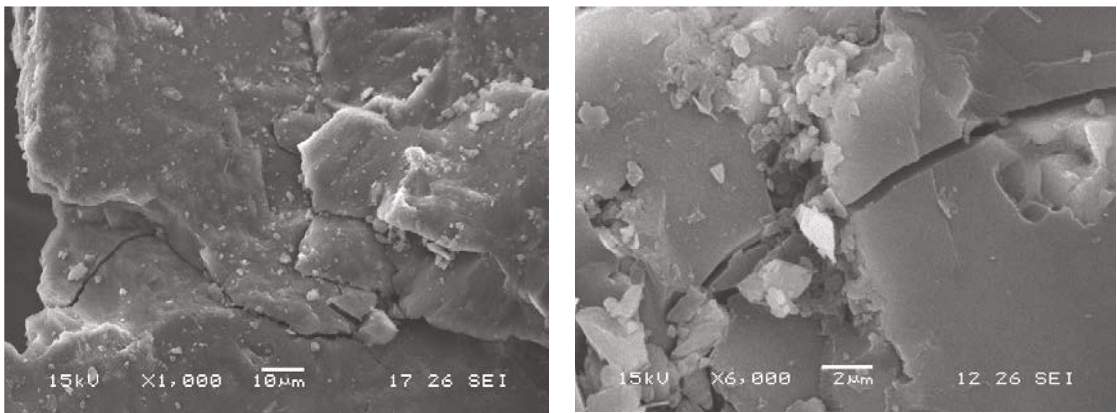
(d) Air vent

FIGURE 3: Pore characteristics under a scanning electron microscope.



(a) Endogenous fissure

(b) Exogenous tensile fissure



(c) Exogenous shear fissure

(d) Exogenous tensile fissure are filled with debris

FIGURE 4: Fissure characteristics under scanning electron microscope.

angular, the size is not uniform, there are few endogenous fissures, and primary bedding and fine bedding are rare. The surface of the coal sample is smooth, the structure development is relatively complete, there are few and thin holes on the surface, the connectivity between holes is poor, and the fissures are not developed. Friction pores (Figures 3(b) and 3(c)) and air vents (Figure 3(d)) were

developed. Under the action of compressive stress, and due to friction or the sliding movement between the coal face and the surface, there is the formation of grooves, round lines, and long triangular or linear holes (namely friction holes) that are exogenous holes. The pore diameters vary from 1 to 2 µm to dozens of microns. The pores are partially connected, which has a certain effect on the migration of

coalbed methane. The pores exist in cataclastic coal and crushed coal. The air vent is a kind of metamorphic pore, which is mostly round, oval and tubular with smooth edge and formed by “gas generation” and “gas accumulation” due to coalification in the coal-forming period. The common stomata size is 0.1 to 3 μm , the development is more concentrated, about 1 μm is more common, the stomata are independent of each other, the connectivity between the pores is not good, and the pores are developed in both primary coal and structural coal.

3.2. Analysis of Coal Fissure Characteristics. The fissure in the coal body is due to the coal seam in the coal-forming period by the nature of various stresses, such as tectonic stress and geological stress, resulting in the coal body fissure, section opening or fissure, and other non-closed-state fissure phenomena. Research on coal microfissures began last century, but research progress is relatively slow. It was not until the 1960s, when Ammosov and Eremin [24], both scholars of the former Soviet Union, put forward their ideas in the book “Fissures in Coal.” Since then, the research on coal body fissures gradually became mature. Later, the term “cleat” was proposed to describe endogenous fissures, and cleat can be divided into facet cleat and end cleat [25]. On the basis of previous research, this paper also divides the fissures in the coal into two types: endogenous and exogenous.

As can be seen from Figure 4, there are endogenous fissures and exogenous fissures developed in the coal samples, and their morphology, size, and genesis are different. In the endogenous fissure, coal is densely developed, with few fillings and no scratches on the surface, which are relatively flat and have tensile characteristics (as shown in Figure 4(a)). Fills in cleats are generally autogenic minerals and rarely fill broken coal particles. Under certain tectonic action, dislocation or extrusion occurs between coal bodies, resulting in fissures or openings, and exogenous tensile fissures and shear fissures can be seen (as shown in Figures 4(c) and 4(d)). Due to the effect of tensile stress, the exogenous tensile fissure has a large opening, appearing as a narrow and long opening (as shown in Figure 4(d)). There is no scratch on the surface, and some debris will be filled in the fissures, with cracks ranging from a few microns to dozens of microns. Exogenous shear fissures rupture due to the action of shear force, showing staggered small fissures and long extension. The fissure has a small opening and is basically closed (as shown in Figure 4(c)). Most fissures are imbricated or stepped, and some are also X-shaped, with good ductility and debris filling.

4. Analysis of Low-Temperature Liquid Nitrogen Adsorption Experiment Results

The pore structure of coal is complex, and the pore diameter distribution varies from millimeter to nanometer. Therefore, the study of the pore structure of coal not only needs qualitative characterization but also needs to be combined with quantitative calculation to be more accurate. The above SEM results are used to qualitatively characterize the morphological characteristics of pore fissures on the surface of

a coal body. The observed coal body morphological characteristics were relatively rough. The characteristics of micron and millimeter pores and fractures in coal samples can be clearly observed, but the nanosized pores cannot be detected. Therefore, the low-temperature liquid nitrogen adsorption experiment can be used to characterize the finer pore structure and morphological characteristics in coal.

4.1. Isothermal Adsorption Curve Analysis. Isotherm adsorption curve can well reflect the surface adsorption characteristics of coal samples, and pore morphology characteristics of experimental coal samples and pore diameter distribution which plays a major role in adsorption can be seen from the adsorption curve and desorption loop. The adsorption isotherm of each coal sample is shown in Figure 5.

The International Union of Pure and Applied Chemistry (IUPAC) classify the isotherm adsorption curve into six types [26]. Compared with the six adsorption isotherms, the nitrogen adsorption isotherm of coal samples tends to belong to the IV adsorption isotherm as a whole, but it is not the same as it. The overall adsorption curve shows an upward trend, and the adsorption curve is lower, while the desorption curve is higher. When the relative pressure is greater than 0.9, the curve rises steeply, and the adsorption volume increases sharply. The curves show that at the beginning, the single-layer adsorption transitions to multilayer adsorption at the low pressure stage. As the relative pressure continues to increase, multilayer adsorption begins to appear, and the adsorption amount gradually increases until the multilayer adsorption gradually forms, and the adsorption layer is infinite when the saturated vapor pressure is reached. In the middle and high pressure stage (the relative pressure is greater than 0.5), the separation phenomenon of the adsorption curve and the desorption curve gradually appears, and the hysteresis loop is produced, namely, the hysteresis loop. The appearance of the adsorption hysteresis ring is caused by capillary condensation on the surface of coal under high pressure (the relative pressure is greater than 0.9).

It can be seen from the hysteresis loop of the coal sample in this experiment that its hysteresis loop type does not strictly belong to the specific type divided by IUPAC. Each type of adsorption hysteresis loop represents different pore structures and reflects the adsorption capacity and air permeability of coal. Referring to the study of adsorption experiments on a large number of coal samples by Chen and Tang [27], the adsorption isothermal hysteresis curve characteristics of coal samples in this experiment were observed and compared, and the adsorption isothermal hysteresis curves were divided into two types:

- (1) I type: nos. 1, 2, 3, and 4 coal samples are representative, the normal type curve produces a loop, the desorption curve and the adsorption curve do not completely coincide, the curve “hysteresis loop” is obvious, and the inflection point is not obvious, indicating that there is no “ink bottle” like hole in the coal sample. The adsorption curve and desorption

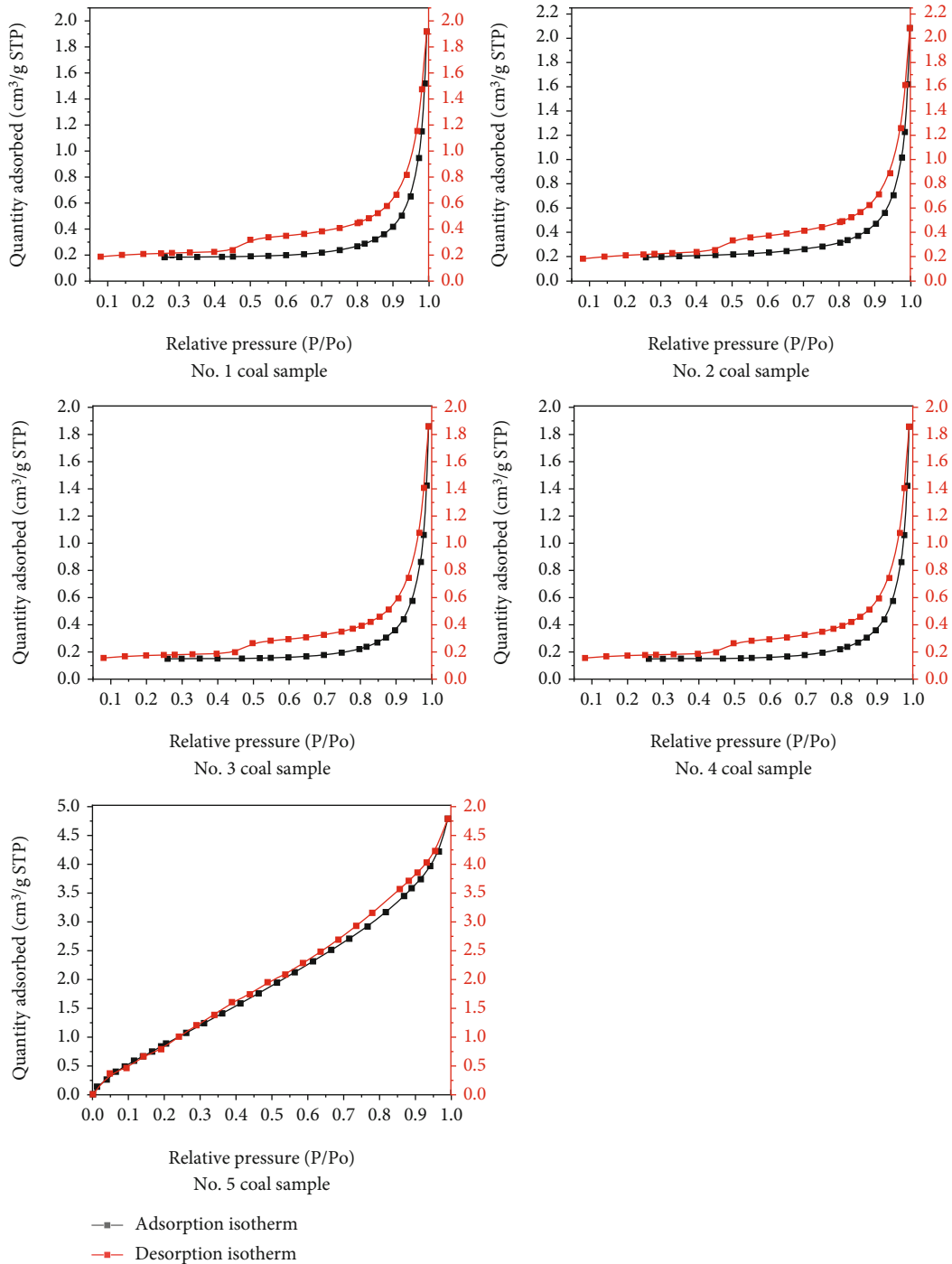


FIGURE 5: Adsorption isotherm of coal sample.

curve basically overlap at low and high relative pressure, and the inflection point occurs when the relative pressure is about 0.5. In the region of 0.45 to 0.95, the capillary condensation phenomenon occurs in the coal body, and the “hysteresis loop” is generated, which is because the pressure required for the capillary condensation of the coal body is less than that of evaporation. It shows that there are closed holes at one end in the low pressure and high pres-

sure stages, which mainly include cylindrical holes, parallel plate holes, wedge-shaped holes, and tapered holes at one end. In the middle and high pressure stage, the pore system is mainly composed of open pores, including cylindrical pores at both ends and parallel plate pores at four sides, and part of slit pores. Such pore structure is conducive to the migration of coalbed methane, and has good permeability and connectivity

TABLE 2: Pore structure parameters of coal samples.

Coal sample	BET surface area (m ² /g)	BJH surface area (m ² /g)	Single point total pore volume (cm ³ /g)	BJH pore volume (cm ³ /g)	BJH average pore width (nm)
1	0.3699	0.6433	0.002967	0.002942	18.2940
2	0.4405	0.7358	0.003224	0.003252	17.6790
3	0.2810	0.5686	0.002865	0.002864	20.1501
4	0.5509	0.8529	0.004229	0.004188	19.6399
5	4.7569	6.7164	0.007375	0.007377	4.3935
Average	1.27984	1.9034	0.004132	0.0041246	16.0313

(2) II type: the no. 5 coal sample is representative, the normal type curve does not produce the adsorption back line, the desorption curve and the adsorption curve almost completely coincide, and the hysteresis phenomenon is not obvious, i.e., there is no obvious inflection point; this is because this kind of coal sample coal capillary condensation and evaporation required pressure that is basically equal. This shows that the pore structure of this kind of coal sample is mainly composed of impermeable pores with one end closed, including cylindrical holes, parallel plate holes, wedge-shaped holes, and tapered holes with one end closed. The pore connectivity is poor, which is not conducive to the exploitation and migration of coalbed methane. The poor connectivity between pores is not conducive to the exploitation and migration of coalbed methane

4.2. Specific Surface Area and Pore Volume Analysis. As a solid material of porous medium, coal's specific surface area is a powerful index to show the adsorption capacity of coal seam, and the adsorption capacity of coal presents a positive correlation with the change of the specific surface area. The specific surface area results obtained by different calculation models are also different. The specific surface area obtained by the BET calculation model is the most common method. In this experiment, the BET equation [28] based on the multimolecular layer adsorption theoretical model is used to characterize the specific surface area:

$$\frac{1}{W[(p_0/p) - 1]} = \frac{1}{W_m C} + \frac{C - 1}{W_m C} \left(\frac{p}{p_0} \right), \quad (1)$$

where W is the weight of adsorbed gas at the relative pressure (P/P_0); W_m is the weight of adsorbed gas covered by a single surface; P/P_0 is the adsorption relative pressure; P is the equilibrium partial pressure of adsorbed mass; P_0 is the saturated vapor pressure of the adsorbent; C is the BET constant, which is related to the adsorption energy of the first adsorption layer.

In physical adsorption, the adsorption between solid and gas is dependent on the intermolecular gravity and occurs. The molecules that have been adsorbed still have gravity; so, on top of the first layer of adsorption, they can also adsorb a second layer, a third layer ..., that is, multimolecular layer adsorption. Pore volume (also called pore volume) mainly shows the total pore volume per unit mass. Table 2

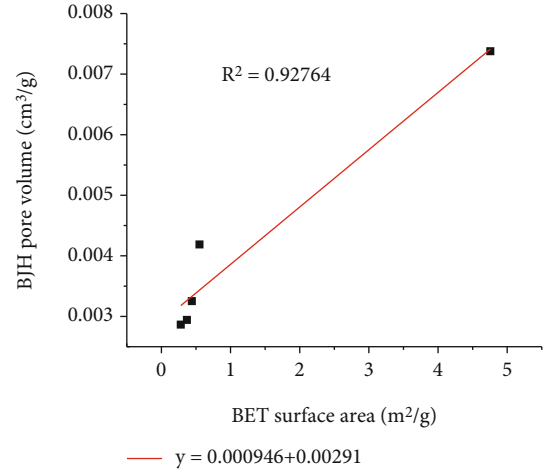


FIGURE 6: BET specific surface area and BJH pore volume fitting curve.

shows the distribution characteristics of pore structure parameters of coal samples obtained under the low-temperature liquid nitrogen adsorption experiment.

The results show that the BET specific surface area of coal samples ranges from 0.2810 to 4.7569 m²/g, with an average of 1.27984 m²/g. The specific surface area of BJH ranges from 0.5686 to 6.7164 m²/g, with an average of 1.9034 m²/g. The BJH specific surface area is larger than that of BET on the whole, but the changing trend remains consistent. The total pore volume of the single point method of a coal sample ranges from 0.002865 to 0.007375 cm³/g, with an average of 0.004132 cm³/g. BJH pore volume ranges from 0.002864 to 0.007377 cm³/g, with an average of 0.0041246 cm³/g. Generally speaking, the difference between the two is very small. The BJH average pore diameter of a coal sample varies greatly from 4.3935 nm to 20.1501 nm, with an average of 16.0313 nm.

Figure 6 is the fitting curve of the relationship between specific surface area and pore volume. It can be seen that there is a positive correlation between specific surface area and pore volume, and both specific surface area and pore volume of coal samples in the mining area are small.

Figure 7 shows the pore specific surface area and pore volume increment diagram under different pore diameters. The relation diagram of the pore specific surface area and pore diameter shows that the curve trends of coal samples 01, 02, 03, and 04 are similar, with peaks at about 3 to

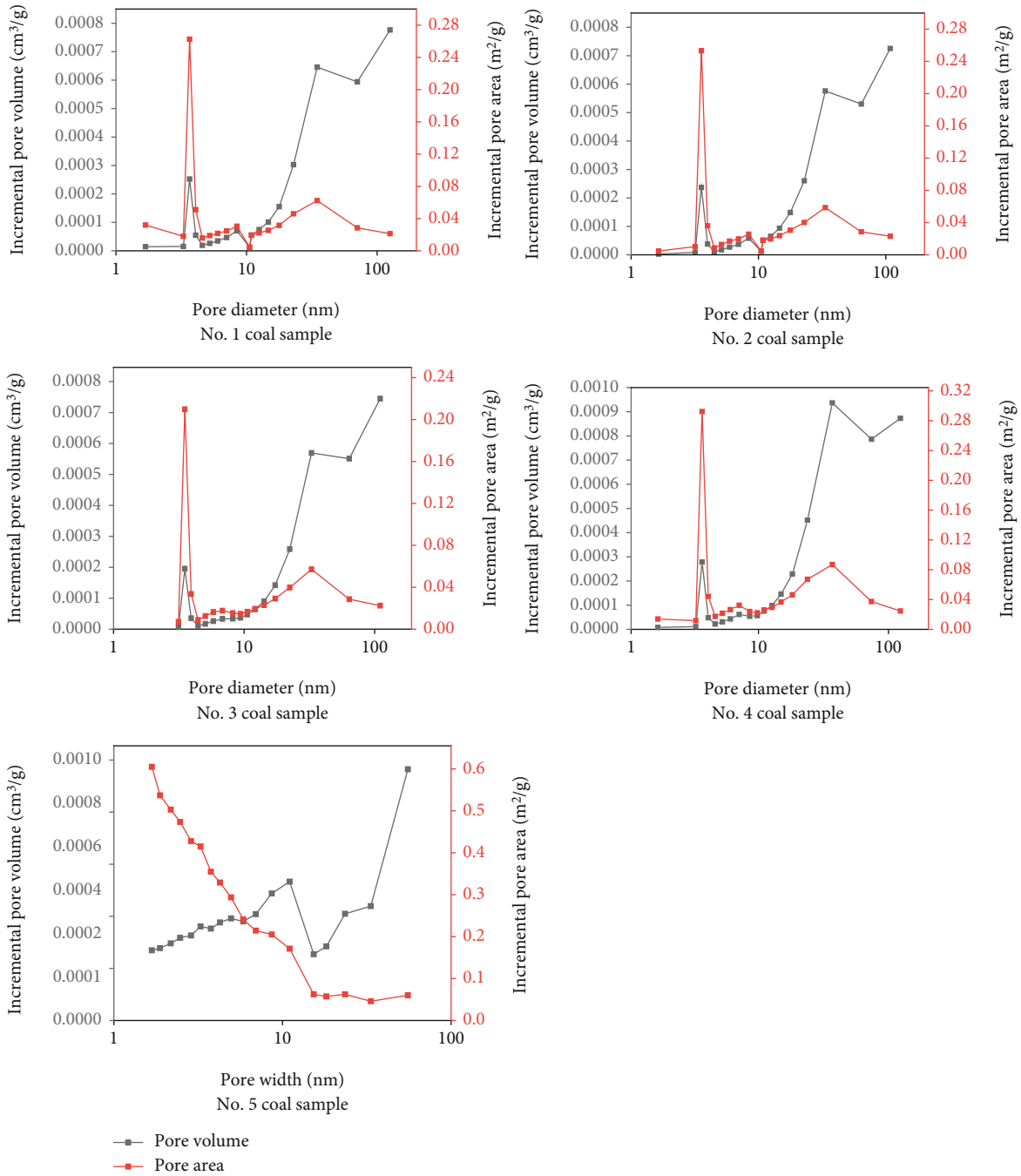


FIGURE 7: Increment diagram of specific surface area and pore volume of coal sample.

4 nm and 20 to 40 nm, indicating that micropores and transition pores have a large contribution to the specific surface area of coal samples. However, the curve of coal sample 05 is different from the other four coal samples. As can be seen from the figure, the peak appears at the aperture of about 2 nm, and then it gradually decreases, but it still keeps a large value. After 10 nm, it becomes very low and flattens out, indicating that the micropores within the range of 2 to 10 nm make a great contribution to the specific surface area of coal samples.

As can be seen from the diagram of the relationship between pore volume increment and pore diameter, the pore

volume increment increases continuously with the increase of pore diameter. The peak value of coal samples 01, 02, 03, and 04 is mostly at the aperture of 30 nm and 100 nm, while the peak value of coal sample 05 is at 10 nm and 50 nm, indicating that the transition hole plays a major contribution to the pore volume of coal sample.

4.3. Analysis of Pore Diameter Distribution Characteristics. The classification methods of apertures usually include the B.B. Hodot decimal division and the IUPAC classification. There are many calculation models for apertures, including BJH, D-H, HK, DFT, and NLDFT. [29] In this paper, the

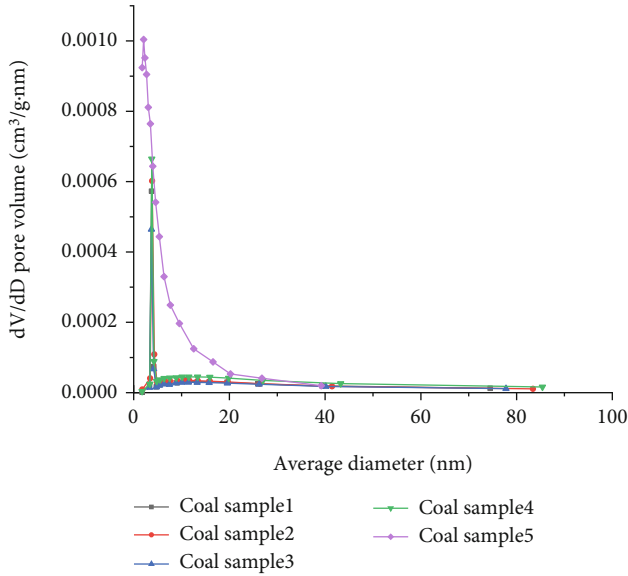


FIGURE 8: Distribution characteristics of pore diameter of a coal sample.

BJH theoretical model is used for pore diameter analysis of coal samples, and the B.B. Hodot decimal division method [30] is used for the coal pore type division system. According to the classification system, the pore diameters of coal can be divided into four types: macropore (>1000 nm), mesopore (100-1000 nm), transition pore (10-100 nm), and micropore (<10 nm). The pore diameter distribution range of each sample recorded by the instrument in this experiment is 1.7 nm to 300 nm. Figure 8 shows the pore diameter distribution characteristics of a coal sample obtained under the low-temperature liquid nitrogen adsorption experiment.

In Figure 8, dV/dD represents the differential of total pore volume to pore diameter, and it represents the distribution function of pore volume density. The peaks protruding from this curve represent the most concentrated pore diameter range in the measured coal sample. As shown in Figure 8, the pore diameter distribution of each coal sample in the region of 2 to 20 nm presents a single peak distribution phenomenon, which indicates that the pore diameter of a coal sample is mainly distributed in the region of 2 to 20 nm, and the main peak is mainly around 2 to 5 nm. Therefore, the micropores and transition pores larger than 2 nm contribute greatly to the pore volume. Generally speaking, pores with pore diameter less than 100 nm, especially micropores, are the main factors that determine gas adsorption, storage, and migration. Therefore, the distribution of micropore diameter in coal plays a leading role in gas storage and migration in coal seams.

According to the classification of coal samples according to the low-temperature liquid nitrogen adsorption isotherm above, the pore diameter distribution curve is also divided into two kinds. The peak value of coal samples 1 to 4 appears at around 4 nm, and both ends of the peak value plummet, indicating that the pore diameter distribution is most concentrated when the pore diameter is 4 nm. The curve has a flat trend in the range of 5 to 20 nm, indicating that there

are a large number of micropores and transition pores in this range, and the pore diameter distribution is uniform, but there is no particularly concentrated distribution of pores. The peak value of coal sample 05 appears at 2 nm, indicating that the pore diameter distribution is most concentrated at the pore diameter of 2 nm. The curves at both ends of the peak value did not drop suddenly, but the peak value gradually decreased with the increase of pore diameter until 20 nm, indicating that the micropores and transition pores at 2 to 20 nm accounted for the majority of the coal sample 05. In general, micropores and transition pores play an absolute role in controlling the specific surface area and pore volume of coal samples, respectively.

Table 3 shows the pore diameter distribution and proportion characteristics of coal samples obtained under the low-temperature liquid nitrogen adsorption experiment, and Figure 9 shows the specific surface area and pore volume proportion of each pore diameter segment. It can be seen that the percentage of pore volume in each pore diameter section of a coal sample is dominated by transition pores, and transition pores make the largest contribution to pore volume. Micropore volume accounts for 12.4% to 61.1% of the total pore volume, transition pore volume accounts for 25.8% to 66.2%, and middle pore volume accounts for 13.1% to 26.1%. The specific surface area of each pore section of a coal sample is dominated by the proportion of micropores, which contributes the most to the specific surface area. The proportion of micropores was 56.2% to 91.2%, the proportion of transitional pore specific surface area was 7.6% to 40.87%, and the proportion of middle pore specific surface area was 1.2% to 3.9%. The results of aperture ratio analysis are consistent with those in Figure 8. The distribution of pore volume in each pore section of a coal sample has the rule that the transition pore is larger than the micropore, and the micropore is larger than the mesopore, and the maximum proportion is 66.2%. The distribution of pore specific surface area show that the micropore is larger than the transition pore, and the transition pores are larger than the mesopores. The maximum ratio is 91.2%.

5. Discussions

By comparing the results of scanning electron microscopy of the coal samples in the study area, it can be found that there are metamorphic pores, exogenous pores, and mineral pores in the coal, and there are endogenous fractures, exogenous tensile fractures, and exogenous shear fractures in the coal. This is because the tectonic stress fields or external factors cause different degrees of damage to the coal body, resulting in different types of pore fractures. By comparing the isothermal adsorption curves of coal samples and referring to previous studies and distinguishing from their classification criteria, the analysis shows that the isothermal adsorption curves of coal samples in the study area can be divided into two types, and the pore structure system of coal samples is mainly composed of open pores and impermeable pores closed at one end. This condition is because different holes will produce different hysteretic curves.

TABLE 3: Characteristics of pore diameter distribution proportion of coal sample.

Coal sample	Pore volume (cm ³ /g)	Pore size ratio (%)			Surface area (m ² /g)	Pore size ratio (%)		
		<10 nm	10 ~ 100 nm	>100 nm		<10 nm	10 ~ 100 nm	>100 nm
1	0.002967	15	60	25	0.3699	61.1	35.3	3.6
2	0.003224	16.4	59.7	23.9	0.4405	64.5	32.6	2.9
3	0.002865	12.4	61.5	26.1	0.2810	56.2	39.9	3.9
4	0.004229	12.92	66.2	20.9	0.5509	56.3	40.9	2.8
5	0.007375	61.1	25.8	13.1	4.7569	91.2	7.6	1.2

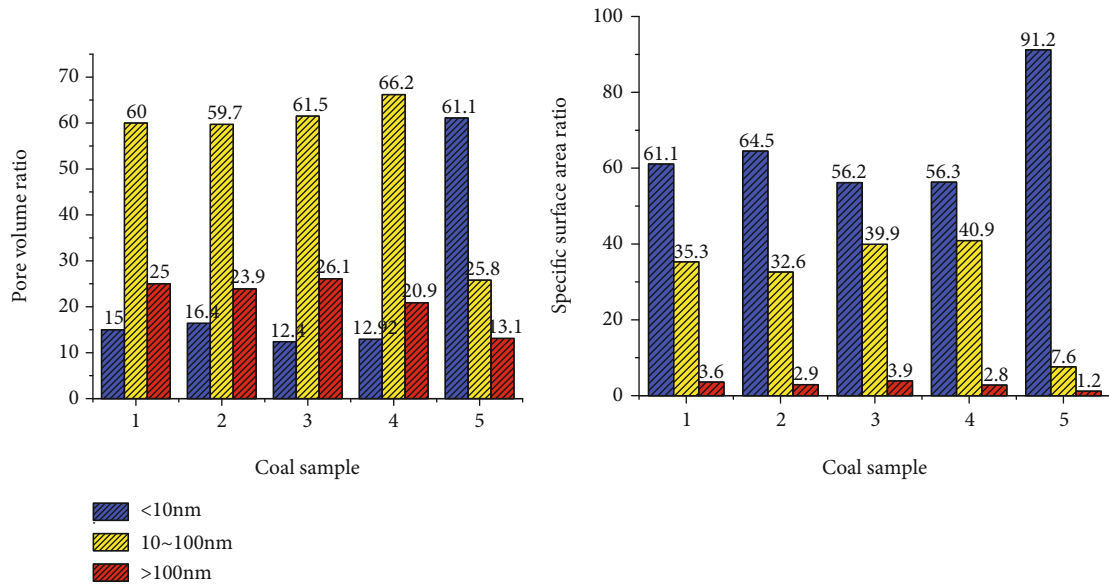


FIGURE 9: Specific surface area and pore volume ratio of each pore diameter segment of a coal sample.

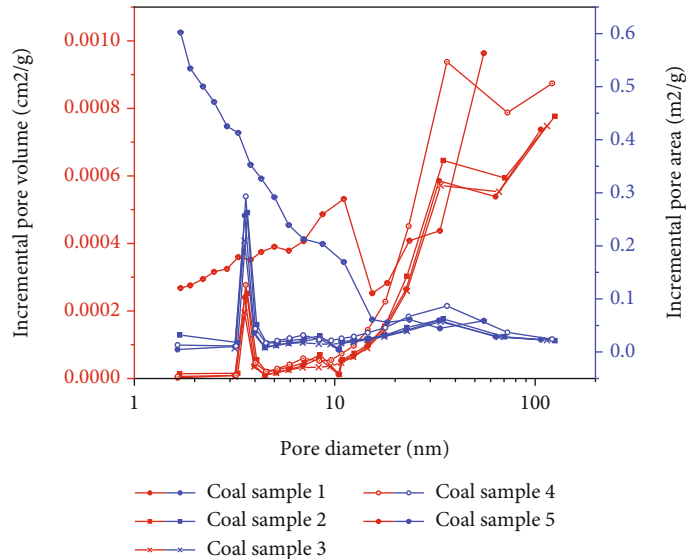


FIGURE 10: Distribution trend of specific surface area and pore volume of coal sample.

According to Figure 10, qualitative analysis was made on the variation of specific surface area and pore volume with pore diameter of coal samples in the study area. It can be seen from the overall trend of the relation curve between

incremental pore area and pore diameter that there are different peaks in the range of the pore diameter of coal, especially in the range of a micropore, indicating that a micropore has a large contribution to the specific surface

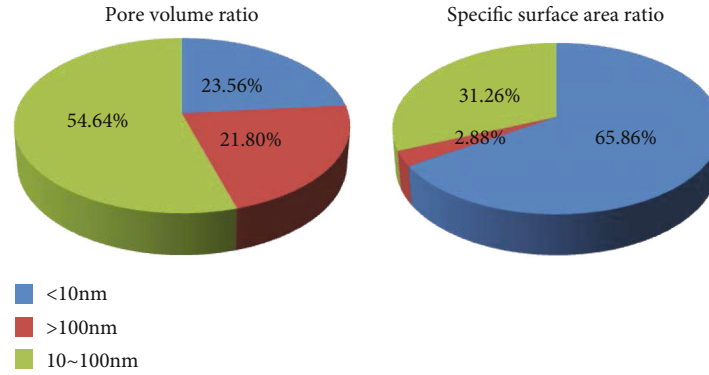


FIGURE 11: Figure of average proportion of specific surface area and pore volume of coal sample.

area of a coal sample, accounting for the largest proportion. From the overall trend of the relation curve between incremental pore volume and pore diameter, it can be seen that the incremental pore volume increases with the increase of pore diameter and presents the characteristics of multipeak distribution. The most obvious peak value is mostly located within the range of the transition hole, indicating that the transition hole plays a major contribution to the pore volume of a coal sample and accounts for the largest proportion.

On the basis of qualitative analysis, quantitative analysis was carried out on the average proportion of specific surface area and pore volume of each pore section of coal sample. As can be seen from Figure 11, the micropores accounted for 23.56% of the total pore volume, the transition pores accounted for 21.80%, and the mesopores accounted for 54.64%. The specific surface area of micropores, transition pores, and mesopores accounted for 65.86%, 31.26%, and 2.88%, respectively. The results show that the distribution of pore volume in each pore section of a coal sample has the rule that the transition pore is larger than the micropore, and the micropore is larger than the mesopore. The distribution of the pore specific surface area has the rule that the micropore is larger than the transition pore, and the transition pore is larger than the mesopore. This is because micropores and transition pores make major contributions to the pore specific surface area and pore volume of coal samples, respectively, and the greater the contribution, the greater the proportion. The research results have certain practical significance for the design of gas extraction, coal seam mining, and migration in the study area.

6. Conclusion

- (1) SEM results show that there are three types of pores, namely, metamorphic pores, exogenous pores, and mineral pores, and there are five subtypes of pores with different genetic types, such as air vent, granular hole, breccia pores, friction pores, and intergranular pores. The pore diameter is generally in the transition range from nanometer to micron. There are endogenous fractures, exogenous tensile fractures, and exogenous shear fractures developed in the coal body. The overall development is relatively compact

and flat. The research on fractures is on the micron scale, generally ranging from a few to dozens of microns

- (2) The low-temperature liquid nitrogen adsorption experiments show that there are two main types of hysteresis curve. The I type curve produces a loop. A “hysteresis loop” is obvious, and an inflection point appears, but it is not obvious. The II type curve does not produce an adsorption back line and has no obvious inflection point. The pores of coal samples are mainly composed of open pores and impermeable holes closed at one end. The average pore diameter is 16.0313 nm, and the pore specific surface area and total pore volume are small, averaging $1.27984 \text{ m}^2/\text{g}$ and $0.0041246 \text{ cm}^3/\text{g}$, respectively
- (3) The pore specific surface area and pore volume of coal are mainly contributed by micropores and transition pores at 2 to 20 nm. The distribution of pore volume in each pore section of a coal sample has the rule that the transition pore is larger than the micropore, and the micropore is larger than the mesopore, and the maximum ratio is 66.2%. The distribution of specific surface area has the rule that the micropore is larger than the transition pore, and the transition pore is larger than the mesopore, and the maximum ratio is 91.2%.

Data Availability

The data used to support the findings of this study have not been made available because the original data relate to the intellectual property rights of the author, and all the original data cannot appear in the paper, and the experimental data that cannot appear is related to privacy.

Conflicts of Interest

All authors declare no conflict of interest.

Acknowledgments

This work was supported by the Key Project of Hubei Province Education Department (D20201506), the Postdoctoral


Innovation Project of Hebei Province (No. B2019005005), and the Wuhan Institute of Technology Science Fund (No. K201855).

References

- [1] S. Zhou, D. Liu, Y. Cai, Z. Karpyn, and Y. Yao, "Petrographic controls on pore and fissure characteristics of coals from the southern Junggar Coalfield, Northwest China," *Energies*, vol. 11, no. 6, p. 1556, 2018.
- [2] J. Huang, G. Hu, G. Xu, B. Nie, N. Yang, and J. Xu, "The development of microstructure of coal by microwave irradiation stimulation," *Journal of Natural Gas Science and Engineering*, vol. 66, pp. 86–95, 2019.
- [3] M. Zhang, M. Lin, H. Zhu, D. Zhou, and L. Wang, "An experimental study of the damage characteristics of gas-containing coal under the conditions of different loading and unloading rates," *Journal of Loss Prevention in the Process Industries*, vol. 55, pp. 338–346, 2018.
- [4] L. Guannan, Y. Dayu, Y. Boming, G. Feng, and C. Peijian, "A study on gas drainage considering coupling process of fracture-pore microstructure and coal deformation," *Fractals*, vol. 29, no. 2, 2021.
- [5] H. Gan, S. P. Nandi, and P. L. Walker Jr., "Nature of the porosity in American coals," *Fuel*, vol. 51, no. 4, pp. 272–277, 1972.
- [6] S. Liu, D. Wang, G. Yin, M. Li, and X. Li, "Experimental study on the microstructure evolution laws in coal seam affected by temperature impact," *Rock Mechanics and Rock Engineering*, vol. 53, 2020.
- [7] Q. Cheng, B. Huang, and Z. Li, "Research progress of experimental methods for pore fractures in coal and rock mass," *China Mining Industry*, vol. 21, no. 1, pp. 115–118, 2012.
- [8] Z. Liwei, *Analysis of Pore Structure and Controlling Factors of Coal Reservoir in Xishanyao Formation, Santanghu Basin*, [M.S. thesis], China University of Geosciences, 2019.
- [9] L. Qin, C. Zhai, J. Xu, S. Liu, C. Zhong, and G. Yu, "Evolution of the pore structure in coal subjected to freeze–thaw using liquid nitrogen to enhance coalbed methane extraction," *Journal of Petroleum Science and Engineering*, vol. 175, pp. 129–139, 2019.
- [10] W. Li, H. Yao, H. Liu, Z. Kang, X. Song, and Z. Feng, "Three-dimensional pore fine characterization of coal with different coal structure based on microscopic CT," *Journal of China Coal Society*, vol. 39, no. 6, pp. 1127–1132, 2014.
- [11] Q. Meng, Y. Zhao, Y. Hu, Z. Feng, and Y. Yu, "Experimental study on pore structure morphology of coking coal," *Journal of China Coal Society*, vol. 36, no. 3, pp. 487–490, 2011.
- [12] A. H. Thompson, A. J. Katz, and C. E. Krohn, "The microgeometry and transport properties of sedimentary rock," *Advances in Physics*, vol. 36, no. 5, pp. 625–694, 1987.
- [13] B. H. Kueper and E. O. Frind, "Two-phase flow in heterogeneous porous media: 1. Model development," *Water resources research*, vol. 27, no. 6, pp. 1049–1057, 1991.
- [14] F. Wang, Y. Cheng, S. Lu, K. Jin, and W. Zhao, "Influence of coalification on the pore characteristics of middle–high rank coal," *Energy & Fuels*, vol. 28, no. 9, pp. 5729–5736, 2014.
- [15] B. Nie, X. Liu, L. Yang, J. Meng, and X. Li, "Pore structure characterization of different rank coals using gas adsorption and scanning electron microscopy," *Fuel*, vol. 158, no. 15, pp. 908–917, 2015.
- [16] M. M. Mahamud López, "Textural characterization of active carbons using fractal analysis," *Fuel Processing Technology*, vol. 87, no. 10, 2006.
- [17] Y. D. Cai, D. M. Liu, Z. J. Pan, Y. B. Yao, J. Q. Li, and Y. K. Qiu, "Pore structure of selected Chinese coals with heating and pressurization treatments," *Science China Earth Sciences*, vol. 57, no. 7, pp. 1567–1582, 2014.
- [18] A. Y. Klimentko, D. N. Saulov, P. Massarotto, and V. Rudolph, "Conditional model for sorption in porous media with fractal properties," *Transport in Porous Media*, vol. 92, no. 3, pp. 745–765, 2012.
- [19] X. Li, Z. Li, L. Zhang, J. Gao, B. Nie, and Y. Meng, "Characterization of pore structure of coal samples with different coal rank and its influence on gas desorption and diffusion," *Journal of China Coal Society*, vol. 44, no. S1, pp. 142–156, 2019.
- [20] W. Jiang, X. Song, and L. Zhong, "Pore characteristics of coal with different coal structure and its influence on gas outburst based on low temperature liquid nitrogen experiment," *Journal of China Coal Society*, vol. 36, no. 4, pp. 609–614, 2011.
- [21] Y. Sun, "Experimental study on the influence of preoxidation on specific surface area and pore diameter distribution of coal," *Coal Mine Safety*, vol. 51, no. 10, 2020.
- [22] T. Li and H. Wang, "Study on pore structure characteristics of low-rank coal under different detemperatures-taking lignite from Xishanyao Formation, Turpan-Hami Basin, Xinjiang as an example [J/OL]," *Journal of China Coal Society*, 2010.
- [23] Y. Li, Y. Zhang, L. Zhang, and J. Hou, "Characterization of pore structure of coal based on mercury injection, low temperature N₂ adsorption and CO₂ adsorption," *Journal of China Coal Society*, vol. 44, no. 4, pp. 1188–1196, 2019.
- [24] I. Ammosov and I. V. Eremin, *Fissuring in Coal*, IZDAT Publishers Moscow, Office Technical Services, Washington, DC, USA, 1963.
- [25] Y. Zeng, Y. Qu, and J. Song, "Fracture system of coal seam and its influence on coalbed methane production," *Journal of Geology*, vol. 24, no. 2, pp. 91–94, 2000.
- [26] X. Fu, Y. Qin, and C. W., *Coal Bed Methane Geology*, Xuzhou: China University of Mining and Technology Press, China, 2007.
- [27] P. Chen and X. Tang, "Study on low-temperature nitrogen adsorption method and characteristics of micropores in coal," *Journal of China Coal Society*, vol. 26, no. 5, pp. 552–556, 2001.
- [28] S. Brunauer, P. H. Emmett, and E. Teller, "Adsorption of gases in multimolecular layers," *Journal of the American Chemical Society*, vol. 60, no. 2, pp. 309–319, 1938.
- [29] M. Thommes, "Physisorption of gases, with special reference to the evaluation of surface area and pore size distribution (IUPAC technical report)," *Chemistry International the News Magazine of IUPAC*, vol. 38, no. 1, p. 25, 2016.
- [30] B. B. Hodot, *Outburst of Coal and Coalbed Gas*, China Industry Press, Beijing, China, 1966.

Research Article

Study on the Permeability Evolution Model of Mining-Disturbed Coal

Hengyi Jia ^{1,2} and Delong Zou³

¹China Coal Research Institute, Beijing 100013, China

²State Key Lab of Coal Resources High Efficient Mining and Clean Utilization, Beijing 100013, China

³Shenyang Research Institute of CCTEG, Shenyang 113122, China

Correspondence should be addressed to Hengyi Jia; jiahengyi2@163.com

Received 29 June 2021; Revised 29 July 2021; Accepted 13 August 2021; Published 26 August 2021

Academic Editor: Feng Du

Copyright © 2021 Hengyi Jia and Delong Zou. This is an open access article distributed under the Creative Commons Attribution License, which permits unrestricted use, distribution, and reproduction in any medium, provided the original work is properly cited.

Coal permeability plays an important role in the simultaneous exploitation of coal and coal-bed methane (CBM). The stress of mining-disturbed coal changes significantly during coal mining activities, causing damage and destruction of the coal mass, ultimately resulting in a sharp increase in permeability. Conventional triaxial compression and permeability tests were conducted on a triaxial creep-seepage-adsorption and desorption experimental device to investigate the permeability evolution of mining-disturbed coal. The permeability evolution models considering the influence of the stress state and stress path on the fracture propagation characteristics were established based on the permeability difference in the deformation stages of the coal mass. The stress-strain curve of the coal was divided into an elastic stage, yield stage, and plastic flow stage. As the axial stress increased, the permeability decreased and then increased, and the curve's inflection point corresponded to the yield point. The permeability models exhibited a good agreement with the experimental data and accurately reflected the overall trends of the test results. The results of this study provide a theoretical basis for coal mine disaster prevention and the simultaneous exploitation of coal and CBM.

1. Introduction

Coal-bed methane that is also called gas is an unconventional natural gas generated during coalification and accumulates in coal seams. Although CBM is a clean and efficient energy source, it is also a disaster factor and greenhouse gas in coal mining. The exploitation of CBM can reduce the occurrence of coal mine accidents and greenhouse gas emissions and minimize energy shortages. The permeability of coal seams is the decisive parameter affecting CBM exploitation. In China, coal seams are characterized by high in situ stress, strong adsorption features, and low permeability, making the extraction of CBM relatively difficult [1, 2]. Therefore, improving the permeability of coal seams is crucial for the efficient extraction of CBM. When coal seams are mined, the stress of mining-disturbed coal undergoes complex changes, resulting in the deformation,

damage, and permeability enhancement of the coal. Therefore, the simultaneous exploitation of coal and CBM has been widely promoted and applied in China.

Permeability models of coal are the basis for planning gas drainage boreholes and improving gas drainage efficiency. Scholars conducted numerous studies on coal seam permeability models. Shi and Durucan [3] presented a permeability model that considered gas desorption in linear elastic coal-beds under uniaxial strain conditions. Liu et al. [4] established a dual-porosity model considering coal deformation caused by gas adsorption. Connel et al. [5] established a permeability model of coal for triaxial stress and gas adsorption conditions based on the porous elastic theory. Perera et al. [6] derived a triaxial stress coal permeability model based on the theory of elasticity with the gas injection pressure, confining stress, axial load, and gas adsorption as control variables. Lu et al. [7] calculated porosity changes

from the perspective of coal matrix-fracture interactions and established permeability models with different mechanical boundaries under the joint action of effective stress and adsorption deformation. The above permeability models do not consider the effect of coal damage and destruction on permeability. In coal mining activities, the stress of the mining-disturbed coal changes significantly, causing damage and destruction of the coal mass, ultimately resulting in a sharp increase in permeability. Therefore, it is urgent to study the permeability evolution model of mining-disturbed coal.

Scholars have focused on the effect of damage and destruction on coal permeability in recent years. Xie et al. [8] considered the damage caused by the shrinkage of the coal matrix after gas drainage and established a coal permeability model to describe the spatial and temporal distribution of coal permeability within the effective influence zone of the borehole. Zhang et al. [9] established a damage variable that is directly related to the effective strain and developed a dynamic model of the permeability evolution using a scalar damage variable. Xue et al. [10] considered the influence of excavation damage on coal permeability and established a postpeak permeability model based on the parallel plate model. The stress path experienced by the coal mass determines the propagation characteristics of the fractures, determining the change law of permeability. On the other hand, the initial stress state also significantly influences fracture propagation and permeability. However, few studies investigated the influence of the initial stress state and stress path on the propagation characteristics of fractures and permeability changes.

In this study, mechanical and seepage experiments of coal were conducted to obtain the evolution law of permeability with the strain. The permeability models considering the influence of the initial stress state and stress path on the fracture propagation characteristics were established and verified by experimental data. The results of this study provide a theoretical basis for coal mine disaster prevention and the simultaneous exploitation of coal and CBM.

2. Experimental Study on Permeability Evolution of Mining-Disturbed Coal

2.1. Specimens. The coal used in the test was collected from the No. 2 coal seam of the Zhongxing coal mine. The coal deposits are broken and have low strength because of tectonic stress, making it difficult to obtain a raw coal specimen. Studies have shown that although reconstituted coal specimens have larger deformation and permeability than raw coal specimens, their deformation characteristics and permeability evolution are similar [11]. Therefore, reconstituted coal specimens were used in the test.

Coal particles sieved through a 40-60 mesh were mixed with a small amount of water and packed into a mold. A pressure of 200 kN was applied to the mold for 1 h, and specimens with a diameter of 50 mm and a height of 100 mm were obtained. The specimens were placed in a 60°C vacuum oven for 48 h and wrapped with fresh film after cooling for the subsequent analysis.

2.2. Experimental Method. Conventional triaxial compression and permeability tests were conducted on the triaxial creep-seepage-adsorption and desorption experimental device. The device consisted of a servo loading system, adsorption-desorption-seepage system, gas pressure control system, temperature control system, and deformation measurement system.

The steady-state method was adopted to measure the permeability of the specimens. The permeability was calculated as follows:

$$k = \frac{2\mu P_0 L Q}{A(P_1^2 - P_0^2)}, \quad (1)$$

where k is the permeability (m^2), μ is the gas kinematic viscosity, P_0 is the gas pressure at the outlet of the specimens (0.1 MPa), L is the length of the specimens (m), Q is the gas permeation rate (m^3/s), A is the cross-sectional area of the specimens (m^2), and P_1 is the gas pressure at the inlet of the specimens (MPa).

Three specimens were selected, and the axial stress and confining stress were applied at the same speed to the hydrostatic pressure state of 2, 4, and 8 MPa, respectively. Subsequently, the confining stress remained unchanged, and the axial stress was applied at the speed of 100 N/s until the specimens failed. During the test, the deformation and gas seepage characteristics were recorded. For the convenience of analysis, the unit of permeability (m^2) was converted to millidarcy; their relationship is $1 \text{ m}^2 = 10^{15} \text{ mD}$.

2.3. Results and Analysis. Figure 1 shows the relationship between the stress-strain curve and permeability-strain curve. The stress-strain curve can be divided into the elastic stage, yield stage, and plastic flow stage. After the yield stage, the strain exhibits the characteristics of plastic flow, and the specimens show no apparent signs of failure. The experiments were stopped after the specimens showed plastic flow characteristics to prevent the strain from exceeding the measurement range and damaging the strain sensor. In Figure 1, the #1 coal specimen is used as an example, and the points A , B , C , and D represent the starting point of loading, the expansion point, the yield point, and the end of the test, respectively. In the initial stage, the volume of the specimen is compressed continuously, and the volumetric strain increases gradually. From point B , the specimen expands, and the volumetric strain decreases. As the axial stress increases, the permeability decreases and then increases, and the curve's inflection point corresponds to point C .

During the deformation, the permeability depends on the effective porosity. There are few new fractures in the A - B stage, and the primary fractures are elastically compacted under the increasing axial stress. In this stage, the specimen is in an elastic deformation state, and the permeability decreases with the volume compression. From point B , the volume expands, and the permeability continues to decline. Tensile microfractures are gradually formed in the coal parallel to the direction of the axial stress, causing volume expansion. However, these microfractures are not connected, and the effective porosity does not increase. At the

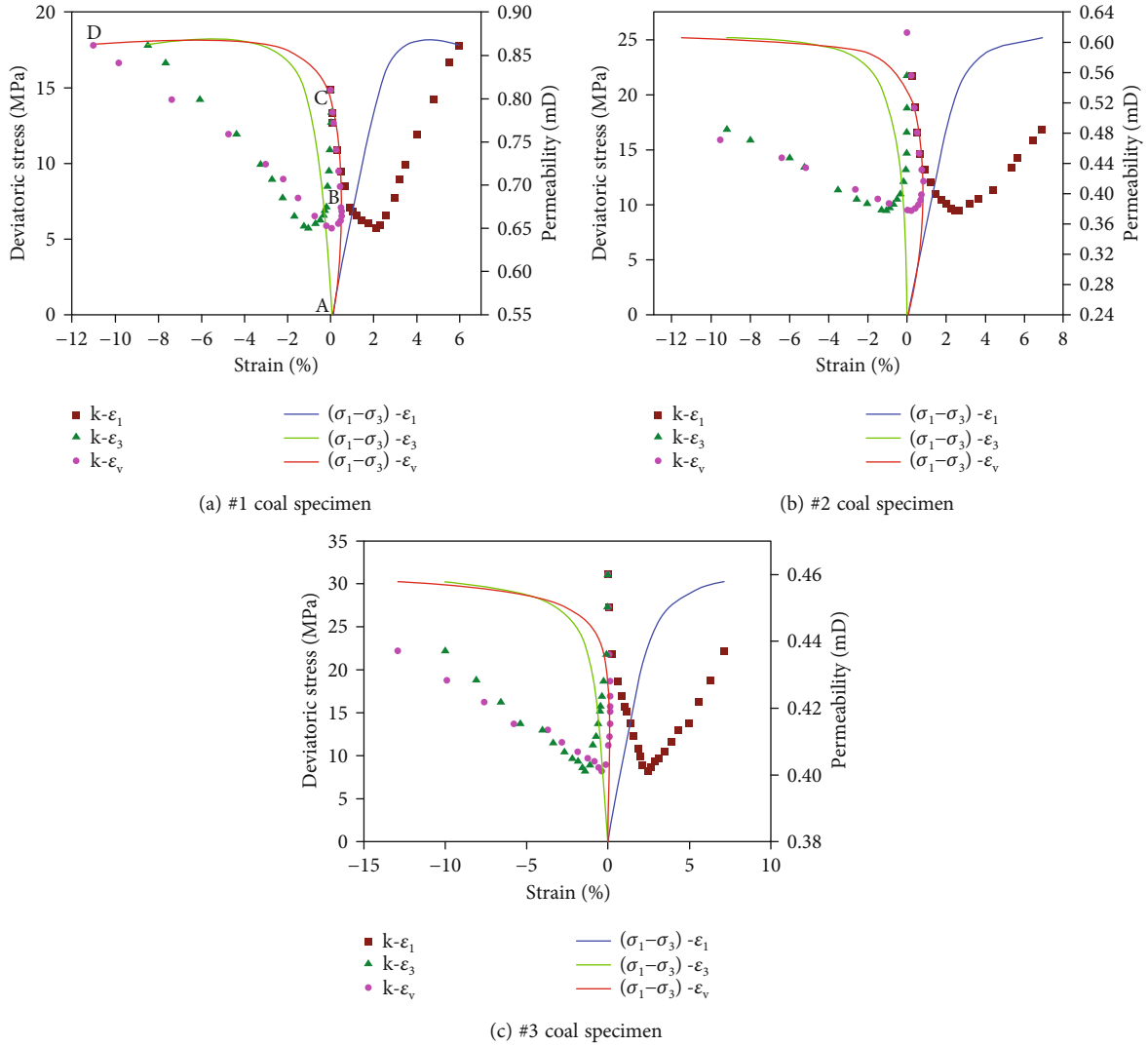


FIGURE 1: The curve of permeability-strain and stress-strain of coal specimens.

same time, the increasing axial stress causes the closure of the primary fractures. Therefore, even if the volume expands, the permeability continues to decrease. From point C, the connectivity of the new fractures increases, and the permeability increases with the volume expansion.

Figure 2 shows the failure characteristics of the coal specimens after the experiments. The three specimens all suffered shear failure, and the angle between the failure crack and the axial direction increases with an increase in the confining pressure. Specimens #2 and #3 also showed tensile failure, which was likely caused by the mechanical properties of the specimens and the limitations of the equipment performance.

3. Permeability Model of Mining-Disturbed Coal

3.1. *Permeability Model in the Elastic Stage.* The pores in which the fluid can flow are called effective pores, whereas the other pores are called invalid pores. Effective and invalid pores exist in both raw coal and reconstituted coal under

certain stress conditions, and only the effective pores affect the permeability.

The permeability of coal can be expressed using the Kozeny-Carman equation as follows:

$$k = \frac{\phi'^3}{CS^2(1-\phi')^2}, \quad (2)$$

where k is the permeability (m^2), ϕ' is the effective porosity, S is the surface area of the pores per unit volume of coal, and C is a coefficient related to the tortuosity of the coal fractures.

When the coal undergoes elastic deformation due to external stress, only the opening and shape of the fractures change. Thus, the parameter S can be regarded as a constant. Equation (1) can be rewritten as follows:

$$\frac{k}{k_0} = \frac{C_0}{C} \left(\frac{\phi'}{\phi'_0}\right)^3 \left(\frac{1-\phi'_0}{1-\phi'}\right)^2 = \alpha \left(\frac{\phi'}{\phi'_0}\right)^3 \left(\frac{1-\phi'_0}{1-\phi'}\right)^2, \quad (3)$$

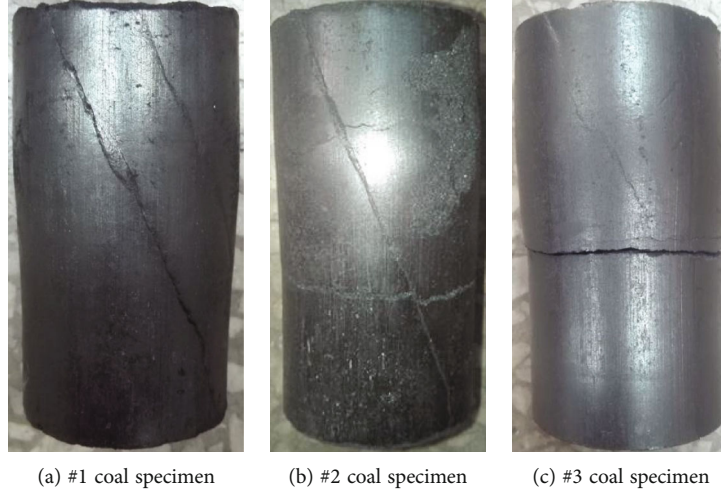


FIGURE 2: Failure characteristics of coal specimens.

where C_0 , k_0 , and ϕ'_0 and C , k , and ϕ' are the coefficient, the permeability, and the effective porosity before and after coal mass deformation, respectively, ($\alpha = C_0/C$).

The total porosity of coal can be expressed by the following equation:

$$\begin{aligned} \phi &= \frac{V_{p0} + \Delta V_p}{V_{b0} + \Delta V_b} = 1 - \frac{V_{s0} + \Delta V_s}{V_{b0} + \Delta V_b} = 1 - \frac{V_{s0}(1 + \Delta V_s/V_{s0})}{V_{b0}(1 + \Delta V_b/V_{b0})} \\ &= 1 - \frac{(1 - \phi_0)}{1 + \varepsilon_V} \left(1 + \frac{\Delta V_s}{V_{s0}}\right), \end{aligned} \quad (4)$$

where ϕ_0 and ϕ are the total porosity before and after deformation, respectively; V_{p0} , V_{b0} , and V_{s0} are the initial pore volume, coal mass volume, and solid skeleton volume of the coal, respectively; ΔV_p , ΔV_b , and ΔV_s are the increment of the pore volume, coal mass volume, and solid skeleton volume, respectively; and ε_V is the volumetric strain.

If $\Delta V_s = 0$, i.e., regardless of changes in the volume of the skeleton, then

$$\phi = \frac{\phi_0 + \varepsilon_V}{1 + \varepsilon_V}. \quad (5)$$

The volumetric strain in Equation (5) is solely caused by pores in coal.

Only a change in the effective pores will affect the permeability during the coal mass deformation. Here, a coefficient λ_1 is introduced to represent the ratio of the volumetric strain caused by the effective pores to the total volumetric strain in this stage ($\varepsilon_{V\text{-effective}}/\varepsilon_V = \lambda_1$, $0 \leq \lambda_1 \leq 1$). According to Equation (5), the effective porosity of coal after deformation is

$$\phi' = \frac{\phi'_0 + \varepsilon_{V\text{-effective}}}{1 + \varepsilon_V} = \frac{\phi'_0 + \lambda_1 \varepsilon_V}{1 + \varepsilon_V}, \quad (6)$$

where $\varepsilon_{V\text{-effective}}$ is the volumetric strain caused by the effective pores.

By substituting Equation (6) into Equation (3), we obtain

$$\frac{k}{k_0} = \frac{\alpha}{1 + \varepsilon_V} \left(1 + \frac{\lambda_1 \varepsilon_V}{\phi'_0}\right)^3 \left(\frac{1 - \phi'_0}{1 + \varepsilon_V - \phi'_0 - \lambda_1 \varepsilon_V}\right)^2. \quad (7)$$

Because the initial stress state and stress path affect the propagation characteristics of the fractures, Equation (7) reflects the influence of the initial stress state and stress path on the fracture propagation characteristics and permeability of the coal mass.

3.2. Permeability Model in the Damage Stage. When the coal mass is damaged, the primary fractures expand, and new fractures are created. Thus, the parameter S in Equation (1) is no longer a constant, and the equation can be rewritten as follows:

$$k = \frac{\phi'^3}{CS^2(1 - \phi')^2} = \frac{\phi'^3}{C(A_s/V_b)^2(1 - \phi')^2}, \quad (8)$$

where A_s is the total surface area of the pores in the coal mass, and V_b is the coal mass volume.

Then, the initial permeability becomes

$$k_0 = \frac{\phi_0'^3}{C_0(A_{s0}/V_{b0})^2(1 - \phi_0')^2}. \quad (9)$$

When the coal mass is damaged, the surface area of the pores changes:

$$A_s = A_{s0}(1 + \psi). \quad (10)$$

The permeability becomes

$$k = \frac{\phi'^3}{C((A_{s0}(1 + \psi))/(V_{b0}(1 + \varepsilon_V)))^2(1 - \phi')^2}. \quad (11)$$

We obtain

$$\frac{k}{k_0} = \alpha \left(\frac{\phi'}{\phi'_0} \right)^3 \left(\frac{1-\phi'_0}{1-\phi'} \right)^2 \left(\frac{1+\varepsilon_V}{1+\psi} \right)^2. \quad (12)$$

We assume that the change in the pore surface area can be ignored; thus, Equation (12) can be simplified as

$$\frac{k}{k_0} = \alpha \left(\frac{\phi'}{\phi'_0} \right)^3 \left(\frac{1-\phi'_0}{1-\phi'} \right)^2 (1+\varepsilon_V)^2. \quad (13)$$

As shown in Figure 1, point *B* is the starting point of the expansion and damage. For the *B-C* stage, Equation (13) should be rewritten as

$$\frac{k}{k_{\text{expansion}}} = \alpha \left(\frac{\phi'}{\phi'_{\text{expansion}}} \right)^3 \left(\frac{1-\phi'_{\text{expansion}}}{1-\phi'} \right)^2 (1+\varepsilon_V - \varepsilon_{V-\text{expansion}})^2, \quad (14)$$

where $k_{\text{expansion}}$, $\phi'_{\text{expansion}}$, and $\varepsilon_{V-\text{expansion}}$ are the permeability, effective porosity, and volumetric strain at the starting point of the expansion, respectively, and k , ϕ' , and ε_V are the permeability, effective porosity, and volumetric strain in the *B-C* stage, respectively.

The coal specimen is being damaged from point *B*, and the volume continues to expand. However, the effective porosity has not increased because the tensile microfractures generated in this stage are not connected. In addition, as the axial stress increases, the primary fractures continue to close, resulting in a decrease in permeability. The coefficient λ_2 is introduced to express the ratio of the volumetric strain caused by the effective pores to the total volumetric strain in this stage, i.e., $\varepsilon_{V-\text{effective}}/(\varepsilon_V - \varepsilon_{V-\text{expansion}}) = \lambda_2$. The trend of the volumetric strain caused by the effective pores is opposite to that of the total volumetric strain; thus, $-1 \leq \lambda_2 \leq 0$.

According to Equation (5), the effective porosity in *B-C* stage can be obtained as

$$\phi' = \frac{\phi'_{\text{expansion}} + \lambda_2 (\varepsilon_V - \varepsilon_{V-\text{expansion}})}{1 + \varepsilon_V - \varepsilon_{V-\text{expansion}}}. \quad (15)$$

According to Equation (6), we obtain

$$\phi'_{\text{expansion}} = \frac{\phi'_0 + \lambda_1 \varepsilon_{V-\text{expansion}}}{1 + \varepsilon_{V-\text{expansion}}}. \quad (16)$$

By substituting Equations (15) and (16) into Equation (14), we derive

$$k = k_{\text{expansion}} \alpha (1 + \varepsilon_V - \varepsilon_{V-\text{expansion}}) \left[1 + \frac{\lambda_2 (1 + \varepsilon_{V-\text{expansion}}) (\varepsilon_V - \varepsilon_{V-\text{expansion}})}{\phi'_0 + \lambda_1 \varepsilon_{V-\text{expansion}}} \right]^3 \times \left\{ \frac{1 + \varepsilon_{V-\text{expansion}} - \phi'_0 - \lambda_1 \varepsilon_{V-\text{expansion}}}{[(1 - \lambda_2) (\varepsilon_V - \varepsilon_{V-\text{expansion}}) + 1] (1 + \varepsilon_{V-\text{expansion}}) - \phi'_0 - \lambda_1 \varepsilon_{V-\text{expansion}}} \right\}^2. \quad (17)$$

Equation (17) is the theoretical model of permeability in the *B-C* stage.

If the yield point is the initial condition, Equation (13) should be rewritten as

$$\frac{k}{k_{\text{yield}}} = \alpha \left(\frac{\phi'}{\phi'_{\text{yield}}} \right)^3 \left(\frac{1-\phi'_{\text{yield}}}{1-\phi'} \right)^2 (1+\varepsilon_V - \varepsilon_{V-\text{yield}})^2, \quad (18)$$

where k_{yield} , ϕ'_{yield} , and $\varepsilon_{V-\text{yield}}$ and k , ϕ' , and ε_V are the permeability, effective porosity, and volumetric strain of the coal at the yield point and in the *C-D* stage, respectively.

The permeability increases from point *C* because of the increasing of effective porosity. The coefficient λ_3 is introduced to express the ratio of the volumetric strain caused by the effective pores to the total volumetric strain at this stage ($\varepsilon_{V-\text{effective}}/(\varepsilon_V - \varepsilon_{V-\text{yield}}) = \lambda_3$, $0 \leq \lambda_3 \leq 1$).

According to Equation (5), the effective porosity in the *C-D* stage can be obtained:

$$\phi' = \frac{\phi'_{\text{yield}} + \lambda_3 (\varepsilon_V - \varepsilon_{V-\text{yield}})}{1 + \varepsilon_V - \varepsilon_{V-\text{yield}}}. \quad (19)$$

According to Equation (15), we obtain

$$\phi'_{\text{yield}} = \frac{\phi'_{\text{expansion}} + \lambda_2 (\varepsilon_{V-\text{yield}} - \varepsilon_{V-\text{expansion}})}{1 + \varepsilon_{V-\text{yield}} - \varepsilon_{V-\text{expansion}}}. \quad (20)$$

By substituting Equations (16), (19), and (20) into Equation (18), we obtain

$$k = k_{\text{yield}} \alpha (1 + \varepsilon_V - \varepsilon_{V\text{-yield}}) \left[1 + \frac{\lambda_3 (\varepsilon_V - \varepsilon_{V\text{-yield}}) (1 + \varepsilon_{V\text{-yield}} - \varepsilon_{V\text{-expansion}}) (1 + \varepsilon_{V\text{-expansion}})}{\phi'_0 + \lambda_1 \varepsilon_{V\text{-expansion}} + \lambda_2 (\varepsilon_{V\text{-yield}} - \varepsilon_{V\text{-expansion}}) (1 + \varepsilon_{V\text{-expansion}})} \right]^3 \times \left\{ \frac{[(1 - \lambda_2) (\varepsilon_{V\text{-yield}} - \varepsilon_{V\text{-expansion}}) + 1] (1 + \varepsilon_{V\text{-expansion}}) - \phi'_0 - \lambda_1 \varepsilon_{V\text{-expansion}}}{[(1 - \lambda_2) (\varepsilon_{V\text{-yield}} - \varepsilon_{V\text{-expansion}}) + 1 + (1 + \varepsilon_{V\text{-yield}} - \varepsilon_{V\text{-expansion}}) (1 - \lambda_3) (\varepsilon_V - \varepsilon_{V\text{-yield}})] (1 + \varepsilon_{V\text{-expansion}}) - \phi'_0 - \lambda_1 \varepsilon_{V\text{-expansion}}} \right\}^2. \quad (21)$$

Equation (21) is the theoretical model of permeability in the *C-D* stage. Equations (17) and (21) also reflect the influence of the initial stress and stress path on the fracture propagation characteristics and permeability of the coal mass.

3.3. Verification of the Permeability Model. In the previous section, the permeability evolution models in different deformation stages were obtained through theoretical derivation. Subsequently, the results of conventional triaxial compression and permeability tests were used to verify the permeability models. The initial effective porosity of the specimens was determined first. According to the test protocol [12, 13], the effective porosity of the specimens with different confining stress values was measured using the triaxial creep-seepage-adsorption and desorption experimental device. The effective porosities are 0.08, 0.06, and 0.043 when the confining stress values are 2 MPa, 4 MPa, and 8 MPa, respectively. As the confining stress increases, the effective porosity decreases. In the permeability experiment, it is stipulated that ε_V is a positive value when the specimen is compressed and a negative value when it is expanded, which is opposite to the stipulation in the permeability models. Therefore, negative signs were added to the volumetric strains in the permeability models. We used Equation (7) to fit the test data of the *A-B* stage, Equation (17) to fit the test data of the *B-C* stage, and Equation (21) to fit the test data of the *C-D* stage. When fitting the test data with Equation (17), the value of λ_1 is the fitting result of Equation (7). Similarly, when Equation (21) is used to fit the test data, the values of λ_1 and λ_2 are the fitting results of Equations (7) and (17), respectively.

Figures 3–5 show the fitting results of the permeability, and Table 1 lists the results of the parameters. It can be seen that the permeability models of the *A-B* stage and the *C-D* stage fit the permeability data well. The parameters λ_1 and λ_3 decrease with an increase in confining stress, indicating that the ratio of the volumetric strain caused by the effective pores to the total volumetric strain decreases with an increase in the confining stress, and the sensitivity of the permeability to the volumetric strain decreases. The fitting results of the *B-C* stage are slightly worse, and the change law of λ_2 with confining stress is not obvious. However, the overall trends of the permeability model and the test data are the same.

4. Discussion

The stress state of mining-disturbed coal is changed by mining activities, causing elastic deformation and even damage and changing the coal permeability [14–16]. The results of the experiments show that the effective porosity of the coal decreases with the increasing axial stress during the elastic deformation stage, resulting in a decrease in permeability. Tensile microfractures begin to form in the coal from point *B*, and the coal begins to expand. However, the tensile microfractures are not connected, and the effective porosity does not increase. At the same time, the original pores decrease with the increasing axial stress. Therefore, although the coal continues to expand, the permeability is still decreasing in the *B-C* stage. From point *C*, the tensile microfractures are connected, and the effective porosity increases. The permeability increases with the expanding coal volume. Therefore, the evolution law of permeability is closely related to the propagation characteristics of the coal fractures.

Establishing a suitable permeability model of mining-disturbed coal is crucial for understanding the fluid seepage mechanism in coal [17, 18]. Most existing permeability models are based on CBM exploitation and ignore the influence of damage on permeability. Xie et al. [19] considered the volumetric change of damage coal with cracks induced by coupling of the abutment pressure under different mining conditions, pore pressure, and expansion caused by gas adsorption and proposed a new word of mining-enhanced permeability meaning the change in permeability by volumetric change of coal. Cheng et al. [20] put forward a new model with strain as a variable for unloading fractured coal by considering the effective stress and gas adsorption/desorption deformation effects. Although these studies have laid a foundation for describing the permeability evolution law of mining-disturbed coal, they all ignored the influence of the pore type on permeability. The permeability models established in this paper consider the influence of the effective and invalid pores on permeability. The initial stress state and stress path affect the propagation characteristics of coal fractures [21, 22]. Therefore, the proposed models accurately reflect the influence of the initial stress state and stress path on permeability.

The permeability distribution law of mining-disturbed coal is the basis for achieving the simultaneous exploitation of coal and CBM. The initial stress affects the evolution characteristics of the coal fractures, which, in turn, affect

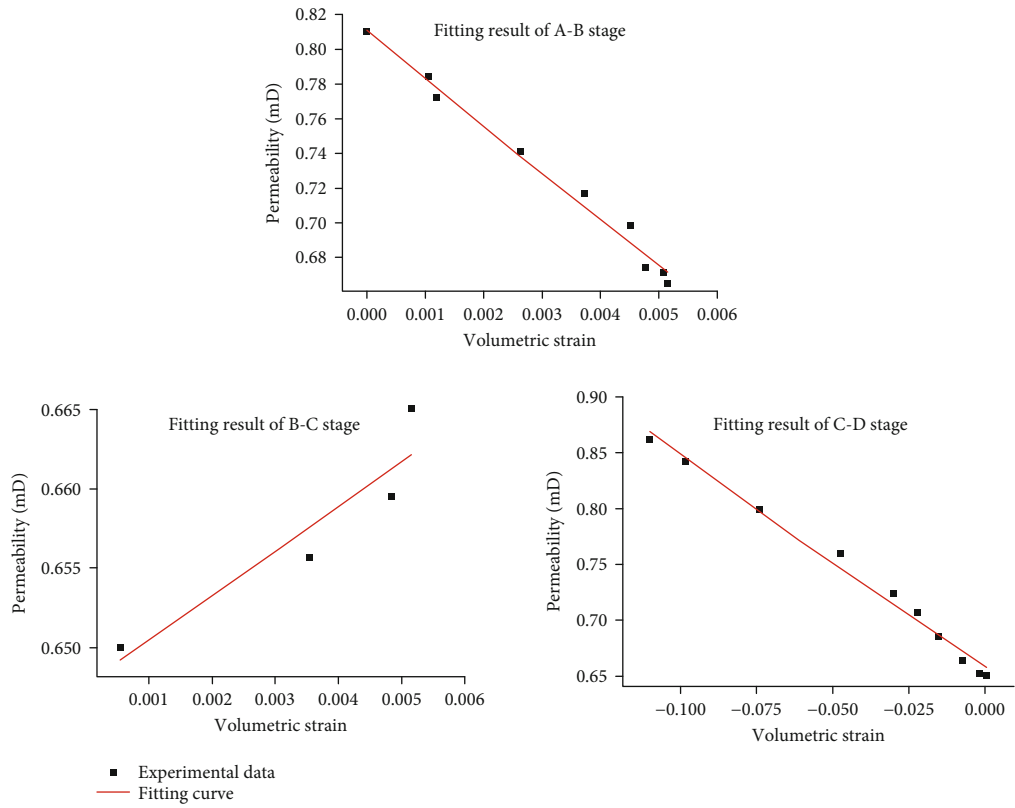


FIGURE 3: Fitting results of #1 coal specimen.

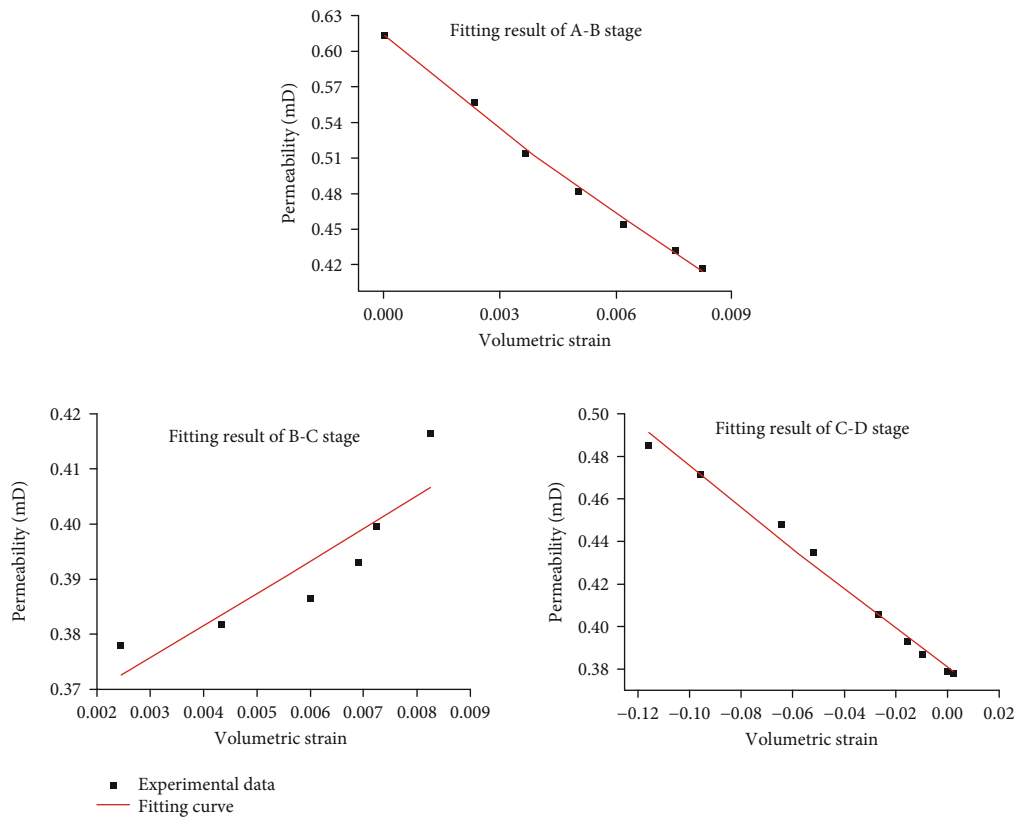


FIGURE 4: Fitting results of #2 coal specimen.

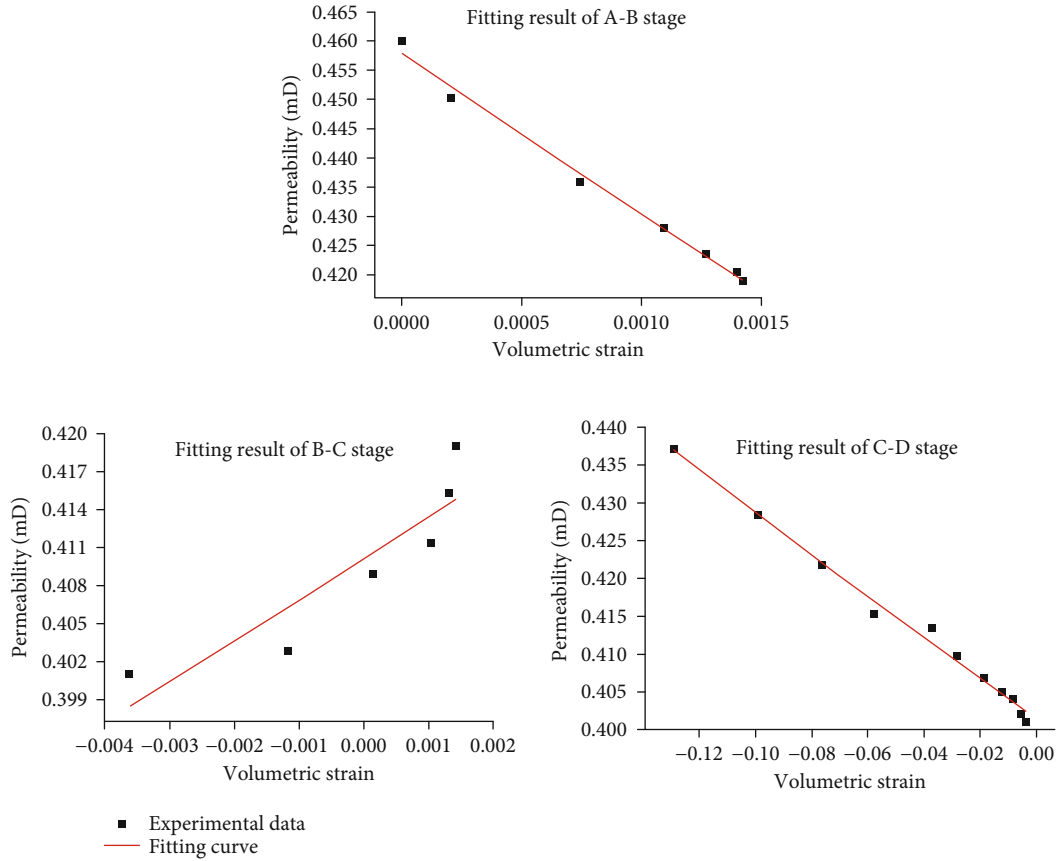


FIGURE 5: Fitting results of #3 coal specimen.

TABLE 1: Fitting results of the parameters.

Specimen	A-B stage			B-C stage			C-D stage		
	α	λ_1	R^2	α	λ_2	R^2	α	λ_3	R^2
#1	1.0019	0.9748	0.9848	0.9957	-0.0745	0.8076	1.0117	0.0912	0.9866
#2	0.9996	0.9142	0.9959	0.9769	-0.2348	0.7424	1.0026	0.038	0.9883
#3	0.9954	0.8948	0.9916	0.99	-0.0923	0.7738	1.0035	0.0232	0.9911

the permeability. The experimental results indicate that the higher the initial confining stress, the lower the sensitivity of the permeability to the volumetric strain is, explaining the poor permeability enhancement of long-distance protected coal seams. The permeability distribution law can be obtained using the proposed permeability models with the volumetric strain of the protected coal seam, enabling the simultaneous exploitation of coal and CBM.

5. Conclusion

- (i) The stress-strain curve of coal was divided into the elastic stage, yield stage, and plastic flow stage. As the axial stress increased, the permeability decreased and then increased, and the inflection point of the curve corresponded to the yield point
- (ii) The stress state of the coal mass is changed during mining activities, causing elastic deformation and

even damage. Effective and invalid pores exist in both raw coal and reconstituted coal under certain stress conditions, but only the effective pores affect the permeability

- (iii) As the confining stress increased, the ratio of the volumetric strain caused by the effective pores to the total volumetric strain decreased, and the sensitivity of the permeability to the volumetric strain decreased. The initial stress state and stress path affected the propagation characteristics of the coal fractures, influencing the evolution law of permeability

Data Availability

The data used to support the findings of this study are available from the corresponding author upon request.

Conflicts of Interest

The authors declare that they have no conflicts of interest.

Acknowledgments

This research was financially supported by the National Natural Science Foundation of China (Grant No. 51704164).

References

- [1] T. Xia, F. Zhou, J. Liu, S. Hu, and Y. Liu, "A fully coupled coal deformation and compositional flow model for the control of the pre-mining coal seam gas extraction," *International Journal of Rock Mechanics and Mining Sciences*, vol. 72, pp. 138–148, 2014.
- [2] H. Wang, X. Yang, F. du et al., "Calculation of the diffusion coefficient of gas diffusion in coal: the comparison of numerical model and traditional analytical model," *Journal of Petroleum Science and Engineering*, vol. 205, p. 108931, 2021.
- [3] J. Q. Shi and S. Durucan, "Drawdown induced changes in permeability of coalbeds: a new interpretation of the reservoir response to primary recovery," *Transport in Porous Media*, vol. 56, no. 1, pp. 1–16, 2004.
- [4] J. Liu, Z. Chen, D. Elsworth, X. Miao, and X. Mao, "Evaluation of stress-controlled coal swelling processes," *International Journal of Coal Geology*, vol. 83, no. 4, pp. 446–455, 2010.
- [5] L. D. Connell, M. Lu, and Z. Pan, "An analytical coal permeability model for tri-axial strain and stress conditions," *International Journal of Coal Geology*, vol. 84, no. 2, pp. 103–114, 2010.
- [6] M. S. A. Perera, P. G. Ranjith, and S. K. Choi, "Coal cleat permeability for gas movement under triaxial, non-zero lateral strain condition: a theoretical and experimental study," *Fuel*, vol. 109, pp. 389–399, 2013.
- [7] S. Lu, Y. Cheng, and W. Li, "Model development and analysis of the evolution of coal permeability under different boundary conditions," *Journal of Natural Gas Science and Engineering*, vol. 31, pp. 129–138, 2016.
- [8] J. Xie, M. Gao, B. Yu, R. Zhang, and W. Jin, "Coal permeability model on the effect of gas extraction within effective influence zone," *Geomechanics and Geophysics for Geo-Energy and Geo-Resources*, vol. 1, no. 1-2, pp. 15–27, 2015.
- [9] N. Zhang, X. Li, H. Cheng, and T. Teng, "A coupled damage-hydro-mechanical model for gas drainage in low-permeability coalbeds," *Journal of Natural Gas Science and Engineering*, vol. 35, pp. 1032–1043, 2016.
- [10] Y. Xue, F. Gao, X. Liu, J. Li, M. Liang, and X. Li, "Theoretical and numerical simulation of the mining-enhanced permeability model of damaged coal seam," *Geotechnical and Geological Engineering*, vol. 34, no. 5, pp. 1425–1433, 2016.
- [11] G. Z. Yin, D. K. Wang, D. M. Zhang, and W. Z. Wang, "Test analysis of deformation characteristics and compressive strengths of two types of coal specimens containing gas," *Chinese Journal of Rock Mechanics and Engineering*, vol. 28, no. 2, pp. 410–417, 2009.
- [12] F. Du and K. Wang, "Unstable failure of gas-bearing coal-rock combination bodies: insights from physical experiments and numerical simulations," *Process Safety and Environmental Protection*, vol. 129, pp. 264–279, 2019.
- [13] D. Wang, M. Peng, J. Wei, Q. Fu, and Y. Xia, "Development and application of tri-axial creep-seepage-adsorption and desorption experimental device for coal," *Journal of China Coal Society*, vol. 3, pp. 644–652, 2016.
- [14] F. Du, K. Wang, X. Zhang, C. Xin, L. Shu, and G. Wang, "Experimental study of coal-gas outburst: insights from coal-rock structure, gas pressure and adsorptivity," *Natural Resources Research*, vol. 29, no. 4, pp. 2481–2493, 2020.
- [15] D. Y. Guo, P. F. Lv, J. C. Zhao, and C. Zhang, "Research progress on permeability improvement mechanisms and technologies of coalbed deep-hole cumulative blasting," *International Journal of Coal Science and Technology*, vol. 7, no. 2, pp. 329–336, 2020.
- [16] K. Wang, F. Du, and G. Wang, "Investigation of gas pressure and temperature effects on the permeability and steady-state time of Chinese anthracite coal: an experimental study," *Journal of Natural Gas Science and Engineering*, vol. 40, pp. 179–188, 2017.
- [17] X. Wu, Y. Peng, J. Xu, Q. Yan, W. Nie, and T. Zhang, "Experimental study on evolution law for particle breakage during coal and gas outburst," *International Journal of Coal Science & Technology*, vol. 7, no. 1, pp. 97–106, 2020.
- [18] C. Xin, F. du, K. Wang, C. Xu, S. Huang, and J. Shen, "Damage evolution analysis and gas–solid coupling model for coal containing gas," *Geomechanics and Geophysics for Geo-Energy and Geo-Resources*, vol. 7, no. 1, p. 7, 2021.
- [19] H. Xie, X. Zhao, J. Liu, R. Zhang, and D. Xue, "Influence of different mining layouts on the mechanical properties of coal," *International Journal of Mining Science and Technology*, vol. 22, no. 6, pp. 749–755, 2012.
- [20] Y. Cheng, H. Liu, P. Guo, R. Pan, and L. Wang, "A theoretical model and evolution characteristic of mining-enhanced permeability in deeper gassy coal seam," *Journal of China Coal Society*, vol. 8, pp. 1650–1658, 2014.
- [21] K. Wang and F. du, "Coal-gas compound dynamic disasters in China: a review," *Process Safety and Environmental Protection*, vol. 133, pp. 1–17, 2020.
- [22] C. Wu, C. Yuan, G. Wen, L. Han, and H. Liu, "A dynamic evaluation technique for assessing gas output from coal seams during commingling production within a coalbed methane well: a case study from the Qinshui Basin," *International Journal of Coal Science and Technology*, vol. 7, no. 1, pp. 122–132, 2020.

Research Article

Combining K-Means Clustering and Random Forest to Evaluate the Gas Content of Coalbed Bed Methane Reservoirs

Jie Yu,^{1,2} Linqi Zhu³,,³ Ruibao Qin,² Zhansong Zhang,¹ Li Li,² and Tao Huang²

¹Yangtze University, Wuhan 430100, China

²CNOOC Research Institute, Beijing 100027, China

³Institute of Deep-Sea Science and Engineering, Chinese Academy of Sciences, Sanya 572000, China

Correspondence should be addressed to Linqi Zhu; zhulq@idsse.ac.cn

Received 27 June 2021; Revised 19 July 2021; Accepted 30 July 2021; Published 21 August 2021

Academic Editor: Wei Zhao

Copyright © 2021 Jie Yu et al. This is an open access article distributed under the Creative Commons Attribution License, which permits unrestricted use, distribution, and reproduction in any medium, provided the original work is properly cited.

The accurate calculation of the gas content of coalbed bed methane (CBM) reservoirs is of great significance. However, due to the weak correlation between the logging response of coalbed methane reservoirs and the gas content parameters and strong nonlinear characteristics, it is difficult for conventional gas content calculation algorithms to obtain more reliable results. This paper proposes a CBM reservoir gas content assessment method combining K-means clustering and random forest. The K-means clustering is used to divide the reservoirs and distinguish the types to establish a random forest model. Judging from the evaluation effect of the research block, the prediction accuracy of the new method is significantly higher than that of the original method, and more accurate gas content prediction values can be obtained for different types of reservoirs. Studies have shown that this method can help the gas content evaluation of CBM reservoirs, improve the accuracy of gas content evaluation, and better support the exploration and development of CBM reservoirs. The results of this study show that the random forest method based on clustering can effectively distinguish the relationship between different logging responses and gas content. On this basis, the random forest algorithm modeling can effectively characterize the complex relationship between gas content and logging curve response. In the case of poor correlation between gas content and logging curve, the gas content of the reservoir can also be accurately calculated.

1. Introduction

With the continuous progress of exploration and development, research on various unconventional reservoirs such as coalbed bed methane (CBM) and shale gas is in full swing, and they are the key growth points of reserves [1–3]. CBM is natural gas that is generated by biochemistry and pyrolysis during the formation and evolution of coal seams and is stored in coal seams. At present, the United States, Canada, Australia, Russia, India, China, and other countries have all started exploration and development of CBM [4–6].

The gas content of a CBM reservoir is a very important parameter, which determines the reserves and final production of the reservoir [7, 8]. However, compared with other reservoirs, it is more difficult to calculate the gas content of CBM reservoirs, which extremely restricts the determination of high-quality reservoirs and the formulation of develop-

ment plans, resulting in unclear understanding of CBM reservoirs. For the core gas content calculation method, Kim proposes to combine the moisture and ash content with the coal bed temperature and pressure and the equilibrium water state correction amount to calculate the coalbed gas content [9]. Ahmed et al. provided the establishment of an isotherm adsorption model to describe the gas content using an isotherm adsorption experiment [10]. Hawkins et al. proposed to use the Langmuir coal rank equation to predict gas content [11]. However, none of the above methods can predict the vertical continuity of the gas content in the formation. Logging is currently the only method that can accurately predict the vertical gas content change of a single well. It is of great significance to establish an accurate gas content logging evaluation model.

Some scholars have studied the logging calculation method of the gas content of CBM reservoirs. Liu et al. [12]

, Meng et al. [13] and Shao et al. [14] both proposed a statistical method for evaluating the gas content of CBM reservoirs. Jin et al. [15] and Fu et al. [16] also used this method. In addition to the use of statistical models or volume models for gas content evaluation, the relationship between gas content and logging response is too complicated. At present, methods for evaluating coal reservoir gas content using machine learning algorithms have gradually emerged. Hou and Wang [17] used the error back propagation neural network to predict the air content and achieved certain results. Pan and Huang [18] and Wu also used BPNN to predict the air content. Lian et al. [19] introduced support vector machines to the evaluation of air content. Guo et al. [20, 21] used the grey system and random forest to predict the gas content. Xiang et al. [22] proposed the application method of deep learning in CBM logging interpretation and believed that the effect of deep belief network in CBM gas content prediction is better than BPNN, multiple regression, and Langmuir equation method.

Although many scholars have proposed a variety of methods for evaluating the gas content of CBM, it cannot be ignored that the complexity of CBM reservoirs is greater, even higher than that of shale gas reservoirs. The logging response of such a complex reservoir is affected very diversely, and the main controlling factors of logging response of different reservoirs are different. No matter how strong the approximation ability of the model is, it is difficult to accurately evaluate the gas content parameters by establishing a single evaluation model. The innovative part of this article is to use clustering methods to classify data with different feature relationships, so that machine learning algorithms can predict different data more targeted, and use more efficient machine learning algorithms to improve the prediction effect.

Based on this idea, this paper proposes a K-means clustering+random forest air content evaluation method, that is, first collect data and use the clustering method to classify the data. After that, the classified data is used to establish a model separately and evaluate the gas content. Finally, a series of established models are used to apply the logging curve to obtain the final gas content prediction curve for the entire well section. In this way, the influence of different main control factors on the prediction can be eliminated as much as possible, so that the model is more targeted and the prediction effect of the model is improved. Although this approach seems to be a more complicated modeling method, the prediction effect of the actual reservoir gas content has been greatly improved. From the perspective of the prediction effect of the research block, the method proposed in this paper is effective and can help the exploration and development of CBM.

2. Data

The study block is located in the southeast of Qinshui Basin in Central China. Drilling revealed that there are 16 coal seams in Taiyuan formation and Shanxi formation, with the maximum total thickness of 23.6 m. Among them, No. 15 coal seam in Taiyuan formation and No. 3 coal seam in

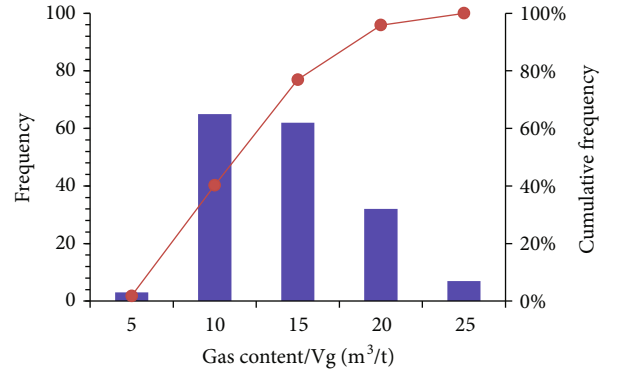


FIGURE 1: Distribution histogram of measured gas content in No. 3 coal.

Shanxi formation are stably distributed in the whole basin. The main mining coal seam is No. 3 coal seam, and No. 15 coal seam is only involved in individual wells. At present, there are more than 1000 coalbed methane wells in the block. The production of wells in different positions varies greatly, and the gas content distribution is unclear, which restricts the exploration and development of coalbed methane. We collected 169 coring gas content measured data from 22 CBM parameter wells in this block, and 6 logging curves including natural gamma ray, spontaneous potential, borehole diameter, deep shallow lateral resistivity, and bulk density. The measured gas content data shows that the gas content of No. 3 coal seam is mainly distributed between 5 and 20 m³/t (Figure 1).

3. Method

3.1. K-Means Clustering. Although we often use classification or regression algorithms in supervised learning methods to predict categories or values, we still often encounter situations where we need to use unsupervised learning methods to obtain a set of data categories. When the amount of data is large, you can consider using clustering algorithms to get different data categories. Clustering is subordinate to unsupervised learning, which does not rely on the defined classes and training examples of class labels. Among them, K-means clustering is a very classic clustering method [23].

At the beginning of K-means clustering, we first need to figure out how to quantitatively calculate the difference between two comparable elements. The smaller the degree of difference, the greater the direct correlation between the two samples, and the more likely it is a rock sample of one type of rock. We define the degree of dissimilarity mathematically here.

Suppose $X = \{x_1, x_2, x_3, \dots, x_n\}$, $Y = \{y_1, y_2, y_3, \dots, y_n\}$, where X and Y are two-element items, each with n measurable characteristic attributes; then, the degree of dissimilarity between X and Y is defined as

$$d(X, Y) = f(X, Y) \longrightarrow R. \quad (1)$$

Among them, R is the real number field. That is to say, the degree of dissimilarity is a mapping of two elements to

the real number field, and the real number quantitatively represents the degree of dissimilarity of the two elements. The calculation of dissimilarity can use Euclidean distance, Manhattan distance, Minkowski distance, and so on. Usually, we use Euclidean distance:

$$d(X, Y) = \sqrt{(x_1 - y_1)^2 + (x_2 - y_2)^2 + \dots + (x_n - y_n)^2}. \quad (2)$$

The above method of calculating dissimilarity has a problem, that is, attributes with a large value range have a higher impact on distance than attributes with a small value range. In order to solve this problem, it is generally necessary to normalize the attribute value. The so-called normalization is to map each attribute value proportionally to the same value interval, so as to balance the influence of each attribute on the distance. Usually, each attribute is mapped to the interval [0,1], and the mapping formula is

$$a'_i = \frac{a_i - \min(a_i)}{\max(a_i) - \min(a_i)}. \quad (3)$$

Among them, $\max(a_i)$ and $\min(a_i)$ represent the maximum and minimum values of the i th attribute in all element items. The so-called clustering problem is to give a set of elements D , where each element has n observable attributes, use a certain algorithm to divide D into k subsets, and require the degree of difference between the elements within each subset as much as possible low, and the element dissimilarity of different subsets is as high as possible. Concentration, each subset is called a cluster. Different from classification, classification is exemplary learning, which requires that each category be clarified before classification and that each element is mapped to a category, while clustering is observational learning, and the category may not be known or even the number of categories may not be known before clustering.

K-means tries to find the natural category of the data. The user sets the number of categories to find a good category center. The algorithm flow is as follows:

- (1) Enter the number of data sets and categories K
- (2) Randomly assign the center point of the category
- (3) Put each point into the set of the category center point closest to it
- (4) Move the category center point to the set where it is
- (5) Go to step 3 until convergence

After a number of cycles, the best classification effect can be obtained. Different from marine shale reservoirs, the relationship between gas content of coal reservoirs and logging response of the coal reservoirs is relatively poor, and the laws are inconsistent, which also leads to the unreliability of the final prediction model. This is because coal reservoirs are more complex than shale reservoirs and have worse continuity, which causes the logging of coal seams to be affected by multiple factors. Using the clustering method to obtain multiple categories and establishing corresponding prediction

models based on different categories can greatly improve the prediction results.

3.2. Random Forest. Random forest is a highly flexible machine learning algorithm that has just emerged in the 21st century. It refers to a classifier that contains multiple decision trees. The thinking behind it is similar to group wisdom. In the 1980s, Breiman et al. invented an algorithm for classification trees, which performed classification or regression through repeated dichotomy of data, which greatly reduced the amount of calculation. In 2001, Breiman combined the classification trees into a random forest, that is, randomized the use of variables and the use of data, generated many classification trees, and then summarized the results of the classification trees [24]. Random forest improves the prediction accuracy without a significant increase in the amount of calculation. Random forest is not sensitive to multivariate collinearity, and the results are relatively robust to missing data and unbalanced data and can well predict the effect of thousands of explanatory variables.

Random forest uses a random method to build a forest. There are many decision trees in the forest, and there is no correlation between each decision tree in the random forest. After obtaining the forest, when a new input sample enters, let each decision tree in the forest make a judgment separately to see which category the sample belongs to. The class with the most classification times is the predicted class. Random forest can handle quantities whose attributes are discrete values. The construction process of random forest is as follows:

- (1) If there are N samples, N samples are randomly selected for replacement (one sample is randomly selected each time and then returned to continue selection). Use the selected N samples to train a decision tree as the sample at the root node of the decision tree
- (2) When each sample has M attributes, when each node of the decision tree needs to be split, then m attributes are selected from these M attributes, and the condition $m < M$ is satisfied. Then, from these m attributes, strategies such as information gain are used to select one attribute as the split attribute of the node
- (3) In the process of decision tree formation, each node must be split according to step 2 until it can no longer be split. Note that there is no pruning during the entire decision tree formation process
- (4) Follow steps 1-3 to build a large number of decision trees to form a random forest

In the process of building each decision tree, attention should be paid to the impact of sampling and complete splitting. The first is two random sampling processes. Random forest samples the input data in rows and columns. For line sampling, a replacement method is used, that is, in the sample set obtained by sampling, there may be duplicate samples. Assuming that there are N input samples, there are also N

samples sampled. In this way, when training, the input samples of each tree are not all samples, making it relatively difficult to overfitting. Then, perform column sampling, from M features, select m ($m < M$).

After that, a decision tree is built using a completely split method for the sampled data, so that a certain leaf node of the decision tree cannot continue to split, or all the samples in it point to the same category. Generally, many decision tree algorithms have an important step-pruning, but this is not done here. Since the previous two random sampling processes ensure randomness, even if pruning is not performed, overfitting will not occur. Using a random forest method to predict gas content should be able to achieve better results.

3.3. Combination Method of K-Means Clustering and Random Forest. It is difficult to evaluate the gas content of coal reservoirs, because the logging response has been affected by various factors, resulting in a poor relationship between the logging response and the core. Only by using clustering and other methods to truly combine logging responses for classification, different types of data are affected differently, and the relationship between logging responses and gas content in different categories is closer. Therefore, K-means clustering is performed first, and then based on the results of the clustering, a random forest model of different types is established for final application. In fact, the inherent meaning of this model is similar to that of random forests. It uses K-means clustering combined with random forests to form a “forest group” to predict gas content more accurately. The modeling and forecasting process is as follows:

- (1) Use K-means clustering to divide the data into several categories. The measurement method usually used to compare the results of different K values is the average distance between a data point and its cluster centroid. Since increasing the number of clusters will always reduce the distance to the data point, when K is the same as the number of data points, increasing K will always reduce the metric to zero. Therefore, this indicator cannot be used as the sole target. Conversely, the average distance to the center of mass is plotted as a function of K , and the “elbow point” at which the reduction rate changes sharply can be used to roughly determine the K value
- (2) Use K sets of data and random forest algorithm to train K models. After determining the category of the new data, the corresponding model can be used to calculate the gas content
- (3) When predicting new data, first determine the category of the new data by calculating the Euclidean distance between the sample data and the centroids of multiple classes of data. The new data belongs to the category corresponding to the centroid with the smallest Euclidean distance. After the category is determined, the corresponding model is used for prediction, and the predicted value of the gas content of the sample point is obtained, and the reliability of the

algorithm is determined by comparing with the real value

4. Result

First, the data needs to be further analyzed to clarify the relationship between the gas content of the CBM reservoir and the logging response. The corresponding results are shown in Figure 2.

In Figure 2, V_g refers to the total gas content results obtained through experiments. AC refers to the acoustic time difference curve response, CAL refers to the well diameter curve response, and CNL refers to the neutron porosity curve response. DEN refers to the density curve response, GR refers to the natural gamma curve response, and RD refers to the deep resistivity curve response. It can be clearly seen that the correlation between each curve and gas content is poor, which is obviously different from marine shale reservoirs. From the correlation of each curve, deep resistivity logging, neutron logging, and sonic logging have a relatively good relationship with the gas content parameters of the reservoir. It is recommended that the above curves can be used as the input curve of the model. When the gas content increases, the sonic time difference of the coal seam increases significantly. As the gas content of the reservoir increases the hydrogen index of the coal seam, the neutron porosity also increases. In addition, with the increase of gas content, the response value of deep resistivity logging increased significantly, indicating that the adsorbed gas in coal reservoirs can significantly increase the resistivity of the reservoir and reduce the conductivity of the CBM reservoir. We also recommend that the resistivity curve be logarithmically converted during input. Based on the above data, the K-means clustering research is carried out.

Figure 3 reflects the relationship between the clustering results and the sample-particle distance. It can be clearly seen that when there are more than 3 cluster types, the average distance reduction speed slows down significantly, indicating that it is not necessary to select more than 3 clusters. So here, we choose the number of clusters to be 3. After clustering, the gas content prediction model is established in different categories. Use the established model to predict the modeling samples, and the results are shown in Figure 4.

It can be seen from Figure 4 that, first of all, the correlation between the response of the logging curve and the poor total gas content does have a great impact on the prediction of gas content. Even if the random forest algorithm has strong approximation and generalization capabilities, the prediction effect obtained is very poor. It can be clearly seen from the results on the right that the prediction effect of the classification modeling after clustering is obviously better than that of Figure 4(a). The prediction effect is poor only when the total gas content is less than $5 \text{ cm}^3/\text{g}$, and the reservoirs with total gas content less than $5 \text{ cm}^3/\text{g}$ are not the reservoirs of our concern. Through the clustering method, data with relatively consistent main control factors are unified and classified, and the model established on this basis is more targeted. Judging from the core prediction results, the ideas

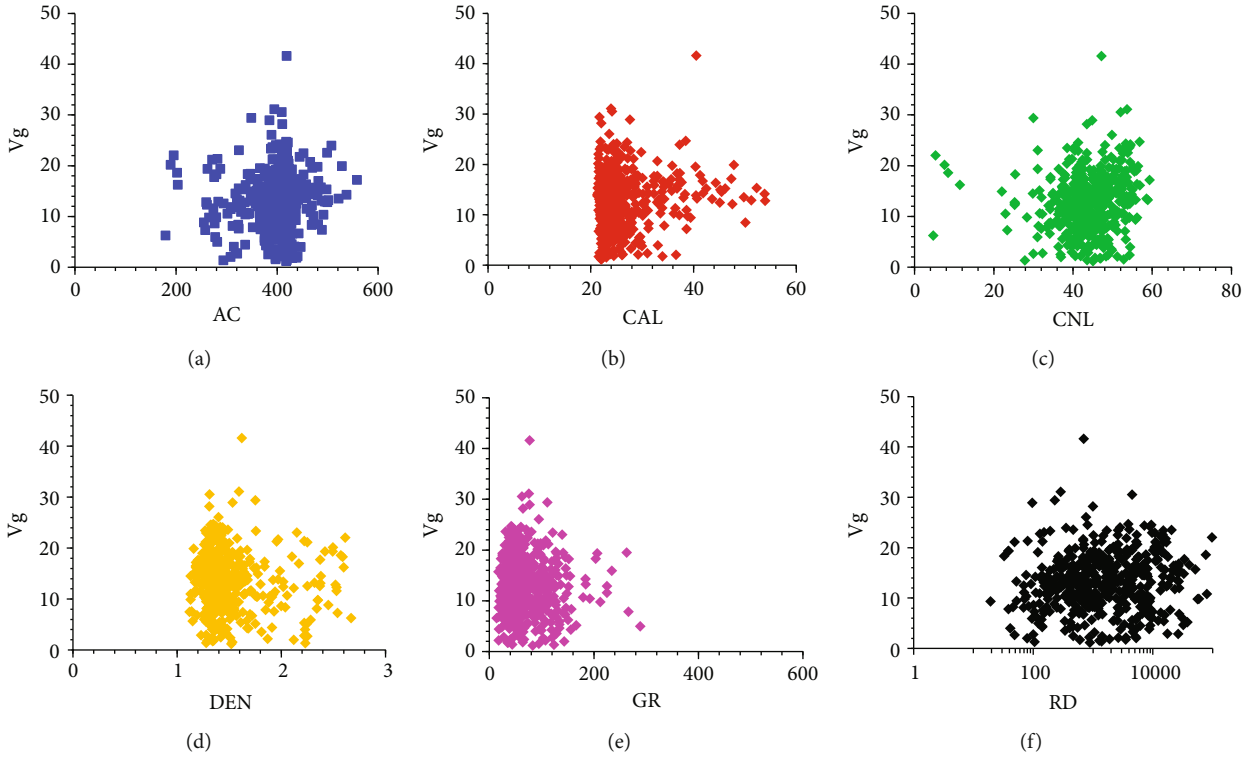


FIGURE 2: Display of the relationship between logging curve response and gas content.

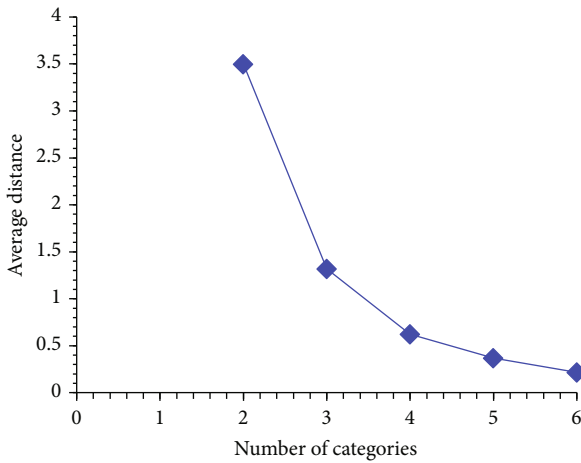


FIGURE 3: Display the relationship between clustering results and the distance between sample and mass point.

proposed in this article are very helpful for the gas content prediction of coal-measure reservoirs.

This method is used to predict the gas content of test wells A and B in the study area. The results are shown in Figures 5 and 6, respectively.

In Figures 5 and 6, the first track is the depth track, and the second track is the caliper curve measured by the four-arm caliper tool. In the third track, the SP curve is the spontaneous potential logging curve, the GR curve is the natural gamma logging curve, Rxo is the microsphere focused resistivity logging curve, RS is the shallow lateral resistivity log-

ging curve, and RD is the deep lateral resistance. Rate logging curve. In the fifth track, DEN is the density logging curve, AC is the sonic logging curve, and CNL is the neutron porosity logging curve. In the sixth channel, Vg_{RF} is the gas content curve directly predicted by random forest, and Vg_{core} is the gas content value of the core. In the seventh track, Vg_{KRF} is the gas content curve obtained by random forest prediction after clustering, Category is the clustering result of the curve, and Conclusion is the interpretation conclusion of the CBM reservoir.

It can be seen from Figure 5 that the correspondence between the Vg_{KRF} curve and the core is much higher than the Vg_{RF} curve, indicating that the random forest modeling effect based on the clustering method is better. Through the analysis of the curve, it can be seen that the gas content of type I reservoirs is relatively low, and the corresponding natural gamma curve content is relatively high. This indicates that the mud content of this type of reservoir is high, which affects the logging response and causes the previous. The prediction of gas content is inaccurate when the unified model is established. In addition, it can be found that the natural gamma response value of coal reservoirs corresponding to category III is low, the density response value is low, the acoustic wave response value is relatively high, and the resistivity response value is relatively high. This shows that type III coal reservoirs are high-quality coal reservoirs with higher coal content, and their gas content should also be higher than other reservoirs. From the perspective of the prediction effect, it is obvious that the gas content prediction results directly based on the random forest algorithm predict low gas content in type III reservoirs, especially in the interval

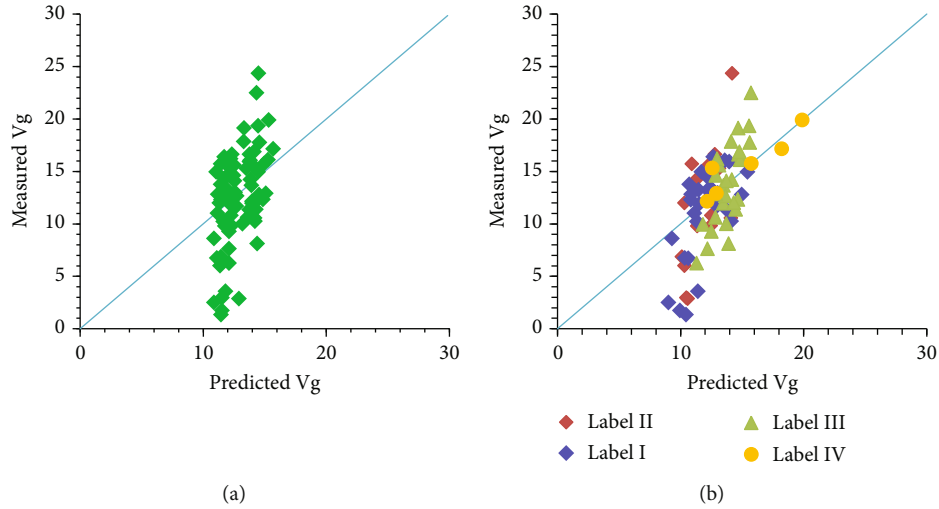


FIGURE 4: The predicted total gas content is compared with the experimental results. (a) The result of direct use of random forest algorithm prediction, and (b) the prediction result obtained by combining K-means clustering and random forest algorithm.

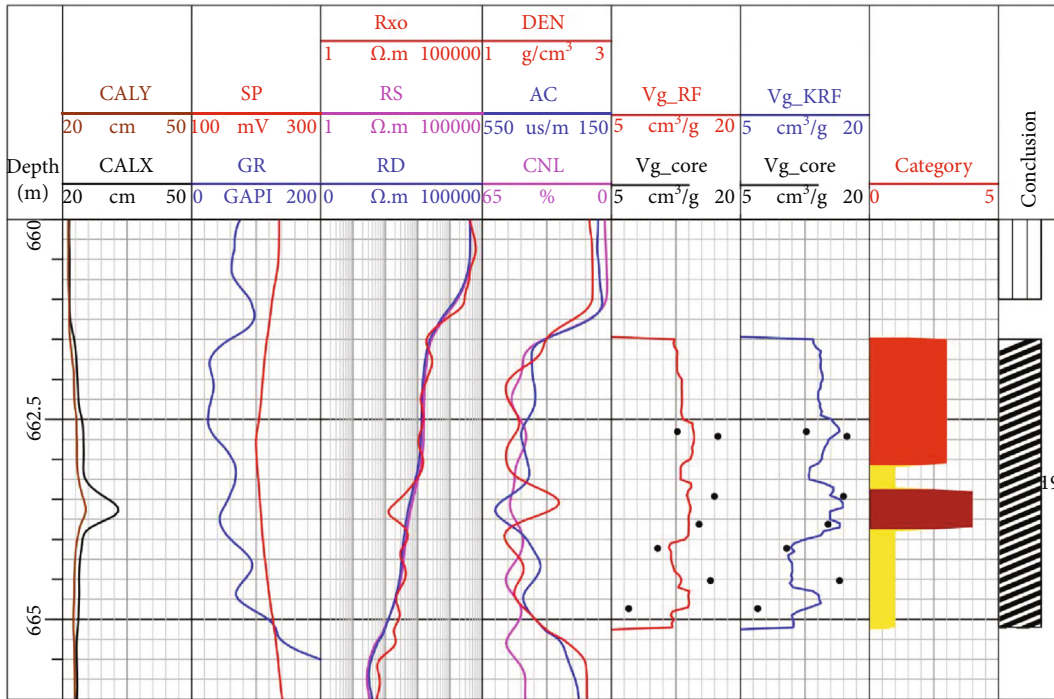


FIGURE 5: Gas content prediction results of well A in the study area.

with very high gas content. In reality, this will make it difficult for us to find the best quality reservoirs. In addition, it has to be mentioned that although we only use the acoustic log response value, resistivity log response value, and neutron log response value, other curves also have a good corresponding relationship with the category, which proves that the accuracy of the class. Type IV reservoirs obviously correspond to the expanded diameter interval, and targeted modeling for this interval can enhance the reliability of the model as much as possible. Therefore, from the application effect of well A, the gas content evaluation method proposed in this paper is more reliable than previous methods.

Figure 6 shows the importance of targeted models. The coal reservoir in Figure 6 is basically a type I reservoir. The gas content curve obtained by directly using random forest for modeling and prediction has very small fluctuations and is not very specific, which makes it difficult for us to directly use the results for high-quality reservoir recognition. The prediction effect of Vg_KRF is relatively more accurate and can be used for high-precision characterization of gas content. However, it can be seen that at 1243.1 m-1245.5 m, the predicted result of Vg_KRF is too small, but the predicted trend is consistent with the actual core trend, indicating that the clustering results need to be adjusted. Or, due to the

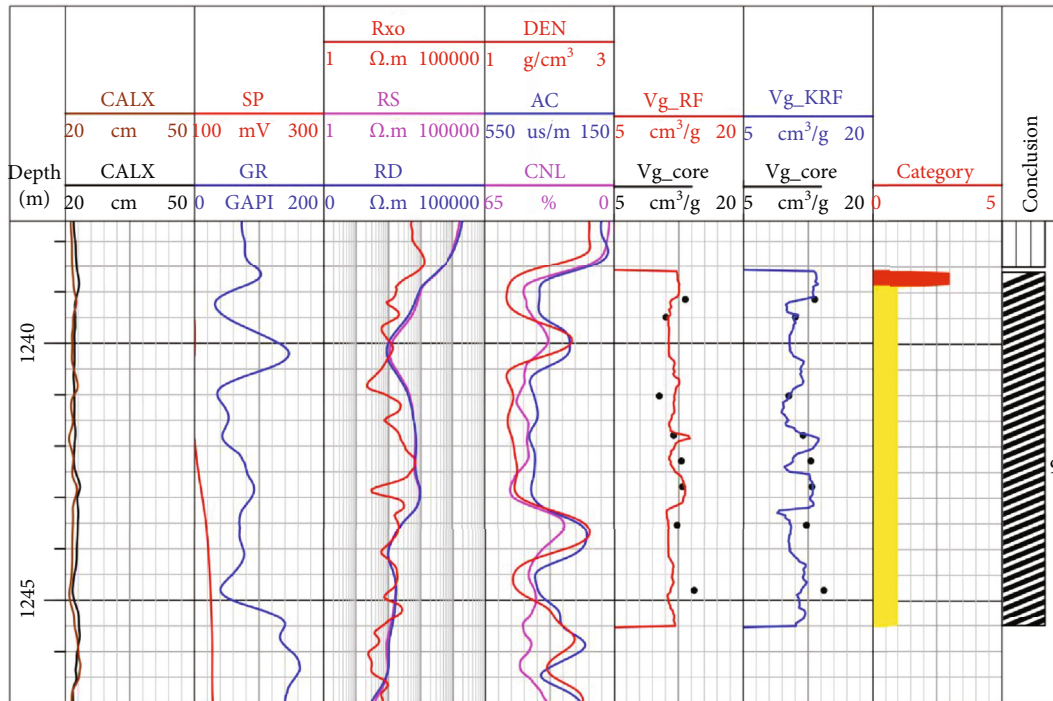


FIGURE 6: Gas content prediction results of well B in the study area.

saving of CBM reservoir development costs, the resolution of the logging tools used for measurement is not enough, and the logging response is disturbed when the vertical change of the reservoir is severe, which ultimately leads to inaccurate classification. Therefore, in the next step of the study, we can focus on the study of log curve superresolution based on wavelet transform and other methods to further improve the prediction effect. In general, the method proposed in this paper is of great help to the gas content evaluation of coal reservoirs with poor correlation between logging response and reservoir parameters.

5. Summary and Conclusions

The calculation of the gas content of CBM reservoirs is more complicated than other reservoirs. Various characteristics of coal reservoirs will have a series of effects on the logging response. This paper proposes a combination of K-means clustering and random forest algorithm to solve the difficult problem of calculating the gas content of CBM reservoirs. The research conclusions are as follows:

- (1) The fact that the calculation of the gas content of CBM reservoirs is more complicated is that the CBM reservoir itself is relatively complex, which causes the logging response to be affected by multiple factors. It further affects the relationship between CBM logging response and gas content, making the correlation poor
- (2) First, the samples are clustered, and the gas content prediction model of random forest is established for each type of sample. Through clustering results com-

pared with actual logging curve analysis, it can be clearly seen that through clustering algorithms, different types of CBM reservoirs can be effectively divided. Furthermore, by comparing the prediction results of CBM gas content, it can be seen that the gas content model established after clustering is more targeted and can evaluate the gas content more accurately. The method proposed in this paper can improve the calculation accuracy of pure CBM gas content and provide a way of thinking for parameter evaluation when the relationship between logging response and reservoir parameters is poor

Nomenclature

- CBM: Coalbed bed methane
- RF: Random forest
- Vg: Gas content
- AC: Sonic log
- CAL: Caliper log
- CNL: Neutron log
- DEN: Density log
- GR: Gamma log
- RD: Resistivity log.

Data Availability

All our data has been fully displayed in the pictures in the article.

Conflicts of Interest

The authors declare that they have no conflicts of interest.

Acknowledgments

This work is supported by the CNOOC information construction major project (No. 2019-KJZC-010); the Laboratory for Marine Geology, Qingdao National Laboratory for Marine Science and Technology (No. 2MGQNLN-KF202004); China Postdoctoral Science Foundation (Nos. 2021M690161 and 2021T140691); Post-doctorate Funded Project in Hainan Province; the Chinese Academy of Sciences-Special Research Assistant Project; China Engineering Technology Development Strategy Hainan Research Institute Consulting Research Project (No. 20-HN-ZT-01); and Open Fund of Key Laboratory of Exploration Technologies for Oil and Gas Resources (Yangtze University), Ministry of Education (Nos. K2021-03 and K2021-08).

References

- [1] L. Tian, Y. Cao, S. Liu, B. Shi, J. Liu, and D. Elsworth, "Coalbed methane reservoir fracture evaluation through the novel passive microseismic survey and its implications on permeable and gas production," *Journal of Natural Gas Science and Engineering*, vol. 76, p. 103181, 2020.
- [2] L. He, H. Mei, X. Hu, M. Dejam, Z. Kou, and M. Zhang, "Advanced flowing material balance to determine original gas in place of shale gas considering adsorption hysteresis," *SPE Reservoir Evaluation and Engineering*, vol. 22, no. 4, pp. 1282–1292, 2019.
- [3] L. Zhang, Z. Kou, H. Wang et al., "Performance analysis for a model of a multi-wing hydraulically fractured vertical well in a coalbed methane gas reservoir," *Journal of Petroleum Science and Engineering*, vol. 166, pp. 104–120, 2018.
- [4] J. Kumar, V. A. Mendhe, A. D. Kamble et al., "Coalbed methane reservoir characteristics of coal seams of south Karanpura coalfield, Jharkhand, India," *International Journal of Coal Geology*, vol. 196, pp. 185–200, 2018.
- [5] R. Baouche and D. A. Wood, "Characterization and estimation of gas-bearing properties of Devonian coals using well log data from five Illizi Basin wells (Algeria)," *Advances in Geo-Energy Research*, vol. 4, pp. 356–371, 2020.
- [6] Z. Yang, Y. Li, Y. Qin et al., "Development unit division and favorable area evaluation for joint mining CBM," *Petroleum Exploration and Development*, vol. 46, no. 3, pp. 559–568, 2019.
- [7] O. Esen, S. C. Özer, A. Soyulu, A. Ramazani Rend, and A. Fişne, "Geological controls on gas content distribution of coal seams in the Kimik coalfield, Soma Basin, Turkey," *International Journal of Coal Geology*, vol. 231, p. 103602, 2020.
- [8] Q. Chen, F. Zhang, F. Qiu et al., "Quantitatively determining gas content using pulsed neutron logging technique in closed gas reservoir," *Journal of Petroleum Science and Engineering*, vol. 198, p. 108149, 2021.
- [9] A. G. Kim, "Estimating methane content of bituminous coal beds from adsorption data," *United States Department of the Interior, Report of Investigations-Bureau of Mines*, vol. 8245, pp. 1–11, 1977.
- [10] U. Ahmed, D. Johnston, and L. Colson, "An advanced and integrated approach to coal formation evaluation," in *SPE Annual Technical Conference and Exhibition*, Dallas, Texas, October 1991.
- [11] J. M. Hawkins, R. A. Schraufnagel, and A. J. Olszewsk, "Estimating coal bed gas content and sorption isotherm using well log data," in *SPE Annual Technical Conference and Exhibition*, Washington, D.C., October 1992.
- [12] R. Liu, J. Wang, W. Liu, S. Guo, and Z. Li, "CBM logging evaluation method based on coal seam structure," *China Coalbed Methane*, vol. 11, no. 4, pp. 22–25, 2014.
- [13] Z. Meng, Y. Guo, and J. Zhang, "Application and prediction model of CBM content based on logging parameters," *Coal Science and Technology*, vol. 42, no. 6, pp. 25–30, 2014.
- [14] X. Shao, Y. Sun, J. Sun et al., "Logging interpretation of coal petrologic parameters: a case study of Hancheng mining area," *Petroleum Exploration and Development*, vol. 40, no. 5, pp. 559–565, 2013.
- [15] Z. Jin, H. Xue, H. Gao, X. Zhao, and G. Bai, "Technology for evaluation of CBM reservoir logging and its application," *Coal Geology & Exploration*, vol. 41, no. 2, pp. 42–45, 2013.
- [16] X. Fu, Y. Qin, G. G. X. Wang, and V. Rudolph, "Evaluation of gas content of coalbed methane reservoirs with the aid of geophysical logging technology," *Fuel*, vol. 88, no. 11, pp. 2269–2277, 2009.
- [17] J. Hou and Y. Wang, "Interpretation of well logging data for CBM using BP neural network," *Fuel*, vol. 35, no. 3, pp. 41–45, 1999.
- [18] H. Pan and Z. Huang, "Discussion on the interpretation method of CBM content," *Coal Geology and Exploration*, vol. 26, no. 2, pp. 58–60, 1998.
- [19] C. Lian, Y. Zhao, H. Li, F. Qu, F. Cai, and J. Zhang, "Prediction of coalbed gas content based on support vector machine regression," *Journal of Xi'an University of Science and Technology*, vol. 28, no. 4, pp. 707–710, 2008.
- [20] J. Guo, Z. Zhang, and C. Zhang, "Prediction and application of CBM content based on gray system and logging method," *Geophysical and Geochemical Exploration*, vol. 44, no. 5, pp. 1190–1200, 2020.
- [21] J. Guo, Z. Zhang, and C. Zhang, "The exploration of predicting CBM content by geophysical logging data: a case study based on slope correlation random forest method," *Geophysical and Geochemical Exploration*, vol. 45, no. 1, pp. 18–28, 2021.
- [22] M. Xiang, X. Qi, F. Zhang, and R. An, "Application of deep learning to CBM logging interpretation," *Geology and Exploration*, vol. 56, no. 6, pp. 1305–1312, 2020.
- [23] H. Yang, H. Pan, H. Ma, A. A. Konaté, J. Yao, and B. Guo, "Performance of the synergetic wavelet transform and modified K-means clustering in lithology classification using nuclear log," *Journal of Petroleum Science and Engineering*, vol. 144, pp. 1–9, 2016.
- [24] Y. Ao, H. Li, L. Zhu, S. Ali, and Z. Yang, "The linear random forest algorithm and its advantages in machine learning assisted logging regression modeling," *Journal of Petroleum Science and Engineering*, vol. 174, pp. 776–789, 2019.

Research Article

Disastrous Mechanism and Concentration Distribution of Gas Migration in Fully Mechanized Caving Stope in Wuyang Coal Mine

Li Chong,^{1,2} He Sifeng ,¹ and Xu Zhijun¹

¹School of Mines, Key Laboratory of Deep Coal Resource Mining, Ministry of Education, China University of Mining and Technology, Xuzhou, 221116 Jiangsu, China

²School of Mines, Jiangsu Engineering Laboratory of Mine Earthquake Monitoring and Prevention, China University of Mining & Technology, Xuzhou, 221116 Jiangsu, China

Correspondence should be addressed to He Sifeng; sifenghe541@163.com

Received 6 May 2021; Accepted 6 August 2021; Published 20 August 2021

Academic Editor: Yu Wang

Copyright © 2021 Li Chong et al. This is an open access article distributed under the Creative Commons Attribution License, which permits unrestricted use, distribution, and reproduction in any medium, provided the original work is properly cited.

The overrunning disaster of harmful gas tends to occur in the working face in thick coal seam with high gas concentration, as the fully mechanized caving stope has the characteristics of high mining intensity, high remnant coal, and high gas content. Therefore, the disastrous mechanism and concentration distribution of gas migration in fully mechanized caving stope are the theoretical basis for gas control scheme. Based on the 7607 working face in Wuyang coal mine, the gas emission quantity in working face is comprehensively analyzed by field measurement in this paper. The gas leakage field, oxygen concentration field, and gas concentration field in 7607 working face are simulated by establishing the equal proportional numerical model. Due to the increase of air leakage in working face caused by the high alley pumping drainage, the risk of coal spontaneous combustion is also analyzed, when gas extraction in goaf is carried out. The research results show that the gas drainage technology in high drainage roadway has a remarkable effect on the gas overrunning phenomenon. The gas concentration near the upper corner of the working surface has been reduced from 0.7%-1% to 0.5%. At the same time, it is necessary to pay attention to the risk of coal spontaneous combustion in the goaf for gas drainage in the high drainage roadway. The width of the oxidation zone in the goaf is about 25 m deeper than that before the drainage. Research results provide the references for gas control technology and coal spontaneous combustion prevention in similar working faces.

1. Introduction

Gas overrunning disaster not only directly threatens the safety of coal miners but also restricts the production capacity in coal mine [1, 2]. The coal output of fully mechanized caving stope is large, while the gas emission is uneven [3–5]. Meanwhile, the gas concentration in fully mechanized caving stope changes greatly in a short time, which is easy to cause gas accidents [6, 7]. Long-term production practice shows that gas migration and gas concentration distribution are important parts of gas control in fully mechanized caving stope [8–10]. For coal mine with complex production conditions, such as high gas and thick coal seams, it is particularly important to understand the gas migration status in the

working face and choose a reasonable gas control scheme [11–13]. Only by figuring out the factors affecting the gas concentration in fully mechanized caving stope can the occurrence of gas disaster be prevented, and the high yield and high efficiency of the mine be realized. Therefore, it is necessary to carry out the research on the disastrous mechanism and concentration distribution of gas migration in fully mechanized caving stope.

The gas outburst from the goaf to the working face is one of the main reasons for the gas overrunning disaster [14–16]. In high-gas mines, there are more remnant coal in goaf with low-position top coal caving mining technology, and the gap between the remnant coal is large [17, 18]. Therefore, after gas is gushing out, it is easy to flow through the goaf and flow

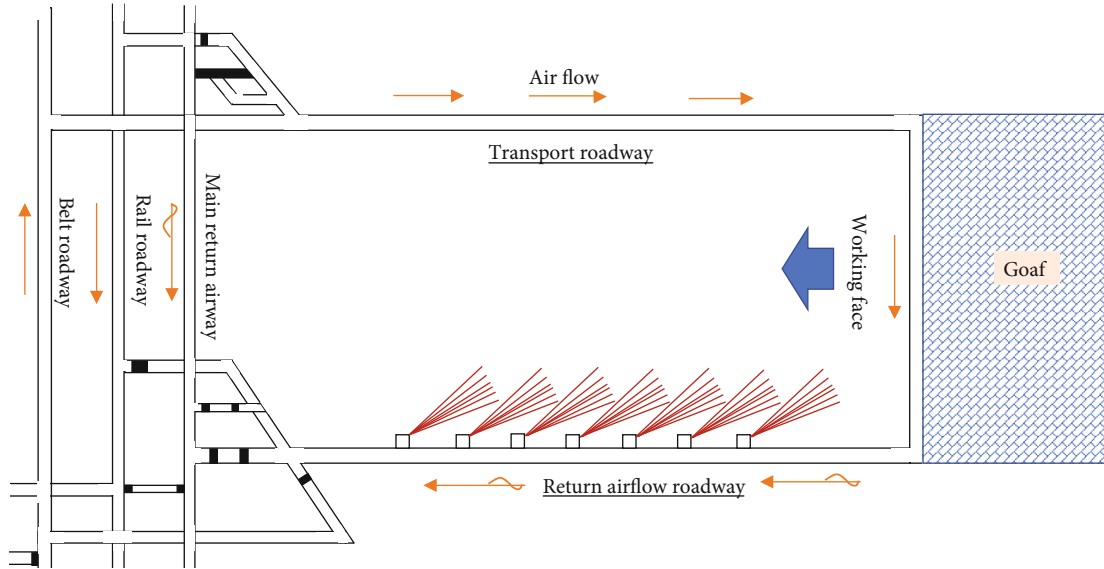


FIGURE 1: Schematic diagram in 7607 working face.

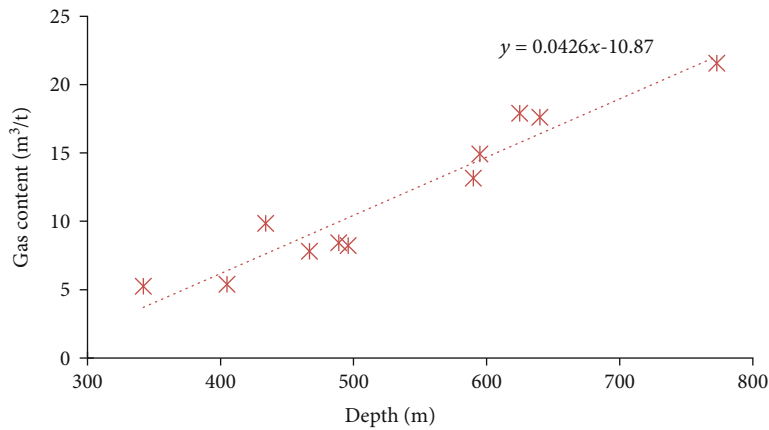


FIGURE 2: The relationship between the gas content and the buried depth of the 3# coal seam.

under the drive of air pressure. In the “U” type ventilation working face, when the air flow enters the stope from the inlet roadway, the gas in the goaf brings out to the working face, causing the gas concentration in the working face [19–21].

The gas drainage technology in high drainage roadway is widely used in China, which plays a good role in preventing the overrunning of gas concentration in the working face [22, 23]. For the working face in coal seam with high gas and spontaneous combustion, gas extraction through high drainage roadway alleviates the gas emission disaster but increases the air leakage in the working face to a certain extent and accelerates the process of spontaneous combustion of remnant coal in goaf [24, 25]. Xia et al. [26] studied the disaster mechanism of coexistence of gas and coal spontaneous combustion and the action mechanism of coupling effect. Chu et al. [27] analyzed the disturbance effect of roof roadway gas drainage on goaf spontaneous combustion area.

Therefore, it is of practical significance to study the characteristics of air leakage and the distribution of three zones for the prevention and control of coal spontaneous combus-

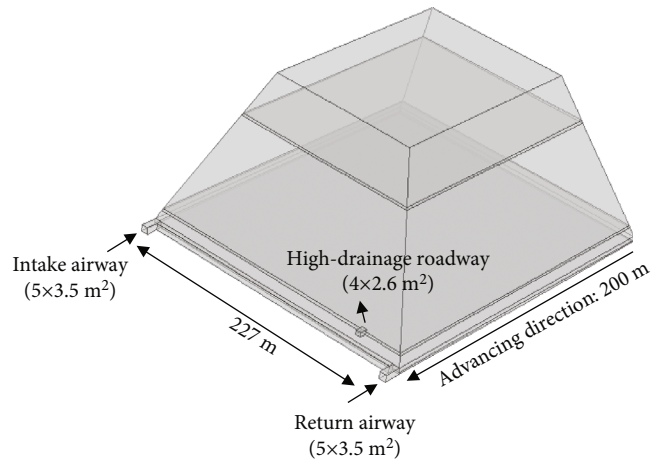


FIGURE 3: Numerical calculation model of 7607 working face.

tion in goaf. Therefore, aiming at the problem of gas overrunning in the high gas fully mechanized caving stope, this paper adopts the actual production conditions in the 7607 working



FIGURE 4: Schematic diagram of mesh division.

TABLE 1: Numerical simulation parameters.

Mark	Value	Meaning
rho_CH4	0.717 (kg/m ³)	Gas density under standard condition
rho_air	1.29 (kg/m ³)	Air density
D	1e-5 (m ² /s)	Gas diffusion coefficient
Mug	1.8e-5 (Pa*s)	Gas dynamic viscosity
pn	-2 (KPa)	Pressure at return air exit
Gp_c	260 (m ³ /min)	Extraction quantity of high pumping roadway
k0	1.45	Natural expansion coefficient
k1	1.15	Residual expansion coefficient
u0	5.1 (m/s)	Flow velocity of intake airflow roadway
u_15	5e-7 (m/s)	Gas emission rate of residual coal in goaf
u_14	8e-7 (m/s)	Gas emission rate of adjacent coal seam
v_mol	22.4 (l/mol)	Molar volume of gas
M_O2	32 (g/mol)	Molar mass of oxygen
M_N2	28 (g/mol)	Molar mass of nitrogen
M_CH4	16 (g/mol)	Molar mass of methane

face in Wuyang coal mine and analyzes the gas emission situation by field measurement in the working face.

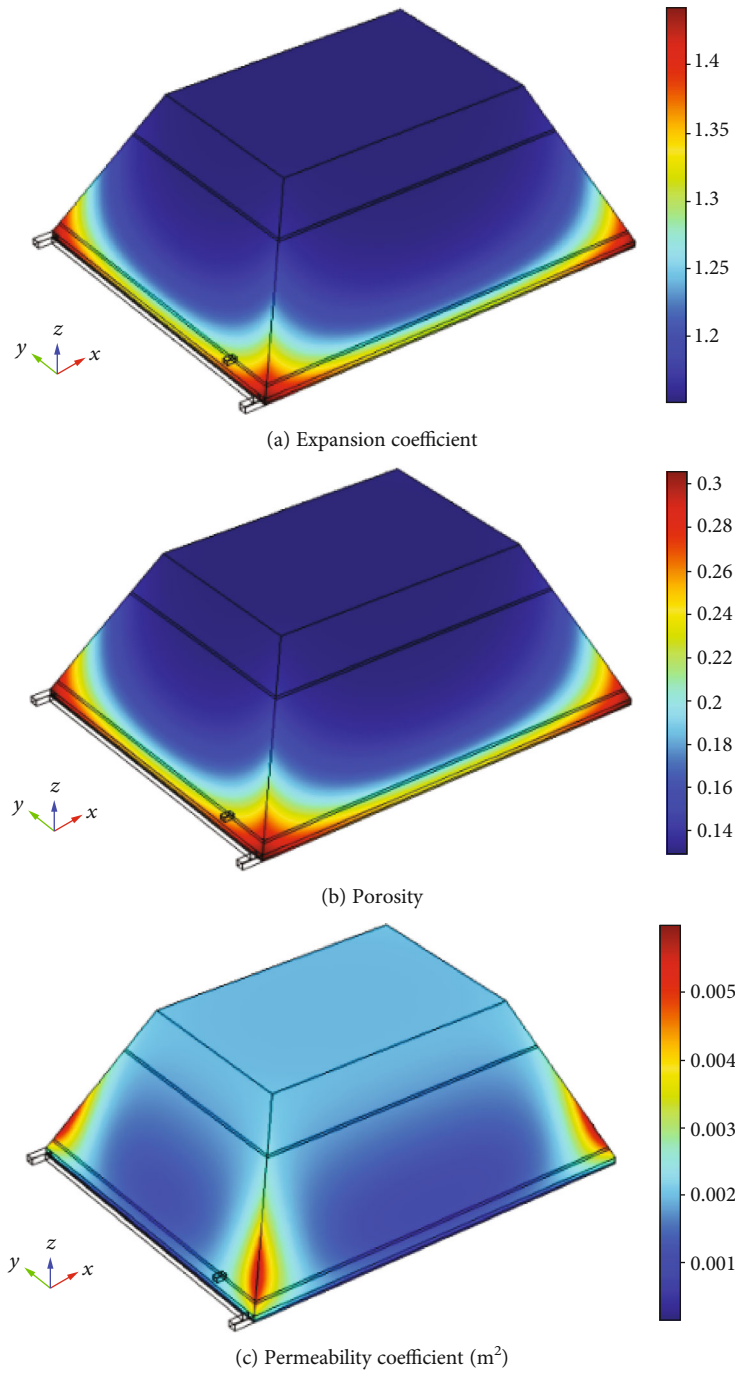
2. Gas Occurrence Law in 7607 Working Face

2.1. Basic Overview of Mining Area and Working Face. Wuyang coal mine is a large modern mine of Lu'an Group, which is located in Xiangyuan County, Changzhi City, Shanxi Province. It is about 13 km long from north to south and 10 km wide from east to west, covering an area of 78.3649 km². There are thirteen coal seams in the minefield, including two mineable seams, one most mineable seam, and ten locally and occasionally mineable seams, with a total thickness of 13.31 m and a coal content coefficient of 8.17%. Among them, 3# coal seam is located in the middle and lower part of Shanxi formation, with an average thickness of 5.75 m. The whole area is generally stable, which is the coal seam being mined. The ventilation mode in Wuyang coal

mine is divided into diagonal type, and the ventilation method is the extraction type.

The layout of 7607 working face in Wuyang coal mine is shown in Figure 1. Fully mechanized top coal caving is adopted in the working face, which has the characteristics of high yield and high efficiency. However, due to high mining intensity, fast advancing speed, and large gas emission in the working face, it is easy to cause gas overrunning in the upper corner or mine return air roadway, which brings great potential safety hazard for production.

2.2. Law of Gas Occurrence in Working Face. Fitting the gas content measured in Wuyang coal mine to the buried depth of the coal seam, the relationship between the gas content of the coal seam and the buried depth of the coal seam is obtained. The corresponding relationship between the gas content in the 3# coal seam and the buried depth is shown in Figure 2.



(a) Expansion coefficient

(b) Porosity

(c) Permeability coefficient (m^2)

FIGURE 5: Continued.

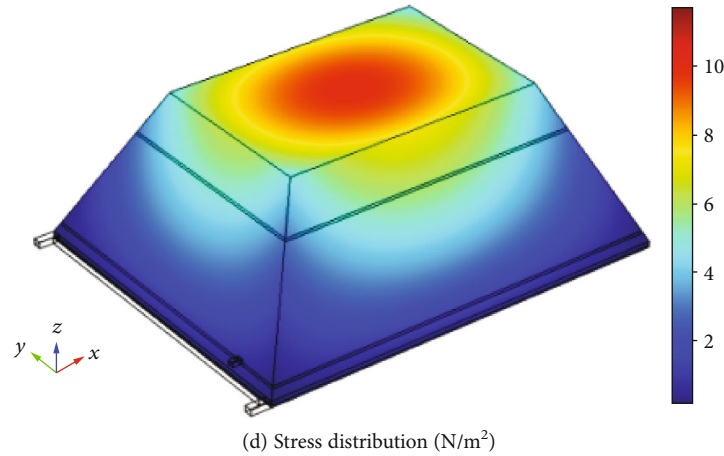


FIGURE 5: Distribution of seepage parameters in goaf.

The buried depth of coal seam at 7607 working face in Wuyang Coal Mine is 512 m-593 m. According to the formula of relation between gas content and buried depth, the coal seam gas content at 7607 working face is calculated to be $10.63 \text{ m}^3/\text{t}$ - $13.95 \text{ m}^3/\text{t}$.

3. Gas Migration Law and Coal Spontaneous Combustion Risk under U-Type Ventilation

3.1. Numerical Calculation Model. The 7607 working face adopts the comprehensively top coal mining technology scheme, with the open-cut length of 227 m and the advancing length of 1002 m. The average depth of coal seam in the working face is 600 m, and the thickness is 6.06 m, and the mining height is 3 m, and the coal discharge is 3 m, and the raw coal gas content in the working face is $9.1 \text{ m}^3/\text{t}$, and the air distribution volume is $4000 \text{ m}^3/\text{min}$. On the basis of the U-shaped ventilation scheme, the 7607 working face adopts gas drainage technology in high drainage roadway. Taking the intersection of the return airway and the working face as the origin of the coordinates in the COMSOL numerical analysis software, the direction of mined-out area is the x-axis direction, and the inclination is the y-axis direction, and the vertical direction is the z-axis direction to establish the geometric model, as shown in Figure 3. The section size of intake airway and return airway is 17.5 m^2 ($5 \text{ m} \times 3.5 \text{ m}$). The section size of high drainage roadway is 10.4 m^2 ($4 \text{ m} \times 2.6 \text{ m}$).

According to the actual situation in the 7607 working face, the strike length of the model is 200 m, and the inclination length is 227 m. The mesh of the working face area in the numerical calculation model is encrypted, shown in Figure 4. Tetrahedral mesh is used for mesh generation, the total number of meshes is 6×10^5 , and mesh encryption is carried out at the working face.

The intake airflow roadway is the entrance of speed, and the return air roadway is the free flow, and the high suction roadway is the mass exit, and the four sides which contact the high suction roadway and the goaf are the interface. The gas emission law in working face, the air leakage flow field in goaf, the distribution law of oxygen concentration

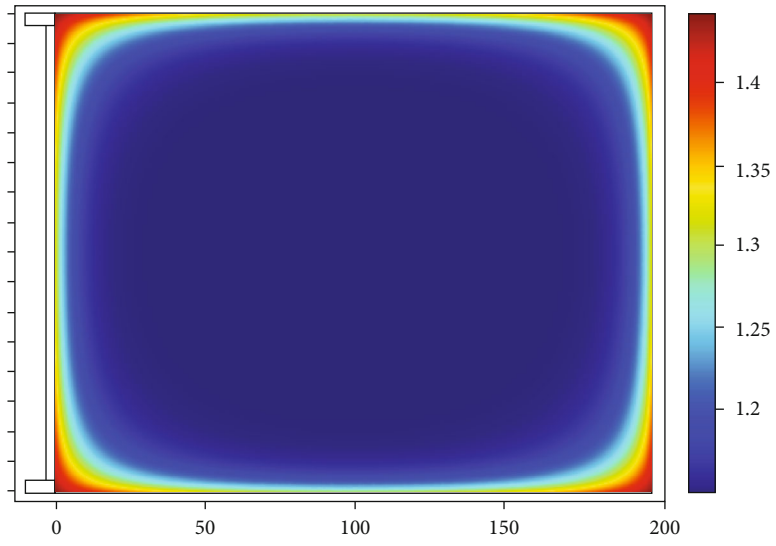
field, and gas concentration field are calculated. The numerical simulation parameters are shown in Table 1.

According to the mass conservation equations, the momentum conservation equations, and the diffusion motion equations, the mathematical model of oxygen and gas transport in the working face and the mined-out area is established, combined with the actual conditions in fully mechanized caving stope. The numerical simulation software COMSOL is employed to solve the model.

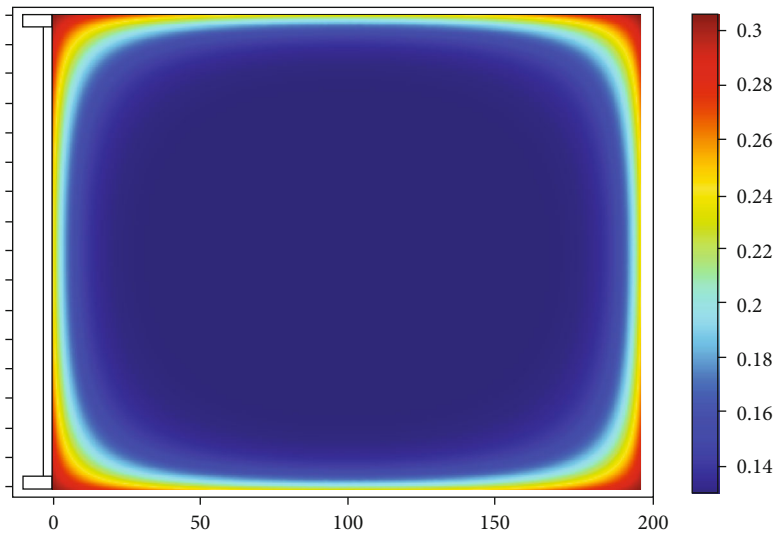
3.2. Distribution of Seepage Parameters in Goaf. Under the effect of air leakage pressure difference in goaf, the air flows between these pores. The surface of coal adsorbs the oxygen in the air leakage and reacts with it to form spontaneous combustion, which is the main reason for spontaneous combustion of residual coal in goaf. The distribution of porosity in goaf is closely related to the lithology of coal roof, compressive strength of coal seam, and distribution of mine pressure in goaf. The distribution of seepage parameters in goaf is shown in Figure 5.

Due to the collapse of the overlying strata in the goaf, the stress distribution in the goaf meets the “O” ring distribution theory. At the end of the working face and two roadway positions, the coefficient of coal and rock crushing expansion and porosity and permeability are larger, while the coefficient of coal and rock fragmentation and porosity and permeability are smaller in the middle of the goaf due to stress compaction. In order to further analyze the gas seepage environment in the goaf, the seepage parameters at the position of $z = 1.5 \text{ m}$ at the floor of the goaf are further extracted, shown in Figure 6.

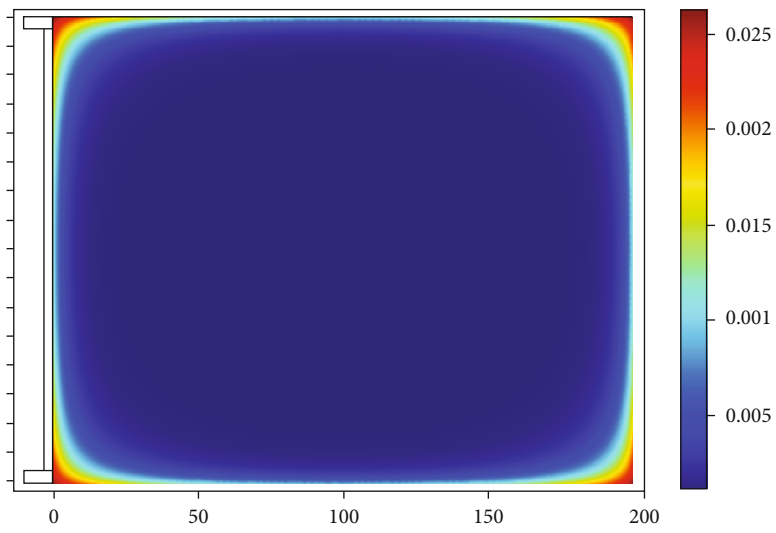
There are some differences in the distribution of seepage parameters in different positions of goaf. From the goaf near the end of the working face and two roadways, the porosity is larger, and the porosity in the middle and deep is smaller. Due to the collapse of overlying strata, the crushing expansion coefficient, porosity, and permeability at the inlet and return air roadway near the working face and the upper and lower angle of the deep solid wall boundary of the goaf are all large; the influence range is about 20 m. The porosity near the end of working face reaches the maximum value of



(a) Expansion coefficient



(b) Porosity



(c) Permeability coefficient (m²)

FIGURE 6: Continued.

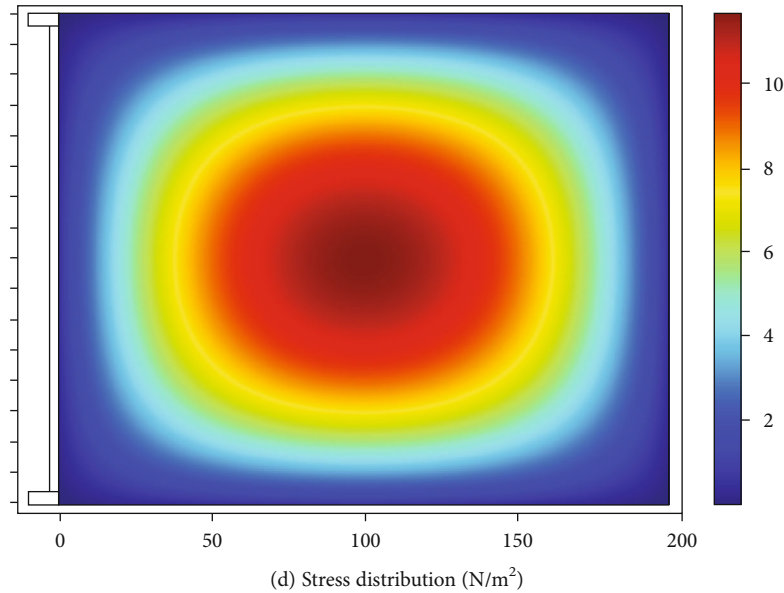


FIGURE 6: Distribution of seepage parameters at $z = 1.5$ m of goaf floor.

0.3 at the inlet and return air. The stress distribution of the goaf reaches the maximum in the middle of the goaf and decreases with the extension of the wall around the goaf.

3.3. Distribution of Flow Field and Concentration Field in Goaf. The change of gas composition in goaf, especially the content of oxygen and gas, depends on the distribution of air leakage and airflow. Therefore, the study of goaf seepage flow is an important theoretical basis for residual coal spontaneous combustion and gas emission and accumulation. The study of goaf seepage distribution provides an important basis for the study of goaf gas distribution and residual coal spontaneous combustion. When the inlet air volume is 4000 m³/min, the distribution of air leakage velocity at the floor $z = 1.5$ m of goaf is shown in Figure 7.

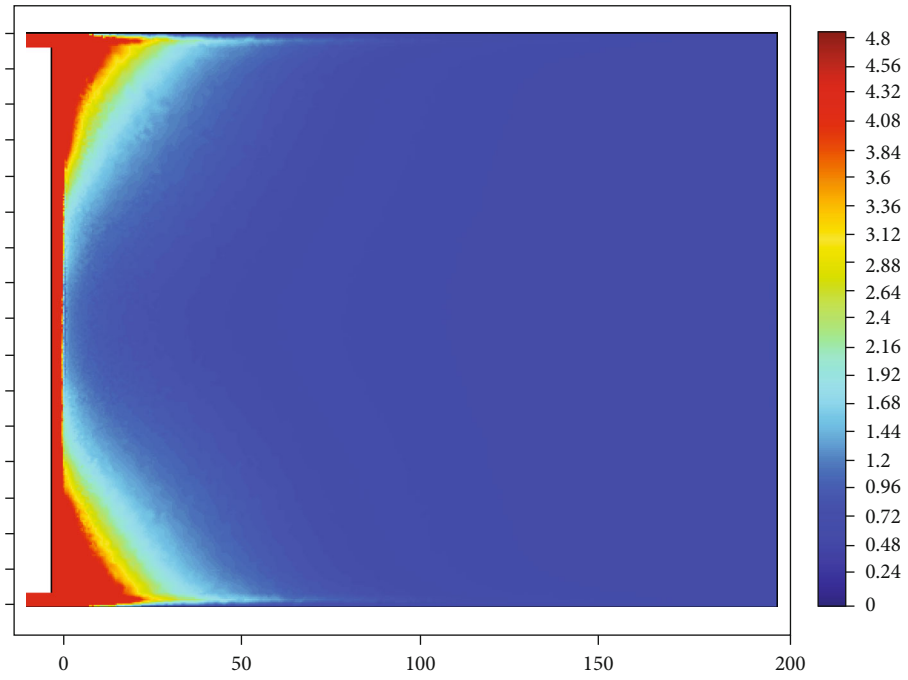
The air leakage rate in the goaf is relatively large at about 20 m near the end of the working face on the strike in Figure 7(a). When it reaches 50 m deep into the goaf, the air leakage rate gradually decreases and is less than 1 m/min. The reason for this phenomenon is the “O” circle distribution of coal mass in goaf. With the development of mining, the roof of goaf collapses. Therefore, there are a lot of air leakage into the goaf in the upper and lower corners in the goaf. The oxygen concentration distribution in the goaf is uneven in Figure 7(b). Due to the velocity inertia of the air leakage flow on the inlet side, the oxidation depth on the inlet side is greater than that on the return side.

In order to analyze the law of gas distribution in the stope and effectively control the gas level in the working face, the three-dimensional gas concentration distributions in goaf and floor are shown in Figures 7(c) and 7(d). Due to the dilution effect of the air leakage flow on the gas in the goaf, the gas concentration in the air inlet side is significantly lower than that in the air return side. Because the influence scope of air leakage is limited, the dilution effect of air flow on gas is relatively weak, when it reaches the middle and deep part

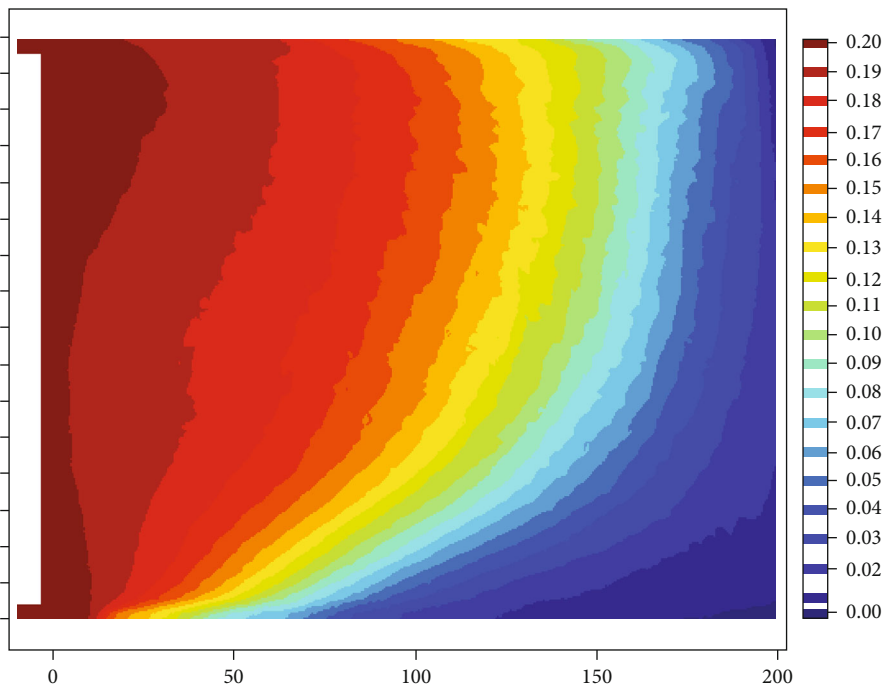
of goaf. Therefore, the gas concentration in the middle and deep part of goaf is higher.

3.4. Division of Spontaneous Combustion Oxidation Zone in Goaf. In order to further analyze the location of spontaneous combustion oxidation zone in goaf, the “three zones” in the goaf are divided by 0.004 m/s (0.24 m/min) and 0.001 m/s (0.1 m/min). The distribution range of spontaneous combustion oxidation zone based on air leakage wind speed is shown in Figure 8(a). The spontaneous combustion oxidation zone in goaf is distributed in the range of 50 m-150 m behind the goaf. On the inlet and return wind side, the isoline of 0.004 m/s is deep to about 120 m in the goaf strike. Based on the analysis of the distribution law of oxygen concentration in goaf, the oxygen concentration contour with $z = 1.5$ m at the floor is extracted for analysis, in order to clearly understand the distribution pattern of spontaneous combustion oxidation zone in goaf.

The distribution of oxidation zone in goaf with 18%-10% oxygen concentration as the division index is shown in Figure 8(b). The white area near the working face is the tropical zone, the colored area between 18% and 10% oxygen concentration contour is the spontaneous combustion zone, and the area with oxygen concentration less than 10% is the asphyxiation zone. When the spontaneous combustion zone extends from the air inlet side of the goaf to the air return side of the goaf, its width gradually decreases. The width of the oxidation zone on the air return side of the goaf is relatively narrow, compared with the central part of the goaf and the air inlet side. In one side of the inlet roadway, the range of spontaneous combustion zone is 75 m-160 m, and the width of spontaneous combustion zone is 85 m, and the width of spontaneous combustion zone is 85 m. The spontaneous combustion zone in the middle of goaf is 85 m-150 m, and the width of spontaneous combustion zone is 65 m. The range of spontaneous combustion zone on one side of the

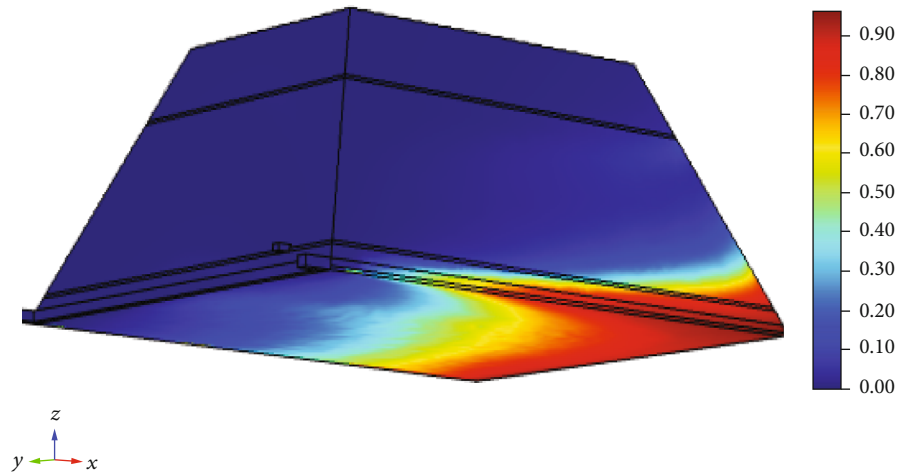


(a) Air leakage velocity

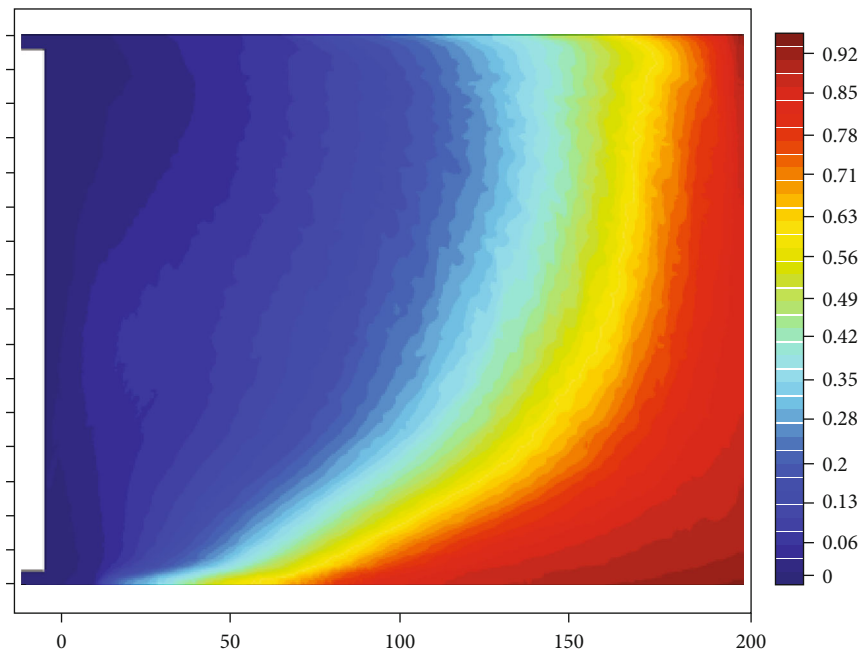


(b) Distribution of oxygen density

FIGURE 7: Continued.



(c) Gas concentration distribution in goaf



(d) Gas concentration distribution in floor

FIGURE 7: Distribution of flow field and concentration field at $z = 1.5$ m of goaf floor.

return air roadway is 20 m-45 m, and the width of spontaneous combustion zone is 25 m. Combined with the oxidation zone range divided by air leakage wind speed and oxygen concentration, the oxidation zone range is determined to be 20 m-150 m, in order to reduce the risk of coal spontaneous combustion in goaf.

4. Multicomponent Gas Migration and Coal Spontaneous Combustion Risk under the Condition of High Pumping Roadway

4.1. *The Distribution of Flow Field and Concentration Field in Goaf.* In order to further control the gas level in the goaf, gas extraction is carried out in the high pumping roadway above the roof of the goaf, and the extraction rate is $260 \text{ m}^3/\text{min}$.

Firstly, the air leakage velocity distribution at $z = 1.5$ m in the goaf floor under the condition of high pumping roadway is shown in Figure 9(a). In order to further analyze the change rule of oxygen concentration on the inlet and outlet side under the action of high pumping roadway, the changes of oxygen concentration at 30 m away from the inlet and outlet side are extracted, shown in Figure 9(b). The oxygen concentration at the air inlet side drops to 18% after entering the goaf about 110 m, and the oxygen concentration at the air inlet side about 170 m is 10%. The three-dimensional gas concentration distribution in goaf under the effect of high pumping roadway is shown in Figure 9(c). In order to clearly understand the gas concentration distribution in working face and goaf, the contour map of gas concentration at the goaf floor $z = 1.5$ m is extracted, shown in Figure 9(d).

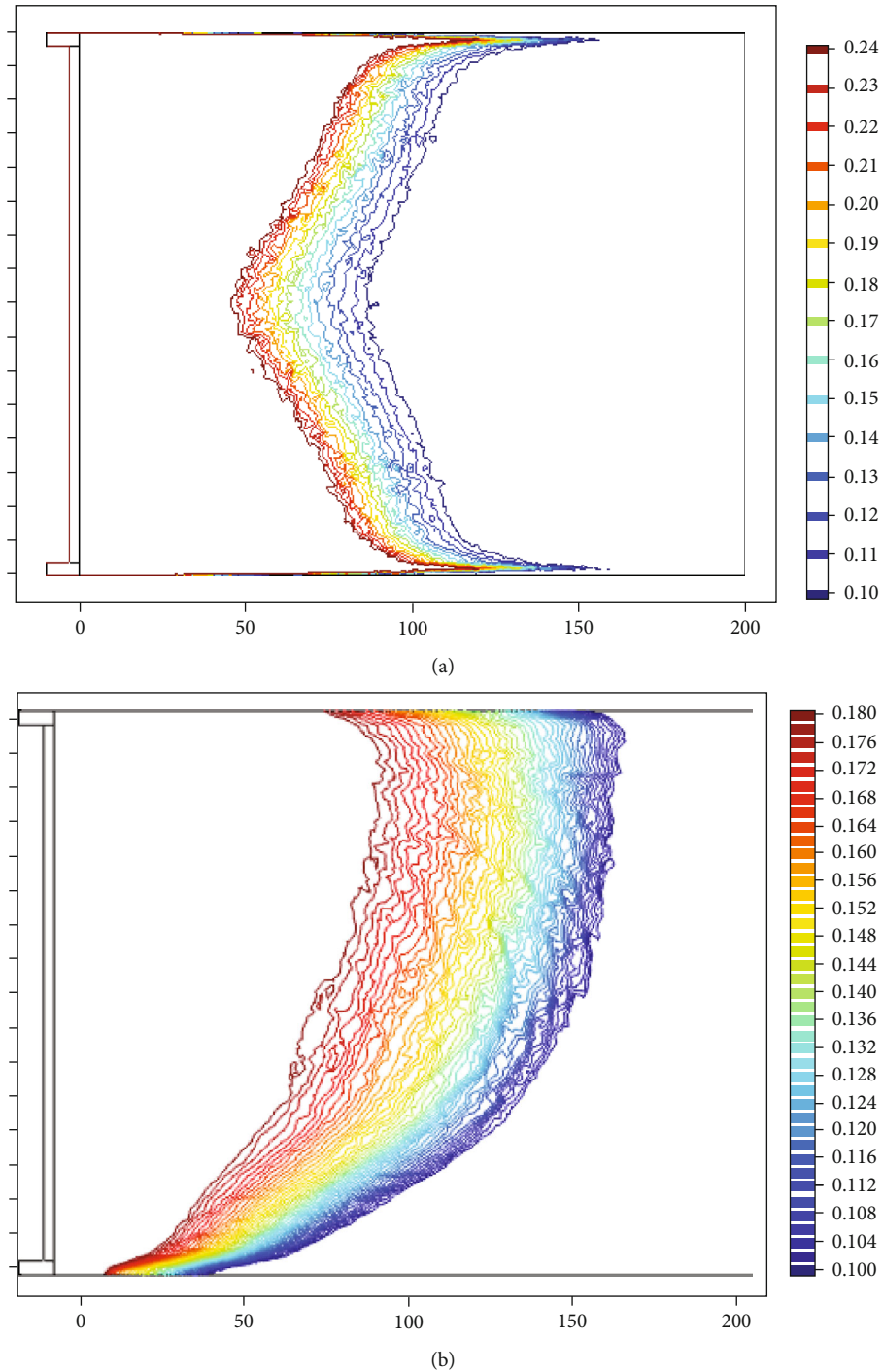
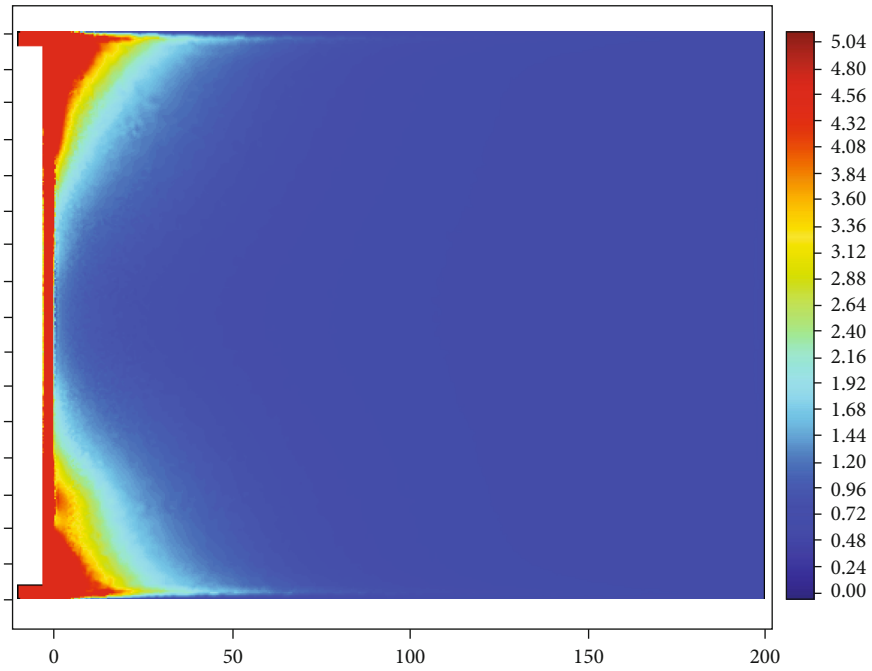


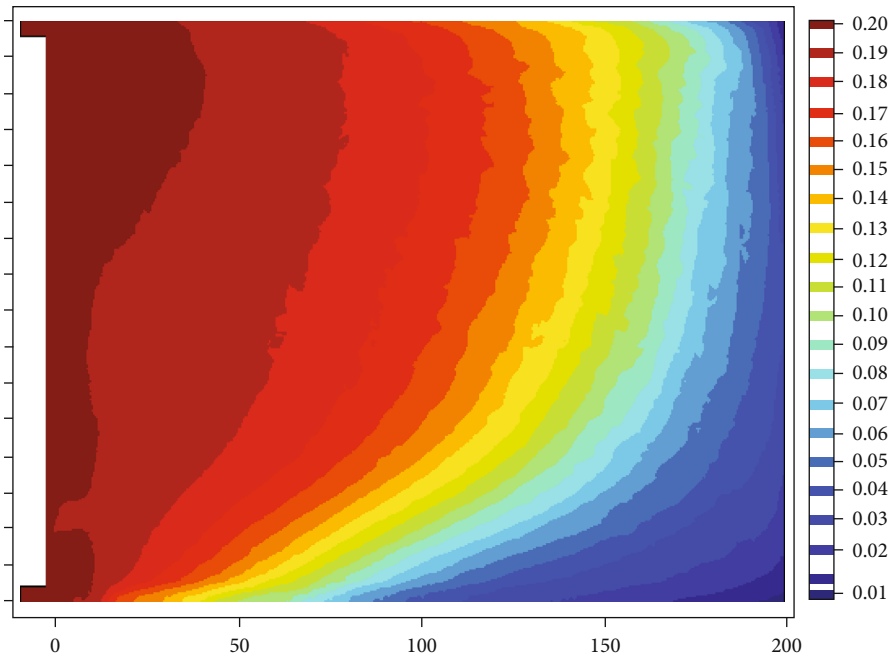
FIGURE 8: Distribution of oxidation zone at $z = 1.5$ m of goaf floor.

4.2. Division of Spontaneous Combustion Oxidation Zone in Goaf. Compared with the leakage field under U -shaped ventilation, the air leakage velocity range at the return air corner becomes larger due to the influence of gas extraction in the high pumping roadway; especially, the air leakage velocity at the position of the return air roadway is significantly increased. The three-zone distribution of goaf under the condition of gas extraction in high pumping roadway is shown in Figure 10(a), which is divided by air leakage speed as an indi-

cator. The spontaneous combustion oxidation zone in goaf is distributed in the range of 60 m-160 m behind goaf. The red area is the tropic zone, the blue area is the suffocation zone, and the gradient area between them is the spontaneous combustion oxidation zone. Compared with the distribution of air leakage velocity under U -type ventilation, the depth of oxidation zone in goaf under high extraction roadway is larger. On the inlet and return wind side, the 0.24 m/min isoline is deep to about 140 m of the goaf strike. In Figure 11(b),

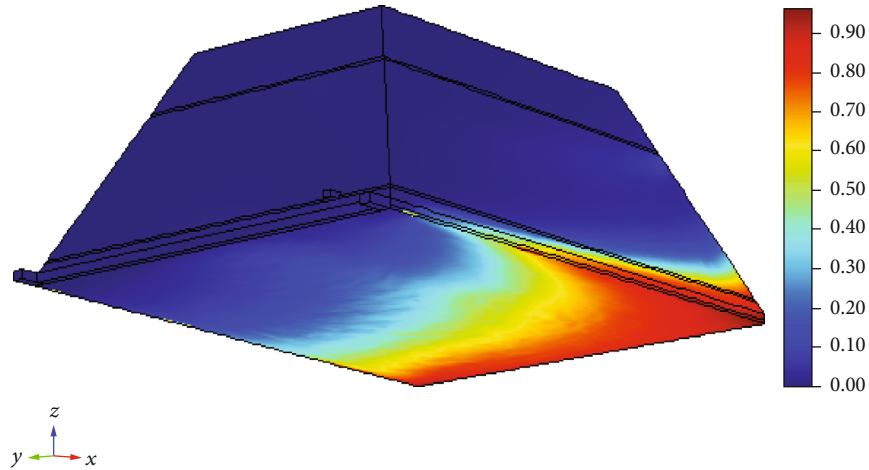


(a) Air leakage velocity

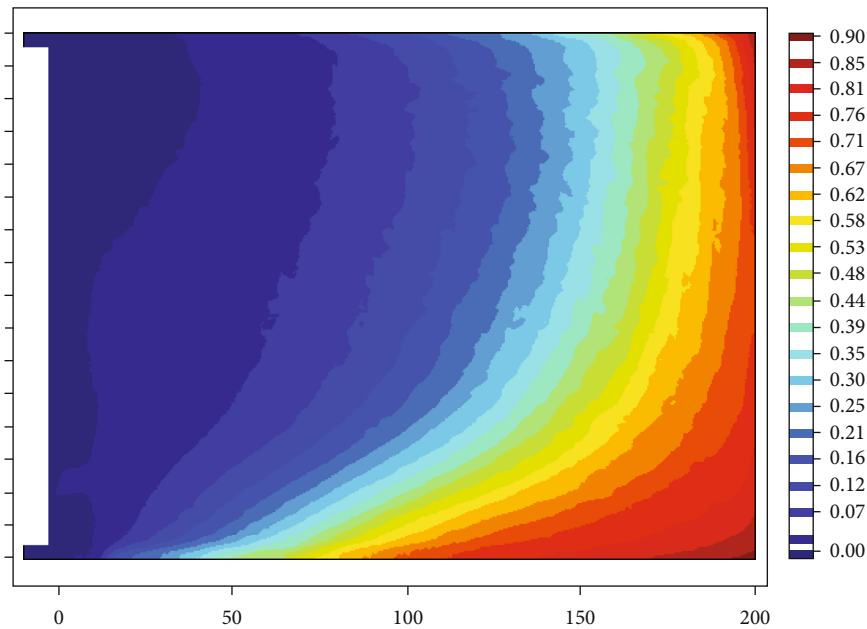


(b) Distribution of oxygen density

FIGURE 9: Continued.



(c) Gas concentration distribution in goaf



(d) Gas concentration distribution in floor

FIGURE 9: Distribution of flow field and concentration field at $z = 1.5$ m in the goaf floor under the condition of high pumping roadway.

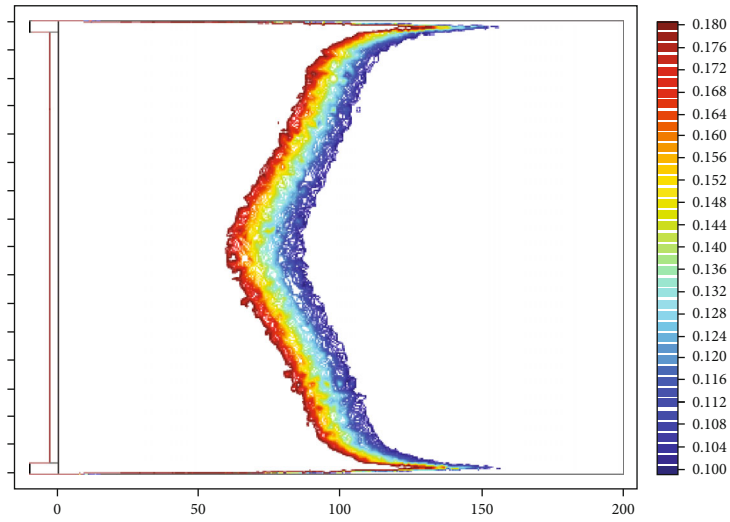
the white area near the working face is the scattered tropical zone, the colored area between the 18% and 10% oxygen concentration contour lines is the spontaneous combustion zone, and the area with oxygen concentration less than 10% is the asphyxiation zone. The range of spontaneous combustion zone on one side of the air inlet roadway is 90 m-175 m in Figure 10(b), and the width of spontaneous combustion zone is 85 m; the range of spontaneous combustion zone in the middle of the goaf is 100 m-160 m, and the width of spontaneous combustion zone is 60 m; the range of spontaneous combustion zone on one side of the air return roadway is 20 m-75 m, and the width of spontaneous combustion zone is 55 m.

Compared with the U -type ventilation, the width of oxidation zone at the inlet side and the middle of goaf has little change, and the oxidation depth moves back about 10 m. The 18% isoline of the oxidation zone on the return side changes

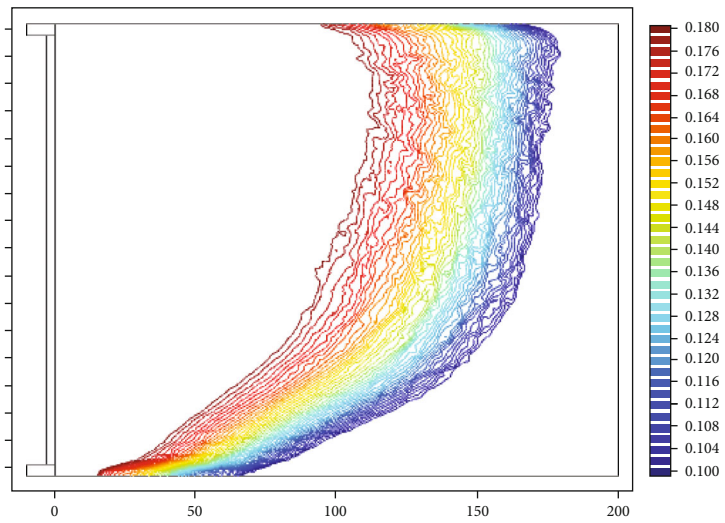
little, and the 10% isoline moves backward obviously. The width of oxidation zone on the return air side changed greatly, which increased by 30 m compared with the previous 25 m width.

4.3. Comparison of Oxygen and Gas Concentration in Goaf before and after Gas Drainage in High Drainage Roadway.

The volume fraction of oxygen and gas on both sides of air intake airway and air return airway in goaf before and after gas extraction in high drainage roadway is compared, as shown in Figures 11 and 12. It can be seen from Figure 11 that the air leakage in goaf is increased after gas extraction in high drainage roadway, and the oxygen volume fraction in the inlet and return air side is increased significantly. When the depth of goaf is 50 m, the oxygen volume fraction at the inlet airway and return airway side increases by 2% and 5%, respectively. Gas drainage in high drainage roadway

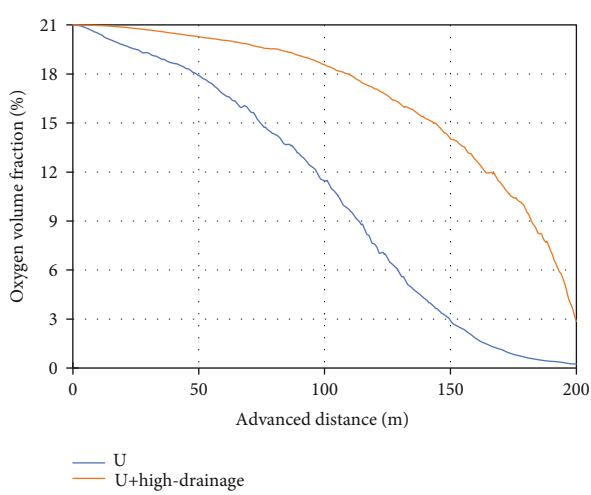


(a)

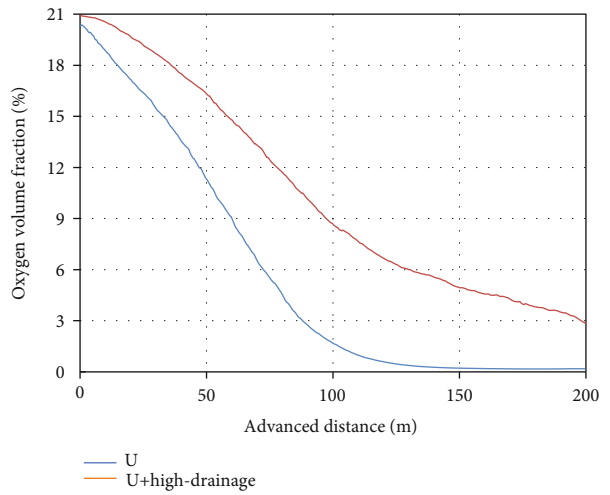


(b)

FIGURE 10: Distribution of oxidation zone at $z = 1.5$ m in goaf floor.



(a)



(b)

FIGURE 11: Volume fraction of oxygen in intake (a) and return (b) airway before and after high drainage.

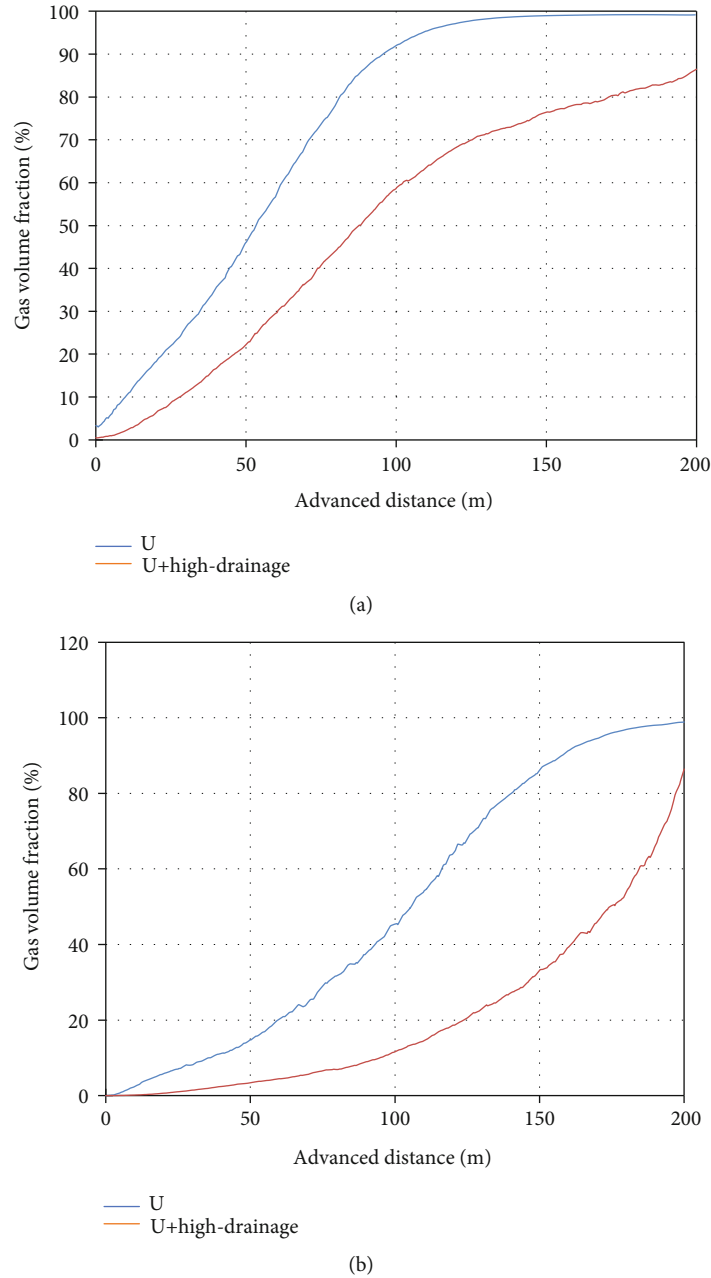


FIGURE 12: Volume fraction of gas in intake (a) and return (b) airway before and after high drainage.

obviously reduces the gas volume fraction in goaf, and the gas volume fraction on both sides of inlet and return airway decreases obviously, as shown in Figure 12. When the depth of goaf is 50 m, the gas volume fraction at the air inlet and air return side decreases by 10% and 20%, respectively. Especially, the gas concentration near the upper corner of the working face is obviously reduced, which effectively inhibits the gas emission from the goaf to the working face.

5. Conclusions

(1) The buried depth of coal seam is the key factor affecting gas occurrence. The relationship between coal

seam gas content and coal seam buried depth is obtained, the growth gradient of gas content is $4.2 \text{ m}^3/\text{t}/\text{hm}$, and the coal seam gas content in the 7607 working face is predicted to be $10.63 \text{ m}^3/\text{t}$ - $13.95 \text{ m}^3/\text{t}$. Through the measurement of gas content, it is proved that the gas occurrence law is consistent with the actual situation

(2) The measured gas emission from the coal wall and falling coal mass in the working face is $26.09 \text{ m}^3/\text{min}$, the gas entering the goaf with air leakage is $1.12 \text{ m}^3/\text{min}$, and the air leakage in the working face is $581 \text{ m}^3/\text{min}$. The simulation results show that the range of spontaneous combustion oxidation zone

in goaf in 7607 working face is 50 m-160 m at the inlet roadway side, 50 m-150 m at the central goaf, and 20 m-150 m at the return air roadway side

- (3) By measuring the gas accumulation concentration in different areas in the working face and determining the natural oxidation zone (seepage area) in goaf in numerical simulation, the gas accident area is comprehensively determined. Through the gas control effect monitoring, it is confirmed that the gas concentration in the upper corner of the fully mechanized top coal caving stope in Wuyang coal mine is not more than 0.8%, and the gas concentration in the return air roadway is not more than 0.8%.

Data Availability

The data used to support the findings of this study are included within the article.

Conflicts of Interest

The authors declare that they have no conflicts of interest.

Acknowledgments

The study was supported by the National Natural Science Foundation of China (51874277).

References

- [1] Y. Cao, Y. Li, and Z. Zhou, "Spatial-temporal variation features and law of gas concentration in the fully mechanized working face under the condition of intermittent ventilation," *International Journal of Mining Science and Technology*, vol. 29, no. 6, pp. 963–969, 2019.
- [2] L. Zhu, F. Dang, Y. Xue, K. Jiao, and W. Ding, "Multivariate analysis of effects of microencapsulated phase change materials on mechanical behaviors in light-weight aggregate concrete," *Journal of Building Engineering*, vol. 42, article 102783, 2021.
- [3] H. Wang, X. Yang, F. Du et al., "Calculation of the diffusion coefficient of gas diffusion in coal: the comparison of numerical model and traditional analytical model," *Journal of Petroleum Science and Engineering*, vol. 205, article 108931, 2021.
- [4] F. Du and K. Wang, "Unstable failure of gas-bearing coal-rock combination bodies: insights from physical experiments and numerical simulations," *Process Safety and Environmental Protection*, vol. 129, pp. 264–279, 2019.
- [5] W. L. Shen, J. B. Bai, W. F. Li, and X. Y. Wang, "Prediction of relative displacement for entry roof with weak plane under the effect of mining abutment stress," *Tunnelling and Underground Space Technology*, vol. 71, pp. 309–317, 2018.
- [6] L. Cheng, L. Shugang, and Y. Shouguo, "Gas emission quantity prediction and drainage technology of steeply inclined and extremely thick coal seams," *International Journal of Mining Science and Technology*, vol. 28, no. 3, pp. 415–422, 2018.
- [7] Y. Xue, F. Gao, Y. Gao, X. Liang, Z. Zhang, and Y. Xing, "Thermo-hydro-mechanical coupled mathematical model for controlling the pre-mining coal seam gas extraction with slot-
ted boreholes," *International Journal of Mining Science and Technology*, vol. 27, no. 3, pp. 473–479, 2017.
- [8] H. W. Zhou, H. P. Xie, and J. P. Zuo, "Development in researches on mechanical behaviors of rocks under the condition of high ground pressure in the depths," *Advances in Mechanics*, vol. 1, pp. 91–99, 2005.
- [9] Y. Xue, T. Teng, F. Dang, Z. Ma, S. Wang, and H. Xue, "Productivity analysis of fractured wells in reservoir of hydrogen and carbon based on dual-porosity medium model," *International Journal of Hydrogen Energy*, vol. 45, no. 39, pp. 20240–20249, 2020.
- [10] D. Ma, H. Duan, W. Liu, X. Ma, and M. Tao, "Water-sediment two-phase flow inrush hazard in rock fractures of overburden strata during coal mining," *Mine Water and the Environment*, vol. 39, no. 2, pp. 308–319, 2020.
- [11] B. H. Yao, Z. Chen, J. Wei, T. Bai, and S. Liu, "Predicting erosion-induced water inrush of karst collapse pillars using inverse velocity theory," *Geofluids*, vol. 2018, Article ID 2090584, 18 pages, 2018.
- [12] F. Du, K. Wang, X. Zhang, C. Xin, L. Shu, and G. Wang, "Experimental study of coal-gas outburst: insights from coal-rock structure, gas pressure and adsorptivity," *Natural Resources Research*, vol. 29, no. 4, pp. 2481–2493, 2020.
- [13] L. L. Si, J. Wei, Y. Xi et al., "The influence of long-time water intrusion on the mineral and pore structure of coal," *Fuel*, vol. 290, article 119848, 2021.
- [14] Z. Z. Cao, P. Xu, Z. H. Li, M. X. Zhang, Y. Zhao, and W. L. Shen, "Joint bearing mechanism of coal pillar and backfilling body in roadway backfilling mining technology," *CMC-Computers Materials & Continua*, vol. 54, no. 2, pp. 137–159, 2018.
- [15] Y. Xue, P. G. Ranjith, F. Dang et al., "Analysis of deformation, permeability and energy evolution characteristics of coal mass around borehole after excavation," *Natural Resources Research*, vol. 29, no. 5, pp. 3159–3177, 2020.
- [16] Z. Z. Cao, F. Du, Z. H. Li, Q. T. Wang, P. Xu, and H. X. Lin, "Research on instability mechanism and type of ore pillar based on the fold catastrophe theory," *CMES-Computer Modeling in Engineering & Science*, vol. 113, no. 3, pp. 287–306, 2017.
- [17] Y. Xue, J. Liu, F. Dang, X. Liang, S. Wang, and Z. Ma, "Influence of CH₄ adsorption diffusion and CH₄-water two-phase flow on sealing efficiency of caprock in underground energy storage," *Sustainable Energy Technologies and Assessments*, vol. 42, article 100874, 2020.
- [18] X. X. Miao, H. Pu, and H. B. Bai, "Principle of water-resisting key strata and its application in water-preserved mining," *Journal of China University of Mining and Technology*, vol. 1, pp. 1–4, 2008.
- [19] M. G. Qian and J. L. Xu, "Study on the "O shape" circle distribution characteristics of mining induced fracture in the overburden strata," *Journal of China Coal Industry*, vol. 5, pp. 20–23, 1998.
- [20] L. L. Si, H. Zhang, J. Wei, B. Li, and H. Han, "Modeling and experiment for effective diffusion coefficient of gas in water-saturated coal," *Fuel*, vol. 284, article 118887, 2021.
- [21] Z. Z. Cao, Y. Ren, Q. Wang, B. Yao, and X. Zhang, "Evolution mechanism of water-conducting channel of collapse column in karst mining area of southwest China," *Geofluids*, vol. 2021, Article ID 6630462, 8 pages, 2021.
- [22] D. Ma, J. Wang, and Z. Li, "Effect of particle erosion on mining-induced water inrush hazard of karst collapse pillar,"

- Environmental Science and Pollution Research*, vol. 26, no. 19, pp. 19719–19728, 2019.
- [23] S. G. Li, C. S. Li, H. F. Lin, and L. H. Cheng, “Technique of drawing relieved methane and simultaneous extraction of coal and coakbed methane,” *Journal of Xi’an University of Science and Technology*, vol. 263, pp. 247–249, 2002.
- [24] Y. Xue, J. Liu, P. G. Ranjith, X. Liang, and S. Wang, “Investigation of the influence of gas fracturing on fracturing characteristics of coal mass and gas extraction efficiency based on a multi-physical field model,” *Journal of Petroleum Science and Engineering*, vol. 206, article 109018, 2021.
- [25] Y. P. Cheng, J. H. Fu, and Q. X. Fu, “Development of gas extraction technology in coal mines of China,” *Journal of Mining and Safety Engineering*, vol. 23, pp. 127–139, 2009.
- [26] T. Q. Xia, F. Zhou, X. Wang et al., “Controlling factors of symbiotic disaster between coal gas and spontaneous combustion in longwall mining gobs,” *Fuel*, vol. 182, pp. 886–896, 2016.
- [27] T. X. Chu, M. Yu, and D. Jiang, “Experimental investigation on the permeability evolution of compacted broken coal,” *Transport in Porous Media*, vol. 116, no. 2, pp. 847–868, 2017.

Research Article

Laws of Gas Diffusion in Coal Particles: A Study Based on Experiment and Numerical Simulation

Yongjiang Hao , Xiaofeng Ji , and Jiewen Pang 

School of Safety and Emergency Management Engineering, Taiyuan University of Science and Technology, Taiyuan 030024, China

Correspondence should be addressed to Yongjiang Hao; haoyongjiang@163.com

Received 26 June 2021; Accepted 28 July 2021; Published 19 August 2021

Academic Editor: Feng Du

Copyright © 2021 Yongjiang Hao et al. This is an open access article distributed under the Creative Commons Attribution License, which permits unrestricted use, distribution, and reproduction in any medium, provided the original work is properly cited.

In order to research on the law of methane released through the pore in coal particles, the methane desorption experiments were conducted, respectively, on four types of particle size of coal samples under three different initial adsorption pressures. The cumulative methane desorption quantity (CMDQ) with time increasing was obtained to show that the reciprocal of CMDQ was in linear relation with the reciprocal of the square root of time, and the correlation coefficients were all above 0.99, on basis of which an empirical formula of CMDQ was established. Then, according to Fick diffusion law and Darcy percolation law, the mathematical models of methane emission from the spherical coal particles were created, respectively, and the corresponding calculating software was programmed by the finite difference method to obtain the simulated CMDQ of each sample under different conditions. The methane emission rate functions (MERF) of the simulation and the experiment were also calculated, respectively. Comparative analysis between the numerically simulated outcomes and the assay results reveals that the simulation outcomes as per Darcy's law match the experimental data better, while the simulated results by Fick's law deviate greatly, which indicates that the methane flowing through coal particles is more in accordance with Darcy's law.

1. Introduction

In China, there are large reserves of coalbed methane (CBM) [1–3]. CBM can be taken as a kind of resource for comprehensive use [4, 5], but it is also a hazardous factor underground, which directly threatens the normal production on the frontline and could easily cause gas explosion [6–8]. Thereby, it should be controlled [9–11], while the exploitation of CBM has always been a research hot spot. However, as a research of basic theory, the pore structure of coal, the methane desorption process, and the mechanism of methane flow in coal seam should be studied first [12].

Coal carries a double-porosity structure [13] full of pores and cracks [14], which have a great influence [15] on the adsorption and desorption of coal body. There are many classification standards about the pores and cracks [13, 16, 17], but the most widely used criterion in the coal industry of China is the standard of Xodot et al. [18], in which the pores are divided into five types by the pore diameter, and micropores and transition pores are the pores with diameters of 10 nm and 10~100 nm, respectively. Research [19] shows that

micropores and transitional pores account for more than 80% of the total pore volume in coal particles, which are the main space for methane adsorption and desorption.

Methane attached to the internal surface of coal pores is the solid state, which constantly exchanges with the gaseous methane molecules in pores. When the adsorption rate is equal to the desorption rate, the exchange reaches a dynamic balance [20]. Once the dynamic equilibrium is destroyed, the gas in pores will begin to flow, which should cause the reduction of interaction force between the internal surface molecules of pores and gas molecules, so the methane molecules in solid state will struggle from the adsorption force of the internal surface, turning into free gaseous molecules in the pore space [21], which forms the process of methane desorption from the coal internal surface. However, the law of the free gas migration and flow in coal body has yet to reach a consensus.

In the early period, most of the scholars agreed that gaseous methane flow in coal seam roughly accords with the Darcy law. Barrer [22] took the linear seepage to describe the gas flowing in coal seam. Later, Zhou and Sun [23]

believed that the gas flow conformed to the Darcy law in coal seam and put forward the linear gas seepage theory by the seepage mechanics. Based on the theory, an equation of gas seepage was established and preliminarily testified to be correct by the actual test results [24–26]. However, many scholars [27, 28] considered that the law of gas flow is diverse in pores with different diameters, i.e., the gas flow obeys molecular diffusion in the small pores but laminar flow in the larger pores and cracks. On this basis, Zhou and Lin [29] established a coalbed structure of the diffusion-seepage model of gas, shown in Figure 1. The coalbed is similar to the brick wall, in which the gas diffuses in the bricks (i.e., the smaller pores). Once into the brickwork joints (i.e., the large pores or cracks), the gas flows outward in filtration. The shape of the brick can be rectangular or round here. Therefore, coalbed can be considered as an object full of globular coal particles, in which micropores and transition pores take up the vast majority of space, and the crack system is between the coal particles. So the laws of methane desorption through coal particles are the fundamental theories for researching the methane flow in coalbed.

Methane emission from the coal particles includes two processes: (1) the desorption of methane molecules from the pore internal surface; (2) the desorbed gas molecules move from the pores to the exterior surface of coal particles. From the molecular motion standpoint, the adsorption or desorption of methane molecules in the pore internal surface is instantaneous, but in fact, the methane escaping from the coal particle needs a certain amount of time, which means the gas flows in the pores should follow certain rules. Yang [30, 31] believed that the methane escaping from the coal particles coincided with the Fick diffusion law, i.e., the gas flow rate is proportionate to the gas content gradient, and then, the equation of gas diffusion in coal particles was established. In his paper [30], the theoretical calculating results of the equation accorded with the gas emission measurements. Smith and Williams [32, 33] had also presented similar diffusion models. In coal particles, the majority of pores are micropores or transition pores, so most researchers believe that the gas flowing in micropores and transition pores obeys the Fick diffusion law, but in the larger pores, such as mesoporous, macropores, and cracks, it conforms to Darcy’s law [34, 35]. Based on this precondition, some important researches were done. He and Nie [36] and Nie et al. [37] analyzed the gas diffusion modes in coal pores, which included Fick diffusion, Knudsen diffusion, transitional diffusion, surface diffusion, and crystal diffusion, and the transitional diffusion was the main pattern of gas flowing in coal seam. Ruckenstein et al. [38] and Smith and Williams [39] set up a double-pore structure of the spherical diffusion model to explain the gas spreading to the surface of coal particles. However, a lot of experimental results [40, 41] have larger deviation with the theoretical calculation values by the Fick diffusion model.

In the present research, the experiment of methane desorption from coal particle will be carried out, and the mathematical model of methane escaping from spherical coal particles will be established, respectively, based on Fick’s law and Darcy’s law for the further simulation research. Then,

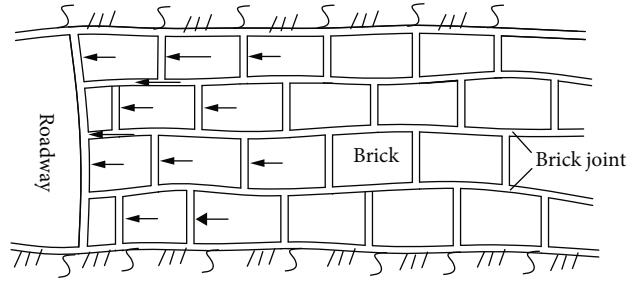


FIGURE 1: Coalbed structure of the diffusion-seepage model of methane.

TABLE 1: Particle dimension (Φ) of coal samples.

Coal sample number	Range of mesh	Particle diameter (μm)
1	4–5	4000–4750
2	15–16	1000–1180
3	30–35	425–550
4	50–60	250–270

the simulated results will be compared with the experimental results, so as to obtain a more reasonable methane flow pattern in coal particles.

2. Methane Desorption Experiment from Coal Particle

2.1. Coal Sample Preparation. The coal samples in our assay came from Yang Caogou Coal Mine, China. In the lab, they were dried in the nitrogen environment at 105°C. When cooled to room temperature, the samples were crushed to screen out four types of granularities, namely, 4-5 mesh, 15-16 mesh, 30-35 mesh, and 50-60 mesh, so the samples are made up of coal particles, which are considered to be spherical particles. The specific parameters are shown in Table 1.

2.2. Experimental Apparatus and Process. The physical methane desorption includes four types: (1) the reducing pressure desorption; (2) the increasing temperature desorption; (3) the substitution desorption; (4) the diffusion desorption. At the present stage, the depressurization is the main method for the desorption experiment [42], so a reducing pressure desorption system has been used in our experiment, which consisted of the ventilating device, heat regulation system, isothermal adsorption system, and data collection system, as shown in Figure 2. V1~V7 are needle valves, which can be opened or closed by different combinations of valves to complete the relevant operation of the experiment, and P is the pressure sensor used to test the pressure value in the reference tank and sample tank.

Before the experiment, the air tightness of the system was tested. Later, the volume of reference tank and the free space volume of coal sample tank were determined by the vacuum filling helium. At room temperature, the coal sample tank

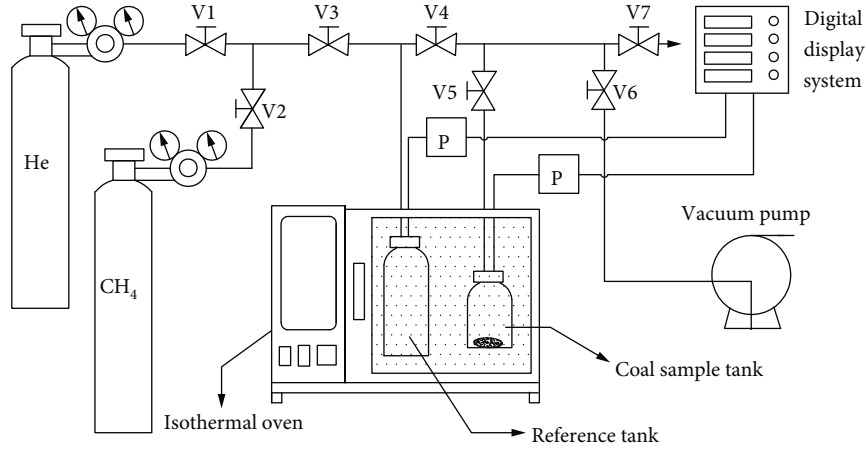


FIGURE 2: Experiment system schematic view.

underwent vacuum-pumping, and then, a certain pressure of methane, respectively, at 1 MPa, 2 MPa, and 4 MPa, was taken into for the coal sample to adsorb sufficiently. When the adsorption reached equilibrium, the desorption experiment began. The pressure in the sample tank is slowly released through the reference tank until it is equal to atmospheric pressure. After that, the coal sample desorption started. If the pressure value of the sample tank rose by 0.01 MPa, the operations would be performed to make the pressure of sample tank recover to atmospheric pressure. The same procedure was repeated N times until the end of desorption. In the experiment, the differential pressure value between pre- and postmoments was collected to compute the methane reduction in the free space of coal sample tank, so the methane desorption quantity per unit time can be obtained as

$$Q_j = \frac{p_j V_f - p_{j-1} V_f}{ZGRT_0 M}, \quad (1)$$

where Q_j denotes the methane desorption volume of coal samples at time j , ml/g; p_j , p_{j-1} is the methane pressure of the sample tank at time j , $j-1$, MPa; V_f denotes the free space volume of sample tank, ml; Z refers to the compressibility factor of CH_4 at pressure p_j ; G reflects the quality of coal samples, g; T_0 denotes the experimental temperature, K; M reflects the molar mass of CH_4 , g/mol.

Therefore, the cumulative methane desorption quantity (CMDQ) can be represented as

$$Q_t = \sum_{j=1}^t Q_j, \quad (2)$$

in which, Q_t denotes the CMDQ in time t , ml/g.

2.3. Experimental Data Processing and Analysis. Through the experiment, the results of CMDQ of each coal sample at different initial adsorbing pressures were obtained. By analyz-

ing, it can be found that the relationship between CMDQ and desorption time accorded with

$$\frac{1}{Q_t} = c_0 \frac{1}{\sqrt{t}} + d_0, \quad (3)$$

where c_0 and d_0 are the equation coefficient; t is the desorption time, h.

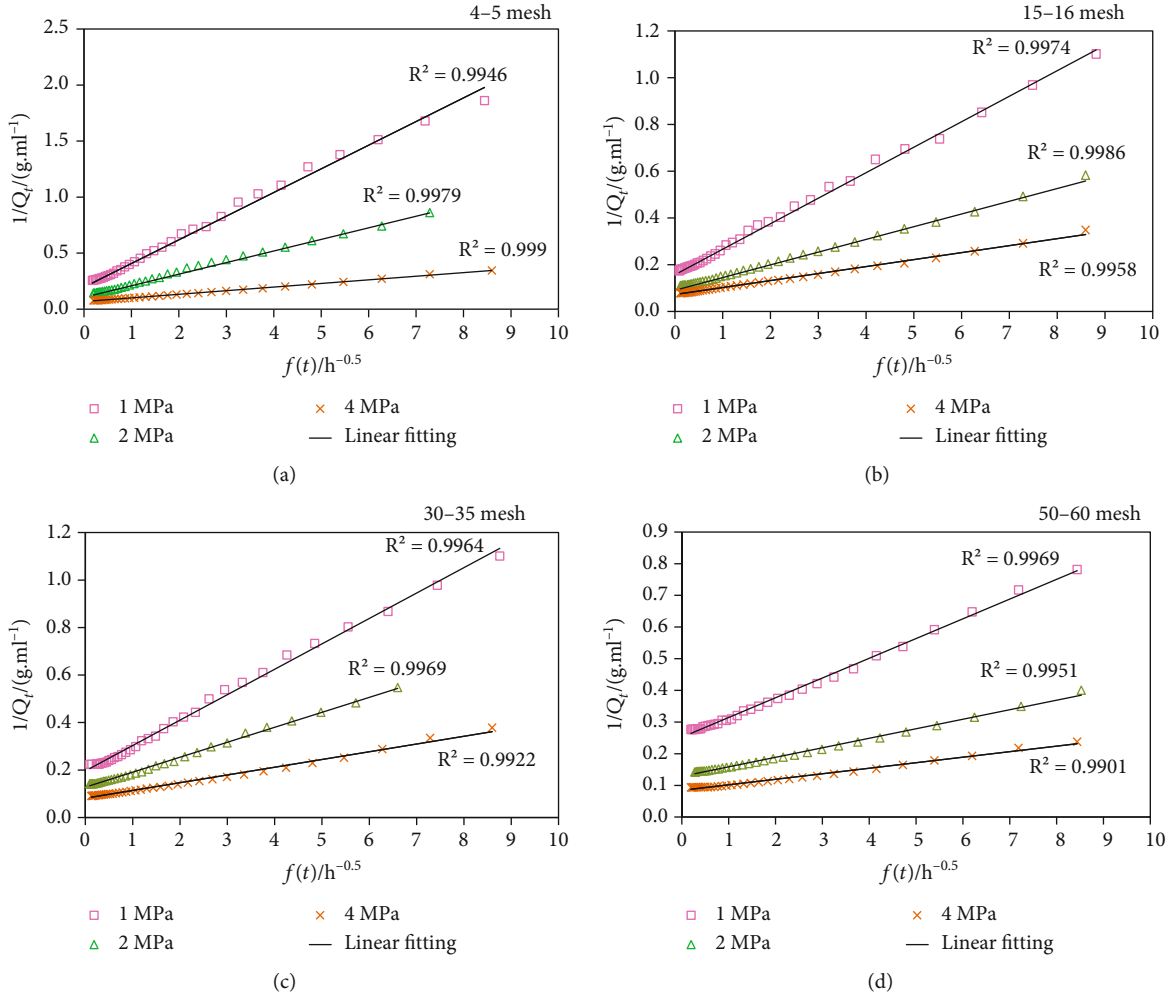
Here, we define $f(t)$ as time function, $f(t) = 1/\sqrt{t}$, and then to draw out the relationship curves of each case between $1/Q_t$ and $f(t)$ in Figure 3.

From Figure 3, all of the curves between $1/Q_t$ and $f(t)$ are better in linear relationship, and the correlation coefficients R^2 are all above 0.99. Therefore, based on formula (3), the theoretical calculation model of CMDQ can be expressed as formula (4), which is similar in the form as the Langmuir equation.

$$Q_t = \frac{A_0 B_0 \sqrt{t}}{1 + B_0 \sqrt{t}}, \quad (4)$$

where A_0 is the ultimate desorption quantity, $A_0 = 1/d_0$, ml/g; B_0 is a constant to reflect the desorption rate, $B_0 = d_0/c_0$, $1/s^{0.5}$. Their values in our experiment are shown in Table 2.

Formula (4) can be used to calculate the CMDQ accurately. The value of A_0 will not increase unlimitedly, which tends to a constant value when the time increases to infinity, so the A_0 indicates the maximum methane desorption quantity of coal particles. In Table 2, the greater the initial pressure is, the greater the value of A_0 becomes, which means that the peak methane desorption volume increases with the initial adsorption pressure rising. However, it seems that the value of A_0 registers no evident change associated with the coal grain dimension. Some scholars [43, 44] believed the reason was that the smaller particle size only increased the outside surface area of coal particle but had no effect on the pore interior surface area which was the main area for methane adsorption. The B_0 is a physical quantity to reflect the

FIGURE 3: Curves of $1/Q$ and $f(t)$ under different initial pressures.TABLE 2: Parameter values of A_0 and B_0 .

Initial pressure (MPa)	4-5 mesh		15-16 mesh		30-35 mesh		50-60 mesh	
	A_0	B_0	A_0	B_0	A_0	B_0	A_0	B_0
1	5.49	0.77	7.94	0.83	5.59	1.39	4.10	3.43
2	9.71	0.99	12.50	1.48	9.17	1.56	7.81	4.41
4	19.23	1.63	15.38	2.24	13.69	2.81	12.05	4.61

desorption rate. The experimental results show that the smaller the particle size or the larger the pressure is, the shorter the time of methane desorption to the end will take, so the value of B_0 is larger.

3. Fick Diffusion Model

3.1. The Establishment of the Mathematical Model. Sevenster [45] established the classical methane diffusion mathematical model in coal particle, and the assumptions are as follows: (1) the coal particle is spherical, and there is a large amount of micropore in the coal sphere; (2) the coal particle is homoge-

neous and isotropic body; (3) the methane flowing in microporous and transition pores accords with Fick's law.

In Fick's law, the methane diffusion velocity is proportionate to the methane content gradient, but the direction is opposite.

$$J = -D \frac{\partial X}{\partial n}, \quad (5)$$

in which J denotes the diffusion speed, $m^3/(m^2 \cdot h)$; D reflects the methane diffusion coefficient, m^2/h ; X reflects the

methane content in per unit volume coal, m^3/m^3 ; \vec{n} refers to the diffusion distance in normal direction, m.

The methane diffusion in coal particles is a process of unstable state. In the globular coal particle, the globular shell in the thickness dr is studied. As per the mass conservation law, the methane variable quantity between inflow and outflow of the shell is equivalent to the methane change quantity in the globular shell, so the methane emission equation of coal particle was set up under the spherical coordinates, as follows:

$$\frac{\partial X}{\partial t} \left[\frac{4}{3} \pi (r + dr)^3 - \frac{4}{3} \pi r^3 \right] + \frac{\partial}{\partial r} \left(-D \frac{\partial X}{\partial \vec{n}} \cdot 4\pi r^2 \right) dr = 0. \quad (6)$$

Here, $(dr)^2 \approx 0$, $(dr)^3 \approx 0$, the D is constant, and then, formula (6) can be deduced as

$$\frac{\partial X}{\partial t} = \frac{D}{r^2} \frac{\partial}{\partial r} \left(r^2 \frac{\partial X}{\partial r} \right), \quad (7)$$

where r denotes the radius, m.

When desorption begins, the exterior pressure of coal particle is still constant, so the initial conditions and boundary conditions are as follows:

$$\begin{cases} X = X_0, 0 \leq r \leq R, t = 0, \\ \frac{\partial X}{\partial r} = 0, r = 0, t > 0, \\ X = X_W, r = R, t > 0, \end{cases} \quad (8)$$

in which X_0 reflects the initial methane content of coal particle, m^3/m^3 ; X_W refers to the methane content at surface of coal particles, m^3/m^3 ; R reflects the radius of coal particles, m.

3.2. Finite Difference Model. Firstly, the globular coal grain from center to exterior surface is separated into N parts alongside the radius and the intersections are the nodes, documented as $0, 1, 2, 3 \dots N$, which are expressed as the solid lines in Figure 4. Considering that the variations of pressure, methane content, and diffusion velocity in the center are less than those near the spherical surface, the node spacing from the center to surface declines in a geometric sequence. Secondly, the N homocentric spheres taking the node 0 as circle center are drew in the coal particle, which are through the middle of the two neighboring nodes separately, presented as the dotted lines in Figure 4. So the coal particle is separated into one center solid sphere and N globular shells by the dotted lines.

Apart from the central solid sphere and the globular shell of the N th node, the rest spherical shells all have interior and exterior spherical surfaces, which are through the middle point of the node spacing. So the difference equations of

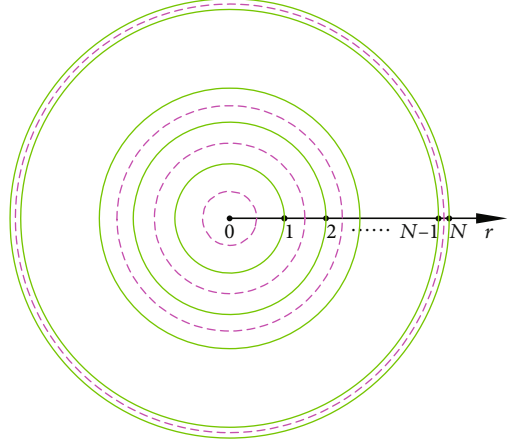


FIGURE 4: Node division under the spherical coordinate system.

unstable flow of methane from 1 to $N - 1$ nodes could be considered as follows:

$$\begin{aligned} & \frac{4}{3} \pi \left[\left(\frac{r_{i+1} + r_i}{2} \right)^3 - \left(\frac{r_{i-1} + r_i}{2} \right)^3 \right] \times \frac{X_i^{j-1} - X_i^j}{\Delta t_j} \\ &= D \frac{\left(\left(\frac{X_i^j - X_{i+1}^j}{2} \right) + \left(\frac{X_i^{j-1} - X_{i+1}^{j-1}}{2} \right) \right)}{r_{i+1} - r_i} \times 4\pi \left(\frac{r_i + r_{i+1}}{2} \right)^2 \\ & \quad - D \frac{\left(\left(\frac{X_{i-1}^j - X_i^j}{2} \right) + \left(\frac{X_{i-1}^{j-1} - X_i^{j-1}}{2} \right) \right)}{r_i - r_{i-1}} \\ & \quad \times 4\pi \left(\frac{r_i + r_{i-1}}{2} \right)^2 \quad (i = 1, 2, \dots, N - 1; j = 1, 2, \dots), \end{aligned} \quad (9)$$

in which the subscript $i - 1$, i , and $i + 1$ denote the node quantity; the superscript $j - 1$ and j denote the time node quantity; Δt_j refers to the time step j .

For the center solid sphere, namely, the 0 node, the difference equation is established as follows:

$$\begin{aligned} & D \frac{\left(\left(\frac{X_0^j - X_1^j}{2} \right) + \left(\frac{X_0^{j-1} - X_1^{j-1}}{2} \right) \right)}{r_1} \times 4\pi \left(\frac{r_1}{2} \right)^2 \\ &= \frac{4}{3} \pi \left(\frac{r_1}{2} \right)^3 \times \frac{X_0^{j-1} - X_0^j}{\Delta t_j}. \end{aligned} \quad (10)$$

For the N node, which refers to the exterior surface of coal particles, namely, $r = R$, as per the boundary conditions:

$$X_N^j = X_W. \quad (11)$$

Formula (9) to (11) forms a complete equation set of the methane flow in coal particles as per Fick's law, in which the methane contents from 0 to N node are the unknown quantities at the j th moment.

After the methane contents of coal particles at each moment are calculated, the methane desorption quantity of spherical coal particle in the j th time step is as

$$\Delta Q_j = 2\pi R^2 \Delta t_j D \frac{(X_{N-1}^j + X_{N-1}^{j-1}) - (X_N^j + X_N^{j-1})}{r_N - r_{N-1}}. \quad (12)$$

The CMDQ of coal particles is the sum of the methane desorption quantity in each time step.

4. Darcy Percolation Model

4.1. Establishment of the Mathematical Model. Zhou and Sun [23] proposed the methane emission pattern from coal particles as per Darcy's law, in which the methane pressure, the gas permeability coefficient, and the adsorption constants are the basic influence factors. The assumptions are as follows: (1) the coal particle is spherical, and there is a large amount of micropore and transition pore in the sphere; (2) the porosity and gas permeability coefficient in coal particles are not affected by the internal methane pressure change; (3) the methane absorption satisfies the Langmuir equation, and the free methane is ideal gas. The methane content could be described as follows:

$$X' = \frac{abp}{1 + bp} + Bmp, \quad (13)$$

where X' denotes the methane content of coal in unit mass, m^3/t ; a reflects the first adsorption constant, m^3/t ; b marks the second adsorption constant, $1/MPa$; p reflects the internal methane pressure of coal body, MPa ; B denotes the coefficient, $m^3/(t \cdot MPa)$; m refers to the porosity.

(4) As the methane flows in coal particles, the temperature is unchanged; (5) the methane flowing in the coal particles is the laminar flow motion, obeying Darcy's law:

$$u = -\frac{k}{\mu} \nabla p. \quad (14)$$

in which u reflects the velocity of methane flow, m/s ; k denotes the permeability of coal seam, m^2 ; μ reflects the gas viscosity coefficient, $MPa \cdot s$; ∇p reflects the methane pressure gradient, MPa/m .

The flowed methane quantity can be determined by the volume flow under one normal atmosphere, so formula (15) can be transformed as

$$q = -\lambda \frac{\partial P}{\partial \vec{n}}, \quad (15)$$

in which q denotes the methane flow per unit area, $m^3/(m^2 \cdot s)$; λ is the gas permeability coefficient, $m^2/(MPa^2 \cdot s)$, $\lambda = k/2\mu$; p_n, P_n reflects the standard atmospheric pressure; P is the square of methane pressure, $P = p^2$, MPa^2 ; \vec{n} denotes the penetration distance on the normal direction, m .

The spherical shell in thickness dr is analyzed in the same way, and the methane emission equation is established as follows:

$$\frac{\partial X'}{\partial t} \rho \left[\frac{4}{3} \pi (r + dr)^3 - \frac{4}{3} \pi r^3 \right] + \frac{\partial}{\partial r} \left(-\lambda \frac{\partial P}{\partial r} \cdot 4\pi r^2 \right) dr = 0, \quad (16)$$

where ρ denotes the apparent density of coal, t/m^3 .
Simplification to get

$$\frac{\partial X'}{\partial t} = \frac{\lambda}{\rho} \left(\frac{\partial^2 P}{\partial r^2} + \frac{2}{r} \frac{\partial P}{\partial r} \right). \quad (17)$$

Taking formula (13) into (17) to get

$$\frac{\partial \left(\left((ab\rho\sqrt{P})/(1+b\sqrt{P}) \right) + Bm\rho\sqrt{P} \right)}{\partial t} = \lambda \frac{1}{r^2} \frac{\partial}{\partial r} \left(r^2 \frac{\partial P}{\partial r} \right). \quad (18)$$

The initial conditions and boundary conditions are as follows:

$$\begin{cases} P = P_0 = p_0^2, 0 \leq r \leq R, t = 0, \\ \frac{\partial P}{\partial r} = 0, r = 0, t > 0, \\ P = P_w = p_w^2, r = R, t > 0, \end{cases} \quad (19)$$

in which p_0 denotes the initial methane pressure of coal particles, MPa ; p_w reflects the methane pressure at the outside surface of coal particles, MPa .

4.2. Finite Difference Model. In the element division, the Darcy model is the same as the Fick model, shown in Figure 4. So the difference equations from 1 to $N-1$ nodes are established as

$$\begin{aligned} & \lambda \frac{\left(\left((P_i^j - P_{i+1}^j)/2 \right) + \left((P_{i-1}^{j-1} - P_{i+1}^{j-1})/2 \right) \right)}{r_{i+1} - r_i} \times 4\pi \left(\frac{r_{i+1} + r_i}{2} \right)^2 \\ & - \lambda \frac{\left(\left((P_{i-1}^j - P_i^j)/2 \right) + \left((P_{i-1}^{j-1} - P_i^{j-1})/2 \right) \right)}{r_i - r_{i-1}} \\ & \times 4\pi \left(\frac{r_{i-1} + r_i}{2} \right)^2 = \frac{4}{3} \pi \left[\left(\frac{r_{i+1} + r_i}{2} \right)^3 - \left(\frac{r_{i-1} + r_i}{2} \right)^3 \right] \\ & \times \left[\frac{abp}{2 \left(1 + b \sqrt{(P_i^j + P_{i+1}^{j-1})/2} \right)^2 \sqrt{(P_i^j + P_{i+1}^{j-1})/2}} + \frac{Bmp}{2 \sqrt{(P_i^j + P_{i+1}^{j-1})/2}} \right] \\ & \cdot \frac{P_i^{j-1} - P_i^j}{\Delta t_j} \quad (i = 1, 2, \dots, N-1; j = 1, 2, \dots). \end{aligned} \quad (20)$$

As to the spherical center point, the difference equation is expressed as follows:

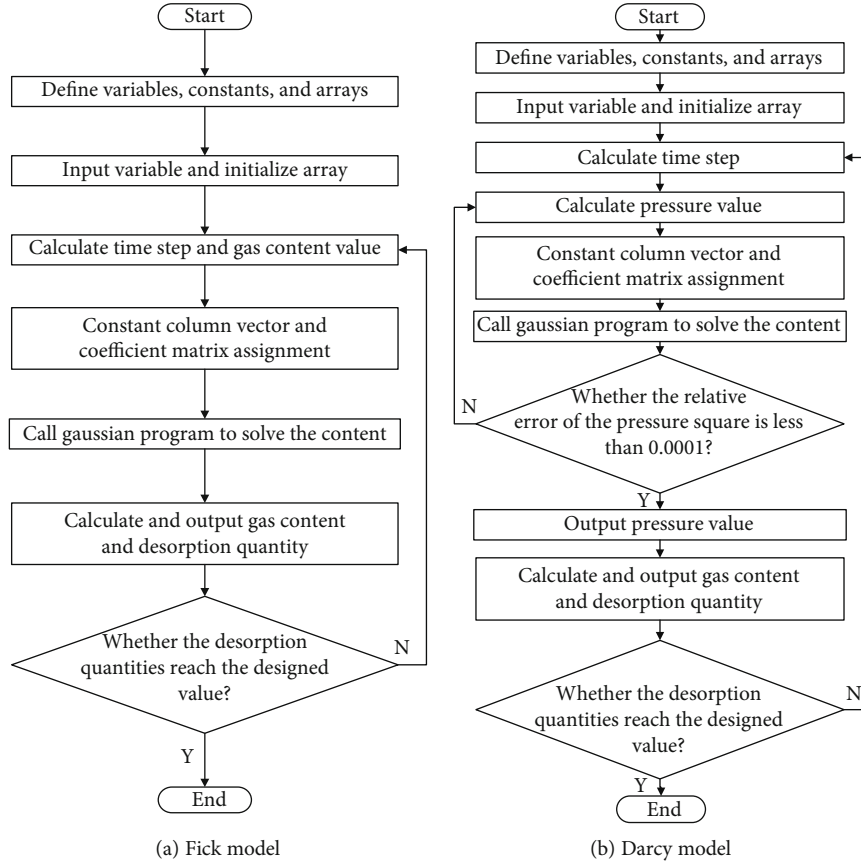


FIGURE 5: Flowchart of program structure.

$$\begin{aligned}
& \lambda \frac{\left((P_0^j - P_1^j)/2 \right) + \left((P_0^{j-1} - P_1^{j-1})/2 \right)}{r_1} \times 4\pi \left(\frac{r_1}{2} \right)^2 \\
& = \frac{4}{3} \pi \left(\frac{r_1}{2} \right)^3 \times \left[\frac{ab\rho}{2 \left(1 + b \sqrt{(P_0^j + P_0^{j-1})/2} \right)^2 \sqrt{(P_0^j + P_0^{j-1})/2}} \right. \\
& \quad \left. + \frac{Bm\rho}{2 \sqrt{(P_0^j + P_0^{j-1})/2}} \right] \frac{P_0^{j-1} - P_0^j}{\Delta t_j}. \tag{21}
\end{aligned}$$

As to the exterior surface, namely, $r = R$, according to the boundary conditions:

$$P_N^j = P_w. \tag{22}$$

Formula (20) to (22) forms a complete equation set of the methane flow in coal particles as per Darcy's law, in which the methane pressures from 0 to N node are the unknown quantities at the j th moment.

After the methane pressure square at each moment is calculated, the methane desorption quantity of coal particles in the j th time step is as

$$\Delta Q_j = 2\pi R^2 \Delta t_j \lambda \frac{(P_{N-1}^j + P_{N-1}^{j-1}) - (P_N^j + P_N^{j-1})}{r_N - r_{N-1}}. \tag{23}$$

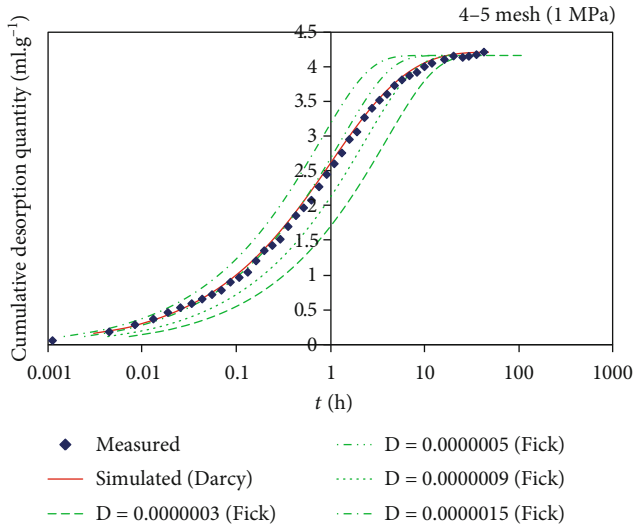
The CMDQ of coal particle is the sum of the methane desorption quantity in each time step.

5. Programming and Operation

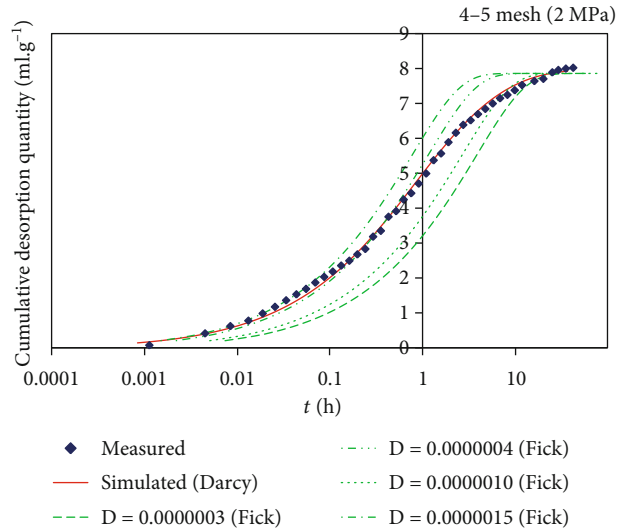
Based on the above difference model and boundary conditions, the corresponding calculating software is designed and compiled.

For the Fick diffusion difference model, the content is unknown. In the process of calculating, given a time step and the eventual methane content, the following methane content could be computed. By analogy, the methane content value at each time node can be obtained. Due to the methane desorption rate diminishing with time prolonging, the time step in calculation increases according to a geometric sequence which gradually enlarges. In this way, the calculated time is saved but the calculated precision is still high. The program structure process is shown in Figure 5(a).

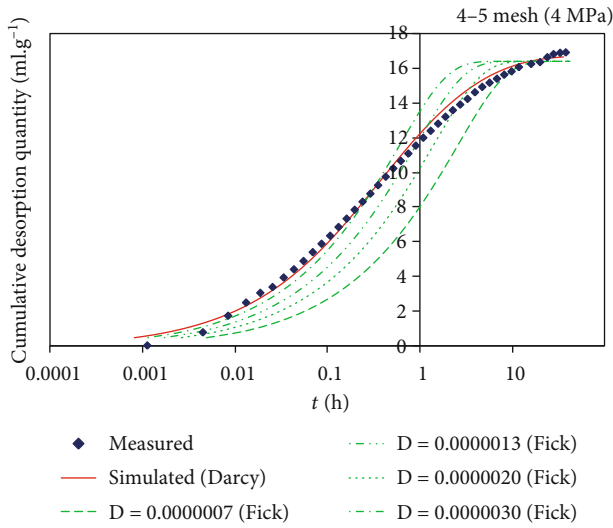
For the Darcy percolation differential model, the square of methane pressure is unknown. In calculating, given a time step and the eventual pressure, the following pressure could be obtained. The methane pressure in the coal particle



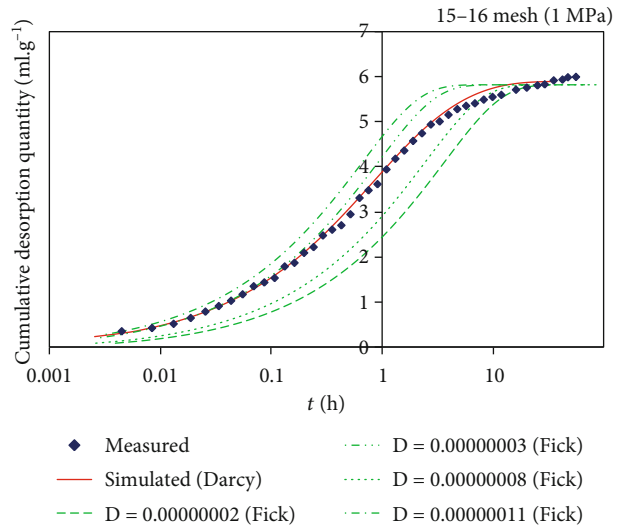
(a)



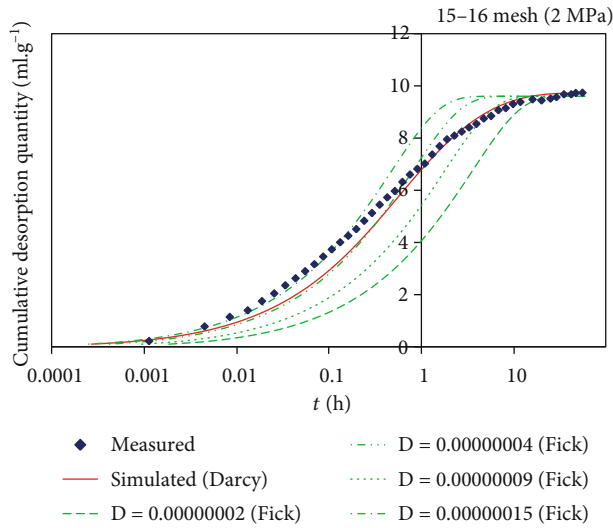
(b)



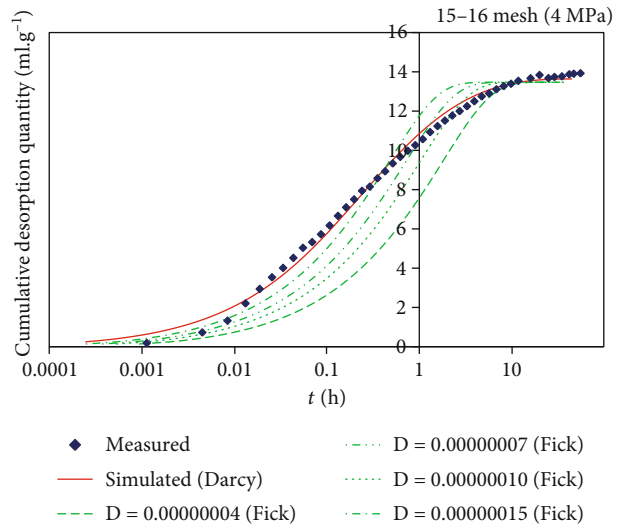
(c)



(d)

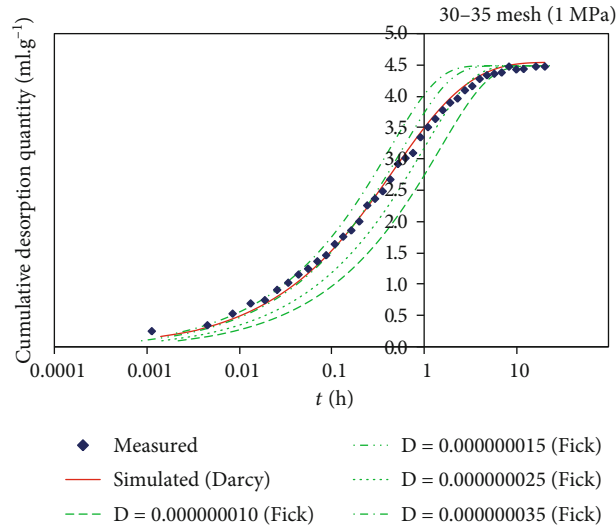


(e)

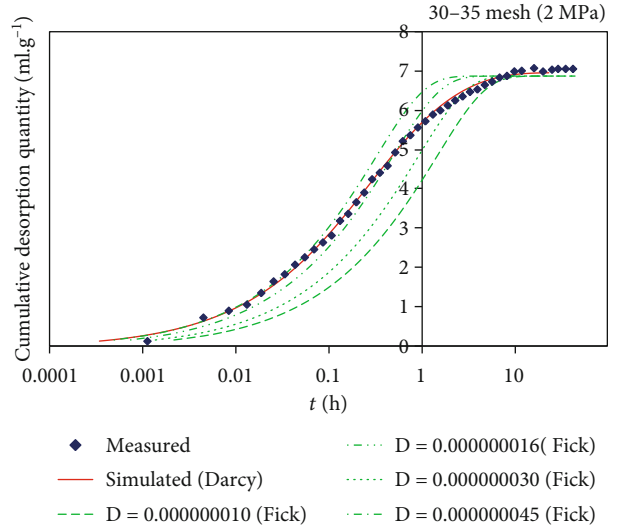


(f)

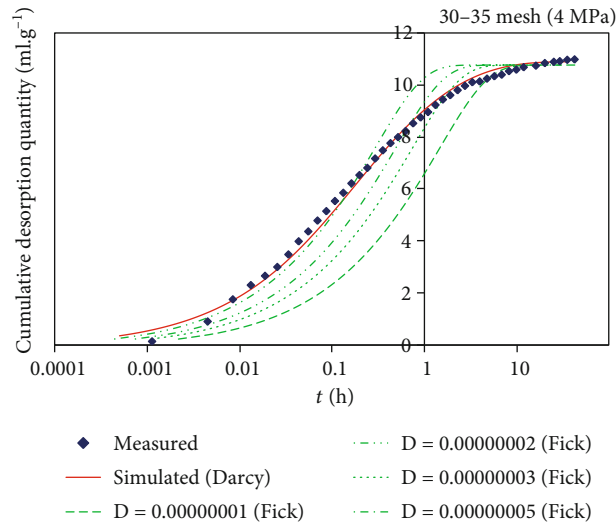
FIGURE 6: Continued.



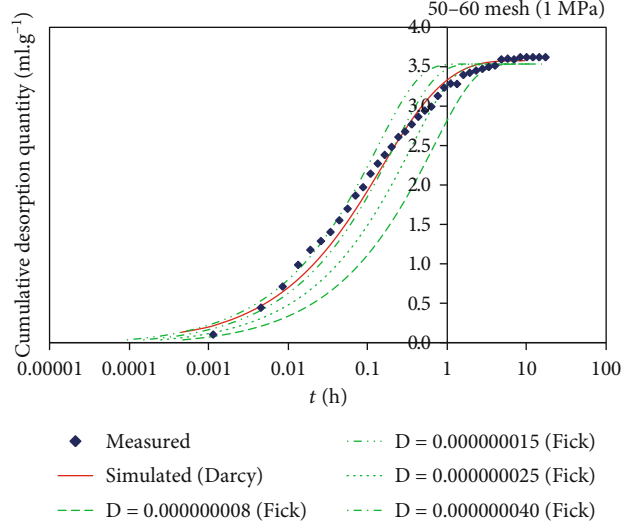
(g)



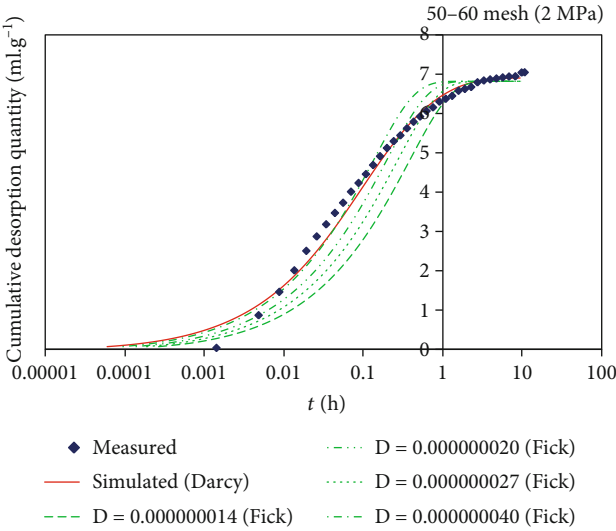
(h)



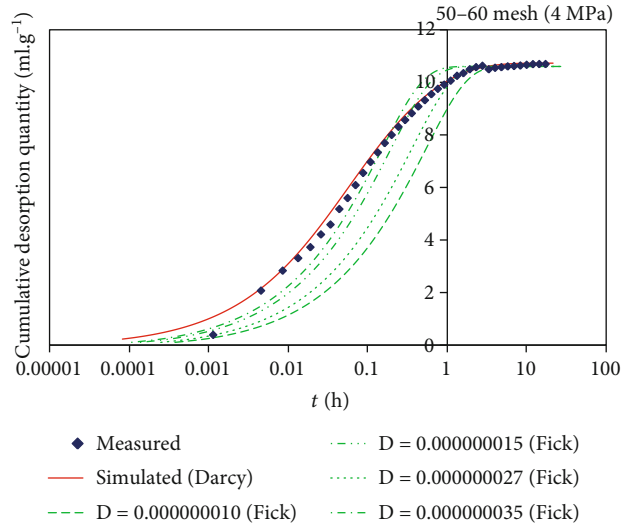
(i)



(j)



(k)



(l)

FIGURE 6: Contrast curves between simulated CMDQ and experimental CMDQ.

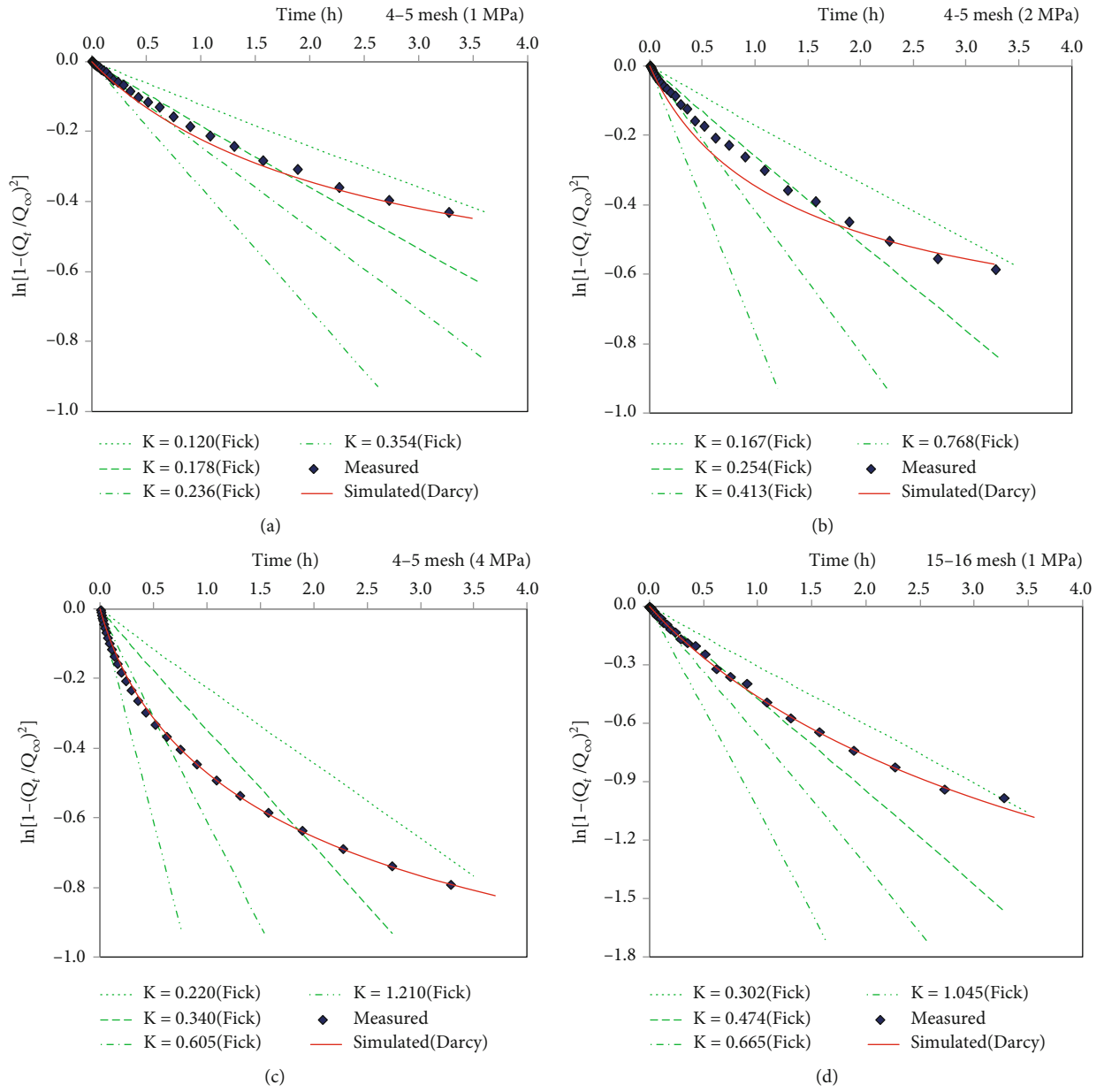


FIGURE 7: Continued.

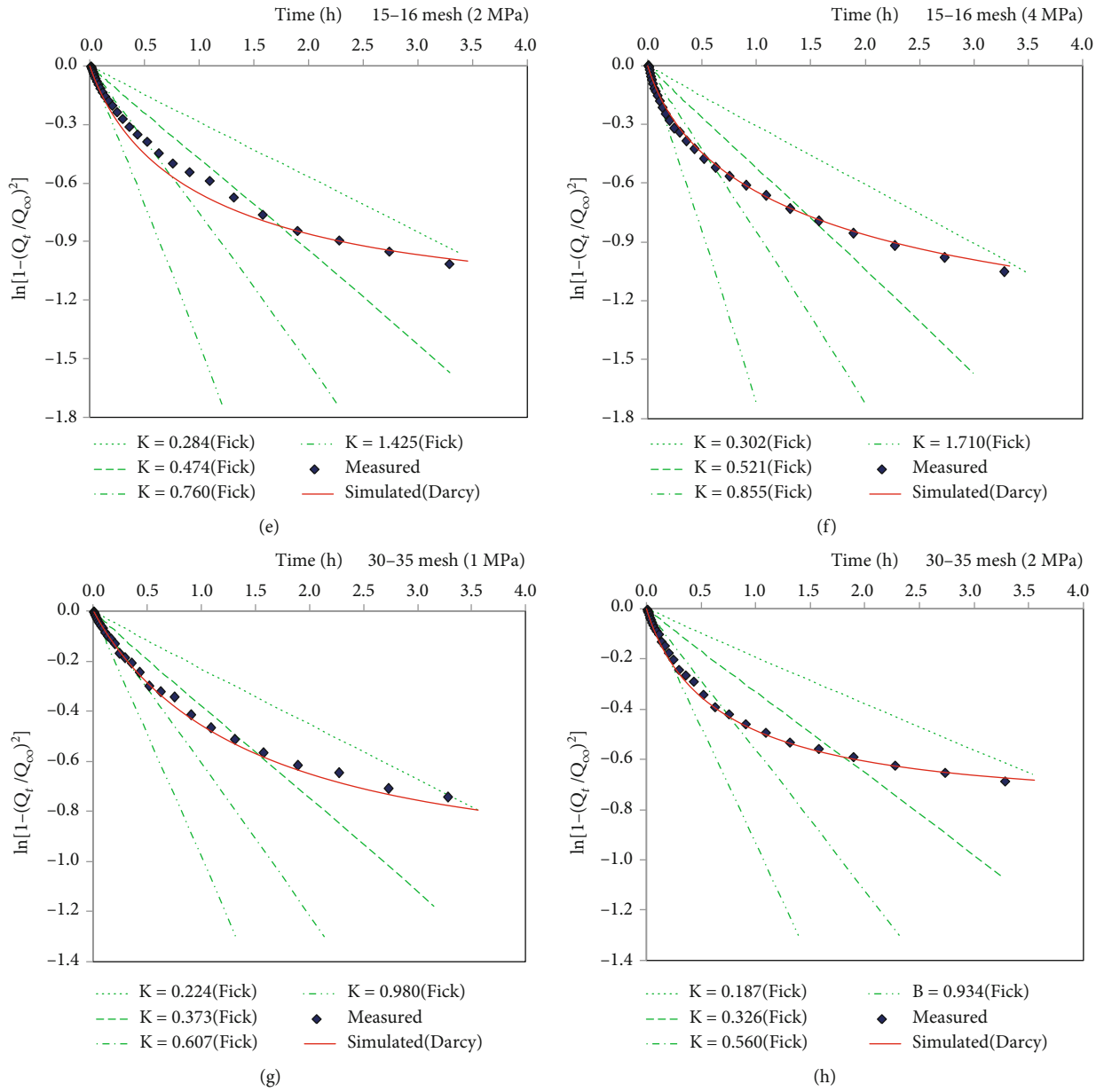


FIGURE 7: Continued.

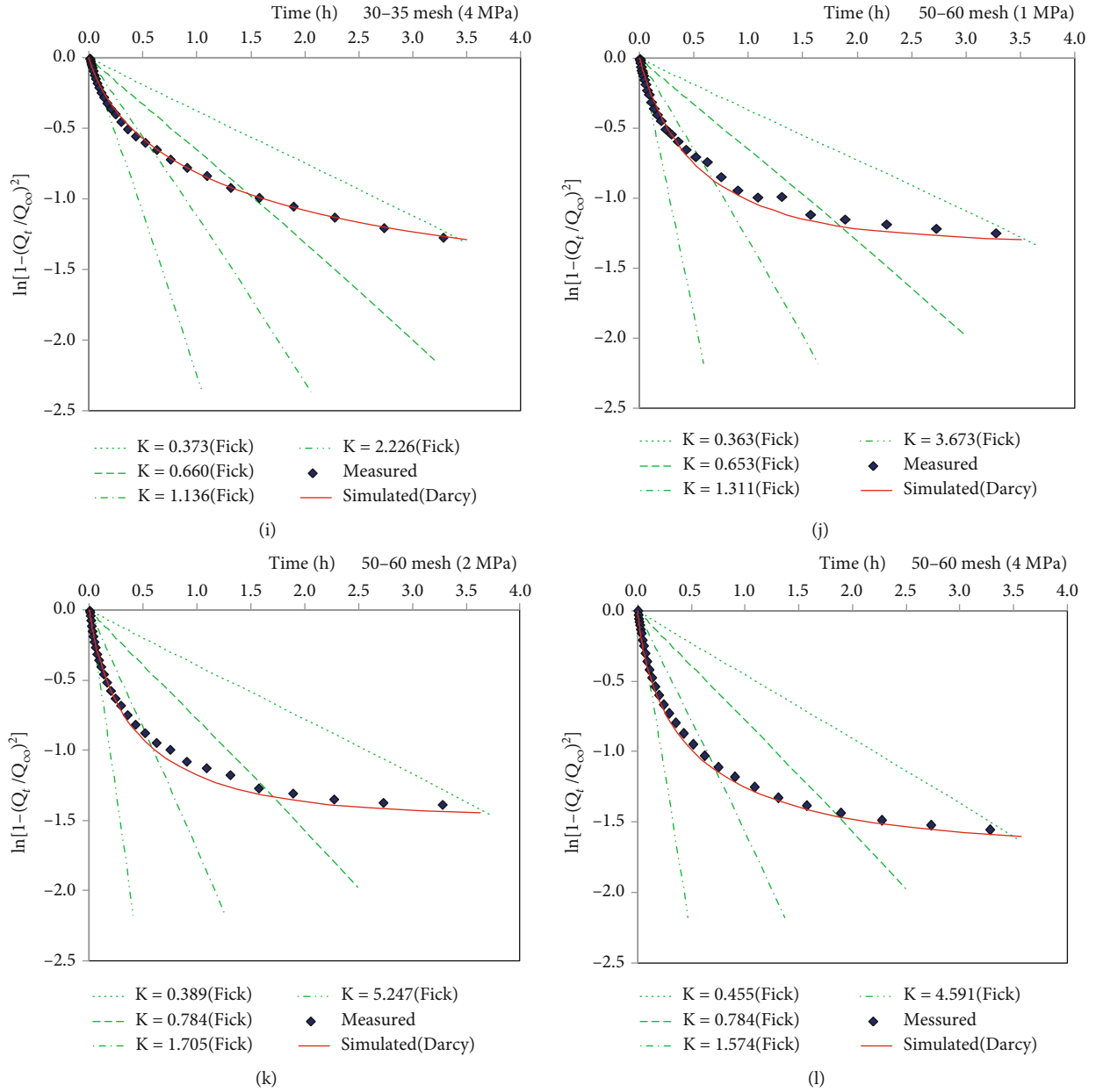


FIGURE 7: Contrast curves between simulation and experimental MERF.

can be calculated at any time, and the time step also uses a geometric progression step length. The right side of formulas (20) and (21) is the nonlinear expression of the node's pressure square at the j th moment, so the iteration method should be used. Assumed $P_i^j = cP_i^{j-1}$, the numerical value under the square root is calculated to get quasilinear equations and the solution, and then, the solution is employed to compute the value under the square root, so new quasilinear equations and the new solution should be obtained again. We repeat the calculation until the relative error of the pre- and postcomputational value is less than a small value. The program structure process is shown in Figure 5(b).

6. Comparative Analyses between the Simulated and Experimental Results

In the Darcy model, the methane adsorption parameters and the porosity of coal derived from the relevant experimental results where a is $26 \text{ m}^3/\text{t}$, b is 0.3 MPa^{-1} , m is 0.5 , and ρ is $1.2 \text{ m}^3/\text{t}$. Through the trial calculation, when the gas permeability coefficient is at $1 \times 10^{-5} \text{ m}^2/(\text{MPa}^2 \cdot \text{s})$, the simulated results of CMDQ fit better with the experimental results. For the Fick model, if the coal particle radius, the initial methane pressure, and content are given, the diffusion coefficient D will be the only influence factor for the methane desorption, and its scope of the trial calculation is taken

from 2×10^{-9} to $2 \times 10^{-5} \text{ m}^3/(\text{m}^2 \cdot \text{d})$. So when the exterior pressure of coal particles is at a normal atmosphere, the variation processes of CMDQ of different coal samples can be calculated, and the results will be compared with the experimental results.

6.1. Comparison of CMDQ. Figure 6 shows the curves of the experiment and simulation of each coal sample under different initial pressures. In order to observe the matching degree of curves more easily, the logarithmic coordinate is used in the figure.

It can be concluded from Figure 6 (1) that the variation trend of Darcy's simulated results is basically identical to the experimental results, but Fick's results have large difference; (2) Darcy's results are pretty consistent with the experimental results in most time, and the differences mainly appear in the initial period. This is because limited by the experimental conditions, the external pressure of coal particles cannot realize the constant pressure in the initial phase; (3) when the diffusion coefficient D becomes larger, Fick's results are more close to the experimental results in the initial stage, but the simulated results reach the desorption balance earlier than that of the experiment, so great deviations emerge later. It indicates that no matter how the D changes, Fick's curves do not always match well with the experimental curves.

6.2. Comparison of Methane Emission Rate Function. Yang and Wang [46] put forward the methane emission rate function (MERF), which was expressed as $\ln [1 - (Q_t/Q_\infty)^2]$. In their paper, the methane emission rates of six kinds of particle size of coal samples were studied by Fick's law to obtain that MERF registered linear change with time t .

$$\frac{\ln [1 - (Q_t/Q_\infty)^2]}{t} = -K, \quad (24)$$

where Q_∞ is the CMDQ when t tends to infinity, ml/g; $-K$ is the slope of MERF with t .

The change rules between MERF and t are studied, respectively, under Fick's diffusion, Darcy's seepage, and the experimental measure. The simulated and measured data are processed and shown in Figure 7. Here, the values of Q_∞ take the A_0 in Section 2.3.

From Figure 7, (1) the MERF of Darcy's simulation are all curving changes as the time increases, which have the similar variation trend to the experiment, but all of Fick's MERF are growth in straight lines over time; (2) Darcy's simulation results mostly accord with the experimental results; (3) Fick's simulated results are only close to the measured results at the initial stage and appear deviation later, in which the gap became larger and larger as time increases. No matter how the D changes, the curves of Fick's results register linear variation and cannot match well with the experimental curves.

7. Discussion

The CMDQ of Fick's simulation, Darcy's simulation, and experimental measure are compared to show that Darcy's

results highly agree with the experimental results. While no matter how we change the size of the methane diffusion coefficient D , the curves of CMDQ in Fick diffusion can never well accord with the experimental curve. This indicates that the methane emission process in coal particles is more accordant with Darcy's law. For the theory analysis, the vast majority of methane is adsorbed at the pore internal surface of coal particle, which is relatively static and almost without flow. So the movement of free methane gas becomes the main form for methane flowing in coal particles, and its flow velocity exhibits no direct association with methane content but is closely related to the gas pressure gradient. Therefore, the methane flow in coal particles should accord with Darcy's law.

The change law of MERF in coal particles is also analyzed in this paper and shows that the experimental MERF are all curving changes with the time growing. The literature [41] also obtained the same experimental conclusion. The MERF under Darcy's condition are also curving change and coincident with the experimental results. However, the MERF under Fick's condition linearly change as time increases and obviously do not follow the measured trends, which indicates that the methane emission from coal particles should not conform to Fick's law, and at least, the situation that the diffusion coefficient D is constant in methane emission can be excluded. From the mechanism of methane emission, in the early emission period, the emitted methane is primarily from the outside surface or the macropores of coal particles, flowing out rapidly, so the emission quantity is fast. But, later, emission source mainly comes from the internal surface of microporous and transition pores. As the diameter of these pores is smaller, the path becomes lengthier and the resistance is also greater, which decreases the emission quantity gradually. Therefore, in the process of the methane emission from coal particle, the MERF will not change linearly, so some scholars [12, 47] believed the methane diffusion coefficient in coal particles is attenuated over time, which still needs a further research.

8. Conclusions

- (1) The methane isothermal desorption experiment of coal particles was performed to obtain that the relationship between the reciprocal of cumulative methane desorption quantity (CMDQ) and the reciprocal of square root of time was linear, and the correlation coefficients R^2 are all above 0.99. The basis on the experiment, an empirical formula of CMDQ was given, which can be used to calculate the CMDQ accurately
- (2) The methane flow mathematic models of spherical coal particle were established, respectively, according to Fick diffusion law and Darcy percolation law. The corresponding calculating software was programmed with the finite difference method. By the software, the simulated CMDQ and the calculated methane emission rate function (MERF) of the two models were obtained under different initial adsorption pressures

- (3) Comparative analyses between the simulation results and the assay outcomes indicate that Darcy's simulated outcomes are consistent with the experimental results, whereas all Fick's results, no matter how the diffusion coefficient changes, have a comparatively large difference from the experimental data. Therefore, the studies in this paper show that the methane flow obeys Darcy's law even in the tiny pore system of coal particles, which provides the basis for further study on the law of methane flow in coalbed

Data Availability

The data used to support the findings of this study are available from the corresponding author upon request.

Conflicts of Interest

The authors declare that they have no conflicts of interest.

Acknowledgments

The research is financially supported by the Applied Basic Research Plan of Shanxi Province (No. 201901D211294) and Universities Science and Technology Innovation Project in Shanxi Province (No. 2020L0365).

References

- [1] C. J. Bibler, J. S. Marshall, and R. C. Pilcher, "Status of worldwide coal mine methane emissions and use," *International Journal of Coal Geology*, vol. 35, no. 1-4, pp. 283-310, 1998.
- [2] P. Liu, J. Fan, D. Jiang, and J. Li, "Evaluation of underground coal gas drainage performance: mine site measurements and parametric sensitivity analysis," *Process Safety and Environmental Protection*, vol. 148, pp. 711-723, 2021.
- [3] T. A. Moore, "Coalbed methane: a review," *International Journal of Coal Geology*, vol. 101, no. 1, pp. 36-81, 2012.
- [4] S. Su, A. Beath, H. Guo, and C. Mallett, "An assessment of mine methane mitigation and utilisation technologies," *Progress in Energy and Combustion Science*, vol. 31, no. 2, pp. 123-170, 2005.
- [5] P. Liu, A. Liu, F. Zhong, Y. Jiang, and J. Li, "Pore/fracture structure and gas permeability alterations induced by ultrasound treatment in coal and its application to enhanced coalbed methane recovery," *Journal of Petroleum Science and Engineering*, vol. 205, pp. 108862-108877, 2021.
- [6] X. P. Yuan, "The characters and trend of accidents in the coal mining in China," *Disaster Advances*, vol. 86, no. 2-3, pp. 867-870, 2012.
- [7] A. Liu, P. Liu, and S. M. Liu, "Gas diffusion coefficient estimation of coal: a dimensionless numerical method and its experimental validation," *International Journal of Heat and Mass Transfer*, vol. 162, pp. 120336-120351, 2020.
- [8] Q. Ye, Z. Z. Jia, and H. Z. Wang, "Characteristics and control technology of gas explosion in gob of coal mines," *Disaster Advances*, vol. 86, no. 2-3, pp. 112-118, 2013.
- [9] R. M. Flores, "Coalbed methane: from hazard to resource," *International Journal of Coal Geology*, vol. 35, no. 1-4, pp. 3-26, 1998.
- [10] C. Ö. Karacan, "Modeling and prediction of ventilation methane emissions of U.S. longwall mines using supervised artificial neural networks," *International Journal of Coal Geology*, vol. 73, no. 3-4, pp. 371-387, 2008.
- [11] C. Ö. Karacan, "Forecasting gob gas venthole production performances using intelligent computing methods for optimum methane control in longwall coal mines," *International Journal of Coal Geology*, vol. 79, no. 4, pp. 131-144, 2009.
- [12] A. D. Alexeev, E. P. Feldman, and T. A. Vasilenko, "Methane desorption from a coal-bed," *Fuel*, vol. 86, no. 16, pp. 2574-2580, 2007.
- [13] H. Gan, S. P. Nandi, and P. L. Walker, "Nature of the porosity in American coals," *Fuel*, vol. 51, no. 4, pp. 272-277, 1972.
- [14] S. Harpalani and G. L. Chen, "Estimation of changes in fracture porosity of coal with gas emission," *Fuel*, vol. 74, no. 10, pp. 1491-1498, 1995.
- [15] G. Amarasekera, M. J. Scarlett, and D. E. Mainwaring, "Micropore size distributions and specific interactions in coals," *Fuel*, vol. 74, no. 1, pp. 115-118, 1995.
- [16] P. C. Kearney, "International Union of Pure and Applied Chemistry," *Pure and Applied Chemistry*, vol. 13, pp. 499-500, 1955.
- [17] C. R. Clarkson and M. R. Bustin, "Variation in micropore capacity and size distribution with composition in bituminous coal of the Western Canadian Sedimentary Basin: implications for coalbed methane potential," *Fuel*, vol. 75, no. 13, pp. 1483-1498, 1996.
- [18] B. B. Xodot, S. Z. Song, and Y. A. Wang, *Coal and Gas Outburst*, China Industrial Press, Beijing, China, 1966.
- [19] G. Liu, Z. Zhang, X. Zhang, and R. S. Lu, "Pore distribution regularity and absorption-desorption characteristics of gas coal and coking coal," *Chinese Journal of Rock Mechanics and Engineering*, vol. 28, no. 8, pp. 1587-1592, 2009.
- [20] E. Salehi, V. Taghikhani, C. Ghotbi, E. N. Lay, and A. Shojaei, "Theoretical and experimental study on the adsorption and desorption of methane by granular activated carbon at 25°C," *Journal of Natural Gas Chemistry*, vol. 4, pp. 415-422, 2007.
- [21] L. Xiangchun, N. Baisheng, Z. Ruming, and C. Leilei, "Experiment of gas diffusion and its diffusion mechanism in coal," *International Journal of Mining Science and Technology*, vol. 22, no. 6, pp. 885-889, 2012.
- [22] R. M. Barrer, *Diffusion in and through Solid*, Cambridge University Press, Cambridge, UK, 1951.
- [23] S. N. Zhou and J. Z. Sun, "Flow theory and application of coal seam gas," *Journal of China Coal Society*, vol. 2, pp. 24-36, 1965.
- [24] E. M. Airey, "Gas emission from broken coal. An experimental and theoretical investigation," *International Journal of Rock Mechanics and Mining Sciences*, vol. 5, no. 6, pp. 475-494, 1968.
- [25] Y. Y. Guo and S. N. Zhou, "Complete solution of flow law in one dimensional flow field of coal seam gas," *Journal of China University of Mining and Technology*, vol. 13, pp. 19-28, 1984.
- [26] H. G. Yu, W. T. Fan, and M. Y. Sun, "Study on fitting models for methane isotherms adsorption of coals," *Journal of China Coal Society*, vol. 29, pp. 463-467, 2004.
- [27] F. S. Karn, R. A. Friedel, and A. G. Sharkey, "Mechanism of gas flow through coal," *Fuel*, vol. 54, no. 4, pp. 279-282, 1975.
- [28] H. Li, Y. Ogawa, and S. Simada, "Mechanism of methane flow through sheared coals and its role on methane recovery*," *Fuel*, vol. 82, no. 10, pp. 1271-1279, 2003.

- [29] S. N. Zhou and B. Q. Lin, *The Theory of Gas Flow and Storage in Coal Seams*, China Coal Industry Publishing House, Beijing, China, 1999.
- [30] Q. L. Yang, "Coal gas diffusion characteristics and its application," *Safety In Coal Mines*, vol. 5, pp. 1–6, 1987.
- [31] Q. L. Yang and Y. A. Wang, "Mathematical simulation of the radial methane flow in spherical coal particles," *Journal of China University of Mining and Technology*, vol. 3, pp. 55–61, 1988.
- [32] D. M. Smith and F. L. Williams, "Diffusion models for gas production from coal: determination of diffusion parameters," *Fuel*, vol. 63, no. 2, pp. 256–261, 1984.
- [33] D. M. Smith and F. L. Williams, "Diffusion models for gas production from coals: application to methane content determination," *Fuel*, vol. 63, no. 2, pp. 251–255, 1984.
- [34] S. N. Zhou, "Mechanism of gas flow in coal seams," *Journal of China Coal Society*, vol. 15, pp. 61–67, 1990.
- [35] S. Y. Wu and Y. Y. Guo, "Study on the characteristics of coalbed methane migration," *Journal of China Coal Society*, vol. 24, pp. 65–69, 1999.
- [36] X. Q. He and B. S. Nie, "Diffusion mechanism of porous gases in coal seams," *Journal of China University of Mining and Technology*, vol. 30, pp. 1–4, 2001.
- [37] B. S. Nie, Y. Y. Guo, and S. Y. Wu, "Mathematical model of gas diffusion in coal particle and analytical solution," *Journal of China University of Mining and Technology*, vol. 30, pp. 19–22, 2001.
- [38] E. Ruckenstein, A. S. Vaidyanathan, and G. R. Youngquist, "Sorption by solids with bidisperse pore structures," *Chemical Engineering Science*, vol. 26, no. 9, pp. 1305–1318, 1971.
- [39] D. M. Smith and F. L. Williams, "Diffusional effects in the recovery of methane from coalbeds," *Society of the Petroleum Engineers Journal*, vol. 24, no. 5, pp. 529–535, 1984.
- [40] Y. P. Qin, C. X. Wang, and J. Wang, "Mathematical model of gas emission in coal particles and the numerical solution," *Journal of China Coal Society*, vol. 37, no. 9, pp. 1466–1471, 2012.
- [41] Y. W. Liu, J. P. Wei, Z. G. He, and M. J. Liu, "Influence rules and mechanisms of temperature on dynamic process of gas diffusion from coal particles," *Journal of China Coal Society*, vol. 38, no. 86, pp. 100–105, 2013.
- [42] J. Luo, Y. Liu, C. Jiang, W. Chu, W. Jie, and H. Xie, "Experimental and modeling study of methane adsorption on activated carbon derived from anthracite," *Journal of Chemical & Engineering Data*, vol. 56, no. 12, pp. 4919–4926, 2011.
- [43] T. C. Ruppel, "Adsorption of methane on dry coal at elevated pressure," *Fuel*, vol. 53, no. 3, pp. 152–162, 1974.
- [44] Z. Xiao-dong, S. Shu-xun, Q. Yong, Z. Jing, and T. Jia-xiang, "Isotherm adsorption of coal samples with different grain size," *Journal of China University of Mining and Technology*, vol. 34, no. 4, pp. 427–432, 2005.
- [45] P. G. Sevenster, "Diffusion of gases through coal," *Fuel*, vol. 38, no. 4, pp. 403–418, 1959.
- [46] Q. L. Yang and Y. A. Wang, "Diffusion theory and application of coal gas," *Journal of China Coal Society*, vol. 9, pp. 87–93, 1986.
- [47] Y. W. Liu, *Study on Gas Emission Rules, Mechanism and Dynamic Model from Coal Particle*, Henan Polytechnic University, Jiaozuo, China, 2011.

Research Article

Influences of Coal Properties on the Principal Permeability Tensor during Primary Coalbed Methane Recovery: A Parametric Study

Jie Zang^{1,2,3}, Ze Ma,² Yong Ge,² and Chengxin Li²

¹Beijing Key Laboratory for Precise Mining of Intergrown Energy and Resources, China University of Mining and Technology, Beijing 100083, China

²School of Emergency Management and Safety Engineering, China University of Mining and Technology, Beijing 100083, China

³State Key Laboratory Cultivation Base for Gas Geology and Gas Control, Jiaozuo 454150, China

Correspondence should be addressed to Jie Zang; jiezang@cumtb.edu.cn

Received 13 April 2021; Accepted 17 July 2021; Published 14 August 2021

Academic Editor: Andrew H. Manning

Copyright © 2021 Jie Zang et al. This is an open access article distributed under the Creative Commons Attribution License, which permits unrestricted use, distribution, and reproduction in any medium, provided the original work is properly cited.

Coal permeability is intrinsically anisotropic because of the cleat structure of coal. Therefore, coal permeability can be denoted by a second-order tensor under three-dimensional conditions. Our previous paper proposed an analytical model of the principal permeability tensor of coal during primary coalbed methane (CBM) recovery. Based on this model, 18 modeling cases were considered in the present study to evaluate how the principal permeabilities were influenced by representative coal properties (the areal porosity, the internal swelling ratio, and the Young modulus) during primary CBM recovery. The modeling results show that with regard to the influences of the areal porosity on the principal permeabilities, an increase in cleat porosity reduces the sensitivity of each principal permeability to pore pressure change. The magnitudes of the principal permeabilities are positively proportional to the internal swelling ratio. The principal permeabilities thus tend to monotonically increase with a depletion in the pore pressure when the internal swelling ratio increases. Because the internal swelling ratio represents the extent of gas-sorption-induced matrix deformation, an increase in the internal swelling ratio increases desorption-induced matrix shrinkage and thus induces an increase in permeability. The principal permeabilities are positively proportional to the isotropic principal Young moduli and the synchronously changing anisotropic principal Young moduli. On the other hand, the principal Young modulus within the plane of isotropy influences the principal permeabilities within this plane in diverse patterns depending on both the dip angle of the coalbed and the pitch angle of the cleat sets. The principal permeability perpendicular to the plane of isotropy is positively proportional to this principal Young modulus, and this correlation pattern is independent of both the dip angle and pitch angle.

1. Introduction

Coal permeability is a property that predominantly determines whether a coalbed methane (CBM) reservoir can be commercially recovered [1–3]. Therefore, the investigation on coal permeability has attracted worldwide attention, and various approaches such as experimental measurements, field observations, mathematical modeling, and numerical simulations have been used for the investigation [4–6].

CBM production triggers a series of coal-gas interactions such as changes in the effective stress and gas desorption from the coal matrix [3, 7, 8]. These interactions influence coal permeability during CBM production. When methane is extracted from a coalbed, the effective stress decreases and cleats are compressed; the compression causes a reduction in permeability. On the other hand, the extraction makes methane desorb from the coal matrix and causes the matrix block to shrink. This

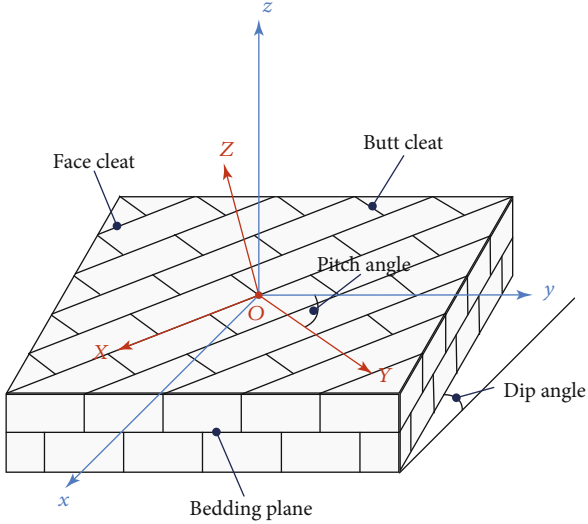


FIGURE 1: Schematic of CCS and UCS [19].

shrinkage increases permeability. Therefore, the manner in which coal permeability varies during CBM production is dependent on the net effects of the effective stress and gas desorption [9, 10].

The net effects of the effective stress and gas desorption on the variation pattern of coal permeability are influenced by coal properties such as porosity, Young's modulus, Poisson's ratio, and sorption strain. The influences of these properties have been evaluated on the basis of theoretical permeability models. Chen et al. [11] documented the influences of Young's modulus, Poisson's ratio, and sorption strain on the variation pattern of coal permeability. Cui and Bustin [12] evaluated how Poisson's ratio influences the variation pattern. Guo et al. [13] evaluated the influences of sorption strain on the variation pattern. Liu et al. [14] discussed the influences of cleat porosity and sorption strain on the pattern. Liu and Harpalani [15] evaluated how porosity influences the pattern.

The abovementioned studies have considered coal permeability to be isotropic. However, coal permeability is intrinsically anisotropic because the fracture structure of coal is heterogeneously distributed [16]. Coalbed fractures are typically composed of three cleat sets: face cleats, butt cleats, and bedding planes [3, 16]. These three cleat sets are normally orthogonal to each other, and coal permeability is intrinsically anisotropic because of this orthogonal fracture structure [3]. Anisotropic permeabilities can be denoted by a second-order diagonal tensor under three-dimensional (3D) conditions. This tensor can be referred to as the "principal permeability tensor" [17, 18], and the diagonal elements of this tensor can be referred to as "principal permeabilities." The principal permeabilities may have different responses to coal properties during primary CBM recovery. However, these responses have not been well documented in the literature.

The present study uses 18 modeling cases to evaluate how coal properties influence the principal permeabilities during

primary CBM recovery. The modeling cases are considered on the basis of a permeability model developed in one of our previous studies [19].

2. Modeling Influences of Coal Properties on Principal Permeability Tensor during Primary CBM Recovery

2.1. Representations of Principal Permeability Tensor. Because the components of the uniaxial strain conditions are aligned along the vertical and horizontal directions, these components are noncoaxial to the cleat sets when the coalbed is inclined. Two coordinate systems can be formulated to align the components of the uniaxial strain conditions with the cleat sets. One is the uniaxial coordinate system (UCS), which is used to accommodate the uniaxial strain conditions, and the other is the cleat coordinate system (CCS), which is used to accommodate the cleat sets. Figure 1 shows the schematic of the two coordinate systems, which can be correlated to two featured properties. One is the dip angle of the inclined coalbed, and the other is the pitch angle of the cleat sets [19].

Our previous paper [19] proposed a model of the principal permeability tensor during primary CBM recovery. The representations of this model are shown in equation (1), equation (2), and equation (3). The present paper will only summarize the basic assumptions and representations of this model. More details can be obtained from our previous paper. The model was developed for a coalbed that is subjected to uniaxial strain conditions. The model assumes that only elastic deformation occurs in the coalbed. The coalbed contains three orthogonal cleat sets (Figure 1). The orientations of the principal permeability tensor are coaxial to those of the cleat sets. Although stress change may induce fracture initiation or propagation in fractured rocks like coal [20, 21], our proposed model assumes that no fracture initiation or propagation occurs in coal during CBM recovery. These assumptions are seemingly simple, but they are widely adopted in the literature and have been validated against both experimental and field data [4, 22, 23].

$$\left\{ \begin{array}{l} k_x = k_{x0} \left\{ 1 + \frac{1}{\phi_{ax0}} \left[\left(\frac{1-\nu}{E_Y} \Delta\sigma_{eYY} + \frac{1-\nu}{E_Z} \Delta\sigma_{eZZ} - \frac{2\nu}{E_X} \Delta\sigma_{eXX} \right) - \frac{F_{in}\epsilon_{LY}P_{LY}(p-p_0)}{(P_{LY}+p)(P_{LY}+p_0)} - \frac{F_{in}\epsilon_{LZ}P_{LZ}(p-p_0)}{(P_{LZ}+p)(P_{LZ}+p_0)} \right] \right\}^3, \\ k_y = k_{y0} \left\{ 1 + \frac{1}{\phi_{ay0}} \left[\left(\frac{1-\nu}{E_Z} \Delta\sigma_{eZZ} + \frac{1-\nu}{E_X} \Delta\sigma_{eXX} - \frac{2\nu}{E_Y} \Delta\sigma_{eYY} \right) - \frac{F_{in}\epsilon_{LZ}P_{LZ}(p-p_0)}{(P_{LZ}+p)(P_{LZ}+p_0)} - \frac{F_{in}\epsilon_{LX}P_{LX}(p-p_0)}{(P_{LX}+p)(P_{LX}+p_0)} \right] \right\}^3, \\ k_z = k_{z0} \left\{ 1 + \frac{1}{\phi_{az0}} \left[\left(\frac{1-\nu}{E_X} \Delta\sigma_{eXX} + \frac{1-\nu}{E_Y} \Delta\sigma_{eYY} - \frac{2\nu}{E_Z} \Delta\sigma_{eZZ} \right) - \frac{F_{in}\epsilon_{LX}P_{LX}(p-p_0)}{(P_{LX}+p)(P_{LX}+p_0)} - \frac{F_{in}\epsilon_{LY}P_{LY}(p-p_0)}{(P_{LY}+p)(P_{LY}+p_0)} \right] \right\}^3, \end{array} \right. \quad (1)$$

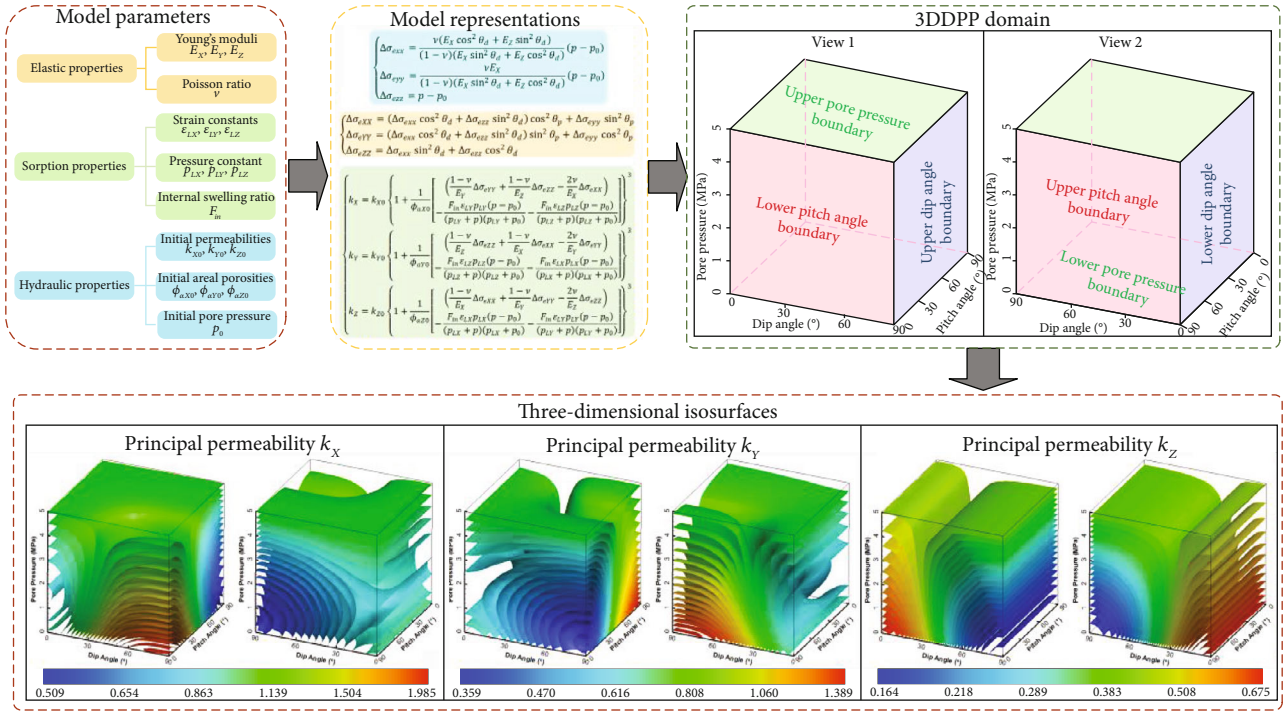


FIGURE 2: Workflow for 3D visualization of principal permeabilities.

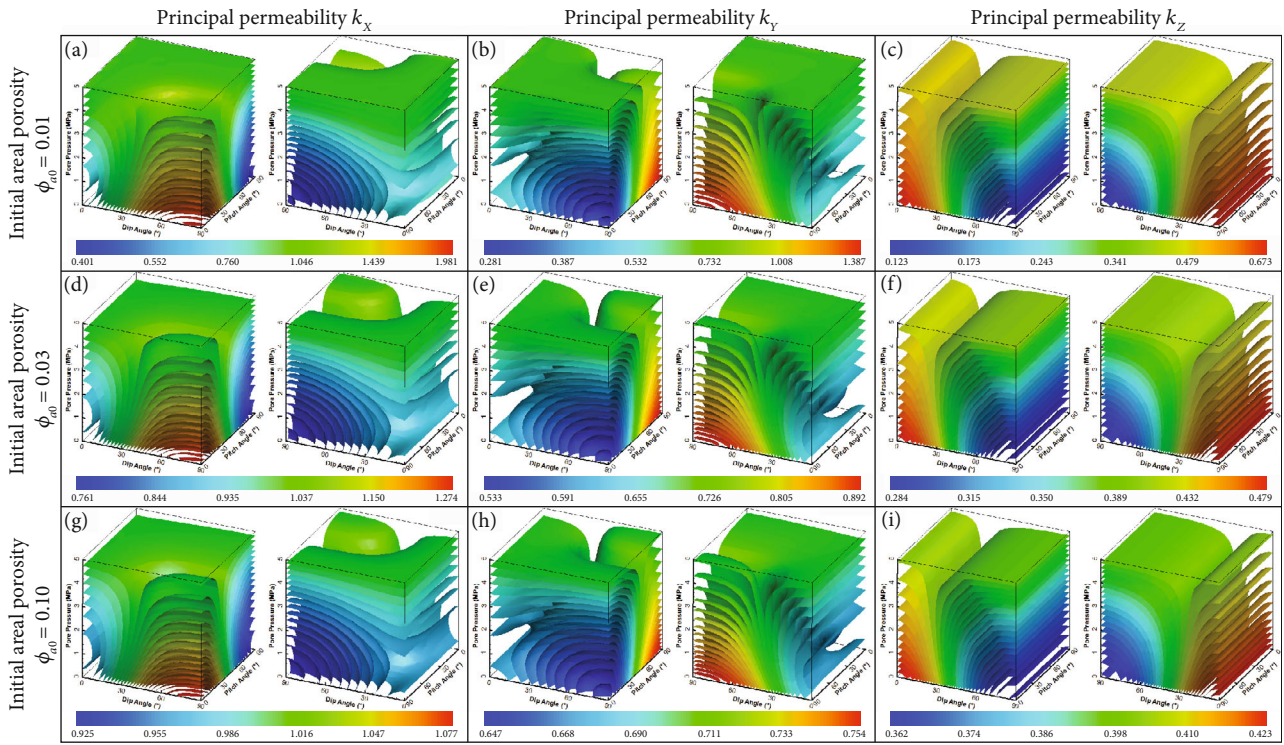


FIGURE 3: 3D isosurfaces showing principal permeabilities within the 3DDPP domain for Cases 1, 2, and 3. The color legends in these images have a uniform measurement unit of “millidarcy (mD).”

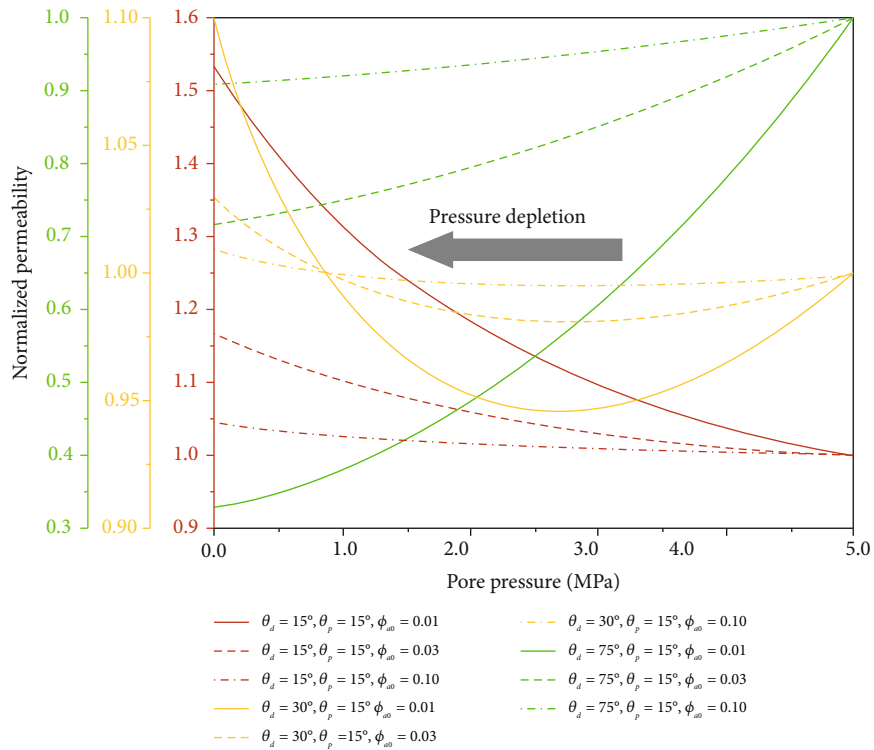


FIGURE 4: Normalized curves showing how areal porosity influences principal permeability k_z during primary CBM recovery.

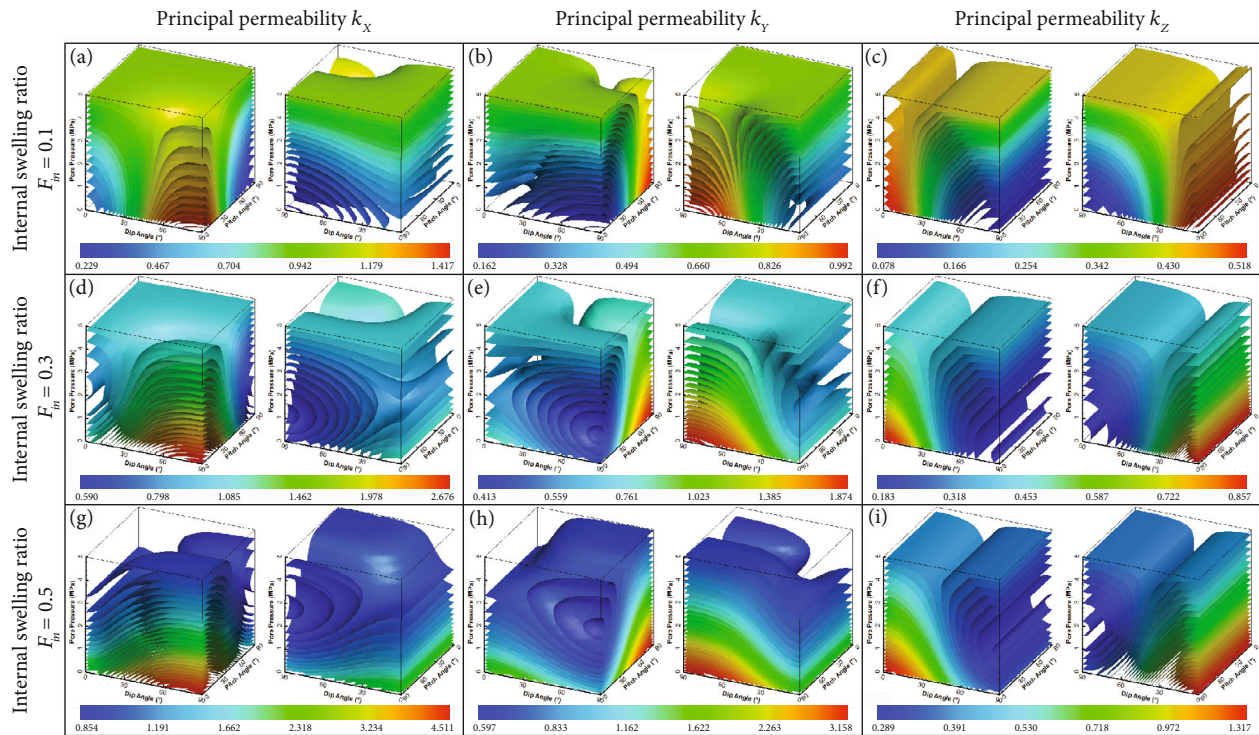


FIGURE 5: 3D isosurfaces showing principal permeabilities within the 3DDPP domain for Cases 4, 5, and 6. The color legends in these images have a uniform measurement unit of “millidarcy (mD).”

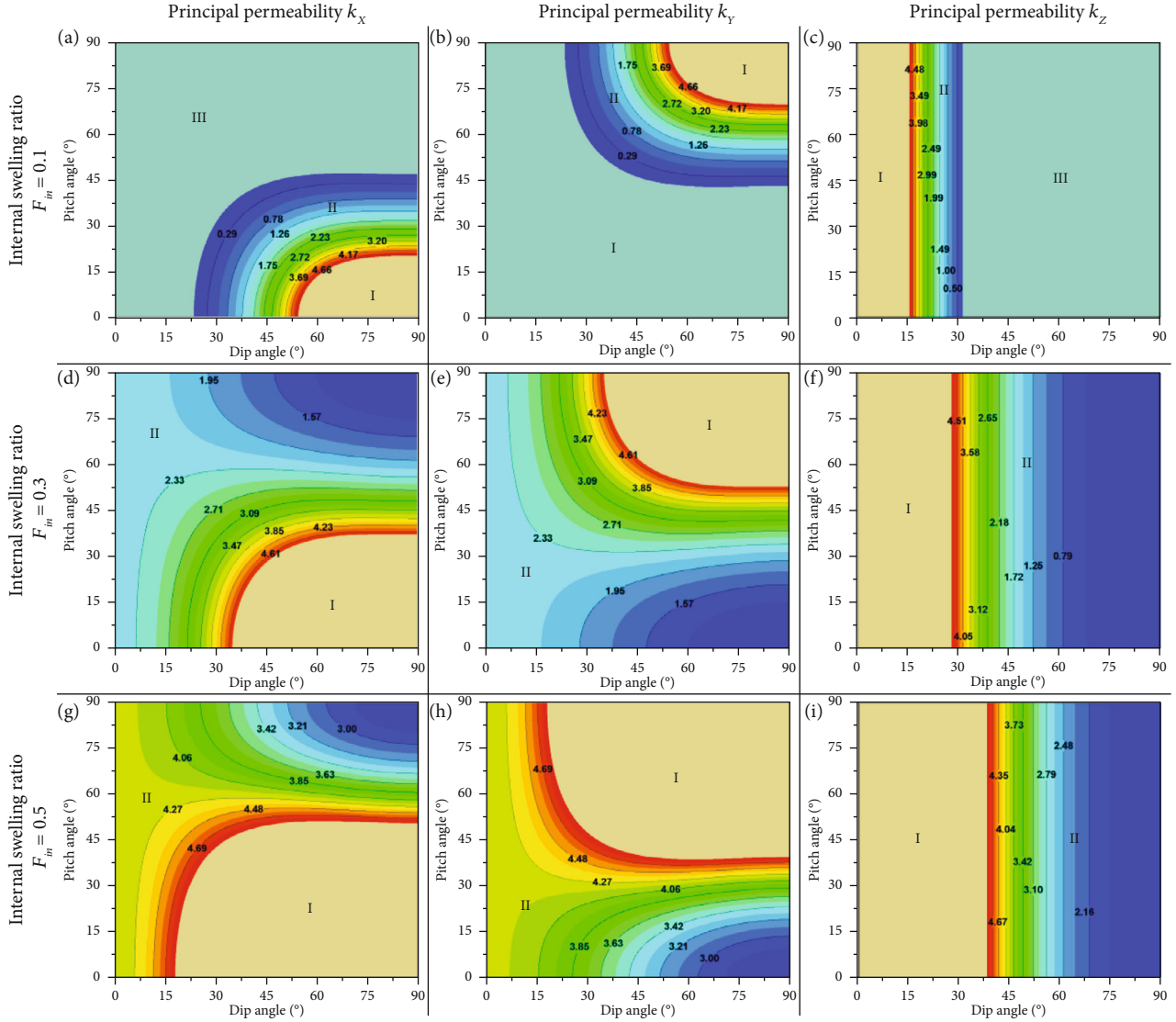


FIGURE 6: 2D contours showing distribution of rebound pressure within the 2DDP domain for Cases 4, 5, and 6. Domain I represents the region where the rebound pressure is greater than 5.0 MPa and the principal permeabilities increase monotonically with a depletion in the pore pressure. Domain II represents the region where the rebound pressure is 0.0–5.0 MPa and the principal permeabilities vary nonmonotonically with a depletion in the pore pressure. Domain III represents the region where the rebound pressure is lower than 0.0 MPa and the principal permeabilities decrease monotonically with a depletion in the pore pressure.

$$\begin{cases} \Delta\sigma_{eXX} = (\Delta\sigma_{eXX} \cos^2\theta_d + \Delta\sigma_{eZZ} \sin^2\theta_d) \cos^2\theta_p + \Delta\sigma_{eYY} \sin^2\theta_p, \\ \Delta\sigma_{eYY} = (\Delta\sigma_{eXX} \cos^2\theta_d + \Delta\sigma_{eZZ} \sin^2\theta_d) \sin^2\theta_p + \Delta\sigma_{eYY} \cos^2\theta_p, \\ \Delta\sigma_{eZZ} = \Delta\sigma_{eXX} \sin^2\theta_d + \Delta\sigma_{eZZ} \cos^2\theta_d, \end{cases} \quad (2)$$

$$\begin{cases} \Delta\sigma_{eXX} = \frac{\nu(E_X \cos^2\theta_d + E_Z \sin^2\theta_d)}{(1-\nu)(E_X \sin^2\theta_d + E_Z \cos^2\theta_d)} (p - p_0), \\ \Delta\sigma_{eYY} = \frac{\nu E_X}{(1-\nu)(E_X \sin^2\theta_d + E_Z \cos^2\theta_d)} (p - p_0), \\ \Delta\sigma_{eZZ} = p - p_0, \end{cases} \quad (3)$$

where E_X , E_Y , and E_Z are the principal Young moduli in CCS; F_{in} is the internal swelling ratio, which represents

the ratio of the internal swelling to the known sorption-induced strain of coal block; k_X , k_Y , and k_Z are the principal permeabilities in CCS; k_{X0} , k_{Y0} , and k_{Z0} are the initial principal permeabilities in CCS; p is the pore pressure; p_0 is the initial pore pressure; p_{LX} , p_{LY} , and p_{LZ} are the principal Langmuir pressure constants in CCS; X , Y , and Z are the axes of CCS; x , y , and z are the axes of UCS; ε_{LX} , ε_{LY} , and ε_{LZ} are the principal Langmuir strain constants in CCS; θ_d is the dip angle of coalbeds; θ_p is the pitch angle representing the acute angle between the strike direction of the inclined coalbed and butt cleat; ν is the Poisson's ratio; σ_{eXX} , σ_{eYY} , and σ_{eZZ} are the normal effective stresses in CCS; σ_{eXX} , σ_{eYY} , and σ_{eZZ} are the normal effective stresses in UCS; ϕ_{aX0} , ϕ_{aY0} , and ϕ_{aZ0} are the initial principal areal porosities in CCS.

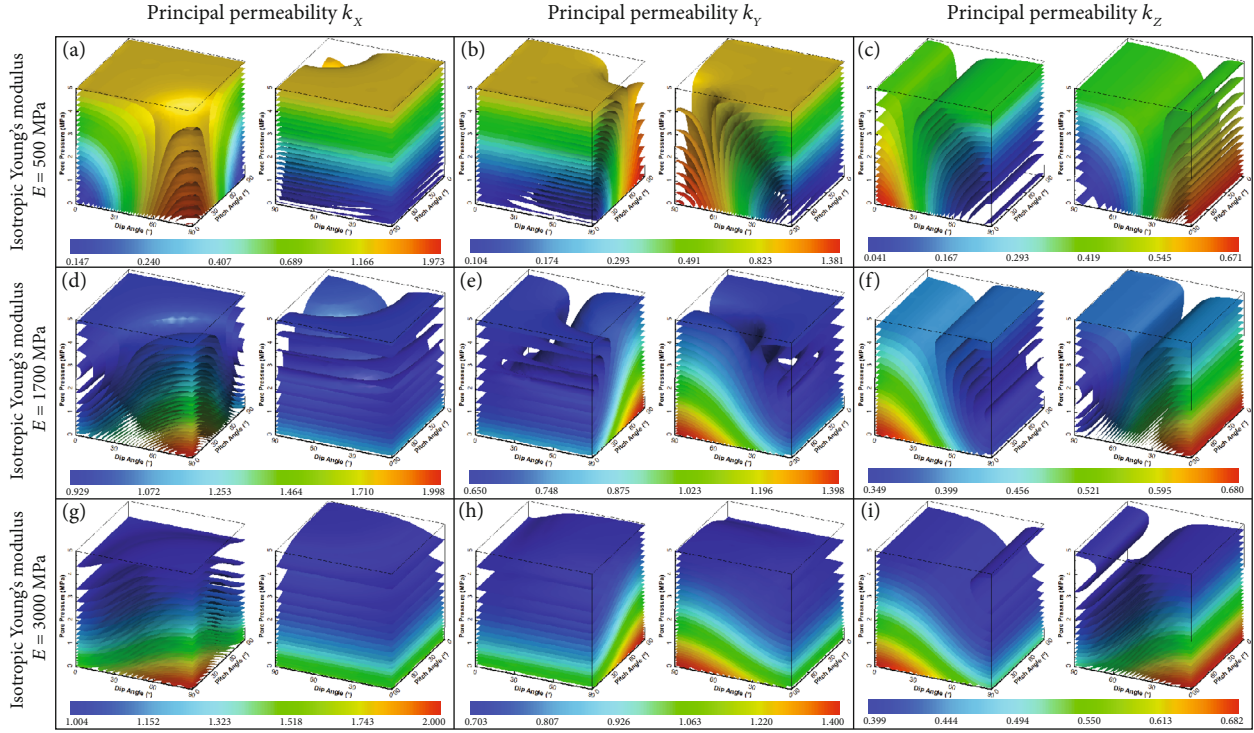


FIGURE 7: 3D isosurfaces showing principal permeabilities within the 3DDPP domain for Cases 7, 8, and 9. The color legends in these images have a uniform measurement unit of “millidarcy (mD).”

Equation (1) shows how the principal permeabilities vary during gas sorption and effective stress change. The normal effective stresses in the CCS ($\Delta\sigma_{eXX}$, $\Delta\sigma_{eYY}$, and $\Delta\sigma_{eZZ}$) can be represented by the normal effective stresses in the UCS, as expressed in equation (2). The normal effective stresses $\Delta\sigma_{exx}$, $\Delta\sigma_{eyy}$, and $\Delta\sigma_{ezz}$ under uniaxial strain conditions can be represented by equation (3). Note that in equation (3), the principal Young moduli are assumed to be transversely isotropic. The combination of equation (1), equation (2), and equation (3) can represent the variation in the principal permeabilities during primary CBM recovery. In our previous papers [3, 19], the formulations of equation (1), equation (2), and equation (3) have been described and these equations have been validated against experimental and field data. Hence, these details are not repeated in this paper.

2.2. Modeling Configuration. Equation (1), equation (2), and equation (3) show that the principal permeability tensor can be influenced by multiple properties. These properties include the dip angle, the pitch angle, the areal porosity, the internal swelling ratio, and the Young modulus. The influences of both the dip angle and pitch angle have been evaluated in our previous study. This study will use 18 modeling cases (divided into six groups) to evaluate how the areal porosity, the internal swelling ratio, and the Young modulus influence the principal permeabilities during primary CBM recovery. The parameters used in each modeling case are presented in Table 1.

Group 1 evaluates how the isotropic areal porosity influences the principal permeabilities. Group 2 focuses on the influences of the isotropic internal swelling ratio. Because the internal swelling ratio is the rate-controlling parameter of sorption strain, this group represents the influences of gas sorption. Because the Young modulus is anisotropic, the influences of the Young modulus will be discussed in four groups. Group 3 evaluates the influences of the isotropic Young modulus. Group 4 evaluates the influences of the anisotropic and synchronously changing principal the Young moduli. Groups 5 and 6 evaluate the influences of the principal Young moduli E_X and E_Z , respectively.

In each modeling case, the principal permeabilities were plotted within a 3D domain formulated by the dip angle, pitch angle, and pore pressure. This domain is referred to as the “3DDPP domain” in this paper. The workflow for the 3D visualization of the principal permeabilities is shown in Figure 2. Equation (1), equation (2), and equation (3) and the related properties were implemented in the 3DDPP domain to compute each principal permeability in this domain. This step was achieved using a self-writing C++ code. The 3DDPP domain was surrounded by three pairs of two-dimensional (2D) boundaries. The computed data were then implemented in the Tecplot 360 Package for 3D visualization.

3. Modeling Results and Discussion

3.1. Influences of Areal Porosity. Figure 3 shows the principal permeabilities within the 3DDPP domain for Cases 1, 2, and

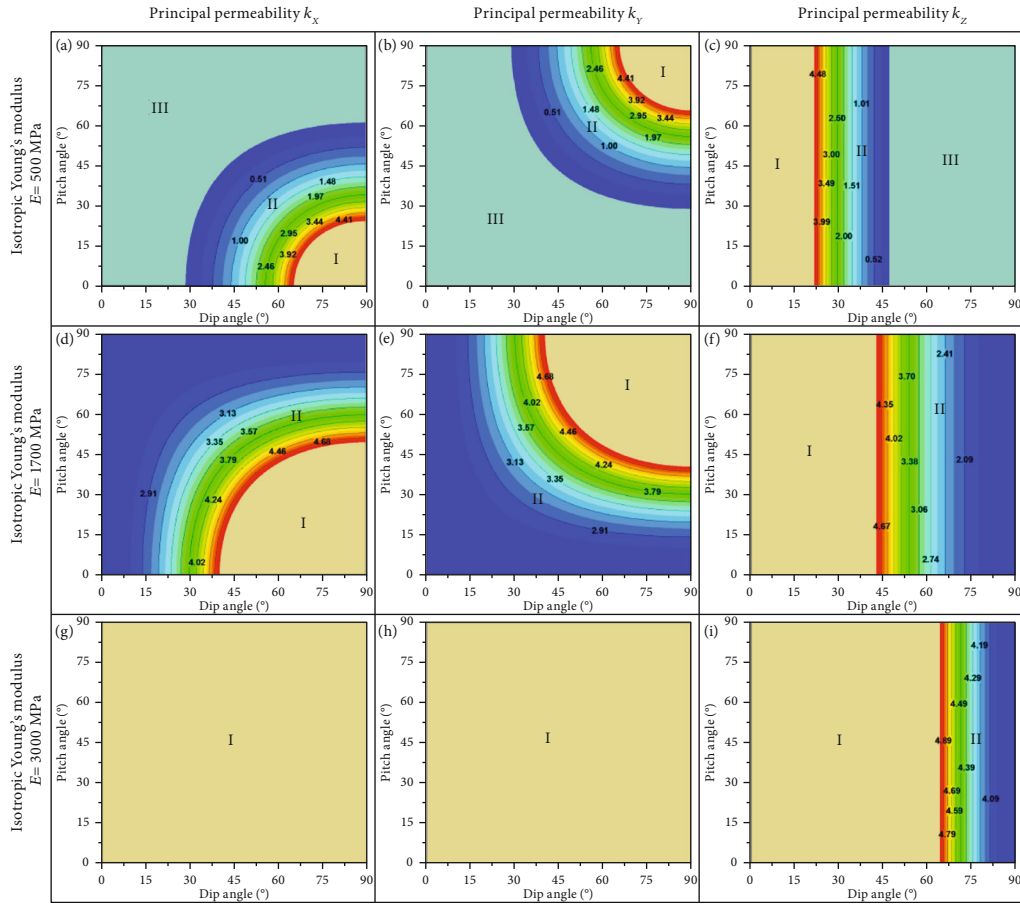


FIGURE 8: 2D contours showing distribution of rebound pressure within the 2DDP domain for Cases 7, 8, and 9. These images were plotted in the same manner as Figure 6.

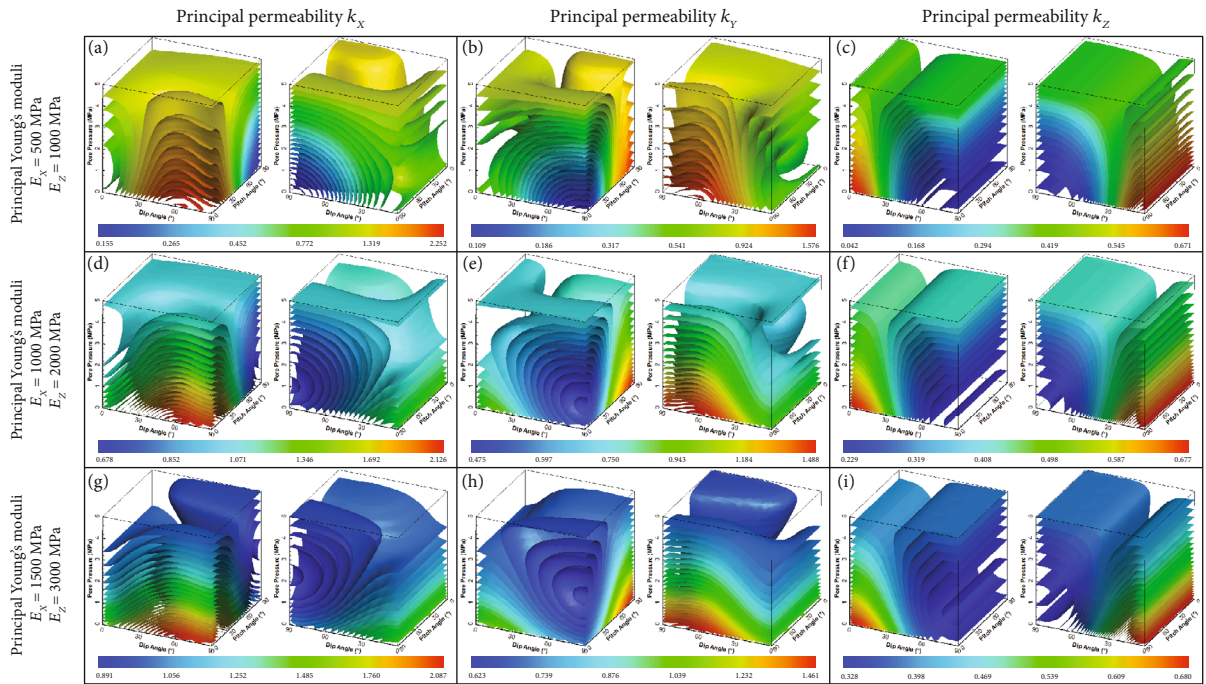


FIGURE 9: 3D isosurfaces showing principal permeabilities within the 3DDP domain for Cases 10, 11, and 12. The color legends in these images have a uniform measurement unit of “millidarcy (mD).”

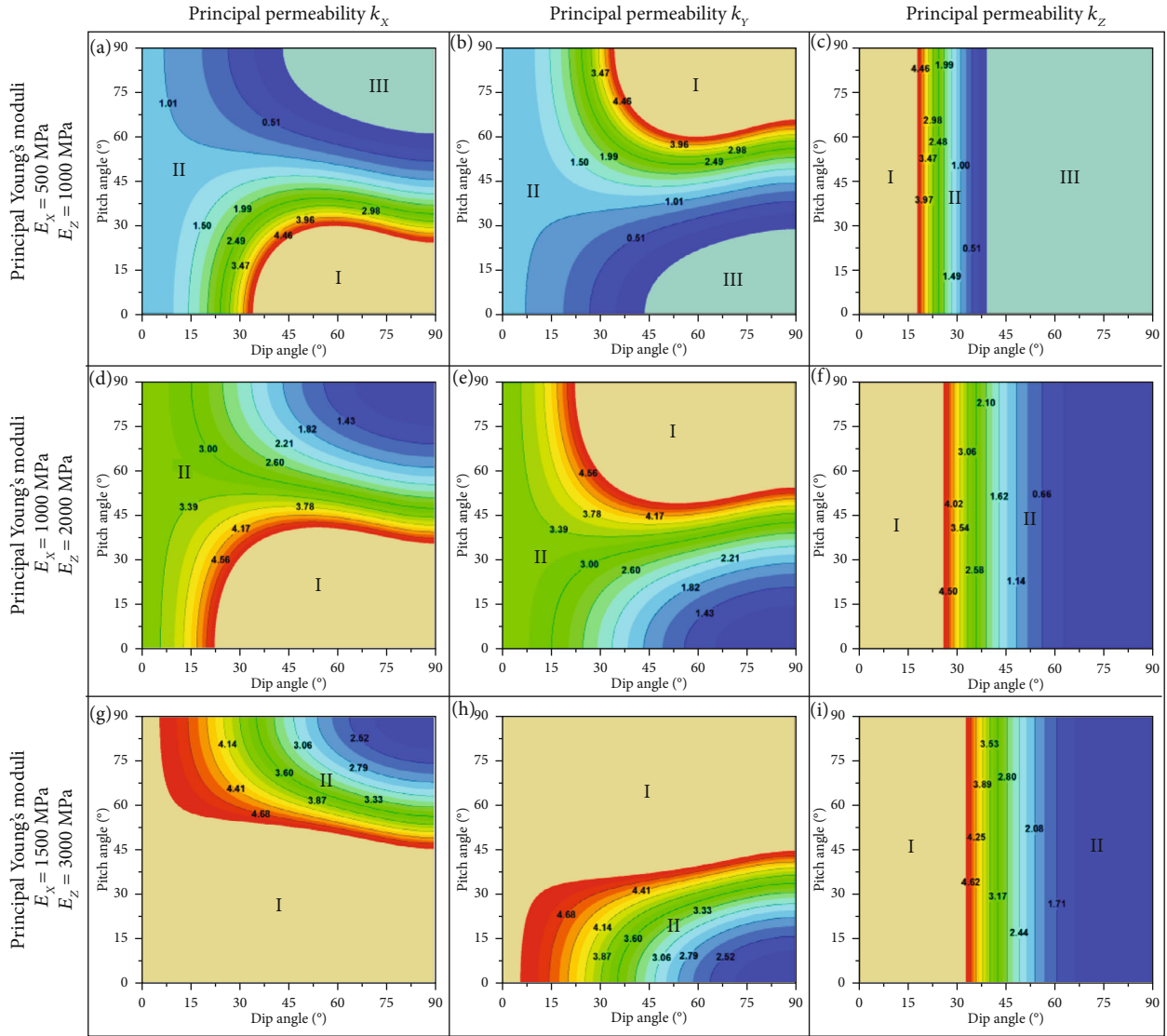


FIGURE 10: 2D contours showing rebound pressure within the 2DDP domain for Cases 10, 11, and 12. The images were plotted in the same manner as Figure 6.

3. For each principal permeability, the structure of the isosurfaces in the 3DDPP domain remains invariant with an increase in the areal porosity. The color legends in Figure 3 show that the increasing areal porosity increases the lower bound but decreases the upper bound of each principal permeability.

Figure 4 provides further details regarding the influences of the areal porosity on the evolution of each principal permeability during primary CBM recovery. When the principal permeability k_z increases monotonically with a depletion in the pore pressure, the acceleration of k_z reduces with an increase in the areal porosity. In this case, k_z is negatively proportional to the areal porosity, as shown by the red curves in Figure 4. When k_z decreases monotonically with a depletion in the pore pressure, the deceleration of k_z reduces with an increase in the areal porosity. In this case, k_z is positively proportional to the areal porosity, as shown by the green

curves in Figure 4. When k_z evolves nonmonotonically with a depletion in the pore pressure, the increasing areal porosity reduces the deceleration of k_z when the pore pressure is greater than the rebound pressure but increases the acceleration of k_z when the pore pressure is lower than the rebound pressure. In this case, k_z is always positively proportional to the areal porosity when the pore pressure is higher than the rebound pressure, as indicated by the yellow curves in Figure 4. When the pore pressure is lower than the rebound pressure, k_z can be either positively proportional or negatively proportional to the areal porosity depending on the acceleration of k_z in different cases. Based on the curves shown in Figure 4, the influences of the areal porosity on the principal permeabilities can be summarized as follows: an increase in cleat porosity reduces the sensitivity of each principal permeability to pore pressure change.

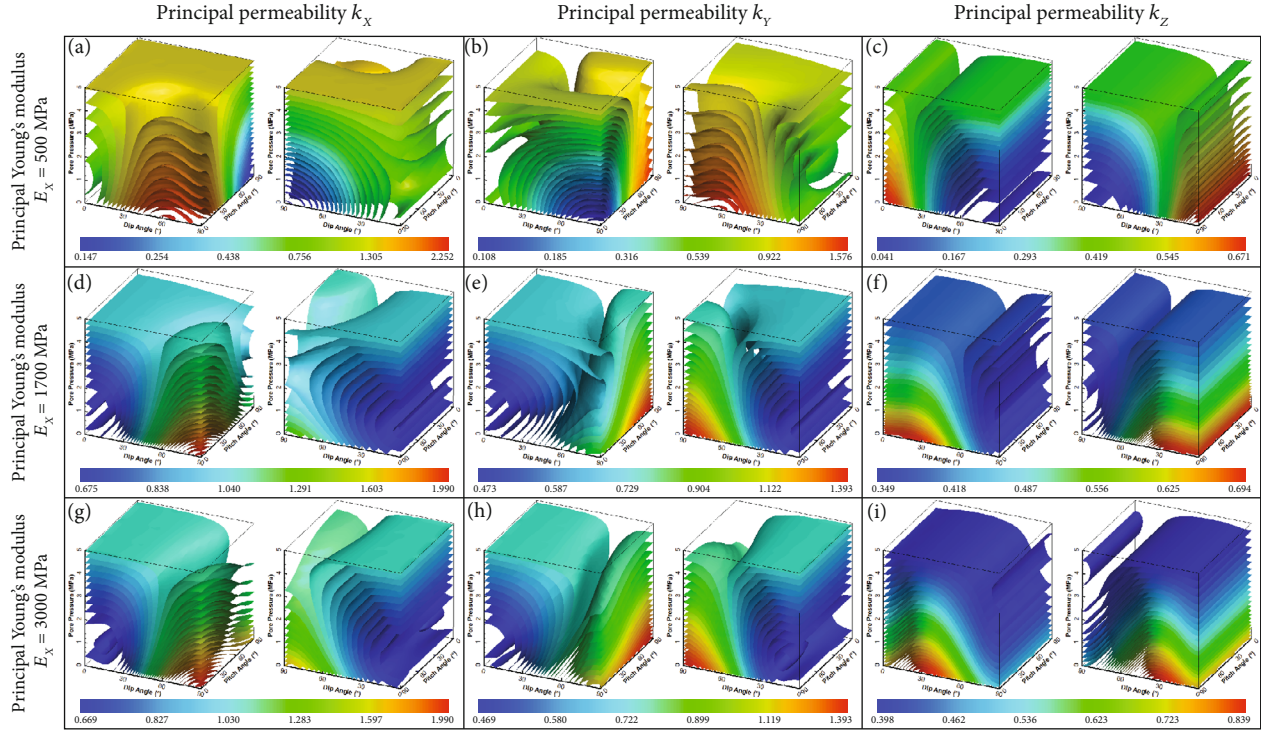


FIGURE 11: 3D isosurfaces showing principal permeabilities within the 3DDPP domain for Cases 13, 14, and 15. The color legends in these images have a uniform measurement unit of “millidarcy (mD).”

The modeling cases described in this subsection are based on the assumption of isotropic cleat porosity. The isotropic nature of cleat porosity is consistent with the experimental observations of Gash et al. [26], who reported that the anisotropy between the cleat porosities in different directions is minor for Fruitland Formation coals. However, the literature also contains reports on cases where the anisotropy of cleat porosity has been found to be substantial. Wang et al. [27] observed that the cleat porosity parallel to the bedding plane could be four times that normal to the bedding plane for coals from the Junggar Basin. When cleat porosity has substantial anisotropy, the principal permeability along the direction of the minimum cleat porosity will have a greater sensitivity to pore pressure or stress change than the principal permeabilities along the directions of the medium and maximum cleat porosities.

3.2. Influences of Internal Swelling Ratio. Equation (1) indicates that all the three principal permeabilities are positively proportional to the internal swelling ratio. The 3D isosurfaces shown in Figure 5 confirm this correlation. The isosurfaces can be classified into two categories for each principal permeability: isosurfaces having values higher than the initial value of each principal permeability, and isosurfaces having values lower than the initial value of each principal permeability. In this study, the first category is referred to as “initial-value greater” (IVG) isosurfaces, whereas the second category is referred to as “initial-value lower” (IVL) isosurfaces. Because the principal permeabilities are positively proportional to the internal swell-

ing ratio, the IVG isosurfaces encroach on the IVL isosurfaces with an increase in the internal swelling ratio. In addition to this encroachment, the increasing internal swelling ratio also increases the maximum and minimum values of each principal permeability, as shown by the color legends in Figure 5.

Because the magnitudes of the principal permeabilities change with the internal swelling ratio, their variation pattern changes according to changes in the pore pressure. The changing variation pattern affects the rebound pressure of the principal permeabilities. The increasing internal swelling ratio changes the distribution of the rebound pressure in the 2D domain formed by the dip angle and pitch angle (2DDP domain), as shown in Figure 6. Figure 6 shows that the rebound pressure increases with an increase in the internal swelling ratio in the entire 2DDP domain for each principal permeability. Because of the increasing rebound pressure, the gray-yellow Domain I tends to encroach on the other two domains. This encroachment indicates that all the three principal permeabilities tend to increase monotonically during pore pressure depletion with an increase in the internal swelling ratio.

The influences of gas sorption on permeability evolution have been widely discussed in the literature [10, 22, 28–32]. Generally, pore pressure depletion induces gas desorption and matrix shrinkage. This process causes cleat dilation and results in increased permeability. On the other hand, an increase in the pore pressure causes gas adsorption and matrix swelling. This process compresses the cleats and reduces permeability. Because the internal swelling ratio

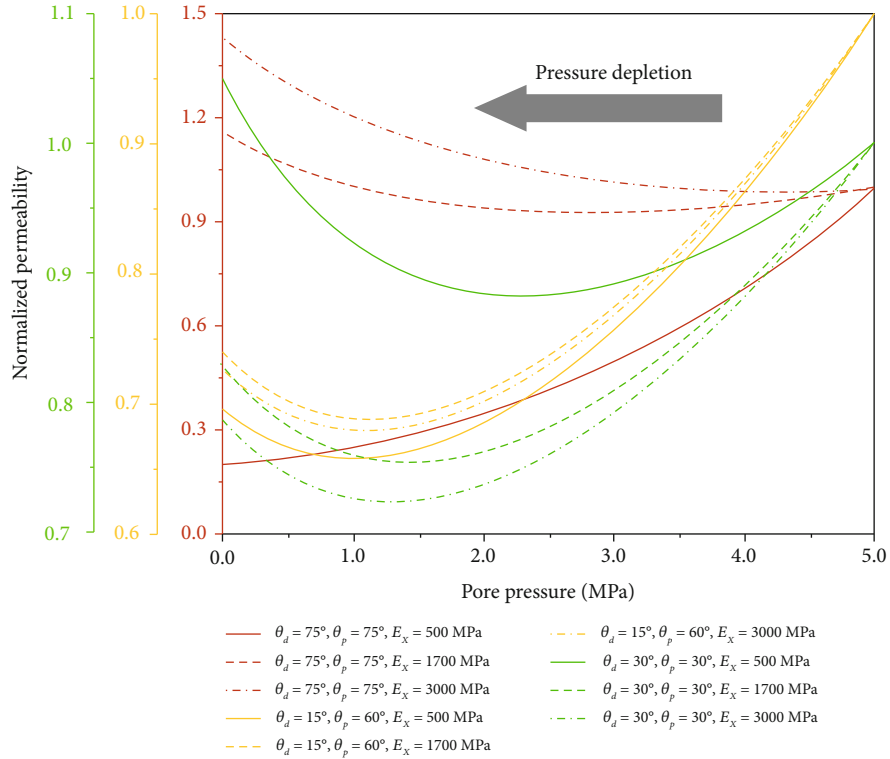


FIGURE 12: Normalized curves showing how E_X affects variation in k_X during pore pressure depletion.

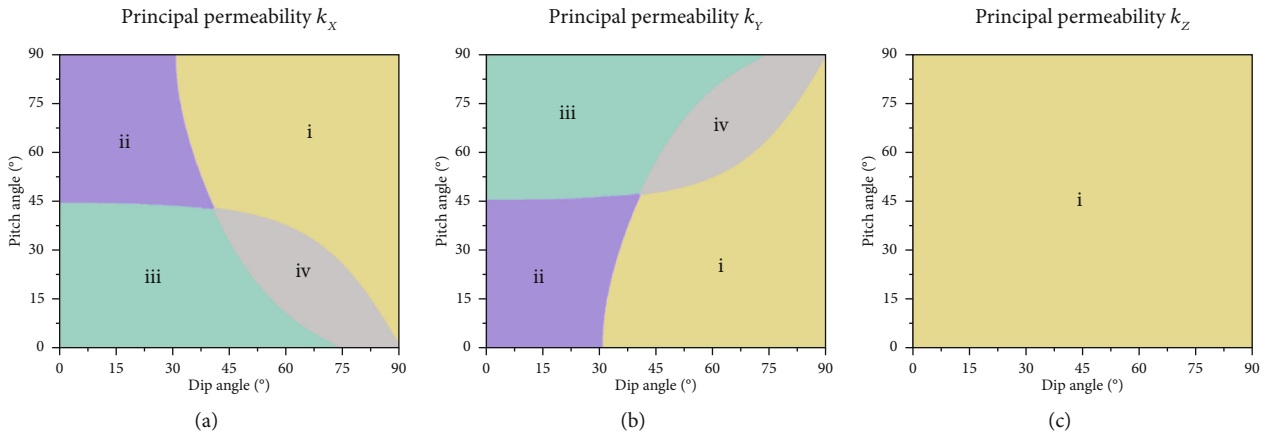


FIGURE 13: Division of the 2DDP domain in terms of variation patterns of principal permeabilities with respect to increasing E_X . In Domain i, the principal permeabilities increase monotonically with an increase in E_X . In Domain ii, the principal permeabilities vary nonmonotonically with an increase in E_X , and the curve of each principal permeability has one maximum point. In Domain iii, the principal permeabilities evolve nonmonotonically with an increase in E_X , and the curve of each principal permeability has one minimum point. In Domain iv, the principal permeabilities decrease monotonically with an increase in E_X .

represents the extent of gas-sorption-induced matrix deformation, an increase in the internal swelling ratio increases desorption-induced matrix shrinkage and thus induces an increase in permeability.

3.3. Influences of Young's Modulus. When Young's modulus is isotropic, the representations of the principal permeabil-

ities are reduced to those expressed in equation (4). This equation set shows that the normal effective stresses in the CCS are independent of the isotropic Young modulus. When the isotropic Young modulus increases, the influences of the effective stress decrease and each principal permeability increases accordingly. All the three principal permeabilities are thus positively proportional to the

isotropic Young's modulus in the entire 3DDPP domain. The 3D isosurfaces shown in Figure 7 confirm this correlation. Figure 7 shows that the IVG isosurfaces gradually encroach on the IVL isosurfaces in the 3DDPP domain for each principal permeability. The maximum and minimum values of each principal permeability also increase with an increase in the isotropic Young modulus, as shown by the color legends in Figure 7.

$$\left\{ \begin{array}{l} k_X = k_{X0} \left\{ 1 + \frac{1}{\phi_{aX0}} \left[\left(\frac{1-\nu}{E} \Delta\sigma_{eYY} + \frac{1-\nu}{E} \Delta\sigma_{eZZ} - \frac{2\nu}{E} \Delta\sigma_{eXX} \right) - \frac{F_{in}\epsilon_{LY}P_{LY}(p-p_0)}{(P_{LY}+P)(P_{LY}+P_0)} - \frac{F_{in}\epsilon_{LZ}P_{LZ}(p-p_0)}{(P_{LZ}+P)(P_{LZ}+P_0)} \right] \right\}^3, \\ k_Y = k_{Y0} \left\{ 1 + \frac{1}{\phi_{aY0}} \left[\left(\frac{1-\nu}{E} \Delta\sigma_{eZZ} + \frac{1-\nu}{E} \Delta\sigma_{eXX} - \frac{2\nu}{E} \Delta\sigma_{eYY} \right) - \frac{F_{in}\epsilon_{LZ}P_{LZ}(p-p_0)}{(P_{LZ}+P)(P_{LZ}+P_0)} - \frac{F_{in}\epsilon_{LX}P_{LX}(p-p_0)}{(P_{LX}+P)(P_{LX}+P_0)} \right] \right\}^3, \\ k_Z = k_{Z0} \left\{ 1 + \frac{1}{\phi_{aZ0}} \left[\left(\frac{1-\nu}{E} \Delta\sigma_{eXX} + \frac{1-\nu}{E} \Delta\sigma_{eYY} - \frac{2\nu}{E} \Delta\sigma_{eZZ} \right) - \frac{F_{in}\epsilon_{LX}P_{LX}(p-p_0)}{(P_{LX}+P)(P_{LX}+P_0)} - \frac{F_{in}\epsilon_{LY}P_{LY}(p-p_0)}{(P_{LY}+P)(P_{LY}+P_0)} \right] \right\}^3, \\ \Delta\sigma_{eXX} = \frac{[\nu(\cos^2\theta_d - \sin^2\theta_d) + \sin^2\theta_d] \cos^2\theta_p + \sin^2\theta_p}{(1-\nu)} (p-p_0), \\ \Delta\sigma_{eYY} = \frac{[\nu(\cos^2\theta_d - \sin^2\theta_d) + \sin^2\theta_d] \sin^2\theta_p + \nu \cos^2\theta_p}{(1-\nu)} (p-p_0), \\ \Delta\sigma_{eZZ} = \frac{\nu(\sin^2\theta_d - \cos^2\theta_d) + \cos^2\theta_d}{(1-\nu)} (p-p_0), \end{array} \right. \quad (4)$$

where E is the isotropic Young modulus.

Figure 7 also shows that the increasing isotropic Young modulus changes the variation in the principal permeabilities with a depletion in the pore pressure. Generally, as the isotropic Young modulus increases, all the three principal permeabilities tend to increase monotonically when the pore pressure depletes. The rebound pressure also increases with an increase in the isotropic Young modulus, as illustrated in Figure 8. The increasing rebound pressure causes the gray-yellow Domain I to expand for all the three principal permeabilities.

When the Young modulus is anisotropic and the principal Young moduli increase synchronously, the principal Young moduli E_X and E_Z can be correlated by a ratio constant (R_c), as expressed in equation (5). The principal permeabilities can thus be expressed by equation (6). This equation set shows that the normal effective stresses in the CCS are independent of both E_X and E_Z but are dependent on their ratio R_c . When E_X and E_Z increase synchronously, the effects of the effective stress reduce and the principal permeabilities increase accordingly. Therefore, the magnitudes of the principal permeabilities are positively proportional to the synchronously increasing E_X and E_Z in the entire 3DDPP domain. The 3D isosurfaces in Figure 9 confirm this correlation.

$$E_Z = R_c E_X, \quad (5)$$

$$\left\{ \begin{array}{l} k_X = k_{X0} \left\{ 1 + \frac{1}{\phi_{aX0}} \left[\left(\frac{1-\nu}{E_X} \Delta\sigma_{eYY} + \frac{1-\nu}{R_c E_X} \Delta\sigma_{eZZ} - \frac{2\nu}{E_X} \Delta\sigma_{eXX} \right) - \frac{F_{in}\epsilon_{LY}P_{LY}(p-p_0)}{(P_{LY}+P)(P_{LY}+P_0)} - \frac{F_{in}\epsilon_{LZ}P_{LZ}(p-p_0)}{(P_{LZ}+P)(P_{LZ}+P_0)} \right] \right\}^3, \\ k_Y = k_{Y0} \left\{ 1 + \frac{1}{\phi_{aY0}} \left[\left(\frac{1-\nu}{R_c E_X} \Delta\sigma_{eZZ} + \frac{1-\nu}{E_X} \Delta\sigma_{eXX} - \frac{2\nu}{E_X} \Delta\sigma_{eYY} \right) - \frac{F_{in}\epsilon_{LZ}P_{LZ}(p-p_0)}{(P_{LZ}+P)(P_{LZ}+P_0)} - \frac{F_{in}\epsilon_{LX}P_{LX}(p-p_0)}{(P_{LX}+P)(P_{LX}+P_0)} \right] \right\}^3, \\ k_Z = k_{Z0} \left\{ 1 + \frac{1}{\phi_{aZ0}} \left[\left(\frac{1-\nu}{E_X} \Delta\sigma_{eXX} + \frac{1-\nu}{E_X} \Delta\sigma_{eYY} - \frac{2\nu}{R_c E_X} \Delta\sigma_{eZZ} \right) - \frac{F_{in}\epsilon_{LX}P_{LX}(p-p_0)}{(P_{LX}+P)(P_{LX}+P_0)} - \frac{F_{in}\epsilon_{LY}P_{LY}(p-p_0)}{(P_{LY}+P)(P_{LY}+P_0)} \right] \right\}^3, \\ \Delta\sigma_{eXX} = \frac{[\sin^2\theta_d(\sin^2\theta_d + R_c \cos^2\theta_d) + \nu(\cos^2\theta_d - \sin^2\theta_d)] \cos^2\theta_p + \nu \sin^2\theta_p}{(1-\nu)(\sin^2\theta_d + R_c \cos^2\theta_d)} (p-p_0), \\ \Delta\sigma_{eYY} = \frac{[\sin^2\theta_d(\sin^2\theta_d + R_c \cos^2\theta_d) + \nu(\cos^2\theta_d - \sin^2\theta_d)] \sin^2\theta_p + \nu \cos^2\theta_p}{(1-\nu)(\sin^2\theta_d + R_c \cos^2\theta_d)} (p-p_0), \\ \Delta\sigma_{eZZ} = \frac{[\nu R_c(\sin^2\theta_d - \cos^2\theta_d) + \cos^2\theta_d(\sin^2\theta_d + R_c \cos^2\theta_d)]}{(1-\nu)(\sin^2\theta_d + R_c \cos^2\theta_d)} (p-p_0). \end{array} \right. \quad (6)$$

Because the magnitudes of the principal permeabilities are positively proportional to the synchronously increasing principal Young moduli E_X and E_Z within the entire 3DDPP domain, the principal permeabilities tend to increase monotonically during pore pressure depletion, as indicated by the 3D isosurfaces shown in Figure 9. The rebound pressure thus increases accordingly for each principal permeability, as illustrated in Figure 10. The increasing rebound pressure causes the gray-yellow Domain I to expand for all the three principal permeabilities.

When E_X increases and E_Z remains invariant, the normal effective stresses in the CCS are dependent on both E_X and E_Z . In this case, the influences of E_X on the principal permeabilities cannot be seen visually from the representation of each principal permeability. Figure 11 shows the 3D isosurfaces for the principal permeabilities within the 3DDPP domain for Cases 13, 14, and 15. Figure 11 shows how the isosurface distribution changes with an increase in E_X for each principal permeability. The IVG isosurfaces gradually encroach on the IVL isosurfaces with an increase in E_X for k_Z . The maximum and minimum values of k_Z are positively proportional to E_X . This correlation indicates that k_Z is positively proportional to E_X within the entire 3DDPP domain.

However, the influences of E_X on k_X and k_Y seem to present diverse patterns depending on both the dip angle and pitch angle. First, the IVG and IVL isosurfaces encroach on each other with an increase in E_X for k_X and k_Y . The IVL isosurfaces encroach on the IVG isosurfaces along the lower pitch angle boundary, whereas the IVG isosurfaces invade the IVL isosurfaces along the upper dip angle boundary for k_X , as illustrated in

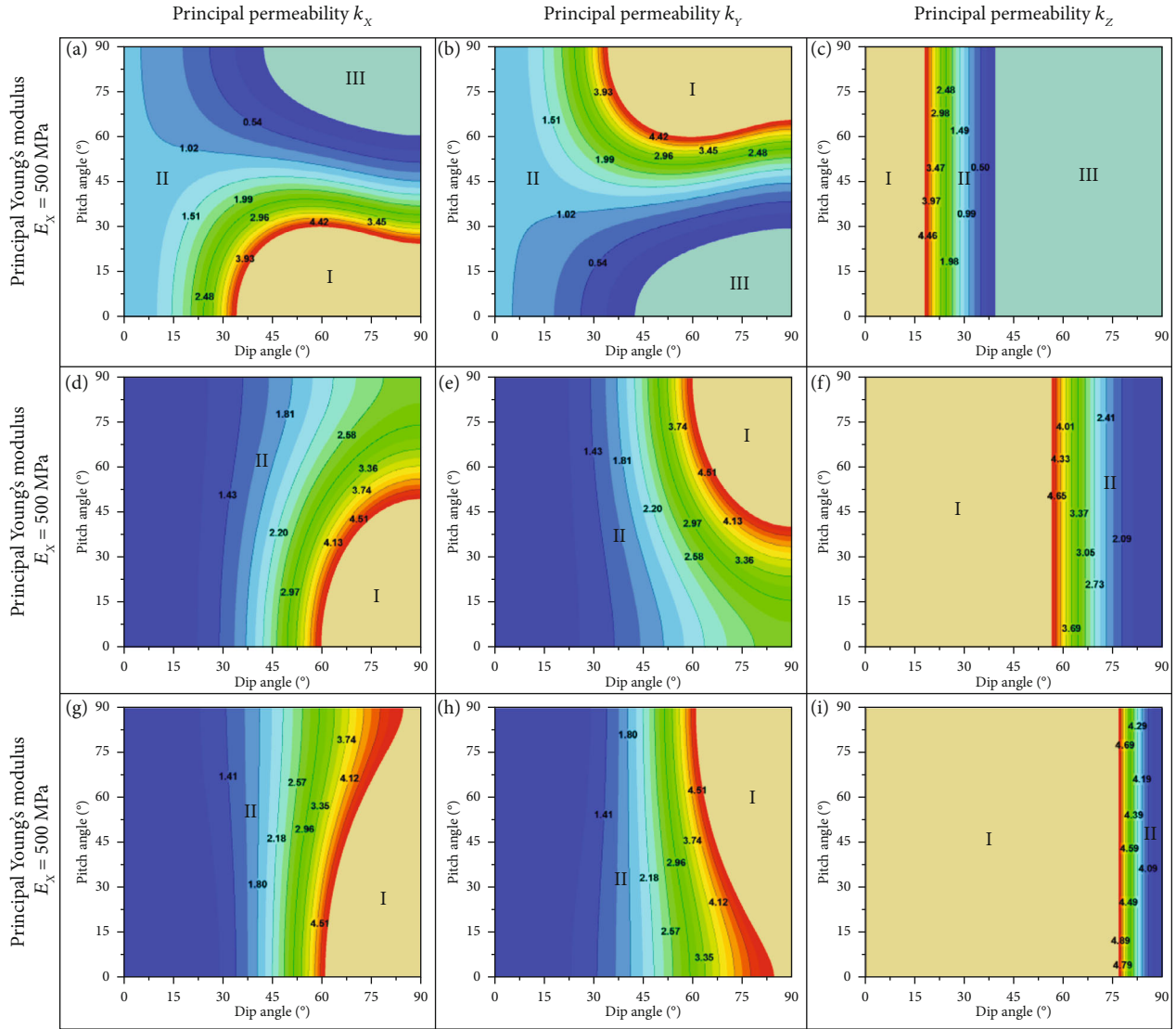


FIGURE 14: 2D contours showing distribution of rebound pressure within the 2DDP domain for Cases 13, 14, and 15. The images were plotted in the same manner as Figure 6.

Figures 11(a), 11(d), and 11(g). Similarly, for k_Y , the IVG isosurfaces encroach on the IVL isosurfaces along the upper dip angle boundary, whereas the IVL isosurfaces invade the IVG isosurfaces along the lower pitch angle boundary, as shown in Figures 11(b), 11(e), and 11(h). Second, the maximum and minimum values of both k_X and k_Y are not positively proportional to E_X . When E_X increases from 500 to 1700 MPa, the minimum values of k_X and k_Y increase, whereas their maximum values decrease. When E_X increases from 1700 to 3000 MPa, the minimum values of k_X and k_Y decrease, whereas their maximum values do not change. Finally, the normalized curves of k_X are plotted (Figure 12), showing the diverse patterns formed by the influences of E_X with a variation in the dip angle and pitch angle. The curves in Figure 12 indicate that the patterns showing the influences of E_X on k_X are independent of the pore pressure. The red

curves show that k_X increases monotonically with an increase in E_X . The green curves show that k_X decreases monotonically with an increase in E_X . The yellow curves indicate that k_X evolves nonmonotonically with an increase in E_X .

Because the patterns showing the influences of E_X on k_X and k_Y are dependent on the dip angle and pitch angle, the 2DDP domain can be divided according to these diverse patterns, as shown in Figure 13. Figures 13(a) and 13(b) indicate that k_X and k_Y evolve differently, showing diverse patterns, with an increase in E_X . These patterns include a monotonically increasing pattern, nonmonotonically evolving pattern with a maximum point, nonmonotonically evolving pattern with a minimum point, and monotonically decreasing pattern. Figure 13(c) shows that k_Z is positively proportional to E_X , and this pattern is independent of both the dip angle and pitch angle.

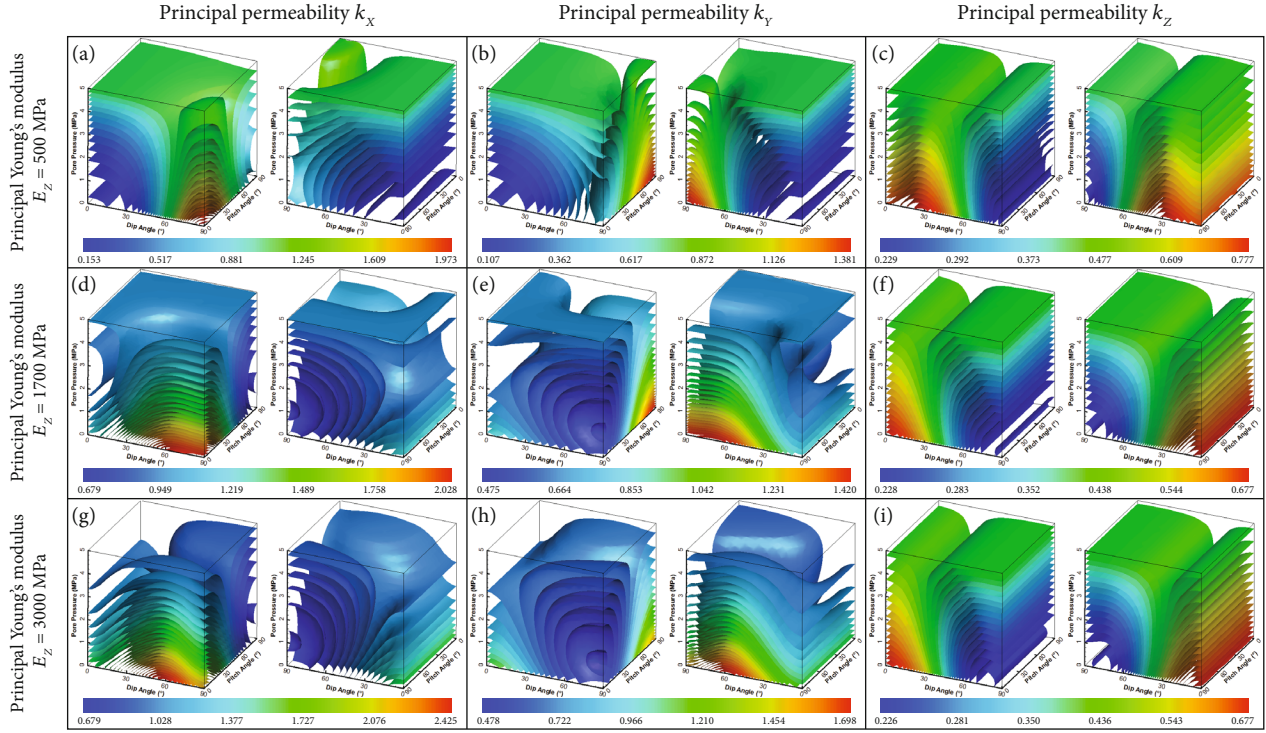


FIGURE 15: 3D isosurfaces showing principal permeabilities within the 3DDPP domain for Cases 16, 17, and 18. The color legends in these images have a uniform measurement unit of “millidarcy (mD).”

The variation in the principal permeabilities with a depletion in the pore pressure also shows a complex dependence on E_X because of the effects of the dip angle and pitch angle. Figure 14 shows how the rebound pressure varies with an increase in E_X . The rebound pressures of k_X and k_Y are dependent on E_X in diverse ways. Domains I and II encroach on each other with an increase in E_X for both k_X and k_Y . Domain I encroaches on Domain II along the right edge of the 2DDP domain. In this encroached domain, the k_X - p and k_Y - p curves change from nonmonotonically evolving ones to monotonically increasing ones with an increase in E_X . Domain II encroaches on Domain I along the bottom edge of the 2DDP domain for k_X and along the top edge of the 2DDP domain for k_Y . In this encroached domain, the k_X - p and k_Y - p curves change from monotonically increasing ones to nonmonotonically evolving ones with an increase in E_X . The images in the right column of Figure 14 show that the rebound pressure of k_Z is positively proportional to E_X in the entire 2DDP domain. Accordingly, Domain I always tends to encroach on Domains II and III with an increase in E_X for k_Z . This encroachment indicates that the k_Z - p curves tend to become positively proportional to E_X within the 2DDP domain.

When E_Z increases and E_X remains invariant, the normal effective stresses in the CCS are dependent on both E_X and E_Z . In this case, the influences of E_Z on the principal permeabilities cannot be seen visually from their representations. Figure 15 shows the principal permeabilities within the 3DDPP domain for Cases 16, 17, and 18. The

IVG isosurfaces gradually encroach on the IVL isosurfaces with an increase in E_Z for k_X and k_Y . This indicates that the magnitudes of k_X and k_Y seem to be positively proportional to E_Z within the entire 3DDPP domain. However, for k_Z , the IVL isosurfaces encroach on the IVG isosurfaces with an increase in E_Z . This indicates that the magnitudes of k_Z seem to be negatively proportional to E_Z within the 3DDPP domain.

Figure 16 shows that the rebound pressures of k_X and k_Y are positively proportional to E_Z . Accordingly, Domain I tends to encroach on Domains II and III with an increase in E_Z . This encroachment indicates that the k_X - p and k_Y - p curves tend to become positively proportional to E_Z . The images in the right column of Figure 16 show that the rebound pressure of k_Z is negatively proportional to E_Z in the entire 2DDP domain. Accordingly, Domain II tends to encroach on Domain I with an increase in E_Z . This indicates that the k_Z - p curves tend to become negatively proportional to E_Z .

A comparison of the modeling results for Groups 6 and 7 indicates that an increase in E_X or E_Z causes an increase in their respective normal principal permeabilities. However, the influences of E_X or E_Z on their respective parallel principal permeabilities are distinct. The variation in k_X and k_Y shows diverse patterns with a depletion in the pore pressure and an increase in E_X , and this variation depends on both the dip angle and pitch angle. The principal permeability k_Z is negatively proportional to E_Z , and this pattern of correlation is independent of both the dip angle and pitch angle.

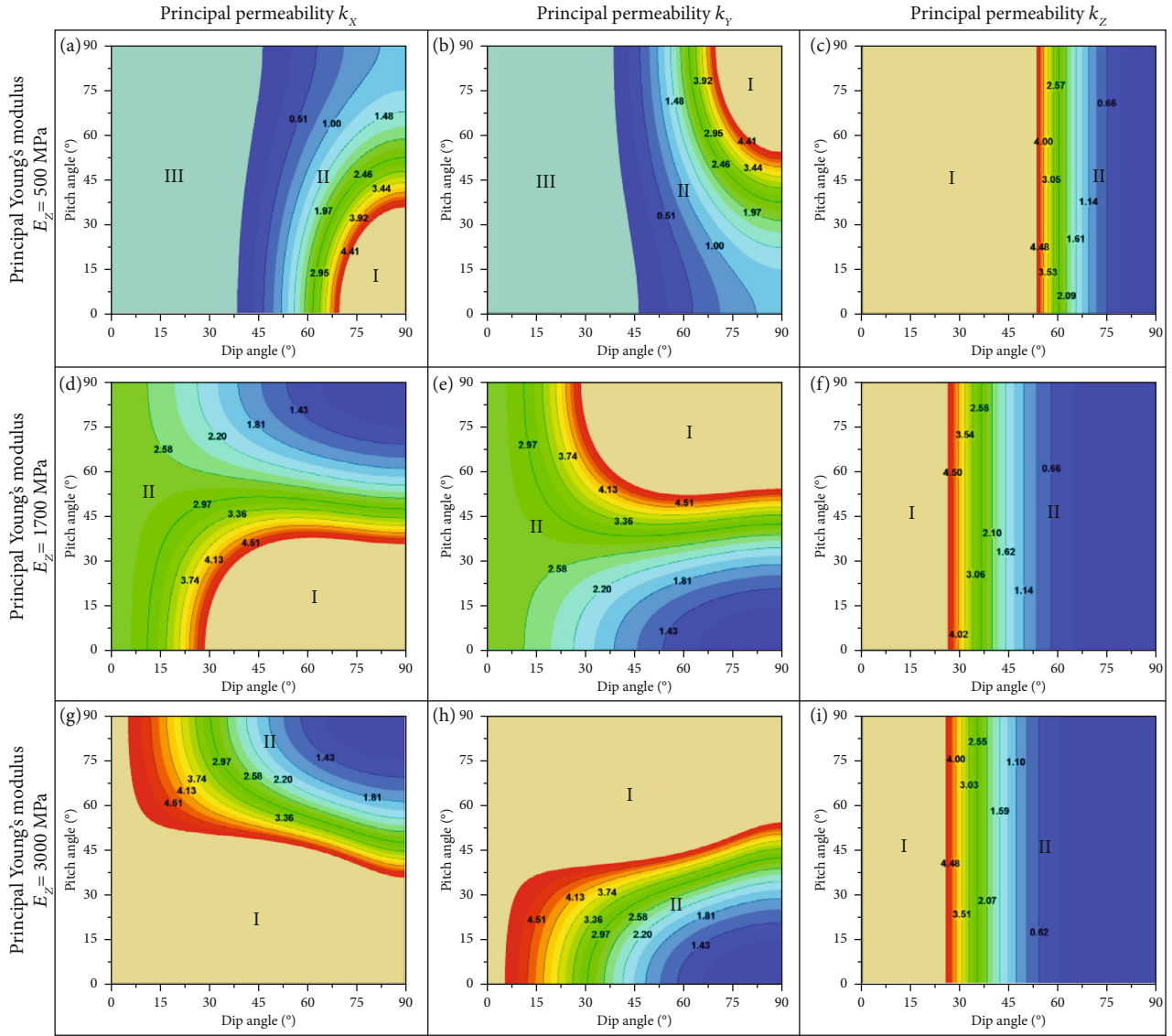


FIGURE 16: 2D contours showing distribution of rebound pressure within the 2DDP domain for Cases 16, 17, and 18. The images were plotted in the same manner as Figure 6.

4. Conclusions

In this study, 18 modeling cases were used to evaluate how the variation patterns of principal permeabilities during primary CBM recovery were influenced by three representative coal properties: the areal porosity, the internal swelling ratio, and Young’s modulus. Based on the study results, the following conclusions are drawn:

- (1) The correlation between the principal permeabilities and the areal porosities is complex and depends on the dependence of the principal permeabilities on pore pressure. The influences of the areal porosity on the principal permeabilities can be summarized as follows: an increase in cleat porosity reduces the sensitivity of each principal permeability to pore pressure change
- (2) The principal permeabilities thus tend to increase monotonically with a depletion in the pore pressure

when the internal swelling ratio increases. Because the internal swelling ratio represents the extent of gas-sorption-induced matrix deformation, an increase in the internal swelling ratio increases desorption-induced matrix shrinkage and thus induces an increase in permeability

- (3) The principal permeabilities are positively proportional to the isotropic principal Young moduli and the synchronously changing anisotropic principal Young moduli. An increase in the principal Young modulus E_x or E_z causes an increase in their respective normal principal permeabilities. However, the influences of E_x or E_z on their respective parallel principal permeabilities are distinct

Data Availability

There is no experimental data in this manuscript.

Conflicts of Interest

The authors declare that they have no conflicts of interest.

Acknowledgments

The authors gratefully acknowledge the support of the National Natural Science Foundation of China (51804312, 51704184, and 51874314), the State Key Laboratory Cultivation Base for Gas Geology and Gas Control (WS2019A03), and the Fundamental Research Funds for the Central Universities (2021YQAQ01).

References

- [1] T. Moore, "Coalbed methane: a review," *International Journal of Coal Geology*, vol. 101, pp. 36–81, 2012.
- [2] R. Rogers, *Coalbed Methane: Principles and Practices*, PTR Prentice Hall, New Jersey, 1994.
- [3] K. Wang, J. Zang, G. D. Wang, and A. T. Zhou, "Anisotropic permeability evolution of coal with effective stress variation and gas sorption: model development and analysis," *International Journal of Coal Geology*, vol. 130, pp. 53–65, 2014.
- [4] J. S. Liu, Z. W. Chen, D. Elsworth, H. Y. Qu, and D. Chen, "Interactions of multiple processes during CBM extraction: a critical review," *International Journal of Coal Geology*, vol. 87, no. 3–4, pp. 175–189, 2011.
- [5] Z. J. Pan and L. Connell, "Modelling permeability for coal reservoirs: a review of analytical models and testing data," *International Journal of Coal Geology*, vol. 92, pp. 1–44, 2012.
- [6] H. B. Zhang, J. S. Liu, and D. Elsworth, "How sorption-induced matrix deformation affects gas flow in coal seams: a new FE model," *International Journal of Rock Mechanics and Mining Sciences*, vol. 45, no. 8, pp. 1226–1236, 2008.
- [7] J. Zang and K. Wang, "A numerical model for simulating single-phase gas flow in anisotropic coal," *Journal of Natural Gas Science and Engineering*, vol. 28, pp. 153–172, 2016.
- [8] J. Zang, K. Wang, and Y. X. Zhao, "Evaluation of gas sorption-induced internal swelling in coal," *Fuel*, vol. 143, pp. 165–172, 2015.
- [9] L. Connell, M. Lu, and Z. J. Pan, "An analytical coal permeability model for tri-axial strain and stress conditions," *International Journal of Coal Geology*, vol. 84, no. 2, pp. 103–114, 2010.
- [10] J. Zang and K. Wang, "Gas sorption-induced coal swelling kinetics and its effects on coal permeability evolution: model development and analysis," *Fuel*, vol. 189, pp. 164–177, 2017.
- [11] Z. W. Chen, J. S. Liu, Z. J. Pan, L. Connell, and D. Elsworth, "Influence of the effective stress coefficient and sorption-induced strain on the evolution of coal permeability: model development and analysis," *International Journal of Greenhouse Gas Control*, vol. 8, pp. 101–110, 2012.
- [12] X. J. Cui and R. Bustin, "Volumetric strain associated with methane desorption and its impact on coalbed gas production from deep coal seams," *AAPG Bulletin*, vol. 89, no. 9, pp. 1181–1202, 2005.
- [13] P. Guo, Y. Cheng, K. Jin, W. Li, Q. Tu, and H. Liu, "Impact of effective stress and matrix deformation on the coal fracture permeability," *Transport in Porous Media*, vol. 103, no. 1, pp. 99–115, 2014.
- [14] J. S. Liu, Z. W. Chen, D. Elsworth, X. X. Miao, and X. B. Mao, "Evolution of coal permeability from stress-controlled to displacement-controlled swelling conditions," *Fuel*, vol. 90, no. 10, pp. 2987–2997, 2011.
- [15] S. M. Liu and S. Harpalani, "Permeability prediction of coalbed methane reservoirs during primary depletion," *International Journal of Coal Geology*, vol. 113, pp. 1–10, 2013.
- [16] S. E. Laubach, R. A. Marrett, J. E. Olson, and A. R. Scott, "Characteristics and origins of coal cleat: a review," *International Journal of Coal Geology*, vol. 35, no. 1–4, pp. 175–207, 1998.
- [17] J. R. Fanchi, "Directional permeability," *SPE Reservoir Evaluation & Engineering*, vol. 11, pp. 565–568, 2006.
- [18] P. S. Lang, A. Paluszny, and R. W. Zimmerman, "Permeability tensor of three-dimensional fractured porous rock and a comparison to trace map predictions," *Journal of Geophysical Research: Solid Earth*, vol. 119, no. 8, pp. 6288–6307, 2014.
- [19] J. Zang, Y. Ge, and K. Wang, "The principal permeability tensor of inclined coalbeds during pore pressure depletion under uniaxial strain conditions: developing a mathematical model, evaluating the influences of featured parameters, and upscaling for CBM recovery," *Journal of Natural Gas Science and Engineering*, vol. 74, p. 103099, 2020.
- [20] X.-P. Zhou, Y.-D. Shou, Q.-H. Qian, and M.-H. Yu, "Three-dimensional nonlinear strength criterion for rock-like materials based on the micromechanical method," *International Journal of Rock Mechanics and Mining Sciences*, vol. 72, pp. 54–60, 2014.
- [21] X. P. Zhou, Y. X. Zhang, Q. L. Ha, and K. S. Zhu, "Micromechanical modelling of the complete stress-strain relationship for crack weakened rock subjected to compressive loading," *Rock Mechanics and Rock Engineering*, vol. 41, no. 5, pp. 747–769, 2008.
- [22] I. Palmer and J. Mansoori, "How permeability depends on stress and pore pressure in coalbeds: a new model," *SPE Reservoir Evaluation & Engineering*, vol. 1, no. 6, pp. 539–544, 1998.
- [23] Z. Pan, *Modeling of Gas Adsorption Using Two-Dimensional Equations of State*, Oklahoma State University, Ann Arbor, 2003.
- [24] S. M. Liu, S. Harpalani, and M. Pillalamarry, "Laboratory measurement and modeling of coal permeability with continued methane production. Part 2. Modeling results," *Fuel*, vol. 94, pp. 117–124, 2012.
- [25] Z. J. Pan and L. Connell, "Modelling of anisotropic coal swelling and its impact on permeability behaviour for primary and enhanced coalbed methane recovery," *International Journal of Coal Geology*, vol. 85, no. 3–4, pp. 257–267, 2011.
- [26] B. Gash, R. Volz, G. Potter, and J. Corgan, *The Effects of Cleat Orientation and Confining Pressure on Cleat Porosity, Permeability and Relative Permeability in Coal*, the SPWLA/SCA Symposium, Oklahoma City, 1992.
- [27] Z. Wang, J. Pan, Q. Hou, B. Yu, M. Li, and Q. Niu, "Anisotropic characteristics of low-rank coal fractures in the Fukang mining area, China," *Fuel*, vol. 211, pp. 182–193, 2018.
- [28] S. Harpalani and R. Schraufnagel, "Shrinkage of coal matrix with release of gas and its impact on permeability of coal," *Fuel*, vol. 69, no. 5, pp. 551–556, 1990.
- [29] J. Levine, "Model study of the influence of matrix shrinkage on absolute permeability of coal bed reservoirs," *Geological Society Special Publication*, vol. 109, no. 1, pp. 197–212, 1996.

- [30] S. Liu, Y. Wang, and S. Harpalani, "Anisotropy characteristics of coal shrinkage/swelling and its impact on coal permeability evolution with CO₂ injection," *Greenhouse Gases: Science and Technology*, vol. 6, no. 5, pp. 615–632, 2016.
- [31] J. Q. Shi and S. Durucan, "Drawdown induced changes in permeability of coalbeds: a new interpretation of the reservoir response to primary recovery," *Transport in Porous Media*, vol. 56, no. 1, pp. 1–16, 2004.
- [32] J. Q. Shi, S. Durucan, and S. Shimada, "How gas adsorption and swelling affects permeability of coal: a new modelling approach for analysing laboratory test data," *International Journal of Coal Geology*, vol. 128–129, pp. 131–139, 2014.

Research Article

Variation Law of Infrared Radiation Temperature of Unloading Fracture of Composite Coal-Rock

Xin Li , Xue Wang , Zhen Yang , Hao Li , Yan Li , and Weiman Sun 

Faculty of Electrical and Control Engineering, Liaoning Technical University, Huludao 125105, China

Correspondence should be addressed to Xue Wang; 1016238726@qq.com

Received 1 June 2021; Accepted 16 July 2021; Published 14 August 2021

Academic Editor: Feng Du

Copyright © 2021 Xin Li et al. This is an open access article distributed under the Creative Commons Attribution License, which permits unrestricted use, distribution, and reproduction in any medium, provided the original work is properly cited.

For composite mining coal-rock dynamic disaster, combining the theory of thermodynamics, damage mechanics, and other disciplines, the thermodynamic coupling mathematical model of composite coal-rock under an unloading condition is deduced, and the simulation model of composite coal-rock is established for numerical simulation. And the variation law of thermal infrared radiation under triaxial loading and unloading of composite coal-rock is analyzed and verified by experiments. The results show the following findings: (1) The distribution of thermal infrared radiation temperature of composite coal-rock is different in different stages of stress. The overall temperature of the temperature field is lower than the initial temperature field in the three-dimensional stress loading stage and the stage of stress-keeping pressure, but the internal temperature of the coal body is the highest. In the first stage of “loading and unloading,” the temperature of a coal seam increases slightly, and the temperature of other parts of the rock layer increases except for the circular low-temperature zone. In the second stage of “loading and unloading,” an alternating zone of high and low temperatures appears in the rock mass, and the temperature field is enhanced, among which the temperature field reaches the strongest after unloading the confining pressure. After jumping over the maximum stress, the temperature field decreases as a whole at the instability and rupture stage. (2) The variation of surface average thermal infrared radiation temperature (T_{ave}) of composite coal-rock can be divided into the initial fluctuation stage, the linear heating stage, the local decline stage, the temperature sudden increase stage, and the fracture decline stage. At three different unloading rates of 0.003 MPa/s, 0.03 MPa/s, and 0.05 MPa/s, the T_{ave} of coal body, floor rock, and roof rock reach the maximum before composite coal-rock instability and fracture, and the temperature change of the coal body is the most obvious. (3) Under different confining pressure unloading rates, the T_{ave} of roof rock, coal body, and floor rock shows a strong linear relationship with stress after linear fitting. And the correlation between simulation and experimental results after fitting is above 0.89. The larger the confining pressure unloading rate is, the shorter the peak time of T_{ave} arrives, and the larger the peak value. The comparison between the experimental results and the simulation analysis shows that the two results are consistent, and the research results can provide a theoretical basis for the prevention and control of dynamic disasters in coal and rock mining.

1. Introduction

With the increasing depth of coal mining, coal and rock dynamic disasters such as coal and gas outburst and rock burst are becoming more and more serious [1]. Reference [2] shows that nearly half of coal mine disasters in China have been found to occur in groups or accompanied by nearby earthquakes, and all types of disasters are involved. The stress disturbance appears to exist between mining areas. The process of coal mining is an unloading process essentially. This mechanical process will cause a lot of thermal infrared radiation and temperature

change in coal and rock mass [3–6]. At the same time, the temperature change during the mining process will further affect the physical parameters and mechanical properties of the material, thus making the actual unloading process more complex. At present, most studies on the mechanical properties of coal and rock are carried out under uniaxial loading conditions. Reference [7] studied the brittle failure model of coal-rock composites under uniaxial compression through laboratory tests and numerical simulation. Reference [8] analyzed stress characteristics and mechanical properties and compared the similarities and differences of composite coal mass with soft

and hard coal mass in deformation and failure characteristics. Moreover, the mechanical properties and deformation and failure laws of the composite coal mass under unidirectional loading were investigated. Reference [9] studied the mechanical properties of coal-like rocks and the law of damage evolution under different loading rates. The results show that the higher the loading rate, the earlier the specimen enters the stage of stable development of damage. In [10], the particle flow method was used to establish the composite model of coal and rock with different inclination angles, and the impact instability characteristics after unloading were analyzed.

Relevant results at home and abroad show that by studying the distribution and variation rule of thermal infrared radiation in composite coal-rock, the dynamic disaster of coal and rock can be effectively predicted [11–14]. Reference [15, 16] used an infrared thermal imager to conduct a simulation test on the failure process of rock strata caused by excavation, and found that infrared radiation temperature can reflect the change of rock strata stress at different depths, while an infrared thermal image can reflect the failure process of rock mass. Reference [17] believes that infrared precursors are mainly manifested as infrared thermography and average infrared radiation temperature anomaly. Reference [18] carried out the infrared radiation observation test on the stress disaster of granite, studied the mechanism of the infrared anomaly phenomenon before the earthquake, and found that the infrared radiation temperature on the outer surface of the rock also changed with the constant change of the stress. Reference [19] carried out uniaxial compression loading tests on aqueous concrete samples, and tested and studied the variation characteristics of infrared radiation temperature, infrared thermography, and acoustic emission, as well as the precursor information of fracture. Reference [20] used infrared thermal imaging technology to study the changes in infrared radiation during coal-rock deformation. The research showed that the infrared radiation temperature on the coal and rock surface would be changed with the increase of the loadings. There was a stage differential in infrared radiation temperature variation in the cracking-developed zone, stress-concentrated area, and broken zone. Reference [21] carried out an observation test of infrared radiation characteristics in the process of loading failure of coal samples, discussed the infrared precursor information of instability failure of coal samples with different bursting liabilities, and obtained the infrared radiation temperature precursor characteristics of coal samples under the condition of no flushing, weak flushing, and strong flushing. Reference [22] monitored the change of an infrared radiation temperature field in surrounding rock of a roadway through infrared radiation technology, and verified that the radiation temperature field had a good corresponding relationship with roadway failure characteristics. Reference [23] found that infrared radiation changes would occur along with stress adjustment in the process of mechanical fracture of coal and rock. Reference [24] quantitatively analyzed the characteristic parameters of infrared radiation temperature and the evolution law of coal and rock damage in the process of coal and rock loading. Reference [25] studied the internal

infrared radiation temperature change law of composite coal-rock under load. The results show that the composite coal-rock has thermoelastic effects and thermal friction effects during the loading process. In addition, the heat generated by the displacement and friction between the fissure surfaces of the coal is significantly higher than the heat generated by the thermoelastic effect, and the thermoelastic effect in the rock mass plays a leading role. Reference [26] found that the thermal infrared radiation temperature temporal evolution in the process of a fracture of coal and rock can be divided into four stages, namely, the T_{ave} calm stage, the T_{ave} slight fluctuation stage, the T_{ave} rapid increase stage, and the T_{ave} rapid decrease stage, which accurately described the infrared radiation law of coal and rock under uniaxial loading and unloading state. Reference [27] found in their study that the infrared radiation precursor of coal-rock fracture and instability showed a trend of step and type spurt upward. In summary, predecessors have studied the characteristics of thermal infrared radiation temperature and precursor laws of coal and rock under uniaxial loading, but there are few related studies on unloading failure of deep coal and rock mass.

Based on the above research results, related scholars have carried out related research on unloading fracture of coal and rock and multifield coupling research. However, there are few studies on the thermal-mechanical coupling mechanism of anisotropic coal and rock masses, and the research on thermal infrared radiation under the condition of triaxial unloading of composite coal-rock is not thorough enough. Reference [28] conducted a three-axis unloading compression test based on the pressure path of the underground engineering excavation. The research results show that the infrared radiation characteristics of rock specimens under different intermediate principal stresses are different, revealing that as the intermediate principal pressure increases, the failure mode of the rock is also different. Reference [29] conducted conventional triaxial compression (CTC) tests on the gas-bearing coal, gas-bearing coal-mudstone combination, and gas-bearing coal-sandstone combination using the RLW-500G triaxial experimental system. Reference [30] conducted laboratory tests under two stress paths, namely, conventional triaxial compression and prepeak unloading confining pressure, in order to explore the failure mechanism of the unloading side of coal roadway excavation, and analyzed its mechanical characteristics. According to the damage and failure law, the results show that under the unloading stress path, the coal body failure is a composite state in which shear failure is the main part, but there is still partial split failure. Based on the unloading mechanics path of the fixed axial displacement and the unloading surrounding pressure, the study on the damage features during the unloading process was conducted on the reconstituted coal with high plasticity with CT value, CT damage, and CT image of each scanning layer obtained from CT imaging experiments [31]. Reference [32] established a temperature-stress numerical coupling model of rock at high temperature, carried out numerical simulation on the evolution law of the temperature field and fracture field of overburden rock in a combustion cavity under the temperature-stress coupling condition, and studied the

relationship between stress and temperature in the state of rock thermal damage. Reference [33] carried out physical experiments and numerical simulations on the system instability faults of gas coal-bearing rock under different circumstances, comprehensively analyzed the multiphysical coupling mechanism of gas coal-bearing rock damage and the occurrence conditions of outbreak-rock coupling dynamic disaster, and improved the understanding of the mechanism of outbreak-rock coupling dynamic disaster. Reference [34] conducted an unloading coal and rock destruction experiment under the multiphase coupling action of water, force, and heat. By optimizing the noise reduction and the infrared radiation information of three-dimensional fusion, the three-dimensional infrared radiation field was reconstructed. And by considering the surface damage characteristics, the three-dimensional infrared radiation field and simulation software results reveal the spatiotemporal evolution of the infrared radiation information of the unloading damage of composite coal-rock, and realize the noncontact prediction of coal and rock dynamic disasters. Reference [35] proposed a thermal-mechanical coupling method for large-volume concrete on the inner wall of deep wells, considering various boundary conditions such as internal heat source, external cold source, plastic plate friction constraint, overlying shaft wall load, and formation lateral pressure. The early temperature-stress field evolution characteristics of the inner wall of the deep frozen wellbore were obtained, and the high-risk areas prone to early temperature cracks were determined. The abovementioned research results have made a very useful exploration of thermal infrared radiation precursors before unloading and rupture of coal and rock, and laid the foundation for subsequent research.

In summary, a large number of coal and rock mining dynamic disaster events show that before the occurrence of dynamic disaster events, there will be various degrees of precursor information, such as changes in stress and strain, temperature, and acoustic emission. By monitoring the changing trends and abnormal values of these signals, it is possible to provide effective early warning of shock disaster hazards, and timely effective control measures can be taken to reduce the casualties and equipment damage caused by rock shock disasters, which has engineering application prospects. However, most of the current researches on the prediction and prediction of coal and rock mining dynamic disasters are based on uniaxial conditions, which is far from the actual three-axis mining situation. The research on the infrared radiation temperature law based on the three-axis unloading condition needs to be in-depth. There is still much room for improvement in analyzing the unloading rupture mechanism from the perspective of multiphysics coupling. There are few studies on the thermodynamics of anisotropic coal and rock masses. Aiming at the problem of effectively predicting and forecasting coal and rock mining dynamic disasters, this paper intends to study not only the distribution of thermal infrared radiation temperature during the unloading and fracture process of anisotropic composite coal-rock, but also the relationship between thermal infrared radiation and stress on the surface of composite coal-rock and its changing law based on thermodynamics and damage mechanics. Joint early-warning simulations and experiments

on coal and rock instability through multiphysics fields to explore the characteristics of infrared radiation temperature changes and coal and rock rupture precursor laws have important theoretical significance for the development of coal and rock mining dynamic disaster prediction and forecast.

2. Materials and Methods

2.1. Thermal-Mechanical Coupling Model of Composite Coal-Rock Unloading. According to the Stefan-Boltzman Law, the thermal infrared radiation energy of the coal and rock surface is proportional to the power of the physical temperature and emittance. When the material type and surface finish of coal-rock are constant, the thermal infrared radiation intensity received by the surface is only related to the physical temperature of coal-rock [26]. Therefore, during the loading-unloading process, when the thermal infrared radiation intensity of the composite coal-rock under the action of stress changes, the reason is that the external stress causes the change of the thermal field of the coal-rock, which leads to the alienation of the temperature field of thermal infrared radiation on the surface of the coal-rock. This thermal change is actually a thermodynamic coupling effect, in which the thermal stress will produce thermal damage and other effects and accelerate the instability failure of the coal and rock mass [36].

According to the Elastic Damage Theory, the equivalent elastic modulus E of coal-rock after damage can be expressed as follows:

$$E = (1 - D)E_0, \quad (1)$$

where E_0 is the initial elastic modulus before damage; D is the damage variable, which is used to describe the damage degree and evolution of coal-rock under the action of external load.

Taking the interior elements of coal and rock mass as the research object, the magnitude of the three principal stresses in the loading-unloading process is not zero [37], which conforms to the generalized Hooke law on the whole. The principal strain equation is as follows:

$$\begin{cases} \varepsilon_x = \frac{1}{E} [\sigma_x - \mu(\sigma_y + \sigma_z)], \\ \varepsilon_y = \frac{1}{E} [\sigma_y - \mu(\sigma_x + \sigma_z)], \\ \varepsilon_z = \frac{1}{E} [\sigma_z - \mu(\sigma_x + \sigma_y)], \end{cases} \quad (2)$$

where ε_i ($i = x, y, z$) is the principal strain; E is the elastic modulus; σ_i ($i = x, y, z$) is the principal stress; μ is the Poisson ratio.

The shear strain equation is as follows:

$$\begin{cases} \gamma_{xy} = \frac{1}{G} \tau_{xy} = \frac{2(1 + \mu)}{E} \tau_{xy}, \\ \gamma_{yz} = \frac{1}{G} \tau_{yz} = \frac{2(1 + \mu)}{E} \tau_{yz}, \\ \gamma_{zx} = \frac{1}{G} \tau_{zx} = \frac{2(1 + \mu)}{E} \tau_{zx}, \end{cases} \quad (3)$$

where γ_{ii} ($ii = xy, yz, zx$) is the shear stress; τ_{ii} ($ii = xy, yz, zx$) is the shear strain; $G = E/(2(1 + \mu))$ is the Lamé constant.

Equation (2) and equation (3) jointly express the stress-strain relationship of composite coal-rock under unloading conditions. In a three-dimensional elastic system, strain can be characterized by principal strain and shear strain components. According to the principles of thermodynamics and reference [38], the relationship between temperature changes and strains of each component of the composite coal-rock is further deduced as follows:

$$\Delta T = \frac{T_0 V}{C} \left(\sum \beta \varepsilon_i + \sum \beta \tau_{ii} \right), \quad (4)$$

where T_0 is the initial temperature of different components of the composite coal-rock ($^{\circ}\text{C}$); V is the volume of the different components of the composite coal-rock (m^3); C is the specific heat capacity of the different components of the composite coal-rock ($\text{J}/(\text{kg}\cdot\text{K})$); $\beta = (\partial \sigma_i / \partial T_0)_{\varepsilon}$, ($i = x, y, z$) or $(\partial \tau_{ii} / \partial T_0)_{\varepsilon}$, ($ii = xy, yz, zx$) is the thermal stress coefficient.

Then, the temperature field T of different components of composite coal-rock at any time is as follows:

$$T = T_0 + \Delta T. \quad (5)$$

Substitute equation (1), equation (2), and equation (3) into equation (4). And according to equation (5), the specific relationship between temperature field and strain of each component of composite coal-rock can be obtained as follows:

$$T = T_0 \left\{ \left(1 + \frac{V}{C} \right) \left[\frac{(1-2\mu)}{(1-D)E_0} (\beta_x \sigma_x + \beta_y \sigma_y + \beta_z \sigma_z) + \frac{(1-D)E_0}{(1-2\mu)} (\beta_{xy} \sigma_{xy} + \beta_{yz} \sigma_{yz} + \beta_{zx} \sigma_{zx}) \right] \right\}. \quad (6)$$

In order to establish the thermodynamic coupling model, the heat conduction equation should be added to determine the distribution of temperature field T in composite coal-rock. According to the principle of heat balance in thermodynamics, it is assumed that the specific heat capacity C and thermal conductivity λ_i ($i = x, y, z$) of composite coal-rock are constants that do not change with temperature. Introduce the solid three-dimensional anisotropic heat conduction differential equation [39] to describe the internal temperature field of composite coal-rock. The specific differential equation is as follows:

$$\frac{\partial T}{\partial t} = \frac{f(t)}{\rho C} \left[\frac{\partial}{\partial x} \left(\lambda_x \frac{\partial T}{\partial x} \right) + \frac{\partial}{\partial y} \left(\lambda_y \frac{\partial T}{\partial y} \right) + \frac{\partial}{\partial z} \left(\lambda_z \frac{\partial T}{\partial z} \right) \right], \quad (7)$$

where ρ is the density of material (kg/m^3); λ_x , λ_y , and λ_z are the thermal conductivity coefficients of the material in three directions ($\text{W}/(\text{m}\cdot\text{K})$); $f(t)$ is the rate of heat release.

However, when coal and rock are damaged under external force, the damage will lead to the increase of thermal conductivity and specific heat capacity of coal-rock. It is assumed that the influence of damage D on the specific heat capacity C and thermal conductivity λ_i ($i = x, y, z$) of composite coal-rock meets the following functional relationship [40]:

$$\begin{aligned} C &= C_0 e^{D/\alpha_C}, \\ \lambda_i &= \lambda_0 e^{D/\alpha_{\lambda_i}}, \end{aligned} \quad (8)$$

where C_0 and C are the specific heat capacity of composite coal-rock of different components before and after damage ($\text{J}/(\text{kg}\cdot\text{K})$). λ_0 and λ_i ($i = x, y, z$) are the thermal conductivity before and after damage of coal and rock of different components ($\text{W}/(\text{m}\cdot\text{K})$). α_C and α_{λ_i} are the influence coefficients of damage on the specific heat capacity and thermal conductivity of different components of composite coal-rock, respectively.

By substituting equation (8) into equation (6) and equation (7), the temperature of different components of composite coal-rock and the instantaneous temperature of each point in coal and rock can be calculated. The average infrared radiation temperature (T_{ave}) refers to the average value of the infrared radiation temperature corresponding to each point on the coal and rock surface at a certain moment, which reflects the variation characteristics of the infrared radiation temperature field on the coal and rock surface on the whole [25]. The specific equation is as follows:

$$T_{\text{ave}} = \frac{1}{n} \sum_{i=1}^n T_i, \quad (9)$$

where T_i is the radiation temperature of the i th point in the temperature field ($^{\circ}\text{C}$). T_{ave} is the average of T_i ($^{\circ}\text{C}$). n is the number of selected composite coal-rock points.

To sum up, the coupling mathematical model of the thermal infrared radiation temperature field and the stress field in the process of unloading and fracture of composite coal-rock is as follows:

$$\begin{cases} T = T_0 \left\{ \left(1 + \frac{V}{C_0 e^{D/\alpha_C}} \right) \left[\frac{(1-2\mu)}{(1-D)E_0} (\beta_x \sigma_x + \beta_y \sigma_y + \beta_z \sigma_z) + \frac{(1-D)E_0}{(1-2\mu)} (\beta_{xy} \sigma_{xy} + \beta_{yz} \sigma_{yz} + \beta_{zx} \sigma_{zx}) \right] \right\}, \\ \frac{\partial T}{\partial t} = \frac{\lambda_0 f(t)}{\rho C_0 e^{D/\alpha_C}} \left[\frac{\partial}{\partial x} \left(e^{\frac{D}{\alpha_{\lambda_x}}} \frac{\partial T}{\partial x} \right) + \frac{\partial}{\partial y} \left(e^{\frac{D}{\alpha_{\lambda_y}}} \frac{\partial T}{\partial y} \right) + \frac{\partial}{\partial z} \left(e^{\frac{D}{\alpha_{\lambda_z}}} \frac{\partial T}{\partial z} \right) \right], \\ T_{\text{ave}} = \frac{1}{n} \sum_{i=1}^n T_i. \end{cases} \quad (10)$$

2.2. Simulation Model of Composite Coal-Rock Unloading. FLAC^{3D} software is used to establish a standard cylindrical composite coal-rock 3D model with the size of $\Phi 50 \text{ mm} \times 100 \text{ mm}$. The ratio of component rock-coal-rock is 1 : 1 : 1. The physical parameters of the top slate and the bottom slate in the model are the same. The model is generally divided into 79200 units and 80,581 nodes. The constitutive relation of the three-dimensional composite coal-rock model in the mechanical mode is set as the commonly used Mohr-Coulomb Plastic Model [41], and the constitutive model in the thermal mode is the anisotropic heat conduction model. The material property parameters of the simulation model are shown in Table 1.

According to the ‘‘Coal Mine Safety Regulations,’’ the working surface temperature does not exceed 26°C [42], and the temperature conditions are those that can be achieved by indoor experiments. Set the initial temperature and ambient temperature of the composite coal-rock simulation model in thermal mode to room temperature 20°C. The steps of the three-axial load-unloading simulation in the mechanical mode are as follows: (1) Apply fixed constraints and axial stress to the top and bottom of the model, and apply 10 MPa confining pressure. (2) Keep the confining pressure constant, and load at a displacement rate of 0.05 mm/min. (3) Record the stress loading curve until the composite coal-rock fracture, and record the peak stress intensity. (4) Under the simulation conditions in steps (1) and (2), triaxial loading is carried out again. When the stress reaches 80% of the peak intensity recorded in step (3), under the condition of ensuring that the simulation results are not distorted, three commonly used slow unloading confining pressure rates of 0.003 MPa/s, 0.03 MPa/s, and 0.05 MPa/s [43, 44] are selected for unloading simulation until the composite coal and rock rupture, and the simulation ends.

3. Results and Discussion

3.1. Simulation Research

3.1.1. Distribution Law of Thermal Infrared Radiation Temperature. In order to better study the relationship between the unloading fracture mechanics stage of coal-rock and its infrared radiation temperature, the stress change process must first be clarified. The stress-time (σ - t) curve of triaxial loading-unloading under the unloading rate of 0.05 MPa/s confining pressure is shown in Figure 1. It is divided into five stages. OA is the three-dimensional stress loading stage. At this stage, due to the combined action of axial pressure and confining pressure, the primary voids and tiny cracks in the composite coal are gradually compacted, and the internal structure begins to change. This stage is similar to the compaction stage in uniaxial loading. AB is the stage of stress-keeping pressure. This stage is a process in which the axial pressure and the confining pressure resist each other, and the axial pressure presents a nonlinear change. BC is the first stage of ‘‘loading-unloading,’’ which is elastic. The stress shows a linear increase trend. CD is the second stage of ‘‘loading-unloading,’’ which is the process of converting elasticity to plasticity. The stress at this stage shows a transition from linear to nonlinear. DE is the instability and rupture stage. After unloading the confining

TABLE 1: Physical parameters of materials.

Physical parameters	Coal	Rock
Bulk modulus (GPa)	1	4.5
Shear modulus (GPa)	0.8	3
Cohesion (MPa)	1	2.5
Tensile strength (MPa)	1	2
Density (kg/m^3)	1450	2400
Specific heat capacity ($\text{J}/(\text{kg}\cdot\text{K})$)	1200	920
Thermal expansion coefficient ($^{\circ}\text{C}$)	6.435×10^{-6}	3.9×10^{-5}
Thermal conductivity ($\text{W}/(\text{m}\cdot\text{K})$)	0.258	3.081

pressure at a rate of 0.05 MPa/s at 142.5 s, until the peak stress at point D reaches the maximum value of 45.45 MPa, the composite coal-rock fractures, the curve drops rapidly, and the simulation ends.

In the simulation process, there is no need to slice the composite coal-rock simulation model, that is, the distribution of T_{ave} can be observed through the overall infrared radiation temperature distribution cloud map. Figure 2 is a cloud map of the overall infrared radiation temperature distribution of the composite coal-rock under the confining pressure unloading at a rate of 0.05 MPa/s. At each stage of stress and after unloading the confining pressure, a time point is selected for analysis at 25 s, 60 s, 90 s, 130 s, 146 s, and 175 s, respectively. It can be seen from Figure 2 that the temperature distribution is different at different stages. However, due to the coal body’s low density and low thermal conductivity, it has a large degree of force deformation and high-temperature accumulation. But the coal body has slow heat transfer and small temperature changes, and finally presents the characteristics of high-temperature distribution in the coal body.

From the perspective of different stages, the overall temperature of the temperature field during the three-dimensional stress loading (Figure 2(a)) and stress-keeping pressure stage (Figure 2(b)) is lower than the initial temperature. In the first stage of ‘‘loading-unloading’’ (Figure 2(c)), as the effect of axial stress becomes more obvious, the temperature of the coal body rises slightly. Except for the circular low-temperature zone, the temperature of the rest of the rock formation increases. In the second stage of ‘‘loading-unloading’’ (Figure 2(d)), the high-temperature area of the coal body spreads up and down on both sides of the rock mass. And the temperature field of part of the rock mass is significantly enhanced compared with the previous stage, and there is an alternating phenomenon of high- and low-temperature regions in the lateral direction. After the confining pressure is relieved (Figure 2(e)), the temperature distribution of the temperature field expands according to the trend of the previous stage, and the temperature field reaches the strongest. After jumping over the highest point of stress, the coal-rock loses stability and ruptures, and the temperature field decreases during the instability and rupture stage (Figure 2(f)).

3.1.2. Changes of Thermal Infrared Radiation Temperature and Stress

(1) *Study on Different Unloading Confining Pressure Rates.* Figure 3 shows the stress-time (σ - t) curve of composite

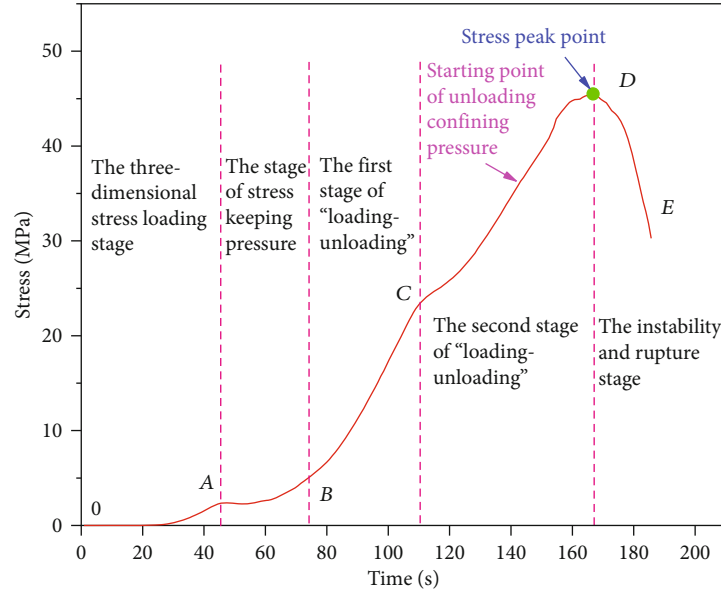


FIGURE 1: The stress-time curve of compound coal-rock. The confining pressure is set to 10 MPa, the unloading rate is 0.05 MPa/s, and D is the stress peak point. The three-axis loading and unloading of composite coal-rock is divided into five stages.

coal-rock triaxial loading-unloading simulation under different unloading confining pressure rates. By comparison, when the confining pressure and other conditions are the same and only the unloading rate is changed, the stress stages remain unchanged, and can still be divided into five stages. The overall stress trend is the same, and the previous loading curves are completely coincident. However, with the increase of unloading rate, the stress peak point of composite coal-rock fracture is reduced, the time from loading to fracture becomes shorter, and the overall stiffness and strength of composite coal-rock decreases, making it easier to fracture.

It can be seen from the foregoing that T_{ave} can reflect the average radiation intensity of the infrared radiation released from the surface of the composite coal-rock, so this paper uses T_{ave} as the analysis parameter for research. Figure 4 shows the average thermal infrared radiation temperature-time ($T_{ave}-t$) curve of the coal surface under the condition of different rates of unloading confining pressure. It can be seen from Figure 4 that the three curves start to change from 142.5 s after unloading. And the peak arrival time of T_{ave} at 0.05 MPa/s unloading confining pressure is earlier than that at 0.03 MPa/s and 0.003 MPa/s unloading confining pressure. The peak temperature is 22.49°C, which is greater than the 22.28°C and 22.03°C of the latter two. That is to say, under the same conditions, the greater the confining pressure unloading rate, the shorter peak time of T_{ave} and the greater the peak value.

(2) *The Law of Thermal Infrared Radiation Temperature Change.* Figure 5 shows the $T_{ave}-\sigma-t$ curves of different components of composite coal-rock under the above three different confining pressure unloading rates, and the trends of the three are consistent. According to the average thermal infrared radiation temperature change curve of the coal surface, the temperature change process is divided into five stages:

the initial fluctuation stage, the linear heating stage, the local decline stage, the temperature sudden increase stage, and the fracture decline stage. Take Figure 5(c) as an example for analysis. The five stages are as follows:

- (1) Initial fluctuation stage: T_{ave} of different components of composite coal-rock shows a fluctuating trend of decreasing, increasing, and then decreasing to varying degrees. The difference is that the wave peak of the coal body appears later than the floor rock and the roof rock in sequence, and the T_{ave} fluctuation degree is larger, and the maximum fluctuation is 0.38°C. At the same time, combined with Figure 1, it can be seen that, compared with the three-dimensional stress loading stage (OA), the internal stress field of the composite coal-rock gradually stabilizes after entering the stage of stress-keeping pressure (AB), and the degree of T_{ave} fluctuation becomes smaller
- (2) Linear heating stage: the change trend of T_{ave} of roof rock, coal, and floor rock is the same as the change trend of the first stage “loading-unloading” (BC) of stress, both of which have a linear rise. The T_{ave} of the coal body at this stage has the most obvious change, increasing by 1.21°C. And at 110.49 s, the T_{ave} of the coal body reaches a local maximum of 21.15°C, and the time is earlier than floor rock and roof rock
- (3) Local decline stage: T_{ave} of roof rock, coal, and floor rock all show a trend of decreasing first and then becoming stable. Among them, the T_{ave} of the coal body has decreased by about 0.35°C, which is in the early stage of the second stage “loading-unloading” (CD) of stress. In this stage, the T_{ave} of floor rock

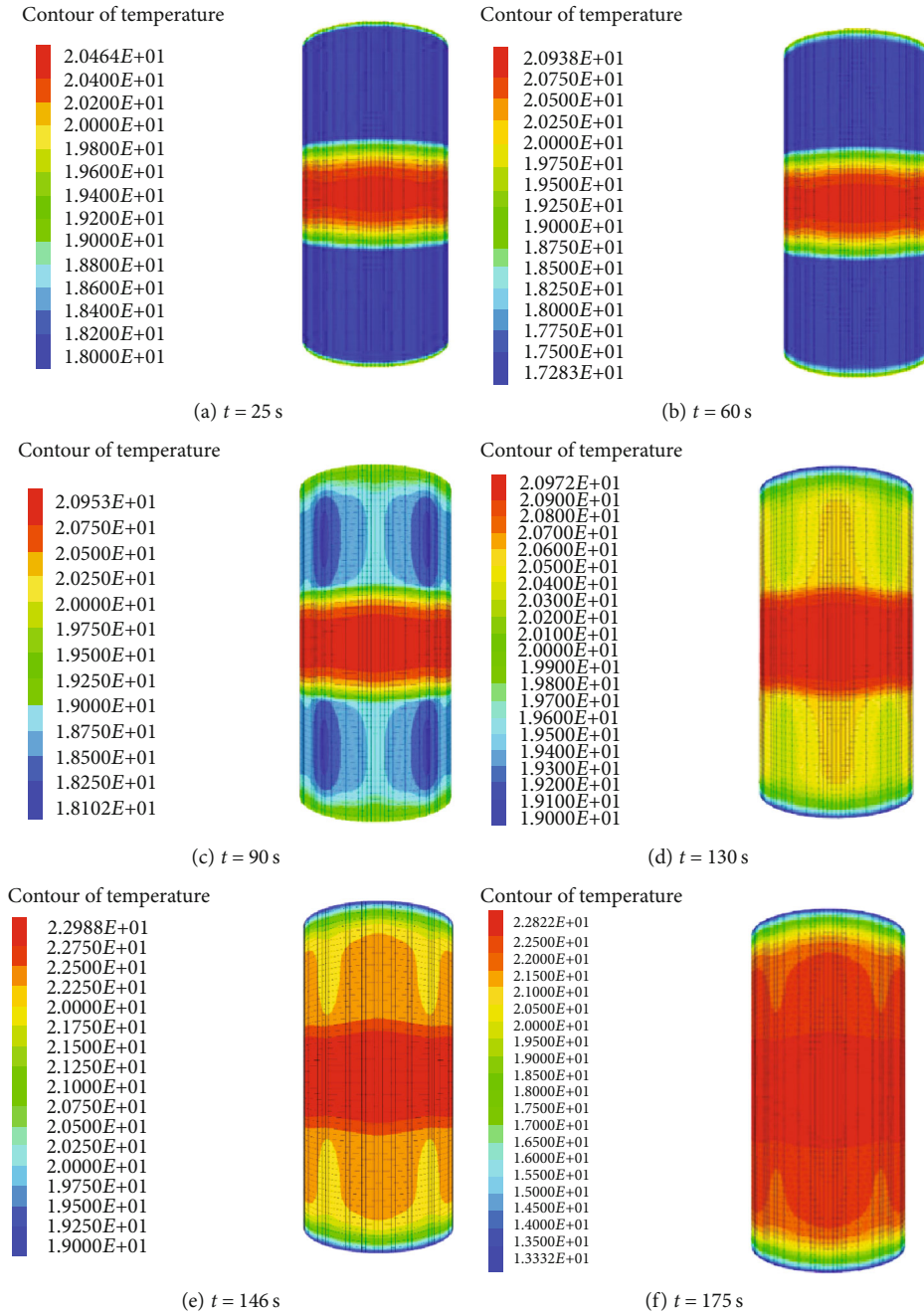


FIGURE 2: Cloud map of temperature distribution of composite coal-rock. When the simulation time is 25 s, 60 s, 90 s, 130 s, 146 s and 175 s, cloud maps of temperature distribution of composite coal-rock at different times correspond to different stress stages in Figure 1, in which 146 s is the time point after unloading confining pressure.

and roof rock continued the upward trend of the previous stage, and reached the local maximums of 21.06°C and 21.01°C at 114.27 s and 116.78 s successively. In the gentle trend interval after the decline, the T_{ave} of the coal body is successively higher than the floor rock and the roof rock

- (4) Temperature sudden increase stage: during this stage, T_{ave} tends to decrease after a sudden increase, and it is in the middle and late stage of the second stage “loading-unloading” (CD) of stress. After the confin-

ing pressure is unloaded at 142.5 s, the confining pressure constraint on the composite coal-rock gradually decreased, and the T_{ave} of the coal body increased suddenly in a short time. At 142.7 s, it first reached the global maximum of 22.53°C , and then showed a downward trend, decreasing by 0.28°C . The floor rock and roof rock reached the global maximum of 22.33°C and 22.15°C successively at 145.23 s and 146.03 s

- (5) Fracture decline stage: after experiencing the combined effect of the previous stress and temperature,

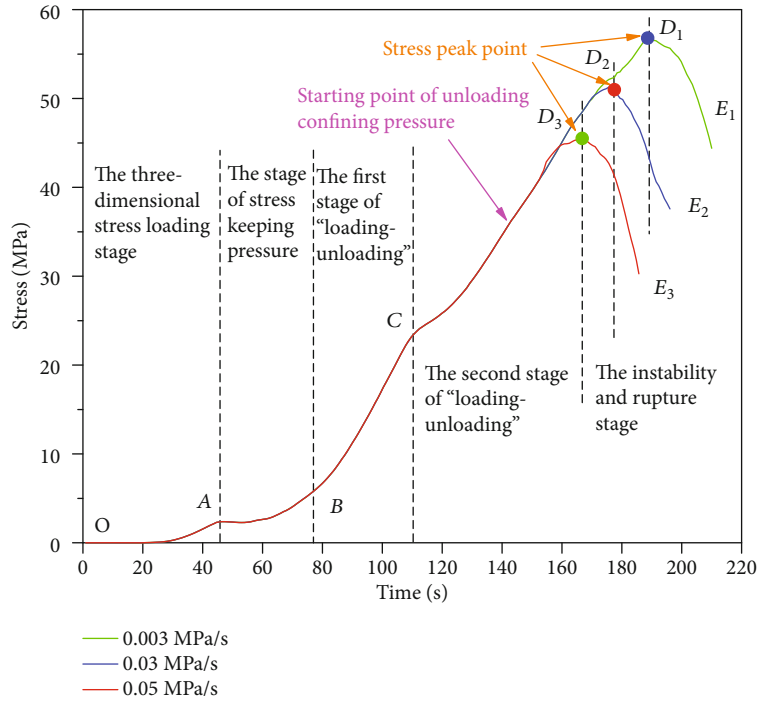


FIGURE 3: Stress-time curves at different pressure unloading rates. Under the confining pressure of 10 MPa and the unloading rates of 0.003 MPa/s, 0.03 MPa/s, and 0.05 MPa/s, the comparison of stress stages in the process of triaxial loading-unloading of composite coal-rock was made. Here, D_1 , D_2 , and D_3 are the stress peak points under the unloading confining pressure rate of 0.003 MPa/s, 0.03 MPa/s, and 0.05 MPa/s, respectively.

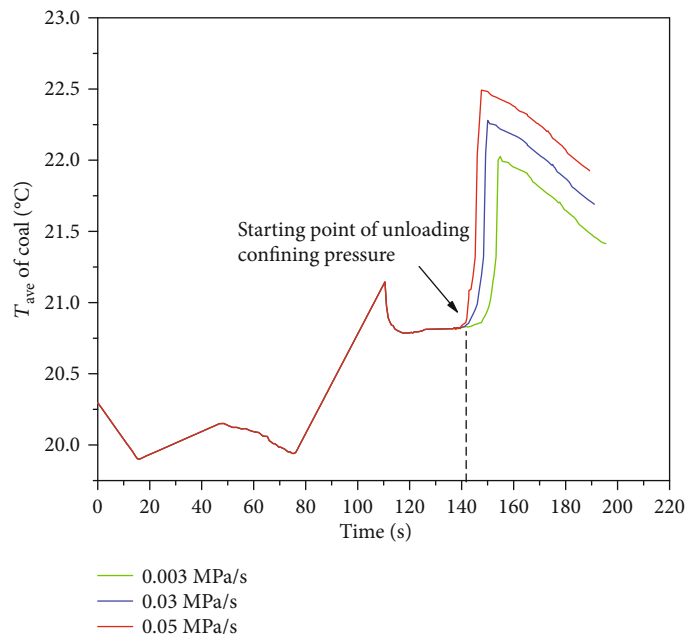
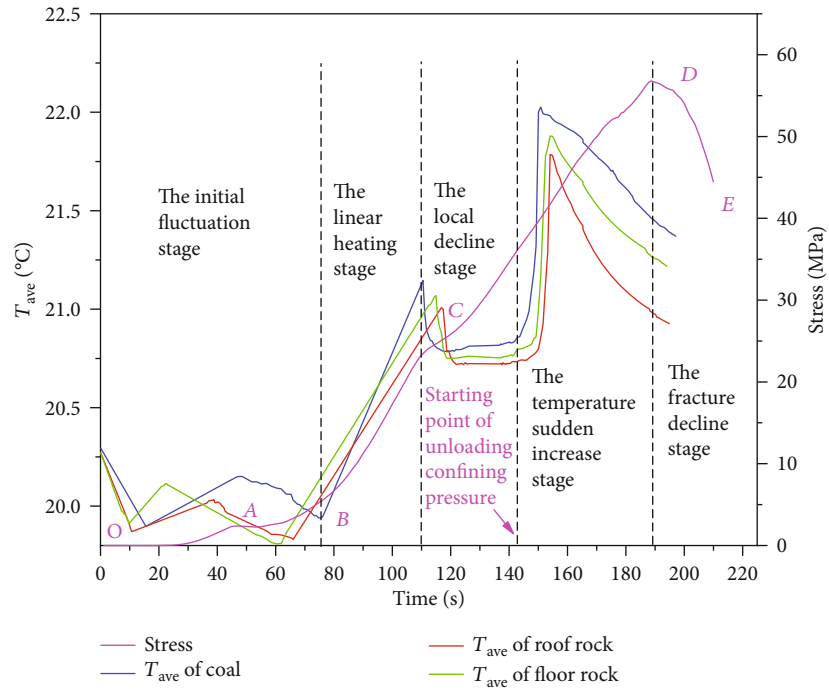
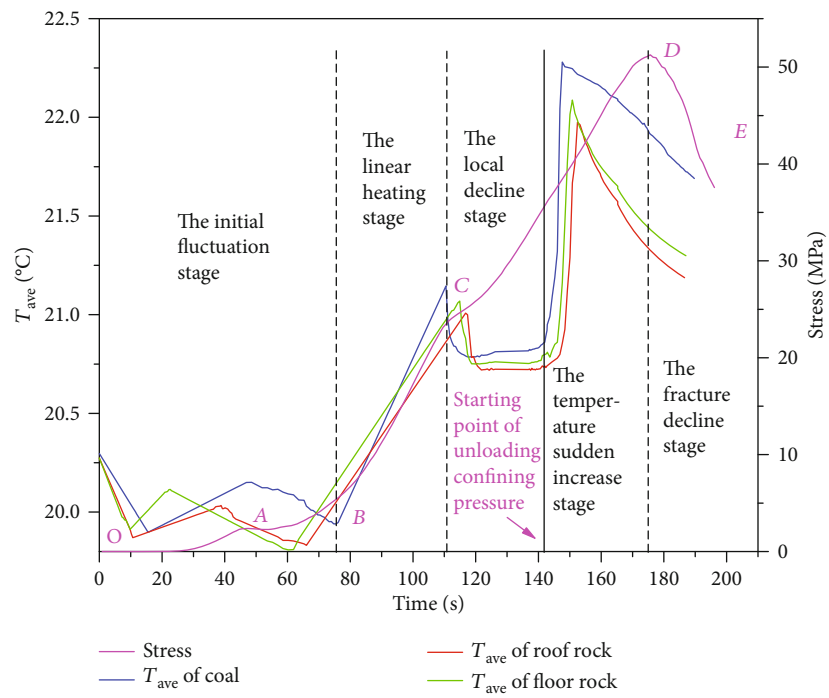


FIGURE 4: T_{ave} - t curves of thermal infrared radiation at different confining pressure unloading rates. Under the confining pressure of 10 MPa and the unloading rates of 0.003 MPa/s, 0.03 MPa/s, and 0.05 MPa/s, the temperature changes during the triaxial loading-unloading process of composite coal were compared, and the confining pressure unloading time was 142.5 s.



(a)



(b)

FIGURE 5: Continued.

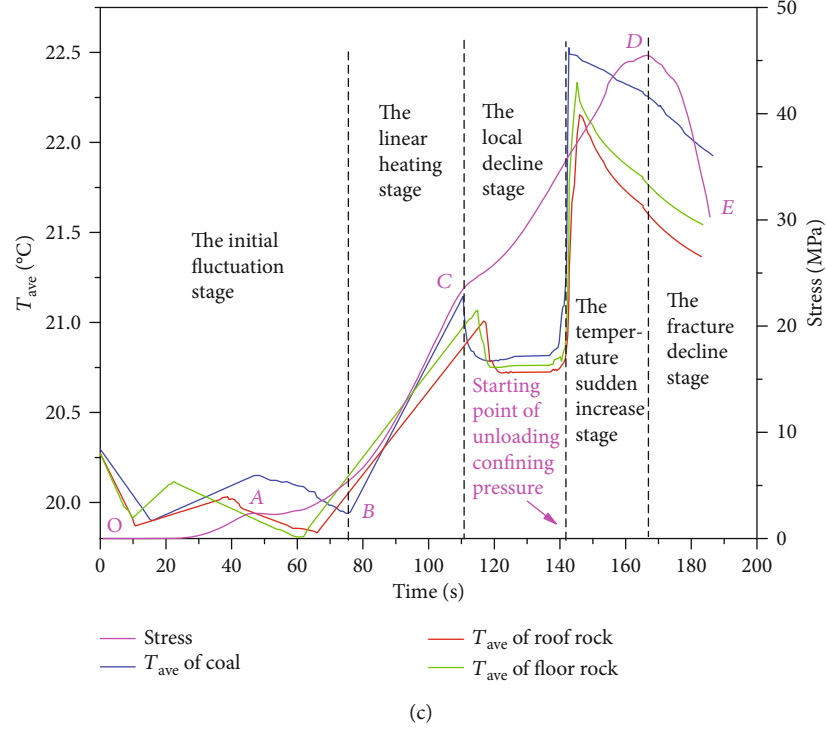


FIGURE 5: T_{ave} - σ - t curve of composite coal-rock. Among them, (a), (b), and (c) are the T_{ave} - σ - t curves of composite coal-rock under the conditions of 0.003 MPa/s, 0.03 MPa/s, and 0.05 MPa/s confining pressure unloading rate, respectively.

the composite coal-rock has reached the bearing limit at 167.6 s and it is unstable and damaged at point D. At this stage, the T_{ave} continues to decline as in the previous stage, and it is in the instability and rupture stage (DE) of stress

3.1.3. The Correlation between Thermal Infrared Radiation Temperature and Stress. The surface average infrared radiation temperature and stress of the composite coal body, roof rock, and floor rock are fitted to obtain the linear fitting relationship expression between the average thermal infrared radiation temperature and stress:

$$T_{ave} = K\sigma + T_1, \quad (11)$$

where T_{ave} is the surface average thermal infrared radiation temperature of each component of the composite coal-rock at any time (°C), K is the slope of the fitting curve, σ is the stress (MPa), T_1 is the starting temperature of the linear heating stage (°C).

Figure 6 shows the fitting curves of the T_{ave} and stress on the surface of the composite coal-rock with different components under different unloading rates. The expression of the linear relationship between the T_{ave} and stress on the coal surface in Figure 6(c) is as follows:

$$T_{ave} = 0.06204\sigma + 19.63599, \quad (12)$$

where the linear correlation coefficient obtained by fitting is 0.924.

A linear fitting is performed on the T_{ave} and the axial stress of the roof rock surface, and the linear relationship between the T_{ave} and the stress is obtained as follows:

$$T_{ave} = 0.04479\sigma + 19.77547, \quad (13)$$

where the linear correlation coefficient obtained by fitting is 0.93553.

A linear fitting is performed on the T_{ave} and the axial stress of the floor rock surface, and the linear relationship between the T_{ave} and the stress is obtained as follows:

$$T_{ave} = 0.04776\sigma + 19.80128, \quad (14)$$

where the linear correlation coefficient obtained by fitting is 0.92295.

According to the fitting parameters in Table 2 (unloading confining pressure at a rate of 0.003 MPa/s and 0.03 MPa/s), the linear correlation coefficients of the T_{ave} and stress after fitting are all greater than 0.89. So, there is a strong linear correlation between the average thermal infrared radiation temperature and the stress on the surface of composite coal-rock under different working conditions.

3.1.4. Experimental Verification. Figure 7 is a schematic diagram of the triaxial test equipment and field testing. The test system consists of a triaxial test machine, dynamic data acquisition, power control cabinet, and computer. In order to ensure that temperature data can be collected in a closed environment, an observation window is set at the confining cylinder of the test machine. This article uses the TAW-

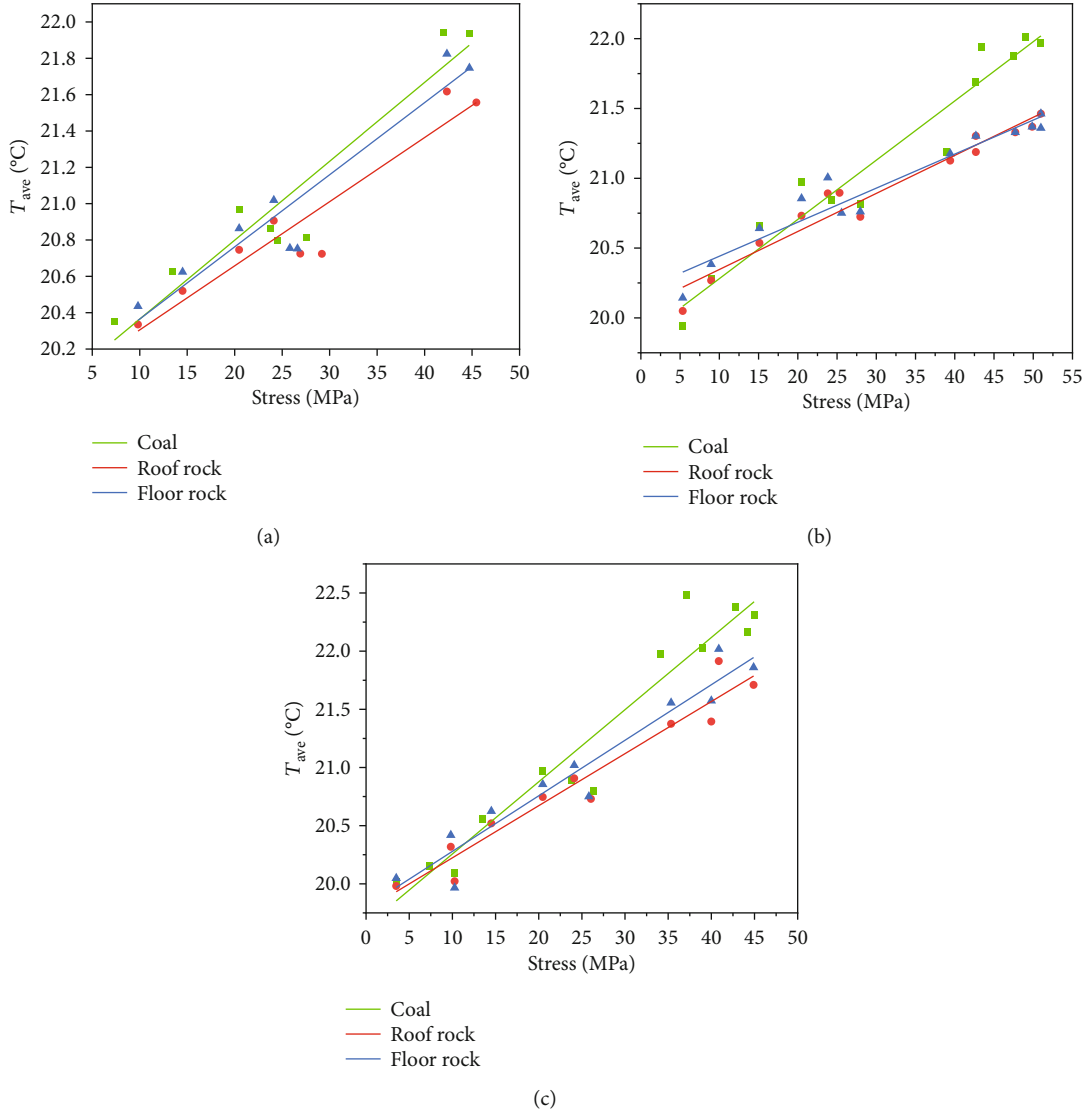


FIGURE 6: Linear fitting of mean thermal infrared radiation temperature and stress. Here, (a), (b), and (c) are linear fitting results of composite coal-rock under confining pressure unloading rates of 0.003 MPa/s, 0.03 MPa/s, and 0.05 MPa/s, respectively.

TABLE 2: Linear fitting parameters between T_{ave} and stress at different pressure unloading rates.

Discharge confining pressure rate (MPa/s)	Sample	Correlation coefficient	Slope	Intercept
0.003	Coal	0.90224	0.04342	19.93063
	Roof rock	0.90156	0.03529	19.95223
	Floor rock	0.89696	0.03969	19.96863
0.03	Coal	0.93408	0.04243	19.85666
	Roof rock	0.9459	0.02726	20.07382
	Floor rock	0.9212	0.02439	20.19758

2000 microcomputer-controlled high-temperature rock triaxial testing machine for testing. This equipment can collect, store, process, and display test data and test curves in real time during the test. The average infrared radiation tem-

perature of the sample is collected by the ThermoView™ Pi20 infrared thermal imager; that is, the average infrared radiation temperature corresponds to all the pixels on the thermal infrared image of the sample surface at a certain moment. The spectral response of the infrared thermal imager is 8 ~ 14 μm, and the sensitivity is 0.03°C.

The coal and rock samples were selected from the coal seams with strong impact at Feng Shuigou Coal Mine in Pingzhuang, Inner Mongolia. In the actual coal mine, the coal seam is mostly sandwiched in the rock layer, which basically presents the three-layer structure of “rock-coal-rock.” According to this characteristic, the composite coal-rock samples used in the test are processed [45]. Through field exploration and comparison, materials were taken from the field, and fresh coal samples with both roof and floor siltstone were drilled. In the laboratory, the roof rock, coal sample, and floor rock were cut and bonded at a ratio of 1:1:1 into 20 cylindrical samples with a diameter of 50 mm and a height

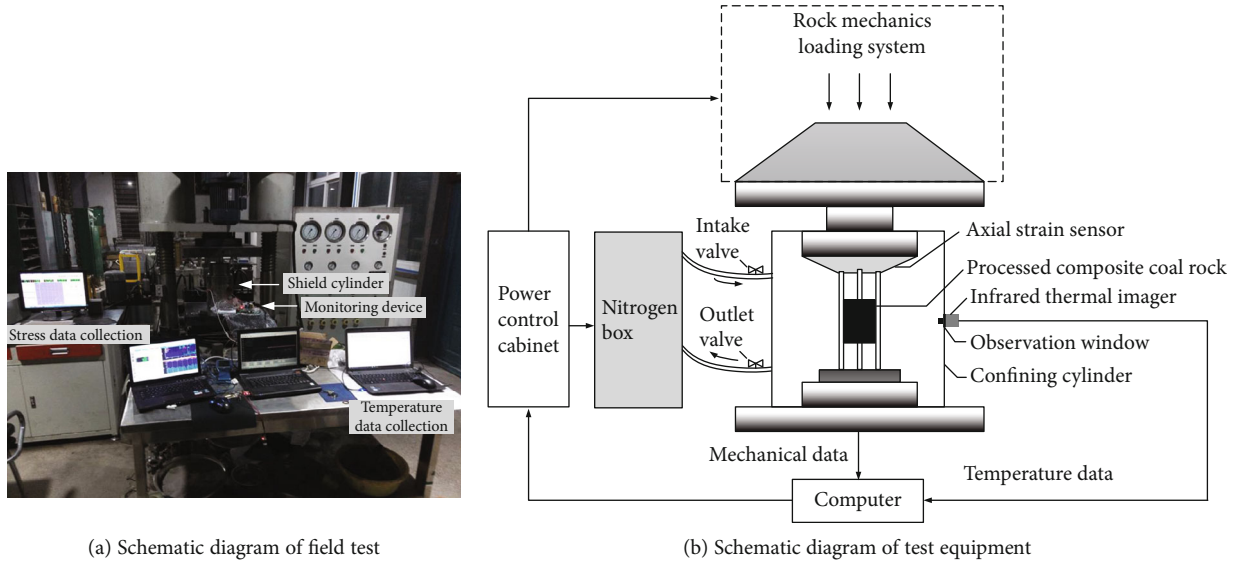


FIGURE 7: Schematic diagram of test equipment and field test. Figure 7(a) is the schematic diagram of the field test, and Figure 7(b) is the schematic diagram of the test equipment. The test equipment is mainly composed of a triaxial test machine, a power control cabinet, a nitrogen box, an infrared thermal imager, and a computer. Power is supplied by the power control cabinet during the experiment. The inlet valve and outlet valve of the nitrogen tank are responsible for controlling the pressurization of the processed composite coal-rock. An observation window is set on the shielding cylinder of the three-axis testing machine, and an infrared thermal imager is placed here to collect the T_{ave} data of the samples. The mechanics and temperature data are uniformly transmitted to the computer for display and storage.

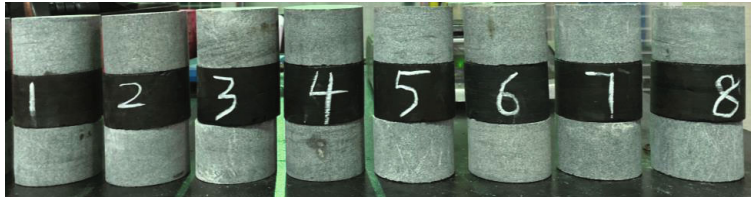


FIGURE 8: Partial composite coal-rock specimen.

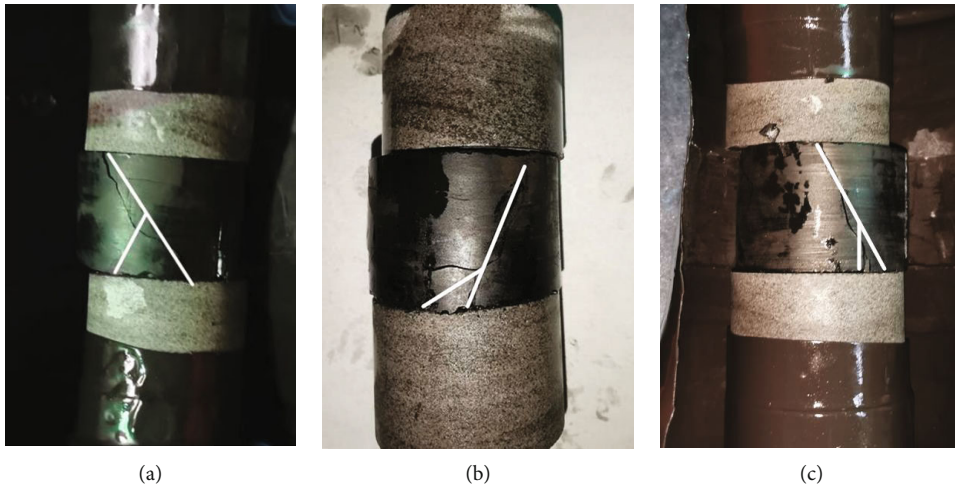
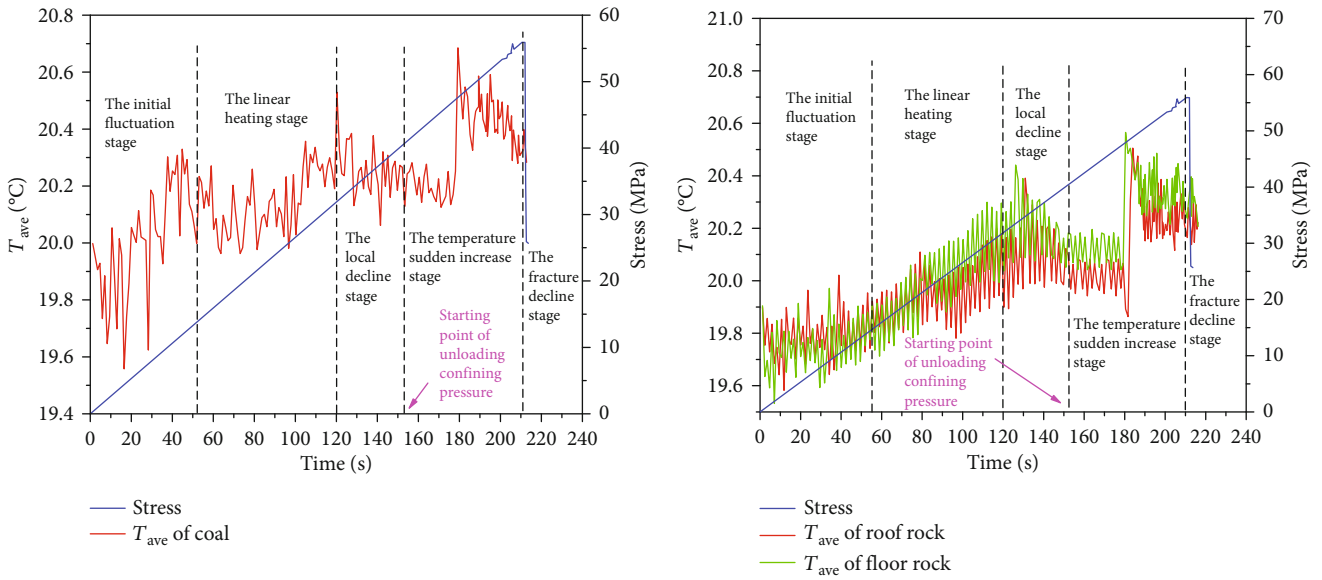


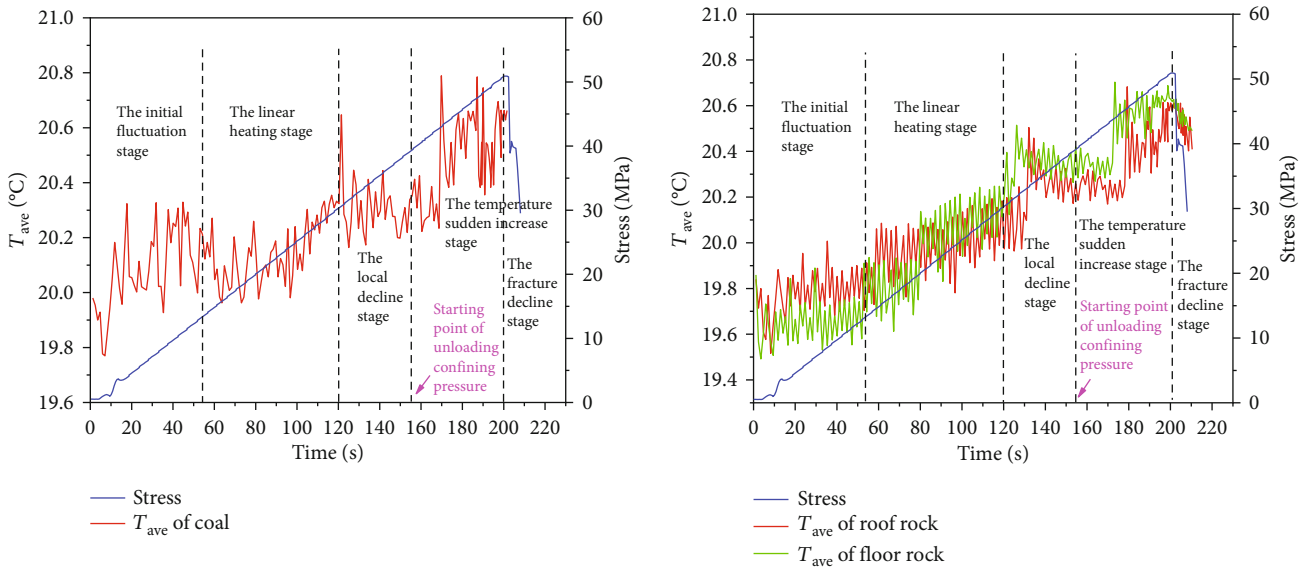
FIGURE 9: Experimental results of samples 1[#], 6[#], and 11[#]. Among them, (a) is the $T_{ave}-\sigma-t$ experimental curve of sample 1[#] when the unloading confining pressure rate is 0.003 MPa/s; (b) is the $T_{ave}-\sigma-t$ experimental curve of sample 6[#] when the unloading confining pressure rate is 0.03 MPa/s; (c) is the $T_{ave}-\sigma-t$ experimental curve of sample 11[#] when the unloading confining pressure rate is 0.05 MPa/s.

of 100 mm. Five samples are reserved for a composite coal-rock pretest, and the remaining samples are subjected to triaxial loading-unloading tests at different unloading confining

pressure rates, numbered 1[#], 2[#], 3[#], 4[#], 5[#], 6[#], 7[#], 8[#], 9[#], 10[#], 11[#], 12[#], 13[#], 14[#], and 15[#]. Some composite coal-rock samples are shown in Figure 8.

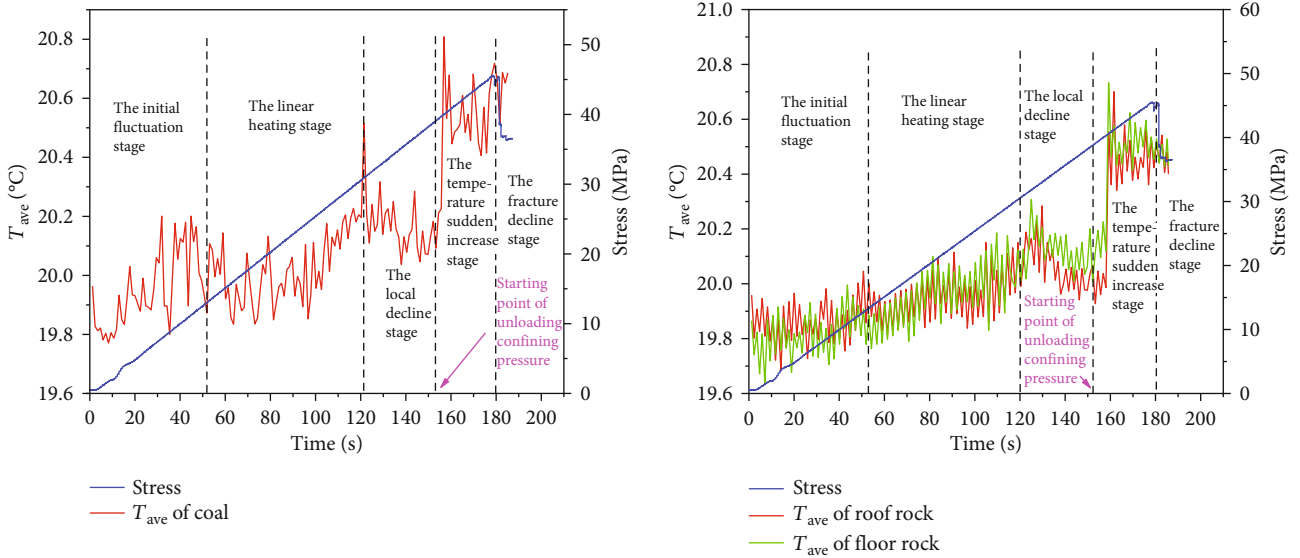


(a) T_{ave} - σ - t experimental curves of different components of sample 1[#]



(b) T_{ave} - σ - t experimental curves of different components of sample 6[#]

FIGURE 10: Continued.



(c) $T_{ave}-\sigma-t$ experimental curves of different components of sample 11[#]

FIGURE 10: $T_{ave}-\sigma-t$ experimental curves of different components of composite coal-rock. Among them, (a), (b), and (c) are the $T_{ave}-\sigma-t$ experimental curves of the samples 1[#], 6[#], and 11[#] at the unloading confining pressure rate of 0.003 MPa/s, 0.03 MPa/s, and 0.05 MPa/s, respectively.

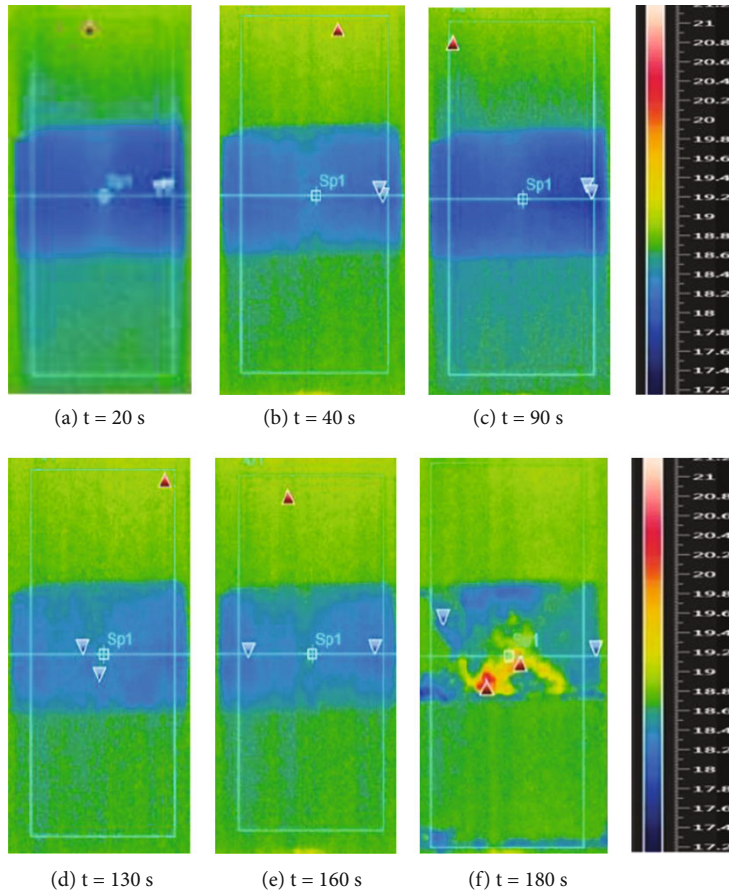


FIGURE 11: Thermal imaging of the sample 11[#]. Here, (a), (b), (c), (d), (e), and (f) are the thermal infrared imaging images of the sample 11[#] at the rate of 0.05 MPa/s when the experimental times are 20 s, 40 s, 90 s, 130 s, 160 s, and 180 s, respectively. Among them, 160 s is the thermal infrared image after the confining pressure has just been unloaded.

TABLE 3: Comparison of T_{ave} and peak stress parameters of coal body under different pressure relief rates.

Confining pressure unloading rate (MPa/s)	Sample	T_{ave}		Stress	
		Peak time (s)	Peak size (°C)	Peak time (s)	Peak size (MPa)
0.003	1 [#]	179.3	20.69	210.7	55.92
	2 [#]	180.7	20.52	213.9	57.67
	3 [#]	182.5	20.45	212.5	56.81
	4 [#]	179.1	20.66	210.3	55.70
	5 [#]	180.3	20.71	213.4	57.49
0.03	6 [#]	169.8	20.79	200.9	50.91
	7 [#]	170.4	20.73	199.8	50.69
	8 [#]	169.7	20.76	198.5	49.83
	9 [#]	168.6	20.75	201.3	49.74
	10 [#]	168.4	20.73	201.1	49.69
0.05	11 [#]	156.9	20.81	180.7	45.46
	12 [#]	157.1	20.92	183.4	46.79
	13 [#]	156.3	20.87	181.9	45.51
	14 [#]	155.8	20.94	177.1	45.39
	15 [#]	156.8	20.73	180.2	45.37

The symbol “#” constitutes the label of the “coal-rock-coal” sample, which is explained in Section 3.1.4.

The experiment steps are as follows:

- (1) At room temperature, seal the composite coal-rock sample with a thermoplastic tube and put it in a confining cylinder
- (2) Connect the thermal imaging camera to the computer, aim the front of the thermal imaging camera at the observation window to the observation surface of the sample, turn on the power, open the software to connect the thermal imaging camera, and check the thermal imaging camera status
- (3) Open the nitrogen valve of the testing machine to inject nitrogen, and close the gas valve when it is full
- (4) Apply three-dimensional stress to the sample to a predetermined confining pressure value of 10 MPa
- (5) Pretest: keep the confining pressure unchanged, load the sample under axial compression at a displacement rate of 0.05 mm/min. Record the peak stress intensity, and obtain the average value of the peak stress intensity of the five samples
- (6) Triaxial loading-unloading test: divide samples 1[#]~15[#] into three groups equally, repeat steps (1), (2), (3), and (4), set the same triaxial loading conditions as the pretest. When the stress reaches about 80% of the average value of the peak strength, the confining pressure will be relieved. And the unloading rate is set to 0.003 MPa/s (samples 1[#], 2[#], 3[#], 4[#], and 5[#]), 0.03 MPa/s (samples 6[#], 7[#], 8[#], 9[#], and 10[#]), and 0.05 MPa/s (samples 11[#], 12[#], 13[#], 14[#], and 15[#]), keep the axial pressure to continue loading during the unloading process. When the axial stress exceeds the peak stress and the sample is damaged, immediately stop the confining pressure unloading

operation. Keep the confining pressure unchanged, and continue to apply the axial stress until the stress curve no longer changes with the change of strain, and the test ends

In the pretest, the average value of unloading confining pressure is 39 MPa. Since the samples are randomly grouped, the first samples, namely, sample 1[#], 6[#], and 11[#], are selected for comparison in the three groups of different confining pressure unloading rate tests. Figure 9 shows the test results of samples 1[#], 6[#], and 11[#]. It can be seen from Figure 9 that the cracks of the sample mainly exist in the coal seam and show an inverted “Y-shaped” splitting fracture. And the rock mass has microcracks, but these are not obvious. This is due to the relatively high strength of the sample, the more prominent end effect, and the end is in a three-way stress state due to friction restraint.

The T_{ave} - σ - t curves of samples 1[#], 6[#], and 11[#] are shown in Figure 10, and the trends of the three curves are the same. Combining Figures 9 and 10, the greater the confining pressure relief rate, the greater the T_{ave} peak, the more severe the mechanical changes caused by heat, the more obvious the thermal-mechanical coupling effect, and the shorter the sample rupture time. Therefore, the cracks in the sample are too late to fully expand, and the more the damage is concentrated on a certain macroscopic fracture surface, the lower the overall degree of fracture. During the loading-unloading process, the formation, expansion and fusion of microcracks within the coal sample occur. As the stress increases, the T_{ave} shows an upward trend, and local peak value and global maximum value appear. Since the strength of the roof and floor rocks is much greater than the coal body, the coal body was unstable and fractured at the end of the test. Although cracks propagated inside the rock mass, the rock mass itself did not break obviously. The T_{ave} of the roof and floor rocks showed an upward trend. After the confining pressure was relieved, the

TABLE 4: Fitting equations at different pressure release rates.

Confining pressure unloading rate (MPa/s)	Number	Sample	Fitting equation	Correlation coefficient
0.003	1 [#]	Coal	$T_{ave} = 0.00605\sigma + 19.87015$	0.93496
		Roof rock	$T_{ave} = 0.00546\sigma + 19.8574$	0.90399
		Floor rock	$T_{ave} = 0.00539\sigma + 19.84124$	0.94312
	2 [#]	Coal	$T_{ave} = 0.0053\sigma + 19.86009$	0.92674
		Roof rock	$T_{ave} = 0.00684\sigma + 19.84865$	0.91652
		Floor rock	$T_{ave} = 0.007169\sigma + 19.83063$	0.93705
	3 [#]	Coal	$T_{ave} = 0.00746\sigma + 19.83876$	0.94878
		Roof rock	$T_{ave} = 0.006098\sigma + 19.87914$	0.93514
		Floor rock	$T_{ave} = 0.006134\sigma + 19.88518$	0.94677
	4 [#]	Coal	$T_{ave} = 0.0061\sigma + 19.89534$	0.92781
		Roof rock	$T_{ave} = 0.00587\sigma + 19.86495$	0.92695
		Floor rock	$T_{ave} = 0.00693\sigma + 19.84713$	0.91746
	5 [#]	Coal	$T_{ave} = 0.0053\sigma + 19.86009$	0.91462
		Roof rock	$T_{ave} = 0.00684\sigma + 19.84865$	0.90857
		Floor rock	$T_{ave} = 0.007169\sigma + 19.83063$	0.91039
6 [#]	Coal	$T_{ave} = 0.00664\sigma + 19.89496$	0.96174	
	Roof rock	$T_{ave} = 0.00956\sigma + 19.77254$	0.96367	
	Floor rock	$T_{ave} = 0.0091\sigma + 19.79735$	0.95806	
7 [#]	Coal	$T_{ave} = 0.00796\sigma + 19.89691$	0.95763	
	Roof rock	$T_{ave} = 0.008565\sigma + 19.76841$	0.91875	
	Floor rock	$T_{ave} = 0.009197\sigma + 19.84372$	0.93548	
8 [#]	Coal	$T_{ave} = 0.008097\sigma + 19.90263$	0.94097	
	Roof rock	$T_{ave} = 0.007156\sigma + 19.77987$	0.95875	
	Floor rock	$T_{ave} = 0.00785\sigma + 19.80753$	0.96864	
9 [#]	Coal	$T_{ave} = 0.00608\sigma + 19.90534$	0.93254	
	Roof rock	$T_{ave} = 0.00896\sigma + 19.72962$	0.92175	
	Floor rock	$T_{ave} = 0.00873\sigma + 19.78641$	0.91867	
10 [#]	Coal	$T_{ave} = 0.00749\sigma + 19.74125$	0.92671	
	Roof rock	$T_{ave} = 0.00928\sigma + 19.70962$	0.91538	
	Floor rock	$T_{ave} = 0.009143\sigma + 19.6831$	0.91274	
11 [#]	Coal	$T_{ave} = 0.00829\sigma + 19.83793$	0.93825	
	Roof rock	$T_{ave} = 0.00676\sigma + 19.87256$	0.9199	
	Floor rock	$T_{ave} = 0.00731\sigma + 19.86935$	0.95169	
12 [#]	Coal	$T_{ave} = 0.008754\sigma + 19.83763$	0.94761	
	Roof rock	$T_{ave} = 0.002570\sigma + 19.87754$	0.92867	
	Floor rock	$T_{ave} = 0.00571\sigma + 19.83333$	0.94652	
13 [#]	Coal	$T_{ave} = 0.009753\sigma + 19.83659$	0.95173	
	Roof rock	$T_{ave} = 0.004627\sigma + 19.87074$	0.93635	
	Floor rock	$T_{ave} = 0.00478\sigma + 19.87988$	0.94174	
14 [#]	Coal	$T_{ave} = 0.0086\sigma + 19.80651$	0.93045	
	Roof rock	$T_{ave} = 0.00537\sigma + 19.90571$	0.92435	
	Floor rock	$T_{ave} = 0.00548\sigma + 19.88145$	0.92037	
15 [#]	Coal	$T_{ave} = 0.008741\sigma + 19.80253$	0.92754	

TABLE 4: Continued.

Confining pressure unloading rate (MPa/s)	Number	Sample	Fitting equation	Correlation coefficient
		Roof rock	$T_{ave} = 0.00487\sigma + 19.88475$	0.91863
		Floor rock	$T_{ave} = 0.00496\sigma + 19.87033$	0.91384

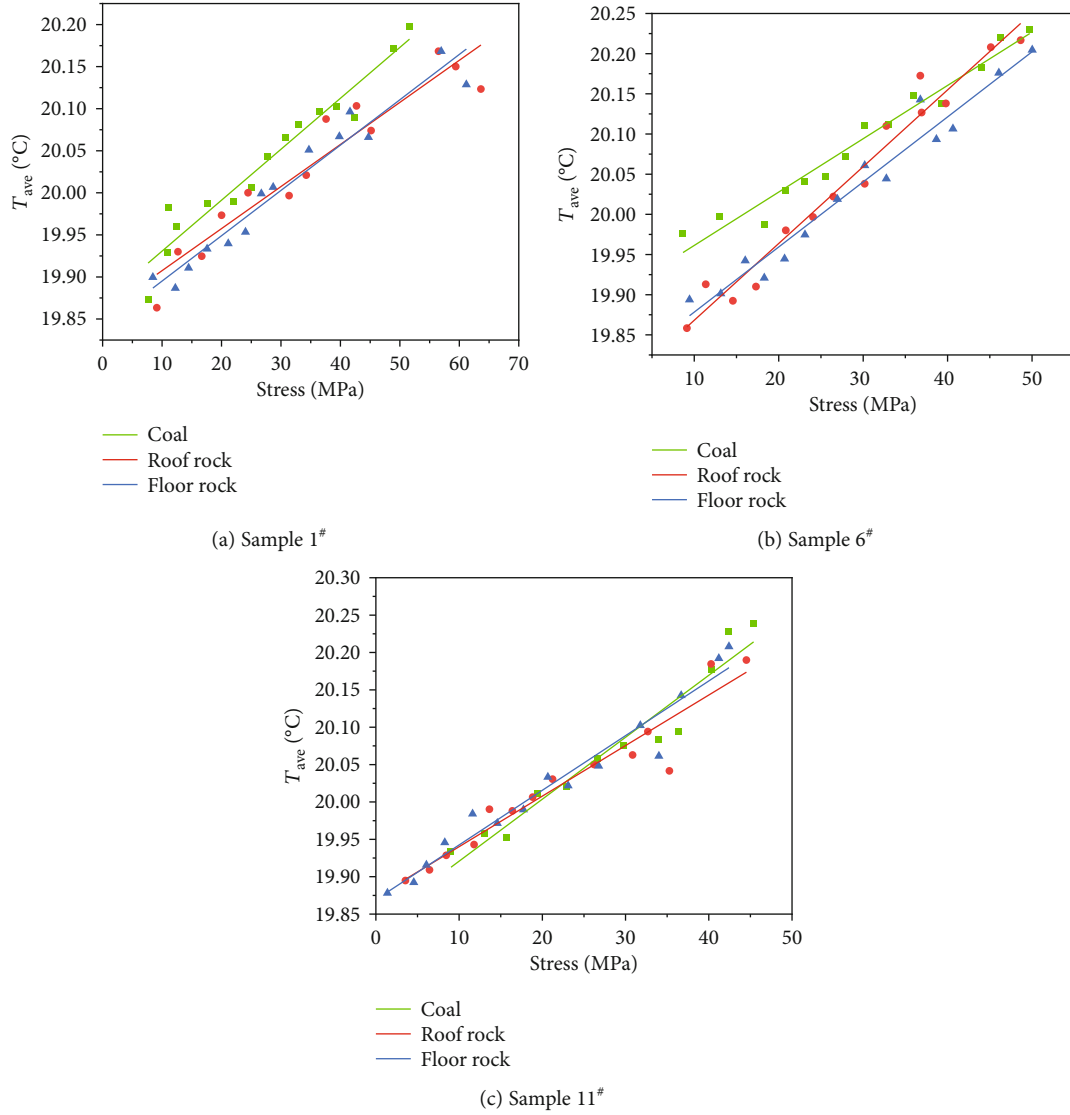


FIGURE 12: The experimental fitting curve of thermal infrared radiation temperature and stress.

T_{ave} reached the maximum value within a short time. Take sample 11# in Figure 10(c) as an example for analysis.

For the coal body, in the initial fluctuation stage, the composite coal-rock, which is an anisotropic and heterogeneous material, has microdefects in the internal framework particles, and the internal microcracks and micropores gradually rupture and close at the initial stage of three-dimensional stress loading. Under the combined action of slight dislocation friction (the apparent damage has not yet begun) and the gas discharged from the pores, coal sample damage begins to occur, and there is a certain degree of heat dissipation. T_{ave} decreases by 0.19°C within 0~19.7s. After entering stage of stress-

keeping pressure, the internal stress field of the coal sample gradually stabilizes, and the damage is not severe at the beginning. At this time, the sample deforms in the elastic range, and the thermoelastic effect plays a leading role. After compaction, the particles in the coal body have a small range of friction, and the heat released causes the T_{ave} fluctuation to rise again by 0.39°C. In the linear heating stage, with the increase of stress, new cracks in the coal sample begin to develop, and microfractures appear and continue to develop. These microcracks continue to rub and heat up during the formation process and are accompanied by friction between the coal and rock interface. For heat production, T_{ave} showed a linear

fluctuation upward trend, and reached a local maximum of 20.52°C at 121.4 s. During the local decline stage, the load-bearing structure of the coal sample began to fail, and different types of microfractures and thermal effects occurred inside. Under the combined action of shear cracks leading to heat generation and local thermal stress-induced local damage, the internal microcracks of the coal sample increase, and the external microcracks appear, which increases the sample volume and expands and absorbs heat. T_{ave} shows a trend that first decreases from the local maximum and then stabilizes, decreasing by 0.43°C within 121.5 s to 152.2 s. During the sudden temperature increase stage, since the confining pressure began to be unloaded at 152.2 s, the confining pressure constraints on the sample gradually decreased, and the development of cracks and frictional slippage in the coal body became more and more intense. The deformation of the sample accelerates, the frictional heat effect occurs, and a large amount of heat is generated. T_{ave} increases suddenly in a short time, reaching a global maximum of 20.81°C at 156.9 s. At the same time, the expansibility of the mineral components in the coal gradually becomes prominent. The superimposed effect induces thermal stress inside the specimen, leading to aggravation of microfractures, the increase in volume is more significant, and some heat is absorbed, and T_{ave} begins to show a downward trend again. In the fracture decline stage, after 180.7 s, due to the further development of original cracks and the production of a large number of new cracks, they clustered towards the main rupture. When the stress reaches the maximum value of 45.46 MPa, the sample reaches the load-bearing limit, the cracks penetrate macroscopically in the coal body, and the sample ruptures. There was violent dislocation friction between the fractured surfaces, resulting in a large number of high-temperature points, and T_{ave} had a small step increase, but the overall trend was still decreasing.

For the roof rock, with the initial load gradually increasing, the cracks and pores are in the compaction stage, the fracture surface does not have frictional heating effect, and the temperature fluctuates up and down. During the linear heating stage, a small amount of microscopic cracks also appeared in the roof rock. The T_{ave} curve showed a nearly linear upward trend, but there was a buffer between 80 and 100 s. T_{ave} lags behind the coal body, reaching a local maximum of 20.28°C at 129.8 s, which increased by about 0.14°C. Due to the increase and expansion of internal microfractures, T_{ave} starts to decrease from the local maximum, and reaches the global maximum at 20.70°C at 161.6 s later than the coal body after the confining pressure is unloaded and is lower than the maximum value of the T_{ave} of the coal body.

The infrared radiation temperature change of the floor rock is similar to that of the roof rock. The difference is that the floor rock bears the gravity from the roof rock and the coal body. During the three-way stress loading stage and the stage of stress-keeping pressure, more gas is discharged from the internal voids, and the phenomenon of heat absorption phenomenon is obvious. The fluctuation trend of T_{ave} is lower than that of the roof rock. In the linear heating stage, the temperature of the roof rock changes more obviously, the temperature is increased by 0.42°C. And the occurrence

time of the local maximum is between the coal body and the roof rock, reaching 20.31°C at 125.03 s. Similarly, the global maximum reaches 20.73°C at 159.2 s, which is between the T_{ave} maximum of the coal body and the roof rock.

Figure 11 is the thermal imaging diagram of sample 11[#] during the loading and unloading process. Six time points of 20 s, 40 s, 90 s, 130 s, 160 s, and 180 s are selected. It can be seen from the Figure 11 that the temperature change of the coal body during the loading and unloading process is more obvious. And the highest point of temperature is located in the middle axial area and the lower part of the coal body, and the temperature change range of the rock body is relatively small.

It can be seen from above that during the unloading and rupture process of the composite coal-rock, the T_{ave} of the coal body appears earlier than the floor rock and the roof rock. In order to explore the precursory changes of infrared radiation temperature, only the T_{ave} of the coal body can be compared with the stress peak time. Table 3 is a comparison of the peak arrival time and peak size of the average thermal infrared radiation temperature and stress on the coal surface under different unloading confining pressure rates for samples 1[#]~15[#]. The average thermal infrared radiation temperature peak arrival time of each sample is earlier than the stress peak arrival time. Combined with Figure 8, before the composite coal-rock is unstable and ruptured, the average thermal infrared radiation temperature of the roof rock, coal body, and floor rock exhibits a sudden increase and stepwise rise. Among them, the occurrence time of the precursors of the average thermal infrared radiation temperature of the coal body is ahead of the floor and roof rock, and the degree of change is the largest.

Table 4 shows the fitting equations and related parameters of some samples at different confining pressure unloading rates. The fitting curves of samples 1[#], 6[#], and 11[#] are shown in Figure 12. It can be seen that the T_{ave} has a good linear correlation with the stress, and the correlation coefficients are all above 0.90. Compared with the fitting result in simulation, the correlation coefficient after experimental fitting is higher. This is the result of the large number of experimental sampling points and artificial points, which further proves that T_{ave} has a good linear correlation with stress.

In summary, the experimental results show that the variation trend of the average thermal infrared radiation temperature on the surface of the sample is consistent with the simulation results. The average thermal infrared radiation temperature on the surface has a good correlation with the stress, which verifies the correctness of the simulation and analysis.

4. Conclusions

- (1) Considering the combined effects of stress and thermal infrared radiation temperature on the unloading and rupture of anisotropic composite coal and rock, based on the basic theory of mechanics and the damage mechanics formula, it is deduced that the different components of the anisotropic composite coal and rock during the unloading and rupture process are at any arbitrary value. The relationship between

thermal infrared radiation temperature and stress is averaged at all times, and a mathematical model of thermal-mechanical coupling under unloading and rupture conditions is established

- (2) The simulation results show that under unloading conditions, the thermal infrared radiation temperature of the composite coal is concentrated in the coal seam. After 142.5 s unloading the confining pressure, the overall temperature field reaches the strongest. The greater the rate of unloading confining pressure, the shorter the peak arrival time of T_{ave} , and the larger the peak value. The T_{ave} changes of roof rock, coal body, and floor rock are mainly divided into five stages, showing a trend of fluctuation, nearly linear rise, slow decline, and the sudden increase after unloading reaches the maximum and then slowly decreases
- (3) The experimental results show that after 152.2 s of unloading the confining pressure, the constraints on the coal and rock gradually decrease, and the development of fissures and frictional slippage becomes more and more intense. The greater the rate of unloading confining pressure, the shorter the peak arrival time of thermal infrared radiation temperature and the greater the peak value. Among them, at 0.003 MPa/s, 0.03 MPa/s, and 0.05 MPa/s unloading confining pressure rates, the T_{ave} of coal, floor rock, and roof rock increase suddenly before the stress peak reaches the maximum value, respectively: 20.69°C, 20.56°C, 20.51°C; 20.79°C, 20.70°C, 20.68°C; and 20.81°C, 20.73°C, 20.70°C. The T_{ave} of each component of the composite coal-rock has a good linear correlation with the stress, and the correlation coefficient is greater than 0.90. The T_{ave} variation law of composite coal-rock under unloading conditions is consistent with the simulation results

The research results provide new ideas and new methods for monitoring and early warning of coal and rock dynamic disasters.

Data Availability

Test data used to support the findings of this study are available from the corresponding author upon request.

Conflicts of Interest

The authors declare no conflict of interest.

Acknowledgments

This work was supported by the discipline innovation team of Liaoning Technical University (LNTU20TD-29), Chinese National Natural Science Foundation (nos. 51604141 and 51204087), and Liaoning Provincial Education Committee Projects (LJ2019JL013 and LJ2020JCL020).

References

- [1] X. Wu, Y. Peng, J. Xu, Q. Yan, W. Nie, and T. Zhang, "Experimental study on evolution law for particle breakage during coal and gas outburst," *International Journal of Coal Science & Technology*, vol. 7, no. 1, pp. 97–106, 2020.
- [2] B. Chen, "Stress-induced trend: the clustering feature of coal mine disasters and earthquakes in China," *International Journal of Coal Science & Technology*, vol. 7, no. 4, pp. 676–692, 2020.
- [3] W. J. Yao, J. Y. Pang, Q. Y. Ma, and H. Lyimo, "Influence and sensitivity analysis of thermal parameters on temperature field distribution of active thermal insulated roadway in high temperature mine," *International Journal of Coal Science & Technology*, vol. 8, no. 1, pp. 47–63, 2021.
- [4] J. Lu, G. Z. Yin, H. Gao, M. H. Li, and B. Deng, "Sure relief of gas-bearing coal under true triaxial loading," *Journal of China Coal Society*, vol. 45, no. 5, pp. 1812–1823, 2020.
- [5] F. R. Huang, S. X. Yan, A. Li, and P. C. Jiang, "Experimental study on infrared radiation of rock under uniaxial compression," *Journal of North China University of Science and Technology (Natural Science Edition)*, vol. 42, no. 4, pp. 24–29, 2020.
- [6] S. D. Wang and W. Y. Hu, "Research on coal and rock mass temperature fields characteristics and control factors in deep mine," *Coal Science and Technology*, vol. 41, no. 8, pp. 18–21, 2013.
- [7] F. Q. Gao, H. P. Kang, and L. Yang, "Experimental and numerical investigations on the failure processes and mechanisms of composite coal-rock specimens," *Scientific reports*, vol. 10, no. 1, p. 13422, 2020.
- [8] Y. Tao, L. Zhenhua, C. Zhiheng, Z. Quanle, C. Jialin, and H. Yanbo, "Deformation and failure characteristics of composite coal mass," *Environmental Earth Sciences*, vol. 80, no. 3, 2021.
- [9] Z. L. Zhao, K. Zhao, and X. Wang, "Study on mechanical characteristics and damage evolution law of coal-rock-like under different loading rates," *Coal science and technology*, vol. 45, no. 10, pp. 41–47, 2017.
- [10] Y. L. Tan and Y. B. Zhang, *Research on Impact Characteristics of Inclined Coal-Rock Composite Body*, Kemerovo, Russia, 2016.
- [11] L. Q. Ma and H. Sun, "Spatial-temporal infrared radiation precursors of coal failure under uniaxial compressive loading," *Infrared Physics & Technology*, vol. 93, pp. 144–153, 2018.
- [12] L. Ma, H. Sun, Y. Zhang, T. Zhou, K. Li, and J. Guo, "Characteristics of infrared radiation of coal specimens under uniaxial loading," *Rock Mechanics and Rock Engineering*, vol. 49, no. 4, pp. 1567–1572, 2016.
- [13] Z. Li, S. Yin, Y. Niu et al., "Experimental study on the infrared thermal imaging of a coal fracture under the coupled effects of stress and gas," *Journal of Natural Gas Science and Engineering*, vol. 55, pp. 444–451, 2018.
- [14] G. Q. Chen, Y. S. Pan, G. Z. Zhang, G. Z. Zhang, and D. Wang, "Thermal infrared precursor information of crack propagation for rock bridges," *Chinese Journal of Geotechnical Engineering*, vol. 41, no. 10, pp. 1817–1826, 2019.
- [15] M. C. He, W. L. Gong, D. J. Li, and H. M. Zhai, "Physical modeling of failure process of the excavation in horizontal strata based on IR thermography," *Mining Science and Technology*, vol. 19, no. 6, pp. 689–698, 2009.

- [16] W. L. Gong, Y. X. Gong, and A. F. Long, "Multi-filter analysis of infrared images from the excavation experiment in horizontally stratified rocks," *Infrared Physics and Technology*, vol. 56, pp. 57–68, 2013.
- [17] C. Wang, Z. Lu, L. Liu, X. Chuai, and H. Lu, "Predicting points of the infrared precursor for limestone failure under uniaxial compression," *International Journal of Rock Mechanics and Mining Sciences*, vol. 88, pp. 34–43, 2016.
- [18] F. T. Freund, "Rocks that crackle and sparkle and glow: strange pre-earthquake phenomena," *Society for Scientific Exploration*, vol. 17, no. 1, pp. 37–71, 2003.
- [19] S. J. Liu, Y. B. Zhang, L. X. Wu, G. L. Li, and Q. L. Chen, "Infrared radiation characteristics of concrete fracture and water seepage process," *Journal of rock mechanics and engineering*, vol. 28, no. 1, pp. 53–58, 2009.
- [20] W. Q. Guo, Y. J. Zhang, and L. Q. An, "Test on infrared radiation exploration technology to predict mine bump pressure," *Coal science and technology*, vol. 35, no. 1, pp. 73–77, 2007.
- [21] Z. J. Xu, Q. X. Qi, and H. Y. Li, "Study on infrared radiation characteristics of loading failure of impact prone coal," *Chinese Journal of safety science*, vol. 23, no. 10, pp. 121–125, 2013.
- [22] Y. B. Zhang, Z. Yang, and X. L. Yao, "Experimental study on real time early warning method of roadway rock burst based on temporal and spatial evolution of infrared radiation," *Journal of mining and safety engineering*, vol. 35, no. 2, pp. 299–307, 2018.
- [23] L. Q. MA, Y. Zhang, H. SUN, S. K. Wang, and A. Najeem, "Experimental study on the control effect of stress on infrared radiation during coal rock fracture," *Chinese journal of coal and rock*, vol. 42, no. 1, pp. 140–147, 2017.
- [24] F. Q. Cheng, Z. H. Li, and Y. Wei, "Damage evolution characteristics of coal rock based on uniaxial compression infrared radiation," *Industrial and mining automation*, vol. 44, no. 5, pp. 64–70, 2018.
- [25] Z. Yang, Q. J. Qi, D. D. Ye, X. Li, and H. Luo, "The change of infrared radiation temperature inside the fracture of composite coal rock under load," *Journal of China Coal Society*, vol. 41, no. 3, pp. 618–624, 2016.
- [26] X. P. Lai, X. M. Liu, and P. F. Shan, "Study on thermal infrared radiation variation of fractured coal-rock mass failure during mining," *Journal of Mining and Safety Engineering*, vol. 36, no. 4, pp. 777–785, 2019.
- [27] X. Li, Z. Yang, S. Dai, B. Qiu, and Y. Xin, "Variation of infrared radiation temperature on fracture surface of loaded composite coal rock," *Chinese journal of safety science*, vol. 27, no. 1, pp. 110–115, 2017.
- [28] K. Du, X. B. Li, D. Y. Li, and L. Weng, "Failure properties of rocks in true triaxial unloading compressive test," *Transactions of Nonferrous Metals Society of China*, vol. 25, no. 2, pp. 571–581, 2015.
- [29] F. Du, K. Wang, G. Wang, Y. Jiang, C. Xin, and X. Zhang, "Investigation of the acoustic emission characteristics during deformation and failure of gas-bearing coal-rock combined bodies," *Journal of Loss Prevention in the Process Industries*, vol. 55, pp. 253–266, 2018.
- [30] Y. L. Feng and W. J. Ju, "Study on mechanical characteristics and damage failure of coal mass from roadway side wall under loading and unloading stress path," *Coal Science and Technology*, vol. 47, no. 4, pp. 210–217, 2019.
- [31] J. W. Zhang, F. Z. Li, X. H. Yu, H. Ding, and L. H. Kong, "Research on evolution characteristics of early-age temperature-stress field of inner lining at deep frozen shaft," *Coal Science and Technology*, vol. 49, no. 2, pp. 69–76, 2021.
- [32] Y. L. Lu, L. G. Wang, F. R. Tang, and Y. He, "Fracture evolution of overburden rock in the combustion zone under the action of temperature-stress coupling during underground coal gasification," *Chinese journal of coal and coal*, vol. 37, no. 8, pp. 1292–1298, 2012.
- [33] F. Du and K. Wang, "Unstable failure of gas-bearing coal-rock combination bodies: insights from physical experiments and numerical simulations," *Process Safety and Environmental Protection*, vol. 129, pp. 264–279, 2019.
- [34] D. P. Shi, "Study on coal and rock damage under multiphase coupling," *Scientific Journal of Intelligent Systems Research*, vol. 2, no. 12, pp. 135–137, 2020.
- [35] H. D. Chen, Y. P. Cheng, Y. B. Pu, H. X. Zhou, and Q. Q. Liu, "Study on reconstituted coal damage features during unloading process," *Coal Science and Technology*, vol. 41, no. 3, pp. 84–87, 2013.
- [36] Y. Y. Du, H. Sun, and L. Q. Ma, "Infrared radiation response characteristics in coal damage evolution process," *Coal science and technology*, pp. 1–9, 2021.
- [37] Q. S. Liu, K. D. Liu, J. B. Zhu, and X. L. Lu, "Study of mechanical properties of raw coal under high stress with triaxial unloading," *Chinese Journal of Rock Mechanics and Engineering*, vol. 33, no. 1, pp. 24–34, 2014.
- [38] S. Y. Chen, L. Q. Liu, P. X. Liu, J. Ma, and G. Q. Chen, "Theoretical and experimental study on the relationship between stress-strain and temperature response," *SCIENCE IN CHINA PRESS*, vol. 39, no. 10, pp. 1446–1455, 2009.
- [39] C. H. Wang and X. J. Shi, "Finite element analysis of effect of temperature variation on temperature stress in mass concrete," *Building Construction*, vol. 30, no. 6, pp. 442–444, 2008.
- [40] W. C. Zhu, C. H. Wei, J. Tian, T. H. Yang, and C. A. Tang, "Coupled thermal-hydraulic-mechanical model during rock damage and its preliminary application," *Rock and Soil Mechanics*, vol. 30, no. 12, pp. 3851–3857, 2009.
- [41] G. J. Zhang and Y. Zhang, "Partition failure characteristics of rock material loading and unloading based on Mohr-Coulomb criterion," *Journal of China Coal Society*, vol. 44, no. 4, pp. 1049–1058, 2019.
- [42] M. C. He and P. Y. Guo, "Deep rock mass thermodynamic effect and temperature control measures," *Chinese Journal of Rock Mechanics and Engineering*, vol. 32, no. 12, pp. 2377–2393, 2013.
- [43] G. Y. Hou, H. Y. Jing, and J. P. Liang, "Experimental study on deformation and acoustic emission characteristics of rectangular roadway under different unloading rates," *Rock and Soil Mechanics*, vol. 40, no. 9, 2019.
- [44] Y. J. Qian, Y. L. Wu, W. W. Pei, and Y. Y. Zhu, "Rock strength and deformation characteristics under different unloading," *Hydro-Science and Engineering*, vol. 6, pp. 48–54, 2020.
- [45] X. Li, H. Li, Z. Yang et al., "Experimental study on triaxial unloading failure of deep composite coal-rock," *Advances in Civil Engineering*, vol. 2021, 2021.

Research Article

Numerical Simulation of the Volumetric Strain Distribution of a Protected Coal Seam

Hengyi Jia ^{1,2}

¹China Coal Research Institute, Beijing 100013, China

²State Key Lab of Coal Resources High Efficient Mining and Clean Utilization, Beijing 100013, China

Correspondence should be addressed to Hengyi Jia; jiahengyi2@163.com

Received 20 May 2021; Accepted 24 July 2021; Published 13 August 2021

Academic Editor: Feng Du

Copyright © 2021 Hengyi Jia. This is an open access article distributed under the Creative Commons Attribution License, which permits unrestricted use, distribution, and reproduction in any medium, provided the original work is properly cited.

To investigate the deformation characteristics of protected coal seams, the numerical simulation of the mining of an upper protective coal seam was carried out in the present study. Based on the basic definition of strain, a method for the extraction of the strain data of the protected coal seam was proposed, and the strain distribution characteristics were obtained. It was found that the x -direction strain is mainly distributed near the coal pillars on both sides and inside the goaf, the y -direction strain is mainly distributed at the working face, the initial mining line, and inside the goaf, and the z -direction strain is mainly distributed at the working face, the initial mining line, the coal pillars on both sides, and inside the goaf. The distribution characteristics and the value of volumetric strain were found to be basically consistent with the z -direction strain. As the working face advances, the protected coal seam undergoes compression and damage expansion in turn. The turning point between compression and damage expansion is approximately 15 m in front of the working face. The variation law of gas drainage in the boreholes of the protected coal seam is closely related to the distribution characteristics of volumetric strain. The results of this research are of great significance for the comprehensive investigation of the effects of pressure relief and the permeability enhancement of protective coal seam mining.

1. Introduction

Coal and gas outburst accidents have long caused substantial casualties and property losses to coal enterprises in China [1, 2]. With the increase of the mining depth, both the in situ stress and gas pressure increase, and the risk of coal and gas outburst is further enhanced [3, 4]. Both theoretical research and production practice demonstrate that the mining of protective coal seams can significantly reduce the in situ stress, expand cracks, discharge gas, and ultimately eliminate the outburst risk of protected coal seams [5–9].

The elimination of the outburst risk of protected coal seams depends on the degree of pressure relief after mining. Scholars have carried out extensive research on the deformation laws of protected coal seams from the perspectives of the relative distance between protective and protected coal seams [10, 11], double protective coal seam mining [12], the mining depth [13], and the impacts of protective coal seam mining

on the roadways of protected coal seams [14]. However, while these studies investigated the deformation of protected coal seams in the vertical direction, the deformation of protected coal seams should be reflected in three directions (the vertical, mining, and tilt directions). Shi and Liu [15] obtained the deformation laws of protected coal seams in both the vertical and mining directions based on the theory of rock fracture and damage, they did not obtain the deformation law along the tilt direction. He et al. [16] proposed a “four fixed point enclosed area” analysis method for the deformation of protected coal seams based on similar simulation experiments and obtained the volumetric strain distribution characteristics. However, it is time-consuming, laborious, and inconvenient to change the simulation conditions to carry out similar simulation experiments. In contrast, in the numerical simulation method, the simulation conditions can easily be changed by modifying the model parameters. Therefore, obtaining the distribution characteristics of the volumetric

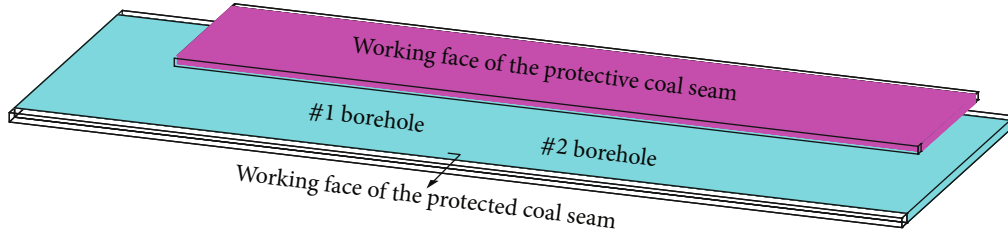


FIGURE 1: Working faces layouts.

strain via numerical simulation is important for the comprehensive investigation of protected coal seam deformation.

In this research, FLAC3D numerical simulation software was employed to study the pressure relief effect of a protected coal seam. According to the definition of strain, a method for extracting the strain data of the protected coal seam was proposed, and the strain distribution characteristics were obtained.

2. Numerical Simulation of Protective Coal Seam Mining

2.1. General Situation of the Coal Mine under Study. The Zhongxing coal mine is located in Shanxi Province, China. The main coal seam of the coal mine is the #2 coal seam, which has low permeability and a severe risk of coal and gas outburst. The locally mineable #02 coal seam is located about 10 m above the #2 coal seam and has a lower risk of outburst and a reduced gas content as compared to the #2 coal seam. To eliminate the outburst risk of the #2 coal seam, the #02 coal seam was mined first as an upper protective coal seam. Because the #02 coal seam is locally mineable, the size of its working face is less than that of the protected coal seam. The sizes of the working faces of the protective and protected coal seam are, respectively, 1160×75 m and 1595×190 m (length \times width). The layouts of the working faces are presented in Figure 1, and their basic parameters are reported in Table 1.

2.2. Establishment of the Numerical Model. Based on the strata conditions of the Zhongxing coal mine, the numerical model shown in Figure 2 was established by FLAC3D numerical simulation software. The strata conditions and mechanical parameters of the coal mine are reported in Table 2. Mining a coal seam will cause the deformation of the rock mass and a reduction in rock strength. Thus, the rock mass can be regarded as elastic-plastic material that exhibits strain-softening characteristics after it is damaged [17]. Therefore, the Mohr-Coulomb strain-softening model was selected, and the tilt angle of the rock strata in the model was set to zero for simplicity.

According to the stress condition of the Zhongxing coal mine, compressive stress of 20 MPa was imposed at the top of the model, and a fixed boundary was imposed at the bottom of the model. The other sides of the model were set as rolling boundaries with an imposed stress of 20 MPa. The length, width, and height of the model were, respectively, 300, 300, and 131 m. The mining length of the working face

TABLE 1: Basic parameters of the coal seams.

Parameter	Protective coal seam	Protected coal seam
Thickness of the coal seam	0.51 m (in average)	2 m (in average)
Tilt angle of the coal seam	7° (in average)	7° (in average)
Original gas pressure	—	0.82 MPa
Original gas content	3.37 m ³ /t	10.4 m ³ /t

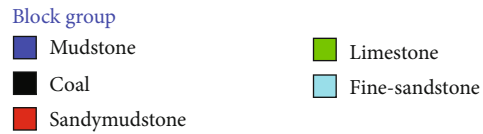
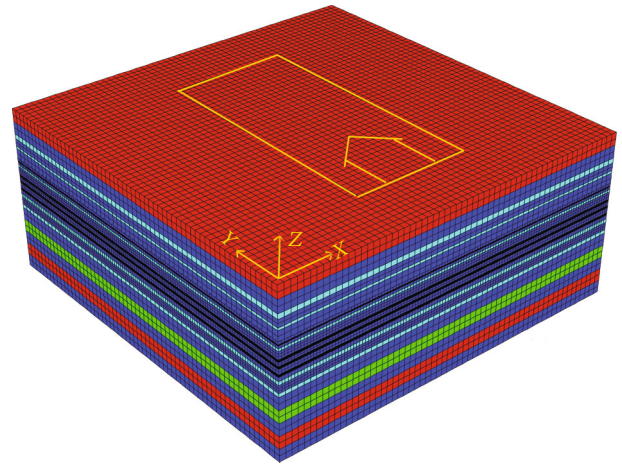


FIGURE 2: Numerical calculation model.

was 200 m, which extends from 50 to 250 m along the y -direction. Moreover, the mining width was 100 m, which extends from 100 to 200 m along the x -direction, and the mining height was 1 m. The model contained 349,200 grids and 400,243 zones (as shown in Figure 2).

2.3. Strain Data Extraction Method. Under the influence of the mining stress, a protected coal seam will be compressed or expand in three directions (the vertical, mining, and tilt directions). In other words, the deformation is mainly reflected in the change of the coal seam volume. The

TABLE 2: Mechanical parameters of coal and rock.

Lithology	Density/kg/m ³	Bulk modulus/GPa	Shear modulus/GPa	Friction angle/°	Cohesion/MPa	Dilatancy angle/°	Uniaxial tensile strength/MPa
Sandy mudstone	2740	3.7	3.1	35	2.6	10	2.4
Mudstone	2690	2.0	1.5	31	1.5	10	1.0
Fine sandstone	2740	3.5	2.2	30	2.0	10	2.0
Coal	1450	1.0	0.8	20	0.6	10	0.5
Limestone	3080	3.9	3.5	43	4.8	10	3.2

volumetric strain of a coal seam is equal to the sum of its strains in the three directions, and the extraction method of the strain data is presented as follows.

The strain in the z -direction (vertical direction) is

$$\eta_z = \frac{d_{\text{floor}} - d_{\text{roof}}}{m}, \quad (1)$$

where η_z is the strain of the protected coal seam in the z -direction, d_{floor} is the vertical displacement of the coal seam floor, d_{roof} is the vertical displacement of the coal seam roof, and m is the initial thickness of the coal seam.

The length and width of the grids in the #2 coal seam were both 2.5 m. When extracting the vertical strain, the vertical displacement of the grid boundary line between $2 \leq x \leq 3$ along the coal seam floor was extracted first. The distance was then increased by 10 m along the x -direction, and the vertical displacement of the grid boundary line between $12 \leq x \leq 13$ was extracted. By analogy, a vertical displacement matrix of the coal seam floor with 120 rows \times 30 columns was obtained. Via the same method, the vertical displacement matrix of the coal seam roof was also obtained. According to Eq. (1), the vertical strain matrix of the #2 coal seam was calculated.

The strain in the x -direction (tilt direction) is

$$\eta_x = \frac{d_{x_i} - d_{x_j}}{l_{x_i \sim x_j}}, \quad (2)$$

where η_x is the strain of the protected coal seam in the x -direction, d_{x_i} is the displacement of the coal seam in the x -direction at position x_i , d_{x_j} is the displacement of the coal seam in the x -direction at position x_j , and $l_{x_i \sim x_j}$ is the initial width from x_i to x_j .

When extracting the strain in the x -direction, the displacement in the x -direction of the grid boundary line between $2 \leq x \leq 3$ was first obtained, which corresponds to the displacement d_{x_i} . Then, the displacement of the grid boundary line between $4.5 \leq x \leq 5.5$ was obtained, which corresponds to the displacement d_{x_j} . The initial width (2.5 m) between the two grid boundary lines corresponds to the $l_{x_i \sim x_j}$. According to Eq. (2), the x -direction strain between the two grid boundary lines can be calculated. The distance was then increased by 10 m along the x -direction, and the strain of the grid boundary lines between $12 \leq x \leq 13$ and that

between $14.5 \leq x \leq 15.5$ were obtained. By analogy, a strain matrix of the coal seam in the x -direction with 120 rows \times 30 columns was obtained.

The strain in the y -direction (mining direction) is

$$\eta_y = \frac{d_{y_i} - d_{y_j}}{l_{y_i \sim y_j}}, \quad (3)$$

where η_y is the strain of the protected coal seam in the y -direction, d_{y_i} is the displacement of the coal seam in the y -direction at position y_i , d_{y_j} is the displacement of the coal seam in the y -direction at position y_j , and $l_{y_i \sim y_j}$ is the initial length from y_i to y_j .

The grid boundary line between $2 \leq x \leq 3$ was first determined, after which the displacements in the y -direction of the grids along the grid boundary line were extracted. For any grid, the side with a smaller y -coordinate corresponds to d_{y_i} , the side with a larger y -coordinate corresponds to d_{y_j} , and the initial length of the grid corresponds to $l_{y_i \sim y_j}$. The strain of each grid can be calculated by substituting the extracted data into Eq. (3). The distance was then increased by 10 m along the x -direction, and the strains of the grids along the grid boundary line between $12 \leq x \leq 13$ were obtained by the same method. By analogy, a strain matrix of the coal seam in the y -direction with 120 rows \times 30 columns was obtained.

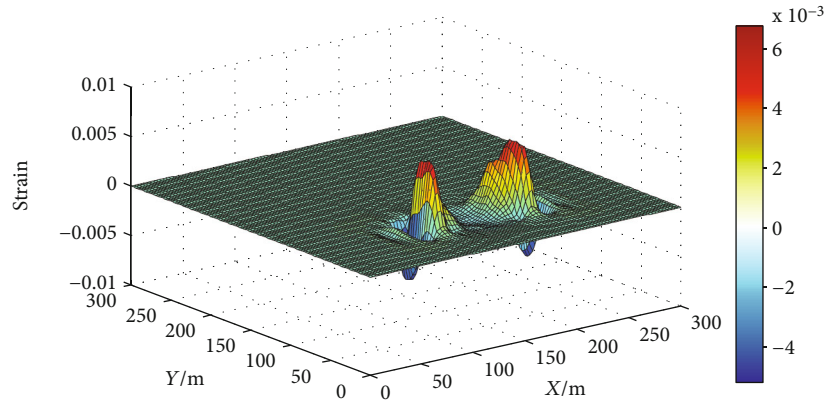
The volumetric strain matrix of the protected coal seam can be obtained by directly adding the elements of the three strain matrices. The calculation formula is as follows:

$$\eta_v = \eta_x + \eta_y + \eta_z, \quad (4)$$

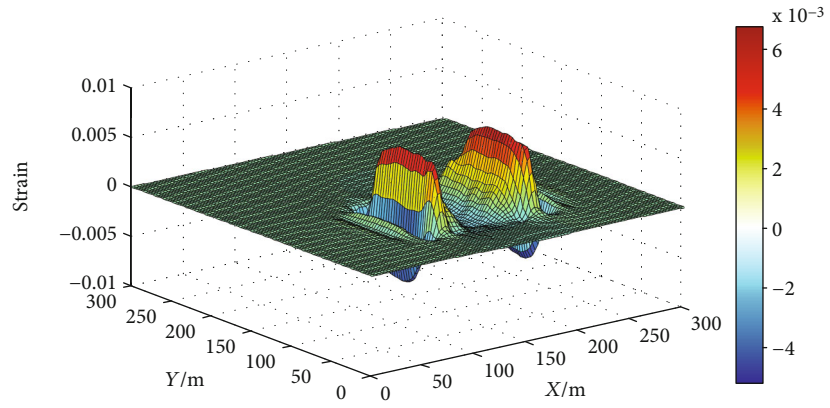
where η_v is the volumetric strain of the protected coal seam.

3. Strain Distribution of the Protected Coal Seam

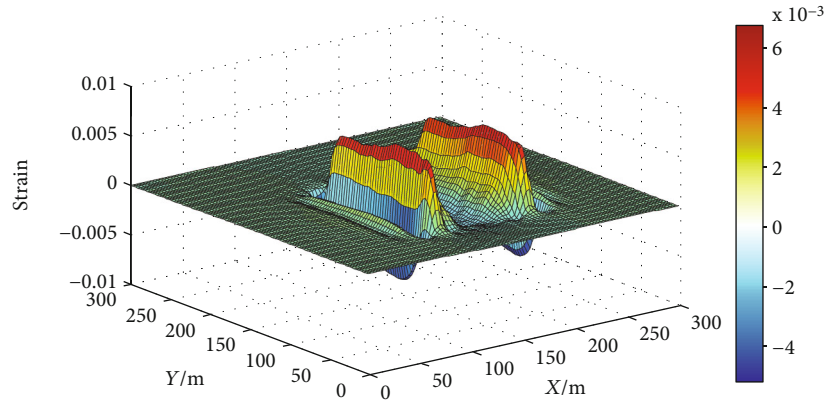
According to the method discussed in the previous section, the strain data of the protected coal seam were extracted. The data were processed by using the "surf" function and "meshgrid" command in MATLAB software, and the strain distributions were obtained. Figures 3–7 present the strain distribution diagrams of the protected coal seam when the working face of the protective coal seam was mined to different distances. In the figures, positive values of strain indicate



(a) Mined 50 m



(b) Mined 100 m



(c) Mined 150 m

FIGURE 3: Continued.

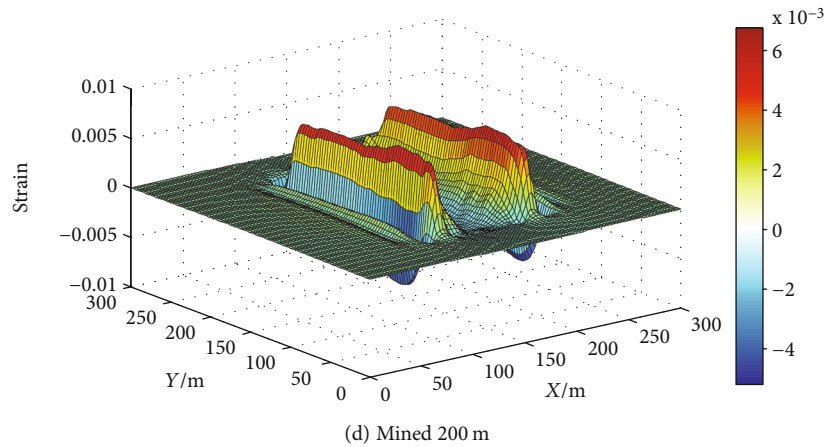


FIGURE 3: X-direction strain of protected coal seam.

that the coal seam underwent compression, while negative values indicate that the coal seam underwent expansion.

Figure 3 presents the x -direction strain of the protected coal seam, which was found to be mainly distributed near the coal pillars on both sides and inside the goaf, while the strain at the working face and the initial mining line was not obvious. The coal seam directly below the coal pillars was in a stress concentration zone, and the significantly increased vertical stress compressed the coal seam in the vertical direction and elongated it in the x -direction. The coal seam at the inner side of the coal pillars was located in a pressure relief zone, in which the vertical stress decreased the most and the coal seam was compressed in the x -direction under the increased horizontal deviatoric stress.

Figure 4 presents the y -direction strain of the protected coal seam, which was found to be mainly distributed at the working face, the initial mining line, and inside the goaf. The strain near the coal pillars on both sides was not obvious. The coal seam directly below the working face was found to expand in the y -direction, which was due to the vertical stress concentration in this area. The coal seam at the inner side of the initial mining line was compressed in the y -direction significantly; it was located in a pressure relief zone, and the degree of unloading of vertical stress in this zone was greater than that of horizontal stress. After the protective coal seam was mined, the floor strata tended to move to the goaf and stop in this zone. Under the dual action of the floor strata movement and vertical stress unloading, the coal seam in this zone was compressed in the y -direction.

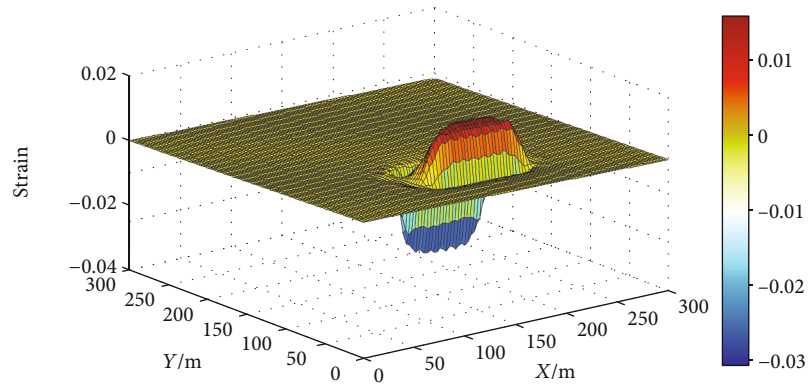
Figure 5 exhibits the z -direction strain of the protected coal seam, which was found to be distributed at the working face, the initial mining line, the coal pillars on both sides, and inside the goaf. The coal seam directly below the working face, the initial mining line, and the coal pillars was compressed along the z -direction, whereas the coal seam in the goaf expanded significantly. In the goaf, the vertical strain was greater than the horizontal strain, which was determined by vertical stress unloading. With the advance of the working face, the stress in the central area of the goaf was gradually restored, and the degree of expansion of the coal seam exhibited a decreasing trend.

Figure 6 displays the volumetric strain of the protected coal seam. The distribution characteristics and the value of volumetric strain were found to be basically consistent with those of the z -direction strain. With the exploitation of the protective coal seam, the scope of the goaf expanded, and the volumetric strain presented an inverted saddle shape. To further investigate the distribution characteristics of the volumetric strain, the main view is shown in Figure 7. It can be seen from the figure that the volumetric strain experienced the stages of increasing, decreasing, and then increasing again from the boundary to the interior of the model. The volumetric strain reached the maximum value in the stress concentration zone and decreased to the minimum value near the working face. The turning point of volumetric strain from increasing to decreasing was found to be about 15 m in front of the working face, which indicates that this was the starting point of the protected coal seam changing from elastic compression to damage expansion.

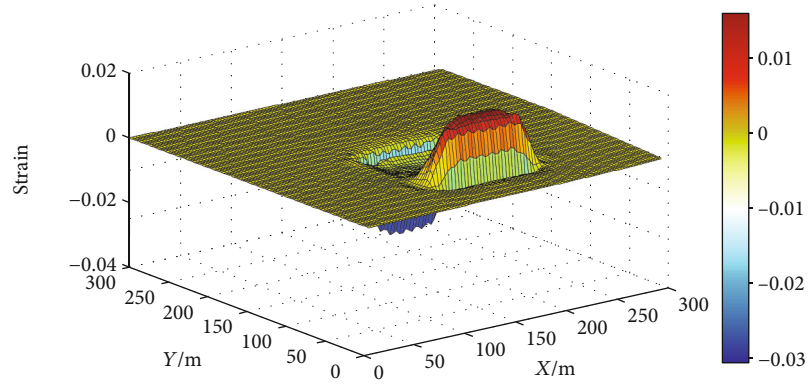
4. Field Observation of the Gas Drainage Effect of the Protected Coal Seam

The changes in the permeability and volumetric strain of protected coal seam both reflect the degree of pressure relief of the coal seam; thus, the permeability and volumetric strain have internal unity. Assuming that the gas pressure of the protected coal seam remains constant during protective coal seam mining, the gas drainage quantity of the coal seam is proportional to the permeability. Therefore, the change law of the gas drainage quantity can be used to verify the correctness of the distribution characteristics of the volumetric strain.

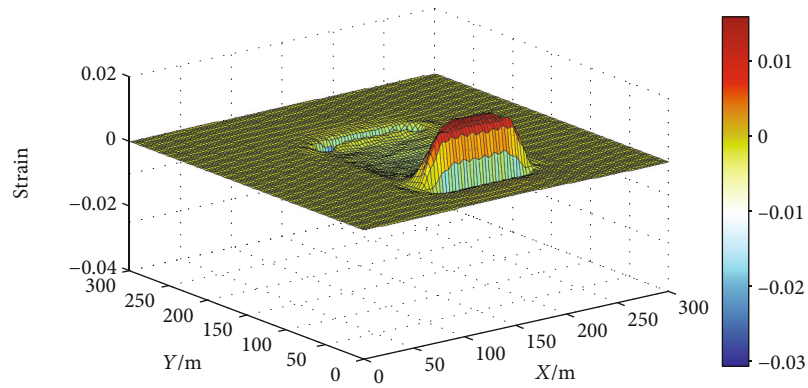
Two gas boreholes were preconstructed in the transportation roadway of the protected coal seam prior to the mining of the protective coal seam. The boreholes were arranged along the coal seam inclination direction and were used to measure the gas drainage quantity and gas drainage concentration with the advance of the working face (as shown in Figure 1). The initial horizontal distances between boreholes #1 and #2 and the working face were 120 and 144 m, respectively. The length of the boreholes was 120 m, and the diameter was 94 mm.



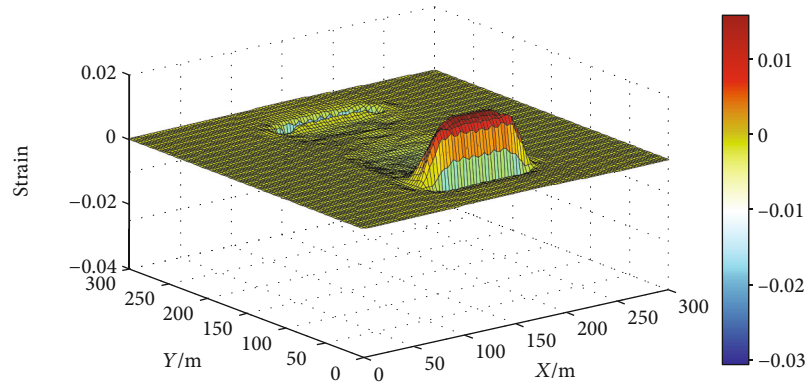
(a) Mined 50 m



(b) Mined 100 m

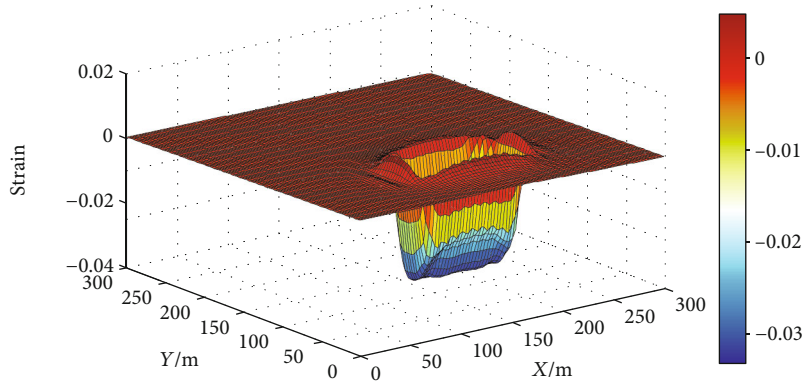


(c) Mined 150 m

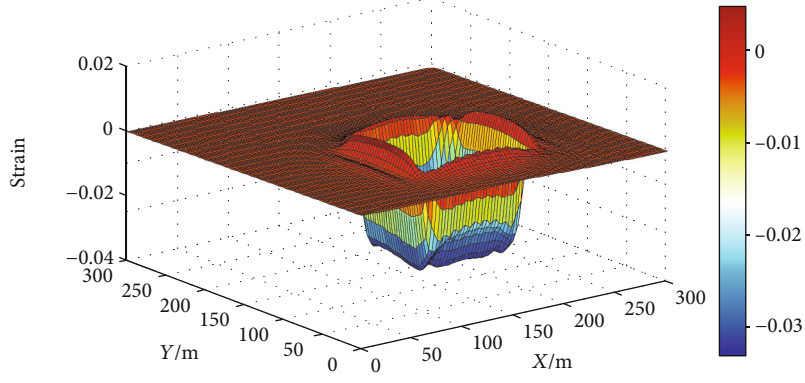


(d) Mined 200 m

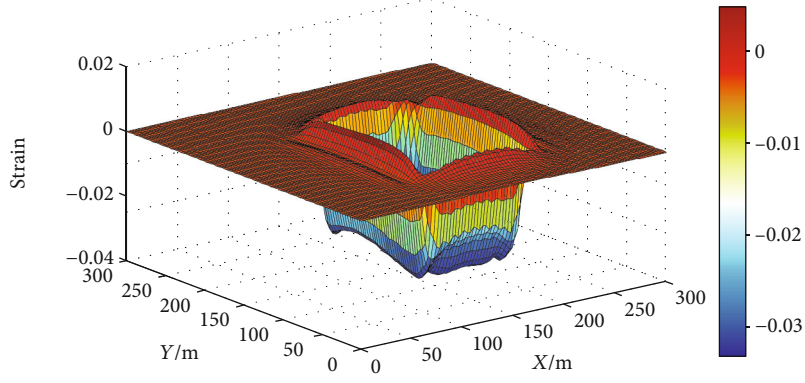
FIGURE 4: Y -direction strain of protected coal seam.



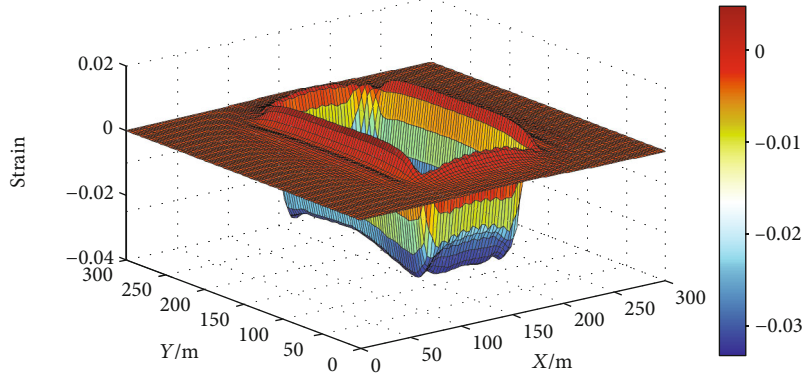
(a) Mined 50 m



(b) Mined 100 m

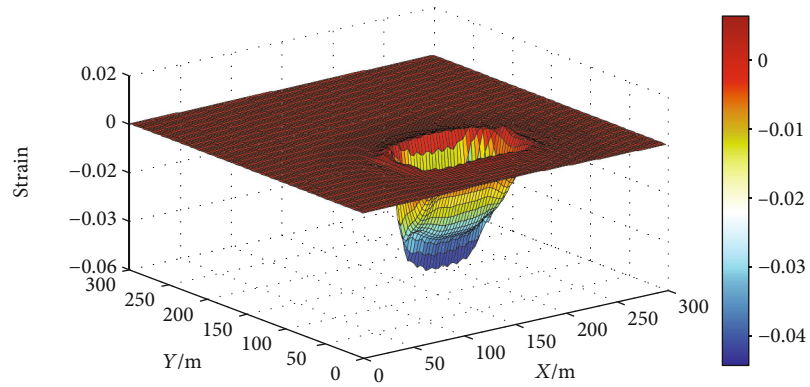


(c) Mined 150 m

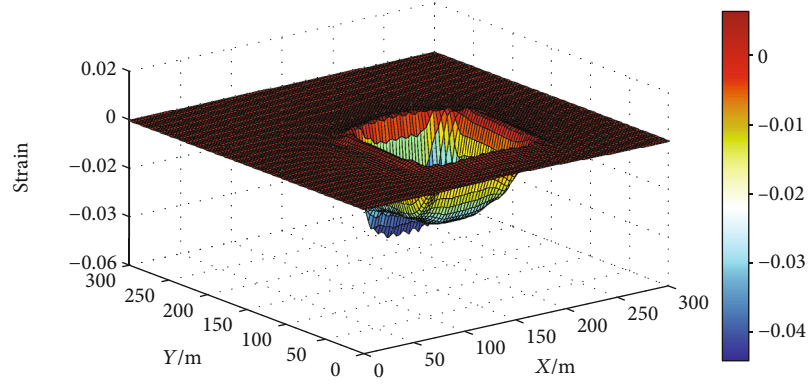


(d) Mined 200 m

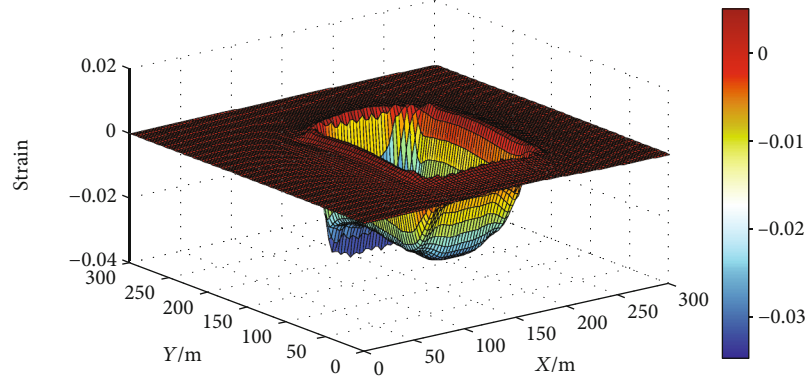
FIGURE 5: Z -direction strain of protected coal seam.



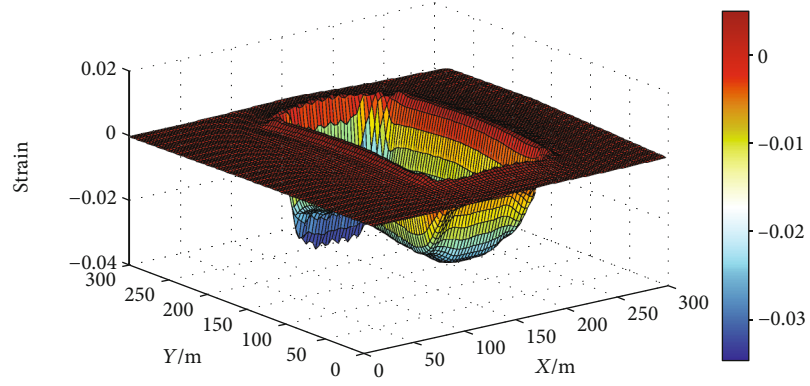
(a) Mined 50 m



(b) Mined 100 m



(c) Mined 150 m



(d) Mined 200 m

FIGURE 6: Volumetric strain of protected coal seam.

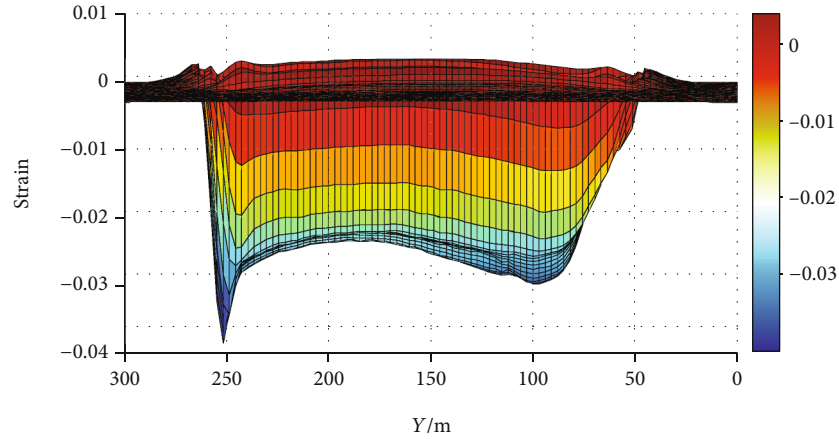


FIGURE 7: The main view of the volumetric strain.

Figure 8 presents the variation laws of the gas drainage quantity and gas concentration of the boreholes. The abscissa in the figure indicates the relative position between the boreholes and the working face. For example, $x = 100$ means that the borehole was located 100 m in front of the working face, and $x = -50$ means that the borehole was located 50 m behind the working face. It can be seen from the figure that the mixed gas drainage quantity was relatively high at the initial stage of mining and decreased in a fluctuating manner with the advance of the working face. From about 15 m in front of the working face, the mixed gas drainage quantity, the pure gas drainage quantity, and the gas concentration began to increase rapidly. When the boreholes entered the goaf, these gas drainage values reached the maximum and remained stable for a period of time, after which they ultimately fluctuated inside the goaf. The variation laws of the gas drainage quantity and the gas concentration were found to be closely related to the distribution characteristics of the volumetric strain; the turning point of the rapid increase of gas drainage coincided with the starting point of damage expansion. These results prove the correctness of the distribution characteristics of the volumetric strain.

5. Discussion

Based on a numerical simulation, a method for the extraction of the strain data of a protected coal seam was proposed, and the strain distribution characteristics were obtained. The x -direction strain was found to be mainly distributed near the coal pillars on both sides and inside the goaf, while the y -direction strain was found to be mainly distributed at the working face, the initial mining line, and inside the goaf. The deformation of the coal seam was affected by the change of stress and the deformable conditions, both of which caused the distribution difference of the horizontal strains. A stress concentration zone was formed around the stope, at which the significantly increased vertical stress caused the compression of the coal seam along the z -direction. The stress inside the goaf was greatly unloaded in all directions, and the coal seam swelled. The simulation results show that the distribution characteristics and the value of the volumet-

ric strain were basically consistent with the z -direction strain, indicating that the z -direction strain has a decisive influence on the volumetric strain. Due to the restrictions of field measurement conditions and technology, scholars have often used vertical strain (z -direction strain in this paper) to express the pressure relief effect of protected coal seams; although this operation is not perfect in theory, it is acceptable in fact.

With the advance of the working face, the protected coal seam entered the stress concentration zone from the original stress zone, and the coal seam experienced compression and damage expansion in turn. The turning point from compression to damage expansion was found to be about 15 m in front of the working face. With the further advance of the working face, the protected coal seam expanded rapidly after entering the goaf and then remained stable. Based on the results of gas drainage, it was determined that the mixed gas drainage quantity was higher in the initial stage and then gradually decreased with the advance of the working face, which was caused by the compression of the coal seam. The mixed gas drainage quantity, pure gas drainage quantity, and gas concentration began to increase rapidly at 15 m in front of the working face and then remained stable after entering the goaf. The variation law of gas drainage data was found to be closely related to the distribution characteristics of the volumetric strain, which proves the correctness of the numerical simulation results. Thus, it is feasible to verify the distribution characteristics of the volumetric strain of a protected coal seam via the gas drainage quantity and gas concentration in the boreholes.

The volumetric strain of a protected coal seam reveals only the degree of pressure relief of the coal seam and does not reveal the degree of permeability increase. If an evolution model of coal permeability with volumetric strain as a variable is established, and if the model is combined with coal seam volumetric strain, the distribution characteristics of permeability can be obtained. Xie et al. [19] considered the volumetric change of damaged coal with cracks induced by the coupling of the abutment pressure under different mining conditions, pore pressure, and expansion caused by gas adsorption, and proposed a new term for mining-enhanced permeability that reflects the change in permeability by the

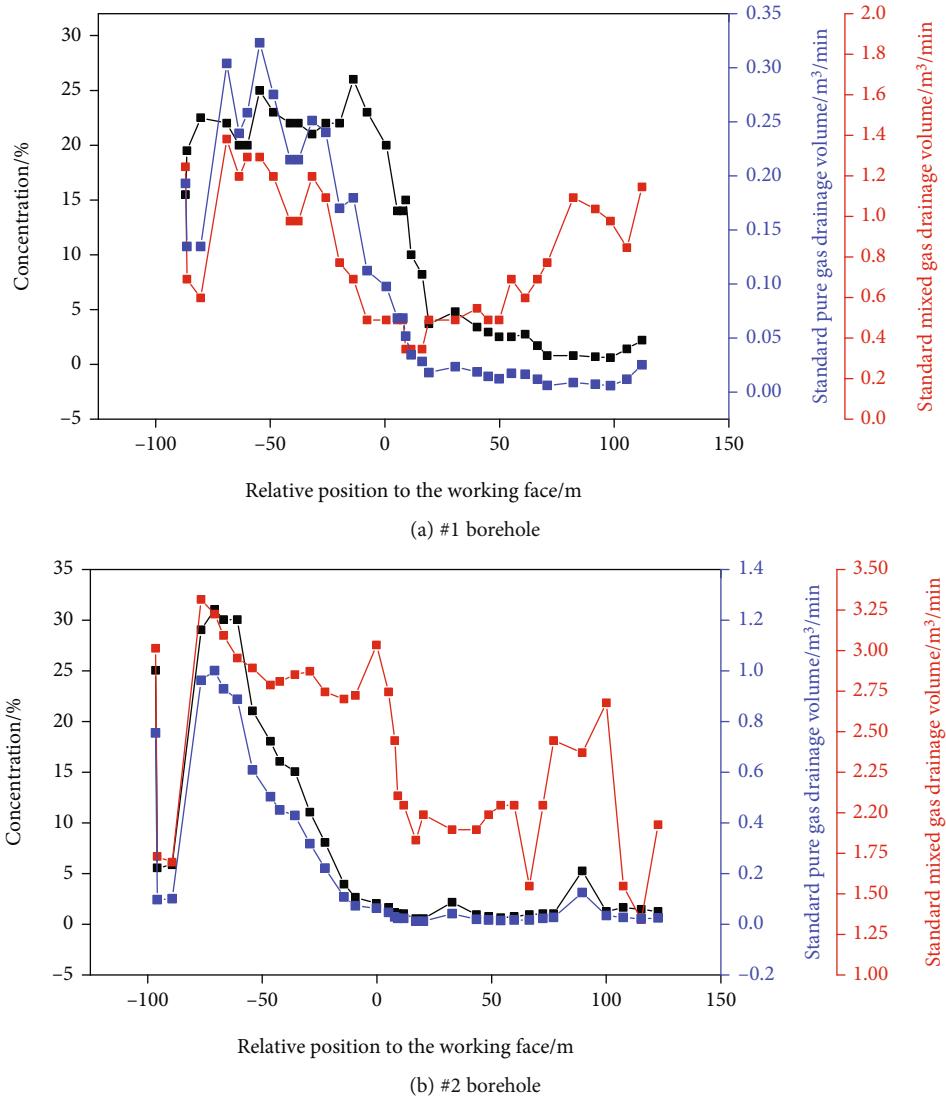


FIGURE 8: Statistics of the gas drainage data [18].

volumetric change of coal. Cheng et al. [20] put forward a new model with strain as a variable for unloading fractured coal by considering the deformation effects of the effective stress and gas adsorption/desorption. These studies laid a theoretical foundation for obtaining the permeability enhancement effect of protected coal seams. However, there is a lack of research on the distribution characteristics of the volumetric strain of protected coal seams. Because coal and gas outburst accidents are becoming increasingly more serious [21–24], the present study both supplements and improves the previous research, and the results are of great significance to revealing the effect of the permeability enhancement of protected coal seams.

6. Conclusion

- (1) The deformation of coal seams is affected by both the change in stress and the deformation conditions. The vertical strain of a coal seam dominates the change law and the value of volumetric strain.

Although it is not comprehensive to use the vertical strain to express the effect of pressure relief of protective coal seam mining in theory, it is acceptable in fact

- (2) The change laws of the gas drainage quantity and gas concentration of a protected coal seam are closely related to the distribution characteristics of the volumetric strain. The turning point of the rapid increase of the gas drainage quantity and gas concentration coincides with the point of damage expansion. Thus, it is feasible to verify the distribution characteristics of the volumetric strain of a protected coal seam via the use of gas drainage data
- (3) The volumetric strain only reveals the degree of pressure relief of a protected coal seam, but does not reveal the degree of permeability increase. The results of this study are of great significance for the comprehensive investigation of the effect of the permeability enhancement of protective coal seam mining

Data Availability

The data used to support the findings of this study are available from the corresponding author upon request.

Conflicts of Interest

The author declares that there is no conflict of interest.

Acknowledgments

This research is financially supported by the National Natural Science Foundation of China (Grant no. 51704164).

References

- [1] H. Wang, Z. Cheng, Q. Zou et al., "Elimination of coal and gas outburst risk of an outburst-prone coal seam using controllable liquid CO₂ phase transition fracturing," *Fuel (Guildford)*, vol. 284, article 119091, 2021.
- [2] F. du, K. Wang, X. Zhang, C. Xin, L. Shu, and G. Wang, "Experimental study of coal-gas outburst: insights from coal-rock structure, gas pressure and adsorptivity," *Natural Resources Research*, vol. 29, no. 4, pp. 2481–2493, 2020.
- [3] M. B. Díaz Aguado and C. González Nicieza, "Control and prevention of gas outbursts in coal mines, Riosa-Olloniego coalfield, Spain," *International Journal of Coal Geology*, vol. 69, no. 4, pp. 253–266, 2007.
- [4] E. Krause and J. Skiba, "Formation of methane hazard in longwall coal mines with increasingly higher production capacity," *International Journal of Mining Science and Technology*, vol. 24, no. 3, pp. 403–407, 2014.
- [5] D. Guowei and Z. Yinhuai, "A novel method for selecting protective seam against coal and gas outburst: a case study of Wangjiazhai coal mine in China," *Sustainability*, vol. 9, no. 6, p. 1015, 2017.
- [6] J. Jiang, Y. Cheng, P. Zhang, K. Jin, J. Cui, and H. du, "CBM drainage engineering challenges and the technology of mining protective coal seam in the Dalong Mine, Tiefsa Basin, China," *Journal of Natural Gas Science and Engineering*, vol. 24, pp. 412–424, 2015.
- [7] F. du and K. Wang, "Unstable failure of gas-bearing coal-rock combination bodies: insights from physical experiments and numerical simulations," *Process Safety and Environmental Protection*, vol. 129, pp. 264–279, 2019.
- [8] Q. Huang, S. Liu, W.-m. Cheng, and G. Wang, "Fracture permeability damage and recovery behaviors with fracturing fluid treatment of coal: an experimental study," *Fuel*, vol. 282, article 118809, 2020.
- [9] Q. Huang, S. Liu, G. Wang, and W. Cheng, "Evaluating the changes of sorption and diffusion behaviors of Illinois coal with various water-based fracturing fluid treatments," *Fuel*, vol. 283, article 118884, 2021.
- [10] M. Tu, X. X. Miao, and N. B. Huang, "Deformation rule of protected coal seam exploited by using the long-distance-lower protective seam method," *Journal of Mining and Safety Engineering*, vol. 23, no. 3, pp. 253–257, 2006.
- [11] Z. Ma, M. Tu, J. MA, B. Zhang, and M. Han, "Rock mass deformation characteristics for coal mining at remote lower protective seam," *Journal of Mining and Safety Engineering*, vol. 25, no. 3, pp. 253–257, 2008.
- [12] Z. Shujin, L. Shaoquan, and L. Shuqing, "Experimental study on swelling deformation law of mining seam in dual protective seam of seam group," *Coal Engineering*, vol. 45, no. 9, pp. 87–90, 2013.
- [13] D. Zhixu and L. Qiang, "Study on pressure unloading effect of lower coal seam under upper protective layer in a kilometer deep well," *Safety in Coal Mines*, vol. 50, no. 4, pp. 6–9, 2019.
- [14] Z. H. Wang-lei, X. I. Zu-qiang, W. A. Hong-yan, and Z. H. Yao-hui, "Study on deformation law of overlying roadway under condition of lower protective seam mining," *Coal Science and Technology*, vol. 42, no. 5, pp. 9–12, 2014.
- [15] S. H. I. Bi-ming and L. I. U. Ze-gong, "Numerical simulation of the upper coal and rock deformation characteristic caused by mining protecting stratum," *Journal of China Coal Society*, vol. 33, no. 1, pp. 17–22, 2008.
- [16] H. Aiping, F. Hua, L. Yangbo, and H. Bingjie, "Analysis method on swelling deformation of protected seam in the process of protective coal seam exploitation," *Journal of Safety Science and Technology*, vol. 12, no. 8, pp. 60–67, 2016.
- [17] W. Yang, B.-q. Lin, Y. A. Qu et al., "Mechanism of strata deformation under protective seam and its application for relieved methane control," *International Journal of Coal Geology*, vol. 85, no. 3-4, pp. 300–306, 2011.
- [18] H. Jia, K. Wang, C. Xu, and Q. Fu, "Permeability distribution characteristics of underlying coal seam disturbed by mining activity," *Energy Sources, Part A: Recovery, Utilization, and Environmental Effects*, pp. 1–16, 2019.
- [19] X. HP, Z. HW, C. GM, and Z. FB, "On theoretical and modeling approach to mining-enhanced permeability for simultaneous exploitation of coal and gas," *Journal of China Coal Society*, vol. 7, pp. 1101–1108, 2013.
- [20] C. YP, L. HY, G. PK, P. RK, and W. LA, "A theoretical model and evolution characteristic of mining-enhanced permeability in deeper gassy coal seam," *Journal of China Coal Society*, vol. 8, pp. 1650–1658, 2014.
- [21] K. Wang and F. Du, "Coal-gas compound dynamic disasters in China: a review," *Process Safety and Environmental Protection*, vol. 133, pp. 1–17, 2020.
- [22] H. Wang, X. Yang, F. Du et al., "Calculation of the diffusion coefficient of gas diffusion in coal: the comparison of numerical model and traditional analytical model," *Journal of Petroleum Science and Engineering*, vol. 205, article 108931, 2021.
- [23] V. Palchik, "Formation of fractured zones in overburden due to longwall mining," *Environmental Geology*, vol. 44, no. 1, pp. 28–38, 2003.
- [24] C. Karacan, F. A. Ruiz, M. Cotè, and S. Phipps, "Coal mine methane: a review of capture and utilization practices with benefits to mining safety and to greenhouse gas reduction," *International Journal of Coal Geology*, vol. 86, no. 2-3, pp. 121–156, 2011.

Research Article

A Statistical Damage Constitutive Model of Anisotropic Rock: Development and Validation

Tenglong Rong ^{1,2}, Can Guan ¹, Kelu Liu ¹, Shuai Heng ^{1,2}, Wenlong Shen ^{1,2}
and Ruiyong Mou ³

¹School of Energy Science and Engineering, Henan Polytechnic University, Jiaozuo 454003, China

²Collaborative Innovation Center of Coal Work Safety and Clean High Efficiency Utilization, Henan Polytechnic University, Jiaozuo 454003, China

³Research Institute of Aero-Engine, Beihang University, Beijing 100191, China

Correspondence should be addressed to Tenglong Rong; rongtenglong@126.com

Received 11 June 2021; Accepted 23 July 2021; Published 13 August 2021

Academic Editor: Feng Du

Copyright © 2021 Tenglong Rong et al. This is an open access article distributed under the Creative Commons Attribution License, which permits unrestricted use, distribution, and reproduction in any medium, provided the original work is properly cited.

The damage constitutive model is of great significance to research the stress-strain relationship and damage evolution of rock under loading in engineering. In order to investigate the effect of anisotropic characteristic on the stress-strain relationship and damage evolution, a statistical damage constitutive model of anisotropic rock under true triaxial condition was developed. In this study, the plane which existed perpendicular to the coordinate axis was extracted from representative volume element (RVE) of rock. The extracted plane was assumed to be composed of abundant mesoscopic elements whose failure strength satisfied the Weibull distribution. According to the number of failure elements on the plane in each direction under loading, the anisotropic damage variable was established based on the proposed concept of areal damage. A statistical damage constitutive model of anisotropic rock was developed by using strain equivalent hypothesis and generalized Hooke constitutive model. Subsequently, the parameters in the anisotropic damage constitutive model were determined by the method of total differential. Thus, the damage evolution of anisotropic rock under various stress conditions can be conveniently evaluated by the anisotropic damage model. The model was validated based on the tests of rocks under the stress conditions of conventional triaxial and true triaxial, respectively. Moreover, for the purpose of studying the influence of parameters on the model, sensitivity analyses of mechanical parameters and model parameters were carried out. The results of statistical damage constitutive clearly demonstrate the stress-strain and damage evolution of anisotropic rock under various stress conditions.

1. Introduction

The stress-strain relationship of rock affected by damage under loading has always been the focus of rock mechanics. It is of great significance to accurately predict the mechanical state and deformation of rock for geotechnical [1], coal mining [2, 3], shale gas exploitation [4], etc. Due to the long-term geological effects in history, rock is a heterogeneous material which includes flaws and geological structure, i.e. pores, voids, defects, joints, fractures, and bedding. Therefore, anisotropy is an obvious characteristic of rock. It is very valuable to investigate the damage and deformation of anisotropic rock under loading. The stress-strain relationship

and damage evolution of anisotropic rock have been studied by laboratory tests in previous researches [4–7].

The damage evolution and stress-strain relationship can also be studied by means of theoretical analysis. The damage constitutive model considering anisotropic characteristics is the theoretical basis of analyzing the anisotropic rock deformation. Based on the previous researches, there are two main theoretical approaches to establish the constitutive relationship of rock under the influence of damage. One approach to establish constitutive model is continuum damage mechanics (CDM). In this approach, rock is regarded as continuous medium. The relationship between damage variable and loading condition is established according to CDM.

The modeling approach based on CDM is developed very early. Some of the models based on CDM involve the anisotropic characteristic [8–12], but the anisotropic damage model based on this approach is complicated.

The other approach to establish constitutive relationship of rock is the statistical damage model (SDM), which is according to the statistics and continuum damage mechanics. In the process of modeling, rock is regarded as clusters composed of abundant mesoscopic elements. The mechanical parameters of mesoscopic elements satisfy a certain mathematical function distribution. Then, the number of destructive mesoscopic elements in rock under loading is calculated by the statistical method. Consequently, damage variable is put forward according to the number of destructive mesoscopic elements to evaluate the damage evolution. Krajcinovic and Silva first proposed a simple statistical damage model to study the material damage evolution under uniaxial tension [13]. Tang and Xu assumed that rock was composed of a large number of mesoscopic elements, which were elastic before failure and useless after failure. The failure strength of mesoscopic elements was based on the normal statistical distribution. Then, the stress-strain of rock under uniaxial condition was analyzed by the continuum damage mechanics [14]. Subsequently, the theory of SDM was improved by Tang and coworkers [15–18]. Cao and coworkers [19–21] made many attempts to improve SDM from different aspects. The attempts included different statistical distribution functions (Weibull distribution and normal distribution) and different strength criteria (Mohr-Coulomb and Drucker-Prager). Meanwhile, the following issues were taken into consideration in these attempts: damage threshold, initial compression, strain softening, and residual strength. Considering scale effect in rock shearing, some statistical damage constitutive models of rock under shear stress were also proposed [22, 23]. In order to research the stress-strain of rock under damage effect more accurately, many mathematical and mechanical theories have been introduced into the SDM [20, 24–27].

In addition to rock damage under loading (compression, tension and shear), the SDM has also been widely used in research of rock damage in the multiphysical environment [28–32]. The factors of porosity, temperature, or freeze-thaw cycles were introduced into the damage variables of SDM under the multiphysical conditions. Moreover, in order to investigate the effect of joints on damage, the factors of crack propagation length, joint friction effect, and joint orientation were drawn into the SDM [33, 34]. There are many statistical damage models that can be used to analyze the progressive damage process of rock under various actions, such as load (compression, tension and shear), high temperature, freeze-thaw, chemistry, and joint. It can be seen that most of the presented SDM are based on isotropic properties. Therefore, the SDM of rock which is based on anisotropic properties needs to be further studied. It is great valuable to develop a SDM which can represent the anisotropic characteristic of rock.

In this study, based on the assumption that any plane of rock was composed of mesoscopic elements whose strength conformed to the Weibull distribution. The concept of areal

damage was proposed to establish the expression of anisotropic damage variable. Then, a statistical damage constitutive model of anisotropic rock (SDAR model) was developed by using strain equivalent hypothesis. Subsequently, the determination of parameters in the anisotropic damage constitutive model was conducted by the method of total differential. Finally, the model was validated based on the tests of two kinds of rocks under different loading stress conditions. One was transversely isotropic shale under conventional triaxial stress condition. And the other was orthogonal anisotropic coal under true triaxial stress condition. In addition, the sensitivity study of parameters was conducted by the developed damage model.

2. Development of the Statistical Damage Constitutive Model of Anisotropic Rock

2.1. Anisotropic Damage Variable. Rock damage refers to the progressive deterioration of mechanical properties caused by the defect accumulation in rock under the action of stress and other factors. In the research on creep behavior of metal under uniaxial tension, Kachanov found that the propagation of microdefects was the main reason for creep damage in material [35]. Consequently, the definition of “continuity” was proposed to quantitatively show the damage behavior of material under loading in Eq. (1), i.e.,

$$\psi = \frac{\tilde{S}}{S}, \quad (1)$$

where ψ is the continuity of material, S is the initial total area of the material, and \tilde{S} is the actual bearing area, which is the result of deducting the failure area from the initial total area.

Rabotnov [36] further proposed the concept of “damage factor ω ,” which is presented as Eq. (2). Therefore, the damage factor is the ratio of the failure area which is invalid caused by the defects to the initial total area.

$$\omega = \frac{S - \tilde{S}}{S}. \quad (2)$$

Damage variable is an important index to measure the damage degree of rock. The evolution of damage variable has an important relationship with the microdefects and fracture of rock. For the purpose of investigating the damage evolution of anisotropic rock in orthogonal directions, representative volume element (RVE) is taken for analysis. One plane which is perpendicular to the coordinate i -axis is extracted from the RVE (Figure 1(a)). The extracted plane is assumed to be composed of abundant initial mesoscopic elements. The number of initial mesoscopic elements is N_{i0} . The damage evolution of the plane can be evaluated under three-dimensional stress condition. The load in the direction of the i -axis is axial compression, and the load in the other two orthogonal directions is confining pressure. Meanwhile, the load in three directions can be changed independently. The plane can also be applied to true triaxial stress condition. Under the effect of three-dimensional stress, the elements

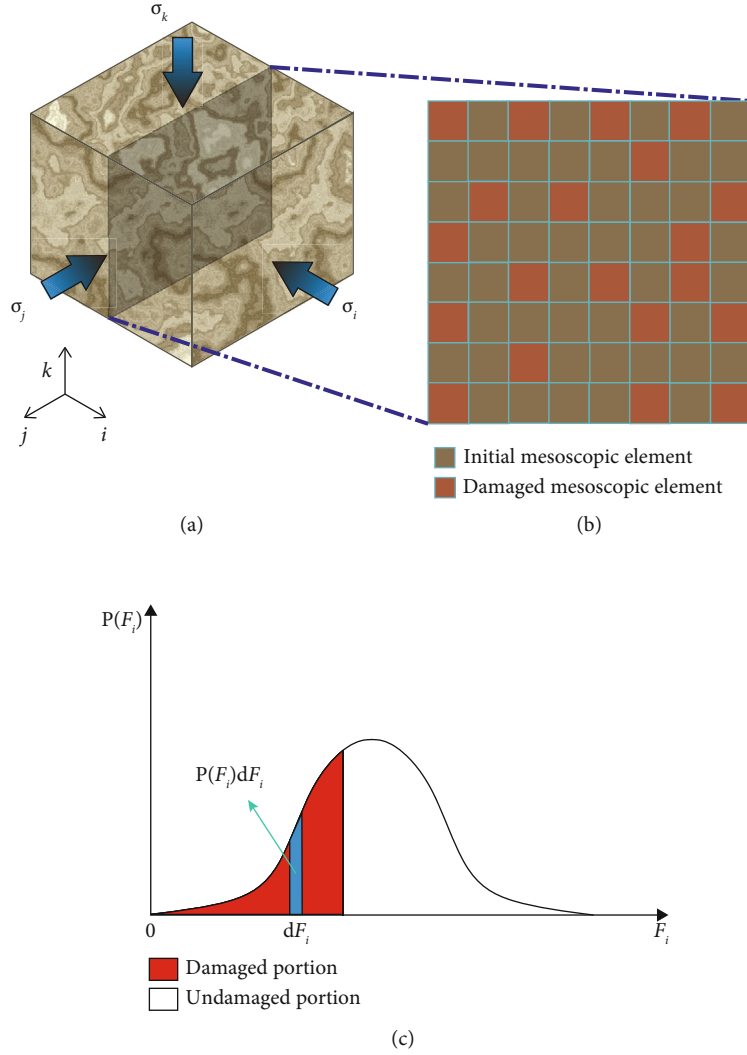


FIGURE 1: The procedures of proposing the areal damage. (a) Extracting the plane perpendicular to the i -axis from RVE. (b) The damaged elements in the plane under loading stress. (c) The failure probability density function of the mesoscopic elements.

are progressive failure, which results in the rock damage. The number of damaged elements in the plane under loading stress is N_{id} (Figure 1(b)).

In this way, the area of rock plane under loading stress can be divided into two parts: damaged area and undamaged area. The undamaged area is regarded as the effective area which supports the loading. According to the concept of damage factor proposed by Rabotnov [36], the definition of areal damage in different directions which is based on the ratio of the failure element number (N_{id}) to the initial element number (N_{i0}) in the extracted plane is given. Because the notation of the i -axis can traverse the coordinate axis of x , y , and z , the extracted plane which is perpendicular to the coordinate i -axis can present the orthogonal anisotropic properties of rocks. Then, the damage evolution of rock in orthogonal directions can be analyzed by the areal damage in orthogonal directions, because the planes are extracted perpendicular to the orthogonal coordinate axes. The areal damage variable D_i of the plane which is perpendicular to the coordinate i

-axis can be given as

$$D_i = \frac{N_{id}}{N_{i0}}. \tag{3}$$

In recent years, on the basis of the assumption that the material was composed of elastic mesoscopic elements and the material properties satisfied the Weibull distribution, some statistical damage constitutive models were established [15, 20, 32]. It is also assumed that the strength of all elements in the plane of each direction are adopted as Weibull distribution in this study. The element would break and fail after the stress reaches to the peak strength. Therefore, the failure probability density function of the mesoscopic elements which are distributed in the plane perpendicular to the i -axis $P(F_i)$ in Figure 1(c) can be expressed as

$$P(F_i) = \frac{w_i}{F_{i0}} \left(\frac{F_i}{F_{i0}}\right)^{w_i-1} \left[-\left(\frac{F_i}{F_{i0}}\right)^{w_i}\right], \tag{4}$$

where F_i is the strength of mesoscopic element, and w_i and F_{i0} are the parameters of the Weibull distribution function.

When the element reaches to any stress level in loading procedure, the number of failure elements in the plane can be calculated as

$$\begin{aligned} N_{id} &= N_{i0} \int_0^{F_i} \frac{w_i}{F_{i0}} \left(\frac{F_i}{F_{i0}} \right)^{w_i-1} \left[- \left(\frac{F_i}{F_{i0}} \right)^{w_i} \right] \\ &= N_{i0} \left\{ 1 - \exp \left[- \left(\frac{F_i}{F_{i0}} \right)^{w_i} \right] \right\}. \end{aligned} \quad (5)$$

Combining Eqs. (3) and (5), the areal damage variable of the plane which is perpendicular to the i -axis can be given by

$$D_i = 1 - \exp \left[- \left(\frac{F_i}{F_{i0}} \right)^{w_i} \right]. \quad (6)$$

2.2. Damage Constitutive Model of the Anisotropic Rock. There are many original defects in rock and some new microcracks will be observed under the damage effect. During the process of loading, the load can be only supported by the effective area without damage. Consequently, the concept of effective stress is put forward. Effective stress refers to the increased actual stress in the material, which is increased due to the decrease of the actual bearing area caused by damage and failure. According to this phenomenon, the strain equivalent hypothesis was proposed by Lemaitre et al. [37]. The constitutive model of strain equivalent hypothesis can be expressed as

$$[\sigma^*] = [\sigma]/[I - D_i] = [C][\varepsilon]/[I - D_i], \quad (7)$$

where $[\sigma^*]$ is the effective stress matrix, $[\sigma]$ is the apparent stress matrix, $[C]$ is the elastic matrix of the material, $[\varepsilon]$ is the strain matrix, and $[I]$ is the identity matrix.

In the laboratory triaxial compression test, the three principal stresses can be measured by the testing machine. The generalized Hooke constitutive model can be transformed to

$$\varepsilon_i = \frac{1}{E_i} \sigma_i^* - \sum_{i \neq j} \frac{\nu_{ij}}{E_j} \sigma_j^*, \quad (8)$$

where ε_i is the component of three principal strains, and E_i and ν_{ij} are the elastic modulus and Poisson's ratio in different directions, respectively. The subscript i represents the direction of the coordinate i -axis. Furthermore, $i, j, k = 1, 2, 3$ and $i \neq j \neq k$. The subscript presents the traversal procedure, but they do not comply with the summation convention.

Substituting Eq. (8) into (7), the three dimensional elastic constitutive equation which includes damage effect can be obtained as

$$\sigma_i = E_i \varepsilon_i (1 - D_i) + \sum_{i \neq j} \frac{E_i \nu_{ij}}{E_j} \sigma_j. \quad (9)$$

Substituting Eq. (6) into (9), a new statistical damage

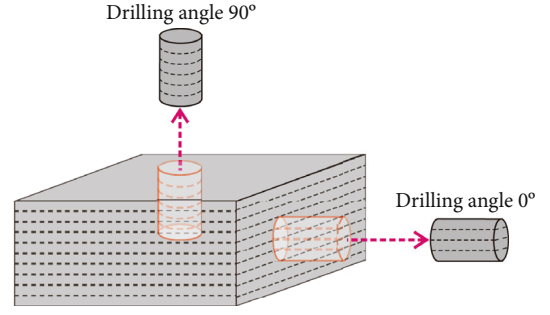


FIGURE 2: Directional coring diagram of shale.

constitutive model of anisotropic rock (SDAR model) is developed as

$$\sigma_i = E_i \varepsilon_i \exp \left[- \left(\frac{F_i}{F_{i0}} \right)^{w_i} \right] + \sum_{i \neq j} \frac{E_i \nu_{ij}}{E_j} \sigma_j. \quad (10)$$

The Drucker-Prager failure criterion is widely used in the researches of rock mechanics [38–40]. In view of this, the Drucker Prager criterion was introduced as the failure criterion of mesoscopic elements in each plane perpendicular to the coordinate axis. Then, the failure strength of element (F_i) in the plane which is perpendicular to the coordinate i -axis can be given by

$$F_i = \alpha_{dp} I_1 + \sqrt{J_2}, \quad (11)$$

where α_{dp} refers to the parameter of material, I_1 is the first invariant of stress, and J_2 is the second invariant of stress deviator.

The three parameters of the Drucker-Prager failure criterion can be calculated by

$$\begin{cases} \alpha_{dp} = \sin \varphi / \sqrt{9 + 3 \sin^2 \varphi}, \\ I_1 = \sigma_1^* + \sigma_2^* + \sigma_3^*, \\ J_2 = \frac{1}{6} \left[(\sigma_1^* - \sigma_2^*)^2 + (\sigma_2^* - \sigma_3^*)^2 + (\sigma_1^* - \sigma_3^*)^2 \right], \end{cases} \quad (12)$$

where φ refers to the friction angle, and σ_1^* , σ_2^* , and σ_3^* are the effective stress in three directions.

2.3. Determination of Parameters in the Anisotropic Damage Constitutive Model. Eqs. (6) and (10) denote the evolution equation of the damage and SDAR model, respectively. There are two important parameters from the Weibull distribution function in the equations, i.e., w_i and F_{i0} , but the values of w_i and F_{i0} are not determined. The method of determining the two parameters needs to be further investigated.

The stress σ_i in the SDAR model is differentiated from Eq. (10), i.e.,

$$d\sigma_i = A_{i1} d\varepsilon_i + A_{i2} dF_i + A_{i3} dw_i + A_{i4} dF_{i0} + \sum_{i \neq j} \frac{E_i \nu_{ij}}{E_j} \sigma_j, \quad (13)$$

where $A_{i1} = \partial\sigma_i/\partial\varepsilon_i$, $A_{i2} = \partial\sigma_i/\partial F_i$, $A_{i3} = \partial\sigma_i/\partial w_i$, and $A_{i4} = \partial\sigma_i/\partial F_{i0}$.

The failure strength of element (F_i) can be regarded as function of σ_1 , σ_2 , σ_3 , and ε_i . The subscript i of ε_i corresponds to that of F_i . Then, the following Eq. (14) can be obtained by differential of F_i .

$$dF_i = \sum F_{ij}d\sigma_j + F_{i*}d\varepsilon_i. \quad (14)$$

The parameters of w and F_0 from the Weibull distribution function in the development of statistical damage constitutive model were assumed to be a function of confining pressure in previous research [41]. And the assumption was validated by comparing with test results. In order to investigate the anisotropic damage of rock, the parameters of w_i and F_{i0} in each direction are assumed to be

functions of loading stress in the other two directions (σ_j , σ_k) by analogy with that assumption. But σ_j and σ_k are not equal in true triaxial compression, the parameters are considered as functions of its average value. By differentiation, we can get

$$\begin{cases} dw_i = w_i^* d\bar{\sigma}_i, \\ dF_{i0} = F_{i0}^* d\bar{\sigma}_i, \end{cases} \quad (15)$$

where $\bar{\sigma}_i = 1/2(\sigma_j + \sigma_k)$.

Substituting Eqs. (14) and (15) into Eq. (13) yields

$$\sum U_{ij}d\sigma_j = -X_i d\varepsilon_i, \quad (16)$$

where

$$[U_{ij}] = \begin{bmatrix} A_{12}F_{11} - 1 & A_{12}F_{12} + \frac{1}{2}A_{13}w_1^* + \frac{1}{2}A_{14}F_{10}^* + \frac{E_1\nu_{12}}{E_2} & A_{12}F_{13} + \frac{1}{2}A_{13}w_1^* + \frac{1}{2}A_{14}F_{10}^* + \frac{E_1\nu_{13}}{E_3} \\ A_{22}F_{21} + \frac{1}{2}A_{23}w_2^* + \frac{1}{2}A_{24}F_{20}^* + \frac{E_2\nu_{21}}{E_1} & A_{22}F_{22} - 1 & A_{22}F_{23} + \frac{1}{2}A_{23}w_2^* + \frac{1}{2}A_{24}F_{20}^* + \frac{E_2\nu_{23}}{E_3} \\ A_{32}F_{31} + \frac{1}{2}A_{33}w_3^* + \frac{1}{2}A_{34}F_{30}^* + \frac{E_3\nu_{31}}{E_1} & A_{32}F_{32} + \frac{1}{2}A_{33}w_3^* + \frac{1}{2}A_{34}F_{30}^* + \frac{E_3\nu_{32}}{E_2} & A_{32}F_{33} - 1 \end{bmatrix}, \quad (17)$$

$$X_i = \begin{bmatrix} A_{11} + A_{12}F_{1*} \\ A_{21} + A_{22}F_{2*} \\ A_{31} + A_{32}F_{3*} \end{bmatrix}.$$

Solving Eq. (16) based on the Kramer's law yields

$$d\sigma_i = (-1)^i \sum \frac{X_j \Delta_{ij}}{\Delta} d\varepsilon_j, \quad (18)$$

where $\Delta = |U_{ij}| = \begin{vmatrix} U_{11} & U_{12} & U_{13} \\ U_{21} & U_{22} & U_{23} \\ U_{31} & U_{32} & U_{33} \end{vmatrix}$, and Δ_{ij} is the remainder of Δ , i.e.,

$$\begin{aligned} \Delta_{11} &= \begin{vmatrix} U_{22} & U_{23} \\ U_{32} & U_{33} \end{vmatrix}, \Delta_{12} = \begin{vmatrix} U_{21} & U_{23} \\ U_{31} & U_{33} \end{vmatrix}, \Delta_{13} = \begin{vmatrix} U_{21} & U_{22} \\ U_{31} & U_{32} \end{vmatrix}, \\ \Delta_{21} &= \begin{vmatrix} U_{12} & U_{13} \\ U_{32} & U_{33} \end{vmatrix}, \Delta_{22} = \begin{vmatrix} U_{11} & U_{13} \\ U_{31} & U_{33} \end{vmatrix}, \Delta_{23} = \begin{vmatrix} U_{11} & U_{12} \\ U_{31} & U_{32} \end{vmatrix}, \\ \Delta_{31} &= \begin{vmatrix} U_{12} & U_{13} \\ U_{22} & U_{23} \end{vmatrix}, \Delta_{32} = \begin{vmatrix} U_{11} & U_{13} \\ U_{21} & U_{23} \end{vmatrix}, \Delta_{33} = \begin{vmatrix} U_{11} & U_{12} \\ U_{21} & U_{22} \end{vmatrix}. \end{aligned} \quad (19)$$

Based on the generalized Hooke constitutive model, the principle stress σ_i can be expressed as a function of three

principal strains ε_1 , ε_2 , and ε_3 . Thus, the total differential of σ_i can be obtained as

$$d\sigma_i = \sum \frac{\partial\sigma_i}{\partial\varepsilon_j} d\varepsilon_j. \quad (20)$$

In the true triaxial stress test, the stress-strain curve of rock in each direction to be solved should reach the following boundary conditions at the peak point, i.e.,

$$\begin{cases} \varepsilon_i = \varepsilon_{icp}, & \sigma_i = \sigma_{icp}, \\ \left. \frac{d\sigma_i}{d\varepsilon_i} \right|_{\varepsilon_i = \varepsilon_{icp}} = 0, \end{cases} \quad (21)$$

where ε_{icp} refers to the peak strain in the loading direction along the i -axis, and σ_{icp} refers to the peak stress in the loading direction along the i -axis.

Comparing Eqs. (18) and (20), it can be known that the coefficients of items at the same position should be the same. Subsequently, Eqs. (18) and (20) are substituted into Eq. (21),

TABLE 1: Mechanical parameters of shale in different directions [44].

Confining pressure (MPa)	Elastic modulus parallel to bedding (GPa)	Elastic modulus perpendicular to bedding (GPa)	Poisson's ratio parallel to bedding	Poisson's ratio perpendicular to bedding	Friction angle (°)
10	22.91	42.94	0.384	0.325	30.3
20	22.77	52.51	0.416	0.263	30.3
30	24.04	56.45	0.422	0.258	30.3

and the Eq. (22) can be obtained.

$$\frac{\partial \sigma_i}{\partial \varepsilon_i} = (-1)^i \frac{X_i \Delta_{ii}}{\Delta} = 0. \quad (22)$$

For the reason that $\Delta_{ii} \neq 0$, the equation that $X_i = 0$ can be obtained. By solving $X_i = 0$, the calculated expressions of w_i and F_{i0} can be derived as

$$w_i = \frac{1}{\ln \left(E_i \varepsilon_{icp} / \sigma_{icp} - \sum_{i \neq j} (E_i \nu_{ij} / E_j) \sigma_j \right)}, \quad (23)$$

$$F_{i0} = F_{ic} (w_i)^{1/w_i}. \quad (24)$$

Eqs. (23) and (24) denote the determination of parameters in the SDAR model, i.e., w_i and F_{i0} . When the material properties of rock are assumed to be isotropic, the elastic modulus and Poisson's ratio in all directions are equal, respectively. In the conventional triaxial test, the two principal stresses in the horizontal direction are equal ($\sigma_2 = \sigma_3 \neq 0$). On this basis, for the conventional triaxial compression test of isotropic rock, the calculated expressions of Eqs. (23) and (24) can be degenerated to

$$w = \frac{1}{\ln \left(E \varepsilon_{cp} / \sigma_{cp} - 2\nu \sigma_3 \right)}, \quad (25)$$

$$F_0 = F_c (w)^{1/w}, \quad (26)$$

where σ_{cp} is the axial peak stress, and σ_3 is the confining pressure.

For the uniaxial triaxial compression condition of isotropic rock, the calculated expressions of parameters illustrated as Eqs. (23) and (24) can be further degenerated for lack of confining pressure ($\sigma_2 = \sigma_3 = 0$). At this time, Eq. (25) for solving parameter w is degenerated to Eq. (27), but Eq. (26) for solving parameter F_0 remains unchanged.

$$w = \frac{1}{\ln \left(E \varepsilon_{cp} / \sigma_{cp} \right)}. \quad (27)$$

Equations (25)–(27) are the calculated expressions of w and F_0 obtained by the degradation of the calculation expressions of w_i and F_{i0} for isotropic rock under conventional triaxial and uniaxial compression, respectively. The calculated expressions of w and F_0 under conventional triaxial compression condition of isotropic rock (Eqs. (25) and (26)) are consistent with those derived by Wang et al. [42]. Further-

more, the expressions under uniaxial compression condition of isotropic rock (Eqs. (26) and (27)) are the same as the research results obtained by Xie and Zhao [43].

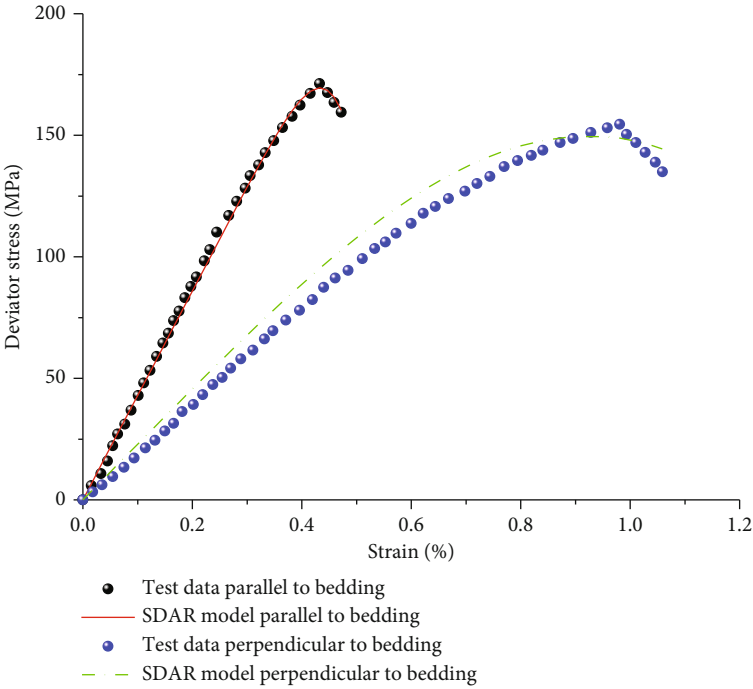
3. Model Validation

3.1. Stress-Strain Relationship

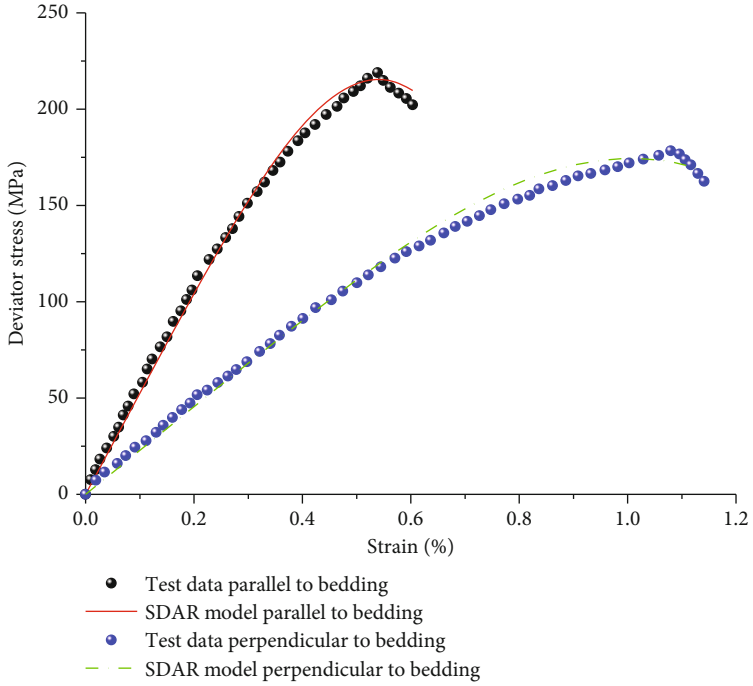
3.1.1. Transversely Isotropic Shale under Conventional Triaxial Stress Condition. As a kind of sedimentary rock, shale is observed to be transversely isotropic. Shale has the same mechanical properties in the horizontal direction, but the mechanical properties in the horizontal direction are different from those in the vertical direction. Heng [44] used shale which is from the Longmaxi Formation in Chongqing to drill tested samples along two orthogonal directions (Figure 2). One is parallel to bedding (drilling angle 0°). The other is perpendicular to bedding (drilling angle 90°). Shale samples drilled from different directions were tested under conventional triaxial compression with confining pressures of 10, 20, and 30 MPa, respectively. Then, the stress-strain relationships of shale which were drilled in orthogonal directions under different confining pressures that are obtained. The parameters used for validation of shale are shown in Table 1.

Comparing the theoretical results of the SDAR model and test data of shale on stress-strain in Figure 3, it can be seen that the theoretical results are very close to the test data in the same drilling direction under confining pressures of 10, 20, and 30 MPa, respectively. The comparison results show that all the stress-strain curves of shale under conventional triaxial compression can well be evaluated by the SDAR model. In the prepeak zone, the curve of theoretical calculation is in good agreement with that of test data. After the peak stress point, the curve of theoretical results present strain softening in the postpeak region. The presentation of strain softening in the SDAR model is also consistent with the mechanical behavior of shale.

Comparing the peak strength of shale in the same drilling direction under each confining pressure (Figure 3), the peak strength of samples in the same drilling direction increases with the increase of confining pressure. Moreover, the peak strength under different confining pressures can be accurately calculated by the SDAR model. Then, comparing the results of samples drilled in different directions under the same confining pressure, it can be found that the peak strength of sample drilled in the direction of parallel to bedding is always bigger than that of perpendicular to bedding. Meanwhile, the peak strain of sample drilled in the direction



(a)



(b)

FIGURE 3: Continued.

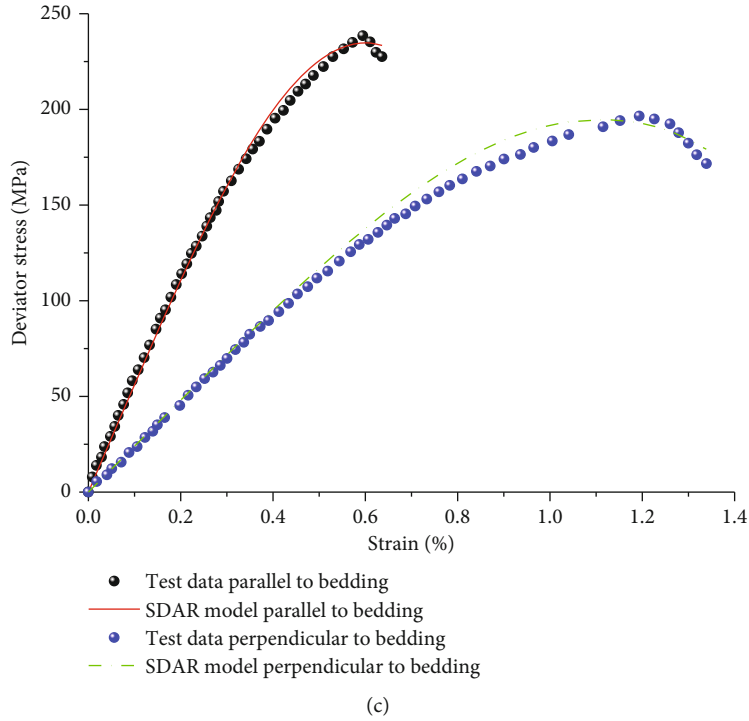


FIGURE 3: Stress-strain curves of shale under different confining pressures: (a) confining pressure 10 MPa, (b) confining pressure 20 MPa, and (c) confining pressure 30 MPa.

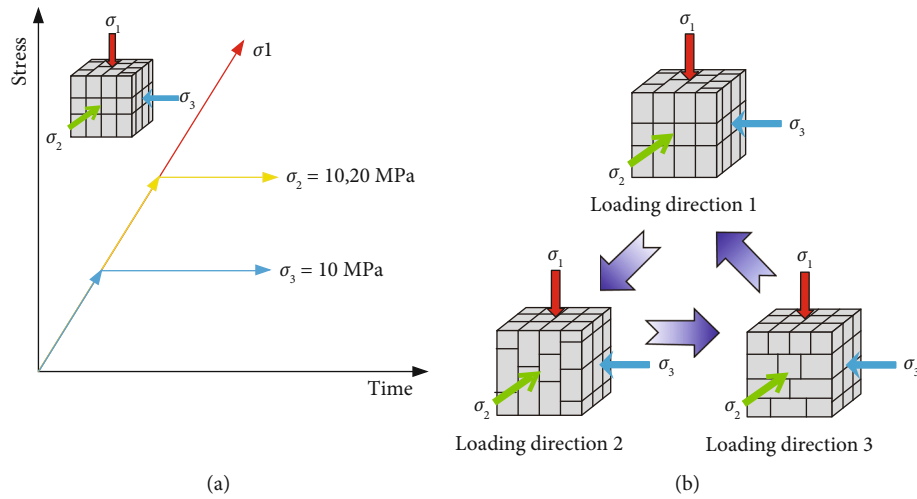


FIGURE 4: Stress loading path and loading direction variations in the true triaxial tests. (a) Stress loading path. (b) Variations of stress loading direction. [49].

TABLE 2: Mechanical parameters of coal in different directions [49, 50].

Stress loading path	Elastic modulus along the face cleat plane direction (GPa)	Elastic modulus along the butt cleat plane direction (GPa)	Elastic modulus along the bedding plane direction (GPa)	Poisson's ratio parallel to bedding	Poisson's ratio perpendicular to bedding	Friction angle ($^{\circ}$)
Path 1 ($\sigma_2 = 20\text{MPa}$, $\sigma_3 = 10\text{MPa}$)	4.11	3.28	3.24	0.14	0.22	28
Path 2 ($\sigma_2 = 30\text{MPa}$, $\sigma_3 = 10\text{MPa}$)	4.55	3.67	2.87	0.14	0.22	28

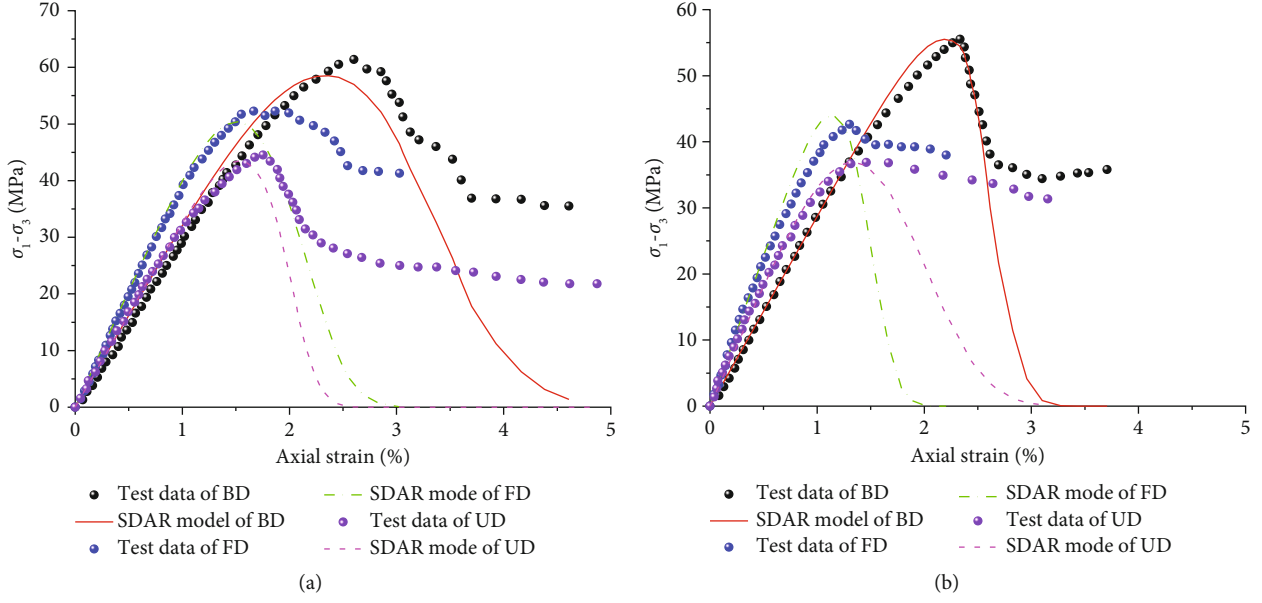


FIGURE 5: Stress-strain of coal in orthogonal directions in different stress loading paths. (a) Path 1 ($\sigma_2 = 20\text{MPa}$, $\sigma_3 = 10\text{MPa}$). (b) Path 2 ($\sigma_2 = 30\text{MPa}$, $\sigma_3 = 10\text{MPa}$).

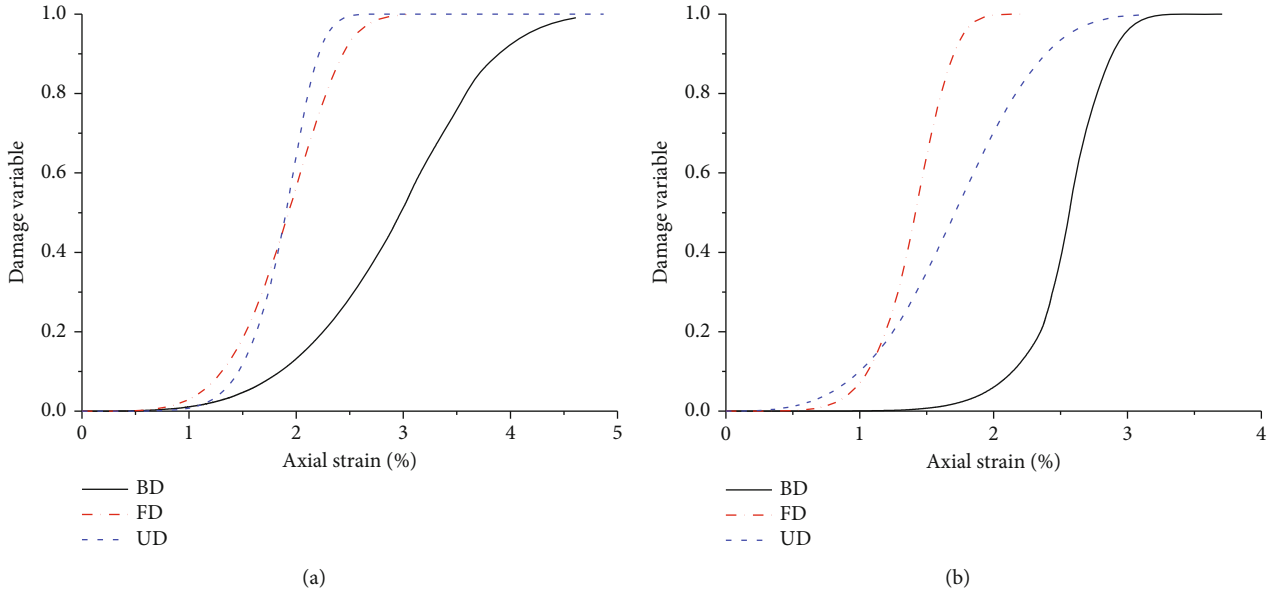


FIGURE 6: Damage evolution of anisotropic coal under different stress loading paths. (a) Path 1 ($\sigma_2 = 20\text{MPa}$, $\sigma_3 = 10\text{MPa}$). (b) Path 2 ($\sigma_2 = 30\text{MPa}$, $\sigma_3 = 10\text{MPa}$).

TABLE 3: Values of elastic modulus in orthogonal directions.

Serial number	Elastic modulus along the face cleat plane direction (GPa)	Elastic modulus along the butt cleat plane direction (GPa)	Elastic modulus along the bedding plane direction (GPa)
Case 1	3	3	3
Case 2	3.5	3	3
Case 3	4	3	3
Case 4	3	3.5	3
Case 5	3	4	3
Case 6	3	3	3.5
Case 7	3	3	4

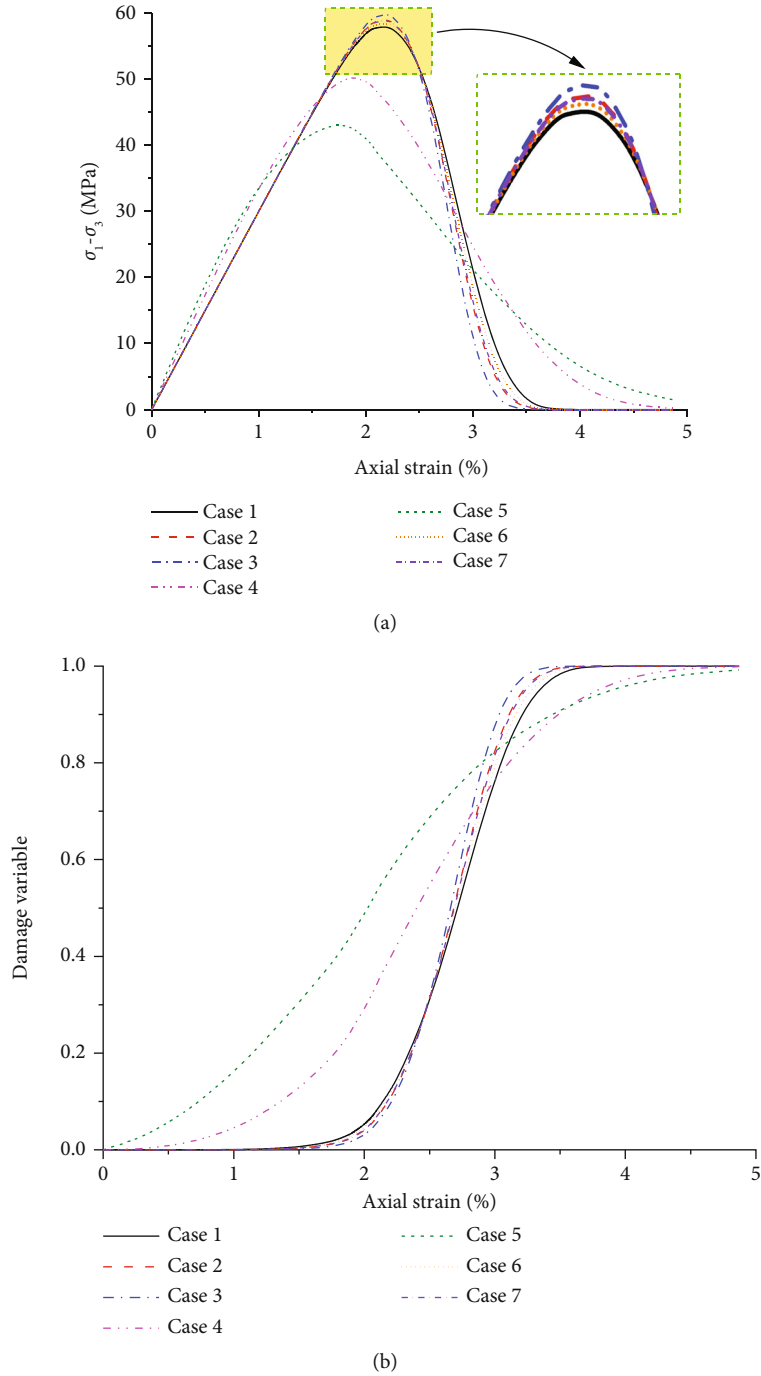


FIGURE 7: Stress-strain and damage evolution of different elastic moduli in orthogonal directions. (a) Stress-strain curves. (b) Damage variable.

of parallel to bedding is smaller than that of perpendicular to bedding. The stress-strain of transversely isotropic shale under conventional triaxial stress can be well calculated by the SDAR model.

3.1.2. Orthogonal Anisotropic Coal under True Triaxial Stress Condition. Under the influence of sedimentation, there is an obvious approximate horizontal bedding plane structure in coal. In addition, there are a lot of cleats in coal, which can be divided into face cleat and butt cleat [45]. These two kinds

TABLE 4: Values of Poisson's ratio in different directions.

Serial number	Poisson's ratio parallel to bedding	Poisson's ratio perpendicular to bedding
Case 1	0.20	0.20
Case 2	0.25	0.20
Case 3	0.35	0.20
Case 4	0.20	0.25
Case 5	0.20	0.35

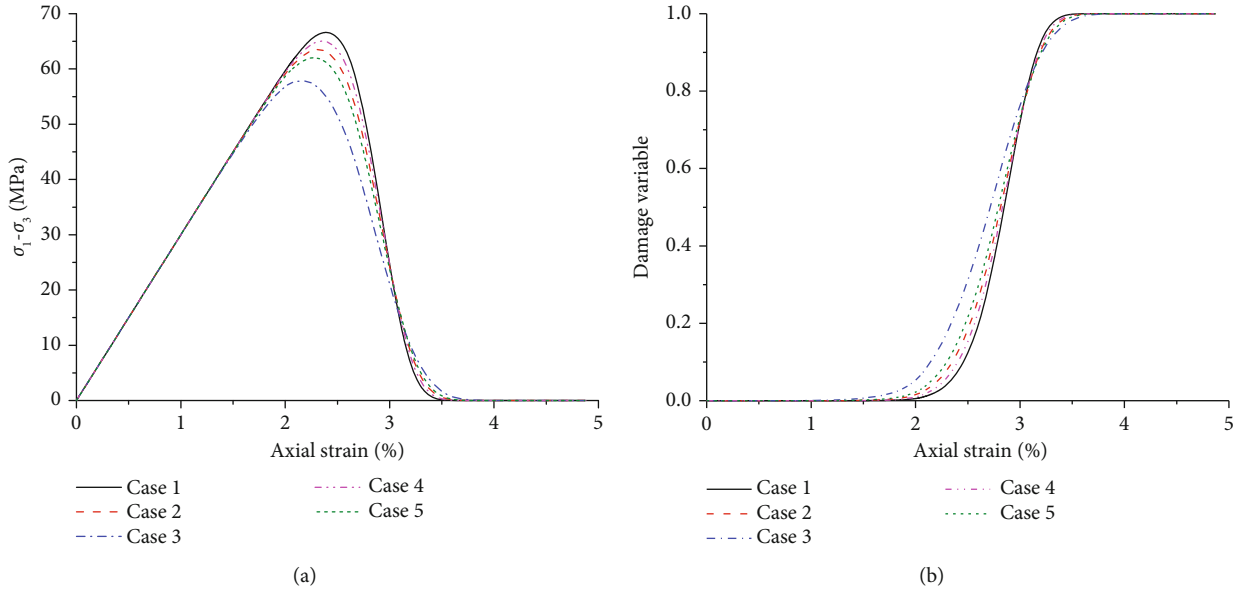


FIGURE 8: Stress-strain and damage evolution of anisotropic Poisson's ratio. (a) Stress-strain curves. (b) Damage variable.

of cleats are approximately orthogonal to each other and perpendicular to the bedding plane (Figure 4(a)) [46, 47]. Due to the existence of cleat and bedding (referred to as fractures), coal is generally divided into matrix and fracture. The coal matrix is also usually simplified to shape of cubes. Therefore, the mechanical properties of coal are considered to be nearly orthotropic [48].

According to the geological structure characteristics of coal seam, the raw cubic coal samples were prepared in the orthogonal fracture directions in Liu's research [49]. The orthogonal fracture directions were bedding plane direction (BD), face cleat plane direction (FD), and butt cleat plane direction (UD), respectively. Then, the true triaxial loading test was carried out with the cubic coal samples in two true triaxial stress paths. The two true triaxial stress paths were conducted as follows (Figure 4(a)). Firstly, the coal sample was loaded to the hydrostatic pressure ($\sigma_1 = \sigma_2 = \sigma_3$) of 10 MPa. Next, σ_3 was kept constant while the σ_1 and σ_2 were increased to the design values of σ_2 simultaneously. The design values of σ_2 were 20 and 30 MPa, respectively. Finally, the σ_2 and σ_3 were kept constant, but the σ_1 was increased until the coal sample failure.

In this way, the complete stress-strain of coal samples under the true triaxial stress condition was tested. The loading directions of three principal stresses ($\sigma_1, \sigma_2, \sigma_3$) were parallel or perpendicular to the original fractures (bedding plane, face cleat, and butt cleat) in the tests. During the whole tests, the directions of the three principal stresses were kept unchanged, but the directions of original fractures in cubic coal sample were changed in turn (Figure 4(b)). Based on the true triaxial test results under different stress paths, the developed SDAR model is validated. The parameters used for validation of coal are illustrated in Table 2.

The theoretical results of the SDAR model and test data of coal on stress-strain are shown in Figure 5. By comparing the stress-strain in each stress path, the peak strength of coal

TABLE 5: Increasing values of w_i .

Serial number	w_i
Case 1	6.32
Case 2	9.32
Case 3	12.32
Case 4	15.32
Case 5	18.32

samples prepared in three directions is in the same order. The peak strength of coal sample along the BD is the largest. And the peak strength of coal sample along UD is the smallest. Moreover, the peak strain also decreased in the order of BD, FD, and UD.

Compared with the test data, the results of the SDAR model can basically represent the stress-strain relationship of coal in different directions under true triaxial condition. In the phase of prepeak, the theoretical results are in good agreement with the test data. The peak stress of the SDAR model is very close to the experimental value of coal in each case. In the postpeak phase, all the theoretical curves obviously present variation of strain softening, which is the same as the test data. All the values of the SDAR model decrease rapidly after the peak stress point. The corresponding tested results also show a decrease trend, but the decrease rate is relatively slow. There is a certain deviation between the SDAR model and the test results in the postpeak phase. In the postpeak phase, there are many reasons for this deviation, including the properties of rock, test conditions, loading procedure, and failure mode of rock [20]. On the whole, stress-strain relationship of orthotropic coal under true triaxial loading can be well evaluated by the SDAR model.

3.2. Evolution of Damage Variable. As a heterogeneous geological material, rock has many original defects. Under the

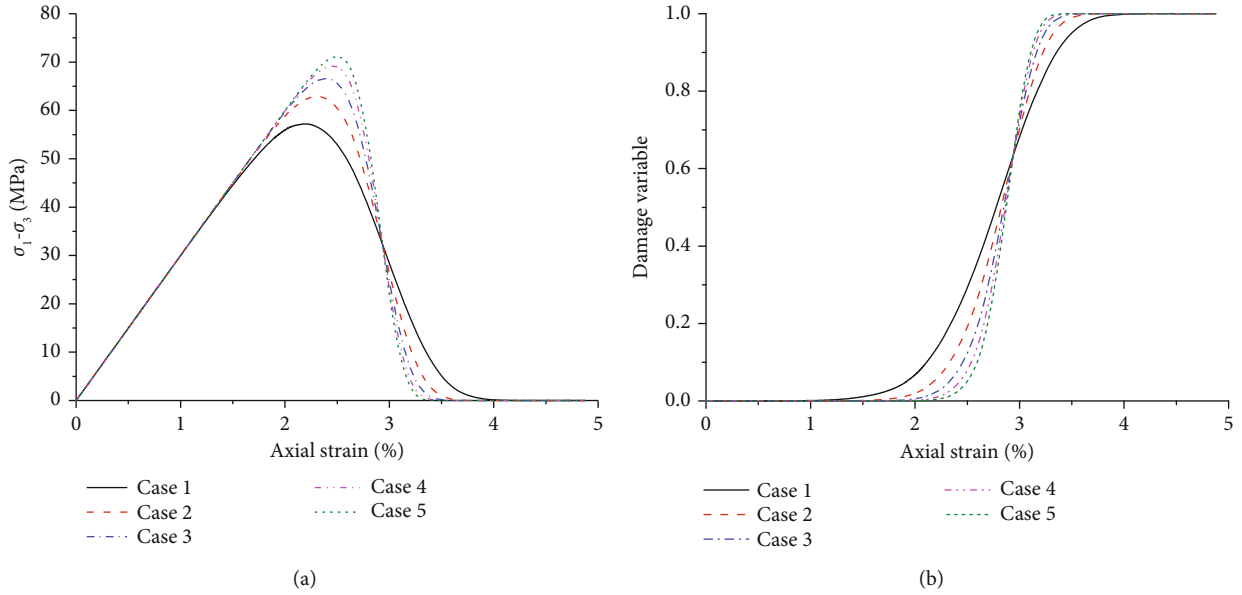


FIGURE 9: Stress-strain and damage evolution of different w_i . (a) Stress-strain curves. (b) Damage variable.

influence of various stresses, the defects continuously emerge and expand, which result in damage accumulation in rock. Damage accumulation is the main reason for progressive failure of rock. It is also the important factor determining the stress-strain relationship of rock. It is of great significance to investigate the rock damage evolution under loading for developing the constitutive model.

Based on Liu's research [49], the damage evolution of orthotropic coal samples drilled in different directions under true triaxial loading is analyzed by the SDAR model. Figure 6 demonstrates the evolution of coal samples prepared in each direction (BD, FD, and UD) under different stress paths. It can be seen that when the axial strain is less than a certain value, the value of damage variable in all directions is 0. In other words, there is no damage in the early phase of loading. In the process of test, the axial strain increases continuously with the increase of loading stress. After the peak stress point, the stress-strain curves present the strain softening with the decrease of stress. But during the whole loading process, both the damage variable and the axial strain are monotonically increase. The value of damage variable increases from 0 to 1.

In stress path 1 ($\sigma_2 = 20\text{MPa}$, $\sigma_3 = 10\text{MPa}$), the damage evolution of coal samples loading along the FD and UD is similar. The initial damage first emerges in the coal sample loaded in FD, but the damage variable of coal sample loaded in UD first reaches 1. The initial damage of coal sample loaded in BD emerges the latest. Meanwhile, the damage accumulation rate of coal loaded in BD is the slowest. Therefore, the increase rate of damage variable in BD is the slowest, and the value of axial strain corresponding to damage variable reaching 1 is the largest.

In stress path 2 ($\sigma_2 = 30\text{MPa}$, $\sigma_3 = 10\text{MPa}$), the initial damage first emerges in the coal sample loaded in UD, but the damage variable of coal sample loaded in FD first reaches 1. The development of damage in the BD is still the slowest. The SDAR model established in this study can well evaluate

TABLE 6: Increasing values of F_{i0} .

Serial number	F_{i0} (MPa)
Case 1	53.57
Case 2	63.57
Case 3	73.57
Case 4	83.57
Case 5	93.57

the damage evolution of anisotropic rock. And the SDAR model also provides a theoretical analysis method for the damage evolution of anisotropic rock under true triaxial condition.

4. Sensitivity Study of Parameters

The sensitivity analysis was based on the test in BD under stress path 1 ($\sigma_2 = 20\text{MPa}$, $\sigma_3 = 10\text{MPa}$) of Liu's research [49]. Sensitivity analysis is conducted from two aspects: mechanical parameters and model parameters. The mechanical parameters include anisotropic elastic modulus and anisotropic Poisson's ratio. The model parameters refer to w_i and F_{0i} .

4.1. Sensitivity of Mechanical Parameters

4.1.1. Anisotropic Elastic Modulus. In order to research the influence of elastic modulus in each direction on the stress-strain relationship and damage evolution, the sensitivity of elastic modulus in orthogonal directions (BD, FD, and UD) is analyzed on the basis of only changing the value of elastic modulus in each direction. The other parameters remain constant. The values of elastic modulus in all three directions are listed in Table 3. Poisson's ratio of coal in all directions is 0.3, and the friction angle of coal is 28° . The loading path of true triaxial stress in the analysis is based on the path 1

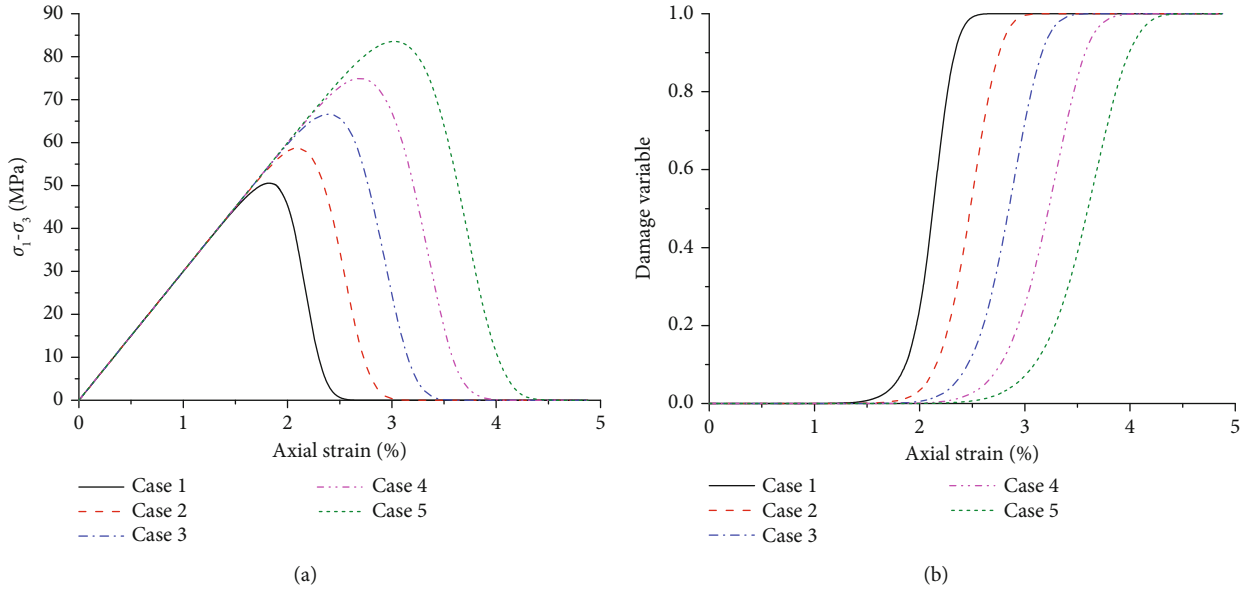


FIGURE 10: Stress strain and damage evolution of different F_0 . (a) Stress-strain curves. (b) Damage variable.

($\sigma_2 = 20\text{MPa}$, $\sigma_3 = 10\text{MPa}$) in Figure 4(a). According to the above parameters and stress path, the axial strain and damage evolution of coal samples prepared along the butt cleat plane direction under true triaxial condition are analyzed.

There are different stress-strain relationships and damage evolution under various combinations of elastic modulus. Figure 7 shows the results of stress-strain and damage under different anisotropic elastic moduli.

Comparing the cases 1, 2, and 3 in Figure 7(a), the results show that the larger the elastic modulus along the face cleat plane direction is, the higher the peak strength of coal is, and the faster the strain softening rate is after peak point. From the comparison among cases 1, 2, and 3 in Figure 7(b), it shows that the larger the elastic modulus along the face cleat plane direction is, the later the accelerated damage accumulation phase emerges. Meanwhile, the increasing rate of damage accumulation becomes faster, and the damage variable reaches 1 earlier.

Then, comparing the cases 1, 4, and 5 in Figure 7(a), it can be obtained that with the increase of elastic modulus along the butt cleat plane direction, the slope of the elastic deformation phase in the stress-strain curve increases while the peak strength of coal decreases. At the same time, the rate of stress dropping increases after peak point. The results of comparison among cases 1, 4, and 5 in Figure 7(b) demonstrate that the larger the elastic modulus along the butt cleat plane direction is, the earlier the accelerated damage accumulation phase emerges. Moreover, the increasing rate of damage accumulation becomes slower, and the value of damage variable reaches 1 later.

By comparing the curves of cases 1, 6, and 7 in Figure 7, we can know that the effects of elastic modulus along the bedding plane direction on the variation of peak stress, stress-strain relationship, and damage are same as the effect caused by the elastic modulus along the face cleat plane direction, but the variation degree of curves under the influence of elas-

tic modulus along the bedding plane direction is smaller. In other words, the sensitivity of elastic modulus along the bedding plane direction is not as high as that of elastic modulus along the face cleat plane direction.

Because the sensitivity analysis is focused on the case that the maximum principal stress (σ_1) is loaded along the butt cleat plane direction, the variation of the elastic modulus along the butt cleat plane direction has a significant influence on the stress-strain and damage, but the change of elastic modulus in the other direction, as the face cleat plane or bedding plane, has little effect on the stress-strain and damage evolution.

4.1.2. Anisotropic Poisson's Ratio. For the purpose of investigating the influence of Poisson's ratio on the stress-strain and damage evolution, the values of Poisson's ratio in different directions are changed while the other parameters are kept constant in the sensitivity analysis. The elastic modulus of coal in all directions is 3 GPa, and the friction angle of coal is 28° . It can be known that the strain in the i -axis direction is only influenced by Poisson's ratio in the other two directions (ν_{ij} and ν_{ik}) from Eqs. (10), (23), and (24). Then, the calculation is carried out according to the case that the maximum principal stress (σ_1) is loaded along the direction of butt cleat plane in Figure 4. The values of Poisson's ratio in all directions are shown in Table 4.

The stress-strain and damage of coal under different Poisson's ratio are shown in Figure 8. The values of the slope concerning elastic deformation phase in the stress-strain curves under different Poisson's ratios are equal (Figure 8(a)). With the independent increase of Poisson's ratio in a certain direction (parallel to bedding or perpendicular to bedding), the peak strength, peak strain, and the rate of stress dropping decrease. Meanwhile, with the increase of Poisson's ratio, both the axial strain corresponding to the initial damage and the increase rate of damage variable decrease (Figure 8(b)).

4.2. Sensitivity of Model Parameters

4.2.1. Parameter of w_i . In order to study the parameter of w_i , the value of w_i is increased at intervals of 3. And the values of w_i are shown in Table 5. On the premise that other parameters remain unchanged, with the increase of w_i , the phase of linear elastic deformation becomes longer, and the peak strength and peak strain increase obviously (Figure 9(a)). Some changes in the damage variable corresponding to the stress-strain are also observed. With the increase of w_i , the axial strain corresponding to initial damage and the rate of damage accumulation become larger (Figure 9(b)). The value of damage variable would reach up to 1 as soon as w_i increases.

4.2.2. Parameter of F_{i0} . In order to analyze the sensitivity of F_{i0} , the values of F_{i0} are changed according to Table 6. The stress-strain and damage variable can be obtained in different values of F_{i0} . As it can be seen in Figure 10(a), with the increase of F_{i0} , the phase of elastic deformation becomes longer, and the peak strength and peak strain increase obviously. Moreover, the stress after peak point decreases based on the same slope at different values of F_{i0} . Meanwhile, the axial strain corresponding to the emergence of initial damage becomes larger with the increase of F_{i0} (Figure 10(b)). It indicates that higher loading stress is required for emergence of coal damage. In addition, the larger the F_{i0} is, the larger the axial strain corresponding to the damage variable reaching 1 becomes.

5. Conclusions

- (1) Based on the proposed concept of areal damage and statistical damage mechanics, a statistical damage constitutive model of anisotropic rock (SDAR model) is established. According to the test validation, it is proved that the model can well evaluate the stress-strain relationship and damage evolution of anisotropic rock in different directions
- (2) The three principal stresses in orthogonal directions are independent of each other in the process of developing the SDAR model. Therefore, the SDAR model can be applied to predict the stress-strain and damage evolution of anisotropic rock under true triaxial loading condition
- (3) The effect of elastic modulus in one direction on the strain of the same direction is more significant than that in other directions. With the increase of elastic modulus in one direction, the slope of elastic deformation in the stress-strain curve of the same direction becomes larger. Meanwhile, the accelerated damage accumulation phase begins. With the increase of Poisson's ratio, the peak strength, peak strain, and the rate of stress dropping in the postpeak zone decrease
- (4) The elastic phase in the stress-strain curve becomes longer with the increased value of w_i . Meanwhile, the peak strength, peak strain, and rate of stress dropping after peak point increase with the increased

value of w_i . Moreover, the rate of damage accumulation increases as well. On the basis of increasing F_{i0} , the elastic deformation phase in the stress-strain curve becomes longer. Both peak strength and peak strain tend to be larger. The rate of stress dropping after peak point is constant. And the axial strain corresponding to the emergence of initial damage becomes larger

Nomenclature

C :	Elastic matrix
D :	Damage variable
E :	Elastic modulus
F :	Failure strength of element
I :	Identity matrix
I_1 :	First invariant of stress
J_2 :	Second invariant of stress deviator
N :	Number of mesoscopic elements
P :	Failure probability density
S :	Initial total area
\tilde{S} :	Actual bearing area
w :	Parameter of Weibull function
α :	Parameter of material
ε :	Strain
ν :	Poisson's ratio
σ :	Apparent stress
σ^* :	Effective stress
φ :	Friction angle
ψ :	Continuity of material
ω :	Damage factor.

Subscripts and Superscripts

cp:	Peak point of stress or strain
d :	Damage
dp:	Drucker-Prager criterion
i, j, k :	Coordinate axes
0:	Initial Value
1, 2, 3:	Direction of principal stress.

Data Availability

The data used to support the findings of this study are included within the article.

Conflicts of Interest

The authors declare that there are no conflicts of interest regarding the publication of this article.

Acknowledgments

This work was supported by the National Natural Science Foundation of China (Nos. 52004081, 51804099, 51904092), the Key Scientific Research Project of Higher Education Institutions in Henan Province (No. 21A440005), and the Natural Science Foundation of Henan Polytechnic University (No. B2020-34). The financial supports are gratefully acknowledged.

References

- [1] H. Niandou, J. F. Shao, J. P. Henry, and D. Fourmaintraux, "Laboratory investigation of the mechanical behaviour of Tournemire shale," *International Journal of Rock Mechanics and Mining Sciences*, vol. 34, no. 1, pp. 3–16, 1997.
- [2] F. Du and K. Wang, "Unstable failure of gas-bearing coal-rock combination bodies: insights from physical experiments and numerical simulations," *Process Safety and Environmental Protection*, vol. 129, pp. 264–279, 2019.
- [3] F. Du, K. Wang, X. Zhang, C. Xin, L. Shu, and G. Wang, "Experimental study of coal–gas outburst: insights from coal–rock structure, gas pressure and adsorptivity," *Natural Resources Research*, vol. 29, no. 4, pp. 2481–2493, 2020.
- [4] S. Heng, Y. Guo, C. Yang, J. J. K. Daemen, and Z. Li, "Experimental and theoretical study of the anisotropic properties of shale," *International Journal of Rock Mechanics and Mining Sciences*, vol. 74, pp. 58–68, 2015.
- [5] H. Song, Y. Jiang, D. Elsworth, Y. Zhao, J. Wang, and B. Liu, "Scale effects and strength anisotropy in coal," *International Journal of Coal Geology*, vol. 195, pp. 37–46, 2018.
- [6] Y. Zhao, H. Song, S. Liu, C. Zhang, L. Dou, and A. Cao, "Mechanical anisotropy of coal with considerations of realistic microstructures and external loading directions," *International Journal of Rock Mechanics and Mining Sciences*, vol. 116, pp. 111–121, 2019.
- [7] C. Li, J. Wang, and H. Xie, "Anisotropic creep characteristics and mechanism of shale under elevated deviatoric stress," *Journal of Petroleum Science and Engineering*, vol. 185, article 106670, 2020.
- [8] J. F. Shao, D. Hoxha, M. Bart et al., "Modelling of induced anisotropic damage in granites," *International Journal of Rock Mechanics and Mining Sciences*, vol. 36, no. 8, pp. 1001–1021, 1999.
- [9] C. L. Chow and T. J. Lu, "On evolution laws of anisotropic damage," *Engineering Fracture Mechanics*, vol. 34, no. 3, pp. 679–701, 1989.
- [10] J. Lemaitre, R. Desmorat, and M. Sauzay, "Anisotropic damage law of evolution," *European Journal of Mechanics-A/Solids*, vol. 19, no. 2, pp. 187–208, 2000.
- [11] Y.-F. Chen, K. Wei, W. Liu, S.-H. Hu, R. Hu, and C.-B. Zhou, "Experimental characterization and micromechanical modeling of anisotropic slates," *Rock Mechanics and Rock Engineering*, vol. 49, no. 9, pp. 3541–3557, 2016.
- [12] F. Marinelli and G. Buscarnera, "Anisotropic breakage mechanics: from stored energy to yielding in transversely isotropic granular rocks," *Journal of the Mechanics and Physics of Solids*, vol. 129, pp. 1–18, 2019.
- [13] D. Krajcinovic and M. A. G. Silva, "Statistical aspects of the continuous damage theory," *International Journal of Solids and Structures*, vol. 18, no. 7, pp. 551–562, 1982.
- [14] C. A. Tang and X. H. Xu, "Statistical damage analysis of the rock complete stress-strain process," *Journal of Northeast University of Technology*, vol. 51, no. 2, pp. 191–195, 1987.
- [15] W. C. Zhu and C. A. Tang, "Micromechanical model for simulating the fracture process of rock," *Rock Mechanics and Rock Engineering*, vol. 37, no. 1, pp. 25–56, 2004.
- [16] C. Tang, "Numerical simulation of progressive rock failure and associated seismicity," *International Journal of Rock Mechanics and Mining Sciences*, vol. 34, no. 2, pp. 249–261, 1997.
- [17] G. Li and C.-A. Tang, "A statistical meso-damage mechanical method for modeling trans-scale progressive failure process of rock," *International Journal of Rock Mechanics and Mining Sciences*, vol. 74, pp. 133–150, 2015.
- [18] C. Tang and S. Tang, "Applications of rock failure process analysis (RFPA) method," *Journal of Rock Mechanics and Geotechnical Engineering*, vol. 3, no. 4, pp. 352–372, 2011.
- [19] W.-g. Cao, X. Li, and H. Zhao, "Damage constitutive model for strain-softening rock based on normal distribution and its parameter determination," *Journal of Central South University of Technology*, vol. 14, no. 5, pp. 719–724, 2007.
- [20] X. Li, W.-G. Cao, and Y.-H. Su, "A statistical damage constitutive model for softening behavior of rocks," *Engineering Geology*, vol. 143–144, pp. 1–17, 2012.
- [21] W. Cao, X. Tan, C. Zhang, and M. He, "Constitutive model to simulate full deformation and failure process for rocks considering initial compression and residual strength behaviors," *Canadian Geotechnical Journal*, vol. 56, no. 5, pp. 649–661, 2018.
- [22] H. Lin, S. Xie, R. Yong, Y. Chen, and S. Du, "An empirical statistical constitutive relationship for rock joint shearing considering scale effect," *Comptes Rendus Mécanique*, vol. 347, no. 8, pp. 561–575, 2019.
- [23] T. Yang, P. Wang, T. Xu et al., "Anisotropic characteristics of jointed rock mass: A case study at Shirengou iron ore mine in China," *Tunnelling and Underground Space Technology*, vol. 48, pp. 129–139, 2015.
- [24] Y. Li, D. Jia, Z. Rui, J. Peng, C. Fu, and J. Zhang, "Evaluation method of rock brittleness based on statistical constitutive relations for rock damage," *Journal of Petroleum Science and Engineering*, vol. 153, pp. 123–132, 2017.
- [25] C. Gao, L. Z. Xie, H. P. Xie et al., "Coupling between the statistical damage model and permeability variation in reservoir sandstone: theoretical analysis and verification," *Journal of Natural Gas Science and Engineering*, vol. 37, pp. 375–385, 2017.
- [26] L. Wang, Y. Yin, B. Huang, and Z. Dai, "Damage evolution and stability analysis of the Jianchuandong dangerous rock mass in the three gorges reservoir area," *Engineering Geology*, vol. 265, article 105439, 2020.
- [27] T.-f. Wong, R. H. C. Wong, K. T. Chau, and C. A. Tang, "Microcrack statistics, Weibull distribution and micromechanical modeling of compressive failure in rock," *Mechanics of Materials*, vol. 38, no. 7, pp. 664–681, 2006.
- [28] Y. Bai, R. Shan, Y. Ju, Y. Wu, P. Sun, and Z. Wang, "Study on the mechanical properties and damage constitutive model of frozen weakly cemented red sandstone," *Cold Regions Science and Technology*, vol. 171, article 102980, 2020.
- [29] S. Huang, Q. Liu, A. Cheng, and Y. Liu, "A statistical damage constitutive model under freeze-thaw and loading for rock and its engineering application," *Cold Regions Science and Technology*, vol. 145, pp. 142–150, 2018.
- [30] X. Li, D. Qu, Y. Luo, R. Ma, K. Xu, and G. Wang, "Damage evolution model of sandstone under coupled chemical solution and freeze-thaw process," *Cold Regions Science and Technology*, vol. 162, pp. 88–95, 2019.
- [31] X. L. Xu and M. Karakus, "A coupled thermo-mechanical damage model for granite," *International Journal of Rock Mechanics and Mining Sciences*, vol. 103, pp. 195–204, 2018.
- [32] H. Zhang, X. Meng, and G. Yang, "A study on mechanical properties and damage model of rock subjected to freeze-thaw cycles and confining pressure," *Cold Regions Science and Technology*, vol. 174, article 103056, 2020.
- [33] S. Chen and C. Qiao, "Composite damage constitutive model of jointed rock mass considering crack propagation length

- and joint friction effect,” *Arabian Journal of Geosciences*, vol. 11, no. 11, p. 283, 2018.
- [34] C. Zhou, M. Karakus, C. Xu, and J. Shen, “A new damage model accounting the effect of joint orientation for the jointed rock mass,” *Arabian Journal of Geosciences*, vol. 13, no. 7, p. 295, 2020.
- [35] L. M. Kachanov, “On the time to failure during creep,” *Izv AN SSSR, OTN*, vol. 8, no. 1, pp. 26–31, 1958.
- [36] Y. N. Rabotnov, “On the equation of state of creep,” *Proceedings of the Institution of Mechanical Engineers, Conference Proceedings*, vol. 178, no. 1, pp. 117–122, 1963.
- [37] J. Lemaitre, *A Course on Damage Mechanics*, Springer, Berlin, 1992.
- [38] V. Mazel, H. Diarra, V. Busignies, and P. Tchoreloff, “Comparison of different failure tests for pharmaceutical tablets: applicability of the Drucker-Prager failure criterion,” *International Journal of Pharmaceutics*, vol. 470, no. 1–2, pp. 63–69, 2014.
- [39] W. Liu, X. Qian, T. Li, Y. Zhou, and X. Zhu, “Investigation of the tool-rock interaction using Drucker-Prager failure criterion,” *Journal of Petroleum Science and Engineering*, vol. 173, pp. 269–278, 2019.
- [40] L. R. Alejano and A. Bobet, “Drucker-Prager Criterion,” *Rock Mechanics and Rock Engineering*, vol. 45, no. 6, pp. 995–999, 2012.
- [41] M. Yang, M. Zhao, and W. Cao, “Method for determining the parameters of statistical damage softening constitutive model for rock,” *Journal of Hydraulic Engineering*, vol. 36, no. 3, pp. 345–349, 2005.
- [42] Z.-l. Wang, Y.-c. Li, and J. G. Wang, “A damage-softening statistical constitutive model considering rock residual strength,” *Computers & Geosciences*, vol. 33, no. 1, pp. 1–9, 2007.
- [43] H. P. Xie and X. Q. Zhao, “Analysis of continuous damage and failure of top-coal,” *Journal of China University of Mining & Technology*, vol. 30, no. 4, pp. 323–327, 2001.
- [44] S. Heng, *Research on the Forming Mechanism of Hydraulic Fracture Network in Shale Gas Reservoir*, University of Chinese Academy of Sciences, Wuhan, 2015.
- [45] K. Wang, J. Zang, G. Wang, and A. Zhou, “Anisotropic permeability evolution of coal with effective stress variation and gas sorption: Model development and analysis,” *International Journal of Coal Geology*, vol. 130, pp. 53–65, 2014.
- [46] H. W. Zhou, T. L. Rong, L. J. Wang, R. Y. Mou, and W. G. Ren, “A new anisotropic coal permeability model under the influence of stress, gas sorption and temperature: development and verification,” *International Journal of Rock Mechanics and Mining Sciences*, vol. 132, article 104407, 2020.
- [47] Z. Wang, J. Pan, Q. Hou et al., “Changes in the anisotropic permeability of low-rank coal under varying effective stress in Fukang mining area, China,” *Fuel*, vol. 234, pp. 1481–1497, 2018.
- [48] Z. Zhang, R. Zhang, H. Xie, M. Gao, E. Zha, and Z. Jia, “An anisotropic coal permeability model that considers mining-induced stress evolution, microfracture propagation and gas sorption-desorption effects,” *Journal of Natural Gas Science and Engineering*, vol. 46, pp. 664–679, 2017.
- [49] Y. Liu, G. Yin, M. Li et al., “Mechanical properties and failure behavior of dry and water-saturated anisotropic coal under true-triaxial loading conditions,” *Rock Mechanics and Rock Engineering*, vol. 53, pp. 4799–4818, 2019.
- [50] J. Lu, G. Huang, H. Gao, X. Li, D. Zhang, and G. Yin, “Mechanical properties of layered composite coal-rock subjected to true triaxial stress,” *Rock Mechanics and Rock Engineering*, vol. 53, pp. 4117–4138, 2020.

Research Article

The Law of Fracture Evolution of Overlying Strata and Gas Emission in Goaf under the Influence of Mining

Cheng Cheng,¹ Xiaoyu Cheng ,^{1,2} Rui Yu,³ Wenping Yue,⁴ and Chao Liu¹

¹*Xi'an University of Science and Technology, Xi'an 710054, China*

²*China Coal Energy Research Institute Co., Ltd., Xi'an 710054, China*

³*China Coal Huajin Group Co., Ltd., Hejin 043300, China*

⁴*Shaanxi Key Laboratory of Safety and Durability of Concrete Structures, Xijing University, Xi'an 710123, China*

Correspondence should be addressed to Xiaoyu Cheng; chengxiaoyu89@126.com

Received 15 June 2021; Revised 16 July 2021; Accepted 27 July 2021; Published 12 August 2021

Academic Editor: Feng Du

Copyright © 2021 Cheng Cheng et al. This is an open access article distributed under the Creative Commons Attribution License, which permits unrestricted use, distribution, and reproduction in any medium, provided the original work is properly cited.

Mining is associated with poor safety due to pressure relief gas emission from the goaf during the production period. The aim of this study was to explore a case study of the Wangjialing coal mine 12322 working face in Shanxi, China, through physical simulation and field observation. The mine is characterized by overlying strata fracture in goaf during the process of working face mining. A mathematical model of gas source emission from the working face and gas migration and the finite element COMSOL software were used to simulate the law of gas migration in the region with overlying strata fissures under the influence of mining. The simulation results were used to explore the law of distribution of pressure relief gas in goaf. Rational parameters of the high-level directional long borehole for the pressure relief gas extraction in goaf were designed based on experimental results. The results showed that the development of the region with overlying strata fissures is affected by mining. In addition, the “trapezoid platform structure” is formed after fracture areas are connected. The maximum height of the stope caving zone was between 26.8 m and 28.1 m, and the maximum height of the fracture zone was approximately 110 m. The gas concentration exhibited a saddle-shaped distribution on the cut surface of the direction of the strike. Furthermore, the gas concentration showed an overall upward trend from the intake airflow roadway to the return airflow roadway and gradually decreased after reaching the maximum. In the vertical direction, gas concentration increased with the increase in the layer, and the position of the highest point of gas concentration gradually shifted to the direction of the intake airflow roadway. Construction parameters of the high directional long borehole were designed through simulation results. After steady extraction and stable extraction, the maximum gas concentration in the upper corner of the working face was 0.49%, and the maximum gas concentration in return airflow was 0.34%. The findings of this study provide information on the law of fracture evolution of overlying strata and gas migration in goaf under the influence of mining. These findings provide a basis for reducing gas overlimit in the working face or return airway corner, thus improving the safety production capacity of the coal mine.

1. Introduction

Currently, many coal seams in China coal mines are thick continuous coal seams. The coal mines account for about 44% of the total coal reserves in China [1]. Coal is one of the main energy sources in China [2–4]. Therefore, the development of high-yield, high-efficiency, and safe mining technology for thick continuous coal seams is important to ensure the high production of coal [5]. However, the rapid development of mining technology in the coal industry

results in an increase in the depth and intensity of mine mining. These features result in an increase in mine gas emission quantity. Gas release limits mine efficient mining [6–9]. The problem of high gas accumulation in the return airway corner caused by high gas emission from goaf during coal seam mining has not been fully solved [10, 11]. Advances in mine gas control technology have significantly improved the pressure-released gas control capacity in goaf through the extraction of the high directional long borehole [12–15]. However, the buried pipe in goaf and the pressure relief gas

drainage technology of the high borehole in coal mining are limited by the uncertainty of the gas emission law of the working face and the unclear law of the gas flow field in goaf and the unclear area of the failure of the overlying strata. High-efficiency control of gas in goaf is restricted, thus significantly affecting the safety production of coal mining. The fracture transfixion area of overburden rock under the influence of mining which leads the gas in goaf into the working face under the influence of airflow significantly affects the safety of coal mining. Therefore, there is a need to explore the distribution characteristics of the overlying strata fracture in the process of working face mining, the law of gas migration in goaf, and gas outbursts from the working face to improve the gas control capacity of mine goaf.

The caving of overlying strata forms three regions including the caving zone, fracture zone, and bending subsidence zone due to the stress effect [16]. The fracture zone is the main channel for gas transportation and seepage. Several studies have explored aspects of the fracture zone, such as empirical formula, numerical simulation, physical simulation, and field measurement. A large number of fracture development models of mining overburden have been established based on theoretical information. Palchik [17, 18] used the drainage method to measure the height of the fracture zone after weak overburden coal seam mining. The findings showed that the ratio of maximum height of the fracture zone to coal seam thickness increases with an increase in the interface number of overlying strata and decreases with an increase in stiffness of the immediate roof. Majdi et al. [19] determined the height of the failure region at the top of the working face using two mathematical models that were established through experimental data. Lin et al. [20] and Zhang and Wang [21] simulated the actual mining process of the working face by establishing a physical similarity model, thus analyzing the fracture evolution law of overlying strata. Furthermore, Gao et al. [22] and Wu et al. [23] simulated the collapse characteristics and fracture zone height distribution characteristics of overlying strata in goaf by establishing two-dimensional discrete element models. In addition, several studies have explored gas emission and migration in goaf based on the distribution law of the fissure zone. Yuan [24] and Danesh et al. [25] report that the law of overburden fracture evolution is correlated with gas migration in goaf. Cao and Li [26] and Liu et al. [27] explored the effect of gas drainage in goaf on gas flow in goaf and the overburden fissure zone. Whittles et al. [28] established the gas seepage model of goaf by numerical simulation and indoor experiments and explored the gas source and the path to the working face of goaf. Several studies have used these findings to explore the goaf gas treatment technology and methods. For instance, Guo et al. [29] evaluated the pressure control of coal seam horizontal drainage and developed a conceptual model on gas drainage. Moreover, Zhang et al. [30] determined the extraction situation of 29 ground boreholes in four working faces and analyzed the law of pressure relief gas extraction. Schatzel et al. [31] evaluated the dynamic influence of coal seam storage conditions and overburden structure on gas drainage in goaf during mining.

The findings from these studies have significantly improved the understanding of the fracture evolution law of mining overburden and the law of gas migration in goaf. However, most studies explore the distribution law of the fracture area in the direction of the working face, whereas the distribution law of the fissure area affected by mining in an inclined direction is not explored; therefore, it is limited in field application. In addition, the dynamic prediction model of gas emission in mining has not been fully explored. Therefore, when using these models to analyze calculations, they significantly affect the distribution of gas migration in goaf. Studies should explore the distribution range of the fissure area and the crack expansion in each area when the overlying strata in goaf are affected by mining. In addition, studies should explore ways to improve the accuracy of the gas emission prediction model in each area of the working face, ensuring accurate prediction of gas distribution in goaf to improve the effect of gas control in goaf.

This study sought to explore the evolution law of overburden fissures through a physical similarity simulation and drilling peep method. In addition, the distribution range of overlying strata fractures under the influence of mining was determined. The dynamic gas emission models of the coal wall, mining-falling coal, and remnant coal in goaf were established to improve the accuracy of gas emission prediction in goaf. Furthermore, the gas distribution and migration of goaf were tested by numerical simulation, and the gas enrichment area of goaf was explored. The results were then used to determine the reasonable drainage parameters of pressure relief gas, and the field application and effect verification were carried out. The findings of this study provide a theoretical basis for guiding mine gas accurate extraction and ensuring mine safety and efficient mining.

2. Project Overview

The case study mine was the Wangjialing coal mine, located in the Shanxi mine area in China. The mine has three layers of mining coal seams with an area of 119.7 km². The minable coal seams include No. 2, No. 3, and No. 10. Currently, the main mining coal seam is the No. 2 coal seam. The main characteristics of the coal seam are low gas content and low permeability. It is a high-gas mine characterized by high yield and high efficiency. The longwall backward mining method and comprehensive mechanized top caving technology are used for this mine.

The 12322 fully comprehensive caving working face was selected as the test face. The location of the working face is shown in Figure 1. The 12322 working face was buried in approximately 400 m depth and had an average coal thickness of 6.2 m, and the coal seam structure was simple. The working face roof comprised sandy mudstone and siltstone, and the working face floor comprised sandy mudstone. The working face strike length was 3300 m, whereas the inclination length was 310 m. The average coal seam gas content was 3.74 m³/t. The averaged absolute gas emission quantity on the working surface is 9.79 m³/min. The total gas content of the working face was low; however, the gas emission was

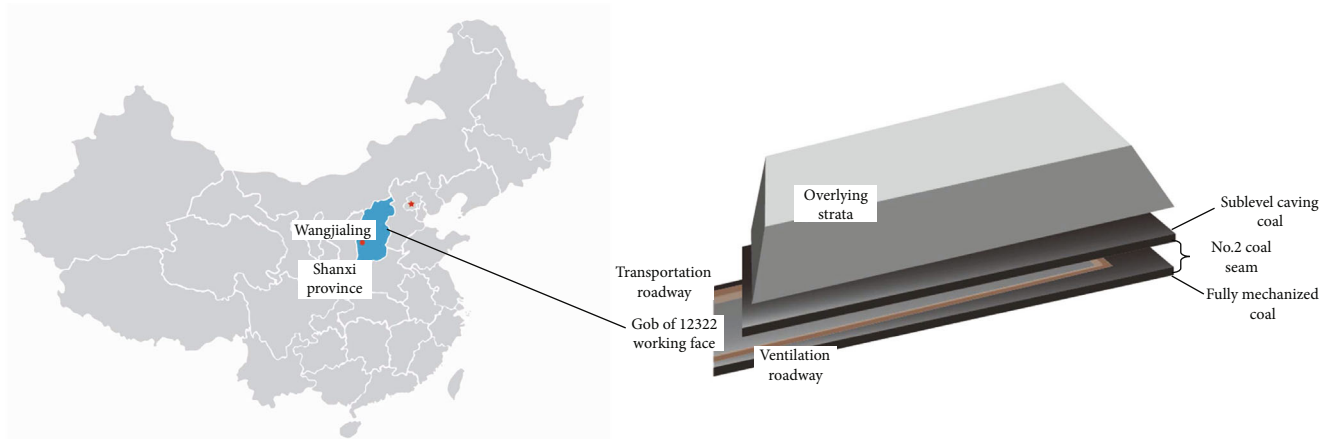


FIGURE 1: Distribution of coal seams in the Wangjialing coal mine.

abnormal in the mining process due to the high yield and high efficiency in the production process.

The lithology of overlying strata in coal seam mining directly affects distribution characteristics of “two-zone” fractures. Lithology characteristics and rock mechanics parameters of the overlying strata in the 12322 working face were determined based on the field drilling coring and laboratory mechanics test of the overlying strata in the 12322 working face (Figure 2).

3. Evolution of Fracture in Overlying Strata

3.1. Physical Experiment of Fracture Evolution of Overlying Strata in Mining

3.1.1. Model Design. According to geological conditions, two identical plane stress similarity simulation models were established when the ratio of geometric similarity is 1:200 (Figure 3). The model size was length \times height = 2500 mm \times 1200 mm. The mining of coal seams was simulated with a length of 500 m and a height of 240 m. The unsimulated rock layer was compensated by an external load, and the pressure of overlying strata was simulated by uniform loading pressure. The thickness of the unsimulated rock layer is 230 m, and the average volume weight of the rock layer is 2600 kN/m³. The added uniform loading pressure q_m is 1993 kPa. The two models used were the step-by-step mining model and the one-time mining model. The step-by-step mining model simulates the working face forward. The excavation step distance was set as 6 m, and the total excavation length was 380 m. During the excavation process, 60 m protective coal pillars were set up on both sides to eliminate the boundary effect. An inclined model was used to simulate the coal seam cutting process, using 310 m obtained from a one-time excavation simulation test.

Fine sand was used as skeletal material, calcium carbonate and gypsum were used as bonding materials, and mica powder was used to simulate the weak joint surface between rock layers. The model comprised 5 survey lines. The 5th survey line was 20 m away from the coal seam, 40 m between the No. 3, No. 4, and No. 5 survey lines, and 60 m between the

No. 1, No. 2, and No. 3 survey lines. One displacement measuring point was placed every 20 m on each survey line, with a total of 24 displacement measuring points.

3.1.2. Analysis of Simulation Results. The overlying rock above the goaf gradually changes from an elastic state to a plastic state when the coal seam is mined. The overlying rock mass above the goaf moves and breaks when the working face advances to a certain distance, forming the caving zone, the fracture zone, and the bending subsidence zone. In the caving zone, the rock strata break into blocks and collapse. In the fracture zone, the fracture of the rock mass is fully developed; therefore, the survey line subsidence in the caving zone is relatively large, and the subsidence of different survey points on the same survey line fluctuates significantly. Although the fracture zone rocks have deformation and fractures, they have good continuity. The subsidence of the measuring point decreases with an increase in the measuring line position, and the subsidence law of each line in the fracture zone is similar. The “three zones” of mining overburden can be effectively categorized based on the above analysis.

The simulation results when working face mining to 380 m are shown in Figures 4(a)–4(c). When the mining area reaches 380 m, the working face experiences 12 cycles of periodic pressure (Figure 4(a)). Statistical analysis showed that the first pressure distance was 50 m, and the periodic pressure distance average was 25 m. The change of the rock strata after each periodic pressure showed a certain regularity. The length of the rock layer collapsed after the periodic pressure was basically the same. All lengths were approximately equal to the periodic pressure step distance. However, the higher the overburden, the more backward the caving boundary was and the farther the projection of the caving boundary on the coal seam from the working face. The fragmented rocks appear irregular after the collapse of the caving zone, and a large difference in the degree of compaction was observed; therefore, it causes the same rock strata subsidence quantity disparity to be big. The sinking situation of each measuring line was drawn based on an analysis of the sinking value of each measuring point (Figure 4(b)). The final vertical displacement changes of the five survey lines of the overlying

Lithology	Columnar	Strata thickness (m)	Density (kg·m ⁻³)	Compressive strength (MPa)	Tensile strength (MPa)	Elastic modulus (GPa)	Poisson's ratio	Geometric similarity ratio
Mudstone		11.0	2643	62.6	2.84	10.45	0.30	1:200
Sandy mudstone		38.9	2635	64.0	2.19	16.90	0.23	
Mudstone		10.1	2643	62.6	2.84	10.45	0.30	
Fine sandstone		6.0	2645	58.5	2.98	18.01	0.21	
Sandy mudstone		7.0	2635	64.0	2.19	16.90	0.23	
Mudstone		6.7	2643	62.6	2.84	10.45	0.30	
Fine sandstone		9.3	2645	58.5	2.98	18.01	0.21	
Mudstone		6.7	2643	62.6	2.84	10.45	0.30	
Sandy mudstone		6.8	2635	64.0	2.19	16.90	0.23	
Mudstone		9.2	2643	62.6	2.84	10.45	0.30	
Sandy mudstone		5.6	2635	64.0	2.19	16.90	0.23	
Siltstone		8.5	2643	55.4	2.75	9.86	0.18	
Sandy mudstone		10.8	2635	64.0	2.19	16.90	0.23	
Mudstone		13.1	2643	62.6	2.84	10.45	0.30	
Sandy mudstone		10.8	2635	64.0	2.19	16.90	0.23	
Fine sandstone		2.8	2645	58.5	2.98	18.01	0.21	
Mudstone		16.5	2643	62.6	2.84	10.45	0.30	
Sandy mudstone		17.1	2635	64.0	2.19	16.90	0.23	
Siltstone		2.0	2643	55.4	2.75	9.86	0.18	
Mudstone		3.9	2643	62.6	2.84	10.45	0.30	
Siltstone		6.2	2643	55.4	2.75	9.86	0.18	
Sandy mudstone		2.1	2635	64.0	2.19	16.90	0.23	
Siltstone		3.4	2643	55.4	2.75	9.86	0.18	
Sandy mudstone		19.5	2635	64.0	2.19	16.90	0.23	
No.2 coal seam		6.0	1301	13.0	0.88	2.43	0.31	
Sandy mudstone		2.0	2635	64.0	2.19	16.90	0.23	

FIGURE 2: Mechanical parameters of overlying strata in the No. 2 coal seam.

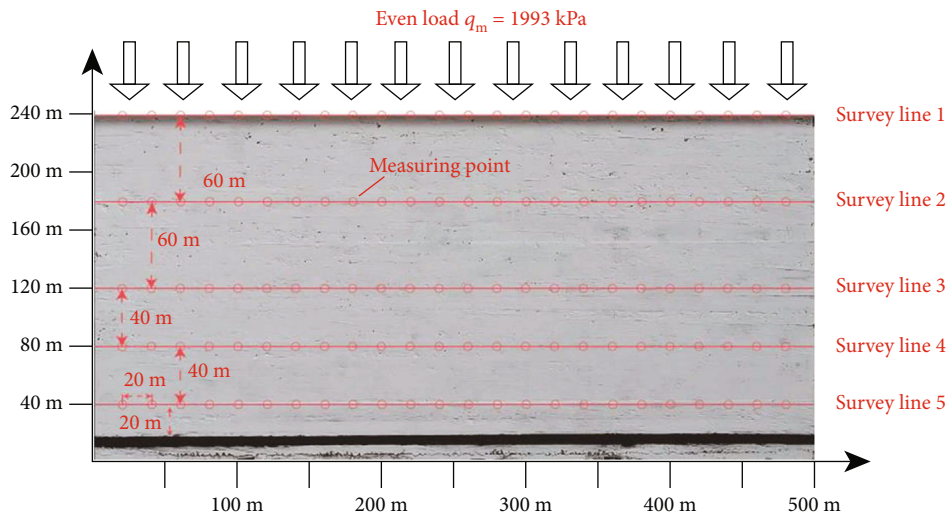


FIGURE 3: Physical similarity model of the working face.

strata after mining were visible. Survey line 5 showed the largest displacement and subsidence, which is close to the mining thickness of the coal seam, with a maximum value of 5.4 m. The subsidence of survey line 4 and survey line 3 decreased sharply with a similar trend, with a maximum of 3.4 m. The sinking amounts of survey line 1 and survey line

2 were the smallest, and the maximum sinking values were 2.3 m and 2.1 m, respectively. These differences occur because survey line 5 is located in the caving zone of the coal roof of the goaf, survey lines 3 and 4 are located in the fracture zone of the coal roof of the goaf, and survey lines 1 and 2 are located above the fracture zone. The overlying

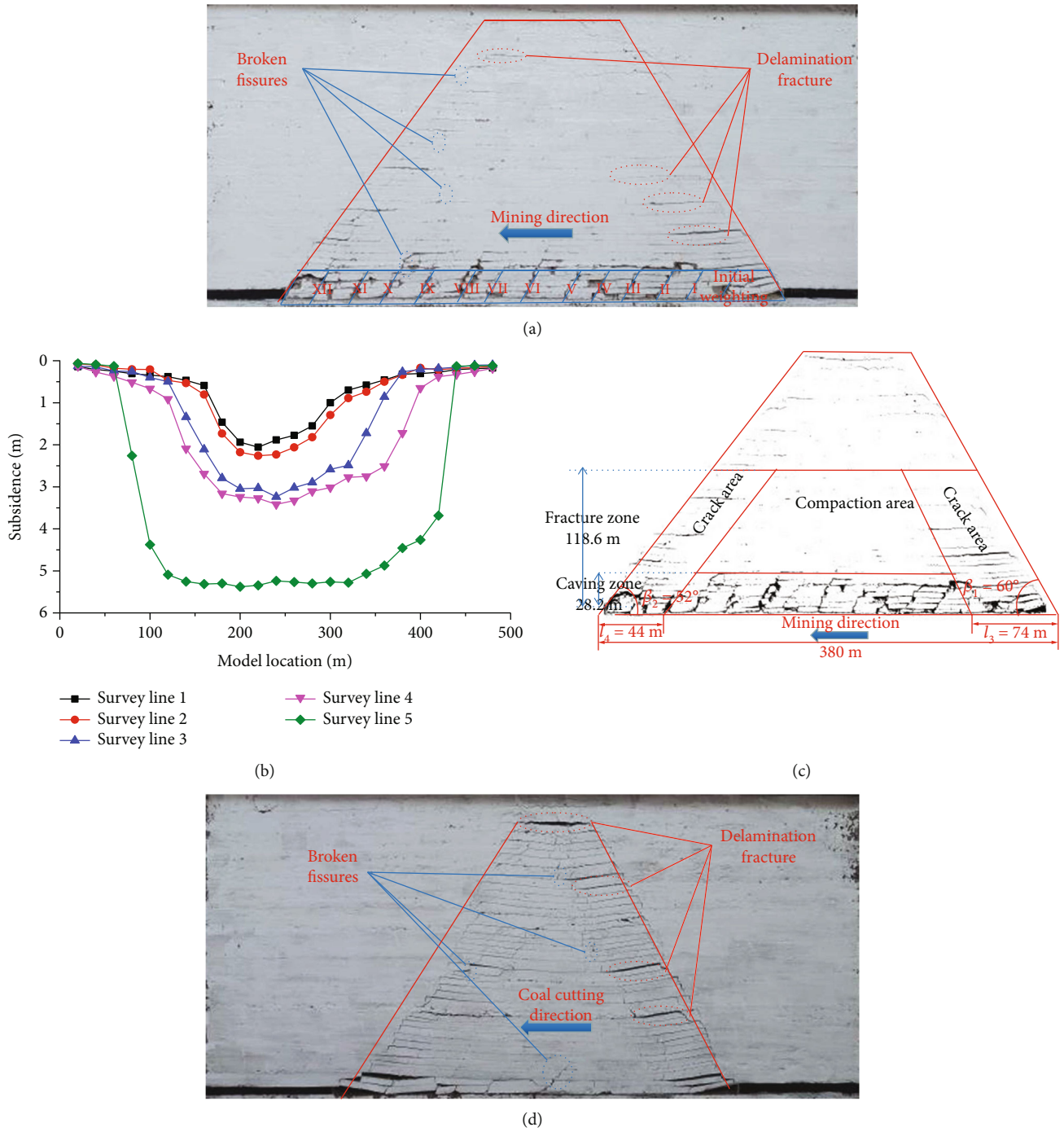


FIGURE 4: Continued.

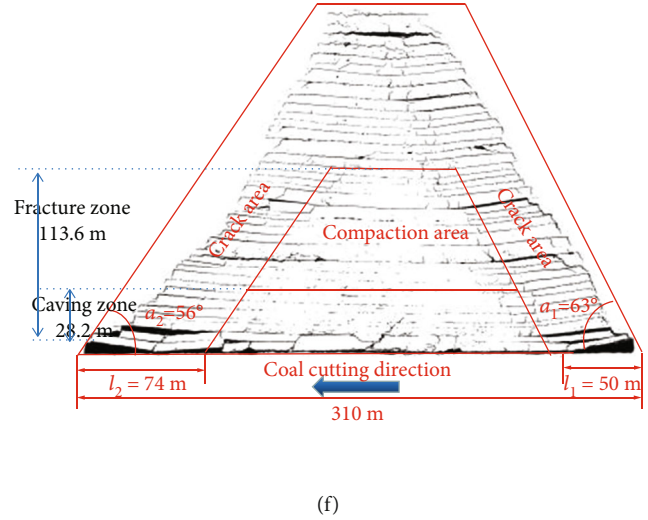
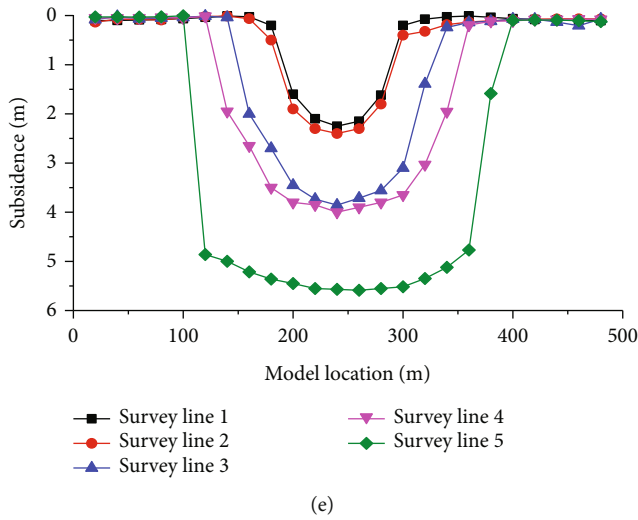


FIGURE 4: Migration and fracture development of overlying strata during coal seam mining.

strata fracture distribution network in the coal mining process is obtained through image processing of Figure 4(a). The distribution law of the caving zone and fissure zone is accurately shown in Figure 4(c). The maximum height of the caving zone of the strike model was 28.2 m, the maximum height of the fracture zone was 118.6 m, the caving angle at the cut eye was 60° , and the caving angle at the working face was 52° .

The simulation result of the one-time mining of the dip model is presented in Figures 4(d)–4(f). The rock formation collapsed after mining. One-time excavation is different from stepwise excavation in that coal cutting speed is faster, resulting in an increased distance of fracture of the rock. Analysis of the sinking value of the measurement points in Figure 4(e) shows that the sinking of the measurement points is generally similar to that of the strike model. The farther away from the roof of the coal seam, the smaller the sinking amount of the displacement measuring point. In addition, the displacement variation of each row of measuring points has a corresponding law. The sinking value of the displacement measuring point of survey line 5, which was 20 m away from the coal seam floor, was between 5.0 m and 5.6 m. The maximum subsidence of survey line 4 from 60 m of the coal seam floor was 4.0 m, and the maximum subsidence of survey line 3 was 3.8 m. These findings show that the farther the distance from the coal roof is, the smaller the subsidence of the survey point. Analysis of the fracture distribution network shows that the cracks in the middle of the goaf are compacted, whereas the cracks on both sides are relatively developed (Figure 4(f)). Several broken fracture gaps occur below 28.2 m from the roof of the coal seam, which are relatively messy, and belong to the caving zone. Fractures from the upper part of the caving zone to a height of 113.6 m are relatively developed and belong to the fracture zone. Measurement of the caving angle of coal seams was inclined to one-off mining. The caving angle of the coal cutter tail was 56° , whereas the caving angle of the coal cutter head was 63° .

3.2. Field Test of Fracture Evolution of Overlying Strata. The field test is the most intuitive and reliable method to study

the development of “three-zone” cracks in overlying strata [32, 33]. Two drill holes are arranged in the coal wall of the return airway of the working face. The location and development of fissures in the borehole under the effect of mining were monitored using the drilling peep method. Borehole layout parameters are shown in Table 1, and the layout is shown in Figure 5.

By observing the development inside the borehole, the fracture area of goaf is analyzed during the process of mining (Figure 6). Analysis of the No. I hole at a depth of 24 m showed that the hole wall was complete, and only small cracks were produced, with no large penetrating cracks. A large number of cracks occurred in the area from 24 m to 59 m, resulting in the collapse of the hole wall. The cracks were developed and irregular. In addition, observation was done from drilling at 59 m to the bottom of the hole. The fissures were stable in this area, and regular penetrating fissures and separation fissures were observed. Analysis of the No. II hole showed that the hole wall was intact within 26 m deep before drilling, and a large amount of broken rock appeared in the area from 26 m to 93 m. Further observation showed that the borehole was significantly deformed. Moreover, it was gradually blocked before the entrance of the bottom of the borehole, indicating that the borehole had reached the goaf compaction zone.

Borehole No. I did not enter the caving area behind the working face before 24 m; therefore, the borehole wall in this area was complete. After entry to the goaf, it first went through the caving zone, resulting in shredding and shedding of rocks in the borehole. The borehole entered the fracture zone at a depth of 59 m. The fracture development was regular, and the rock integrity was good. The front section of borehole No. II was similar to that of borehole No. I. Several rock blocks accumulated in the borehole at a depth of 26 m into the caving zone of goaf, whereas at 93 m deep, the borehole entered the goaf compaction area and was gradually blocked.

The location of the hole was determined by drawing the vertical view and front view of borehole No. I and No. II.

TABLE 1: Drilling parameters.

Drilling number	Hole position	Drilling diameter (mm)	Drilling depth (m)	Inclination (°)	Included angle with laneway midline (°)
1#	The coal wall at 20m away from the working face	$\phi 73$	120	+27.0	12.0
2#			135	+12.0	35.0

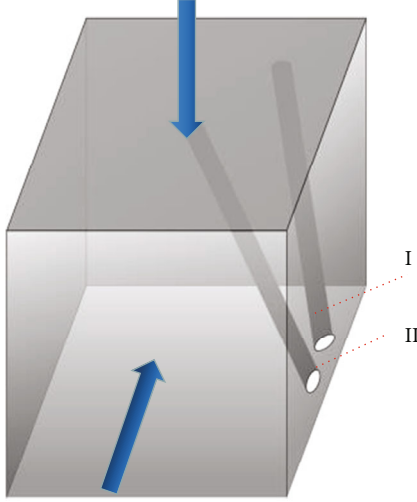


FIGURE 5: Schematic of the peephole.

Analysis of the measured results was done through borehole peeking. Borehole No. I entered the goaf zone and fracture zone but did not enter the compaction zone. Borehole No. II entered the caving zone and compaction zone but did not enter the fracture zone. The height of the caving zone was between 26 m and 28 m, and the compaction area was about 50 m from the mining face and 22 m~52 m from the return air roadway.

4. Law of Gas Migration in Goaf under the Influence of Mining

4.1. Law of Gas Emission from the Fracture Zone

4.1.1. Dynamic Gas Emission Model of the Working Face

(1) *Coal Wall Gas Emission Model.* The fresh coal wall was constantly exposed during the mining process of the working face, and a constant gas pressure gradient was observed in front of the working face. Therefore, the gas in the coal seam flowed to the working face. The intensity of gas emission decreased with an increase in coal wall exposure time. The amount of coal wall gas emission mainly depends on the original coal seam gas pressure, coal seam permeability, and coal gas adsorption performance. Under constant mining conditions, the gas emission intensity has the following function relationship with the exposure time:

$$V_1 = V_r(1+t)^{-n_1}, \quad (1)$$

where V_1 represents the gas emission intensity per unit area of the coal wall at time t , $\text{m}^3/(\text{m}^2 \cdot \text{min})$; V_r represents the gas

emission intensity per unit area of the coal wall at the initial moment, $\text{m}^3/(\text{m}^2 \cdot \text{min})$; t represents the coal wall exposure time, min; and n_1 represents the coal wall gas emission attenuation coefficient, min^{-1} .

The cumulative gas emission per unit area of the coal wall during normal advancement of the working face is

$$q_1 = \int_0^t V_1 dt. \quad (2)$$

Absolute gas emission from the coal wall of the working face is calculated as follows:

$$Q_1 = S \cdot q_1. \quad (3)$$

The effective exposed area of the coal wall of the working face is divided into the front coal wall S_1 and the top coal wall S_2 . Gas emission from the coal wall is the sum of the two parts:

$$S = S_1 + S_2, \quad (4)$$

$$S_1 = l \cdot h_0, \quad (5)$$

$$S_2 = l \cdot w. \quad (6)$$

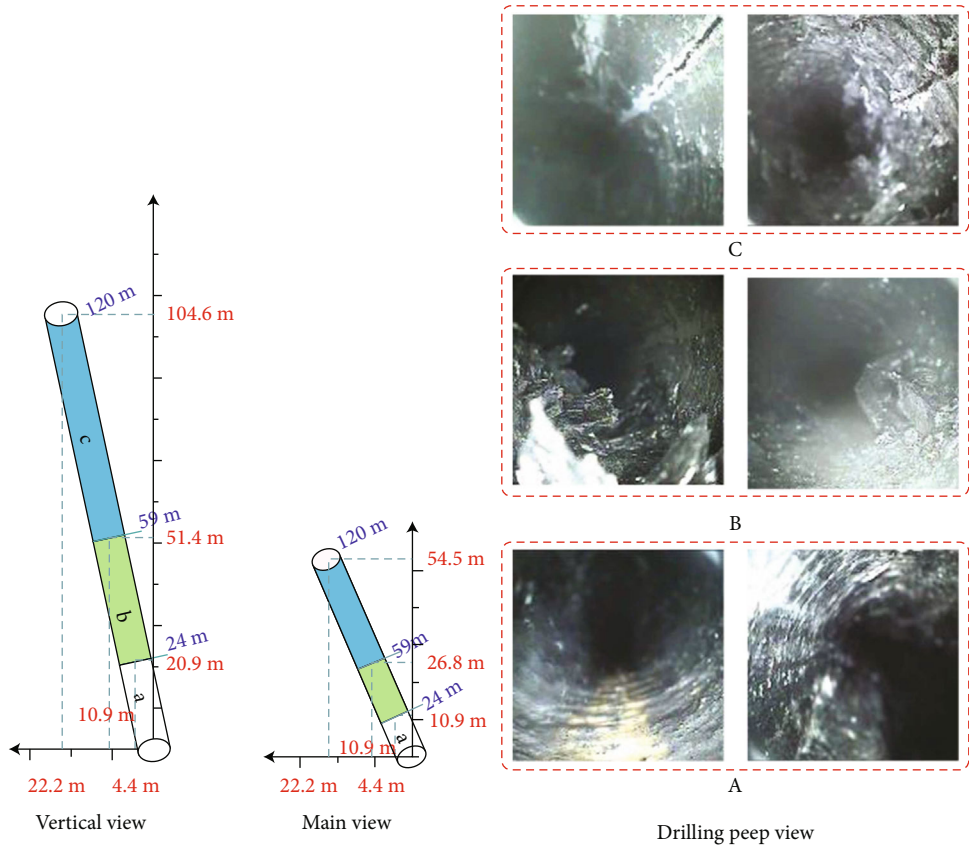
In the formula, S represents the effective exposed area of the coal wall of the working face, m^2 ; l represents the length of the working face, m; h_0 represents the height of the working face, m; and w represents the width of the working surface, m.

The absolute gas emission from the coal wall is calculated through organization and integration of formulas (1)–(6) as follows:

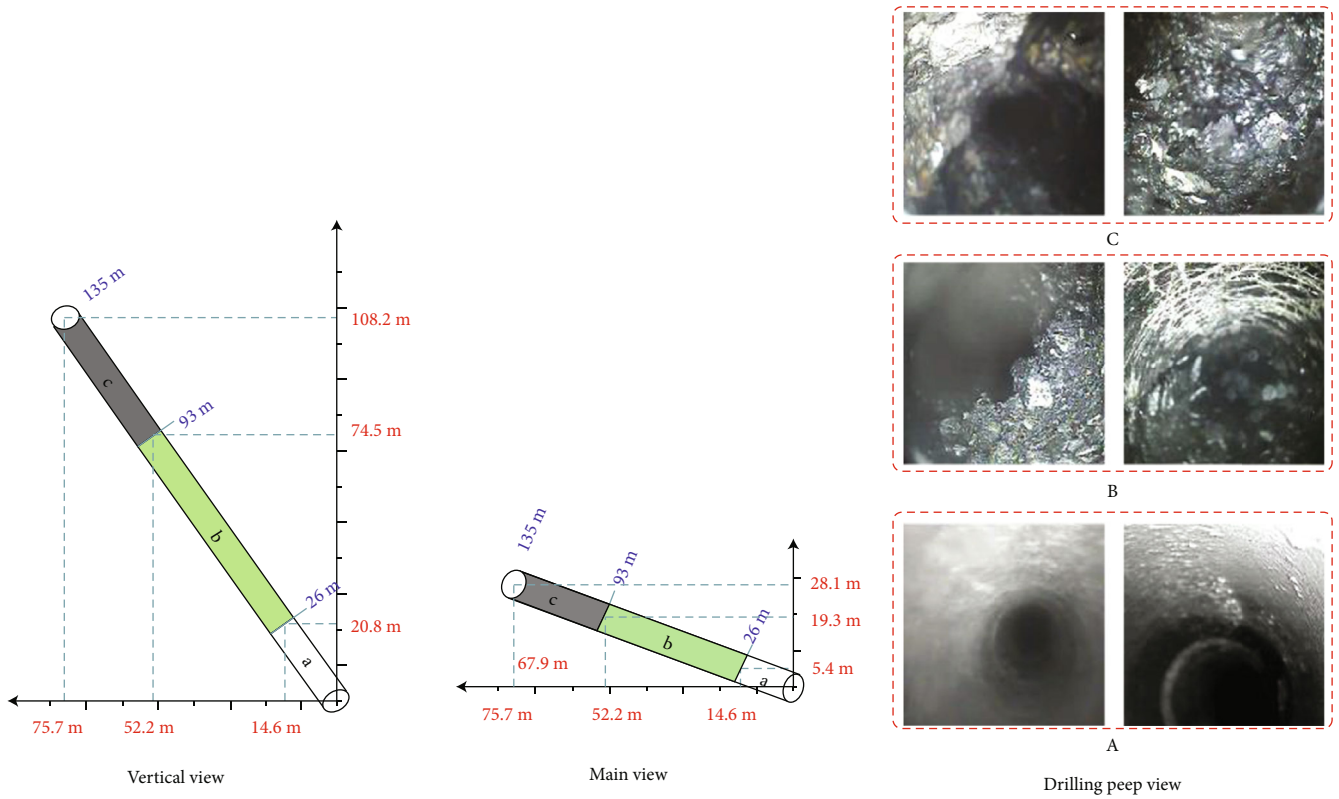
$$Q_1 = V_r \left(\frac{(1+t)^{1-n_1}}{1-n_1} - \frac{1}{1-n_1} \right) l(h_0 + w). \quad (7)$$

(2) *The Law of Coal Gas Emission from Coal Mining.* Part of the gas in the working face is released during the mining process as the coal body is broken into different particle sizes. The amount of emission is mainly related to factors such as coal amount, desorption gas content, desorption strength, and exposure time. In the process of mining, the gas desorption strength of coal is correlated with the exposure time of coal. The mathematical expression of this relationship is

$$V_2 = V_c \cdot e^{-n_2 t}, \quad (8)$$



(a) Borehole No. I



(b) Borehole No. II

FIGURE 6: Observation results of drill holes during mining.

whereby V_2 represents the gas emission intensity at time t when the mined coal stays at the working face, $\text{m}^3/(\text{t}\cdot\text{min})$; n_2 represents the attenuation coefficient of gas emission from coal mining, min^{-1} ; V_c represents the initial gas emission intensity of broken coal, $\text{m}^3/(\text{t}\cdot\text{min})$; and t represents the residence time of mined coal on the working face, min .

During the production period, the coal mine gas emission Q_2 is affected by the mined coal quality and gas desorption strength. The mathematical expression of this relationship is as shown below:

$$Q_2 = \int_0^t dV_2 \cdot M_2 \frac{W_0}{1.5}. \quad (9)$$

In the formula, dV_2 represents the total gas emission intensity of coal mined at time dt , $\text{m}^3/(\text{t}\cdot\text{min})$; M_2 represents the coal mining quality, t ; t represents the time of coal transportation, that is, the time when the coal mass is transported out of the working face through the scraper conveyor and the belt, min ; and W_0 represents the desorption gas content amount of the coal mass, m^3/t .

M_2 is calculated as follows:

$$M_2 = Rh_1\rho dv_0, \quad (10)$$

whereby h_1 represents the coal seam thickness, m ; ρ is the coal density, t/m^3 ; d is the shearer cutting depth, m ; R represents the rate of recovery, $\%$; and v_0 represents the coal cutting speed, m/min .

The amount of gas emission in the coal mining process of the working face can be obtained by combining equations (8)–(10) and integrating t as follows:

$$Q_2 = \frac{2}{3}Rh_1\rho dv_0 W_0 \left[\frac{V_c}{n_2} (1 - e^{-n_2 t}) \right]. \quad (11)$$

(3) *Model of Gas Emission from Remnant Coal in Goaf.* In the process of comprehensive mining, a relationship between the desorption strength of the remnant coal gas and the exposure time of the coal mass is observed. The relationship is similar to the change law of the gas emission intensity of the mined coal. The mathematical expression of this relationship is

$$V_3 = V_c \bullet e^{-n_3 t}. \quad (12)$$

In the formula, V_3 represents the gas emission intensity at time t of unit remnant coal in the goaf, $\text{m}^3/(\text{t}\cdot\text{min})$; n_3 represents the gas emission attenuation coefficient of remnant coal, min^{-1} ; and t represents the stay time of remnant coal in goaf, min .

Gas emission from the goaf is mainly affected by the recovery rate during the process of comprehensive mining. A high recovery rate leads to less remnant coal; therefore, the gas emission in the goaf is lower. The effective gas emission in goaf is calculated as follows:

$$Q_3 = \int_0^t dV_3 \cdot M_3 \frac{W_0}{1.5}. \quad (13)$$

In the formula, Q_3 represents the gas emission from goaf, m^3 ; dV_3 represents the gas emission intensity of remnant coal in goaf at time dt , $\text{m}^3/(\text{t}\cdot\text{min})$; M_3 represents the quality of remnant coal in goaf at time t ; W_0 represents the desorption gas content amount of the coal mass, m^3/t ; and t represents the exposure time of remnant coal in goaf, min .

The quality of the remnant coal in goaf depends on the recovery rate of the working face and is calculated as follows:

$$M_3 = (1 - R)lh_1\rho l_0. \quad (14)$$

In the formula, h_1 represents the coal seam thickness, m ; ρ represents the coal density, t/m^3 ; R represents the rate of recovery, $\%$; l represents the length of the working face, m ; and l_0 represents the depth of goaf, m .

The amount of gas emission from the remnant coal in goaf can be obtained by combining formulas (12)–(14) and integrating

$$Q_3 = \frac{2V_c}{3n_3} (1 - e^{-n_3 t}) (1 - R)lh_1\rho l_0 W_0. \quad (15)$$

4.1.2. Gas Migration Model of the Mining Fracture Area

(1) *Gas Migration Model in the Working Face.* The Navier-Stokes equation accurately describes the flow of fluid in the pipeline. The airflow in the coal mine roadway and mining face can be simplified to pipeline flow [34]. In this study, the Navier-Stokes equation was used as the governing equation of airflow in the working face, and the dependent variables were the velocity vector (u_{ns}) and pressure (p_{ns}). The equation is expressed as follows:

$$-\nabla \bullet \eta \left(\nabla u_{\text{ns}} + (\nabla u_{\text{ns}})^T \right) + \rho u_{\text{ns}} \bullet \nabla u_{\text{ns}} + \nabla p_{\text{ns}} = 0, \quad (16)$$

$$\nabla \bullet u_{\text{ns}} = 0, \quad (17)$$

whereby η represents the viscosity coefficient, $\text{kg}/(\text{m}\cdot\text{s})$; and ρ is the fluid density, kg/m^3 .

(2) *Gas Migration Model in Goaf.* The goaf is affected by the collapse of the roof and is filled with coal, and there are a lot of cracks and cavities around the coal. The state of the gas flow in goaf is between the Darcy seepage and the Navier-Stokes pipeline flow. This state can be described by the Brinkman equations, that is, the fluid flow equation in the porous medium. The equation is mainly affected by the velocity vector (u_{br}), the pressure (p_{br}), and the permeability and porosity of the porous medium. Moreover, the permeability and porosity in goaf are correlated with the coefficient of dilatation of rock collapse. This relationship can be expressed as shown below [35]:

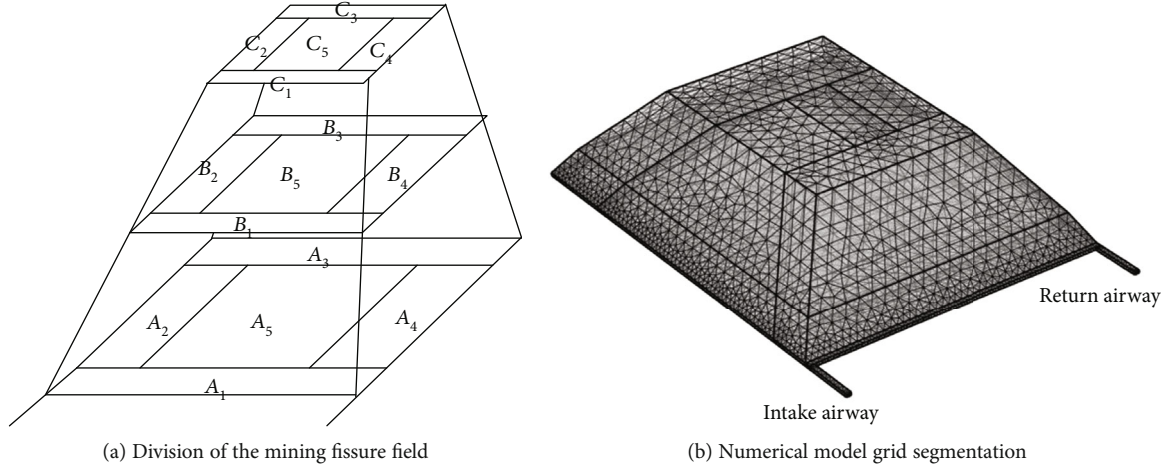


FIGURE 7: Numerical model of gas migration in goaf.

TABLE 2: Coefficient of dilatation of rock collapse of each area.

Area	A_1, B_1	A_2, B_2	A_5, B_5	A_4, B_4	A_3, B_3	C_1, C_3	C_5	C_2, C_4
Dilatation coefficient k_p	1.2	1.14	1.05	1.12	1.07	1.05	1.07	1.06
Porosity	0.17	0.12	0.05	0.11	0.07	0.05	0.07	0.06
Permeability ($10^{-6}/m^2$)	1.45	1.2	0.03	1.2	0.14	0.14	0.007	0.3

$$\frac{\rho}{\varepsilon} \left(\frac{\partial u_{br}}{\partial t} \right) + \left(\frac{\mu}{k} \right) u_{br} = -\nabla p_{br} + \nabla \left(\frac{\mu}{\varepsilon} \left(u_{br} + (\nabla u_{br})^T \right) \right) + F, \quad (18)$$

$$\nabla \bullet u_{br} = 0, \quad (19)$$

$$k = \frac{\varepsilon^3 d_m^2}{150(1 - \varepsilon)^2}, \quad (20)$$

$$\varepsilon = 1 - \frac{1}{k_p}, \quad (21)$$

whereby η represents the viscosity coefficient, kg/(m·s); ρ is the fluid density, kg/m³; ε is the porosity; k is the permeability coefficient; k_p is the coefficient of dilatation of rock collapse; and d_m is the average particle diameter of the porous medium, m.

The fluid flow equations in the porous medium relative to the velocity vector (u_{br}), pressure (p_{br}), and coefficient of dilatation of rock collapse (k_p) can be obtained by reorganizing equations (18)–(21) as follows:

$$\frac{\rho}{\varepsilon} \left(\frac{\partial u_{br}}{\partial t} \right) + \left(\frac{150\mu k_p}{(k_p - 1)^3 d_m^2} \right) u_{br} = -\nabla p_{br} + \nabla \left(\frac{\mu k_p}{k_p - 1} \left(u_{br} + (\nabla u_{br})^T \right) \right) + F. \quad (22)$$

4.2. Numerical Simulation of Gas Migration in Goaf

4.2.1. Numerical Model Establishment. The working face and mining fissure field can be simplified based on the above-

mentioned physical test and the theoretical model of gas migration. The model is divided into 15 regions based on the different coefficients of dilatation of rock collapse of the overburden rock caused by mining (Figure 7(a)).

Based on the physical similarity simulation, a gas migration model in goaf was established by COMSOL numerical simulation, as shown in Figure 7(b).

The length and width of the goaf in the model are 400 m and 310 m, respectively. In the model, the heights of the goaf, caving zone, and fracture zone are 3 m, 28.2 m, and 90.4 m, respectively. And the caving angle in the inner part of the goaf after the coal seam was mined was 60°, the caving angle in the location of the coal face was 52°, the caving angle on the side of the return airflow roadway was 63°, and the caving angle on the side of the intake airflow roadway was 56°.

The height of the working face was 3 m, the width was 5 m, and the length was 310 m based on the actual mine conditions. The wind speed was 2.26 m/s, the air density was 1.29 kg/m³, the gas density was 0.714 kg/m³, the air dynamic viscosity coefficient was 5×10^{-5} Pa·s, and the gas pressure was 0.2 MPa. The outer boundary condition of the simulation model is air-impermeable, which indicates that the gas cannot travel through the boundary. The areas that contain the caving zone and fracture zone are in free seepage conditions. Also, the roadway and working face are both set in the free-flow model of gas.

The gas migration in goaf was affected by permeability and porosity, as shown by the abovementioned gas migration model in goaf. In addition, the porosity and permeability are correlated with the coefficient of dilatation of rock collapse. Therefore, the coefficient of dilatation of rock collapse is calculated based on the actual situation in the field. A_n

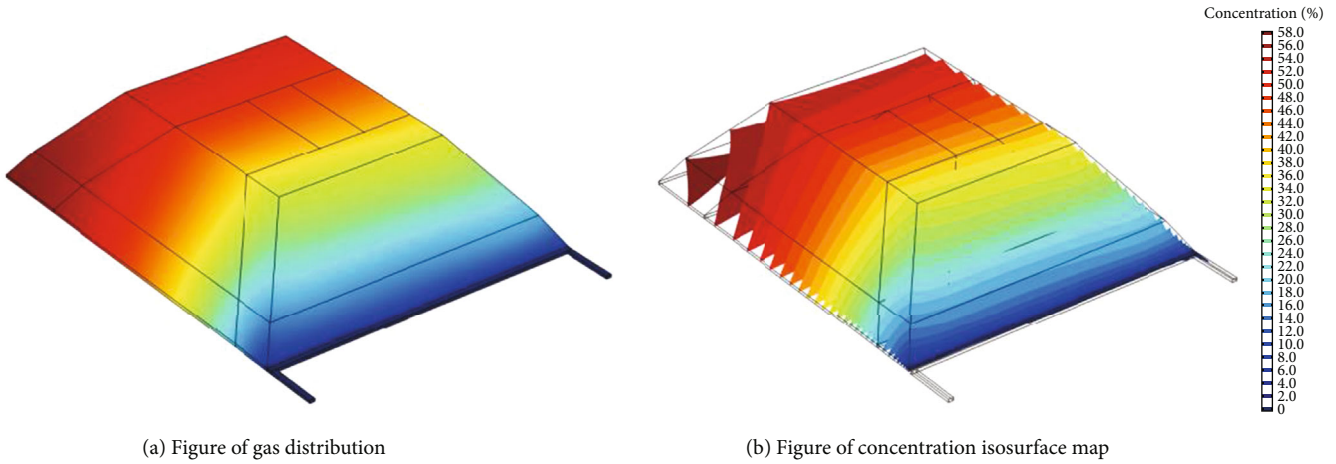


FIGURE 8: Three-dimensional distribution of gas concentration in goaf.

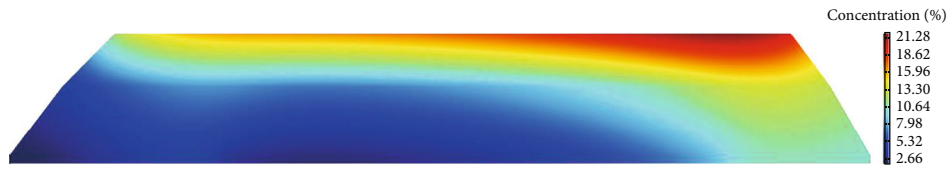


FIGURE 9: Plane diagram of gas concentration distribution at a depth of 45 m in goaf.

represents the goaf, B_n represents the caving zone, and C_n represents the fissure zone. Specific values are shown in Table 2.

4.2.2. Analysis of Numerical Simulation Results. Under the influence of coal seam mining, gas migration is affected by gas concentration and pressure. The development of fissures of the overlying strata in various areas is very different. Therefore, the distribution of gas in different areas of the goaf is also different. During the diffusion of gas in the overburden fissure area, the distribution of the mining fissure field plays a vital role in gas migration. The gas concentration results based on the distribution law of the mining fissure field are shown in Figure 8.

The distribution patterns of gas with different concentrations are shown in Figure 8. The gas concentration increases gradually in the deep area of goaf along the coal seam strike. The gas isosurface was dense, and the gradient of gas concentration was relatively large near the return airway corner of the working face. The gas migrates to the return airway corner direction due to the influence of air leakage near the working face, which makes the gas concentration increase gradually from the inlet wind corner to the return airway corner, in the direction of the coal seam inclination of the working face. The gas reaches the maximum value at the return airway corner. The distribution of gas concentration in the vertical direction shows that the gas concentration in the fracture zone at the return airway corner is significantly higher compared with that in the caving zone.

The plane gas distribution at 45 m inside the extracted working face is shown in Figure 9. On the plane at a depth

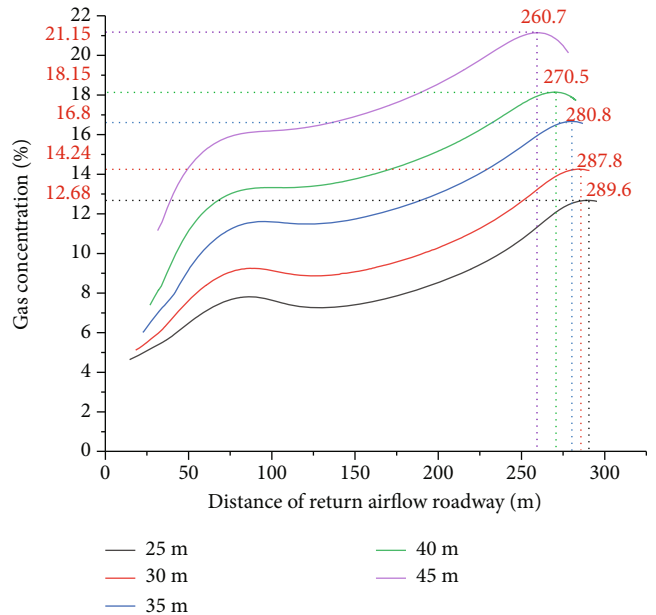


FIGURE 10: Gas concentration against different heights at a depth of 45 m in goaf.

of 45 m in goaf, the gas presents a “saddle-shaped” distribution as a whole. The highest concentration is distributed in the area of the upper caving zone and lower part of the fracture zone. The gas concentration data is extracted from the tangent line at the height of 25 m, 30 m, 35 m, 40 m, and 45 m at a depth of 45 m in goaf for quantitative analysis. A curve of gas concentration variation along coal seam

TABLE 3: Parameters of the high-level directional long borehole.

Drilling site	Drilling number	Design layer (m)	Design horizontal distance (m)	Construction layer (m)	Construction horizontal distance (m)	Length (m)
6#	6-1	45	50	43	50	483
	6-2	40	40	41	40	480
	6-3	35	30	33	29	477
	6-4	25	20	24	19	474

tendency was constructed, as shown in Figure 10. The curve shows that from the intake airflow roadway of the working face to the return airflow roadway, the gas concentration gradually increases, then decreases and increases again. Thereafter, it gradually decreases when it reaches the highest point. The maximum gas concentration of the tangent at different heights is different. When the heights are 25 m, 30 m, 35 m, 40 m, and 45 m, the distances from the highest point of gas concentration to the return airflow roadway are 20.4 m, 22.2 m, 29.2 m, 39.5 m, and 49.3 m, respectively. The highest gas concentration at each height was 12.68%, 14.24%, 16.8%, 18.15%, and 21.15%, respectively, and the gas concentration showed an increasing trend in the vertical direction.

The effective extraction distance of drill holes in the overlying rock fissure of the goaf is affected by the overlying rock collapse. The results from physical simulation show that the drill holes should be located in the gas enrichment zone of the crack area of the overburden rock caused by mining. Moreover, the drill holes should mainly extract gas at a depth of 40 m-50 m from the working face, thereby changing the upper corner gas flow field and ensuring safety production at the working face.

Based on this, the on-site setting of the high directional long borehole is a balanced trade-off with the extraction capacity and economic benefits. The high directional long borehole is set as follows. The high directional long borehole is set within 50 m from the return airflow roadway of the working face. The bottom location of the high directional long borehole is arranged at the position of 20 m, 30 m, 40 m, and 50 m from the horizontal distance of the return airflow roadway, and the design layers of the high directional long borehole are 20-30 m, 30-40 m, 40-50 m, and 40-50 m, respectively.

5. Practical Application

In the normal mining process of the test working face, affected by gas migration in goaf, the gas concentration of the return airway corner of the working face is relatively high, which affects safety production. Unsafe gas emission cannot be effectively solved by ventilation. Reasonable high directional long borehole layout parameters are designed to extract gas in the goaf overburden fracture area based on the analysis of the law of fracture distribution of overlying strata and gas migration in goaf, thus reducing the gas emission in goaf and changing the gas flow field near the return airway corner. The location of the gas enrichment area of the gas migration process can be effectively determined by

tracking the gas concentration of the working face and the return airway corner during the mining process and real-time monitoring of the gas concentration and the gas extraction volume of the high-position long borehole.

5.1. Drilling Location Selection. The primary task of gas extraction in the fracture zone of the goaf is designing the extraction method and parameters based on the determination of the range of the high-concentration gas enrichment area. Regional determination of the gas enrichment area is important for efficient extraction. Choosing the location of the directional long boreholes in the gas enrichment area can help in effectively extracting high-concentration gas and achieving safety production in the mine. A reasonable high-level directional long borehole parameter is designed to carry out pressure relief gas extraction in the fissure zone of goaf based on these findings. The design parameters are shown in Table 3, and a high-level directional long borehole arrangement is shown in Figure 11.

5.2. Effect Investigation

5.2.1. Extraction Effect. The extraction effect was determined through the real-time monitoring of the gas extraction effect of the high-level directional long borehole during the mining of the working face (Figure 12). The findings show that in the normal mining process of the working face, the four high-level directional long boreholes in the drilling site extraction effects were improved. The extraction concentrations of the four boreholes were 11.0%-26.2%, 7.5%-32.6%, 10.0%-20.0%, and 7.3%-19.0%. The average extraction concentrations were 19.6%, 17.5%, 15.2%, and 13.0%. The minimum gas extraction purity of the four boreholes was more than 0.4 m³/min, and the maximum purity was 1.9 m³/min. The average gas extraction purities of the four boreholes were 0.91 m³/min, 0.62 m³/min, 0.99 m³/min, and 0.88 m³/min.

The averaged absolute gas emission quantity on the working face is 9.79 m³/min. When the gas extraction volume reached 1.95 m³/min, it can meet the "provisional requirements for compliance of coal mine gas drainage," while the average total of the gas extraction volume of the four high-level directional long boreholes is 3.42 m³/min. Therefore, the construction locations of the high-level directional long boreholes were all in the gas enrichment area, and the overall drainage effect of the boreholes reached the expected effect.

5.2.2. Investigation on the Effect of Gas Governance. The change of the return airway corner and the return airflow gas concentration of the working face for the high-level directional long borehole extraction pressure relief gas of the goaf

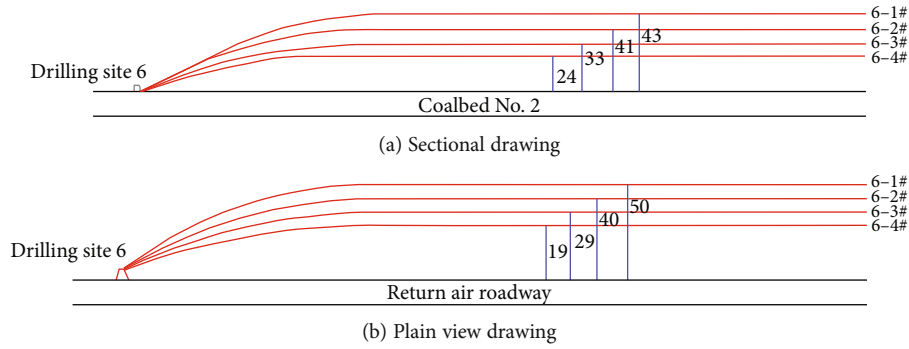


FIGURE 11: High-level directional long drilling layout of the 6# drilling site.

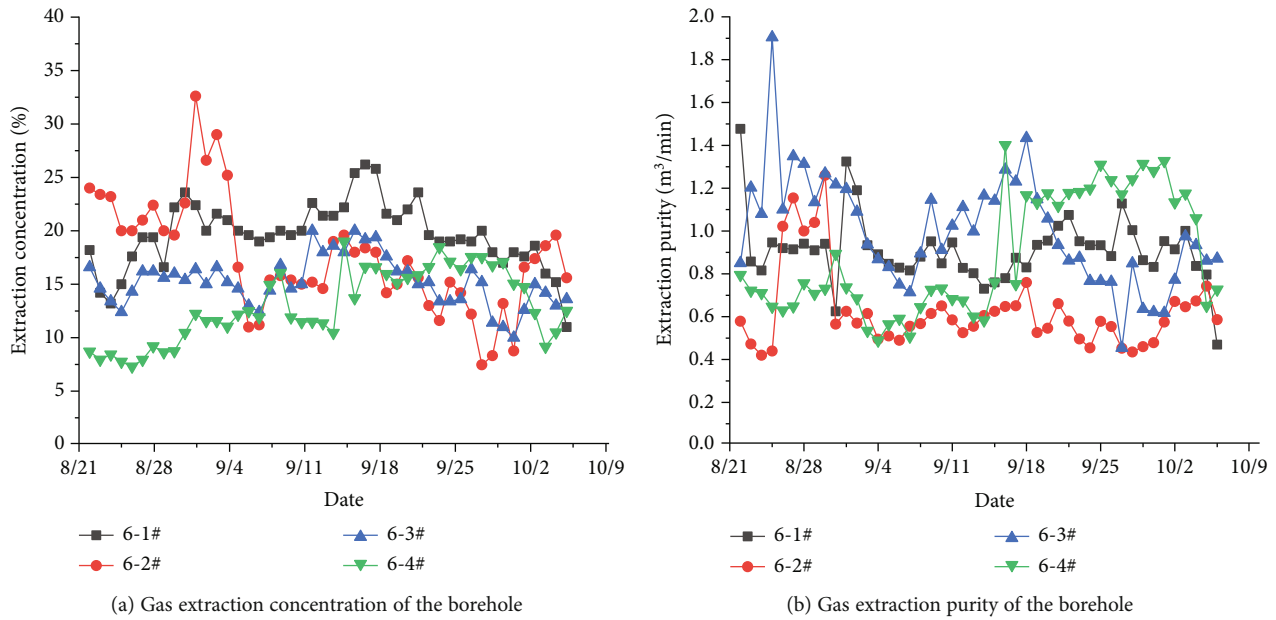


FIGURE 12: Extraction effect of the high-level directional long borehole.

during the stable mining period of the working face is shown in Figure 13. Gas concentration in the return airway corner was between 0.30 and 0.49%, whereas the gas concentration of return airflow was between 0.12% and 0.33%.

According to regulations in Shanxi province, China, when the coal mine return airway corner and the return airflow methane concentration are greater than or equal to 0.8%, the methane sensor will alarm. So the safety threshold of the return airway corner and return airflow gas concentration should be less than 0.8%. The gas concentrations of the return airway corner and the working face are all below the safety threshold when the working face is normally mined, and high-level directional long boreholes are used to extract pressure relief gas.

6. Discussion

The gas migration behavior in goaf can be analyzed by exploring the law of fracture evolution of overlying strata caused by mining. This study used physical similarity simulation to explore gas migration. The fracture area distribution

of the coal seam strike direction and inclined direction under the influence of mining was explored in this study. Physical test results were verified through an on-site drilling peep method.

The fracture area distribution of overlying strata was obtained using comparative on-site drilling peep and analogy simulation test results. The coal mining face was within 70 m of the return airway as a fracture area. After exceeding this area, it entered the compaction zone. The high fracture zone developed to about 100 m and entered the bending subsidence zone, and fissures were less developed.

Therefore, the distribution of the “three zones” of the overlying strata of the working face after mining was determined through comprehensive judgments. The h_2 which represents the final height of the caving zone was 28.2 m, and the h_3 which is the development height of the fracture zone was 113.6 m. In the strike direction, the β_2 of the caving angle in the inner part of the goaf after the coal seam was mined was 60° , and the β_1 of the caving angle in the location of the coal face was 52° . In the inclined direction, the a_1 of the caving angle on the side of the return airflow roadway was

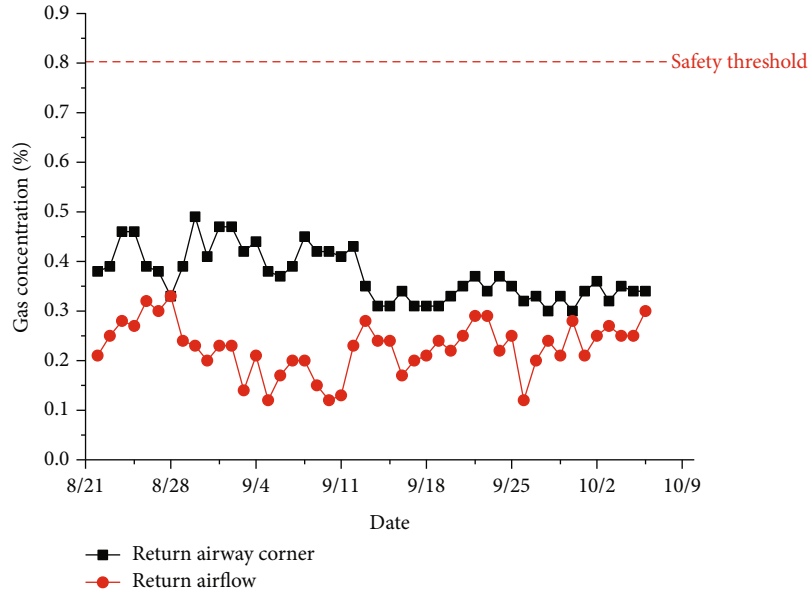


FIGURE 13: Return airway corner and return airflow gas concentration during mining.

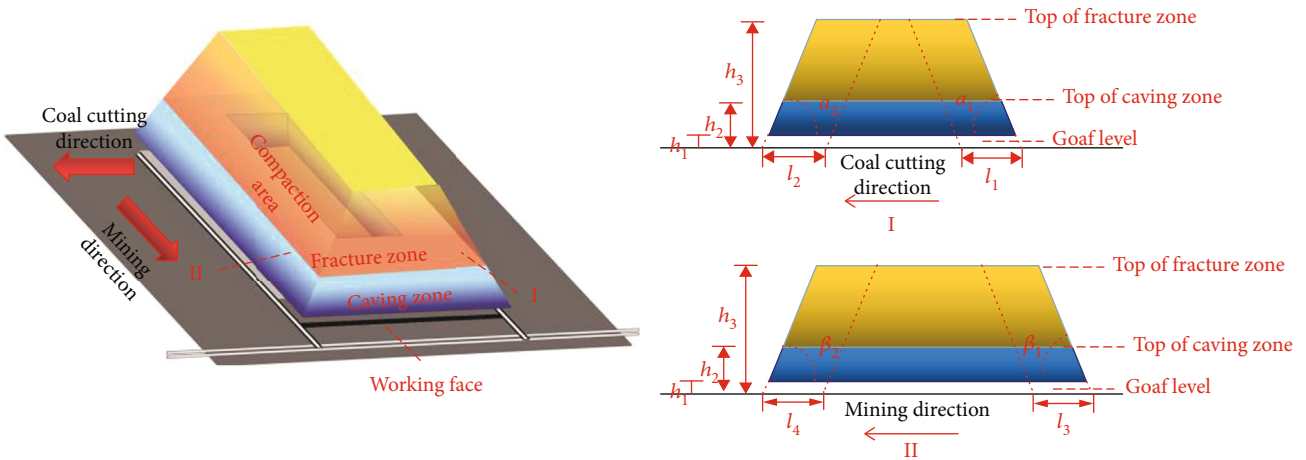


FIGURE 14: Distribution of the “three zones” of overlying strata under the influence of mining.

63°, and the a_2 of the caving angle on the side of the intake airflow roadway was 56°. Analysis of the development of fractures after mining showed a vertical fracture development area above the top of the goaf, which was interpenetrated from the delamination fracture and vertical fracture. This fracture was directly connected to the area of the caving zone to form an “O”-type circle fracture zone [36] (Figure 14). A large number of delamination fractures and a small amount of penetrating fractures were formed in an “O”-type circle. After mining, the pressure relief gas moves and accumulates in this area, thus becoming the enrichment area of the pressure relief gas.

The different laws of gas emission of the coal wall, coal mine, and goaf were used to establish the dynamic emission models of different gas sources in goaf. The gas migration model of the working face and the goaf was established based on the law of gas migration. The gas migration model between the working face and the goaf was also established,

which provides a basic algorithm to explore the law of the solid-gas coupling and gas migration in the fracture zone.

Further borehole peep results, gas emission models, and gas migration models based on physical analogy simulation test results were used to establish a numerical model of gas migration in goaf. The numerical model was used to test the gas migration in goaf. The gas migration law and distribution characteristics were obtained from quantitative analysis of the distribution of the gas enrichment area of overlying strata in goaf. The construction parameters of the high directional long borehole and the high-concentration gas area in the goaf overburden fracture zone were then used to control the gas in goaf. The gas emission in the mining period of the working face was effectively controlled, thus ensuring the safety production of the working face.

The aim of this systematic study was to explore the law of fracture evolution of overlying strata and the law of gas migration in goaf under fixed conditions. However, the law

of the distribution of fracture of overlying strata and the gas emission in goaf under multiple disturbance conditions should be explored further. For instance, the law of the distribution of fracture of overlying strata in mining under the conditions of changes in mining speed, coal and rock properties, and faults should be determined. In addition, studies on the high-level drilling and buried pipe extraction in goaf and the gas migration law in goaf under the dynamic changes of the wind flow in goaf should be explored further to ensure the efficiency of gas control at the working face.

7. Conclusion

- (1) A physical similarity experiment was used to simulate the distribution characteristics of the overlying strata fracture zone in goaf in the process of working face mining. Under the influence of mining, the fracture development of overlying strata in goaf is a "trapezoid platform structure," the maximum height of the caving zone is between 26 m and 28 m, and the maximum height of the fracture zone is about 110 m. Furthermore, the compaction area of goaf is located in the middle area of goaf, about 50 m away from the working face and approximately 22 m to 52 m away from the side of the return air roadway
- (2) The mathematical model of dynamic gas emission in different states such as the coal wall, coal mine, and goaf was established based on the different forms of gas sources in the working face. The model was then used to establish the gas migration model in goaf. Moreover, the model was used to study the law of gas migration in the fracture of overlying strata in goaf under the influence of mining. Quantitative analysis of the gas distribution law at the 45 m depth of the goaf was carried out. The distribution law of the highest point of gas concentration at different heights was determined
- (3) Reasonable high-location directional long borehole construction parameters were designed, and gas drainage in the goaf was carried out to ensure gas control in the fracture zone of the overlying strata in goaf. These processes can effectively solve the problem of high-concentration gas emission from the fracture zone of the overlying strata in goaf, thus effectively controlling the gas in the working face and the return airway corner. These processes ultimately improve mine gas control, thus ensuring safety production in mines

Data Availability

The data used to support the findings of this study are available from the corresponding author upon request.

Conflicts of Interest

The authors declare no conflicts of interest.

Acknowledgments

This research is financially supported by the National Natural Science Foundation of China (51874233, 51734007, and 51974241).

References

- [1] Z. Wen, E. Xing, S. Shi, and Y. Jiang, "Overlying strata structural modeling and support applicability analysis for large mining-height stopes," *Journal of Loss Prevention in the Process Industries*, vol. 57, pp. 94–100, 2019.
- [2] J. Ma, Q. Li, T. Kempka, and M. Kühn, "Hydromechanical response and impact of gas mixing behavior in subsurface CH₄ storage with CO₂-based cushion gas," *Energy & Fuels*, vol. 33, no. 7, pp. 6527–6541, 2019.
- [3] W. Kai and D. Feng, "Coal-gas compound dynamic disasters in China: a review," *Process Safety and Environmental Protection*, vol. 133, pp. 1–17, 2020.
- [4] Y. Z. Shang, P. F. Hei, S. B. Lu et al., "China's energy-water nexus: assessing water conservation synergies of the total coal consumption cap strategy until 2050," *Applied Energy*, vol. 210, pp. 643–660, 2018.
- [5] X. Y. Li, N. Zhang, Z. Z. Xie, D. X. Liang, and Y. M. Zhao, "Study on efficient utilization technology of coal pillar based on gob-side entry driving in a coal mine with great depth and high production," *Sustainability*, vol. 11, no. 6, 2019.
- [6] Z. Liu, H. Yang, W. Cheng, L. Xin, and G. Ni, "Stress distribution characteristic analysis and control of coal and gas outburst disaster in a pressure-relief boundary area in protective layer mining," *Arabian Journal of Geosciences*, vol. 10, no. 16, p. 358, 2017.
- [7] J. Brodny and M. Tutak, "Determination of the zone endangered by methane explosion in goaf with caving of longwalls ventilated on 'Y' system," *Management Systems in Production Engineering*, vol. 4, no. 24, pp. 247–251, 2016.
- [8] J. Brodny, M. Tutak, and A. John, "Analysis of influence of types of rocks forming the goaf with caving on the physical parameters of air stream flowing through these gob and adjacent headings," *Mechanika*, vol. 24, no. 1, pp. 43–49, 2017.
- [9] L. Qin, P. Wang, S. Li et al., "Gas adsorption capacity of coal frozen with liquid nitrogen and variations in the proportions of the organic functional groups on the coal after freezing," *Energy & Fuels*, vol. 35, no. 2, pp. 1404–1413, 2021.
- [10] J. Cheng, X. Zhang, and A. Ghosh, "Explosion risk assessment model for underground mine atmosphere," *Journal of Fire Sciences*, vol. 35, no. 1, pp. 21–35, 2017.
- [11] L. He, S. Yang, Q. Sun, T. Chen, and R. Huang, "Study on gas transportation principle and control in goaf with Y-shape ventilation system," *Journal of Safety Science and Technology*, vol. 7, no. 2, pp. 50–54, 2011.
- [12] F. Wang, T. Ren, S. Tu, F. Hungerford, and N. Aziz, "Implementation of underground longhole directional drilling technology for greenhouse gas mitigation in Chinese coal mines," *International Journal of Greenhouse Gas Control*, vol. 11, pp. 290–303, 2012.
- [13] F. Zhou, T. Xia, X. Wang, Y. Zhang, Y. Sun, and J. Liu, "Recent developments in coal mine methane extraction and utilization in China: a review," *Journal of Natural Gas Science and Engineering*, vol. 31, pp. 437–458, 2016.

- [14] Q. Qu, H. Guo, and M. Loney, "Analysis of longwall goaf gas drainage trials with surface directional boreholes," *International Journal of Coal Geology*, vol. 156, pp. 59–73, 2016.
- [15] F. An, Z. Wang, H. Yang et al., "Application of directional boreholes for gas drainage of adjacent seams," *International Journal of Rock Mechanics and Mining Sciences*, vol. 90, pp. 35–42, 2016.
- [16] D. Zhang, G. Fan, L. Ma, and X. Wang, "Aquifer protection during longwall mining of shallow coal seams: a case study in the Shendong Coalfield of China," *International Journal of Coal Geology*, vol. 86, no. 2-3, pp. 190–196, 2011.
- [17] V. Palchik, "Influence of physical characteristics of weak rock mass on height of caved zone over abandoned subsurface coal mines," *Environmental Geology*, vol. 42, no. 1, pp. 92–101, 2002.
- [18] V. Palchik, "Formation of fractured zones in overburden due to longwall mining," *Environmental Geology*, vol. 44, no. 1, pp. 28–38, 2003.
- [19] A. Majdi, F. P. Hassani, and M. Y. Nasiri, "Prediction of the height of destressed zone above the mined panel roof in longwall coal mining," *International Journal of Coal Geology*, vol. 98, no. 1, pp. 62–72, 2012.
- [20] H. Lin, S. Li, and L. Cheng, "Experimental analysis of dynamic evolution model of mining-induced fissure zone in overlying strata," *Journal of Mining & Safety Engineering*, vol. 28, no. 2, pp. 298–303, 2011.
- [21] J. Zhang and J. Wang, "Similar simulation and practical research on the mining overburden roof strata 'three-zone' height," *Journal of Mining & Safety Engineering*, vol. 31, no. 2, pp. 249–254, 2014.
- [22] F. Gao, D. Stead, and J. Coggan, "Evaluation of coal longwall caving characteristics using an innovative UDEC Trigon approach," *Computers and Geotechnics*, vol. 55, pp. 448–460, 2014.
- [23] W. Wu, J. Bai, X. Wang, S. Yan, and S. Wu, "Numerical study of failure mechanisms and control techniques for a gob-side yield pillar in the Sijiazhuang coal mine, China," *Rock Mechanics and Rock Engineering*, vol. 52, no. 4, pp. 1231–1245, 2019.
- [24] L. Yuan, "Scientific conception of precise coal mining," *Journal of China Coal Society*, vol. 42, no. 1, pp. 1–7, 2017.
- [25] N. N. Danesh, Z. Chen, S. M. Aminossadati, M. S. Kizil, Z. Pan, and L. D. Connell, "Impact of creep on the evolution of coal permeability and gas drainage performance," *Journal of Natural Gas Science & Engineering*, vol. 33, pp. 469–482, 2016.
- [26] J. Cao and W. Li, "Numerical simulation of gas migration into mining-induced fracture network in the goaf," *International Journal of Mining Science and Technology*, vol. 27, no. 4, pp. 681–685, 2017.
- [27] Y. Liu, S. Shao, X. Wang, L. Chang, G. Cui, and F. Zhou, "Gas flow analysis for the impact of gob gas ventholes on coalbed methane drainage from a longwall gob," *Journal of Natural Gas Science and Engineering*, vol. 36, pp. 1312–1325, 2016.
- [28] D. N. Whittles, I. S. Lowndes, S. W. Kingman, C. Yates, and S. Jobling, "Influence of geotechnical factors on gas flow experienced in a UK longwall coal mine panel," *International Journal of Rock Mechanics and Mining Sciences*, vol. 43, no. 3, pp. 369–387, 2006.
- [29] H. Guo, C. Todhunter, Q. Qu, and Z. Qin, "Longwall horizontal gas drainage through goaf pressure control," *International Journal of Coal Geology*, vol. 150-151, pp. 276–286, 2015.
- [30] C. Zhang, S. Tu, Q. Bai, G. Yang, and L. Zhang, "Evaluating pressure-relief mining performances based on surface gas venthole extraction data in longwall coal mines," *Journal of Natural Gas Science and Engineering*, vol. 24, pp. 431–440, 2015.
- [31] S. J. Schatzel, C. Ö. Karacan, H. Dougherty, and G. V. R. Goodman, "An analysis of reservoir conditions and responses in longwall panel overburden during mining and its effect on gob gas well performance," *Engineering Geology*, vol. 127, pp. 65–74, 2012.
- [32] Y. Kang, J. Wang, and F. Kong, "Bore hole survey method for overburden failure," *Coal Science and Technology*, vol. 30, no. 12, pp. 26–28, 2002.
- [33] W.-d. Wu, J.-b. Bai, X.-y. Wang, Z.-j. Zhu, and S. Yan, "Field investigation of fractures evolution in overlying strata caused by extraction of the Jurassic and Carboniferous coal seams and its application: case study," *Case Study, International Journal of Coal Geology*, vol. 208, pp. 12–23, 2019.
- [34] D. Li, C. Xu, and Z. Xiong, "Gas flowing model of mining face and solve it using COMSOL," *Journal of China Coal Society*, vol. 37, no. 6, pp. 967–971, 2012.
- [35] L. Zongxiang, S. Guangyi, and J. Wang, "Numerical simulation for non-homogeneous flow field and romantic movement law of gob," *Chinese Journal of Rock Mechanics and Engineering*, vol. 20, pp. 1578–1581, 2001.
- [36] M. Qian and J. Xu, "Overburden fracture distribution of the 'O' shape of circle features," *Journal of China Coal Society*, vol. 23, no. 5, pp. 466–469, 1998.

Research Article

Effects of Thermal Treatment on Mineral Composition and Pore Structure of Coal

Bin Liu ^{1,2}, Teng Teng ^{1,2}, Zhenhua Jiao ² and Shaobo Li²

¹Key Laboratory of Safety and High-Efficiency Coal Mining, Ministry of Education (Anhui University of Science and Technology), Huainan 232001, China

²State Key Laboratory of Mining Response and Disaster Prevention and Control in Deep Coal Mines, Anhui University of Science and Technology, Huainan 232001, China

Correspondence should be addressed to Bin Liu; bqt1700101012@student.cumtb.edu.cn and Teng Teng; t.teng@cumtb.edu.cn

Received 25 May 2021; Accepted 22 July 2021; Published 12 August 2021

Academic Editor: Wei Zhao

Copyright © 2021 Bin Liu et al. This is an open access article distributed under the Creative Commons Attribution License, which permits unrestricted use, distribution, and reproduction in any medium, provided the original work is properly cited.

With the increasing depth of coalbed methane (CBM) exploitation, temperature becomes the main factor affecting the efficiency of CBM exploitation. The change of temperature has significant influence on the mineral composition and pore structure of coal. To study the effects of thermal treatment on mineral composition and pore structure of coal, X-ray diffraction (XRD) test, scanning electron microscopy (SEM) test, and mercury intrusion test were carried out for three groups of coal. The mineral composition and pore structure of coal specimens after thermal treatment (25, 50, 75, and 100°C) were analyzed. The results show that the main mineral compositions of three groups of coal specimens after different temperatures are basically unchanged, and the maximum diffracted intensity after different temperature treatments decreases first and then increases with the increasing temperature. The count of fissures decreases first and then increases with temperature, and the count of pores increases first and then decreases with the increasing temperature. The velocity of mercury injection in high pressure (100~400 MPa) of coal specimens increases first and then decreases with temperature. The porosity, pore area, median pore diameter, and average pore diameter increase with the increasing temperatures. The volume of microfracture decreases, then increases, and finally decreases. The volume of macropore and mesopore increases slowly, and that of transition pore decreases slowly with the increasing temperature. Meanwhile, the volume of micropore increases first and then decreases during the process of thermal treatment. The fractal dimension of pore size ranges from 2.6 to 2.9 and increases linearly with the increasing temperature.

1. Introduction

With the depletion of shallow coal resources, more and more coal mines are entering the deep mining stages. The high ground stress, high temperature, and high water pressure restrict the safe and efficient mining of deep coal resources [1–3]. Coalbed methane (CBM) is a form of low-carbon clean energy, which is important for optimizing energy production and achieving carbon neutrality goals [4–6]. The temperature has significant influence on permeability and porosity of coal, which is important for the efficiency of CBM exploitation [7–9]. Therefore, it is urgent to study the evolution of mineral composition and microstructure of coal after different temperature treatments.

Previous studies have proved that rocks and rock-like materials have significant thermal effects, and the physical and mechanical properties change significantly after thermal treatment. The physical and mechanical properties of granite after temperature treatments have been a research hotspot for underground nuclear waste disposal, and many scholars have analyzed its physical and mechanical properties, such as fracture toughness [10], rockburst proneness [11], uniaxial compressive strength [12, 13], elastic modulus [13], longitudinal wave velocity [13], mechanical behavior [14, 15], tensile strength [12, 16, 17], acoustic emission characteristics [18, 19], mineral composition [20], pore structure [16, 20, 21], and permeability [22]. The physical and mechanical properties of sandstone after temperature treatments have also

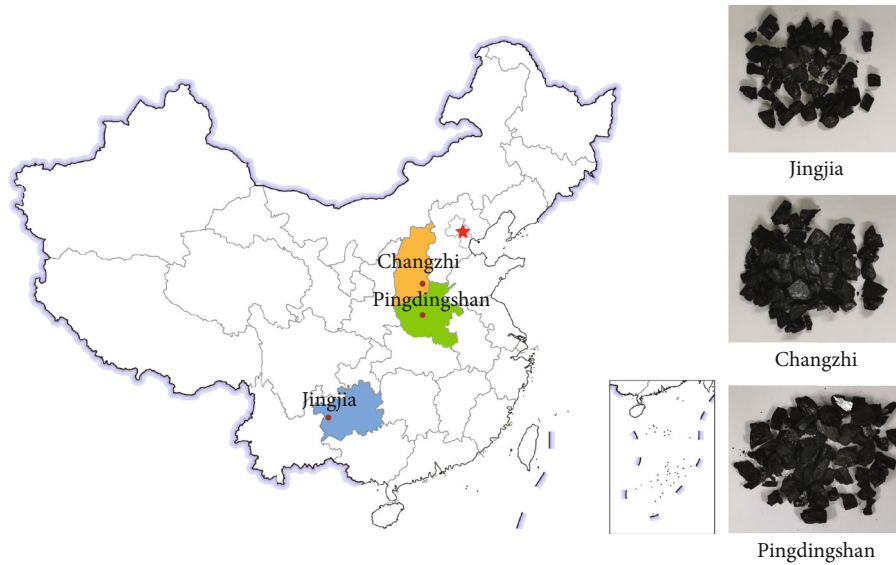


FIGURE 1: Location of the study areas and coal specimens.

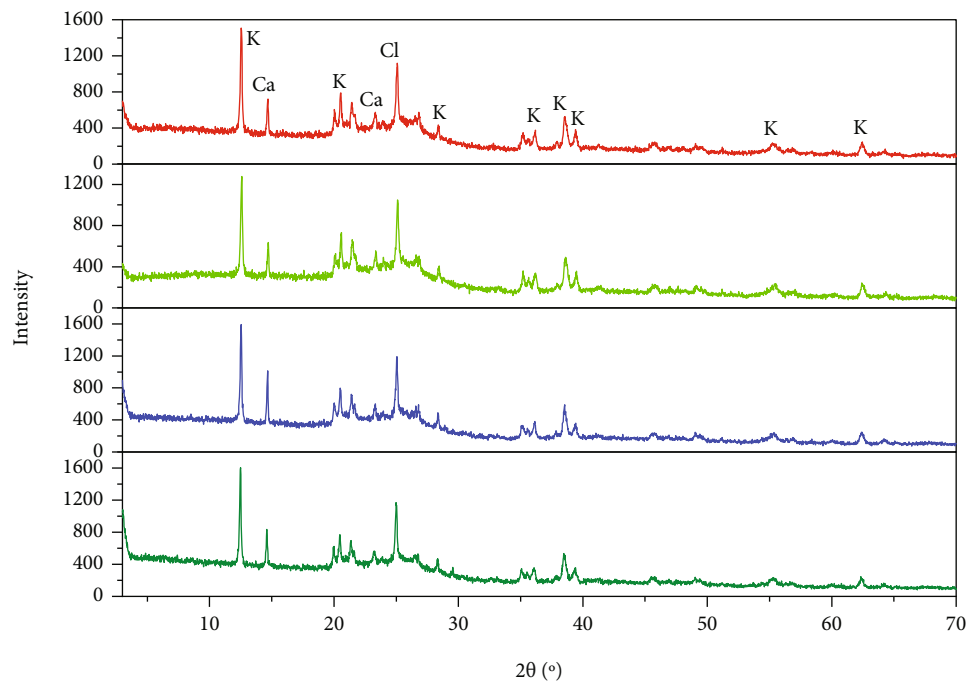
attracted a lot of attention; the properties such as thermal cracking process [23], peak strength [24], mechanical behavior in unloading conditions [25], wave velocity [26, 27], porosity [27], triaxial mechanical behavior [28], permeability behavior [28], microstructure [26], pore characteristics [29, 30], elastic modulus [29], tensile strength [31], energy evolution [32], microstructure deterioration [33], and morphological properties [34] have been investigated in depth. The physical property and tensile strength of shale have been also analyzed [35, 36]. Peng et al. and Rong et al. analyzed the physical and mechanical behaviors of thermal-damaged marble [37, 38]. The microstructure characteristic, mechanical behaviors, pore distribution, and AE characteristic of limestone have been investigated [39–41]. Yavuz et al. [42] investigated the changes of physical properties of five carbonate rocks (two marbles and three limestones) after different heating temperatures. The unconfined compressive strength and elastic moduli of gabbro after thermal loading have been studied by Keshavarz et al. [43]. Brotóns et al. [44] investigated the effect of thermal treatment on physical and mechanical properties of calcarenite. Ugur et al. [45] studied the changes in porosity features of natural stones after thermal treatment. The effect of thermal treatment on petrographic and mineralogical composition of coal mining wastes was analyzed by Nowak [46]. Tian et al. [47] investigated the changes of physical and mechanical behavior of claystone due to the thermal treatment, such as uniaxial compressive strength, triaxial compressive strength, and density. The grain size distribution and mineral composition of flux calcined porcelainites after thermal treatment have been studied by Saidi et al. [48]. Ersoy et al. [49] analyzed the mineralogical and geomechanical properties of volcanic rocks subjected to high temperatures. The effect of temperature on pore structure and mechanical properties of shotcrete was studied by Liu et al. [50]. Miao et al. investigated the evolution of coal pore-fracture during the thermal damage process [51]. The above studies mainly focus on physical and

mechanical properties of dense hard rocks (granite, sandstone, marble, shale, and gabbro). The main reason is that these dense rock strata are often at high temperatures when storing nuclear waste. Meanwhile, the high temperature in those studies generally exceeds 500°C. However, the geothermal temperature increases by 25~30°C with an increase of 1000 m in mining depth, and the geothermal temperature is generally below 100°C in deep coal mining. Therefore, the temperature of thermal treatment ranges from 25 to 100°C in this study.

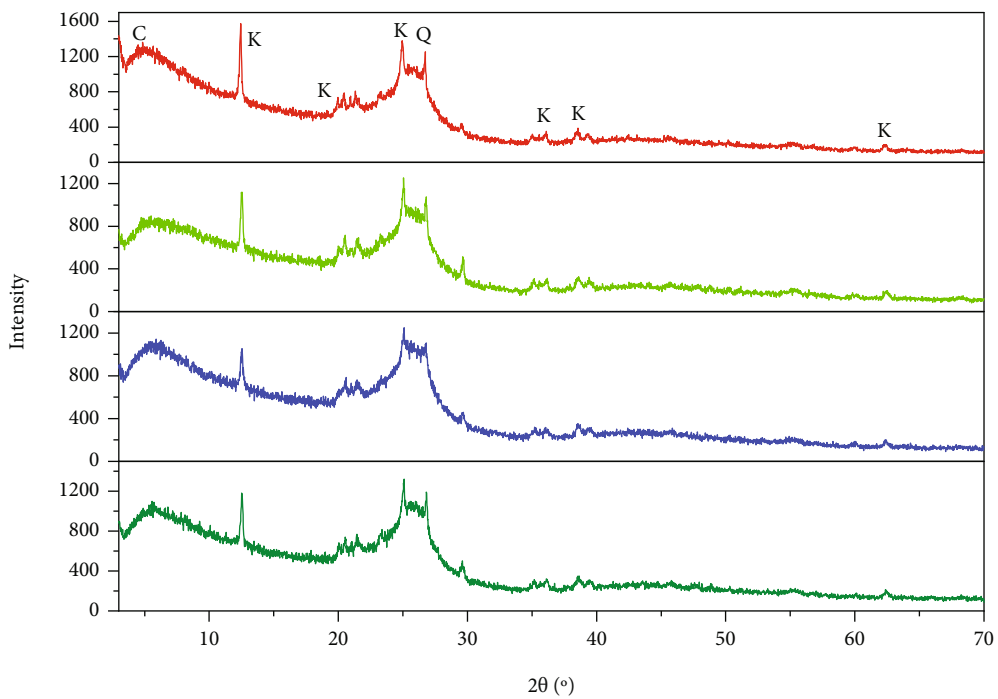
Coal, as an anisotropic medium, is highly sensitive to temperature. The structure and mechanical properties of coal will change significantly when the temperature changes, thus affecting the permeability and porosity of coal. To analyze the changes of physical and mechanical properties from a microscopic point of view, the X-ray diffraction (XRD) tests, mercury intrusion tests, and scanning electron microscopy (SEM) tests were carried out for three groups of coal after thermal treatment at different temperatures (25, 50, 75, and 100°C). The mineral composition and microstructure of coal specimens after thermal treatment were analyzed, and velocity of mercury injection, pore parameters, and distribution of pore size for three groups of coal were investigated based on the mercury intrusion tests. The result is significance for CBM exploitation and gas extraction.

2. Experimental Scheme

2.1. Specimen Preparation. As shown in Figure 1, the coal blocks were collected from Jingjia Coal Mine, Changzhi Coal Mine, and Pingdingshan Coal Mine, respectively. Jingjia Coal Mine is located in southwest of Guizhou Province, China. Changzhi Coal Mine is located in the southeast of Shanxi Province, China. Pingdingshan Coal Mine is located in the middle of Henan Province, China. The coal blocks were crushed into coal lumps with the dimension less than 30 mm in length, width, and height (Figure 1), and the coal



(a)



(b)

FIGURE 2: Continued.

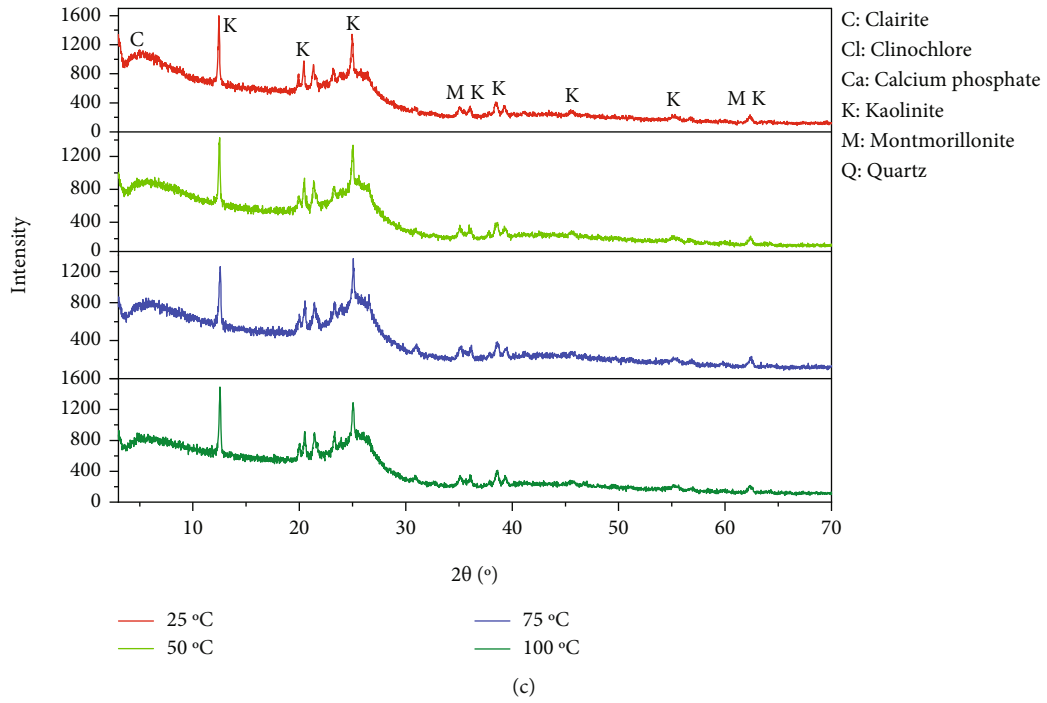


FIGURE 2: XRD patterns of three groups of coal specimens after different temperature treatments: (a) JJ coal specimen, (b) CZ coal specimen, and (c) PDS coal specimen.

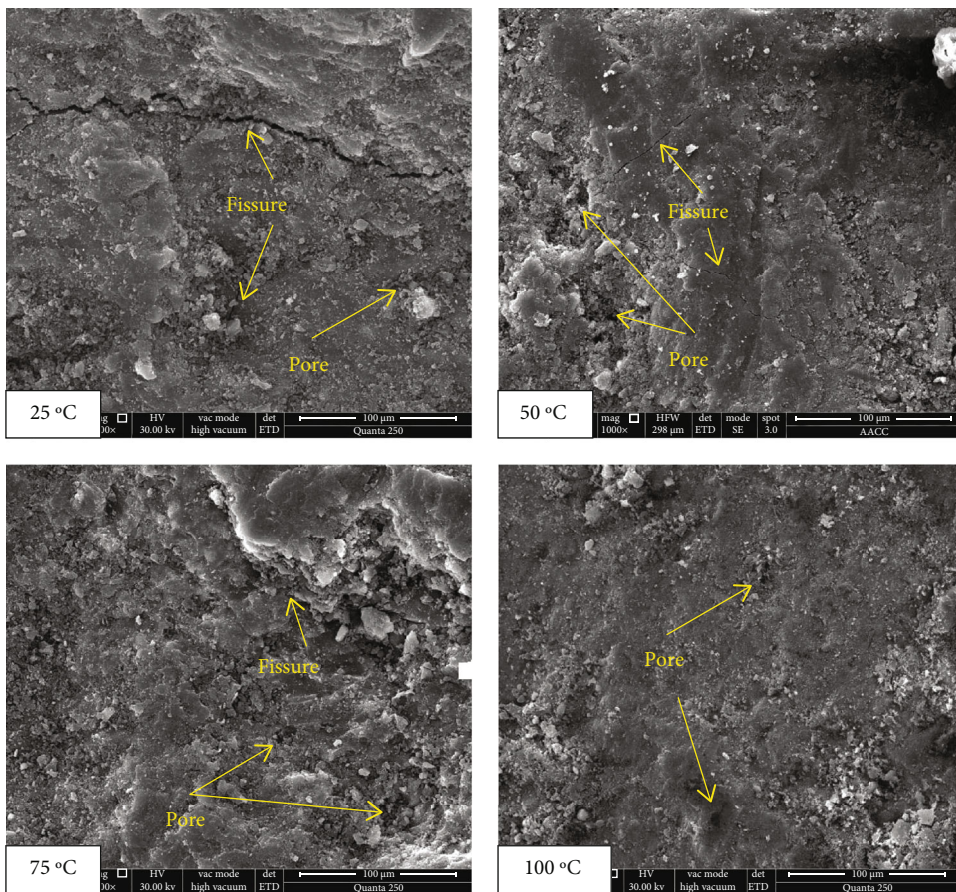


FIGURE 3: The SEM images of JJ coal specimens after different temperature treatments.

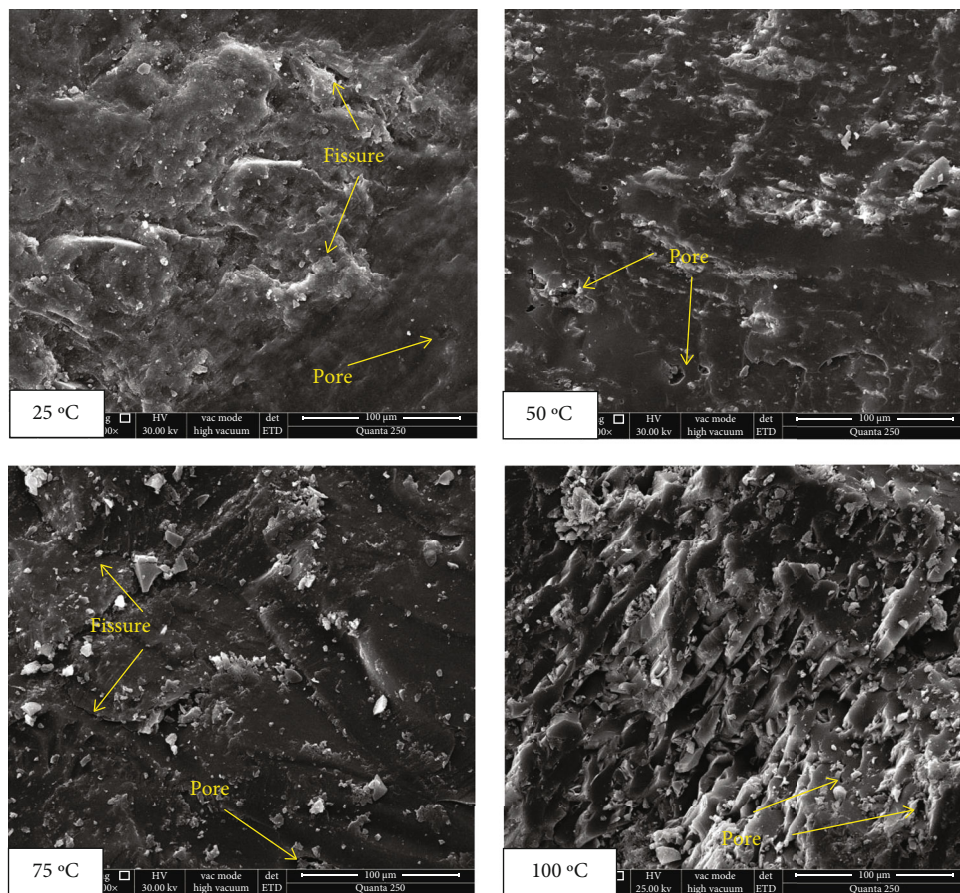


FIGURE 4: The SEM images of CZ coal specimens after different temperature treatments.

lumps with smooth surface were selected for the mercury intrusion tests and SEM tests after thermal treatment. The coal lumps were milled to coal powder for XRD tests after thermal treatment. The coal specimens from Jingjia Coal Mine, Changzhi Coal Mine, and Pingdingshan Coal Mine were marked as JJ, CZ, and PDS, respectively.

2.2. Experimental Equipment and Process. Before the test, the three groups of coal lumps were heated to target temperature (25, 50, 75, and 100°C) in the drying oven and kept at a target temperature for 24 hours, and then, the coal lumps were sealed and cooled naturally to room temperature. The coal lumps after thermal treatments were prepared for the XRD, SEM, and mercury intrusion tests to analyze the variation of mineral composition, microstructure, and pore structure.

The XRD test was performed on D8 ADVANCE X-ray Diffractometer (BRUKER Corporation, Germany). The radius of goniometer is 250 mm, divergence slit is 0.6 mm, and antiscatter slit is 8 mm. The coal powder was milled and sieved to pass through a 325 mesh sieve, and the mass of each group of coal powder was not less than 0.5 g. The coal powder was poured into the center of a clean sample tray and then capped with a clean glass sheet to flatten the surface of the coal powder. Then, the mineral composition can be measured. The next coal powder is measured after the coal powder measurement completed.

The mercury intrusion test was conducted on Autopore IV 9510 Automatic Mercury Porosimeter. The working pressure ranges from 0 to 60000 psi (414 MPa), and the measurement range of pore size is 0.003~1000 μm . According to the previous research [52], the contact angle was set to 130°, and the mercury (Hg) surface tension was set to 0.485 N/m. The mercury intrusion tests were carried out on three groups of coal specimens, and the related parameters such as pore size distribution, total pore volume, and total pore area can be obtained after the test.

The specimens were scanned by Quanta 250™ SEM scanner (FEI, USA). The electron beam voltage ranges from 200 V to 30 kV, and the range of magnification is 6~1000000. Before the test, the sample is first placed in the sample bin and then vacuumed. The region of interest (ROI) was magnified by 400, 1000, 3000, 10000, and 20000 times, respectively, and the SEM images were stored simultaneously.

3. Results and Discussions

3.1. Mineral Composition after Thermal Treatment. XRD tests are commonly used to investigate the mineral composition of coal and rock materials [20, 39, 46, 53, 54]. Therefore, XRD tests were carried out on coal powder after different temperature treatments (25, 50, 75, and 100°C). As shown in Figure 2, the main mineral composition of three groups of coal

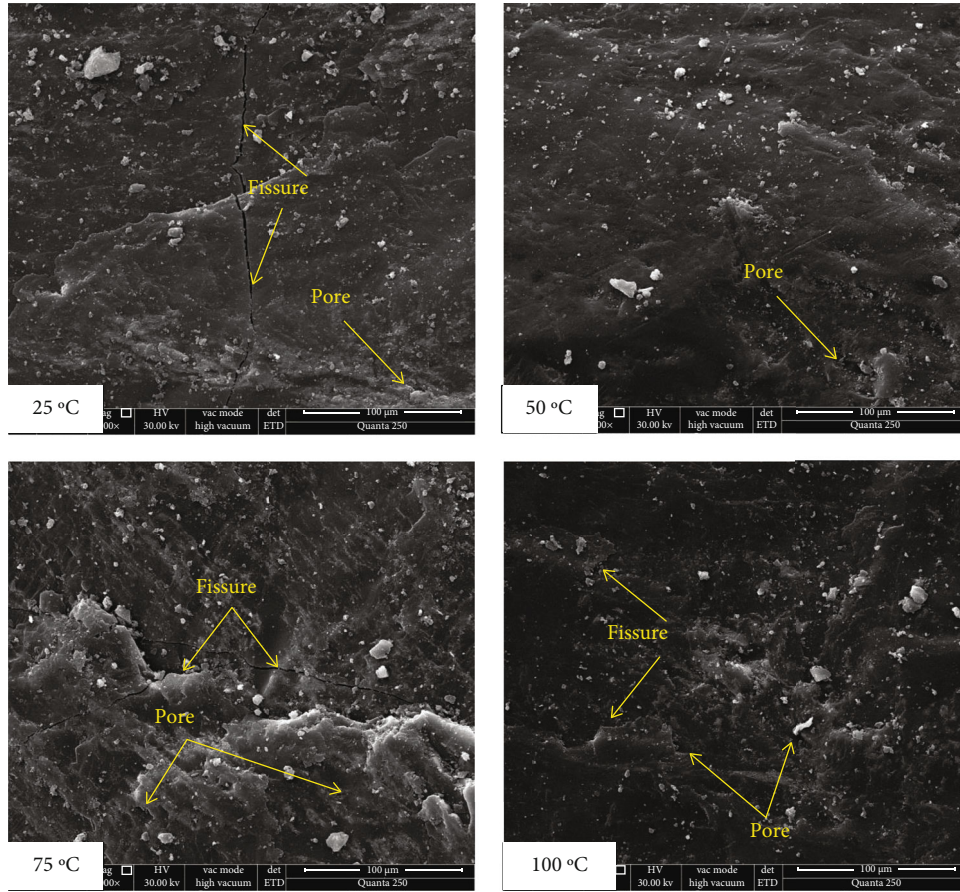


FIGURE 5: The SEM images of PDS coal specimens after different temperature treatments.

specimens is basically unchanged; namely, no chemical changes occur after the thermal treatment. The result is consistent with that of granite [20]. As shown in Figure 2(a), the main mineral compositions of JJ coal specimens are kaolinite, calcium phosphate, and clinocllore. The maximum diffracted intensity is 1506 at 25°C, decreases at 50°C, and then increases to the peak of 1605 at 100°C. As shown in Figure 2(b), the mineral compositions are kaolinite, quartz, and clairite for CZ coal specimens. The maximum diffraction intensity is 1575 at 25°C, decreases to 1250 at 75°C, and then increases to 1323 at 100°C. As shown in Figure 2(c), the mineral compositions of PDS coal specimens are kaolinite, clairite, and montmorillonite. The maximum diffraction intensity is 1601 at 25°C, decreases to 1264 at 75°C, and then increases to 1492 at 100°C. Thus, the maximum diffracted intensity of three groups of coal specimens after different temperature treatments decreases first and then increases with the increasing temperature. The phenomena are mainly caused by thermal treatment and the anisotropy of coal specimens. In summary, there is no change in the main mineral compositions, and the maximum diffracted intensity changes a little after heat treatment. The maximum diffracted intensity after different temperature treatments decreases first and then increases with the increasing temperature.

3.2. Microstructure after Thermal Treatment. SEM tests are commonly used to investigate the microstructure of cross-

sections of coal and rock materials [26, 33, 34, 39, 41, 51, 55]. Therefore, SEM tests were carried out on coal samples after different temperature treatments (25, 50, 75, and 100°C). The regions of interest (ROI) of coal specimens were magnified by 400, 1000, 3000, 10000, and 20000 times, respectively. The SEM images of three groups of coal specimens after different temperature treatments are shown in Figures 3–5, which were magnified by 1000 times. As shown in Figure 3, the fissure width is large at the temperature of 25°C, and there are no obvious fissures at the temperature of 100°C. Thus, the fissure width decreases with the increasing temperature. Meanwhile, there are a few pores generated after thermal treatment. Similarly, it can be seen from Figure 4 that the pores grow with the rise of temperature of thermal treatment, and the fissure width decreases with the increasing temperature. As shown in Figure 5, the fissure width decreases first and then increases with the rise of temperature of thermal treatment, and there are many pores generated after thermal treatment. Thus, thermal treatment has a significant effect on microstructure of coal specimens, which is related to the permeability. In summary, the count of fissures decreases first and then increases with the increasing temperature, which is mainly caused by thermal expansion and thermal cracking of coal matrix. Meanwhile, the count of pores increases first and then decreases with the increasing temperature of thermal treatment, which is mainly due to the thermal shrinkage and thermal expansion of coal matrix.

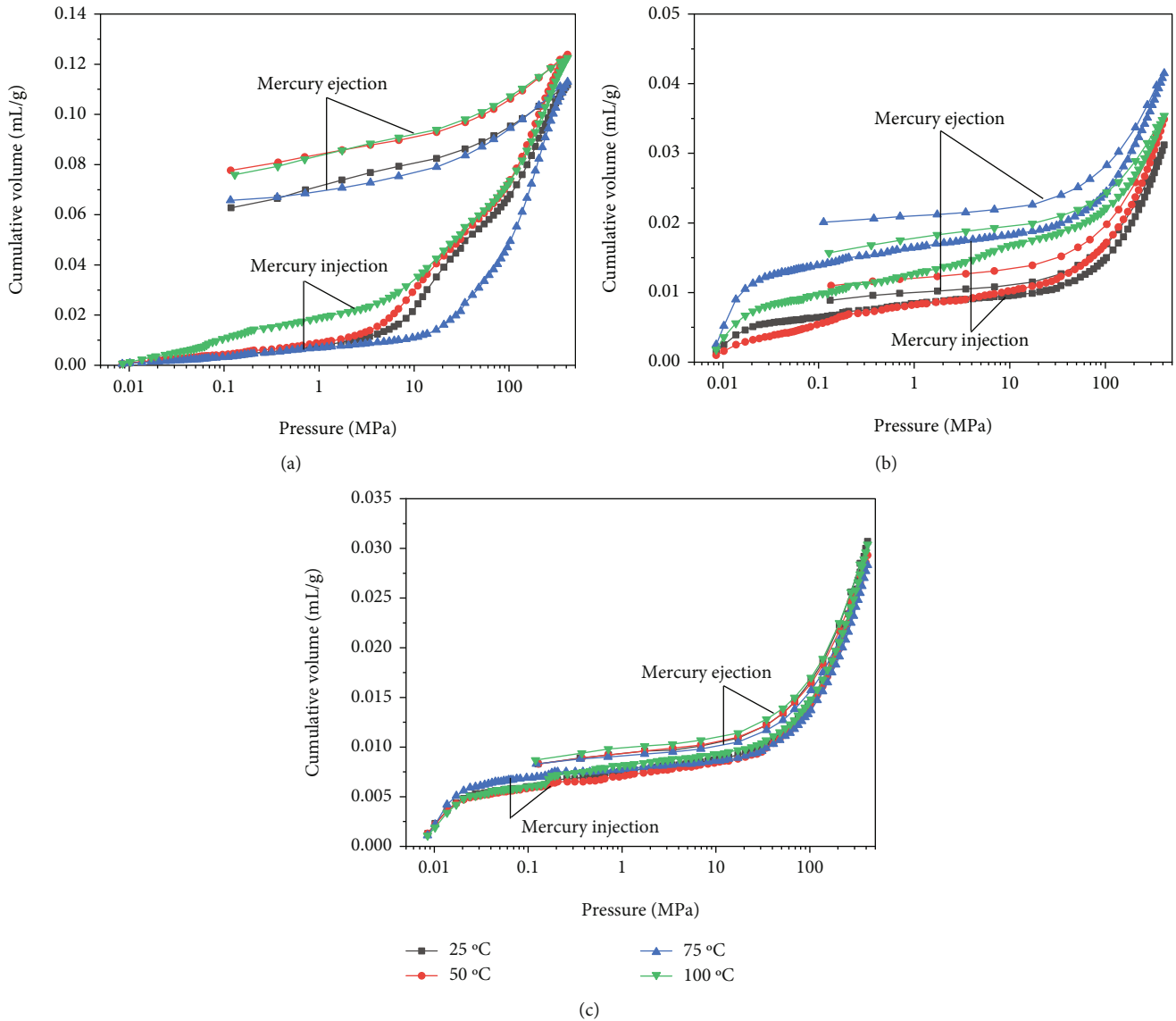


FIGURE 6: Curves of mercury injection and ejection in three groups of coal specimens after different temperature treatments: (a) JJ coal specimen, (b) CZ coal specimen, and (c) PDS coal specimen.

3.3. *Pore and Fissure Distribution.* Mercury intrusion tests are commonly used to investigate the pore and fissure characteristics of coal and rock [20, 50, 51, 56–58]. To obtain the pore and fissure characteristics of coal specimens after thermal treatment, mercury intrusion tests were carried out on coal samples after different temperature treatment (25, 50, 75, and 100 °C). As shown in Figure 6, the mercury injection curve is S-shape, which can be divided into three stages, namely, initial injection stage, slow injection stage, and rapid injection stage. The cumulative pore volume increases fast at the initial injection stage, increases slowly during the slow injection stage, and increases rapidly at the rapid injection stage. There are significant differences in cumulative pore volume for different coal specimens. The cumulative pore volume is 0.03 mL/g in PDS coal specimen, and the cumulative pore volume is 0.12 mL/g in JJ coal specimen, which is 4 times higher than that in PDS coal specimen. The main rea-

son is the differences in microstructure of coal specimens. Similarly, there also exist some differences in mercury injection curve of coal specimens after different temperature treatment. The cumulative pore volume increases first and then decreases with the increasing temperature for CZ coal specimen. For JJ coal specimen, the cumulative pore volume increases first, then decreases, and finally increases with the increasing temperature. The cumulative pore volume decreases first and then increases with the increasing temperature for PDS coal specimen. These phenomena indicate that the mineral composition and pore distribution have a significant effect on the mercury injection curve.

To analyze the velocity of mercury injection of coal specimens after different temperatures, the velocity in high pressure (100~400 MPa) is calculated using the least squares method. As shown in Figure 7, the fitted curves fit well for those data. The velocity of coal specimens after different

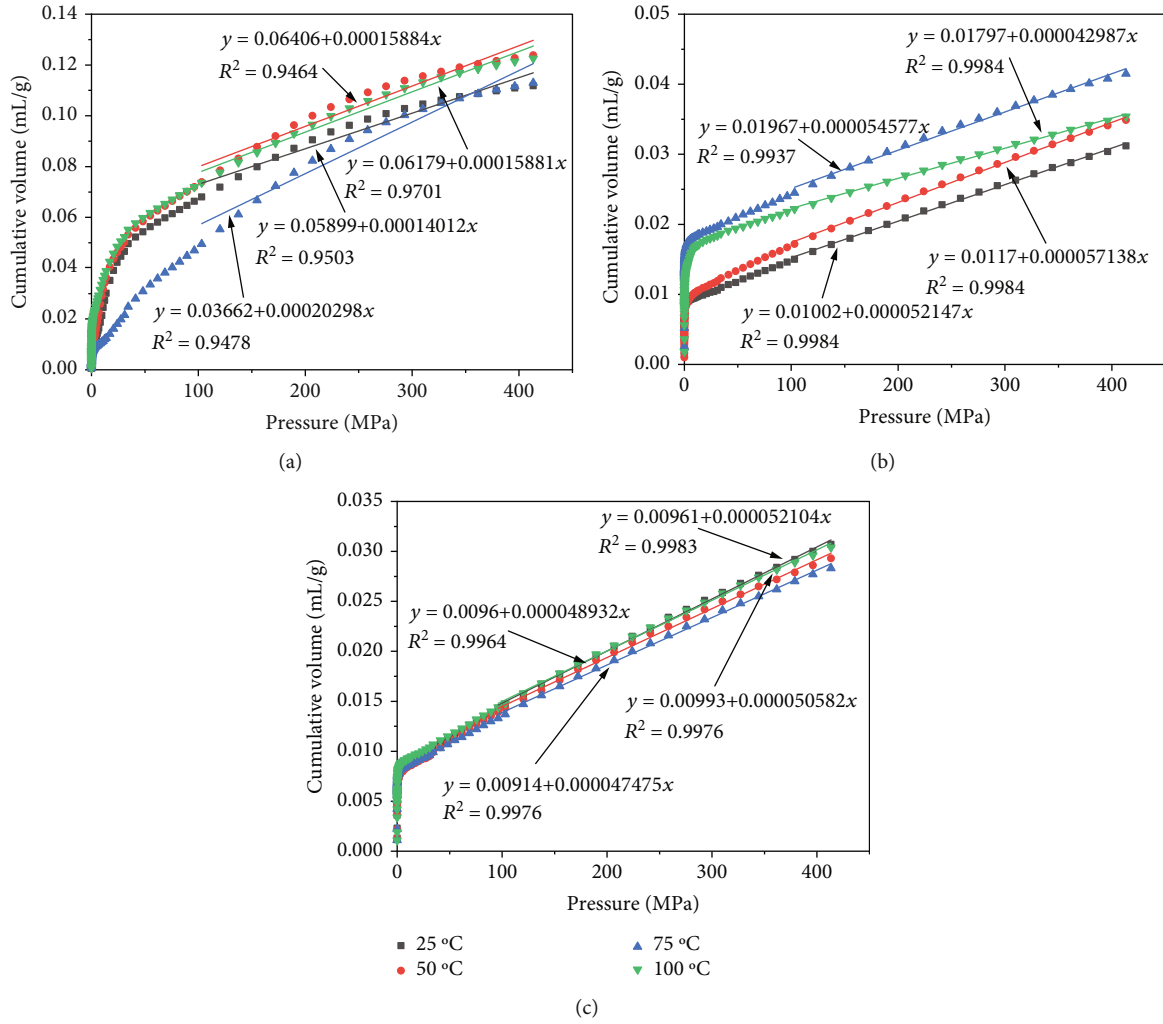


FIGURE 7: Relationship between cumulative volume and pressure in three groups of coal specimens after different temperature treatments: (a) JJ coal specimen, (b) CZ coal specimen, and (c) PDS coal specimen.

temperature treatment is shown in Figure 8. The velocity of JJ coal specimen is higher than 1.4×10^{-4} mL/(g·MPa), and that of CZ and PDS coal samples ranges from 4×10^{-5} to 6×10^{-5} mL/(g·MPa), which is mainly caused by the differences in microstructure of coal specimens. Meanwhile, the velocity of JJ and CZ coal specimen increases first and then decreases with the increasing temperature. However, the velocity of PDS coal specimen decreases first and then increases with the rise of temperature. These phenomena are mainly caused by the mineral composition and pore structure.

The pore distribution of coal specimens can be measured by the mercury intrusion tests, and the relationship between the pore size and the applied pressure can be expressed as follows [52]:

$$p(r) = -\frac{2\gamma \cos \theta}{r}, \quad (1)$$

where $p(r)$ is the applied pressure, r is the radius of pore, θ is the contact angle (130°), and γ is the Hg surface tension (0.485 N/m).

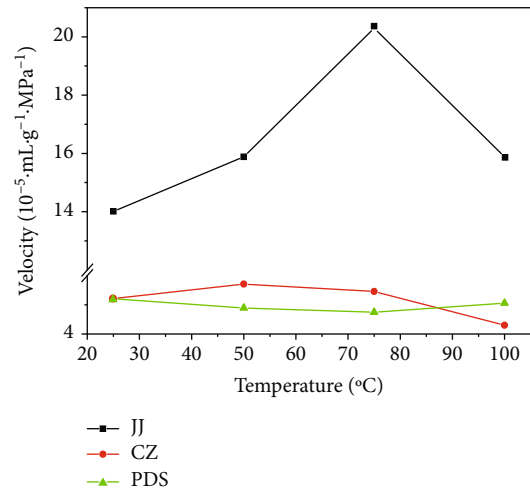


FIGURE 8: Relationship between velocity and temperatures in three groups of coal specimens after different temperature treatments.

TABLE 1: Pore parameters of the three groups of coal specimens after different temperature treatments.

Specimen source	Temperature (°C)	Porosity (%)	Pore area (m ² /g)	Median pore diameter (nm)	Bulk density (g/mL)	Average pore diameter (nm)
Jingjia Coal Mine	25	12.52	36.57	23.4	1.12	12.2
	50	13.70	41.05	21.0	1.11	12.1
	75	12.45	50.61	10.1	1.10	8.9
	100	13.92	41.11	23.5	1.14	11.9
Changzhi Coal Mine	25	3.98	14.06	11.0	1.27	8.9
	50	4.35	15.51	11.6	1.24	9.0
	75	5.34	14.36	27.4	1.29	11.6
	100	4.71	11.59	63.7	1.33	12.2
Pingdingshan Coal Mine	25	3.80	13.98	10.9	1.24	8.8
	50	3.63	13.00	11.4	1.24	9.0
	75	3.61	12.63	11.2	1.27	9.0
	100	3.79	13.45	11.4	1.25	9.0

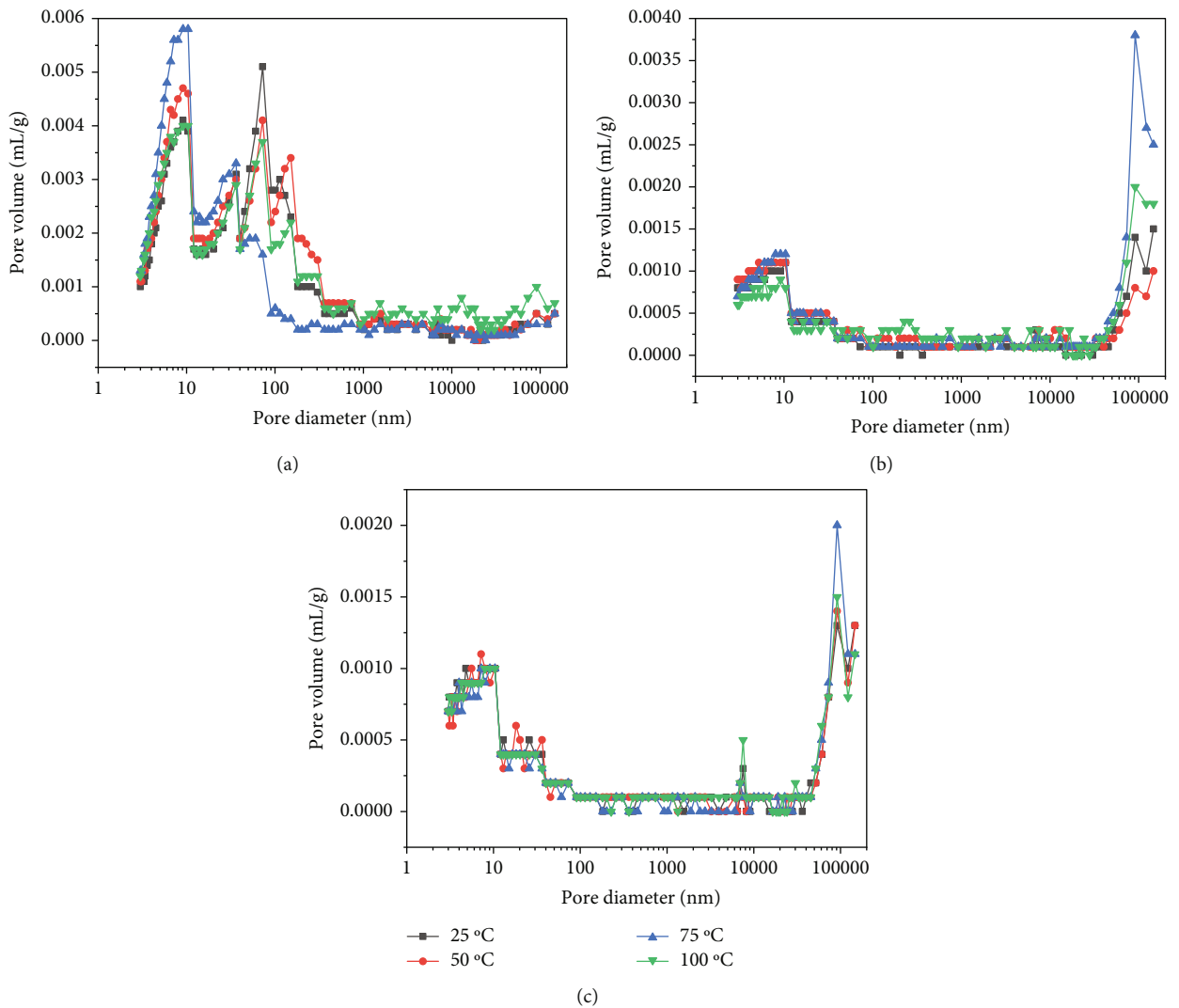


FIGURE 9: Relationship between pore volume and pore diameter in three groups of coal specimens after different temperature treatments: (a) JJ coal specimen, (b) CZ coal specimen, and (c) PDS coal specimen.

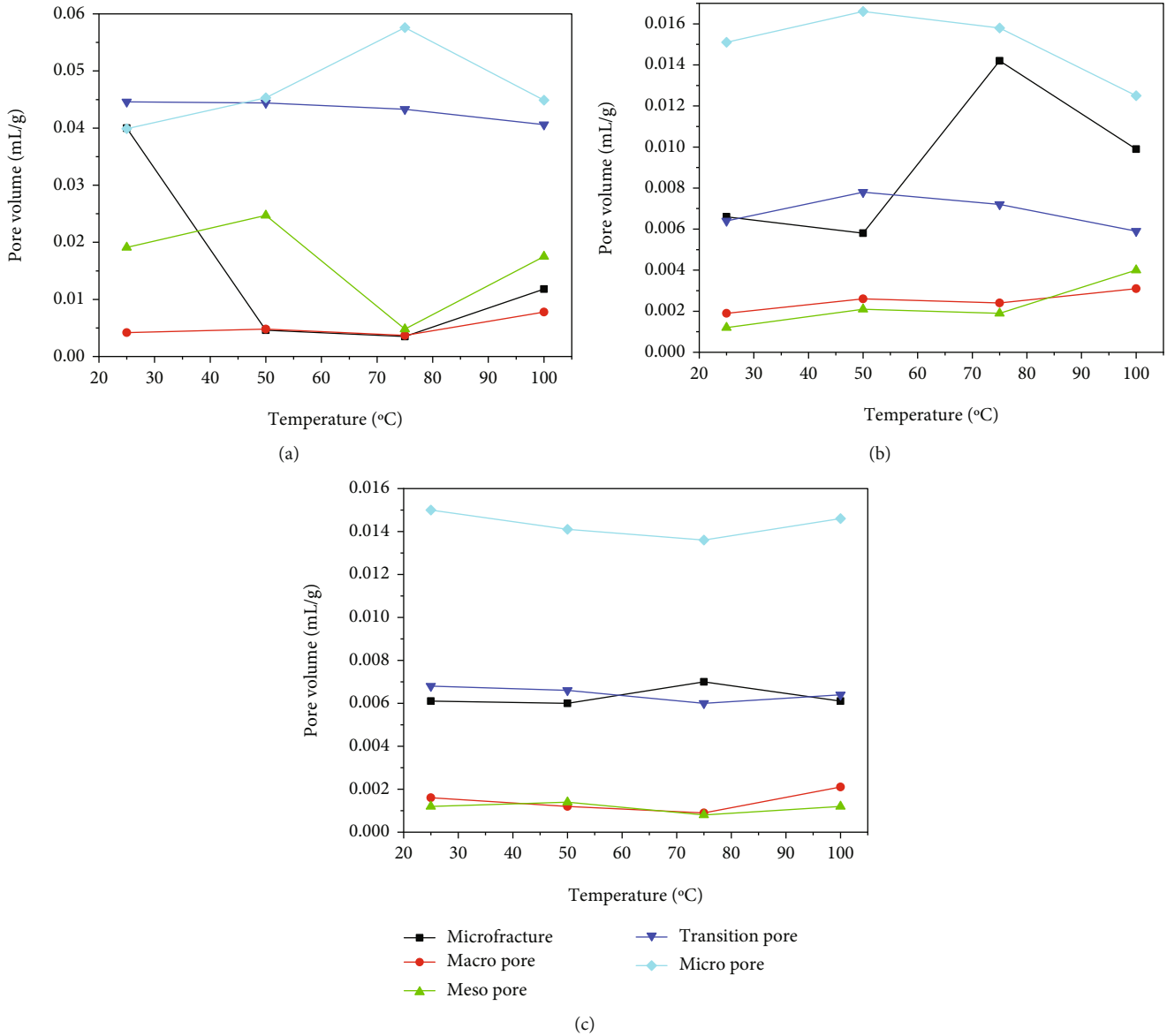


FIGURE 10: Variation of volume for five types of pores with the increasing temperatures: (a) JJ coal specimen, (b) CZ coal specimen, and (c) PDS coal specimen.

The pore parameters of the three groups of coal specimens after different temperature treatments are listed in Table 1. The porosity, pore area, median pore diameter, and average pore diameter for JJ coal specimens are higher than those for CZ and PDS coal specimens. However, the bulk density of JJ coal specimens is lower than that of CZ and PDS coal specimens. In general, the porosity, pore area, median pore diameter, and average pore diameter increase with the increasing temperatures. However, there are some exceptions. These phenomena are mainly caused by the mineral composition and pore structure.

Figure 9 shows the relationship between pore volume and pore diameter in three groups of coal specimens after different temperature treatments, and the pore diameter ranges from 3 nm to 150 μm . Previous studies show that the pore can be classified as microfracture (10~150 μm),

macropore (1~10 μm), mesopore (0.1~1 μm), transition pore (10~100 nm), and micropore (3~10 nm) [52]. As shown in Figure 9, the pore volume of micropore and microfracture increases first and then decreases with the increasing temperature of thermal treatment, and the pore volume of macropore, mesopore, and transition pore changes a little with the increasing temperature. Those phenomena indicate that the micropore and microfracture are strongly influenced by the temperature. However, there exist significant differences among these three coal specimens. The pore diameter of JJ coal specimen is mainly concentrated on 3~100 nm, which mainly consisted of micropores and transition pores. On the contrary, the pore diameter is concentrated on 50~150 μm (microfracture) for CZ and PDS coal specimens.

To quantitatively analyze the pore distribution characteristics after different temperature treatments, the pore volume

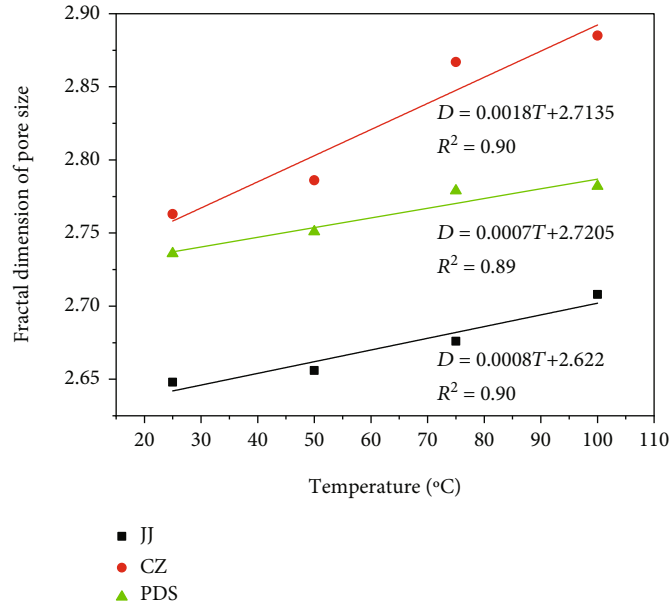


FIGURE 11: Relationship between fractal dimensions of pore size with different temperatures in three groups of coal specimens.

with different diameters after the thermal treatments is calculated. As shown in Figure 10, the volume of microfracture decreases at 50°C, which is mainly caused by thermal expansion of coal matrix; it increases at 75°C due to thermal shrinkage of coal matrix; it decreases at 100°C due to thermal expansion. The volume of macropore and mesopore increases slowly, and that of transition pore decreases slowly with the increasing temperature. Meanwhile, the volume of micropore increases first and then decreases after the thermal treatment. These phenomena indicate that the micropore and microfracture are strongly influenced by the temperature. However, there are some exceptions due to the differences in mineral composition and pore structure.

Previous studies have demonstrated that the pore size distribution of coal and rock conforms to fractal characteristics [51, 59, 60]. Therefore, the effect of temperature on the pore structure of coal after different temperature treatments can be quantitatively analyzed based on fractal theory. According to the methods mentioned in previous studies [51, 59, 60],

$$\lg \frac{dV}{dP} = k \lg P + b, \quad (2)$$

where V is the pore volume, P is the applied pressure, k is the linear slope, and b is the constant.

And the fractal dimension (D) of pore size can be obtained:

$$D = k + 4. \quad (3)$$

As shown in Figure 11, the fractal dimension ranges from 2.6 to 2.9 and increases with the increasing temperature, which indicates that the pore surfaces is less and less smooth as the temperature rises. To analyze the evolution of fractal

dimension with temperature quantitatively, the least squares method was used to fit the above data. As shown in Figure 11, the fractal dimension is nearly linearly related to the temperature. These phenomena indicate the pore surfaces of coal become rougher as the temperature rises.

In summary, thermal treatment has significant effects on mineral composition, microstructure, and pore structure of coal. The main mineral compositions after thermal treatment are basically unchanged, and the maximum diffracted intensity decreases first and then increases with the increasing temperature. The count of fissures decreases first and then increases, and the count of pores increases first and then decreases with the increasing temperature. The porosity, pore area, median pore diameter, and average pore diameter increases with the increasing temperatures. The fractal dimension of pore size ranges from 2.6 to 2.9 and increases linearly with the increasing temperature. The pore structure varies with mineral composition and microstructure due to the thermal shrinkage and thermal expansion of coal matrix. Meanwhile, the macroscopic mechanical properties are related to mineral composition, microstructure, and pore structure.

4. Conclusions

The X-ray Diffraction (XRD) test, scanning electron microscopy (SEM) test, and mercury intrusion test were carried out for three groups of coal, and the mineral composition and pore structure of coal specimens after thermal treatment (25, 50, 75, and 100°C) were analyzed. The main conclusions are as follows:

- (1) The main mineral compositions of three groups of coal specimens after thermal treatment are basically unchanged, and the maximum diffracted intensity

changes a little after heat treatment. The maximum diffracted intensity after different temperature treatments decreases first and then increases with the increasing temperature

- (2) The count of fissures decreases first and then increases with the increasing temperature, and the count of pores increases first and then decreases with the increasing temperature. Thermal treatment has a significant effect on microstructure of coal specimens
- (3) The velocity of mercury injection in high pressure (100–400 MPa) of JJ and CZ coal specimens increases first and then decreases with the increasing temperature, but that of PDS coal specimen decreases first and then increases with the increasing temperature. The porosity, pore area, median pore diameter, and average pore diameter increase with the increasing temperatures
- (4) The volume of microfracture decreases, then increases, and finally decreases. The volume of macropore and mesopore increases slowly, and that of transition pore decreases slowly with the increasing temperature. Meanwhile, the volume of micro-pore increases first and then decreases during the process of thermal treatment. The fractal dimension of pore size ranges from 2.6 to 2.9 and increases with the increasing temperature. The fractal dimension is nearly linearly related to the temperature

Data Availability

The experimental data used to support the findings of this study are included within the article.

Conflicts of Interest

The authors declare no conflict of interest.

Acknowledgments

This work was supported by the Open Fund of the Key Laboratory of Safety and High-efficiency Coal Mining (JYBSYS2019101), the State Key Laboratory of Mining Response and Disaster Prevention and Control in Deep Coal Mines (SKLMRDPC19KF06 and SKLMRDPC20KF04), and the Natural Science Foundation of Anhui Province (1908085QE184).

References






- [1] H. Xie, M. Gao, R. Zhang, G. Peng, W. Wang, and A. Li, “Study on the mechanical properties and mechanical response of coal mining at 1000 m or deeper,” *Rock Mechanics and Rock Engineering*, vol. 52, pp. 1475–1490, 2019.
- [2] M. C. He, H. P. Xie, S. P. Peng, and Y. D. Jiang, “Study on rock mechanics in deep mining engineering,” *Chinese Journal of rock mechanics and engineering*, vol. 24, pp. 2803–2813, 2005.
- [3] Z. Zhang, H. Xie, R. Zhang et al., “Deformation damage and energy evolution characteristics of coal at different depths,” *Rock Mechanics and Rock Engineering*, vol. 52, no. 5, pp. 1491–1503, 2019.
- [4] F. Du, K. Wang, X. Zhang, C. Xin, L. Shu, and G. Wang, “Experimental study of coal–gas outburst: insights from coal–rock structure, gas pressure and adsorptivity,” *Natural Resources Research*, vol. 29, pp. 2481–2493, 2020.
- [5] H. Wang, X. Yang, F. Du et al., “Calculation of the diffusion coefficient of gas diffusion in coal: the comparison of numerical model and traditional analytical model,” *Journal of Petroleum Science and Engineering*, vol. 205, p. 108931, 2021.
- [6] W. Zhao, K. Wang, R. Zhang, H. Dong, Z. Lou, and F. An, “Influence of combination forms of intact sub-layer and tectonically deformed sub-layer of coal on the gas drainage performance of boreholes: a numerical study,” *International Journal of Coal Science & Technology*, vol. 7, pp. 571–580, 2020.
- [7] W. C. Zhu, C. H. Wei, J. Liu, H. Y. Qu, and D. Elsworth, “A model of coal-gas interaction under variable temperatures,” *International Journal of Coal Geology*, vol. 86, no. 2-3, pp. 213–221, 2011.
- [8] C. R. Clarkson and J. M. McGovern, “Optimization of CBM Reservoir exploration and development strategies through integration of simulation and economics,” *SPE Reservoir Evaluation and Engineering*, vol. 8, no. 6, pp. 502–519, 2005.
- [9] M. E. Hossain, S. H. Mousavizadegan, and M. R. Islam, “The effects of thermal alterations on formation permeability and porosity,” *Petroleum Science and Technology*, vol. 26, pp. 1282–1302, 2008.
- [10] M. H. B. Nasser, B. S. A. Tatone, G. Grasselli, and R. P. Young, “Fracture toughness and fracture roughness interrelationship in thermally treated westerly granite,” in *Rock Physics and Natural Hazards*, pp. 801–822, Birkhäuser Basel, 2009.
- [11] Z. Zhang, F. Gao, and Z. Liu, “Research on rockburst proneness and its microcosmic mechanism of granite considering temperature effect,” *Chinese Journal of Rock Mechanics and Engineering*, vol. 29, pp. 1591–1602, 2010.
- [12] Z. Zhao, “Thermal influence on mechanical properties of granite: a microcracking perspective,” *Rock Mechanics and Rock Engineering*, vol. 49, no. 3, pp. 747–762, 2016.
- [13] Z. Z. Zhang, F. Gao, and X. L. Xu, “Experimental study of temperature effect of mechanical properties of granite,” *Rock and Soil Mechanics*, vol. 32, pp. 2346–2352, 2011.
- [14] S. Shao, P. G. Ranjith, P. L. P. Wasantha, and B. K. Chen, “Experimental and numerical studies on the mechanical behaviour of Australian Strathbogie granite at high temperatures: an application to geothermal energy,” *Geothermics*, vol. 54, pp. 96–108, 2015.
- [15] S. Q. Yang, P. G. Ranjith, H. W. Jing, W. L. Tian, and Y. Ju, “An experimental investigation on thermal damage and failure mechanical behavior of granite after exposure to different high temperature treatments,” *Geothermics*, vol. 65, pp. 180–197, 2017.
- [16] P. K. Gautam, A. K. Verma, M. K. Jha, P. Sharma, and T. N. Singh, “Effect of high temperature on physical and mechanical properties of Jalore granite,” *Journal of Applied Geophysics*, vol. 159, pp. 460–474, 2018.
- [17] W. G. P. Kumari, D. M. Beaumont, P. G. Ranjith, M. S. A. Perera, B. L. Avanthi Isaka, and M. Khandelwal, “An experimental study on tensile characteristics of granite rocks exposed to different high-temperature treatments,” *Geomechanics and Geophysics for Geo-Energy and Geo-Resources*, vol. 5, pp. 47–64, 2019.

- [18] X. L. Xu and Z.-Z. Zhang, "Acoustic emission and damage characteristics of granite subjected to high temperature," *Advances in Materials Science and Engineering*, vol. 2018, Article ID 8149870, 12 pages, 2018.
- [19] Z. Wang, A. He, G. Shi, and G. Mei, "Temperature effect on AE energy characteristics and damage mechanical behaviors of granite," *International Journal of Geomechanics*, vol. 18, no. 3, p. 4017163, 2018.
- [20] X. Shang, Z. Zhang, X. Xu, T. Liu, and Y. Xing, "Mineral composition, pore structure, and mechanical characteristics of pyroxene granite exposed to heat treatments," *Minerals*, vol. 9, no. 9, p. 553, 2019.
- [21] Z. Zhang, F. Gao, Y. Gao et al., "Fractal structure and model of pore size distribution of granite under high temperatures," *Chinese Journal of Rock Mechanics and Engineering*, vol. 35, pp. 2426–2438, 2016.
- [22] B. Shu, R. Zhu, J. Tan, S. Zhang, and M. Liang, "Evolution of permeability in a single granite fracture at high temperature," *Fuel*, vol. 242, pp. 12–22, 2019.
- [23] Y. Zhang, X. Zhang, and Y. S. Zhao, "Process of sandstone thermal cracking," *Acta Geophysica Sinica*, vol. 48, pp. 656–659, 2005.
- [24] X. Mao, L. Zhang, R. Liu, and D. Ma, "Mechanical and thermal damage properties of sandstone at high temperatures," *Electronic Journal of Geotechnical Engineering*, vol. 19, pp. 3137–3150, 2014.
- [25] Q. Le Ding, F. Ju, X. B. Mao, D. Ma, B. Y. Yu, and S. B. Song, "Experimental investigation of the mechanical behavior in unloading conditions of sandstone after high-temperature treatment," *Rock Mechanics and Rock Engineering*, vol. 49, pp. 2641–2653, 2016.
- [26] H. Sun, Q. Sun, W. Deng, W. Zhang, and C. Lü, "Temperature effect on microstructure and P-wave propagation in Linyi sandstone," *Applied Thermal Engineering*, vol. 115, pp. 913–922, 2017.
- [27] Q. Sun, W. Zhang, T. Su, and S. Zhu, "Variation of wave velocity and porosity of sandstone after high temperature heating," *Acta Geophysica*, vol. 64, pp. 633–648, 2016.
- [28] S. Q. Yang, P. Xu, Y. B. Li, and Y. H. Huang, "Experimental investigation on triaxial mechanical and permeability behavior of sandstone after exposure to different high temperature treatments," *Geothermics*, vol. 69, pp. 93–109, 2017.
- [29] Y. Zhang, Q. Sun, H. He, L. Cao, W. Zhang, and B. Wang, "Pore characteristics and mechanical properties of sandstone under the influence of temperature," *Applied Thermal Engineering*, vol. 113, pp. 537–543, 2017.
- [30] N. N. Sirdesai, T. N. Singh, and R. Pathegama Gamage, "Thermal alterations in the poro-mechanical characteristic of an Indian sandstone – a comparative study," *Engineering Geology*, vol. 226, pp. 208–220, 2017.
- [31] N. N. Sirdesai, T. N. Singh, P. G. Ranjith, and R. Singh, "Effect of varied durations of thermal treatment on the tensile strength of red sandstone," *Rock Mechanics and Rock Engineering*, vol. 50, pp. 205–213, 2017.
- [32] R. R. Zhang, L. W. Jing, and Q. Y. Ma, "Experimental study on thermal damage and energy evolution of sandstone after high temperature treatment," *Shock and Vibration*, vol. 2018, Article ID 3845353, 9 pages, 2018.
- [33] Y. J. Shen, Y. L. Zhang, F. Gao, G. S. Yang, and X. P. Lai, "Influence of temperature on the microstructure deterioration of sandstone," *Energies*, vol. 11, no. 7, p. 1753, 2018.
- [34] N. N. Sirdesai, B. Mahanta, P. G. Ranjith, and T. N. Singh, "Effects of thermal treatment on physico-morphological properties of Indian fine-grained sandstone," *Bulletin of Engineering Geology and the Environment*, vol. 78, pp. 883–897, 2019.
- [35] L. J. You and Y. L. Kang, "Effects of thermal treatment on physical property of tight rocks," *Progress in Geophysics*, vol. 24, pp. 1850–1854, 2009.
- [36] S. Yang, D. Yang, and Z. Kang, "Experimental investigation of the anisotropic evolution of tensile strength of oil shale under real-time high-temperature conditions," *Natural Resources Research*, vol. 30, no. 3, pp. 2513–2528, 2021.
- [37] J. Peng, G. Rong, M. Cai, M. Di Yao, and C. B. Zhou, "Physical and mechanical behaviors of a thermal-damaged coarse marble under uniaxial compression," *Engineering Geology*, vol. 200, pp. 88–93, 2016.
- [38] G. Rong, J. Peng, M. Yao, Q. Jiang, and L. N. Y. Wong, "Effects of specimen size and thermal-damage on physical and mechanical behavior of a fine-grained marble," *Engineering Geology*, vol. 232, pp. 46–55, 2018.
- [39] Y. Zhang, Q. Sun, and J. Geng, "Microstructural characterization of limestone exposed to heat with XRD, SEM and TG-DSC," *Materials Characterization*, vol. 134, pp. 285–295, 2017.
- [40] W. Zhang, Q. Sun, S. Zhu, and B. Wang, "Experimental study on mechanical and porous characteristics of limestone affected by high temperature," *Applied Thermal Engineering*, vol. 110, pp. 356–362, 2017.
- [41] Y. Zhang, Q. Sun, L. Cao, and J. Geng, "Pore, mechanics and acoustic emission characteristics of limestone under the influence of temperature," *Applied Thermal Engineering*, vol. 123, pp. 1237–1244, 2017.
- [42] H. Yavuz, S. Demirdag, and S. Caran, "Thermal effect on the physical properties of carbonate rocks," *International Journal of Rock Mechanics and Mining Sciences*, vol. 47, pp. 94–103, 2010.
- [43] M. Keshavarz, F. L. Pellet, and B. Loret, "Damage and changes in mechanical properties of a gabbro thermally loaded up to 1,000°C," *Pure and Applied Geophysics*, vol. 167, pp. 1511–1523, 2010.
- [44] V. Brotóns, R. Tomás, S. Ivorra, and J. C. Alarcón, "Temperature influence on the physical and mechanical properties of a porous rock: San Julian's calcarenite," *Engineering Geology*, vol. 167, pp. 117–127, 2013.
- [45] I. Ugur, N. Sengun, S. Demirdag, and R. Altindag, "Analysis of the alterations in porosity features of some natural stones due to thermal effect," *Ultrasonics*, vol. 54, pp. 1332–1336, 2014.
- [46] J. Nowak, "The influence of thermal transformation of coal mining wastes on their petrographic and mineralogical composition," *Gospodarka Surowcami Mineralnymi - Mineral Resources Management*, vol. 30, no. 1, pp. 143–159, 2014.
- [47] H. Tian, M. Ziegler, and T. Kempka, "Physical and mechanical behavior of claystone exposed to temperatures up to 1000°C," *International Journal of Rock Mechanics and Mining Sciences*, vol. 70, pp. 144–153, 2014.
- [48] R. Saidi, A. Tlili, and F. Jamoussi, "The effect of heating on mineral composition and grain size distribution of flux calcined porcelanites from the Gafsa-Metlaoui basin, southwestern Tunisia," *Journal of the African Earth Sciences*, vol. 124, pp. 189–198, 2016.
- [49] H. Ersoy, H. Kolaylı, M. Karahan, H. Harputlu Karahan, and M. O. Sünnetci, "Effect of thermal damage on mineralogical and strength properties of basic volcanic rocks exposed to high

- temperatures,” *Bulletin of Engineering Geology and the Environment*, vol. 78, pp. 1515–1525, 2019.
- [50] P. Liu, S. Cui, Z. Li, X. Xu, and C. Guo, “Influence of surrounding rock temperature on mechanical property and pore structure of concrete for shotcrete use in a hot-dry environment of high-temperature geothermal tunnel,” *Construction and Building Materials*, vol. 207, pp. 329–337, 2019.
- [51] G. Miao, Z. Li, L. Sun, and Y. Yang, “Experimental study on pore-fracture evolution law in the thermal damage process of coal,” *Combustion Science and Technology*, vol. 193, no. 4, pp. 677–701, 2021.
- [52] Y. Li, Y. Jiang, B. Zhang, H. Song, W. Dong, and P. Wang, “Investigation on the pore characteristics of coal specimens with bursting proneness,” *Scientific Reports*, vol. 9, no. 1, p. 16518, 2019.
- [53] C. Sun, G. Li, M. E. Gomah, J. Xu, and H. Rong, “Experimental investigation on the nanoindentation viscoelastic constitutive model of quartz and kaolinite in mudstone,” *International Journal of Coal Science & Technology*, 2021.
- [54] P. Boral, A. K. Varma, and S. Maity, “Nitration of Jharia basin coals, India: a study of structural modifications by XRD and FTIR techniques,” *International Journal of Coal Science & Technology*, 2021.
- [55] X. Liu, S. Yuan, Y. Sieffert, S. Fityus, and O. Buzzi, “Changes in mineralogy, microstructure, compressive strength and intrinsic permeability of two sedimentary rocks subjected to high-temperature heating,” *Rock Mechanics and Rock Engineering*, vol. 49, no. 8, pp. 2985–2998, 2016.
- [56] T. Meng, R. Liu, X. Meng, D. Zhang, and Y. Hu, “Evolution of the permeability and pore structure of transversely isotropic calcareous sediments subjected to triaxial pressure and high temperature,” *Engineering Geology*, vol. 253, pp. 27–35, 2019.
- [57] W. Zhao, K. Wang, L. Wang et al., “Influence of matrix size and pore damage path on the size dependence of gas adsorption capacity of coal,” *Fuel*, vol. 283, p. 119289, 2021.
- [58] W. Zhao, K. Wang, S. Liu et al., “Asynchronous difference in dynamic characteristics of adsorption swelling and mechanical compression of coal: modeling and experiments,” *International Journal of Rock Mechanics and Mining Sciences*, vol. 135, p. 104498, 2020.
- [59] H. Jiang, Y. Cheng, L. Yuan, F. An, and K. Jin, “A fractal theory based fractional diffusion model used for the fast desorption process of methane in coal,” *Chaos*, vol. 23, no. 3, p. 33111, 2013.
- [60] Y. Chen, X. Wang, and R. He, “Modeling changes of fractal pore structures in coal pyrolysis,” *Fuel*, vol. 90, no. 2, pp. 499–504, 2011.

Research Article

Mechanical Characteristics and Energy Dissipation Trends of Coal-Rock Combination System Samples with Different Inclination Angles under Uniaxial Compression

Zhen Wei ^{1,2}, Ke Yang ^{1,2,3}, Xiang He,^{1,2} Xiaolou Chi ^{1,2}, Xinyuan Zhao ^{1,2},
and Jiqiang Zhang ^{1,2}

¹State Key Laboratory of Mining Response and Disaster Prevention and Control in Deep Coal Mines, Anhui University of Science and Technology, Anhui, Huainan 232001, China

²Key Laboratory of Mining Coal Safety and Construction Efficiency of Anhui Province and Ministry of Education, Anhui University of Science and Technology, Huainan, 232001 Anhui, China

³Institute of Energy, Hefei Comprehensive National Science Center, Hefei, 230031 Anhui, China

Correspondence should be addressed to Ke Yang; keyang2003@163.com

Received 17 June 2021; Accepted 26 July 2021; Published 12 August 2021

Academic Editor: Wei Zhao

Copyright © 2021 Zhen Wei et al. This is an open access article distributed under the Creative Commons Attribution License, which permits unrestricted use, distribution, and reproduction in any medium, provided the original work is properly cited.

Coal mines are composed of multiple complex rock strata with different mechanical characteristics and energy accumulation and release performances. This implies uneven energy distribution in the coal-rock combination system (CRCS). To explore the effect of the included angle between the loading direction and the coal-rock contact surface on the mechanical properties, crack propagation mode, and energy evolution characteristics of the CRCS, the uniaxial compression tests were carried out on the CRCS samples with zero and 30° inclination angles. The obtained mechanical properties and energy dissipation trends of the tested samples were similar to those of the pure (raw) coal and rock ones but strongly depended on the inclination angles. The impact energy index of the CRCS samples was smaller than those of the pure coal and pure rock samples, and its impact tendency was less pronounced. The deformation and failure of the CRCS samples occurred in the coal part, the rock part inhibiting the development and deformation of the coal. According to the deformation and failure characteristics of the CRCS, the coal support far away from the contact surface should be strengthened in engineering practice to avoid the rock mass failure caused by the expansion and evolution of cracks in the coal part. At a 30° inclination angle, the CRCS sample was tensioned at the coal-rock contact surface, and the original cracks and pores were gradually compacted under the stress component perpendicular to the contact surface. With an increase in the inclination angle, the difference between the total energy accumulated before the peak and the released energy after the peak was reduced, and the difference between the total energy accumulated before the peak and the dissipated energy increased gradually. CRCS samples with different inclinations exhibited three damage stages: initial damage, stable damage growth, and rapid damage growth. The results obtained are considered instrumental in rockburst preventing, monitoring, and early warning under different stress environments.

1. Introduction

As the depth and intensity of coal mining continue to increase, large deformation of the roadway and dynamic disasters become more and more topical [1, 2]. Isolated coal pillars turn into frequent zones of dynamic disasters. The coal-rock system structure composed of the coal seam and

the surrounding rock is an important carrier of underground mining activities, which plays an important role in supporting the overlying strata and maintaining the roadway stability [3]. Therefore, it is of great significance to study the deformation, failure, and energy evolution mechanism of coal-rock combination systems (CRCS) for prevention, monitoring, and early warning of coal mine disasters.

The laboratory tests and numerical simulation of CRCS are common methods used to study the structure of the coal-rock system [4]. The mechanical characteristics, energy evolution, and impact tendency of the CRCS with different combination modes, coal-rock height ratios, strength ratios, and dip angles became topical for the global research community. Dou et al. [5, 6] experimentally studied the damage evolution in CRCS samples using AE signals and electromagnetic radiation signals. The correlation between the impact tendency of the CRCS and the AE signals was obtained. Zuo et al. [7, 8] carried out the strength and deformation failure tests on CRCS with different coal-rock combinations. They revealed the effect of different combinations on the impact tendency of the coal-rock system. Mou et al. [9] proposed the criteria of stable and unstable failures of the CRCS based on their instability and failure characteristics. Chen et al. [10] studied the variation trends of mechanical parameters of CRCS with different coal-rock height ratios. They analyzed the gradual instability process and failure mode of the coal-rock combination structure. Zhang et al. [11] carried out uniaxial and triaxial compression tests on samples of three different coal-rock combinations and analyzed the influence of combination modes on the CRCS mechanical properties and failure modes. Based on the energy evolution and failure mechanism of the CRCS, the energy driving mechanism of the crack initiation of the combination was determined by the energy storage characteristics, and the inclination angle effect of the whole instability failure of CRCS samples was revealed [12, 13]. Yang et al. [14] studied the energy evolution characteristics of the coal-rock system and proposed the system collaborative control technology. Chen et al. [8] carried out the uniaxial compression tests of CRCS samples and analyzed the evolution process of crack propagation in the CRCS under uniaxial loading based on CT scanning and the AE monitoring technology. Yang et al. [15] experimentally proved that shear fracture and axial splitting failure were the main failure modes of CRCS. The kinetic energy in the CRCS samples during a failure was related to the strength difference of the coal rock. In addition, the numerical simulation method was applied to study the effects of the strength ratio and height ratio of the CRCS samples on their impact tendency and failure mode [16]. The numerical simulation of different lithologic combinations performed in the study [17] revealed the phenomenon of local deformation and fracture migration of samples. The interface parameters of coal-rock combination have obvious influence on the mechanical and acoustic emission signal characteristics, which are mainly concentrated in prefabricated cracks, endogenous cracks, and mechanical and acoustic emission signals under different loading conditions [18, 19], especially the macro- and micromechanical characteristics and failure mechanism of the whole coal-rock combination [20]. There are few reports on the mechanical and energy evolution of different angles between the loading direction and the contact surface of the composite.

Previous studies were focused on the mechanical properties, deformation, and failure mechanism of CRCS. During the loading process, the damage evolution of CRCS was characterized by laboratory tests and numerical simulation, the

AE technology, and the electromagnetic radiation method. However, studies on the energy partition evolution and the multistage damage of CRCS are quite scarce, to explore the mechanical characteristics and energy dissipation trend of CRCS with different inclinations under the uniaxial load. Given the above, this study performed uniaxial compression tests of CRCS samples via an RMT150 rock mechanics testing machine. The energy evolution and failure mechanism of different CRCS samples during loading were clarified. The relationship between the AE signal and the mechanical behavior was monitored in real time. The energy accumulation trends in the CRCS were analyzed to provide references for the prevention and monitoring of dynamic disasters in coal mines.

2. Test Design and Loading Scheme

2.1. Sample Preparation. The coal collected on-site is difficult to be processed into a combination with the inclined contact surface. The heterogeneity of the coal and rock mass causes its physical and mechanical properties to be quite discrete [21]. To unify the variables and highlight the main research object of the test, all the test samples were processed with similar materials, as shown in Figure 1(a). The test setup included the coal monomer, the rock monomer, and the CRCS samples with 50 mm × 100 mm standard samples. The CRCS samples were subdivided into two groups with inclination angles equal to zero and 30°, respectively.

The sample preparation materials included quartz sand, barite powder, iron powder, rosin, pulverized coal, sodium humate, and alcohol. The mass ratio of the standard rock sample was as follows: quartz sand : barite powder : iron powder = 1 : 2 : 1. The alcohol content was 5% of the aggregate mass, and the rosin binder concentration was 25%. The mass ratio of materials for the standard coal sample was as follows: 0–1 mm pulverized coal : 1–3 mm pulverized coal = 19 : 6, and the amount of water was 10% of the aggregate mass. The amount of a single standard rock sample from the trial test was as follows: 132 g of quartz sand, 264 g of barite powder, 132 g of iron concentrate powder, 26.4 g of alcohol, and 6.6 g of rosin. The material consumption of a single standard coal sample was as follows: 197.6 g of 0–1 mm pulverized coal, 62.4 g of 1–3 mm pulverized coal, 26 g of water, and 0.83 g of sodium humate. The material consumption of the standard coal-rock sample was half of the above one.

During the preparation, the material was weighed and stirred evenly according to the required proportion, put into the self-made steel mold, and formed with the testing machine. The forming pressures for the standard rock and standard coal samples were 4.9 and 29.4 kN, respectively, and their duration was 5 min, as shown in Figure 1(b). According to the China national standards and the International Society for Rock Mechanics standards, the nonparallelism of both ends of the formed samples was no more than 0.01 mm; the diameter deviation of both ends did not exceed 0.02 mm. Each formed sample was placed in a dry and well-ventilated place for seven days. Three standard rock samples, three standard coal samples, and six CRCS samples (three



FIGURE 1: Sample preparation materials and standard samples: (a) proportioning materials, (b) mould, and samples.

with a 0° inclination and three with a 30° inclination) were prepared.

2.2. Testing System and Scheme. Laboratory tests were carried out in the State Key Laboratory of Anhui University of Science and Technology. The test system is shown in Figure 2. It mainly includes the loading device, the AE device, and the digital camera. During the test, the three devices were synchronized for later test data processing and analysis. The loading device was a Shenzhen SUNS UTM4000 electronic universal testing machine, servodriven by the AC motor, with good stability, high precision, and a maximum test load of 20 kN. The AE device was a DS2-8B acoustic emission signal analyzer, which was used to monitor the failure process of uniaxial compression in real time. To reduce the influence of external equipment on the AE signal acquisition, the threshold value of the AE system was set at 100 MV, and a Vaseline lubricator was placed between the AE probe and the sample to enhance the sensitivity of AE signal acquisition [22]. A Canon digital camera stage was used to capture the sample’s deformation and failure stage points under the uniaxial load. The load and AE signals were transmitted to the computer for real-time display and storage.

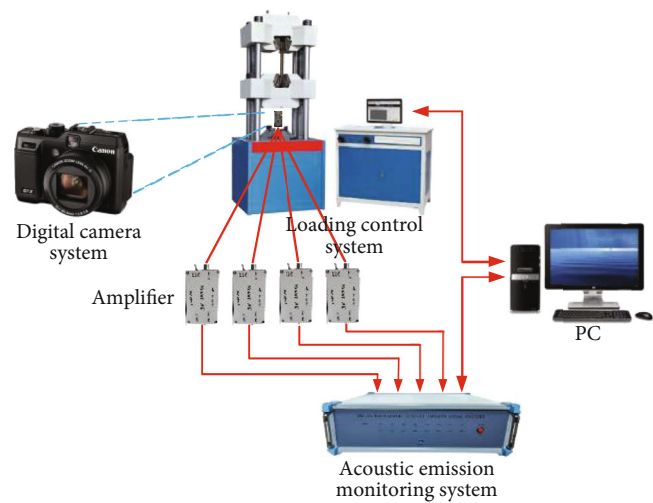


FIGURE 2: Test loading and monitoring system.

Twelve uniaxial compression tests were subdivided into four groups, with three standard samples in each group. Before the test, the prepared standard rock samples, the coal samples, and CRCS samples were numbered and weighed, and the test system was launched by connecting the line. Due to the small strength of samples, to prevent rapid failure, which would make it impossible to measure the continuous stress-strain curve, the displacement-controlled loading mode was adopted. The loading rate was 0.01 mm/s, and the loading was continuous until the sample’s final fracture.

3. Results and Analysis

3.1. Stress-Strain Characteristics of CRCS Samples with Different Inclinations. The stress-strain curves of typical CRCS samples under uniaxial compression are shown in Figure 3. According to the stress-strain curves, the sample deformation could be subdivided into four stages [23]. Due to the differences in material components and proportion

of the samples, the stress-strain curves of the samples with different proportions under the uniaxial load varied greatly. The strength of the CRCS samples slightly exceeded that of pure coal monomers, indicating that the strength of the CRCS sample mainly depended on the coal. The decreasing order of the compressive strength of samples was as follows: pure rock sample > 0°-inclination CRCS sample > 30°-inclination CRCS sample > pure coal sample. The decreasing order of elastic moduli was pure rock sample > 0°-inclination CRCS sample > pure coal sample > 30°-inclination CRCS sample. The peak strains of the pure coal and pure rock samples were 0.878 and 1.026, respectively. The peak strain of the CRCS sample is less than that of the pure coal sample and pure rock sample, mainly because the rock mass part of the CRCS sample experienced no significant deformation under the uniaxial compression load [24, 25]. The brittle failure after the peak of the pure rock sample was strongly pronounced, and the stress dropped, while the CRCS and pure coal samples exhibited good continuity after the peak.

In the stress-strain curves constructed under the uniaxial compression load conditions, the ratio of the accumulated deformation energy before the peak to the loss of

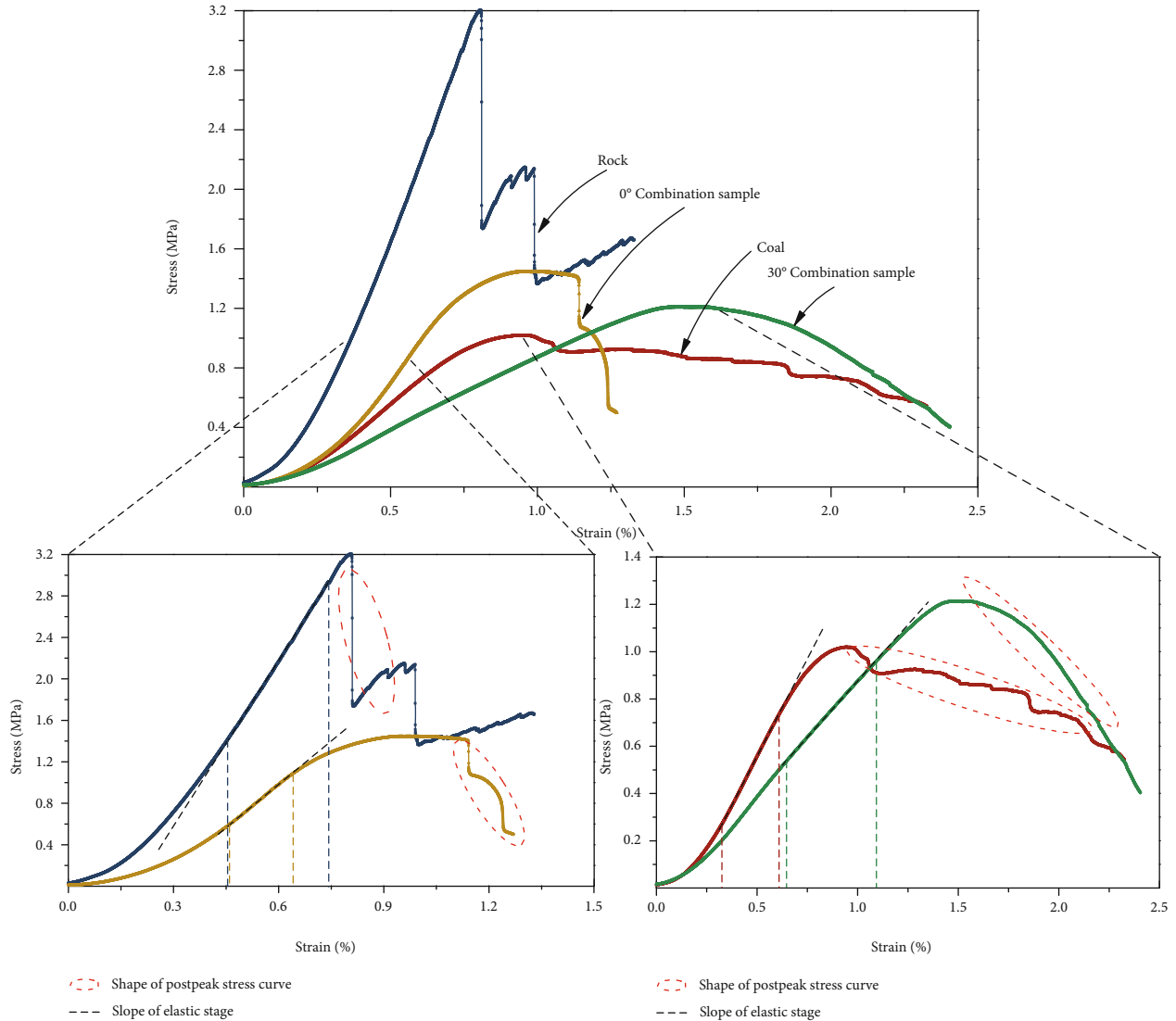


FIGURE 3: Stress-strain curves of typical samples under uniaxial compression.

deformation energy after the peak is referred to as the impact energy index [26]. The impact energy index of the CRCS samples was smaller than that of the pure coal and pure rock samples. That is, the CRCS impact tendency was weak. The deformation and failure of the CRCS samples mainly occurred in the coal part, while the rock part inhibited the development and deformation of the coal body. The coal part expanded and deformed for a long time before the peak stress was reached, so the deformation and failure mechanism of the CRCS sample changed.

The complete stress-strain curve of the rock reflected its damage evolution process. The rock experienced compaction stage (I), elastic stage (II), plastic stage (III), and residual deformation stage (IV). The rock's mechanical properties in each stage were different. The stress state of rock can be revealed by analyzing the four stages of rock deformation. The boundary points of the four stages of the sample are shown in Figure 4. The results show that the strain in the 30° CRCS sample exceeded that of the 0° one, and the residual deformation was large in the four stages. It changed asyn-

chronously with the other three stages, indicating that the sample was seriously damaged and prone to serious disasters.

3.2. AE Response of CRCS Samples with Different Inclinations.

The displacement controlled loading method was used in the test, and the loading rate was 0.01 mm/s until the specimen was destroyed. The sampling frequency of acoustic emission system is 1000 kHz, and the threshold is 40 dB. In order to enhance the coupling effect between the acoustic emission probe and the sample, Vaseline is smeared between the sensor and the sample to reduce the acoustic impedance difference and energy attenuation of the contact surface and improve the effectiveness of AE signal in the test process. The failure characteristics and AE response of CRCS samples with different inclinations are shown in Figure 5. When the inclination of the coal-rock sample increased from 0° to 30°, the CRCS sample's fracture mode evolved from splitting failure of the coal rock to the sliding failure at the interface of the CRCS. There was a close correlation between the AE and the stress drop of the rock sample. The stress curve fluctuated

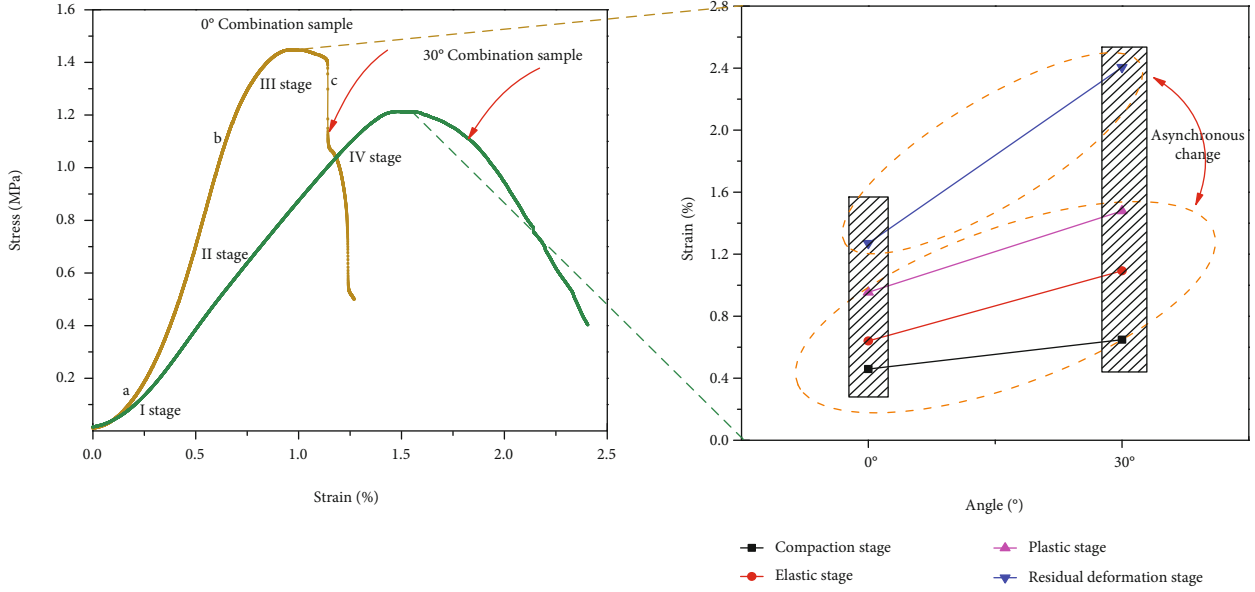


FIGURE 4: Relationship between the 0° and 30° CRCS samples and the strain points.

greatly after the peak, and there existed an obvious stress drop, accompanied by large energy AE events. The AE signal of the coal sample under uniaxial loading was weak, and the correlation with stress drop was low. The AE events of large energy were mainly concentrated in the after-peak stage. The fluctuation of the stress-time curve of the CRCS sample occurred within a small range, and there was only one peak point. The correlation between the AE and the stress drop was not obvious, and numerous AE signals were mainly concentrated in the stable rising stage of stress before the peak.

The AE energy can better characterize the damage and fracture of the coal-rock sample and directly reflect the evolution process of crack initiation, propagation, and penetration in the sample [27, 28]. Therefore, the AE energy was used as a characteristic parameter to further analyze the damage process of the coal-rock samples with different inclinations.

Based on the statistical damage theory, the damage evolution equation of samples under uniaxial loading was established in the following form:

$$\sigma = E(1-D)\varepsilon_1, \quad (1)$$

where σ is the axial stress, in MPa; E is the elastic modulus, in MPa; and D is the damage factor, which is derived as the number of cracks in the microelement in the sample.

Assuming that the strength of the microelement in the sample followed the Weibull distribution law, the relationship between the damage factor and the AE energy parameters was obtained:

$$D = \frac{N_t}{N_a}, \quad (2)$$

where N_t and N_a are the AE cumulative energies at time t and sample's fracture, respectively, in mV·mS units.

The samples had a certain residual strength after the peak under a uniaxial load. The damage factor and the AE energy parameter model based on the Weibull distribution disregarded the residual strength after the peak. It was assumed that the sample was destroyed when the maximum strain was reached, i.e., $D = 1$, which was inconsistent with reality. Therefore, the correction factor m was introduced, with the calculation equation of the damage factor reduced to the following form:

$$D = m \frac{N_t}{N_a}. \quad (3)$$

With an account of the residual strength, the correction factor m can be obtained as follows:

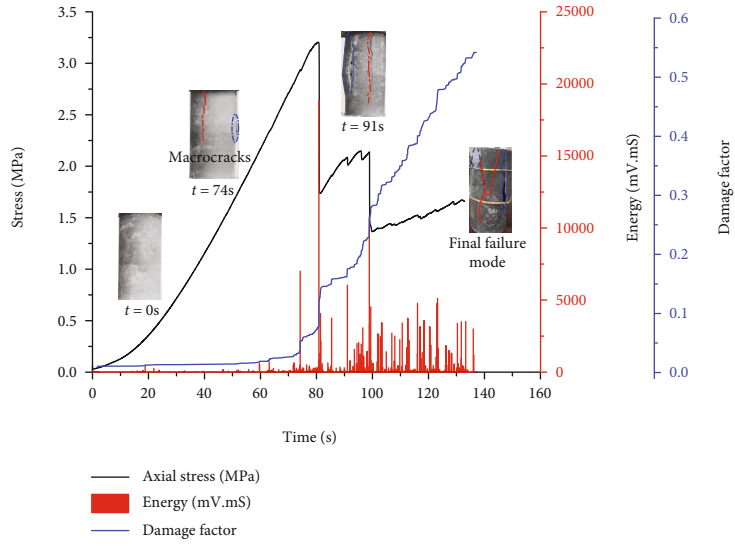
$$m = \frac{\sigma_c - \sigma_p}{\sigma_c}, \quad (4)$$

where σ_c is the compressive strength, in MPa and σ_p is the residual strength, in MPa.

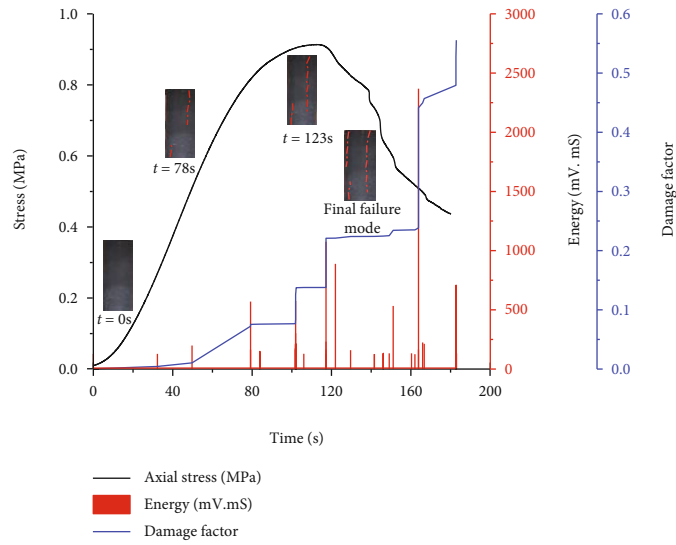
By substituting Equations (3) and (4) into Equation (1), the damage evolution equation of the uniaxial compression of CRCS samples characterized by the AE energy was obtained:

$$\sigma = E \left(1 - \frac{\sigma_c - \sigma_p}{\sigma_c} \frac{N_t}{N_a} \right) \varepsilon_1. \quad (5)$$

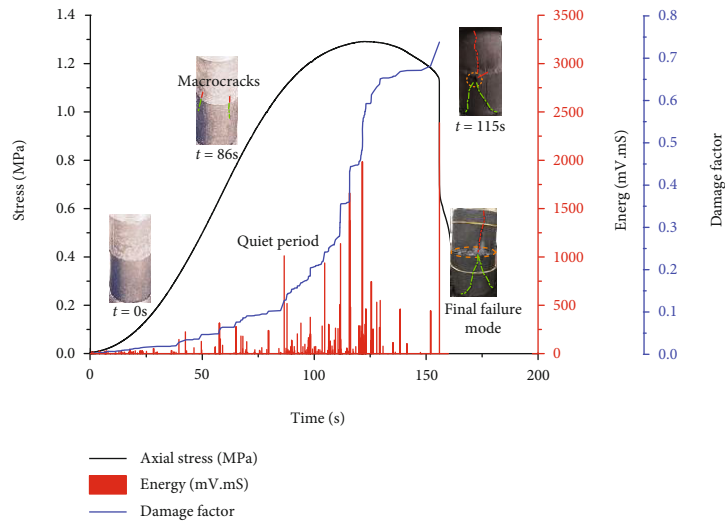
The damage evolution process of a typical sample under uniaxial compression was obtained by transforming the damage variables of the CRCS sample based on the normalization method [29, 30]. As shown in Figure 5, the CRCS samples with different inclinations were characterized by the multistage damage mechanism, which included three stages,



(a)

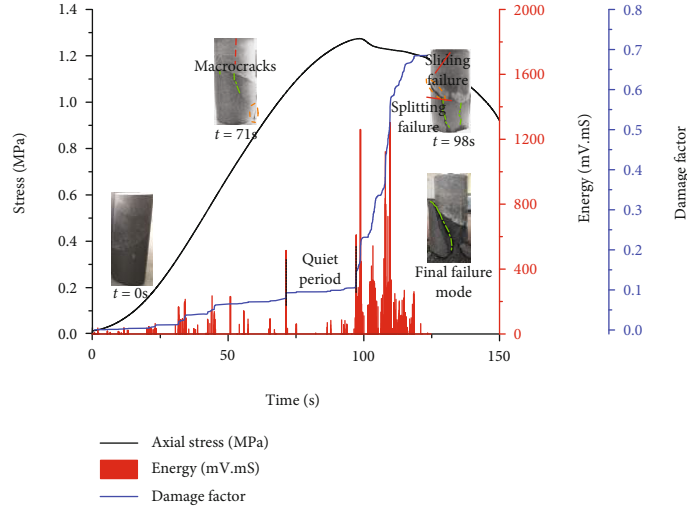


(b)



(c)

FIGURE 5: Continued.



(d)

FIGURE 5: Uniaxial compression stress and AE signal characteristics of typical samples: (a) standard rock sample, (b) standard coal sample, (c) 0° CRCS sample, and (d) 30° CRCS sample.

according to the damage factor-time curve. The first stage was the initial damage stage, with a damage factor of about zero and low damage. It mainly corresponded to the initial stage of the stress-strain compaction and the elastic stage. At this time, the original cracks closed, the internal structure was uniform, and there was no new crack initiation or propagation. The second stage was the stable growth stage of damage, in which the damage factor increased nonlinearly, and the damage degree was high, mainly in the middle and late portions of the elastic stress-strain stage and the early part of the plastic stage. At this time, the primary cracks reached their limit state, and new cracks initiated and propagated with increased loading pressure. The third stage was the rapid growth stage of damage, mainly located in the middle and late portions of the stress-strain plastic stage and the residual stage after the peak. At this time, the internal microcracks in the sample expanded rapidly, converged, formed a network of cracks, and merged, resulting in the macrofracture.

In comparison with Figure 5, acoustic emission signals and damage factors of different dip coal-rock assemblages show the characteristics of stage evolution. The stress-strain curve of rock sample is in drop type after the peak, and the stress-strain curve of the coal-bearing component decreases slowly, indicating that the rock sample has good brittleness [31]. The combined samples first appeared microcracks in the attachment of contact surface, and the microcracks developed gradually until the specimen was destroyed. The rock samples and coal samples first appeared cracks at the loading end and developed and expanded gradually.

3.3. Failure and Instability Characteristics of Coal-Rock Combination with Different Dip Angles. In the same stress state, coal is the first to be destroyed, and microcracks and weak planes appear. With the continuous loading, these microcracks gradually connect and develop with the weak surface, forming the macrofailure characteristics. In the combination, the coal component is mainly longitudinal failure,

and the angle between the crack and the axial direction of the sample is in the range of 0° to 30° which belongs to shear failure. The failure process is that the local point begins to lose stability and then leads to the overall instability [32]. The failure mode of 30° composite specimen is “point type” incomplete failure.

To sum up, with the gradual increase of the dip angle of the coal-like rock combination, the combination failure mode gradually transits from shear failure and “point type” incomplete failure, and with the gradual increase of dip angle, the failure degree changes from complete failure to incomplete failure.

4. Energy Evolution in the CRCS Mass

4.1. Energy Calculation Method. Energy evolution accompanies the whole process of damage and failure of the coal and rock mass, so it is more practical to reveal the coal and rock mass damage from the energy evolution standpoint [33, 34]. Based on this, the energy evolution of CRCS samples with different inclinations under uniaxial compression was performed to analyze the trend of total energy accumulated before the peak, total release energy after peak, elastic energy, dissipated energy, and surplus energy.

The uniaxial stress-strain curve of coal-like rock combination is obtained by the test, and the stress-strain curve is integrated according to the calculus method, as shown in Figure 6. During the cyclic loading experiment, it is found that the unloading curve is curved due to the viscous hysteresis. The elastic energy accumulated before the peak can be approximately calculated by means of elastic stage translation, and the formula is shown below:

$$U^e = \frac{1}{2} \sigma_c \varepsilon^e, \quad (6)$$

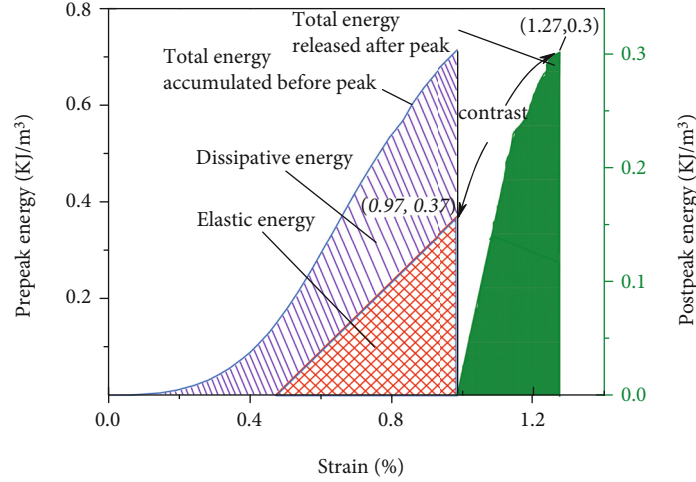


FIGURE 6: Energy conversion trend.

where σ_c is compressive strength, in MPa and ε^e is the elastic strain that can be recovered before the peak, in %.

According to the first law of thermodynamics, assuming that there is no heat exchange between the coal-rock combination and the outside world under uniaxial load, part of the work done by the testing machine is converted into elastic strain energy, which is stored in the sample, and part of it is consumed in the form of dissipative energy, i.e.,

$$U = U^e + U^d, \quad (7)$$

$$U = \int_0^{\varepsilon_1} \frac{\sigma_i + \sigma_{i+1}}{2} d\varepsilon, \quad (8)$$

where U is the total energy before the peak, U^d is the dissipated energy, ε_1 is the strain corresponding to the peak stress, and σ_i and σ_{i+1} are stresses in i th and $i+1$ th microelements, respectively.

The postpeak energy U^f of the sample is

$$U^f = \int_{\varepsilon_1}^{\varepsilon_{\max}} \frac{\sigma_i + \sigma_{i+1}}{2} d\varepsilon, \quad (9)$$

where ε_{\max} is the limit strain after the peak.

Part of the elastic energy stored before the peak is consumed by the sample rupture, and the remaining energy is converted into the initial kinetic energy of the sample ejection. Therefore, the surplus energy is the difference between the pre peak elastic energy and the postpeak released energy.

$$U^y = U^e - U^f, \quad (10)$$

where U^f is the total release energy after peak and U^y is the surplus energy.

4.2. Energy Evolution of CRCS Samples with Different Inclinations. The evolution of rock damage is accompanied by energy transfer and conversion, presenting comprehensive information on stress and strain evolutions. It is of cer-

tain significance to evaluate the process of rock loading to catastrophe based on energy. Figure 7 shows the energy conversion law of CRCS samples with 0° and 30° inclination angles.

As shown in Figure 7, the stress-strain evolution can be subdivided into the following four stages, namely, compression stage (I), elastic stage (II), plastic stage (III), and after-peak stage (IV). The dissipated and elastic energies exist in the compression, elastic, and plastic stages; the released and surplus energies exist in the after-peak stage, while shares and forms of energy in each stage are adjusted. According to Equations (6) to (10), calculations were performed for the total energy accumulated before the peak, released energy after peak, elastic energy accumulated before the peak, dissipated energy, and surplus energy. The performed analysis revealed that the energy characteristics of 0° and 30° CRCS samples were similar, and the dissipated energy of the 30° CRCS sample was small.

Figure 8 shows the law of energy release after the peak in the rock. As expected, the variation trends of 0° and 30° CRCS samples were very similar. All samples with different inclinations satisfied the law of stable energy release in the initial, middle, and later stages exhibited a gradual slowdown in the later stage and maximum energy release. According to the curve's slopes of samples with different inclinations, the energy release after the peak of 30° CRCS was intense.

Figure 9 shows the variation law of total energy, elastic energy, dissipated energy, released energy, and surplus energy accumulated before the peak of 0° and 30° coal-rock combination samples. From the horizon and trend relationship of the curve, it can be seen that the total energy accumulated before the peak is $>$ elastic energy $>$ released energy $>$ dissipated energy $>$ surplus energy, and there is no offside situation. It shows that the variation of samples of 0° and 30° coal-rock assemblages can meet the general law of energy evolution, and only fluctuates in numerical value. With the increase of the inclination angle, the positions of the total energy accumulated before the peak and the elastic deformation energy are closer and closer. The difference between the total energy accumulated before the peak and the released energy after the peak shows a decreasing trend, and the

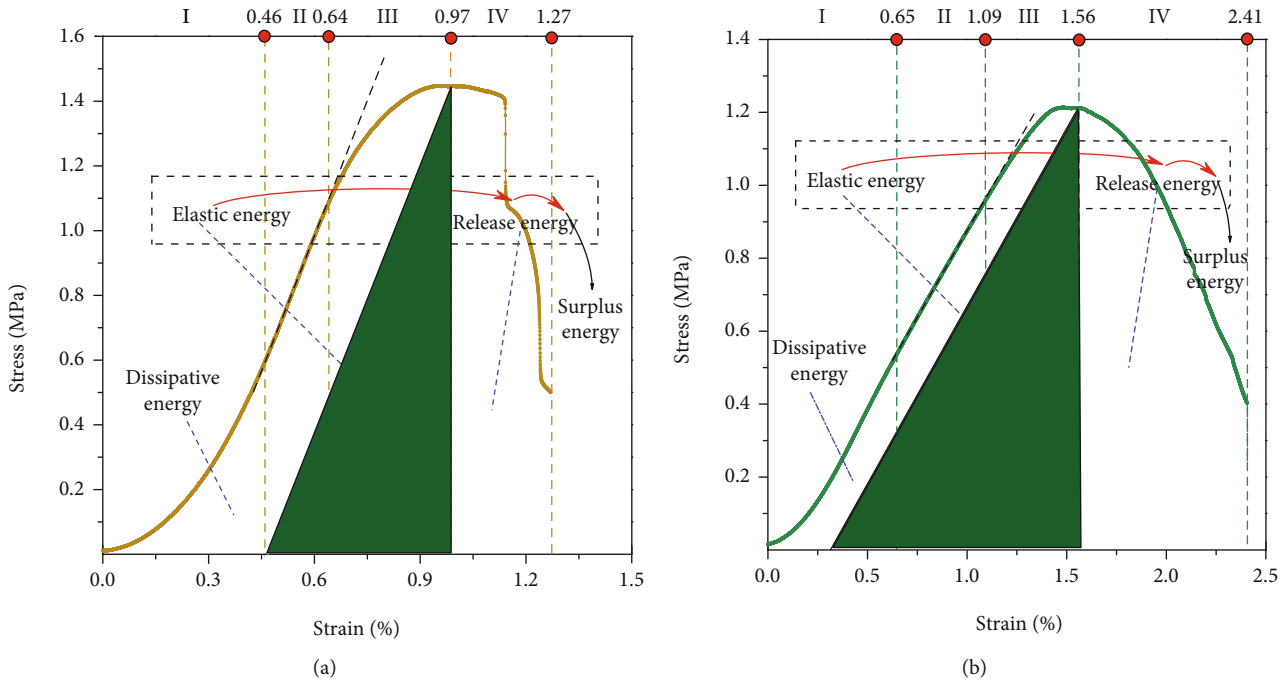


FIGURE 7: Energy conversion law of CRCS samples: (a) 0° CRCS samples and (b) 30° CRCS samples.

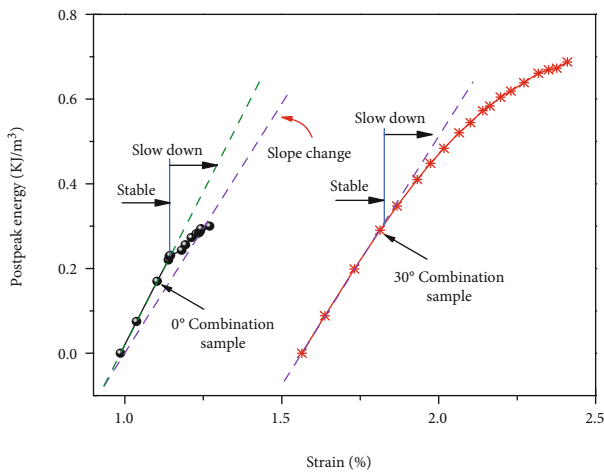


FIGURE 8: Law of energy release after the peak of the 0° and 30° CRCS samples.

difference between the total energy accumulated before the peak and the dissipated energy shows a gradually increasing trend. The results show that with the increase of dip angle, the energy storage characteristics of coal-like rock combination are gradually enhanced.

5. Analysis of Inclination Influence Mechanism in CRCS

The experimental results show that the AE signal is highly consistent with the loading failure process of the specimen, which is consistent with the previous research results. However, the mechanical and acoustic emission characteristics of coal-rock associations with different dip angles are signif-

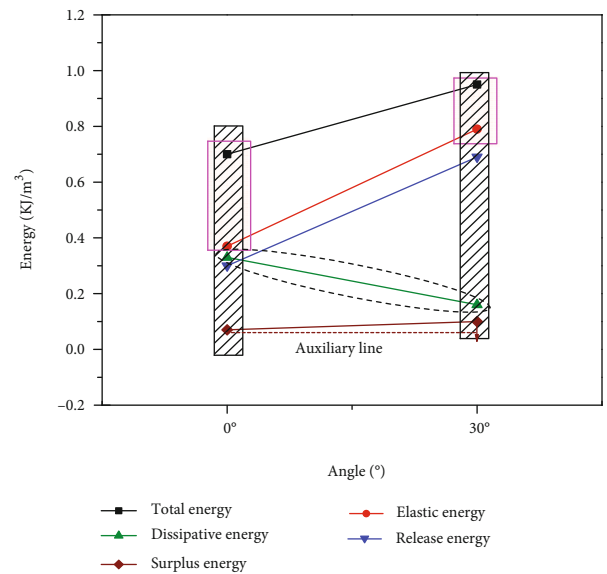


FIGURE 9: Energy conversion law of the 0° and 30° CRCS samples.

icantly different. In order to explore the influence of contact angle on peak load and uniaxial compressive strength, a mechanical model as shown in Figure 10 is established. In the contact surface of the coal rock, $\sigma \sin \alpha$ is the stress of the contact surface of the parallel coal rock, $\sigma \cos \alpha$ is the stress of the contact surface of vertical coal rock, where σ is the axial stress applied and α is the angle between the contact surface and the horizontal direction of the coal rock. With an increase in the inclination of the contact surface of the coal rock, $\sigma \sin \alpha$ increased gradually and $\sigma \cos \alpha$ decreased gradually, that is, the shear slip failure was enhanced during

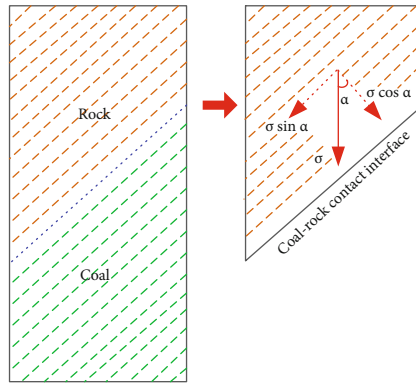


FIGURE 10: Schematic diagram of the inclination angle effect in CRCS.

loading, and the tensile splitting failure was weakened gradually. The crack morphology and mechanical properties of the CRCS samples with different inclinations exhibited different patterns under the external loads.

At $\alpha = 0^\circ$, the axial stress was normal to the contact surface of the coal rock of the combination, the original fractures and pores of the sample were compressed to a large extent, and numerous cracks perpendicular to the contact surface were produced, so the sliding instability failure did not occur easily. When the peak load was reached, the cracks perpendicular to the contact surface were not completely connected, showing good ductility failure. The small cracks perpendicular to the contact surface after the peak were rapidly connected, and the sample was damaged instantly. At $\alpha = 30^\circ$, there was a stress component parallel to the contact surface in the CRCS; the sample was tensioned at the contact surface; cracks were generated under the action of the stress component parallel to the contact surface, and the original cracks and pores of the sample were gradually compacted under the action of the stress component perpendicular to the contact surface. Therefore, the 30° CRCS samples were more prone to losing cohesion and experienced a sliding failure along the contact surface.

The CRCS samples with different inclinations can reflect the characteristics of the coal-rock contact surface. When the coal seam is the same, the angles between the principal stress and the contact surface are different, and the energy dynamic evolution and impact tendency differ as well. The larger strain energy is accumulated before the peak, the shorter the failure time after the peak, and the greater the impact tendency. The test results show that with an increase in the inclination angle α of the contract surface, the elastic energy accumulated before the peak increased, and the failure time decreased. Before the sample was loaded to the peak load, numerous AE signals appeared, and intensive AE signals were detected in the middle of the failure process.

6. Conclusions

The results obtained made it possible to draw the following conclusions:

- (1) The coal and rock mass near the contact surface of the CRCS affected each other. The limiting effect of the rock mass in the failure stage before the peak was obvious, and the coal part effect in the failure stage after the peak was more pronounced. The sample failure mode was closely related to the inclination angle of the contact surface, i.e., the larger the inclination, the greater the shear slip failure
- (2) With an increase in the inclination angle of the contact surface, the positions of the total energy accumulated before the peak and the elastic energy of the CRCS shifted closer to each other. The difference between the total energy accumulated before the peak and the released energy after the peak decreased. The difference between the total energy accumulated before the peak and the dissipated energy tended to increase gradually
- (3) The rock art in the CRCS sample limited the strength of the coal part. Compared with the pure coal monomer, the pressure-bearing time of the sample in the expansion stage after the peak was longer, and the impact tendency of the CRCS sample was weaker. According to the deformation and failure characteristics of the combination, the support of the coal body far from the contact surface should be strengthened in engineering practice to avoid the rock damage caused by the expansion and evolution of cracks in the coal part

Data Availability

The data used for conducting classifications are available from the corresponding author authors upon request.

Conflicts of Interest

The authors declare that there are no conflicts of interest regarding the publication of this paper.

Acknowledgments

We acknowledge the financial support for this work provided by the China National Key Research and Development Program (2019YFC1904304) and 115 innovation team support project in Anhui Province.

References

- [1] M. C. He, H. P. Xie, S. P. Peng, and Y. D. Jiang, "Study on rock mechanics of deep mining," *Chinese Journal of Rock Mechanics and Engineering*, vol. 24, no. 16, pp. 2803–2813, 2005.
- [2] H. P. Xie, H. W. Zhou, D. J. Xue, H. W. Wang, R. Zhan, and F. Gao, "Research and thinking on deep mining and limit mining depth of coal," *Journal of China Coal Society*, vol. 37, no. 4, pp. 535–542, 2012.
- [3] L. Yuan, J. H. Xue, Q. S. Liu, and B. Liu, "Surrounding rock control theory and support technology of deep rock roadway in coal mine," *Journal of China Coal Society*, vol. 36, no. 4, pp. 535–543, 2011.

- [4] S. L. Song, X. S. Liu, Y. L. Tan, D. Y. Fan, Q. Ma, and H. L. Wang, "Study on failure modes and energy evolution of coal-rock combination under cyclic loading," *Shock and Vibration*, vol. 2020, Article ID 5731721, 16 pages, 2020.
- [5] L. M. Dou, J. C. Tian, C. P. Lu et al., "Study on electromagnetic radiation law of impact failure of composite coal and rock," *Chinese Journal of Rock Mechanics and Engineering*, vol. 24, no. 19, pp. 143–146, 2005.
- [6] L. M. Dou, C. P. Lu, Z. L. Mou, X. T. Zhang, and Z. H. Li, "Experimental study on impact propensity of combined coal and rock," *Journal of Mining and Safety Engineering*, vol. 23, no. 1, pp. 43–46, 2006.
- [7] J. P. Zuo, H. P. Xie, A. M. Wu, and J. F. Liu, "Study on failure mechanism and mechanical properties of deep coal rock monomer and combination," *Chinese Journal of Rock Mechanics and Engineering*, vol. 30, no. 1, pp. 84–92, 2011.
- [8] Y. L. Chen, J. P. Zuo, D. J. Liu, and Z. B. Wang, "Deformation failure characteristics of coal-rock combined body under uniaxial compression: experimental and numerical investigations," *Bulletin of Engineering Geology and the Environment*, vol. 78, no. 5, pp. 3449–3464, 2018.
- [9] Z. L. Mou, H. Wang, P. Peng, Z. J. Liu, and X. C. Yang, "Experimental study on failure characteristics and impact tendency of rock coal rock combination," *Journal of Mining and Safety Engineering*, vol. 30, no. 6, pp. 841–847, 2013.
- [10] S. J. Chen, D. W. Yin, N. Jiang, F. Wang, and Z. H. Zhao, "Mechanical properties of oil shale-coal composite samples," *International Journal of Rock Mechanics and Mining Sciences*, vol. 123, article 104120, 2019.
- [11] Z. T. Zhang, J. F. Liu, L. Wang, H. T. Yang, and J. P. Zuo, "Experimental study on influence of combination mode on mechanical properties and failure characteristics of coal rock combination," *Journal of China Coal Society*, vol. 37, no. 10, pp. 1677–1681, 2012.
- [12] F. Du and K. Wang, "Unstable failure of gas-bearing coal-rock combination bodies: insights from physical experiments and numerical simulations," *Process Safety and Environmental Protection*, vol. 129, no. 2019, pp. 264–279, 2019.
- [13] Y. L. Tan, W. Y. Guo, Q. H. Gu et al., "Research on the rockburst tendency and AE characteristics of inhomogeneous coal-rock combination bodies," *Shock and Vibration*, vol. 2016, no. 2, Article ID 9271434, p. 11, 2016.
- [14] K. Yang, Z. Wei, X. L. Chi, Y. G. Zhang, and W. J. Liu, "Experimental research on the mechanical characteristics and the failure mechanism of coal-rock composite under uniaxial load," *Advances in Civil Engineering*, vol. 2020, no. 1, Article ID 8867809, p. 11, 2020.
- [15] S. Yang, J. Wang, J. G. Ning, and P. Q. Qiu, "Experimental study on mechanical properties, failure behavior and energy evolution of different coal-rock combined specimens," *Applied Sciences*, vol. 9, no. 20, pp. 4427–4438, 2019.
- [16] Q. Ma, Y. L. Tan, X. S. Liu, Z. H. Zhao, and D. Y. Fan, "Mechanical and energy characteristics of coal-rock composite sample with different height ratios: a numerical study based on particle flow code," *Environmental Earth Sciences*, vol. 80, no. 8, pp. 309–321, 2021.
- [17] W. R. Liu, W. Yuan, Y. T. Yan, and X. Wang, "Analysis of acoustic emission characteristics and damage constitutive model of coal-rock combined body based on particle flow code," *Symmetry*, vol. 11, no. 8, pp. 1040–1053, 2019.
- [18] C. Zhang and L. Zhang, "Permeability characteristics of broken coal and rock under cyclic loading and unloading," *Natural Resources Research*, vol. 28, no. 3, pp. 1–13, 2018.
- [19] W. Zhao, K. Wang, Y. P. Cheng, S. M. Liu, and L. Fan, "Evolution of gas transport pattern with the variation of coal particle size: kinetic model and experiments," *Powder Technology*, vol. 367, pp. 336–346, 2020.
- [20] F. Du, K. Wang, X. C. P. Xin, L. Y. Shu, and G. D. Wang, "Experimental study of coal-gas outburst: insights from coal-rock structure, gas pressure and adsorptivity," *Natural Resources Research*, vol. 29, no. 4, pp. 2481–2493, 2020.
- [21] F. Du, K. Wang, G. D. Wang, Y. Huang, and L. P. Yi, "The mechanism of damage in gas-bearing coal-rock combination bodies and gas seepage in coals," *Energy Sources, Part A: Recovery, Utilization, and Environmental Effects*, vol. 43, no. 10, pp. 1181–1201, 2019.
- [22] X. Ding, X. C. Xiao, X. F. Lv et al., "Time frequency signal characteristics and evolution mechanism of acoustic emission during coal and rock fracture process," *Journal of China Coal Society*, vol. 44, no. 10, pp. 2999–3011, 2019.
- [23] Z. G. Xia, S. Liu, B. Zhang, J. H. Song, F. Fen, and N. Jiang, "Mechanical properties and damage characteristics of coal-rock combination with different dip angles," *KSCE Journal of Civil Engineering*, vol. 25, no. 5, pp. 1687–1699, 2021.
- [24] Z. H. Zha, W. M. Wang, L. H. Wang, and C. Q. Dai, "Compression-shear strength criterion of coal-rock combination model considering interface effect," *Tunnelling and Underground Space Technology*, vol. 47, no. 2015, pp. 193–199, 2015.
- [25] H. T. Sun, L. C. Dai, Y. B. Liu, and H. W. Jin, "Critical conditions and energy transfer characteristics of the failure process of coal-rock combination systems in deep mines," *Geofluids*, vol. 2021, no. 16, Article ID 6655443, p. 14, 2021.
- [26] X. S. Liu, Y. L. Tan, J. G. Ning, Y. W. Lu, and Q. H. Gu, "Mechanical properties and damage constitutive model of coal in coal-rock combined body," *International Journal of Rock Mechanics and Mining Sciences*, vol. 110, no. 2018, pp. 140–150, 2018.
- [27] Z. P. Meng, P. Zhang, Y. D. Tian, Y. H. Wang, S. N. Li, and C. Li, "Experimental analysis of stress-strain, permeability and acoustic emission of coal reservoir under confining pressure," *Journal of China Coal Society*, vol. 45, no. 7, pp. 2544–2551, 2020.
- [28] M. M. Kou, X. R. Liu, Z. Q. Wang, and S. D. Tang, "Laboratory investigations on failure, energy and permeability evolution of fissured rock-like materials under seepage pressures," *Engineering Fracture Mechanics*, vol. 247, no. 2021, article 107694, 2021.
- [29] X. L. Li, S. J. Chen, E. Y. Wang, and Z. H. Li, "Rockburst mechanism in coal rock with structural surface and the microseismic (MS) and electromagnetic radiation (EMR) response," *Engineering Failure Analysis*, vol. 124, no. 3, article 105396, 2021.
- [30] Y. Yang, C. B. Jiang, X. W. Guo, S. J. Peng, J. J. Zhao, and F. Z. Yan, "Experimental investigation on the permeability and damage characteristics of raw coal under tiered cyclic unloading and loading confining pressure," *Powder Technology*, vol. 389, no. 2021, pp. 416–429, 2021.
- [31] C. Zhang, S. H. Tu, and Y. X. Zhao, "Compaction characteristics of the caving zone in a longwall goaf: a review," *Environmental Earth Sciences*, vol. 78, no. 1, pp. 1–12, 2019.

- [32] K. Wang and F. Du, "Coal-gas compound dynamic disasters in China: a review," *Process Safety and Environmental Protection*, vol. 133, pp. 1–17, 2020.
- [33] P. Wang, H. J. Jia, and P. Q. Zheng, "Sensitivity analysis of bursting liability for different coal-rock combinations based on their inhomogeneous characteristics," *Geomatics, Natural Hazards and Risk*, vol. 11, no. 1, pp. 149–159, 2020.
- [34] J. J. Feng, E. Y. Wang, R. X. Shen, L. Chen, X. L. Li, and N. Li, "A source generation model for near-field seismic impact of coal fractures in stress concentration zones," *Journal of Geophysics and Engineering*, vol. 13, no. 4, pp. 516–525, 2016.

Research Article

Research and Optimization of Gas Extraction by Crossing-Seam Boreholes from Floor Roadway

Gang Li  and **Jiafei Teng**

College of Mining, Liaoning Technical University, Fuxin, Liaoning Province, China

Correspondence should be addressed to Gang Li; ligang@lntu.edu.cn

Received 3 June 2021; Accepted 25 July 2021; Published 10 August 2021

Academic Editor: Feng Du

Copyright © 2021 Gang Li and Jiafei Teng. This is an open access article distributed under the Creative Commons Attribution License, which permits unrestricted use, distribution, and reproduction in any medium, provided the original work is properly cited.

Deep coal seams are characterized by large stress, high gas pressure, and low permeability. The gas disaster threatens the safe production of coal mine seriously. Gas extraction by crossing-seam boreholes from floor roadway (GECMBFR) can reduce the pressure and content of coal seam gas, which is the main measure to prevent gas disaster. Considering the Klinkenberg effect, governing equations of gas adsorption/desorption-diffusion, gas seepage, and stress fields within the coal seam are established to form the seepage-stress coupling model. The governing equations are embodied into a finite element driven software to numerically simulate gas migration and fluid-solid coupling law in coal seam. On this basis, the process of gas extraction under different borehole spacings and diameters is simulated. The effects of these two key parameters on coal seam gas pressure, gas content, and gas permeability were analyzed. The borehole spacing and diameter were determined to be 5 m and 0.09 m, respectively. Combined with the actual situation of a mine, the process of gas extraction from floor roadway with different cross-sectional schemes, ordinary drilling boreholes and punching combined drilling boreholes, is comparatively analyzed. The results show that the gas extraction effect by ordinary drilling boreholes is lower than that of the punching combined drilling boreholes, and the extraction is uneven and makes it difficult to meet the standard. Hydraulic punching was carried out, and coal was washed out of the borehole, which expanded the contact area between the borehole wall and coal seam. The coal seam around the punching borehole is unloaded, which improves coal permeability and accelerates gas migration towards the borehole, thus promoting the efficiency of gas extraction. It is more reasonable to use punching combined drilling borehole scheme when implementing the GECMBFR technology.

1. Introduction

As the mining depth increases, gas pressure and content in coal seam increase. This may lead to gas accidents such as coal and gas outburst and gas explosion, which seriously threaten the safety production of coal mine [1, 2]. Gas extraction by borehole drilling from floor roadway can effectively reduce coal seam gas and eliminate gas disaster risk [3]. Reasonable arrangement parameters of extraction boreholes can avoid blind extraction area among boreholes and improve gas extraction volume. Meanwhile, an optimal scheme will reduce drilling construction and thus decrease the cost of field application. Understanding the law of gas migration in the coal seam is the key to determine the reasonable borehole parameters [4].

Scholars have studied the interaction relationship between coal and gas. They consider that the change of geostress and gas pressure in the coal seam will cause coal deformation and change of porosity and permeability. For instance, Liang et al. [5], Xu et al. [6], and Connell [7] established gas-solid coupling models of coal and gas under different stress conditions. Then, the gas ad/desorption-induced coal deformation is introduced into the gas-solid coupling model [8–10]. In fact, the existence of water in the coal seam will occupy the migration channel of methane and reduce the relative permeability of gas phase [11, 12]. At the same time, the gas flow in the coal seam is very different from the liquid flow, because the effective permeability depends on the compressibility and gas pressure [13]. The dependence of coal seam permeability on gas pressure is called the Klinkenberg

effect. It has important influence on gas flow behavior [14]. In previous studies, the Klinkenberg effect is often ignored, resulting in large errors in borehole design and gas extraction calculation [15, 16].

In this study, considering the action of the Klinkenberg effect, the seepage-stress coupling model for gas extraction from coal seam is established by combining the controlling equations of gas diffusion field in coal matrix, gas seepage field in fractures, and stress field within the coal seam. The mathematical equations were embedded into the finite element (FE) analysis software to model the gas extraction through boreholes from floor roadway. The influence of borehole spacing and borehole diameter on gas extraction through boreholes is analyzed. And the research results provide guidance for optimizing the borehole schedule of gas extraction.

2. Seepage-Stress Coupling Model for Coal Seam Gas Extraction

Considering the occurrence environment of coal seam gas, we put forward the following assumptions [17–19]: (1) coal seam is an elastic continuous medium, which contains both fractures and porous matrix; (2) gas adsorbs on the surface of both pores and fractures, and gas transports in the space of pores and fractures in the state of free; (3) with the process of gas extraction, gas first desorbs from the surface of pores and then diffuses into fractures and finally seepages into boreholes from the fractures, obeying the Langmuir adsorption law, Fick's law, and Darcy's law, respectively; and (4) gas is a kind of ideal gas.

2.1. Controlling Equation of Seepage Field. Coal seam is structured by pores, fractures, and solid phase. Coal seam gas is generated from the solid phase and stored within the pores and fractures. In the coal matrix, gas content includes adsorbed and free gas. The gas content in the coal matrix can be expressed as [20]

$$m_m = V_{sg}\rho_s\rho_{gs} + \varphi_m\rho_{mg}, \quad (1)$$

where V_{sg} is volume of adsorbed coalbed methane, m^3/kg ; ρ_s is density of coal skeleton, kg/m^3 ; ρ_{gs} is gas density in standard state, kg/m^3 ; φ_m is the porosity of the coal matrix; and ρ_{mg} is gas density in the coal matrix, kg/m^3 .

Gas existing in the space of pores and fractures obeys the ideal gas law. The density of free gas is given as

$$\rho_g = \frac{M_g}{RT}p, \quad (2)$$

where M_g is molar mass of gas, kg/mol ; R is molar constant of gas, $J/(mol\cdot K)$; T is geothermal temperature, K ; and p is gas pressure, MPa .

The volume of adsorbed coalbed methane in coal matrix can be defined by Langmuir law [10]:

$$V_{sg} = \frac{V_L p_m}{P_L + p_m}, \quad (3)$$

where V_L and P_L are the Langmuir constants and p_m is gas pressure in matrix, Pa .

Before the operation of gas extraction, the coal seam gas is in the state of equilibrium, namely, gas pressure in pores equals that of gas in fractures. After implementing gas extraction, the equilibrium is disturbed, and the gas desorbs from the surface of pores and diffuses into the fractures driven by concentration gradient. By using Fick's law, the mass conservation in the porous matrix is obtained [13]:

$$\frac{\partial m_m}{\partial t} = -\frac{M_g}{\tau RT}(p_m - p_f), \quad (4)$$

where p_f is gas pressure in coal fracture, MPa , and τ is diffusion time, s .

Combining Equations (1)–(4), the controlling equation of gas migration in the matrix is gained:

$$\frac{\partial}{\partial t} \left(\frac{V_L p_m}{P_L + p_m} \rho_s \frac{M_g}{RT_s} p_s + \varphi_m \frac{M_g}{RT} p_m \right) = -\frac{M_g}{\tau RT} (p_m - p_f). \quad (5)$$

For gas transporting in a fracture system, the diffused gas from the coal matrix acts as the mass source, and the gas mass conservation of the fracture system can be expressed as [21]

$$\frac{\partial (\varphi_f \rho_g)}{\partial t} + \nabla \cdot (\rho_g \vec{q}_g) = (1 - \varphi_f) \frac{M_g}{\tau RT} (p_m - p_f), \quad (6)$$

where φ_f is porosity of fracture and \vec{q}_g is seepage velocity of gas, m/s .

The Klinkenberg effect will increase the apparent permeability especially when the gas pressure is low. Considering this, we define the gas flow rate in the fracture as [21, 22]

$$\vec{q}_g = -\frac{k}{\mu_g} \left(1 + \frac{b_k}{p_f} \right) \nabla p_f, \quad (7)$$

where k is fracture permeability, m^2 ; μ_g is gas dynamic viscosity, $Pa\cdot s$; and b_k is slippage factor, Pa .

Submitting Equation (7) into (6), the controlling equation of seepage field of gas can be obtained:

$$\frac{\partial}{\partial t} \left(\varphi_f \frac{M_g}{RT} p_f \right) + \nabla \cdot \left(-\frac{M_g (p_f + b_k) k}{RT \mu_g} \nabla p_f \right) = (1 - \varphi_f) \frac{M_g}{\tau RT} (p_m - p_f). \quad (8)$$

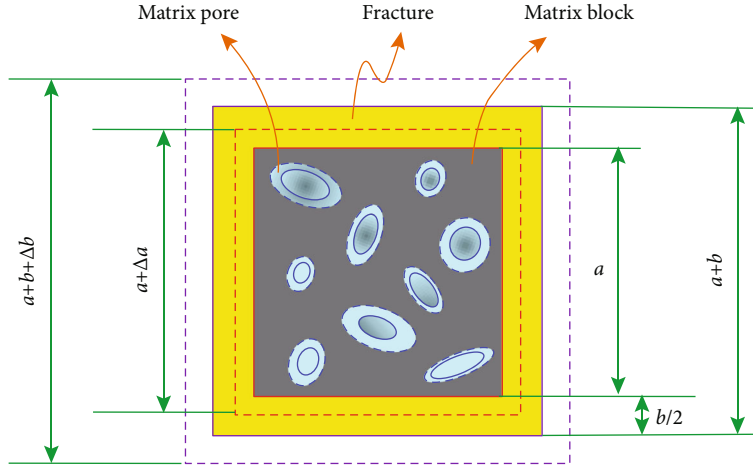


FIGURE 1: Conceptual model of representational element volume of coal mass.

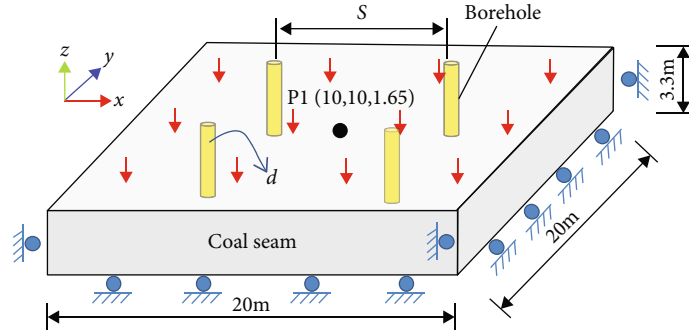


FIGURE 2: Geometric model for investigating the influence of borehole parameters on gas extraction.

2.2. *Controlling Equation of Stress Field.* The strain of coal mass is the sum of strain caused by stress, gas pressure, gas ad/desorption, and temperature change [20]:

$$\varepsilon_{ij} = \frac{1}{2G} \sigma_{ij} - \left(\frac{1}{6G} - \frac{1}{9K} \right) \sigma_{kk} \delta_{ij} + \frac{\alpha_m p_m + \alpha_f p_f}{3K} \delta_{ij} + \frac{\varepsilon_a}{3} \delta_{ij}, \quad (9)$$

where δ_{ij} is Kronecker sign; D is modified elastic modulus, GPa; $D = 1/(1/E_s + 1/(aK_n))$; G is shear modulus of coal, GPa; $G = D/2(1 + \nu)$; K is volume modulus of coal, GPa, $K = D/3(1 - 2\nu)$; K_s is volume modulus of coal skeleton, GPa; K_n is the stiffness of fracture, GPa; ν is the Poisson ratio; α_m and α_f are effective stress coefficients; a is the length of matrix, m; ε_a is gas adsorption-caused strain of coal skeleton, which is proportional to adsorption capacity [13]:

$$\varepsilon_a = \alpha_{sg} V_{sg}, \quad (10)$$

where α_{sg} is strain coefficient of gas adsorption, kg/m^3 .

According to the classical mechanics, the strain-displacement equation and static equilibrium of coal seam can be derived as

$$\begin{cases} \varepsilon_{ij} = \frac{1}{2} (u_{i,j} + u_{j,i}), \\ \sigma_{ij,j} + F_i = 0, \end{cases} \quad (11)$$

where F is volume force, Pa; u is the displacement, m; and the subscript i and j stand for the direction of x , y , and z .

Combining Equations (9)–(11), the controlling equation of stress field can be obtained:

$$Gu_{i,jj} + \frac{G}{1-2\nu} u_{j,ji} - \alpha_m p_{m,i} - \alpha_f p_{f,i} - K\varepsilon_{a,i} + F_i = 0. \quad (12)$$

2.3. *Porosity and Permeability Equations.* The mechanical properties of coal seam are largely dependent on the structure of pores and fractures. Porosity and permeability are the key parameters for evaluating gas migration in coal. The variation of pores and fractures is closely related to the stress state, as well as the mechanical properties of coal seam.

TABLE 1: Relevant parameters for simulation of gas extraction.

Parameter name	Value	Parameter name	Value
Initial gas pressure of coal seam (p_0 , MPa)	1.0	Geothermal temperature (T_0 , K)	300
Gas adsorption volume constant (V_L , m ³ /kg)	0.0256	Adsorption strain coefficient (ϵ_{\max} , kg/m ³)	0.06
Gas adsorption pressure constant (P_L , MPa)	1.07	Molar mass of gas (M_g , g/Mol)	16
Gas dynamic viscosity (μ_g , Pa·s)	1.84×10^{-5}	Molar gas constant (R , J/(Mol·K))	8.314
Hydrodynamic viscosity (μ_w , Pa·s)	1.03×10^{-3}	Standard temperature (T_s , K)	273.5
Gas desorption time (τ , d)	1.21	Standard atmospheric pressure (p_s , kPa)	101
Initial porosity of coal (φ_{m0})	0.035	Coal density (ρ_c , kg/m ³)	1410
Initial fracture degree of coal (φ_{f0})	0.012	Initial permeability (k_{f0} , m ²)	1.8×10^{-17}
Slippage factor (b_k , MPa)	0.36	Poisson's ratio of coal (ν)	0.35

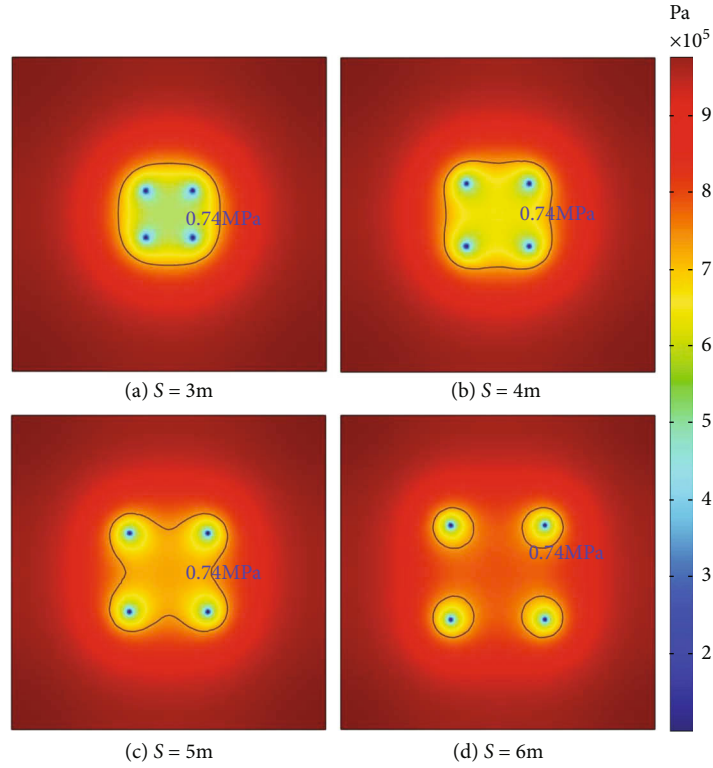


FIGURE 3: Gas pressure with different borehole spacings after 120 days' extraction.

The equation of matrix porosity is taken from a published literature, which is defined as [23]

$$\varphi_m = \frac{\varphi_{m0}(1 + S_0) + \alpha_m(S - S_0)}{(1 + S)}, \quad (13)$$

in which the strain $S = \epsilon_v + p_m/K_s - \epsilon_a$; ϵ_v is the volume strain of coal; and the subscript "0" stands for the initial state.

The conceptual model of presentational element volume (REV) in the coal seam is shown in Figure 1, where a is defined as the length of the matrix and b is the length of the fracture.

Fracture porosity is taken as [24]

$$\phi_f = \phi_{f0} + \frac{\phi_{f0}K_m}{3(K_f + K_m/r_{mt}^3 - K_m)} \left(\Delta\epsilon_a + \frac{\Delta\epsilon_v}{r_{mt}^3} + \frac{\alpha_m\Delta p_m}{K_m} \right), \quad (14)$$

where K_f is improving fracture stiffness, $K_f = bK_n$, GPa; $r_m = a/(a + b)$ is defined as the proportion of matrix length to the REV length; and K_m is the bulk modulus of the matrix, Pa.

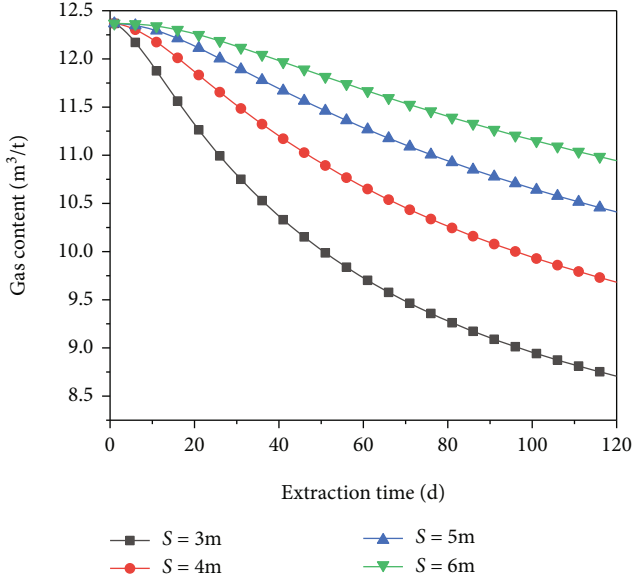


FIGURE 4: Gas content in the coal seam with different borehole spacings.

The cubic law is adopted to illustrate the relation of fracture permeability and fracture porosity [25], which is expressed as

$$\frac{k}{k_0} = \left(\frac{\varphi_f}{\varphi_{f0}} \right)^3. \quad (15)$$

Submitting Equation (14) into Equation (15), the available fracture permeability is

$$k = k_0 \left(1 + \frac{K_m}{3(K_f + K_m/r_{mt}^3 - K_m)} \left(\Delta\varepsilon_a + \frac{\Delta\varepsilon_v}{r_{mt}^3} + \frac{\alpha_m \Delta p_m}{K_m} \right) \right)^3, \quad (16)$$

where k_0 is initial permeability, m^2 .

By using the partial differential equations of Equations (5), (8), and (12)–(16), the seepage-stress coupling model is obtained, and the partial differential equations can be embedded into software by programming to simulate the law of gas extraction by drilling through floor roadway.

3. Effects of Borehole Spacing and Diameter on Gas Extraction through Boreholes

3.1. Geometric Model and Definite Solution Condition. In order to design and optimize the layout scheme of gas extraction through boreholes in floor extraction roadway, the influence of borehole spacing and borehole diameter on gas extraction through boreholes was studied. The three-dimensional geometric model of gas extraction through boreholes in floor roadway is constructed, as shown in Figure 2. Coal seam is a cuboid with a size of $20\text{ m} \times 20\text{ m} \times 3.3\text{ m}$. The four borehole centers are square and

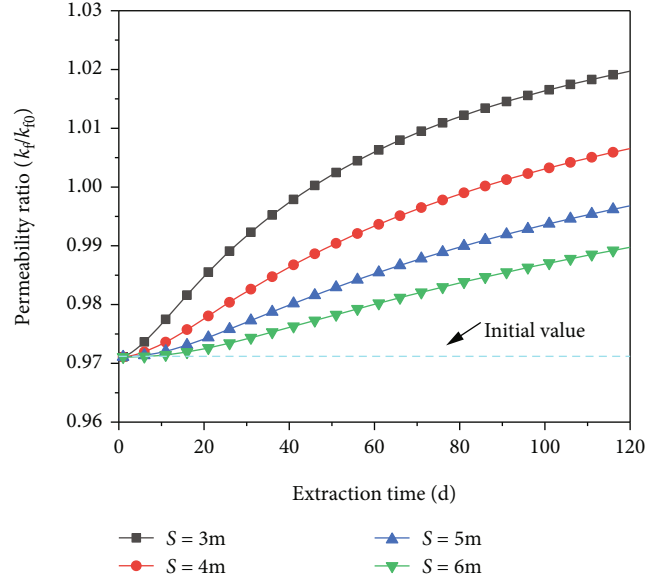


FIGURE 5: Coal permeability with different borehole spacings.

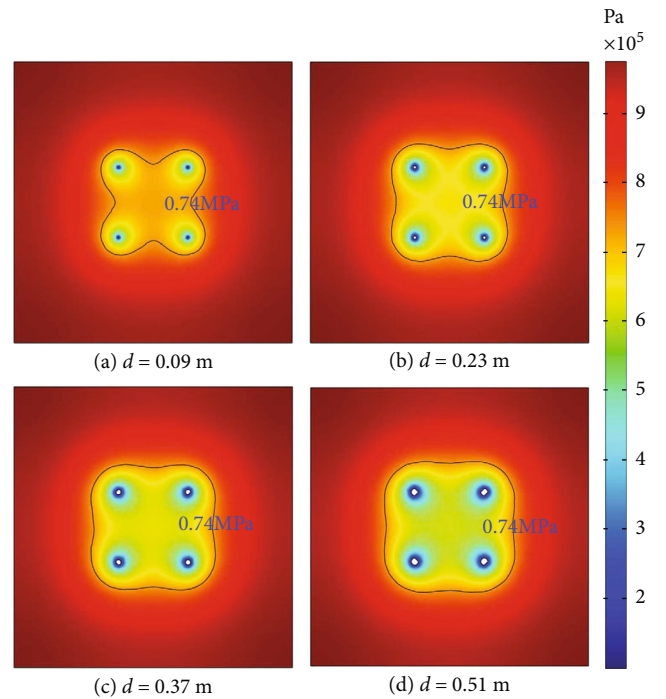


FIGURE 6: Gas pressure in the coal seam with different borehole diameters.

arranged in the center of the model. The borehole spacing is S , while the borehole diameter is d .

When solving the mathematical model, the sliding boundary is around the geometric model in Figure 2. The bottom is fixed boundary, and the top is applied with 15 MPa of vertical stress. The external sides of the model are set as impermeable boundaries, indicating that there are no gas flows at these boundaries. The borehole wall of the extraction borehole is set as the pressure boundary condition,

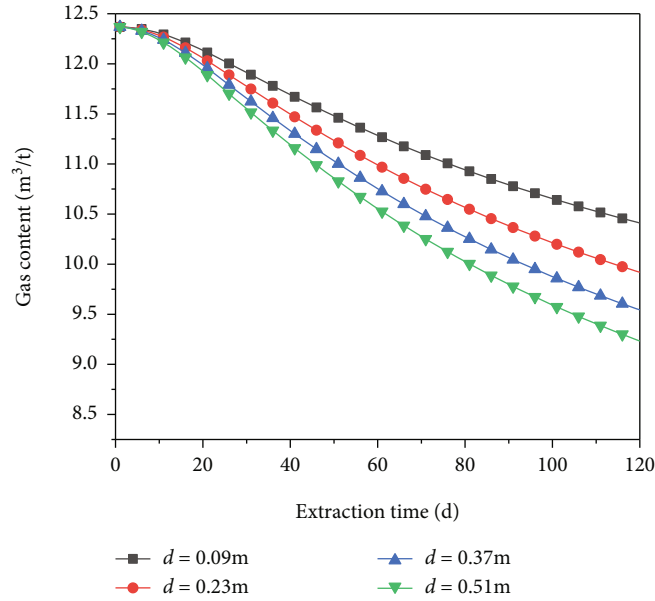


FIGURE 7: Gas content in the coal seam with different borehole diameters.

and the extraction pressure is 20 kPa. For the simulation of gas extraction by crossing-seam boreholes, the initial gas pressure is 1.0 MPa, and the initial permeability is $1.8 \times 10^{-17} \text{ m}^2$. Other relevant parameters are shown in Table 1.

In order to facilitate the analysis, the single variable control method is used. On the basis of keeping other parameters unchanged, the gas extraction law of borehole spacing or diameter in the range of change is discussed. In other words, when the borehole spacing is studied, the borehole diameter is fixed to 0.09 m, and the borehole spacing is set to 3 m, 4 m, 5 m, and 6 m, respectively. To reveal the influencing law of varying borehole diameters on the gas extraction efficiency, we set four sizes of borehole diameter starting from 0.09 m with an interval of 0.14 m. When the borehole diameter is research objectives, the borehole spacing is fixed to 5 m, and the borehole diameter is set to 0.09 m, 0.23 m, 0.37 m, and 0.51 m, respectively.

3.2. Effect of Borehole Spacing on Gas Extraction by Crossing-Seam Boreholes. After 120 days' gas extraction, the contour of gas pressure with a borehole spacing of 3 m, 4 m, 5 m, and 6 m is shown in Figure 3.

The black line represents the gas pressure 0.74 MPa. When the gas pressure is lower than 0.74 MPa, it meets requirements of gas extraction. Under the action of extraction pressure, coal seam gas migrates into the borehole, and the gas pressure near the borehole decreases. With the operation of extraction, the area of gas pressure reduction extends outward. After 120 days' extraction, the volume of effective gas extraction for a borehole spacing of 3 m, 4 m, 5 m, and 6 m is 119.75, 143.65, 152.69, and 69.43 m^3 , respectively. It is visible; the borehole spacing is not the greater the better, nor the smaller the better. When the borehole spacing is 5 m, the effective gas extraction area is the largest and the efficiency of gas extraction is the highest.

Under different borehole spacings, the variation of gas content with time at reference point P1 is shown in Figure 4. With the prolonging of gas extraction, the gas content at the reference point gradually decreases. In the same time interval, the decline of gas content at the initial stage is greater than that at the late stage of extraction. The greater the borehole spacing, the smaller the degree of gas content reduction. Meanwhile, the decrease of gas content is nonlinear with the increase of borehole spacing. For example, at 60 days of extraction, the gas content at the reference point P1 with 3, 4, 5, and 6 m borehole spacing is 9.73, 10.67, 11.29, and 11.68 m^3/t , respectively, which is 21.29%, 13.66%, 8.69%, and 5.49% lower than that of the original gas content. After 120 days' extraction, the gas content is 8.71, 9.68, 10.41, and 10.94 m^3/t , respectively, which is 29.55%, 21.66%, 15.76%, and 11.46% lower than the original gas content, respectively.

Under different borehole spacings, the variation of coal seam permeability with time at position P1 of reference point is shown in Figure 5. From the Equation (16), the actual permeability of coal seam is the result of the competition of permeability in free stress state and the coaction of gas pressure, ground stress, and adsorption deformation. The permeability ratio of coal seam at the reference point P1 at the initial stage of extraction is 0.9713. With the increase of extraction time, the permeability of the reference point position increases gradually. The larger the borehole spacing is, the smaller the increase of permeability is, and the two are nonlinear. After 120 days of extraction, the permeability ratios of coal seams were 1.0197, 1.0065, 0.997, and 0.9897, respectively, which were 5.01%, 3.66%, 2.65%, and 1.93% higher than the original permeability, respectively.

3.3. Effect of Borehole Diameter on Gas Drainage by Crosslayer Boreholes. When gas extraction is conducted for 120 days, the gas pressure distribution in the coal seam with a borehole diameter of 0.09 m, 0.23 m, 0.37 m, and 0.51 m is

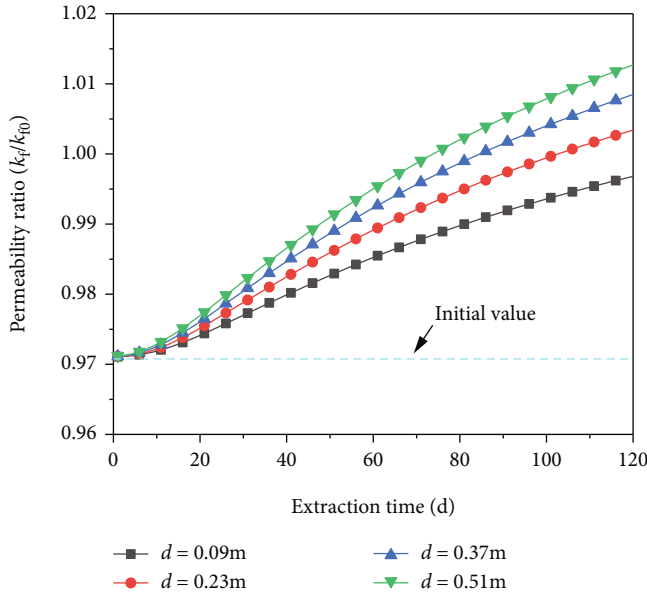


FIGURE 8: Coal permeability with different borehole diameters.

presented in Figure 6. The gas pressure of 0.74 MPa in the coal seam is considered as the requirement of effective gas extraction. The increase of borehole diameter expands the contact area between borehole wall and coal seam, and the area of gas pressure reduction increases. After 120 days of extraction, the effective gas extraction volumes with borehole diameters of 0.09 m, 0.23 m, 0.37 m, and 0.51 m were 152.69 m³, 208.49 m³, 240.18 m³, and 263.78 m³, respectively. The effective gas extraction volume of 0.51 m borehole diameter increased by 111.09 m³ compared with 0.09 m borehole diameter, which increased by 72.75%. When the borehole diameter is 0.09 m, the effective extraction area of the four boreholes has been connected into pieces to meet the extraction requirements.

Gas content at reference point P1 with the different borehole diameters of 0.09 m, 0.23 m, 0.37 m, and 0.51 m varies, as shown in Figure 7. The greater the diameter is, the smaller the residual gas content is. After 120 days' extraction, the gas content of reference point P1 with borehole diameters of 0.09 m, 0.23 m, 0.37 m, and 0.51 m were 10.41 m³/t, 9.92 m³/t, 9.54 m³/t, and 9.23 m³/t, respectively, which were 3.298 m³/t, 3.791 m³/t, 4.166 m³/t, and 4.477 m³/t lower than those of initial gas content -13.71 m³/t. It can be found that the borehole diameter of 0.51 m is 4.67 times larger than that of 0.09 m, while the decrease amplitude of gas content only increases by 0.36 times. Therefore, gas content cannot be reduced multiply when the borehole diameter multiplied. The decrease of gas content is the comprehensive effect of permeability, gas pressure gradient, and borehole diameter.

Figure 8 shows the permeability variation in the coal seam with time at reference point P1 under different borehole diameters. With the development of gas extraction, the permeability of the reference point position increases gradually, which is mainly controlled by the shrinkage of coal matrix. The greater the borehole diameter is, the higher the increment of permeability is, and both of them are nonlinear. After 120 days' extraction, coal permeabilities were

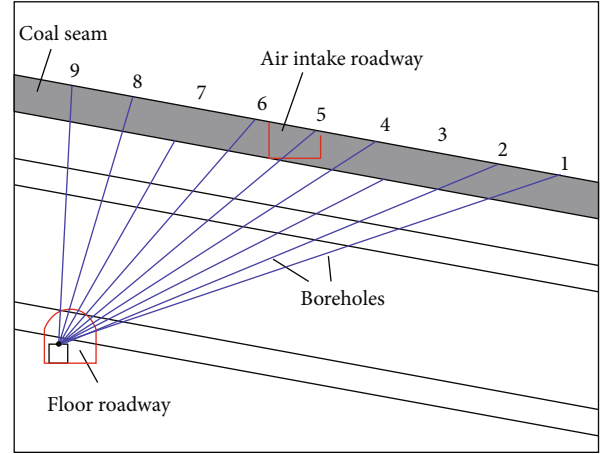


FIGURE 9: Section of gas extraction boreholes drilling from floor roadway.

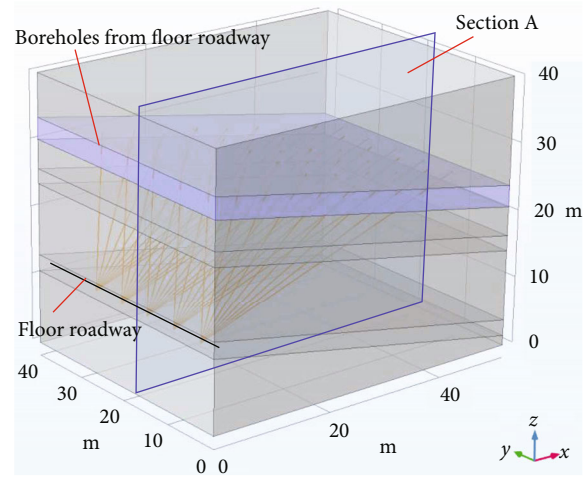


FIGURE 10: Geometric model of gas extraction boreholes drilling from floor roadway.

0.9968, 1.0034, 1.0085, and 1.0127, respectively, which were 2.65%, 3.33%, 3.86%, and 4.95% higher than the original permeability, respectively.

4. Scheme Optimization of Gas Extraction by Crossing-Seam Boreholes from Floor Roadway

The length of the mine field in a coal mine is about 4 km north and south, and the width of the east and west is about 3 km. The mine field area is 12.87 km², and the approved production capacity is 1.4 million t/a. The dynamic phenomena of coal and gas outburst occurred 28 times in total. The types of gas outburst were mainly pressure, outburst, and dumping. The maximum outburst gas amount was 25704 m³, and the maximum outburst coal amount was 293 t. With the depletion of shallow coal resources, coal mining gradually shifts to the deep. The coal seam shows complex occurrence conditions, high geostress, high gas, and low permeability, and the outburst risk increases.

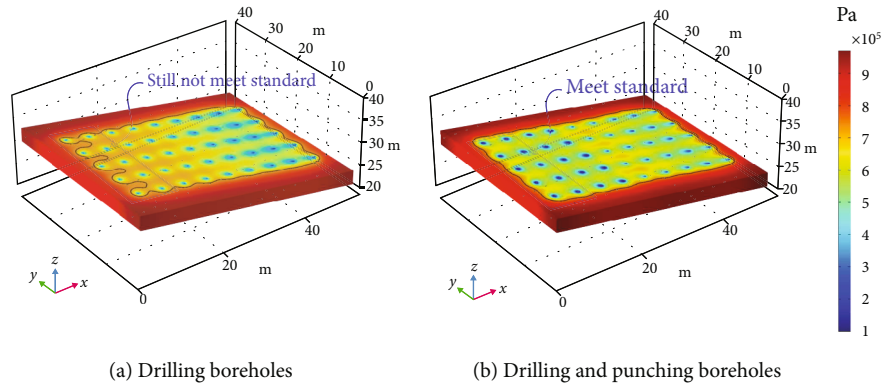


FIGURE 11: Gas pressure in the coal seam after 120 days' extraction.

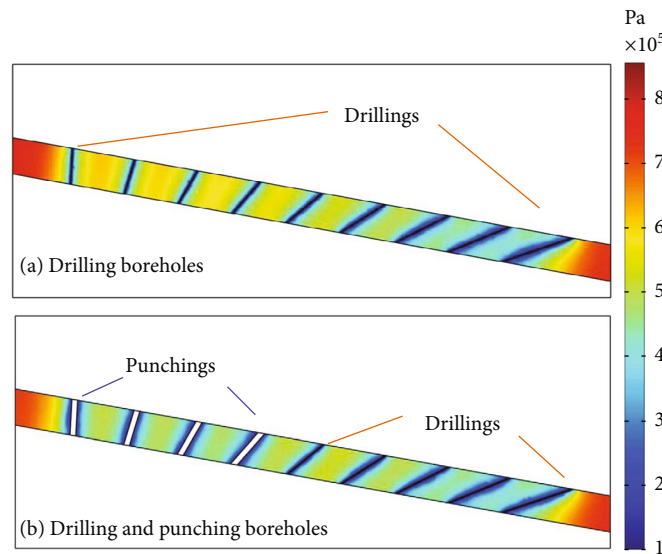


FIGURE 12: Gas pressure distribution on section A under two extraction schemes.

The construction was carried out at 20 m outside the floor gas extraction roadway of intake roadway, and the interval between the two roadway layers was 18 m. Starting at 35 m from the floor roadway opening, a group of boreholes were designed for each 6 m, with 9 boreholes in each group, and the aperture was 89 mm. The borehole control range is 15 m outside the contour line of the two sides of the intake roadway. The depth of the borehole is 0.5 m above the roof of the 15 coal seam. Figure 9 is the plane layout of the gas extraction borehole in the floor roadway. In addition, in order to compare and analyze and optimize the scheme, the pore size of 6 #~9 # borehole is expanded to 500 mm by hydraulic punching in Figure 9; that is, 1 #~5 # is ordinary extraction borehole and 6 #~9 # is hydraulic punching.

According to the gas extraction scheme of intake roadway, a three-dimensional geometric model of numerical calculation is established (Figure 10). Reference section A is set in the geometric model to observe the change of gas pressure in the coal seam.

Figure 11 shows the gas pressure distribution nephogram of the two extraction schemes after 120 days of extraction. In

Figure 11(a), the gas pressure drops faster in coal seams far from the floor extraction roadway and slower in coal seams near the floor extraction roadway. After 120 days of extraction, there are still substandard extraction areas that do not meet the requirement of less than 0.74 MPa near the floor extraction roadway. By comparison, it is found that the gas pressure in the coal seam near or far from the floor extraction roadway in Figure 11(b) decreases rapidly. This is due to the hydraulic punching of four boreholes close to the floor roadway, which expands the borehole diameter. The extraction effect of hydraulic punching is obviously better than that of ordinary drilling. The main reasons may include the following: (1) hydraulic punching flushes the coal out of the borehole, expanding the contact area between the borehole wall and the coal seam; (2) after the coal is washed out, the coal around the hydraulic punching is unloaded. The permeability of coal seam is improved, the speed of gas migration to borehole is accelerated, and the efficiency of gas extraction is promoted.

As illustrated in Figure 12, the gas pressure of coal seam on section A is extracted. Figure 12(a) shows the results of

cross section using a crosslayer drilling scheme, and Figure 12(b) shows the results of gas extraction using five crosslayer drilling and four hydraulic punching. In the case of scheme 1, that is, through-layer drilling scheme is adopted for all sections. The gas pressure decreases significantly in the area far from the floor extraction roadway, while the gas pressure decreases slightly in the area near the floor extraction roadway. The reason is that the inclination angle of the borehole far from the floor extraction roadway is small, the trajectory through the coal seam is longer, and the contact area formed with the coal seam is larger. Under the same negative pressure of extraction, the extraction effect is better. In the case of scheme 2, the hydraulic punching is used near the floor extraction roadway, and the ordinary drilling is used far from the floor extraction roadway. In the area where the hydraulic punching is arranged, the gas pressure decreases rapidly, and the extraction reaches the standard after 120 days. In the case of scheme 2, namely, hydraulic punching is adopted near the floor pumping roadway on the cross section. The scheme of ordinary drilling is adopted far from the floor extraction roadway. In the area where hydraulic punching is arranged, the gas pressure drops rapidly, and the extraction can reach the extraction standard after 120 days of extraction. In summary, using the extraction scheme of full-section ordinary crosslayer drilling, the extraction effect on the side near the floor extraction roadway is lower than that on the side far from the floor extraction roadway due to the short trajectory of crosslayer drilling through the coal seam, which leads to uneven extraction and difficulty in reaching the standard. The gas efficiency will be greatly improved by further hydraulic punching on the basis of the borehole near the floor extraction roadway, expanding the borehole diameter and increasing the exposed area of the borehole coal wall. At the same time, hydraulic punching is not required for all boreholes, which saves the construction cost. Therefore, it is more reasonable to adopt the scheme of common through-layer drilling and hydraulic punching.

5. Conclusions

- (1) The controlling equations of gas adsorption/desorption-diffusion field in coal matrix, gas seepage field, and stress field in coal fracture are derived on the basis of assuming coal seam as pore-fracture dual-porosity medium. Combined with the coupling terms such as porosity and permeability, the seepage-stress coupling model of gas migration considering the Klinkenberg effect is established, which can be used to study the law of coal seam gas extraction
- (2) The gas extraction law of a four-hole model in horizontal coal seam was simulated, and the influence of borehole spacing and diameter on gas pressure, gas content, and coal permeability after different extraction times was analyzed. Under the simulated coal seam conditions, the effective extraction area increases first and then decreases with the borehole spacing. And the borehole spacing of 5 m is more reasonable. The effective extraction area increases with

the increase of borehole spacing. Under the conditions permitted, increasing the borehole diameter will significantly improve the efficiency of gas extraction

- (3) The gas extraction process of floor roadway crossing layer under the full-section ordinary drilling scheme and the hydraulic punching combined with ordinary drilling scheme was compared and analyzed. Adopting hydraulic punching near floor extraction roadway, enlarging borehole diameter, and increasing exposure area of borehole wall will greatly improve gas efficiency. It is more reasonable to adopt the scheme of common crossing-seam drilling combined with hydraulic punching boreholes

Coal seam is characterized by heterogenous properties, while the change of coal seam temperature will have an impact on the results. Therefore, the heterogeneity of coal seam and the thermal effect will be considered in the future works.

Data Availability

The data used in this article were from the simulation results by COMSOL Multiphysics. The equations were written as COMSOL codes independently to conduct these simulations. The data are available from the corresponding author upon request.

Conflicts of Interest

The authors declare no competing financial interest.

Acknowledgments

This research was financially supported by the National Natural Science Foundation of China (Grant No. 51774165) and the project of discipline innovation team of Liaoning Technical University (Grant No. LNTU20TD-05).

References

- [1] I. Palmer, "Coalbed methane completions: a world view," *International Journal of Coal Geology*, vol. 82, no. 3-4, pp. 184-195, 2010.
- [2] C. Fan, S. Li, D. Elsworth, J. Han, and Z. Yang, "Experimental investigation on dynamic strength and energy dissipation characteristics of gas outburst-prone coal," *Energy Science & Engineering*, vol. 8, no. 4, pp. 1015-1028, 2020.
- [3] W. He, F. He, K. Zhang, Y. Zhao, and H. Zhu, "Increasing permeability of coal seam and improving gas drainage using a liquid carbon dioxide phase transition explosive technology," *Advances in Civil Engineering*, vol. 2018, Article ID 3976505, 15 pages, 2018.
- [4] C. Fan, S. Li, M. Luo, W. Du, and Z. Yang, "Coal and gas outburst dynamic system," *International Journal of Mining Science and Technology*, vol. 27, no. 1, pp. 49-55, 2017.
- [5] B. Liang, M. Zhang, and Y. Wang, "Mathematical model and numerical method for coupled gas flow in coal seams and coal deformation," *Chinese Journal of Rock Mechanics and Engineering*, vol. 15, no. 2, pp. 40-47, 1996.

- [6] T. Xu, C. Tang, L. Song, T. Yang, and Z. Liang, "Numerical simulation of coupled gas flow in failure process of gassy coal-rock," *Chinese Journal of Rock Mechanics and Engineering*, vol. 24, no. 10, pp. 1667–1673, 2005.
- [7] L. Connell, "Coupled flow and geomechanical processes during gas production from coal seams," *International Journal of Coal Geology*, vol. 79, no. 1-2, pp. 18–28, 2009.
- [8] P. Guo, S. G. Cao, Z. G. Zhang, Y. Li, Y. B. Liu, and Y. Li, "Analysis of solid gas coupling model and simulation of coal containing gas," *Journal of China Coal Society*, vol. 37, no. 1, pp. 330–335, 2012.
- [9] G. Yin, M. Li, S. Li, W. Li, J. Yao, and Q. Zhang, "3D numerical simulation of gas drainage from boreholes based on solid gas coupling model of coal containing gas," *Journal of China Coal Society*, vol. 38, no. 4, pp. 535–541, 2013.
- [10] T. Xia, F. Zhou, J. Liu, and F. Gao, "Evaluation of the pre-drained coal seam gas quality," *Fuel*, vol. 130, pp. 296–305, 2014.
- [11] S. Chen, *Study on Coupled Deformation and Gas-Water Two Phase Flow Model for Fractured Coal and Rock*, Northeastern University, Shenyang, 2012, (thesis).
- [12] W. Zhao, K. Wang, R. Zhang, H. Dong, Z. Lou, and F. An, "Influence of combination forms of intact sub-layer and tectonically deformed sub-layer of coal on the gas drainage performance of boreholes: a numerical study," *International Journal of Coal Science & Technology*, vol. 7, no. 3, pp. 571–580, 2020.
- [13] W. Zhu, J. Liu, J. Sheng, and D. Elsworth, "Analysis of coupled gas flow and deformation process with desorption and Klinkenberg effects in coal seams," *International Journal of Rock Mechanics and Mining Sciences*, vol. 44, no. 7, pp. 971–980, 2007.
- [14] G. Hu, H. Wang, X. Fan, Z. Yuan, and S. Hong, "Mathematical model of coalbed gas flow with Klinkenberg effects in multiphysical fields and its analytic solution," *Transport in Porous Media*, vol. 76, no. 3, pp. 407–420, 2009.
- [15] C. Fan, D. Elsworth, S. Li, L. Zhou, Z. Yang, and Y. Song, "Thermo-hydro-mechanical-chemical couplings controlling CH₄ production and CO₂ sequestration in enhanced coalbed methane recovery," *Energy*, vol. 173, pp. 1054–1077, 2019.
- [16] T. Liu, B. Lin, X. Fu, Y. Zhao, Y. Gao, and W. Yang, "Modeling coupled gas flow and geomechanics process in stimulated coal seam by hydraulic flushing," *International Journal of Rock Mechanics and Mining Sciences*, vol. 142, article 104769, 2021.
- [17] J. Liu, L. Xie, D. Elsworth, and Q. Gan, "CO₂/CH₄ competitive adsorption in shale: implications for enhancement in gas production and reduction in carbon emissions," *Environmental science & technology*, vol. 53, no. 15, pp. 9328–9336, 2019.
- [18] J. Liu, L. Xie, Y. Yao, Q. Gan, P. Zhao, and L. Du, "Preliminary study of influence factors and estimation model of the enhanced gas recovery stimulated by carbon dioxide utilization in shale," *ACS Sustainable Chemistry & Engineering*, vol. 7, no. 24, pp. 20114–20125, 2019.
- [19] Q. Huang, S. Liu, W. Cheng, and G. Wang, "Fracture permeability damage and recovery behaviors with fracturing fluid treatment of coal: an experimental study," *Fuel*, vol. 282, article 118809, 2020.
- [20] C. Fan, D. Elsworth, S. Li et al., "Modelling and optimization of enhanced coalbed methane recovery using CO₂/N₂ mixtures," *Fuel*, vol. 253, pp. 1114–1129, 2019.
- [21] P. Thararoop, Z. Karpyn, and T. Ertekin, "Development of a multi-mechanistic, dual-porosity, dual-permeability, numerical flow model for coalbed methane reservoirs," *Journal of Natural Gas Science and Engineering*, vol. 8, no. 9, pp. 121–131, 2012.
- [22] C. Wu, C. Yuan, G. Wen, L. Han, and H. Liu, "A dynamic evaluation technique for assessing gas output from coal seams during commingling production within a coalbed methane well: a case study from the Qinshui Basin," *International Journal of Coal Science & Technology*, vol. 7, no. 1, pp. 122–132, 2020.
- [23] Y. Wu, J. Liu, D. Elsworth, X. Miao, and X. Mao, "Development of anisotropic permeability during coalbed methane production," *Journal of Natural Gas Science and Engineering*, vol. 2, no. 4, pp. 197–210, 2010.
- [24] C. Fan, S. Li, H. Zhang, and Z. Yang, "Rational boreholes arrangement of gas extraction from unloaded coal seam," *Advances in Civil Engineering*, vol. 2018, 9 pages, 2018.
- [25] S. Li, C. J. Fan, J. Han, M. K. Luo, Z. H. Yang, and H. J. Bi, "A fully coupled thermal-hydraulic-mechanical model with two-phase flow for coalbed methane extraction," *Journal of Natural Gas Science and Engineering*, vol. 33, pp. 324–336, 2016.

Research Article

Numerical Simulation of Coal Spontaneous Combustion around a Borehole Induced by Negative Pressure Gas Drainage

Youxin Zhao ^{1,2}, Qingjie Qi^{1,2}, Xinlei Jia ^{3,4}, Yingjie Liu ^{1,2} and Jingwen Zhang^{1,2}

¹Emergency Science Research Academy, China Coal Research Institute, China Coal Technology & Engineering Group Co., Ltd., Beijing 100070, China

²State Key Laboratory of Efficient Mining and Clean Utilization of Coal Resources, Beijing 100013, China

³School of Safety Science and Engineering, Liaoning Technical University, Fuxin Liaoning 123000, China

⁴Key Laboratory of Mine Thermodynamic Disasters and Control of Ministry of Education, Fuxin Liaoning 123000, China

Correspondence should be addressed to Xinlei Jia; ybyfz@163.com

Received 22 April 2021; Revised 18 June 2021; Accepted 27 July 2021; Published 9 August 2021

Academic Editor: Bo Tan

Copyright © 2021 Youxin Zhao et al. This is an open access article distributed under the Creative Commons Attribution License, which permits unrestricted use, distribution, and reproduction in any medium, provided the original work is properly cited.

The suction negative pressure is an important factor affecting the spontaneous combustion of coal around a borehole. Because the mechanism of suction negative pressure in the gas extraction process remains unclear, a constant suction negative pressure is often used in coal mines, leading to a low efficiency of gas extraction in deep coal seams. Moreover, the coal body easily undergoes spontaneous combustion during the extraction process, which is not conducive to safe mining. To study the effect of the suction negative pressure near the end sealing section, a numerical model of the combustion process around a borehole under the influence of suction negative pressure was established using COMSOL. The variation laws of the gas seepage velocity, oxygen concentration, and coal temperature in the borehole cycle were analyzed, and the gas suction negative pressure under different sealing parameters was optimized to ensure efficient gas extraction and prevent the spontaneous combustion of coal. The results showed that the negative pressure of extraction provides the power required for gas seepage into the borehole, and the gas flow rate increases with increasing negative pressure of extraction, exhibiting a linear growth trend. The range of the coal suffocation zone around the sealing section decreases with the increase in the negative pressure. With the extension of the gas extraction time, the oxygen concentration decreases rapidly, and the inflection point advances with the increase in the negative pressure. When the negative pressure of gas extraction is <40 kPa, the range of the high-temperature area around the block increases with the negative pressure of gas extraction. Based on the present situation of the spontaneous combustion induced by gas drainage in the Pingdingshan No. 10 Coal Mine, different sealing parameters should be set with different negative pressures of extraction, and the negative pressure of extraction should not exceed -18 kPa when the sealing depth is 20 m and the sealing length is 8 m in the 24130 working face. These parameter settings can help effectively prevent spontaneous combustion during the extraction process.

1. Introduction

The negative pressure of gas extraction is one of the main indices affecting the progress of gas extraction in coal mines [1–5]. In the process of gas drainage along the bed, the negative pressure provides the power for gas extraction, and the gas and surrounding gas continuously flow into the extraction pipe through the fissured coal around the plugging sec-

tion, thus realizing gas extraction. An excessive negative pressure not only reduces the gas concentration in the borehole but also increases the oxygen content around the fissured coal, leading to a spontaneous combustion of the coal around the borehole. A low negative pressure increases the extraction time, and performing the extraction for a long duration can also easily lead to a spontaneous combustion. Therefore, setting a reasonable negative pressure for gas

extraction has important guiding significance for improving the gas extraction efficiency, shortening the construction period, and ensuring the safety of gas extraction [6].

Several theoretical and experimental studies have been conducted on the negative pressure and gas extraction efficiency. Liu et al. [7] proposed a mechanism-based model to theoretically describe the gas desorption, diffusion, and flow through coal around a drainage borehole. The proposed model was numerically solved and verified with borehole drainage data obtained from a mine site. Zhang et al. [8] designed a simulation test platform and performed a numerical simulation on the gas seepage characteristics. The optimal negative pressure of extraction was between 30 kPa and 40 kPa, and the extraction concentration was the highest at 35 kPa. Qi et al. determined the spontaneous combustion area of coal around a gas drainage borehole and optimized the gas drainage negative pressure using numerical simulation software, with the air flow velocity as the criterion [9–11]. The effects of gas concentration and coal spontaneous combustion characteristics on gas seepage and coal spontaneous combustion have been analyzed on the basis of the gas seepage theory, control equation, and combustion calculation model [12–17].

Despite the numerous studies on negative pressure drainage [18, 19], currently, the mechanism of spontaneous combustion induced by the negative pressure remains unclear, and a constant negative pressure is generally used in the gas drainage of coal mines. Some research results have shown that with the change in the sealing parameters, coal seam depth, and geological conditions, the gas leakage channel around the borehole changes significantly [20–22]. Moreover, with the increase in the gas extraction time, the surrounding oxygen concentration, seepage distribution, and coal temperature vary. The use of the constant negative pressure cannot solve the problem of gas extraction and coal spontaneous combustion. Based on the actual conditions in a mine, selecting reasonable drainage parameters is beneficial to improving the efficiency of coal seam gas drainage [23]. However, increasing the negative pressure of extraction aggravates the spontaneous combustion of the coal around the borehole [24–27]. Because of the particularity and complexity of the coal body environment around the gas extraction borehole, it is difficult to directly observe the surrounding gas concentration, seepage velocity distribution, and coal body temperature during the gas extraction process. Moreover, the laws of temporal and spatial evolutions cannot be directly reflected. A reasonable negative pressure for extraction is the key to solving the problems related to the gas extraction and coal spontaneous combustion zone around the borehole [28, 29].

Although considerable research has been conducted on negative pressure drainage, there are few studies on the mechanism of coal spontaneous combustion induced by the negative pressure. Based on the actual sealing situation of the 24130 working face of Pingdingshan No. 10 Mine and considering gas diffusion, permeability variation, coal oxidation reaction, and porous media heat transfer, this study established a gas drainage coupling model under different drainage negative pressure conditions. The simulation results

reveal the variations in the gas concentration, seepage distribution, and coal temperature around the borehole; help analyze the negative pressure of drainage under different sealing parameters; and lay a theoretical foundation for ensuring safe and efficient gas drainage.

2. Mathematical Modeling of Spontaneous Combustion of Coal around Boreholes Induced by Gas Drainage

2.1. Darcy's Law. The fractured coal body around a borehole is considered a porous medium space with nonuniform porosity and permeability. The permeability is a continuous function [30–32]. The gas seepage velocity in the porous medium can be expressed as in

$$\frac{\partial}{\partial t}(\varepsilon_p \rho) + \nabla \cdot (\rho \mu) = Q_m, \quad (1)$$

$$v = -\frac{k}{2\mu p_1} \frac{dP}{dl}. \quad (2)$$

In Equations (1) and (2), ε_p is the porosity, and the unit is 1; ∇ is the flow gradient; ρ is the mixed gas density, kg/m^3 ; p_1 is the negative pressure, Pa; v is the vector velocity of the air flow, m/s ; μ is the dynamic viscosity of the mixed gas; k is the permeability, m^2 .

2.2. Mass Transfer in Porous Media. The combustion of air in the fractured coal body around a borehole is a complicated process, and the volume fraction of the gas in the porous medium is affected by multiphysical parameters.

2.2.1. Governing Equation for the Gas around the Borehole.

$$p_{2,j} \frac{\partial c_i}{\partial t} + p_{1,i} \nabla \cdot \Gamma_i + u \cdot \nabla c_i = R_i + S, \quad (3)$$

$$p_{3,j} = \Delta_p. \quad (4)$$

In Equations (3) and (4) [29], p_2 is the original rock stress, MPa; R_i is the reaction rate, $\text{mol}/(\text{m}^3 \cdot \text{s})$, p_3 is the roadway pressure, MPa; Δ_p is the pressure of the coal body around the borehole, MPa.

The equations governing the gas diffusion process are as follows:

$$p_{1,i} = c_i \frac{\partial \Delta_p}{\partial t},$$

$$N_i = \Gamma_i + u c_i = -D_{e,j} \nabla c_i + u c_i, \quad (5)$$

$$D_{e,j} = \frac{\Delta_p}{\tau_{F,j}} D_{F,j},$$

where $D_{e,j}$ is the diffusion coefficient of different gases, m^2/s .

2.2.2. Coal Oxidation Reaction Equation. The air around the borehole reacts chemically with the coal, and the governing equation for the oxygen consumption reaction is as follows:

$$\frac{\partial c_i}{\partial t} + \nabla \cdot (-D_i \nabla c_i) + u \nabla c_i = R_i. \quad (6)$$

The oxygen consumption rate in Equation (6) is related to factors such as the coal spontaneous combustion characteristics, oxygen concentration, and temperature. The temperature and oxygen volume fraction have a greater impact on the oxygen consumption rate of the fractured coal body around the borehole. According to literature [33], the following is the general expression for the oxygen consumption rate:

$$R_c = -\frac{c(\text{O}_2)}{c^0(\text{O}_2)} \gamma_0 e^{\alpha(T-T_r)}. \quad (7)$$

In Equation (7), R_c is the oxygen consumption coefficient, $\text{mol}/(\text{m}^3 \cdot \text{s})$; $c^0(\text{O}_2)$ is the initial oxygen concentration, 1; $c(\text{O}_2)$ is the actual oxygen concentration, 1; T is the absolute temperature of the coal body, °C; T_r is the initial temperature of the coal seam, °C.

2.2.3. Porous Medium and Heat Transfer Fluid. The coal around the borehole chemically reacts with the outside air, and the heat released increases the temperature of the coal body around the borehole. According to the hypothesis of local heat balance, the heat transfer equation [34] for the spontaneous combustion process of coal is as follows:

$$C_{eq} \frac{\partial T}{\partial t} + \varphi \rho_g C_{pg} \bar{q} \cdot \nabla T - \nabla \cdot (k_{eq} \nabla T) = -R_c Q_T, \quad (8)$$

where C_{eq} is the heat capacity of the gas, $\text{kg} \cdot \text{K}$; k_{eq} is the thermal conductivity of the gas, $\text{J}/(\text{m} \cdot \text{K} \cdot \text{s})$; C_{pg} is the heat capacity of coal, $\text{J}/(\text{m} \cdot \text{K})$; Q_T is the heat of oxidation, kJ/mol .

3. Mathematical Model Construction

3.1. General Situation of 24130 Working Face in Pingdingshan No. 10 Mine. The Pingdingshan No. 10 Coal Mine of China Pingdingshan Coal Group Co., Ltd. is an outburst coal mine. The coal seam easily undergoes spontaneous combustion. The buried depth of the No. 15 coal seam in the 24130 working face is 1200 m. The gas drainage method mainly adopts the through-layer predraining gas technology and the gas prevention technology in the working face. The gas pressure range of the 15th and 16th coals of the No. 10 mine is 0.1–2.95 MPa, and the gas pressure range of the 17th coal is 0.4–1.85 MPa. The amount of gas in the 15th and 16th coals of the No. 10 mine is in the range of 2.15–20.04 m^3/t and that in the 17th coal is in the range of 6.49–12.13 m^3/t . The air permeability of the coal seam at the 24130 working face is 0.0019 MD, and the attenuation coefficient is 0.068 d^{-1} . The coal seam has poor air permeability and is difficult to extract. The inclination angle of the coal seams in the mining area varies significantly. The inclination angle of the coal seams south of the Shikuang syncline is in the range of 10–20°, and the coal seam inclination angles from the north of the Guozhuang anticline to the Likou syncline gradually decrease from 40° to 0–5°.

3.2. Model and Mesh. A 2D axisymmetric model is established for the spontaneous combustion of coal around a borehole induced by negative pressure drainage. The working face length (airway length) is 70 m, the working face width (cut hole length) is 160 m, and the depth of the borehole for gas drainage along the bedding based on an actual drilling diameter of 94 mm, the model drilling diameter is set to 100 mm considering drilling disturbance. Based on the actual situation of the 24130 working face, the coal seam temperature is set to 48°C, the sealing parameter is 20–8 (sealing depth-sealing length), and the suction pressures are 18, 23, 30, and 35 kPa. Figure 1 shows the constructed physical and geometric models. The grid is divided in a distributed manner. The maximum number of grid cells is 3.5, the minimum number of cells is 0.045, the maximum cell increase rate is 1.1, and the curvature factor is 0.3. The entire grid contains 24624 domain cells and 2546 boundary elements.

3.3. Key Parameters and Boundary Conditions. The permeability of the coal body around a drainage borehole is affected by both roadway excavation and drilling construction. The permeability and porosity of the coal body along the borehole direction decrease. The farther away from the center of the borehole, the lower the porosity and permeability. According to literature [32], the formula for the plastic zone radius is as follows:

$$R_L = a_0 \left[\frac{(p_2 + c \cot \varphi)(1 - \sin \varphi)}{p_4 + c \cot \varphi} \right]^{(1 - \sin \varphi)/(2 \sin \varphi)}, \quad (9)$$

where a_0 is the drilling radius, mm; φ is the internal friction angle of the rock mass, °; c is the cohesion of the rock mass, MPa; and p_4 is the support resistance, MPa.

Spontaneous combustion mainly occurs around the borehole; therefore, the coal around a single borehole is selected as the main calculation area. The main parameters of this model (Table 1) are from experimental results and references [30, 35]. Based on the actual situation, the initial and boundary conditions are listed in Table 1. Figure 1 shows the model of the spontaneous combustion around the borehole induced by gas drainage. No displacement constraints were applied to the upper, left, and right sides of the model boundary. The initial conditions of the gas–air seepage pressure conditions are $P_2(0) = 1.6$ MPa and $P_3(0) = 0.1$ kPa. The initial oxygen concentration is 0, the initial roadway temperature is 28°C, and the pressure of AB and BC is set to 0.1 kPa; GH, FG, and IH are $P_2(0) = 1.6$ MPa, oxygen convection AB and BC. The oxygen concentration at the boundary is 9.375 mol/m^3 ; CD, FG, and IH have no diffusive convection; AB, BC, GH, and IH have a thermal convection boundary; and CD and FG are adiabatic.

Table 1 lists the main parameters of the model. Based on a field test, the test borehole depth of the 24130 working face was set to 1200 m; the average bulk density of the overlying rock mass was $2.7 \times 10^4 \text{ N} \cdot \text{m}^{-3}$; the cohesive force was 2.1 MPa. The internal friction angle of the rock mass was 25°. The support resistance was 0.09 MPa. Substituting these parameters into Equation (9), we obtain $R_L = 0.25$ m. The

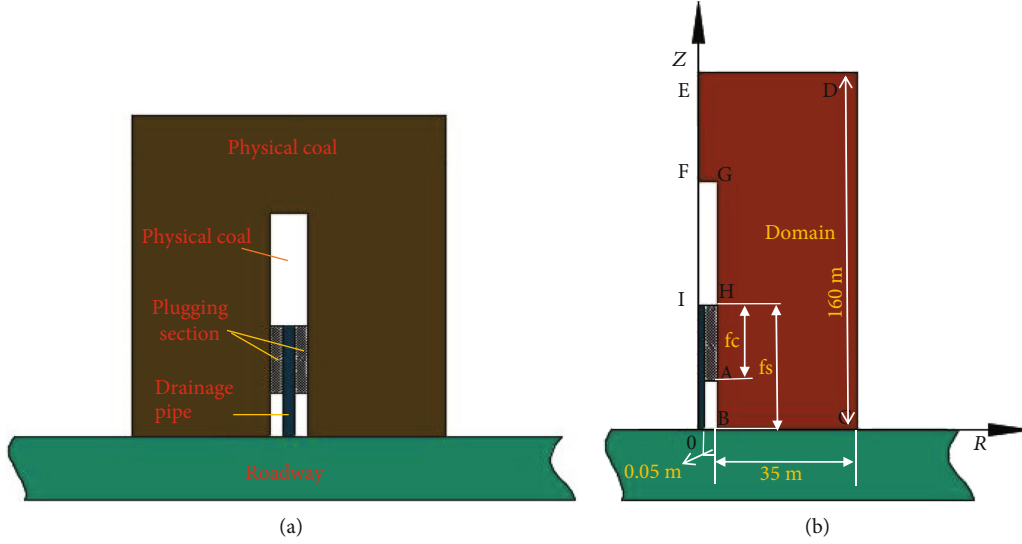


FIGURE 1: (a) Physical model and (b) simulation model of drainage borehole.

TABLE 1: Model parameters.

Parameters	Magnitude and unit	Parameters	Magnitude and unit
Coal density	1250 (kg/m ³)	Initial oxygen volume fraction	9.375 (mol/m ³)
Original coal permeability	0.039 (m ²)	Heat transfer coefficient	180 (W/(m ² ·K))
Methane heat capacity	1625 (J/(kg·K))	Gas viscosity	1.84 × 10 ⁻⁵ (Pa·s)
Coal heat capacity	1260 (J/(kg·K))	Air viscosity	1.79 × 10 ⁻⁵ (Pa·s)
Molar air mass	0.029 (kg/mol)	Oxygen consumption constant	0.036 (mol/(m ³ ·h))
Oxygen diffusion coefficient	1.6 × 10 ⁻⁴ (m ² /s)	Thermal conductivity of coal	0.26 (J/(m·s·K))
Oxidation heat of coal	19744.37 (J/g)		

empirical formula for the borehole permeability obtained by Louis [29] is expressed in Equation (10). Equation (11) expresses the coal seam permeability around the borehole at the 24130 working face of Pingdingshan No. 10 Mine:

$$k = k_0 e^{\eta(b-x)}, \quad (10)$$

$$k = 0.039 e^{1.4(0.156-x)}, \quad (11)$$

where k_0 is the initial coal seam permeability, m²; $b = R_L - r_0$ is the width of the plastic zone, m; η is the permeability growth coefficient of the equivalent fissure field around the borehole, taking a value of 1.4; and x is the coal permeability at a distance from the borehole center, m.

4. Analysis of the Temporal and Spatial Evolution Laws of Coal Spontaneous Combustion Induced by Negative Pressure Drainage

The wind speed of the gas leakage around the gas drainage borehole is a vector, and it is difficult to measure it during the gas drainage process. The oxygen concentration is affected by both the air leakage state and the oxygen state.

The area with a higher oxygen concentration has serious air leakage, the area with a high natural degree consumes more oxygen, and the oxygen concentration is low. The oxygen content reflects the supplying conditions of the coal body around the borehole and the heat storage conditions. The temperature of the coal body around the borehole is the most direct indicator reflecting the spontaneous combustion state around the borehole. Because the surrounding environment of the borehole is complicated, it is difficult to detect the internal temperature of the borehole [31]. Therefore, the numerical simulation method is used to study the spatial evolutions of the gas leakage streamlines, wind speed distribution, oxygen concentration, and temperature around the borehole under different suction negative pressure conditions.

4.1. Influence of Negative Pressure on the Gas Seepage Velocity around a Borehole. Figure 2 shows cloud diagrams of the gas seepage velocity around a gas drainage borehole, where the plugging depth is 20 m, the plugging length is 8 m, and the coal seam temperature is 48°C. As shown, the gas around the drainage borehole mainly flows from the roadway wall and the exposed borehole into the gas drainage pipe. The gas seepage gradient around the gas drainage borehole is high, and the gas gradient area is large. The main channel for gas leakage is via the extraction borehole. In Figures 2(a)–2(d), the seepage

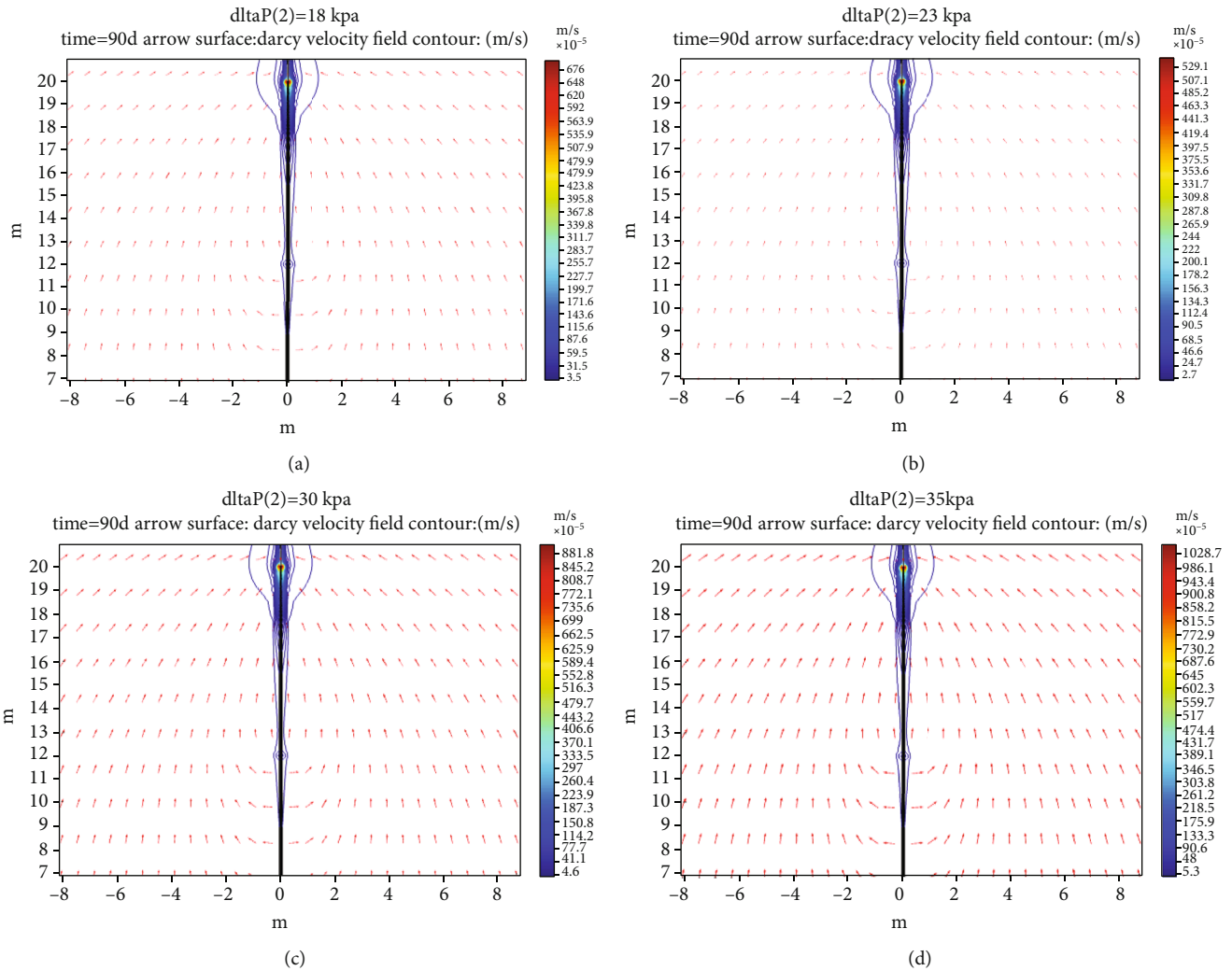


FIGURE 2: Cloud maps of the gas seepage velocity around a gas drainage borehole under suction pressures of (a) 18 kPa, (b) 23 kPa, (c) 30 kPa, and (d) 35 kPa.

velocity on the inner side of the plugging section of the gas drainage borehole is the highest, and when the negative pressures of drainage are 18, 23, 30, and 35 kPa, the maximum wind speeds at the inner end of the plugging section are 0.0053, 0.0068, 0.0081, and 0.01 m/s, respectively. With the increase in the plugging depth, the maximum velocity of the gas around the plugging section decreases, showing a negative correlation. In the range of 12–17 m in the plugging section, the wind flow velocity remains largely unchanged. The greater the negative pressure of drainage, the greater the gas seepage velocity around the gas drainage borehole; the two are positively correlated. The function relationship between the maximum gas seepage velocity around the gas drainage borehole and the negative pressure of drainage is $y = 2.6 \times 10^{-4}x + 5.72 \times 10^{-4}$, $R^2 = 0.98$, where x is the suction negative pressure (kPa), and y is the gas seepage velocity (m/s). The closer to the center of the gas drainage borehole, the greater the gradient of seepage increase, and the denser the seepage distribution line in the figure, the faster the increase in the seepage velocity of the surrounding gas.

Figure 3 shows the seepage distribution law of the monitoring points around the plugging section with different plugging parameters under different suction pressure conditions. The legend “18-20-0.1” indicates that the negative pressure of drainage is 18 kPa, the sealing depth is 20 m, and the distance from the center of the borehole is 0.1 m. Figures 3(a) and 3(b) show the seepage velocity distributions at $R = 0.1$ m and $R = 0.4$ m, respectively. As shown, when the sealing depth is 20 m, the sealing length is 8 m, and $R = 0.1$ m, the maximum wind speed around the plugging section increases with the increase in the inspiratory pressure, and there is a positive correlation between them. In the distance range of 0–7 m in the plugging section, the seepage air flow velocity is low. In this area, combined with the distribution law of the oxygen volume fraction, the oxygen volume fraction is greater than 8%, and when the wind velocity is low, the coal body is prone to spontaneous combustion. In the range of 7–10 m, the airflow velocity around the plugging section has an exponential relationship with the distance of the outer port of the plugging section. Here, the airflow

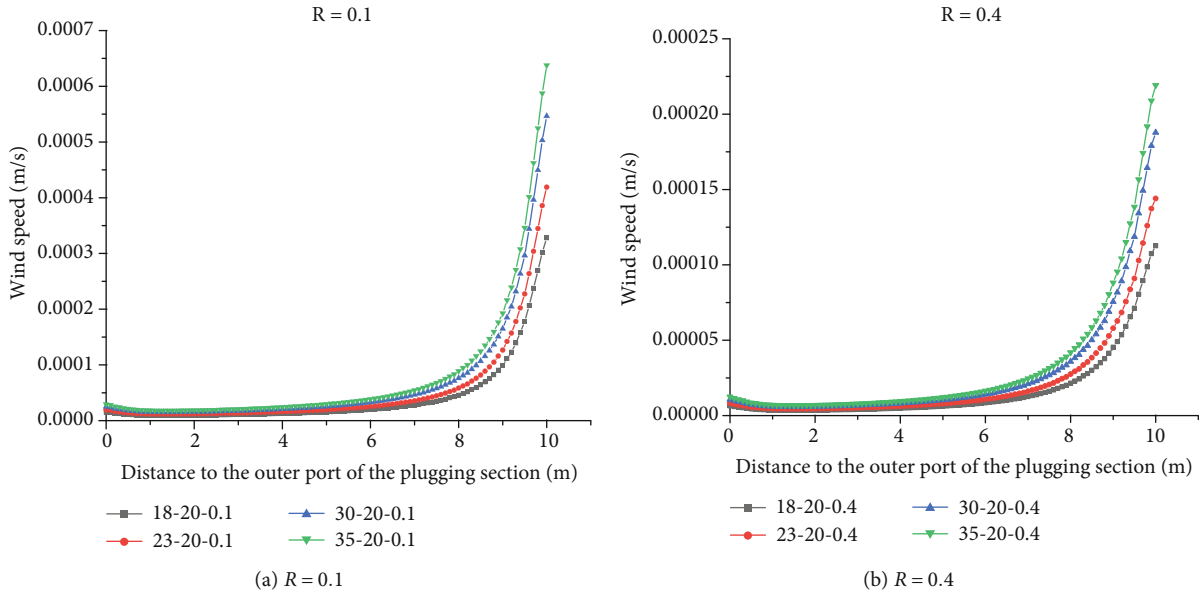


FIGURE 3: Relationship between air velocity and pumping negative pressure.

velocity is high, the oxygen volume fraction is low, and the surrounding coal is not prone to spontaneous combustion. The seepage distribution law at $R=0.4$ m, shown in Figure 3(b), is lower than that shown in Figure 3(a), and the increase rate of the seepage in the range of 6–10 m is evidently reduced.

4.2. Influence of Negative Pressure on the Volume Fraction of Oxygen around the Borehole. The negative pressure of the drainage directly affects the pressure distribution of the fractured coal in the plugging section around the drainage borehole, which leads to the size of the gas and oxygen distribution range in the roadway. Figure 4 shows the variation in the oxygen volume fraction around the plugging section with the gas drainage time when the plugging depth is 20 m, the plugging length is 8 m, and the negative pressures are 18, 23, 30, and 35 kPa. The legend $\Delta P = 18000$ Pa, (0.5, 15) implies that the plugging depth is 15 m, the plugging length is 8 m, the suction pressure is 18 kPa, and the location of the monitoring point is 0.5 m from the borehole radial distance and 15 m from the roadway wall.

Figure 4 shows the variation in the oxygen volume fraction over time at each monitoring point for different suction pressures with a sealing depth of 20 m and a sealing length of 8 m. As shown, the monitoring point moves to the inner side of the plugging section, and the oxygen volume fraction decreases; the oxygen volume fraction at each monitoring point hardly changes with the progress of gas drainage. As shown in Figures 4(a) and 4(b), at suction negative pressures of 18 and 23 kPa, respectively, the oxygen volume fraction is $<8\%$, and the sealing section lengths are 5 and 4 m, respectively. The greater the negative pressure, the wider the range of oxygen diffusion. Within 90 days of gas drainage, the oxygen volume fraction was relatively stable, and the downward trend was relatively slow, indicating that the coal body around the borehole was in a slow oxidation stage and that

there was no spontaneous combustion. As shown in Figures 4(c) and 4(d), at negative extraction pressures of 30 and 35 kPa, the oxygen volume fraction is $<8\%$ in the distance range of 16–20 m from the roadway, with no conditions for a spontaneous ignition. Between 16 m, the oxygen volume fraction is $>8\%$, and the inflection point appears at extraction times of 60 d and 52 d, that is, the point where the oxygen volume fraction begins to drop rapidly. At this time, the surrounding fractured coal enters the rapid oxidation stage. In summary, with the increase in the negative pressure of extraction, the narrower the range of the coal suffocation zone around the plugging section, the earlier the rapid decline in the oxygen concentration, and the shorter the time required by the fissured coal around the plugging section to ignite. Therefore, when the sealing depth is 20 m and the sealing length is 8 m, the oxygen volume fraction is used to determine whether spontaneous combustion occurs in the coal as the standard, and the suction pressure should not be >23 kPa.

4.3. Influence of Negative Pressure on Coal Temperature around Borehole. Figures 5(a)–5(d) show that when the plugging depth is 20 m, the plugging length is 8 m, and the suction pressures are 18, 23, 30, and 35 kPa, respectively, the fissure coal around the plugging section is in the 90th day of gas drainage. The body temperature distribution cloud chart shows that with the increase in the suction pressure, the high-temperature areas around the gas drainage boreholes where the coal temperature is $>70^\circ\text{C}$ expand, and the highest values of the coal body temperature reach 71.3, 83.4, 106, and 128°C . The high-temperature area is within the range of 0–2 m from the outer end of the plugging section. The oxygen concentration in this area is high, and the seepage velocity is low, which are conducive to produce and store heat. In summary, when the plugging depth is 20 m and the plugging length is 8 m, to prevent the spontaneous combustion, the

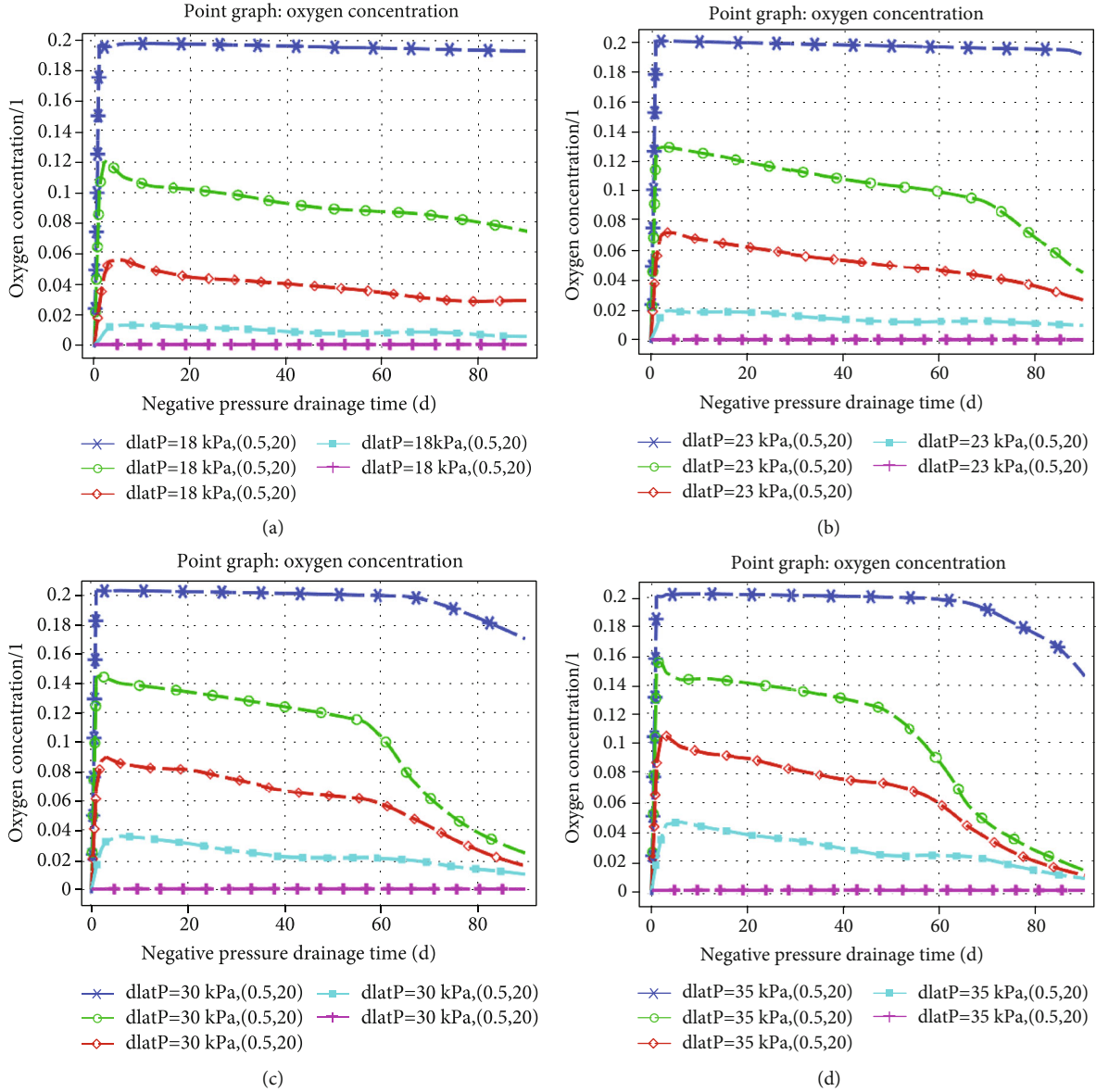


FIGURE 4: Change law of the oxygen concentration at different monitoring points for suction pressures of (a) 18 kPa, (b) 23 kPa, (c) 30 kPa, and (d) 35 kPa.

negative pressure of the drainage should not exceed 18 kPa when the gas drainage time is within 90 days.

Figure 6 shows the temporal and spatial evolutions of the coal temperature around the borehole under different drainage negative pressure conditions at positions (0.5, 12), (0.5, 15), (0.5, 17.5), and (0.5, 20). Figure 6(a) shows the monitoring point (0.5, 12) outside the plugging section. The temperature of the coal body increases with the increase in the gas drainage time, exhibiting a linear trend, and the negative pressure of the drainage increases. The higher the temperature of the coal body around the borehole, when the suction pressure is 35 kPa, the coal temperature reaches 105°C. Figures 6(b) and 6(c) show the evolution laws of the coal body temperature at the monitoring points (0.5, 15) and (0.5, 17.5). As shown, when the negative pressure of drainage is >30 kPa, the gas drainage is approximately 70 days, and the

temperature of the coal body begins to decrease, indicating that the heat dissipation of the coal body is greater than the heat generation. This is mainly because as the degree of coal oxidation increases, the area outside the plugging section consumes a large amount of oxygen; therefore, the closer the plugging section is to the inner side, the more the oxygen consumed and the lower the heat released, thereby decreasing the temperature of the coal body. Figure 6(d) shows that the coal at the monitoring point (0.5, 20) has largely no change in its temperature. This is mainly due to the fact that it is close to the inner side of the plugging section, the gas seepage velocity is high, the oxygen concentration is low, and the heat dissipation is significantly lower than the heat production. The low temperature increase is also due to the heat conduction of the gas. In summary, along the drilling direction, on both sides of the plugging section, the

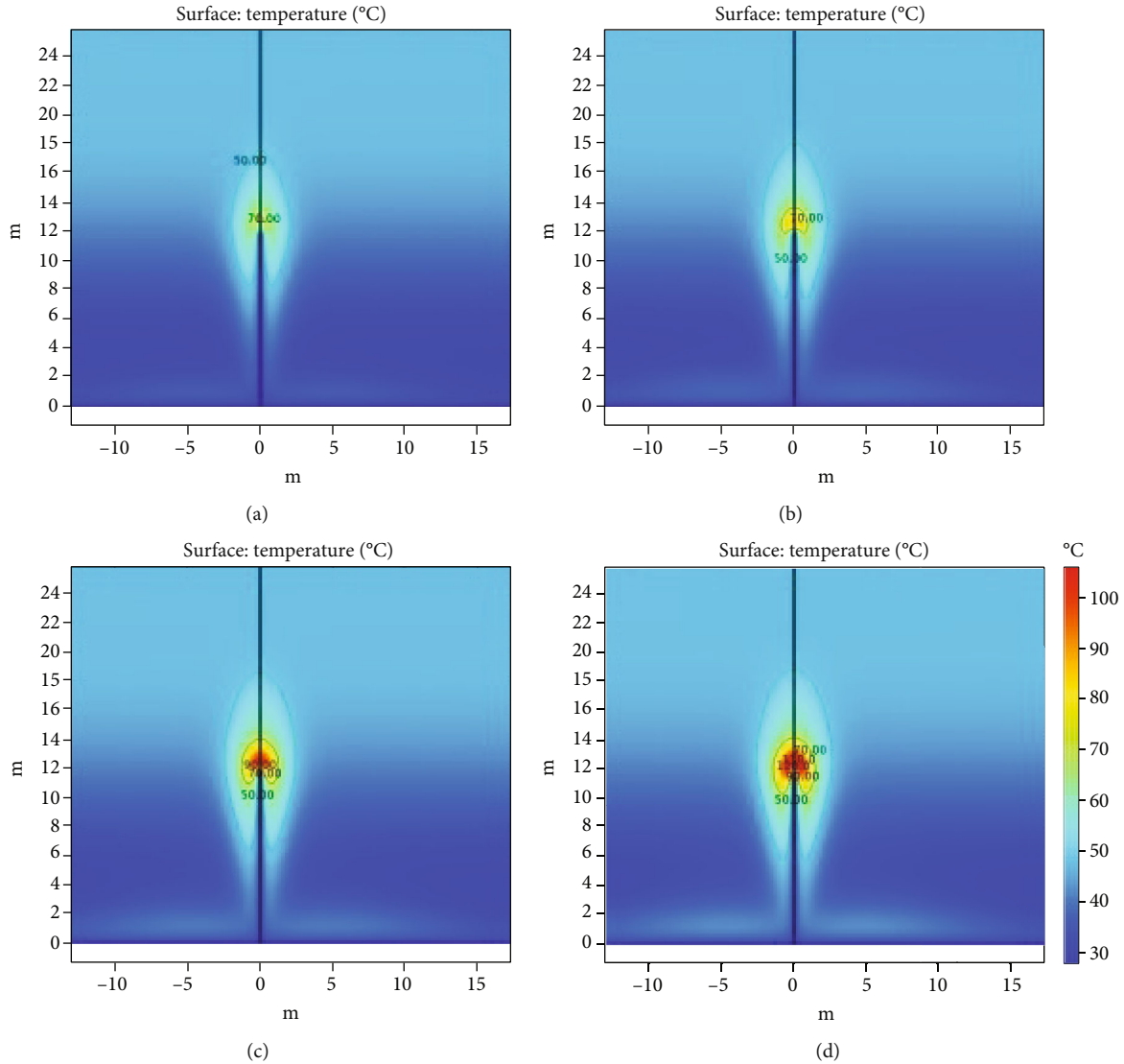


FIGURE 5: Coal temperature cloud maps around a gas borehole at suction pressures of (a) 18 kPa, (b) 23 kPa, (c) 30 kPa, and (d) 35 kPa.

maximum temperature of the coal body temperature decreases, and the area outside the plugging section has the highest heating rate. It is also most prone to fire area and is important for prevention and treatment.

4.4. Model Validation. In this study, the test boreholes in the conveyor roadway of the 24130 working face were taken as examples for a comparative verification. Each test borehole was equipped with two AD590JH temperature sensors to monitor the temperature at two positions 12 m and 14 m away from the borehole orifice. Figure 7 shows the temperature at the numerical simulation point and the test monitoring point. As shown, with the increase in the gas drainage time, the surrounding coal temperature increases. The coal temperature around the borehole at the test point is lower than the simulated point at the test point, and the temperature at the test point (0.5, 12). The initial stage is less than (0.5, 14), but with the increase in the time, when the gas drainage time is 60 d, the coal body temperature (0.5, 12)

on the outer side is higher than (0.5, 14). In the early stage of gas drainage, the heat release of coal oxidation at a lower temperature is lower, and the closer to the outside, the greater the heat dissipation. With the increase in the gas drainage time, the coal near the outside (0.5, 12) is sufficient. The oxidation reaction is accelerated under oxygen conditions, the heat production is far greater than the heat dissipation, and the heating rate is accelerated. Comparing the temperature changes at (0.5, 12) between the simulated and experimental points, the simulation results are largely consistent with the changes in the field test data. The average coal temperature at the simulated point within 90 days is calculated to be 56.4°C. The average coal temperature is 52°C. Similarly, it can be calculated that the average coal temperature within 90 days of gas drainage at (0.5, 14) is 52.6°C, and the temperature at the simulation point is 56.8°C. The errors between the average coal temperature at (0.5, 12) and (0.5, 14) of the numerical simulation monitoring point and the average coal temperature of the test point are 7.8% and 7.4%. The error is

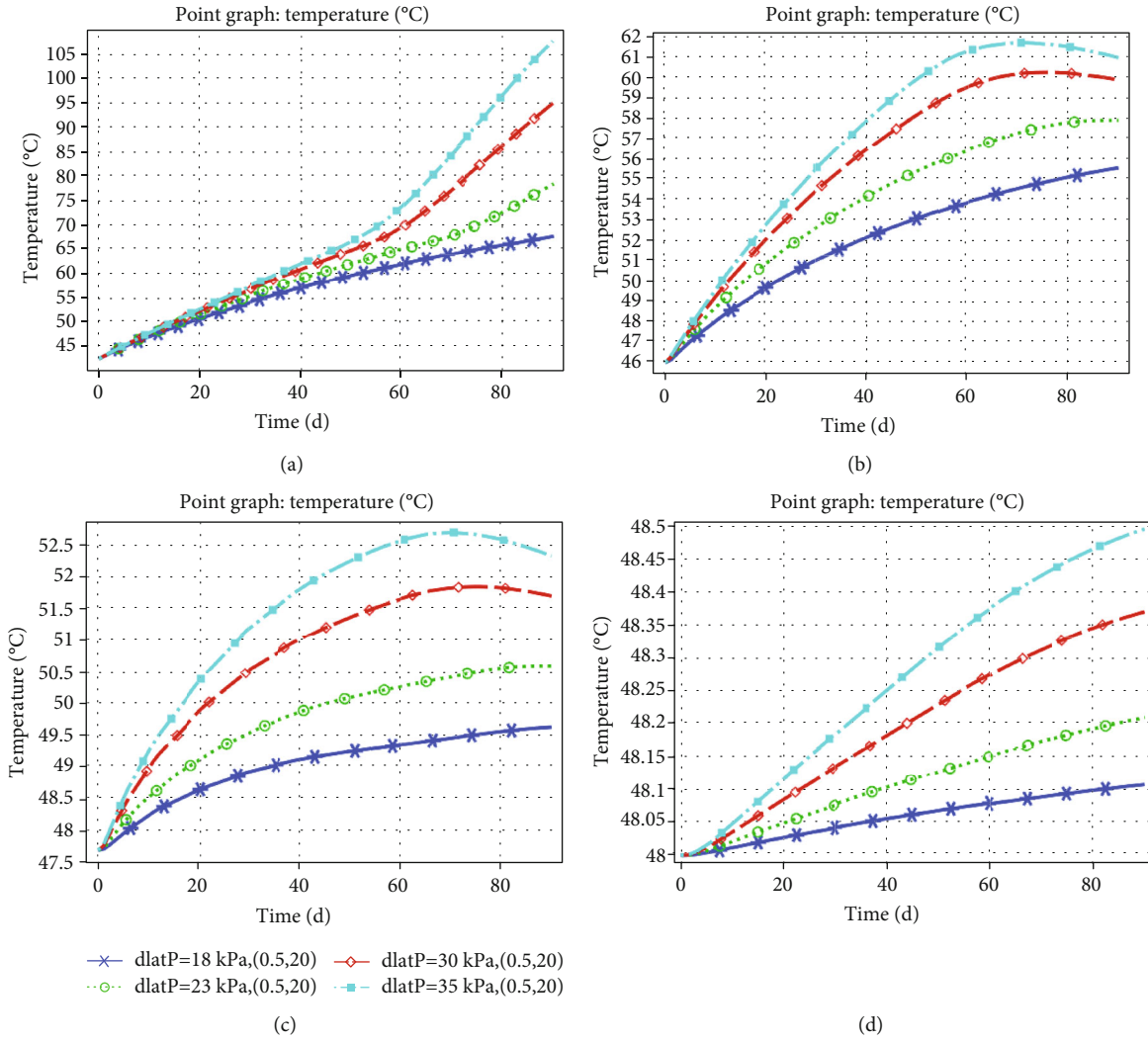


FIGURE 6: Temporal and spatial evolutions of the temperature in the coal body around a borehole at different monitoring points: (a) (0.5, 12), (b) (0.5, 15), (c) (0.5, 17.5), and (d) (0.5, 20).

low, and the monitoring value is in good agreement with the numerical simulation value, indicating the reliability of the numerical simulation. Similarly, by monitoring the temperature in the borehole using the beam tube, the CO volume fraction in the beam tube was detected. Figure 8 shows the obtained data results. The figure shows that the CO volume fraction increases with the increase in the gas drainage time. The CO concentration in the borehole in the early stage of drainage is much lower than that in the later stage of gas drainage, which is largely consistent with the temperature change as the drainage progresses. From the side, the spontaneous combustion of coal around the drainage borehole is verified, which further confirms the model accuracy.

5. Conclusion

To effectively solve the complex problems of gas drainage efficiency and spontaneous combustion of coal around boreholes, we applied Darcy’s law, porous media, mass fluid transfer, and porous media heat transfer to establish a spon-

aneous combustion model for drainage boreholes. The temporal and spatial evolution laws of the borehole gas seepage velocity, concentration, and coal temperature under different negative pressures were determined. The following results were obtained:

- (1) Using the theory of porous medium seepage and heat transfer, the changes in the crack coal seepage field and temperature field around a gas extraction hole were simulated, and the influence of negative pressure on the spontaneous combustion of a cracked coal body was analyzed. Based on the actual situation in the 24130 working face of the Pingdingshan No. 10 Mine, a theoretical analysis method was used to obtain a function formula for the permeability around the borehole under gas drainage in the working face: $k = 0.039e^{1.4(0.156-x)}$. From the formula, we find that the permeability and porosity of the coal body decrease exponentially; the farther the distance from the borehole center, the lower the porosity and permeability

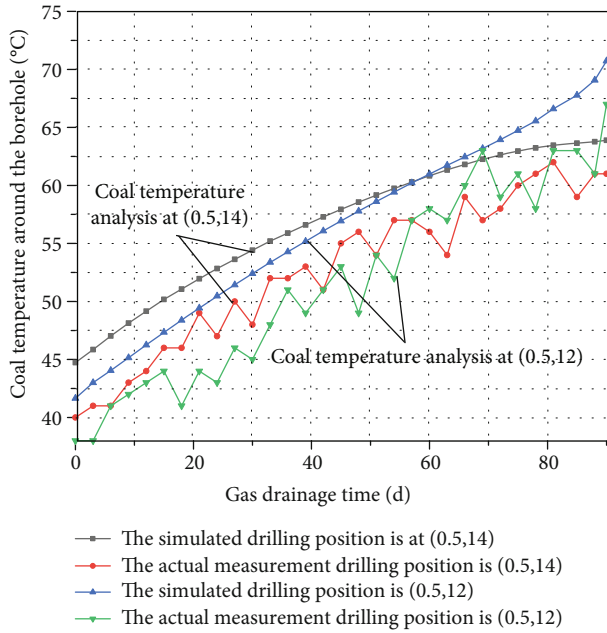


FIGURE 7: Comparative analysis of simulation and experiment.

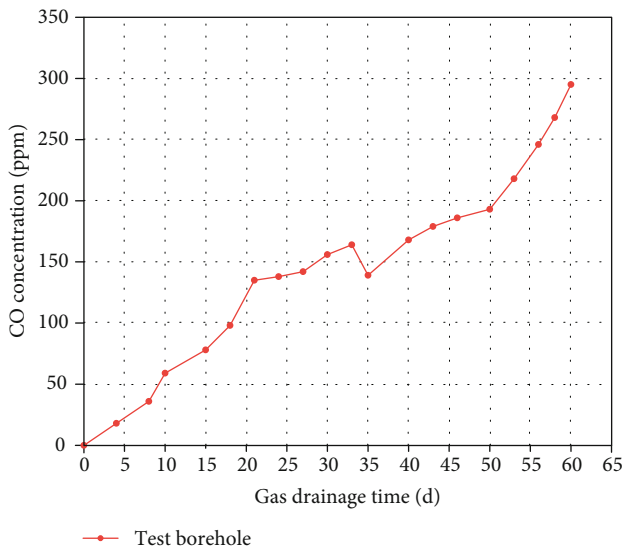


FIGURE 8: CO concentration changes in experimental boreholes.

- (2) A mathematical model of the negative pressure drainage inducing coal spontaneous combustion around the borehole was established. The gas flow velocity increased with the increase in the negative pressure of the drainage, exhibiting a linear growth trend, and the negative pressure of the drainage increased. The narrower the range of the coal suffocation zone around the plugging section, the earlier the rapid decline in the oxygen concentration, the higher the temperature of the coal around the borehole, and the wider the high-temperature area. The high-temperature area around the borehole is at a distance from the outside of the sealing within 1–2 m. At the outer end of the borehole plugging section to the

inner 1–2 m location, the occurrence of heat storage and spontaneous combustion is first observed; it then spread to both ends of the borehole

- (3) The oxygen concentration in the fissures around the borehole, gas seepage velocity, and coal temperature were used to determine the spontaneous combustion of the coal in the 24130 working face. When the sealing depth and sealing length are 20 m and 8 m, respectively, the suction pressure should not exceed 18 kPa

Data Availability

The data used to support the findings of this study are included with the article.

Conflicts of Interest

There are no conflicts of interest regarding the publication of this paper.

Acknowledgments

The authors would like to thank Rodrigo Cabanero for the linguistic assistance during the preparation of this manuscript. This work was supported by the National Key R&D Plan Key Special Funding Project (grant number 2018YFC0807900), China Coal Technology & Engineering Group Co., Ltd. (2019-2-ZD003), National Natural Science Foundation Youth Project of China (grant numbers 51804161 and 51804355), National Natural Science Foundation of China (grant number 52074156), and China Postdoctoral Science Foundation (2020M680490).

References

- [1] C. Wang, "Numerical simulation study on reasonable gas extraction negative pressure in the high-level entry," *Industrial Safety and Environmental Protection*, vol. 37, no. 1, pp. 59–61, 2011.
- [2] K. Wang, X. S. Zhao, and S. G. Li, "Study on the distribution law and application of negative extraction pressure in bedding borehole," *Mining Safety and Environmental Protection*, vol. 48, no. 2, pp. 81–86, 2021.
- [3] J. K. Ma, "Determining reasonable negative pressure of coal seam gas drainage based on statistical analysis of big data," *China Energy and Environmental Protection*, vol. 41, no. 5, pp. 24–27, 2019.
- [4] Y. P. Cheng, J. Dong, W. Li, M. Y. Chen, and K. Liu, "Effect of negative pressure on coal bed methane extraction and application in the utilization of methane resource," *Journal of China Coal Society*, vol. 42, no. 6, pp. 1466–1774, 2017.
- [5] K. J. Zhou, "Study on numerical simulation of negative pressure for rational extraction of coal and gas outburst seam," *Coal*, vol. 23, no. 2, pp. 31–33, 2014.
- [6] H. Y. Wang, S. Guo, Y. Y. Xie, H. Zhao, H. Wang, and W. Wang, "Study on competitive adsorption characteristics of CO/CO₂/CH₄ multi-component low concentration gases in coal," *Energy Sources, Part A: Recovery, Utilization, and Environmental Effects*, vol. 42, pp. 1–15, 2020.

- [7] P. Liu, J. Z. Fan, D. Jiang, and J. Li, "Evaluation of underground coal gas drainage performance: mine site measurements and parametric sensitivity analysis," *Process Safety and Environmental Protection*, vol. 148, pp. 711–723, 2021.
- [8] T. D. Zhang, M. K. Pang, X. K. Jiang, W. Q. Peng, and X. Ji, "Influence of negative pressure on gas percolation characteristics of coal body in perforated drilling hole," *Rock and Soil Mechanics*, vol. 40, no. 7, pp. 2517–2525, 2019.
- [9] Y. H. Wang, Y. Wu, and J. L. Zhang, "Research on determining optimal gas drainage negative pressure based on goaf prevention and control," *China Coal*, vol. 44, no. 10, pp. 143–148, 2018.
- [10] Q. J. Qi, Y. X. Zhao, and X. L. Jia, "Cause analysis and prevention of spontaneous combustion in deep coal seam drilling," *China Safety Science Journal*, vol. 29, no. 1, pp. 37–42, 2019.
- [11] Q. J. Qi, H. Wang, Z. W. Dong, Y. C. Li, and X. H. Li, "Determination on initial coal spontaneous combustion area of coal pile based on COMSOL software," *Coal Science and Technology*, vol. 44, no. 10, pp. 18–23, 2016.
- [12] H. Wang, B. Z. Dlugogorski, and E. M. Kennedy, "Analysis of the mechanism of the low-temperature oxidation of coal," *Combustion and Flame*, vol. 134, pp. 107–117, 2003.
- [13] H. Wang, X. Fang, F. Du et al., "Three-dimensional distribution and oxidation degree analysis of coal gangue dump fire area: a case study," *Science of The Total Environment*, vol. 772, p. 145606, 2021.
- [14] D. Zhang, X. X. Cen, W. F. Wang et al., "The graded warning method of coal spontaneous combustion in Tangjiahui Mine," *Fuel*, vol. 288, p. 119635, 2021.
- [15] H. Wang, B. Tan, Z. Shao, Y. Guo, Z. Zhang, and C. Xu, "Influence of different content of FeS₂ on spontaneous combustion characteristics of coal," *Fuel*, vol. 288, p. 119582, 2021.
- [16] F. Du, K. Wang, X. Zhang, C. Xin, L. Shu, and G. Wang, "Experimental study of coal-gas outburst: insights from coal-rock structure, gas pressure and adsorptivity," *Natural Resources Research*, vol. 29, no. 4, pp. 2481–2493, 2020.
- [17] F. Du and K. Wang, "Unstable failure of gas-bearing coal-rock combination bodies: insights from physical experiments and numerical simulations," *Process Safety and Environmental Protection*, vol. 129, pp. 264–279, 2019.
- [18] W. J. Yao, J. Y. Pang, Q. Y. Ma, and H. Lyimo, "Influence and sensitivity analysis of thermal parameters on temperature field distribution of active thermal insulated roadway in high temperature mine," *International Journal of Coal Science Technology*, vol. 8, no. 1, pp. 47–63, 2021.
- [19] M. Onifade and B. Genc, "Spontaneous combustion liability of coal and coal-shale: a review of prediction methods," *International Journal of Coal Science Technology*, vol. 6, no. 2, pp. 151–168, 2019.
- [20] Q. J. Qi, X. L. Jia, X. H. Zhou, and Y. Zhao, "Instability-negative pressure loss model of gas drainage borehole and prevention technique: a case study," *PLoS One*, vol. 15, no. 11, p. e0242719, 2020.
- [21] Z. M. Wang, S. H. Han, Z. J. You, V. Honari, Y. Sun, and S. Zhang, "Influences of negative pressure on air-leakage of coal seam gas extraction: laboratory and CFD-DEM simulations," *Journal of Petroleum Science and Engineering*, vol. 196, p. 107731, 2021.
- [22] T. Liu, "Modeling air leakage around gas extraction boreholes in mining-disturbed coal seams," *Process Safety and Environmental Protection*, vol. 141, pp. 202–214, 2020.
- [23] Z. X. Li, "CFD simulation of spontaneous coal combustion in irregular patterns of goaf with multiple points of leaking air," *Journal of China University of Mining and Technology*, vol. 18, no. 4, pp. 504–515, 2008.
- [24] H. Y. Wang, X. Y. Fang, Y. C. Li, and Z. Y. Zheng, "Research and application of the underground fire detection technology based on multi-dimensional data fusion," *Tunnelling and Underground Space Technology*, vol. 109, 2021.
- [25] J. J. Liu, D. Wang, and J. L. Gao, "Numerical simulation of drainage negative of high alley pumping effect on the goaf air leakage and spontaneous combustion zone," *Journal of Heilongjiang University of Science and echnology*, vol. 26, no. 4, pp. 362–367, 2016.
- [26] W. R. Zhang, S. Q. Yang, and J. W. Cheng, "Spontaneous heating and gas drainage on a coal face with 'fourgateroad' and overlying drainage tunnel," *Journal of China University of Mining and Technology*, vol. 42, no. 4, pp. 513–518, 2013.
- [27] W. Wang, B. S. Jia, and Y. Qi, "Improved CRITIC modified G2-TOPSIS borehole spontaneous combustion prediction model and application," *Chinese Safety Science Journal*, vol. 29, no. 11, pp. 26–31, 2019.
- [28] S. M. Li, "Study on the influence of negative pressure of gas drainage effect of coal seam," *Energy Technology and Management*, vol. 42, no. 3, pp. 31–36, 2017.
- [29] Q. Y. Chen, *Study on Law of "Three Zones" Distribution in Goaf Based on the Buried Pipe Drainage*, North China University of Science and Technology, 2015.
- [30] F. B. Zhou, X. Wang, and T. Q. Xia, "A model of safe drainage of coal seam gas," *Journal of China Coal Society*, vol. 39, pp. 1659–1666, 2014.
- [31] G. Liu and H. W. Song, "Study on the law of loose surrounding rock in coal roadway," *Journal of China Coal Society*, vol. 39, pp. 31–35, 2002.
- [32] Y. Lu, X. Z. Zou, D. P. Cui, and X. F. Yu, "Theoretical analysis and practice of fragmentation circle in surrounding rock," *Journal of Liaoning University Technology*, vol. 2, pp. 219–221, 2007.
- [33] Z. X. Li, Q. Wu, and Z. Q. Wang, "Distribution characteristic of remaining coal oxygen consumption and spontaneous combustion heating-up in gob," *Journal of China Coal Society*, vol. 34, pp. 667–672, 2009.
- [34] F. Tong, L. Jing, and R. W. Zimmerman, "A fully coupled thermo-hydro-mechanical model for simulating multiphase flow, deformation and heat transfer in buffer material and rock masses," *International Journal of Rock Mechanics and Mining Sciences*, vol. 47, no. 2, pp. 205–217, 2010.
- [35] X. Jia, Q. Qi, and Y. Zhao, "Determination of the spontaneous combustion hazardous zone and analysis of influencing factors in bedding boreholes of a deep coal seam," *ACS Omega*, vol. 6, no. 12, pp. 8418–8429, 2021.

Research Article

Response Surface Method for Strength Analysis and Proportion Optimization of New Type Sealing Materials

Sheng Xue , Xin Guo , Chunshan Zheng, Yaobin Li, and Xiaoliang Zheng

Anhui University of Science & Technology, Huainan 232001, China

Correspondence should be addressed to Xin Guo; guoxin190510@163.com

Received 19 April 2021; Revised 26 June 2021; Accepted 8 July 2021; Published 2 August 2021

Academic Editor: Basim Abu-Jdayil

Copyright © 2021 Sheng Xue et al. This is an open access article distributed under the Creative Commons Attribution License, which permits unrestricted use, distribution, and reproduction in any medium, provided the original work is properly cited.

The influence of the interaction among water-cement ratio, content of expansion agent, water reducing agent, and retarder on the compressive strength of new sealing material was studied. The Design-Expert software was used to design experiments, establish a quadratic polynomial regression model, draw response surface, and optimize parameters. The microstructure morphology of the sample is explored by a scanning electron microscope (hereinafter referred to as SEM). The research results show that the interaction between the water-cement ratio and expansion agent content is the most crucial factor affecting the compressive strength of the new sealing material. Under the optimal condition of 0.4% water reducing agent, 0.04% retarder, 0.8 water-cement ratio, and 8% expansion agent, the compressive strength of the sealing material cured for 3 d and 7 d is 39.247 MPa and 41.044 MPa, with the maximum absolute error of 1.71% and 2.81%, which proves the high accuracy of the model. The main hydration products of the new sealing material are ettringite and C-S-H gel, interlacing each other to form a dense structure, which contributes to the high strength of the new sealing material.

1. Introduction

China is currently faced with the most severe gas disaster in coal mines in the world [1–3]. Gas predrainage is effective for coal mine gas control, and the performance of sealing material is the key to ensuring drainage efficiency. The coal mine gas drilling sealing material can be divided into inorganic grouting material and organic grouting material. Inorganic sealing materials are mainly cement mortar, low-cost but easy to shrink and crack [4, 5]. Organic sealing materials, including polyurethane and modified resin [6–8], have a better sealing effect but are expensive, flammable, and toxic [9, 10]. In recent years, scholars have studied composite sealing materials for coal mines. Some researchers have developed a CF expansion sealing material with cement, the base material, and metal Al powder, gypsum, and other inorganic additives with good expansibility [11, 12]. Glass fiber would reduce the fluidity of pure cement paste, and the higher the content of glass fiber, the more pronounced the effect [13]. Carbon nanofibers can effectively increase the shrinkage

and crack resistance of ultra-fine cement while keeping the hardness unchanged [14]. Fly ash was used as a base material and adding water-retaining agent, expansion agent. This material, with a certain degree of expansion, is not easy to shrink and adheres tightly to coal and could significantly improve the mechanical properties of grouting materials [15–17]. The strength of the sulfoaluminate cement sealing material decreases rapidly with the increase of the water-cement ratio [18]. Portland cement has been used to modify the polyurethane material and developed a new grouting material, which not only keeps good mechanical properties of polyurethane material but also overcomes the shortcoming of flammability [19]. Wang et al. [20–22] developed a new polymer sealing material for underwater tunnels and studied its swelling property, mechanical property, flame retardant property, and creep recovery property. Tan et al. [23] studied the waterproof performance of two kinds of water swellable pad materials: water swellable rubber (WSR) and water swellable polyurethane (WSP). Expansion tests were carried out to determine the expansion ratio under

compression and free expansion conditions. A dynamic mechanics analyzer (DMA) was used to measure the storage modulus under different compression pressures and different saline environments. The morphology of WSR and WSP was observed by scanning electron microscopy (SEM). Liu et al. [24, 25] studied the enhancement effect of expansion agent on the performance of underground mass concrete structure. The field test results show that the expansion strain of concrete can be increased effectively by the postcast and postcast expansion reinforcement belts, which indicates that the expansion agent can enhance the crack prevention performance of concrete structures in situ.

With the increase of coal mining depth, the in situ stress increases gradually. Under the action of high in situ stress, the borehole sealing section is easy to cause hole collapse, resulting in air leakage, which is not conducive to gas extraction. In order to improve the gas extraction efficiency, the compressive strength of grouting materials was studied. This paper investigates the performance of composite sealing materials from the perspective of macromechanics and microstructure with the quadratic polynomial regression model. The results reveal that the interaction between the water-cement ratio, retarder, expansion agent, and water reducing agent in the composite sealing material system significantly affects the compressive strength of the sealing material cured for 3 d and 7 d. The optimal ratio is determined by the verification test, and the mechanism of action of the new sealing material is revealed by SEM analysis.

2. Materials and Methods

2.1. Experimental Materials. The base material used in the experiment is ultrafine Portland cement. The measured values of D90 and D50 are $12.6 \mu\text{m}$ and $5 \mu\text{m}$, respectively, which can be effectively injected into microcracks below 0.1 mm. The seaweed powder with a white appearance, which is easily soluble in water, is used as the retarder. The solution is a colorless and transparent viscous liquid, which can advance the setting time and improve the strength of cement materials [26]. After being added, PCE (polycarboxylic acid water-reducing agent), a white powder, which is easily soluble in water, can disperse cement particles with the water-reduction rate of 20-35% [27, 28]. The compound expansive agent of calcium oxide and calcium sulfate (HCSA), with a gray-white appearance, promotes a good spatial structure of cement hydration products [29, 30]. The composition of ultrafine cement and expansion agent used in the experiment is shown in Table 1.

2.2. Experimental method. 29 groups of experiments with four factors and three levels were designed using Box-Behnken experiment design function in Design-Expert 8.0.5 software. The steps of the parameter optimization process are shown in Figure 1. The four factors are water-cement ratio, retarder content, water reducing agent content, and expansion agent content, as shown in Table 2. The materials were mixed, then water was added, and the mixture was poured into the triple mold ($7.07 \text{ cm} \times 7.07 \text{ cm} \times 7.07 \text{ cm}$).

The mold surface was scraped flat and put into the curing box. After curing the mixture for one day, the mold was removed, and then, the stone body was cured for 3 d and 7 d.

The compressive strength of stones of different ages was tested by the RMT uniaxial press, as shown in Figure 2. The microstructure of the new sealing material and ordinary cement materials was then observed by the FEI Quanta 200 FEG environmental scanning electron microscope. After the experiment, the response surface regression analysis was carried out by Design-Expert 8.0.5 software. By taking compressive strength as the response value, a quantitative regression model of the relationship between the compound dosing amounts of admixtures was obtained [31], which provides a basis for optimizing the sealing material.

3. Experimental Results

It can be seen from Table 3 that after 3 d curing (temperature $20 \pm 2^\circ\text{C}$, relative humidity above 95%), the minimum compressive strength of the new sealing material is 23.997 MPa, and the maximum is 39.918 MPa. After 7 d curing (the curing conditions are the same), the minimum compressive strength is 27.012 MPa and the maximum is 42.197 MPa. These results show that the new sealing material has good mechanical properties.

4. Response Surface Optimization Analysis

According to the experimental results in Table 3, the water-cement ratio, retarder, water reducing agent, and expansion agent were set as independent variables A , B , C , and D , and the compressive strength of the samples cured for 3 d and 7 d was used as the objective function for multiple nonlinear regression fitting.

4.1. Model Variance Analysis and Significance Test. As shown in Table 4, the P values of the two models are both less than 0.0001, indicating a small experimental error [32]. It can be seen from the significance test that the significance order of each factor in the regression equation of the sample cured for 3 d is as follows: A (water-cement ratio) $> D$ (expansion agent) $> C$ (water reducing agent) $> B$ (retarder); interaction of different factors: AD (water-cement ratio, expansion agent) $> AC$ (water-cement ratio, water-reducing agent) $> AB$ (water-cement ratio, retarder) $> CD$ (water-cement ratio, expansion agent) $> BD$ (retarder, expansion agent) $> BC$ (retarder, water reducing agent). The P value of A and D is less than 0.0001, indicating extremely significant influence. The P value of B and C is greater than 0.05, showing the insignificant impact. The P value of AD and AC is less than 0.05, suggesting a significant effect. The P value of AB , BC , BD , and CD is greater than 0.05, indicating insignificant influence. The P value of the BC is 0.8102, meaning the least significant impact. According to the compressive strength of the experimental scheme, a polynomial regression equation of the compressive strength (R_{3d} , R_{7d}) of the independent variables A , B , C , and D can be obtained as

TABLE 1: Chemical composition of raw materials (%).

Chemical composition	w (SiO ₂)	w (Al ₂ O ₃)	w (Fe ₂ O ₃)	w (CaO)	w (MgO)	w (SO ₃)	Loss	Total
HCSA expanding agent	4.96	8.52	0.99	64.18	2.67	16.97	1.19	99.48
Superfine Portland cement	20.57	9.89	3.08	57.65	2	2.7	2.6	98.49

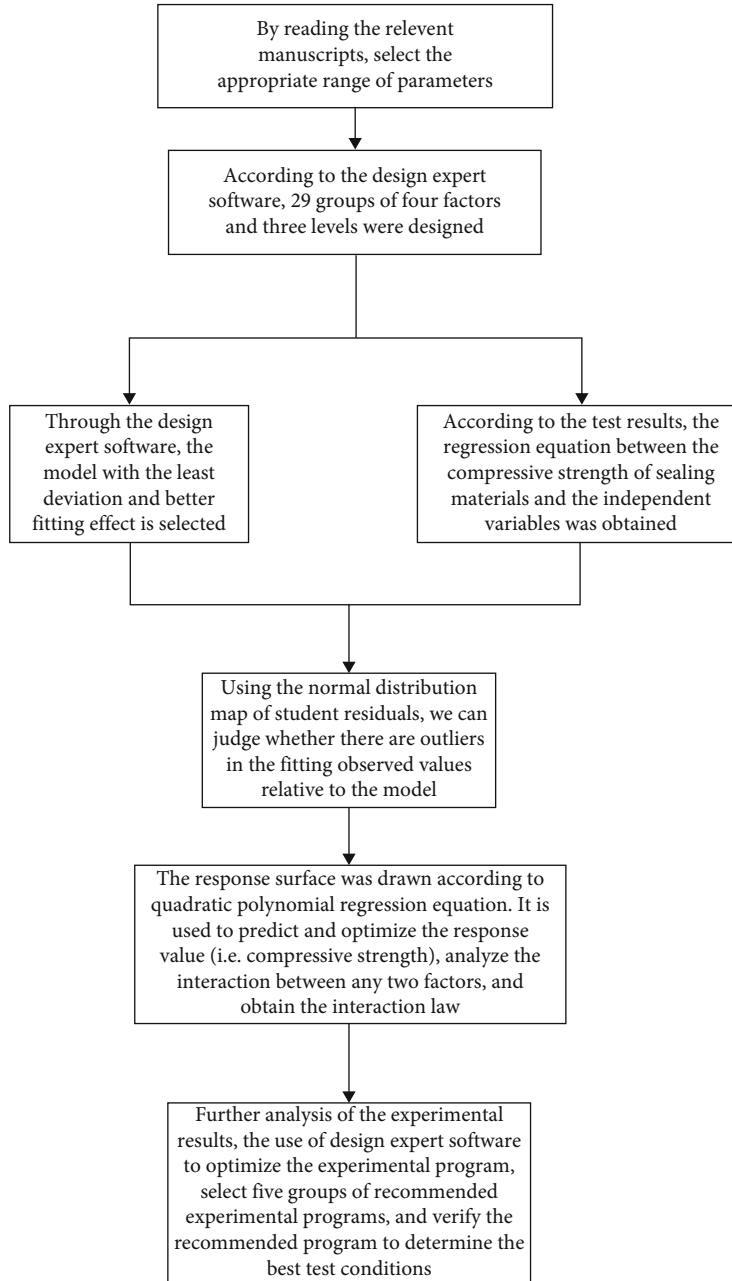


FIGURE 1: Steps of the parameter optimization process.

TABLE 2: Range of factors in the experiment.

Test group	Water-cement ratio	Value range of each factor (%)		
		Retarder	Water-reducing agent	Expanding agent
ZJ1-29	0.8~1.0	0.03~0.05	0.3~0.5	8-10



FIGURE 2: Compressive strength test of composite material specimen.

$$\begin{aligned}
 R_{3d} = & +29.601 - 3.65 * A - 0.47 * B + 0.6 * C - 1.91 * D \\
 & - 1.01 * AB - 1.10 * AC + 1.63 * AD + 0.12 * BC \\
 & + 0.51 * BD - 0.54 * CD + 0.84 * A^2 - 2.86 * B^2 \\
 & + 1.04 * C^2 + 1.61 * D^2,
 \end{aligned}
 \tag{1}$$

$$\begin{aligned}
 R_{7d} = & +30.38 - 3.41 * A - 0.70 * B + 0.79 * C - 2.42 * D \\
 & - 0.58 * AB - 0.62 * AC + 1.54 * AD + 0.048 * BC \\
 & + 0.24 * BD - 0.25 * CD + 1.44 * A^2 - 1.97 * B^2 \\
 & + 1.85 * C^2 + 1.85 * D^2.
 \end{aligned}
 \tag{2}$$

The order of the significance of each factor in the regression equation of specimen cured for 7 days is as follows: A (water-cement ratio) $> D$ (expansion agent) $> C$ (water reducing agent) $> B$ (retarder); interaction of different factors: AD (water-cement ratio, expansion agent) $> AC$ (water-cement ratio, water-reducing agent) $> AB$ (water-cement ratio, retarder) $> CD$ (water-cement ratio, expansion agent) $> BD$ (retarder, expansion agent) $> BC$ (retarder, water reducing agent). The P value of A and D is less than 0.0001, indicating extremely significant influence. The P value of B and C is greater than 0.05, indicating an insignificant impact. The P value of AD is less than 0.05, indicating significant interaction. The P value of the AC changes from 0.0432 to 0.3482, suggesting that the interaction between A and C has a more significant impact on the sample cured for three days, and the longer the sample is cured, the less significant the effect. The P value of BC is 0.9413, indicating the least significant interaction effect.

TABLE 3: Response surface test design and test results.

No.	Water-cement ratio	Parameter value			R_{3d} (MPa)	R_{7d} (MPa)
		Retarder	Water-reducing agent	Expanding agent		
1	0.80	0.04	0.40	8.00	39.918	42.197
2	0.80	0.04	0.40	10.00	30.986	32.991
3	0.80	0.04	0.50	9.00	37.697	38.477
4	0.80	0.05	0.40	9.00	31.652	34.133
5	0.80	0.04	0.30	9.00	33.997	35.010
6	0.80	0.03	0.40	9.00	29.899	32.069
7	0.90	0.03	0.40	10.00	26.943	28.511
8	0.90	0.03	0.30	9.00	27.696	31.233
9	0.90	0.03	0.40	8.00	30.931	32.871
10	0.90	0.03	0.50	9.00	28.479	32.141
11	0.90	0.04	0.40	9.00	29.601	30.381
12	0.90	0.04	0.30	10.00	31.239	32.011
13	0.90	0.04	0.40	9.00	29.601	30.381
14	0.90	0.04	0.40	9.00	29.601	30.381
15	0.90	0.04	0.30	8.00	32.986	36.021
16	0.90	0.04	0.40	9.00	29.601	30.381
17	0.90	0.04	0.50	8.00	35.112	38.021
18	0.90	0.04	0.50	10.00	31.213	32.997
19	0.90	0.04	0.40	9.00	29.601	30.381
20	0.90	0.05	0.50	9.00	27.162	29.133
21	0.90	0.05	0.40	8.00	28.922	30.410
22	0.90	0.05	0.40	10.00	26.993	27.012
23	0.90	0.05	0.30	9.00	25.896	28.033
24	1.00	0.04	0.40	8.00	28.911	31.036
25	1.00	0.04	0.50	9.00	26.976	29.989
26	1.00	0.04	0.40	10.00	26.513	27.978
27	1.00	0.03	0.40	9.00	26.295	28.091
28	1.00	0.05	0.40	9.00	23.997	27.843
29	1.00	0.04	0.30	9.00	27.664	29.008

As the items (F value, R^2) of conformity degree comparison were relatively abstract, it was necessary to verify the selected model in other ways. The studentized residual was used to compare the predicted residual value and the actual value (Figure 3). The points were mostly concentrated in the center of the map in terms of the abscissas and were distributed approximately on a straight line, indicating that the model was reliable.

4.2. Response Surface Analysis. Figure 4 is the three-dimensional surface obtained according to the response value under the interaction of each two independent variables, where the X -axis and the Y -axis show the factor level and Z -axis shows the compressive strength. The interaction and law of the other two factors under the condition that any two of the four factors A (water-cement ratio), B (retarder content), C (water-reducing agent content), and D (expansion agent content) remain unchanged were determined.

TABLE 4: Response surface secondary model and ANOVA results.

Curing age (d)	Source	Sum of squares	df	Mean square		P value	Significance
3	Model	332.63	14	23.76	24.40	<0.0001	***
	A	159.82	1	159.82	164.12	<0.0001	***
	B	2.63	1	2.63	2.70	0.1224	*
	C	4.27	1	4.27	4.39	0.0549	*
	D	43.67	1	43.67	44.85	<0.0001	***
	AB	4.10	1	4.10	4.21	0.0593	*
	AC	4.81	1	4.81	4.94	0.0432	**
	AD	10.67	1	10.67	10.96	0.0052	**
	BC	0.058	1	0.058	0.060	0.8102	*
	BD	1.06	1	1.06	1.09	0.3145	*
	CD	1.16	1	1.16	1.19	0.2940	*
	A ²	4.61	1	4.61	4.73	0.0473	**
	B ²	53.14	1	53.14	54.57	<0.0001	***
	C ²	7.07	1	7.07	7.26	0.0174	**
	D ²	16.88	1	16.88	17.33	0.0010	**
	Residual	13.63	14	0.97			
	Lack of fit	13.63	10	1.36			
	Pure error	0.000	4	0.000			
	Cor total	346.26	28				
	R ² = 0.9606	Adj R ² = 0.9213	***P value [-∞, 0.0001]; **P value [0.0001, 0.05]; *P value [0.05, +∞]				
7	Model	328.94	14	23.50	14.33	<0.0001	***
	A	139.62	1	139.62	85.15	<0.0001	***
	B	5.81	1	5.81	3.55	0.0807	*
	C	7.43	1	7.43	4.53	0.0515	*
	D	70.35	1	70.35	42.91	<0.0001	***
	AB	1.34	1	1.34	0.81	0.3819	*
	AC	1.55	1	1.55	0.94	0.3482	*
	AD	9.45	1	9.45	5.76	0.0308	**
	BC	9.216E - 003	1	9.216E - 003	5.621E - 003	0.9413	*
	BD	0.23	1	0.23	0.14	0.7128	*
	CD	0.26	1	0.26	0.16	0.6981	*
	A ²	13.54	1	13.54	8.26	0.0123	**
	B ²	25.25	1	25.25	15.40	0.0015	**
	C ²	22.23	1	22.23	13.56	0.0025	**
	D ²	22.18	1	22.18	13.53	0.0025	**
	Residual	22.96	14	1.64			
	Lack of fit	22.96	10	2.30			
	Pure error	0.000	4	0.000			
	Cor Total	351.90	28				
	R ² = 0.9348	Adj R ² = 0.8695	***P value [-∞, 0.0001]; **P value [0.0001, 0.05]; *P value [0.05, +∞]				

Figures 4(a) and 4(b) show the influence of the interaction between water-cement ratio and expansion agent on the compressive strength of the sample. The compressive strength of the sample varies greatly with the water-cement

ratio or the value of the expansion agent. At this time, the response surface is steep, which indicates that the interaction of water-cement ratio and expansion agent has a significant influence on the response value. It is consistent with the

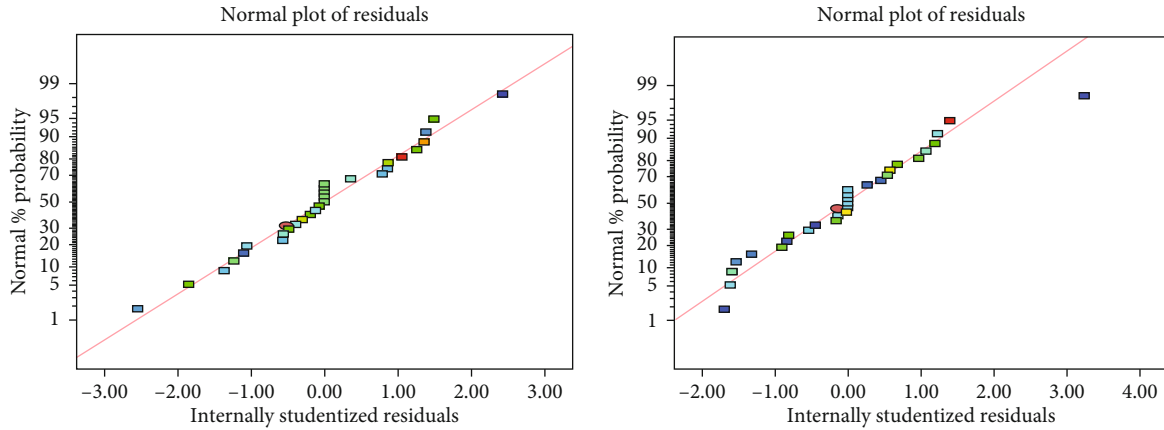


FIGURE 3: Studentized residual distribution.

results of the previous analysis of variance. When the water-cement ratio is low, the compressive strength of the sample increases rapidly with the increase of the expansion agent content. When the water-cement ratio increases to above 0.9, the compressive strength of the sample increases slowly with the increase of the expansion agent content. When the content of expansion agent is low, the compressive strength of the sample increases rapidly as the water-cement ratio decreases. When the content of expansion agent increases to more than 9%, the compressive strength of the sample increases slowly with the decrease of water-cement ratio.

Figures 4(c) and 4(d) show the influence of the interaction between water-cement ratio and water reducing agent on the compressive strength of the sample. The compressive strength of the sample has a steeper change trend, indicating that the interaction between the water-cement ratio and the water reducing agent has a significant impact on the response value.

The smoother response surface in Figures 4(e) and 4(f) indicates less significant influence of the interaction of the retarder and water-cement ratio on the compressive strength. When the water-cement ratio remains unchanged, the compressive strength of the sample increases first and then decreases with the increase of retarder content. When the content of the retarder is constant, the compressive strength of the sample increases rapidly with the decrease of the water-cement ratio, and the steep response surface shows that the retarder has little effect on the compressive strength.

As shown in Figures 4(g) and 4(h), when the content of the expansion agent is constant, the compressive strength increases with the increase of the water reducing agent, indicating that the expansion agent has less influence on the fluidity. When the value of the water reducing agent reaches the upper limit and the value of the expansion agent reaches the lower limit, the response surface is steep, indicating that the interaction of the two factors has the greatest impact on the compressive strength.

Figures 4(i) and 4(j) show the influence of the interaction between the retarder and expansive agent on the compressive strength of the sample. The change rule of the graph is consistent with the influence rule of the two-factor ANOVA on

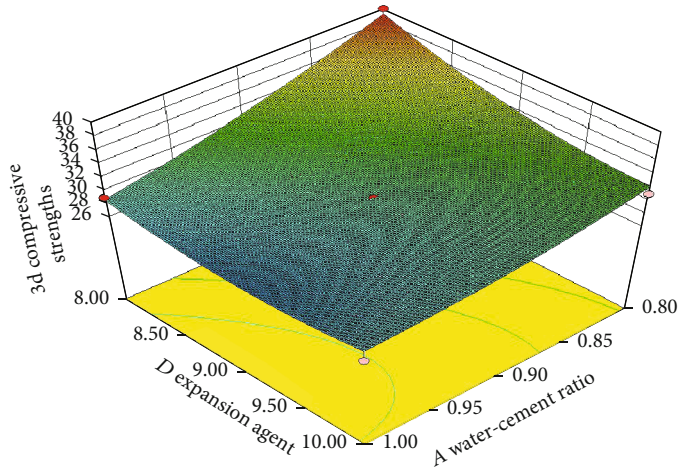
the response value in Table 4. When the content of the expansion agent remains constant, the compressive strength increases and then decreases with the increase of the content of the retarder. When the content of the retarder remains unchanged, the compressive strength of the sample decreases rapidly with the increase of the content of the expansion agent, indicating that the effect of the water-cement ratio on the response value is more significant than that of the retarder. The response surface is relatively flat on the whole, indicating that the influence of the interaction between the retarder and the expansive agent is small.

As shown in Figures 4(k) and 4(l), when the retarder interacts with the expansion agent, the response surface is relatively smooth, indicating that the influence of the interaction on the compressive strength is the least significant, which is consistent with the results of the variance analysis.

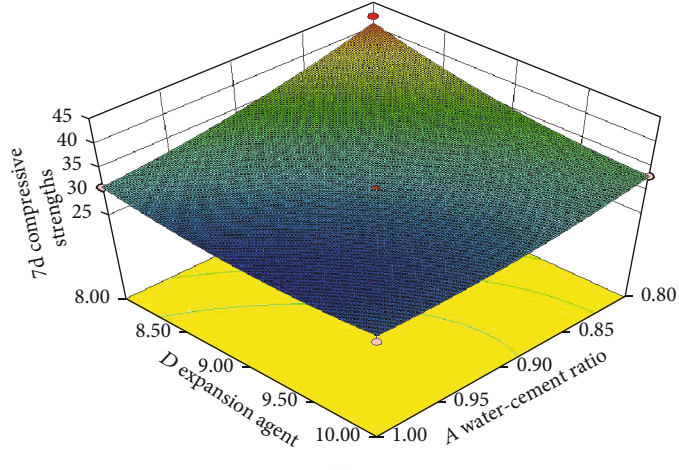
4.3. Response Surface Optimization Prediction and Verification. The experimental results were further analyzed by taking the compressive strength of the sample as the optimization index. The optimized experimental scheme was obtained by the Design-Expert software where the content of water reducing agent is 0.4%, the content of retarder is 0.04%, the water-cement ratio is 0.8, and the content of expansion agent is 8%. The scheme was then verified. Due to limited space, the results were shown in Table 5 without being described in detail. It can be seen that the compressive strength of the specimen cured for 3 d and 7 d under the optimal condition are 39.247 MPa and 41.044 MPa, with the maximum absolute error between the predicted value and actual value of compressive strength as 2.55% and 1.77%. Figures 5(a) and 5(b) shows that the measured and predicted values have a high degree of fitting, and the fitting coefficients are 0.9586 and 0.9298, respectively, indicating that the model is relatively reliable.

5. Microscopic Characterization of Sealing Material

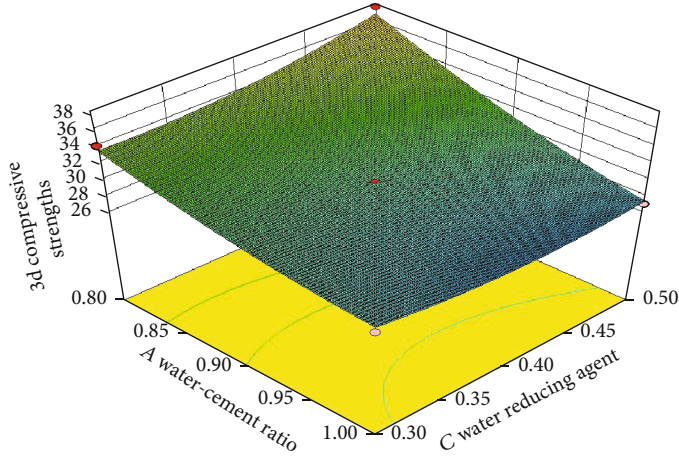
It can be seen from Figures 6(a) and 6(b) that the connection between the hydration products of the ordinary cement



(a)



(b)



(c)

FIGURE 4: Continued.

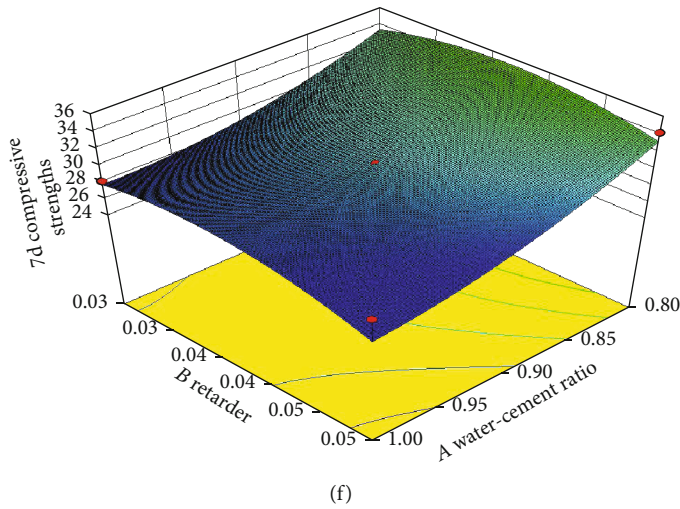
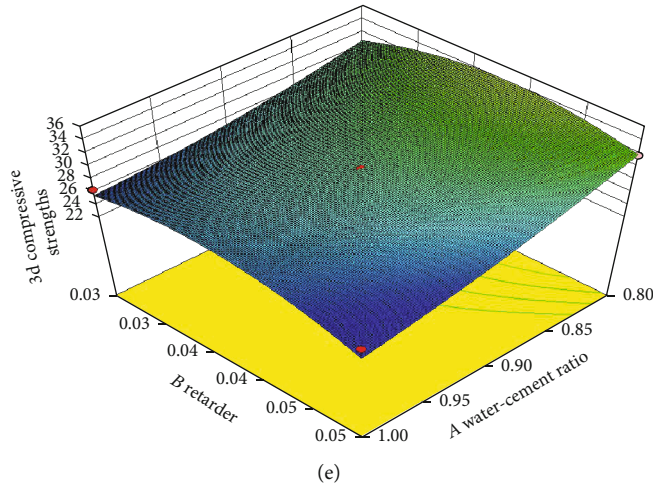
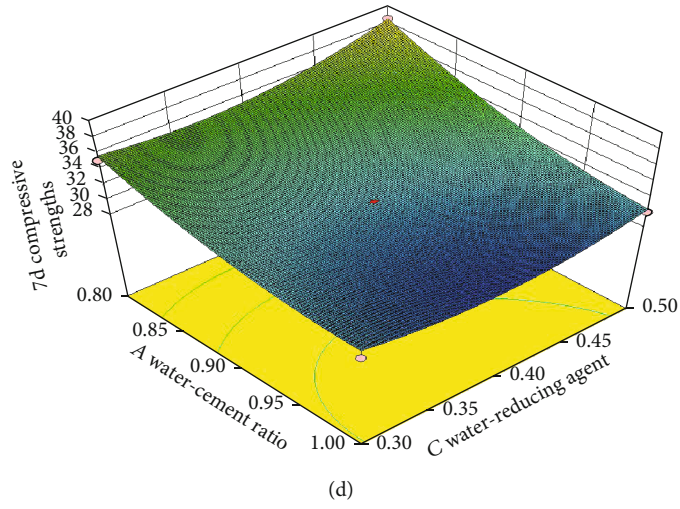
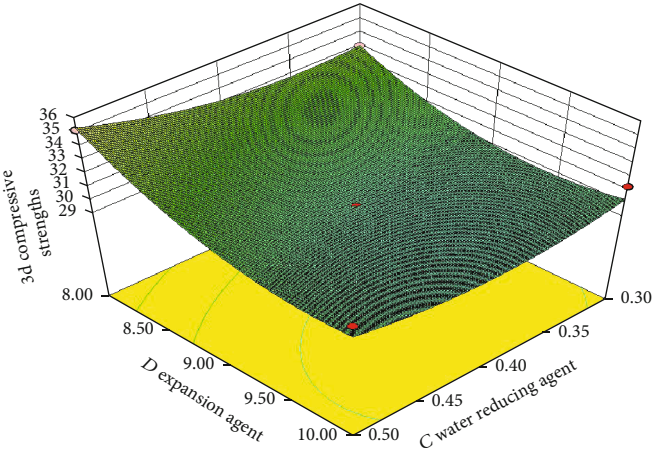
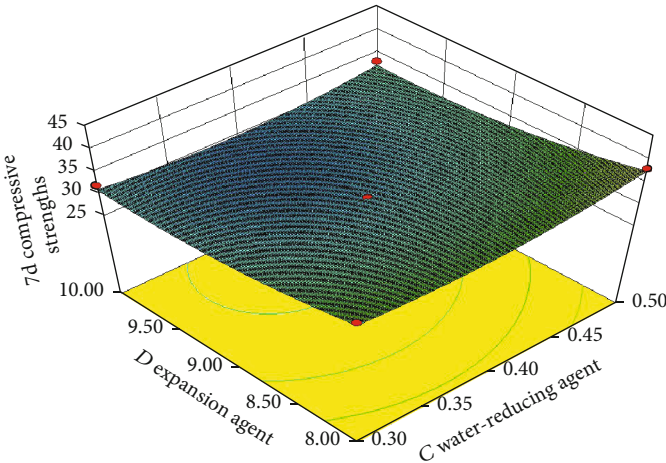


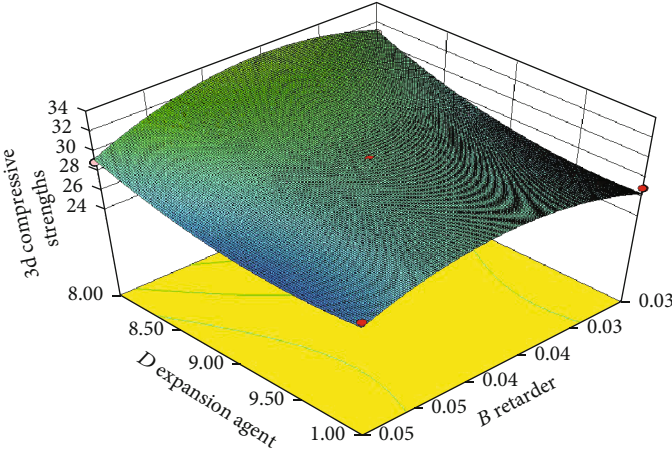
FIGURE 4: Continued.



(g)



(h)



(i)

FIGURE 4: Continued.

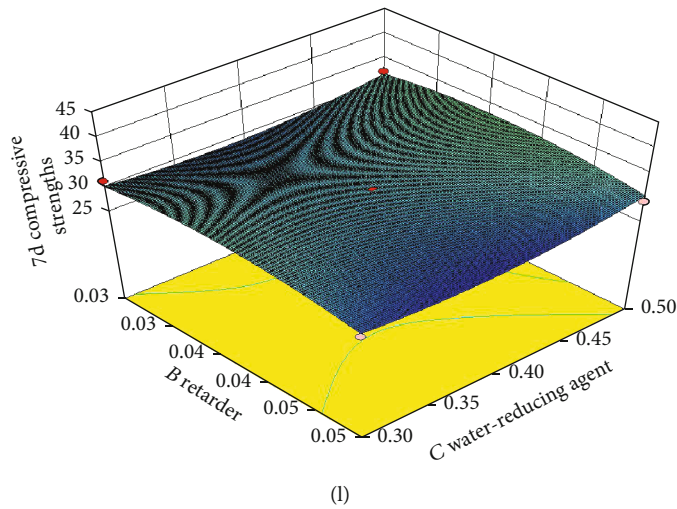
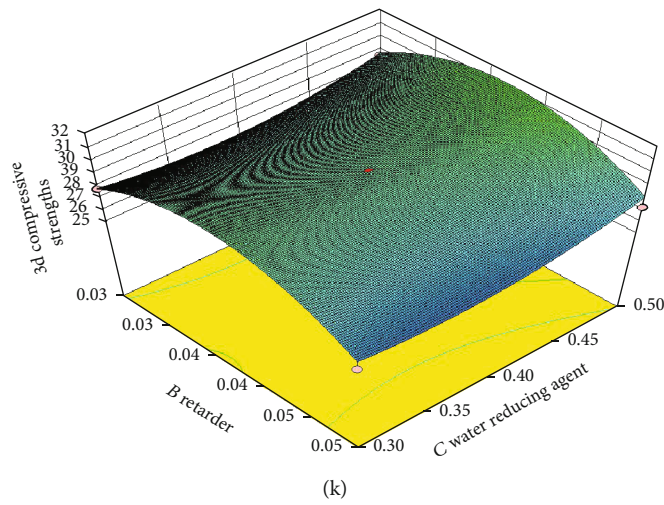
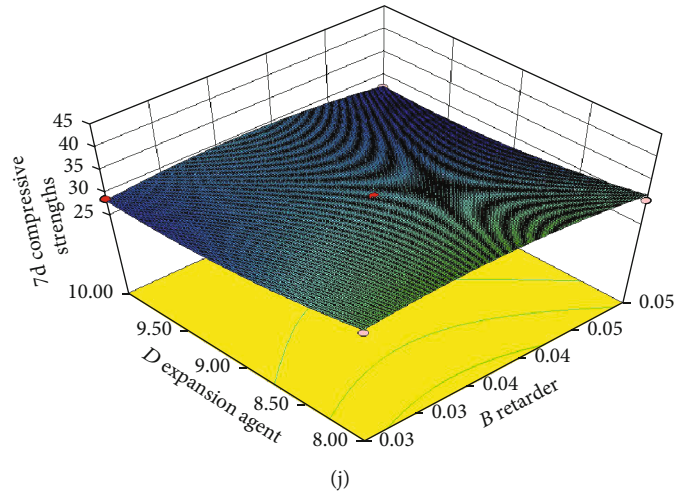


FIGURE 4: Three-dimensional response curve of compressive strength.

material during curing is loose, resulting in a lower compressive strength. When cured for three days, the cement clinker is encapsulated by C-S-H gel with an obvious pore structure and large pore volume. After 7-day curing, the surface area of the C-S-H gel gradually increases, the volume gradually

expands, and the pore becomes smaller. With the hydration reaction, the number of C-S-H gels increases, and some needle-shaped AFt crystals appear.

It can be seen from Figures 6(c) and 6(d) that the gel particles of the new sealing material are interconnected

TABLE 5: Optimum Scheme and Results.

No.	3 d compressive strength (actual) (MPa)	3 d compressive strength (prediction) (MPa)	Error (%)	7 d compressive strength (actual) (MPa)	7 d compressive strength (prediction) (MPa)	Error (%)
1	32.918	32.099	2.55	33.197	33.378	-0.54
2	33.554	33.031	1.58	36.031	35.463	1.61
3	31.487	31.243	0.78	33.717	33.615	0.30
4	26.601	26.490	0.42	27.449	27.381	0.25
5	28.587	28.032	1.98	30.936	30.398	1.77

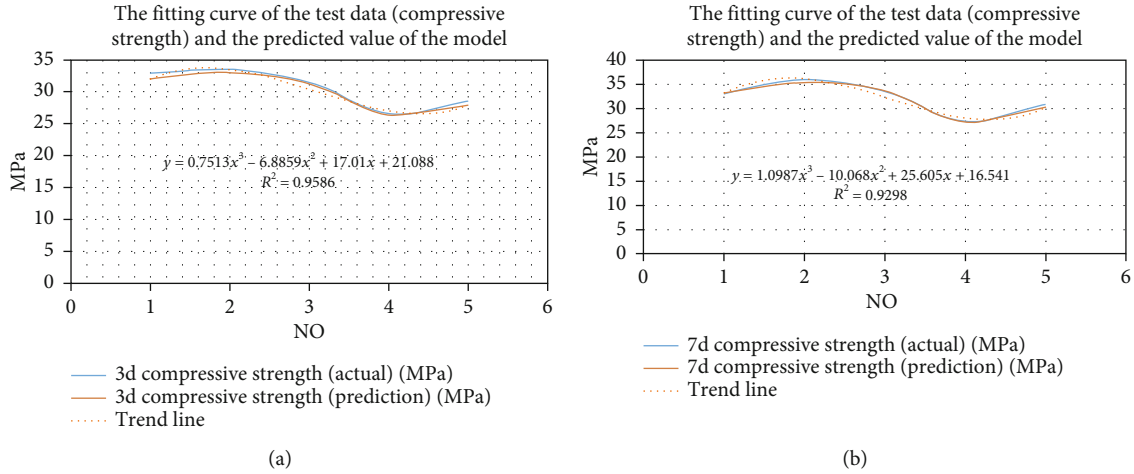


FIGURE 5: The fitting curve of the test data (compressive strength) and the predicted value of the model.

compactly, which increases the strength of the material. After 3 d curing, C-S-H gel with a dense structure and fewer pores was formed, which were wrapped with cement clinker; After 7 d curing, a large number of ettringite crystals were formed, indicating that the admixture can promote cement hydration reaction, and AFt crystals were generated with an expansion effect. The C-S-H gel and AFt were densely and uniformly cross-bonded together, thereby increasing the strength of the material [33–35].

6. Conclusions

- (1) The compressive strength of the samples varies greatly with the water-cement ratio or the amount of expansion agent. The compressive strength of the sample increases rapidly with the increase of the content of expansion agent when the water cement is relatively low. When the water-cement ratio increases to more than 0.9, the compressive strength of the sample increases slowly with the increase of the expansion agent content. When the content of expansion agent is low, the compressive strength of the sample increases rapidly with the decrease of the water-cement ratio. When the expansion agent content increases to more than 9%, the compressive strength of the sample increases slowly with the decrease of the water-cement ratio
- (2) When the water-cement ratio remains unchanged, the compressive strength of the specimen increases

first and then decreases with the increase of the retarder content. When the retarder content is constant, the compressive strength of the sample increases rapidly with the decrease of the water-cement ratio

- (3) When the content of expansion agent is constant, the compressive strength increases with the increase of the content of water reducer. When the content of expander is constant, the compressive strength increases first and then decreases with the increase of retarder content. When the amount of retarder remains unchanged, the compressive strength of the sample decreases rapidly with the increase of the amount of expansion agent
- (4) Through variance analysis and the significance test, the significance order of the influence of each component on the compressive strength were obtained as follows: water cement ratio > expansion agent > water reducing agent > retarder. According to the response surface drawn by the regression equation, the interaction between water-cement ratio and expansion agent has the most significant effect on the compressive strength, and the interaction between retarder and water reducing agent has the least significant effect on the compressive strength
- (5) The optimal experimental condition was obtained by response surface analysis: water reducing agent content of 0.4%, retarder content of 0.04%, the

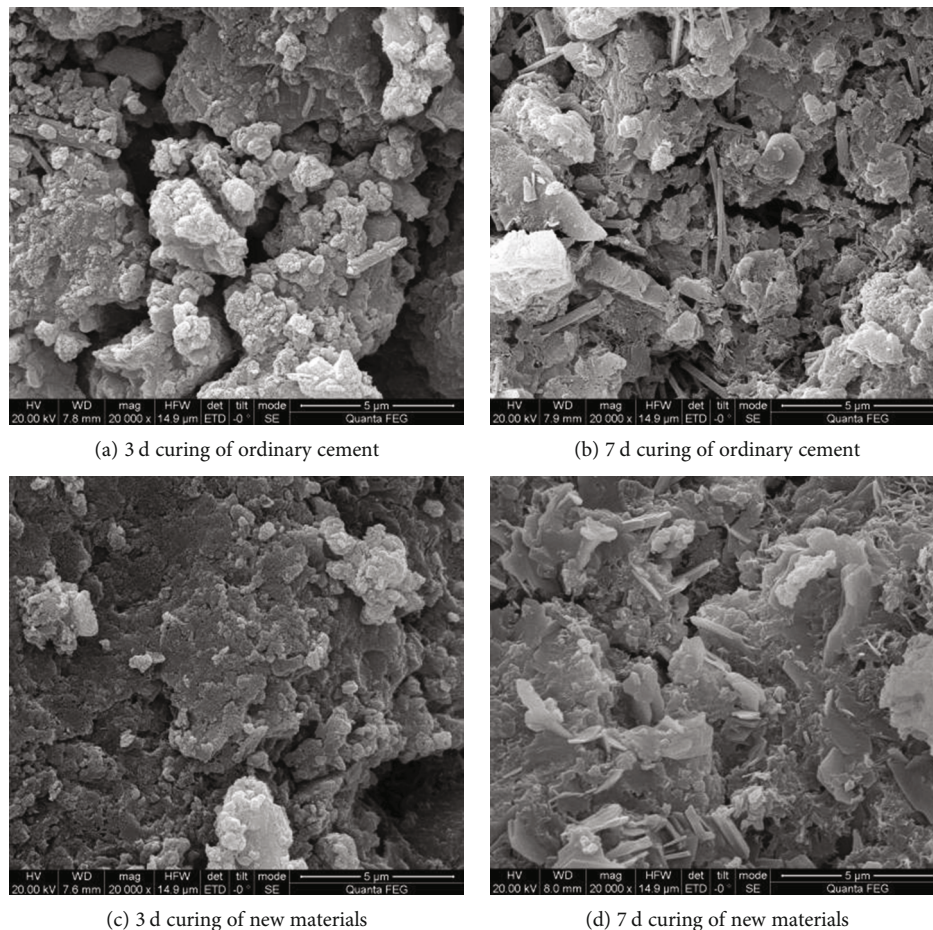


FIGURE 6: SEM micromorphology of hydration products of samples at different ages.

water-cement ratio of 0.8, and expansion agent content of 8%. The compressive strength of the new sealing material cured for 3 d and 7 d was 39.247 MPa and 41.044 MPa, with the maximum absolute error of 1.71% and 2.81%, respectively. The predicted value was highly consistent with the measured value

- (6) Compared with ordinary cement materials, the new sealing material has a denser overall structure and fewer pores. The hydration products C-S-H gel, Aft, and other cementing materials, which are uniformly cross-bonded together, increase the uniformity and compactness of the material, thus improving the strength of the material

Data Availability

The data used to support the findings of this study are available from the corresponding author upon request.

Conflicts of Interest

The authors declared no potential conflicts of interest with respect to the research, authorship, and/or publication of this article.

Authors' Contributions

All authors contributed to this paper. Sheng Xue and Xin Guo prepared the manuscript. Chunshan Zheng and Yaobin Li made a substantial contribution to the data analysis. Xiaoliang Zheng participated in the study and reviewed the manuscript.

Acknowledgments

This research was financially supported by the National Natural Science Foundation of China (Nos. 51934007 and 51904013) and Shandong Key S&T Innovation Engineering Project (2019JZZY020504).

References

- [1] L. Yuan, "Strategic thinking of simultaneous exploitation of coal and gas in deep mining," *Journal of China Coal Society*, vol. 41, no. 1, pp. 1–6, 2016.
- [2] H. Zhang, Y. Cheng, L. Yuan, L. Wang, and Z. Pan, "Hydraulic flushing in soft coal sublayer: gas extraction enhancement mechanism and field application," *Energy Science & Engineering*, vol. 7, no. 5, pp. 1970–1993, 2019.
- [3] S. Xue and L. Yuan, "The use of coal cuttings from underground boreholes to determine gas content of coal with direct desorption method," *International Journal of Coal Geology*, vol. 174, pp. 1–7, 2017.

- [4] Y. Guo, B. L. Zhang, X. G. Zheng, W. Zhou, X. L. Wei, and D. X. Zhu, "Grouting reinforcement technology of superfine cement with wind oxidation zone based on time varying rheological parameters of slurries," *Journal of Mining & Safety Engineering*, vol. 36, no. 2, pp. 338–343, 2019.
- [5] D. X. Zhu, Y. Guo, W. Wang, G. Guo, and T. An, "Grouting reinforcement technique in wind oxidation zone by power law superfine cement slurry considering the time-varying rheological parameters," *Advances in Civil Engineering*, vol. 2019, Article ID 2495850, 10 pages, 2019.
- [6] X. Gao, Y. Wei, F. M. Wang, and Y. H. Zhong, "Fatigue resistant and microstructure evolution of polyurethane grout materials under uniaxial compression," *Acta Materiae Compositae Sinica*, vol. 34, no. 4, p. 5507556, 2017.
- [7] Y. T. Niu, C. J. Zhang, Z. P. Yang, and X. M. Guan, "Recent progress of organic/inorganic grouting material based on polyurethane," *New Chemical Materials*, vol. 46, no. 3, pp. 42–44, 2018.
- [8] Z. P. Yang, W. J. Zhang, X. M. Guan, and C. J. Zhang, "Preparation, characterization, and properties of silicate/polyurethaneurea composites based on dipropylene glycol dibenzoate," *Polymer Composites*, vol. 4, no. 5, pp. 507–517, 2016.
- [9] X. M. Guan, H. B. Zhang, Z. P. Yang et al., "Research of high performance inorganic-organic composite grouting materials," *Journal of China Coal Society*, vol. 45, no. 3, pp. 902–910, 2020.
- [10] W. H. Sui, J. Liu, W. Hu, J. Qi, and K. Zhan, "Experimental investigation on sealing efficiency of chemical grouting in rock fracture with flowing water," *Tunnelling and Underground Space Technology*, vol. 50, pp. 239–249, 2015.
- [11] S. G. Li, J. F. Zhang, C. Zhang, H. F. Lin, and H. J. Yang, "Experimental study on expansion mechanism of new CF sealing material and the key influencing factors," *Journal of Mining & Safety Engineering*, vol. 35, no. 2, pp. 415–421, 2018.
- [12] T. J. Zhang, R. Y. Bao, S. G. Li, C. Zhang, L. Zhang, and X. K. Jiang, "Experimental study on expansion and creep characteristics of new CF sealing material," *Journal of Mining & Safety Engineering*, vol. 36, no. 1, pp. 175–183, 2019.
- [13] Q. B. Wang, Q. K. Zhu, T. S. Shao et al., "The rheological test and application research of glass fiber cement slurry based on plugging mechanism of dynamic water grouting," *Construction and Building Materials*, vol. 189, pp. 119–130, 2018.
- [14] J. Hogancamp and Z. Grasley, "The use of microfine cement to enhance the efficacy of carbon nanofibers with respect to drying shrinkage crack resistance of Portland cement mortars," *Cement & Concrete Composites*, vol. 83, pp. 269–272, 2017.
- [15] C. Zhai, X. W. Xiang, X. Yu, S. Peng, G. H. Ni, and M. Li, "Sealing performance of flexible gel sealing material of gas drainage borehole," *Journal of China University of Mining & Technology*, vol. 42, no. 6, pp. 982–988, 2013.
- [16] J. X. Zhang, Y. N. Sun, Z. D. Sun, Z. M. Wang, Y. Y. Zhao, and T. B. Sun, "Analysis of macroscopic mechanical properties and mechanism of coal dust/polymer composite grouting material," *Chinese Journal of Rock Mechanics and Engineering*, vol. 38, Supplement 1, pp. 2889–2897, 2019.
- [17] C. Zhai, X. W. Xiang, Q. L. Zou, X. Yu, and Y. M. Xu, "Influence factors analysis of a flexible gel sealing material for coal-bed methane drainage boreholes," *Environmental Earth Sciences*, vol. 75, no. 5, 2016.
- [18] X. X. Chen, R. Bi, and L. Zhang, "Effect of water-to-cement ratio on sulfo-aluminate type cementitious grouting materials," *Magazine of Concrete Research*, vol. 71, no. 6, pp. 298–308, 2019.
- [19] Z. Q. Feng, H. P. Kang, and G. Q. Han, "Polyurethane grouting materials modified by inorganic salts in coal mines," *Chinese Journal of Geotechnical Engineering*, vol. 35, no. 8, pp. 1559–1564, 2013.
- [20] Z. N. Wang, S. L. Shen, A. N. Zhou, and H. M. Lyu, "Mechanical, flame-retarding, and creep-recovery properties of ethylene-propylene-diene monomer enhanced with nano-hydroxide for undersea tunnel sealing gasket," *Journal of Applied Polymer Science*, vol. 138, no. 10, 2021.
- [21] Z. N. Wang, S. L. Shen, A. Zhou, and H. M. Lyu, "Experimental investigation of water-swelling characteristics of polymer materials for tunnel sealing gasket," *Construction and Building Materials*, vol. 256, article 119473, 2020.
- [22] Z. N. Wang, S. L. Shen, A. N. Zhou, and Y. S. Xu, "Experimental evaluation of aging characteristics of EPDM as a sealant for undersea shield tunnels," *Journal of Materials in Civil Engineering*, vol. 32, no. 7, article 4020182, 2020.
- [23] J. S. Tan, S. L. Shen, A. Zhou, Z. N. Wang, and H. M. Lyu, "Laboratory evaluation of long-term sealing behaviors of two water-swelling materials for shield tunnel gasket," *Construction and Building Materials*, vol. 249, p. 118711, 2020.
- [24] F. Liu, S. L. Shen, D. W. Hou, A. Arulrajah, and S. Horpibulsuk, "Enhancing behavior of large volume underground concrete structure using expansive agents," *Construction and Building Materials*, vol. 114, pp. 49–55, 2016.
- [25] J. X. Zhang, H. M. Lyu, S. L. Shen, and D. W. Hou, "Investigation of crack control of underground concrete structure with expansive additives," *Journal of Materials in Civil Engineering*, vol. 33, no. 1, p. 04020420, 2021.
- [26] H. C. Du, Y. N. Wang, M. M. He, Z. F. Lin, and Z. Z. Lyu, "Study on the effect of organic retarder on the performance of cement modified emulsified asphalt mastic," *Materials Review*, vol. 33, no. S2, pp. 254–260, 2019.
- [27] L. L. Shui, Z. Sun, H. Yang, X. Yang, Y. Ji, and Q. Luo, "Experimental evidence for a possible dispersion mechanism of polycarboxylate-type superplasticisers," *Advances in Cement Research*, vol. 28, no. 5, pp. 287–297, 2016.
- [28] Y. R. Zhang and X. M. Kong, "Correlation of the dispersing capability of NSF and PCE types of superplasticizer and their impacts on cement hydration with the adsorption in fresh cement pastes," *Cement and Concrete Research*, vol. 65, no. 3, pp. 1–9, 2015.
- [29] J. J. Feng, M. Miao, and P. Y. Yan, "Hydration and expansion properties of shrinkage-compensating composite cementitious materials," *Journal of Building Materials*, vol. 15, no. 4, pp. 439–445, 2012.
- [30] Z. F. Pan, Y. Z. Zhu, D. F. Zhang, N. Chen, Y. C. Yang, and X. N. Cai, "Effect of expansive agents on the workability, crack resistance and durability of shrinkage-compensating concrete with low contents of fibers," *Construction and Building Materials*, vol. 259, p. 119768, 2020.
- [31] W. T. Lan, A. X. Wu, and Y. M. Wang, "Formulation optimization and formation mechanism of condensate expansion and filling composites," *Acta Materiae Compositae Sinica*, vol. 36, no. 6, pp. 1536–1545, 2019.
- [32] R. Y. Bao, *Study on the Instability Mechanism of the Sealing Section of the Borehole in Soft Coal Seam and the New Reinforced Seal Technology*, [Ph.D. Thesis], Xi'an University of Science & Technology, China, 2019.

- [33] B. Li, *Study on the Mechanism of Microscopic Mechanics of hydrated Calcium silicate (C-S-H) Gel*, [Ph.D. Thesis], Harbin Engineering University, China, 2018.
- [34] P. Termkhajornkit, R. Barbarulo, and G. Chanvillard, "Microstructurally-designed cement pastes: a mimic strategy to determine the relationships between microstructure and properties at any hydration degree," *Cement and Concrete Research*, vol. 71, pp. 66–77, 2015.
- [35] W. Sekkal, A. Zaoui, M. Benzerzour, and N. Abriak, "Role of porosity on the stiffness and stability of (001) surface of the nanogranular C-S-H gel," *Cement and Concrete Research*, vol. 87, pp. 45–52, 2016.

Research Article

Failure Analysis of Deep Composite Roof Roadway and Support Optimization of Anchor Cable Parameters

Chen Li ¹, Wenlong Zhang ¹, Tianhong Huo¹, Rui Yu,² Xidong Zhao ³ and Ming Luo¹

¹School of Energy & Mining Engineering, China University of Mining and Technology (Beijing), Beijing 100083, China

²Wang Jialing Coal Mine, China Coal Energy Research Institute Co., Ltd., Yuncheng 043301, China

³School of Safety Engineering, North China Institute of Science & Technology, Langfang 065201, China

Correspondence should be addressed to Chen Li; 13120008810@163.com and Xidong Zhao; xdz523@126.com

Received 9 May 2021; Accepted 1 July 2021; Published 16 July 2021

Academic Editor: Haiyan Wang

Copyright © 2021 Chen Li et al. This is an open access article distributed under the Creative Commons Attribution License, which permits unrestricted use, distribution, and reproduction in any medium, provided the original work is properly cited.

The stability of the roadway surrounding rock is the key factor of underground mining. Roof subsidence occurred during roadway excavation in the Menkeqing Coal Mine. For the sake of safety, it was decided to stop tunneling project and strengthen roadway support, which resulted in a delay of the construction period and economic damage. To maintain the stability of the surrounding rock, we carried out a systematic study through field monitoring, theoretical analysis, and numerical simulation. The deformation and failure law of the surrounding rock, roof structure characteristics, and mechanical properties of the surrounding rock were obtained by field monitoring. The failure characteristics and forms of deep composite roof roadway are further analyzed. The key points of stability of the roadway surrounding rock of soft rock composite laminated roof are obtained by theoretical analysis, i.e., improving the effective stress diffusion efficiency of the anchor cable through the reasonable arrangement of the anchor cable. We use FLAC numerical simulation software to study the influence of different supporting parameters of anchor cable on the stress diffusion in the surrounding rock and put forward the optimal parameters. The optimized support parameters have been applied in the field, and the ideal results have been obtained.

1. Introduction

At present, the mining of coal resources in China is gradually developing to deep mining [1, 2]. Compared with shallow coal mining, deep coal mining is affected by higher stress and a more complex geological structure. The coal measure strata are mostly formed by sedimentation, and the roof of coal seam is mostly a layered structure [3]. Therefore, the deep mining roadway often shows stronger deformation failure and higher repair frequency than the shallow mining roadway [4, 5].

The high deviated stress field around the roadway during mining can be artificially intervened by adjusting the mining layout [6–9]. However, the high-stress field of the first mining face in the tunneling stage cannot be changed, even if the strong support on the regional stress field of the roadway is very little change [10]. In the face of high-stress mining roadway deformation and failure, it is necessary to clearly understand the rock structure and rock strength parameters

[11–13]. These data are the basis for analyzing the deformation and failure mechanism of the surrounding rock and also the basis for putting forward the corresponding control measures of the surrounding rock [14–16]. At present, the surrounding rock stability control of mining roadway mainly depends on the active support of rebar bolt and anchor cable [17, 18]. Because the rebar bolt length is short and the support resistance is small, there are some hidden dangers in the support effect when the damage range of the surrounding rock is larger than the length of the rebar bolt. Anchor cable support resistance is large, but the overall elongation is small and the use cost is high. Besides, the high density of the anchor cable is easy to cause the hanging roof of goaf [19]. Therefore, the reasonable arrangement of the anchor cable is of great significance to the stability control of the surrounding rock [20, 21].

We have carried out detailed mine pressure monitoring and geological investigation on the project site. On this basis, combined with numerical simulation analysis, the instability

mechanism of the composite roof is obtained. In addition, we further study the mechanism of anchor cable and stress diffusion effect of different anchor cable arrangements in the roof. According to the research results, the anchor cable support scheme is optimized, and the research results have a guiding significance for other mining roadway engineering in this mine.

2. Project Profile

2.1. Engineering Geology and Support Conditions. The Menkeqing Coal Mine is located in the Hujert Mining Area, Wushen Banner, Ordos City, Inner Mongolia Autonomous Region. Menkeqing Coal Mine is a typical deep mining mine. The average buried depth of 2-2 coal seam is 760 m, and the average coal thickness is 2.63 m. The designed length of the 2201 return air roadway is 1760 m, and the designed section width \times height of the roadway is 5.4 m \times 2.5 m, which is driven along the floor of the coal seam. The geological exploration borehole of 2-2 coal seam shows that the roof structure is complex, the immediate roof is composed of medium sandstone, sandy mudstone, fine sandstone, and argillaceous interlayer, and the surrounding rock of the roof is rich in water.

The initial support of the roadway is a combined support design of rebar bolt-anchor net-anchor cable. The coal pillar rib and roof are $\Phi 20 \times 2300$ mm rebar bolt support, and the working face rib is 27×2300 mm FRP bolt support. Row spacing between bolts is 800×800 mm. The roof anchor net is made of steel belt made of $\Phi 12$ mm round steel, with a length of 5400 mm. Roof anchor cable specification is $\Phi 21.8 \times 8300$ mm and row spacing 2400×2400 mm, as shown in Figure 1.

2.2. Failure Law of the Surrounding Rock. Water drenching phenomenon appeared in 2201 return air roadway from 800 m. The roof sag tendency was obvious after roadway excavation and even the roof leakage occurred locally. Therefore, to avoid the continuous roof sag, reinforcement support was carried out in the corresponding area, i.e., two rows of anchor cable were supported again in the middle of the two rows of anchor cables and two anchor cables for each row, and combined reinforcement support was carried out with single hydraulic pillar and I-steel. In addition, $\phi 200$ mm pine wooden point post support was set as a warning, as shown in Figure 2. To be on the safe side, roadway excavation was suspended. According to the LBY-2 roof separation instrument installed on the roof during tunneling, the deformation and failure of the surrounding rock within the range of 0 ~ 5 m of the roof can be obtained, as shown in Figure 3.

In the range of 800 m ~ 1200 m, the roof sag of the roadway reached 80~130 mm only under the influence of tunneling. Bedding failure exists in the shallow surrounding rock of 0 ~ 2.5 m and the deep surrounding rock at 2.5 ~ 5 m of the roof. The average bedding separation of the surrounding rock in the shallow part of this section is 59.3 mm, while the average bedding separation of the surrounding rock in the deep part is 48.2 mm. Although the shallow deformation accounted for 55.16%, it did not take an absolute advantage.

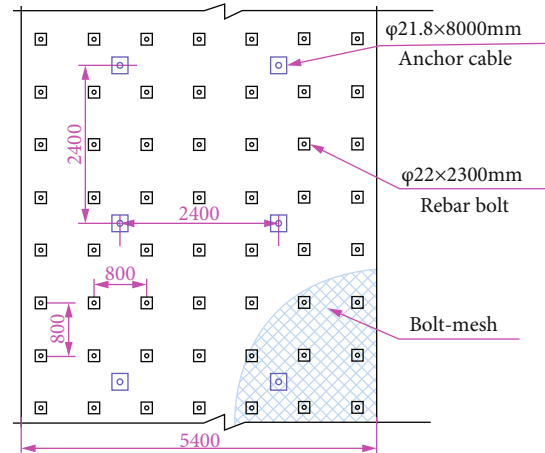


FIGURE 1: The roof support plan of 2201 return air roadway.

Therefore, from the perspective of quantitative analysis, there were potential unstable strata within 5 m of the roadway roof. In general, the bedding separation amount in the shallow part of the roof is larger, as shown in Figure 3(a). Figure 3(b) shows the bed separation curve at 1050 m. It can be seen from the figure that the roof surrounding rock was not completely stable within 15 days after roadway excavation, and the deep roof was basically stable after reinforcement on the 16th day, but the shallow surrounding rock was still stable after 4 days. Therefore, it is still necessary to optimize the original supporting parameters according to the geological conditions.

3. Instability Analysis of Composite Roof

3.1. Roof Structure Detection of Roadway. To clarify the relationship between roof subsidence and rock distribution and understand the development characteristics of roof fractures, a ZXZ20-Z roof borehole detector was used to detect the roof structure at 800-1200 m of 2201 return air roadway. The average spacing of detection points was 65 m, and the detection results of the roadway roof rock distribution were shown in Figure 4.

As can be seen from Figure 4, the roof of 2201 return air roadway has the feature of composite lamination, and there are 6 kinds of rock strata distributed within 8 m from bottom to top of the immediate roof. Especially within the range of 5 m above the roof, the average thickness of the rock layer is only 1 m. The siltstone layer contains an interlayer of mudstone with an average thickness of 0.38 m. Local coal lines are developed in the roof. Peep detection shows that there is still a broken zone in the sandy mudstone layer, and the maximum damage range of the surrounding rock in the deep roof is up to 4.8 m. The borehole in the mudstone interlayer has an obvious bed separation zone. In contrast, the destruction of the shallow surrounding rock is more obvious. The separation, fragmentation, and cavitation are the most serious in the middle sand strata.

The vertical stress of the original rock in 2201 air return roadway is about 19 MPa. According to the mining coefficient of 3, the mining stress of the roadway will be about 57 MPa in the later period. Therefore, the reduction of

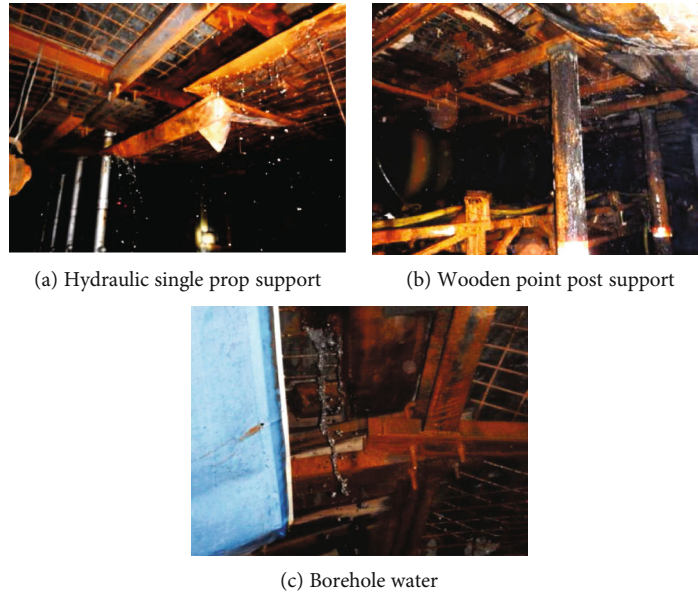


FIGURE 2: Damage of tunneling roadway (roof water spray).

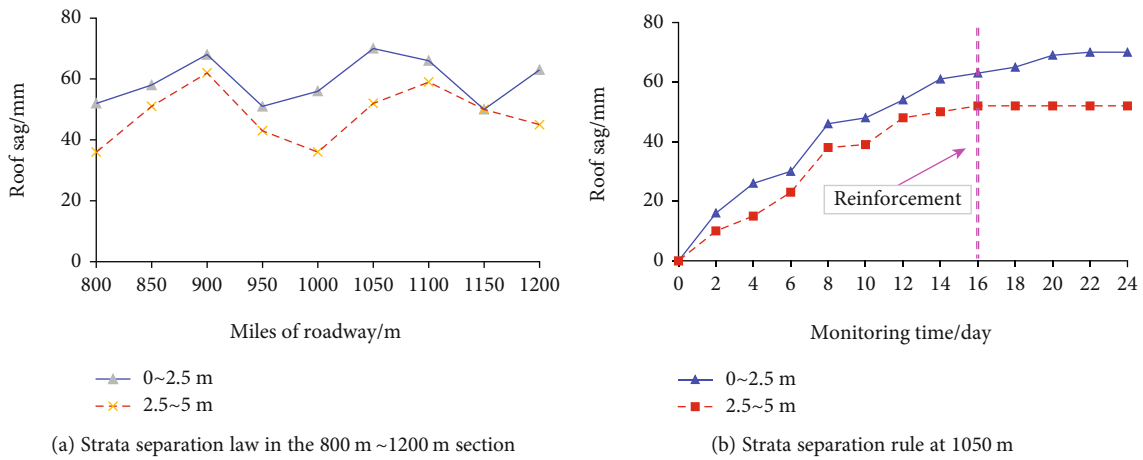


FIGURE 3: Separation curve in roof sag section.

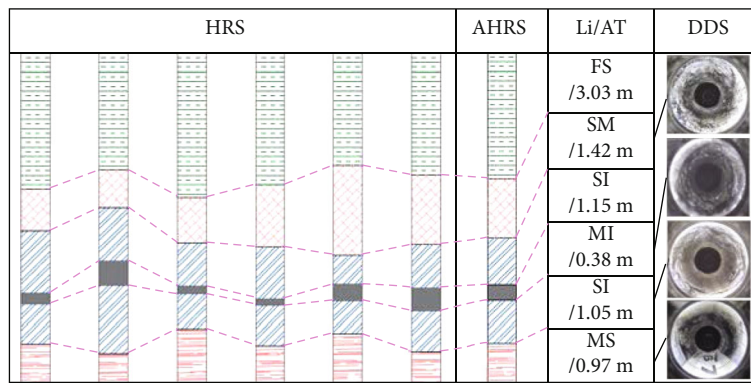


FIGURE 4: Roof structure survey results (where HRS: histogram of roof strata; AHRS: average histogram of roof strata; Li: lithology; AT: average tickness; DDS: drilling detection screenshot; FS: fine sandstone; SM: sandy mudstone; SI: siltstone; MI: mudstone interlayer; MS: medium sandstone).

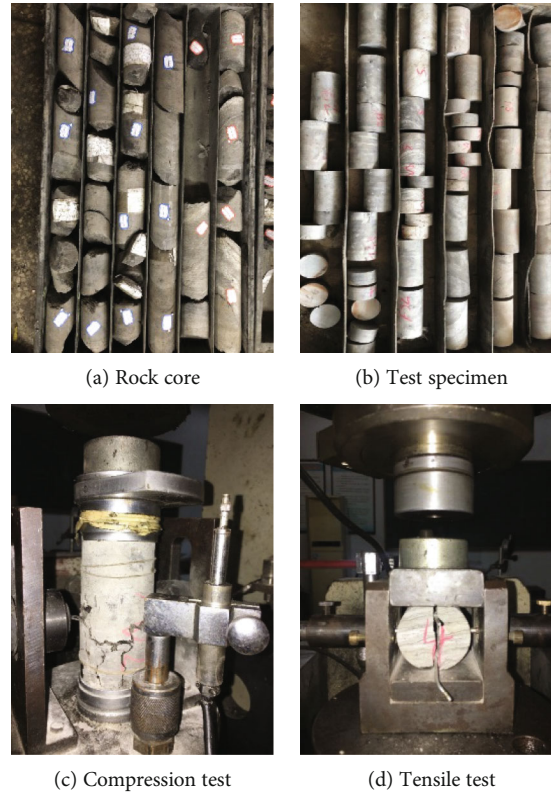


FIGURE 5: Mechanical test process of the surrounding rock.

TABLE 1: Rock mechanic test results.

Li	σ_c /MPa	Normal conditions			σ_c /MPa	Immersion conditions		
		σ_t /MPa	C/MPa	f /°		σ_t /MPa	C/MPa	f /°
GR	40	3.8	5.6	35	34	3.1	4.6	32
MS	35	2.2	4.5	36	26	1.7	3.2	35
FS	38	2.8	5.9	31	28	1.5	1.9	30
SM	15	1.3	2.2	28	8	0.8	0.7	26
SI	32	3.5	4.4	35	23	2.5	2.1	32
MU	18	2.3	2.5	30	5	0.7	0.6	25
SI	33	3.4	4.5	36	24	2.5	1.8	35
MS	30	2.8	3.4	33	19	1.7	2.2	30

Where GR: grit; MU: mudstone; σ_c : compressive strength; σ_t : tensile strength; C: cohesion; f : internal friction angle.

tangential stress under the action of strong mining stress will lead to serious damage to the roadway with small layer thickness, weak interlayer, and water-rich roof [22]. There is a hidden danger of roof caving.

3.2. Mechanical Parameter Test of the Surrounding Rock. To understand the mechanical difference between the normal condition of the roof surrounding rock and the water pouring condition, the core was drilled in the backing chamber at 650 m of 2201 return air roadway. The diameter of the core drilling hole is $\Phi 8$ mm, the length of the core is 15 m, and the inclination is 80° . After the core is encapsulated, the rock mechanic test is carried out in the laboratory. The test pro-

cess is shown in Figure 5, and the rock mechanic test results are shown in Table 1.

When the immediate roof of 2201 air return roadway is in water content condition, the rock strength is affected, among which the sandstone mudstone and mudstone have stronger softening properties. The buried depth of 2201 return air roadway is 670 m, and the vertical stress of the original rock of coal seam is about 19 MPa [3, 12, 22]. Therefore, under the same stress action, the strength of the surrounding rock in the water-pouring area of the roof is weakened, and it is easier to produce a large range of plastic zone. At the same time, the plastic zone of the surrounding rock is accompanied by the strong expansion pressure acting

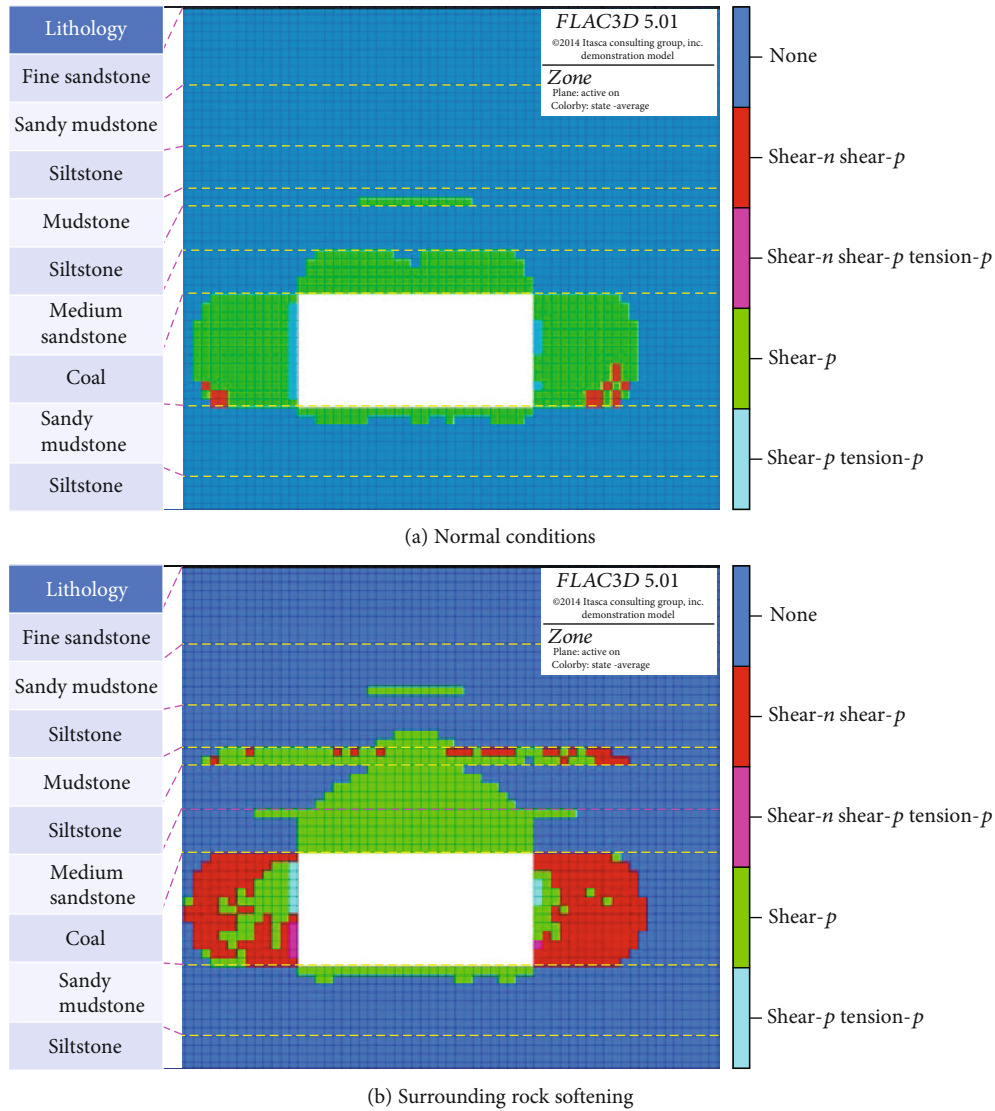


FIGURE 6: Distribution of plastic zone in the roadway surrounding rock.

on the roof, which intensifies the potential instability probability of the roof [23]. In addition, the degree of softening of different rock strata by water is not consistent, which leads to the great strength difference between rock strata. The poor cohesion between layers further aggravates the instability of the roof separation layer.

3.3. Failure Characteristic of the Surrounding Rock. Through the detection of the roof structure of the roadway, it is found that the roof has obvious rock formation and contains mudstone interlayer with an average thickness of 0.4 m. The mechanical properties of different rock strata in the roof were obtained by borehole core test of surrounding rock mechanics. The mechanical properties of the surrounding rock decrease sharply after water softening. Based on this, a 50 m × 50 m FLAC numerical model was established to analyze the influence of interlayer and lithology on the failure of the roadway surrounding rock [24–26]. The rock strata were fine tuned to facilitate mesh division, and the

mesh size was 0.2 m × 0.2 m. The lateral and bottom boundary of the model was fixed, and the upper boundary was compensated with 19 MPa normal stress. The gravity stress gradient and pressure coefficient in the model were 0.025 and 1.2, respectively. The Mohr-Coulomb constitutive model was adopted in the simulation.

The numerical model results are shown in Figure 6. Figure 6(a) shows the plastic zone distribution of the surrounding rock under normal conditions. At this time, due to the weak strength of the coal seam rock, the plastic zone of the surrounding rock at the roadway ribs under strong vertical stress is 2.4 m. The damage range of the immediate roof of the roadway is 1 m, and the whole medium sand strata are reduced to a plastic zone. There is no plastic failure zone in siltstone due to its high rock strength, but there is a small plastic zone with a thickness of 0.2 m in the mudstone interlayer with weaker lithology. Figure 6(b) shows the distribution of plastic zone in surrounding rock of roadway when the surrounding rock is softened. Compared with

Figure 6(a), the softening of rock strength leads to a sharp expansion plastic zone and the failure depth above the roof. In particular, the extension of the mudstone interlayer is particularly obvious.

The change of the position and thickness of interlayer and the change of the strength of the surrounding rock seriously affect the morphology and size of the plastic zone of the surrounding rock. Under normal circumstances, rebar bolt support of roof can maintain the stability of roadway. However, under the condition of water softening of the surrounding rock, the anchorage part of the rebar bolt is located in the plastic zone. It is easy to cause the overall sag of the surrounding rock within the range of rebar bolt. In this case, the function of rebar bolt is limited, and the stability of surrounding rock is mainly maintained by anchor cable. The anchor cable not only needs to suspend the potentially unstable rock strata in the roof stable rock strata but also should have a reasonable arrangement so that the support resistance can fully diffuse in the surrounding rock.

3.4. Analysis of Failure Mode of Composite Roof. The direct roof of 2201 return air roadway is a composite roof with small rock thickness, poor interlayer cohesiveness, and local coal line development. Usually under such roof conditions, if the roadway is excavated, there will be obvious layer separation, and it is difficult to form a self-supporting structure, resulting in roof safety accidents [27].

The failure forms of the composite roof can be summarized into three types, such as flexural failure, integral separation, and weak plane slip [28], as shown in Figure 7. The roof flexural failure is shown in Figure 7(a). At this time, the rebar bolt should pass through multiple separation positions as far as possible, and the rebar bolt should be anchored into the deep of the stable rock strata. In this case, the roof of 2201 return air roadway has the disadvantages of insufficient rebar bolt density and sufficient length due to complex strata stratification within 5 m. The overall roof separation damage is shown in Figure 7(b). At this time, the anchor cable support density should be increased, and the preload should be increased. In this case, the roof support of 2201 return air roadway has the shortcoming of insufficient anchor cable support strength. The situation of the roof with a weak surface is shown in Figure 7(c). At this time, rebar bolt and anchor cable combined support with grouting modification to give full play to the self-supporting capacity of the surrounding rock which is one of the best support methods. The roof of 2201 return air roadway only contains weak interlayers with few weak surfaces. Grouting has not been considered for the time being.

4. Optimization of Strong Supporting Parameters of the Anchor Cable

4.1. Analysis of Supporting Action of the Anchor Cable. In deep mining, the change of anchor cable supporting parameters has a limited effect on the plastic zone of the surrounding rock when the mechanical properties of surrounding rock and the stress environment are given. However, changing the supporting parameters of anchor cable plays an important

role in the stability control of the surrounding rock in the plastic zone [29, 30]. The rebar bolt of layered composite roof roadway is mainly aimed at the shallow surrounding rock and combined with the shallow rock to form the “anchor beam” structure. The anchor cable with stronger support strength can suspend the shallow “anchor beam” structure in the deep stable rock strata. In addition, the strong anchor cable can effectively control the slip of weak surface and restrain the formation of new cracks. The high prestress of anchor cable can increase the friction and shear strength between rock layers by increasing the normal restraint of composite layered rock masses. The length of the anchor cable makes the high prestress of the anchor cable effectively diffuses in the deep strata and improves the integrity of the surrounding rock [31].

The reinforcement of the composite roof surrounding rock by anchor cable support is mainly through the joint action of anchor cable monomer, anchoring agent, and tray. According to the elastic mechanic's theory, the mechanical model of interaction between rock strata and anchor cable of the composite roof is established, as shown in Figure 8.

Assuming that the anchor cable and the rock mass within the influence range meet axisymmetry [31], the axial balance equation of the anchor cable element body is shown in Eq. (1).

$$\frac{\partial \sigma_{zz}}{\partial z} + \frac{1}{r} \left[\frac{\partial (r \tau_{rz})}{\partial r} \right] = 0, \quad (1)$$

where σ_{zz} is the axial stress of anchor cable infinitesimal body; τ_{rz} is the shear stress of anchor cable infinitesimal body.

For anchor cable, the following relationship exists:

$$\frac{d\sigma_{zz}^f(z)}{dz} + \frac{2}{a} \tau(z) = 0, \quad (2)$$

where $\sigma_{zz}^f(z)$ is the average axial stress of the anchor cable; a is the radius of anchor cable.

The constitutive equation of rock mass is

$$\tau(r, z) = G_m \gamma = G_m \frac{dw}{dr}, \quad (3)$$

where G_m is the shear modulus of deep surrounding rock mass; w is the axial displacement of the deep surrounding rock mass.

The equilibrium condition of anchor cable and the cross-section force affecting the microsegment of rock mass is

$$\bar{\sigma}_m = - \frac{a^2}{b^2 - a^2} \sigma^f. \quad (4)$$

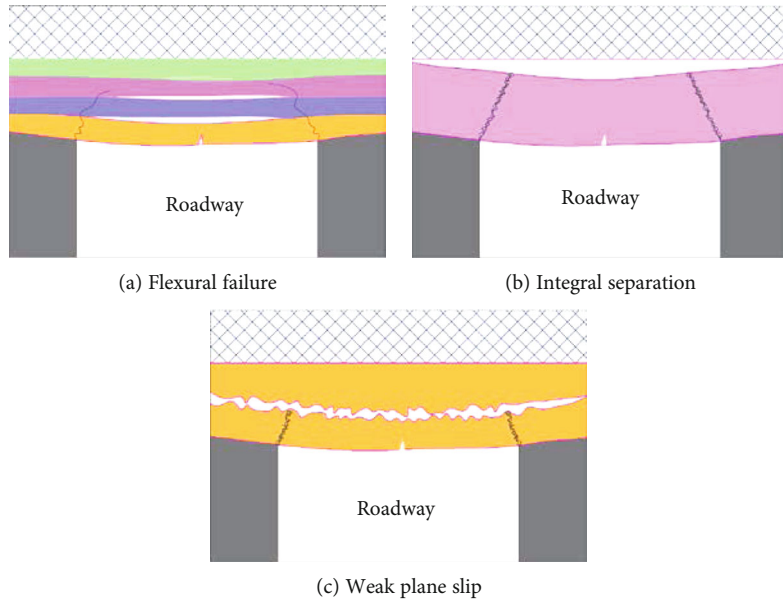


FIGURE 7: Composite roof failure mode.

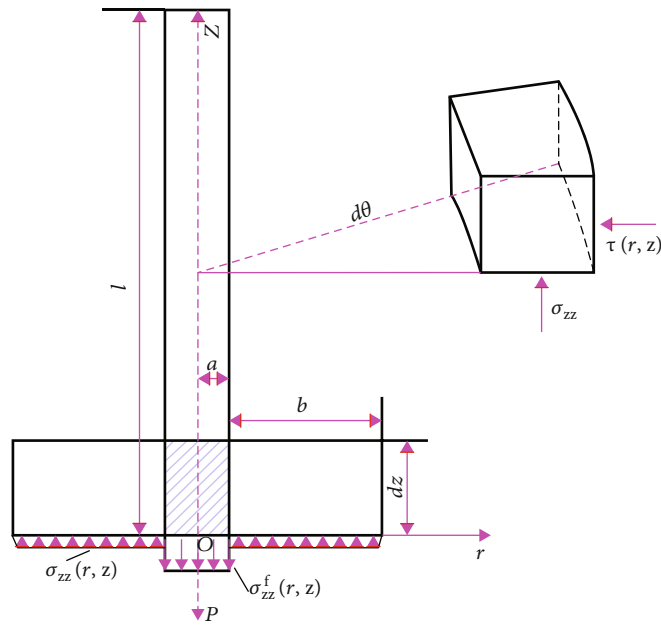


FIGURE 8: The model anchor cable and its influence on rock mass.

The boundary conditions are

$$\begin{cases} z = 0, \sigma^f(z) = \frac{P}{\pi a^2}, \\ z = l, \sigma^f(l) = 0, \end{cases} \quad (5)$$

where P is the pretension; l is the length of anchor cable.

By analyzing the axial stress balance equation of the anchor cable element body through Eq. (1)–(5), the axial stress of the anchor cable and the shear stress of the interface

between the anchor cable and the surrounding rock mass can be obtained, as shown in Eqs. (6) and (7).

Axial stress of anchor cable is as follows:

$$\sigma(z) = \frac{P}{\pi a^2} [\cosh(kz) - c \tanh(kl) \sinh(kz)], \quad (6)$$

where c is the cohesion of the surrounding rock; K is the coefficient of general solution; z is any point along the anchor cable axis.

Interfacial shear stress of surrounding rock mass is as follows:

$$\tau(z) = \frac{kp}{2\pi a} [c \tanh(kl) \cosh(kz) - \sinh(kz)]. \quad (7)$$

The bearing capacity of the anchoring balanced arch bearing structure is as follows:

$$q = \frac{Q(1 + \sin \theta)(l - D)}{D^2(1 - \sin \theta)(R + l - D)}, \quad (8)$$

where q is the bearing capacity of the arch, kN; Q is the anchor cable prestress, kN; D is the anchor cable spacing, m; R is the half of the roadway span, m; θ is the internal friction angle of coal-rock mass, ($^{\circ}$).

According to Eq. (6)–(8), increasing the prestress of the anchor cable (or increasing the support strength in a disguised way by increasing the support density) contributes to the stress diffusion of the anchor cable. It also helps to increase the damage resistance of the weak surface. There is a negative correlation between the anchorage balance arch and the row spacing between the anchors. Under the condition of weak roof lithology and obvious laminated characteristics, increasing the strength of anchor cable support is beneficial to the stability of the roadway surrounding rock.

Strata stratification is obvious within 5 m of the roof of 2201 return air roadway, and rebar bolt obviously cannot effectively control deep separation. The large row spacing between the anchor cable leads to the fact that a single anchor cable acts alone and cannot form an effective superimposed compression body in the same section (as shown in Figure 9). This eventually causes the roof to sag as a whole. Therefore, the anchor cable with row spacing of 2400×2400 mm fails to form an arch-bearing structure. It also fails to maximize the use of the overall stiffness and self-bearing capacity of the surrounding rock within the support range.

4.2. Numerical Analysis of Anchor Cable Support. To effectively maintain the stability of the roof of 2201 return air roadway and reduce engineering rework, the parameters of the roof with composite layered soft rock characteristics were optimized. The original anchor cable support parameters were optimized from 2400×2400 mm interrow spacing, 2-2 layout, to 1600×1600 mm interrow spacing, 2-3-2 layout. The numerical simulation analysis was carried out for different support schemes [32]. The rebar bolt support resistance is 120 kN, and the anchor cable support resistance is 350 kN. Vertical stress nephogram in the mudstone interlayer at 2 m of the roof and between two rows of anchor cables in roadway were, respectively, intercepted, as shown in Figure 10.

Figure 9 shows that the superposition value of the stress field in the bolt support range is the largest under different support schemes. With the change of anchor cable supporting density, the stress gap within the anchor cable supporting range is very large. The stress at 2 m above the roof (in the

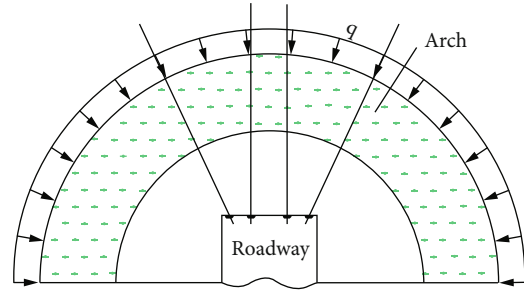
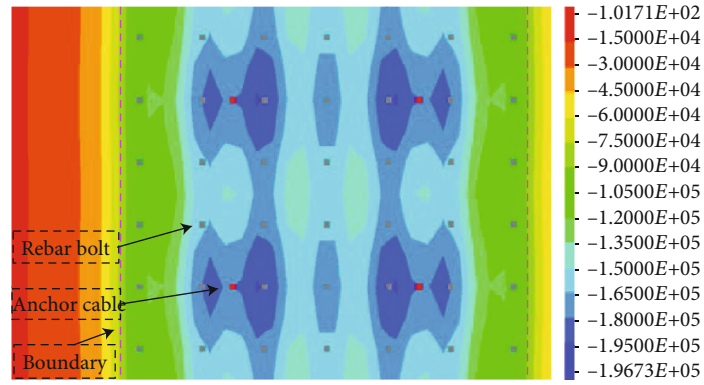


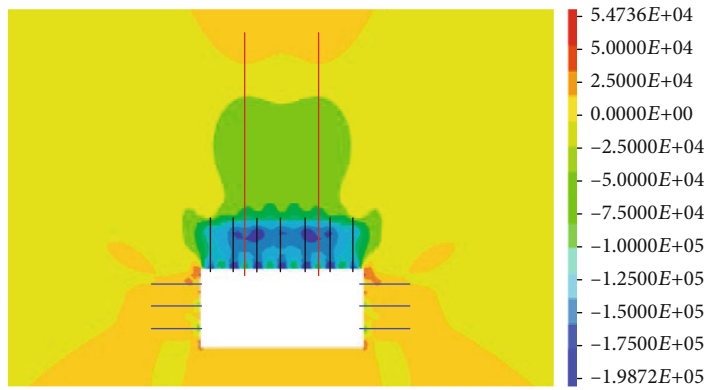
FIGURE 9: Anchorage equilibrium mechanical model.

mudstone interlayer) of the original support scheme does not diffuse effectively. The stress tends to be distributed at the point and was relatively scattered. The stress is concentrated around the anchor cable, and the maximum stress concentration is 0.1967 MPa, as shown in Figure 10(a). The maximum stress between the two rows of anchor cables in the original support is only 0.1987 MPa, as shown in Figure 10(b). In the reinforced support scheme, the stress is effectively diffused at 2 m above the roof, and the high stress under the action of the anchor cable is connected into sheets, with the maximum stress concentration of 0.3000 MPa. However, the stress in the middle of the roadway with the greatest roof caving hidden danger is small, as shown in Figure 10(c). The maximum stress between the two rows of anchor cables in the original support significantly increased to 0.8352 MPa, but the stress diffusion effect was poor, as shown in Figure 10(d). The stress of the optimized support scheme is smaller than that of the reinforcement scheme but larger than that of the original support scheme. In addition, the stress at 2 m above the roof is effectively diffused, and the high stress under the action of the anchor cable is connected into sheets. The maximum stress concentration is 0.2657 MPa, and the maximum stress concentration is in the middle of the roadway, as shown in Figure 10(e). In the optimized support scheme, the maximum stress between the two rows of anchor cables increased significantly to 0.2824 MPa, and the high stress zone was uniform, as shown in Figure 10(f).

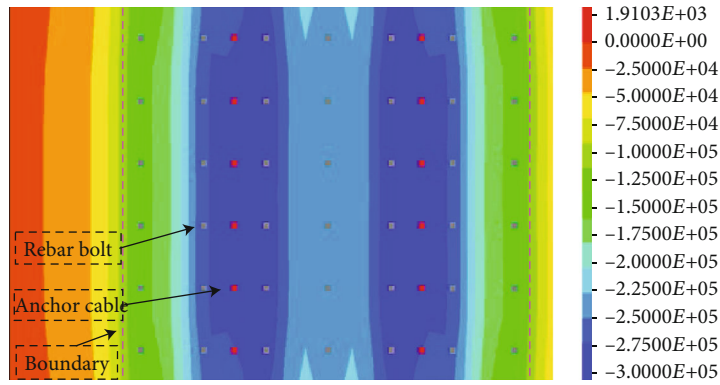
The change of vertical stress caused by the change of anchor cable supporting density is not the same order of magnitude as the original rock stress [19, 30]. However, for the surrounding rock already in the plastic zone, the stress action mode within the supporting range can be effectively improved by changing the supporting parameters and layout of the anchor cable [21, 33]. The effective diffusion of support resistance within the support range can increase the thickness of the bearing ring, increase the bearing capacity, and promote the stability of the surrounding rock [34]. For the roof with a large potential instability range, a certain supporting density can avoid local roof leakage caused by too large row spacing between anchor cable [29, 35, 36]. In addition, compared with the original scheme, the number of anchor cable increased by 0.625/m, but the number of anchor cable decreased by 1.042/m compared with the reinforcement scheme of the 800-1200 m section. It has certain economic advantages.



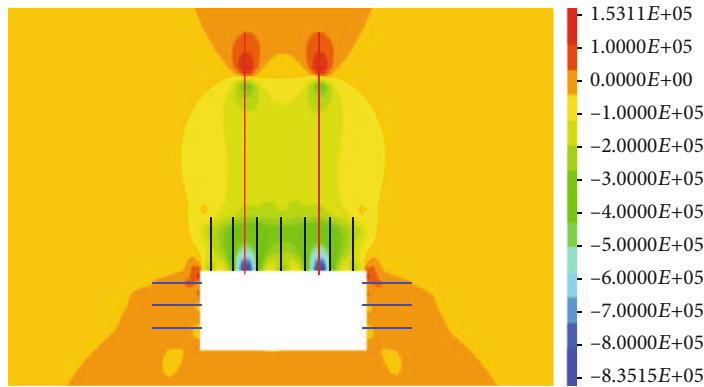
(a) Vertical stress at 2 m above the original supporting roof



(b) Vertical stress of roadway profile under original support

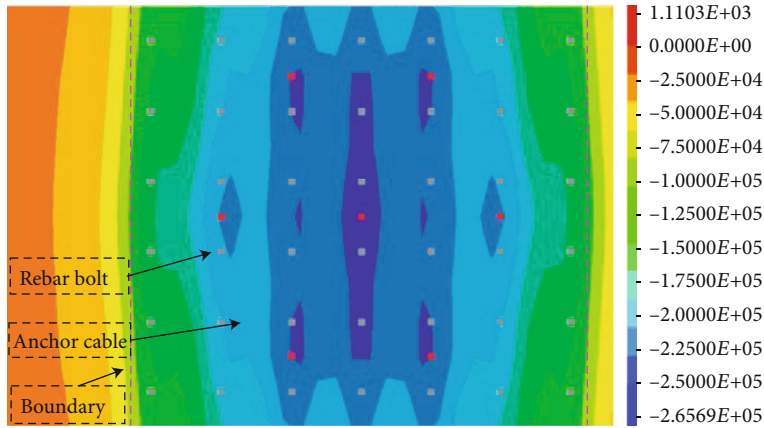


(c) Vertical stress at 2 m above reinforced supporting roof

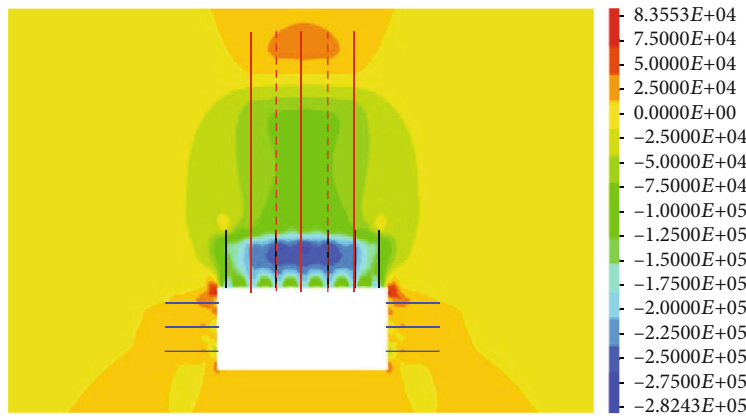


(d) Vertical stress of roadway profile under reinforced support

FIGURE 10: Continued.

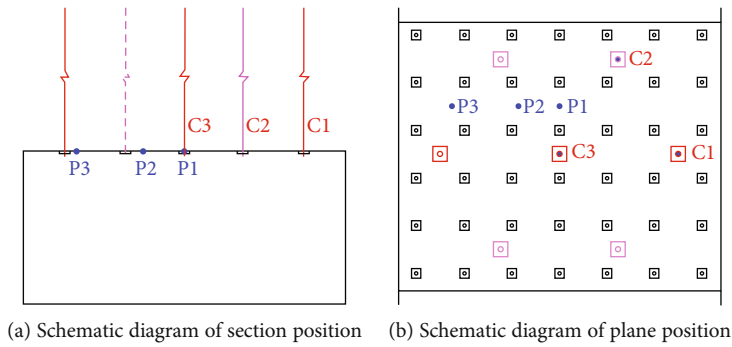


(e) Vertical stress at 2 m above the optimized supporting roof



(f) Vertical stress of roadway profile under optimized support

FIGURE 10: Anchor cable support stress nephogram.



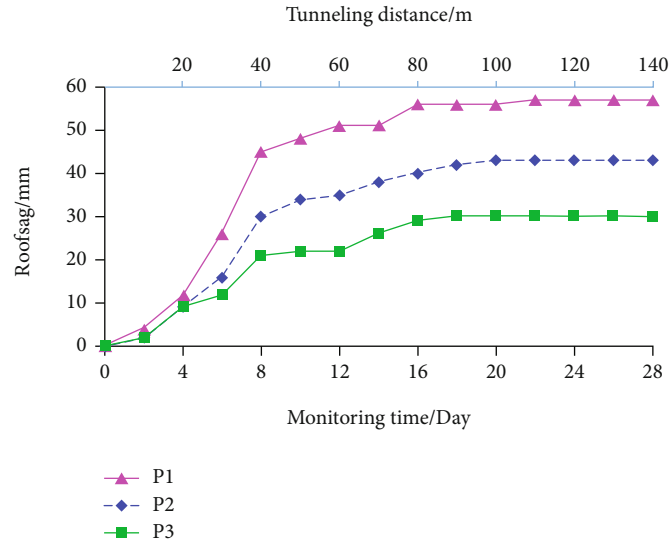
(a) Schematic diagram of section position (b) Schematic diagram of plane position

FIGURE 11: Monitoring point layout schematic.

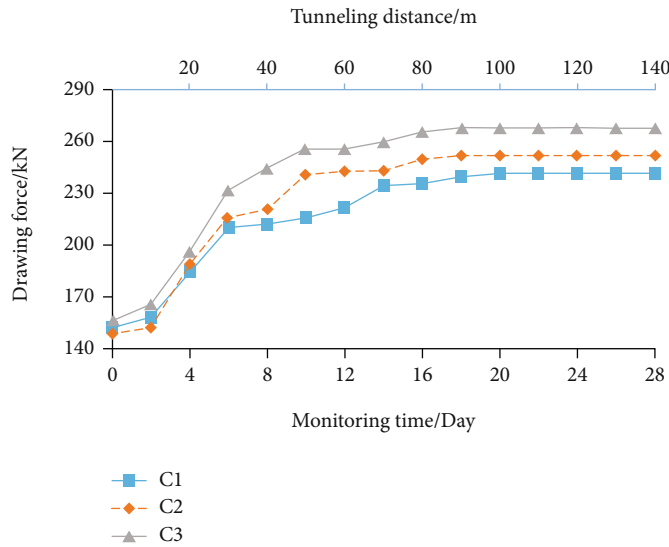
5. Field Application of Optimized Support Parameters

We have carried out the field application of the optimization scheme in 2201 return air roadway at 1200~1760 m in the Menkeqing Coal Mine. The optimization scheme is to optimize the original row spacing 2400 × 2400 mm and 2-2 layout to 1600 × 1600 mm and 2-3-2 layout. The plan of roof optimization scheme is shown in Figure 9(e).

We arranged one measuring point every 50 m within the range of 1210 m ~1710 m, and a total of 11 measuring points were arranged. The roof stability of the roadway is better after the optimized support scheme is applied in the field. After the tunneling is stable, the maximum settlement of each measuring point in the roadway is between 56 and 82 mm, and the stress of anchor cable is between 201 and 260 kN. Representative monitoring points are selected for data analysis. The layout of monitoring points at 1360 m is shown in



(a) Sag monitoring



(b) Anchor cable stress monitoring

FIGURE 12: Monitoring data.

Figure 11, in which P1-P3 are sag monitoring points and C1-C3 are anchor cable stress monitoring points.

Figure 12 shows the data measured at representative monitoring points. During tunneling, the maximum subsidence of the roadway at 1360 m is between 33 and 57 mm, and the maximum subsidence of the roadway is at the central position (P1 point), which is 57 mm. The deformation rate of the roadway reached its maximum within 4-8 days after tunneling, and the monitoring point lagged behind the tunneling working face by about 40 m. 20 days after tunneling, that is, the roadway gradually becomes stable after 100 m behind the working face. Similar to the deformation law of the roof, the stress of the anchor cable is the largest at the measuring point (C3) in the center of the roadway, and the change is the largest in the 4th to 12th day after roadway excavation. After 16 days, that is, after the monitoring

point lagged behind the tunneling work by 80 m, the stress of the anchor cable gradually stabilized.

6. Conclusion

Through the systematic study on the failure characteristics of the surrounding rock and the effect of anchor cable support in deep mining roadway, we mainly get the following conclusions.

- (1) The main reason for the roof subsidence of the mining roadway is that the roof structure of the roadway is complex, and the layer structure is obvious. After softening by water, the strength difference between layers is great, and the bond between layers is poor, which aggravates the roof separation

instability. The failure modes of different composite roofs are analyzed

- (2) The surrounding rock of deep mining roadway is affected by the high stress environment, which leads to a large plastic zone. The roof interlayer structure causes the plastic zone of the roof to expand rapidly in the soft strata. The position, thickness, and strength of the interlayer have a great influence on the morphology and size of the plastic zone of surrounding rock
- (3) Theoretical derivation proves that there is a negative correlation between the anchoring balance arch and the row spacing between the anchoring cables with the composite roof. The distribution of roof support resistance under different anchor cable supporting parameters is verified by numerical simulation. Reasonable arrangement of anchor cable is conducive to the full extension of supporting the resistance in the roof
- (4) Under the condition of weak roof lithology and obvious composite layered characteristics, increasing the strength of anchor cable support is conducive to the stability of the roadway surrounding rock. Based on the research results, the supporting parameters of roadway anchor cable are optimized and applied in the field. No surrounding rock instability occurred after field application

Data Availability

The data used to support the findings of this study are available from the corresponding author upon request.

Conflicts of Interest

The authors declare no conflict of interest.

Authors' Contributions

C. Li and W.L. Zhang performed the conceptualization. C. Li and T.H. Huo performed the methodology. C. Li, R. Yu, and X.D. Zhao performed the investigation. C. Li and M. Luo performed the writing.

Acknowledgments

This work was partially supported by the National Natural Science Foundation of China (Grant no. 51804117).

References

- [1] H. P. Kang, G. Xu, B. M. Wang et al., "Forty years development and prospects of underground coal mining and strata control technologies in China," *Journal of Mining and Strata Control Engineering*, vol. 1, no. 1, pp. 7–39, 2019.
- [2] H. Y. Wang, X. Y. Fang, F. Du et al., "Three-dimensional distribution and oxidation degree analysis of coal gangue dump fire area: a case study," *Science of The Total Environment*, vol. 772, article 145606, 2021.
- [3] M. G. Qian, P. W. Shi, and J. L. Xu, *Mining Pressure and Strata Control*, China University of Mining and Technology Press, 2010.
- [4] C. Zhang, S. H. Tu, and Y. X. Zhao, "Compaction characteristics of the caving zone in a longwall goaf: a review," *Environmental Earth Sciences*, vol. 79, pp. 1–27, 2019.
- [5] X. F. Guo, Z. Q. Zhao, X. Gao, X. Y. Wu, and N. J. Ma, "Analytical solutions for characteristic radii of circular roadway surrounding rock plastic zone and their application," *International Journal of Mining Science and Technology*, vol. 29, no. 2, pp. 263–272, 2019.
- [6] Z. Q. Zhao, N. J. Ma, H. Liu, and X. F. Guo, "A butterfly failure theory of rock mass around roadway and its application prospect," *Journal of China University of Mining & Technology*, vol. 47, no. 5, pp. 969–978, 2018.
- [7] Y. Yu, L. Y. Zhang, J. F. Lu, B. C. Chen, X. Q. Zhao, and L. M. Liu, "Research on the evolution characteristics of floor stress and reasonable layout of roadways in deep coal mining," *Geofluids*, vol. 2021, 14 pages, 2021.
- [8] B. Ghabraie, G. Ren, X. Zhang, and J. Smith, "Physical modelling of subsidence from sequential extraction of partially overlapping longwall panels and study of substrata movement characteristics," *International Journal of Coal Geology*, vol. 140, no. 15, pp. 71–83, 2015.
- [9] P. K. Kaiser, S. Yazici, and S. Maloney, "Mining-induced stress change and consequences of stress path on excavation stability - a case study," *International Journal of Rock Mechanics and Mining Sciences*, vol. 38, no. 2, pp. 167–180, 2001.
- [10] N. J. Ma, X. D. Zhao, Z. Q. Zhao, J. Li, and X. F. Guo, "Stability analysis and control technology of mine roadway roof in deep mining," *Journal of China Coal Society*, vol. 40, pp. 2287–2295, 2015.
- [11] Y. Sun, G. Li, J. Zhang, and D. Qian, "Experimental and numerical investigation on a novel support system for controlling roadway deformation in underground coal mines," *Energy Science & Engineering*, vol. 8, no. 2, pp. 490–500, 2020.
- [12] C. Li, X. F. Guo, T. H. Huo, and R. Liu, "Coal pillar design of pre-excavated double equipment withdrawal channel and its surrounding rock stability control," *Journal of Huazhong University of Science and Technology (Natural Science Edition)*, vol. 49, no. 4, pp. 1–7, 2021.
- [13] F. Du, K. Wang, X. Zhang, C. Xin, L. Shu, and G. Wang, "Experimental study of coal-gas outburst: Insights from coal-rock structure, gas pressure and adsorptivity," *Natural Resources Research*, vol. 29, pp. 2481–2493, 2020.
- [14] Y. Y. Li, K. Xie, Y. M. Sun, S. H. Li, and X. H. An, "Stress and deformation analysis and reinforcement time selection of composite foundations in shallow loess tunnels," *Chinese Journal of Rock Mechanics and Engineering*, vol. 38, no. 11, pp. 2332–2343, 2019.
- [15] M. Rezaei, M. F. Hossaini, and A. Majdi, "Development of a time-dependent energy model to calculate the mining-induced stress over gates and pillars," *Journal of Rock Mechanics and Geotechnical Engineering*, vol. 7, no. 3, pp. 306–317, 2015.
- [16] Q. C. Zhao and B. J. Fu, "Study on loose zone testing and support technology of roadway surrounding rock affected by dynamic pressure," *Journal of Mining and Strata Control Engineering*, vol. 2, pp. 49–56, 2020.

- [17] H. P. Kang, "Spatial scale analysis on coalmining and strata control technologies," *Journal of Mining and Strata Control Engineering*, vol. 2, no. 2, pp. 5–30, 2020.
- [18] X. F. Guo, Z. Q. Zhao, X. Gao, Z. K. Ma, and N. J. Ma, "The criteria of underground rock structure failure and its implication on rockburst in roadway: a numerical method," *Shock and Vibration*, vol. 2019, 12 pages, 2019.
- [19] J. Li, "The coal pillar design method for a deep mining roadway based on the shape of the plastic zone in surrounding rocks," *Arabian Journal of Geosciences*, vol. 13, no. 12, article 5501, 2020.
- [20] G. Li, F. S. Ma, J. Guo, H. J. Zhao, and G. Liu, "Study on deformation failure mechanism and support technology of deep soft rock roadway," *Engineering Geology*, vol. 264, article 105262, 2020.
- [21] G. R. Feng and P. F. Wang, "Simulation of recovery of upper remnant coal pillar while mining the ultra-close lower panel using longwall top coal caving," *International Journal of Mining Science and Technology*, vol. 30, no. 1, pp. 55–61, 2020.
- [22] C. Jia and C. C. Hu, "Instability mechanism and control technology of longwall entries driving along the gob in a thick coal seam," *Journal of Mining and Strata Control Engineering*, vol. 2, no. 4, pp. 38–45, 2020.
- [23] Z. Q. Zhao, N. J. Ma, X. F. Guo, X. D. Zhao, and L. Fan, "Falling principle and support design of butterfly-failure roof in large deformation mining laneways," *Journal of China Coal Society*, vol. 41, no. 12, pp. 2932–2939, 2016.
- [24] F. Q. Gao, "Use of numerical modeling for analyzing rock mechanic problems in underground coal mine practices," *Journal of Mining and Strata Control Engineering*, vol. 1, no. 1, pp. 21–28, 2019.
- [25] H. Molladavoodi and M. Rahmati, "Dilation angle variations in plastic zone around tunnels in rocks-constant or variable dilation parameter," *Journal of Central South University*, vol. 25, no. 10, pp. 2550–2566, 2018.
- [26] F. Du and K. Wang, "Unstable failure of gas-bearing coal-rock combination bodies: insights from physical experiments and numerical simulations," *Process Safety and Environmental Protection*, vol. 129, pp. 264–279, 2019.
- [27] M. K. Jia, "Research on roof falling mechanism of deteriorative strata combination supported by bolts," *Rock and Soil Mechanics*, vol. 28, no. 7, pp. 1333–1337, 2007.
- [28] T. Yu, G. M. Zhao, X. R. Meng, X. Cheng, and G. J. Li, "Stability analysis and supporting parameter design of composite roof," *Coal Science and Technology*, vol. 48, no. S1, pp. 19–24, 2020.
- [29] C. Li, W. L. Zhang, N. Wang, and C. Hao, "Roof stability control based on plastic zone evolution during mining," *Journal of Mining & Safety Engineering*, vol. 36, no. 4, pp. 753–761, 2019.
- [30] C. Yuan, L. Fan, J. F. Cui, and W. J. Wang, "Numerical simulation of the supporting effect of anchor rods on layered and nonlayered roof rocks," *Advances in Civil Engineering*, vol. 2020, 14 pages, 2020.
- [31] J. K. Li and H. Wang, "Ground support of interbedded rock roof in a deep roadway with fully-anchored cables," *Journal of Mining and Strata Control Engineering*, vol. 2, no. 3, pp. 14–22, 2020.
- [32] F. Pellet, M. Roosefid, and F. Deleruyelle, "On the 3D numerical modelling of the time-dependent development of the damage zone around underground galleries during and after excavation," *Tunnelling and Underground Space Technology*, vol. 24, no. 6, pp. 665–674, 2009.
- [33] M. F. Cai, "Key theories and technologies for surrounding rock stability and ground control in deep mining," *Journal of Mining and Strata Control Engineering*, vol. 2, no. 3, pp. 5–13, 2020.
- [34] H. P. Kang, "Analysis on load-bearing ring in surrounding rock of roadway," *Rock and Soil Mechanics*, vol. 17, no. 4, pp. 84–89, 1996.
- [35] C. Li, Z. Wu, W. L. Zhang, Y. H. Sun, C. Zhu, and X. H. Zhang, "A case study on asymmetric deformation mechanism of the reserved roadway under mining influences and its control techniques," *Geomechanics and Engineering*, vol. 22, no. 5, pp. 449–460, 2020.
- [36] C. X. Zhao, Y. M. Li, G. Liu, and X. Meng, "Mechanism analysis and control technology of surrounding rock failure in deep soft rock roadway," *Engineering Failure Analysis*, vol. 115, article 104611, 2020.

Research Article

Analysis of Key Factors Affecting Water Disaster in Deep Mining and Establishment of a Water Disaster Evaluation Method Suitable for Different Mining Depths

Jianghui He ¹, Wenping Li ¹, Wei Qiao,¹ Zhi Yang,² and Qiqing Wang ¹

¹School of Resources and Geosciences, China University of Mining & Technology, Xuzhou 221116, China

²School of Environment and Spatial Informatics, China University of Mining & Technology, Xuzhou 221116, China

Correspondence should be addressed to Wenping Li; hjh@cumt.edu.cn

Received 5 April 2021; Revised 24 May 2021; Accepted 16 June 2021; Published 6 July 2021

Academic Editor: Wei Zhao

Copyright © 2021 Jianghui He et al. This is an open access article distributed under the Creative Commons Attribution License, which permits unrestricted use, distribution, and reproduction in any medium, provided the original work is properly cited.

Deep mining is the current and future mining focus in the coalfield of North China. Therefore, it is necessary to establish a water inrush assessment method suitable for deep mining. The conventional water inrush coefficient (T) method is simple to use, but its accuracy is low when the mining depth is very small or large because it neglects the role of the aquifer water yield. The main purpose of this paper is to introduce a simple water inrush risk assessment method that is more applicable in deep mining than the T method. In this study, the hydrogeological characteristics in deep mining were studied and the role of the aquifer water yield in water inrush was analyzed. Afterwards, an improved T method considering the aquifer specific yield (q) was established. In the new method, the critical water inrush coefficient changes with changing q following a negative correlation. The parameter thresholds were determined based on systematic data analyses of 186 mining cases. The results of the statistical analysis show that the accuracy of the new method at different mining depths is higher than that of the T method.

1. Introduction

Coal will remain the major energy source in China for a long time. From the coal resources in China, 53% are located below a depth of 1 km [1]. Following the depletion of shallow coal resources, the coal mining depth (D_m) has increased. However, the exploitation of deep coal seams in the North China coalfield (Figure 1) faces a threat from the underlying confined aquifers in Ordovician limestone.

Floor karst water inrush has been extensively studied in literature. For example, Wu et al. have conducted extensive and detailed research on water inrush from mine floors, proposing some risk-assessment methods, such as the master-control index method and the vulnerability index method and its improved version [2, 3]. These methods were successfully applied to practical mining. Liu and Hu adopted the water-resistance coefficient method to identify floor water inrush risks [4]. Meng et al. presented a geological-assessment method to evaluate the vulnerability of the floor water inrush by considering its lithology, structure, and water

inrush coefficient [5]. Wang et al. used a secondary fuzzy comprehensive evaluation system to analyze the risk of mine water inrush [6]. He et al. developed a $P-H-q$ evaluation system for risk assessment of water inrush based on the water-pressure-transfer theory [7]. Hong-fei et al. established a coal floor water inrush model that considered the structural characteristics of floor strata to evaluate the antipermeability strength of an aquiclude [8]. Bai et al. explained the groundwater inrush mechanism in terms of variable mass and non-linear dynamics [9]. Chen et al. used an engineering analogy method to predict the water inrush risk areas in mining, using Fisher's discriminant analysis [10]. Physical simulations performed by Zhang et al. revealed that the permeability of floor rocks had regional and temporal characteristics [11]. Gao et al. found that the water inflow increased with an increasing permeability coefficient following a power function [12]. Many other methods are available to evaluate the possibility of mine water inrush and related water-rock coupling problems [13–34]. Some scholars have specially studied floor water inrush through faults [35–39]. In

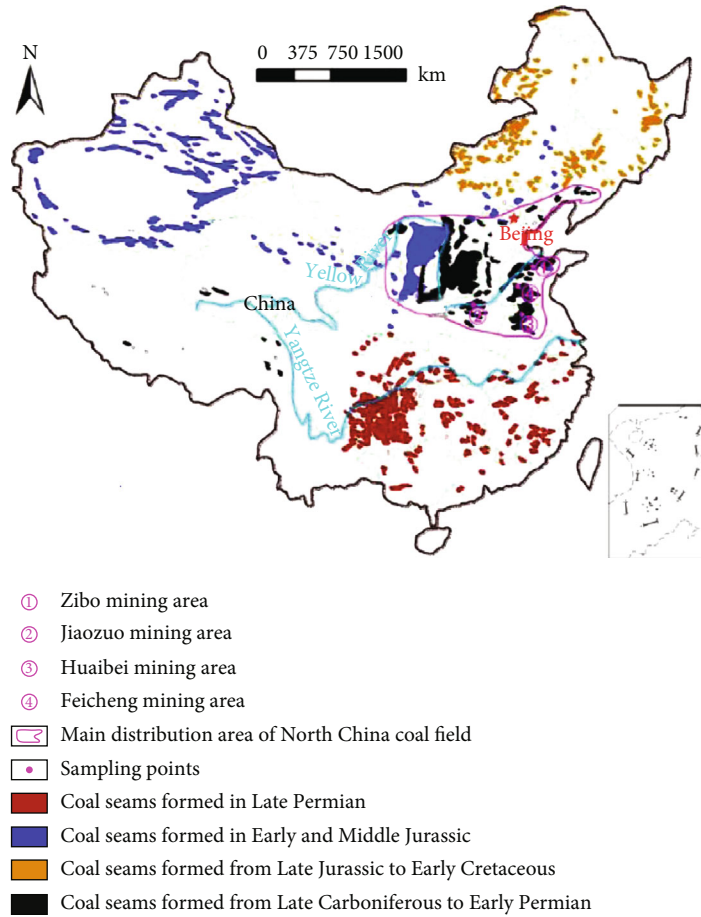


FIGURE 1: Distribution of coal resources in China.

summary, the common methods used to predict the mine floor water inrush can be categorized as (1) empirical formula and GIS technology, (2) mathematical analysis, (3) nonlinear mathematical analysis, and (4) simulation experiments [40]. However, most of these methods require sophisticated software, equipment, and/or operational technology as well as complex analyses and calculations. Therefore, widespread implementation of these methods is difficult.

The conventional water inrush coefficient (T) method is the most practical method used to predict water inrush in coal mines under various conditions. T (in MPa/m) is obtained from the following empirical equation based on large water inrush data:

$$T = \frac{P}{M}, \quad (1)$$

where P (in MPa) is the water pressure in a confined aquifer in the coal-seam floor and M (in m) is the thickness of the aquiclude of the coal seam floor.

T denotes the water pressure that can be supported by a unit thickness of the coal seam floor aquiclude and can quantitatively indicate the risk of water inrush from an underlying confined aquifer during coal mining. A larger T value indicates more susceptibility to water inrush accidents. The minimum value of T that can initiate water inrush is called

the critical water inrush coefficient (T_s), which ranges from 0.06 to 0.1 MPa/m, as provided in the *Stipulation on Prevention and Control of Coal Mine Water* of China [41]. Floor water inrush incidents are likely to occur when $T > T_s$. This formula is simple and practical because it incorporates two important parameters that govern the characteristics of the aquifer and aquiclude (P and M , respectively). Therefore, it has been incorporated in relevant standards and coal mine water prevention and control regulations.

Practical mining data collected from the North China coalfield, which include 186 water inrush cases and 92 safety mining cases, have proven that the results predicted using the T method are generally consistent with the actual results when $2.5 \text{ MPa} < P < 3.5 \text{ MPa}$ (Figure 2).

In addition, according to the data collected from the North China coalfield [42], P exhibits a linear positive correlation with the aquifer depth (D) (Figure 3).

The following equation can be obtained from Figure 3:

$$D = 101.28P + 11.212. \quad (2)$$

Because D will change with D_m (Figure 4), it is necessary to analyze the change in the accuracy of the T method with changing D_m .

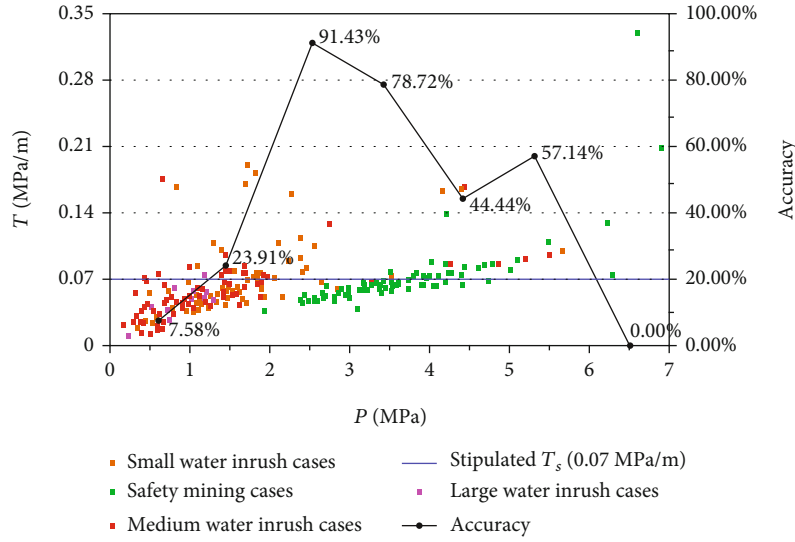


FIGURE 2: Change in the accuracy of the prediction results from the water inrush coefficient method (T) under different water pressures (P).

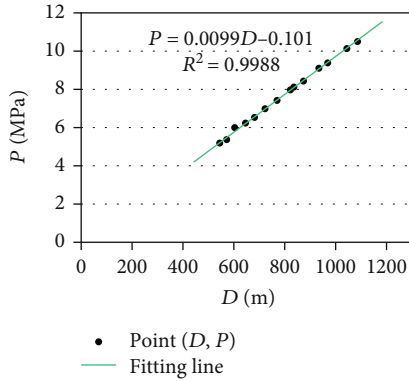


FIGURE 3: Distribution of the water pressure (P) at different depths (D).

Figure 4 shows that the relationship between D and D_m can be expressed by the following formula:

$$D_m = D - M. \tag{3}$$

After statistically analyzing the data in Figure 2 with the help of Equations (2) and (3), the variation of the prediction accuracy from the T method with changing D_m can be obtained (Figure 5).

The T method was put forward in 1964 in Jiaozuo’s hydrogeological work. The corresponding T_s was also the empirical value based on the mining conditions at that time. Because the average value of D_m was about 300 m at that time, the empirical value of T_s obtained according to the mining conditions at that time was more suitable when D_m was about 300 m. This conclusion is basically consistent with the law of fitting line in Figure 5, which shows that the accuracy of the T method is the highest when D_m is equal to 311.16 m. Figure 5 shows that when D_m is very shallow or very deep, the prediction accuracy from the T method is very low. Because coal seams buried at great depths are the object

of future exploitation in the North China coalfield, evaluation of water hazards during mining of deeply buried coal seams is the focus of the present study. The D_m of deeper coal seams is generally more than 400 m, mostly exceed 700 m, or exceed 1000 m in the 33 mines in the North China coalfield [43]. Hence, the T method is unsuitable for deep-mining risk assessment.

In addition to the T method, a common method is the GIS-based multifactor superposition analysis (represented by the vulnerability index method). The GIS-based multifactor superposition analysis method is a good method because many related factors are considered. However, in the discriminant map obtained by this method, we can only obtain the relative magnitude of water inrush risk in different positions, but not the absolute magnitude of the possibility of water inrush in different positions. When applying the GIS-based multifactor superposition analysis method, a specific boundary which can divide the safety zone and water inrush zone is needed, such as T_s in the T method. Therefore, it is necessary to study the hydrogeological conditions in deep mining and to establish a simple water inrush risk assessment method that is more applicable than the T method.

2. Hydrogeological Conditions in Deep Mining

The coal seams in some mines are buried at depths of 1,200 m and face the threat of limestone aquifers (Figure 6), which cause the P and T values to reach 13 MPa and 0.144–1.256 MPa/m, respectively. In addition, when D is large, aquifers have low porosity (ϕ) and permeability (K) owing to high ground stress (Figures 7 and 8). Φ determines the size of the water-storage space in aquifers, and K determines the movement efficiency of water in aquifers. Reduced ϕ and K lead to a reduced water yield (or effluent capacity) of the aquifer.

The water yield of aquifers is often described in terms of the specific yield (q , in $L/(s \cdot m)$), which indicates the sustainable water yield from a drill hole with a diameter of 91 mm

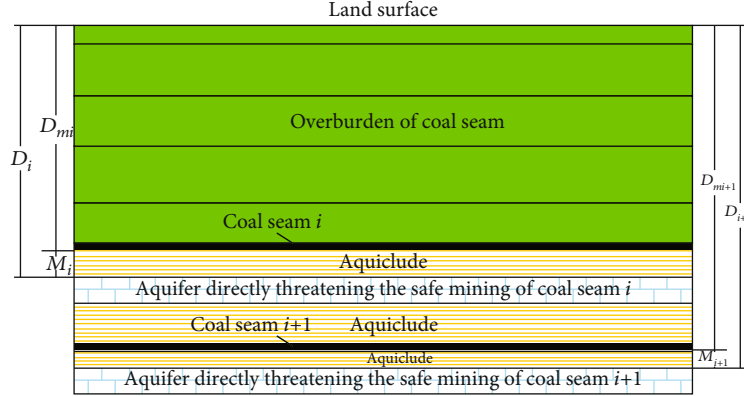


FIGURE 4: Relationship between D and D_m . D_i : buried depth of the aquifer directly threatening the safety mining of coal seam i ; D_{mi} : mining depth of the coal seam i ; M_i : thickness of the aquiclude directly protecting the safe mining of coal seam i .

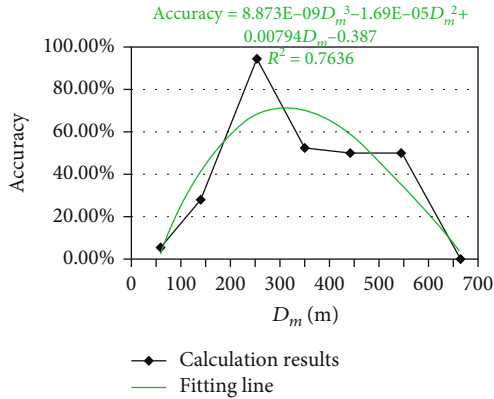


FIGURE 5: Change in the prediction accuracy of the T method with changing D_m .

when the water levels drop by 1 m per unit time during a pumping test. Figure 9 shows a steady-flow pumping test in a confined aquifer. In this figure, h_0 , Q , R_0 , s_w , R_w , a , and K denote the initial water head of the confined aquifer, the pump flow, the radius of the cone of depression, the drop of the water level in the well, the radius of the pumping well, the thickness of the aquifer, and its permeability, respectively. Under these conditions, the Dupuit formula of the confined pumping well can be obtained as follows:

$$Q = \frac{2\pi K a s_w}{\ln(R_0 - R_w)}. \quad (4)$$

According to the definition of q , it can be calculated as follows:

$$q = \frac{Q}{s_w} = \frac{2\pi K a}{\ln(R_0 - R_w)}. \quad (5)$$

The value of q decreases with increasing D because both ϕ and K decrease (Figure 10). Qiao et al. and Zhao reached the same conclusion [44, 45].

3. Analysis of the Role of q in the Occurrence of Water Inrush

q reflects the effluent capacity of the aquifer. The water inrush process involves draining water from the aquifer to other spaces. Therefore, theoretically, q is closely related to the occurrence of water inrush. In contrast, water scarcity significantly reduces the likelihood of the confined water to break through an aquiclude. Some mining cases have proven that water inrush is related to the q value. When the T method is used to evaluate the risk of water inrush, unrealistic results are produced if q is neglected (Table 1). The list in Table 1 indicates that from the first to the fifth cases, because the q values were all small, no water inrush occurred, although $T > T_s$. From the sixth to the tenth cases (Table 1), q was large and water inrush occurred during the mining process, although T did not exceed T_s . Therefore, it is confirmed that q significantly influences the occurrence of water inrush. Thus, in order to improve the accuracy of the results, the change in q in deep mining must be considered. Shi et al. reached the same conclusion [46].

This analysis revealed that under deep mining conditions, the aquifer related to water inrush is characterized by large P and low q , and q is positively correlated with the possibility of water inrush. Therefore, in deep mining, the possibility of water inrush can be reduced using small q , even if $T > T_s$. Thus, the conventional T method is oversimplified for assessing the water inrush possibility because it only considers P , while neglecting q . The water yield of aquifers that recharge the mine must be considered to accurately assess water inrush risk. Therefore, the objectives of this study are to analyze the role of q in water inrush and to establish a convenient method for water inrush risk assessment that considers q .

3.1. Before Formation of Water Inrush. From the point of view of mechanics, the floor water inrush involves breaking the aquiclude under continuous water pressure within a certain period followed by the gushing of water from the aquifer below the aquiclude, along the rupture surface, into the goaf. Because the aquiclude breakage only occurs after a period of deformation, a time limit exists for the occurrence of water

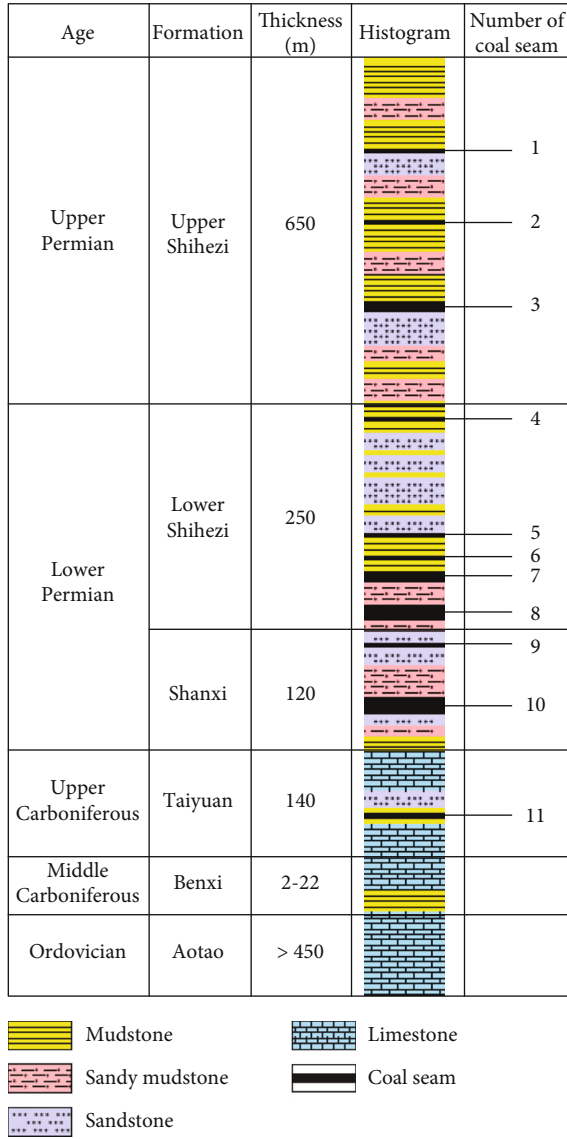


FIGURE 6: Stratigraphic column of the Permian coal-bearing strata in the Huaibei mining area, China.

inrush. First, the aquiclude takes time to deform to its critical breaking state. After a goaf with length L is formed, the aquiclude gradually bends and deforms under the water pressure to reach its critical breaking state. The time required to reach this condition is called required time (t_r). Second, the deformation and breaking of the aquiclude must be completed before the goaf is filled and compacted by the caved overburden [47, 48]. The time before the goaf is filled and compacted is called the available time (t_a) for water inrush formation. Water inrush can only occur when $t_r < t_a$.

The water pressure that is continuously exerted on the aquiclude, called the aquiclude bending pressure (P_b), constitutes the external force directly responsible for the eventual breakage of the aquiclude. P_b also refers to the water pressure accumulated in the cavity caused by the deformation of the aquiclude (i.e., ③ in Figure 11). Unless otherwise stated, this is the cavity referred to hereafter. P refers to the water pressure or undisturbed water pressure in the confined aquifer

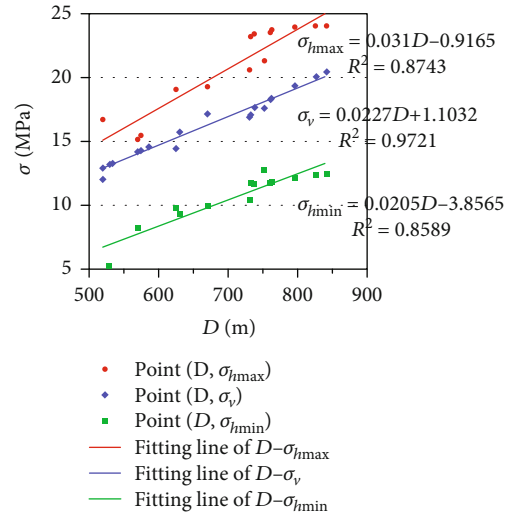


FIGURE 7: Changes in ground stress (σ) at different depths (D): σ_{hmax} : maximum horizontal principal stress; σ_{hmin} : minimum horizontal principal stress; σ_v : vertical principal stress.

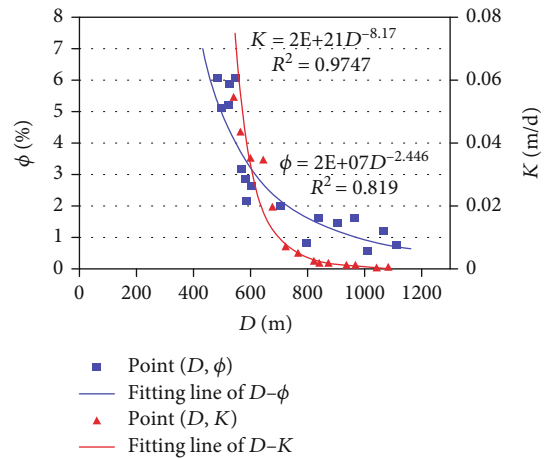


FIGURE 8: Changes in the porosity (ϕ) and permeability (K) of aquifers with changing depth (D).

before or after mining, respectively. The water-pressure variation and water runoff in the aquifer after mining are shown in Figure 11. The persistence of P_b is assured by the continuous flow of water into the cavity. The efficiency of the water movement in the aquifer is related to the water yield of the aquifer. Obviously, a lower water yield in the confined aquifer results in lower efficiency of the seepage flow to the cavity, slower deformation in the aquiclude, longer time for the aquiclude to deform to its breaking state, greater possibility for t_r to exceed t_a , and less possibility of water inrush. The water yield of aquifers is often described in terms of q . In other words, the smaller the q value, the lower the possibility of water inrush.

For water inrush caused by dangerous geological structures (i.e., faults, collapse columns, etc.), the initiation process involves erosion of the filler in the cracks of these structures owing to water flow, which is also caused by the continuity of seepage. Similar to the water inrush in the

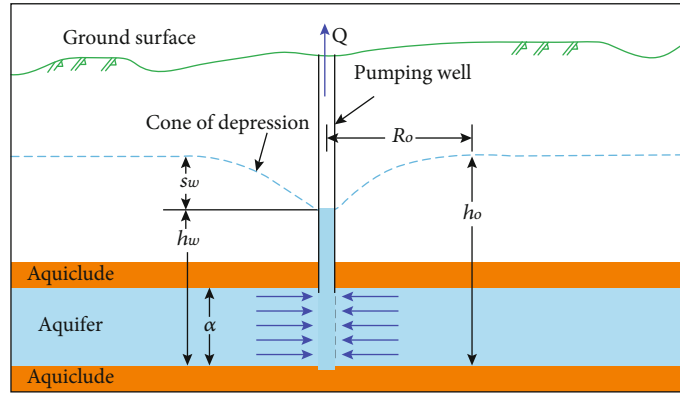


FIGURE 9: Pumping test of a steady well flow in a confined aquifer.

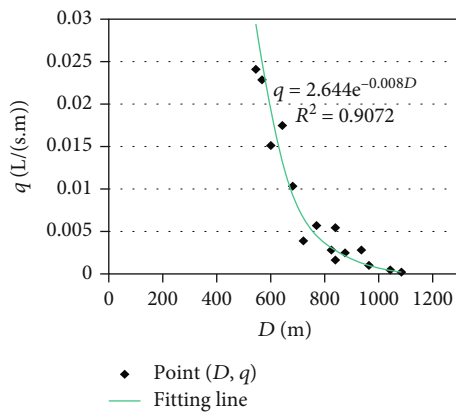


FIGURE 10: Change in the specific yield (q) for different depths (D).

cavity described earlier, the smaller the q , the lower is the possibility of water inrush in the dangerous geological structures.

3.2. After Formation of Water Inrush. Water inrush data from 186 excavation faces in the North China coalfield (Tables 2–4) were collected to analyze the role of q in the water inrush.

Usually, according to the volume of water inflow (Q) recorded in each case, water inrush is classified as a small case ($0 < Q \leq 60 \text{ m}^3/\text{h}$), medium case ($60 < Q < 600 \text{ m}^3/\text{h}$), or large case ($Q \geq 600 \text{ m}^3/\text{h}$). Among the 186 water inrush cases studied, 79 were small, 95 were medium, and 12 were large.

The statistical summary of the 186 water inrush cases (Table 5) shows that almost all the small- Q cases were located in areas with $0.06 \leq q < 1.7 \text{ L}/(\text{s} \cdot \text{m})$, almost all the medium- Q cases were located in areas with $1.7 \leq q < 16.7 \text{ L}/(\text{s} \cdot \text{m})$, and all the large- Q cases were located in areas with $q \geq 16.7 \text{ L}/(\text{s} \cdot \text{m})$. No water inrush cases occurred when $q < 0.06 \text{ L}/(\text{s} \cdot \text{m})$.

After a water inrush occurs, the larger the value of q , the greater the amount of water poured out because of the greater water yield of the aquifer, the larger the amount of water released from the aquifer in a short period, and the larger the amount of water that flows into the mining area. Therefore, q can determine the magnitude of the water inrush after an event.

4. Establishment and Application of the T - q Method

In this section, the development of a convenient method for water inrush risk assessment that considers q is discussed.

A confined aquifer is a source of power and the medium for the water inrush. An aquiclude is the medium that can obstruct water inrush. Water inrush is related not only to the potential of the confined water to break through the aquiclude but also to the extent of release of this potential (unless otherwise stated, this is the potential referred to hereafter). P and M parametrize the potential of the confined water to break through the aquiclude, and q is a nonnegligible parameter that determines the extent of this potential release. The contributions of these parameters to the possibility of water inrush are described below.

First, when P is big and M is small, the potential for water inrush is high. Therefore, the ratio of P to M (i.e., T) can be used to indicate the potential for water inrush. The greater the value of T , the higher the potential for water inrush. Second, the greater the value of q , the better the hydrodynamic conditions in the aquifer, the greater the extent of this potential release, and the higher the possibility of water inrush. Therefore, the possibility of water inrush is positively correlated with both T and q values.

4.1. Division of Water Inrush and Safety Zones in the T - q Method. From the previous analysis, the possibility of water inrush was determined in terms of T and q . When the potential for water inrush is greater, the energy that can be directly applied to break through the aquiclude or the water inrush channels is larger and the possibility of water inrush is greater. In other words, for constant q , the greater the value of T , the higher the possibility of water inrush. Figure 12 shows the 186 water inrush cases used to obtain the T_s - q function curve. Because T_s is the minimum T that can initiate occurrence of water inrush, the T_s points should be in the area where T is relatively small for a certain q value of the aquifer. The points marked by the symbol “ \times ” in Figure 12 were selected as the critical points, and the T_s - q function curve was obtained by fitting these points. The points in the area above the T_s - q curve were identified as the water inrush points, and those in the area below the T_s - q curve were the

TABLE 1: Mining cases in the North China coalfield, wrongly evaluated by the T method.

No.	Mining face	P (MPa)	q (L/(s·m))	T (MPa/m)	T_s (MPa/m)	Evaluation results	Field verification
1	III628, Zhuzhuang mine, Huaibei mining area	4.22	0.016	0.140	0.07	Danger	Safety
2	III616, Yangzhuang mine, Huaibei mining area	5.50	0.052	0.110	0.07	Danger	Safety
3	1044, Liudian mine, Huaibei mining area	6.93	0.024	0.210	0.07	Danger	Safety
4	1037, Liudian mine, Huaibei mining area	6.60	0.024	0.330	0.07	Danger	Safety
5	1088, Heishan mine, Zibo mining area	6.23	0.032	0.130	0.07	Danger	Safety
6	11022, Jiulishan mine, Jiaozuo mining area	1.19	24.450	0.052	0.07	Safety	Danger, $Q = 714 \text{ m}^3/\text{h}$
7	9507, Xiangzhuang mine, Feicheng mining area	0.92	8.330	0.038	0.07	Safety	Danger, $Q = 300 \text{ m}^3/\text{h}$
8	4221, Jiaoxi mine, Jiaozuo mining area	1.00	12.620	0.053	0.07	Safety	Danger, $Q = 201 \text{ m}^3/\text{h}$
9	12031, Jiulishan mine, Jiaozuo mining area	0.92	11.330	0.041	0.07	Safety	Danger, $Q = 588 \text{ m}^3/\text{h}$
10	1007, Fucun mine, Zibo mining area	1.46	7.120	0.043	0.07	Safety	Danger, $Q = 256 \text{ m}^3/\text{h}$

Note: Q refers to the water inflow in a water inrush case.

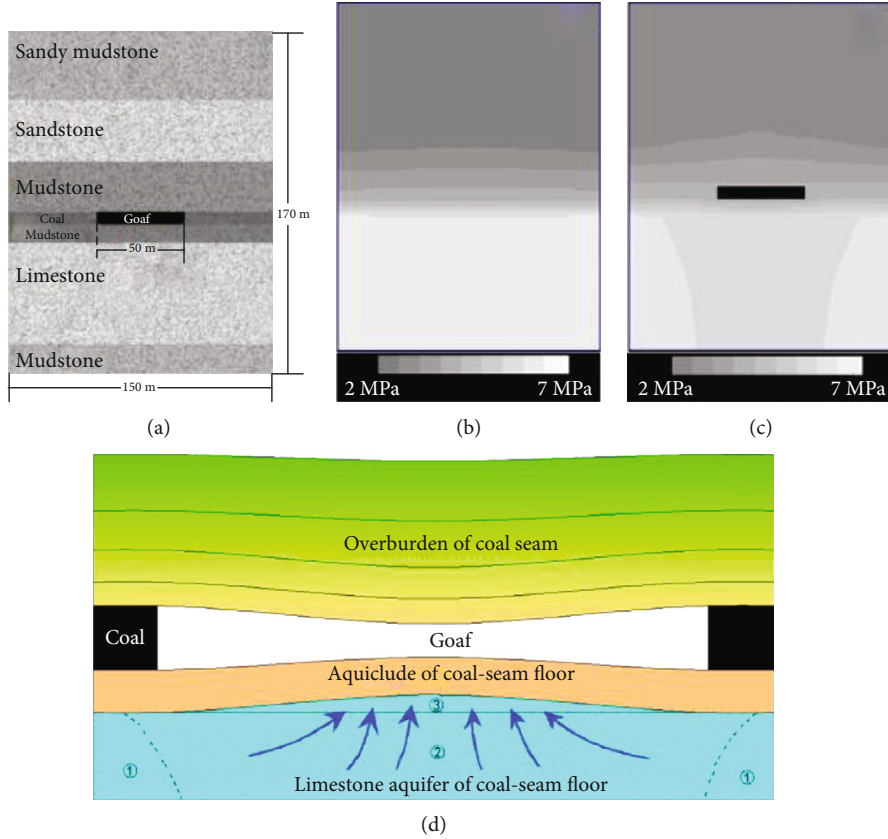


FIGURE 11: Definition of terms used for risk assessment of water inrush from the coal-seam floor. (a) Numerical model designed by RFP software. (b) Water pressure distribution after self-stable equilibrium of the model before excavation. (c) Water pressure distribution after excavation. (d) Schematic diagram of water migration characteristics in floor aquifer. ①: areas with undisturbed water pressure; ②: area with disturbed water pressure; ③: cavity caused by the deformation of the aquiclude, which is situated between the aquiclude and the aquifer. The blue arrows indicate the water seepage direction.

safety points. Figure 12 shows that except for the fitting points; all the other water inrush points are above the T_s - q curve. The water inrush points between the T_s - q and the stipulated T_s curves were wrongly evaluated as safety points by

the T method, because at these points, T was less than the stipulated T_s . Therefore, the new method is more practical than the T method in determining the water inrush and safety zones.

TABLE 2: Specific yield (q) and water inrush coefficient (T) values in small water inrush cases.

q (L/(s-m))	T (MPa/m)	q (L/(s-m))	T (MPa/m)	q (L/(s-m))	T (MPa/m)	q (L/(s-m))	T (MPa/m)	q (L/(s-m))	T (MPa/m)
1.667	0.024	1.333	0.025	0.167	0.108	0.583	0.068	1.417	0.070
1.167	0.030	1.117	0.045	1.167	0.052	0.955	0.042	0.333	0.051
1.333	0.056	0.167	0.047	1.300	0.037	1.000	0.057	1.628	0.089
1.167	0.040	1.210	0.168	0.333	0.052	1.333	0.057	1.117	0.078
0.733	0.089	1.650	0.047	1.333	0.082	0.417	0.062	1.250	0.079
1.000	0.051	0.167	0.092	0.860	0.058	0.083	0.058	1.580	0.100
1.450	0.054	1.033	0.108	0.667	0.162	1.667	0.060	0.767	0.046
0.717	0.063	0.083	0.114	0.443	0.065	0.700	0.055	0.500	0.052
1.667	0.018	0.167	0.161	1.133	0.059	0.443	0.077	0.500	0.046
1.167	0.057	0.667	0.161	0.500	0.166	1.312	0.069	1.333	0.045
1.167	0.047	0.500	0.170	0.500	0.046	1.210	0.083	1.417	0.050
0.833	0.046	0.500	0.182	0.333	0.027	0.443	0.072	0.083	0.069
2.000	0.191	0.083	0.052	0.390	0.079	0.067	0.073	0.500	0.045
1.333	0.038	1.018	0.067	0.583	0.061	0.125	0.105	0.333	0.055
0.500	0.037	0.083	0.101	1.697	0.056	0.167	0.060	0.817	0.056
1.667	0.038	0.333	0.085	0.390	0.078	1.000	0.072		

TABLE 3: Specific yield (q) and water inrush coefficient (T) values in medium water inrush cases.

q (L/(s-m))	T (MPa/m)	q (L/(s-m))	T (MPa/m)	q (L/(s-m))	T (MPa/m)	q (L/(s-m))	T (MPa/m)	q (L/(s-m))	T (MPa/m)
8.333	0.028	8.333	0.038	3.750	0.051	2.450	0.052	5.882	0.071
12.500	0.018	10.000	0.046	0.867	0.057	4.000	0.036	6.147	0.065
11.00	0.024	11.500	0.043	12.833	0.074	11.667	0.046	4.578	0.054
4.000	0.017	2.500	0.076	1.783	0.068	9.167	0.048	6.378	0.051
4.667	0.018	10.417	0.022	2.533	0.052	3.333	0.059	2.167	0.060
11.000	0.016	12.617	0.053	10.55	0.061	2.663	0.059	3.883	0.068
13.000	0.018	7.167	0.074	4.167	0.051	5.000	0.049	2.717	0.043
14.167	0.043	8.833	0.034	11.333	0.041	3.333	0.021	9.167	0.075
3.333	0.015	3.053	0.079	3.467	0.056	10.000	0.096	5.000	0.062
5.167	0.026	9.633	0.056	15.500	0.069	10.000	0.052	2.500	0.026
8.333	0.023	7.600	0.065	6.667	0.012	7.117	0.043	2.667	0.078
13.333	0.018	3.333	0.039	4.533	0.176	10.750	0.052	11.700	0.034
5.000	0.044	5.583	0.083	9.733	0.064	6.667	0.024	5.417	0.087
3.333	0.026	2.533	0.061	4.033	0.072	3.333	0.043	3.667	0.086
4.667	0.021	2.167	0.085	1.833	0.041	2.500	0.055	4.333	0.085
8.333	0.021	2.767	0.077	3.783	0.031	4.333	0.053	6.167	0.097
16.667	0.013	4.167	0.046	2.283	0.037	6.250	0.070	3.000	0.091
13.333	0.022	2.00	0.045	5.417	0.025	3.543	0.167	9.500	0.091
8.333	0.024	4.00	0.128	4.833	0.026	2.417	0.069	4.000	0.085

TABLE 4: Specific yield (q) and water inrush coefficient (T) values in large water inrush cases.

q (L/(s-m))	T (MPa/m)	q (L/(s-m))	T (MPa/m)	q (L/(s-m))	T (MPa/m)	q (L/(s-m))	T (MPa/m)
20.000	0.050	28.000	0.011	21.667	0.049	24.333	0.057
19.283	0.052	24.450	0.052	19.817	0.037	20.667	0.057
16.700	0.028	25.000	0.041	23.183	0.075	17.067	0.061

TABLE 5: Number of water inrush cases for each volume of water inflow (Q) and different magnitudes of specific yield (q).

Magnitude of q (L/(s·m))	Number of water inrush cases		
	Small- Q water inrush cases	Medium- Q water inrush cases	Large- Q water inrush cases
$q < 0.06$	0	0	0
$0.06 \leq q < 1.7$	78	1	0
$1.7 \leq q < 16.7$	1	94	0
$q \geq 16.7$	0	0	12

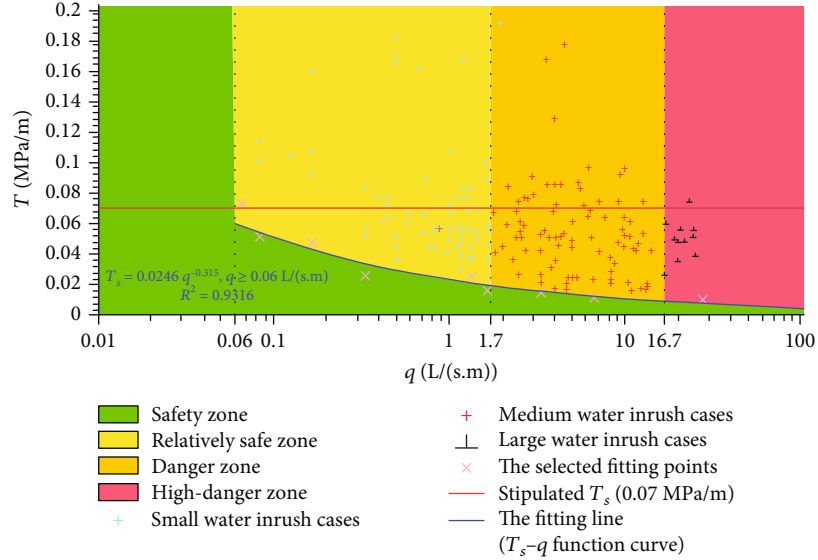


FIGURE 12: Discrimination diagram using the T - q method.

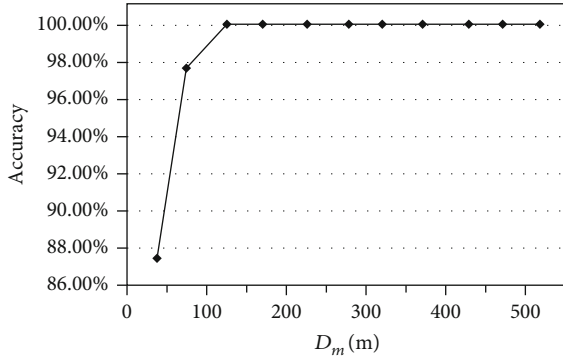


FIGURE 13: Change in the accuracy of the prediction with different mining depths (D_m) using the T - q method.

The T_s - q curve also shows that T_s is not fixed but changes with changing q . There is a negative correlation between T_s and q . The relationship between them is expressed as follows:

$$T_s = 0.0246q^{-0.315}, q \geq 0.06 \text{ L/(s} \cdot \text{m)}. \quad (6)$$

The areas below and above the T_s - q curve were defined as the safety and water inrush zones, respectively.

The list in Table 5 indicates that no water inrush accidents occurred when $q < 0.06 \text{ L/(s} \cdot \text{m)}$. Therefore, the line

at $q = 0.06 \text{ L/(s} \cdot \text{m)}$ can also be used as the division between the water inrush and safety zones, considering that the area with $q < 0.06 \text{ L/(s} \cdot \text{m)}$ is the safety zone. In this interval, T_s was not affected by q . A larger but not definitive value could be considered as the value of T_s , which is represented by the symbol ∞ .

$$T_s = \infty, q < 0.06 \text{ L/(s} \cdot \text{m)}. \quad (7)$$

4.2. Risk Level Classification in Water Inrush Zone in the T - q Method. For the area above the T_s - q curve, the risk level was determined by the value of q in the aquifer.

Table 5 and Figure 12 show that the boundary between the small and medium water inrush cases was $q = 1.7 \text{ L/(s} \cdot \text{m)}$. The area where the small water inrush cases were distributed was defined as a relatively safe zone because Q in these cases was sufficiently small to be easily drained and could not affect mine production. The boundary between the medium and large water inrush cases was $q = 16.7 \text{ L/(s} \cdot \text{m)}$. The area where the medium water inrush cases were distributed was defined as a danger zone because Q was relatively large and would have a negative influence on mine production. Applying the same logic, the area where the large water inrush cases were distributed was called a high-danger zone because Q was too large for rapid draining and would jeopardize safe mine production.

TABLE 6: Application cases in the North China coalfield evaluated by the $T - q$ method.

No.	Mining face	D_m (m)	P (MPa)	q (L/(s·m))	T (MPa/m)	T_s (MPa/m)	Evaluation results	Field verification
A	III628, Zhuzhuang mine, Huaibei mining area	408.47	4.22	0.016	0.140	∞	Safety	Safety
B	III616, Yangzhuang mine, Huaibei mining area	518.25	5.50	0.052	0.110	∞	Safety	Safety
C	1044, Liudian mine, Huaibei mining area	680.08	6.93	0.024	0.210	∞	Safety	Safety
D	1037, Liudian mine, Huaibei mining area	659.66	6.60	0.024	0.330	∞	Safety	Safety
E	1088, Heishan mine, Zibo mining area	594.26	6.23	0.032	0.130	∞	Safety	Safety
F	11022, Jiulishan mine, Jiaozuo mining area	108.85	1.19	24.450	0.052	0.0090	Water inrush with $Q \geq 600 \text{ m}^3/\text{h}$ (high danger)	Water inrush with $Q = 714 \text{ m}^3/\text{h}$
G	9507, Xiangzhuang mine, Feicheng mining area	80.18	0.92	8.330	0.038	0.0126	Water inrush with $60 < Q < 600 \text{ m}^3/\text{h}$ (danger)	Water inrush with $Q = 300 \text{ m}^3/\text{h}$
H	4221, Jiaoxi mine, Jiaozuo mining area	93.62	1.00	12.620	0.053	0.0111	Water inrush with $60 < Q < 600 \text{ m}^3/\text{h}$ (danger)	Water inrush with $Q = 201 \text{ m}^3/\text{h}$
I	12031, Jiulishan mine, Jiaozuo mining area	81.95	0.92	11.330	0.041	0.0115	Water inrush with $60 < Q < 600 \text{ m}^3/\text{h}$ (danger)	Water inrush with $Q = 588 \text{ m}^3/\text{h}$
J	1007, Fucun mine, Zibo mining area	125.13	1.46	7.120	0.043	0.0133	Water inrush with $60 < Q < 600 \text{ m}^3/\text{h}$ (danger)	Water inrush with $Q = 256 \text{ m}^3/\text{h}$
K	4231, Jiaoxi mine, Jiaozuo mining area	109.88	1.17	3.33	0.059	0.0168	Water inrush with $60 < Q < 600 \text{ m}^3/\text{h}$ (danger)	Water inrush with $Q = 91 \text{ m}^3/\text{h}$
L	9304, Shida mine, Zibo mining area	182.12	1.96	5.88	0.071	0.0141	Water inrush with $60 < Q < 600 \text{ m}^3/\text{h}$ (danger)	Water inrush with $Q = 210 \text{ m}^3/\text{h}$
M	10401, Taoyang mine, Feicheng mining area	43.40	0.54	1.67	0.024	0.0209	Water inrush with $0 < Q \leq 60 \text{ m}^3/\text{h}$ (relatively safe)	Water inrush with $Q = 60 \text{ m}^3/\text{h}$
N	42013, Jiaoxi mine, Jiaozuo mining area	72.24	0.8	1.17	0.04	0.0234	Water inrush with $0 < Q \leq 60 \text{ m}^3/\text{h}$ (relatively safe)	Water inrush with $Q = 42 \text{ m}^3/\text{h}$
O	11051, Jiulishan mine, Jiaozuo mining area	139.32	1.5	0.72	0.063	0.0273	Water inrush with $0 < Q \leq 60 \text{ m}^3/\text{h}$ (relatively safe)	Water inrush with $Q = 26 \text{ m}^3/\text{h}$
P	9301, Shida mine, Zibo mining area	225.28	2.42	0.39	0.078	0.0331	Water inrush with $0 < Q \leq 60 \text{ m}^3/\text{h}$ (relatively safe)	Water inrush with $Q = 14 \text{ m}^3/\text{h}$
Q	9302, Shida mine, Zibo mining area	176.57	1.91	0.58	0.068	0.0292	Water inrush with $0 < Q \leq 60 \text{ m}^3/\text{h}$ (relatively safe)	Water inrush with $Q = 21 \text{ m}^3/\text{h}$
R	9307, Shida mine, Zibo mining area	148.54	1.64	1	0.057	0.0246	Water inrush with $0 < Q \leq 60 \text{ m}^3/\text{h}$ (relatively safe)	Water inrush with $Q = 36 \text{ m}^3/\text{h}$
S	9019, Shida mine, Zibo mining area	140.63	1.54	0.08	0.058	0.0545	Water inrush with $0 < Q \leq 60 \text{ m}^3/\text{h}$ (relatively safe)	Water inrush with $Q = 3 \text{ m}^3/\text{h}$
T	1095, Xiazhuang mine, Zibo mining area	190.36	2.05	1	0.072	0.0246	Water inrush with $0 < Q \leq 60 \text{ m}^3/\text{h}$ (relatively safe)	Water inrush with $Q = 36 \text{ m}^3/\text{h}$

Note: ∞ indicates a larger, but not definitive, value of T_s ; the distribution of the cases can be seen in Figure 14.

4.3. *Novelty Analysis of the T - q Method.* The abovementioned analysis enabled the development of the T - q method.

Figure 12 shows the discrimination diagram with T on the y -axis and q on the x -axis. The $T_s - q$ curve separates the safety zone from the water inrush zone. The water inrush zone consists of relatively safe, danger, and high-danger zones, which are indicated by different colors. The risk level of the water inrush from the coal-seam floor can be easily

and quickly determined by introducing the q and T values of an excavation face onto Figure 12. Thus, the $T - q$ method provides a quick and handy risk assessment in mining. Smaller q indicates lower possibility of water inrush, whereas larger q correlates with higher magnitude of water inrush after the water inrush initiation.

The novelty of this study is reflected in the following two aspects.

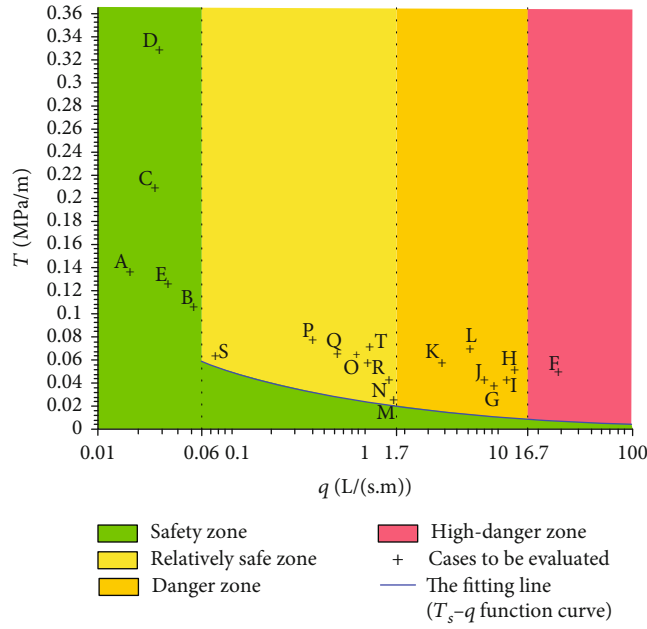


FIGURE 14: Distribution of application cases recorded in Table 6 in the T - q discrimination diagram.

4.3.1. *The T - q Method Is More Accurate and Practical.* The occurrence of water inrush actually includes two stages: (1) the formation stage of a water inrush channel and (2) the water-discharge stage from the aquifer into the excavation face. In the formation stage of the water inrush channel, the instability and breakage of the intact aquiclude or dangerous geological structure occur under the action of continuous water pressure. The continuity of water pressure is guaranteed by the water movement in the aquifer. Therefore, when the possibility of water inrush is evaluated, the efficiency of water movement in the aquifer must be considered to obtain more accurate results. In the water-discharge stage from the aquifer to the excavation face, the amount of water inflow into the excavation face is also determined by the efficiency of the water movement in the aquifer. The efficiency of water movement in the aquifer is related to q . Therefore, the q of the aquifers that recharge the mine must be considered to accurately assess the water inrush risk. Compared with the traditional T method, the T - q method proposed herein provides a more realistic risk assessment in deep mining because q is considered.

As it can be seen from Figure 13, the method proposed in this paper has high accuracy for different D_m . The accuracy is generally higher than 80%. Given that the results of this paper were obtained through the statistical analysis of the existing sample data, the accuracy of the method will inevitably be affected by the number of samples and the distribution range of the D_m of the samples. If we get a large number of sample data with different D_m , the accuracy of the method will increase. Although the accuracy of the method is affected by the number of samples, the conclusion stating that the accuracy of the method is higher than that of the T method is convincing because T_s is treated as a q -related variable. Especially when the mining depth is very shallow or deep, the accuracy of the method is higher than that of the T method.

4.3.2. *The T - q Method Is Simple and Can Be Quickly Used.* Many factors related to water inrush exist, including the size of the excavation face, D_m , and complexity of the geological structure. Therefore, as more factors are considered in the evaluation of water inrush risk, more accurate are the evaluation results. However, considering more factors involves a more complex analysis and calculation, which can make difficult its application. Therefore, the selection of the most decisive factors needs to consider both the accuracy of the results and the simplicity of the discrimination process. Several decades of mining practice have proven that the results of the water inrush risk assessment based solely on the size of P , M , and q can fully provide a guide to the prevention and control of mine floods. Compared with the existing multifactor superposition and analytical methods with complex operating process, the proposed method provides a quicker risk assessment in deep mining because only one T - q discrimination diagram is needed to complete the discrimination.

4.4. *Application and Verification of the T - q Method.* Water inrush cases and safety cases are used to verify the accuracy of the proposed method (Table 6). According to Equations (6) and (7), the T_s values of each sampling point in Table 6 can be obtained.

It can be seen from Table 6 that since the q values of points A–E are very small, the T_s of points A–E are all ∞ , which is greater than their actual T values, indicating that water inrush will not occur at these points. The T_s values of points F–T are smaller than their actual T values, indicating that water inrush will occur at these points. Furthermore, the water quantity range of these water inrush points can be predicted according to the magnitudes of q . The actual results show that the risk level of water inrush at all points and the water quantity range of each water inrush point are

accurately predicted (Figure 14, Table 6). On the contrary, it can be seen from Table 1 that if q is not considered, the water inrush risk of these points will not be predicted accurately. Compared with Tables 1 and 6, we can conclude that the T - q method is reliable, and q is a key factor that cannot be ignored in water inrush assessment.

5. Conclusions

The main contribution of this paper is to improve the T method by obtaining a simple and easy to use method with a higher accuracy. Through this study, the following findings are obtained.

The conventional T method is mostly applicable when D_m is about 300 m. The corresponding T_s is also extracted based on the prevention and control experience of water disaster in those mines whose D_m is about 300 m. The accuracy of the T method is low when D_m is very shallow or very deep because in the T method, the T_s of different D_m is set as a fixed value. Thus, the method neglects the fact that T_s is a variable related to q , affected by D_m .

The possibility of water inrush is positively correlated with both T and q . T indicates the potential of the confined water to break through the aquiclude, and q is the key parameter that determines the extent of this potential release. The value of the critical T_s is not fixed but changes with changing q and has a negative correlation with q . The T - q method proposed in this paper has high accuracy for different D_m , generally being higher than 80%. The risk level of water inrush from the coal seam floor can be easily and quickly determined by introducing the q and T values of an excavation face onto the T - q discrimination diagram. The evaluation results of 20 application cases show that the T - q method has high accuracy at different D_m .

Compared with the traditional T method and the multi-factor superposition analysis method, the method established in this paper has the characteristics of convenient field application and high accuracy. The establishment process of the T - q method can provide reference for the establishment of relevant methods in other coal fields.

Data Availability

All data used during the study appear in the submitted article are available from the corresponding author upon request.

Conflicts of Interest

The authors declare that there is no conflict of interest regarding the publication of this paper.

Acknowledgments

This research was jointly supported by the Project funded by the China Postdoctoral Science Foundation (Grant No. 2019M652015), Fundamental Research Funds for the Central Universities (Grant No. 2017XKZD07), and Natural Science Foundation of China (Grant No. 41772302).

References

- [1] L. Yuan, N. Zhang, J. G. Kan, and Y. Wang, "The concept, model and reserve forecast of green coal resources in China," *Journal of China University of Mining and Technology*, vol. 47, no. 1, pp. 1–8, 2018.
- [2] Q. Wu, Z. L. Zhang, and J. F. Ma, "A new practical methodology of the coal floor water bursting evaluating I: the master controlling index system construction," *Journal of China Coal Society*, vol. 32, pp. 42–47, 2007.
- [3] Q. Wu, Z. L. Zhang, S. Y. Zhang, and J. F. Ma, "A new practical methodology of the coal floor water bursting evaluating II: the vulnerable index method," *Journal of China Coal Society*, vol. 32, pp. 1121–1126, 2007.
- [4] Q. M. Liu and J. W. Hu, "Research on method of water-resisting coefficient for distinguishing floor water inrush danger," *Procedia Earth and Planetary Science*, vol. 3, pp. 238–245, 2011.
- [5] Z. P. Meng, G. Q. Li, and X. T. Xie, "A geological assessment method of floor water inrush risk and its application," *Engineering Geology*, vol. 143–144, pp. 51–60, 2012.
- [6] Y. Wang, W. F. Yang, M. Li, and X. Liu, "Risk assessment of floor water inrush in coal mines based on secondary fuzzy comprehensive evaluation," *International Journal of Rock Mechanics and Mining Sciences*, vol. 52, pp. 50–55, 2012.
- [7] J. H. He, W. P. Li, and W. Qiao, "P-H-q evaluation system for risk assessment of water inrush in underground mining in North China coal field, based on rock-breaking theory and water-pressure transmission theory," *Geomatics, Natural Hazards and Risk*, vol. 9, no. 1, pp. 524–543, 2018.
- [8] H. F. Duan, Z. Q. Jiang, S. Y. Zhu, L. J. Zhao, and J. G. Liu, "A expansive limits anti-permeability strength methodology of the coal mine floor water inrush evaluating," *Procedia Environmental Sciences*, vol. 12, pp. 372–378, 2012.
- [9] H. B. Bai, D. Ma, and Z. Q. Chen, "Mechanical behavior of groundwater seepage in karst collapse pillars," *Engineering Geology*, vol. 164, pp. 101–106, 2013.
- [10] L. W. Chen, X. Q. Feng, W. P. Xie, and D. Q. Xu, "Prediction of water-inrush risk areas in process of mining under the unconsolidated and confined aquifer: a case study from the Qidong coal mine in China," *Environment and Earth Science*, vol. 75, no. 8, 2016.
- [11] S. C. Zhang, W. J. Guo, and Y. Y. Li, "Experimental simulation of water-inrush disaster from the floor of mine and its mechanism investigation," *Arabian Journal of Geosciences*, vol. 10, no. 22, pp. 502–512, 2017.
- [12] R. Gao, H. Yan, F. Ju, X. C. Mei, and X. L. Wang, "Influential factors and control of water inrush in a coal seam as the main aquifer," *International Journal of Mining Science and Technology*, vol. 28, no. 2, pp. 187–193, 2018.
- [13] W. H. Shi and T. H. Yang, "A coupled nonlinear flow model for particle migration and seepage properties of water inrush through broken rock mass," *Geofluids*, vol. 2020, Article ID 1230542, 14 pages, 2020.
- [14] T. Li, T. T. Mei, X. H. Sun, Y. G. Lv, J. Q. Sheng, and M. Cai, "A study on a water-inrush incident at Laohutai coalmine," *International Journal of Rock Mechanics and Mining Sciences*, vol. 59, pp. 151–159, 2013.
- [15] Q. S. Bai, S. H. Tu, C. Zhang, and D. F. Zhu, "Discrete element modeling of progressive failure in a wide coal roadway from water-rich roofs," *International Journal of Coal Geology*, vol. 167, pp. 215–229, 2016.

- [16] B. Li and Y. L. Chen, "Risk assessment of coal floor water inrush from underlying aquifers based on GRA-AHP and its application," *Geotechnical and Geological Engineering*, vol. 34, no. 1, pp. 143–154, 2016.
- [17] J. S. Wu, S. D. Xu, R. Zhou, and Y. P. Qin, "Scenario analysis of mine water inrush hazard using Bayesian networks," *Safety Science*, vol. 89, pp. 231–239, 2016.
- [18] S. L. Liu, W. T. Liu, and J. J. Shen, "Stress evolution law and failure characteristics of mining floor rock mass above confined water," *KSCE Journal of Civil Engineering*, vol. 21, no. 7, pp. 2665–2672, 2017.
- [19] M. Qiu, L. Q. Shi, C. Teng, and Y. Zhou, "Assessment of water inrush risk using the fuzzy Delphi analytic hierarchy process and grey relational analysis in the Liangzhuang coal mine, China," *Mine Water and the Environment*, vol. 36, no. 1, pp. 39–50, 2017.
- [20] L. Q. Shi, W. F. Gao, J. Han, and X. P. Tan, "A nonlinear risk evaluation method for water inrush through the seam floor," *Mine Water and the Environment*, vol. 36, no. 4, pp. 597–605, 2017.
- [21] B. B. Yang, W. H. Sui, and L. H. Duan, "Risk assessment of water inrush in an underground coal mine based on GIS and fuzzy set theory," *Mine Water and the Environment*, vol. 36, no. 4, pp. 617–627, 2017.
- [22] B. Y. Yu, Z. Q. Chen, J. Y. Wu, and L. Z. Wang, "Experimental study of non-Darcy flow seepage properties of cemented broken rocks with mass loss," *Journal of China University of Mining and Technology*, vol. 46, pp. 321–327, 2017.
- [23] G. L. Dai, X. Y. Xue, K. Xu, L. Dong, and C. Niu, "A GIS-based method of risk assessment on no. 11 coal-floor water inrush from Ordovician limestone in Hancheng mining area, China," *Arabian Journal of Geosciences*, vol. 11, no. 22, p. 714, 2018.
- [24] Z. Huang, X. Z. Li, S. J. Li, K. Zhao, and R. Zhang, "Investigation of the hydraulic properties of deep fractured rocks around underground excavations using high-pressure injection tests," *Engineering Geology*, vol. 245, pp. 180–191, 2018.
- [25] Q. Li, X. X. Meng, Y. B. Liu, and L. F. Pang, "Risk assessment of floor water inrush using entropy weight and variation coefficient model," *Geotechnical and Geological Engineering*, vol. 37, no. 3, pp. 1493–1501, 2019.
- [26] B. Li, Q. Wu, X. Q. Duan, and M. Y. Chen, "Risk analysis model of water inrush through the seam floor based on set pair analysis," *Mine Water and the Environment*, vol. 37, no. 2, pp. 281–287, 2018.
- [27] W. T. Liu, Q. Li, and J. Y. Zhao, "Application on floor water inrush evaluation based on AHP variation coefficient method with GIS," *Geotechnical and Geological Engineering*, vol. 36, no. 5, pp. 2799–2808, 2018.
- [28] W. B. Sun and Y. C. Xue, "An improved fuzzy comprehensive evaluation system and application for risk assessment of floor water inrush in deep mining," *Geotechnical and Geological Engineering*, vol. 37, no. 3, pp. 1135–1145, 2019.
- [29] Y. F. Zeng, "Vulnerability index method based on partition variable weight theory," in *Research on risk evaluation methods of groundwater bursting from aquifers underlying coal seams and applications to coalfields of North China. Springer Theses (Recognizing Outstanding nnnnnnnD. Research)*, Springer, Cham, 2018.
- [30] D. K. Zhao, Q. Wu, F. P. Cui et al., "Using random forest for the risk assessment of coal-floor water inrush in Panjiayao coal mine, northern China," *Hydrogeology Journal*, vol. 26, no. 7, pp. 2327–2340, 2018.
- [31] G. Li and W. T. Liu, "Uncertainty analysis of water-inrush from floor induced by deep mining," *Geotechnical and Geological Engineering*, vol. 37, no. 1, pp. 317–325, 2019.
- [32] T. T. Li and C. Y. Wang, "Numerical simulation study on formation and evolution process of water-inrush channel in floor under high water pressure," *Geotechnical and Geological Engineering*, vol. 37, no. 4, pp. 3007–3012, 2019.
- [33] Z. E. Ruan, C. P. Li, A. X. Wu, and Y. Wang, "A new risk assessment model for underground mine water inrush based on AHP and D-S evidence theory," *Mine Water and the Environment*, vol. 38, no. 3, pp. 488–496, 2019.
- [34] X. T. Wang, S. C. Li, Z. H. Xu, P. Lin, J. Hu, and W. Y. Wang, "Analysis of factors influencing floor water inrush in coal mines: a nonlinear fuzzy interval assessment method," *Mine Water and the Environment*, vol. 38, no. 1, pp. 81–92, 2019.
- [35] J. Han, L. Q. Shi, X. G. Yu, J. C. Wei, and S. C. Li, "Mechanism of mine water-inrush through a fault from the floor," *Mining Science and Technology (China)*, vol. 19, no. 3, pp. 276–281, 2009.
- [36] X. Y. Hu, L. G. Wang, Y. L. Lu, and M. Yu, "Analysis of insidious fault activation and water inrush from the mining floor," *International Journal of Mining Science and Technology*, vol. 24, no. 4, pp. 477–483, 2014.
- [37] S. L. Liu, W. T. Liu, and D. W. Yin, "Numerical simulation of the lagging water inrush process from insidious fault in coal seam floor," *Geotechnical and Geological Engineering*, vol. 35, no. 3, pp. 1013–1021, 2017.
- [38] W. H. Shi, T. H. Yang, H. L. Liu, and B. Yang, "Numerical modeling of non-Darcy flow behavior of groundwater outburst through fault using the Forchheimer equation," *Journal of Hydrologic Engineering*, vol. 23, no. 2, p. 04017062, 2018.
- [39] S. C. Li, J. Wu, Z. H. Xu, and W. M. Yang, "Mechanics criterion of water inrush from the coal floor under influence of fault and its engineering application," *International Journal of Geomechanics*, vol. 19, no. 5, article 04019022, 2019.
- [40] B. Li, W. Q. Zhang, B. Gao, and J. D. Yuan, "Research status and development trends of mine floor water inrush grade prediction," *Geotechnical and Geological Engineering*, vol. 36, no. 3, pp. 1419–1429, 2018.
- [41] State Administration of Work Safety and State Administrative of Coal Mine Safety, *Stipulation on Prevention and Control of Coal Mine Water*, China Coal Industry Publishing House, Beijing, 2009.
- [42] W. Qiao, *Study on the Water Abundance Regularity of Deep Fracture-Karst Aquifer and the Critical Evaluation of Water Inrush from Coal Floor in Coal Mine*, China University of Mining and Technology, Xuzhou, 2011.
- [43] W. Y. Hu, "The characteristics of karst and deep coal mine karst water hazards in eastern North China," *Coal Geology & Exploration*, vol. 38, pp. 23–27, 2010.
- [44] W. Qiao, W. P. Li, and C. X. Zhao, "Water inrush coefficient-unit inflow method for water inrush evaluation of coal mine floor," *Chinese Journal of Rock Mechanics and Engineering*, vol. 28, pp. 2466–2474, 2009.
- [45] C. X. Zhao, *The Water Inrush Mechanism and Governmental Mode of Deep Karst in Huaibei Mine*, China University of Mining and Technology, Xuzhou, 2015.
- [46] L. Q. Shi, M. Qiu, W. X. Wei, D. J. Xu, and J. Han, "Water inrush evaluation of coal seam floor by integrating the water

inrush coefficient and the information of water abundance,” *International Journal of Mining Science and Technology*, vol. 24, no. 5, pp. 677–681, 2014.

- [47] J. Sun, Y. Hu, and G. M. Zhao, “Relationship between water inrush from coal seam floors and main roof weighting,” *International Journal of Mining Science and Technology*, vol. 27, no. 5, pp. 873–881, 2017.
- [48] B. H. Guo, T. Cheng, L. Wang, T. Luo, and X. Y. Yang, “Physical simulation of water inrush through the mine floor from a confined aquifer,” *Mine Water and the Environment*, vol. 37, no. 3, pp. 577–585, 2018.

Research Article

Crack Propagation Law and Failure Characteristics of Coal-Rock Combined Body with the Different Inclination Angle of Prefabricated Fissure

Chunlei Zhang¹, Yun Dong¹, Ruimin Feng², Ningbo Peng¹, Jihua Zhang¹,
Jingke Wu¹ and Wei Shen¹

¹Faculty of Architecture and Civil Engineering, Huaiyin Institute of Technology, Huai'an, Jiangsu 223001, China

²Department of Civil Engineering, University of Arkansas, 4190 Bell Engineering Center, Fayetteville, AR 72701, USA

Correspondence should be addressed to Chunlei Zhang; leizhewudi@hyit.edu.cn and Yun Dong; dyunhyit@hyit.edu.cn

Received 26 April 2021; Accepted 18 June 2021; Published 5 July 2021

Academic Editor: Feng Du

Copyright © 2021 Chunlei Zhang et al. This is an open access article distributed under the Creative Commons Attribution License, which permits unrestricted use, distribution, and reproduction in any medium, provided the original work is properly cited.

Few studies have been conducted on the crack propagation law and failure characteristics of coal-rock combined body (CRCB) with prefabricated fissure. A sliding crack model was firstly presented to analyze the failure law of rock with a single fracture and the influence of the inclination angle of the fracture on the strength of the rock. The RFP numerical models of the CRCB with different inclination angles of prefabricated fracture were then established to simulate the dynamic change process of crack propagation and shear stress of the CRCB with prefabricated fracture under uniaxial compression. The influence of the inclination angle of the fracture in the rock on the fracture expansion and failure characteristics of CRCB was further analyzed based on the acoustic emission data. The results showed that (1) when $2\beta = \arctan 1/\mu$, σ_{cw} takes the minimum value, and crack initiation is most likely to occur; (2) the strength of coal-rock assemblage shows different changing trends with the fracture inclination angle; (3) the secondary cracks of CRCB with prefabricated fracture of 0° , 15° , and 30° initiated and expanded near the tip of the main crack, and the secondary cracks of 45° , 60° , and 75° initiated and expanded from the tip of the main crack; (4) there are three failure modes of CRCB with prefabricated crack, the double-shear failure mode Λ , the tensile-shear composite failure mode along the fracture surface, and the tensile failure mode along the fracture surface; and (5) intact CRCB and CRCB with prefabricated crack when $\alpha = 75^\circ$ and $\alpha = 90^\circ$ have strong brittleness, and other CRCB with different prefabricated fracture inclination angles show a certain degree of postpeak plasticity. The results on the mechanical properties and damage characteristics of CRCB are of great significance for the safety and efficient mining of deep coal resources.

1. Introduction

Coal is the main resource of energy supply in China. As coal in the shallow subsurface is gradually exhausted, coal mining depth is constantly increasing, which leads to the frequent occurrence of dynamic disasters such as coal and gas outburst and rock burst under deep high geostress environment [1, 2]. The deformation damage of coal-rock combined body (CRCB) in the deep environment is affected by multiple factors such as its own physical and mechanical properties and geological structure, but more importantly, it is affected by the coexistence of the coal-rock combination structure [3]. The damage and break of rock mass and coal in the engineer-

ing scale are tightly associated with their fine structural features. Research in microscopic view provides a powerful tool to better understand and master the damage and breakage of coal and rock mass in the engineering scale [4]. A better understanding of damage characteristics and fracture mechanisms of CRCB is much helpful for us to make a reasonable interpretation on mining-induced breakage, fracture development, and stress change in the field. Therefore, research on the mechanical properties and damage characteristics of CRCB is of great significance for the safety and efficient mining of deep coal resources.

In recent years, many scholars have carried out mechanical tests of CRCB under different conditions either by

numerical simulations or laboratory tests, aiming to explore the mechanical response characteristics of CRCB [5]. Gong et al. [6, 7] obtained outburst proneness of different CRCB using the axial loading test based on prepeak energy distribution and different loading rates. Zuo et al. [8, 9] studied the failure modes and mechanical behavior differences of different CRCB under uniaxial and triaxial compression. Cao et al. [10] considered the influence of the interface inclination angle of CRCB on its strength and failure mechanism. Liu et al. and Xie et al. [11, 12] studied the crack propagation law of CRCB with different combinations and found that the failure of coal and the propagation of cracks further led to the failure of the rock. Du and Wang [13] explored the failure characteristics of CRCB through the true triaxial test. Chen et al., Zhao et al., and Dong et al. [14–16] obtained the fracture propagation mode of CRCB under different loading conditions through theoretical analysis and laboratory experiments. The above research on the failure characteristics of CRCB is mainly aimed at intact coal-rock assemblages. However, considering the influence of geological movement during the formation of coal and rock masses, there are a large number of original fissures in the coal and rock masses which affect the “coal-rock” structural strength and failure characteristics, so it is worth investigating the role of the fissures in the mechanical behavior of the rocks. Li et al. and Yin et al. [17–19] used Split Hopkinson Pressure Bar (SHPB) and PFC numerical simulation methods to perform shock compression and uniaxial compression tests on CRCB with prefabricated cracks and obtained the crack inclination and position on the influence of the strength and failure characteristics of the CRCB, but the influence of the cracks in the rock mass is not considered.

Therefore, this paper will use RFPA software to carry out numerical simulations of CRCB with prefabricated cracks in different inclination angles, explore the influence of cracks in rock mass on the mechanical properties and failure characteristics of the CRCB, and further explore the mechanical response characteristics of the CRCB.

2. Sliding Crack Model of Rock with Single Fracture

At present, there are two main views on the compression-induced crack propagation of brittle materials: one is compression-tension fracture and the other is sliding fracture. Comparing the two views in explaining the microcrack propagation of brittle materials, the sliding crack model reflecting the mechanism of microcrack sliding opening fracture gradually prevails and has been widely accepted in academia. Natural rock material has the characteristics of discontinuity, inelasticity, heterogeneity, and anisotropy. Its structural composition is relatively complex, and it belongs to the brittle material. In 1963, Brace and Bombolakis [20] first proposed the sliding crack model, which was later popularized and applied to the study of the mechanical mechanism of fractured brittle materials under compressive loading by Horii and Nemat-Nasser [21].

2.1. Sliding Crack Model. The frictional sliding crack model is the most extensive model for studying coal and rock mass damage [22]. It is believed that when coal and rock mass is compressed, original cracks will produce secondary tensile cracks that propagate in the direction of maximum principal stress, and secondary cracks are the main cause of splitting and destruction of coal and rock mass. The friction crack model under compressive stress is shown in Figure 1.

The following assumptions are made for the model in Figure 1. The problem is a plane strain problem, the confining pressure is σ_3 , and the axial pressure is σ_1 , and the following assumptions are satisfied: The rock mass is homogeneous and isotropic; both the rock strength and fracture strength obey the Mohr-Coulomb strength criterion. The angle between the penetration crack and the axial stress is β , the internal friction angle is φ_w , the cohesion of the fracture surface is c_w , the normal stress vertical to fracture surface is σ , and the shear stress along the fracture surface is τ .

Decompose the shear stress and normal stress on the original crack surface PP_1 to get

$$\begin{cases} \sigma_n = \sigma_1 \cos^2\theta + \sigma_3 \sin^2\theta, \\ \tau_e = \frac{1}{2}(\sigma_1 - \sigma_3) \sin 2\theta. \end{cases} \quad (1)$$

It is assumed that the failure of coal and rock mass satisfies the Mohr-Coulomb criterion. The actual effective shear stress of friction sliding can be then expressed as

$$\tau_{\text{eff}} = (\sigma_1 - \sigma_2) \cos \theta \sin \theta - \tau_c - \mu(\sigma_1 \cos^2\theta + \sigma_2 \sin^2\theta), \quad (2)$$

where μ is the internal friction coefficient of coal and rock mass and τ_c is the cohesion. The critical condition for frictional sliding of cracks is $\tau_{\text{eff}} = 0$, and we have

$$\sigma_1 = \frac{\sigma_2 \sin \theta \cos \theta - \tau_c - \mu \sigma_2 \cos^2\theta}{\mu \sin^2\theta + \sin \theta \cos \theta}. \quad (3)$$

According to the above equation, when $\theta_0 = \tan^{-1}(\mu + \sqrt{\mu^2 + 1})$, σ_1 gets the minimum value; then, we obtain the critical stress condition causing frictional sliding:

$$\sigma_{1cs} = \frac{\sigma_2 \sin \theta_0 \cos \theta_0 - \tau_c - \mu \sigma_2 \cos^2\theta_0}{\mu \sin^2\theta_0 + \sin \theta_0 \cos \theta_0}. \quad (4)$$

When $\sigma_1 < \sigma_{1cs}$, the coal and rock mass materials exhibit elastic characteristics, and the original cracks do not cause friction sliding. When $\sigma_{1cs} \leq \sigma_1 < \sigma_{1c}$, the coal and rock mass exhibits nonlinear strengthening characteristics, and some cracks have self-similar propagation and frictional sliding.

Continuing to load, some cracks will self-similarly propagate. The crack gradually expands to a certain characteristic length c_b , with the increase of axial pressure, and c_b is related to the material composition of coal and rock mass.

In the rock loading test, the cracks of the rock sample experience a process from opening to closing to expansion

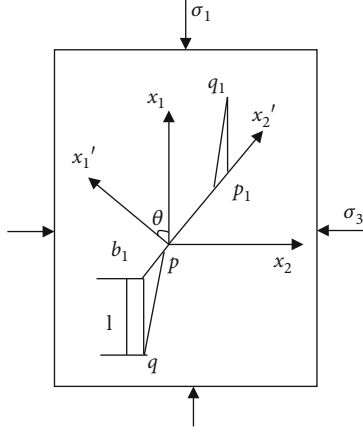


FIGURE 1: Frictional sliding crack model under compressive loading (the overall coordinate system $o-x_1x_2$ and the local coordinate system $o-x_1'x_2'$; the ox_1' axis is parallel to the crack's outer normal line; the length of the crack is $2c$, and the azimuth angle is θ).

and rupture. Therefore, to study the influence of cracks on the strength of the rock in the compression test, it is necessary to start with the closed crack [23]. Because the crack is closed, the effective shear stress on the crack causes relative sliding on the crack surface, which can be regarded as a pure type II crack at the crack initiation stage, that is, $K_I = 0$ [24]; according to the theory of fracture mechanics, the stress intensity factor at the crack tip is

$$k_{II} = \tau_e \sqrt{\pi c}. \quad (5)$$

Taking $\sigma_3 = 0$ and $\sigma = \sigma_1$ and substituting Equation (2) into Equation (5), we have

$$k_{II} = \tau_e \sqrt{\pi c} = \sigma \cos \theta \sin \theta \sqrt{\pi c} - \tau_c \sqrt{\pi c} - \mu \sigma \cos^2 \theta \sqrt{\pi c}. \quad (6)$$

For shear fracture under compression, the following formula is adopted as the criterion:

$$\lambda_{12} k_I + k_{II} = k_{IIc}. \quad (7)$$

In the formula, λ_{12} is the compression reduction coefficient, and k_{IIc} is the shear toughness under compression. Since $k_I = 0$, the failure criterion of the crack surface is $k_{II} = k_{IIc}$.

The criterion of stable growth of microcracks can be expressed as

$$K_{IIc} = \frac{1}{2} [(\sin 2\theta - \mu - \mu \cos 2\theta)\sigma - 2\tau_c] \sqrt{\pi c}, \quad (8)$$

where a is the type II fracture toughness of the weak surface.

Since the cohesion τ_c of the crack surface during uniaxial compression is very small, take $\tau_c = 0$ and $\beta = 90^\circ - \theta$, the initial fracture strength of the crack is

$$\sigma_{cw} = \frac{2K_{IIc}}{\sqrt{\pi c}(\sin 2\theta - \mu - \mu \cos 2\theta)} = \frac{2K_{IIc}}{\sqrt{\pi c}(\sin 2\beta - \mu + \mu \cos 2\beta)}. \quad (9)$$

2.2. The Influence of Fissure Angle on the Strength of Rock Mass. No unified standard has been reported for the testing of type II fracture factor k_{IIc} ; however, when the test model size, material, and the external conditions are all the same, the value of fracture toughness k_{IIc} only varies in a very small range if using the same loading method, and it can be considered that it remains unchanged during the experiment [25]. Under uniaxial compression, the strength and failure mode of a rock mass with a single closed crack are determined by the strength of the rock and the strength of the crack surface. It can be seen from Equation (9) that σ_{cw} is a function of β , c , and μ . When the crack length c and the friction coefficient μ of the crack surface is fixed, σ_{cw} is only related to the crack inclination angle. $\beta < \pi/2 - \psi_w$ is the discontinuity point of the function σ_{cw} . When $\beta > \pi/2 - \psi_w$, $\sigma_{cw} < 0$. At this time, the failure of the rock mass is due to tensile stress, which does not conform to the assumption. In order to obtain the extreme value of σ_{cw} , we take the derivative of Equation (9):

$$\frac{\partial \sigma_{cw}}{\partial \beta} = 0, \quad \frac{\partial^2 \sigma_{cw}}{\partial \beta^2} > 0. \quad (10)$$

It can be seen from Equation (10) that when $\beta = 1/2 \arctan 1/\mu$, Equation (10) holds. When $\beta = 1/2 \arctan 1/\mu$, σ_{cw} takes the minimum value, crack initiation is most likely to occur, and the corresponding crack initiation stress is the smallest. When μ is 0.1, $\beta = 42.145^\circ$ [25].

3. Numerical Simulation

The RFPA (rock failure process analysis) software is adopted to study on the crack propagation law and failure characteristics of CRCB with prefabricated fissure. RFPA2D is a rock failure process analysis system with elastic mechanics as stress analysis tools, elastic damage theory, and modified Coulomb failure criterion as medium deformation and failure analysis module [26, 27], enabling to simulate the microcracking process of rock during the deformation process.

3.1. Model Construction and Parameter Selection. Figure 2 shows the model established for numerical simulation. The sample model is a rectangular CRCB with 100 mm height and 50 mm width. Both the height of coal and the height of rock in the model are 50 mm, and the model is divided into 200,000 units. Mohr-Coulomb is used as the constitutive relationship. The length of the crack is $20\sqrt{2}$ mm, and the closing cracks are in contact with each other, the crack surface friction coefficient is 0.1, and the fracture is located in rock, and the angles with the minimum principal stress are 0° , 15° , 30° , 45° , 60° , 75° , and 90° , respectively. Mechanical parameters of CRCB with prefabricated fissure are shown in Table 1. The uniaxial compression test was performed on the CRCB. The loading method was axial displacement

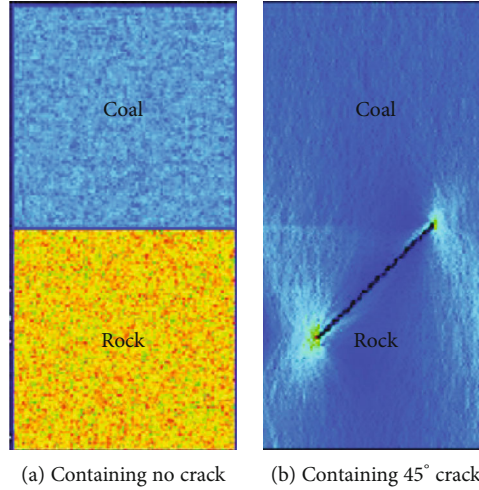


FIGURE 2: Numerical models.

TABLE 1: Mechanical parameters of CRCB with prefabricated fissure.

Type	σ (MPa)	E (GPa)	ψ ($^{\circ}$)	μ	ρ ($\text{kg}\cdot\text{m}^{-3}$)	m
Coal	50	12	32	0.25	1800	5
Rock	140	50	38	0.2	3500	10

loading with a one-step increment of 0.002 mm/step, and the load was carried out until the sample failed.

3.2. Analysis of Strength and Deformation Characteristics.

The crack initiation stress σ_{ci} and the damage stress σ_{cd} are not only important characteristic values of CRCB strength but also the boundary point of different stages in the crack propagation process. There are many methods to determine the rock initiation stress and damage stress [28, 29]; in this paper, the axial stress corresponding to the crack initiation point is taken as the crack initiation stress σ_{ci} , and the damage stress σ_{cd} is determined by the axial stress corresponding to the rapid growth point of the crack. According to the fracture process of the CRCB (Figure 2), Table 2 shows the σ_{ci} and σ_{cd} of intact CRCB and CRCB with prefabricated fissure and their relationship with the uniaxial compressive strength σ of intact CRCB.

Figure 3 shows the fracture evolution process of CRCB with prefabricated fracture of different inclination angles (Due to space limitation, only the shear stress diagrams when the inclination angles of the fractures are $\alpha = 15^{\circ}$ and $\alpha = 45^{\circ}$ are listed). The generation, propagation, and penetration of microcracks formed the macroscopic failure surface of the CRCB, which in turn caused its failure and instability. As the axial strain increases, the evolution of the number of microcracks in CRCB with different inclination angles of crack is basically the same. There is initially no microcracks; microcracks slowly grow, then grow rapidly, and finally stabilize. The number of cracks increases sharply near the peak strain area, especially in a certain stage after the peak strain, which indicates that the microcracks within this stage are

rapidly generated (step 26-2 of Figure 3(a) and step 27-4 of Figure 3(b)), expanded, and penetrated, forming macrocracks. The crack propagation and failure mode in intact CRCB and CRCB with prefabricated fracture of 90° are almost the same. The cracks have almost no effects on the crack propagation mode of the CRCB under uniaxial compression. The cracks start and propagate in the coal part, and no cracks show up in the rock part. The secondary cracks of CRCB with prefabricated fracture of 0° , 15° , and 30° initiated and expanded near the tip of the main crack, and the secondary cracks of 45° , 60° , and 75° initiated and expanded from the tip of the main crack. It can be seen from Figure 3 that the failure of the CRCB with $\alpha = 15^{\circ}$ and $\alpha = 45^{\circ}$ all experienced crack initiation, propagation, and final macroscopic failure, and the CRCB slipped along the crack surface during the failure process. The difference is that when $\alpha = 15^{\circ}$, the initiation and propagation of secondary cracks do not appear at the tip of the main crack, but near the tip of the main crack. The crack propagation is relatively easy before the stress reaches the peak value, but the crack initiation stress is large. When step = 17, the crack initiation occurs, and the CRCB sample reaches its peak strength at step 39. When $\alpha = 45^{\circ}$, the initiation and propagation of secondary cracks mainly spread around the tip of the main crack. As the loading continues, the stress intensity factor of the crack tip increases, and the microcracks penetrate through the tip of the main crack and at both ends of the main crack. Wing cracks are formed and propagate toward the crack end along the main loading direction. In addition, when $\alpha = 45^{\circ}$, the crack initiation is much easier; when step = 10, the cracks start to initiate, and CRCB has been completely broken when the load reaches 29 steps, which is much easier to break compared with $\alpha = 15^{\circ}$. Compared with $\alpha = 45^{\circ}$, when $\alpha = 75^{\circ}$, the crack angle is close to parallel to the axial loading direction, crack initiation is also easy, but the crack growth is strongly suppressed, which leads to an increase in its peak strength (Figure 4).

Figure 4 shows the stress-strain curves of CRCB with different prefabricated crack inclination angles. It can be seen that the CRCB with prefabricated fissure went through three

TABLE 2: Peak strength and peak strain of prefabricated fractured rock-coal combined body.

Angle ($^{\circ}$)	σ_{ci}	Step	σ_{cd}	Step	Peak strength (σ) (MPa)	Peak strain (%)	Step	σ_{ci}/σ	σ_{cd}/σ
Intact	14.1	46	16.7	55	17.3	0.11	57	0.815	0.965
0	3.95	16	6.39	35	6.58	0.068	36	0.600	0.971
15	4.03	17	4.87	26	5.16	0.05	27	0.781	0.944
30	3.18	14	5.24	24	5.93	0.05	27	0.536	0.884
45	2.95	13	4.36	19	6.38	0.054	29	0.462	0.683
60	5.87	22	9.03	33	10.8	0.084	44	0.592	0.836
75	8.18	27	13.4	45	16.2	0.106	55	0.504	0.827
90	12.1	40	16.1	53	16.9	0.108	56	0.715	0.953

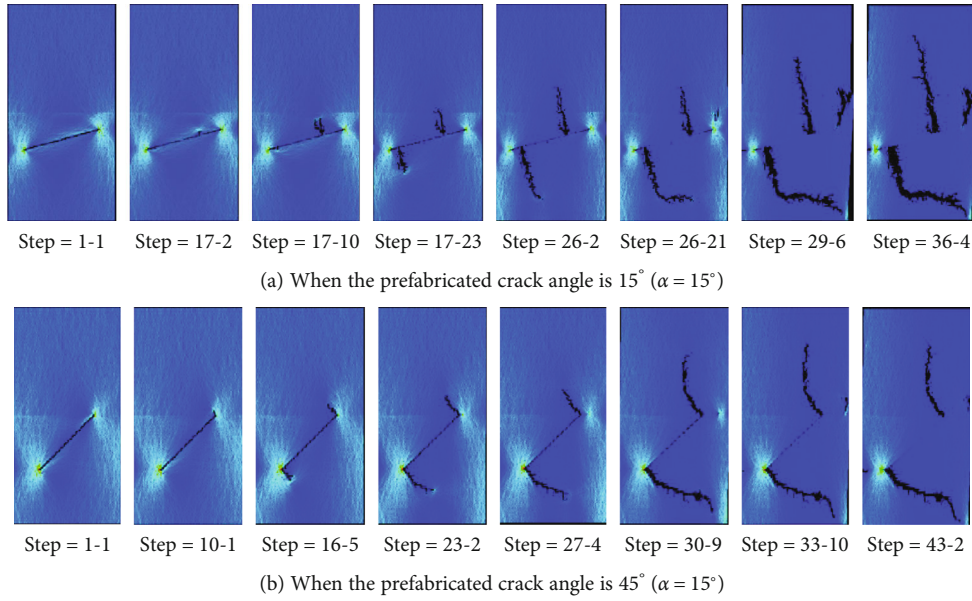


FIGURE 3: Shear stress evolution processes for different prefabricated crack angles of CRCB.

stages under uniaxial compression: linear elastic deformation stage, fracture development stage, and failure stage. Different from the real rock test, the initial compaction stage does not show up obviously, which is mainly related to the constitutive model setting of the simulation software. The stress-strain curve basically rises linearly at the beginning of loading. When the stress reaches the peak strength, the CRCB begins to break, and meanwhile, the stress begins to drop. In addition, the peak strengths of CRCB with different fracture angles are different. Figure 5 shows the relationship between the peak strength of the CRCB and the inclination angle of the crack. It can be seen that the crack inclination angle affects the strength of the CRCB under uniaxial compression. As the crack inclination angle increases, the strength of the CRCB firstly decreases and then increases. CRCB has the lowest peak strength when $\alpha = 15^{\circ}$. When $\alpha < 15^{\circ}$, the peak strength of the CRCB decreases with the increase of the crack inclination angle. When $\alpha > 15^{\circ}$, the peak strength of the CRCB increases with the increase of the inclination angle of the prefabricated fissure.

Compared with the intact CRCB, the bearing capacity of the CRCB with prefabricated fracture is reduced to a certain extent, that is, deterioration. In order to quantitatively

express the degradation characteristics, the deterioration factor w is introduced and is expressed as

$$\omega = \left(1 - \frac{\sigma_0}{\sigma_w}\right) \times 100\%. \quad (11)$$

In the formula, σ_0 is the uniaxial compressive strength of the CRCB with prefabricated fissure (MPa) and σ_w is the uniaxial compressive strength of the CRCB with different prefabricated crack inclination angles (MPa).

Figure 6 shows the relationship between the deterioration factor and the crack inclination angle of the CRCB. As the inclination angle increases, the deterioration factor firstly increases and then decreases and reaches the maximum value when $\alpha = 15^{\circ}$; as the inclination angle continues to increase, the deterioration factor decreases continuously until $\alpha = 75^{\circ}$. When $\alpha = 90^{\circ}$, the deterioration factor further decreases, which is close to the intact CRCB.

3.3. Failure Characteristic Analysis. Failure of the CRCB is caused by macroscopic cracks formed by the propagation of the prefabricated cracks in the rock and interpenetrating with each other, which in turn leads to the overall failure of the

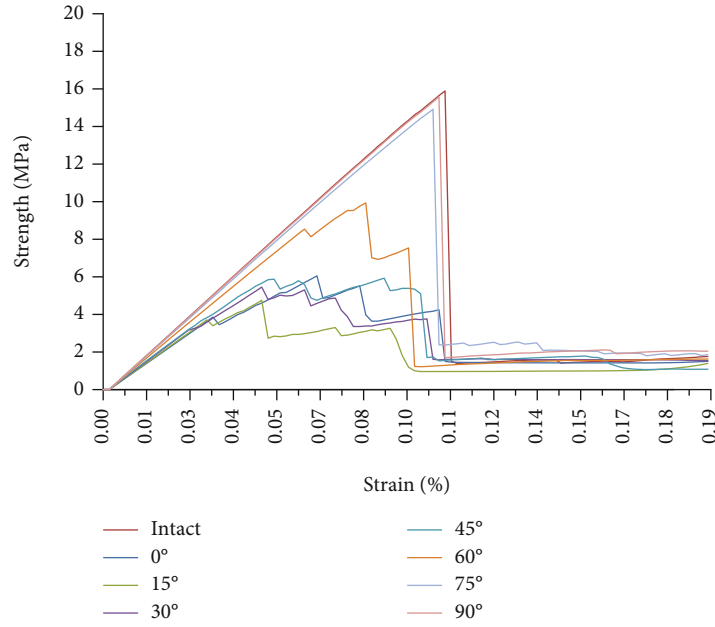


FIGURE 4: Stress-strain curves of coal-rock combined bodies.

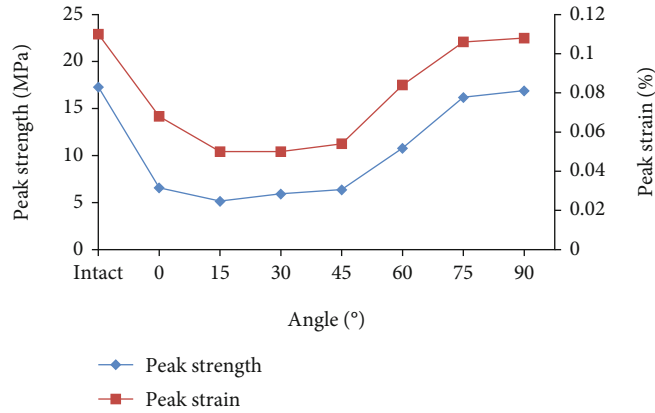


FIGURE 5: Curves of peak strength and peak strain of coal-rock combined body with prefabricated fissure.

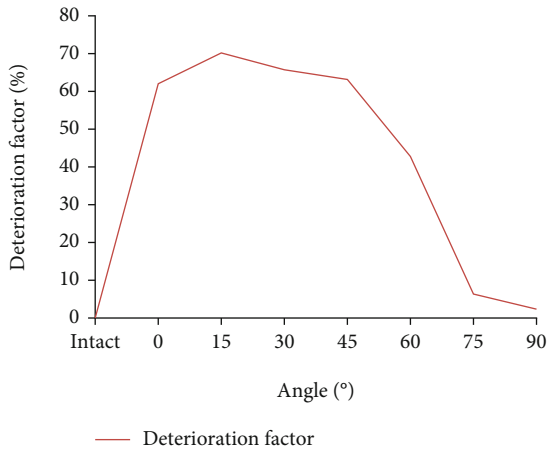


FIGURE 6: Deterioration factor curve.

CRCB. Therefore, the destruction of the rock mass in CRCB leads to its failure, and the inclination angle of the prefabricated cracks in the rock mass affects its failure mode. As shown in Figure 7, there are three failure modes of CRCB with prefabricated crack, the double-shear failure mode Λ (Figures 7(a), 7(g), and 7(h)), the tensile-shear composite failure mode along the fracture surface (Figures 7(b)–7(d)), and the tensile failure mode along the fracture surface (Figures 7(e) and 7(f)). The failure of the intact CRCB and the CRCB with 90° prefabricated fissures mainly occurs in the coal. This is mainly due to the fact that the strength of the coal sample is much smaller than that of the rock sample, and it is a double-shear failure mode, and the crack propagation is type Λ ; the angle between the shear failure surface and the vertical direction is 47.3° and 33.8°, respectively; when the prefabricated fracture is 75° ($\alpha = 75^\circ$), the CRCB also exhibits Λ -type double-shear failure, the difference is that the fracture expansion angle is reduced to 34.2° and 32°, and the crack tip

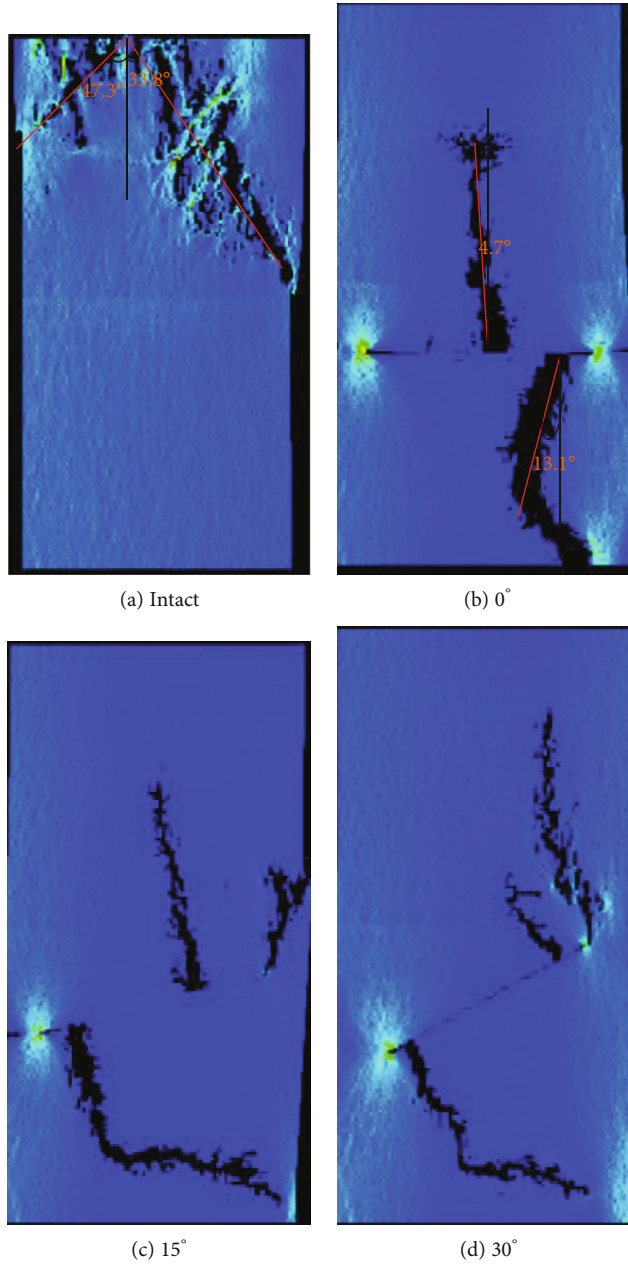


FIGURE 7: Continued.

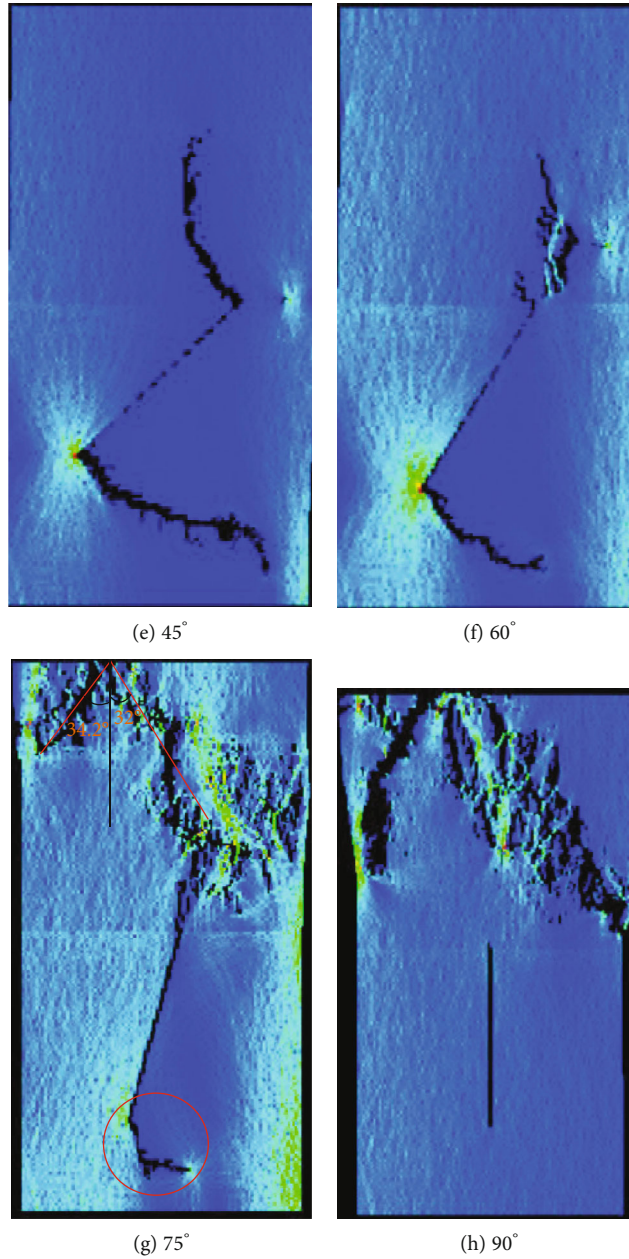
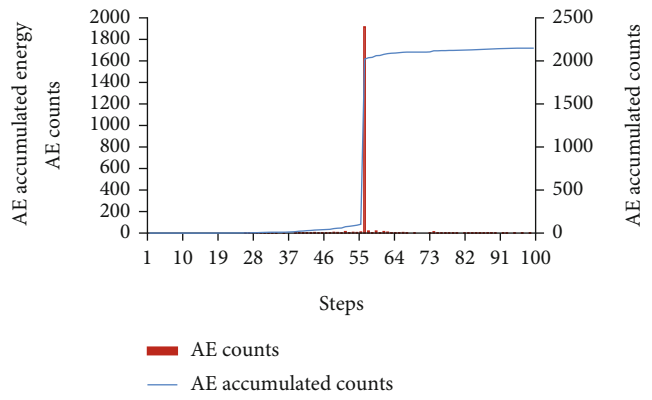
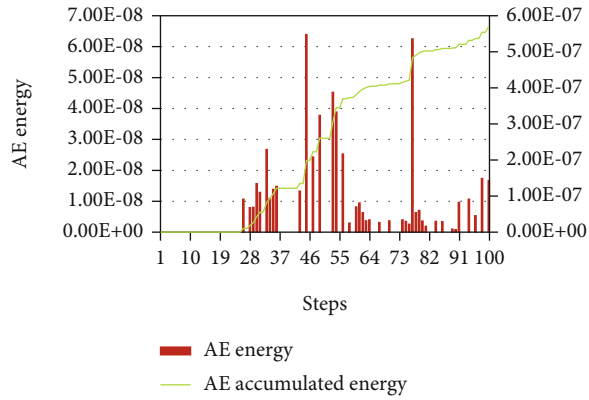


FIGURE 7: Failure modes of different coal-rock combined bodies with different prefabricated fissure angles.

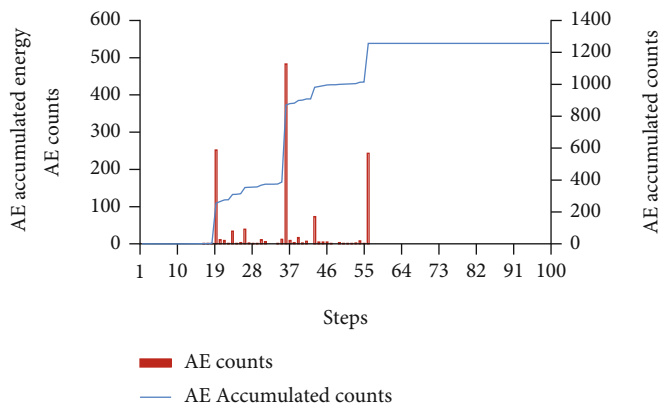
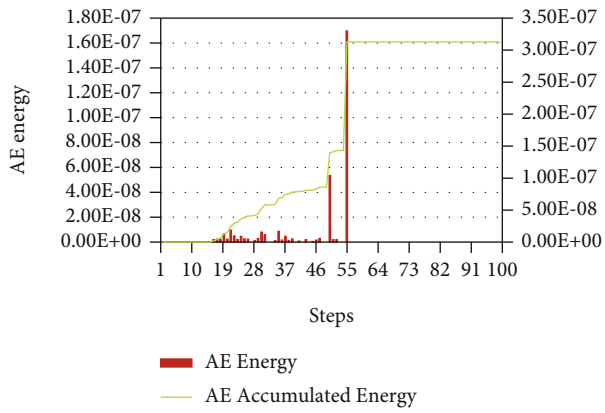
propagates inside the rock mass, as shown in the circle in Figure 7(g). When the inclination angles of the prefabricated cracks are 0° , 15° , and 30° , the failure mode of the CRCB is tensile-shear composite failure. The coal and rock masses in the CRCB are damaged, and the cracks first start propagating near the tip of the prefabricated crack, and then, expanding and penetrating cause the CRCB to reach the peak strength and eventually fail. When the inclination angles of the prefabricated cracks are 45° and 60° , both the coal and rock samples of the CRCB are damaged. Among them, the coal samples are mainly shear failure, and the rock samples are tensile failure with the increase of axial stress. The failure surface and the vertical direction form a certain angle to gradually deflect and finally coincide with the vertical direction. The crack expansion shape in the rock mass is basically

S-shaped. The crack propagation and failure process are as follows: under the axial stress, the prefabricated crack of the rock mass slips, a small number of microcracks are generated on both sides of the joint surface, and an upward extending tensile crack is formed on the upper part of the joint surface. At the same time, the microcracks near the two tips of the joint gather and nucleate; when the axial stress increases, they expand upward in the coal sample and the rock sample to form tensile cracks, while the joint surface will continue to slip and expand; when the axial stress continues to increase, the tensile cracks will continue to increase. The extension crack continues to propagate until the total failure of CRCB.

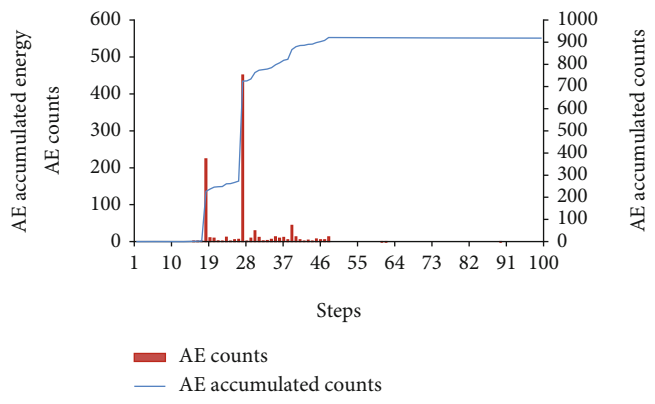
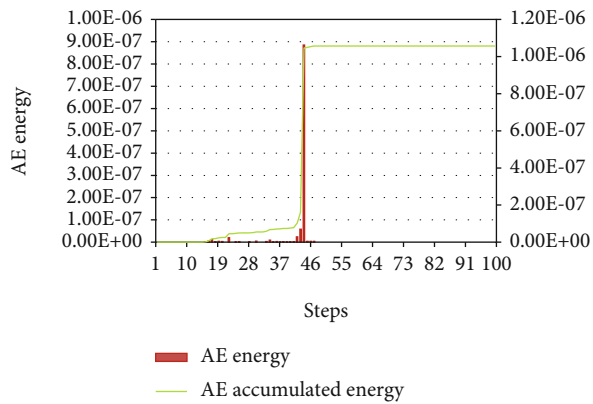
3.4. Acoustic Emission Characteristic Analysis. Coal and rock will release energy in the form of elastic waves (acoustic



(a) intact

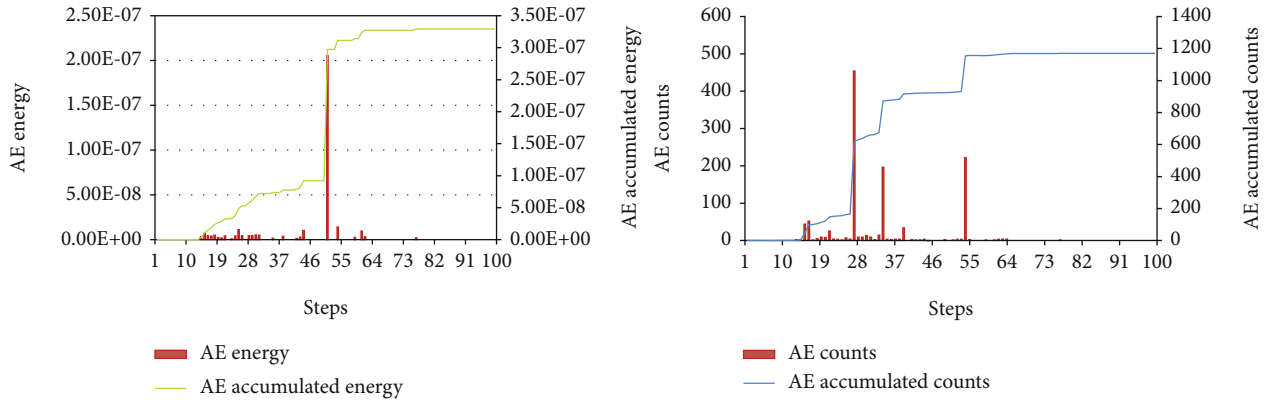


(b) $\alpha=0^\circ$

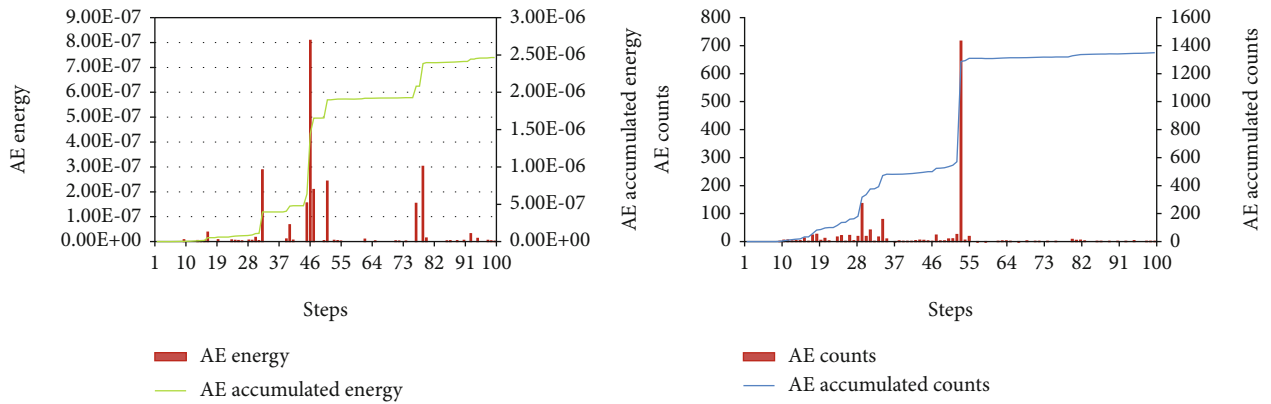


(c) $\alpha=15^\circ$

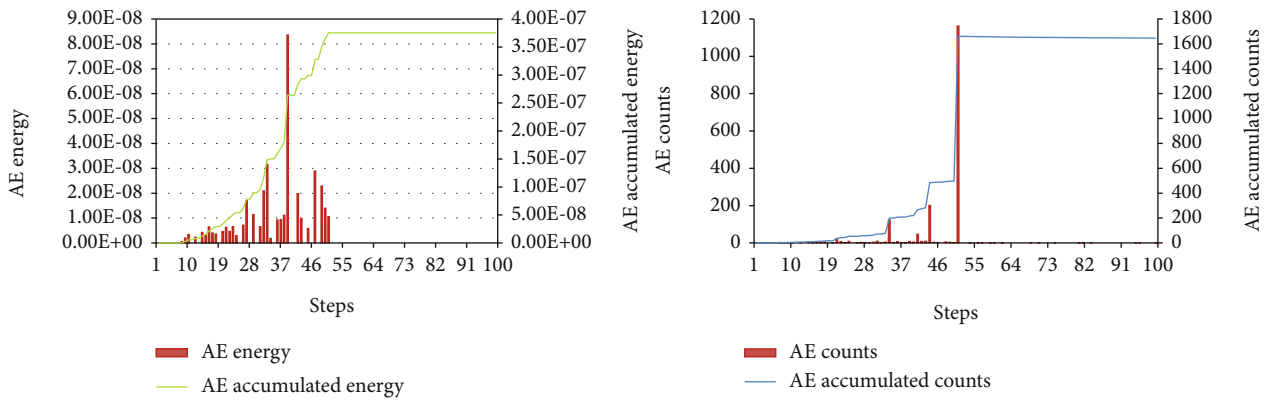
FIGURE 8: Continued.



(d) $\alpha=30^\circ$



(e) $\alpha=45^\circ$



(f) $\alpha=60^\circ$

FIGURE 8: Continued.

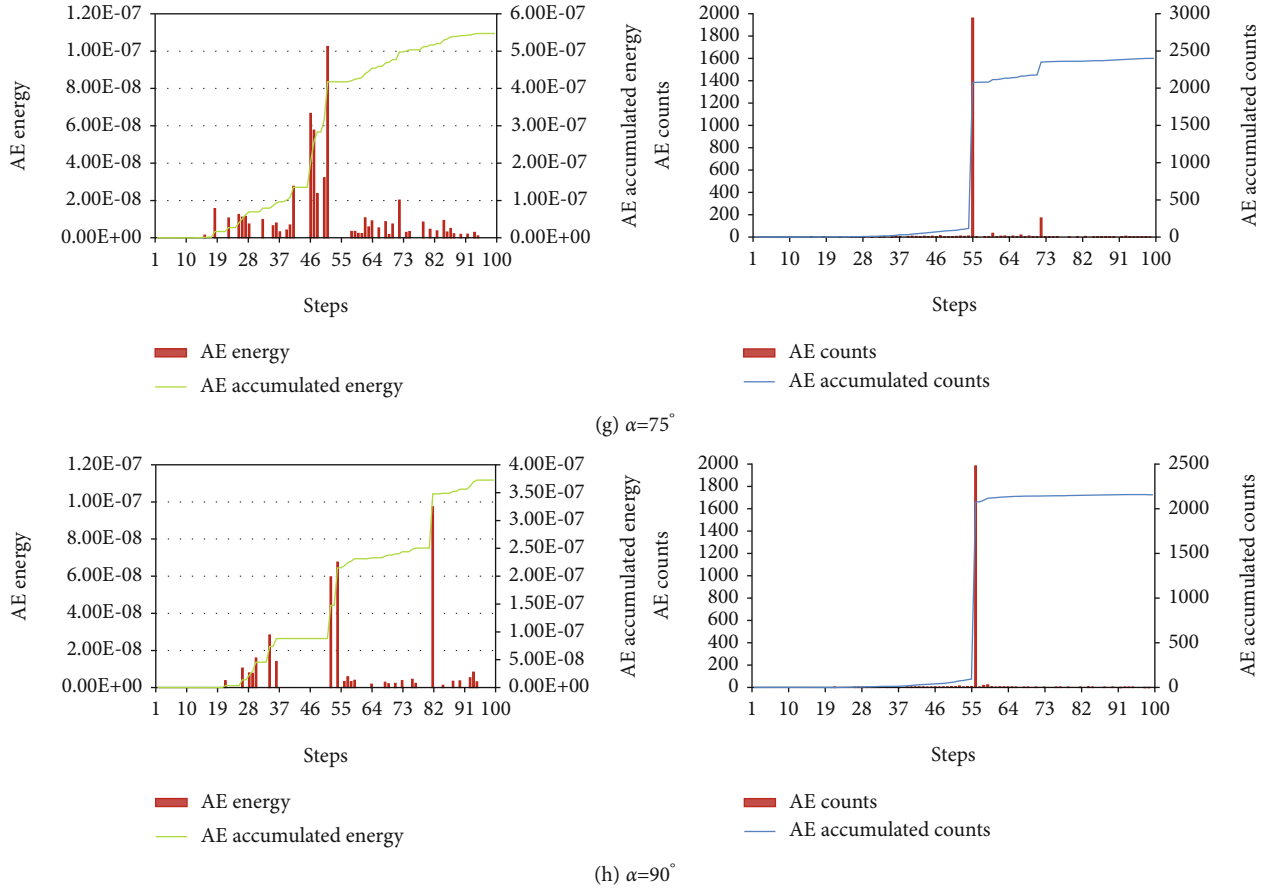


FIGURE 8: Acoustic emission characteristic curves of coal-rock combined bodies with different prefabricated fissure angles.

emission) during its deformation and failure process [16]. By analyzing acoustic emission parameters, the characteristics of coal and rock deformation and failure can be better understood.

The acoustic emission of the rock in the process of failure and deformation reflects the evolution process of its internal crack initiation, propagation, and penetration failure. It can be seen from Figure 8 that the acoustic emission characteristics of the CRCB with prefabricated fracture of different inclination angles have a general law: At the beginning of loading, no acoustic emission events can be detected because the internal crack is closed; and then, only a small amount of acoustic emission events are generated in the elastic phase. As the load continues to increase to the plastic deformation stage, the internal cracks expand, and more acoustic emission events are generated. Near the peak loading, a large number of acoustic emissions are produced, and the number of acoustic emission events reaches the maximum, which can be used as a precursor to the failure of the CRCB. In the postpeak stage, a certain acoustic emission signal will be generated due to the further propagation and penetration of cracks. At the same time, as shown in Figure 8, the influence of the prefabricated crack inclination angle in CRCB on its acoustic emission characteristics under uniaxial compression can be found: the total number of acoustic emission events as a whole decreases first and then increases with the increase of the prefabricated fracture inclination angle. The CRCB has the highest number of acoustic emis-

sion events (2399) when $\alpha = 75^\circ$ (Figure 8(f)), followed by the intact CRCB (2148), which is mainly caused by the development and expansion of the crack tip. The single largest acoustic emission events first decrease and then increase with the increase of the prefabricated fracture inclination angle, and its ratio to the total number of cumulative acoustic emission events is 0.89, 0.38, 0.78, 0.38, 0.53, 0.70, 0.81, and 0.93, respectively, which are consistent with the stress-strain curve in Figure 3 and indicate that intact CRCB and CRCB with prefabricated crack when $\beta = 75^\circ$ and $\beta = 90^\circ$ have strong brittleness, while other CRCB with different prefabricated fracture inclination angles show a certain degree of postpeak plasticity. The single peak acoustic emission events of the CRCB is located after its peak strength when $\alpha = 45^\circ$ (Figure 8(d)) and $\alpha = 60^\circ$ (Figure 8(e)). The number of steps (strain) corresponding to the peak acoustic emission counts of the other CRCB first decreases and then increases with the increase of the inclination angle of the prefabricated fracture, which is consistent with the peak strength of the CRCB. The single peak acoustic emission events and the peak strength correspond to the same strain, indicating that after the peak strength, the CRCB with 45° and 60° prefabricated cracks further expand and penetrate, so it is unreliable to confirm the failure of CRCB by single peak acoustic emission events.

The failure of coal and rock mass under stress is a process of energy absorption and release, and the energy of acoustic

emission reflects the elastic energy released when the cracks inside the coal and rock are generated or expanded [30, 31]. From Figure 8, the accumulative amount of acoustic emission energy increases with the increase of strain. In the initial stage of loading, although the number of acoustic emission events of the CRCB is small, the acoustic emission energy gradually accumulates. When the energy accumulates to a certain extent, the CRCB reaches its peak strength, and the acoustic emission count increases rapidly. It can also be seen from Figure 7 that during the uniaxial compression of different CRCB, the cumulative energy of acoustic emission in descending order is as follows: 45°, 15°, intact CRCB, 75°, 60°, 90°, 30°, and 0°, indicating that the cumulative energy of acoustic emission has a nonlinear relationship with the strength of the CRCB with different inclination angles of prefabricated fracture. The cumulative energy before the peak value of acoustic emission events is as follows: 75°, intact CRCB, 60°, 90°, 45°, 0°, 30°, and 15°, so from the perspective of acoustic emission energy, the outburst proneness of the CRCB with 75° prefabricated fissure is higher than that of the intact CRCB. The single peak acoustic emission energy is located before the peak strength of CRCB for $\alpha = 60^\circ$, $\alpha = 75^\circ$, and intact CRCB, while it is located after the peak strength of CRCB for $\alpha = 0^\circ$, 15°, 30°, 45°, and 90°, which shows the influence of the cracks in the rock mass and their inclination angle on the postpeak characteristics of the CRCB under uniaxial compression.

4. Conclusion

- (1) The inclination angle of the cracks in CRCB will affect its crack initiation stress. When the crack inclination angle is around 45°, the crack initiation stress is the smallest, and the numerical simulation results are consistent with the theoretical analysis
- (2) The inclination angle of CRCB affects the propagation mode of the crack. The secondary cracks of CRCB with prefabricated fracture of 0°, 15°, and 30° initiated and expanded near the tip of the main crack, and the secondary cracks of 45°, 60°, and 75° initiated and expanded from the tip of the main crack
- (3) The inclination angle of CRCB will affect its strength. When $\alpha = 15^\circ$, the peak strength of the CRCB is the lowest. When $\alpha < 15^\circ$, the peak strength of the CRCB decreases with the increase of the crack inclination angle. When $\alpha > 15^\circ$, the peak strength of the CRCB increases with the increase of the inclination angle of the prefabricated fissure
- (4) The inclination angle of CRCB will affect its failure modes. The failure of the intact CRCB and the CRCB with 90° and 75° prefabricated fissures mainly occurs in the coal, and it is a double-shear failure mode, and the crack propagation is type Λ . When the inclination angles of the prefabricated cracks are 0°, 15°, and 30°, the failure mode of the CRCB is tensile-shear composite failure. When the inclination angles of the prefabricated cracks are 45° and 60°, the coal

samples are mainly shear failure, and the rock samples are tensile failure with the increase of axial stress

- (5) The existence of cracks in CRCB will affect its brittleness and plastic characteristics. The acoustic emission results indicate that intact CRCB and CRCB with prefabricated crack when $\alpha = 75^\circ$ and $\alpha = 90^\circ$ have good brittleness, and other CRCB with different prefabricated fracture inclination angles show a certain degree of postpeak plasticity

Data Availability

All data used to support the findings of this study are included within the article, and there are not any restrictions on data access.

Conflicts of Interest

The authors declare no conflicts of interest.

Acknowledgments

This paper was supported by the Natural Science Foundation of the Jiangsu Higher Education Institutions of China (No. 20KJB440002), the National Natural Science Foundation of China (Project Nos. 51804129, 51808246, and 51904112), China Postdoctoral Science Foundation (No. 2020M671301), the Postdoctoral Science Foundation of Jiangsu Province (Nos. 2019K139 and 2019Z107), the Huai'an Science and Technology Plan project (No. HAB201836), the Industry Education Research Cooperation Projects in Jiangsu Province (No. BY2020007), the Undergraduate Innovation and Entrepreneurship Training Program (No. 202011049111XJ), and the Foundation of Huaiyin Institute of Technology (No. Z301B20530).

References

- [1] K. Wang and F. Du, "Coal-gas compound dynamic disasters in China: a review," *Process Safety and Environmental Protection*, vol. 133, pp. 1–17, 2020.
- [2] L. Yang, F. Gao, X. Wang, and J. Li, "Energy evolution law and failure mechanism of coal-rock combined specimen," *Journal of China Coal Society*, vol. 44, no. 12, pp. 3894–3902, 2019.
- [3] J. Zuo, H. Xie, A. Wu, and J. Liu, "Investigation on failure mechanism and mechanical behaviors of deep coal-rock single body and combined body," *Chinese Journal of Rock Mechanics and Engineering*, vol. 30, no. 1, pp. 84–92, 2011.
- [4] F. du, K. Wang, X. Zhang, C. Xin, L. Shu, and G. Wang, "Experimental study of coal-gas outburst: Insights from coal-rock structure, gas pressure and adsorptivity," *Natural Resources Research*, vol. 29, no. 4, pp. 2481–2493, 2020.
- [5] J. Zuo, J. Wang, and Y. Jiang, "Macro/meso failure behavior of surrounding rock in deep roadway and its control technology," *International Journal of Coal science & Technology*, vol. 6, no. 3, pp. 301–319, 2019.
- [6] F. Gong, H. Ye, and Y. Luo, "Rate effect on the burst tendency of coal-rock combined body under low loading rate range," *Journal of China Coal Society*, vol. 42, no. 11, pp. 2852–2860, 2017.

- [7] F. Gong, H. Ye, and Y. Luo, "The effect of high loading rate on the behaviour and mechanical properties of coal-rock combined body," *Shock and Vibration*, vol. 2018, Article ID 4374530, 9 pages, 2018.
- [8] J. Zuo, Y. Chen, H. Song, and X. Wei, "Evolution of pre-peak axial crack strain and nonlinear model for coal-rock combined body," *Chinese Journal of Geotechnical Engineering*, vol. 39, no. 9, pp. 1609–1615, 2017.
- [9] Y. Chen, J. Zuo, D. Liu, Y. Li, and Z. Wang, "Experimental and numerical study of coal-rock bimaterial composite bodies under triaxial compression," *International Journal of Coal Science & Technology*, 2021.
- [10] J. Cao, Q. Dai, Y. Zhou, and D. Ma, "Failure mechanism and strength of coal-rock combination bodies considering dip angles and fractal characteristics of interface," *Journal of Central South University (Science and Technology)*, vol. 49, no. 1, pp. 175–182, 2018.
- [11] X. Liu, Y. Tan, J. Ning, Y. Lu, and Q. Gu, "Mechanical properties and damage constitutive model of coal in coal-rock combined body," *International Journal of Rock Mechanics and Mining Sciences*, vol. 110, pp. 140–150, 2018.
- [12] Z. Xie, N. Zhang, F. Meng, C. Han, Y. An, and R. Zhu, "Deformation field evolution and failure mechanisms of coal-rock combination based on the digital speckle correlation method," *Energies*, vol. 12, no. 13, pp. 1–14, 2019.
- [13] F. Du and K. Wang, "Unstable failure of gas-bearing coal-rock combination bodies: Insights from physical experiments and numerical simulations," *Process Safety and Environmental Protection*, vol. 129, pp. 264–279, 2019.
- [14] Y. Chen, J. Zuo, H. Song, L. Feng, and G. Shao, "Deformation and crack evolution of coal-rock combined body under cyclic loading-unloading effects," *Journal of Mining & Safety Engineering*, vol. 35, no. 4, pp. 826–833, 2018.
- [15] Z. Zhao, W. Wang, L. Wang, and C. Dai, "Compression-shear strength criterion of coal-rock combination model considering interface effect," *Tunnelling and Underground Space Technology*, vol. 47, no. 3, pp. 193–199, 2015.
- [16] S. Dong, A. Li, Y. Ji, Y.-x. Yang, and Q. Mu, "Mechanical and failure characteristics of rock-coal-rock combined body under different strain rates: a numerical study from micro perspective," *Geotechnical and Geological Engineering*, vol. 39, no. 1, pp. 185–191, 2021.
- [17] C. Li, Y. Xu, Y. Zhang, and H. Li, "Study on energy evolution and fractal characteristics of cracked coal-rock-like combined body under impact loading," *Chinese Journal of Rock Mechanics and Engineering*, vol. 38, no. 11, pp. 2231–2241, 2019.
- [18] D. Yin, S. Chen, B. Chen, X. Liu, and H. Ma, "Strength and failure characteristics of the rock-coal combined body with single joint in coal," *Geomechanics and Engineering*, vol. 15, no. 5, pp. 1113–1124, 2018.
- [19] D. Yin, S. Chen, B. Chen, L. Jiang, T. Meng, and W. Wang, "Simulation study on effects of coal persistent joint on strength and failure characteristics of rock-coal combined body," *Journal of Mining & Safety Engineering*, vol. 35, no. 5, pp. 1054–1062, 2018.
- [20] W. F. Brace and E. G. Bombolakis, "A note on brittle crack growth in compression," *Journal of Geophysical Research*, vol. 68, no. 12, pp. 3709–3713, 1963.
- [21] H. Horii and S. Nemat-Nasser, "Compression-induced micro-crack growth in brittle solids: axial splitting and shear failure," *Journal of Geophysical Research*, vol. 90, no. B4, pp. 3105–3125, 1985.
- [22] X. Zhou and Y. Zhang, *Constitutive Theory of Stress Relief Rock Mass and Its Application*, Science Press, Beijing, 2007.
- [23] P. Lin, K. Huang, R. Wang, and W. Zhou, "Crack growth mechanism and failure behavior of specimen containing single flaw with different angles," *Chinese Journal of Rock Mechanics and Engineering*, vol. 24, pp. 5652–5658, 2005.
- [24] E. Lajtai, "Strength of discontinuous rocks in direct shear," *Geotechnique*, vol. 19, no. 2, pp. 218–233, 1969.
- [25] Huiwang, *Numerical simulation of fractured rock failure process and related laws*, [Dissertation], Anhui University of Science & Technology, 2015.
- [26] C. Tang, S. Wang, and F. Yufang, *Numerical Experiment of Rock Failure Process*, Science Press, Beijing, 2012.
- [27] Z. Liang, C. Tang, H. Li, T. Xu, and T. Yang, "A numerical study on failure process of transversely isotropic rock subjected to uniaxial compression," *Rock and Soil Mechanics*, vol. 26, no. 1, pp. 57–63, 2005.
- [28] L. Cunbao, H. Xie, and L. Xie, "Experimental and theoretical study on the shale crack initiation stress and crack damage stress," *Journal of China Coal Society*, vol. 42, no. 4, pp. 969–976, 2017.
- [29] M. Gao, T. Li, L. Meng et al., "The method to identify characteristic stresses of rock in different stages during failure process," *Chinese Journal of Rock Mechanics and Engineering*, vol. 35, no. S2, pp. 3577–3588, 2016.
- [30] D. Zhang, C. Liu, Y. Zhou, and D. Ma, "Characteristics of fracture mechanism and acoustic emission of rock-coal combined body with prefabricated fissure," *Geotechnical and Geological Engineering*, vol. 38, pp. 6245–6254, 2020.
- [31] F. du, K. Wang, G. Wang, Y. Jiang, C. Xin, and X. Zhang, "Investigation of the acoustic emission characteristics during deformation and failure of gas-bearing coal-rock combined bodies," *Journal of Loss Prevention in the Process Industries*, vol. 55, pp. 253–266, 2018.

Research Article

Analysis on the Shape and Impact Pressure of the High-Pressure Water Jet during the Hydraulic Flushing Cavity Technique

Shouqing Lu,^{1,2} Chengfeng Wang,^{1,2} Wei Wang^{ORCID},³ Mingjie Li,^{1,2} and Dongti Zhang⁴

¹Department of Safety Engineering, Qingdao University of Technology, Qingdao 266520, China

²Shandong Key Industry Field Accident Prevention Technology Research Center (Non-Ferrous Metallurgy), Qingdao 266520, China

³Shanghai Fire Research Institute of MEM, Shanghai 200032, China

⁴School of Civil and Resource Engineering, University of Science and Technology Beijing, Beijing 100083, China

Correspondence should be addressed to Wei Wang; wangweiwangwei0037@163.com

Received 13 April 2021; Accepted 22 May 2021; Published 18 June 2021

Academic Editor: Feng Du

Copyright © 2021 Shouqing Lu et al. This is an open access article distributed under the Creative Commons Attribution License, which permits unrestricted use, distribution, and reproduction in any medium, provided the original work is properly cited.

A large proportion of minable coal seams in China belong to low-permeability soft coal seams. Such coal seams suffer serious coal and gas outburst hazards and endure a high incidence of major disasters in coal mines. The adoption of the high-pressure water jet (HPWJ) hydraulic flushing cavity can effectively promote the gas drainage efficiency and volume and eliminate the hidden danger of gas disasters. Nevertheless, the shape and impact pressure of rotating HPWJ are rarely researched. In this study, on the basis of the numerical simulation, the axial and radial stress distributions of HPWJ and the energy-gathering effect of a conical-cylindrical combined nozzle were analyzed. It is concluded that the submerged condition will accelerate the attenuation of jet velocity and reduce the impact strength of the jet. The jet diffusion angle grows with the increases in the nozzle diameter and water pressure, and 24° is the optimal contraction angle. Finally, the influences of factors such as the rotation speed on the shape and impact pressure of HPWJ were explored, and the results show that the rotation speed should be controlled within 90 r/min. The research findings lay the foundation of the study on the mechanism of coal crushing by HPWJ and provide technical support for the research and development of drilling and flushing integrated equipment.

1. Introduction

China, a country where over 95% of coal mines are recovered by means of underground mining [1–4], is suffering the most serious coal and gas outburst disasters in the world [5–7]. It contains a large number of outburst coal mines where outburst disasters occur intensely and frequently [8]. Low-permeability coal seams where gas can hardly be drained refer to the coal seams whose permeability λ is smaller than 0.1 m²/(MPa²·d) [9], and soft coal seams refer to the coal seams whose hardness coefficient f is smaller than 1 [10]. Low-permeability soft coal seams account for a large proportion of mineable coal seams in China. For a long time, it is difficult to control gas in high-gas soft coal seams due to low permeability and poor drilling stability [11, 12], and the fatality rate of gas accidents in coal mines remains high [13–15]. Therefore, high-gas soft coal seams endure a high incidence of major disasters in coal mines [16, 17]. The

hydraulic flushing cavity technique works by drilling along-measure boreholes or cross-measure boreholes into the coal body and then flushing out large quantities of coal and gas through the high-pressure water jet (HPWJ) [18, 19]. The multiple large-diameter cavities formed in the coal seam are conducive to pressure relief and gas release. This technique, together with gas drainage measures, serves to reduce the ground stress and gas pressure of coal. It can effectively promote the gas drainage efficiency and volume and eliminate the hidden danger of mine gas disasters, thus providing a new approach for gas control in high-gas soft coal seams.

HPWJ, a coal/rock crushing technique, is widely applied to coal and petroleum fields in recent years [20]. The technique boasts multiple advantages such as concentrated energy transfer, no spark, no wear, no generation of high temperature or static electricity, dust reduction, and strong adaptability. Thanks to these advantages, it is particularly competent to crush coal and release gas in high-gas low-

permeability coal seams [21, 22]. Scholars all over the world have conducted extensive research studies on rock crushing by HPWJ and have proposed a variety of theories, including the water hammer effect theory, the stress wave effect theory, the impact effect theory, the water wedge effect theory, the cavitation effect theory, and the pulsed load-induced fatigue damage theory [23–26]. The stress wave effect theory proposed by Singh and Hartman [27] in 1961 is the earliest accessible theory about rock crushing and failure under the action of jets. Based on this theory, Farmer and Attewell [28] put forward an empirical formula for the jet cutting depth and the P-wave velocity, i.e., the sound velocity.

Pan and Yao [29] and Bai and Cao [30] established a simulation model of rock crushing by pulsed water jets based on the arbitrary Lagrangian-Eulerian (ALE) algorithm, simulated the process of rock crushing with different-velocity jets, and studied the process of rock crushing damage evolution. Ma et al. [31] and Wang et al. [32] established a model of material cutting by HPWJ and a model of material erosion by abrasive jets by means of finite element modeling (FEM) and smoothed particle hydrodynamics (SPH). Based on the simulation data, they obtained the variation curves of the maximum cutting depth with the HPWJ velocity and the abrasive jet velocity, respectively, and verified the feasibility of the model by comparing the simulation data with the experimental results. Maniadaki et al. [33] and Gong et al. [34] established a numerical model of material erosion by HPWJ and a model of material cutting by premixed abrasive water jets based on the ALE algorithm.

Ni et al. [35–38] researched the process and mechanism of HPWJ flushing. By regarding the damage variable as the criterion of rock failure, they established a coupling model of HPWJ-induced macro/micro rock damage. Wang et al. [39, 40] simulated the process of HPWJ-induced rock crushing by means of nonlinear dynamic FEM and rock dynamic damage modeling. They drew the following conclusions. (1) HPWJ can crush the rock in milliseconds. (2) The rock crushing mechanism of ordinary continuous HPWJ is to cause tensile failure as a result of pressure relief and jet impact. (3) The process of rock crushing proceeds stepwise. Song and Chen [41] simulated the process of HPWJ-induced rock crushing based on the SPH algorithm and analyzed the energy conversion in this process, the impact force of HPWJ, and the evolution of HPWJ-induced rock crushing. Lu et al. [42] simulated the stress wave effect of the pulsed water jet in the process of rock crushing by using the SPH algorithm, concluding the failure modes of rocks with different lithologies under the pulsed water jet stress wave. By employing the ALE algorithm, Liu and Si [43] revealed that the confining pressure caused by HPWJ impact had a significant effect on the axial damage of rock and a slight effect on the radial damage. Lu et al. [24] conducted a test study on the mechanism of rock crushing by cavitating HPWJ, and Tian and Lin [25, 26] probed into the mechanism of jet-assisted rock crushing from two aspects, i.e., bubble cavitation and water drop impact. Si et al. [44] established a model of rock crushing by abrasive water jets from two perspectives, i.e., continuous damage mechanics and meso-damage mechanics.

Li [45] consolidated coal blocks with cement and obtained the variation of erosion depth with the pump pressure and target distance. Jiang [46] prepared coal rock specimens by mixing coal, sand, and cement at a certain ratio and performed experiments with an impeller rotary nozzle. Through these experiments, he found variations of erosion depth and width with the spray distance and nozzle diameter. Zhang [47] simulated the process of coal rock (replaced with concrete in his simulation) cutting by HPWJ and discussed the relationship among jet pressure, discharge quantity, and cutting volume and depth. Wang et al. [48] adopted an abrasive jet cutting system to cut argillaceous limestone in a coal seam floor and elaborated on the relationship between the cutting depth and the factors including the target distance, nozzle movement velocity, and number of reciprocation times. Sun et al. [49] simulated HPWJ-induced rock crushing in light of the dynamic nonlinear FEM and the Hoffman crushing criterion. They disclosed that the rock crushing efficiency could be promoted by increasing the impact velocity, jet diameter, transverse movement velocity, and jet beam number and reasonably selecting a jet incident angle in the range of 35~40°. Lin et al. [50] simulated the process of rock crushing by abrasive water jets through SPH-FEM. On the basis of the simulation results, they analyzed the range of rock damage by different-velocity abrasive water jets under the abrasive concentration of 30%.

The HPWJ, of which the medium is water, refers to a jet stream with a high impact velocity and a high dynamic pressure produced via a pressurizing device (pump station) and a nozzle of a specific shape. Its shape and impact pressure are mainly affected by conditions such as the pump pressure, pipeline resistance, nozzle structure, nozzle rotation speed, and environmental medium. In this study, numerical simulation was carried out with the assistance of ANSYS Fluent software. On the basis of the simulation, the axial and radial stress distributions of HPWJ and the energy-gathering effect of a conical-cylindrical combined nozzle were analyzed. Furthermore, the influences of the submergence conditions, nozzle diameter and angle, pump station pressure, rotation speed on the shape, and impact pressure of HPWJ were explored. The research findings facilitate the study on the mechanism of HPWJ-induced coal crushing and provide technical support for the research and development of drilling and flushing integrated equipment.

2. Impact Characteristics and Shape of HPWJ

2.1. Impact Characteristics of HPWJ. According to its different mechanisms, the HPWJ impact pressure on rock can be divided into two stages, namely, the water hammer pressure stage and the stagnation pressure stage. Sevda [51] generated an impact jet by dropping a hammer from a height to impact the piston. In this way, he successfully monitored the variations of impact pressure on different solid materials (Figure 1). The value of the rising angle θ is related to the transient reaction rate of the impacted material, and the reaction rate of metal materials is higher than that of polymer materials.

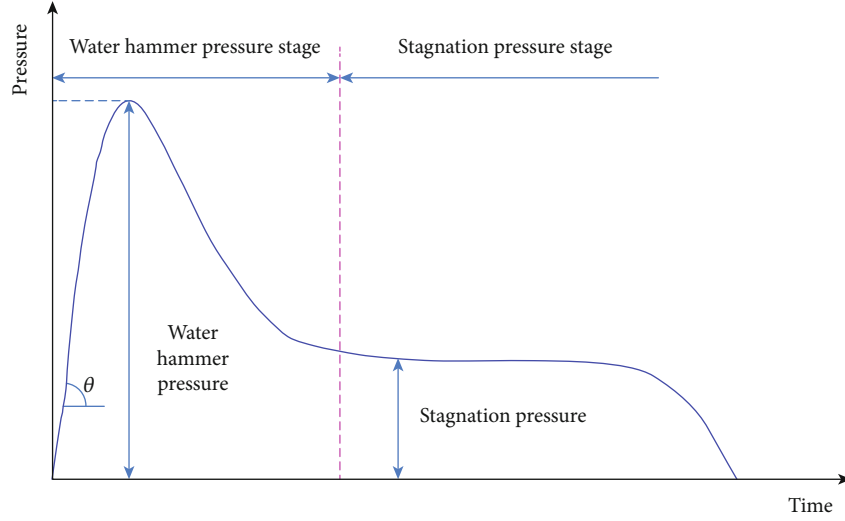


FIGURE 1: Division of the HPWJ impact pressure stage.

The inertia and compressibility of water are the main reasons for the generation of water hammer pressure. The shape of HPWJ is simplified as a cylinder (Figure 2). In the initial stage, the jet compression zone will be formed under the high-speed collision between the jet and the target. And the peak pressure with strong erosion force will be formed on the target surface when the water is compressed, that is, the water hammer pressure [52]. According to the law of conservation of momentum [53], the water hammer pressure can be derived as follows:

$$P_{wh} = \frac{\nu \rho_w c_w \rho_s c_s}{\rho_w c_w + \rho_s c_s}, \quad (1)$$

where P_{wh} is the water hammer pressure, Pa; ν is the velocity of water jet impact, m/s; ρ_w and c_w are the density of water and the velocity of shock wave propagation in the water medium, respectively, kg/m^3 and m/s ; ρ_s and c_s are the density of rock and the velocity of shock wave propagation in rock, respectively, kg/m^3 and m/s .

The duration of water hammer pressure, which is generally in nanoseconds (ns), can be expressed as

$$t_r = \frac{r}{c_w}, \quad (2)$$

where r is the radius of the jet, m; t_r is the duration of water hammer pressure, s.

After the water jet gets stabilized, it gradually enters the stagnation pressure stage where the Bernoulli stagnation pressure P_s is

$$P_s = \frac{\rho_w v^2}{2}, \quad (3)$$

where P_s is the Bernoulli stagnation pressure, Pa.

2.2. Influence of Submerged/Nonsubmerged Conditions on the Impact Characteristics and Shape of HSWJ. At present,

scholars all over the world mostly adopt a high-speed camera for recording the shape of HPWJ [55–57] and analyzing its radial and axial structural characteristics. After the HPWJ is ejected from the nozzle, its front end gradually diffuses in the shape of an arc. Afterwards, the jet profile continues to expand and the diameter gradually increases until the water flow is completely dispersed. As exhibited in Figure 3, the HPWJ is of varying shapes in four primary sections, i.e., the compact section, the core section, the fracture section, and the dissipation section [58].

According to media in the surrounding environment, water jets can be divided into submerged water jets and nonsubmerged water jets. The analysis on a nonsubmerged water jet is chiefly focused on its diffusion law and core section length [59]. The core section where a great deal of energy is accumulated plays a decisive role in jet impact performance, while the outer boundary generally expands linearly in accordance with the angle. From statistics obtained by different research methods, Huang [60] found that the core section length of the jet is generally 400%~922% of the nozzle diameter and the jet diffusion angle generally ranges from 26.6° to 29.9° . Within the basic section, jet diffusion is rarely affected by the boundary layer and the nozzle, and it follows Equation (4) [61]:

$$d = k\sqrt{x}, \quad (4)$$

or

$$\frac{d}{R_0} = k_1 \sqrt{\frac{x}{R_0}}, \quad (5)$$

where d is the jet diameter, m; x is the distance from the nozzle outlet, m; R_0 is the radius of the nozzle outlet, m; k and k_1 are the coefficients related to the nozzle, where $k_1 = 0.12 \sim 0.18$.

To explore the influence of the submerged condition on the impact characteristics and shape of HPWJ, the numerical

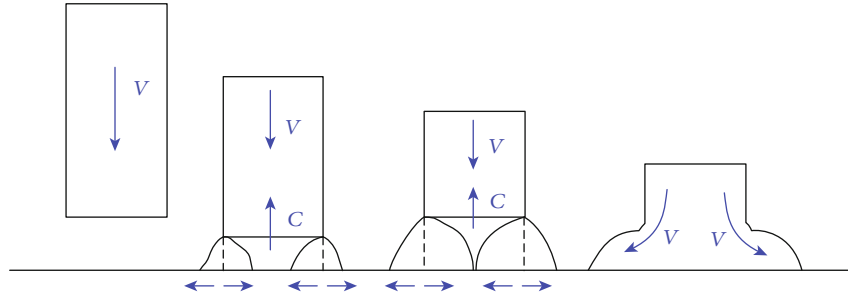
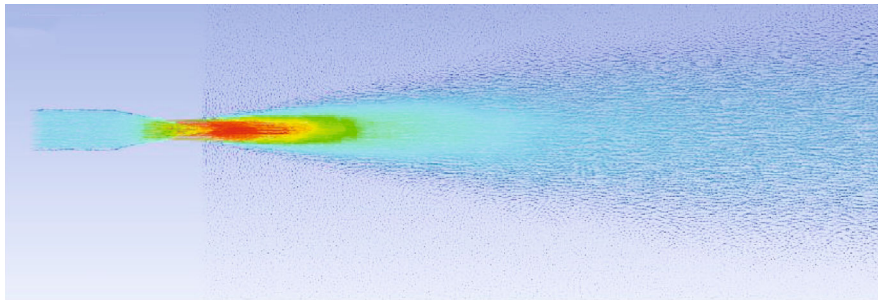
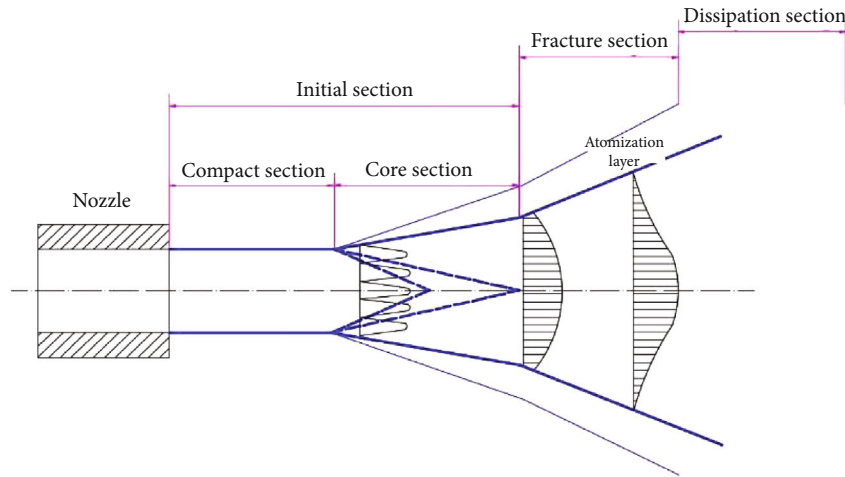


FIGURE 2: Schematic diagram of the initial stage of water jet impact on the solid surface [54].



(a)



(b)

FIGURE 3: Shape of the water jet.

models of nonsubmerged and submerged jets were constructed, respectively, as shown in Figure 4(a). In the models, the jet impact distance (i.e., the target distance) was set to 100 mm, and the diameter of the circular rigid plate is 60 mm. Next, the jets under the submerged and nonsubmerged conditions were numerically calculated, respectively, with the calculation results displayed in Figures 4(b) and 4(c).

Under the nonsubmerged condition, the jet corresponds to slower velocity attenuation, a smaller diffusion angle, a larger initial section length, and a longer effective impact distance. The jet impact force on the axis of the rigid plate with the target distance of 100 mm can reach 80.7 MPa under the nonsubmerged condition, while it decreases to 65.2 MPa by 19.2% under the submerged condition. This demonstrates that the submerged condition will weaken the jet impact

strength, thus affecting the coal crushing effect and the flushing efficiency. Therefore, in underground coal mines, HPWJ flushing operations should be carried out under the nonsubmerged condition. To achieve this goal, it is necessary to keep the drainage channel unobstructed.

2.3. Axial Dynamic Pressure Distribution of HPWJ. Dynamic pressure, which can be expressed by Equation (6), refers to the kinetic energy of the water jet per unit volume. Primarily influenced by density and velocity, it can reflect the variations of jet velocity attenuation and entrained air quality.

$$P = \frac{1}{2} \rho v^2. \quad (6)$$

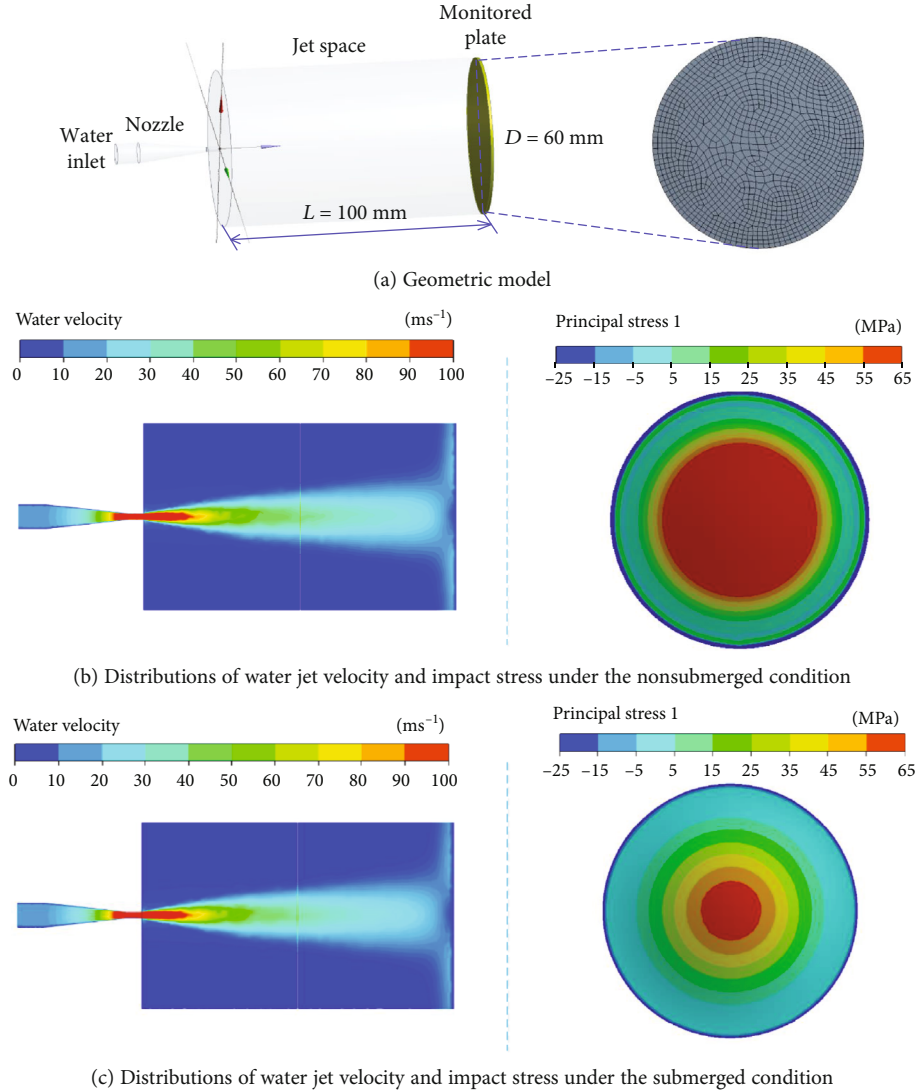


FIGURE 4: Comparison between jet impact effects under the nonsubmerged and submerged conditions.

Under the nonsubmerged condition, the basic section is the major section that acts to crush the rock. The impact dynamic pressure distribution on each cross-section at different target distances in the initial section can be expressed as follows:

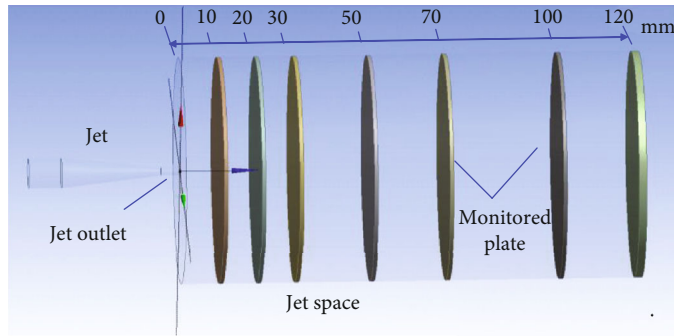
$$\frac{P}{P_m} = f(\eta) = \left(1 - \left(\frac{Y}{R}\right)^{1.5}\right)^2, \quad (7)$$

where P is the impact dynamic pressure, MPa; P_m is the dynamic pressure on the jet axis, MPa; R is the radius of the water jet cross-section, m; Y is the radial distance from the monitored point to the axis, m.

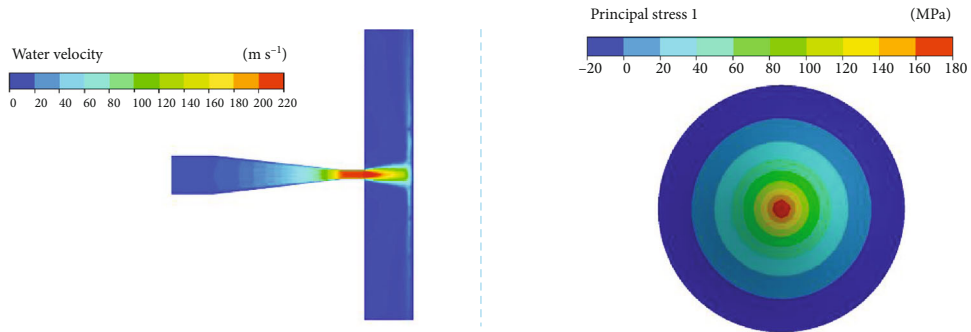
To investigate the impact dynamic pressure variations of HPWJ at different target distances (distances from the nozzle x) and different radial distances from the jet axis y , rigid plates were set at different target distances so that the problem was converted into HPWJ impact on the plate, as illustrated in Figure 5(a). The variations of maximum impact

pressure on the monitored plate at different impact distances are presented in Figure 6. Among them, the contour maps of jet velocity and the distributions of maximum principal stress on the plate at the target distances of 10 mm, 30 mm, 70 mm, and 120 mm are shown in Figures 5(b)–5(e).

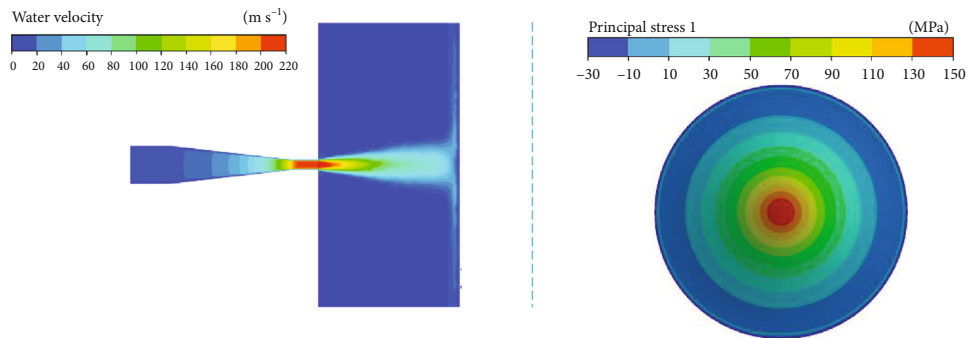
With the increase in the target distance, the jet velocity and the maximum impact pressure decrease gradually. The maximum impact pressure is as high as 188.1 MPa at the target distance of 10 mm, but it drops by 71.8% to 53.1 MPa at the target distance of 120 mm. The stress concentration zone at the cross-section center gradually expands with the increase in the target distance, which corresponds to the radial diffusion that occurs during jet impact. As the water jet keeps expanding forward, its cross-sectional area grows gradually. After being blocked by the plate, the water jet deflects to both sides. Gradually, the fluid on the jet axis expands and deflects to both sides for a longer distance. However, it fails to diffuse effectively in a short time and thus accumulates there. A fluid accumulation area with a lower jet velocity can be observed in the middle of the contact surface



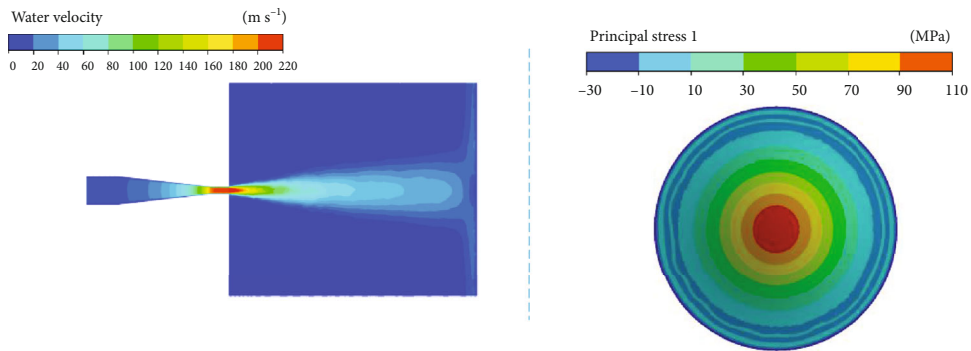
(a) Geometric model



(b) Jet velocity and impact stress distribution on the plate at a target distance of 10 mm

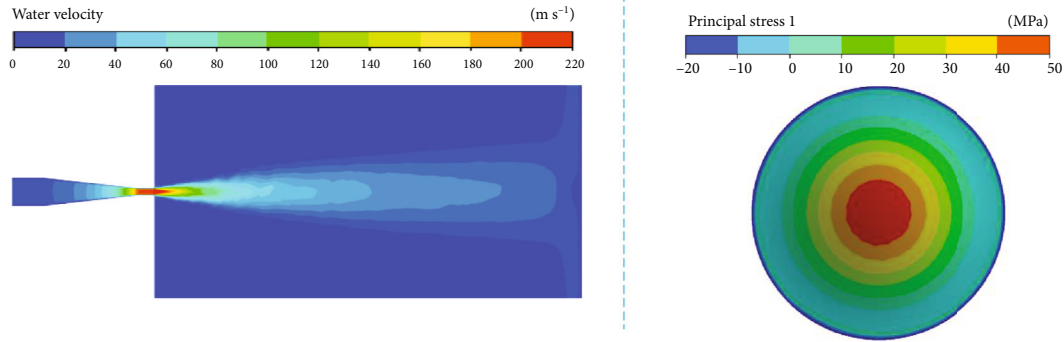


(c) Jet velocity and impact stress distribution on the plate at a target distance of 30 mm



(d) Jet velocity and impact stress distribution on the plate at a target distance of 70 mm

FIGURE 5: Continued.



(e) Jet velocity and impact stress distribution on the plate at a target distance of 120 mm

FIGURE 5: Velocity and stress distribution of HPWJ impact on the plate at different target distances.

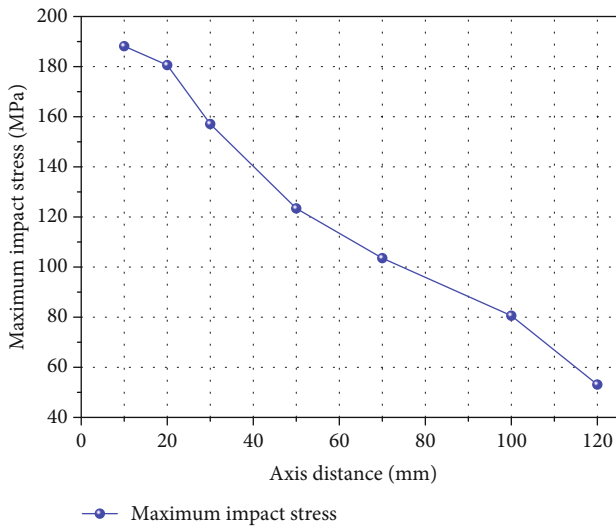


FIGURE 6: Impact pressure of HPWJ on the plate at different target distances.

between the jet and the plate in Figures 5(d) and 5(e). Despite the low jet velocity in this area, the transmission of fluid impact force is not affected.

3. Energy-Gathering Effect of the Conical-Cylindrical Combined Nozzle

3.1. Influence of the Nozzle Structure on the Jet Impact Effect. The nozzle, the executive element of the HPWJ generator, is responsible for converting energy. It gathers the pressure energy of the high-pressure water flow through the contraction of its internal cross-section, hence ensuring the excellent flow characteristics and dynamic performance of the water jet [62]. The nozzle structure has a crucial effect on jet properties such as the impact force, diffusion angle, and effective impact distance. The common nozzle structure and jet flow characteristics are illustrated in Figure 7.

The nozzle characteristic parameters affecting the jet impact performance mainly include the contraction angle α , length-diameter ratio l/d , contraction section length, and outlet diameter. With the aid of a high-speed camera, Lu et al.

[63] captured the shape of water jet impact under different nozzle diameters and jet pressures. Besides, they made a statistical analysis on the jet diffusion angle and drew the following conclusions. First, when the water pressure is constant, the jet diffusion angle grows notably with the increase in the nozzle diameter. Second, when the nozzle diameter is constant, the diffusion angle changes slightly with the change in the water pressure. The second conclusion deviates from the conclusion given in Section 2.3 of this paper, probably due to limitations of the test equipment or the monitoring method.

Aiming at discussing the influence of the contraction angle on jet velocity attenuation, nonsubmerged water jet models whose contraction angles were 13° , 24° , 60° , 90° , and 180° were constructed, respectively. The water jet space in the model was a cylinder space with a diameter of 60 mm and a length of 200 mm. The inlet and outlet diameters of the nozzles were 4 mm and 1 mm, respectively. The contour maps of jet velocity formed by the nozzles are presented in Figure 8, and the jet velocity attenuation on the jet axis is shown in Figure 9. The contraction angle significantly influences the jet velocity. As the contraction angle grows, the jet velocity at the nozzle outlet falls and the jet attenuation rate rises. After the inlet and outlet diameters are determined, the total length of the nozzle is mainly determined by the contraction section length which is negatively correlated with the contraction angle. The nozzle adopted for hydraulic flushing in underground coal mines should not be too long, and the energy-gathering effect and the jet velocity attenuation amplitude are both acceptable under the contraction angle of 24° . Considering the two factors, 24° is the recommended contraction angle.

After being accelerated by the nozzle, the water jet is ejected in a cone shape. The jet velocity declines gradually in the axial direction, while it expands and diffuses gradually to both sides in the radial direction. When the nozzle contraction angle is set to 13° , the variations of jet velocity on the radial cross-sections at different axial distances are exhibited in Figure 10.

3.2. Influence of the Nozzle Angle on the Jet Shape. The nozzle, arranged on the side of the drill bit or drill pipe, forms a certain angle (denoted as α) with the drill pipe axis. The angle between the water jet and the normal of the coal wall

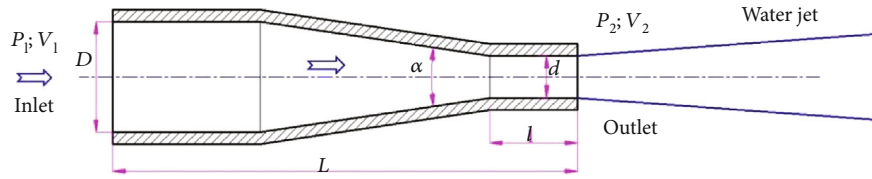


FIGURE 7: Nozzle structure and jet flow characteristics.

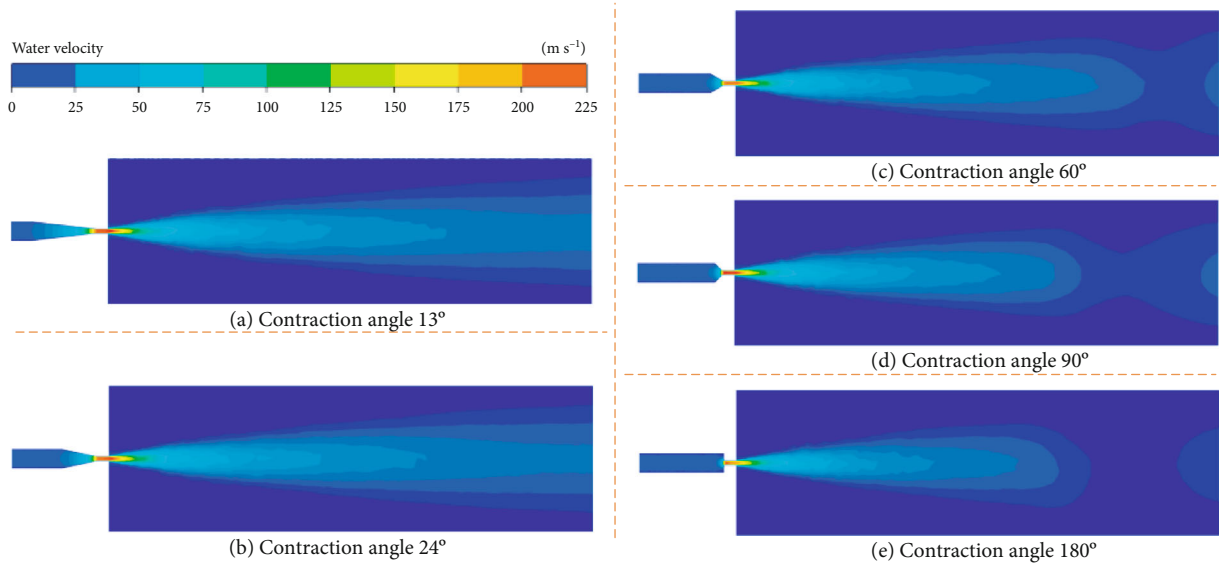


FIGURE 8: Contour maps of jet velocity formed by nozzles with different contraction angles.

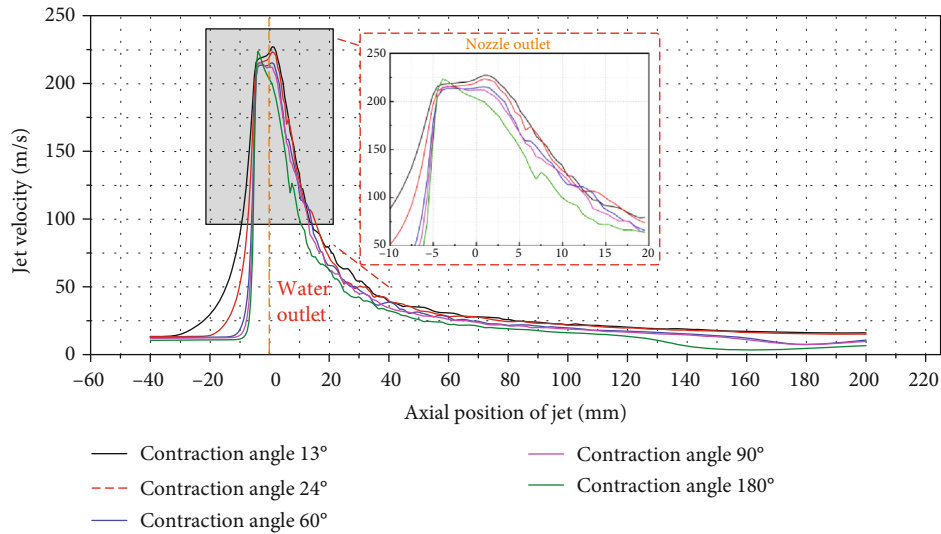


FIGURE 9: Variations of jet velocity on the jet axis under different contraction angles.

(denoted as β) whose value is determined by α shares a complementary angle with α . In this section, the influence of the nozzle angle on the jet shape and impact force is discussed in three cases, $\alpha = 90^\circ$, $\alpha = 60^\circ$, and $\alpha = 30^\circ$. The simulation results are shown in Figure 11. With the decrease in the nozzle angle, the turbulence degree of the fluid at the nozzle inlet decreases; the jet velocity increases; and the effective impact distance lengthens.

4. Influence of the Rotation Rate on the Impact Shape and Stress of HPWJ

4.1. Influence of Pump Pressure on HPWJ. The pressure of the high-pressure water pump station used for hydraulic flushing in underground coal mines generally lies within 10~60 MPa (10~40 MPa in most cases). In this study, the HPWJs generated at the pump pressures of 45 MPa, 35 MPa, 25 MPa, 15

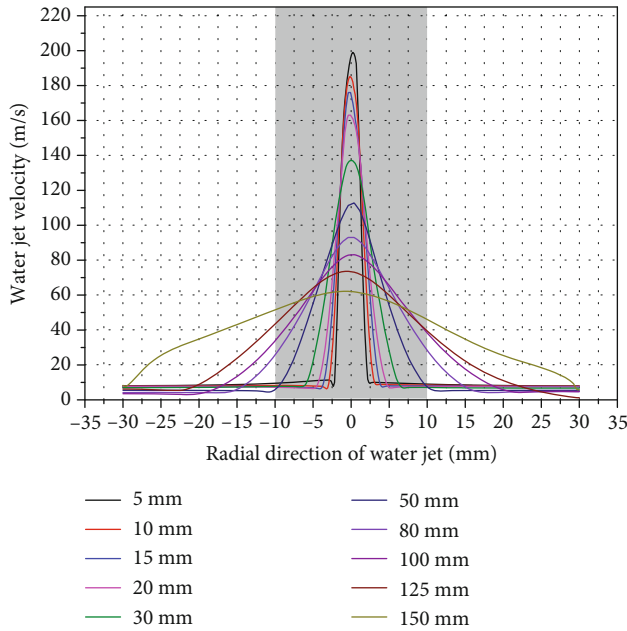


FIGURE 10: Variations of jet velocity on the radial cross-sections at different target distances.

MPa, and 10 MPa were numerically simulated. The simulation results are displayed in Figures 12 and 13.

The jet velocity on the jet axis rises gradually with the increase in the pump pressure, so does the acceleration of the jet when it passes through the nozzle. The maximum jet velocity at the nozzle outlet is as high as 305 m/s at the pump pressure of 45 MPa, while it drops to 143 m/s when the pump pressure is reduced to 10 MPa. On the other hand, an excessive pump pressure will result in an increase in the jet diffusion angle and a strong interaction between the jet and the air. The large amount of entrained air promotes the breakage and separation of water. As a result, the atomization of water intensifies. In the case of constant sizes of the jet pipe and nozzle, when the pump pressure remains low, the effective impact distance (compact section and core section) of the jet lengthens with the increase in it; when the pump pressure increases to a certain extent, raising it further will lead to the atomization of water; that is, water breaks into small droplets under the action of air. Under a higher pump pressure, the atomization of water is more intensified, and thus, the effective impact distance is shorter. For underground hydraulic flushing operation equipment in coal mines, there exists an optimal range of pump pressure where the jet can reach the best effective impact distance and impact force. Moreover, since the distance between the nozzle and the coal wall gradually expands as the flushing proceeds, the pump pressure needs to be constantly adjusted to keep the coal wall within the effective impact distance. When the distance between the nozzle and the coal wall reaches a certain limit, raising the pump pressure further will strengthen the atomization of water, failing to prolong the effective impact distance of the jet. Hence, an upper limit exists for the depth of coal crushing by the same equipment.

4.2. Different Stages of Coal Crushing by HPWJ. According to the shape of the coal pit formed by HPWJ impact, the process of coal crushing can be roughly divided into three stages, namely, the concave stage, the conical pit stage, and the cylindrical pit stage. In the initial stage of coal crushing, the jet rushes to the coal wall almost vertically after being accelerated by the nozzle, as shown in Figure 14(a). The coal at the jet axis, which undergoes the largest impact force, starts to break and fall off first, and a conical pit with a certain angle appears on the coal wall there, as presented in Figure 14(b). As the coal keeps breaking and falling off, the pit deepens and becomes cylindrical, as exhibited in Figure 14(c). The difference in the coal wall shape exerts an enormous effect on the distribution of jet velocity. Blocked by the coal wall, the jet changes its direction to varying degrees. In this process, part of the momentum in the original jet direction will be lost and transferred to the coal in the form of force. On the other hand, the jet velocity gradually attenuates with the increase in the target distance, and the increase in the pit depth will induce water accumulation at the bottom of the pit. In this study, the coal wall formed by HPWJ impact was appropriately simplified into a regular smooth slope, and the influence of crushed coal slag on the jet was ignored. Under this assumption, a numerical model was built to investigate the influence of different coal wall shapes on the jet impact effect (Figure 15).

As the impacted coal breaks and separates gradually, the jet experiences the plane impact stage, the conical impact stage, and the cylindrical impact stage in turn. Blocked by the coal wall, water at the bottom of the pit is discharged at a decelerated rate and accumulates there, forming a cushion on the coal wall surface. Consequently, the nonsubmerged jet is progressively converted to a submerged jet at the bottom of the pit. The HPWJ can hardly directly act on the coal surface so that the jet impact force is greatly reduced. In addition, due to the increase in the pit depth, the broken coal slag on the coal wall has to cross a longer distance to be discharged. Meanwhile, the decelerated discharge of the jet from the pit will weaken its slag removal ability. The crushed coal slag that cannot be discharged in time also buffers the coal wall from the jet impact. Under the comprehensive effect of the above factors, the HPWJ finds it difficult to crush the coal in a deeper area.

4.3. Influence of the Rotation Rate on the Jet Shape. During borehole construction in soft broken coal, the borehole collapses and gets blocked easily. To ensure the successful construction of boreholes, drilling is often conducted at a high rotation speed using a large-blade spiral drill pipe so that the coal slag can be discharged smoothly. In the hydraulic flushing process, the drill pipe also needs to rotate at a certain speed, which is not only required by the nozzle for rotary coal crushing but also conducive to the discharge of coal slag. The influence of rotation on the jet in the rotary flushing process is exhibited in Figure 16. When the jet leaves the nozzle to impact the coal wall, it deflects as a result of inertia, and the jet axis is no longer straight. The jet becomes less continuous, and the rear jet has a weaker effect on the front jet. Resultantly, the jet impact force becomes too

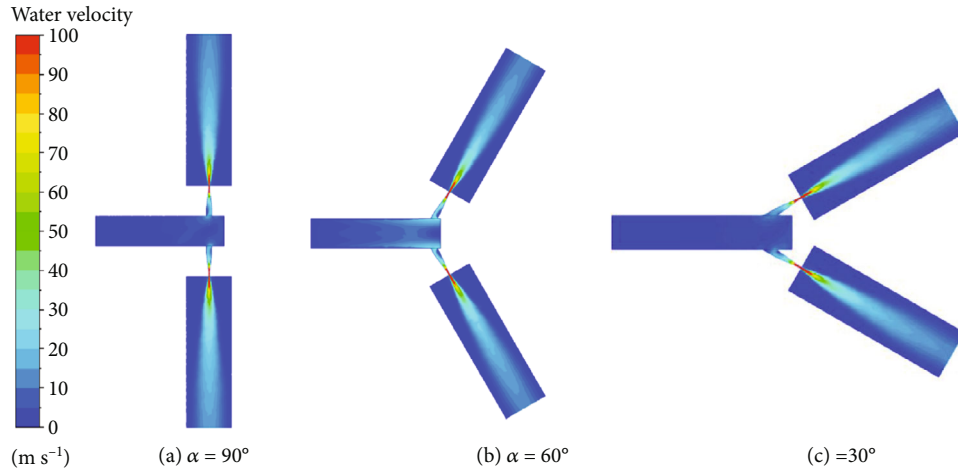


FIGURE 11: Contour maps of jet velocities under different nozzle angles.

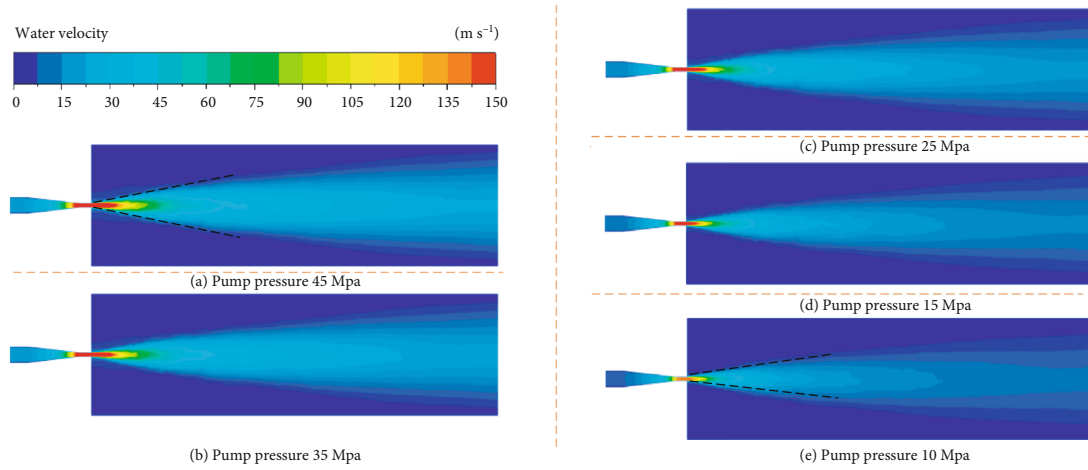


FIGURE 12: HPWJs generated at different pump pressures.

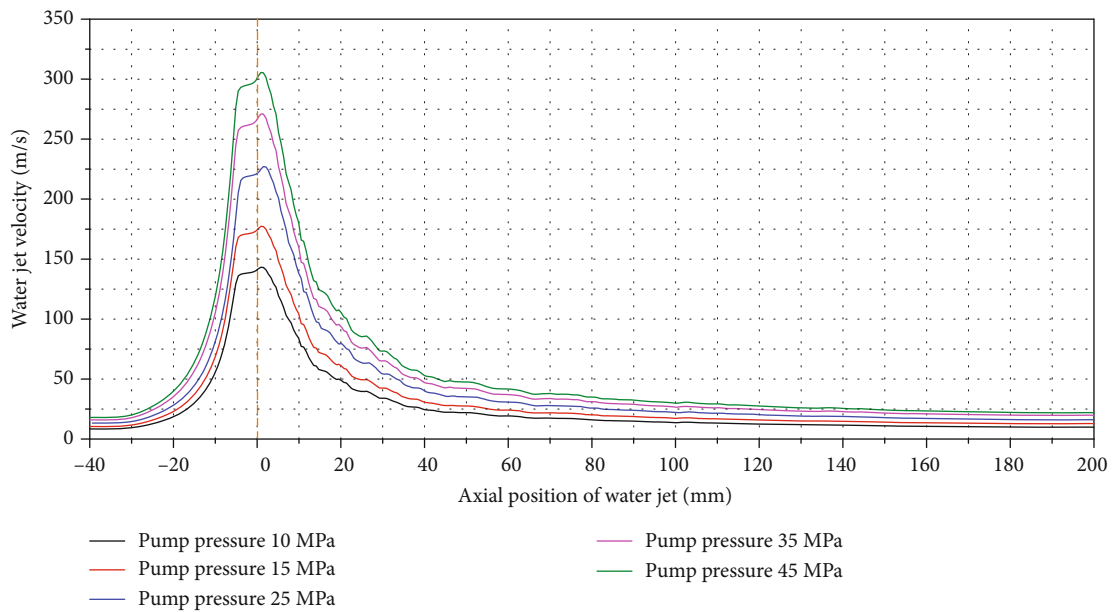


FIGURE 13: Variations of jet velocity on the jet axis at different pump pressures.

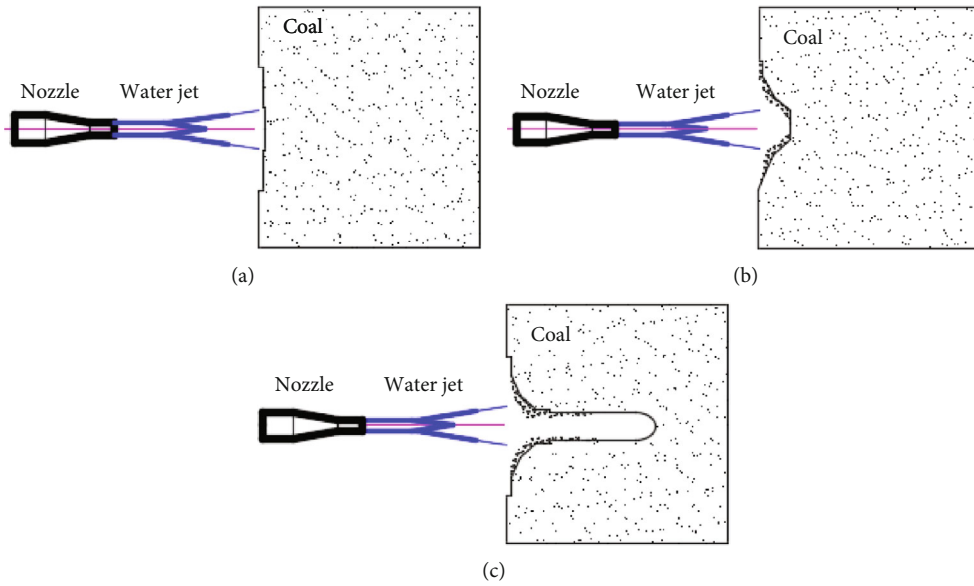


FIGURE 14: Different stages of HPWJ-induced coal crushing.

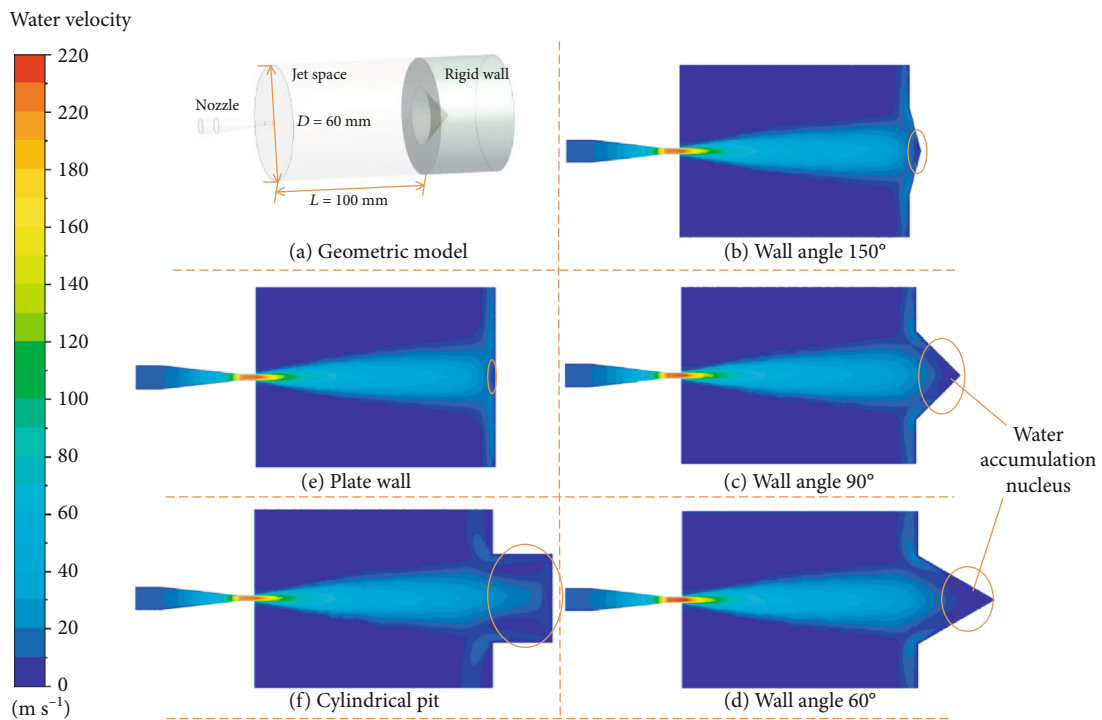


FIGURE 15: Contour maps of jet velocity in different coal crushing stages.

weak to guarantee the impact distance. The rotation speeds commonly used in drilling and hydraulic operations in coal mines lie in the range of 30-300 r/min. In this study, the jet shapes in this range were comparatively analyzed. The simulation results for the two-nozzle combination and the three-nozzle combination are given in Figures 17 and 18, respectively.

Under both combination modes, the jet shapes exhibit resembling variation trends with the rotation speed. For the

two-nozzle combination, when the rotation speed is as high as 300 r/min, the jet deviates sharply for approximately 90° after leaving from the nozzle, with the maximum impact distance being about 20 mm. When the rotation speed is reduced to 180 r/min, the jet deviates less violently, with the maximum impact distance being about 80 mm. As the rotation speed decreases to 120 r/min, the jet deviation angle continues to narrow while the impact distance lengthens. As the rotation speed decreases to 90 r/min, the jet gradually

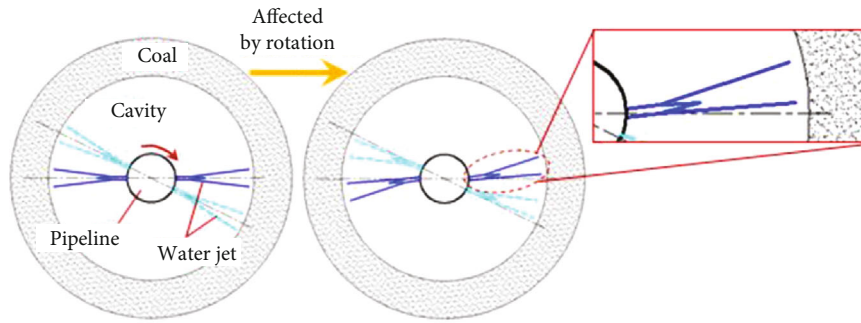


FIGURE 16: Influence of the rotation speed on the shape of HPWJ.

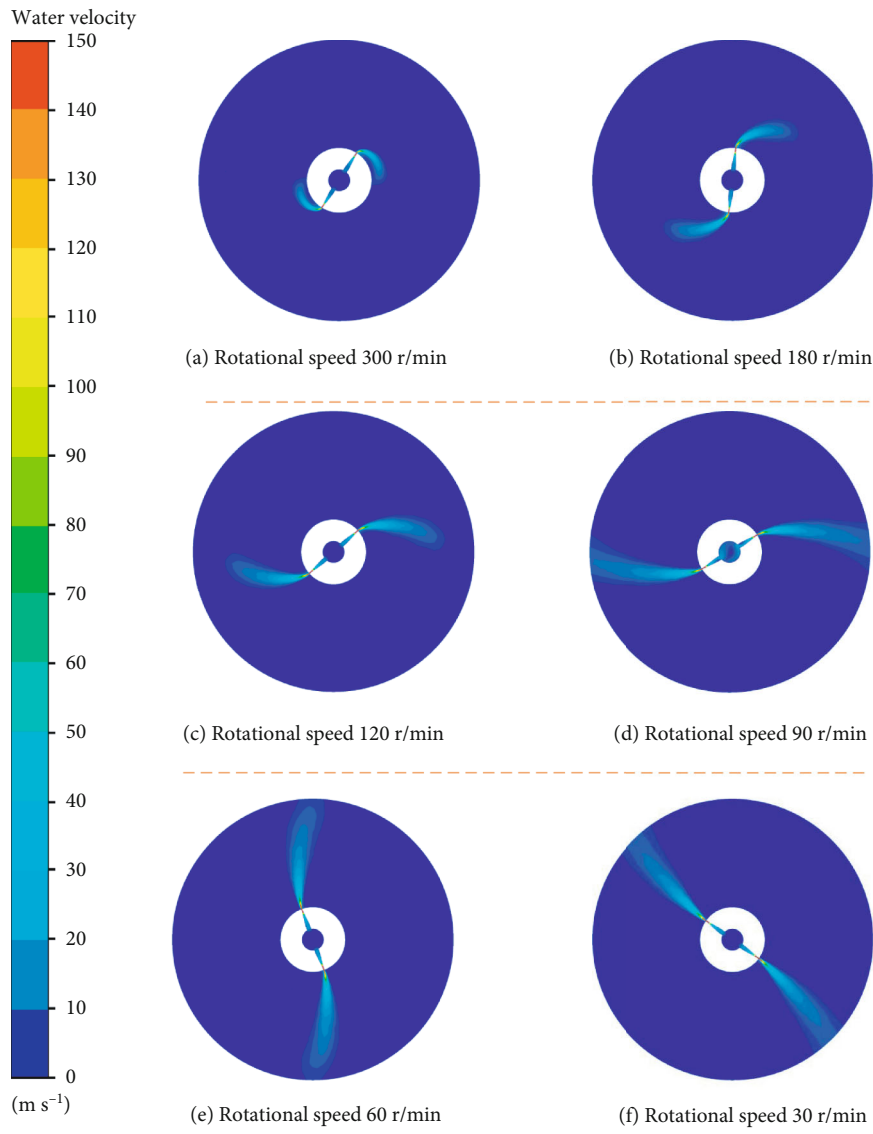


FIGURE 17: Contour maps of jet velocity for the two-nozzle combination at different rotation speeds.

reaches the boundary (200 mm) of the model. Compared with the front end of the jet, the initial section has a smaller deflection angle. As the rotation speed drops to 30 r/min, the jet only has a small deflection angle.

In summary, the nozzle rotation speed remarkably influences the jet shape and the impact distance. Rotation of the nozzle will lead to the deflection of the jet. The deflection angle grows with the increase in the rotation speed. It can

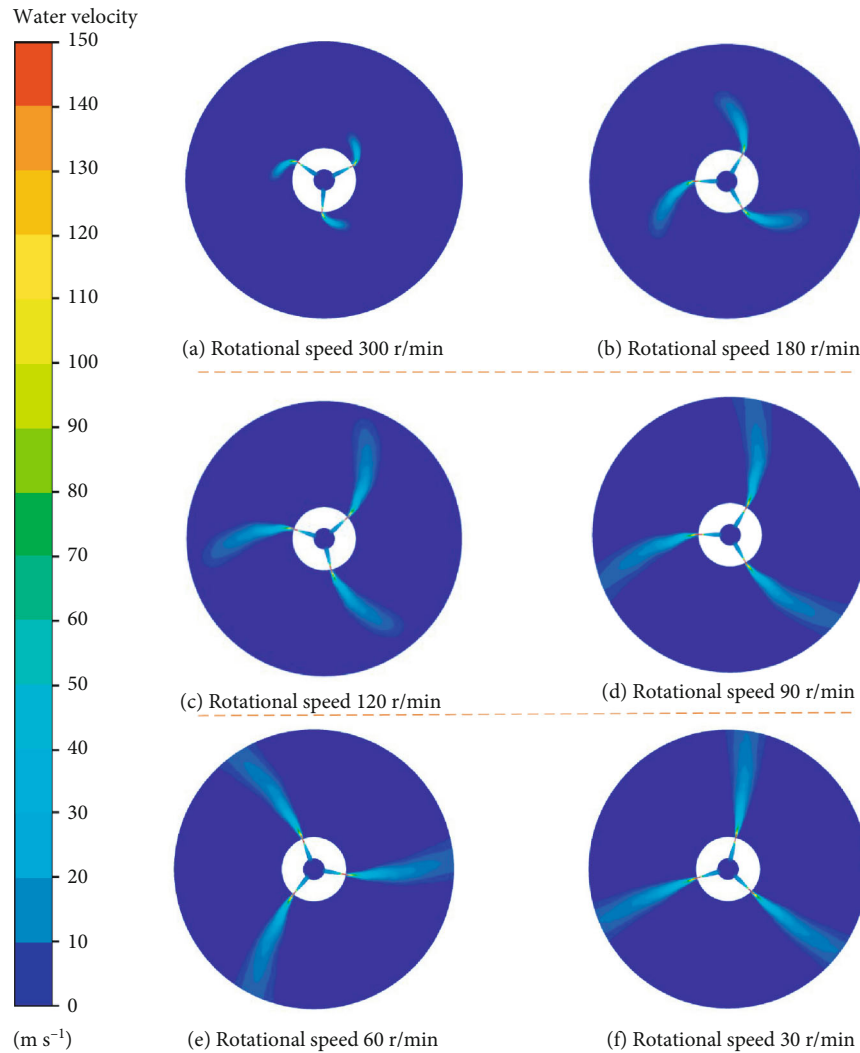


FIGURE 18: Contour maps of jet velocity for the three-nozzle combination at different speeds.

be as high as 90° when the rotation speed is high enough. Besides, the influence of the rotation speed on the deflection angle is more significant at a longer impact distance. The deflection of the jet worsens the jet continuity, shortens the impact distance, and weakens the impact force. When the rotation speed is low, only the fracture section and the dissipation section are affected. As the rotation rate rises, the initial section is also affected. An excessively high rotation speed will shorten the effective impact distance, reduce the coal crushing depth, and lower the coal crushing efficiency. On the other hand, as can be known from the analysis in the previous section, an upper limit exists for the depth of coal crushing by the same equipment under a constant pump pressure. When this upper limit is reached, the pit no longer changes with the passage of flushing time. If the nozzle rotation speed is too low, the flushing will be time-consuming and unable to achieve an improved flushing effect, which will not only delay the construction period but also waste water resources. Moreover, after the jet sweeps over the coal surface, the reflection of compression waves generated in the coal also contributes to coal crushing. An excessively

low rotation speed will weaken the reflection and coal crushing performance of compression waves.

5. Conclusions

In this paper, the axial and radial stress distributions of the high-pressure water jet (HPWJ) and the energy-gathering effect of a conical-cylindrical combined nozzle were analyzed by simulation. Furthermore, the influences of the submergence conditions, nozzle angle, pump station pressure, rotation speed on the shape, and impact pressure of HPWJ were explored. The main conclusions are as follows:

- (1) In the radial direction, the submerged condition will accelerate the attenuation of jet velocity and reduce the impact strength of the jet. The jet impact force on the axis of the rigid plate with the target distance of 100 mm can reach 80.7 MPa under the nonsubmerged condition, while it drops to 65.2 MPa by 19.2% under the submerged condition. In the axial direction, the jet velocity and the impact force both

decline gradually with the increase in the target distance under the nonsubmerged condition. The maximum impact pressure is as high as 188.1 MPa at the target distance of 10 mm, but it weakens to 53.1 MPa by 71.8% at the target distance of 120 mm

- (2) After the nozzle inlet and outlet diameters are determined, the total length of the nozzle is mainly determined by the contraction angle. Considering that the nozzle adopted for hydraulic flushing in underground coal mines should not be too long, 24° is the recommended contraction angle
- (3) During coal wall crushing by HPWJ, blocked by the coal wall, water at the bottom of the pit is discharged at a decelerated rate and accumulates there. Consequently, the nonsubmerged jet is gradually converted to the submerged jet at the bottom of the pit. In addition, the rotation speed should be controlled within 90 r/min in order to increase the coal crushing efficiency

Data Availability

The data used to support the results of this study are available from the corresponding author upon request.

Conflicts of Interest

The authors declare that they have no conflicts of interest.

Acknowledgments

This research was financially supported by the Shanghai Rising-Star Program (20QB1401000), National Science Foundation of China (51804176, 51706122), Natural Science Foundation of Shanghai (19ZR1411500), Natural Science Foundation of Shandong Province (ZR2018PEE001), Science & Technology Foundation of Guizhou Province ([2020]4Y055), China Postdoctoral Science Foundation (2019M652346), and Project of Shandong Province Higher Educational Science and Technology Program (J18KA187).

References



- [1] J. Liu, R. Zhang, D. Z. Song, and Z. Q. Wang, "Experimental investigation on occurrence of gassy coal extrusion in coal-mine," *Safety Science*, vol. 113, pp. 362–371, 2019.
- [2] S. Q. Lu, Y. L. Zhang, Z. Y. Sa, S. F. Si, L. Y. Shu, and L. Wang, "Damage-induced permeability model of coal and its application to gas predrainage in combination of soft coal and hard coal," *Energy Science & Engineering*, vol. 7, no. 4, pp. 1352–1367, 2019.
- [3] Q. Ma, W. Nie, S. Yang et al., "Effect of spraying on coal dust diffusion in a coal mine based on a numerical simulation," *Environmental Pollution*, vol. 264, p. 114717, 2020.
- [4] Z. Xiu, W. Nie, J. Yan et al., "Numerical simulation study on dust pollution characteristics and optimal dust control air flow rates during coal mine production," *Journal of Cleaner Production*, vol. 248, p. 119197, 2020.
- [5] Y. Hua, W. Nie, Q. Liu, H. Peng, W. Wei, and P. Cai, "The development and application of a novel multi-radial-vortex-based ventilation system for dust removal in a fully mechanized tunnelling face," *Tunnelling and Underground Space Technology*, vol. 98, p. 103253, 2020.
- [6] W. Niu, W. Nie, M. Yuan et al., "Study of the microscopic mechanism of lauryl glucoside wetting coal dust: environmental pollution prevention and control," *Journal of Hazardous Materials*, vol. 412, p. 125223, 2021.
- [7] H. Wang, Z. Y. Sa, W. M. Cheng, R. Zhang, and S. Yang, "Effects of forced-air volume and suction region on the migration and dust suppression of air curtain during fully mechanized tunneling process," *Process Safety and Environmental Protection*, vol. 145, pp. 222–235, 2021.
- [8] H. Xu, S. Sang, J. Yang, and H. Liu, "CO₂ storage capacity of anthracite coal in deep burial depth conditions and its potential uncertainty analysis: a case study of the No. 3 coal seam in the Zhengzhuang Block in Qinshui Basin, China," *Geosciences Journal*, 2021.
- [9] J. Liu, "Technic study on increasing permeability of deep-hole presplitting blasting and its application in low permeability coal seam," AnHui University of Science and Technology, Ph.D., 2008.
- [10] W. L. Quan, J. M. Xv, S. H. Tu, D. S. Zhang, and X. Q. Liang, *Introduction to Mining Engineering*, China University of Mining and Technology Press, Xuzhou, 2004.
- [11] F. Du and K. Wang, "Unstable failure of gas-bearing coal-rock combination bodies: insights from physical experiments and numerical simulations," *Process Safety and Environmental Protection*, vol. 129, pp. 264–279, 2019.
- [12] S. Lu, C. Wang, M. Li et al., "Gas time-dependent diffusion in pores of deformed coal particles: model development and analysis," *Fuel*, vol. 295, p. 120566, 2021.
- [13] Q. Bao, W. Nie, C. Liu et al., "The preparation of a novel hydrogel based on crosslinked polymers for suppressing coal dusts," *Journal of Cleaner Production*, vol. 249, pp. 119–343, 2020.
- [14] F. Chen, A. Cao, L. Dou, and G. Jing, "A quantitative evaluation method of coal burst hazard based on zone division and an analytic hierarchy process: a case study on Yanbei coal mine, Gansu Province, China," *Geosciences Journal*, vol. 23, no. 5, pp. 833–848, 2019.
- [15] S. Lu, C. F. Wang, Q. Q. Liu et al., "Numerical assessment of the energy instability of gas outburst of deformed and normal coal combinations during mining," *Process Safety and Environmental Protection*, vol. 132, pp. 351–366, 2019.
- [16] F. Du, K. Wang, X. Zhang, C. P. Xin, L. Y. Shu, and G. D. Wang, "Experimental study of coal-gas outburst: insights from coal-rock structure, gas pressure and adsorptivity," *Natural Resources Research*, vol. 29, no. 4, pp. 2481–2493, 2020.
- [17] X. Liu, W. Nie, Y. Hua, C. Liu, L. Guo, and W. Ma, "Behavior of diesel particulate matter transport from subsidiary transportation vehicle in mine," *Environmental Pollution*, vol. 270, p. 116264, 2021.
- [18] M. Y. Chen, Y. P. Cheng, J. C. Wang, H. R. Li, and N. Wang, "Experimental investigation on the mechanical characteristics of gas-bearing coal considering the impact of moisture," *Arabian Journal of Geosciences*, vol. 12, no. 18, 2019.
- [19] S. Q. Lu, L. Li, Y. Q. Cheng, Z. Y. Sa, Y. L. Zhang, and N. Yang, "Mechanical failure mechanisms and forms of normal and deformed coal combination containing gas: model development and analysis," *Engineering Failure Analysis*, vol. 80, pp. 241–252, 2017.

- [20] R. Zhang, J. Liu, Z. Y. Sa, Z. Q. Wang, S. Q. Lu, and C. F. Wang, "Experimental investigation on multi-fractal characteristics of acoustic emission of coal samples subjected to true triaxial loading-unloading," *Fractals-Complex Geometry Patterns and Scaling in Nature and Society*, vol. 28, 2020.
- [21] Y. Han, B. W. Dong, F. Y. Zhang, S. Lv, and W. D. Li, "Process of hydraulic punching technology for relieving pressure and enhancing permeability in China," *China Mining Magazine*, vol. 30, pp. 95–100, 2021.
- [22] H. M. Yang, X. L. Qiu, and X. L. Lv, "Numerical simulation of effective influence radius of hydraulic cavitation model of "one hole and multiple cavitation"," *Coal Technology*, vol. 40, 2021.
- [23] H. L. Liao, G. S. Li, and J. L. Niu, "Influential factors and mechanism analysis of rock breakage by ultra-high pressure water jet under submerged condition," *Chinese Journal of Rock Mechanics and Engineering*, vol. 27, pp. 1243–1250, 2008.
- [24] Y. Y. Lu, X. H. Li, and W. Y. Xiang, "Rock erosion mechanism of cavitating water jets," *Rock and Soil Mechanics*, vol. 26, pp. 1233–1237, 2005.
- [25] F. B. Tian and M. Lin, "Studies on the mechanism of water jet - assisted drilling technology(1)—cavitation and erosion," *Mechanics in Engineering*, vol. 29, pp. 29–33, 2007.
- [26] F. B. Tian and M. Lin, "Studies on the mechanism of water jet - assisted drilling technology(2)— high-speed drip impacting with solid target," *Mechanics in Engineering*, vol. 29, pp. 34–39, 2007.
- [27] M. M. Singh and H. L. Hartman, "Hypothesis for the mechanism of rock failure under impact," *The 4th U.S. Symposium on Rock Mechanics (USRMS) University Park*, 1961 American Rock Mechanics Association, Pennsylvania, 1961.
- [28] I. W. Farmer and P. B. Attewell, "Rock penetration by high velocity water jet: a review of the general problem and an experimental study," *International Journal of Rock Mechanics and Mining Sciences & Geomechanics Abstracts*, vol. 2, no. 2, pp. 135–153, 1965.
- [29] C. Pan and Y. Yao, "The numerical simulation of rock fragmentation by high-pressure jet," *China Rural Water and Hydropower*, vol. 12, pp. 59–62, 2005.
- [30] Z. H. Bai and L. W. Cao, "Numerical simulation and analysis of rock breaking under pulse water jet," *Journal of Chongqing University of Technology(Natural Science)*, vol. 23, pp. 31–35, 2009.
- [31] L. Ma, R. Bao, and Y. M. Guo, "Waterjet penetration simulation by hybrid code of SPH and FEA," *International Journal of Impact Engineering*, vol. 35, 2007.
- [32] J. Wang, N. Gao, and W. Gong, "Abrasive waterjet machining simulation by coupling smoothed particle hydrodynamics/finite element method," *Chinese Journal of Mechanical Engineering*, vol. 23, no. 5, pp. 568–573, 2010.
- [33] K. Maniadaki, T. Kestis, N. Bilalis, and A. Antoniadis, "A finite element-based model for pure waterjet process simulation," *The International Journal of Advanced Manufacturing Technology*, vol. 31, no. 9-10, pp. 933–940, 2007.
- [34] W. J. Gong, J. M. Wang, and N. Gao, "Numerical simulation for abrasive water jet machining based on ALE algorithm," *The International Journal of Advanced Manufacturing Technology*, vol. 53, no. 1-4, pp. 247–253, 2011.
- [35] H. J. Ni and R. H. Wang, "A theoretical study of rock drilling with a high pressure water jet," *Petroleum Science*, vol. 1, no. 4, pp. 72–76, 2004.
- [36] H. J. Ni, R. H. Wang, and Y. H. Bai, "Finite element method for analyzing high-pressure water jet breaking rock," *Journal of China University of Petroleum(Edition of Natural Science)*, vol. 37, p. 40, 2002.
- [37] H. J. Ni, R. H. Wang, and H. K. Ge, "Numerical simulation on rock breaking under high pressure water," *Chinese Journal of Rock Mechanics and Engineering*, vol. 23, pp. 550–554, 2004.
- [38] H. J. Ni, R. H. Wang, and Y. Q. Zhang, "Numerical simulation study on rock breaking mechanism and process under high pressure water jet," *Applied Mathematics and Mechanics*, vol. 26, no. 12, pp. 1445–1452, 2005.
- [39] R. H. Wang and H. J. Ni, "Research of rock fragmentation mechanism with high-pressure water jet," *Journal of China University of Petroleum(Edition of Natural Science)*, vol. 26, pp. 118–122, 2002.
- [40] R. H. Wang, Z. H. Shen, and W. D. Zhou, "Experimental study on rock breaking borehole by high pressure water jet," *Oil Drilling & Production Technology*, vol. 20-25, pp. 99-100, 1995.
- [41] Z. C. Song and J. M. Chen, "Numerical simulation for high-pressure water jet breaking rock mechanism based on SPH algorithm," *Oil Field Equipment*, vol. 38, pp. 39–43, 2009.
- [42] Y. Y. Lu, S. Zhang, Y. Liu, Z. H. Lu, and L. Y. Jiang, "Analysis on stress wave effect during the process of rock breaking by pulsed jet," *Journal of Chongqing University*, vol. 35, pp. 117–124, 2012.
- [43] J. L. Liu and H. Si, "Numerical simulation on damage field of high pressure water jet breaking rock under high ambient pressure," *Journal of Chongqing University*, vol. 34, pp. 40–46, 2011.
- [44] H. Si, Y. M. Xie, and C. H. Yang, "Numerical simulation of rock damage field under abrasive water jet," *Rock and Soil Mechanics*, vol. 32, pp. 935–940, 2011.
- [45] Q. Li, "Research on drilling long hole in soft coal seam by high pressure water jets," Chongqing University, 2008.
- [46] W. Z. Jiang, "Research on theory of slotting and enhancing permeability by high pressure rotational jetting in low permeability coal seam and its application," China University of Mining and Technology, 2009.
- [47] X. Zhang, "The study on the mechanism and experiment of high pressure water jet slotted," Liaoning Technical University, 2009.
- [48] X. C. Wang, Y. Y. Lu, Y. Kang, B. W. Xia, and S. Zhang, "Experimental study of abrasive waterjet cutting coal-rock mass," *Journal of China University of Mining & Technology*, vol. 40, pp. 246–251, 2011.
- [49] Q. D. Sun, Z. M. Wang, J. Q. Yu, and W. H. Zhang, "A disquisition on breaking mechanism of high pressure jet impacting on rock," *Rock and Soil Mechanics*, vol. 26, pp. 978–982, 2005.
- [50] X. D. Lin, Y. Y. Lu, J. R. Tang, X. Ao, and L. Zhang, "Numerical simulation of abrasive water jet breaking rock with SPH-FEM coupling algorithm," *Journal of Vibration and Shock*, vol. 33, pp. 170–176, 2014.
- [51] D. Sevda, "Experimental and numerical study of rock breakage by pulsed water jets," Australia University of Queensland, PhD, Brisbane, 2011.
- [52] F. J. Heymann, "High-speed impact between a liquid drop and a solid surface," *Journal of Applied Physics*, vol. 40, no. 13, pp. 5113–5122, 1969.
- [53] S. S. Cook, "Erosion by water-hammer," *Proceedings of the Royal Society of London Series A, Containing Papers of a*

- Mathematical and Physical Character*, vol. 119, no. 783, pp. 481–488, 1928.
- [54] J. E. Field, “Stress waves, deformation and fracture caused by liquid impact,” *Philosophical Transactions of the Royal Society of London Series A, Mathematical and Physical Sciences*, vol. 260, pp. 86–93, 1966.
- [55] J. E. Field, “ELSI conference: invited lecture: liquid impact: theory, experiment, applications,” *Wear*, vol. 233-235, pp. 1–12, 1999.
- [56] K. Pianthong, S. Zakrzewski, M. Behnia, and B. E. Milton, “Supersonic liquid jets: their generation and shock wave characteristics,” *Shock Waves*, vol. 11, no. 6, pp. 457–466, 2002.
- [57] W. K. Soh, B. C. Khoo, and W. Y. D. Yuen, “The entrainment of air by water jet impinging on a free surface,” *Experiments in Fluids*, vol. 39, no. 3, pp. 498–506, 2005.
- [58] X. Q. Ma, *Impact Dynamics*, Beijing Institute of Technology Press, Beijing, 1992.
- [59] R. H. Wang and H. J. Ni, “Study on rock breaking mechanism of high pressure water jet,” China University of Petroleum Press, 2010.
- [60] F. Huang, “On the transient dynamics of water jet impinging target and the mechanism of water jet breaking rock,” Chongqing University, 2015.
- [61] A. Ohashi and K. Yanaida, “The fluid mechanics of capsule pipelines : 1st report, analysis of the required pressure drop for hydraulic and pneumatic capsules,” *JSME International Journal Series B-fluids and Thermal Engineering*, vol. 29, no. 252, pp. 1719–1725, 1986.
- [62] Y. S. Yang, J. P. Zhang, and S. L. Nie, “Energy loss of nozzles in water jet system,” *Journal of Mechanical Engineering*, vol. 49, no. 2, pp. 139–145, 2013.
- [63] T. K. Lu, H. Yu, and Y. Dai, “Longhole waterjet rotary cutting for in-seam cross panel methane drainage,” *Mining Science and Technology*, vol. 20, pp. 378–383, 2010.

Research Article

Pore Structure Characteristics and Evolution Law of Different-Rank Coal Samples

Zhihui Wen ^{1,2,3}, Qi Wang ^{1,2}, Yunpeng Yang^{1,2} and Leilei Si^{1,2,3}

¹School of Safety Science and Engineering, Henan Polytechnic University, Jiaozuo 454000, China

²State Key Laboratory Cultivation Base for Gas Geology and Gas Control (Henan Polytechnic University), Jiaozuo 454000, China

³Collaborative Innovation Center of Coal Work Safety and Clean High Efficiency Utilization, Jiaozuo 454000, China

Correspondence should be addressed to Zhihui Wen; wenzhihui@hpu.edu.cn

Received 30 April 2021; Accepted 1 June 2021; Published 17 June 2021

Academic Editor: Feng Du

Copyright © 2021 Zhihui Wen et al. This is an open access article distributed under the Creative Commons Attribution License, which permits unrestricted use, distribution, and reproduction in any medium, provided the original work is properly cited.

In this study, the full-size pore structure characteristics of six different-rank coal samples were investigated and analyzed from three perspectives, namely, pore shape, pore volume, and pore specific surface area, by performing a high-pressure mercury injection experiment and a low-temperature nitrogen adsorption experiment. Next, the full-size pore volumes and pore specific surface areas of the six coal samples were accurately characterized through a combination of the two experiments. Furthermore, the relationships between volatile matter content and pore volume and between volatile matter content and pore specific surface area were fitted and analyzed. Finally, the influences of metamorphic degree on pore structure were discussed. The following conclusions were obtained. The pore shapes of different-rank coal samples differ significantly. With the increase of metamorphic degree, the full-size pore volume and pore specific surface area both decrease first and then increase. Among the pores with various sizes, micropores are the largest contributor to the full-size pore volume and pore specific surface area. The fitting curves between volatile matter content and pore volume and between volatile matter content and pore specific surface area can well reflect the influence and control of metamorphic degree on pore volume and pore specific surface area, respectively. With the increase of volatile matter content, the pore volume and the pore specific surface area both vary in a trend resembling a reverse parabola.

1. Introduction

China is a country boasting abundant coal resources. According to *National Energy Development Strategy (2030-2050)* formulated by the Chinese Academy of Engineering, coal resources will account for about 55% of the whole energy structure of China in 2030 and will still account for over 50% in 2050 [1, 2]. That is, coal will still occupy the most important position in China's primary energy structure in the future [3]. Coal is a typical heterogeneous porous medium whose pore structure is one of the key parameters for evaluating it [4]. Pore structure not only determines the physical and mechanical properties of coal, but also controls the process of gas adsorption, desorption, diffusion, and seepage in a coal seam [5-7]. In particular, the adsorption capacity of

coalbed methane (CBM) is closely related to the pore development degree and pore structure characteristics. Therefore, the research on the pore structure characteristics of coal is meaningful for gas disaster prevention and CBM extraction and utilization [8-10]. As specified by the Hodot decimal classification standard [11-13], the pores in coal can be divided into five categories according to the pore size, i.e., micropores (<10 nm), small pores (10-100 nm), mesopores (100-1,000 nm), macropores (>10,000 nm), and visible pores (>100,000 nm). Among them, micropores, also referred to as adsorption pores, are the main space for gas adsorption. The commonly used methods to measure the pore structure characteristics of coal include high-pressure mercury injection, nuclear magnetic resonance, micro CT, low-temperature nitrogen adsorption, and transmission electron microscope

[14–20]. Due to the limitations of different measurement methods, the pore structure of coal can hardly be accurately characterized with a single method [21].

In previous studies, high-pressure mercury injection and low-temperature nitrogen adsorption are considered to be two effective methods for pore structure testing [22–24]. The principle of high-pressure mercury injection is to enable mercury to enter pores by applying an external force. When the external force is larger, mercury can enter pores with a smaller diameter. High-pressure mercury injection can measure pores whose diameters range from 5.5 nm to 1,000,000 nm. When the mercury injection pressure is higher than 200 MPa, mercury is able to enter pores with the diameter of 7 nm. However, in this case, the excessive external force may pose the risk of deformation and damage to coal. Thus, this method cannot accurately measure the distribution of nanoscale pores [25].

The principle of low-temperature nitrogen adsorption is based on physical adsorption caused by intermolecular forces [26]. At -195.8°C , the energy of nitrogen molecules is reduced, and nitrogen molecules reach the adsorption equilibrium of approximate monolayer on the surface of solid material under the action of van der Waals forces. At this time, the adsorption surface area of the solid substance is proportional to its adsorption capacity. In this way, the specific surface area of the substance to be measured can be calculated. Meanwhile, with the volume of pores in the solid substance being equivalent to the volume of liquid nitrogen entering the pores, the rate of variation of pore volume with the pore size can be measured by means of theoretical analysis. The most commonly used calculation method is to calculate pore volume, pore size distribution, and pore specific surface area by using the Barrett-Joyner-Halenda (BJH) theory [27]. Despite its inability to measure the distribution of macropores, low-temperature nitrogen adsorption is able to accurately characterize the distribution of micropores and small pores. Accordingly, some scholars propose to combine the above two methods for the purpose of accurately characterizing the full-size pore structure of coal [28–30].

Considering the important position of coal in China's energy structure, investigating the pore structure distribution characteristics of typical coal samples from different mining areas in China conduces to conducting an in-depth study on the control mechanism of pore structure on the gas adsorption, desorption, and seepage characteristics of coal. Such an investigation is of great significance for gas disaster prevention and CBM extraction in typical mining areas in China. In this paper, six different-rank coal samples were collected from different mining areas and then subjected to the high-pressure mercury injection experiment and the low-temperature nitrogen adsorption experiment. Based on the experimental results, the mercury injection-ejection curves of different coal samples and their corresponding pore shapes, pore volumes, and pore specific surface areas were analyzed, and the low-temperature nitrogen adsorption-desorption isotherms of these samples and their corresponding pore characteristics, pore volumes, and pore specific surface areas were also probed into. Moreover, the accuracy

of these two methods in terms of measuring the pore volumes and pore specific surface areas under different pore diameters was discussed. Besides, the two methods were combined to characterize the full-size pore shapes, pore volumes, and pore specific surface areas of different coal samples. Ultimately, the influences and control mechanisms of coal rank on the pore structure characteristics were clarified.

2. Materials and Methods

2.1. Sampling Regions and Sample Preparation. The coal samples used in the experiment were selected from six different typical mining areas in China. The sampling regions are shown in Figure 1. Then, the water contents, ash contents, volatile contents, and vitrinite reflectance values of the samples were tested in accordance with the preparation process displayed in Figure 2. The sampling locations and the test results of relevant basic parameters are given in Table 1.

2.2. High-Pressure Mercury Injection Experiment. The device used in the high-pressure mercury injection experiment is the Auto Pore 9505 automatic mercury porosimeter in the Key Laboratory of Gas Geology and Gas Control of Henan Polytechnic University (Figure 3). The test pore diameter ranges from 5 nm to 360,000 nm, and the maximum working pressure is 228 MPa. The application of pressure enables mercury to enter the pores. The functional relationship between the pore size that mercury can reach and the applied external force satisfies the Washburn equation [31, 32].

$$r = \frac{-2\gamma \cos \theta}{P}, \quad (1)$$

where P is the mercury injection pressure, Pa; r is the radius of pores, m; θ is the contact angle, and it takes the value 130° ; γ is the surface tension of mercury, and it equals $4.85 \times 10^{-3} \text{ N/m}$.

The specific surface area of pores in the sample can be further calculated via the mercury injection pressure according to the Young-Duper equation.

$$-PdV = \gamma \cos \theta dS, \quad (2)$$

where S is the specific surface area of pores, m^2/g .

2.3. Low-Temperature Nitrogen Adsorption Experiment. The device used in the low-temperature nitrogen adsorption experiment is the ASAP2020M automatic specific surface area and pore size analyzer in the Key Laboratory of Gas Geology and Gas Control of Henan Polytechnic University. The test pore size ranges from 0.35 nm to 500 nm, and the lower limit of specific surface area measurement is $0.0005 \text{ m}^2/\text{g}$. The schematic diagram of the low-temperature nitrogen adsorption experimental device is shown in Figure 4.

In the experiment, the processed sample was put into the sample tube before the experimental device was connected, and then, the liquid nitrogen cup was filled with liquid nitrogen. Next, the entire system was vacuumized, and the volume of free space in the sample tube was calibrated using helium. After a certain amount of nitrogen was injected into the

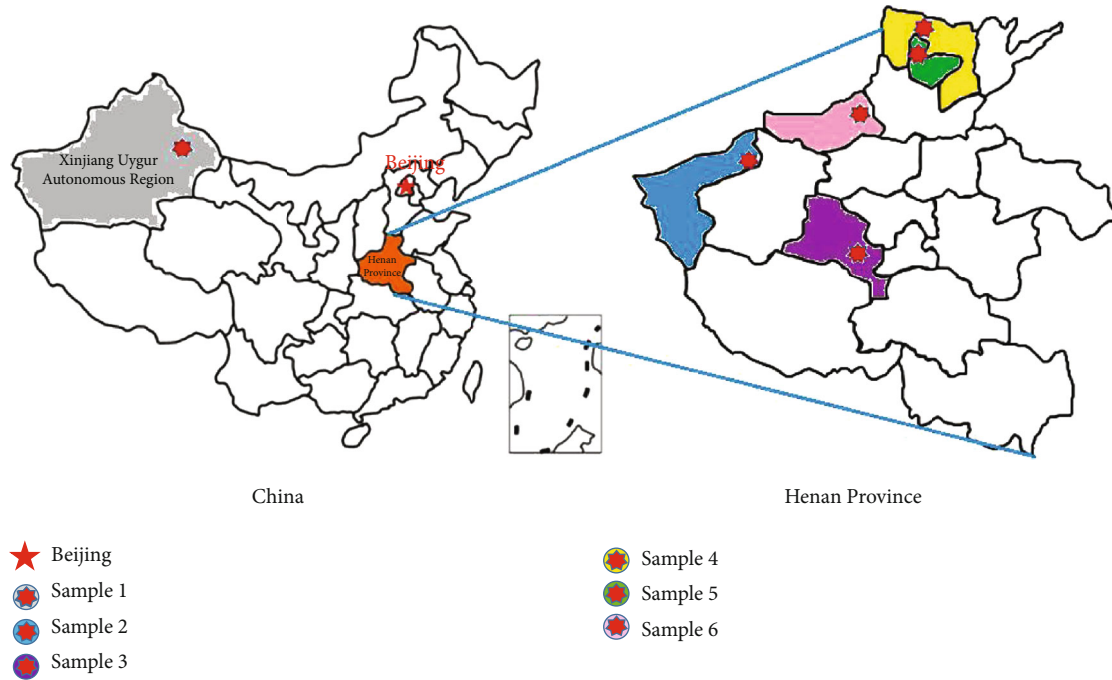


FIGURE 1: Sampling locations of experimental coal samples.

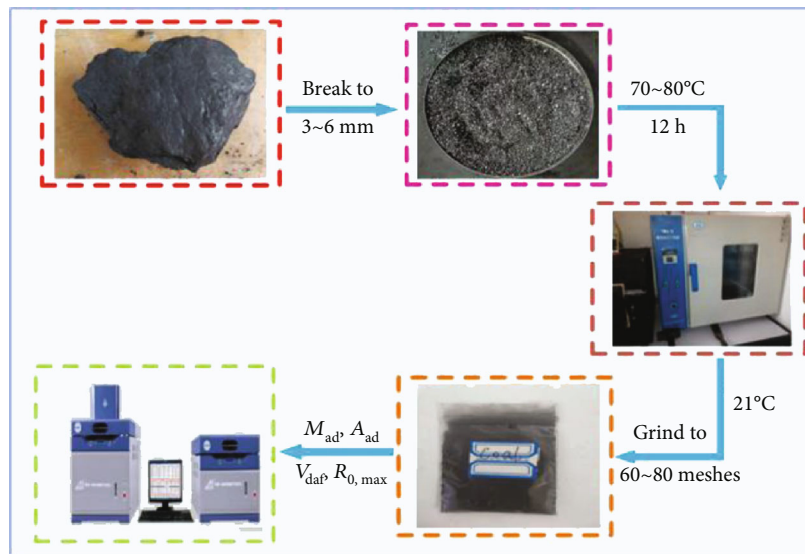


FIGURE 2: Sample preparation process and experimental steps.

TABLE 1: Basic information and parameters of experimental coal samples.

Sample	Sampling location	M_{ad} (%)	A_{ad} (%)	V_{daf} (%)	$R_{0,max}$ (%)
Sample 1	Dananhu No. 1 mine, Hami mining area	8.02	15.36	42.35	0.43
Sample 2	Gengcun mine, Yima mining area	2.11	11.92	38.16	0.52
Sample 3	Pingdingshan No. 5 mine, Pingdingshan mining area	1.23	15.82	28.82	1.05
Sample 4	Zhujiao mine, Anyang mining area	1.62	11.85	22.16	1.30
Sample 5	Hebi No. 9 mine, Hebi mining area	1.37	12.86	12.93	1.76
Sample 6	Jiulishan mine, Jiaozuo mining area	2.32	12.92	7.68	2.55

Note: M_{ad} , A_{ad} , and V_{daf} are the moisture, ash, and volatile matter contents on the air-dried basis, respectively. $R_{0,max}$ is the maximum vitrinite reflectance.



FIGURE 3: Auto Pore 9505 automatic mercury porosimeter.

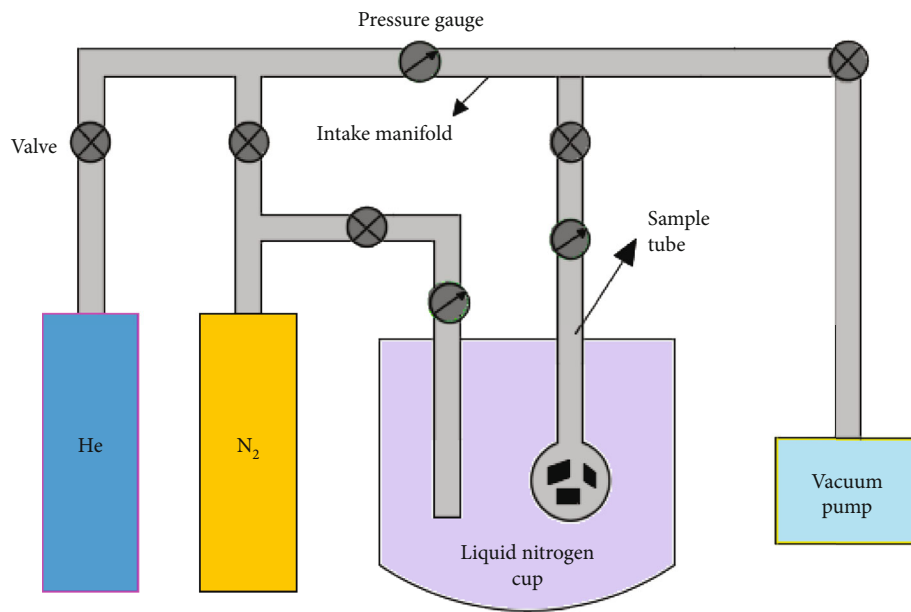


FIGURE 4: Schematic diagram of the low-temperature nitrogen adsorption experimental device.

intake manifold, the initial pressures, initial temperatures, and initial gas weights of the intake manifold and the sample tube were recorded. Afterwards, a certain amount of nitrogen was injected from the intake manifold to the sample tube. When the sample reached adsorption equilibrium, the pressures, temperatures, and gas weights of the intake manifold and the sample tube were recorded again. On the basis of the acquired data, the adsorption capacity of the sample was calculated. Then, the nitrogen adsorption-desorption isotherm can be obtained by taking the relative pressure as the abscissa and the adsorption capacity as the ordinate.

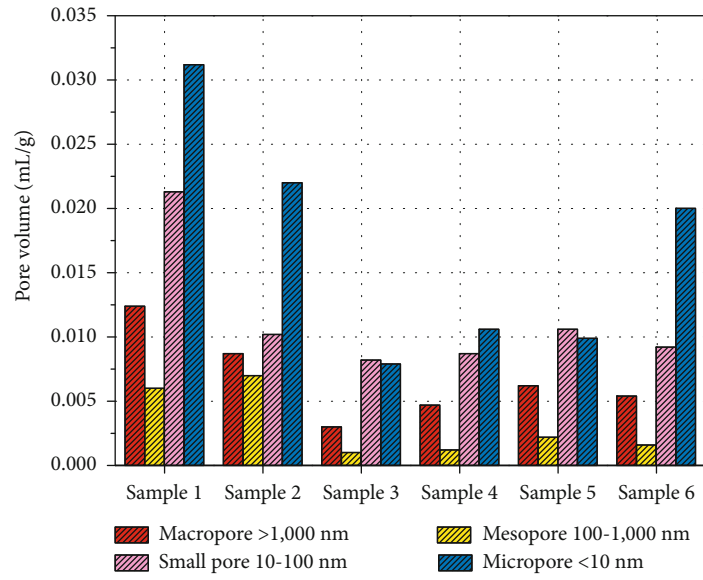
Generally, the pore volume, pore size distribution, and the specific surface area are calculated by using the BJH method [33].

3. Experimental Results

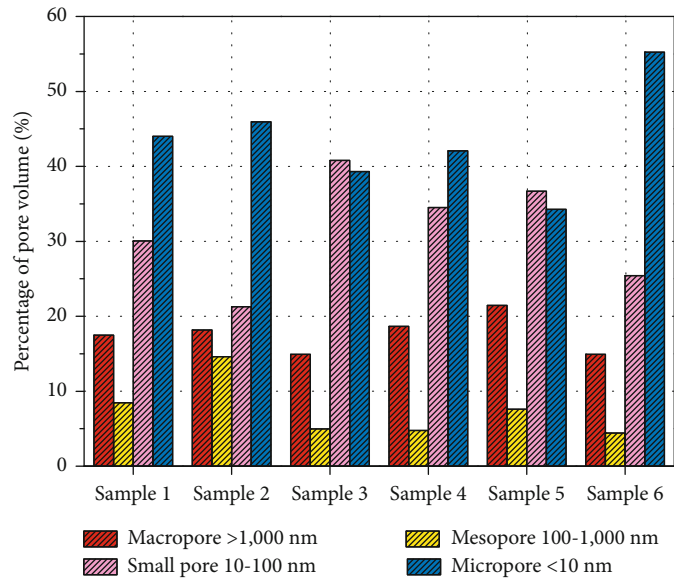
3.1. Results of the High-Pressure Mercury Injection Experiment

3.1.1. Pore Volume and Pore Specific Surface Area. The pore volumes and pore specific surface areas of the six coal samples were tested by performing a high-pressure mercury injection experiment. The results are exhibited in Figure 5.

The pores in the six different-rank coal samples mainly belong to small pores and micropores, followed by macropores and mesopores, as displayed in Figures 5(a) and 5(b). Besides, the total pore volume decreases first and then increases with the rise of coal rank, as illustrated in Figure 5(e).

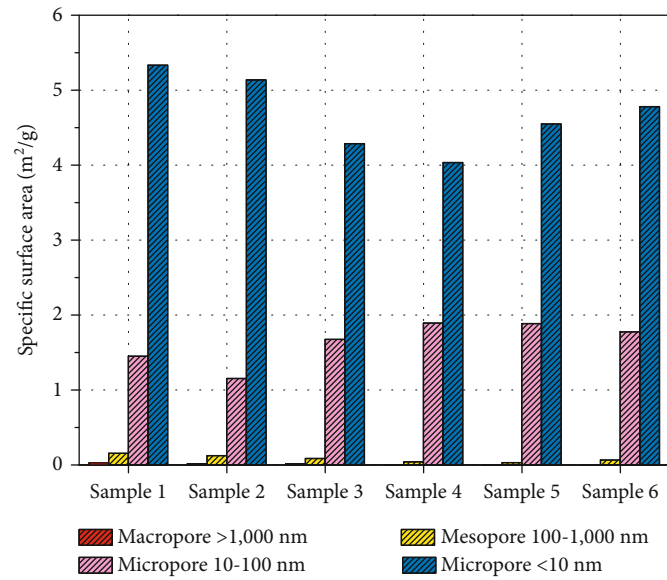


(a)

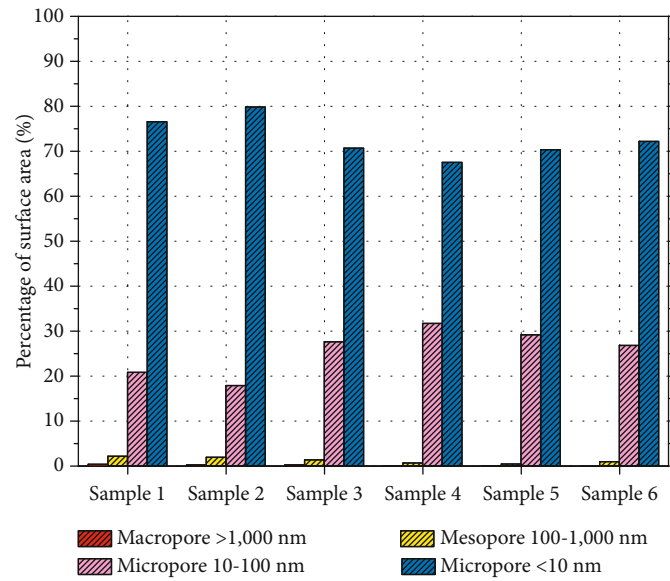


(b)

FIGURE 5: Continued.



(c)



(d)

FIGURE 5: Continued.

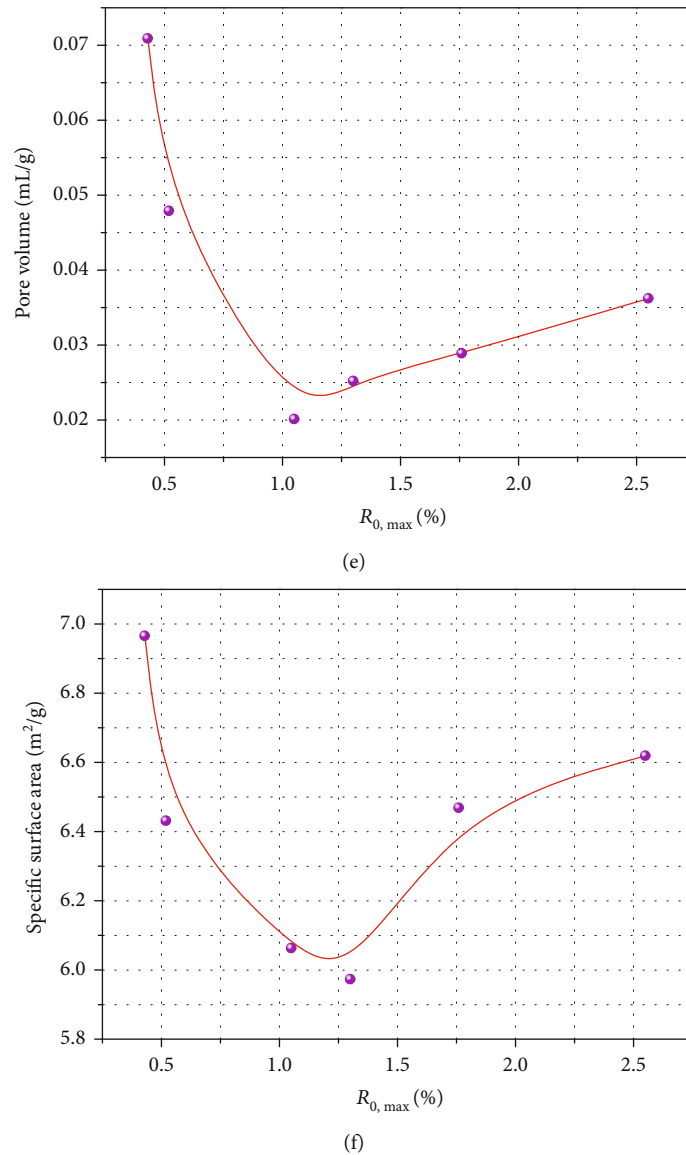


FIGURE 5: Results of the high-pressure mercury injection experiment. (a) Pore volume distribution; (b) pore volume proportion; (c) pore specific surface area distribution; (d) pore specific surface area proportion; (e) shows the relationship between total pore volume and metamorphic degree; (f) shows the relationship between total specific surface area and metamorphic degree.

Meanwhile, the pore specific surface areas of micropores account for the largest proportion (over 67.57%) for all the six coal samples, followed by those of small pores, whereas those of macropores and mesopores account for relatively smaller proportions, as presented in Figures 5(c) and 5(d). Hence, it can be concluded that the total pore specific surface areas of coal samples are primarily determined by micropores, and the total specific surface area decreases first and then increases with the rise of coal rank, as illustrated in Figure 5(f).

3.1.2. Mercury Injection Curve and Pore Shape Characteristics. The pores in coal can be divided into effective pores and isolated pores. The effective pores can be further divided into semiclosed pores, open pores, and ink-bottle-shaped pores. The pore shapes are illustrated in Figure 6 [34].

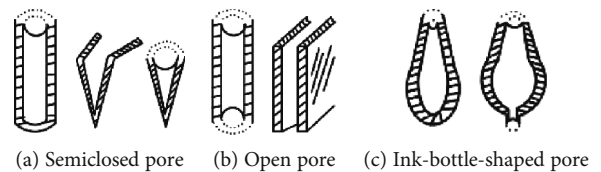


FIGURE 6: Classification of pore shapes corresponding to the mercury injection curves.

The mercury injection-ejection curves obtained from the high-pressure mercury injection experiment are shown in Figure 7. The mercury injection-ejection curves of different samples differ obviously. Although hysteresis loops are formed by the curves of all the six samples, these hysteresis loops are quite different, which reflects the differences in

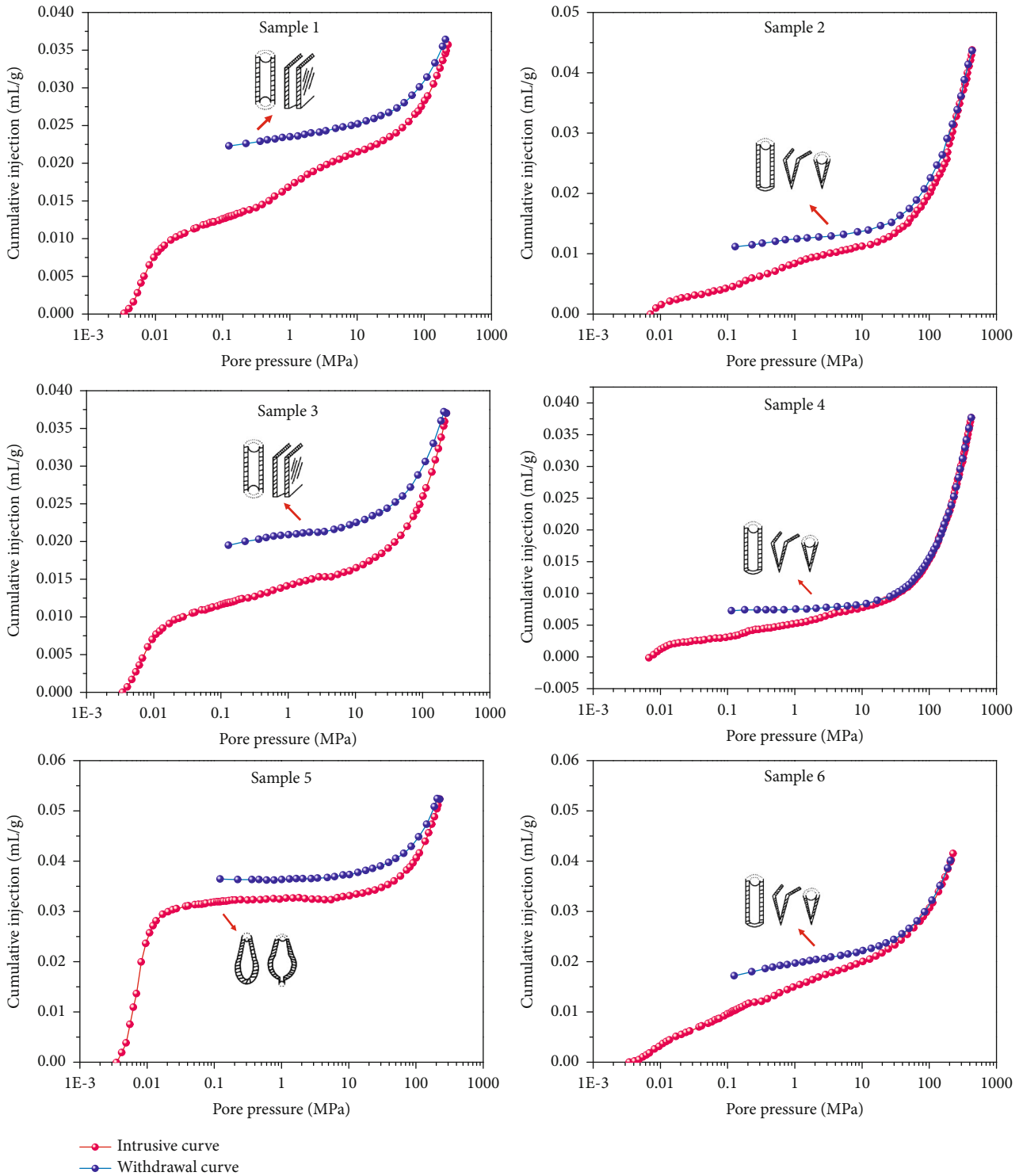
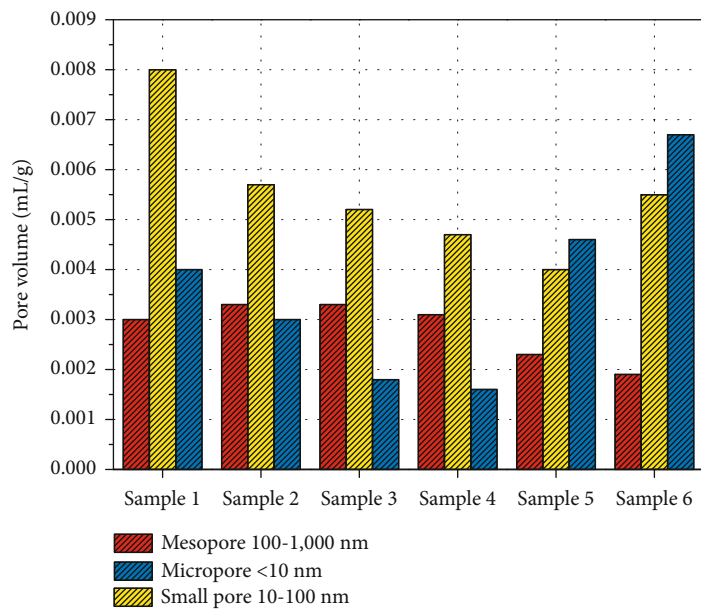


FIGURE 7: Mercury injection curves of experimental coal samples.

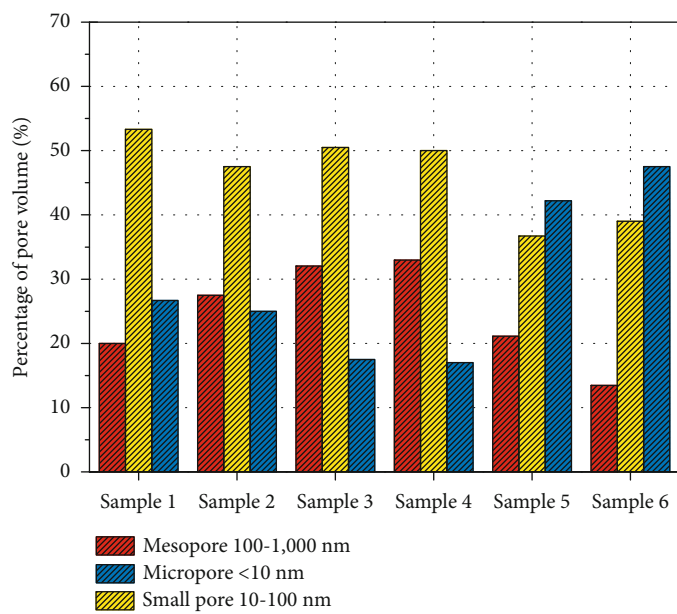
the basic pore shapes and connectivities of different coal samples. According to the classification method of pore shapes in Figure 6, the six coal samples can be divided into 3 categories:

- (1) *Samples 1 and 3*. Their values of mercury injection-ejection curves differ notably, and obvious hysteresis

loops are formed by their curves, which suggests that the two samples possess open pores and a certain number of ink-bottle-shaped pores. In addition, the cumulative amounts of mercury injection of the two samples increase slowly with the rise of pressure, which demonstrates the development of different-sized pores in the samples.

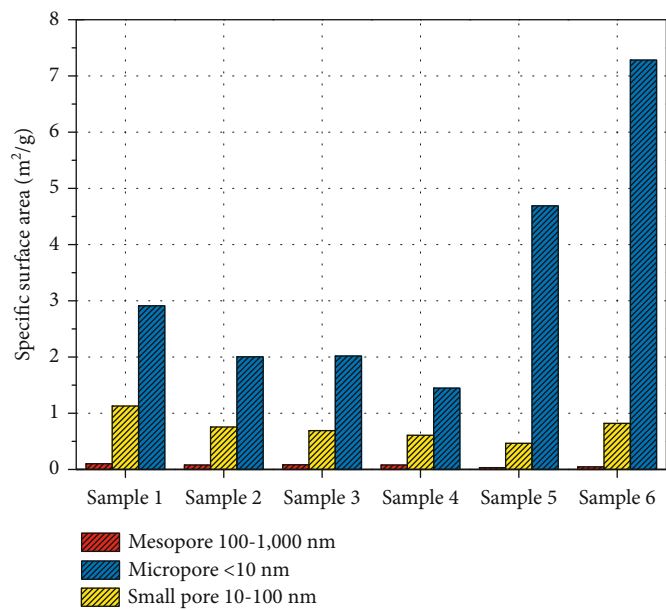


(a)

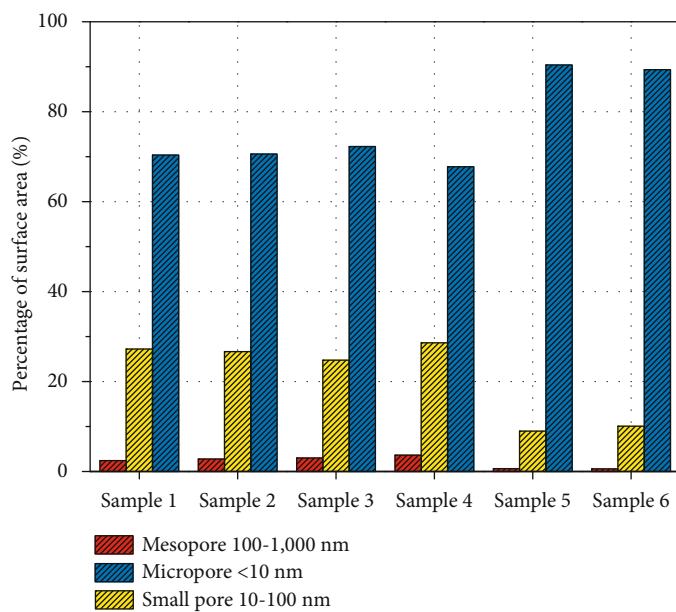


(b)

FIGURE 8: Continued.



(c)



(d)

FIGURE 8: Continued.

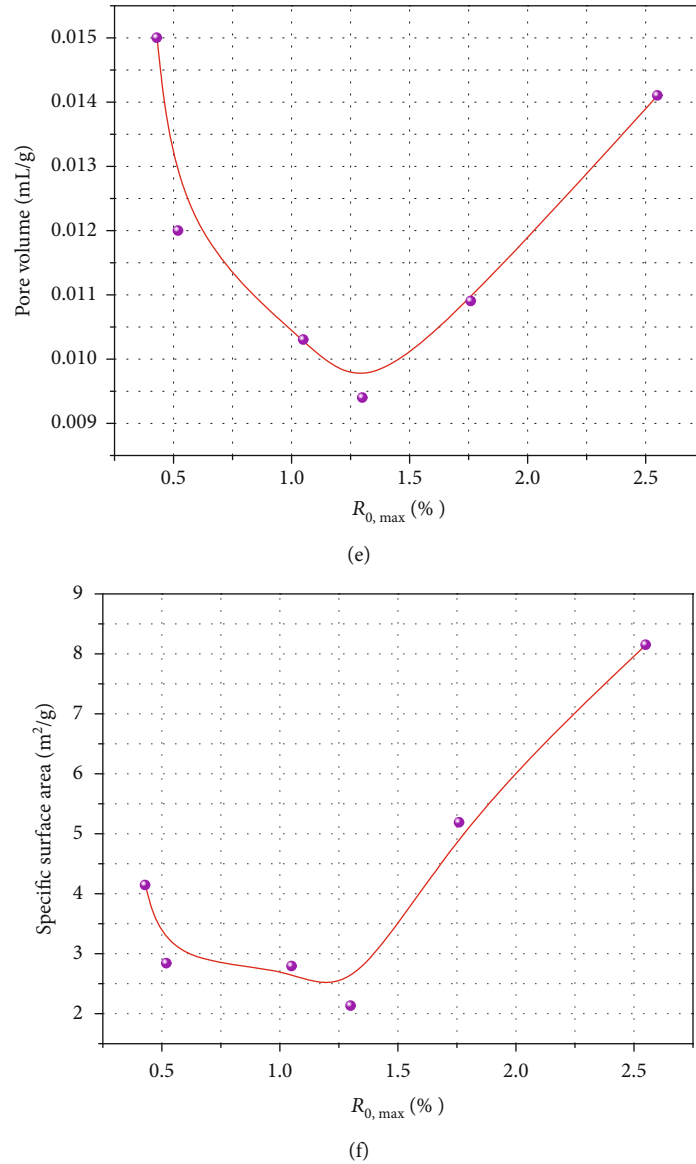


FIGURE 8: Results of the low-temperature nitrogen adsorption experiment. (a) Pore volume distribution; (b) pore volume proportion; (c) pore specific surface area distribution; (d) pore specific surface area proportion; (e) shows the relationship between total pore volume and metamorphic degree; (f) shows the relationship between total specific surface area and metamorphic degree.

- (2) *Sample 5*. When the pressure is lower than 0.01 MPa, its cumulative pore volume jumps sharply, indicating the wide development of large pores. When the pressure is higher than 10 MPa, its cumulative pore volume grows rapidly, suggesting the wide development of micropores. Besides, a hysteresis loop is formed by the curve, which is a sign of the existence of ink-bottle-shaped pores.
- (3) *Samples 2, 4, and 6*. The hysteresis loops of the three samples are the smallest, and they even disappear when the relative pressure gets higher than 10 MPa, which shows that the pores in the three samples are not so open and gradually close in the later stage. This demonstrates that micropores and transition pores are semiclosed. Meanwhile, the samples con-

tain a large number of semiopen pores whose connectivities are poor.

3.2. Results of the Low-Temperature Nitrogen Adsorption Experiment

3.2.1. Pore Volume and Pore Specific Surface Area. The pore volumes and pore specific surface areas of the six coal samples were tested through a low-temperature nitrogen adsorption experiment. The results are exhibited in Figure 8.

The pores in the six different-rank coal samples mainly belong to small pores and micropores, followed by macropores and mesopores, as displayed in Figures 8(a) and 8(b). In addition, the total pore volume decreases first and then increases with the rise of coal rank, as illustrated in Figure 8(e).

Meanwhile, the pore specific surface areas of micropores account for the largest proportion (over 67.57%) for all the six coal samples, whereas those of mesopores and small pores account for relatively smaller proportions, as presented in Figures 8(c) and 8(d). Hence, it can be concluded that the total pore specific surface areas of coal samples are mainly determined by micropores, and the total specific surface area decreases first and then increases with the rise of coal rank, as illustrated in Figure 8(f).

3.2.2. Adsorption Isotherms and Pore Shape Characteristics. The shape of adsorption isotherm obtained through the low-temperature nitrogen adsorption experiment can reflect the pore shape. According to whether an adsorption loop is formed by the nitrogen adsorption isotherm, Chen and Tang [35] divided the pore shapes into parallel plate pores, cylindrical pores, and ink-bottle-shaped pores. The pore shapes are exhibited in Figure 9.

Figure 10 shows the nitrogen adsorption isotherms of the six coal samples. The adsorption capacities of different samples differ significantly. To be specific, the maximum adsorption capacities of samples 1-6 are 1.569 cm³/g, 0.762 cm³/g, 7.135 cm³/g, 8.668 cm³/g, 8.055 cm³/g, and 10.566 cm³/g, respectively. Among them, sample 2 has the smallest adsorption capacity while sample 6 has the largest adsorption capacity. The adsorption capacity varies in a U-shaped trend, i.e., it decreases first and then increases, with the rise of coal rank.

Based on the nitrogen adsorption isotherms, the six coal samples can be classified into the following three categories in accordance with the pore shapes given in Figure 9.

- (1) *Samples 1, 2, 5, and 6.* Their adsorption isotherms and desorption isotherms are separated, not overlapping even at a low relative pressure. This shows that the micropores are relatively developed in the four samples, and most of the pores belong to parallel plate pores with four open edges. In the adsorption process, a turning point which corresponds to the ink-bottle-shaped pores appears on the desorption isotherm of sample 1 at the relative pressure of about 0.5.
- (2) *Sample 3.* Its adsorption isotherms and desorption isotherms roughly overlap, indicating that it primarily consists of cylindrical pores with one closed end. Since such pores require equal relative pressures during adsorption and desorption, the adsorption isotherms and the desorption isotherms are basically not separated.
- (3) *Sample 4.* Its adsorption isotherms and desorption isotherms do not completely overlap in the whole nitrogen adsorption process. Instead, they merely roughly overlap at relatively low pressures and high relative pressures, indicating the existence of open permeable and impermeable pores in the sample. Moreover, a turning point which corresponds to the ink-bottle-shaped pores appears at the relative pressure of about 0.5.

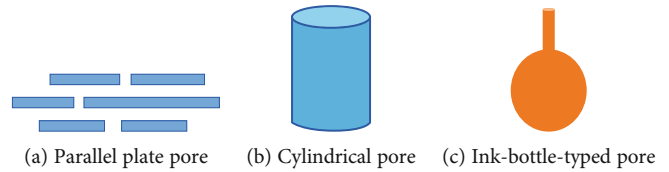


FIGURE 9: Pore shapes corresponding of the adsorption isotherms.

3.3. Joint Characterization of Pore Volume. The volumes of mesopores and macropores can be accurately tested through the high-pressure mercury injection experiment, while those of micropores and small pores can be accurately determined through the low-temperature nitrogen adsorption experiment. Thus, in this study, the two experiments were combined to jointly characterize the full-size pore volumes of the six experimental coal samples.

The principle of joint characterization of full-size pore characteristics is to take the mesopore and macropore volume data from the high-pressure mercury injection experiment and the micropore and small pore data from the low-temperature nitrogen adsorption experiment as the full-size pore volumes of the coal samples. The joint characterization results are listed in Table 2.

The total pore volumes of the experimental six coal samples lie in the range of 0.0115-0.0284 mL/g. Among them, sample 1 has the largest pore volume and sample 3 has the smallest one. The total pore volume varies in a U-shaped trend, i.e., it decreases first and then increases, with the increase of coal rank. Specifically, with respect to macropores and mesopores, Sample 1 and sample 3 correspond to the largest and smallest pore volumes, respectively. With respect to small pores, sample 1 and sample 6 correspond to the largest and smallest pore volumes, respectively. With respect to micropores, sample 6 and sample 4 correspond to the largest and smallest pore volumes, respectively. In the measured data, micropores share a relatively consistent variation trend with the total pore volume.

3.4. Joint Characterization of Pore Specific Surface Area. According to the principle of joint characterization given in Section 3.3, the pore specific surface areas of the six coal samples are characterized. The characterization results are listed in Table 3.

The total pore specific surface areas of the six experimental coal samples lie in the range of 2.099-8.168 m²/g. Among them, sample 4 has the smallest pore specific surface area and sample 6 has the largest one. The total pore specific surface area also varies in an approximately W-shaped trend with the rise of coal rank. The pore specific surface areas of all the six coal samples present the following variation trend: micropores > small pores > mesopores > macropores. In addition, under the condition of the same coal rank, the pore specific surface areas of small pores and micropores are much larger than those of mesopores and macropores. This means that mesopores and macropores contribute little to the pore specific surface area of coal, while micropores are the main contributor to it. Generally, the coal with a larger total pore

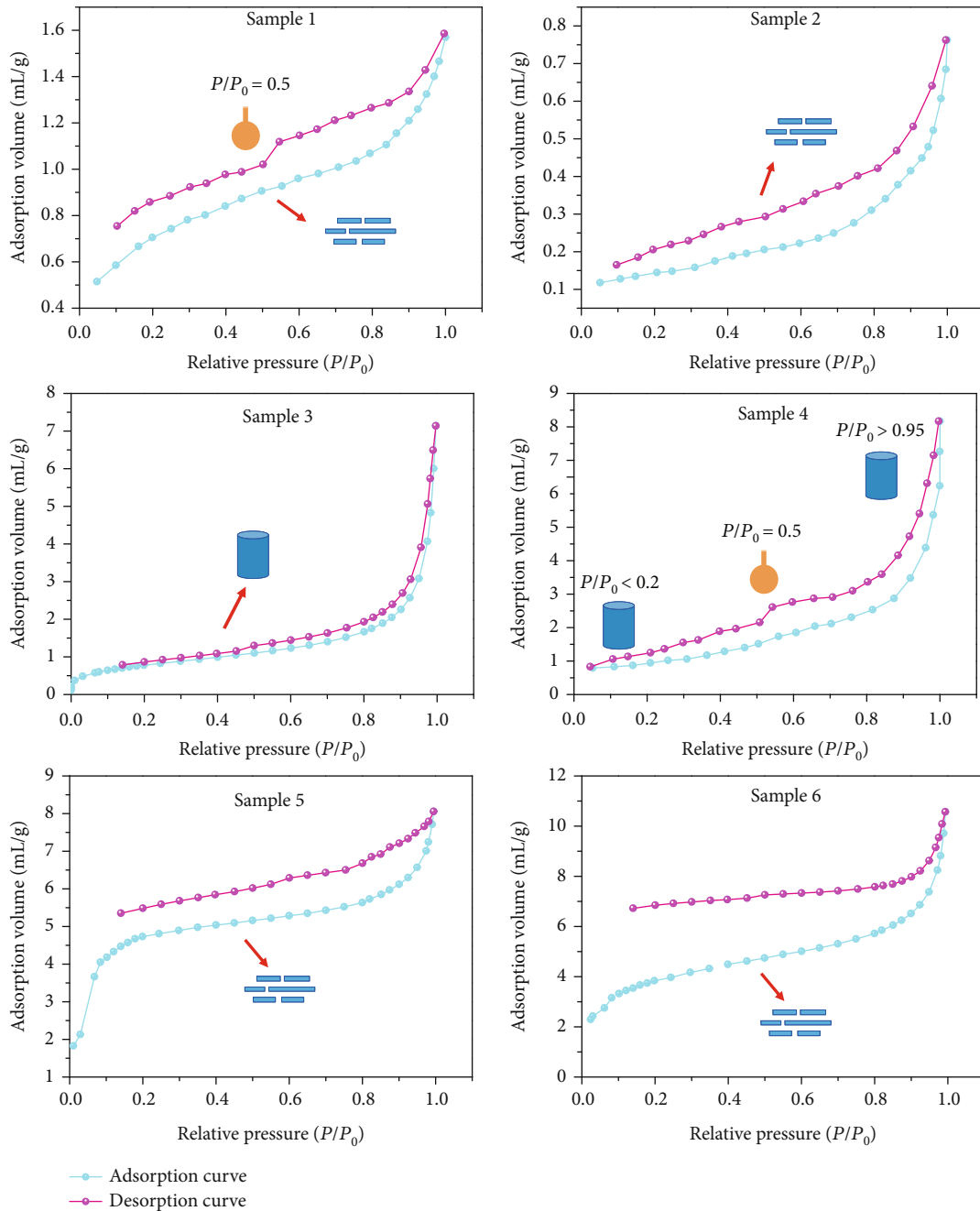


FIGURE 10: Nitrogen adsorption isotherms of experimental coal samples.

specific surface area boasts stronger adsorption capacity. Hence, micropores are the main controlling factor that determines the adsorption capacity of coal.

4. Discussion

4.1. Effect of Metamorphic Degree on Pore Volume. In this section, correlation analysis was conducted on the pore volumes and volatile matter contents of the six coal samples after joint characterization. Through fitting, it is found that the relationship between pore volume and volatile matter content conforms to a binomial relationship. For all the six

coal samples, the pore volume varies in a trend resembling a reverse parabola with the increase of the volatile matter content (Figure 11).

Based on the correlation analysis on the results of fitting between pore volume and volatile matter content, the following conclusions can be drawn.

- (1) The fitting degrees R^2 of macropores, mesopores, and micropores are all above 0.75, which means that the fitting curves can well reflect the relationship between volatile matter content and pore volume. In the stage of low metamorphic degree ($V_{daf} > 25\%$), the volumes

TABLE 2: Joint characterization results of pore volume.

Sample	Pore volume (mL/g)				Total pore volume (mL/g)
	Macropore	Mesopore	Small pore	Micropore	
Sample 1	0.0124	0.0040	0.0080	0.0040	0.0284
Sample 2	0.0087	0.0030	0.0057	0.0030	0.0204
Sample 3	0.0030	0.0010	0.0052	0.0018	0.0110
Sample 4	0.0047	0.0012	0.0047	0.0016	0.0122
Sample 5	0.0062	0.0022	0.0040	0.0046	0.0170
Sample 6	0.0054	0.0026	0.0055	0.0067	0.0202

TABLE 3: Joint characterization results of pore specific surface area.

Sample	Specific surface area (m ² /g)				Total specific surface area (m ² /g)
	Macropore	Mesopore	Small pore	Micropore	
Sample 1	0.027	0.154	1.127	2.913	4.221
Sample 2	0.017	0.126	0.757	2.005	2.905
Sample 3	0.017	0.085	0.691	2.017	2.810
Sample 4	0.003	0.042	0.610	1.444	2.099
Sample 5	0.002	0.030	0.467	4.689	5.188
Sample 6	0.001	0.065	0.820	7.282	8.168

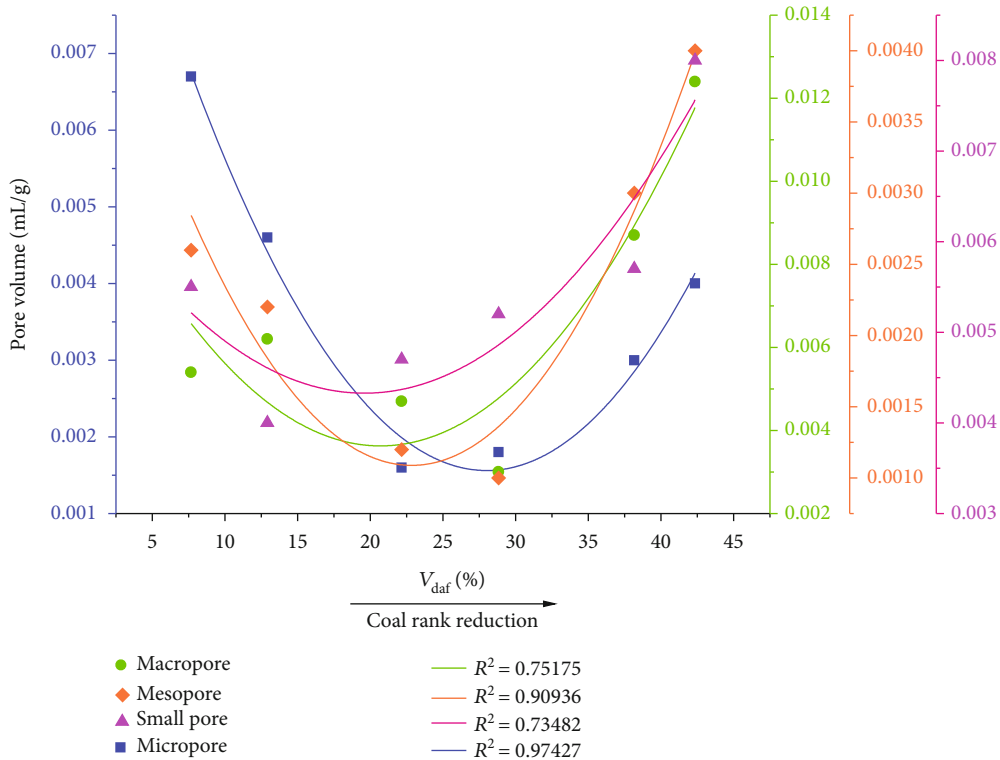


FIGURE 11: Curves of fitting between volatile matter content and pore volume.

of various pores all surge notably with the increase of volatile matter content. In the stage of medium metamorphic degree ($15\% < V_{daf} < 25\%$), they are rarely affected by the volatile matter content, just changing slightly. In the stage of high metamorphic degree ($V_{daf} < 15\%$), they drop considerably with the increase of volatile matter content

(2) The fitting degree R^2 of small pores is 0.73, which means that the fitting curves can roughly reflect relationship between volatile matter content and pore volume. The pore volume grows continuously with the increase of volatile matter content, indicating that the volume of small pores is greatly affected by the volatile matter content

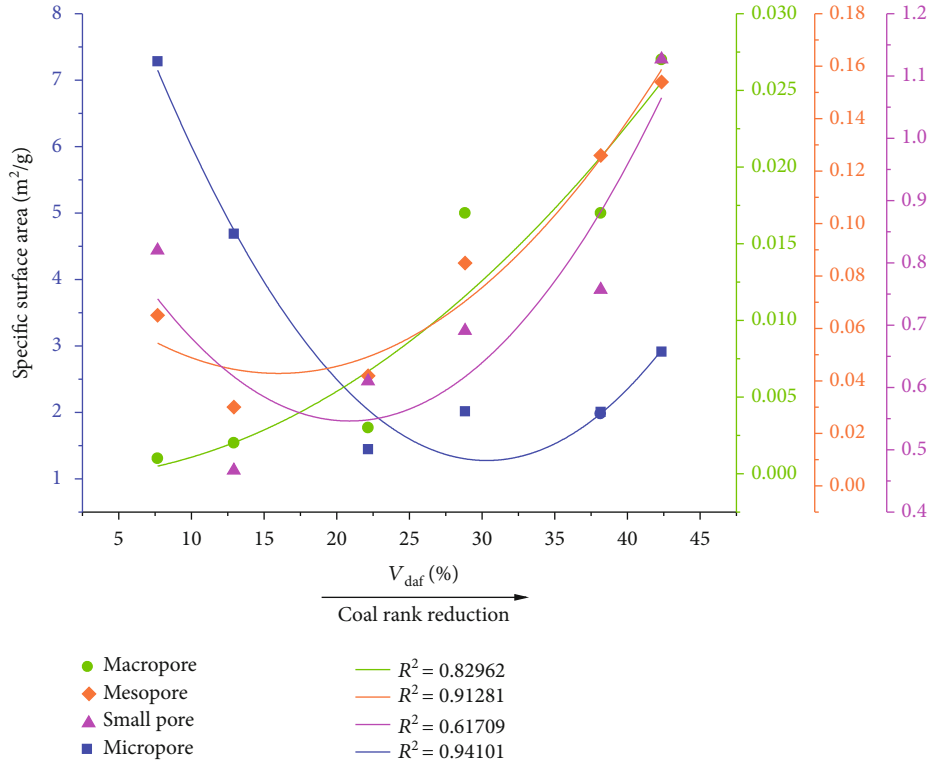


FIGURE 12: Curve of fitting between volatile matter and pore specific surface area.

4.2. *Effect of Metamorphic Degree on Pore Specific Surface Area.* In this section, correlation analysis was conducted on the pore specific surface areas and volatile matter contents of the six coal samples after joint characterization. Through fitting, it is disclosed that the relationship between pore specific surface area and volatile matter content conforms to a binomial relationship. For all the six coal samples, the pore specific surface area also varies in a trend resembling a reverse parabola with the increase of the volatile matter content (Figure 12).

Based on the correlation analysis on the results of fitting between pore specific surface area and volatile matter content, the conclusions are as follows.

- (1) The fitting degrees R^2 of macropores and mesopores are both higher than 0.8, which means that the relationship between volatile matter content and pore specific surface area is well reflected. With the increase of volatile matter content, the fitting curves of specific surface areas of macropores and mesopores present an upward trend, which demonstrates that the numbers of macropores and mesopores grow gradually
- (2) The fitting degree R^2 of small pores is 0.62, which means that the relationship between volatile matter content and pore specific surface area is roughly reflected. In the stage of low metamorphic degree, the pore specific surface area surges sharply, indicating the rapid growth of the number of small pores. In the stage of medium metamorphic degree, it is

barely affected by the volatile matter content, and the number of small pores changes slightly. The stage of high metamorphic degree witnesses the rapid decreases of pore specific surface area and number of small pores

- (3) The fitting degree R^2 of micropores is 0.94, which means that the relationship between volatile matter content and pore specific surface area is excellently reflected. In the stage of medium metamorphic degree, the pore specific surface area changes insignificantly, suggesting the small change of the number of micropores. In the stages of low and high metamorphic degrees, it changes sharply, showing the great change of the number of micropores

5. Conclusions

In this study, the pore size, pore size distribution, and pore specific surface area of six different-rank coal samples from typical mining areas in China were calculated based on the results of high-pressure mercury injection and low-temperature liquid nitrogen adsorption experiments. Furthermore, the full-size pore characteristic parameters of coal samples were jointly characterized by the two methods. Finally, the influences of metamorphic degree on pore structure were discussed. The following main conclusions were drawn:

- (1) The results of the high-pressure mercury injection experiment and the low-temperature nitrogen adsorption experiment on the six coal samples reveal that the

specific surface area of micropores accounts for the largest proportion, which indicates that micropores determine the adsorption capacities of coal samples and are the main space for gas adsorption. Besides, with the increase of metamorphic degree, the pore volumes and pore specific surface areas of the six coal samples all decrease first and then increase

- (2) The results of the two experiments also disclose that the pore shape characteristics of the six coal samples differ notably. Such differences are a proof of the heterogeneity of surface properties of coal samples
- (3) According to the results of joint characterization, the volumes and specific surface areas of micropores, small pores, mesopores, and macropores exhibit varying variation trends with the change of metamorphic degree. Specifically, the pore volume varies in a U-shaped trend while the pore specific surface area changes in an approximately U-shaped trend with the increase of coal rank
- (4) The fitting degrees of volatile matter content and pore volume and those of volatile matter content and pore specific surface area are all greater than 0.6. The fitting curves can well reflect the influences and controlling mechanisms of metamorphic degree on pore volumes and pore specific surface areas of coal samples. With the increase of volatile matter content, the pore volume and the pore specific surface area both vary in a trend resembling a reverse parabola

Data Availability

The data used to support the findings of this study are included within the article.

Conflicts of Interest

The authors declare that they have no conflicts of interest.

Acknowledgments

This work was supported by the National Natural Science Foundation of China (Grant No.: 51974109), the Program for Leading Talents in Scientific and Technological Innovation of Henan Province (Grant No.: 204200510032), the Scientific and Technological Projects of Henan Province (Grant No.: 202102310220), the Plan of Key Scientific Research Project of Colleges and Universities in Henan Province (Grant No.: 20A620001), the Fundamental Research Funds for the Universities of Henan Province (Grant No.: NSFRF210301), and the Doctoral Fund of Henan Polytechnic University (Grant No.: B2019-55).

References

- [1] X. Z. Wang, "Strategic consideration of China coal industry development during energy revolution and new normal of economic development," *China Coal*, vol. 41, no. 4, pp. 5–8, 2015.
- [2] L. Yuan, N. Zhang, J. G. Han, and Y. Wang, "The concept, model and reserve forecast of green coal resources in China," *Journal of China University of Mining and Technology*, vol. 47, no. 1, pp. 1–8, 2018.
- [3] F. Wu and Z. M. Zhao, "The development status and future forecast of China's coal supply," *China Coal*, vol. 44, no. 7, pp. 5–8, 2018.
- [4] F. Du, K. Wang, X. Zhang, C. P. Xin, L. Y. Shu, and G. D. Wang, "Experimental study of coal-gas outburst: insights from coal-rock structure, gas pressure and adsorptivity," *Natural Resources Research*, vol. 29, no. 4, pp. 2481–2493, 2020.
- [5] Y. P. Yang, Z. H. Wen, L. L. Si, and X. Y. Xu, "Experimental study on variation law of electrical parameters and temperature rise effect of coal under DC electric field," *Scientific Reports*, vol. 11, no. 1, pp. 1–11, 2021.
- [6] L. L. Si, H. T. Zhang, J. P. Wei, B. Li, and H. K. Han, "Modeling and experiment for effective diffusion coefficient of gas in water-saturated coal," *Fuel*, vol. 284, article 118887, 2021.
- [7] H. J. Zhang, L. Zhang, D. Wang, and J. L. Hou, "Gas emission characteristics of tectonic coal and microscopic explanation of pore structure," *Journal of China Coal Society*, vol. 43, no. 12, pp. 3404–3410, 2018.
- [8] Z. H. Wen, Y. P. Yang, Q. Wang, and B. H. Yao, "Mechanism and characteristics of CH₄/CO₂/H₂O adsorption in lignite molecules," *Geofluids*, vol. 2021, Article ID 5535321, 11 pages, 2021.
- [9] J. W. Yue, Z. F. Wang, J. S. Chen, M. H. Zheng, Q. Wang, and X. F. Lou, "Investigation of pore structure characteristics and adsorption characteristics of coals with different destruction types," *Adsorption Science and Technology*, vol. 37, no. 7–8, pp. 623–648, 2019.
- [10] F. Du and K. Wang, "Unstable failure of gas-bearing coal-rock combination bodies: insights from physical experiments and numerical simulations," *Process Safety and Environmental Protection*, vol. 129, pp. 264–279, 2019.
- [11] S. B. Chen, X. H. Xia, Y. Qin, C. Q. Fu, and L. Hu, "Classification of pore structures in shale gas reservoir at the Longmaxi Formation in the south of Sichuan Basin," *Journal of China Coal Society*, vol. 38, no. 5, pp. 760–765, 2013.
- [12] Z. W. Liao, X. F. Liu, D. Z. Song et al., "Micro-structural damage to coal induced by liquid CO₂ phase change fracturing," *Natural Resources Research*, vol. 30, no. 2, pp. 1613–1627, 2020.
- [13] J. Zhu, B. Zhang, Y. Zhang, J. Tang, and Y. D. Jiang, "Coal pore characteristics in different coal mine dynamic disasters," *Arabian Journal of Geosciences*, vol. 11, no. 17, pp. 1–10, 2018.
- [14] Y. B. Yao and D. M. Liu, "Petrophysical properties and fluids transportation in gas shale: a NMR relaxation spectrum analysis method," *Journal of China Coal Society*, vol. 43, no. 1, pp. 181–189, 2018.
- [15] Q. Q. Gan, J. Xu, S. J. Peng, F. Z. Yan, R. F. Wang, and G. L. Cai, "Effects of heating temperature on pore structure evolution of briquette coals," *Fuel*, vol. 296, no. 2, article 120651, 2021.
- [16] L. L. Si, J. P. Wei, Y. J. Xi et al., "The influence of long-time water intrusion on the mineral and pore structure of coal," *Fuel*, vol. 290, no. 1, article 119848, 2021.
- [17] F. D. Xin, H. Xu, D. Z. Tang et al., "Pore structure evolution of low-rank coal in China," *International Journal of Coal Geology*, vol. 205, pp. 126–139, 2019.
- [18] S. Tao, Z. J. Pan, S. D. Chen, and S. L. Tang, "Coal seam porosity and fracture heterogeneity of marcolithotypes in the Fanzhuang

- Block, southern Qinshui Basin, China,” *Journal of Natural Gas Science and Engineering*, vol. 66, pp. 148–158, 2019.
- [19] Z. P. Meng, S. S. Liu, B. Y. Wang, Y. D. Tian, and J. Wu, “Adsorption capacity and its pore structure of coals with different coal body structure,” *Journal of China Coal Society*, vol. 40, no. 8, pp. 1865–1870, 2015.
- [20] X. F. Liu, D. Z. Song, X. Q. He, Z. P. Wang, M. R. Zeng, and L. K. Wang, “Quantitative analysis of coal nanopore characteristics using atomic force microscopy,” *Powder Technology*, vol. 346, pp. 332–340, 2019.
- [21] J. P. Wei, S. H. Dai, Z. H. Wen, X. C. Ren, and M. G. Li, “Research on comprehensive characterization method of different rank coal porosity,” *Journal of Henan Polytechnic University (Natural Science)*, vol. 34, no. 3, pp. 305–310, 2015.
- [22] Y. W. Ju, B. Jiang, Q. L. Hou, G. L. Wang, and A. M. Fang, “Structural evolution of nano-scale pores of tectonic coals in southern North China and its mechanism,” *Acta Geologica Sinica*, vol. 79, no. 2, pp. 269–285, 2005.
- [23] Y. Li, Y. G. Zhang, L. Zhang, and J. L. Hou, “Characterization on pore structure of tectonic coals based on the method of mercury intrusion, carbon dioxide adsorption and nitrogen adsorption,” *Journal of China Coal Society*, vol. 44, no. 4, pp. 1188–1196, 2019.
- [24] L. L. Qi, Z. F. Wang, H. M. Yang, and X. J. Chen, “Study on porosity of coal samples based on low temperature nitrogen adsorption method and mercury porosimetry,” *Coal Science and Technology*, vol. 40, no. 8, pp. 36–39, 2012.
- [25] L. Qin, S. G. Li, C. Zhai et al., “Joint analysis of pores in low, intermediate, and high rank coals using mercury intrusion, nitrogen adsorption, and nuclear magnetic resonance,” *Powder Technology*, vol. 362, pp. 615–627, 2020.
- [26] G. H. Ni, S. Li, S. Rahmin et al., “Effect of nitric acid on the pore structure and fractal characteristics of coal based on the low-temperature nitrogen adsorption method,” *Powder Technology*, vol. 367, pp. 506–516, 2020.
- [27] Z. Y. Wang, Y. P. Cheng, Y. X. Qi, R. P. Wang, L. Wang, and J. Y. Jiang, “Experimental study of pore structure and fractal characteristics of pulverized intact coal and tectonic coal by low temperature nitrogen adsorption,” *Powder Technology*, vol. 350, pp. 15–25, 2019.
- [28] J. T. Pu, *Experimental Study of Pore Structure Characteristics of Full-Aperture Section of Middle and Low Rank Coal in Xinjiang Mining Area*, [M. S. thesis], Xi’an University of Science and Technology, Xi’an, China, 2019.
- [29] J. Shen, Y. Qin, and J. Zhao, “Maceral contribution to pore size distribution in anthracite in the South Qinshui Basin,” *Energy & Fuels*, vol. 33, no. 8, pp. 7234–7243, 2019.
- [30] D. F. Zhao, Y. H. Guo, X. X. Mao, C. G. Lu, M. Li, and F. C. Qian, “Characteristics of macro-nanopores in anthracite coal based on mercury injection, nitrogen adsorption and FE-SEM,” *Journal of China Coal Society*, vol. 42, no. 6, pp. 1517–1526, 2017.
- [31] J. Zhu, M. Zhang, L. J. Chuan, J. Tang, and F. Zhao, “Experimental study on coal strain induced by methane sorption/desorption and effect of pore features,” *Chinese Journal of Rock Mechanics and Engineering*, vol. 35, no. S1, pp. 2620–2626, 2016.
- [32] C. X. Wang, W. Liu, and J. K. Liu, “Research on pore structure characteristics of gas coal in Fukang mining area,” *Industry and Mine Automation*, vol. 45, no. 7, pp. 92–96, 2019.
- [33] W. Q. Zhu, D. Z. Tang, H. Xu, Y. X. Yu, and L. Wang, “Characteristics of pore structure and specific surface area of lignite,” *Coal Geology & Exploration*, vol. 44, no. 6, pp. 59–63, 2016.
- [34] L. Wang, G. X. Zhang, J. Liu, X. J. Chen, and Z. Q. Li, “Effect of the pore structure on adsorption and diffusion migration of different rank coal samples,” *Energy & Fuels*, vol. 34, no. 10, pp. 12486–12504, 2020.
- [35] P. Chen and X. Y. Tang, “The research on the adsorption of nitrogen in low temperature and micro-pore properties in coal,” *Journal of China Coal Society*, vol. 26, no. 5, pp. 552–556, 2001.